

**ANALYTICAL AND EXPERIMENTAL STUDY ON SLENDER
CONCRETE-FILLED STEEL TUBE COLUMNS AND BEAM-COLUMNS**

A Ph.D. Thesis
Submitted to
The Academic Faculty

by
Tiziano Perea

In partial Fulfillment
of the Requirements for the Degree
Doctor of Philosophy in Civil Engineering

Georgia Institute of Technology
December 2010

ANALYTICAL AND EXPERIMENTAL STUDY ON SLENDER CONCRETE-FILLED STEEL TUBE COLUMNS AND BEAM-COLUMNS

Approved by:

Dr. Roberto T. Leon, Advisor

School of Civil and Environmental
Engineering

Georgia Institute of Technology

Dr. Jerome F. Hajjar, Co-Advisor

School of Civil and Environmental
Engineering

Northeastern University

Dr. Donald W. White

School of Civil and Environmental
Engineering

Georgia Institute of Technology

Dr. Reginald DesRoches

School of Civil and Environmental
Engineering

Georgia Institute of Technology

Dr. Lawrence F. Kahn

School of Civil and Environmental
Engineering

Georgia Institute of Technology

Dr. Richard W. Neu

School of Mechanical Engineering

Georgia Institute of Technology

Date Approved: November 9, 2010

I dedicate this thesis to my Family

and

to the memory of

Enrique Martínez Romero, M.S.C.E., P.E.

and

José Manuel Fernández Herrera, M.S.C.E., P.E.

*Pioneers of composite structures and other innovative systems in Mexico
who dedicated their entire lives to the world of the structural engineering*

ACKNOWLEDGEMENTS

Many individuals and institutions have contributed to this research and my graduate studies. Although I certainly cannot fully thank them in few pages, I would like to recognize, at least briefly, their assistance and support.

Firstly, I truly appreciate all of the guidance, support, opportunity, and insight provided by my graduate advisor Dr. Roberto T. Leon, and co-advisor Dr. Jerome F. Hajjar. I am very thankful for the unique opportunity and the privilege of working on this remarkable research project that has become one of the best experiences in my professional career and my personal life.

I would like to extend my appreciation to the members of my advisory committee: Dr. Donald W. White, Dr. Lawrence F. Kahn, Dr. Reginald DesRoches, and Dr. Richard W. Neu for their insights and critical assessment.

A special note of appreciation goes to: Dr. Theodore V. Galambos (Professor Emeritus of the University of Minnesota) for his insights and constructive advice to the project. My colleague on the project, Mark D. Denavit (Ph.D. Candidate at the University of Illinois at Urbana-Champaign) who provided invaluable help and strong complementary work to this research, mainly with analytical tools and calibrations.

The experimental part of this project would not have been possible without the use of a state-of-the-art facility such as the MAST Laboratory of the University of Minnesota, an equipment site of the Network for Earthquake Engineering Simulation. Beyond use of the first-class system at MAST, I received friendship, kind hospitality and invaluable assistance from the MAST director Dr. Carol Shield, the MAST staff: Paul Bergson, Angela Kingsley, Drew Daugherty, Jonathan Messier, Mitch Reiersen, Rachel Gaulke, and many students at the University of Minnesota.

I extend my sincere appreciation to my colleagues in the department of Civil and Environmental Engineering at the Georgia Institute of Technology who have made my time in Atlanta memorable at a personal level. I am convinced that the experience I had with the Georgia Tech faculty and fellow students will result in many future and productive academic interactions.

In addition, another special note of appreciation goes to my colleagues at the Universidad Autónoma Metropolitana in Mexico City, who encouraged me to pursue doctoral studies abroad. I extend this appreciation to my colleagues at UNAM, GIIS-RIIS, UPAEP and CICEPAC in Mexico for the early encouragement as a young engineer.

My graduate studies were possible by financial support from the Academic Program PROMEP of the Mexican Department of Education (SEP) and the National Science Foundation (NSF). Their generous support enabled me to pursue my graduation education as the sole professional focus during my tenure as a graduate student.

The experimental work described in this thesis is part of a NEESR project supported by the National Science Foundation under Grant No. CMMI-0619047, the American Institute of Steel Construction, the Network for Earthquake Engineering Simulation, the Georgia Institute of Technology, and the University of Illinois at Urbana-Champaign. In-kind material and labor was provided by Atlas Tube Inc. and LeJeune Steel Co. Any opinions, findings, and conclusions expressed in this document are those of the authors and do not necessarily reflect the views of the National Science Foundation or other sponsors.

Last but not least, I would like to thank my family for their endless support and encouragement. Undoubtedly, none of this would have been possible without the unconditional support, love and tremendous patience from my wife Veronica and our child Emiliano. They made this enterprise possible and worthwhile. Finally, I would like to thank God for every blessing He has given me, above all, for the privilege and the joy of being *Emiliano's dad*.

TABLE OF CONTENTS

LIST OF TABLES	XII
LIST OF FIGURES	XIV
ABBREVIATIONS	XXXI
NOTATION.....	XXXII
SUMMARY	XXXV
 CHAPTER 1. INTRODUCTION.....	 1
1.1. Background and Motivation	7
1.2. Problem definition	8
1.3. Scope and Objectives	10
1.4. Methodology	11
1.5. Brief research project description	12
1.6. Dissertation outline	15
1.7. Original contributions	16
 CHAPTER 2. PRELIMINARY RESEARCH STUDIES	 18
2.1. Previous experimental research studies	18
2.1.1. Introduction.....	18
2.1.2. Review of previous experimental studies on CFT columns and beam-columns.....	21
2.1.3. Brief comparison of CFT specimens previously tested	23
2.1.4. Review of previous experimental studies on CFTs under torsional loading	24
2.2. Compiled experimental databases.....	25
2.2.1. Previous compilation of experimental databases.....	25
2.2.2. Gaps in the experimental databases	27
2.3. Concrete casting effects	33
2.4. Previous analytical research studies.....	37
2.4.1. Material constitutive models.....	37
2.4.1.1. Sakino et al. (2004)	41

2.4.1.2. Tort and Hajjar (2007) and Denavit and Hajjar (2010).....	44
2.4.2. Comparison of constitutive models applicable to CFTs.....	53
2.4.3. Fiber-based analysis.....	57
2.4.4. Finite Element Analysis.....	60
CHAPTER 3. EXPERIMENTAL PROGRAM	67
3.1. MAST Laboratory.....	67
3.2. Description of specimens	71
3.3. Instrumentation plan	78
3.4. Pretest settings	83
3.5. Load protocol	85
3.5.1. LC1 – Incremental axial compression until buckling.....	86
3.5.2. LC2 – Unidirectional lateral displacement with constant gravity force	88
3.5.2.1. Monotonic displacement with reversal at the maximum lateral strength	88
3.5.2.2. Incremental cyclic displacement with reversal at a target displacement	90
3.5.3. LC3 – Multidirectional lateral displacement with constant gravity force	92
3.5.3.1. Monotonic displacement with reversals at the peak lateral capacity	92
3.5.3.2. Incremental cyclic displacement turning around once the target displacement is reached.....	94
3.5.4. LC4 – Final load case set.....	95
3.5.4.1. Repetition of some previous load cases	95
3.5.4.2. Monotonic twisting with constant gravity force	95
3.5.4.3. Monotonic uniaxial or biaxial displacement towards the maximum system stroke.....	96
CHAPTER 4. WET CONCRETE EFFECTS	98
4.1. Introduction.....	98
4.2. Analytical prediction.....	98
4.2.1. Closed-form solutions in circular tubes	98
4.2.2. Analytical solutions for rectangular tubes	99
4.2.3. Finite Element Analysis.....	100
4.3. Experimental investigation	104

4.3.1. Construction of the specimens	104
4.3.2. Strain gages and principal strain and stress computation	106
4.3.3. Experimental strains measured during the concrete casting	107
4.3.4. Observations during the tests	110
4.4. Recommendations to minimize the effects of the wet concrete pressure	112
CHAPTER 5. BUCKLING CAPACITY	114
5.1. Introduction	114
5.2. Buckling load by the AISC Specifications	115
5.3. Experimental results from the raw data	122
5.4. Differences between analytical and experimental maximum loads	136
5.4.1. System compliance	138
5.4.2. Frictional forces in the clevises	144
5.4.3. Initial imperfections	147
5.4.4. Lack of perfect control of the DOFs	152
5.4.5. Specimens with axial load strength above the MAST capacity	165
5.5. Experimental buckling loads from processed data	172
5.6. Advanced computational analysis	175
5.6.1. Monotonic compression loading with no parasitic forces	176
5.6.2. Step-by-step analysis	188
5.6.3. Column curves with ideal conditions	194
5.7. Experimental extraction of the effective stiffness	199
CHAPTER 6. P-M INTERACTION DIAGRAMS	205
6.1. Introduction	205
6.2. P-M interaction diagram by the AISC Specifications	206
6.3. Methodology for the determination of the P-M interaction diagram of beam-columns	214
6.4. Experimental tests	223
6.4.1. Uniaxial bending	227
6.4.2. Biaxial bending	237
6.5. Determination of the interaction diagrams using computational analyses	250
6.6. Conclusions	253

CHAPTER 7. RESPONSE TO LATERAL FORCES AND	
EVOLUTION OF THE FLEXURAL RIGIDITY	255
7.1. Introduction.....	255
7.2. Experimental tests	256
7.2.1. Lateral force – column drift response ($F-\Delta$)	256
7.2.2. Moment – curvature response ($M-\phi$)	279
7.3. Evolution of flexural rigidity	312
7.4. Advanced computational analysis.....	327
7.5. Conclusions.....	349
 CHAPTER 8. EVALUATION OF LIMIT STATES.....	 351
8.1. Introduction.....	351
8.2. Local buckling	352
8.2.1. Introduction.....	352
8.2.2. Wall slenderness limits in the AISC Specifications	353
8.2.3. Theoretical wall slenderness limits in circular tubes	355
8.2.4. Theoretical wall slenderness limits in rectangular tubes	357
8.2.5. Previous empirical calibrations on the initiation of local buckling	359
8.2.6. Experimental extraction of local buckling from the experimental tests	364
8.3. Identification of limits states.....	380
8.4. Experimental plastic hinge lengths	394
8.5. Postmortem evaluation.....	404
8.6. Conclusions.....	409
 CHAPTER 9. TORSION.....	 411
9.1. Introduction.....	411
9.2. Previous studies	412
9.2.1. Analytical research	412
9.2.2. Experimental research	414
9.3. Specifications and Codes	415
9.4. Experimental results.....	417
9.5. Calibration of the experimental data.....	422

9.5.1. Torsional capacity.....	423
9.5.2. Torsional rigidity	426
9.6. Conclusions.....	437

CHAPTER 10. PROPOSE METHODOLOGY FOR

THE STRENGTH CALCULATION.....	438
10.1. Introduction.....	438
10.2. Material and geometric properties	439
10.3. Axial strength of CFT cross-sections based on the plastic stress method	442
10.4. Axial and flexural strength of CFT cross-sections based on the plastic stress method	443
10.5. Axial strength of CFT columns.....	450
10.6. Axial and flexural strength of CFT beam-columns	451
10.7. Axial and flexural strength of CFT cross-sections with non-compact steel tubes.....	455
10.7.1. Wall slenderness limits for steel sections in CFTs	455
10.7.2. Interaction diagram for CFTs with slender section	456
10.7.3. Interaction surface at the first steel yielding.....	463
10.8. Application examples.....	465

CHAPTER 11. CONCLUSIONS..... 488

11.1. Summary and Conclusions	488
11.2. Conclusions.....	489
11.2.1. Wet concrete effects on RCFT members.....	490
11.2.2. Nominal axial load capacity of CFT columns	491
11.2.3. P-M interaction diagrams for CFT cross-sections an beam columns	492
11.2.4. Flexural rigidity for CFT members.....	493
11.2.5. Steel local buckling in CFT members	495
11.2.6. Plastic hinge length in CFT members.....	496
11.2.7. Torsional strength and stiffness of CFT members.....	496
11.2.8. Forensic analysis.....	497
11.3. Impact and contributions.....	497
11.4. Suggested topics for future research studies	499

APPENDIX A. MATERIAL PROPERTIES	500
A.1. On-site concrete filling properties.....	500
A.2. Coupon test results	501
APPENDIX B. EXPERIMENTAL RESULTS	507
B.1. Specimen 1C5-18-5.....	507
B.2. Specimen 2C12-18-5.....	514
B.3. Specimen 3C20-18-5.....	524
B.4. Specimen 4Rw-18-5.....	534
B.5. Specimen 5Rs-18-5	544
B.6. Specimen 6C12-18-12.....	552
B.7. Specimen 7C20-18-12.....	562
B.8. Specimen 8Rw-18-12.....	567
B.9. Specimen 9Rs-18-12	574
B.10. Specimen 10-C12-26-5	581
B.11. Specimen 11C20-26-5.....	590
B.12. Specimen 12Rw-26-5.....	599
B.13. Specimen 13Rs-26-5	608
B.14. Specimen 14C12-26-12.....	617
B.15. Specimen 15C20-26-12.....	627
B.16. Specimen 16Rw-26-12.....	636
B.17. Specimen 17Rs-26-12	645
B.18. Specimen 18C5-26-12.....	653
REFERENCES.....	661
VITA.....	668

LIST OF TABLES

Table 2.1. Summary of experimental studies in CFT columns and beam columns	19
Table 2.2. Some material constitutive models in the literature developed for CFT	39
Table 2.3. Summary of analytical studies with fiber analysis in composite elements	58
Table 3.1. Capacity of the MAST system	68
Table 3.2. Test matrix of the CFT specimens with nominal values	71
Table 3.3. Test matrix of the CFT specimens with measured values	72
Table 4.1. Maximum analytical response of steel tubes under hydrostatic pressure	102
Table 4.2. Braces plan for the RCFTs	104
Table 5.1. Maximum experimental axial loads obtained from the raw data	125
Table 5.2. Deflections of the compliance test at 750 kips of compression	141
Table 5.3. Experimental buckling loads in specimens with adjusted effective length	151
Table 5.4. Maximum lateral forces (F_{max}) and top bending moments (M_{lmax}) during LC1	153
Table 5.5. Extracted axial loads at the time the system lost ideal control	164
Table 5.6. Summary of the maximum axial loads obtained for the specimens where buckling was not reached in the test	170
Table 5.7. Experimental buckling loads from the processed data	173
Table 5.8. Buckling loads from computational analysis	186
Table 5.9. Effective flexural stiffness extracted from moment-curvatures during LC1	200
Table 6.1. DOFs controlled during LC2 in the CCFT specimens	224
Table 6.2. Motion shapes of the top, gravity loads, and reversal events at LC2 and LC3	226
Table 6.3. Summary of extracted P-M interaction points from the uniaxial loading LC2	235
Table 7.1. Flexural rigidity (EI_{exp}) extracted from the measured response	319
Table 7.2. Averaged concrete contribution factor ($C_{3,test}$) to the effective stiffness	325
Table 8.1. Wall slenderness limits in the AISC Specifications for steel and composite sections	354
Table 8.2. Classification of the steel cross-section in terms of the wall slenderness	355
Table 8.3. Strain at the first occurrence of local buckling during the testing	367
Table 8.4. Summary of the maximum strains measured within load cases LC1 and LC2	381
Table 8.5. Summary of extracted plastic hinge length	398
Table 9.1. DOF's controlled during the torsional loading	417
Table 9.2. Summary of results from torsional loading	418
Table 9.3. Calibration for the torsional capacity of CFTs	425
Table 9.4. Effectiveness factor (α_T) of the concrete in the torsion capacity	425
Table 9.5. Experimental torsional stiffness	430

Table 9.6. Equations to estimate the effectiveness factor of the concrete in torsional stiffness.....	430
Table 10.1. Geometric properties for CFTs	441
Table 10.2. Equations to calculate the axial and flexural capacity (anchor points 1, 2 and 3) in CFT cross-sections with compact, non-compact or slender steel section	461

Tables in Appendix A

Table A.1. Concrete mix design used for 5 ksi of nominal strength.....	500
Table A.2. Concrete mix design used for 12 ksi of nominal strength.....	500

Tables in Appendix B

Table B.1. Load protocol summary for the specimen 3C20-18-5	508
Table B.2. Load protocol summary for the specimen 3C20-18-5	515
Table B.3. Load protocol summary for the specimen 3C20-18-5	525
Table B.4. Load protocol summary for the specimen 4Rw-18-5.....	535
Table B.5. Load protocol summary for the specimen 5Rs-18-5.....	545
Table B.6. Load protocol summary for the specimen 6C12-18-12	553
Table B.7. Load protocol summary for the specimen 7C20-18-12	563
Table B.8. Load protocol summary for the specimen 8Rw-18-12.....	568
Table B.9. Load protocol summary for the specimen 9Rs-18-12.....	575
Table B.10. Load protocol summary for the specimen 10C12-26-5.....	582
Table B.11. Load protocol summary for the specimen 11C20-26-5.....	591
Table B.12. Load protocol summary for the specimen 12Rw-26-5.....	600
Table B.13. Load protocol summary for the specimen 13Rs-26-5.....	609
Table B.14. Load protocol summary for the specimen 14C12-26-12.....	618
Table B.15. Load protocol summary for the specimen 15C20-26-12.....	628
Table B.16. Load protocol summary for the specimen 16Rw-26-12.....	637
Table B.17. Load protocol summary for the specimen 17Rs-26-12.....	646
Table B.18. Load protocol summary for the specimen 17Rs-26-12.....	654

LIST OF FIGURES

Figure 1.1. Some possible cross-sections configurations in composite columns.....	3
Figure 1.2. Construction process for a building with SRC columns (Viest et al. 1997)	5
Figure 1.3. Erection and construction process for the first four stories of a building with SRC composite columns (Martinez-Romero 2003)	6
Figure 1.4. Floor system of a building with CCFT columns (Davids and Merriel, 2004)	6
Figure 2.1. Histograms obtained from the unified database	29
Figure 2.2. Experimental vs. analytical column curve for RCFTs	30
Figure 2.3. Experimental vs. analytical column curve for CCFTs	30
Figure 2.4. Normalized experimental strength obtained for CCFT beam-columns for different slenderness parameter (λ) ranges.	31
Figure 2.5. Experimental vs. analytical column curve for SRCs.....	31
Figure 2.6. Concrete filling procedure on site of a RCFT	34
Figure 2.7. Hydrostatic pressure from wet concrete and temporal reinforcement in RCFTs that reduces the radial expansions (Uy and Das, 1999)	34
Figure 2.8. Lateral deflection estimated by Uy and Das (1999) for a double-pinned square steel-box column with different lateral brace spacing (N_b) and upper story pressure (N_s)	35
Figure 2.9. Deflected shape tendency in RCFTs (adapted from Uy and Das, 1999)	36
Figure 2.10. Fully-plastic stress distribution in composite cross-sections.....	38
Figure 2.11. Stress-strain (σ - ϵ) curves obtained from the Sakino model for a 5 ksi strength concrete confined by a steel tube with different width-to-thickness ratios.	41
Figure 2.12. Scale effect factor on compressive strength of circular plain concrete columns	43
Figure 2.13. Stress-strain (σ - ϵ) curves obtained from the Sakino model for a 5 ksi strength concrete confined by a steel tube with different width-to-thickness ratios.	43
Figure 2.14. Stress-strain (σ - ϵ) for the steel tubes used with the Sakino model	44
Figure 2.15. Confined concrete strength (f_{cc}) vs. wall slenderness ratio ($\lambda = D/t$) of circular steel tubes from the calibration by Sakino et al. (2004) and by Denavit and Hajjar (2010) for CCFTs	46
Figure 2.16. Stress-strain constitutive model implemented in Tort and Hajjar (2007) for the concrete core in RCFTs.....	47
Figure 2.17. Stress-strain constitutive model implemented in Denavit and Hajjar (2010) for the concrete core in CCFTs.....	48
Figure 2.18. Wall-slenderness ratio vs. strain at occurrence of local buckling.....	49
Figure 2.19. Monotonic Shen σ - ϵ model for the steel component in CFTs.....	51
Figure 2.20. Shen σ - ϵ model for steel vs. coupon test.....	52
Figure 2.21. Different stress-strain model available for concrete in CFTs	54
Figure 2.22. Different stress-strain models available for steel in CFTs.....	56

Figure 2.23. Frame element with ends coupled to fiber cross-sections	57
Figure 2.24. Model and results from the FEA presented by Varma (2000).....	62
Figure 2.25. Stress-strain curves obtained from FEA (Varma, 2000)	63
Figure 2.26. Finite element model of a CFT cylinder, and its displaced shape of the CFT with a preload in the steel tube followed by a compression force in the concrete	65
Figure 2.27. Variation of the hoop stresses with the compression force, and the uniaxial stress- strain (σ - ϵ) obtained from the finite element analysis.	66
Figure 3.1. Multi-Axial Sub-assembly Testing system (MAST)	69
Figure 3.2. Typical configuration of MTS actuators	69
Figure 3.3. Schematic drawings of specimens placed at MAST	70
Figure 3.4. Finite Element Analysis performed for the base plates	74
Figure 3.5. Circular CFT specimen with an HSS5.563x0.134	75
Figure 3.6. Circular CFT specimen with an HSS12.75x0.25	75
Figure 3.7. Circular CFT specimen with an HSS20x0.25	76
Figure 3.8. Rectangular CFT specimen with an HSS20x12x0.3125	76
Figure 3.9. Photographs taken before and during the concrete casting and testing	77
Figure 3.10. Details of strain gages on the specimens.....	79
Figure 3.11. Details of LVDTs on the specimens	80
Figure 3.12. Details of string pots on the specimens.....	80
Figure 3.13. Krypton LEDs on the specimens	81
Figure 3.14. Robotic towers for video and photo collection at MAST.....	82
Figure 3.15. Example of the data streamed online through RDV and Webex.	82
Figure 3.16. Expected column response with LC1 under an incremental axial displacement on the CFT specimens with the initial out-of-plumbness	87
Figure 3.17. Expected column response with LC2 under a constant axial load, incremental uniaxial lateral displacement, and reversals at the peak lateral strength	89
Figure 3.18. Expected column response with LC2 under a constant axial load and cyclic biaxial lateral displacement towards different drift targets.....	91
Figure 3.19. Expected response under a constant axial load and biaxial lateral displacement towards different probes with reversals at the peak lateral strength. (a) Free body diagram. (b) Displacement path of the top with 8 probes. (c) Displacement path of the top with 1 probe and different sub-probes. (d) Interaction surface M_x - M_y . (e) 3D P - M_x - M_y interaction diagram.	93
Figure 3.20. Expected column response with LC3 under a constant axial load and cyclic biaxial lateral displacement towards different drift targets.....	94
Figure 3.21. Expected column response with LC4 under a constant axial load and incremental torsional displacement towards the maximum system rotation.....	96

Figure 3.22. Final displacement path under a high constant axial load and incremental lateral displacement towards the maximum system translation	97
Figure 4.1. Free body diagram of a half circular tube with internal pressure	99
Figure 4.2. F.E. Model of a steel tube under hydrostatic pressure.....	101
Figure 4.3. Contour of transverse stresses at the L/4 bottom of the HSS from FEA	101
Figure 4.4. Distribution of maximum transverse stresses in the rectangular cross-section.....	103
Figure 4.5. Distribution of temporal braces to restrain expansion due to the casting	105
Figure 4.6. Strain gages Tokyo Sokki WF series	106
Figure 4.7. Transverse strains measured during the casting on the 20" face at 2' 6" from the base for the specimens 4-Rw-18-5 (restrained) and 5-Rs-18-5 (non-restrained).	108
Figure 4.8. Transverse strains and stresses measured during the concrete casting on the 20" face at 2' 6" from the base for the specimens 8-Rw-18-12 and 9-Rs-18-12.....	109
Figure 4.9. Average at 1' 6" and 2' 6" from the base of the transverse strains and stresses measured during the concrete casting on the 20" face for the 26 feet long RCFTs.	110
Figure 4.10. Local buckling position at the end of the testing.....	111
Figure 5.1. Column tolerances as specified in the AISC and the ACI Specifications.....	118
Figure 5.2. Theoretical and suggested K factors for different BCs (AISC Commentary, 2005)	119
Figure 5.3. Column curve by the AISC (2010) Specifications	121
Figure 5.4. Definition of out-of straightness (Δ_o), out-of-plumbness (δ_o), and the different boundary conditions for the buckling load case.....	122
Figure 5.5. Initial profile shape at the beginning of the loading case LC1	124
Figure 5.6. Maximum experimental load ratios (P_{exp}/P_o) from the raw data.....	126
Figure 5.7. Compressive loading vs. midspan distortion for the C5 set of CCFTs.....	127
Figure 5.8. Compressive loading vs. Drift for the C12 set of CCFTs.....	128
Figure 5.9. Compressive loading vs. Drift for the C20 set of CCFTs.....	128
Figure 5.10. Compressive loading vs. Drift for the Rw set of RCFTs.....	129
Figure 5.11. Compressive loading vs. Drift for the Rs set of RCFTs	129
Figure 5.12. Compressive loading vs. midspan moment ($P-M_{CL}$) for the C5 set of CCFTs	131
Figure 5.13. Compressive loading vs. base moment ($P-M_2$) for the C12 set of CCFTs.....	132
Figure 5.14. Compressive loading vs. base moment ($P-M_2$) for the C20 set of CCFTs.....	133
Figure 5.15. Compressive loading vs. base moment ($P-M_2$) for the Rw set of RCFTs.....	134
Figure 5.16. Compressive loading vs. base moment ($P-M_2$) for the Rs set of RCFTs	135
Figure 5.17. Instrumentation setup to verify the crosshead compliance	139
Figure 5.18. Crosshead deflections along the span from averaged measurements in compliance test (relative vertical displacement, $\Delta_r=0.11$ in).....	141
Figure 5.19. FEM analysis for the crosshead under critical conditions	142

Figure 5.20. Experimental vs. analytical axial-lateral displacement	144
Figure 5.21. Data reported by the controller from the empty crosshead test	146
Figure 5.22. Effect of out-of-plumbness on the axial load capacity	147
Figure 5.23. Initially imperfect shapes for cantilever columns (ASCE, 1997)	148
Figure 5.24. Initial deflected shape	149
Figure 5.25. Fixed-free and fixed-spring boundary conditions	152
Figure 5.26. Histories of test response for the Specimen 10-C12-26-5	155
Figure 5.27. Histories of test response for the Specimen 14-C12-26-12	156
Figure 5.28. Histories of test response for the Specimen 15-C20-26-12	157
Figure 5.29. Axial force (P) vs. lateral force (F) of the most slender specimens	158
Figure 5.30. Axial force (P) vs. lateral force (F) of the CCFTs with 5.5 in. of diameter	159
Figure 5.31. Axial force (P) vs. lateral force (F) of the CCFTs with 12.75 in. of diameter	160
Figure 5.32. Axial force (P) vs. lateral force (F) of the CCFTs with 20 in. of diameter	161
Figure 5.33. Axial force (P) vs. lateral force (F) of the RCFTs oriented in weak axis	162
Figure 5.34. Axial force (P) vs. lateral force (F) of the RCFTs oriented in strong axis	163
Figure 5.35. Linear relationship in columns with elastic buckling	166
Figure 5.36. Proposed tangent form for elastic and inelastic buckling of columns	167
Figure 5.37. Application of the tangent form on CCFTs with different slenderness	168
Figure 5.38. Application of the tangent form on a CCFT with different imperfections	169
Figure 5.39. Application of the tangent and the secant form on the CCFT specimens that did not buckle with the full compressive capacity of the MAST system	171
Figure 5.40. Experimental critical load ratios (P_{exp}/P_o) from processed data.....	174
Figure 5.41. Experimental response vs. Analytical prediction for the Specimen 2C12-18-5	178
Figure 5.42. Experimental response vs. Analytical prediction for the Specimen 6C12-18-12	178
Figure 5.43. Experimental response vs. Analytical prediction for the Specimen 10C12-26-5	179
Figure 5.44. Experimental response vs. Analytical prediction for the Specimen 14C12-26-5	179
Figure 5.45. Experimental response vs. Analytical prediction for the Specimen 3C20-18-5	180
Figure 5.46. Experimental response vs. Analytical prediction for the Specimen 7C20-18-12	180
Figure 5.47. Experimental response vs. Analytical prediction for the Specimen 11C20-26-5	181
Figure 5.48. Experimental response vs. Analytical prediction for the Specimen 15C20-26-12	181
Figure 5.49. Experimental response vs. Analytical prediction for the Specimen 4Rw-18-5	182
Figure 5.50. Experimental response vs. Analytical prediction for the Specimen 5Rs-18-5.....	182
Figure 5.51. Experimental response vs. Analytical prediction for the Specimen 8Rw-18-12	183
Figure 5.52. Experimental response vs. Analytical prediction for the Specimen 9Rs-18-12.....	183
Figure 5.53. Experimental response vs. Analytical prediction for the Specimen 12Rw-26-5	184

Figure 5.54. Experimental response vs. Analytical prediction for the Specimen 13Rs-26-5.....	184
Figure 5.55. Experimental response vs. Analytical prediction for the Specimen 16Rw-26-12	185
Figure 5.56. Experimental response vs. Analytical prediction for the Specimen 17Rs-26-12.....	185
Figure 5.57. Critical load ratios (P_{exp}/P_o) from computational analysis.....	187
Figure 5.58. Experimental and analytical critical load ratios and AISC column curve	187
Figure 5.59. Experimental response vs. Analytical prediction for the C12 Specimens	190
Figure 5.60. Experimental response vs. Analytical prediction for the C20 Specimens	191
Figure 5.61. Experimental response vs. Analytical prediction for the Rw Specimens	192
Figure 5.62. Experimental response vs. Analytical prediction for the Rs Specimens.....	193
Figure 5.63. Shape function used to represent the initial imperfection	195
Figure 5.64. Analytical column curves for a CCFT cross-section with 12.75 inches of diameter.....	196
Figure 5.65. Analytical column curves for a CCFT cross-section with 20 inches of diameter	197
Figure 5.66. Analytical column curves for a RCFT cross-section.....	198
Figure 5.67. Moment-Curvature from LC1 for the C5 set.....	200
Figure 5.68. Moment-Curvature from LC1 for the C12 set.....	201
Figure 5.69. Moment-Curvature from LC1 for the C20 set.....	202
Figure 5.70. Moment-Curvature from LC1 for the Rw set.....	203
Figure 5.71. Moment-Curvature from LC1 for the Rs set.....	204
Figure 6.1. Plastic stress distribution method.....	206
Figure 6.2. Strain compatibility method.....	207
Figure 6.3. P-M interaction diagrams obtained with the plastic stress method and the strain compatibility method.....	208
Figure 6.4. Components of the interaction diagram: fully-plastic stress method to RCFTs	209
Figure 6.5. Transition of the plastic interaction diagram from the steel component on CFTs	210
Figure 6.6. Transition of the plastic interaction diagram from the concrete component on CFTs.....	210
Figure 6.7. Reduction by the AISC (2005) Specifications on the P-M cross-section by the stability effects factor χ to get the P-M strength on composite beam columns	213
Figure 6.8. P-M interaction diagram for composite cross-sections (stocky columns) and beam columns (reduced by stability effects) by the AISC (2005) Specifications.....	213
Figure 6.9. P-M paths to approach the beam-column capacity.....	214
Figure 6.10. Beam column under axial-flexural loading	216
Figure 6.11. Reduction in the P-M interaction diagram to account stability effects.....	216
Figure 6.12. Reduction in the P-M interaction diagram to account initial imperfection.....	218
Figure 6.13. Total vs. Net P-M interaction diagrams	219
Figure 6.14. P-M interaction diagram used for calibration of steel beam columns (ASCE 1997).....	220

Figure 6.15. Components of the P-M interaction diagram for steel members	221
Figure 6.16. Components of the P-M interaction diagram for composite members	222
Figure 6.17. Horizontal displacement path at the top during LC2.....	223
Figure 6.18. Horizontal displacement path at the top during LC3.....	223
Figure 6.19. Schematic illustration of the extraction of P-M Interaction points from the uniaxial loading (left), and schematic definition of the limit point at the incipient buckling (right)	228
Figure 6.20. Definition of the limit point at the incipient buckling from experimental data	228
Figure 6.21. Extraction of P-M Interaction points from the uniaxial loading LC2 on the circular CFTs with 12.75 inches of diameter.....	231
Figure 6.22. Extraction of P-M Interaction points from the uniaxial loading LC2 on the circular CFTs with 20 inches of diameter.....	232
Figure 6.23. Extraction of P-M Interaction points from the uniaxial loading LC2 on the rectangular CFTs oriented in the weak axis.....	233
Figure 6.24. Extraction of P-M Interaction points from the uniaxial loading LC2 on the rectangular CFTs oriented in the strong axis	234
Figure 6.25. Experimental net moments normalized to the AISC strength	236
Figure 6.26. Illustration of the interaction surface from the biaxial loading (LC3)	237
Figure 6.27. Extraction of P-M Interaction points for the Specimen 2C12-18-5 from LC3	239
Figure 6.28. Extraction of P-M Interaction points for the Specimen 6C12-18-12 from the biaxial bending loading LC3	240
Figure 6.29. Extraction of P-M Interaction points for the Specimen 3C20-18-5 from the biaxial bending loading LC3	241
Figure 6.30. Extraction of P-M Interaction points for the Specimen 4Rw-18-5 from the biaxial bending loading LC3	242
Figure 6.31. Extraction of P-M Interaction points for the Specimen 5Rs-18-5 from the biaxial bending loading LC3	243
Figure 6.32. Displacement of the beam-column top, Specimen 9Rs-18-12 (Denavit et al., 2010)	244
Figure 6.33. Experimental interaction surface (adapted from Denavit et al., 2010)	244
Figure 6.34. Biaxial moment path for the specimens 10-C12-26-5 and 14-C12-26-12 during LC3.....	245
Figure 6.35. Biaxial moment path for the specimen 15-C20-26-12 during LC3	246
Figure 6.36. Biaxial moment path for the specimens 8Rw-18-12 and 9Rs-18-12 during LC3.....	247
Figure 6.37. Biaxial moment path for the specimen 12-Rw-26-5 during LC3	247
Figure 6.38. Biaxial moment path for the specimen 13Rs-26-5 during LC3.....	248
Figure 6.39. Biaxial moment path for the specimens 12-Rw-26-5 (blue path) and 13-Rs-26-5 (red path) during LC3	248
Figure 6.40. Biaxial moment path for the specimens 16-Rw-26-12 and 17-Rs-26-12 during LC3	249
Figure 6.41. Biaxial moment path for the specimens 16-Rw-26-12 (blue) and 17-Rs-26-12 (red)	249

Figure 6.42. P-M interaction diagrams for the composite CFT beam columns	252
Figure 7.1. Force relaxation at the testing pauses (schematic)	257
Figure 7.2. Lateral force (F, kip) vs. Drift (Δ/L , %) from the uniaxial load cases (LC2, reversal at peak force) for the Specimen 2C12-18-5.....	261
Figure 7.3. Lateral force (F, kip) vs. Drift (Δ/L , %) from the uniaxial load cases (LC2, reversal at peak force) for the Specimen 6C12-18-12.....	261
Figure 7.4. Lateral force (F, kip) vs. Drift (Δ/L , %) from the uniaxial load cases (LC2, reversal at peak force) for the Specimen 3C20-18-5.....	262
Figure 7.5. Lateral force (F, kip) vs. Drift (Δ/L , %) from the uniaxial load cases (LC2, reversal at peak force) for the Specimen 7C20-18-12.....	262
Figure 7.6. Lateral force (F, kip) vs. Drift (Δ/L , %) from the uniaxial load cases (LC2, reversal at peak force) for the Specimen 4Rw-18-5.....	263
Figure 7.7. Lateral force (F, kip) vs. Drift (Δ/L , %) from the uniaxial load cases (LC2, reversal at peak force) for the Specimen 8Rw-18-12.....	263
Figure 7.8. Lateral force (F, kip) vs. Drift (Δ/L , %) from the uniaxial load cases (LC2, reversal at peak force) for the Specimen 5Rs-18-5	264
Figure 7.9. Lateral force (F, kip) vs. Drift (Δ/L , %) from the uniaxial load cases (LC2, reversal at peak force) for the Specimen 9Rs-18-12	264
Figure 7.10. Lateral force (F, kip) vs. Drift (Δ/L , %) from the uniaxial load cases (LC2, K=1) for the Specimen 1C5-18-5.....	265
Figure 7.11. Lateral force (F, kip) vs. Drift (Δ/L , %) from the uniaxial load cases (LC2, K=1) for the Specimen 18C5-26-12	265
Figure 7.12. Lateral force (F, kip) vs. Drift (Δ/L , %) from the uniaxial load cases (LC2, reversal at desired drift) for the Specimens 10C12-26-5.....	266
Figure 7.13. Lateral force (F, kip) vs. Drift (Δ/L , %) from the uniaxial load cases (LC2, reversal at desired drift) for the specimen 14C12-26-12.....	266
Figure 7.14. Lateral force (F, kip) vs. Drift (Δ/L , %) from the uniaxial load cases (LC2, reversal at desired drift) for the Specimen 11C20-26-5	267
Figure 7.15. Lateral force (F, kip) vs. Drift (Δ/L , %) from the uniaxial load cases (LC2, reversal at desired drift) for the Specimen 15C20-26-12	267
Figure 7.16. Lateral force (F, kip) vs. Drift (Δ/L , %) from the uniaxial load cases (LC2, reversal at desired drift) for the Specimen 12Rw-26-5	268
Figure 7.17. Lateral force (F, kip) vs. Drift (Δ/L , %) from the uniaxial load cases (LC2, reversal at desired drift) for the Specimen 16Rw-26-12	268
Figure 7.18. Lateral force (F, kip) vs. Drift (Δ/L , %) from the uniaxial load cases (LC2, reversal at desired drift) for the Specimen 13Rs-26-5	269
Figure 7.19. Lateral force (F, kip) vs. Drift (Δ/L , %) from the uniaxial load cases (LC2, reversal at desired drift) for the Specimen 17Rs-26-12	269
Figure 7.20. Lateral force (F, kip) vs. Drift (Δ/L , %) from the uniaxial load case (LC2, K=1) for the Specimen 14C12-26-12 (P=300 kip)	270

Figure 7.21. Lateral force (F, kip) vs. Drift (Δ/L , %) from the biaxial load cases (LC3, diamond-shape) for the Specimen 3C20-18-5	270
Figure 7.22. Lateral force (F, kip) vs. Drift (Δ/L , %) from the biaxial load cases (LC3, diamond-shape) for the Specimen 2C12-18-5	271
Figure 7.23. Lateral force (F, kip) vs. Drift (Δ/L , %) from the biaxial load cases (LC3, diamond-shape) for the Specimen 6C12-18-12	271
Figure 7.24. Lateral force (F, kip) vs. Drift (Δ/L , %) from the biaxial load cases (LC3, diamond-shape) for the Specimen 4Rw-18-5	272
Figure 7.25. Lateral force (F, kip) vs. Drift (Δ/L , %) from the biaxial load cases (LC3, diamond-shape) for the Specimen 5Rs-18-5.....	272
Figure 7.26. Lateral force (F, kip) vs. Drift (Δ/L , %) from the biaxial load cases (LC3, eight-shape) for the Specimen 7C20-18-12	273
Figure 7.27. Lateral force (F, kip) vs. Drift (Δ/L , %) from the biaxial load cases (LC3, eight-shape) for the Specimen 8Rw-18-12 (P=800 kip)	273
Figure 7.28. Lateral force (F, kip) vs. Drift (Δ/L , %) from the biaxial load cases (LC3, eight-shape) for the Specimen 10C12-26-5	274
Figure 7.29. Lateral force (F, kip) vs. Drift (Δ/L , %) from the biaxial load cases (LC3, eight-shape) for the Specimen 14C12-26-12	274
Figure 7.30. Lateral force (F, kip) vs. Drift (Δ/L , %) from the biaxial load cases (LC3, eight-shape) for the Specimens 11C20-26-5.....	275
Figure 7.31. Lateral force (F, kip) vs. Drift (Δ/L , %) from the biaxial load cases (LC3, eight-shape) for the Specimen 15C20-26-12	275
Figure 7.32. Lateral force (F, kip) vs. Drift (Δ/L , %) from the biaxial load cases (LC3, eight-shape) for the Specimen 12Rw-26-5	276
Figure 7.33. Lateral force (F, kip) vs. Drift (Δ/L , %) from the biaxial load cases (LC3, eight-shape) for the Specimen 13Rs-26-5.....	276
Figure 7.34. Lateral force (F, kip) vs. Drift (Δ/L , %) from the biaxial load cases (LC3, eight-shape) for the Specimen 16Rw-26-12	277
Figure 7.35. Lateral force (F, kip) vs. Drift (Δ/L , %) from the biaxial load cases (LC3, eight-shape) for the Specimen 17Rs-26-12.....	277
Figure 7.36. Lateral force (F, kip) vs. Drift (Δ/L , %) from the biaxial load case (LC3, K=1, eight-shape) for the specimens 18C5-26-12 (P=20 kip)	278
Figure 7.37. Lateral force (F, kip) vs. Drift (Δ/L , %) from the biaxial load cases (LC3, probe-subprobe) for the Specimens 9Rs-18-12 (P=800 kip).....	278
Figure 7.38. Second order moment at the base (M, kip-ft) vs. Curvature (ϕ , 1/in) from the uniaxial load cases (LC2) for the specimen 2C12-18-5	282
Figure 7.39. Second order moment at the base (M, kip-ft) vs. Curvature (ϕ , 1/in) from the uniaxial load cases (LC2) for the specimen 6C12-18-12	283
Figure 7.40. Second order moment at the base (M, kip-ft) vs. Curvature (ϕ , 1/in) from the uniaxial load cases (LC2) for the specimen 3C20-18-5	284

Figure 7.41. Second order moment at the base (M, kip-ft) vs. Curvature (ϕ , 1/in) from the uniaxial load cases (LC2) for the specimen 7C20-18-12	285
Figure 7.42. Second order moment at the base (M, kip-ft) vs. Curvature (ϕ , 1/in) from the uniaxial load cases (LC2) for the specimen 4Rw-18-5.....	286
Figure 7.43. Second order moment at the base (M, kip-ft) vs. Curvature (ϕ , 1/in) from the uniaxial load cases (LC2) for the specimen 8Rw-18-12.....	287
Figure 7.44. Second order moment at the base (M, kip-ft) vs. Curvature (ϕ , 1/in) from the uniaxial load cases (LC2) for the specimen 5Rs-18-5.....	288
Figure 7.45. Second order moment at the base (M, kip-ft) vs. Curvature (ϕ , 1/in) from the uniaxial load cases (LC2) for the specimen 9Rs-18-12.....	289
Figure 7.46. Second order moment at the base (M, kip-ft) vs. Curvature (ϕ , 1/in) from the uniaxial load cases (LC2) for the specimen 10C12-26-5	290
Figure 7.47. Second order moment at the base (M, kip-ft) vs. Curvature (ϕ , 1/in) from the uniaxial load cases (LC2) for the specimen 14C12-26-12.....	291
Figure 7.48. Second order moment at the base (M, kip-ft) vs. Curvature (ϕ , 1/in) from the uniaxial load cases (LC2) for the specimen 11C20-26-5	292
Figure 7.49. Second order moment at the base (M, kip-ft) vs. Curvature (ϕ , 1/in) from the uniaxial load cases (LC2) for the specimen 15C20-26-12.....	293
Figure 7.50. Second order moment at the base (M, kip-ft) vs. Curvature (ϕ , 1/in) from the uniaxial load cases (LC2) for the specimen 12Rw-26-5.....	294
Figure 7.51. Second order moment at the base (M, kip-ft) vs. Curvature (ϕ , 1/in) from the uniaxial load cases (LC2) for the specimen 16Rw-26-12.....	295
Figure 7.52. Second order moment at the base (M, kip-ft) vs. Curvature (ϕ , 1/in) from the uniaxial load cases (LC2) for the specimen 13Rs-26-5.....	296
Figure 7.53. Second order moment at the base (M, kip-ft) vs. Curvature (ϕ , 1/in) from the uniaxial load cases (LC2) for the specimen 17Rs-26-12.....	297
Figure 7.54. Second order moment at the base (M, kip-ft) vs. Curvature (ϕ , 1/in) from the uniaxial load cases (LC2) for the specimen 2C12-18-5	298
Figure 7.55. Second order moment at the base (M, kip-ft) vs. Curvature (ϕ , 1/in) from the uniaxial load cases (LC2) for the specimen 3C20-18-5	299
Figure 7.56. Second order moment at the base (M, kip-ft) vs. Curvature (ϕ , 1/in) from the uniaxial load cases (LC2) for the specimen 4Rw-18-5.....	300
Figure 7.57. Second order moment at the base (M, kip-ft) vs. Curvature (ϕ , 1/in) from the uniaxial load cases (LC2) for the specimen 5Rs-18-5.....	301
Figure 7.58. Second order moment at the base (M, kip-ft) vs. Curvature (ϕ , 1/in) from the uniaxial load cases (LC2) for the specimen 6C12-18-12	302
Figure 7.59. Second order moment at the base (M, kip-ft) vs. Curvature (ϕ , 1/in) from the uniaxial load cases (LC2) for the specimen 14C12-26-12 and 7C20-18-12.....	303
Figure 7.60. Second order moment at the base (M, kip-ft) vs. Curvature (ϕ , 1/in) from the uniaxial load cases (LC2) for the specimen 10C12-26-5	304

Figure 7.61. Second order moment at the base (M, kip-ft) vs. Curvature (ϕ , 1/in) from the uniaxial load cases (LC2) for the specimen 11C20-26-5	305
Figure 7.62. Second order moment at the base (M, kip-ft) vs. Curvature (ϕ , 1/in) from the uniaxial load cases (LC2) for the specimen 12Rw-26-5.....	306
Figure 7.63. Second order moment at the base (M, kip-ft) vs. Curvature (ϕ , 1/in) from the uniaxial load cases (LC2) for the specimen 13Rs-26-5	307
Figure 7.64. Second order moment at the base (M, kip-ft) vs. Curvature (ϕ , 1/in) from the uniaxial load cases (LC2) for the specimen 15C20-26-12.....	308
Figure 7.65. Second order moment at the base (M, kip-ft) vs. Curvature (ϕ , 1/in) from the uniaxial load cases (LC2) for the specimen 16Rw-26-12.....	309
Figure 7.66. Second order moment at the base (M, kip-ft) vs. Curvature (ϕ , 1/in) from the uniaxial load cases (LC2) for the specimen 17Rs-26-12.....	310
Figure 7.67. Second order moment at the base (M, kip-ft) vs. Curvature (ϕ , 1/in) from the uniaxial load cases (LC2) for the specimens 8Rw-18-12 and 9Rs-18-12.....	311
Figure 7.68. Flexural rigidity for the circular specimens with 12 inches of diameter.....	321
Figure 7.69. Flexural rigidity for the circular specimens with 20 inches of diameter.....	322
Figure 7.70. Flexural rigidity for the rectangular specimens oriented in the weak axis.....	323
Figure 7.71. Flexural rigidity for the rectangular specimens oriented in the strong axis	324
Figure 7.72. Average of the C_3 parameter obtained for each specimen (squares) and for all the specimens (dashed line)	326
Figure 7.73. Experimental vs. Analytical response with a different initiation of steel local buckling for the Specimen 4Rw-18-5 during the first loading cycle in LC2b	329
Figure 7.74. Force relaxation with time at the testing pauses (data taken from the Specimen 4Rw-18-5 at the second positive peak in LC2a).....	331
Figure 7.75. Force relaxation at the testing pauses (schematic)	331
Figure 7.76. Experimental vs. Analytical response for the Specimen 2C12-18-5 during LC2	332
Figure 7.77. Experimental vs. Analytical response for the Specimen 3C20-18-5 during LC2	333
Figure 7.78. Experimental vs. Analytical response for the Specimen 4Rw-18-5 during LC2	334
Figure 7.79. Experimental vs. Analytical response for the Specimen 5Rs-18-5 during LC2	335
Figure 7.80. Experimental vs. Analytical response for the Specimen 6C12-18-12 during LC2	336
Figure 7.81. Experimental vs. Analytical response for the Specimen 7C20-18-12 during LC2	337
Figure 7.82. Experimental vs. Analytical response for the Specimen 8Rw-18-12 during LC2	338
Figure 7.83. Experimental vs. Analytical response for the Specimen 9Rs-18-12 during LC2	339
Figure 7.84. Experimental vs. Analytical response for the Specimen 10C12-26-5 during LC2	340
Figure 7.85. Experimental vs. Analytical response for the Specimen 11C20-26-5 during LC2	341
Figure 7.86. Experimental vs. Analytical response for the Specimen 12Rw-26-5 during LC2	342
Figure 7.87. Experimental vs. Analytical response for the Specimen 13Rs-26-5 during LC2	343

Figure 7.88. Experimental vs. Analytical response for the Specimen 14C12-26-5 during LC2	344
Figure 7.89. Experimental vs. Analytical response for the Specimen 15C20-26-12 during LC2	345
Figure 7.90. Experimental vs. Analytical response for the Specimen 16Rw-26-12 during LC2	346
Figure 7.91. Experimental vs. Analytical response for the Specimen 17Rs-26-12 during LC2	347
Figure 7.92. Experimental vs. Analytical response for the Specimen 3C20-18-5 during the biaxial load case LC3b (P=750 kip, 16 probes around the Specimen)	348
Figure 7.93. Experimental vs. Analytical response for the Specimen 11C20-26-5 during the biaxial load case LC3a (P=450 kip, figure eight)	348
Figure 8.1. Local buckling failure (Leon et al., 2007).....	353
Figure 8.2. Buckling strength calibration of CCFTs by Bradford et al. (2002)	357
Figure 8.3. Critical stress in hollow and filled rectangular tubes in the AIJ (2001). Figure adapted from Sakino et al. (2004).....	359
Figure 8.4. Calibration of the strain at local buckling by Tort and Hajjar (2007).....	361
Figure 8.5. Calibration of the strain at local buckling by Denavit and Hajjar (2010)	362
Figure 8.6. Wall-slenderness ratio vs. strain at occurrence of local buckling.....	363
Figure 8.7. Local buckling deformation at the end of the test for the C5 group	364
Figure 8.8. Calibration of the local buckling initiation for CCFTs.....	368
Figure 8.9. Calibration of the local buckling initiation for RCFTs.....	369
Figure 8.10. Proposed limits for compact, non-compact and slender sections in CCFTs.....	371
Figure 8.11. Proposed limits for compact, non-compact and slender sections in RCFTs.....	371
Figure 8.12. Local buckling deformation at the end of the test for the C5 group	372
Figure 8.13. Local buckling deformation at the end of the test for the C12 group	373
Figure 8.14. Local buckling deformation at the end of the test for the C12 group	374
Figure 8.15. Local buckling deformation at the end of the load protocol in RCFTs	375
Figure 8.16. Development of local buckling during the load case LC2 (uniaxial bending).....	378
Figure 8.17. Local buckling mechanism in CCFTs with normal and high strength concrete infill.....	379
Figure 8.18. Occurrence of limit states in the specimen 2C12-18-5.....	385
Figure 8.19. Occurrence of limit states in the specimen 6C12-18-12.....	385
Figure 8.20. Occurrence of limit states in the specimen 10C12-26-5.....	386
Figure 8.21. Occurrence of limit states in the specimen 14C12-26-12.....	386
Figure 8.22. Occurrence of limit states in the specimen 3C20-18-5.....	387
Figure 8.23. Occurrence of limit states in the specimen 7C20-18-12.....	387
Figure 8.24. Occurrence of limit states in the specimen 11C20-26-5.....	388
Figure 8.25. Occurrence of limit states in the specimen 15C20-26-12.....	388
Figure 8.26. Occurrence of limit states in the specimen 4Rw-18-5.....	389
Figure 8.27. Occurrence of limit states in the specimen 8Rw-18-12.....	389

Figure 8.28. Occurrence of limit states in the specimen 12Rw-26-5	390
Figure 8.29. Occurrence of limit states in the specimen 16Rw-26-12	390
Figure 8.30. Occurrence of limit states in the specimen 5Rs-18-5	391
Figure 8.31. Occurrence of limit states in the specimen 9Rs-18-12	391
Figure 8.32. Occurrence of limit states in the specimen 13Rs-26-5	392
Figure 8.33. Occurrence of limit states in the specimen 17Rs-26-12	392
Figure 8.34. Occurrence of limit states in the specimen 18C5-26-12	393
Figure 8.35. Occurrence of limit states in the specimen 1C5-18-5	393
Figure 8.36. Schematic determination of the plastic hinge length (Paulay and Priestley, 1992)	394
Figure 8.37. Derivation of the plastic hinge length in a cantilever beams	395
Figure 8.38. Computation of the yield curvature in the cross-section	398
Figure 8.39. Curvatures vs. length at the peak displacement	399
Figure 8.40. Curvatures vs. length at the peak displacement	400
Figure 8.41. Curvatures vs. length at the peak displacement	401
Figure 8.42. Curvatures vs. length at the peak displacement	402
Figure 8.43. Curvatures vs. length at the peak displacement for the Specimens C5	403
Figure 8.44. Post-mortem images from the specimen 7C20-18-12	405
Figure 8.45. Post-mortem photos from the specimen 8Rw-18-12	407
Figure 9.1. Results from FE analysis under pure torsion in CFTs by Han, Yao, and Tao (2007)	413
Figure 9.2. Interaction diagrams with torsion in CFTs presented by Han, Yao, and Tao (2007b)	413
Figure 9.3. Torsional loading vs. twisting angle ($T-\theta_z$) of the Specimen 1C5-18-5 with $P=0$. The blue curve is a filtered and smoothed response of the raw data included in green.	419
Figure 9.4. Torsional loading vs. twisting angle for the Specimens 2C12-18-6 and 6C12-18-12	420
Figure 9.5. Torsional loading vs. twisting angle for the Specimens 3C20-18-5 and 7C20-18-12	420
Figure 9.6. Torsional loading vs. twisting angle ($T-\theta$) obtained for the Specimens 4, 5 and 8	421
Figure 9.7. Change of the tangent torsional stiffness (GJ_{exp}) in Specimen 7 ($P=0$ kip)	428
Figure 9.8. Elastic torsional stiffness for the Specimens 2C12-18-5 and 6C12-18-12	431
Figure 9.9. Tangent torsional stiffness for the Specimens 2C12-18-5 and 6C12-18-12	432
Figure 9.10. Elastic torsional stiffness for the Specimen 3C20-18-5	433
Figure 9.11. Tangent torsional stiffness for the Specimen 3C20-18-5	433
Figure 9.12. Elastic torsional stiffness obtained for the Specimen 4Rw-18-5	434
Figure 9.13. Tangent torsional stiffness obtained for the Specimen 4Rw-18-5	434
Figure 9.14. Elastic torsional stiffness obtained for the Specimen 5Rs-18-5	435
Figure 9.15. Tangent torsional stiffness obtained for the Specimen 5Rs-18-5	435
Figure 9.16. Torsional stiffness obtained for the Specimen 8Rw-18-12 ($P=0$)	436

Figure 10.1. Stress-strain (σ - ϵ) curves that are typically applicable to CFTs	440
Figure 10.2. Notation in geometric dimensions for RCFTs and CCFTs	441
Figure 10.3. Plastic stress distribution of CFTs in pure compression.....	442
Figure 10.4. Plastic stress distribution for a given position of the PNA	443
Figure 10.5. P-M interaction diagram for a CFT cross-section based on the plastic stress method.....	444
Figure 10.6. Interaction diagram from a set of P-M points for the cross-section capacity	449
Figure 10.7. Schematic representation of the P-M components in slender CFT members	451
Figure 10.8. Schematic representation of the capacity components in different arrangements	454
Figure 10.9. Stress distribution in a CFT cross-section composed by a slender tube ($\lambda = \lambda_r$), assuming that local buckling achieves when steel yields in compression.....	458
Figure 10.10. Schematic P-M interaction diagram for a CFT with slender steel cross-section which wall slenderness ratio equals λ_r	460
Figure 10.11. Schematic net or usable capacity in a CFT with slender steel cross-section which wall slenderness ratio equals λ_r	462
Figure 10.12. Elastic stress distribution in a CFT cross-section related to the first yielding (either compression or tension) in the steel tube.....	464
Figure 10.13. Schematic P-M interaction diagram for a CFT with first yielding in the steel tube	465

Figures in Appendix A

Figure A.1. Coupon tests from the steel corresponding to the Specimens 1 and 18	501
Figure A.2. Coupon tests from the steel corresponding to the Specimens 2 and 6	501
Figure A.3. Coupon tests from the steel corresponding to the Specimens 3 and 7	502
Figure A.4. Coupon tests from the steel corresponding to the Specimens 4, 5, 8 and 9	502
Figure A.5. Coupon tests from the steel corresponding to the Specimen 10	503
Figure A.6. Coupon tests from the steel corresponding to the Specimen 11	503
Figure A.7. Coupon tests from the steel corresponding to the Specimen 12	504
Figure A.8. Coupon tests from the steel corresponding to the Specimen 13	504
Figure A.9. Coupon tests from the steel corresponding to the Specimen 14	505
Figure A.10. Coupon tests from the steel corresponding to the Specimen 15	505
Figure A.11. Coupon tests from the steel corresponding to the Specimen 16	506
Figure A.12. Coupon tests from the steel corresponding to the Specimen 17	506

Figures in Appendix B

Figure B.1. Specimen 1C5-18-5	507
Figure B.2. Experimental results from LC1 in the specimen 1C5-18-5	509
Figure B.3. Experimental results from LC1a in the specimen 1C5-18-5.....	510
Figure B.4. Experimental results from LC1b in the specimen 1C5-18-5	511
Figure B.5. Experimental results from LC2 in the specimen 1C5-18-5	512
Figure B.6. Experimental results from LC4 in the specimen 1C5-18-5	513
Figure B.7. Specimen 2C12-18-5.....	514
Figure B.8. Experimental results from LC1 in the specimen 2C12-18-5	517
Figure B.9. Experimental results from LC2a in the specimen 2C12-18-5.....	518
Figure B.10. Experimental results from LC3a in the specimen 2C12-18-5.....	519
Figure B.11. Experimental results from LC3b in the specimen 2C12-18-5	520
Figure B.12. Experimental results from LC2b in the specimen 2C12-18-5	521
Figure B.13. Experimental results from LC4a in the specimen 2C12-18-5.....	522
Figure B.14. Experimental results from LC4b in the specimen 2C12-18-5	522
Figure B.15. Experimental results from LC4c in the specimen 2C12-18-5.....	523
Figure B.16. Specimen 3C20-18-5.....	524
Figure B.17. Experimental results from LC1 in the specimen 3C20-18-5	526
Figure B.18. Experimental results from LC2a in the specimen 3C20-18-5.....	527
Figure B.19. Experimental results from LC2b in the specimen 3C20-18-5	528
Figure B.20. Experimental results from LC3a in the specimen 3C20-18-5.....	529
Figure B.21. Experimental results from LC3b in the specimen 3C20-18-5	530
Figure B.22. Experimental results from LC3c in the specimen 3C20-18-5.....	531
Figure B.23. Experimental results from LC4a in the specimen 3C20-18-5.....	532
Figure B.24. Experimental results from LC4b in the specimen 3C20-18-5	532
Figure B.25. Experimental results from LC4c in the specimen 3C20-18-5.....	533
Figure B.26. Specimen 4Rw-18-5.....	534
Figure B.27. Experimental results from LC1 in the specimen 4Rw-18-5.....	536
Figure B.28. Experimental results from LC2a in the specimen 4Rw-18-5.....	537
Figure B.29. Experimental results from LC2b in the specimen 4Rw-18-5.....	538
Figure B.30. Experimental results from LC3a in the specimen 4Rw-18-5.....	539
Figure B.31. Experimental results from LC3b in the specimen 4Rw-18-5.....	540
Figure B.32. Experimental results from LC3c in the specimen 4Rw-18-5.....	541
Figure B.33. Experimental results from LC4a in the specimen 4Rw-18-5.....	542

Figure B.34. Experimental results from LC4b in the specimen 4Rw-18-5.....	542
Figure B.35. Experimental results from LC4c in the specimen 4Rw-18-5.....	543
Figure B.36. Specimen 5Rs-18-5.....	544
Figure B.37. Experimental results from LC1 in the specimen 5Rs-18-5.....	546
Figure B.38. Experimental results from LC2 in the specimen 5Rs-18-5.....	547
Figure B.39. Experimental results from LC3a in the specimen 5Rs-18-5.....	548
Figure B.40. Experimental results from LC3b in the specimen 5Rs-18-5.....	549
Figure B.41. Experimental results from LC4a in the specimen 5Rs-18-5.....	550
Figure B.42. Experimental results from LC4b in the specimen 5Rs-18-5.....	550
Figure B.43. Experimental results from LC4c in the specimen 5Rs-18-5.....	551
Figure B.44. Specimen 6C12-18-12.....	552
Figure B.45. Experimental results from LC1 in the specimen 6C12-18-12.....	554
Figure B.46. Experimental results from LC2a in the specimen 6C12-18-12.....	555
Figure B.47. Experimental results from LC2b in the specimen 6C12-18-12.....	556
Figure B.48. Experimental results from LC3a in the specimen 6C12-18-12.....	557
Figure B.49. Experimental results from LC3b in the specimen 6C12-18-12.....	558
Figure B.50. Experimental results from LC3c in the specimen 6C12-18-12.....	559
Figure B.51. Experimental results from LC4a in the specimen 6C12-18-12.....	560
Figure B.52. Experimental results from LC4b in the specimen 6C12-18-12.....	560
Figure B.53. Experimental results from LC4c in the specimen 6C12-18-12.....	561
Figure B.54. Specimen 7C20-18-12.....	562
Figure B.55. Experimental results from LC1 in the specimen 7C20-18-12.....	564
Figure B.56. Experimental results from LC2 in the specimen 7C20-18-12.....	565
Figure B.57. Experimental results from LC3 in the specimen 7C20-18-12.....	566
Figure B.58. Specimen 8Rw-18-12.....	567
Figure B.59. Experimental results from LC1 in the specimen 8Rw-18-12.....	569
Figure B.60. Experimental results from LC2a in the specimen 8Rw-18-12.....	570
Figure B.61. Experimental results from LC2b in the specimen 8Rw-18-12.....	571
Figure B.62. Experimental results from LC3a in the specimen 8Rw-18-12.....	572
Figure B.63. Experimental results from LC4 in the specimen 8Rw-26-12.....	573
Figure B.64. Experimental results from LC4 in the specimen 8Rw-18-12.....	573
Figure B.65. Specimen 9Rs-18-12.....	574
Figure B.66. Experimental results from LC1 in the specimen 9Rs-18-12.....	576
Figure B.67. Experimental results from LC2 in the specimen 9Rs-18-12.....	577
Figure B.68. Experimental results from LC3a in the specimen 9Rs-18-12.....	578

Figure B.69. Experimental results from LC3b in the specimen 9Rs-18-12	579
Figure B.70. Experimental results from LC3c in the specimen 9Rs-18-12	580
Figure B.71. Specimen C12-26-5.....	581
Figure B.72. Experimental results from LC1 in the specimen 10C12-26-5	584
Figure B.73. Experimental results from LC2a in the specimen 10C12-26-5.....	585
Figure B.74. Experimental results from LC2b in the specimen 10C12-26-5.....	586
Figure B.75. Experimental results from LC3a in the specimen 10C12-26-5.....	587
Figure B.76. Experimental results from LC3b in the specimen 10C12-26-5.....	588
Figure B.77. Experimental results from LC4 in the specimen 10C12-26-5	589
Figure B.78. Specimen 11C20-26-5.....	590
Figure B.79. Experimental results from LC1 in the specimen 11C20-26-5	593
Figure B.80. Experimental results from LC2a in the specimen 11C20-26-5.....	594
Figure B.81. Experimental results from LC2b in the specimen 11C20-26-5.....	595
Figure B.82. Experimental results from LC3a in the specimen 11C20-26-5.....	596
Figure B.83. Experimental results from LC3b in the specimen 11C20-26-5.....	597
Figure B.84. Experimental results from LC4 in the specimen 11C20-26-5	598
Figure B.85. Specimen 12Rw-26-5.....	599
Figure B.86. Experimental results from LC1 in the specimen 12Rw-26-5.....	602
Figure B.87. Experimental results from LC2a in the specimen 12Rw-26-5.....	603
Figure B.88. Experimental results from LC2b in the specimen 12Rw-26-5.....	604
Figure B.89. Experimental results from LC3a in the specimen 12Rw-26-5.....	605
Figure B.90. Experimental results from LC3b in the specimen 12Rw-26-5.....	606
Figure B.91. Experimental results from LC4 in the specimen 12Rw-26-5.....	607
Figure B.92. Specimen 13Rs-26-5	608
Figure B.93. Experimental results from LC1 in the specimen 13Rs-26-5.....	611
Figure B.94. Experimental results from LC2a in the specimen 13Rs-26-5	612
Figure B.95. Experimental results from LC2b in the specimen 13Rs-26-5	613
Figure B.96. Experimental results from LC3a in the specimen 13Rs-26-5	614
Figure B.97. Experimental results from LC3b in the specimen 13Rs-26-5.....	615
Figure B.98. Experimental results from LC4 in the specimen 13Rs-26-5.....	616
Figure B.99. Specimen 14C12-26-12.....	617
Figure B.100. Experimental results from LC1 in the specimen 14C12-26-12.....	620
Figure B.101. Experimental results from LC2a in the specimen 14C12-26-12.....	621
Figure B.102. Experimental results from LC2b in the specimen 14C12-26-12.....	622
Figure B.103. Experimental results from LC3a in the specimen 14C12-26-12.....	623

Figure B.104. Experimental results from LC2a' in the specimen 14C12-26-12.....	624
Figure B.105. Experimental results from LC3a' in the specimen 14C12-26-12.....	625
Figure B.106. Experimental results from LC4 in the specimen 14C12-26-12.....	626
Figure B.107. Specimen 15C20-26-12.....	627
Figure B.108. Experimental results from LC1 in the specimen 15C20-26-12.....	630
Figure B.109. Experimental results from LC2a in the specimen 15C20-26-12.....	631
Figure B.110. Experimental results from LC2b in the specimen 15C20-26-12.....	632
Figure B.111. Experimental results from LC3a in the specimen 15C20-26-12.....	633
Figure B.112. Experimental results from LC3b in the specimen 15C20-26-12.....	634
Figure B.113. Experimental results from LC4 in the specimen 15C20-26-12.....	635
Figure B.114. Specimen 16Rw-26-12.....	636
Figure B.115. Experimental results from LC1 in the specimen 16Rw-26-12.....	639
Figure B.116. Experimental results from LC2a in the specimen 16Rw-26-12.....	640
Figure B.117. Experimental results from LC2b in the specimen 16Rw-26-12.....	641
Figure B.118. Experimental results from LC3a in the specimen 16Rw-26-12.....	642
Figure B.119. Experimental results from LC3b in the specimen 16Rw-26-12.....	643
Figure B.120. Experimental results from LC4 in the specimen 16Rw-26-12.....	644
Figure B.121. Specimen 17Rs-26-12.....	645
Figure B.122. Experimental results from LC2a in the specimen 17Rs-26-12.....	648
Figure B.123. Experimental results from LC2b in the specimen 17Rs-26-12.....	649
Figure B.124. Experimental results from LC3a in the specimen 17Rs-26-12.....	650
Figure B.125. Experimental results from LC3b in the specimen 17Rs-26-12.....	651
Figure B.126. Experimental results from LC4 in the specimen 17Rs-26-12.....	652
Figure B.127. Specimen 18C5-26-12.....	653
Figure B.128. Experimental results from LC1 in the specimen 18C5-26-12.....	656
Figure B.129. Experimental results from LC2a in the specimen 18C5-26-12.....	657
Figure B.130. Experimental results from LC2b in the specimen 18C5-26-12.....	658
Figure B.131. Experimental results from LC3 in the specimen 18C5-26-12.....	659
Figure B.132. Experimental results from LC4 in the specimen 18C5-26-12.....	660

ABBREVIATIONS

AISC	American Institute of the Steel Construction
ACI	American Concrete Institute
EC	Eurocode
AIJ	Architectural Institute of Japan
RC	Reinforced concrete
SRC	Steel reinforced concrete, encased steel by concrete or embedded steel into concrete
CFT	Concrete-filled steel tube
CCFT	Circular CFT
RCFT	Rectangular CFT
HSS	Hollow structural section
FEA	Finite element analysis
FEM	Finite element method
DOF	Degree of freedom
PNA	Plastic neutral axis
ENA	Elastic neutral axis
MAST	Multi-Axial Subassemblage Testing
NEES	Network for Earthquake Engineering Simulation

NOTATION

α	Concrete confinement factor on the Sakino model
β	Steel triaxial stresses factor on the Sakino model
χ	P_n/P_o ratio
δ	Small or local deflections
Δ	Large or global deflections
ε	Strain
ε_c	Concrete strain
ε_{co}	Concrete strain at f_c'
ε_{cc}	Confined concrete strain at f_{cc}'
ε_{cu}	Ultimate concrete strain
ε_{lb}	Compressive strain related to the initiation of the steel local buckling
ϕ	Cross-section curvature
ϕ	Strength reduction factor by AISC or ACI
λ	Slenderness parameter related to flexural buckling
λ_w	Wall slenderness ratio (D/t , h/t , b/t) of the steel cross-section related to its local buckling
ρ	Total steel ratio in the cross-section
ρ_s	Structural steel ratio in the cross-section
ρ_{sr}	Longitudinal reinforcement ratio in the cross-section
σ	Normal stress
τ	Shear stress
θ	Rotation
Ω	Safety factor by AISC
b	Base of an HSS rectangular steel cross-section
b_c	Base of a rectangular concrete cross-section ($b_c = b - 2t$)
b_f	Flange base of a steel W cross-section
c_r	Concrete cover
d	Effective depth of a rectangular cross-section
f_c	Concrete strength as a function of the strain (ε)
f_c'	Compressive strength of a 28 days concrete cylinder
f_{cc}'	Compressive strength of confined concrete
f_{cu}	Ultimate concrete strength linked to ε_{cu}
h	Depth of a W or an HSS rectangular steel cross-section
h_c	Depth of a rectangular concrete cross-section ($h_c = h - 2t$)
r	Radius of gyration of the cross-section
t	Thickness of steel plate or tube
y	Variable distance between the neutral axis and the centroidal axis
y_o	Distance “y” related to the pure bending capacity (M_o)
y_n	Distance “y” related to the critical axial load capacity (P_n)
A	Gross cross-section area
A_c	Concrete cross-section area
A_s	Steel cross-section area
A_{sr}	Longitudinal reinforcement area
A_w	Web area of a steel cross-section

A_λ	Point A on the P- M diagram reduced by χ
C_λ	Point C on the P-M diagram reduced by χ
D	External diameter of a circular o tubular cross-section
E_c	Concrete modulus of elasticity
E_s	Steel modulus of elasticity
E_{sr}	Steel reinforcement modulus of elasticity
E_{eff}	Effective modulus of elasticity on a composite element
E_m	Modified or effective flexural stiffness of a composite element
El_c	Concrete contribution to the flexural stiffness of a composite element
El_s	Steel contribution to the flexural stiffness of a composite element
El_{sr}	Longitudinal reinforcement contribution to the flexural stiffness of a composite element
El_{eff}	Effective flexural stiffness of a composite element
F	Lateral force
F_c	Block stress for the concrete in compression
F_y	Yield stress of the steel
F_r	Residual stress in the steel
F_s	Effective stress in the steel ($F_y - F_r$)
F_{yr}	Yield stress of the steel reinforcement
I_c	Concrete cross-section moment of inertia
I_s	Steel cross-section moment of inertia
I_{sr}	Longitudinal reinforcement moment of inertia
I_{eff}	Effective composite cross-section moment of inertia
K	Effective length coefficient
KL	Effective length of an element
L	Length of an element
M	Bending moment
M_b	Flexural strength of the cross-section at the balance point (equal to M_D)
M_c	Flexural strength of the concrete cross-section
M_s	Flexural strength of the steel cross-section
M_o	Pure bending strength of the composite cross-section (equal M_B)
M_p	Plastic flexural strength of a steel cross-section (ZF_y , or M_o if composite)
M_x	Flexion about the strong axis cross-section
M_y	Flexion about the weak axis cross-section
M_{exp}	Experimental strength in flexion
M_u	Ultimate flexural demand
M_B	Flexural strength at the point B on the P-M interaction diagram (equal to M_o)
M_C	Flexural strength at the point C on the P-M interaction diagram (equal to M_B)
M_D	Flexural strength at the point D on the P-M interaction diagram (equal to M_b)
M_E	Flexural strength at the point E on the P-M interaction diagram
M_1	Moment from a first order analysis
M_2	Moment from a second order analysis
P	Axial force in compression (negative value if tension)
P_b	Compressive strength of the cross-section at the balance point (equal to P_D)
P_c	Compressive strength of the concrete cross-section (equal to P_C)
P_s	Compressive strength of the steel cross-section
P_e	Euler or elastic critical load

P_{cr}	Critical load
P_n	Nominal compressive strength of the element
P_{exp}	Experimental compressive strength
P_o	Nominal compressive strength of the cross-section or a short element
P_y	Nominal compressive strength of the steel cross-section (equal to P_s)
P_u	Ultimate compressive demand
P_A	Compressive strength at the point A of the P-M interaction diagram (also labeled as P_o)
$P_{A\lambda}$	Compressive strength at the point A_λ of the P-M interaction diagram (equal to χP_A)
P_C	Compressive strength at the point C of the P-M interaction diagram (equal to $2P_D$)
$P_{C\lambda}$	Compressive strength at the point C_λ of the P-M interaction diagram (equal to χP_C)
P_D	Compressive strength at the point D of the P-M interaction diagram (equal a $P_C/2$)
P_E	Compressive strength at the point E of the P-M interaction diagram
R_y	Overstrength coefficient for the nominal yield stress in the steel
R_u	Overstrength coefficient for the nominal ultimate stress in the steel
T	Torsion force
V	Shear force
V_n	Nominal shear strength
Z_c	Plastic section modulus of concrete
Z_s	Plastic section modulus of steel
Z_{sr}	Plastic section modulus of reinforcement

SUMMARY

The use of composite steel-concrete columns and beam-columns in many structural systems is increasing globally due to the intrinsic synergy when these materials are designed and detailed together properly. However, limited test data are available to justify the structural system response factors and comprehensive design equations in current design specifications. This research, through the testing of 18 full-scale, slender concrete-filled steel tube (CFT) beam-columns, attempts to address the latter need. The circular and rectangular CFT specimens tested for this research are by far the longest and the most slender full-scale CFT members tested worldwide. These CFT specimens were subjected to a complex load protocol that includes pure compression, uniaxial and biaxial bending combined with compression, pure torsion, and torsion combined with compression. In addition, data from the hydrostatic pressure on the steel tubes due to the fresh concrete at casting was evaluated. The single most important contribution of this research is the clarification of the interaction between strength and stability in slender composite concrete-filled columns and beam-columns. Parallel to the experimental study, advanced computational analyses were carried out to calibrate material and element models that characterize the salient features of the observed CFT response, such as steel local buckling and residual stresses, concrete confinement, stability effects, strength, and stiffness degradation, among others. Based on the observed behavior, simplified guidelines for the computation of the strength and stiffness parameters for CFT columns and beam-columns are proposed for design purposes.

CHAPTER 1

INTRODUCTION

One of the critical decisions that face the structural designer is the selection of materials to be used in a civil construction. This decision is frequently based on structural and economic reasons, and it is supported by the designer's judgment and experience. The central goal is to achieve an economic structure with good performance.

Two materials that have been widely used in civil constructions are concrete and steel. The advantages of both materials are well known. Concrete is very stiff, inexpensive and has good fire resistance; meanwhile, steel is strong, ductile and lightweight. The “smart” combination of these two materials, or synergy, results in a system with a much higher efficiency than that of the individual components. The designation given to such systems include the terms hybrid, mixed or composite construction. Composite systems have been successfully used in columns, beams and slabs of midrise and high-rise buildings, and in piers and beams of bridges.

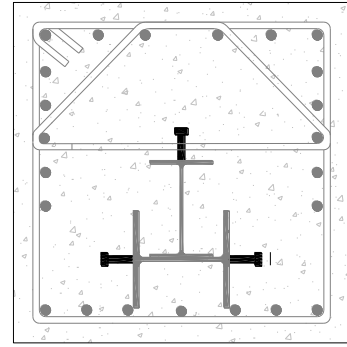
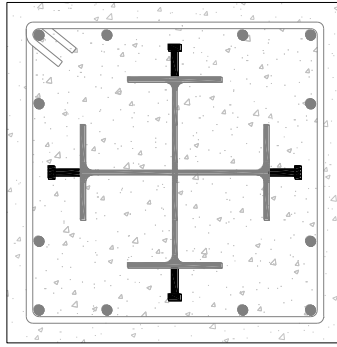
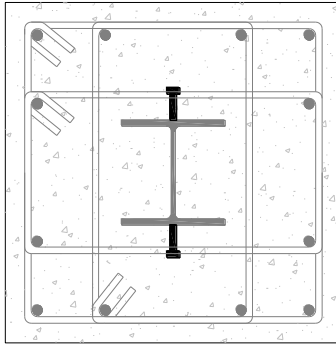
The use of composite columns in many structural systems is increasing worldwide due to the intrinsic synergy when these materials are designed and detailed properly together. Composite columns provide not only many advantages in construction (i.e. speed and economy), but also a substantial improvement of the mechanical properties of structural members when compared to either steel or reinforced concrete elements.

A composite column, if designed and detailed properly, will result in a synergistic behavior that highlights the best of the concrete properties (stiffness, high compressive strength, fire proofing) and the best of the steel properties (ductility, high tensile strength, lightweight). Due to this synergistic effect, less conservative behavior factors (i.e. the lateral strength reduction factor R_{μ} , the lateral displacement amplification factor C_{\square} , the overstrength factor Ω_o , or the design strength reduction factor ϕ) could be used as compared to those used for either reinforced concrete or structural steel columns. For example, if the strength reduction factor obtained by reliability-based analysis is $\phi=0.65$ for a reinforced concrete column (ACI-318, 2008) and $\phi=0.90$ for a steel column (AISC, 2005), then the ϕ for a composite column with implicit synergistic properties should be higher than these values.

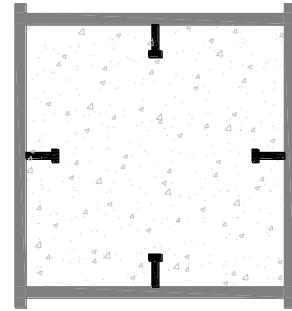
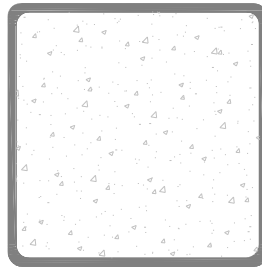
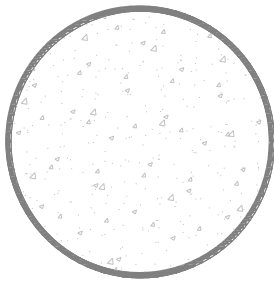
Additional advantages of composite columns can be achieved if they are detailed as part of a mixed structural system. For example, if they are properly connected with the floor system (beams and slab), a higher strength and a better behavior can be achieved in the beam-column connection, thus increasing the redundancy and toughness. Once the construction complexities are overcome (i.e. the interdisciplinary coordination between steel and concrete workers, and forming of the beam-column connection), more advantages will be obtained in the construction process (i.e. speed construction, formwork savings, reduced loads on foundation, increased useful space, lower construction and maintenance costs, etc.). Moreover, as new areas of the U.S. are reclassified to higher seismic design accelerations and the need to limit nonstructural damage becomes more important, replacement of either congested concrete columns or flexible steel columns with composite columns is a clear solution for brand-new and existing structures.

Composite columns can be made up with different configurations; some of these are shown in Figure 1.1. While there is great variety in these configurations, composite columns have been classified into two general types in terms of the position of steel and concrete. These are:

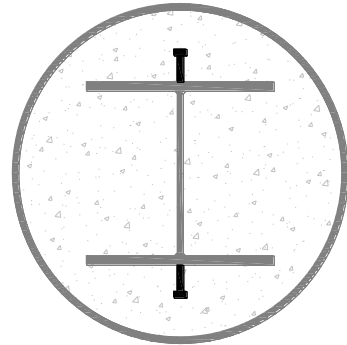
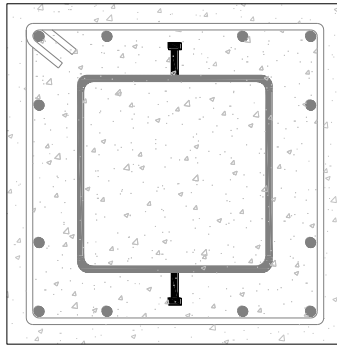
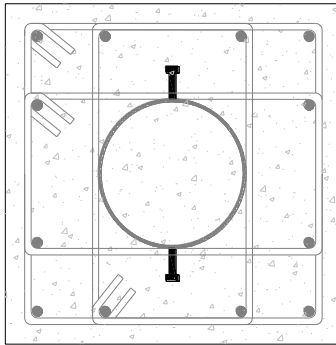
- Encased or steel reinforced concrete (SRC) elements, where the steel section is embedded or encased by the concrete; in other words, the concrete section is reinforced by a rolled or a built-up steel section.
- Concrete-filled steel tubes (CFT), where the steel is a rolled or built-up hollow section filled with concrete.



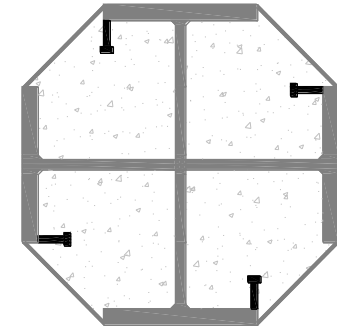
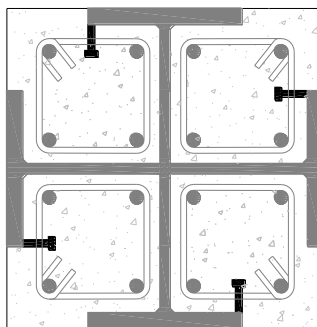
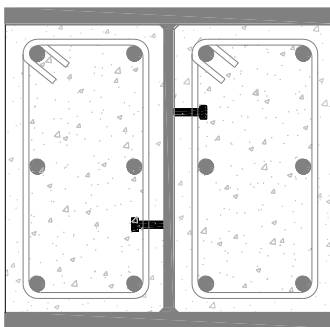
(i) SRC cross-sections



(ii) CFT cross-sections



(iii) Combined SRC-CFT cross-sections



(iv) Partially encased cross-sections

Figure 1.1. Some possible cross-sections configurations in composite columns

Composite columns, either as SRCs or as CFTs, offer different advantages to the structural engineer. Some of these advantages include, but are not limited to:

- *Optimal location of steel section:* Due to its location at the periphery of the cross section, the steel in CFTs has an optimal distribution that increases the strength and stiffness of the element. In SRC configurations, the column is ideally located for fast erection.
- *Fast construction of the structure:* As illustrated in Figure 1.2 through Figure 1.4, the steel columns are erected and connected to the floor system to support the construction loads (beams, girders, metal deck, etc.). This is followed by the casting of the concrete slabs and columns in the lower levels, while the steel structure erection may continue in upper levels. Once the concrete has hardened, and thus the composite action has been developed, the system can achieve its final strength and stiffness to support the designated gravity and lateral loads.
- *Higher flexural strength in embedded beam-column connections of SRCs:* Since the steel beam – steel column connection in SRC elements is embedded in a massive reinforced concrete section, the rotational stiffness of the steel connection is increased by the loads transferred between the beam and concrete in the embedded zone. In addition, the bending moment that can be sustained by the connection is higher than that capacity given by the initial steel connection or beam section alone.
- *Delay of the steel local buckling:* In composite cross-sections, the steel column (either as compact, non-compact or slender section) is stiffened by the contact with the hardened concrete, delaying or avoiding local buckling of the steel. Thus, the local buckling is delayed until the steel-concrete contact is lost (i.e. if the concrete cracks or a separation of concrete-steel occurs). Even if the concrete cracks, the delay of local buckling in CFT sections will still occur since the concrete expands and bears against the steel tube, maintaining the concrete-steel contact. Since the concrete core forces all local buckling modes outward, thinner steel sections may be used that still ensure the yield strength will be reached in the tube before buckling occurs.
- *Higher confinement in the concrete:* The steel column section adds confinement to the concrete core, which induces an increment in strength and ductility in the concrete. Due

to the shape of the section and the higher hoop stresses than can be achieved, circular CFT cross-sections provide a higher confinement than either rectangular CFT and SRC cross-sections. This confinement is also influenced by the diameter-to-thickness (D/t) ratio of the tubes.

- *Savings in the construction costs:* Constructions costs may be reduced due to the fast erection and an optimal design. Because of its higher strength, a composite column is lighter than a typical RC column with a similar strength, which reduces the loads on and cost of the foundation, the cost and amount of reinforcement bars, and thus the cost of construction. The steel section, which act as formwork and is stiffened by the concrete in CFT columns, is much lighter than a conventional steel column, which also reduces substantially the steel costs. Finally, the beam-column connections can be designed as efficiently (or even better) as a conventional steel or concrete column.
- *Fireproofing:* In SRC cross-sections, the concrete works as a fireproofing to the steel section.

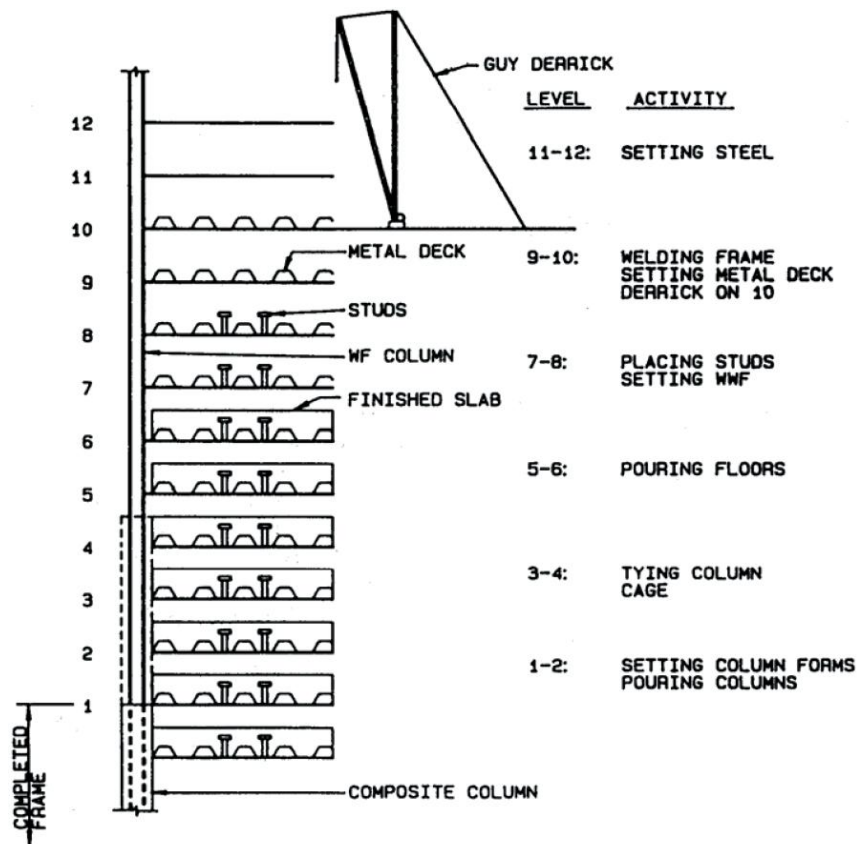


Figure 1.2. Construction process for a building with SRC columns (Viest et al. 1997)

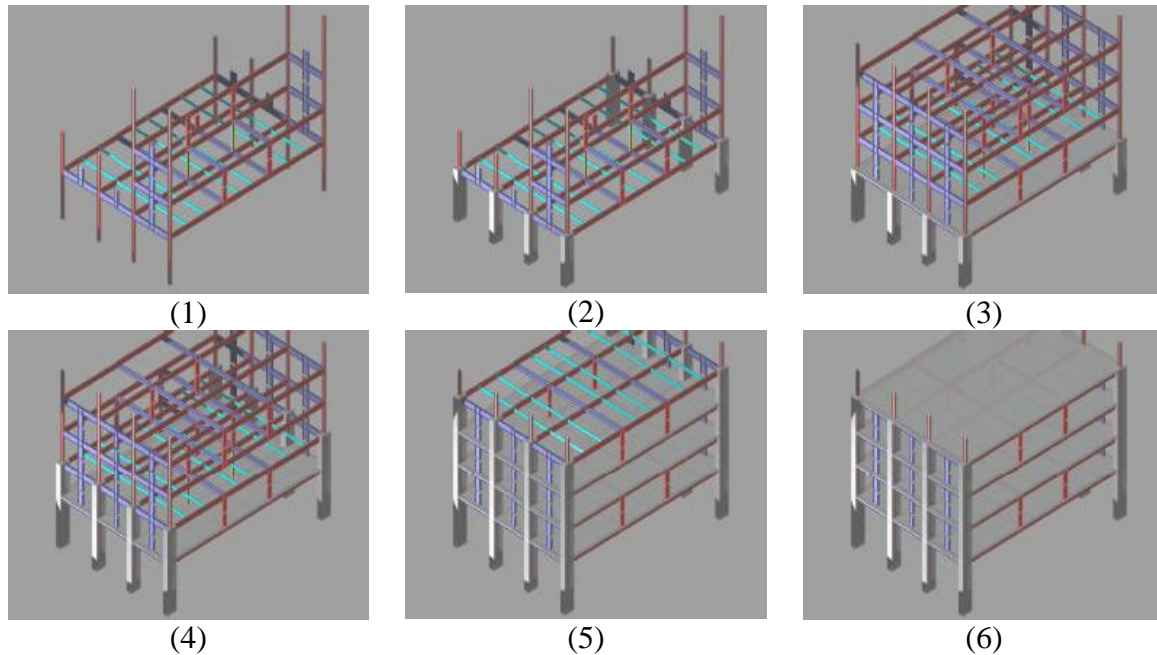


Figure 1.3. Erection and construction process for the first four stories of a building with SRC composite columns (Martinez-Romero 2003)

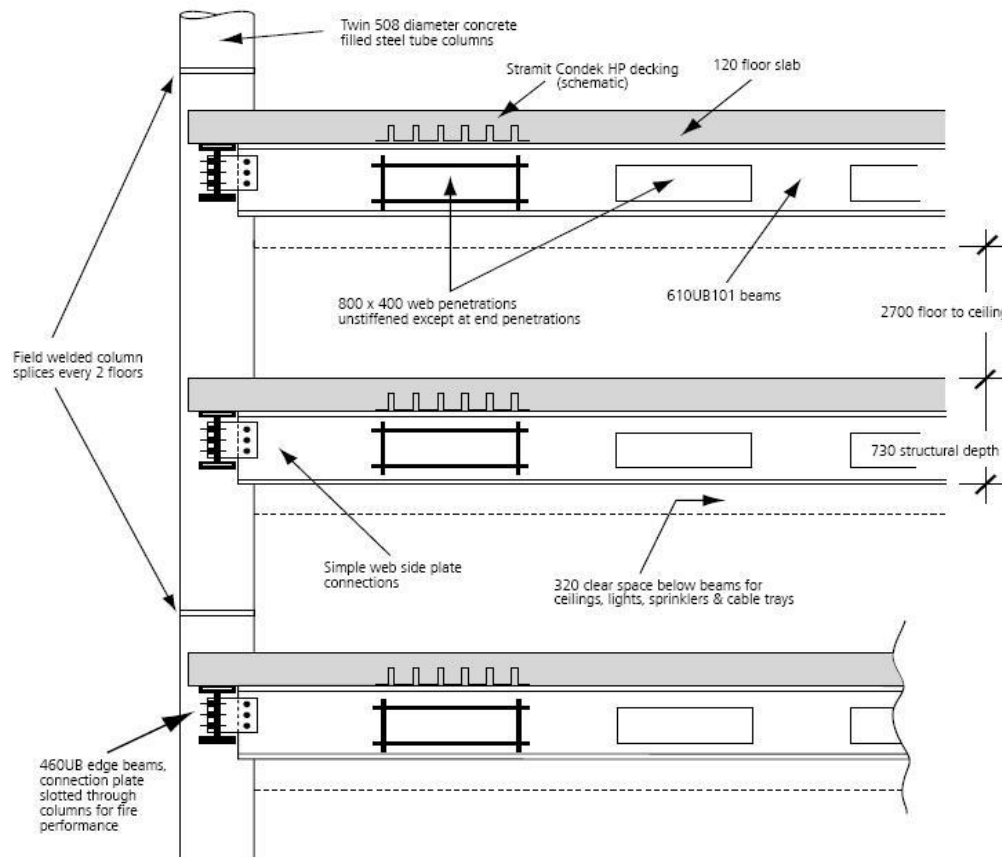


Figure 1.4. Floor system of a building with CCFT columns (Davids and Merriel, 2004)

1.1. Background and Motivation

Even though composite columns in buildings and other systems have been widely used for more than 50 years and their use is increasing worldwide, it is still very common in practice to either neglect the synergetic contribution of either the steel or the concrete or to treat the synergetic action in a simplistic manner. In other words, a composite column is treated as an equivalent steel or concrete one, a practice that is in most cases unduly conservative. Efficient use of composite columns requires that differences in behavior between composite and steel or concrete columns be incorporated clearly into the design process.

In ultimate strength design for seismic forces, it is customary to design based on elastic models for reduced forces and larger deformations. The reduced forces and larger deformations come from a series of so-called system factors (R_μ for the forces and C_d for the deformations). In the absence of extensive field experience with composite building subjected to ultimate loads or laboratory data on large composite substructures, code committees and practitioners have assumed behavior factors for composite systems by analogy to similar concrete or steel systems. Consequently, the estimation of the inter-story drifts and force distribution in the frames in many cases is probably inaccurate. The determination of appropriate system behavior factors will improve the accuracy in the calculation of lateral inelastic forces, displacements and inter-story drifts.

Current code provisions (i.e. AISC, 2005; ACI-318, 2008; EC-4, 2004; AIJ, 2001; etc.) have filled many gaps in the design of composite elements such as columns. However, in the author's opinion, there still exist some knowledge gaps in their behavior in areas such as the effective stiffness under lateral forces, instability effects in slender beam-columns, and the steel-concrete contact interaction effects, among others.

At the present time it is still difficult to predict the maximum structural response of a frame system with composite columns based on a typical frame analysis. Fiber Analysis (FA) or Finite Element Analysis (FEA) can be used to get a better response prediction; however, their application in conventional high-rise buildings is neither practical nor very common yet.

For these reasons, the development of design parameters or behavior factors applicable solely to composite systems incorporating SRC and CFT columns is needed. It is important that these factors also satisfy the limit cases, or in other words, with a smooth transition to concrete

factors when the steel ratio is very low, and vice versa, a smooth transition to steel factors when the steel ratio is very high. To reach these goals, it is essential to conduct a comprehensive experimental program that includes the tests of slender and full-scale beam-columns and slender cross-sections to fill the gaps in the experimental databases, and thus, account for the effects that do not affect short beam-columns or compact sections. This experimental program is the primary objective of the research reported herein.

The development of guidelines for composite frames will have immediate practical impact on construction for either constructing new structures or retrofitting old structures. In the next four sections, the work to be accomplished as part of this dissertation is described from different points of view. This is followed by a summary of expected original contributions.

1.2. Problem definition

Use of composite and mixed systems in low to moderate height construction in seismic areas of the United States is not common. The primary reason for this is that while some current design codes allow their use, there are major gaps in the provisions due to lack of targeted and coordinated prior research on composite columns and frames using U.S construction practices. Few design codes worldwide have developed provisions to design composite columns with robust reliability. AISC (2005), Eurocode 4 (2004) and AIJ (2001) are some of the codes with a good understanding in the behavior of composite columns. However, there remain some uncertainties in the behavior of such elements, such as:

- *Behavior of slender beam-columns:* Due to all the structural benefits and the synergy effects on composite construction, CFT columns tend to have smaller concrete cross sections than concrete-only columns, and lighter (thinner or smaller) steel cross-sections than steel-only columns. Thus, frames with composite columns (as well as with concrete or steel columns) are susceptible to buckling due to second order effects, either $P-\delta$ for braced frames or $P-\Delta$ for unbraced frames. Consequently, stability effects have to be accounted in the analysis process; in these calculations the effective stiffness (EI_{eff}) has an important role in the accuracy of these calculations. Current EI_{eff} have been derived mostly from curve fitting to data and do not represent a robust mechanical representation of actual behavior.

- *Effective stiffness for lateral forces:* Analysis programs still assume, in most cases, linear elastic (bar or frame) elements to assemble a global stiffness matrix. The solution of the equations results in the calculation of the lateral displacements (or drifts). A main concern using this approach for the analysis of composite frames is the accuracy in displacements because of the assumptions made for either the effective Young's modulus (E_{eff}) or the effective lateral stiffness (EI_{eff}). The use of fiber elements (instead of linear elements) will provide a more accurate approach for the structural analysis but a more complex problem to solve, especially if an irregular multistory 3D-frame is going to be analyzed. For this reason, some structural engineers, in the absence of good supporting information on effective stiffness, have assumed conservatively for analysis and design purposes the stiffness as that of either reinforced concrete or steel. A very careful set of experiments is needed to generate EI_{eff} for both the cases of columns subjected to axial loads and beam-columns subjected to lateral loads.
- *Effective torsional stiffness in 3D frame analysis:* Like the shear strength, research for torsional strength has not been widely explored for CFT columns. Consequently, it is not clear what the effective participation for each component to resist torsional loading is. Like flexural rigidity, this research will evaluate an effective torsional rigidity and will be presented in simplified design equations for CCFTs and RCFTs. The predicted equivalent torsional rigidity will allow to better account for the effects on structural asymmetries or irregularities on 3D frame analyses with CFT columns.
- *Shear strength:* The knowledge gaps on the investigation of the shear strength in composite columns are also reflected in the code provisions with few details on the calculation of this parameter. Specifications currently require designers to take the shear strength of either the steel component or the concrete component, or a superposition of those with reduced values. Again, in this case, little or no solid data is available to validate these recommendations.
- *Bond stress between concrete and structural steel:* Many of the CFT columns benefits depend on the steel-concrete interaction. Since the steel used in composite columns has a smooth surface, it is expected that low bond strength arise in the link between steel and concrete unless shear studs are provided. The benefits of a higher concrete confinement and the delay in the steel local buckling may be drastically reduced due to relative

differences in lateral strains or slip between the steel and the concrete surfaces. Very little data is available on this topic.

This research intends to address a number of these issues primarily from an experimental standpoint and at the element level. The data generated herein will be used in a companion dissertation focused on behavior of frames and development of system behavior factors.

1.3. Scope and Objectives

The main objectives of this research are to develop experimental data to:

- Evaluate the effect of the wet concrete in the steel tubes during the casting
- Determine the critical load of slender composite CCFT and RCFT full-scale columns with different boundary conditions.
- Determine a number of points of the axial load-moment (P - M) interaction diagram for composite CFT beam-columns.
- To obtain the experimental response of CFT beam-columns under cyclic lateral forces, and from this, both evaluate the strength and ductility of the composite specimens for seismic loading and identify limits states that characterize the response. In addition, this research pursues the evaluation and the degradation of the stiffness in the composite element throughout the load protocol.
- To evaluate the strength and torsional stiffness of CFT specimens under cyclic torsional loading.

The experimental data will be used to:

- Improve the analytical prediction of structural systems with CFT elements through evaluation and calibration of both material constitutive models and element models.
- Provide recommendations for the construction and the design of circular and rectangular composite CFT elements.

1.4. Methodology

In order to achieve the previous objectives, an experimental and an analytical research program will be conducted. The experimental program is carried out utilizing state-of-the-art equipment for the testing of 18 CFT full-scale, fixed-free specimens subjected to a set of different loading conditions.

The following methodology is used to achieve the objectives described in the previous section:

- *Wet concrete effects*: Instrumentation for measuring the effect of the wet concrete consists of rosette strain gauges for measuring both longitudinal and transverse strains at points where highest values of strains are expected. Strains are tracked during different stages of the testing, starting from before the concrete is cast into the tubes and ending after the last load case in the load protocol.
- *Experimental buckling load*: Each of the specimens is subjected to an incremental vertical displacement until reaching the maximum axial capacity. The columns are tested as vertical cantilevers; depending on the desired boundary conditions, the horizontal DOFs are either in displacement control or in force control.
- *P-M interaction values*: For this case, the specimen is subjected to a constant gravity load and a progressive lateral top displacement. As the displacement grows in a given direction, and so the $P\Delta$ effects, the lateral strength starts to flatten out (maximum capacity), then decreases (up to when failure occurs), and eventually the displacements are reversed to stabilize the system. Thus, *P-M* values coupled to the maximum capacity and the failure states are rededuced by imperfections, and then compared to the analytical predictions.
- *Response to seismic loading*: For this case, the specimen is subjected to constant gravity load and incremental cyclic lateral top displacements. The direction of these displacements are both unidirectional and bidirectional, so uniaxial and biaxial response can be evaluated. Moment-curvature response reflects the change between cycles and load cases, so the degradation in both strength and stiffness will be tracked throughout the load protocol.

- *Torsional loading*: In this case, the specimen is controlled with a monotonic top twisting. Experimental values from the torsion-twisting curve, such as the torsional strength and stiffness, are calibrated to simplified equations.
- *Improve analytical models*: Analyses based on fiber elements (using the software OpenSees, 2010) are performed with the aim of improving the prediction of the observed experimental response. The evaluation and calibration of both material constitutive models and the structural model that best reflects the test conditions are essential to developing better simulation tools for these structural elements.

1.5. Brief research project description

To implement the methodology described above, a work plan, comprising seven main tasks, was devised. Each of these phases is described briefly below.

Review of the previous experimental and analytical research on CFTs

Previous research studies will provide a guide on what has been done and what is needed to be investigated on CFT members, and so avoid research duplication and keep focus on where the knowledge gaps are. This review includes both analytical and experimental research studies on CFT columns and beam columns subjected to monotonic and cyclic loads. Review of the experimental past research will help in the evaluation of the test data gaps and for the update of the experimental databases.

Review of the available experimental databases on CFTs

Review of the existing experimental CFT databases (Leon et al., 2005; Goode, 2007; Gourley et al., 2008) will allow the identification of the test data ranges, limits and gaps. This review will include the identification of data ranges and gaps for the geometry of previous CFT specimens such as the specimen length (L), the cross-section shape (rectangular vs. circular, weak vs. strong axis, etc.) and the cross-section sizes (D , b , h , t , available cross-sections). In addition, it will identify ranges and gaps for the materials strength and properties (f_c' , F_y , width-thickness ratios, etc.), the load test protocol (monotonic, cyclic, concentric or eccentric compression, uniaxial or biaxial bending, torsion, etc.), the boundary conditions, and any other test conditions (i.e. instrumentation used, testing rates, etc.). The available databases collected

are going to be merged and updated with the most recent experimental data so a unified database can be used to find the data gaps. The selection of the CFT specimens to be tested in this research is going to be based on the identification of gaps from this unified and updated database, and on the observations from the review of previous research studies.

Preliminary analysis of postulated CFT specimens

Once a preliminary selection of CFT specimens and other main parameters (i.e. boundary conditions, load cases, etc.) has been made, key results are calculated based on both the simplified models from AISC (2005) Specifications and from computational methods based on Fiber Analysis (FA) and/or Finite Element Analysis (FEA). These key results include the analytical determination of the cross-section strength to axial force, bending moment, and the P-M interaction diagram. Stability reduction due to second order effects are determined from computational analyses that account for geometric and material non-linearities, as well as other behavior effects (i.e. concrete confinement and steel local buckling and residual stresses).

In addition, analyses for the secondary elements (i.e. base plates, bolted and welded connections, and the capacities for crosshead, the strong floor and the strong wall) are performed to guarantee the occurrence of the expected failure mode. Complementary analyses are performed to account for loads during the construction (i.e. hydrostatic pressure in steel tubes due to the casting of wet concrete) or during the erection or connection to the testing machine; all of these may affect the behavior during the testing. The idea behind of all these analyses is to have a better understanding of the behavior of the CFT specimens before, during and after the testing, and avoid unexpected failures.

Development of the experimental work plan

Based on the preliminary analyses results and the laboratory constraints, details of the CFT test matrix will be finalized and the whole work plan developed (i.e. construction, instrumentation, testing, etc.). As mentioned before, identification of the critical points from the preliminary analyses with postulated load cases will give information about what type and where the instrumentation is needed. On the other hand, these analyses will also help to identify key load cases such that neither the lab capacities are exceeded or wasted, nor early or unexpected failures take place. In addition to the construction, instrumentation and testing details, there is

also of the need to develop a careful data management plan, a risk-hazard management plan, and a post-mortem investigation plan.

Execution of the experimental program

A comprehensive experimental program is planned to be conducted for this research at the Multi-Axial Sub-assembly Testing (MAST) laboratory at the University of Minnesota, a NEES facility. The experimental program consists of testing a series of 18 full-scale circular and rectangular concrete-filled steel tube (CFT) beam-columns subjected to a very complex load protocol. The CFT specimens proposed for this research will be the world largest beam-columns tested in an experimental program. Additional information about the CFT specimens, the instrumentation and the testing plan are explained with more detail in the following chapter.

Advanced computational analyses

Parallel to the experimental study, advanced computational analyses are performed. Analytical models that account for the geometric and material non-linearities and the effects of the steel-concrete contact interaction (i.e. concrete confinement or the steel local buckling) are calibrated and verified with the experimental results. In addition, the computational models are calibrated to follow the accumulation of damage and the strength-stiffness degradation observed in the experimental tests. The calibrated analytical models will be used to establish guidelines on the computation of equivalent composite beam-column rigidity to be used in seismic analysis and design of composite frames, and eventually for parametric studies aimed at developing system response factors (i.e. R_{μ} , C_{μ} , Ω , ϕ) for composite frame structures with CFT columns.

Development of analysis and design recommendations

Based on the results from the experimental tests and the computational analyses, qualitative and quantitative analysis and design recommendations will be provided. In addition, preliminary work to prepare or augment design recommendations for the use of advanced materials and composite action in brand-new or existing structure will be presented.

1.6. Dissertation outline

This dissertation is organized into the following chapters:

- CHAPTER 2 describes briefly a review of the previous investigation on composite CFT columns and beam-columns. Previous experimental and analytical research studies and their main contributions are summarized and commented upon.
- CHAPTER 3 describes in detail the experimental setup used in the 18 CFT specimens tested in this project. The MAST laboratory capabilities, a description of the specimens, the instrumentation plan, the pre-test settings and the load protocol are documented in this chapter.
- CHAPTER 4 discusses the effects of the wet concrete during its casting into the steel HSS tubes. The strain measurements in the steel exterior walls are compared with those strains obtained from closed-form solution and with those obtained from finite element analyses under hydrostatic pressure. The effects of the wet concrete in the steel local buckling are also documented in this chapter. Recommendation to minimize the effects on CFT members are given at the end of this chapter.
- CHAPTER 5 discusses the results and the issues associated with the buckling loads obtained experimentally. These results are compared with predictions based on the specifications and computational simulations.
- CHAPTER 6 presents experimental values of the axial load and bending moment capacity (P-M) extracted from the uniaxial and biaxial bending tests, and these are compared with the P-M interaction diagrams obtained from the specifications.
- CHAPTER 7 discusses the experimental cyclic flexural response to lateral forces of the composite CFT specimens under load cases with unidirectional and bidirectional bending. The experimental response is compared with predictions based on computational analyses. The evolution of the effective flexural rigidity of the composite specimens within the load protocol is also presented in this section.
- CHAPTER 8 presents an evaluation of different limit states reach during the entire loading testing. Occurrence of the first yielding in compression and tension in the steel, the start of development of local buckling in the steel tube, and estimation on the

occurrence of the concrete crushing is discussed in this Chapter. In addition, this chapter presents the results of the obtained plastic hinge lengths and the post-mortem or forensic analysis of the CFT specimens tested in this project.

- CHAPTER 9 discusses the torsional response of the CFT specimens. The torsional stiffness obtained experimentally is compared with that obtained for the concrete and the steel independent components. Recommendation to determine the torsional strength and rigidity on CFT members are given at the end of this chapter.
- CHAPTER 10 proposes an approach to estimate the axial and flexural capacity of CFT members. This methodology includes observations obtained from the experimental test data collected and analyzed in this project and the observations from other studies.
- CHAPTER 11 gives general conclusions and recommendations obtained in this research.
- APPENDIX A documents some results as the concrete mix design, the concrete cylinders tests and the steel coupons tests.
- APPENDIX B summarizes the main experimental results obtained in the tests for each specimen during each load case.

1.7. Original contributions

The present research project is distinctive in many ways. Some points that make this project unique include:

- Providing qualitative and quantitative recommendations to evaluate and minimize the effects of the wet concrete pressure in the steel tubes during the pouring.
- Completing a comprehensive experimental program that consisted of testing 18 circular and rectangular CFTs, with an extensive and advanced instrumentation, and subjected to a very complex load protocol. All these will make possible to fill many of the gaps found in the experimental CFT databases. These results are expected to become the benchmarks by which future analytical models for composite beam-columns will be evaluated.
- Selecting a test matrix unique for (1) the length and the slenderness of the specimens (the world largest CFT columns and beam columns), (2) the use of the larger and thinner

fabricated HSS cross-section sizes (low width-thickness ratios D/t or h/t), and (3) the range in material properties. This research will provide much needed data to calibrate material constitutive models and the element models for composite structures.

- Improving the analytical prediction for strength and deformation capacity of CFT columns and beam-columns with fiber-based or finite-based analysis with respect to:
 - Second order analysis accounting for geometric and material non-linearities
 - Cyclic behavior of beam-columns with strength and stiffness degradation
 - Accumulated damage accounting for effective confinement and local buckling
- Improving the analytical prediction for strength and deformation capacity of CFT columns and beam-columns with simplified design equations, including:
 - Effective flexural (EI_{eff}) and torsional rigidity (GJ_{eff}) for 3D frame analysis
 - Critical load (P_n) and column curves ($P_n-\lambda$) for slender columns
 - P-M interaction diagrams for both cross-sections and beam-columns
- Developing a design procedure for CFT columns with compatible transition from reinforced concrete to steel elements, and vice versa. Also, include some recommendations for design procedure on composite frames with CFT columns subjected to gravity and seismic load conditions.

In summary, this research project provides a unique set of data that can and has been used to verify advanced computational models and provide support for the development of both simplified and advanced analysis techniques for composite CFT members.

In addition, this research study is an effort at (1) developing new fundamental knowledge, (2) improving our understanding of composite beam-column behavior, (3) extending design ranges, (4) providing calibration data, and (5) improving the accuracy of the response prediction on concrete-filled tube members.

The author expects that, based on the results and conclusion obtained in this research project, CFT members have an immediate practical impact on analysis, design and, as a consequence, on construction on composite frames system for either constructing new structures or retrofitting old structures.

CHAPTER 2

PRELIMINARY RESEARCH STUDIES

2.1. Previous experimental research studies

2.1.1. Introduction

Even though there have been numerous experimental test series for composite columns in the past, in particular for CFT elements, most of the documentation in the specialized literature is limited to columns with certain characteristics (i.e. small cross-sections, short elements, small D/t ratios, conventional strength materials, etc). Specimens with these characteristics are the only viable option when the capabilities of the laboratory equipment are limited, making the testing of full-scale specimens impractical. The results from specimens with lower slenderness but a wide range of cross-section sizes have been useful for the quantification of the cross-section strength and behavior of short elements, where the length effects do not have a critical impact. In turn, data results from slender specimens, which are mostly made of small cross-section sizes and tested in a horizontal position, have been useful for parametric studies accounting for the length effects and effective confinement of CFT columns and beam-columns. However, the extrapolation to elements with sizes closer to those used in practice for real structures may not be entirely correct and the conclusions from these research efforts may need to be adjusted accordingly.

This section reviews some of the previous research that focused on the experimental tests of CFT elements. Innovations, principal contributions and main conclusions of selected previous research studies relevant to this work are briefly discussed. There is no intent to provide a complete summary of all efforts; such summaries are available elsewhere (Aho, 1997; Kim, 2005; Leon *et al.*, 2005; (Goode 2007); Gourley *et al.*, 2008).

Table 2.1 summarizes chronologically the material and geometric properties of CFT specimens tested in previous experimental research studies. The information in this table was extracted from the collected databases (Leon *et al.*, 2005; Goode, 2007; Gourley *et al.*, 2008), which will be discussed in the following section.

Table 2.1. Summary of experimental studies in CFT columns and beam columns

Reference	Type	KL (ft)	tube size (in) (D) or (b)x(h)	wall thickness (in)	Max D/t or h/t	f_c' (ksi)
Kloppel and Goder (1957)	CCFT	2.8 – 7.6	3¾ – 8½	1/8 – 1/2	55	3 – 4
Salani and Sims (1964)	CCFT	5	1 – 3	1/32 – 3/32	55	3 – 4
Chapman and Neogi (1966)	CCFT	1.3 – 6.8	5 – 14	1/16 – 3/8	78	3 – 9.6
	RCFT	1.3	4.5x4.5	3/16, 3/8	25	4.6
Furlong (1967)	CCFT	3	4.5, 5, 6	1/16, 3/32, 1/8	98	3 – 6.6
	RCFT		4x4, 5x5	3/32, 1/8, 3/16	46	
Gardner and Jacobson (1967), Gardner (1968)	CCFT	0.5 – 7.5	3 – 6 ² / ₃	1/16 – 3/16	65	2.6 – 6.3
Knowles and Park (1969)	CCFT	0.8 – 5.7	3¾, 3½	1/16, 1/4	60	5.4 – 6
	RCFT		3x3	1/8	21	5 – 6.8
Neogi, Sen and Chapman (1969)	CCFT	4.6 – 10.9	5 – 6 ² / ₃	1/16 – 3/8	78	2.7 – 9.7
	RCFT	1.3	4.5x4.5	3/16 – 3/8	24	4.7
Janss and Guiaux (1970)	CCFT	1.7 – 14.3	3 ³ / ₄ – 8 ² / ₃	1/8 – 1/4	36	4.5
Janss (1974)	CCFT	3.9 – 5.3	10.8 – 16	3/16 – 3/8	81	4 – 5.5
	RCFT	4.3 – 4.6	13x13	3/16 – 7/16	72	4 – 4.5
Bridge (1976)	RCFT	7, 10	6x6, 8x8	1/4 – 7/16	21	4.5 – 5.1
Zhong (1978)	CCFT	0.8 – 16.4	3 ³ / ₄ – 19 ¹ / ₂	3/32 – 1/2	84	3.2 – 7.9
Tang (1978)	CCFT	1.4 – 4.9	4.2	1/8	35	5.4
Tomii and Sakino (1979a, 1979b)	RCFT	1.0	4x4	3/32, 1/8, 3/16	43	3 – 4.6
SSRC Task Group 20 (1979)	CCFT	3.4 – 7.6	3 ³ / ₄ – 8 ¹ / ₂	5/32 – 1/4	53	3 – 4.3
Cai (1981)	CCFT	2.3 – 12.1	6 ¹ / ₂	3/16	33	4, 5.5, 6
Tang et al. (1982)	CCFT	0.5 – 6.5	3 – 11.8	1/16 – 7/16	100	3 – 8
Zhou (1983)	CCFT	6.7 – 9.7	4, 5 ³ / ₁₆	5/32 – 7/32	30	3.6, 5.4
Zhong (1983)	CCFT	1.1 – 5.3	4¼	1/16 – 7/32	57	3.1, 4.5
Cai and Jiao (1984)	CCFT	0.9 – 12.1	3 ³ / ₄ – 12.6	3/32 – 1/2	102	3.9 – 6.8
Cai and Gu (1985)	CCFT	1.1 – 18.2	4 ¹ / ₄	1/8	27	4.2
Wang and Yang (1985)	CCFT	0.9	5 ¹ / ₄	3/32 – 1/4	55	2.5, 3.9
Sakino et al. (1985)	CCFT	0.7	4	1/32 – 1/4	192	2.6, 5.4
Sakino et al. (1985)	CCFT	0.7	4	1/32 – 1/4	192	2.6, 5.4
Chen et al. (1988)	CCFT	0.6 – 2.2	2 – 6½	1/8 – 3/16	38	4.8
Pan (1988)	CCFT	8 – 11.9	6½	3/16	38	6.3

Table 2.1. Summary of experimental studies in CFT columns and beam columns (cont)

Reference	Type	KL (ft)	tube size (in) (D) or (b)x(h)	wall thickness (in)	Max D/t or h/t	f_c' (ksi)
Lin (1988)	CCFT	1.6, 2.6	6	$1/32 - 3/32$	214	3, 5
	RCFT		6x6, 6x8		284	3.3, 5.1
Sakino and Hayashi (1991)	CCFT	0.8, 1.2	7	$1/8 - 3/8$	58	3.2, 6.6
Bergmann (1994)	RCFT	3.3, 13.1	7x7, 10 $\frac{1}{4}$ x10 $\frac{1}{4}$	$5/16$	35	13.4
Matsui et al. (1995, 1997)	CCFT	2.2 – 16.3	6 $\frac{1}{2}$	$3/16$	40	4.6 – 5.9
	RCFT	2 – 14.8	6x6	$3/16$	33	
Shakir-Khalil (1996)	RCFT	9.6 – 16.1	4x6	$3/16$	33	5.2 – 6
Inai and Sakino (1996)	RCFT	1.2 – 3.2	several square sizes	$3/16 - 3/8$	72	3.7 – 13.2
Roeder and Cameron (1999)	CCFT	2.7 – 6.3	10 $\frac{1}{4}$ – 23 $\frac{3}{4}$	$1/4 - 1/2$	108	6.4 – 6.9
Bridge and O'Shea (1997, 2000)	CCFT	1.8 – 2.2	6 $\frac{1}{2}$, 7 $\frac{1}{2}$	$1/32 - 1/8$	220	5.5 – 16.5
Nakahara and Sakino (1998)	RCFT	2	8x8	$1/8 - 1/4$	63	17.3
Varma (2000)	RCFT	4	12x12	$1/4, 3/8$	50	16
Seo and Chung (2002); Seo, Tsuda and Nakamura (2002)	RCFT	1.6 – 12.3	5x5	$1/8$	40	9.3 – 14
Mursi et al. (2003)	RCFT	9.9	4.7, 6.7, 8.7, 10.6	$3/16$	52	3
Han and Yao (2003)	CCFT	1 – 6.6	4 – 8	$1/8$	65	3 – 6.8
	RCFT	1.8 – 7.7	several rect. sizes		134	2.7 – 8.5
Lam and Williams (2004)	RCFT	1.0	4x4	$5/32 - 3/8$	23	3.6 – 11.5
Hardika and Gardner (2004)	RCFT	5.9	8x8	$3/16 - 3/8$	44	6.4 – 14
Han and Yao (2004)	CCFT	6.6	8	$1/8$	65	6.8
	RCFT	2, 7.6	8x8			
Ghannam et al. (2004)	CCFT	7.2, 8.1	4 $\frac{1}{3}$ – 6.5	$3/32 - 3/16$	58	1.5 – 4.8
	RCFT	6.6, 8.2	4x4, 4x8, 5 $\frac{1}{2}$ x5 $\frac{1}{2}$, 3 $\frac{1}{2}$ x6		48	

2.1.2. Review of previous experimental studies on CFT columns and beam-columns

Kloppel and Goder performed the first documented experimental research on CCFTs in 1957. This research, originally published in German, is cited in English by Knowles and Park (1970) and Roik and Bergmann (1989), who also described the experimental results and other details. These authors performed collapse load tests on hollow and concrete-filled steel tubes. Three tests were examined in detail, with stresses and strains in both the steel and concrete tabulated for incremental values of concentric load. Based on the experimental data analysis, these authors established the initial design formulas for CFT columns.

One of the first comprehensive experimental research study using both CCFT and RCFT columns and beam-columns was published by Furlong (1967), who tested CFT specimens with both concentric and eccentric loads. Based on this experimental data, design equations were proposed to estimate the ultimate strength of beam-columns. In addition, the concrete-steel interaction was taken into account explicitly for the first time. Furlong observed that the two materials behave independently of one another at strains below 0.001, where the Poisson's ratio of concrete is lower than that of steel; this difference in lateral expansion resulted in a non-contact state between these two materials at low levels of strain. As strains increased, the concrete expanded laterally at a greater rate than the steel, and above 0.001, the concrete Poisson ratio began to approach that of steel and, as a consequence, the steel starts providing confinement to the concrete. Simultaneously, the concrete core stabilizes the steel wall of the tubes, preventing premature local buckling and allowing the tube to attain its full yield capacity. Data from these tests also show that creep had an influential effect on the specimen behavior.

Tomii and Sakino (1979a) conducted an experimental research on square CFT specimens to determine moment-curvature ($M-\phi$) relationships. Under a constant axial load, moment was applied to the section in uniformly increasing amounts. In addition to the very detailed experimental study, the authors proposed analytical equations to estimate the ultimate moment of a RCFT section. Analytical moment-curvature ($M-\phi$) relationships were developed and compared to the experimental results. The concentrically loaded columns produced strengths in excess of those calculated analytically, a fact that these authors attributed to differences in the estimated concrete strength. Columns subjected to both axial load and bending moment displayed behavior that was highly dependent on the D/t ratio and the magnitude of the axial

load, especially in the inelastic range of strains. Moment-curvature ($M-\phi$) plots show an increase in ductility with a decrease in D/t ratio. Specimens with $D/t=24$ behaved in a ductile manner, while columns with $D/t=44$ and high axial load had a falling branch in the $M-\phi$ diagram. Even though this last set of columns failed in a rather brittle manner, the tension side of the steel tube still yielded. It was suggested that the ductility increase as the D/t ratio decreased was due largely to the lateral confinement of the concrete by the steel.

In Tomii and Sakino (1979b), additional square CFT tests were reported in five series. Each series contained different material properties and h/t ratios, and the parameters evaluated were the shear span ratio (a/h) and axial load ratio (P/P_o). The tubes were annealed to remove residual stresses and the specimens were tested with double fixed boundary conditions ($K=0.5$). This research indicated a negligible effect due to the a/h ratio. It was also observed that for specimens with a high axial load ratio ($P/P_o = 0.5$), after a certain amount of decrease in the lateral strength, the hysteretic loops tended to stabilize and even showed a slight increase in lateral resistance. The authors attributed this to a transformation in shape of the buckled tube (from square to circular-like), which effectively increased the amount of confinement of the concrete and resulted in the stabilization of the hysteretic loops. A considerable amount of axial shortening was observed for columns with a P/P_o of 0.5 due to the combination of steel local buckling and concrete crushing. The experimental ultimate moment was 1.0 to 1.2 times the calculated value by the method described in Tomii and Sakino (1979a, 1979b); the authors suggested that this was due to a combination of strain hardening in the steel tube and moment gradient effects in the confined concrete at the critical section.

2.1.3. Brief comparison of CFT specimens previously tested

Before the present research, the tallest CFT specimens tested and documented in the specialized literature were conducted by Cai and Gu (1985) for CFTs with 18.2 feet of effective length and 4¼ inches of diameter, and by Shakir-Khalil and Al-Rawdan (1996) with 16.1 feet of effective length and 4x6 inches of cross-section size. Cai and Gu's results on slender columns show elastic buckling failures that were well predicted by the Euler's formulation; they also mentioned that the behavior of slender CCFTs is highly influenced by all the initial imperfections (i.e. the out-of-straightness and the loading eccentricity). For RCFTs, Shakir-Khalil and Al-Rawdan (1996) reported lower strength with an increase in length due to local buckling, that generally took place on the longer side of the tubes. After testing, the concrete was reported crushed but with a good integrity.

At the present time, the specimens with the biggest circular CFTs cross-section size have been conducted by Luksha and Nesterovich (1991) using spiral welded tubes with 40.2 inches of diameter and 10 feet of effective length. Two types of failure were observed in this study: (1) small diameter specimens, for which failure is characterized by the local buckling of the steel and the crushing of the concrete; (2) large diameter specimens, for which failure was reported as a shear failure. In turn, the previous biggest square CFT cross-section was conducted by Janss (1974) with 13x13 inches of size and 4.36 feet of effective length. For rectangular CFT shapes, Han and Yao (2003) tested tubes with 14.2x9.4 inches of size and 4.7 feet of effective length.

In contrast, the specimens with the highest width-thickness ratio documented were performed by O'Shea and Bridge (1997) for CCFTs with a D/t ratio equal to 221, and by Lin (1988) for RCFTs with an h/t ratio equal to 284. Both studies used special tubes with 1/32 inches in thickness, 7½ inches diameter, and 2.2 feet of effective length in the CCFTs, and 6x8 in. and 2.6 feet of effective length in the RCFTs.

On the other hand, specimens that have been filled with high performance concrete include those tested by O'Shea and Bridge (1997) using concrete with a compressive strength of 16.5 ksi in CCFTs, and those tested by Nakahara and Sakino (2000) and Varma (2000) in RCFTs with concrete strengths of 17.3 and 16 ksi, respectively.

2.1.4. Review of previous experimental studies on CFTs under torsional loading

Although few CFT specimens have been tested under torsional loading, in general, it is expected a good performance due to the position of the steel tube at the perimeter of the CFT cross-section. Additionally, circular CFT's behavior is excellent due to the shape of the circular steel tube. Among the few studies of experimental studies of circular CFTs under torsion are those reported by Lee *et al.* (1991) and u *et al.* (1991)

u *et al.* (1991)

u *et al.* (1991)

Xu *et al.* (1991).

Lee *et al.* (1991) tested short CCFTs under monotonic and cyclic torsional loading with and without compression; results of this study show higher torsional resistance in the CCFTs with higher compression loads.

Xu *et al.* (1991), in contrast, tested short ($L=7D$), medium ($L=13D$) and long ($L=20D$) CCFTs under torsional loading, also with and without compression; the diameter of these specimens were 3½ and 4½ inches. These authors reported non-abrupt torsional failures at rotation angles of 5, 9, and 14 degrees for the short, medium, and long columns, respectively. Contrary to Lee et al.'s results, the ultimate torsional moment resistance decreased with an increase in the axial load ratio, so the highest torsional moment was attained in the pure torsion case. The characteristic failure mechanism was a cracking of the concrete followed by a propagation of the cracks along the length of the tube in a spiral pattern.

Lack of experimental data is evident for rectangular and square CFT specimens under torsional loading. Chapter 8 of this thesis closes this gap by showing the experimental results obtained for both CCFTs and RCFTs under torsional loading.

2.2. Compiled experimental databases

2.2.1. Previous compilation of experimental databases

There have been several large-scale efforts to compile an experimental database that summarizes the principal results of composite columns tests, either as CCFT, RCFT or SRC cross-sections, and/or as columns or beam columns tests. The first effort of this type was by an SSRC committee in 1979 (SSRC Task Group 20, 1979), which reported a collection of 179 tests that included 73 tests on axially loaded CFTs, 30 tests on axially loaded SRCs, 32 test on eccentrically loaded CFTs and 44 tests on eccentrically loaded SRCs. As a result of this database analysis, this SSRC committee proposed a design specification for composite columns which was adopted in the Chapter I of the LRFD Specification in AISC (1986).

Three years later, Roik and Bergmann (1989) collected experimental data from 208 tests reported at the time in the specialized literature, and used this database for the development and calibration of the Eurocode specifications EC-4 (1992) for composite columns.

In the mid 1990s, a research team guided by Galambos gathered experimental test results on composite columns with the purpose to investigate through Monte-Carlo simulations reliability indices for CFT and SRC columns designed by the existing EC-4 (1992) Eurocode (Sulyok and Galambos 1995) and the AISC (1993) LRFD Specifications (Lundberg and Galambos 1996). This database contained data for 389 available tests that included 119 tests on CFT columns and 128 CFT beam columns, and 59 tests on SRC columns and 83 SRC beam columns. All the data compiled was for tests with monotonic loads, and the material and geometric properties, as well as the experimental peak strength are reported.

In 1996, Aho and Leon collected a database for SRC, CCFT and RCFT columns and beam columns. Insofar as materials and geometric properties were concerned, there were no other specific limitations on the database. In total, this research reported nine databases, six for SRC, CCFT and CFT columns and beam columns, and three for those data (mainly coming from shear critical specimens tested cyclically in Japan) that had parameters that could not be compared with the rest of the data. These databases were used for the evaluation of the existing AISC-LRFD Specifications (AISC, 1993) and Eurocode (EC4, 1992), and their corresponding

reliability indices. Additionally, the data analysis aided the authors in developing design equations, which eventually were used as the base of the current AISC Specifications (AISC, 2005). In 2005, Kim and Leon added new information and edited these databases, resulting again in six databases for SRC, CCFT and RCFT of columns and beam columns. These updated databases were used in the evaluation of the current AISC Specifications (AISC, 2005) and Eurocode (EC4, 1994).

Kawaguchi *et al.* (1998) compiled an experimental database for CFT beam-columns from tests conducted in Japan. The collected data included monotonic and cyclic loads and documented material and geometric properties, experimental stiffness, and strengths and deformations associated to the peak and other characteristic levels (i.e. post-peak strength dropped 5%, maximum rotation reached the 1/100 value). Based on the experimental data, these authors developed analytical models for the calculation of the flexural strength and the rotational capacity of CFT beam-columns. Four years later, Nishiyama *et al.* (2002) gathered data from tests conducted in Japan as part of the U.S.-Japan Cooperative Research Program on Composite and Hybrid Structures. This database included test results for specimens under monotonic and cyclic loads, and was divided for both CCFTs and RCFTs in (1) centrally-loaded stub-columns, (2) eccentrically-loaded stub columns, (3) beam-columns, and (4) sub-assemblages. The database also reported material and geometric properties, calculated stiffness, period of vibration and costs, among other particular information of each test. Based on this collected data, the authors developed design formulas to calculate the strength and deformation capacities of CFT elements.

Another team that gathered experimental results and collected them in databases from 2001 was led by Hajjar (Gourley *et al.*, 2008). Gourley and Hajjar (1993) is the first version of a synopsis for CFT beam-columns subjected to monotonic and cyclic loads. This database has been updated and refined with more data in later versions in 1995, 2001 and 2008 (Gourley *et al.*, 2008). The latest compilation in Gourley *et al.* (2008) provides a summary of the behavior and experimental work of concrete filled steel tube members, connections, and frames that are reported in detail in the literature. These published studies have been summarized with an emphasis on experimental setup and properties, analytical methods presented, and key results from the work under various loading conditions.

More recently, Goode published online in 2006 a database for CFT columns and beam columns, with an update in 2007 (Goode 2007). His first database compilation was divided in short ($L/D < 4$) and long elements, in columns (no moment) and beam-columns (with uniaxial or biaxial bending moment with and without a preload), and for circular, rectangular and polygonal cross-section shapes. Goode's latest updated compilation published online in 2007 (<http://web.ukonline.co.uk/asccs2>) is composed of 13 databases that summarize the experimental results of 1819 CFT specimens. This database has been used by Goode and Lam (2008) for the evaluation of the strength predicted by the Eurocode EC-4 (2004); the comparison between the experimental strength and the EC-4 prediction in this studies have shown good predictions in general for CFTs, except in RCFTs with concrete above 75 MPa (10.9 ksi) of strength where the EC-4 prediction has underestimated the experimental strength.

2.2.2. Gaps in the experimental databases

One of the premises for the selection of the test matrix in the present research was the election of specimens that fill gaps with respect to the available experimental data. This motivated an analysis of the existing data to find out where the gaps were and what parameters should be accounted to fulfill this goal. To accomplish this objective, the databases compiled by Leon *et al.* (2005), Goode (2007) and Gourley *et al.*, 2008 were joined and edited into a “unified database”. The so-called “unified database” used in this research excludes duplicated data, and those “suspicious” tests data where inconsistencies were found or correspond to specimens that do not share the main database characteristics (i.e. steel only specimens, concrete only specimens, cross sections with a non-circular or non-rectangular geometry, etc). In addition, this database was updated with new data published up to 2009. Thus, this refined database included results for 1387 CCFTs (from which 912 are columns and 475 are beam-columns), 826 RCFTs (with 524 columns and 302 beam-columns) and 267 SRCs (with 119 columns and 148 beam-columns).

The following figures summarize the analysis of the unified database for composite SRC, CCFT and RCFT columns and beam-columns. Although this dissertation focuses in CFT cross-sections only, the results from SRC tests are also given for future reference.

In Figure 2.1, histograms of the experimental data from both columns and beam-columns are shown with respect to the slenderness parameter (λ), the concrete strength (f_c'), the steel yield stress (F_y), the longitudinal steel ratio ($\rho_s=A_s/A$), the D/t ratio for CFTs, the h/t ratio for RFCTs, and the reinforcement steel ratio for SRCs ($\rho_{sr}=A_{sr}/A$).

A comparison of the experimental strength normalized with the analytical column curve as given by the Chapter I in the AISC 2005 Specifications (P_{exp}/P_o) are illustrated for RCFT columns (Figure 2.2), CCFT columns (Figure 2.3) and SRC columns (Figure 2.5). These figures show a big dispersion, mainly for short columns. This big dispersion is justified by the confinement effects that are influenced by the depth-thickness ratio and the size of the cross-section, among other uncertainties.

Figure 2.4 shows the normalized experimental strength obtained for CCFT beam-columns with different slenderness parameter (λ). For reference, the continuous line represents the P-M interaction diagram of a steel element as described by equations H1-1a and H1-1b in the AISC 2005 Specifications. As illustrated in these figures, the slenderness, which impact second order moments, reduce the P-M strength as expected.

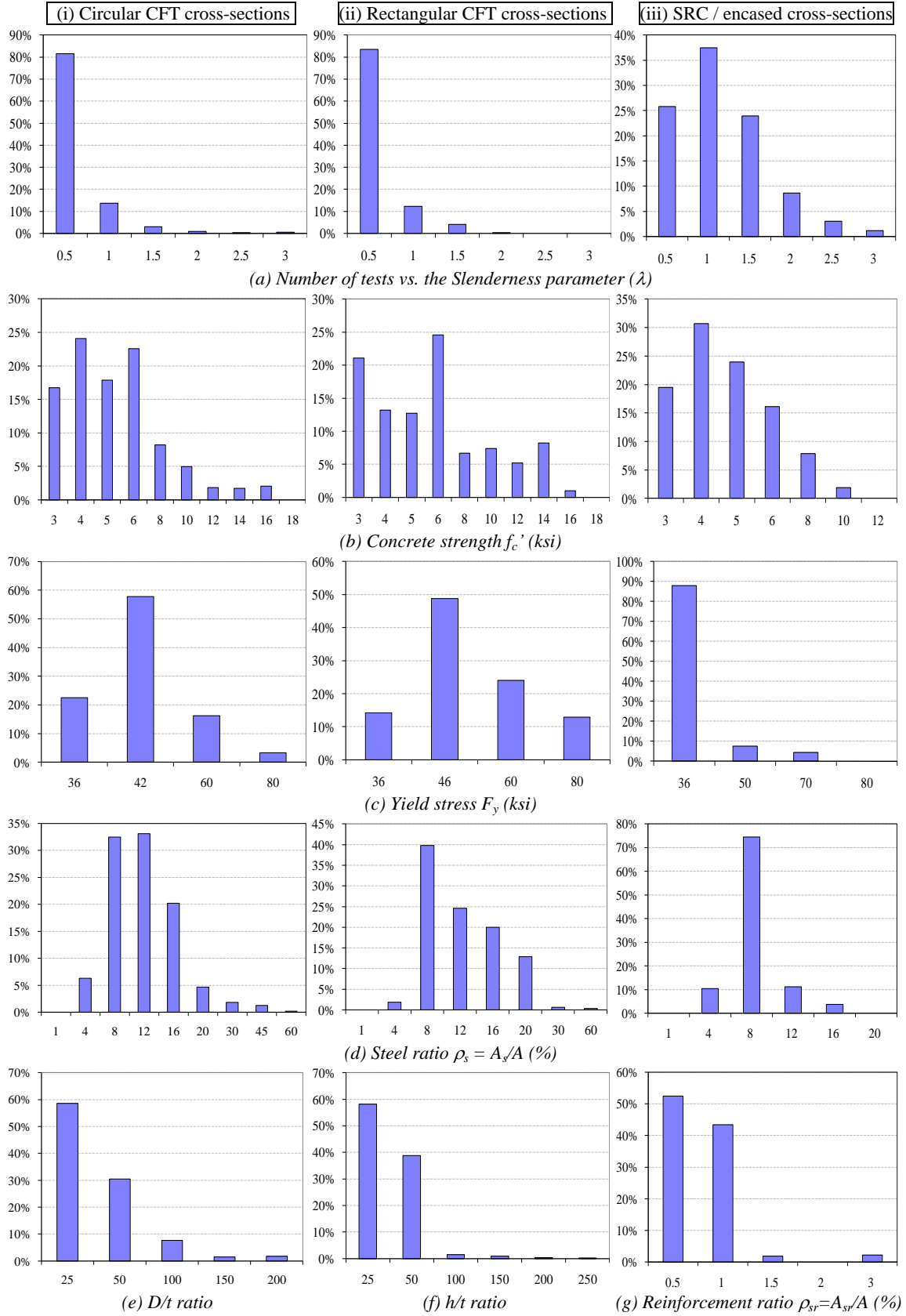


Figure 2.1. Histograms obtained from the unified database

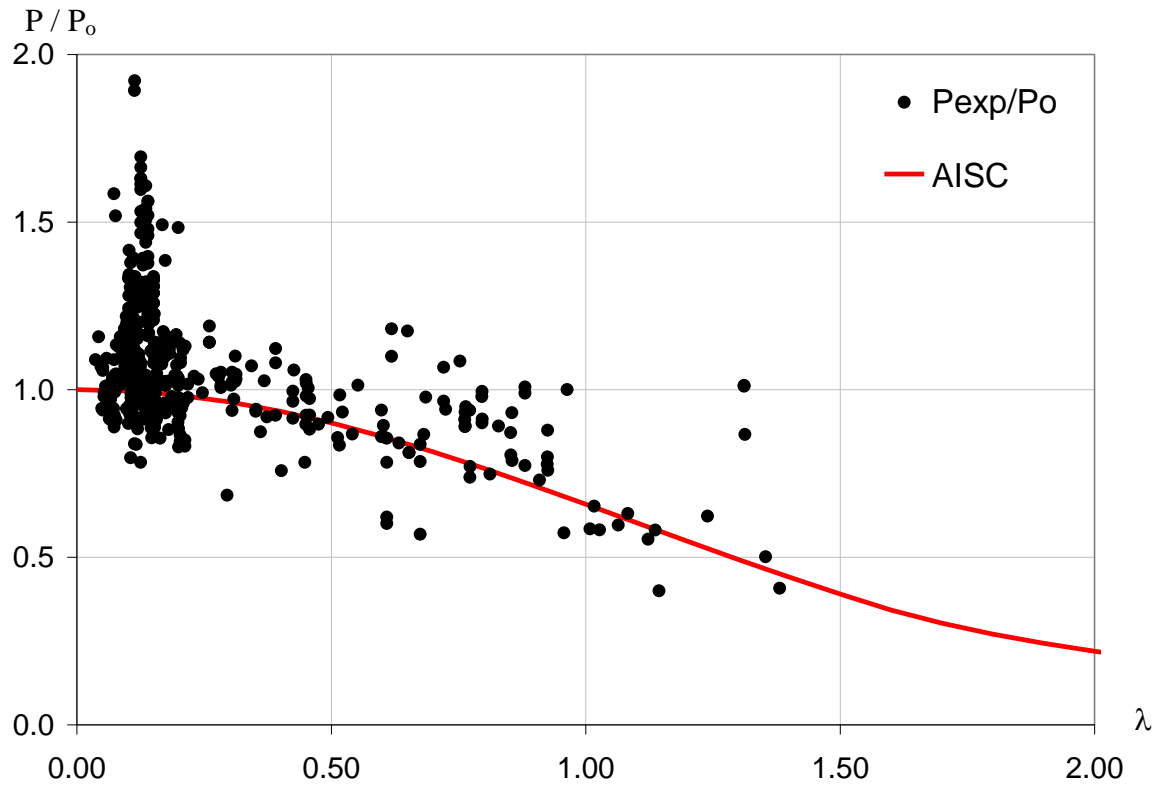


Figure 2.2. Experimental vs. analytical column curve for RCFTs

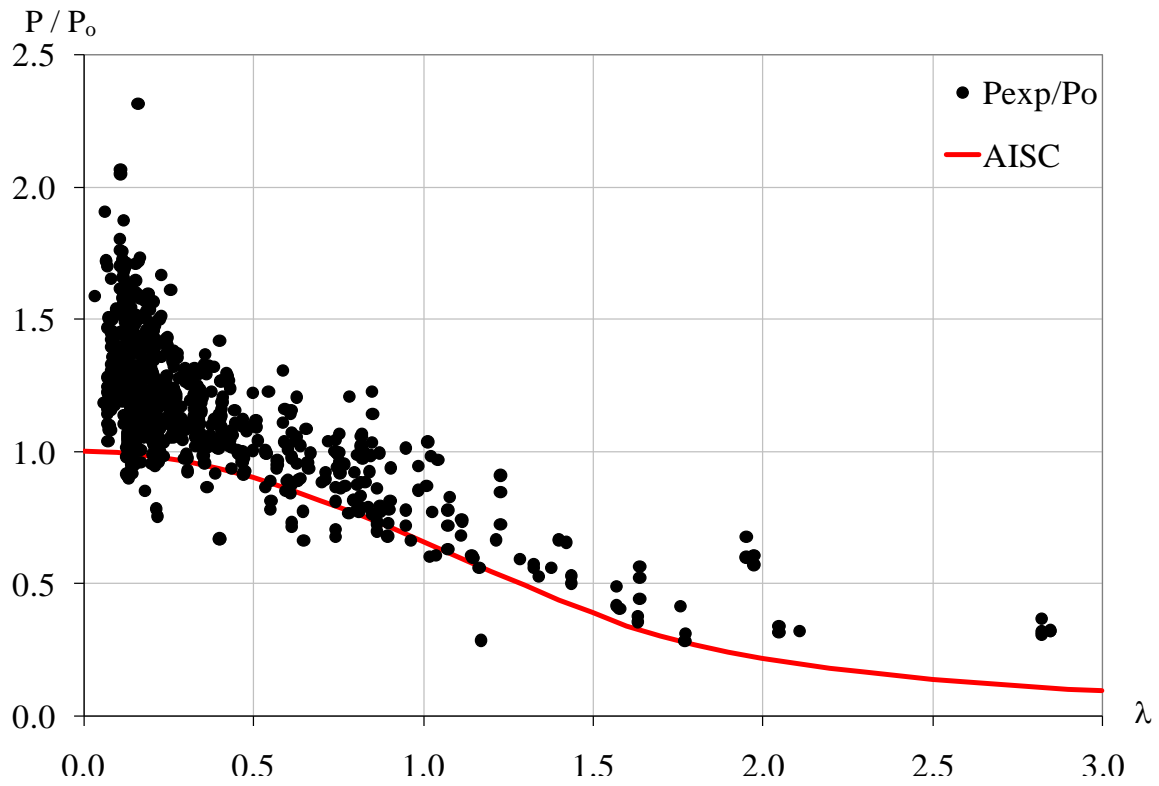


Figure 2.3. Experimental vs. analytical column curve for CCFTs

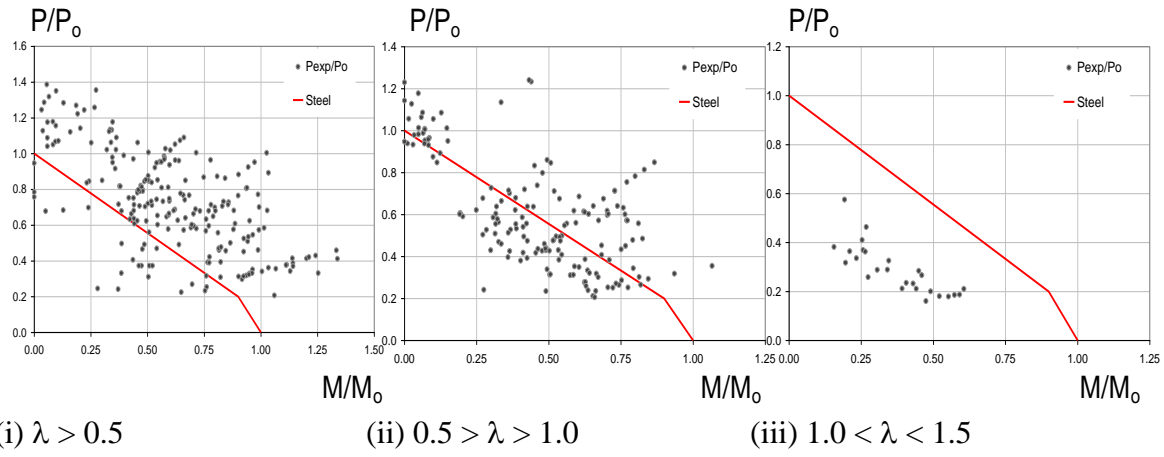


Figure 2.4. Normalized experimental strength obtained for CCFT beam-columns for different slenderness parameter (λ) ranges.

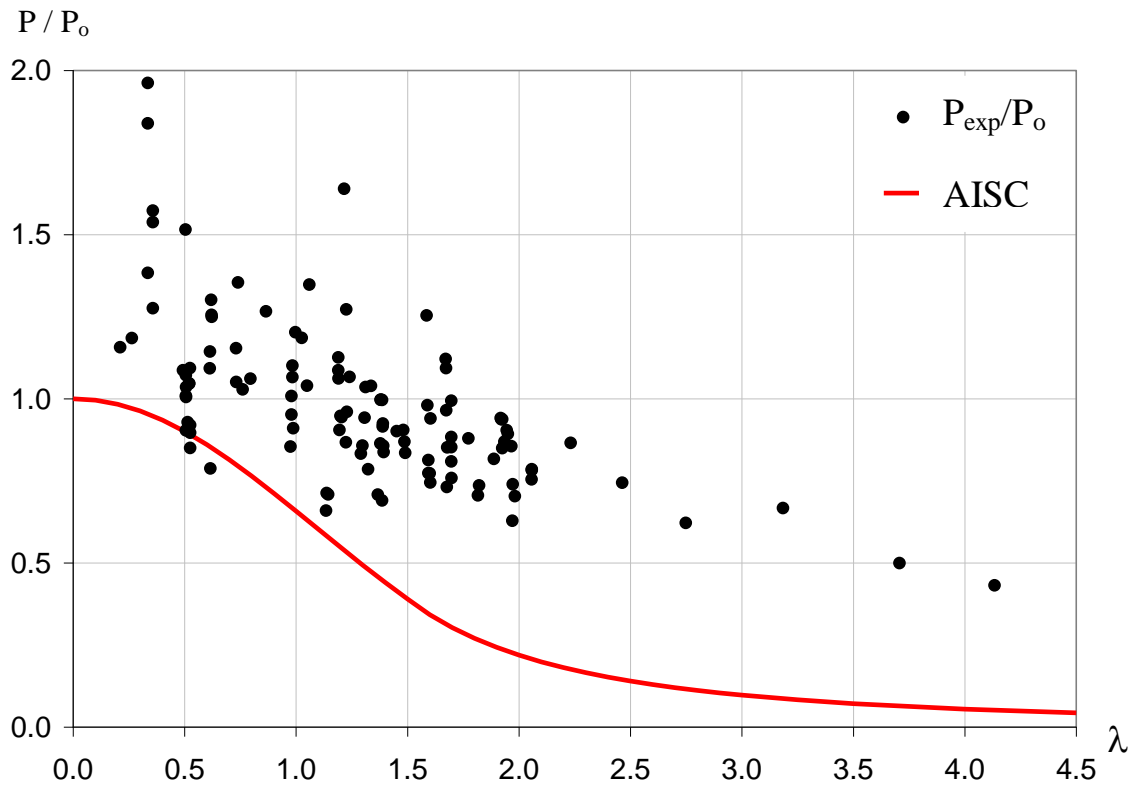


Figure 2.5. Experimental vs. analytical column curve for SRCs

All these plots clearly show where the lack of experimental data is or, conversely, what parameters have been explored in most of the experimental tests. In summary, and as illustrated in these figures, most experimental data is concentrated in:

- Short and intermediate slender columns ($\lambda < 1.5$), a range where the inelastic buckling strength governs.
- Mainly normal strength concrete ($f_c' < 4$ ksi).
- Conventional yield stress ($36 \text{ ksi} < F_y < 50 \text{ ksi}$) in the steel.
- Low D/t ratios in CFT specimens ($D/t < 20$).
- Low steel reinforcement ratio in SRC specimens ($\rho < 1\%$).

These observations guided the selection of CFT specimens with the following characteristics for this experimental work:

- Slender columns ($\lambda > 1.5$) were preferable, to study a range where the second order effects are higher and elastic buckling strength governs.
- CFTs filled with moderate strength concrete ($f_c' = 5$ ksi) and high strength concrete ($f_c' = 12$ ksi).
- Section with the highest D/t ratios available in the HSS steel market.
- A wide variety of HSS cross-sections, from tubes with small cross-section size where the slenderness and so the second order effects dominate, up to tubes with the highest available cross-section size that are common in real civil constructions.
- Specimens with a length that can be handle in the laboratory ($17'6'' < L < 26'6''$).
- Specimens with a strength that can be achieved in the laboratory ($P_n < 1320$ kips, $M_D < 8000$ kip-ft, $V < 880$ kips).

The final selection and discussion of the experimental CFT test matrix used in this research is shown in Chapter 3.

2.3. Concrete casting effects

Similarly to conventional steel frame construction, buildings with CFT columns are commonly constructed with the erection of continuous columns that stretch over a number of stories, followed by the connection to the girder-beam system and the metal deck. In composite system with CFTs, the casting of the concrete in columns is a critical task in the construction process since the pre- and post-construction sequence, as well as the final strength and stiffness of the composite element, depends on this task. Thus, a careful concrete casting is needed to ensure good quality and integrity of the concrete and the composite element once this hardens.

The common process to cast-in-place the concrete in practice is either casting the concrete through the hollow section at the top (Figure 8.a), or pumping the concrete from a cut opening close to the bottom (Figure 8.b). Each of these approaches offers different advantages, but the main purpose of both pursues the same goal, the integrity of the concrete. Modern pumping concrete techniques reduce concrete segregation, but they require a repair (plug welded) for the pump opening once the concrete hardens. Pouring concrete from the top avoids the hassle of cutting and repairing the steel tube, but it may require a careful concrete placement to avoid segregation and voids. This can be solved introducing the pumping hose as deep as possible into the tubes so as to minimize the dropping distance, and/or using special concrete (i.e. Self-Consolidating Concrete, *SCC*) that minimizes segregation. Either the casting or the pumping techniques have the same issues as regards to vibration of conventional concrete. Since *SCC* does not require vibration, this special concrete is advantageous for the casting of composite CFT members.

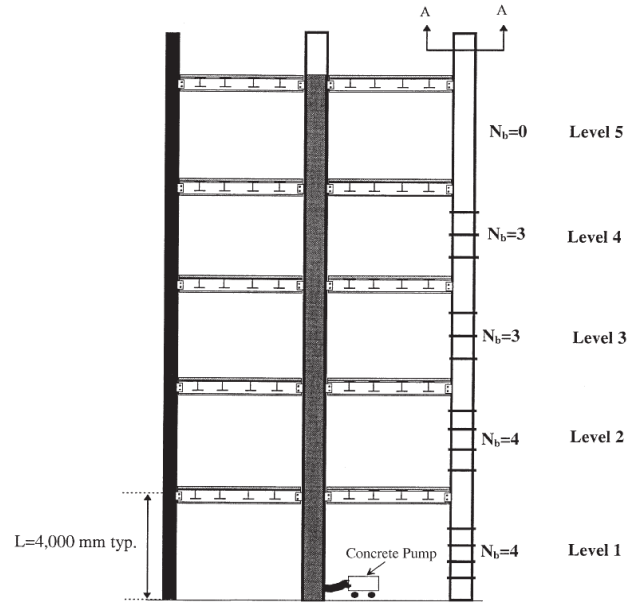
When the concrete is placed into the steel tubes (with either technique), the concrete introduces hydrostatic pressures on the walls that force the steel tube to distort. This radial expansion can be critical for rectangular shapes under a high hydrostatic pressure (i.e. casting of either long columns, or bottom columns when several upper stories are also being cast).

In high-rise buildings, concrete casting for several stories is common to speed up the construction process, but the amount of hydrostatic pressure coming from the wet concrete can be significant, even when the connected beams restrain the expansion at each story. The pressure between stories swells the tubes, with this distortion being critical in the lower columns. The practical solution to avoid this issue is adding temporal braces or lateral reinforcement to

minimize the expansion (Figure 6.b and 7.b). Eventually, the concrete sets with the shape given by the steel tube acting as a formwork, and finally the concrete hardens and the elements start working in composite action.



(a) Pouring (Bergmann *et al.*, 1995)



(b) Pumping (Uy and Das, 1999)

Figure 2.6. Concrete filling procedure on site of a RCFT

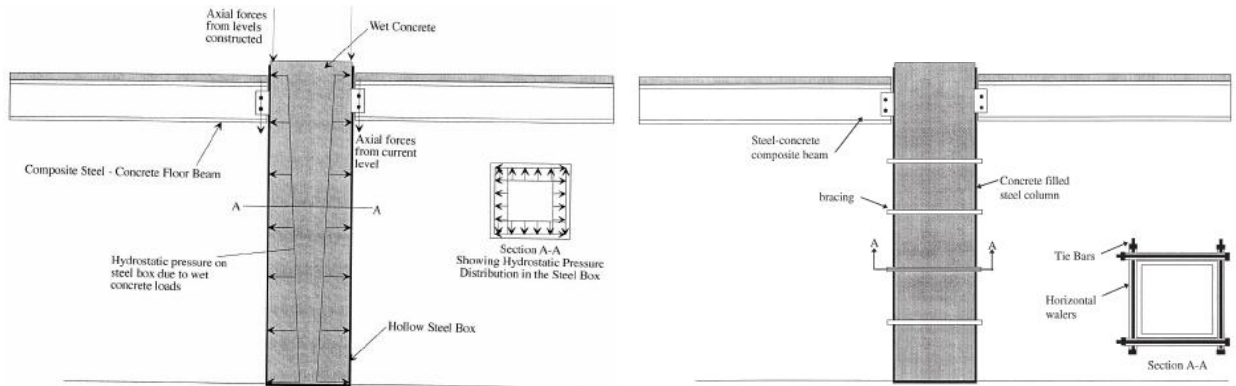


Figure 2.7. Hydrostatic pressure from wet concrete and temporal reinforcement in RCFTs that reduces the radial expansions (Uy and Das, 1999)

Analytical investigation of the wet concrete effects has been previously reported by Uy and Das (1997, 1999) through a folded plate finite element approach for thin-walled steel boxes with and without a temporal lateral reinforcement. The variables investigated by these authors in their parametric study included: number of simultaneous stories being casted (N_s), number of equally-distributed braces between floor stories (N_b), h/t ratios, and boundary conditions.

Figure 2.8 shows the results for the estimated lateral deflection in a double-pinned square steel-box column ($L=4$ m, $h=150$ cm, $h/t=40$) with different amounts of lateral braces (N_b) and wet concrete pressure from the upper stories (N_s). As expected, their results for the estimated lateral deflection are reduced with closer brace spacing and increased for higher spacing when simultaneously cast with upper stories. These authors pointed out that, as shown in Figure 2.9, the maximum lateral deflection in the lower columns moves from a low position towards the column mid-span with an increase in the number of simultaneous upper stories being cast.

For this research, the effects of the wet concrete are also investigated. The results of the experimental results are shown in Chapter 4.

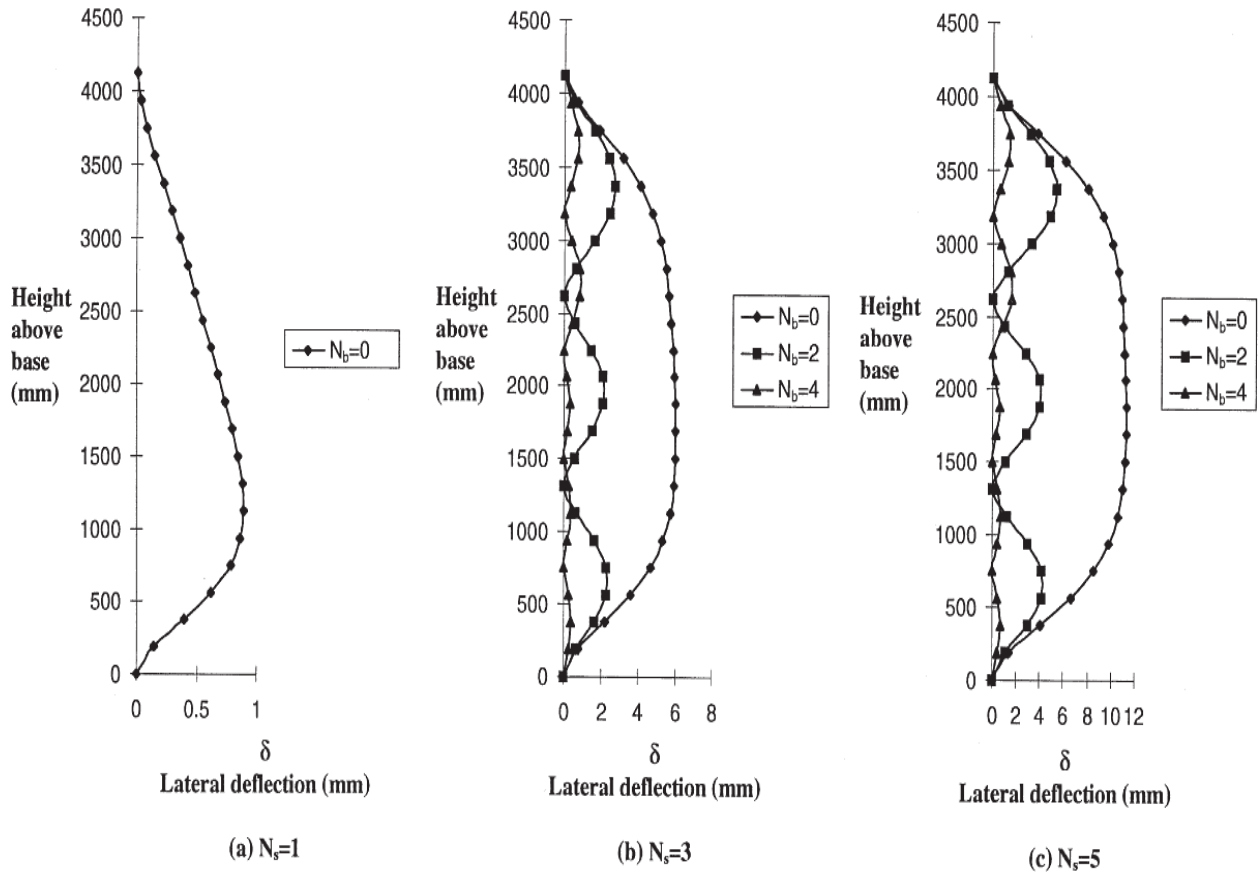


Figure 2.8. Lateral deflection estimated by Uy and Das (1999) for a double-pinned square steel-box column with different lateral brace spacing (N_b) and upper story pressure (N_s)

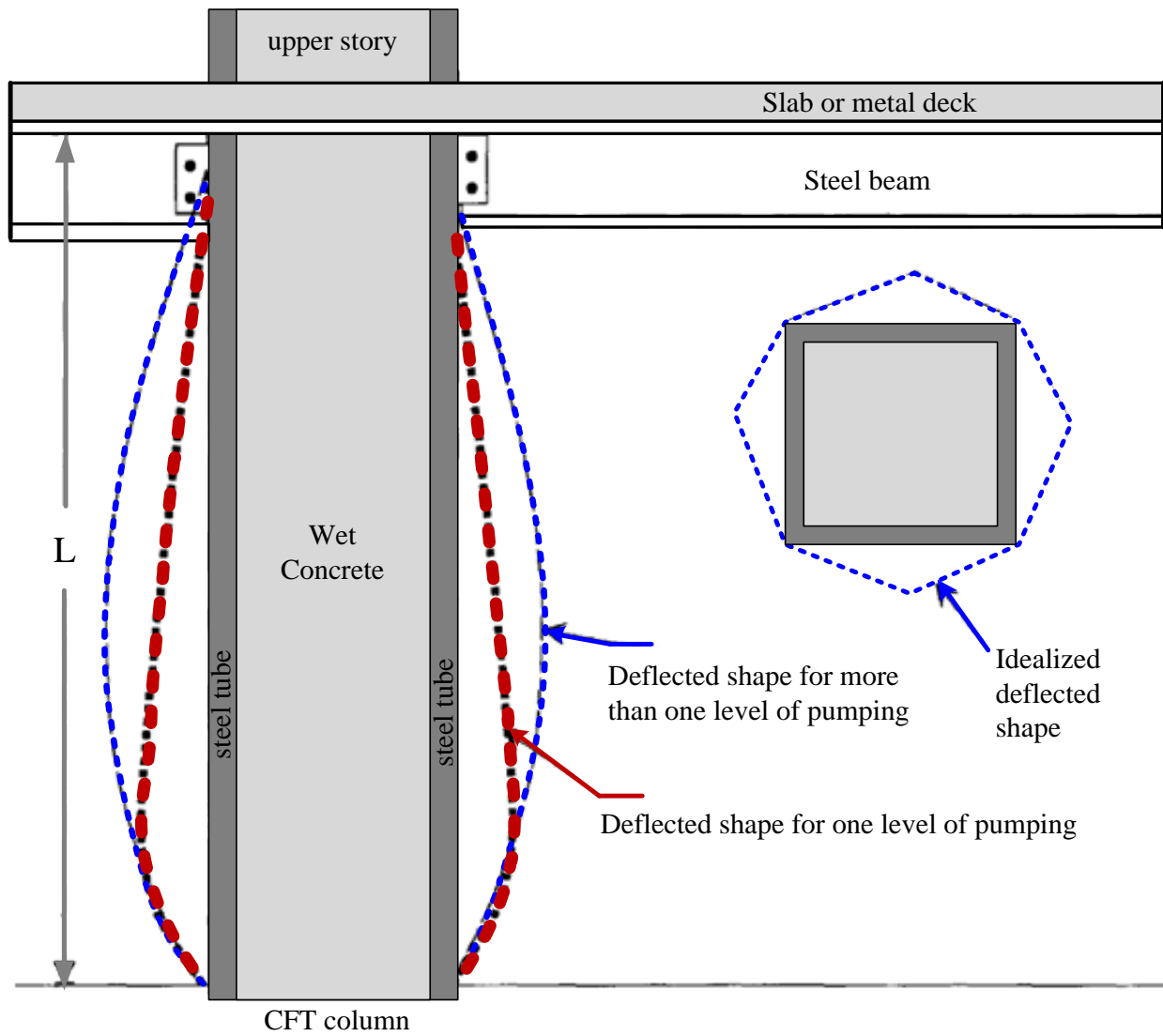


Figure 2.9. Deflected shape tendency in RCFTs (adapted from Uy and Das, 1999)

2.4. Previous analytical research studies

2.4.1. Material constitutive models

When CFT columns are subjected to compression force, both the steel tube and the concrete core expand laterally due to Poisson's effect. In the early stages, the steel tube expands at a greater rate than the concrete core since its Poisson's ratio ($\nu_s \approx 0.3$) is larger than the corresponding value in the concrete ($\nu_c \approx 0.2$). However, as the loading continues the rate of lateral expansion, the concrete core starts developing micro-cracks that increase the rate of its lateral expansion until, eventually, the radial contact interaction between the steel and the concrete occurs, thus developing a confinement pressure on the concrete and a hoop stress in the steel. This interaction vanishes on those spots when the steel-concrete contact is lost due to some flexural buckling, steel local buckling, or any other loading or effects that tend to reduce the composite action on the member. This steel-concrete interaction is more difficult to track with more complex loading protocols (i.e. cyclic loading), and so a comprehensive formulation on the constitutive materials is needed to better estimate the overall response.

The accuracy of the analytical response prediction of CFT members and structures depends strongly on the ability of the constitutive relations to provide realistic estimations on its monotonic and cyclic behavior. Initial analytical studies on CFT members used the available material constitutive models initially developed for reinforced concrete only and structural steel only without the steel-concrete composite interaction between these two materials that accounts for the salient features of CFT members.

For simplicity, elastic-perfectly-plastic or rigid-plastic models (Figure 2.10) were initially used for both the steel and concrete in order to estimate the maximum strength of composite cross-sections (i.e. Roik and Bergmann, 1992). The use of these simplistic models, demonstrated an accurate estimation in the ultimate capacity of CFT cross-sections through simplified equations that have been adopted in many code provisions for design purposes (i.e. AISC, 2005; EC-4, 2004, AIJ, 2003). The application of the set of equations developed based on the rigid plastic model is also known as the plastic stress method.

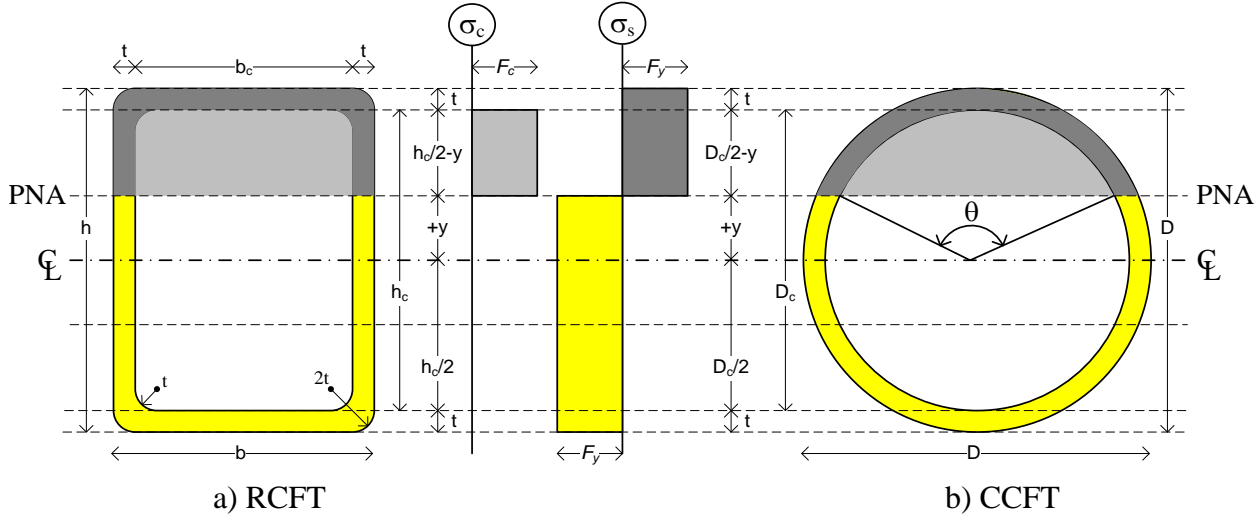


Figure 2.10. Fully-plastic stress distribution in composite cross-sections

When the entire non-linear response is of interest, more complex uniaxial stress-strain curves are needed. The application of the material properties using their actual stress-strain curves and the assumption that plane section always remains plane is also known as the strain compatibility method.

In the literature, numerous of constitutive relations have been derived as explicit functions of stress and strain and are commonly utilized in nonlinear analysis of steel and reinforced concrete structures (i.e. Ramberg and Osgood, 1943; Menegotto and Pinto, 1973; Balan et al., 1998 to give but a few examples).

In addition, numerous research studies have focused on the stress-strain response of reinforced concrete, and some are relevant to the response of CFT members such as those developed by Kent and Park (1971), Popovics (1973), Chen and Chen (1975), Sheikh and Uzumeri (1982), Mander *et al.* (1988), Collins and Mitchell (1990), Saatcioglu and Razvi (1992), Chang and Mander (1994), Amer-Moussa and Buyukozturk (1990), Cusson and Paultre (1995), Attard and Setunge (1996), Lee and Fenves (1998), Palermo and Vecchio (2003), Grassl and Jirasek (2006), among others. For structural steel, the relation between stress and strain has been associated through a set of hardening and flow rules (Dafalias and Popov, 1975; Cofie and Krawinkler, 1985; Mizuno *et al.*, 1992; Shen *et al.*, 1995). Cyclic characteristics of these formulations are modeled by introducing internal variables and incorporating them with the constitutive relations.

Table 2.2 shows a list of some available constitutive material models developed for reinforced concrete members, steel members, and CFT members. Even though the references listed in this table is not comprehensive, it gives an idea of the diversity of the models that can be applicable in CFT members.

Table 2.2. Some material constitutive models in the literature developed for CFT

Members	Reference	Comment
Reinforced Concrete	Kent and Park (1971)	Composed by a function up to the peak stress, and a bilinear function for the post-peak
	Popovics (1973)	Continuous function for the pre- and post-peak
	Mander <i>et al.</i> (1988)	Confinement due to the lateral reinforcement is accounted in circular and rectangular sections
	Chang and Mander (1994)	Confinement, cracking, degradation for monotonic and cyclic behavior is modeled
Steel	Menegotto and Pinto (1973)	Smooth elastic-to-plastic transition, elastic unloading, isotropic and kinematic hardening, and Bauschinger effects
	Shen <i>et al.</i> , 1995	Smooth elastic-to-plastic transition, elastic unloading, isotropic and kinematic hardening, Bauschinger effects, stiffness and strength degradation, and local buckling
	Mizuno <i>et al.</i> , 1992	Plasticity model with yield plateau, reduction of elastic range, movement of bounding lines, decrease and disappearance of yield plateau during cyclic loading
CFT	Elremaily and Azizinamini (2002)	Chang-Mander model used for concrete and elastic-perfectly-plastic model used for steel
	Sakino <i>et al.</i> (2004)	Concrete model proposed with confinement effects. Elastic-perfectly-plastic used for steel with a softening for local buckling
	Nakahara <i>et al.</i> (1998))	Stress-strain relationships for concrete with confinement and steel tubes with local buckling
	Susantha <i>et al.</i> (2001)	Uniaxial stress–strain relationship for the concrete confined by various shaped steel tubes
	Varma (2000)	Stress–strain curves for steel and concrete were obtained from FEA, implicitly accounting for the effects of local buckling and biaxial stresses in the steel tube and the confinement in concrete
	Hatzigeorgiou (2008)	Monotonic stress–strain relationship for confined concrete is proposed. Elastic-perfectly-plastic model was used to model the steel
	Tort and Hajjar (2007)	Based on Chang-Mander for concrete, Mizuno and Shen for steel, with adjustments for RCFTs
	Denavit and Hajjar (2010)	Based on Chang-Mander for concrete and Shen for steel, with adjustments for CCFTs

The constitutive models adopted to simulate the monotonic and cyclic behavior of CFT members should be comprehensive enough to capture the characteristics that have influence on the overall response. Among the desired features recommended by Hajjar (2000) for the concrete constitutive model to capture the response of CFT members are:

- Smooth transition from elastic to plastic response, following the monotonic compressive envelope in the pre- and post-peak range
- Capture of the effective tensile response and the cracking opening-closing effects under cycling loading
- Increment in ductility and strength due to the confinement effects in the concrete as a consequence of the contact with the steel tube
- Elastic unloading following the load reversal. However, the elastic stiffness degrades due to the concrete crushing and cracking with monotonic or cyclic loading
- Decreasing in the size of the elastic zone in cycling loading due to the concrete crushing and cracking
- Complex strength and stiffness degradation rules as a result of cyclic loading

Among the desired features for the steel constitutive model to capture the response of CFT members, as recommended by Hajjar (2000), are:

- Smooth transition between elastic and plastic response, rather than formation of a significant yield plateau
- Elastic unloading following the load reversal
- Bauschinger effect causing a reduction in the yield stress when the direction of strain changes
- Decreasing elastic zone and gradual stiffness reduction as a result of a cyclic loading
- Gradient of the yield stress along the perimeter of the steel tube
- A bounding stiffness that is attained near the end of the tests due to the stabilizing action of the steel tube
- Residual stresses as a consequence of the manufacturing process of the steel.
- When cold-formed steel tube sections are used, the effects of the cold-forming process must be considered
- Local buckling of the steel tube

- Steel fracture may be neglected in CFTs since these are robust members that rarely fracture until very late in cyclic loading histories or with an extremely high load and displacement condition

The following section briefly describes some of the uniaxial constitutive models developed for CFT members.

2.4.1.1. Sakino et al. (2004)

Sakino and Sun (1994) proposed a unified stress-strain model for concrete confined by steel tubes and/or conventional hoops. Based on this model, Sakino *et al.* (2004) enhanced this constitutive materials model for circular and rectangular CFT members accounting for confinement, local buckling, and biaxial stresses. The latter model was based on empirical data calibration of centrally loaded short CFT columns, as part of fifth phase of the U.S. – Japan Cooperative Earthquake Research Program. The proposed stress-strain envelope for both concrete in compression and the structural steel are shown in Figure 2.11 and Figure 2.14, respectively.

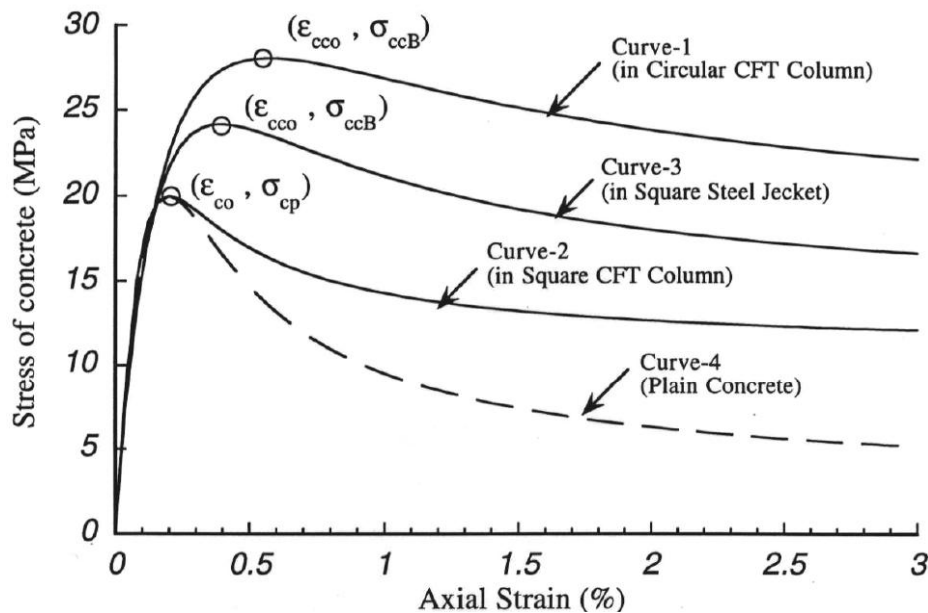


Figure 2.11. Stress-strain (σ - ϵ) curves obtained from the Sakino model for a 5 ksi strength concrete confined by a steel tube with different width-to-thickness ratios.

Equation 2.1 describes the monotonic σ - ε curve for concrete proposed by Sakino *et al.* (2004), which is in terms of the effective hoop stresses (σ_{re}) and the peak concrete strength.

$$\sigma(\varepsilon) = f_{cc}' \left(\frac{V(\varepsilon/\varepsilon_{cc}) + (W-1)(\varepsilon/\varepsilon_{cc})^2}{1 + (V-2)(\varepsilon/\varepsilon_{cc}) + W(\varepsilon/\varepsilon_{cc})^2} \right) \quad (2.1)$$

The parameters V and W are defined by:

$$V = \frac{E_c \varepsilon_{cc}}{f_{cc}'} \quad (2.2)$$

$$W = 1.5 - 0.0171 f_c' [MPa] + 2.39 \sqrt{\sigma_{re} [MPa]}$$

The effective hoop stresses (σ_{re}) and the peak strength values for circular CFTs are:

$$\sigma_{re} = \frac{0.0677 F_y}{D/t - 2}$$

$$f_{cc}' = \gamma_u f_c' + \frac{1.558 F_y}{D/t - 2} \quad (2.3)$$

$$\varepsilon_{cc} = \begin{cases} \varepsilon_c \left[1 + 4.7 \left(\frac{f_{cc}'}{f_c'} - 1 \right) \right] & \text{if } f_{cc}' < 1.5 f_c' \\ \varepsilon_c \left[3.35 + 20 \left(\frac{f_{cc}'}{f_c'} - 1.5 \right) \right] & \text{if } f_{cc}' \geq 1.5 f_c' \end{cases}$$

Correspondingly, for rectangular CFTs the values are:

$$\sigma_{re} = \frac{2(b/t - 1) F_y}{(b/t - 2)^3}$$

$$f_{cc}' = \gamma_u f_c' \quad (2.4)$$

$$\varepsilon_{cc} = \varepsilon_c = 0.94 \times 10^{-3} (f_c' [MPa])^{0.25}$$

In the previous equations, γ_u is a factor that accounts for the scale effects of the structural members. This factor was calibrated with experimental tests (Figure 2.12) of both circular and rectangular concrete sections as: $\gamma_u = 1.67 (D - 2t)^{-0.112}$.

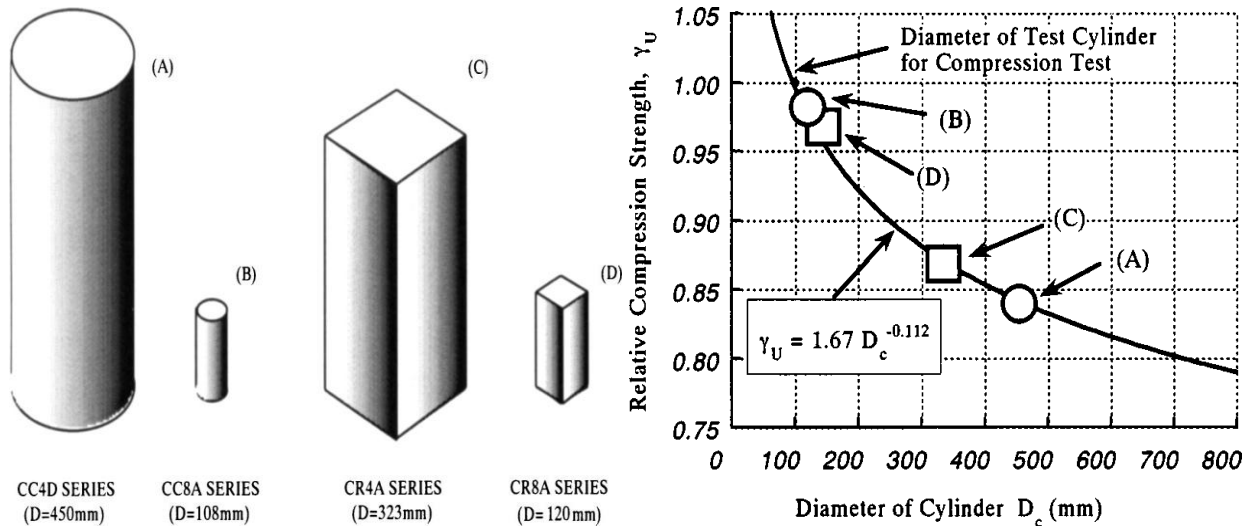


Figure 2.12. Scale effect factor on compressive strength of circular plain concrete columns

Figure 2.13 shows σ – ϵ curves obtained with the Sakino concrete model for a 5 ksi strength concrete that is confined by circular and rectangular steel tubes with width-to-thickness ratios (D/t , b/t) of 50 and 100, respectively. As shown in this figure, confinement improves strength and ductility in circular CFTs but only ductility in rectangular CFTs.

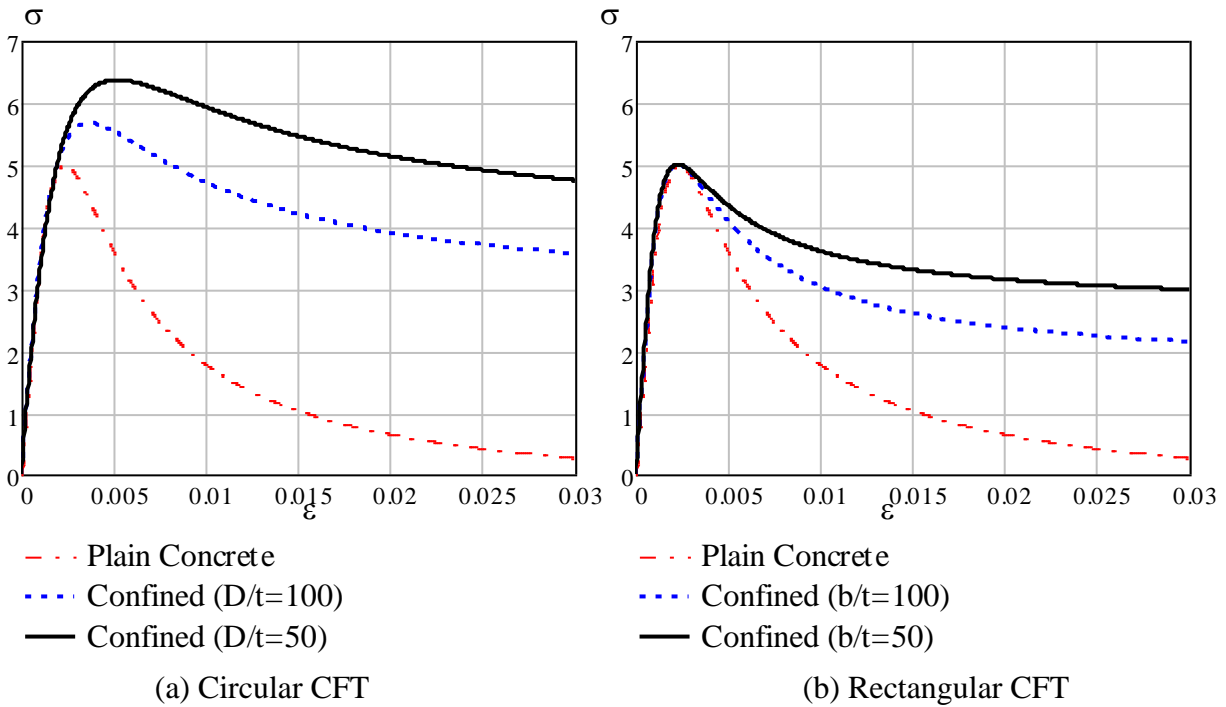


Figure 2.13. Stress-strain (σ – ϵ) curves obtained from the Sakino model for a 5 ksi strength concrete confined by a steel tube with different width-to-thickness ratios.

Conversely, steel tubes in CFT members are proposed to be modeled through an unsymmetrical σ – ε curve with yielding stress equals to $1.09F_y$ in tension and $0.89F_y$ in compression that satisfies biaxial stresses with the Von Misses yield criteria, where F_y is the nominal yield stress of the steel. Depending on the width/thickness ratio, local buckling in RCFTs can be handled by a descending branch of the σ – ε curve at a critical strain. A careful calibration of the experimental data is needed to obtain the strain when local buckling takes place. Sakino model postulates that the strain at local buckling in CCFTs is reached at high values of strain, and therefore, local buckling effects can be neglected. This approach is tied to the Japanese design requirements for width/thickness ratios, which preclude this failure mode.

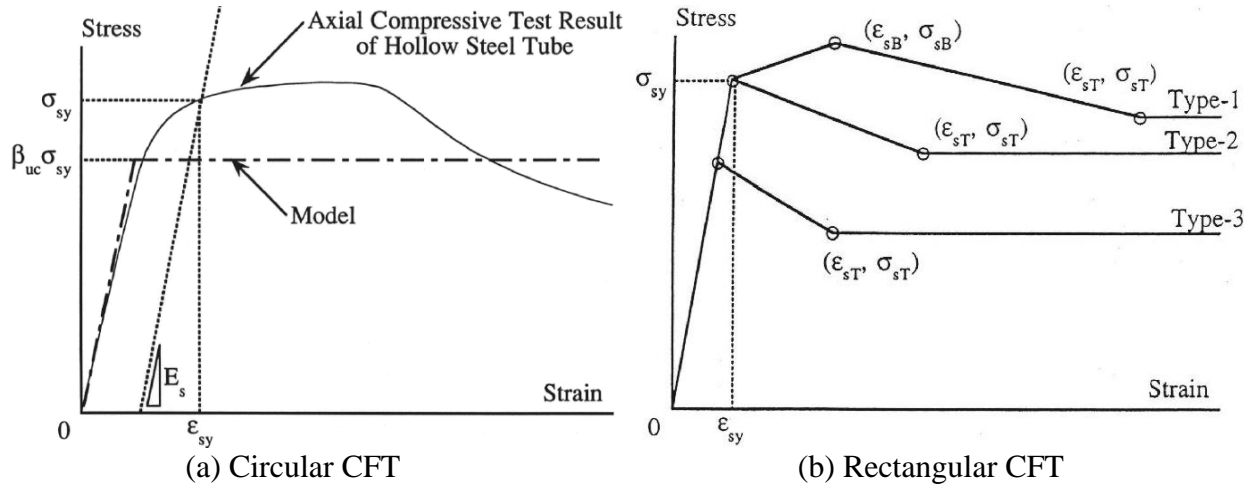


Figure 2.14. Stress-strain (σ – ε) for the steel tubes used with the Sakino model

2.4.1.2. Tort and Hajjar (2007) and Denavit and Hajjar (2010)

A three-dimensional distributed plasticity beam element formulation was developed for rectangular CFTs by Tort and Hajjar (2007) and for circular CFTs by Denavit and Hajjar (2010). Similar to the Sakino model, these two references utilize uniaxial cyclic constitutive models for the concrete core and steel tube that account for the salient features of each material, as well as the interaction between the two, including concrete confinement, concrete tensile strength, and local buckling of the steel tube. Robust hysteretic rules for the non-linear cyclic response were adopted in these comprehensive models.

The concrete material models used in both references are based in the model proposed by Chang and Mander (1994) and Tsai (1988), with improvements to better predict the concrete response to monotonic and cyclic loading of all possible cases for RCFTs (Tort and Hajjar, 2007) and CCFTs (Denavit and Hajjar, 2010).

The monotonic response in compression as proposed by Chang and Mander (1994) is defined by the Equation 2.5, where the parameter $D(\varepsilon)$ is defined by the Equation 2.6:

$$\sigma(\varepsilon) = f_{cc} \frac{n}{D(\varepsilon)} \frac{\varepsilon}{\varepsilon_{cc}} \quad (2.5)$$

$$D(\varepsilon) = \begin{cases} 1 + \frac{\varepsilon}{\varepsilon_{cc}} \left(n - \frac{r}{r-1} \right) + \frac{(\varepsilon/\varepsilon_{cc})^r}{r-1} & \text{for } r \neq 1 \\ 1 + \frac{\varepsilon}{\varepsilon_{cc}} \left(n - 1 + \ln \frac{\varepsilon}{\varepsilon_{cc}} \right) & \text{for } r = 1 \end{cases} \quad (2.6)$$

The parameters n and r depend on the concrete strength and stiffness. The parameter for the post-peak factor in compression (r) is given by:

$$r = \begin{cases} f'_c [\text{MPa}] / 5.2 - 1.9 & \text{for } \varepsilon > \varepsilon_{cc} \\ 0.4 + 0.016(D/t)(f'_c/F_y) & \text{for } \varepsilon \leq \varepsilon_{cc} \text{ and CCFT} \\ 0.3 + 0.11(D/t)(f'_c/F_y) & \text{for } \varepsilon \leq \varepsilon_{cc} \text{ and RCFT} \end{cases} \quad (2.7)$$

The peak stress (f_{cc}) and the corresponding strain (ε_{cc}) of concrete confined by the steel in RCFTs are equal to those obtained for unconfined concrete. The strain at the peak stress (ε_c) for unconfined concrete (applicable to RCFTs) is given by Chang and Mander (1994) as:

$$\varepsilon_c = \frac{f'_c [\text{MPa}]^{1/4}}{28} \quad (2.8)$$

The strain at the peak stress (ε_{cc}) for confined concrete (applicable to CCFTs) is given by Richart et al. (1929) as:

$$\varepsilon_{cc} = \varepsilon_c \left(1 + 5 \left(\frac{f_{cc}}{f'_c} - 1 \right) \right) \quad (2.9)$$

For CCFTs, the peak stress (f_{cc}) as proposed by Mander *et al.* (1988) is equal to:

$$f_{cc} = f_c' \left(-1.254 + 2.254 \sqrt{1 + \frac{7.94 f_l}{f_c'}} - 2 \frac{f_l}{f_c'} \right) \quad (2.10)$$

The confinement pressure (f_l) in CCFTs proposed by Denavit and Hajjar (2010) is:

$$f_l = \left(0.138 - 0.00174 \frac{D}{t} \right) \frac{2F_y}{D/t - 2} \geq 0 \quad (2.11)$$

The initial concrete stiffness used in this model is defined as:

$$E_c [\text{MPa}] = 8,200 f_c' [\text{MPa}]^{3/8} \quad (2.12)$$

Figure 2.15 illustrates the strength of confined concrete (f_{cc}) by a circular steel tube with given wall slenderness ratios ($\lambda = D/t$) as obtained from Equation 2.10 calibrated by Denavit and Hajjar (2010), and from Equation 2.3 proposed by Sakino *et al.* (2004). The values in this figure are obtained assuming an unconfined concrete of 5 and 12 ksi of strength, and the steel tube with a nominal yielding stress of 42 ksi. This figure shows higher values of confined concrete strength from the Sakino's equation. As seen in Figure 2.15, Denavit and Hajjar's calibration illustrates no influence on the concrete strength when the CCFT cross-section is composed by circular tubes with D/t ratios greater than 79; according to Equation 2.11, the confinement pressure (f_l) above this value becomes zero and so the concrete is controlled by its unconfined strength.

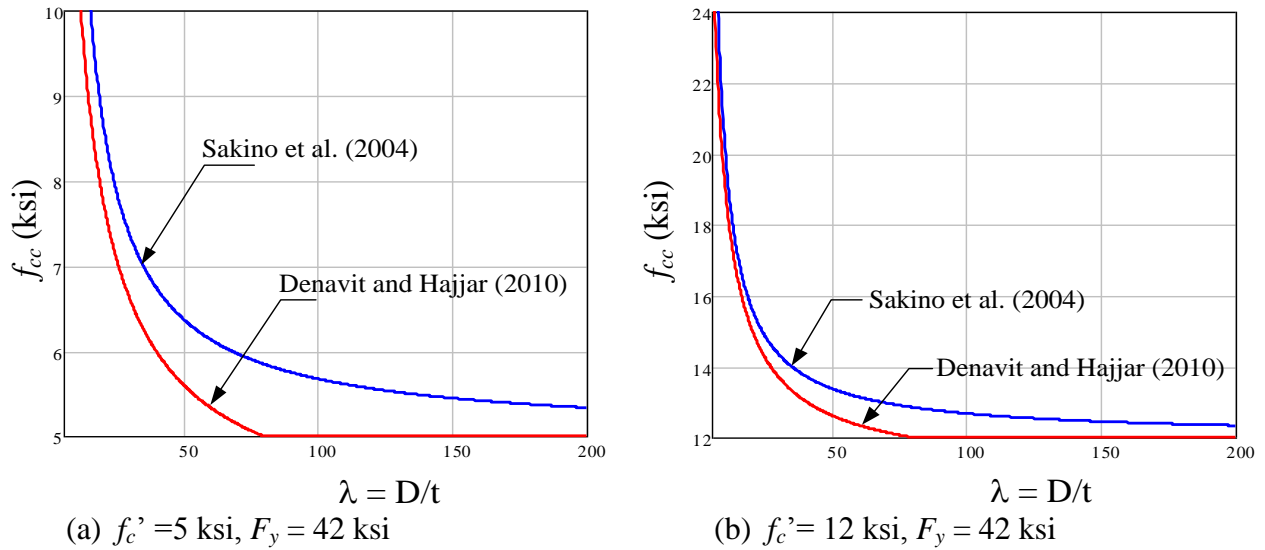


Figure 2.15. Confined concrete strength (f_{cc}) vs. wall slenderness ratio ($\lambda = D/t$) of circular steel tubes from the calibration by Sakino *et al.* (2004) and by Denavit and Hajjar (2010) for CCFTs

Figure 2.16 shows the monotonic and cyclic stress-strain response implemented in Tort and Hajjar (2007) for the concrete core in RCFTs. The robustness of the hysteretic rules in cycling loading is illustrated in Figure 2.16.b through a complex determination of the hysteretic loops in the confined concrete by the rectangular tube and its tension strength.

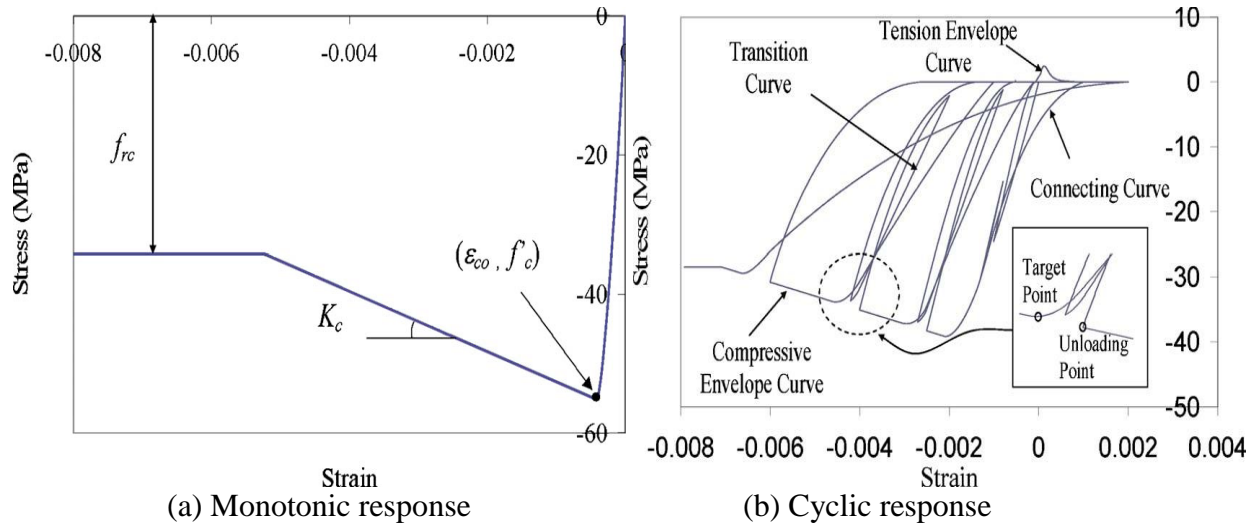


Figure 2.16. Stress-strain constitutive model implemented in Tort and Hajjar (2007) for the concrete core in RCFTs

Similarly, Figure 2.17 shows the backbone stress-strain curve implemented in Denavit and Hajjar (2010) for the concrete core in CCFTs. The influence of the concrete strength filled into tube with a given diameter-thickness ratio (constant $D/t=50$) is shown in Figure 2.17.a. In turn, the influence of the confinement effects is shown in Figure 2.17.b, where a CCFT cross-section hold the same concrete strength ($f'_c = 50$ MPa) and is confined by tubes of different D/t ratios ($30 < D/t < 80$). As illustrated in the Figure 2.17.b, the peak stress increased as the confinement increased with D/t decrements; the strain ductility also increase with lower D/t values.

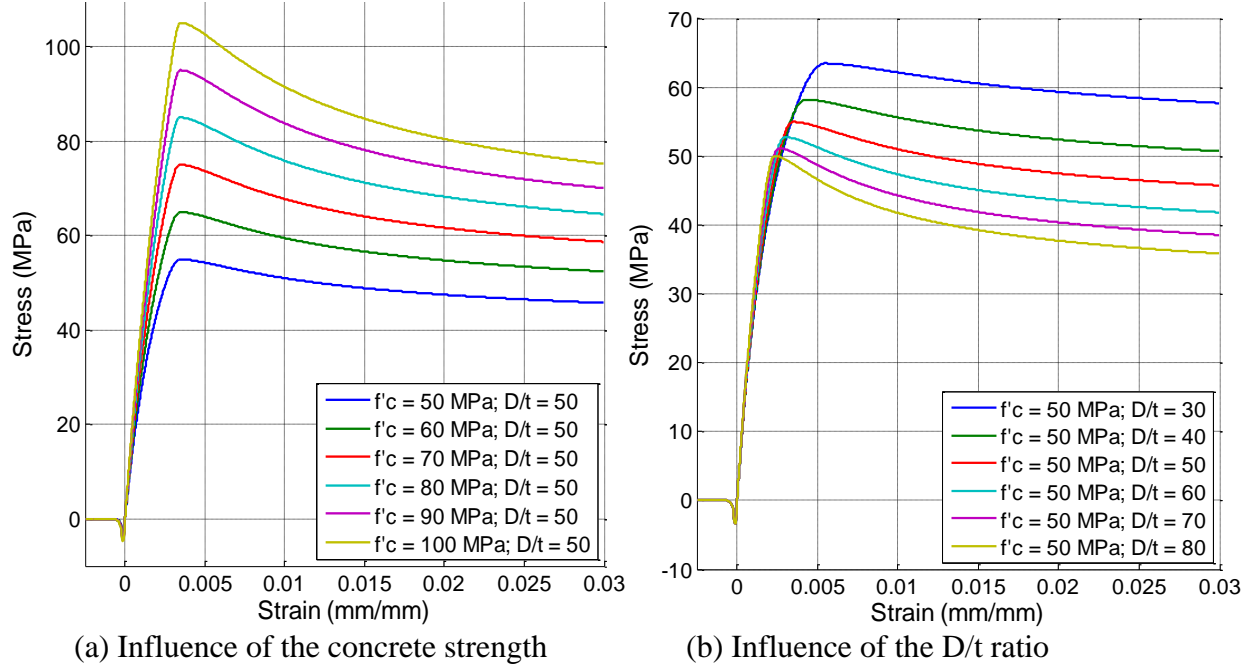


Figure 2.17. Stress-strain constitutive model implemented in Denavit and Hajjar (2010) for the concrete core in CCFTs

With respect to the steel component, the stress-strain backbone curves used by Tort and Hajjar (2007), and Denavit and Hajjar (2010) are based on the incremental bounding surface formulation proposed by Shen *et al.* (1995), with modifications for CFT members to better account for local buckling, residual strains and the hysteretic rules in the non-linear cyclic response. The improved rules on this cyclic plasticity model reproduce elastic unloading, decreasing elastic zone, Bauschinger effect, bounding stiffness and local buckling degradation.

According with Tort and Hajjar (2007) and Denavit and Hajjar (2010), the initiation of the local buckling starts at a strain given by:

$$\varepsilon_{lb} = \begin{cases} 0.214R^{-1.41} \left(F_y / E_s \right) & \text{for CCFT} \\ 3.14R^{-1.48} \left(F_y / E_s \right) & \text{for RCFT} \end{cases} \quad (2.13)$$

Where the factor R is given by:

$$R = \begin{cases} \frac{D}{t} \cdot \frac{F_y}{E_s} & \text{for CCFT} \\ \frac{h}{t} \sqrt{\frac{F_y}{E_s}} & \text{for RCFT} \end{cases} \quad (2.14)$$

The previous equations, calibrated with experimental data of CFT tests available in the literature, can be rewritten in terms of the yielding strain (ε_y) and the wall-slenderness ratio (λ) of the steel tube as shown in Equation 2.15.

$$\varepsilon_{lb} = \begin{cases} 0.214\lambda^{-1.41}\varepsilon_y^{-0.41} & \text{For CCFTs} \\ 3.14\lambda^{-1.48}\varepsilon_y^{0.26} & \text{For RCFTs} \end{cases} \quad (2.15)$$

This pair of equations is plotted in Figure 2.18, with the wall-slenderness ratio ($\lambda = D/t$ or h/t) vs. the strain at occurrence of local buckling normalized with the strain at yielding. The corresponding limiting wall-slenderness ratios (λ_p) in AISC (2010) for compact filled-tubes are marked in this figure. These limits intersect the local buckling strain of these calibrations at about one and three times the yielding strain for RCFTs and CCFTs, respectively. These comparisons suggest a reasonable limit λ_p for RCFTs, while the limit for CCFTs is quite conservative.

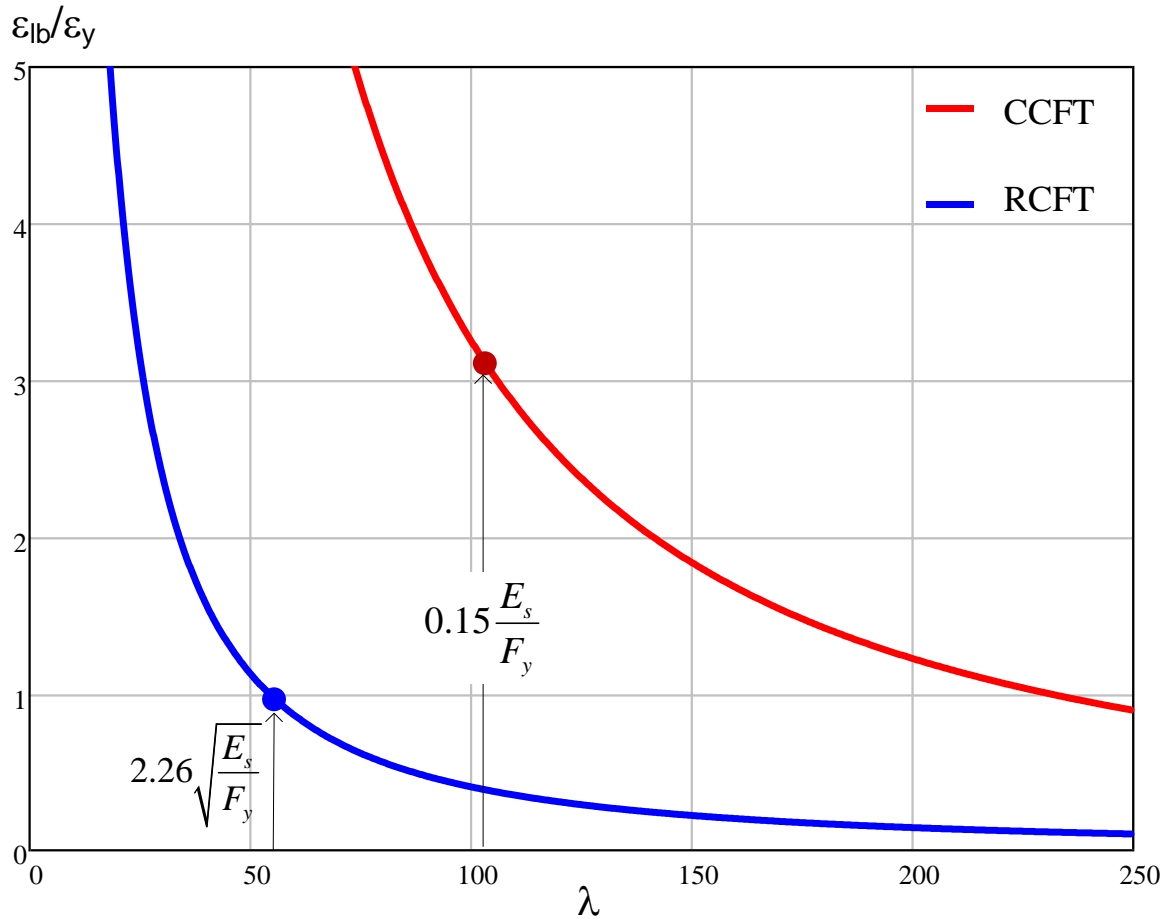


Figure 2.18. Wall-slenderness ratio vs. strain at occurrence of local buckling

Once the local buckling strain calculated with the previous equation has been exceeded, the stress-strain curve decays with a degradation slope calculated as:

$$K_s = \begin{cases} -E_s / 30 & \text{for CCFT} \\ \min(0, -3.22E_s (R - 0.08)) & \text{for RCFT} \end{cases} \quad (2.16)$$

The previous descending branch becomes constant once the residual stress is achieved with a value defined as:

$$f_{rs} = \begin{cases} \max[F_{lb}, 0.17F_{lb}/R] & \text{for CCFT} \\ \max[F_{lb}, 0.16 - 0.73RF_{lb}] & \text{for RCFT} \end{cases} \quad (2.17)$$

In turn, the residual stresses are accounted in these formulations with an initial plastic strain, which is given by:

$$\varepsilon_o^p = \begin{cases} 0.0006 & \text{for CCFT} \\ 0.0004 & \text{for RCFT flat} \\ 0.0006 & \text{for RCFT corner} \end{cases} \quad (2.18)$$

Figure 2.19 illustrates the backbone curves for the steel component for RCFTs (Tort and Hajjar, 2007) and CCFTs (Denavit and Hajjar, 2010). In Figure 2.19.a, local buckling for a rectangular tube cross-section is shown by the descending branch at the strain ε_{lb} , with a slope of K_s , until the constant stress f_{rs} is achieved. In Figure 2.19.b, a set of stress-strain curves is shown that shares the same yielding strength, but different values of the wall slenderness (D/t) in circular cross-sections. This figure illustrates compressive yielding and full plasticity without local buckling for the case with $D/t=30$, and yielding and partial plasticity for the case with $D/t=60$ (compact cross-sections). In addition, Figure 2.19.b displays a descending branch at the yielding for the case with $D/t=90$ (non-compact cross-sections), and a descending branch before yielding for the cases with $D/t=120$ and 150 (slender cross-sections).

Figure 2.20 compares the Shen's constitutive model, which includes the enhancements implemented by Denavit and Hajjar (2010), with a coupon tension test performed for a sample taken from one of the specimens tested in this research. The material and geometric properties measured (F_y , F_u , E_s) in the coupon test were used in the definition of the analytical model. With the aim of illustrating as reference the influence of local buckling in the analytical model, the tensile stress-strain obtain in the coupon test were also plotted in the compression side where a

cyclic response is illustrated. In addition, Figure 2.20 shows the analytical model for different load history paths. All these cases illustrate that the analytical model follow the coupon test envelope in tension within a low range of strains ($\epsilon < 0.005$). This range of strains, however, is wide enough to obtain a good part of the non-linear response of the element since the concrete cracking in tension, the steel local buckling, and concrete crushing in compression occur generally within this range.

Besides the material non-linearities, these authors also developed an element to account for the geometric nonlinearities. For this purpose, a distributed-plasticity mixed finite element formulation was used to allow for accurate modeling of both geometric and material nonlinearities with a favorable balance of computational efficiency and accuracy.

The distributed plasticity mixed beam finite element formulations developed previously by Tort and Hajjar (2007) was intended for the analysis of rectangular CFT members with slip between the steel tube and concrete core included. In turn, Denavit and Hajjar (2010) developed a similar element for the analysis of circular CFT members. Previously, Nukala and White, 2004 developed an element for the analysis of steel structures with section warping included.

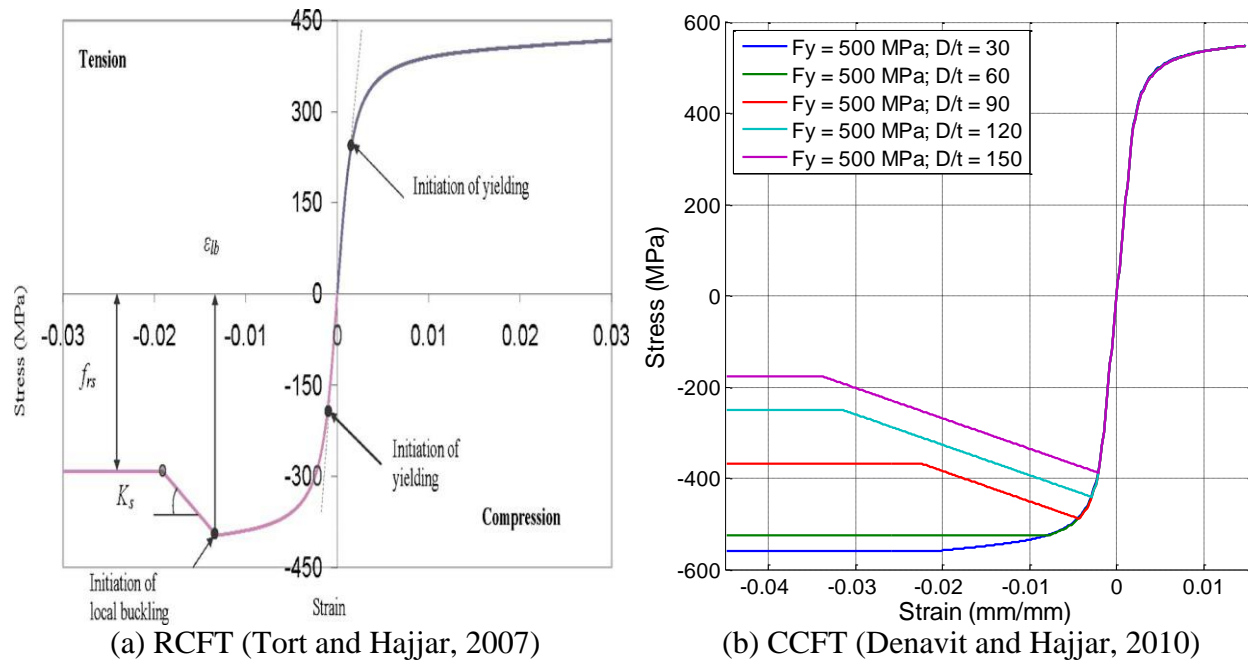


Figure 2.19. Monotonic Shen σ - ϵ model for the steel component in CFTs

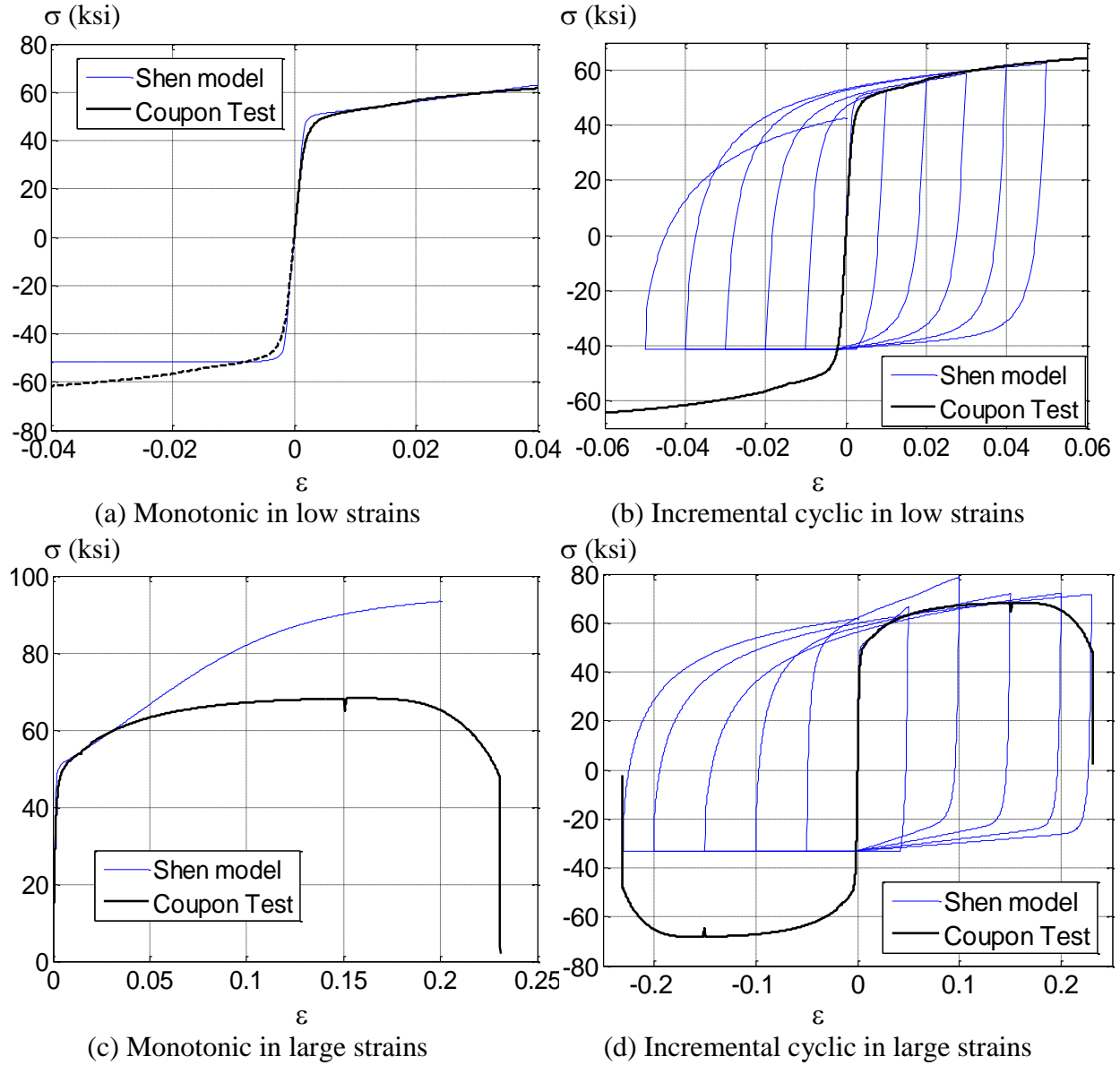


Figure 2.20. Shen σ - ϵ model for steel vs. coupon test

The material and element models developed by Tort and Hajjar (2007) and Denavit and Hajjar (2010) described in this section will be used to obtain the analytical response of the rectangular and circular CFT specimens tested in this project. For these analyses, the software OpenSees (2010) is used via a compiled version by Denavit and Hajjar (2010) with material models and mixed elements developed explicitly for CCFT and RCFT composite members, as well as the standard material and element models already built-in and developed in OpenSees.

2.4.2. Comparison of constitutive models applicable to CFTs

As commented before, there are many options to account for the material properties of CFT members. Some of these were originally developed for reinforced concrete members or steel-only members, but have been adapted to CFT composite members. The main differences in all these models are the assumptions in the parameters that influence the stress-strain envelope, and mainly on the hysteretic rules and the strength-stiffness degradation on the cyclic non-linear response.

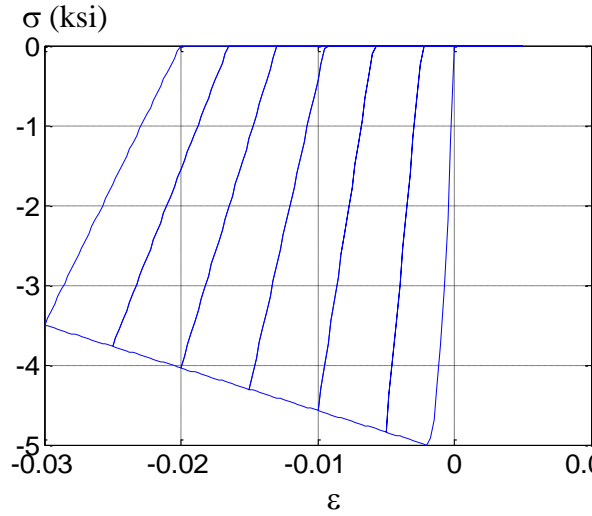
Figure 2.21 shows the cyclic response of different uniaxial stress-strain models that may be applicable to predict the response of the concrete components in CFT members. The concrete models shown in Figure 2.21.a to Figure 2.21.b are already integrated in the latest version of OpenSees (2010) that incorporate both unconfined and confined reinforced concrete.

The monotonic concrete model in Figure 2.21.e proposed by Sakino *et al.* (2004) was implemented in the OpenSees source code (Appendix C) using the same cyclic rules that were programmed in the Concrete04-Popovics model.

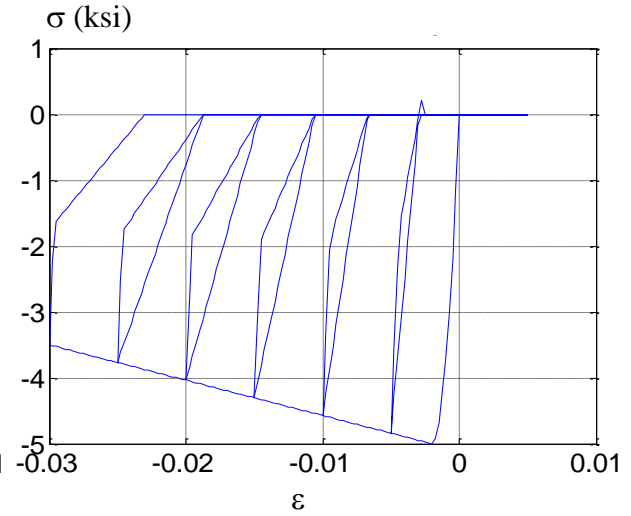
The concrete model shown in Figure 2.21.f was implemented by Denavit and Hajjar (2010) based on the Chang-Mander model and, as commented before, with enhancements to account for the concrete confinement and the non-cyclic response in CFT members. With exception of the model shown in Figure 2.21.a, all the material models shown in Figure 2.21 account for the tension capacity of concrete.

The material properties and parameters that origin the stress-strain curves in Figure 2.21.e and Figure 2.21.f correspond to those obtain for a CCFT integrated by a steel tube HSS20x¼ A-500 Gr. B, and the confined concrete in-fill with 5 ksi of strength. The material properties and parameters that origin the stress-strain curves in Figure 2.21.a to Figure 2.21.b were adopted to mimic the confined concrete response of the CCFT obtained in Figure 2.21.e and Figure 2.21.f.

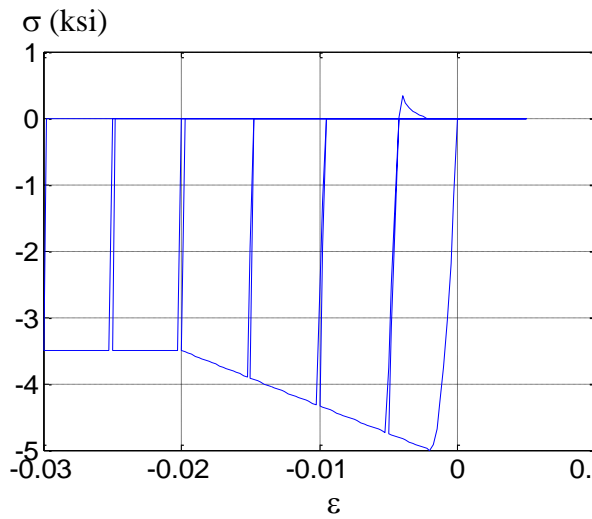
As can be noticed in these figures, the stress-strain response with the Chang-Mander model (Figure 2.21.f) illustrates the more complex and robust uniaxial response in cyclic loading.



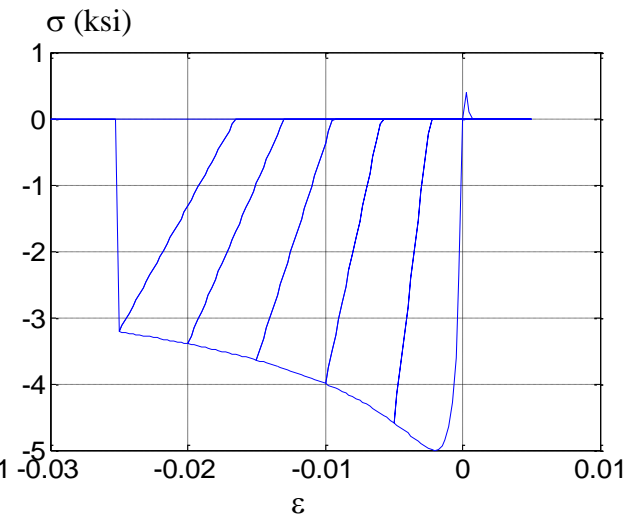
(a) Concrete01, Kent-Scott-Park



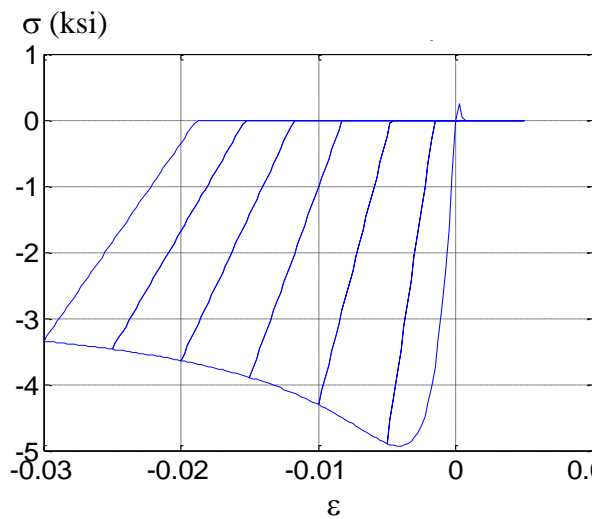
(b) Concrete02, linear tension softening



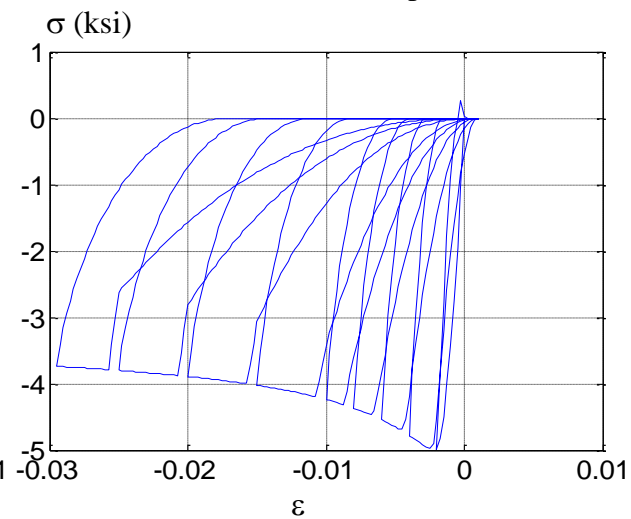
(c) Concrete03, non-linear tension softening



(d) Concrete04, Popovics



(e) Sakino



(f) Chang-Mander

Figure 2.21. Different stress-strain model available for concrete in CFTs

Similarly, Figure 2.22 shows the cyclic response of different uniaxial stress-strain models that may be applicable to predict the response of the steel component in CFT members. In addition, this figure shows the stress-strain curve obtained from a coupon test of a sample taken from one of the specimens tested in this research. To illustrate the influence of local buckling in the analytical model, the tensile stress-strain obtained in the coupon test were also plotted in the compression side.

Figure 2.22.f shows the implementation of the Shen model by Denavit and Hajjar (2010) to the steel component in CFTs, with enhancements to account for local buckling, residual strains, and non-cyclic response; this figure was obtained for a steel tube which $D/t=86$. With exception of the Shen model, all the material models shown in Figure 2.22 are integrated in the latest version of OpenSees (2010).

The curve in Figure 2.22.e is an elastic-perfectly plastic material shifted to account for biaxial stresses as proposed by Sakino *et al.* (2004).

The model in Figure 2.22.d and Figure 2.22.f exhibit softening after the local buckling strain in compression is exceeded.

The model in Figure 2.22.b, and without a smoother transition the models in Figure 2.22.a and Figure 2.22.c, follow with some accuracy the monotonic tensile response of the coupon test, although none of these include the local buckling effects.

As noticed in all these figures, the stress-strain response with the Shen model (Figure 2.22.f) illustrates the more complex and robust uniaxial response for cyclic loading within the strain interval shown, with a good prediction of the monotonic envelope in tension, and with a rational degradation due to the local buckling in compression.

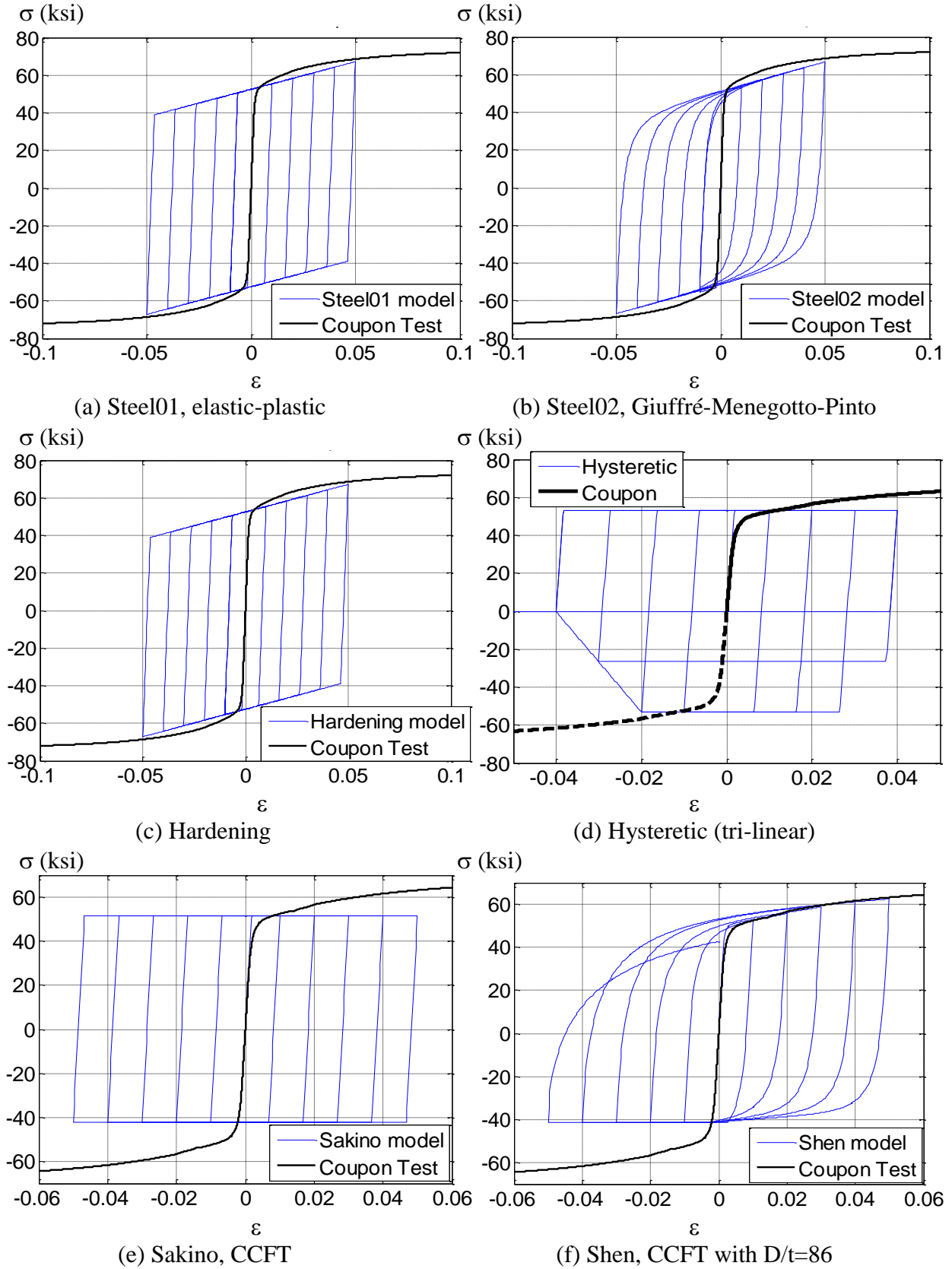


Figure 2.22. Different stress-strain models available for steel in CFTs

2.4.3. Fiber-based analysis

Fiber element analysis have been widely used to understand and predict the behavior of steel (i.e. White, 1986; Liew and Chen, 2004; etc.), reinforced concrete (i.e. Taucer *et al.*, 1991; Izzuddin *et al.*, 1994; Spacone and Filippou, 1995; etc.) and composite steel-concrete elements. Table 2.3 summarizes briefly a number of analytical studies that have looked at fiber analysis of composite elements. This table is not meant to be comprehensive: however, it gives an idea of the maturity and breath of the approach.

Fiber element analysis is a numerical technique which models a structural element by dividing it into a number of two-end frame elements, and by linking each boundary to a discrete cross-section with a grid of fibers (Figure 2.23). The material stress-strain response in each fiber is integrated to get stress-resultant forces and rigidity terms, and from these, forces and rigidities over the length are obtained through finite element interpolation functions which must satisfy equilibrium and compatibility conditions.

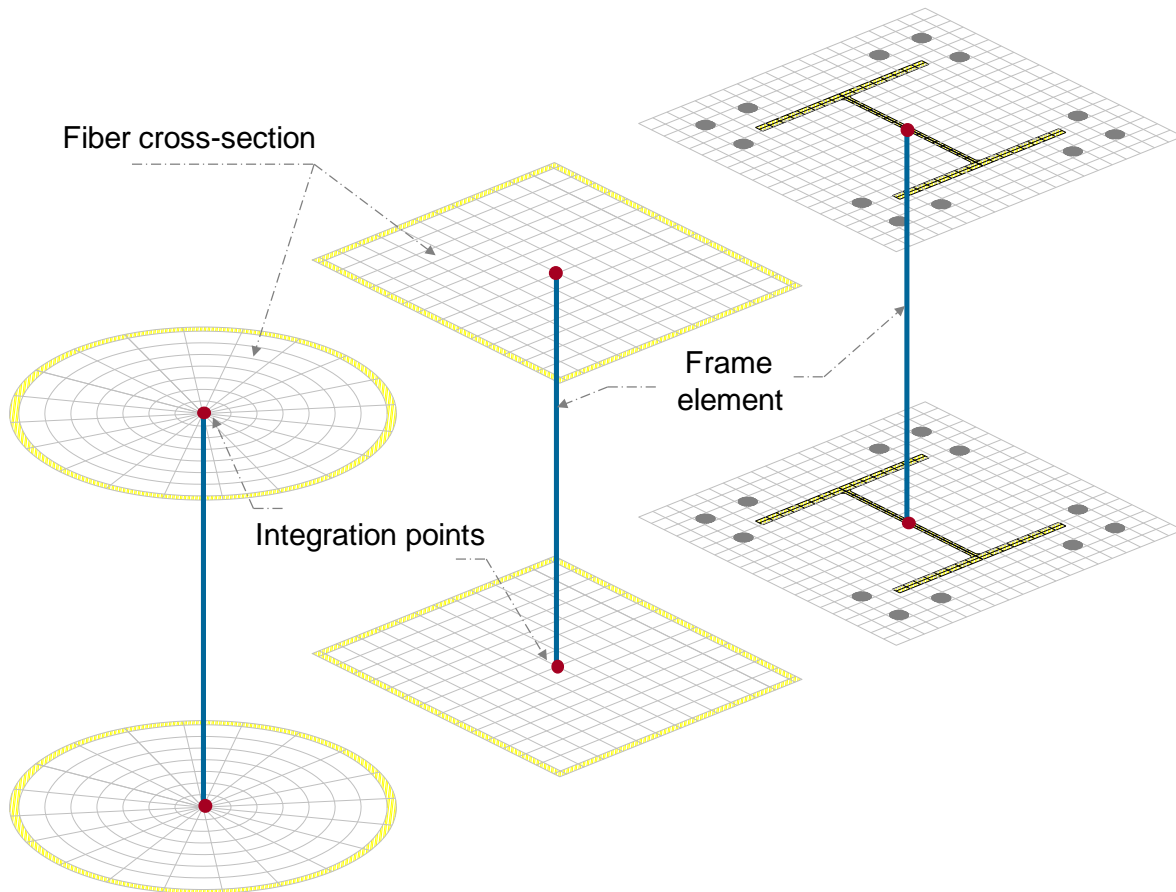


Figure 2.23. Frame element with ends coupled to fiber cross-sections

Table 2.3. Summary of analytical studies with fiber analysis in composite elements

Reference	Applied to:	Brief comments
Tomii and Sakino (1979)	CCFT and RCFT cross-sections	Calibrated fiber M- ϕ results with experimental results adjusting σ - ϵ curve in concrete, keeping steel as elastic-perfectly-plastic.
Elnashai and Elghazouli (1993)	SRC beam-columns	Developed a non-linear model for SRC frame structures subjected to cyclic and dynamic loads, accounting for geometric nonlinearities, material inelasticity, confinement effects in concrete, and local buckling and cyclic degradation in the steel. The model is calibrated and compared with experimental data.
Ricles and Paboojian (1994)	SRC beam-columns	Analyzed SRC beam-columns with fiber analysis, which accounted for strain compatibility, material nonlinearity, and confinement effects using the Mander model.
Hajjar and Gourley (1996)	RCFT cross-sections	Developed a polynomial expression to represent a 3D axial-bending interaction equation for square CFT cross-sections. This polynomial equation was fitted based on results from nonlinear fiber element analysis.
El-Tawil and Dierlein (1999)	SRC cross-sections	Compared experimental and fiber-based results of monotonic M- ϕ curves. From the fiber-based model, interaction curves were obtained for 3 SRC cross-sections with different steel ratios, which were compared with the ACI and AISC strength.
Lakshimi and Shanmugan (2000)	CFT beam-columns	Used fiber models to predict behavior of biaxially-loaded CFT beam-columns and axially-loaded slender CFT columns.
Uy (2000)	CFT columns	Used fiber models in CFT columns with thin-walled steel tubes. Buckling and post-buckling behavior were incorporated through a finite strip method and an effective width approach.
Aval et al. (2002)	CCFT and RCFT beam-columns	Developed a fiber element accounting for bond/slip interaction between concrete and steel (due to the difference between axial elongation and curvatures). The effect of semi- and perfect bond is investigated and compared with experiments.
Fujimoto et al. (2004)	RCFT cross-sections	Used the empirical σ - ϵ curves developed by Nakahara-Sakino-Inai in fiber analysis to predict monotonic M- ϕ curves.
Inai et al. (2004)	RCFT cross-sections	Used the empirical σ - ϵ curves developed by Nakahara-Sakino-Inai in fiber analysis to predict cyclic M- ϕ curves.
Varma (2000)	RCFT beam-columns	Adapted and implemented σ - ϵ curves for both high strength steel and concrete to predict the response of square CFT elements. These curves were adapted from results of 3D finite element analyses, which implicitly accounts for local buckling of the steel tube, transverse interaction between steel and concrete infill, and confinement of the concrete infill.
Lu et al. (2006)	RCFT cross-sections	Obtained M- ϕ curves and interaction P-M _u diagrams, which accounted for residual stresses in the steel and confinement effects in concrete, as well as the material nonlinearity.
Choi et al. (2006)	RCFT cross-sections	Developed a parametric study to determine the P-M interaction diagram varying with the b/t and f_c'/F_y ratios.
Kim and Kim (2006)	RCFT beam-columns	Compared fiber-based cyclic M- ϕ and force-displacement (F- Δ) curves with those obtained experimentally.
Liang (2008)	RCFT cross-sections	Determined P-M interaction diagrams for short CFT beam-columns assuming material nonlinearity. Fiber element results are compared with experimental data and existing solutions. Evaluated the influence of steel ratios, f_c' and F_y .

There are several advantages which justify the use of fiber analysis. Some of these advantages include but are not limited to their ability to handle:

- *Complex cross-sections*: A fiber cross-section can have any general geometric configuration formed by sub-regions of simpler shapes; geometric properties of the more complex section are calculated through the numerical integration.
- *Tapered elements*: Since the length of the fiber is not considered, the cross-section defined at each of the two ends can be different, and therefore, the response of tapered members can be roughly estimated. Precision can be increased with more integration points.
- *Complex strength-strain behavior*: Since each fiber can have any stress-strain response, this technique allows modeling nonlinear behavior in steel members (steel σ - ϵ and residual stresses), reinforced concrete members (unconfined and confined concrete σ - ϵ , and steel reinforced σ - ϵ), and composite members.
- *Accuracy and efficiency*: Since each fiber is associated to a given uniaxial stress-strain (σ - ϵ) material response, higher accuracy and more realistic behavior effects can be captured by a fiber-based model than in a frame-based model, and at less computing time than for a 3D finite-based model.

As described previously, the uniaxial σ - ϵ curve can directly account for the material nonlinearity under monotonic or cyclic loads or displacements, and the residual stresses in the structural steel members. However, some researchers have calibrated, based on experimental or analytical 3D finite-based results (i.e. Varma, 2000; Tort and Hajjar, 2007), the uniaxial σ - ϵ to account for additional behavior effects like:

- Confinement effects in the concrete due to either steel reinforcement (as in RC or SRC cross-sections) or a steel tube (as in CFT cross-sections). Concrete confinement in CFT elements remain while the steel-concrete contact is present.
- Local buckling in steel tubes through a degradation of the compressive σ - ϵ beyond the corresponding strain (ϵ_{lb}) when local buckling take place. Local buckling in CFT

elements can be reached when the steel is highly stressed and the steel-concrete contact is lost.

Stability effects through geometric nonlinearity and initial imperfections can be captured directly within the frame-based analysis. In turn, slip between concrete and steel has been modeled in the frame-based formulation by adding degrees-of-freedom (i.e. Hajjar *et al.*, 1998; Aval *et al.*, 2002; Tort and Hajjar, 2007).

2.4.4. Finite Element Analysis

Finite Element Analysis (FEA) is a numerical technique that models a structural system by a set of appropriate finite elements (1D, 2D or 3D) interconnected at the exterior nodes, and all together models the entire system as accurate as possible. Nodes will have the desired degrees of freedom that may include translations, rotations, and for special applications, higher order derivatives of displacements. When the nodes displace, they will drag the elements along in a certain manner dictated by the element formulation, so the displacements at any point in the element can be interpolated from the nodal displacements through the finite element interpolation or shape functions, which must satisfy equilibrium and compatibility conditions as well.

Several advantages justify the use of finite element analysis. Some of these advantages include but are not limited to their ability to handle:

- Complex 3D geometries: 1D, 2D or 3D elements may be used to generate any 2D or 3D shape of any structural system.
- True material non-linearity: Since the analysis account for size and shape changes, true stress-strain “ σ – ϵ ” values are used in the calculations instead of the engineering stress-strain $(\sigma-\epsilon)_{\text{eng}}$ values.
- Geometric nonlinearity and initial conditions (like residuals stress or strains, out-of-plumbness, out-of straightness, etc.) may be included in the model.

- Definition of surfaces in contact allows giving a better modeling of the true steel-concrete interaction. In composite columns, for example, the normal and tangential contact interaction between the steel and concrete's surfaces may allowed to account directly for effects which in fiber analysis are indirectly implicit in the uniaxial σ - ϵ . Thus, as long as the steel-concrete remain in contact, neither local buckling, loss of confinement, nor slip can take place.

Accounting for contact in finite element analysis may include but are not limited to their ability to handle:

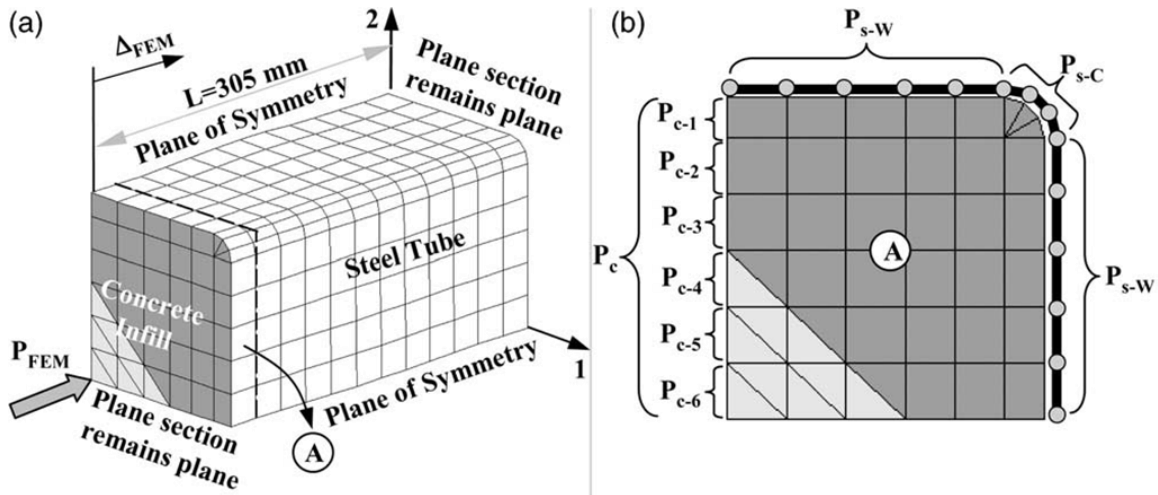
- Confinement directly provided by the normal pressure between the surfaces in contact; modification in the uniaxial σ - ϵ curve is not needed.
- Local buckling of the steel tube is delayed until loss of normal contact takes place.
- Slip or unbonding in concrete-steel surfaces takes place when tangential contact is lost.
- Wear can be predicted in mechanical parts with friction or relative motion between contact surfaces, mainly when these are subjected to high cycle fatigue.

Since the model may have a large amount of elements, computing time or resources are an important issue to consider. In order to obtain good accuracy without excessive processing, the following is often recommended:

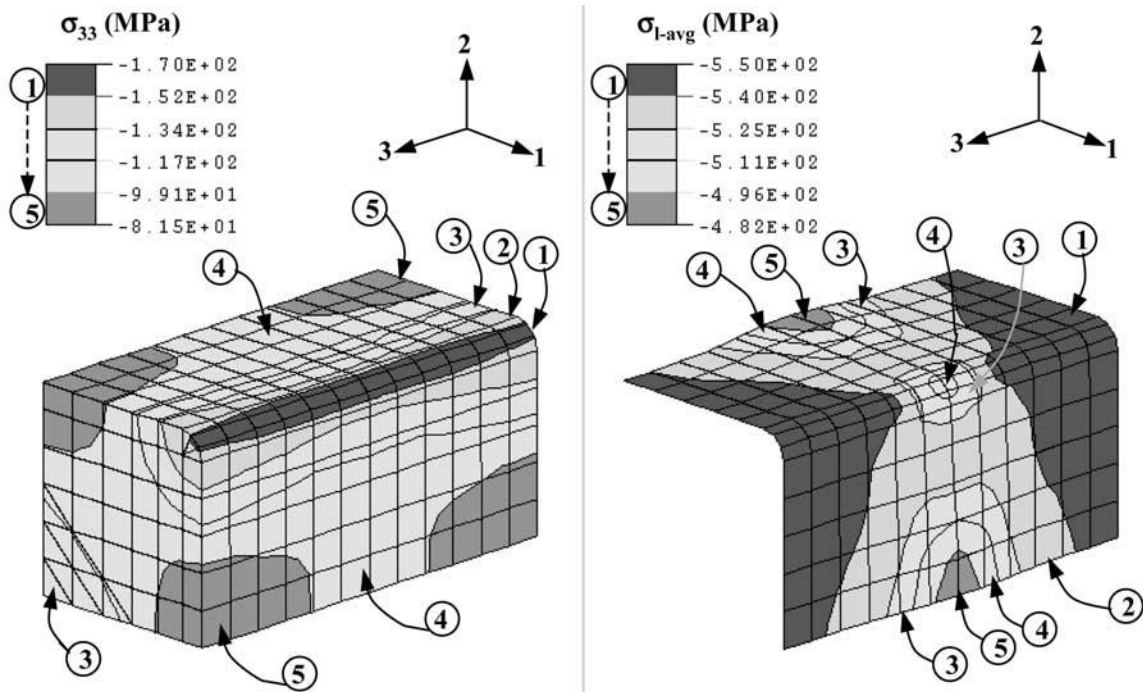
- Symmetry or anti-symmetry conditions are exploited in order to reduce the size of the system. Compatibility of displacements of many nodes can be imposed via constraint relations; proper support constraints are imposed with special attention paid to nodes on symmetry axes.
- The element mesh should be fine enough in order to have acceptable accuracy. To assess accuracy, the mesh is refined until results show little change. For higher accuracy, the elements' aspect ratio should be as close to unity as possible and smaller elements can be used over the parts of higher stress gradient.

Since the computing time and resources are high demanded in this type of analyses, fewer research studies have used this technique to obtain the response of CFT members. A summary of some of the available literature using the FEA approach is given next.

Varma (2000) derived strain curves for the steel and concrete from three-dimensional nonlinear finite element analyses of the CFT failure segments (Figure 2.24). As a result, the finite element model-based stress–strain curves implicitly account for the effects of local buckling and biaxial stresses in the steel tube and the confinement of the concrete infill (Figure 2.25).

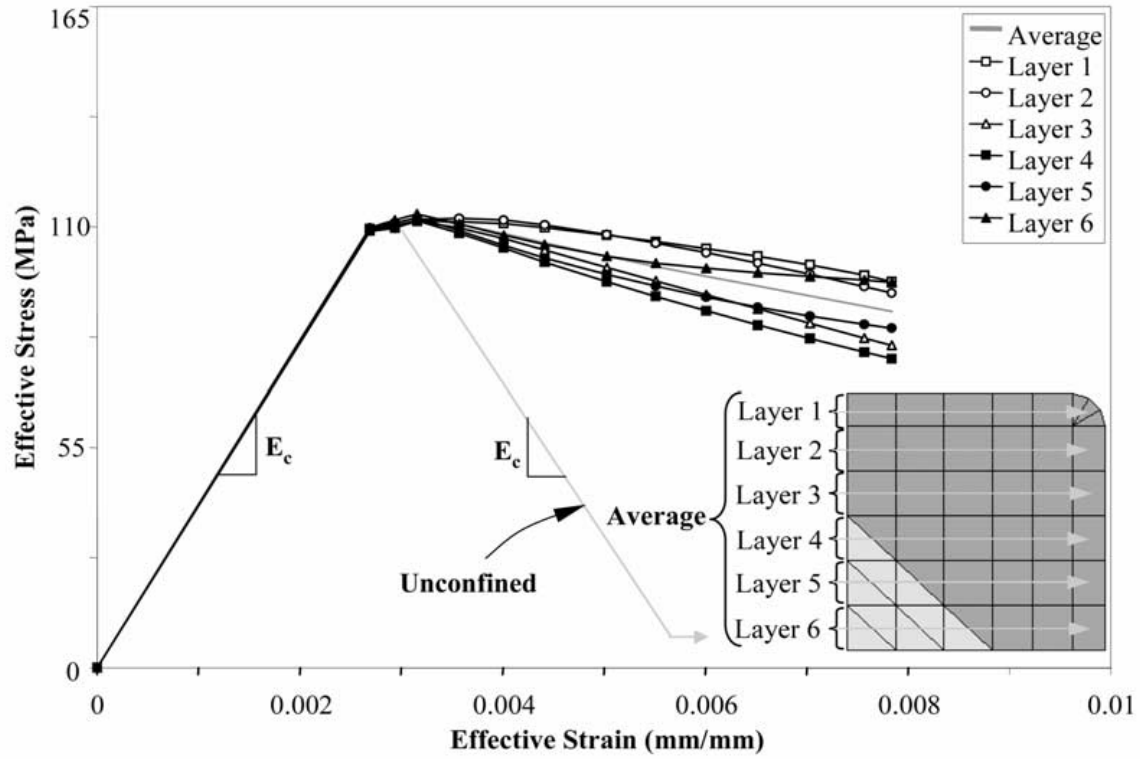


(i) 3D finite element model for a segment of CFT

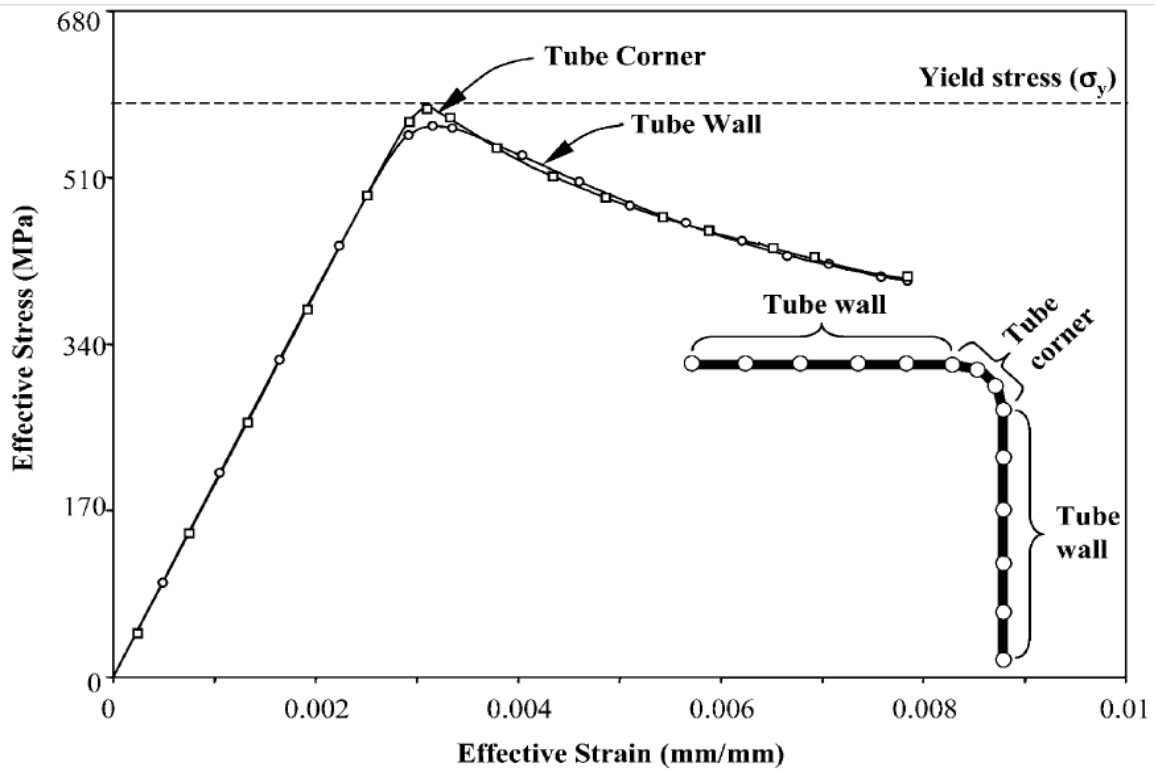


(ii) Longitudinal stresses in steel tube and concrete infill

Figure 2.24. Model and results from the FEA presented by Varma (2000)



(i) Compression stress–strain curves for concrete extracted in different layers



(ii) Compression stress–strain curves for steel extracted at walls and corners

Figure 2.25. Stress-strain curves obtained from FEA (Varma, 2000)

Perea and Leon (2004) evaluated the effects of confinement in short columns based on a finite element analyses using the software ABAQUS (2010). For this purpose, a cylinder of concrete confined by a steel tube was analyzed. The steel tube is modeled by 20-joint 3D solids (C3D20R) and an elastoplastic stress-strain curve with a yielding stress of $F_y=42$ ksi. The concrete is modeled by 8-joint 3D-solids (C3D8R) and 6-joint wedges (C3D6), and a monotonic stress-strain curve as proposed by Popovics (1973) with plain or unconfined properties and $f'_c=5$ ksi of strength. After assembling the CFT element (Figure 2.26.a), interaction of steel-concrete surfaces in contact was defined by the normal-hard contact model, which allows separation but avoids overclosure; a small adjustment zone was defined to avoid inaccuracy due to the numerical noise range.

The loading in the composite cylinder was applied in two steps:

(1) A pre-compression on the steel tube only. Three cases of pre-compression were considered in the study.

- (i) No preload in the steel tube ($\varepsilon_s=0$);
- (ii) A preload compression in the steel tube such that the maximum strains in the tube reach the yielding strain of the steel ($\varepsilon_s=\varepsilon_y=F_y/E_s$);
- (iii) A high preload compression in the steel tube such that the maximum strain in the steel tube reached five times the yielding strain ($\varepsilon_s=5\varepsilon_y$). The deformation shape of the cylinder under this pre-compression is illustrated in Figure 2.26.b.i.

(2) After the pre-compression on the steel is achieved and sustained, a monotonic compression only on the concrete core was applied until the concrete reached a large degree of strength softening. The deformation shape of the cylinder under the constant pre-compression applied on the steel tube in step 1 and the maximum compression on the concrete core are illustrated in Figure 2.26.b.ii.

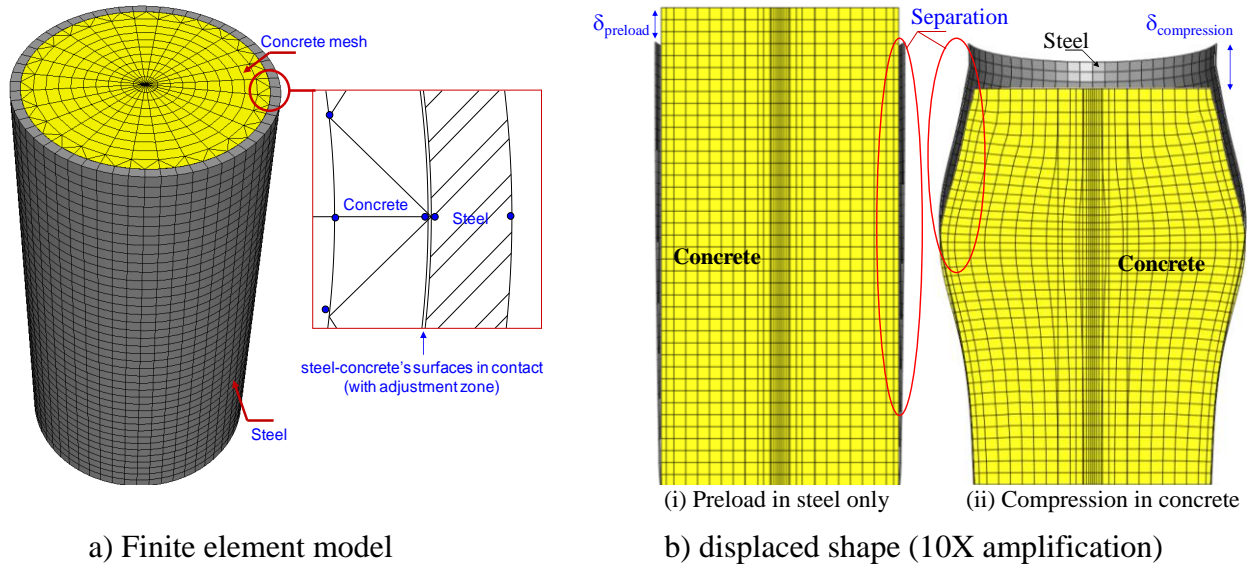
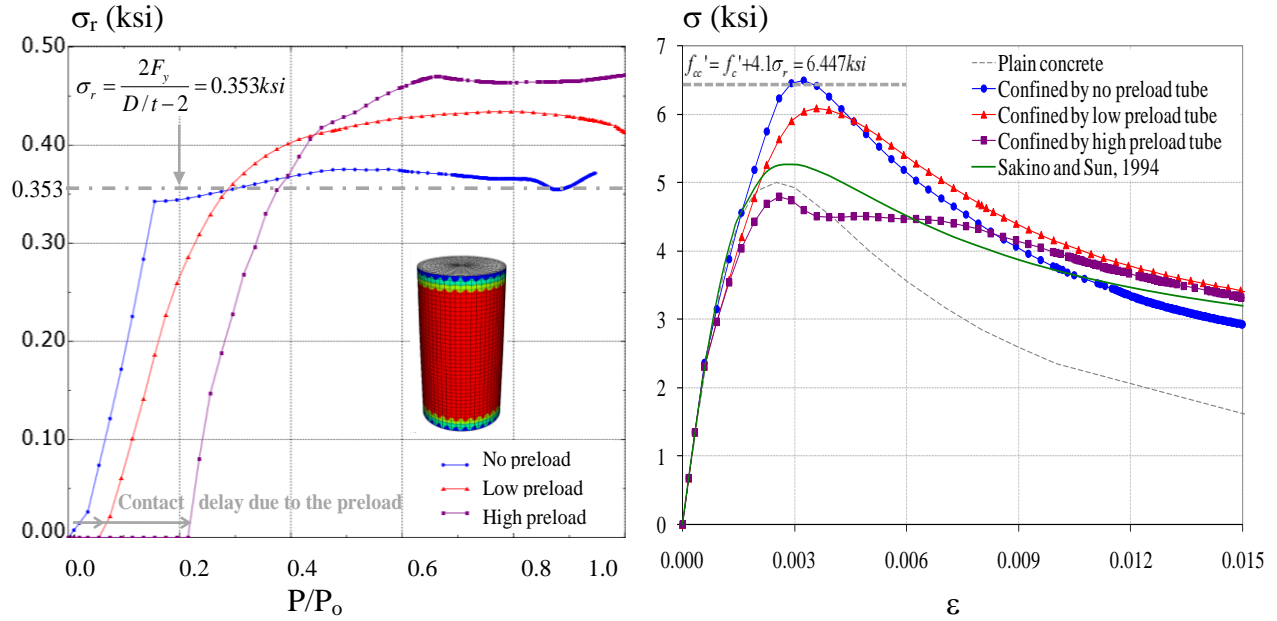


Figure 2.26. Finite element model of a CFT cylinder, and its displaced shape of the CFT with a preload in the steel tube followed by a compression force in the concrete

The results of the hoop stresses in the concrete confined by the steel tube, and the corresponding σ – ϵ for confined concrete proposed by Sakino *et al.* (2004) are illustrated in Figure 2.27.

As seen in Figure 2.27.a, the concrete-steel contact in the tube increases the hoop stresses as the compression force increments. As seen in Figure 2.27.b.i, the cases with an initial preload in the steel tube produce an initial separation (or a contact delay) which is eventually closed as the compression in the concrete makes it expand and then go back in contact; however, as soon as the steel and concrete surfaces are in contact, the σ – ϵ tends to go from the plain concrete curve to the confined concrete curve. Notice that both maximum hoop stresses and maximum confined strength from FEA are very close to those estimated with the empirical equations proposed by Richart (1928). Sakino's prediction is very similar in strength and ductility to the σ – ϵ curve when the tube had an initial preload in the steel.



a) Hoop stress vs. Normalized compression

b) Uniaxial stress-strain (σ - ϵ)

Figure 2.27. Variation of the hoop stresses with the compression force, and the uniaxial stress-strain (σ - ϵ) obtained from the finite element analysis.

The conclusions from this study state that 3D finite element analysis with contact models can deal with the salient features of CFTs in a straightforward manner. Definition of contact surfaces between concrete and steel allows a more realistic interaction within these materials, and therefore, confinement, local buckling and triaxial stresses can be directly integrated in the behavior (with no influence on the material model). More computing resources and time will be required by this 3D-FEA than with other modeling and analysis techniques (i.e. concentrated or distributed plasticity analysis).

CHAPTER 3

EXPERIMENTAL PROGRAM

A comprehensive experimental program was conducted for this research. The experimental program consisted in testing 18 full-scale concrete-filled steel tube (CFT) beam-columns subjected to a very complex load protocol. These complex full-scale tests were possible due to the capabilities of the Multi-Axial Sub-assembly Testing Laboratory (MAST), a part of the NEES Collaboratory (Hajjar *et al.*, 2002). At the time this program was conducted, these 18 CFT specimens were the most slender and longest CFT columns and beam-columns tested in the world as far as the author knows.

3.1. MAST Laboratory

The Multi-Axial Sub-assembly Testing system (MAST), shown in Figure 3.1, consist of a stiff steel crosshead in the shape of a cruciform connected to the strong floor with four vertical actuators and connected to the L-shaped strong wall with four horizontal actuators (two in each wall).

The eight actuators are connected at the ends to the crosshead and the strong floor/wall using swivels with low-friction bearings. Each vertical actuator has a static load capacity of ± 330 kips and ± 20 inches of piston stroke. In turn, each horizontal actuator has a load capacity of 440 kips and ± 16 inches of piston stroke. The configuration of a typical actuator is illustrated in Figure 3.2 (*MTS Systems Corporation*).

Thus, the MAST system has the capability of controlling the top 6 DOFs independently with a total capacity of $P_z = 1320$ kips in vertical force, $F_x = F_y = 880$ kips in shear, and a maximum stroke of ± 20 and ± 16 inches respectively for the horizontal and the vertical displacement. A summary of the overall MAST system capacity is condensed in Table 3.1 (Hajjar *et al.*, 2002). The information in this table is referenced to the MAST coordinate system that is shown in Figure 3.3.a; this coordinate system is used as reference in all the data presented in this research. Schematics drawings of the MAST system with a CCFT and a RCFT connected to the crosshead are shown in Figure 3.3.b and 3.3.c.

Table 3.1. Capacity of the MAST system

(a) Total System Capacity

Component	Capacity
Vertical Forces:	$\pm 1,320$ kips
Lateral Forces:	± 880 kips
Lateral Displacements:	± 16 inches
Vertical Displacements:	± 20 inches
Subassembly size (W x L x H):	20'-0" x 20'-0" x 28'-9"

(b) Non-concurrent Capacities of MAST DOFs

Axis	DOF - Degree of Freedom	Load	Stroke / Rotation
X	Translation	± 880 kips	± 16 inches
	Rotation	$\pm 8,910$ kip-ft	± 7 degrees
Y	Translation	± 880 kips	± 16 inches
	Rotation	$\pm 8,910$ kip-ft	± 7 degrees
Z	Translation	$\pm 1,320$ kips	± 20 inches
	Rotation	$\pm 13,200$ kip-ft	± 10 degrees

(c) Capacity of each actuator

Type	Vertical Actuator	Horizontal Actuator
Quantity:	4	4
Static load capacity:	± 330 kips	± 440 kips
Piston stroke:	± 20 inches	± 16 inches
Swivels at actuator ends:	Low-friction hydrostatic bearings, $\pm 30^\circ$ travel	Low-friction mechanical U-joint style swivels, $\pm 25^\circ$ travel

The MAST system is driven by a sophisticated MTS controller that enables multi-axial cyclic static tests of large-scale structural sub-assemblies. The six-degree-of-freedom (DOF) control technology employed by the MAST system advances the current state of technology by allowing the experimental simulation of complex boundary effects through its multi-axial capabilities, which can impose multiple-degree-of-freedom states of deformation and load (Hajjar *et al.*, 2002). The controller seamlessly converts the 6-DOF space into drive commands for each of the eight actuators, accounting for geometric nonlinearity. The HCC controller provides mixed-mode control, which allows each DOF to be controlled either in displacement or force control. Moreover, the controller can slave any DOF to any combination of other DOFs.

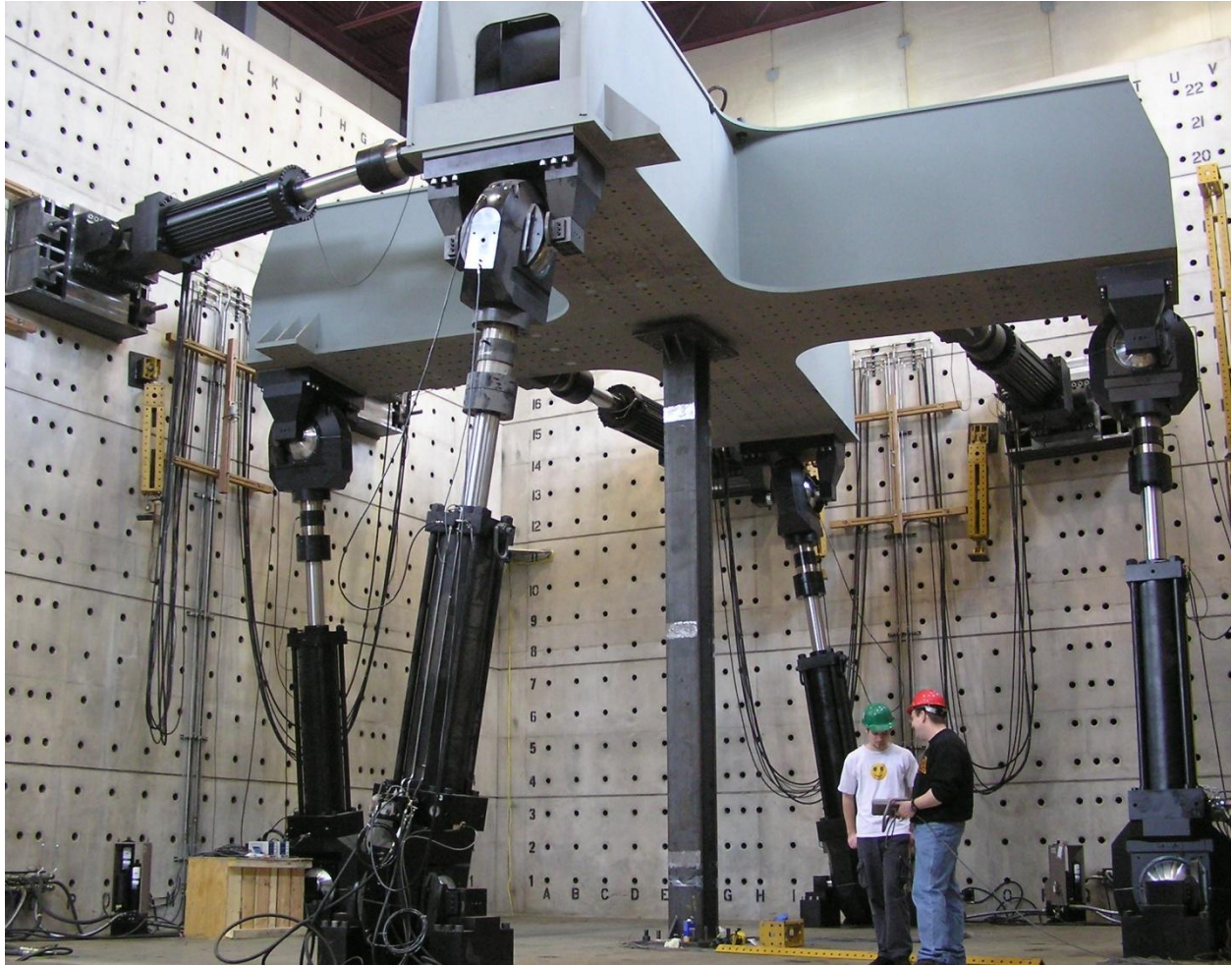


Figure 3.1. Multi-Axial Sub-assembly Testing system (MAST)

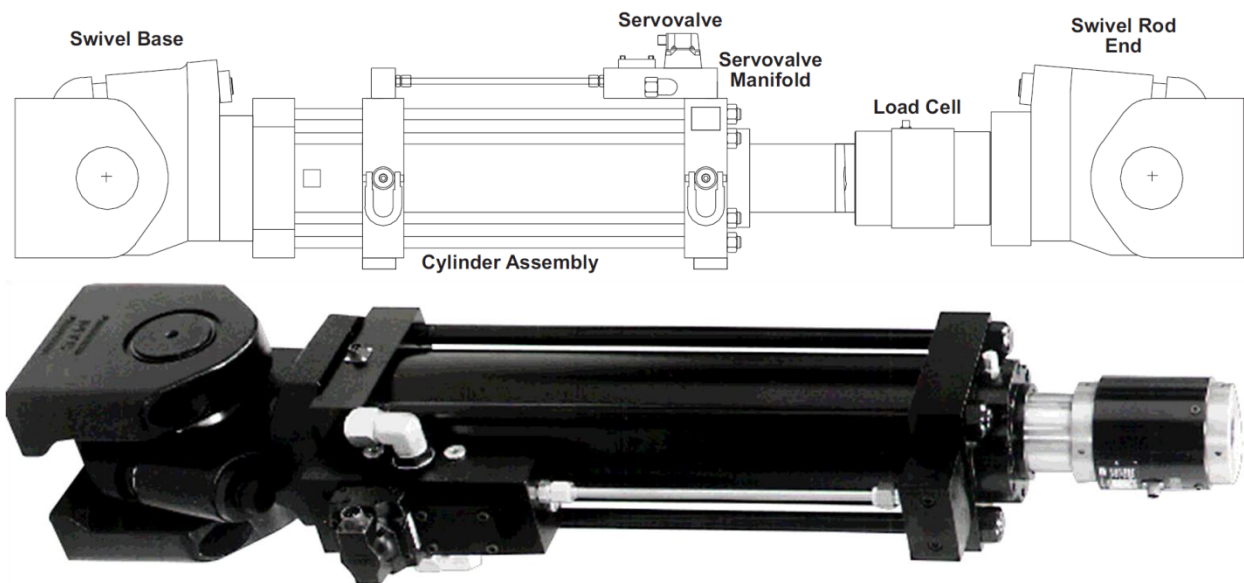
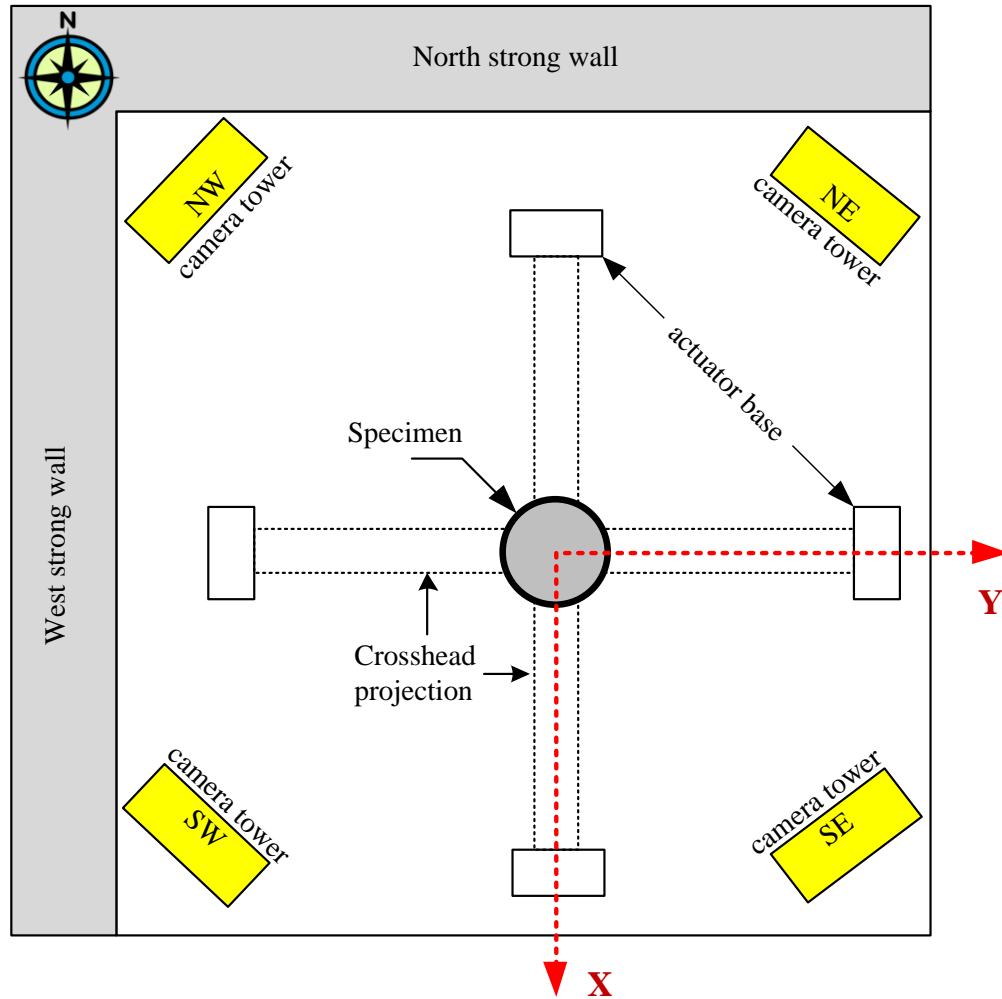


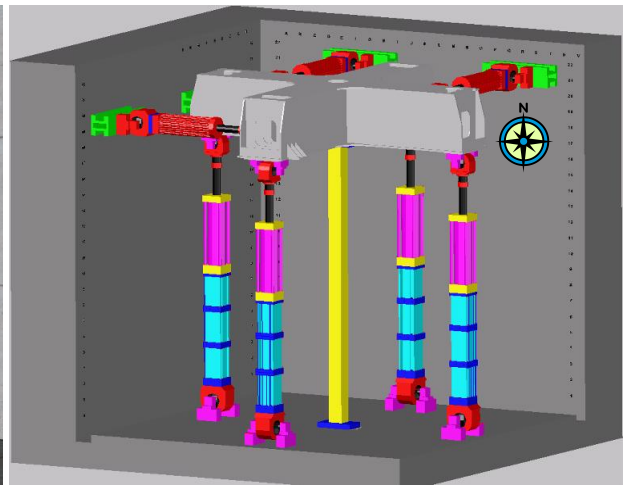
Figure 3.2. Typical configuration of MTS actuators



(a) Coordinate system of the MAST Lab (plan view)



(b) 3D view with a CCFT



(c) 3D view with a RCFT

Figure 3.3. Schematic drawings of specimens placed at MAST

3.2. Description of specimens

The test matrix selected aims to fill gaps found in the available experimental databases (Leon *et al.*, 2005; Goode; 2007). Specimens with different steel tube shapes, high h/t ratios and lengths, and filled with normal and high strength concrete were preferred. Due to constructability constraints when casting the tubes, self consolidating concrete (SCC) was used in this project to avoid concrete segregation and vibration issues. Table 3.2 presents a summary of the selected test matrix along with nominal properties of the CFT specimens tested. In total, these tests represent 20 kips of steel in weight and 22 cubic yards of self consolidating concrete in volume.

Table 3.2. Test matrix of the CFT specimens with nominal values

Specimen Name	Length (ft)	Steel section HSS D x t	D/t	Fy (ksi)	f_c' (ksi)
1C5-18-5	18	HSS5.563x0.134	45	42	5
2C12-18-5	18	HSS12.75x ¹ / ₄	55	42	5
3C20-18-5	18	HSS20.00x ¹ / ₄	86	42	5
4Rw-18-5	18	HSS20x12x ⁵ / ₁₆	67	46	5
5Rs-18-5	18	HSS20x12x ⁵ / ₁₆	67	46	5
6C12-18-12	18	HSS12.75x ¹ / ₄	55	42	12
7C20-18-12	18	HSS20.00x ¹ / ₄	86	42	12
8Rw-18-12	18	HSS20x12x ⁵ / ₁₆	67	46	12
9Rs-18-12	18	HSS20x12x ⁵ / ₁₆	67	46	12
10C12-26-5	26	HSS12.75x ¹ / ₄	55	42	5
11C20-26-5	26	HSS20.00x ¹ / ₄	86	42	5
12Rw-26-5	26	HSS20x12x ⁵ / ₁₆	67	46	5
13Rs-26-5	26	HSS20x12x ⁵ / ₁₆	67	46	5
14C12-26-12	26	HSS12.75x ¹ / ₄	55	42	12
15C20-26-12	26	HSS20.00x ¹ / ₄	86	42	12
16Rw-26-12	26	HSS20x12x ⁵ / ₁₆	67	46	12
17Rs-26-12	26	HSS20x12x ⁵ / ₁₆	67	46	12
18C5-26-12	26	HSS5.563x0.134	45	42	12

Material and geometric properties were measured for all the specimens and are shown in Table 3.3. As seen in this table, the measured length (*L*) of the steel tubes (not including the base plates) exceeded the requested nominal length by ¹/₂ to 2³/₄ inches. The averaged values of the measured thickness (*t*) on the steel tubes equaled the design thickness reported by the manufacturer.

Concerning the material properties for the steel, a set of three coupon samples were extracted and tested in tension for each heat used in the tube manufacture as reported by the manufacturer. The yield and ultimate stress obtained from the coupon tests are also reported in Table 3.3, as well as the Young's modulus results, which averaged very close to the nominal value ($E_s = 29,000$ ksi).

In addition, concrete properties were obtained from testing of cylinders made at the time of the concrete casting. The casting of the specimens was arranged in four groups due to logistic with the testing sequence. These groups are: (1) specimens 1 to 5, (2) specimens 6 to 9, (3) specimens 10 to 13, and (4) specimens 14 to 18. A set of 40 cylinders were made for each casting group, from which compression and split cylinder tests were performed to obtain the concrete strength and stiffness at different ages. Average values of the compressive strength at the 28th day (f_c') and at the day of the test (f_c) are presented in Table 3.3, as well as the tensile strength (f_t) and the Young's modulus (E_c) obtained from the cylinder tests.

Table 3.3. Test matrix of the CFT specimens with measured values

Specimen name	Length L	thickness t (in)	F_y (ksi)	F_u (ksi)	E_s (ksi)	f_c' (ksi)	f_c (ksi)	f_t (ksi)	E_c (ksi)
1C5-18-5	18' $\frac{1}{2}$ "	0.124	55.6	70.7	28,135	5.5	5.5	1.10	4,000
2C12-18-5	18' $\frac{1}{2}$ "	0.233	48.9	64.7	28,886	5.5	5.6	1.10	4,000
3C20-18-5	18' $1\frac{1}{2}$ "	0.233	47.6	68.3	29,045	5.5	5.8	1.10	4,000
4Rw-18-5	18' 2"	0.291	53.0	72.8	29,352	5.5	5.9	1.10	4,000
5Rs-18-5	18' 2"	0.291	53.0	72.8	29,352	5.5	5.9	1.10	4,000
6C12-18-12	18' $\frac{1}{2}$ "	0.233	48.9	64.7	28,886	12.7	13.2	1.65	6,070
7C20-18-12	18' $1\frac{7}{8}$ "	0.233	47.6	68.3	29,045	12.7	13.2	1.65	6,070
8Rw-18-12	18' $2\frac{5}{8}$ "	0.291	53.0	72.8	29,352	12.7	13.3	1.65	6,070
9Rs-18-12	18' $2\frac{5}{8}$ "	0.291	53.0	72.8	29,352	12.7	13.3	1.65	6,070
10C12-26-5	26' 1"	0.233	48.6	68.1	29,038	7.3	7.9	0.60	5,000
11C20-26-5	26' $2\frac{3}{4}$ "	0.233	44.3	69.2	29,254	7.3	8.1	0.60	5,000
12Rw-26-5	26' $1\frac{1}{4}$ "	0.291	58.9	77.4	29,024	7.3	8.2	0.60	5,000
13Rs-26-5	26' $1\frac{3}{4}$ "	0.291	55.5	73.2	29,033	7.3	8.3	0.60	5,000
14C12-26-12	26' $1\frac{1}{2}$ "	0.233	55.5	66.8	28,763	11.5	11.6	0.76	5,800
15C20-26-12	26' 2"	0.233	42.5	65.8	29,027	11.5	11.6	0.76	5,800
16Rw-26-12	26' $1\frac{1}{4}$ "	0.291	55.2	73.4	29,078	11.5	11.7	0.76	5,800
17Rs-26-12	26' $1\frac{1}{2}$ "	0.291	55.1	71.9	29,020	11.5	11.7	0.76	5,800
18C5-26-12	26' $\frac{5}{8}$ "	0.124	55.6	70.7	28,135	11.5	11.7	0.76	5,800

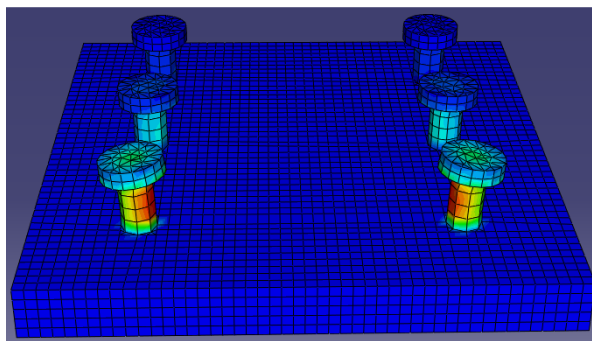
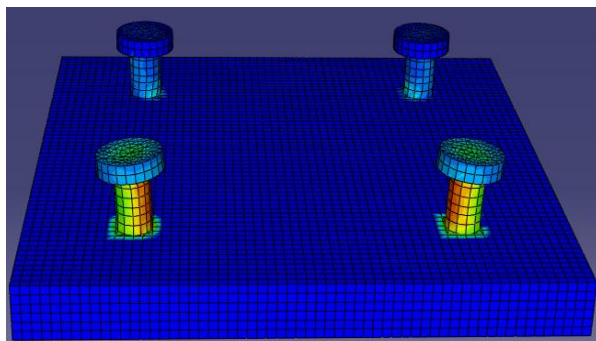
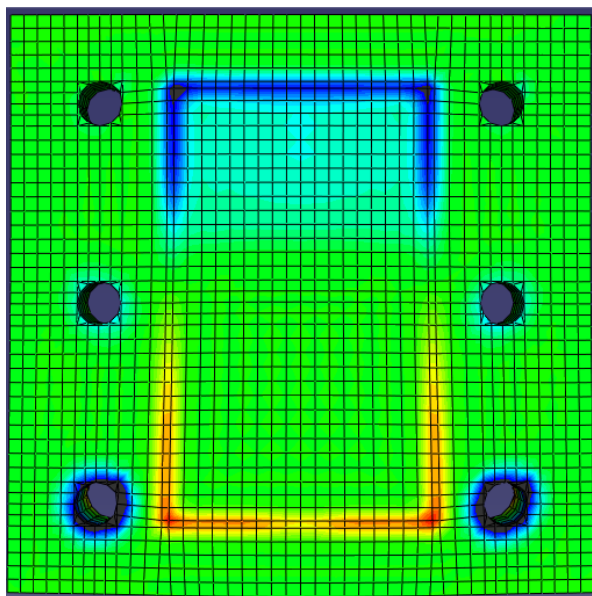
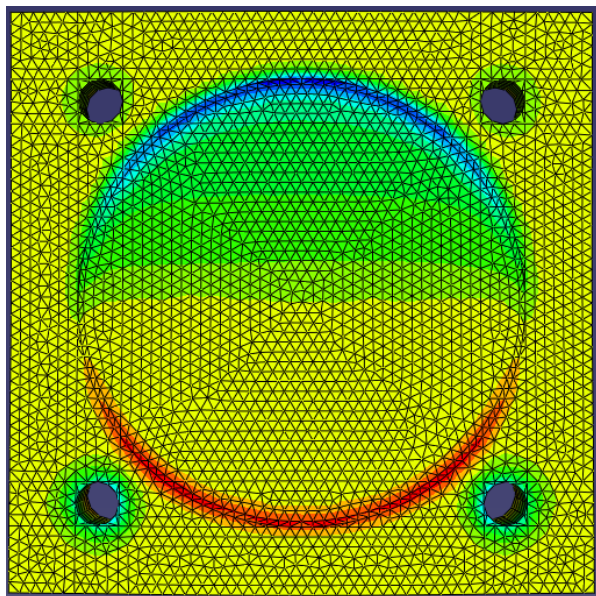
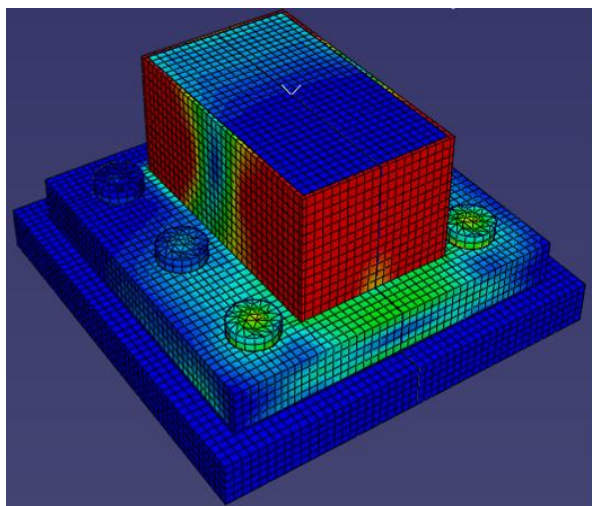
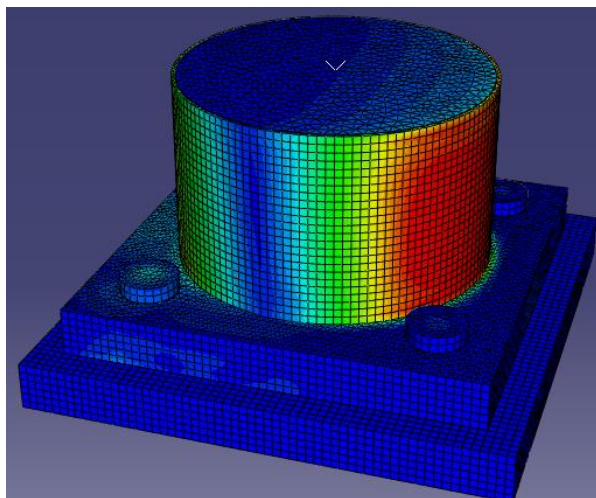
The material and geometric properties summarized in Table 3.3 are used in the analysis and prediction calculations for comparison to the experimental data obtained in this study.

Appendix B shows more details about the materials used in this project, including the stress-strain curves obtained from the steel coupon tests, and the details on the proportioning in the concrete mixes.

Concerning the construction of the specimens, the steel tubes were cut at the shop (*LeJeune Steel, Minneapolis, MN*) and welded with complete penetration welds to base plates at both ends. These base plates are designed in order to connect the full-scale specimens to the strong floor and to the crosshead. The plates were analyzed and designed based on a capacity design approach to avoid an early failure in the connection or base plate welds. Relatively thick plates were used to ensure that rigid boundary conditions could be approximated. Finite element analyses were also conducted to check the strength and the deformations of the base plates, the weld sizes and the entire connection. Figure 3.4 illustrates a distribution of the stresses obtained from the FEA. The location of the bolts connecting the specimen to the MAST equipment was predetermined by the location of the loading points in the testing machine. Thus, these base plates may not reflect typical practice. The final design details of the CFT specimens are shown in Figure 3.5 to Figure 3.8.

Once the tubes were fabricated, they were shipped and stored at the MAST Laboratory for the concrete casting and curing prior to testing. The specimens with 18 feet of length were sent and tested first; once this group was tested and disposed of, the second set of specimens with 26 feet of length was brought in for casting and testing.

In order to provide storage and support during the casting prior the testing, the specimens were secured, as shown in Figure 3.4.a, to a braced frame with a work platform to provide a work space during the concrete casting. As commented before, self consolidated concrete (*SCC*) was used in this project to avoid segregation and vibration issues since the concrete was pumped and dropped from the hose introduced inside the tubes from the top; this filling process is illustrated in Figure 3.4.b. More details about the concrete casting are discussed in Chapter 4. As an illustration of the following steps, Figure 3.4.c and Figure 3.4.d shows specimens before and during the testing; more details about the pre-test settings and the load protocol in the testing is described in the following sections.



a) CCFT20x0.25 Specimen

b) RCFT20x12x0.3125 Specimen

Figure 3.4. Finite Element Analysis performed for the base plates

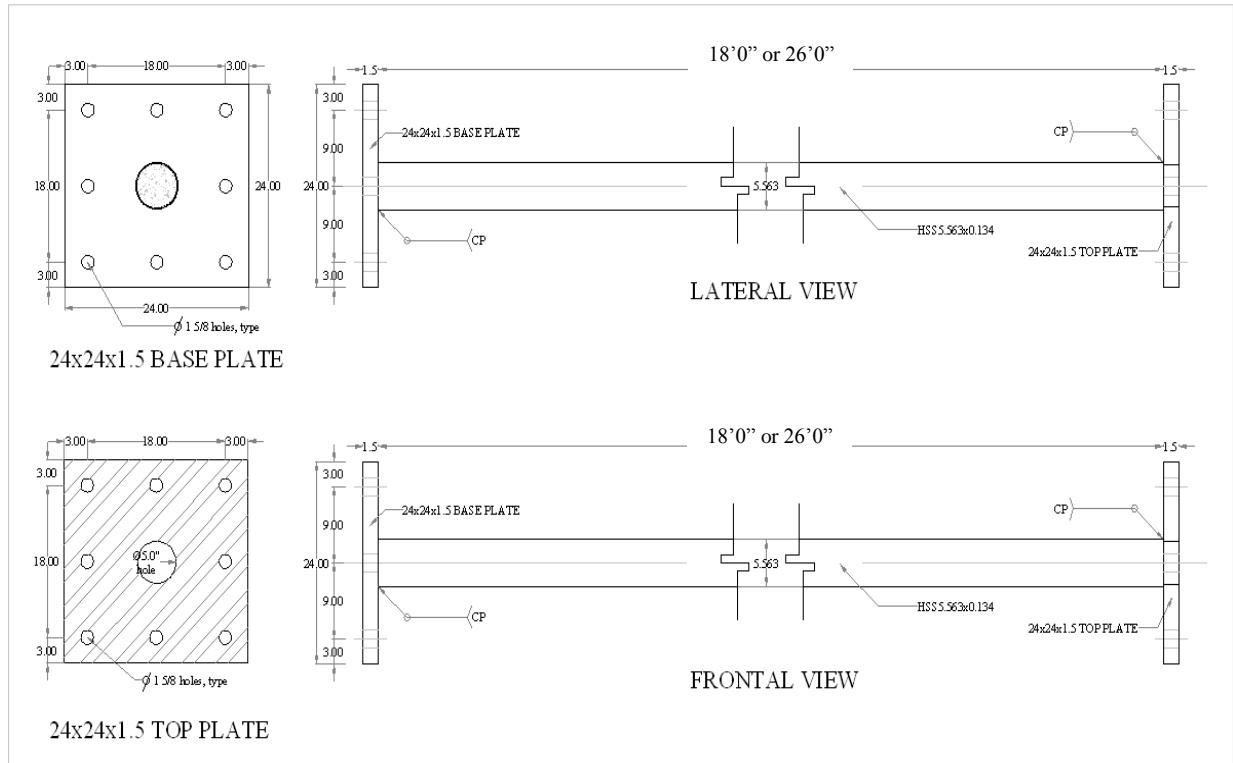


Figure 3.5. Circular CFT specimen with an HSS5.563x0.134

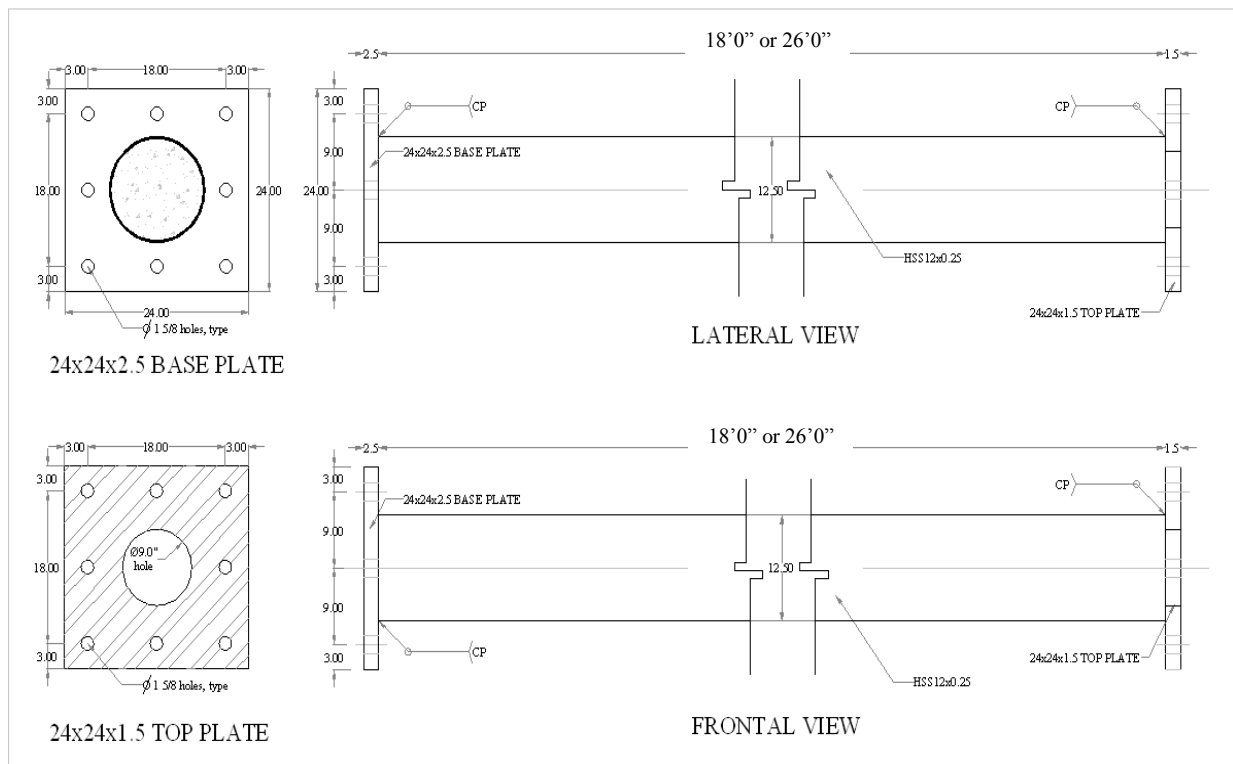


Figure 3.6. Circular CFT specimen with an HSS12.75x0.25

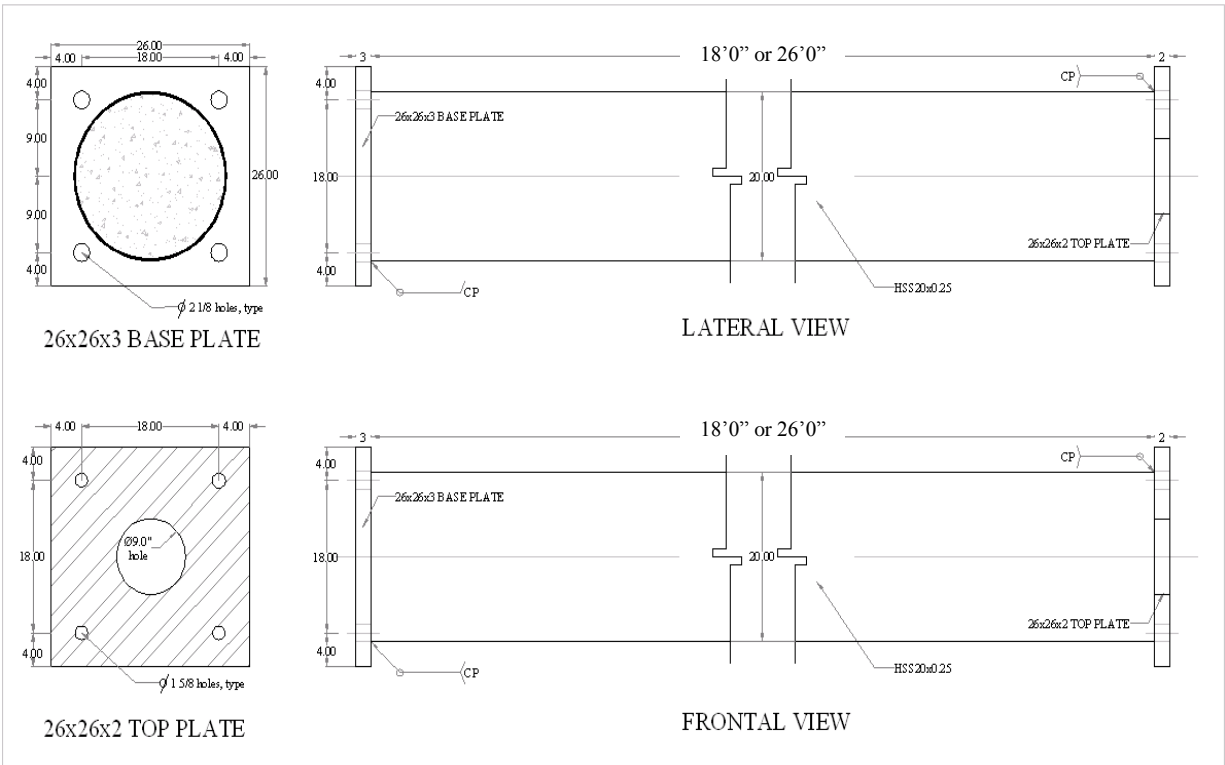


Figure 3.7. Circular CFT specimen with an HSS20x0.25

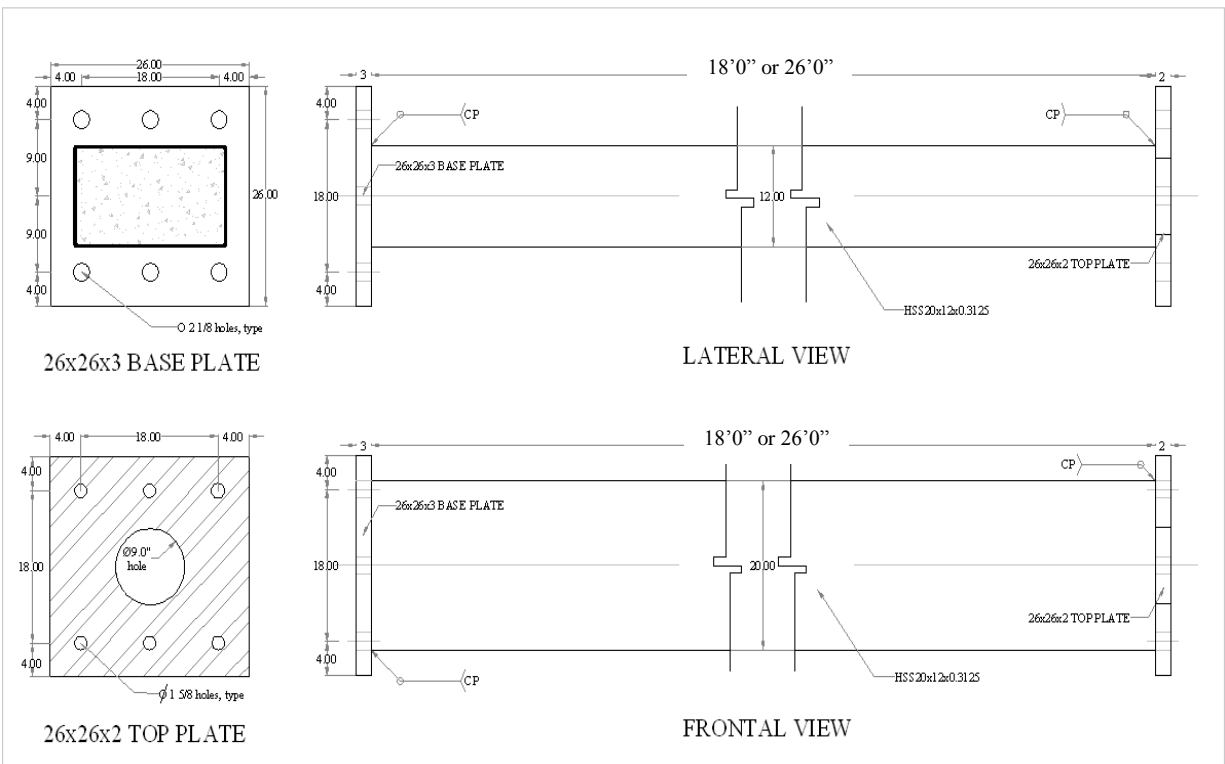


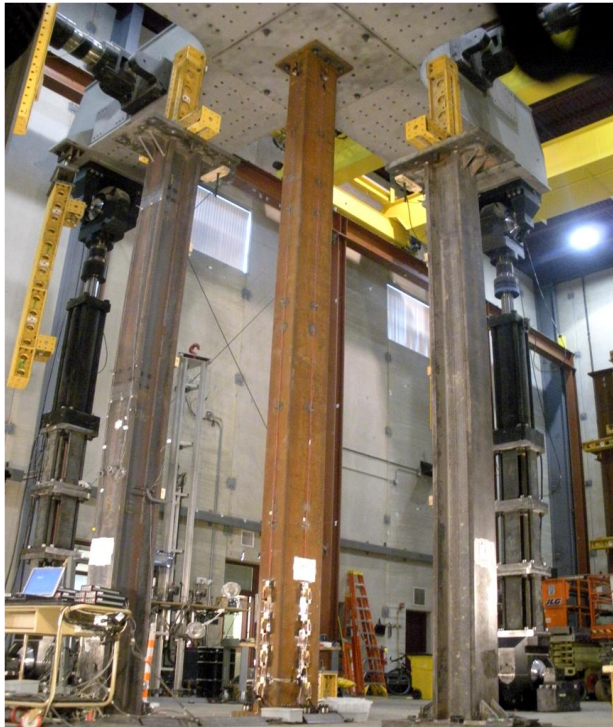
Figure 3.8. Rectangular CFT specimen with an HSS20x12x0.3125



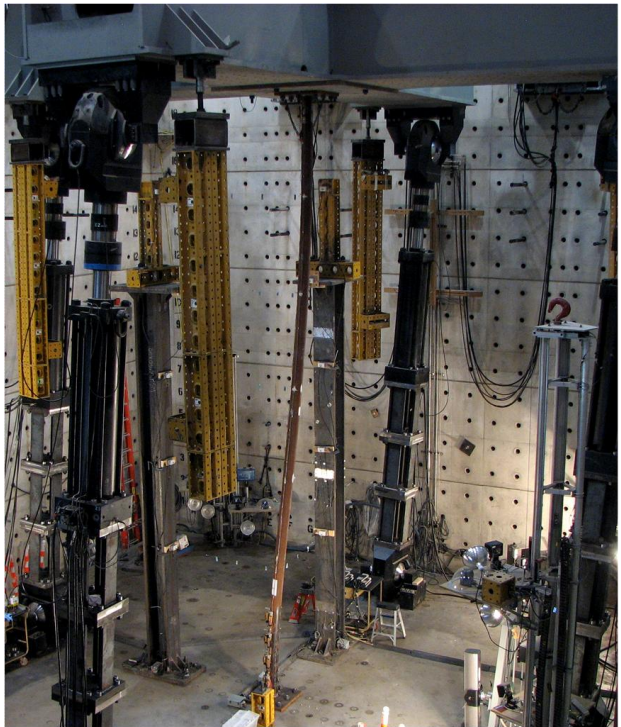
(a) Specimens stored ready for casting



(b) Filling of the steel tubes with SCC



(c) Specimen connected ready for testing



(d) Specimen during the testing

Figure 3.9. Photographs taken before and during the concrete casting and testing

3.3. Instrumentation plan

As noted before, in the MAST system the crosshead is connected to a set of actuators, which are instrumented with built-in (MTS/Lebow) load cells and magnetostrictive (Temposonic) linear position sensors that allow measuring the acting force and the relative displacement in each of the actuators. From these measurements, calculation of the resultant crosshead forces, moments, displacements and rotations associated with the horizontal and vertical axes are obtained by the controller and stored in the DAQ system.

The MAST Data Acquisition (DAQ) system is based on the National Instruments SCXI high performance data acquisition platform. The key features include: (1) simultaneous sampling of 172 voltage channels at ± 10 V and 248 channels of quarter bridge 120 ohm strain gauge input; (2) sampling rate of up to 10 Hz for all channels; (3) lowpass filtering at 2 Hz for voltage channels and 10Hz for strain channels; (4) 16-bit A-to-D conversions; (5) software-controlled shunt and null-offset calibration of all strain channels, which provides wiring checks and allows better use of measurement range; and (6) integrated wiring system. In addition to collecting sensor data, the DAQ system collects feedback from the control system through analog outputs of the MTS controller, and 3D positional information through the Metris DMM metrology hardware (see data path diagram). The DAQ software was locally developed for controlling National Instruments hardware.

The instrumentation on the specimens consisted of:

- Strain gages for measuring both longitudinal and transverse strains. The strain gages were placed in three (in some cases, four) faces of the exterior steel wall of the tubes. At least three measurements at the same level of the column allow the complete calculation of strain within the cross-section assuming plane sections remain plane. Details about location and layout of the strain gages on the specimens are shown in Figure 3.10.
- LVDTs for measuring relative displacements (elongation of shortening) along the specimen. As with the strain gages, LVDTs were placed in three faces to allow the calculation of the relative displacement in any point within the cross-section assuming plane sections remain plane. LVDTs were attached to the specimen through a set of brackets bolted and studs welded to the steel (Figure 3.11).

- String-pots for measuring lateral displacements and obtaining the displaced profile in both horizontal axes. Location and layout of the string-pots in the specimens are shown in Figure 3.12.
- LEDs for measuring the position change of a set of points. These measurements are captured by the Krypton system (Metris K600 Dynamic Measuring Machine, DMM). The layout of the LED target points on the specimens is shown in Figure 3.13.

Additional calculated channels were obtained from the measured data. Some of these calculations include, but are not limited to:

- Moments at the base, and at different points along the specimen
- Rotations and curvatures at different cross-sections
- Evolution of the displaced shape of the column and deformations in selected segments.
- Stresses at different positions through the cross-section and the specimen length.

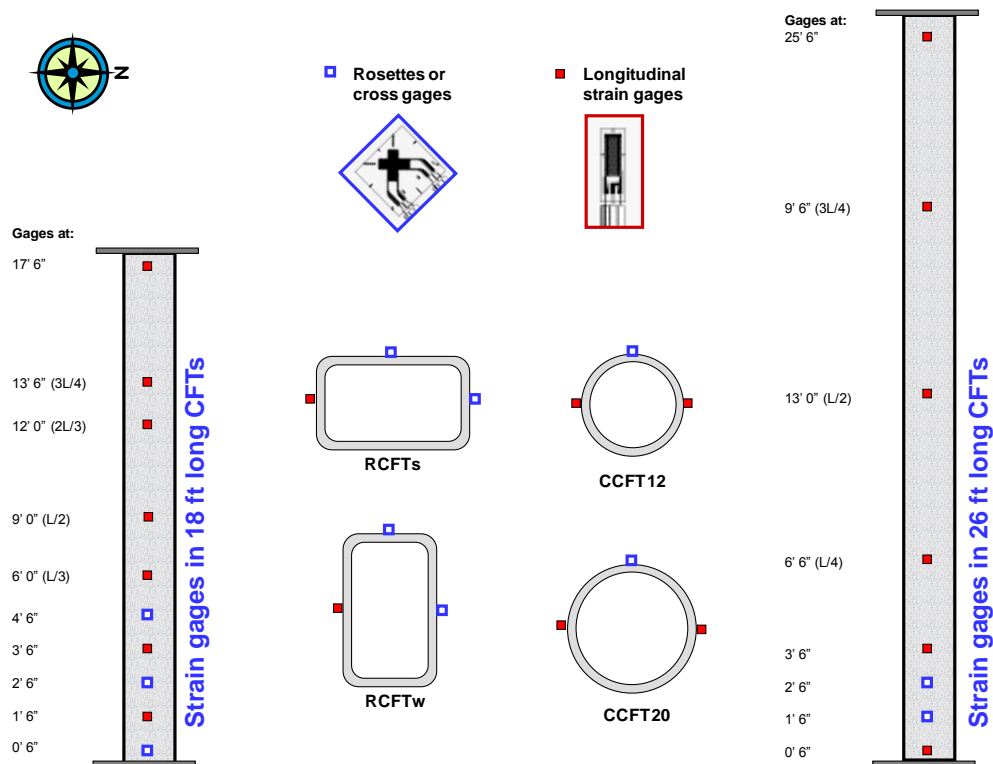


Figure 3.10. Details of strain gages on the specimens

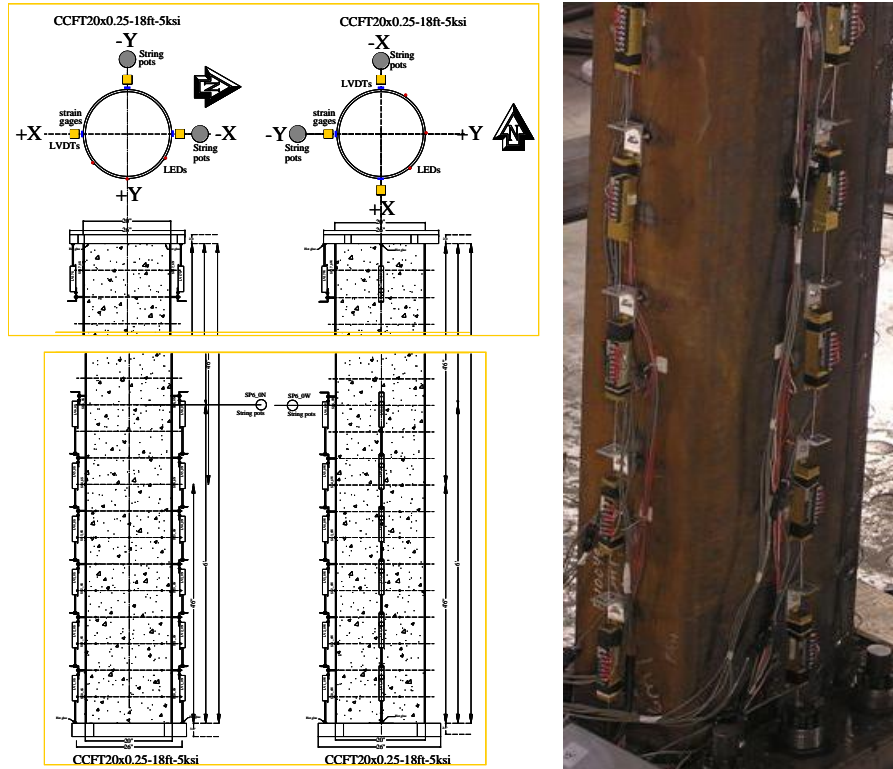


Figure 3.11. Details of LVDTs on the specimens

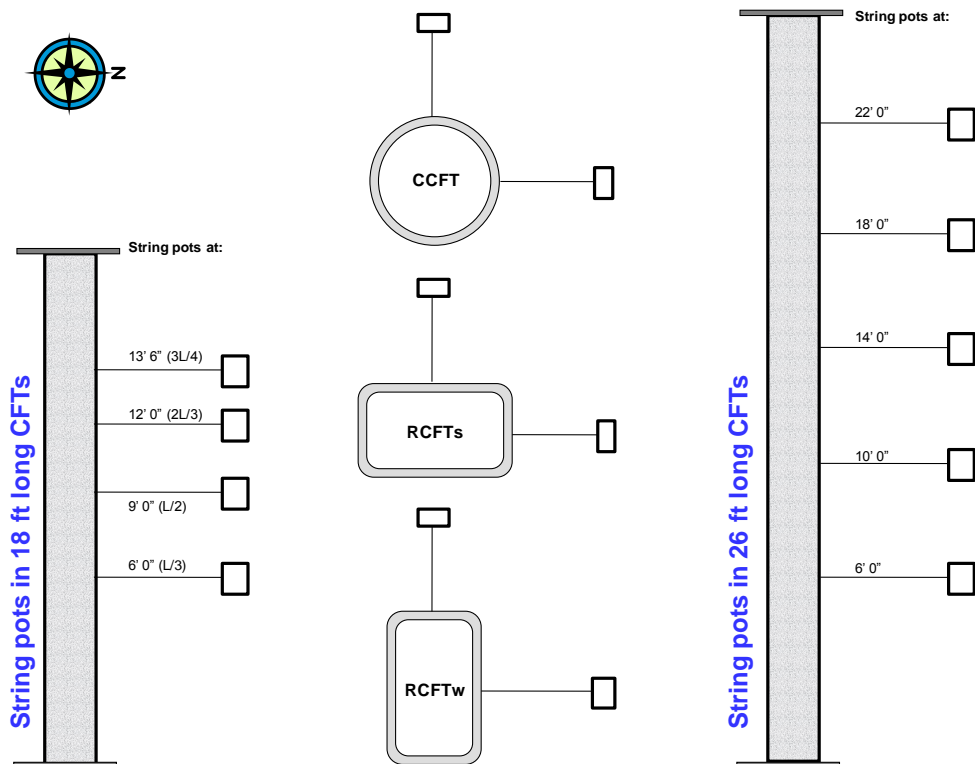


Figure 3.12. Details of string pots on the specimens

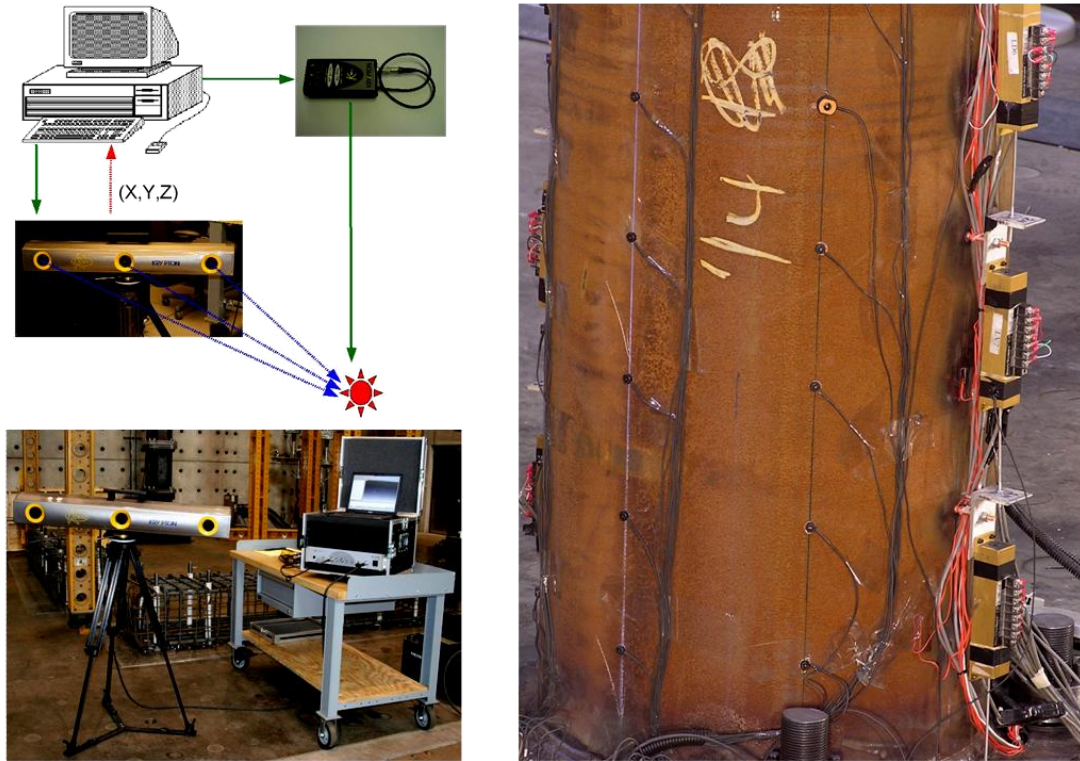


Figure 3.13. Krypton LEDs on the specimens

The MAST Laboratory has one Metris Dynamic Measuring Machine (DMM) system. The system consists of a camera, infrared Light Emitting Diodes (LEDs), and control hardware and software. The key features include: (1) 3D position detection of up to 81 LEDs at 100Hz (expandable up to 256 LEDs) in the camera's 17 m³ field of view; (2) $\sim \pm 0.0008''$ resolution; (3) synchronization of data samples and archives using TTL signals fed from the NI DAQ system (see data path diagram); (4) ability to perform as-built verifications of specimens, to generate metadata associated with sensor locations, and to measure 3-D displacements of the structural surface; and (5) measurement noise (1σ) = 0.00039 in.

In addition, 8 still cameras and 8 video cameras distributed in 4 robotic towers were used to capture images and videos of the whole specimen and some interest points during the entire test (Figure 3.14). All the numeric and visual data were also streamed online by the interface Real-time Data Viewer (RDV) which allowed the PI's to observe and analyze the live time-synchronized data remotely. These data was also stored at the NEES Central Repository.

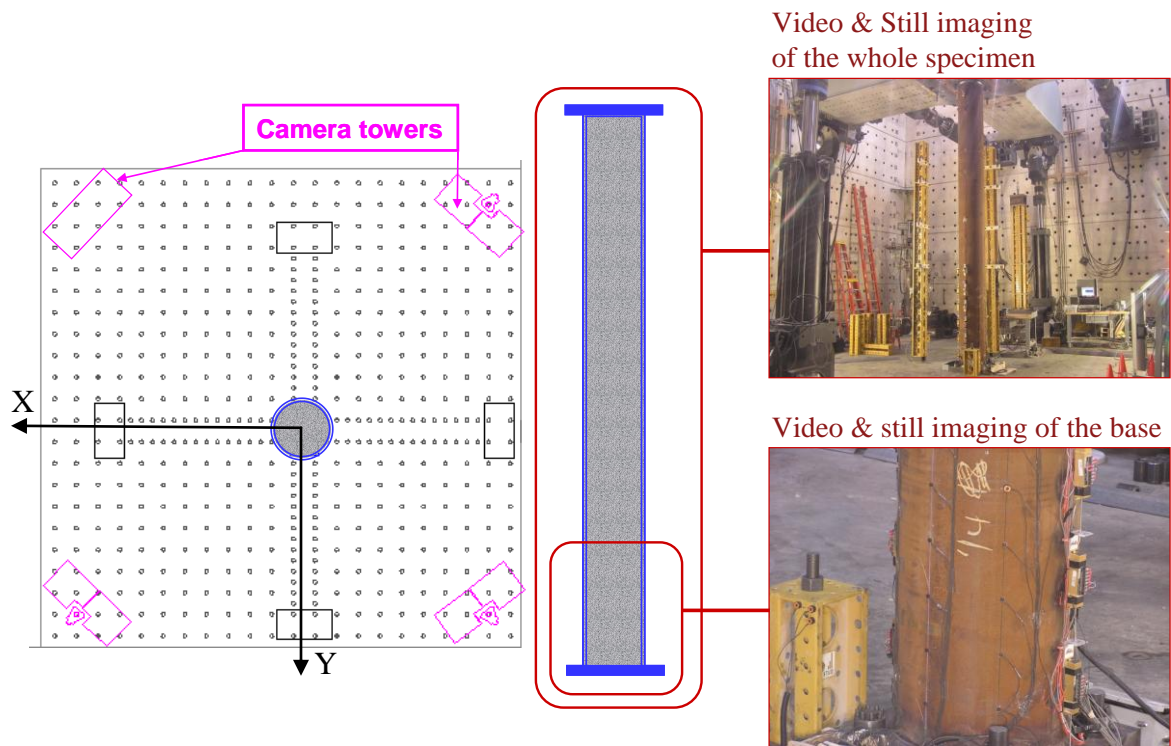


Figure 3.14. Robotic towers for video and photo collection at MAST

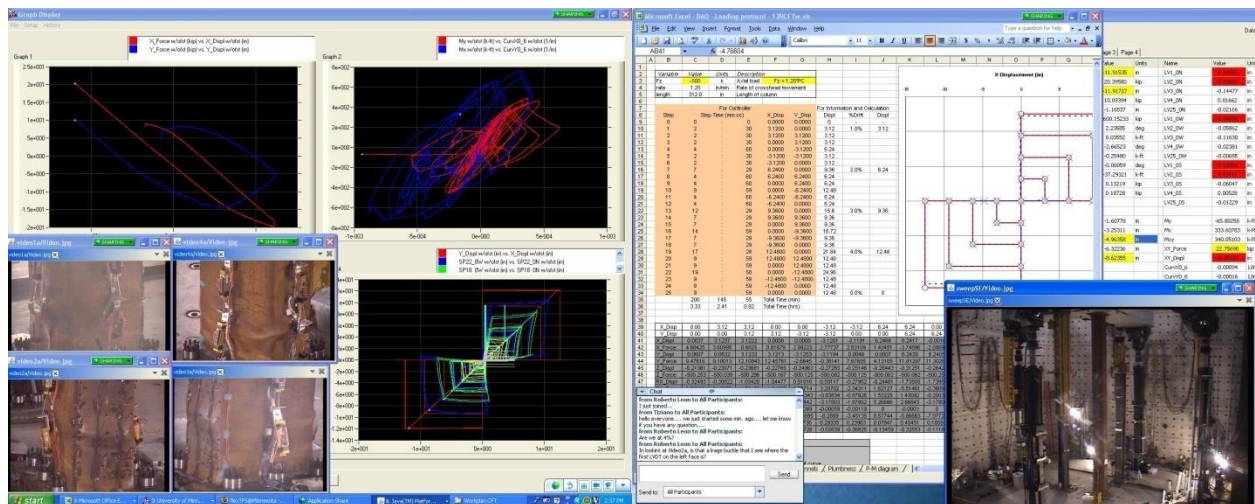


Figure 3.15. Example of the data streamed online through RDV and Webex.

3.4. Pretest settings

The pretest setup in the CCFT specimens for each tests had the following sequence:

- *Moving of the specimen to the center of the testing machine:*

In this step, the crosshead was moved (usually to the NW corner of the lab) so the overhead crane could move the specimen as close as possible to the center of the testing machine. This was followed by a temporal connection of the column base plate to the strong floor. Then, the crosshead was moved directly above the test specimen, bolts were temporarily installed to the crosshead, the temporal base connection released and finally, the crosshead was used as a crane to move the specimen to the center position.

- *Final connection and tensioning of the base plate to the strong floor:*

The base plate was connected rigidly to the strong floor with threaded rods (ASTM A193 Grade B7) and super nuts (with multi-jackbolt stud tensioners, ASTM A193 Grade B7) that were pre-tensioned up to 60% of the ultimate capacity. The amount, size and layout of the threaded rods were constrained by the strong floor layout, but they were optimally designed to guarantee a rigid base; FE analyses (as illustrated in Figure 3.4) under critical conditions of axial load and bending confirmed low values of stresses and deformations (i.e. uplift or twisting).

- *Surveying of the out-of-plumbness and the out-of-straightness with respect to the X and Y axes* (Figure 3.14). Two approaches were used:

1. Plum bob – Getting the profile from the relative distance between a plumb bob (attached to the top plate) and the closest normal point to the specimen.
2. Theodolite – Getting the initial imperfection from the relative distance between a reference vertical line (defined by the transit) and the closest normal point to the specimen.

As consistent measurements were obtained from the two approaches, the specimen profile then was assumed as the average of both measurements. Chapter 5 shows the initial profile measured for each case. Because out-of-straightness has a great influence on the results, these measurements are essential to the post-processing of the data.

- *LVDTs and string potentiometers calibration:*

These devices were calibrated before every test. Correlations between voltage and displacement measurements in LVDTs and string potentiometers at multiple positions (i.e. zero, half range and full range) was performed for every test.

- *Instrumentation mounting and connecting:*

Strain gages, LVDTs, LEDs and string potentiometers were mounted to the specimen and connected to the DAQ system at this stage.

- *DAQ setup:*

The crosshead and the instrumentation connected to the DAQ were configured with the corresponding conversion factors.

- *Offsets:*

With all the instrumentation connected to the DAQ, data started being recorded with offsets or baseline corrected. At the starting step, the instrumentation measurements for the crosshead position and the string potentiometers were set such that their values matched the specimen profile surveyed in a previous step. The rest of the instrumentation measurements were set nominally to zero (varying within the resolution range). All the displacements were set according to the MAST coordinate system and relative to the top-center of the bottom plate or the center of the cross section (Figure 3.1.b).

- *Final connection and tensioning of the top plate to the crosshead:*

Threaded rods to the top crosshead were tensioned until 60% of the yield stress was reached. The connection process created forces and moments that were monitored and recorded. As illustrated in following sections, the forces made during the connection were higher for the specimens with a higher flexibility. One specimen at this stage connected to the strong floor and the crosshead and ready for testing is shown in Figure 3.4.c.

- *Removal of the forces and moments induced during the connection:*

The crosshead was moved until the system came back to the initial state of zero forces and moments. The data taken during this process was named LC0.

3.5. Load protocol

The CFT specimens were subjected to a complex load protocol that consisted of a series of different load cases. Each of these load cases addresses the measurement of different parameters. Some of these parameters are:

- Buckling load of the CFT columns accounting for the effectiveness of the composite stiffness on the stability effects with given boundary conditions. The post-processing of this data is analyzed and discussed in Chapter 5.
- Determination of the maximum flexural capacity under different gravity conditions that allow the determination of the P-M interaction diagram for CFT beam-columns. The results related to the extraction of some experimental set of points for the P-M interaction diagram are presented in Chapter 6.
- Determination of the cyclic behavior response of the beam-columns for the calibration of the computational analysis. The cyclic loading response of the specimens due to constant axial load and cyclic lateral forces is documented and discussed in Chapter 7.
- Evolution of the flexural (EI_{eff}) and torsional (GJ_{eff}) stiffness. The discussion on the evolution of the flexural and torsional rigidities are documented and analyzed in Chapter 7 and Chapter 9, respectively. In addition, Chapter 7 shows the results from the load cases under uniaxial and biaxial cyclic bending loading, and Chapter 9 presents the results from the torsional cyclic loading.
- Determination of some limits state such as steel yielding and local buckling, cracking and crushing of concrete, as well as and the plastic hinge length developed in cyclic loading. The post-processing analysis of the experimental data collected and the determination of such limit states are are presented in Chapter 8.

In order to achieve these targets, different load cases were used. The type and number of cycles for each depends on the particular characteristics and the desired information in each specimen.

The following section is a summary of the four load cases that constitute the basis for the load protocol used in this experimental research. In the following chapters, the nomenclature LC1 to LC4 is used to refer to these particular load cases.

3.5.1. LC1 – Incremental axial compression until buckling

This initial load case (or LC1) consists of driving the crosshead in displacement control with an incremental downward vertical displacement (Δ_z) at a fixed rate of $0.04 \text{ in}/\text{min}$, and in load control by holding zero top forces and moments so the specimen tip moves free in lateral translation (Δ) and rotation (θ). Since the base is rigidly connected to the strong floor and top DOF's are controlled as mentioned, the full-scale specimens will behave as a slender fixed – free member with an effective length of $K=2$ (Figure 3.16). Since the rigidity in the circular specimens is equal in any direction, both principal translations (Δ_x and Δ_y) and rotations (θ_x and θ_y) were controlled as free in the CCFTs ($K_x = K_y = 2$). The rigidity is different in the two perpendicular directions in the case of the RCFTs, and so the Y-axis was kept fixed ($\Delta_y = \theta_y = 0$) and only the X-axis was controlled free ($K_x = 2, K_y = 0.5$). All the specimens are subjected to this LC1 with at least two repetitions or cycles under fixed-free conditions, except in the weakest specimens (1C5-18-5, 18C5-26-12) where the boundary conditions were set as fixed-fixed ($K=0.5$) in order to have a strength less closer to the system resolution and avoid issues with the control on these flexible specimens.

At the beginning of the load case, the cross-head holds zero forces and moments, and its position matches the values of the measured out-of-plumbness (Δ_o). The horizontal forces and moments will be controlled around zero (varying within the noise level) during the entire load case in order to keep the fixed-free condition.

Once the crosshead starts moving downward at a fixed rate of $0.04 \text{ in}/\text{min}$, both the vertical reaction (P) and the lateral top displacement (Δ) start increasing. As a consequence, a second order bending moment at the base ($M=P\Delta$) increases to maintain equilibrium. Eventually, the column reaches the buckling limit state at the critical load (P_n) and, since the system is in displacement control, the vertical force P starts decreasing to maintain equilibrium. Once the critical buckling load (P_n) is reached, the crosshead will be moved upward to unload the specimen up to zero force. The described path axial force and moment at the base (P - M) during this load case is schematically illustrated in Figure 3.16. As reference, this figure also shows schematic representation of the interaction diagrams for a cross-section and a beam-column, highlighting the reduction in axial strength due to stability effects on slender columns with imperfections.

Among the parameters intended to address with this load case LC1 are:

- Experimental determination of the buckling critical load (P_n) and its relationship to the initial imperfections (Δ_o).
- Evaluation of the effective flexural stiffness (EI_{eff}) of the composite column from the buckling load achieved and the measurements of the moment-curvature at the base.
- Calibration of the analytical buckling strength obtained with the design equations of the AISC Specification.
- Calibration of the analytical models to improve their ability to predict the full response (forces, displacements, strains) with the incorporation of the salient behavioral features of CFT members (i.e. confinement, residual stresses, local buckling, etc.).

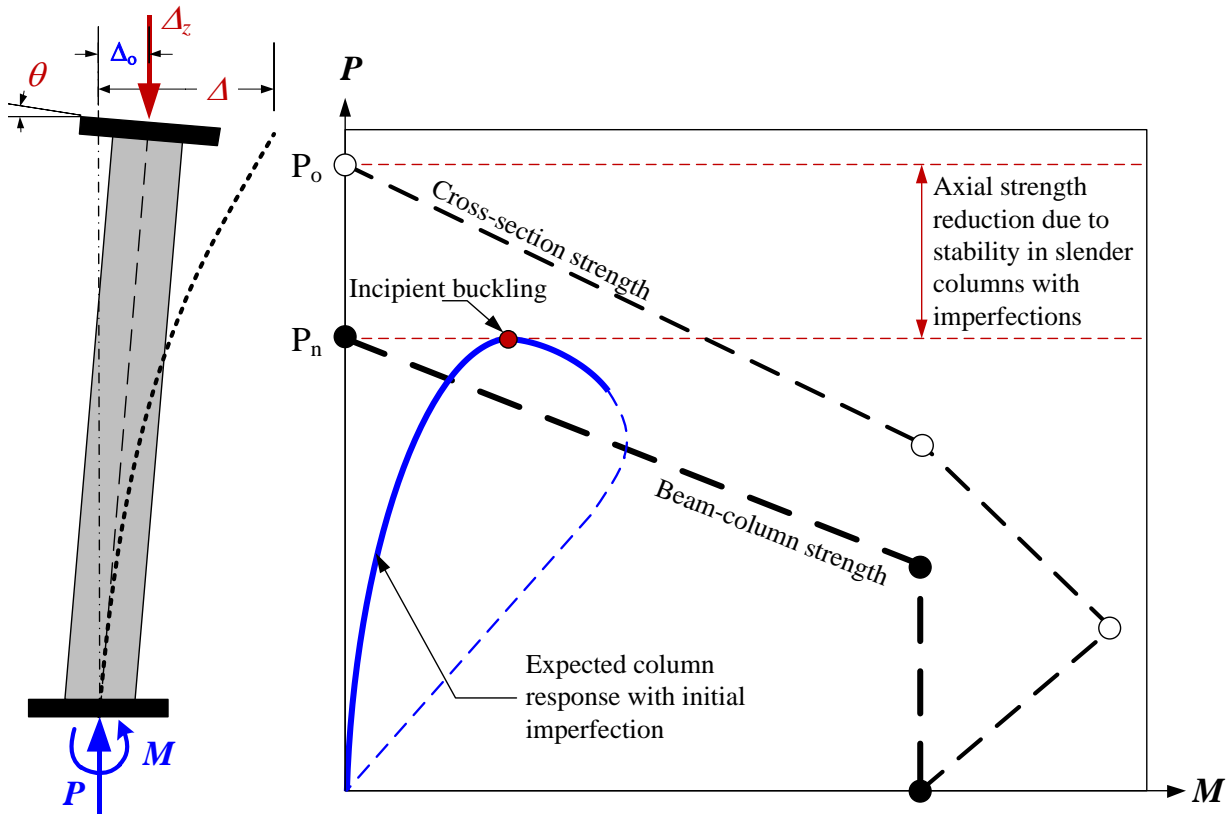


Figure 3.16. Expected column response with LC1 under an incremental axial displacement on the CFT specimens with the initial out-of-plumbness

3.5.2. LC2 – Unidirectional lateral displacement with constant gravity force

3.5.2.1. Monotonic displacement with reversal at the maximum lateral strength

The application of a desired gravity load ($P < P_n$) while the top position is held at zero displacement is the preliminary step to the main motion in LC2. Right after the load P is preset and maintained, the second load case (or LC2) consists of driving the specimen tip sideways while it is under the given constant gravity load (P). The motion of the crosshead during this load case (in fact, during all the LC2 and LC3 types) took place with a fixed rate of $1 \text{ in}/\text{min}$ in the axis of motion, although in some cases a rate of $1.5 \text{ in}/\text{min}$ was used.

Similar to the previous load case, the rotations (θ) at the top are controlled during the entire load case as free (or with moments at the top equal to zero). The motion at the top follows the axis delineated by the path in the previous load case LC1, which follows the axis defined by the initial imperfection in the CFT specimens and the X-axis in the RCFTs.

As the specimen starts moving sideways, the lateral strength of the specimen will be activated as demanded. For this particular case, the reversal of displacement will take place when the lateral strength of the specimen slightly passes its peak value (F_{max}), when incipient instability is detected. At the peak, the critical section at the base is loaded in flexure by the overturning moment ($\approx F_{max} \cdot L$) plus the second order component ($P\Delta$). Since this load case is in displacement control, an increment in displacement after the peak results in a decrease of the lateral force to maintain equilibrium. Also, decreasing the displacement would unload F as well, and then activate the lateral strength in the opposite direction. Calibration of the P-M interaction diagram may be possible through a set of different pairs of the maximum stable moments at each sustained axial load; inclusion of the moments consumed by the imperfections is needed in the calibration, and this may be possible with the results from LC1 and/or its calibration.

Figure 3.17 describes schematically the axial force – moment path on LC2 and the expected reversals (blank squares). As reference, this figure also shows a representation of the interaction diagrams for a cross-section and a beam-column, highlighting the unusable flexural capacity due to stability of the slender beam-column.

Among the parameters intended to address with load case LC2 are:

- Experimental determination of the net flexural uniaxial capacity for different levels of gravity force (experimental P-M set points, uniaxial bending).
- Comparison with the analytical interaction diagrams obtained with the design equations of the AISC Specifications.
- Experimental determination of the effective flexural stiffness (EI_{eff}) of the composite column from the lateral force –displacement and moment-curvature responses.
- Calibration of the analytical models to fully predict the full response (forces, displacements, strains, local buckling occurrence) of these slender beam-columns.

The first half of specimens was tested with this LC2 type and with different values of gravity force (P), each with two cycles up to both positive and negative peaks. The remaining half was tested with the variant explained in the next section.

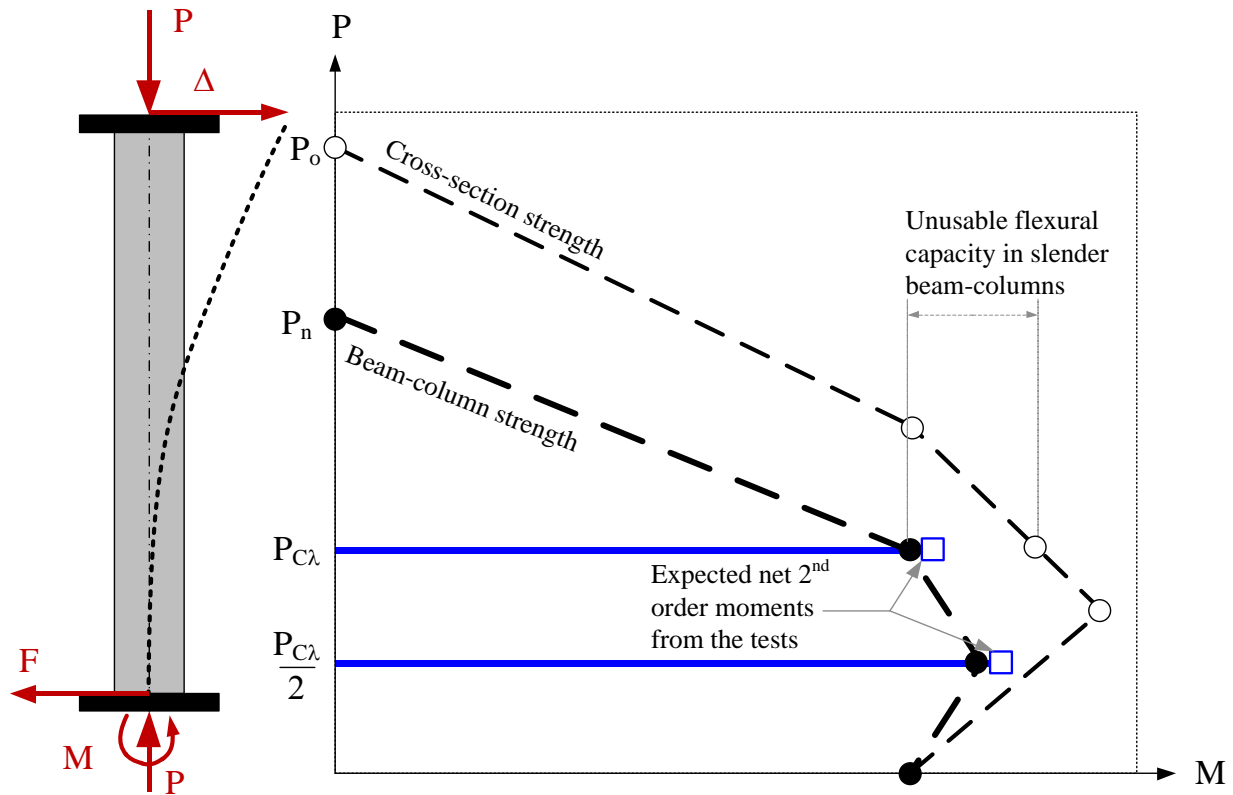


Figure 3.17. Expected column response with LC2 under a constant axial load, incremental uniaxial lateral displacement, and reversals at the peak lateral strength

3.5.2.2. Incremental cyclic displacement with reversal at a target displacement

This type is a variant of the previous LC2 used for the second half of specimens. As for the first half of the specimens, this case starts with the application of the desired gravity load, followed by a cyclic sideways movement as illustrated in Figure 3.18.a. This motion also follows the axis delineated by the path in the previous load case LC1, which is the axis of initial out-of-plumbness in the circular specimens, and the X axis in the rectangular specimens (Figure 3.18.b).

Same than in the previous LC2 type, the lateral motion of the specimen tip was controlled with input commands that moves the crosshead from the origin position to the target displacement with a fixed rate of the order of $1 \text{ in}/_{\text{min}}$ in the axis of motion, although this rate was increased to $1.5 \text{ in}/_{\text{min}}$ in some cases where no negative influence was expected. The purpose of the higher rate aims to save time of testing of the order of 50%, and it was only used occasionally in those load cases under a low axial loading (P under the balance point) and in those specimen with the larger cross-sections such as the CCFTs with 20" diameter, or the RCFTs oriented in the strong axis.

The difference with the previous case is that the reversals for this LC2 type occurs at desired drifts, whether or not this displacement is before or after the peak lateral capacity. Thus, the displacement path was cyclic with reversals mostly from 1% to the maximum stroke of the MAST system (between 4% to 6% drift) with increments of 1% of drift. Figure 3.18 shows the cyclic response ($M-\Delta$, $F-\Delta$, $M-\theta$, $M-\phi$) during LC2 with reversals at every 1% of incremental drifts.

Among the parameters intended to address with this LC2 type are those of the previous LC2 type (with reversal at peak lateral capacity), plus the following characteristics.

- Evaluation of the strength and stiffness degradation.
- Progression of the steel local buckling and its interaction with previous limit states (i.e. steel yielding in compression and tension)

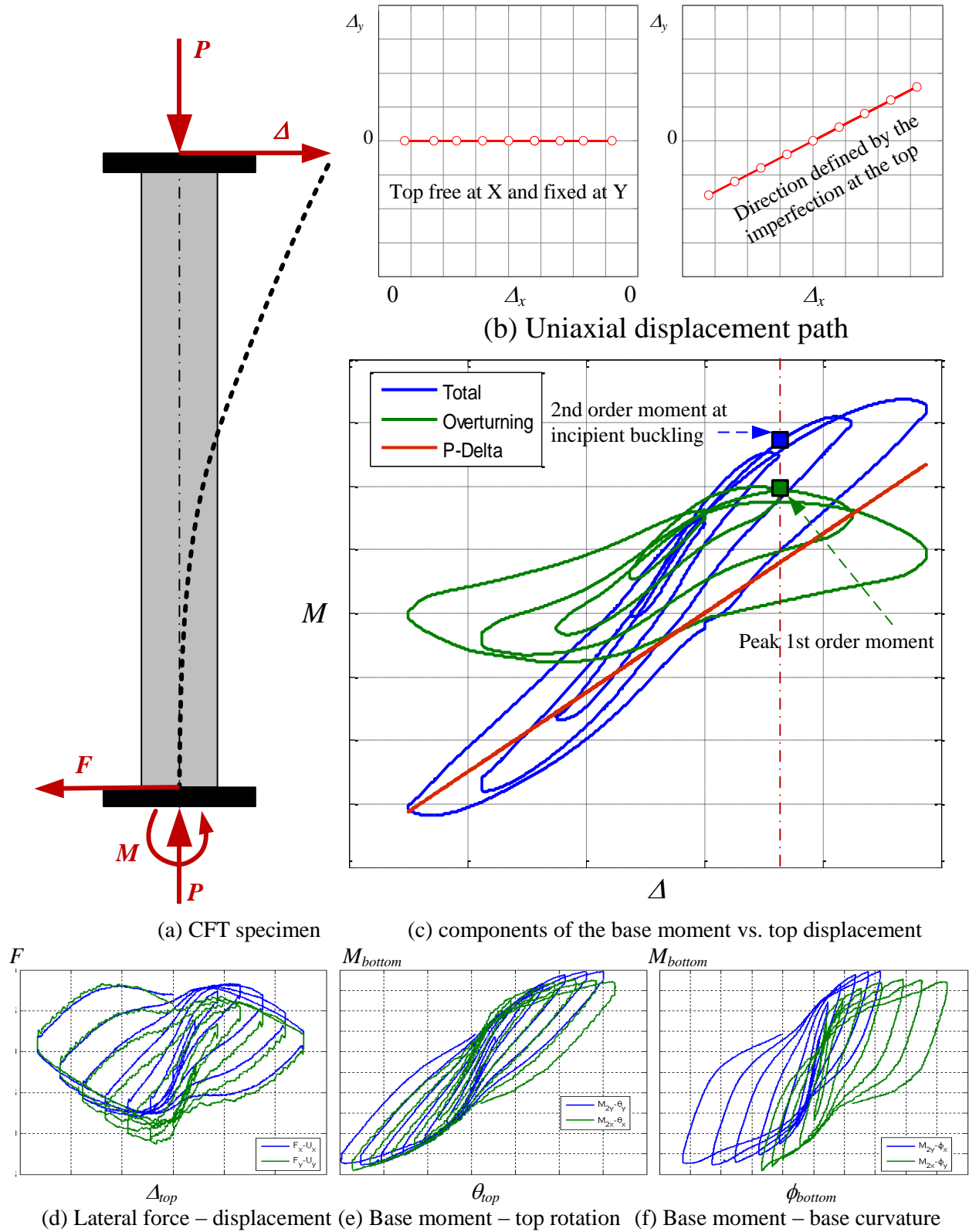


Figure 3.18. Expected column response with LC2 under a constant axial load and cyclic biaxial lateral displacement towards different drift targets

3.5.3. LC3 – Multidirectional lateral displacement with constant gravity force

3.5.3.1. Monotonic displacement with reversals at the peak lateral capacity

This third load case LC3, used for the first half of specimens, is similar to the uniaxial load case LC2 with reversal at peak capacity, with the difference that the path of motion is multidirectional along different probes around the specimen (Figure 3.19.a, b, c). The purpose of this LC3 type is the determination of the interaction surface (M_x - M_y) for different values of compression force (P) such that analytical 3D interaction diagrams can be calibrated with experimental data (Figure 3.19.d, e). Similar to the 2D interaction diagram, inclusion of the moments consumed by the imperfections is needed in the calibration and this may be possible with the results from LC1 and/or its calibration.

Figure 3.19.b shows the displacement path used primarily in the first half of the specimens. This LC3 type started by holding the desired gravity load P , followed by a probe moving laterally from *point 0* towards *point 1* at a rate of 1.0 to 1.5 in/min in the axis of motion, and with reversal at the peak lateral capacity (blank circle) with the same lateral motion rate (1.0 to 1.5 in/min). The reversal stops near the midpoint towards the zero position, and then the specimen was moved along the diamond path shown, with a new probe towards *point 2*. This process continues with the same speed rate for the 8 probes, and finally completing the diamond cycle and returning to the starting *point 0*. This 8-probe path was used from the specimens 4 to 8. Likewise, specimen 3 used a similar path with 16-probes around the diamond. Specimen 9 was controlled with a set of main probes, each with different sub-probes paths as shown in Figure 3.19.c.

The union of the lateral strength peaks for all the probes (represented by the blank circles from *point 1* to 8) delineates the interaction surface in either the displacement space (as shown in Figure 3.19.b and c) or in the moment space (as shown in Figure 3.19.d and e). All the latter processes are repeated for up to 3 different compression loads.

Among the parameters intended to address with this LC3 type are:

- Experimental determination of the net flexural biaxial capacity for different levels of gravity force (experimental P - M_x - M_y set points, biaxial bending). The shape of the biaxial interaction surface (M_x - M_y) may be controlled by the cross-section type, the axial

load level in the column, and the accumulated degradation experienced from previous probes or load cased.

- Calibration of the analytical interaction diagrams obtained with the design equations of the AISC Specifications.
- Evaluation of the effective flexural stiffness (EI_{eff}) associated to the different axis of motion.
- Calibration of the analytical models to be able in predicting the 3D full response (forces, displacements, strains) of these slender beam-columns. The analytical response must be able to predict the accumulated damage response (i.e. steel local buckling, concrete crushing and cracking) and the corresponding degradation.

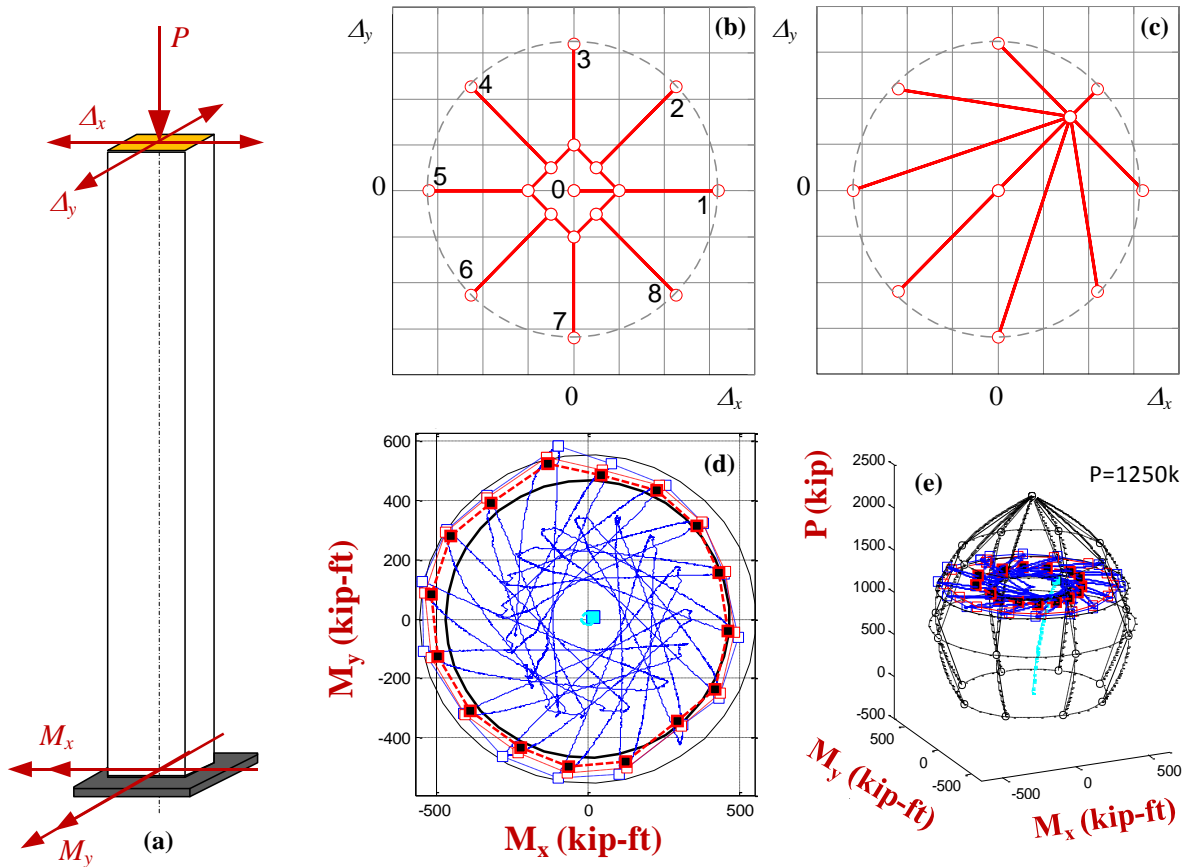


Figure 3.19. Expected response under a constant axial load and biaxial lateral displacement towards different probes with reversals at the peak lateral strength. (a) Free body diagram. (b) Displacement path of the top with 8 probes. (c) Displacement path of the top with 1 probe and different sub-probes. (d) Interaction surface M_x - M_y . (e) 3D P - M_x - M_y interaction diagram.

3.5.3.2. Incremental cyclic displacement turning around once the target displacement is reached

This LC3 type was used for specimen 8 and the second half of tests (specimen 10 to 12). In contrast to the biaxial load case LC3 with reversal at peak capacity, in this LC3 the reversals take place at target drift levels (Δ/L) as shown in Figure 3.20.b, starting from 1% in both positive and negative sides, with increments of 1% up to the maximum stroke of the system (which varies from 4 to 6% drift). Same than before, the crosshead and the specimen tip are driven at a fixed speed rate of the order of $1.0 \text{ in}/\text{min}$ (and up to $1.5 \text{ in}/\text{min}$ in few cases). Figure 3.20 also shows the cyclic response ($M-\Delta$, $F-\Delta$, $M-\phi$) during LC3 with reversals at every 1% of incremental drifts.

Among the parameters intended to address with this LC3 type are those of the previous type (with reversal at peak lateral capacity), plus the following characteristics.

- Evaluation of the strength and stiffness degradation.
- Progression of the damage (i.e. steel local buckling) and its interaction with previous limit states (i.e. steel yielding in compression and tension).

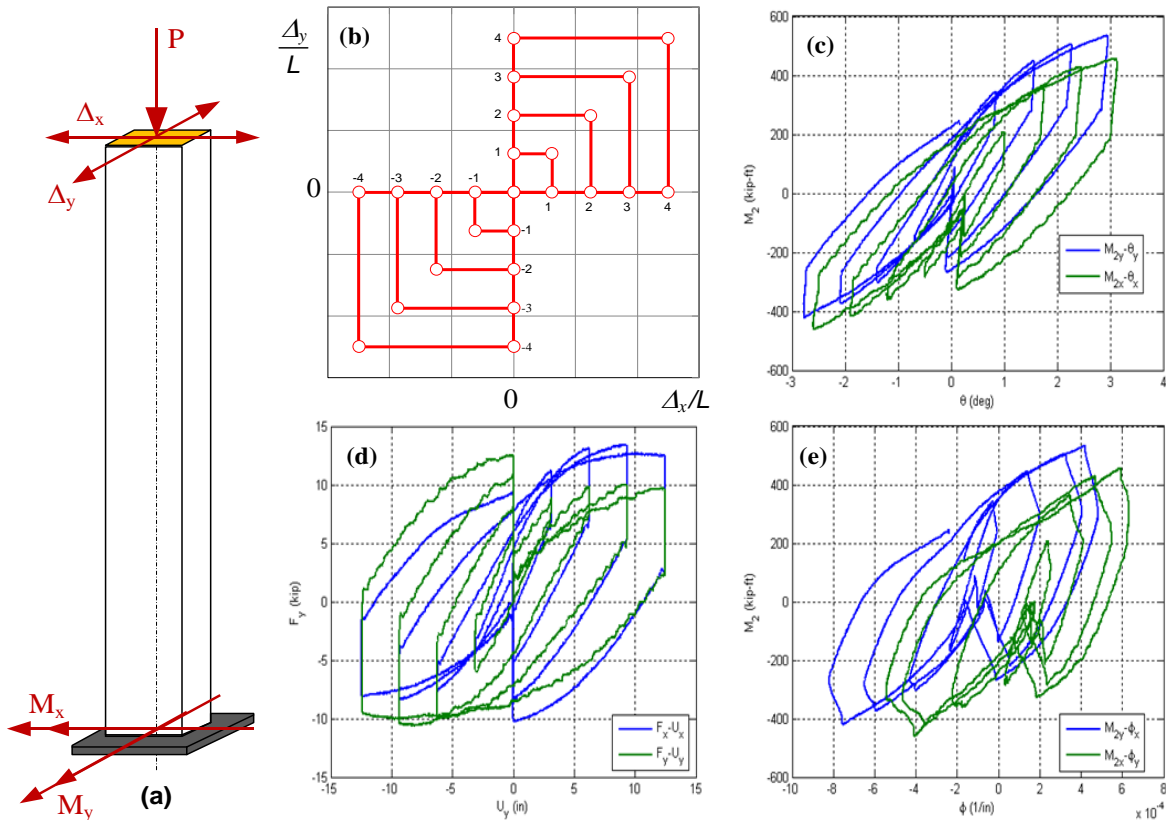


Figure 3.20. Expected column response with LC3 under a constant axial load and cyclic biaxial lateral displacement towards different drift targets

3.5.4. LC4 – Final load case set

After the previous three load cases, with all the different cycles and cases, a final load case is applied to finalize the load protocol. The intention of this final load case was to extend the amount of damage until an irreversible failure (i.e. steel fracture) took place. Fracture in the steel was never observed in any test, even when different load paths were applied to target this failure.

The following section summarizes different choices used for the latest load case. In some cases, combinations of these were used to increase the damage.

3.5.4.1. Repetition of some previous load cases

In some cases, the previous load cases LC1, LC2 or LC3 was repeated with and/or without the same previous conditions; these conditions include but are not limited to the corresponding boundary or control conditions (i.e. fixed-fixed $K=0.5$), load or displacement values (i.e. different gravity loads P , or different target drifts), etc.

3.5.4.2. Monotonic twisting with constant gravity force

This LC4 type, used for the first half of specimens, consists in twisting the specimen by rotating the crosshead towards the maximum rotations of the system ($\approx \pm 10^\circ$). In order to evaluate the effect of the axial force on the torsion strength, this twisting load case was applied with no compression force (pure torsion) and 20% of the squashing strength ($P=0.2P_o$), and the lateral displacements and top bending rotations were held at zero. Figure 3.21 shows schematically the torsion-twisting response expected during this LC4 type.

Among the parameters intended to address with this LC3 type are:

- Experimental determination of the torsional capacity with and without presence of axial compression force.
- Experimental determination of the effective torsional stiffness (JG_{eff}) of the composite column from the torsion moment –rotation response.
- Calibration of the analytical models to be able in predicting the 3D full response (i.e. torsion, twisting, strains) of these slender beam-columns.

3.5.4.3. Monotonic uniaxial or biaxial displacement towards the maximum system stroke

This load case LC4 type, used for the second half of specimens, has the intent to induce the highest possible damage in the specimen through a motion of the top towards the maximum possible displacement of the system (the four corners) and with a very high axial gravity load. Figure 3.22 shows schematically the path-displacement path during this LC4 type, driving the specimen with the probes towards the points 1 to 4.

Among the parameters intended to address with this LC3 type are:

- Evaluation of the highest strength and stiffness degradation in these slender specimens.
- Calibration of the analytical models to be able in predicting the final response.

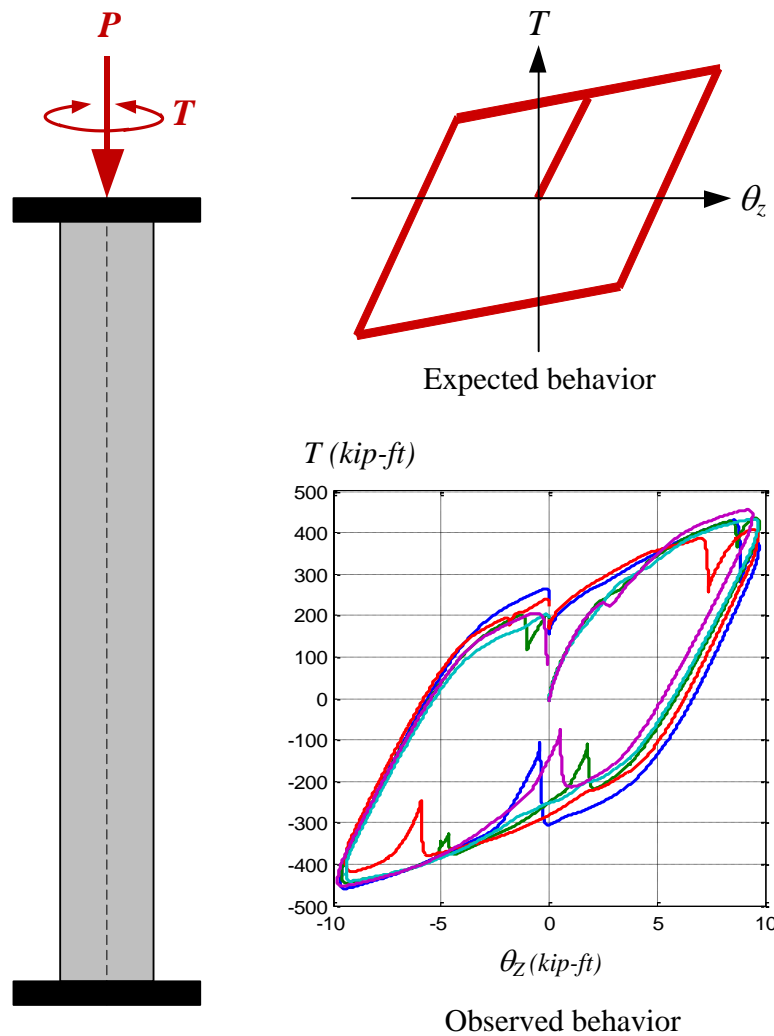


Figure 3.21. Expected column response with LC4 under a constant axial load and incremental torsional displacement towards the maximum system rotation

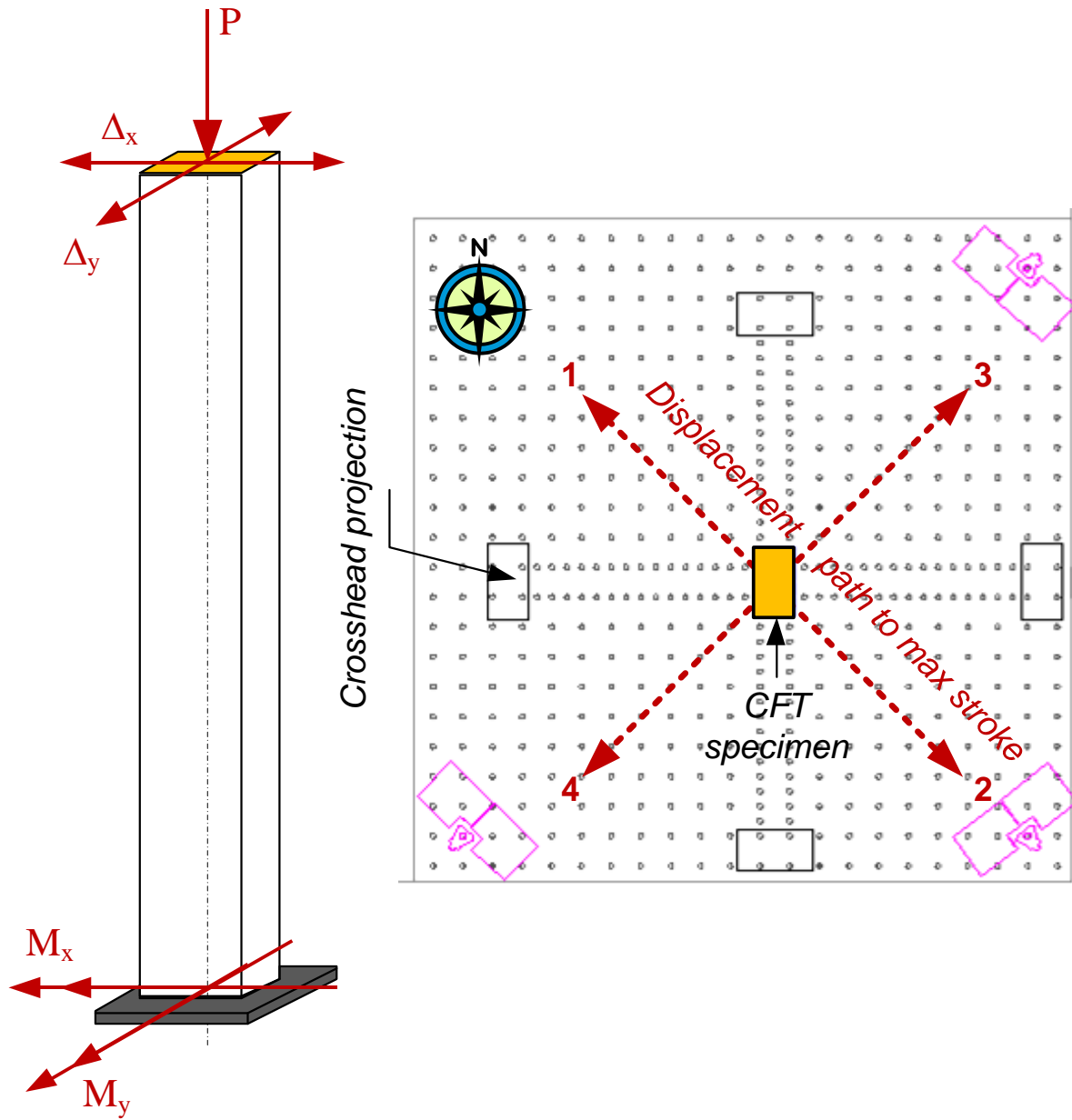


Figure 3.22. Final displacement path under a high constant axial load and incremental lateral displacement towards the maximum system translation

CHAPTER 4

WET CONCRETE EFFECTS

4.1. Introduction

Evaluation of the wet concrete acting on the tube as a hydrostatic pressure was discussed early in this project since the experimental program included very long columns, large cross-sections and very thin steel tubes. Chapter 2 discussed some of the available research studies on the concrete casting effects as well as common practices for cast-in-place CFT columns. These descriptions indicated that casting effects could have potentially large impacts on the behavior of these specimens.

In this chapter, the effects of the wet concrete during the casting are discussed. The stresses, strains and deformations are first calculated based on closed-form solutions and Finite Element Analyses (FEA). These analytical results are then compared with the experimental measurements obtained during casting. The influence of the initial deformations and transverse stresses created by the hydrostatic pressure on the steel local buckling are discussed. Finally, design recommendations for handling casting effects are proposed.

4.2. Analytical prediction

4.2.1. Closed-form solutions in circular tubes

The closed-form solution for circular tubes under hydrostatic pressure (or thin-walled pressurized vessels) is well known, and can be found in any strength of materials book (i.e. (Timoshenko 1930); (Budynas 1999)). The solution is based on the equilibrium of forces at the cross-section as shown in Figure 4.1. From this figure, values of the elastic transverse stresses (σ_r) and deformation (δ) for thin-walled circular pressures vessels can be obtained with the aid of Equations 4.1 and 4.2.

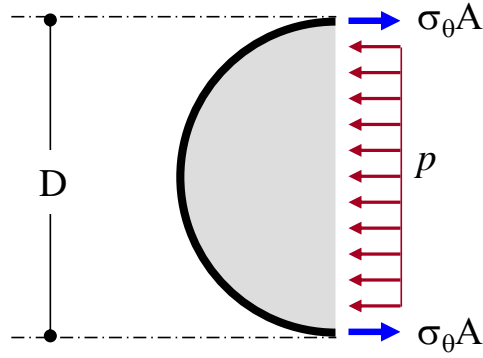


Figure 4.1. Free body diagram of a half circular tube with internal pressure

$$\sigma_t = \frac{p(D - 2t)}{2t} = \frac{p \cdot R}{t} \quad (4.1)$$

$$\delta = \Delta R = \frac{p \cdot R^2}{E_s \cdot t} \quad (4.2)$$

where D is the diameter of a circular tube, t is the wall thickness, and E_s is the Young's modulus of the steel. The hydrostatic pressure is $p = w_c \cdot L_p$, where w_c is the unit weight of the wet or fresh concrete ($\approx 150 \text{ lb/ft}^3$ for normal weight concrete) and L_p is the height of the linear pressure at the point of interest.

4.2.2. Analytical solutions for rectangular tubes

Closed-form solution for rectangular pressure vessels is not as simple as for circular shapes. One approximate solution is assuming plate bending behavior on the steel walls; this assumption will be illustrated in the next section with results obtained from finite element analysis. Based on plate bending theory (Budynas, 1999; Young and Budynas, 2001), equations for the calculation of the elastic transverse stresses (σ_t) and deformations (δ) for rectangular steel tubes under hydrostatic pressure can be approximated with Equations 4.3.a and 4.4.

$$\sigma_t = \beta_1 \frac{p \cdot (h - 2t)^2}{t^2} \leq F_y \quad (4.3)$$

$$\delta = \beta_2 \frac{p \cdot (h - 2t)^4}{E_s \cdot t^3} \quad (4.4)$$

In the previous equations h is the width of the rectangular cross-section, t is the wall thickness, and E_s is the Young's modulus of the steel. The hydrostatic pressure ($p=w_c \cdot L_p$) depends on the unit weight of the wet or fresh concrete ($w_c \approx 150 \text{ lb/ft}^3$ for normal weight concrete) and the high of the linear pressure of interest (L_p). The stiffness parameters β_1 and β_2 are related to the geometry and the effective boundary conditions of the steel walls. For conventional HSS tubes these can be approximated with the following equations derived assuming plate bending theory:

For the stresses at the ends of the longer face on the rectangular tube:

$$\beta_1 = \frac{2h_c}{b_c + 4h_c} \quad (4.5)$$

For the stresses at the middle of the longer face on the rectangular tube:

$$\beta_1 = \frac{1}{3} \left(\frac{3b_c + 4h_c}{b_c + 4h_c} \right) \quad (4.6)$$

Deformation at the middle of the longer face of the rectangular tube:

$$\beta_2 = \frac{1}{32} \left(\frac{5b_c + 4h_c}{b_c + 4h_c} \right) \quad (4.7)$$

where h_c and b_c are, respectively, the longer and the shorter inner widths of the rectangular cross-section ($h_c = h - 2t$; $b_c = b - 2t$). The stresses and deformations of the shorter face are lower than those estimated for the longer side; these can be estimated by switching the cross-section size dimensions in Equation 4.7. The calculation of the stresses and the deformation is strictly valid if the stresses, either at the ends or the center, are lower than F_y . If the stresses are within the elastic range, the corresponding strains can be calculated by the Hooke's law as: $\varepsilon_t = \sigma_t \cdot E_s$.

4.2.3. Finite Element Analysis

In order to verify the effects of the concrete casting in the 18 and 26 feet long CFTs, FEAs were performed using the software ABAQUS (2010) for the circular and rectangular steel shapes used in this research. The steel tubes were modeled with quadratic isoparametric solids (20-node bricks, C3D20R) with a size that ensures 5 nodes through the thickness and an aspect ratio lower than 12.5. The hydrostatic pressure applied on the internal steel walls was calculated

based on the column height and the concrete unit weight (Figure 4.2). Typical contour stresses of transverse stresses are plotted in Figure 4.3. Table 4.1 shows a summary of the results from the analysis.

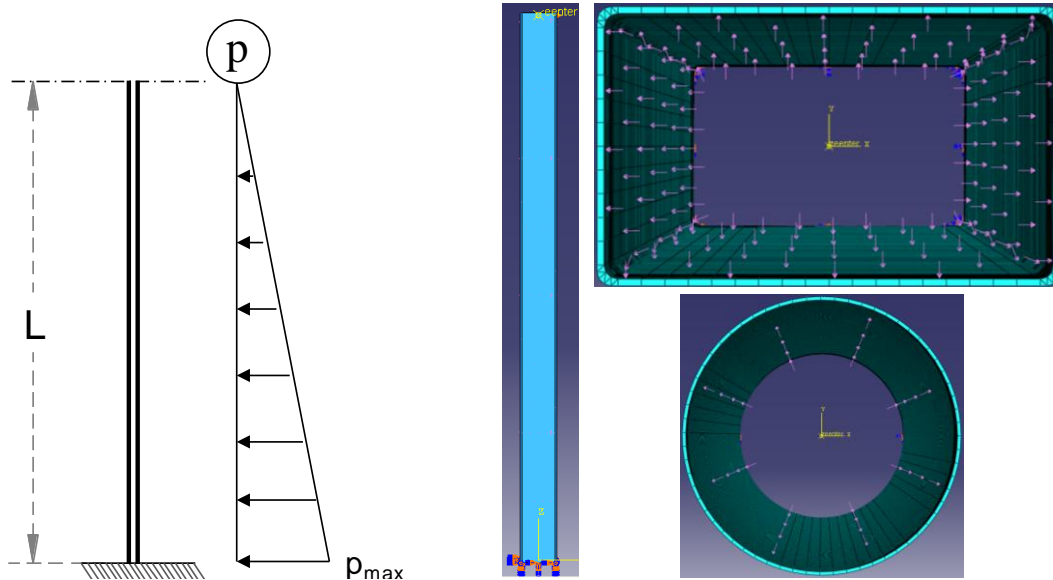


Figure 4.2. F.E. Model of a steel tube under hydrostatic pressure

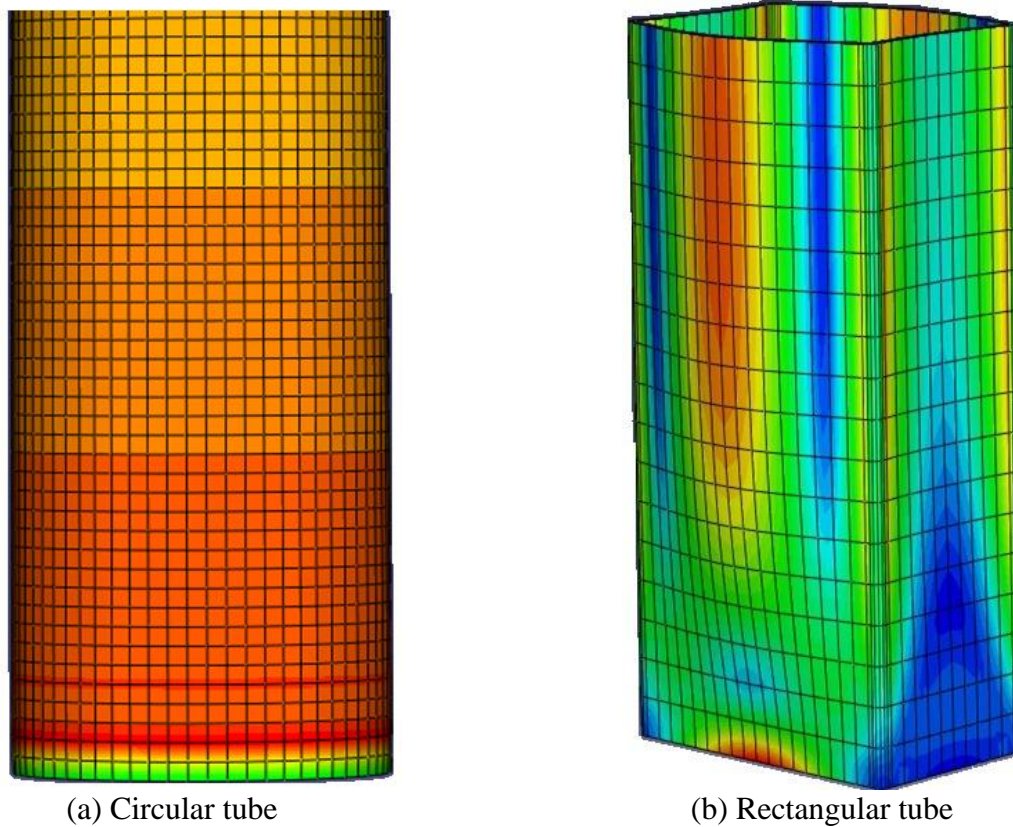


Figure 4.3. Contour of transverse stresses at the $L/4$ bottom of the HSS from FEA

Table 4.1. Maximum analytical response of steel tubes under hydrostatic pressure

Steel shape	L (ft)	σ_t (ksi)	ϵ_t ($\times 10^{-6}$)	δ (in)
HSS5.563x $\frac{1}{8}$	18	0.425	15	0.00005
	26	0.614	21	0.00007
HSS12.75x $\frac{1}{4}$	18	0.490	17	0.00013
	26	0.708	25	0.00019
HSS20x $\frac{1}{4}$	18	0.730	25	0.00024
	26	1.132	39	0.00045
HSS20x12x $\frac{5}{16}$	18	25.90	893	0.188
	26	36.13	1246	0.241

As summarized in the Table 4.1, very low response values were obtained for the circular tubes, even for the longer columns or the thinner cross-sections. Results obtained with the FEA on the circular specimens matched closely those calculated from closed-form solution of thin-wall cylindrical pressure vessels. Transverse stresses obtained with FEA exhibited plate bending behavior since the stresses across the tube thickness remained constant. The calculated values indicated no concerns due to the fluid concrete in the circular cross-sections, so no additional action was taken for the construction of the CCFTs.

The opposite case occurred for the rectangular tubes, where the maximum computed transverse stresses and strains reached nominal yield values up to 60% and 80% of the for the shorter (L=18 ft) and the longer (L=26 ft) HSS tubes, respectively. The maximum response in the rectangular HSS20x12x $\frac{5}{16}$ was located in the longer 20" side and between 2 to 2.5 feet from the base. The contour of transverse stresses through the thickness (at the cross-section where the maximum values were obtained) is illustrated in the Figure 4.4. As shown in this figure, bending stresses are linearly distributed through the thickness, with maximum tension stress at the center-external fiber and about the same tension stress value at both extreme-internal fibers of the 20" wall. Linear distribution of the transverse stresses, varying from tension to compression and

passing through zero at the central node, confirm primarily bending behavior in the plates as initially assumed. The outward deflection in the longer 20" walls due to the internal concrete pressure reduced and induced inward deflection in the shorter 12" walls. In case no action is taken, the concrete would take the shape of the deflected tube when it hardens.

FEA results on the rectangular specimen showed some dependency with the mesh size. Solutions converged with a fine mesh. The results from these analyses were well approximated with those obtained from simple calculations assuming bending behavior of the tube walls (Equations 4.1 and 4.2).

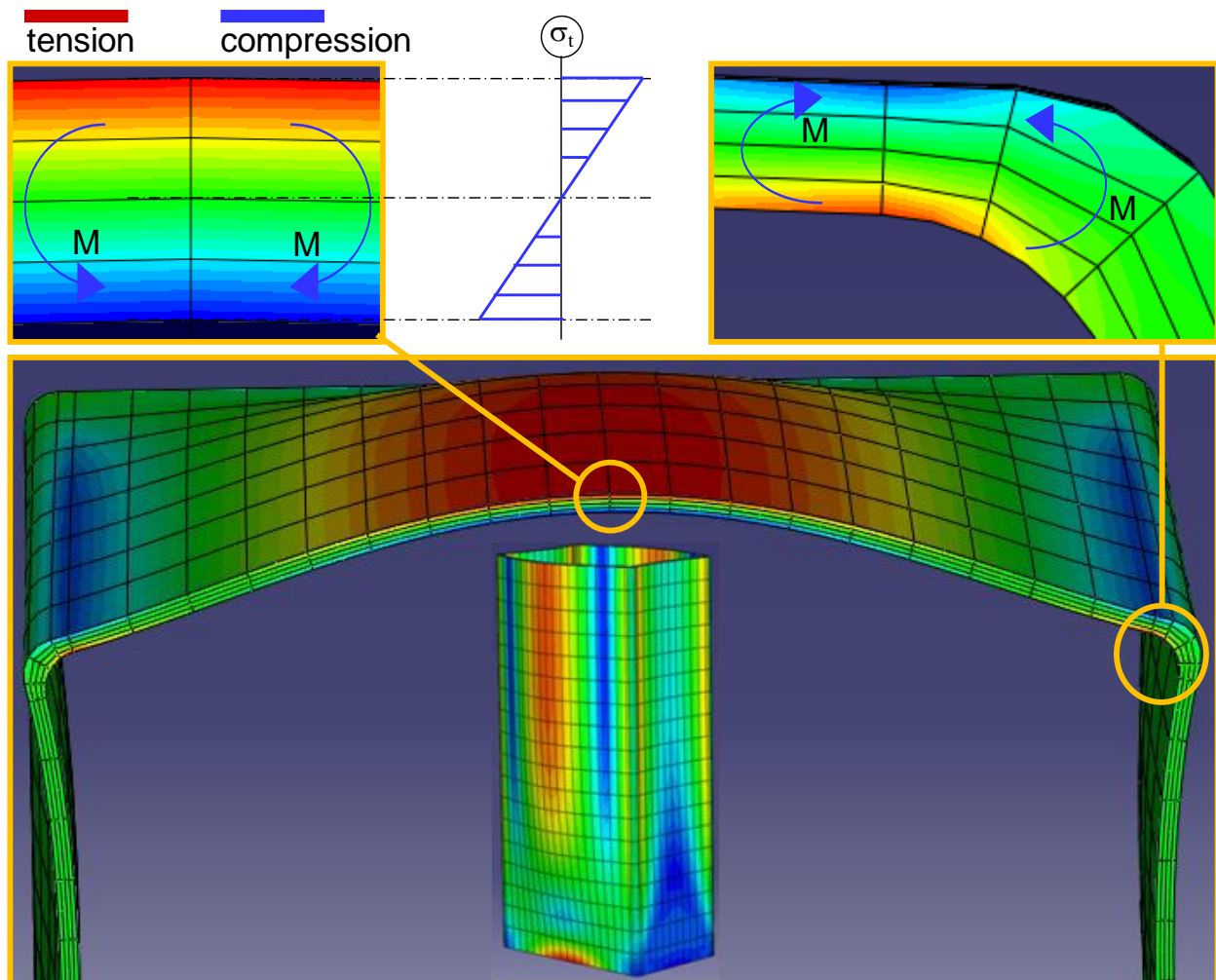


Figure 4.4. Distribution of maximum transverse stresses in the rectangular cross-section

4.3. Experimental investigation

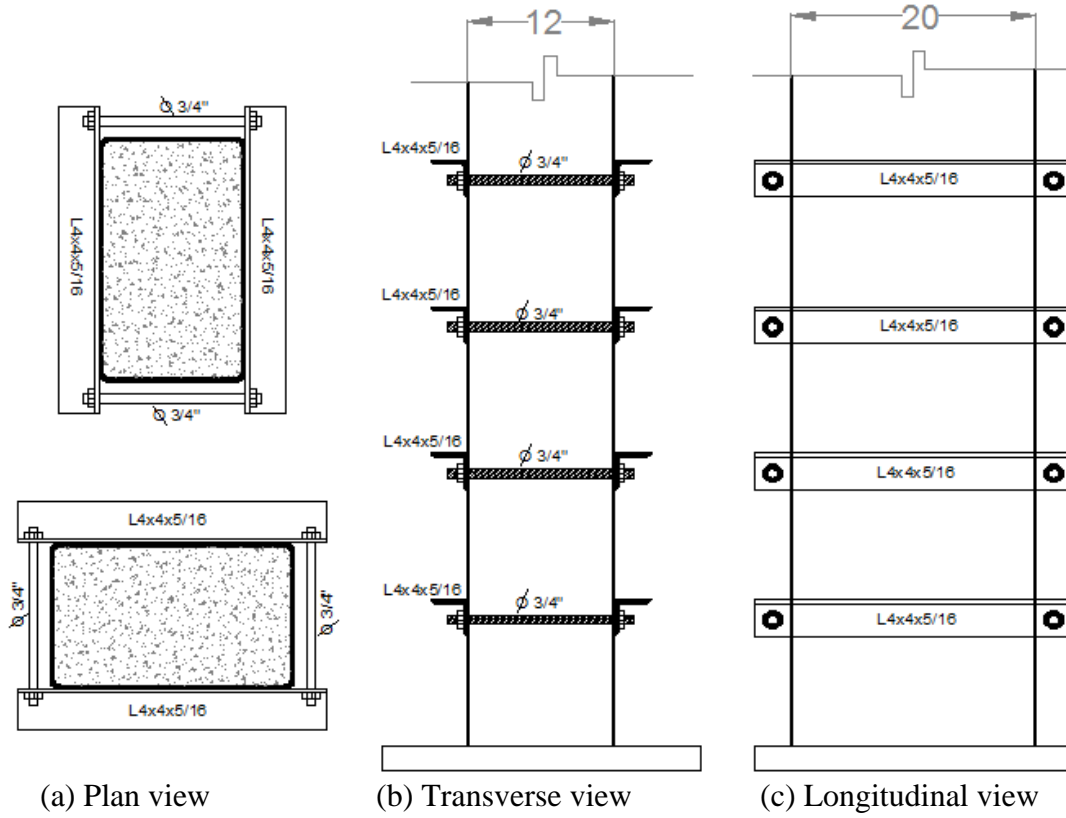
4.3.1. Construction of the specimens

Based on the analytical results, the following actions were taken for the construction of the rectangular CFTs.

- Installation of rosettes or cross strain gages at critical points so transverse strains could be measured during the concrete casting and the hardening process. Measurements of transverse strains during the casting process allow comparisons of the experimental response with that predicted from the analyses.
- Installation of temporary braces in some tubes at the critical sections (as described in Table 4.2 and shown in Figure 4.5), so the expansion due to the internal pressure can be reduced. These temporary braces consisted of two angles (ASTM A36, 4x4x5/16 inches) in contact with the longer 20 in. sides, and tensioned with two threaded rods (ASTM A193 Grade B7, $\frac{3}{4}$ in. diameter) along the shorter 12 in. sides (Figure 4.5). This temporary lateral reinforcement intended to diminish the expansion of the rectangular steel tubes during the casting, thus reducing the difference in shape between the assumed perfect rectangular column and the actual deflected shape after hardening. As illustrated in Figure 4.5, the braces were located at the bottom from 1 to 4 feet at every foot.

Table 4.2. Braces plan for the RCFTs

Specimen	Notes
4-Rw-18-5	This specimen was not braced, so expansion took place as expected and calculated (see Table 4.1). Strains were measured since casting until hardening of concrete (3 days).
5-Rs-18-5	This specimen was braced before the concrete casting. These braces were removed just before the specimen testing (147 days). Strains were measured since casting until hardening of concrete (3 days).
8-Rw-18-12 9-Rs-18-12	These specimens were braced about one and a half hours after the concrete was poured into the steel tubes. These braces were removed just before the specimens testing (92 days and 103 days, respectively). Strains were measured during the concrete casting, during the braces installation, and until the concrete hardening (5 days).
12-Rw-26-5 13-Rs-26-5 16-Rw-26-12 17-Rs-26-12	All these specimens were braced before the concrete casting. These braces were removed once the concrete hardens (3 days after casting). Strains were measured during the concrete casting and after the braces were removed (5 days).



(d) 5Rs-18-5



(e) 12Rw-26-5



(f) 13Rs-26-5

Figure 4.5. Distribution of temporal braces to restrain expansion due to the casting

4.3.2. Strain gages and principal strain and stress computation

As commented in the Chapter 3, specimens were extensively instrumented with uniaxial strain gages; in some critical points, cross or rosette strain gages were placed. All these strain gages are Tokyo Sokki waterproofed foil gages (WF series). Single strain gages were placed such that longitudinal strains due to either axial forces or bending were measured; cross and rosette strain gages were placed such that both longitudinal and transverse strains were measured (Figure 4.6). In rosette strain gages, a third component at 45° is also measured to make the calculation of the principal strains (ε_1 , ε_2) and its direction (ϕ) possible (Equations 4.8 and 4.9, respectively). If the principal strains are lower than the yield strain ($\varepsilon_y = F_y / E_s$), then the principal stresses (σ_1 , σ_2) and the von Mises (σ_{VM}) stresses can also be computed with Equations 4.11, 4.12 and 4.13, respectively.

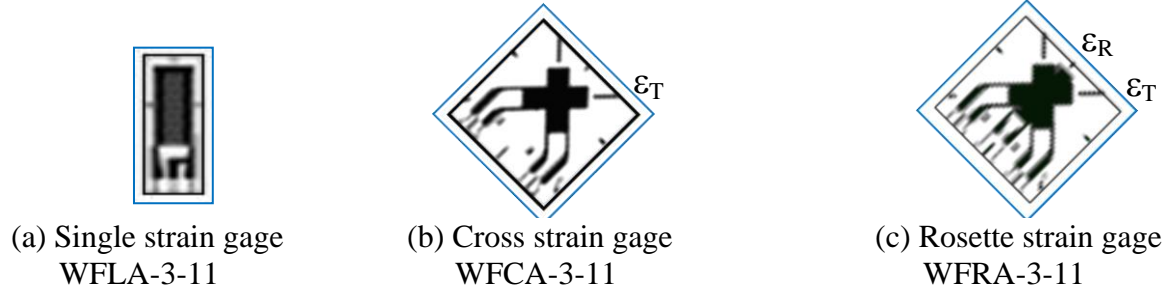


Figure 4.6. Strain gages Tokyo Sokki WF series

$$\varepsilon_{1,2} = \frac{\varepsilon_L + \varepsilon_T}{2} \pm \sqrt{\frac{(\varepsilon_L - \varepsilon_R)^2 + (\varepsilon_T - \varepsilon_R)^2}{2}} \quad (4.8)$$

$$\phi = \frac{1}{2} \tan^{-1} \left(\frac{\varepsilon_L + \varepsilon_T - 2\varepsilon_R}{\varepsilon_T - \varepsilon_L} \right) \quad (4.9)$$

$$\gamma_{xy} = 2\varepsilon_{xy} = 2\varepsilon_R - \varepsilon_L - \varepsilon_T \quad (4.10)$$

$$\sigma_1 = \frac{E}{(1-\nu^2)} (\varepsilon_1 + \nu\varepsilon_2) \quad (4.11)$$

$$\sigma_2 = \frac{E}{(1-\nu^2)} (\varepsilon_2 + \nu\varepsilon_1) \quad (4.12)$$

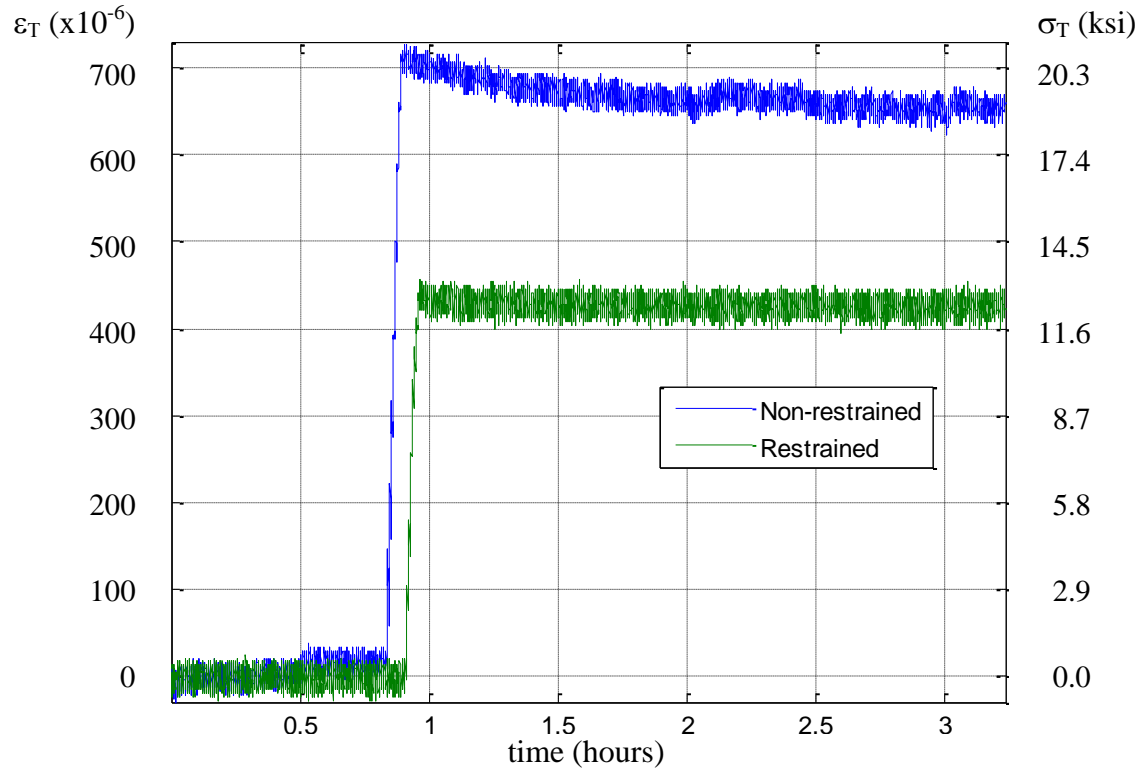
$$\sigma_{VM} = \sqrt{\sigma_1^2 - \sigma_1 \cdot \sigma_2 + \sigma_2^2} \quad (4.13)$$

4.3.3. Experimental strains measured during the concrete casting

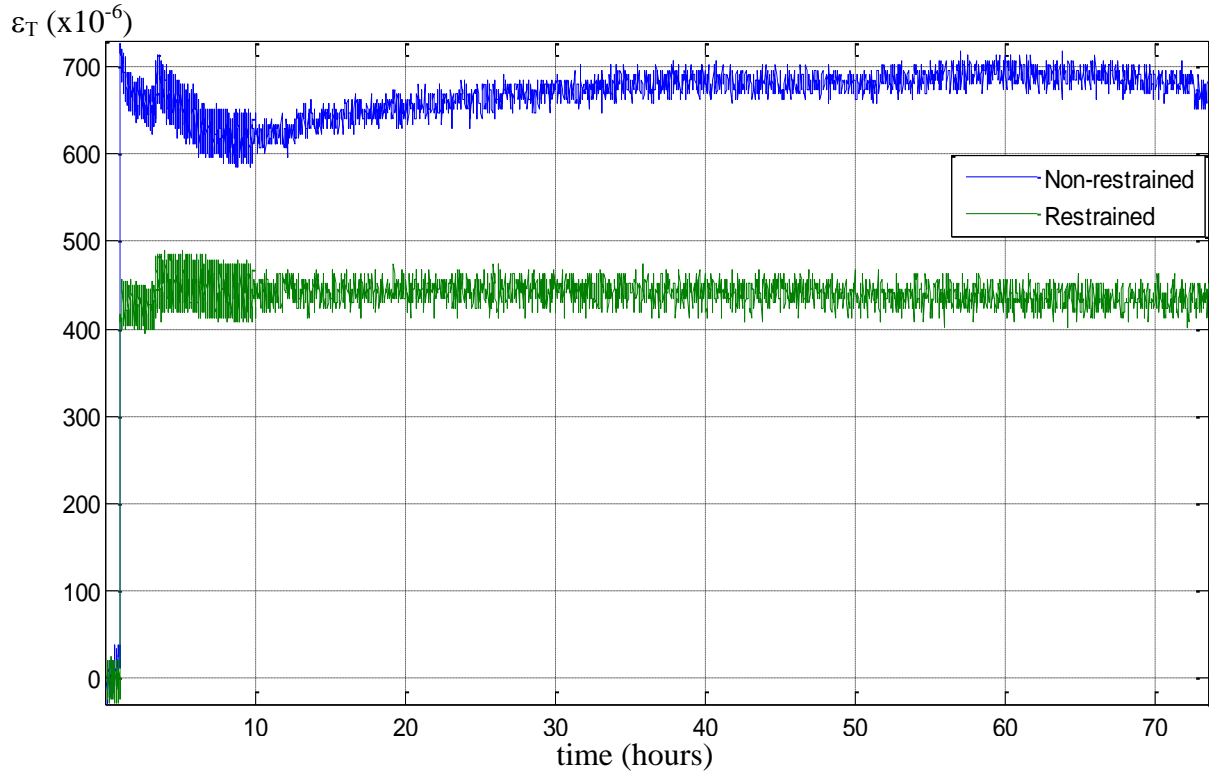
As shown in Table 4.2, specimens 4-Rw-18-5 (without the bracing restrainers) and 5-Rs-18-5 (with the bracing restrainers) were filled with concrete and the transverse strains were measured for 3 days. Figure 4.7 shows the transverse strains and stresses measured during the concrete casting for the restrained (4-Rw-18-5) and the non-restrained (5-Rs-18-5) cases and at the point where the critical value was expected (on the 20" face at 2' 6" from the base) for these 18 feet long specimens. As shown in this figure, the concrete started and finished being cast between 0.8 to 0.9 hr, so the hydrostatic pressure increased the transverse strain at this points up to 720 micro-strains (for the non-restrained case) and 470 micro-strains (for the restrained case). This figure illustrates the benefit of the bracing system, which reduced the level of maximum strains and stressed by about 35%. Strains were measured from casting until hardening of concrete (3 days), but the braces in the specimen 5-Rs-18-5 were removed just before the specimen testing (147 days).

Figure 4.8 shows the transverse strains and stresses measured during the concrete casting on the 20" face at 2' 6" from the base for the specimens 8-Rw-18-12 and 9-Rs-18-12. As shown in this figure, the concrete started and finished being cast between 1.9 to 2.0 hrs and, since both columns did not have the braces, the hydrostatic pressure increased the transverse strain up to 740 micro-strains. One to two hours later, the 3 braces (at 1, 2 and 3 feet from the base) were placed in each of these two 18 feet long specimens, reducing the transverse strains to 425 micro-strains. Again, the benefit of the bracing system reduced the level of maximum strains and stressed by about 43%. Strains were measured during the concrete casting, during brace installation, and until the concrete hardened (5 days). These braces were removed just before the specimens testing (92 days and 103 days, respectively).

Figure 4.9 shows the average transverse strains and stresses measured during the concrete casting at 1' 6" and 2' 6" from the base on the 20" face for specimens 12-Rw-26-5, 13-Rs-26-5, 16-Rw-26-12, 17-Rs-26-12. The concrete started being cast between 0.5 to 2.0 hrs and, since all these 26 feet long columns had the braces on (at 1, 2, 3 and 4 feet from the base), the hydrostatic pressure increased the transverse strains between 203 and 676 micro-strains. From the FEA without the restrainers, 1246 micro-strains were calculated for these specimens, and so the bracing system reduced the level of maximum strains between 46 to 84%.

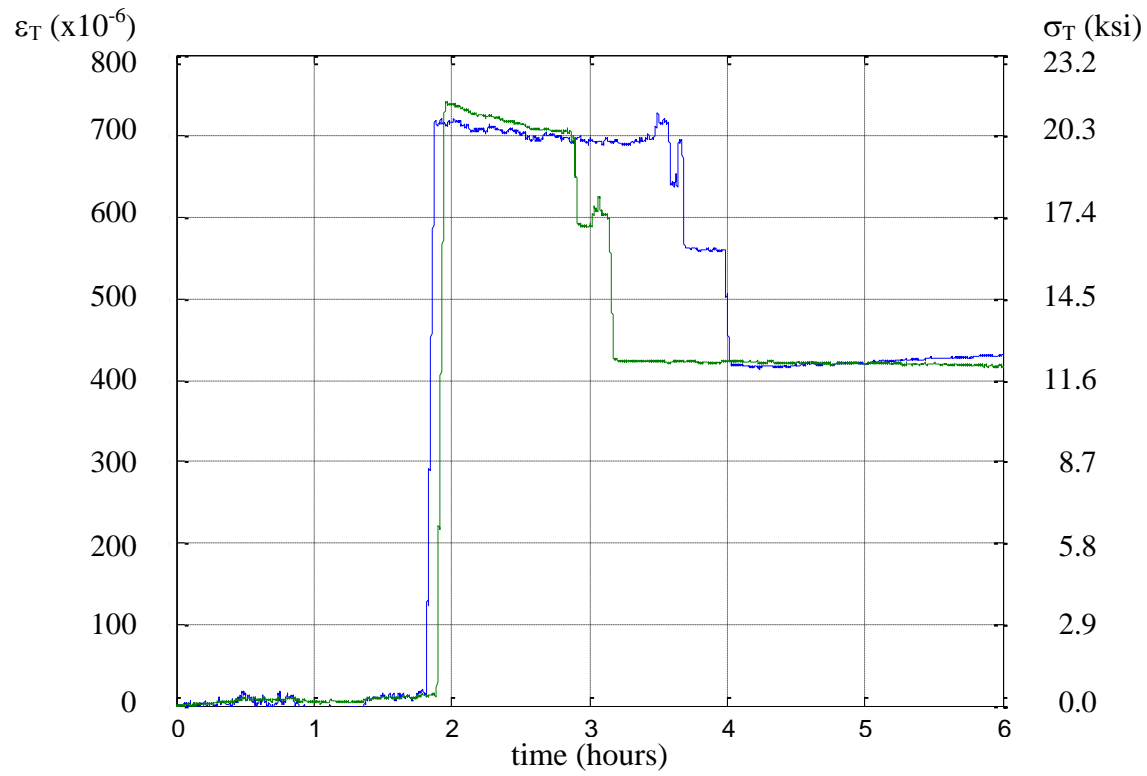


(a) Initial 3 hours during the concrete casting

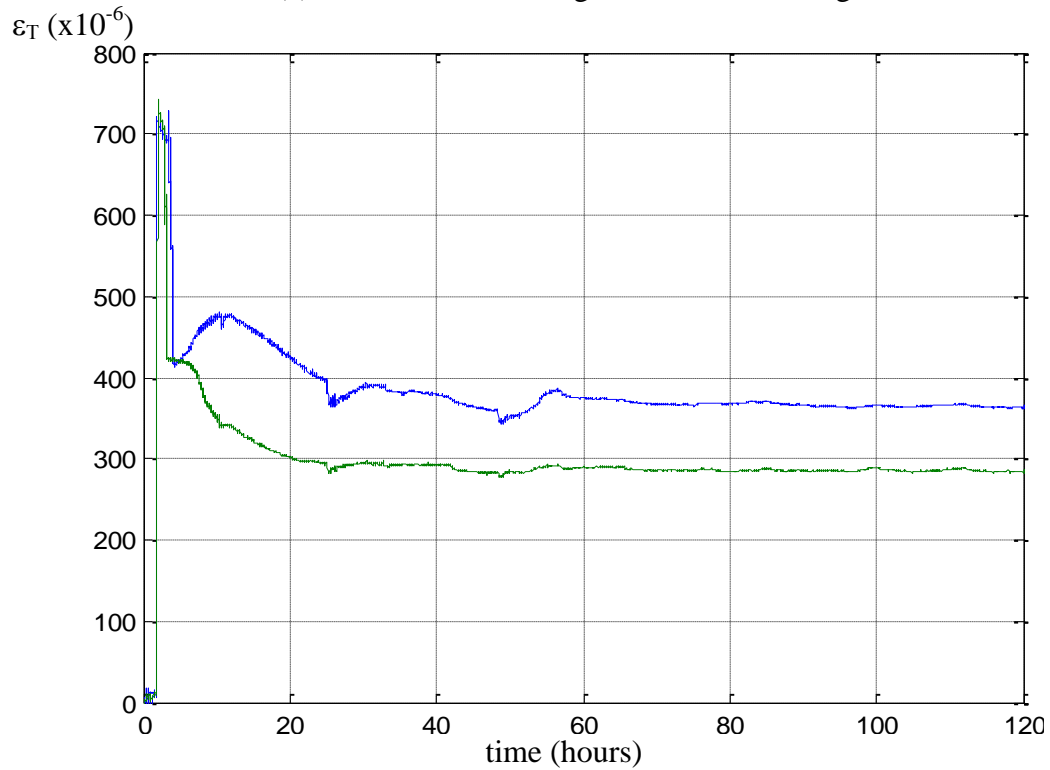


(b) Entire record

Figure 4.7. Transverse strains measured during the casting on the 20" face at 2' 6" from the base for the specimens 4-Rw-18-5 (restrained) and 5-Rs-18-5 (non-restrained).



(a) Initial 6 hours during the concrete casting



(b) Entire record

Figure 4.8. Transverse strains and stresses measured during the concrete casting on the 20" face at 2' 6" from the base for the specimens 8-Rw-18-12 and 9-Rs-18-12.

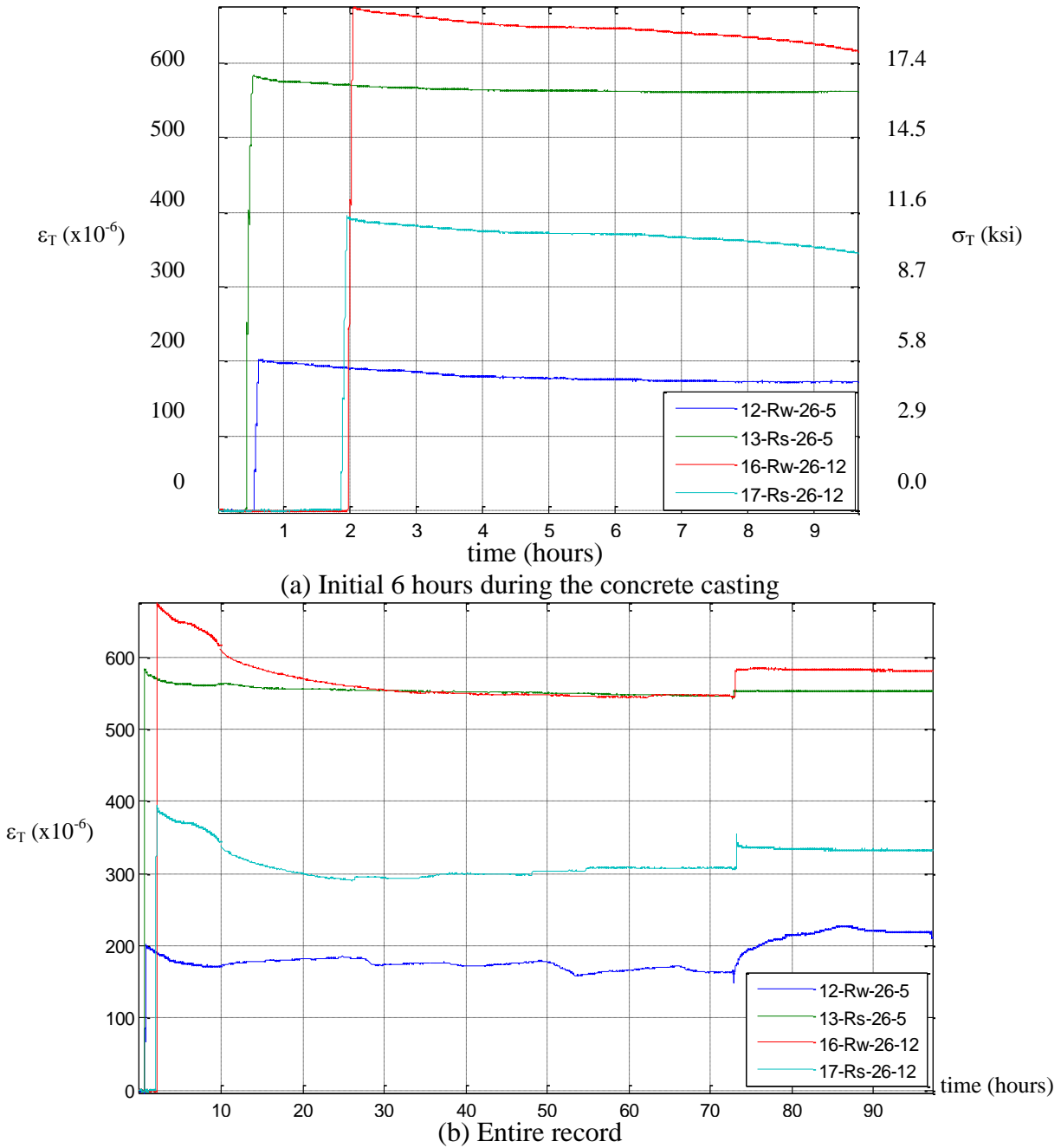
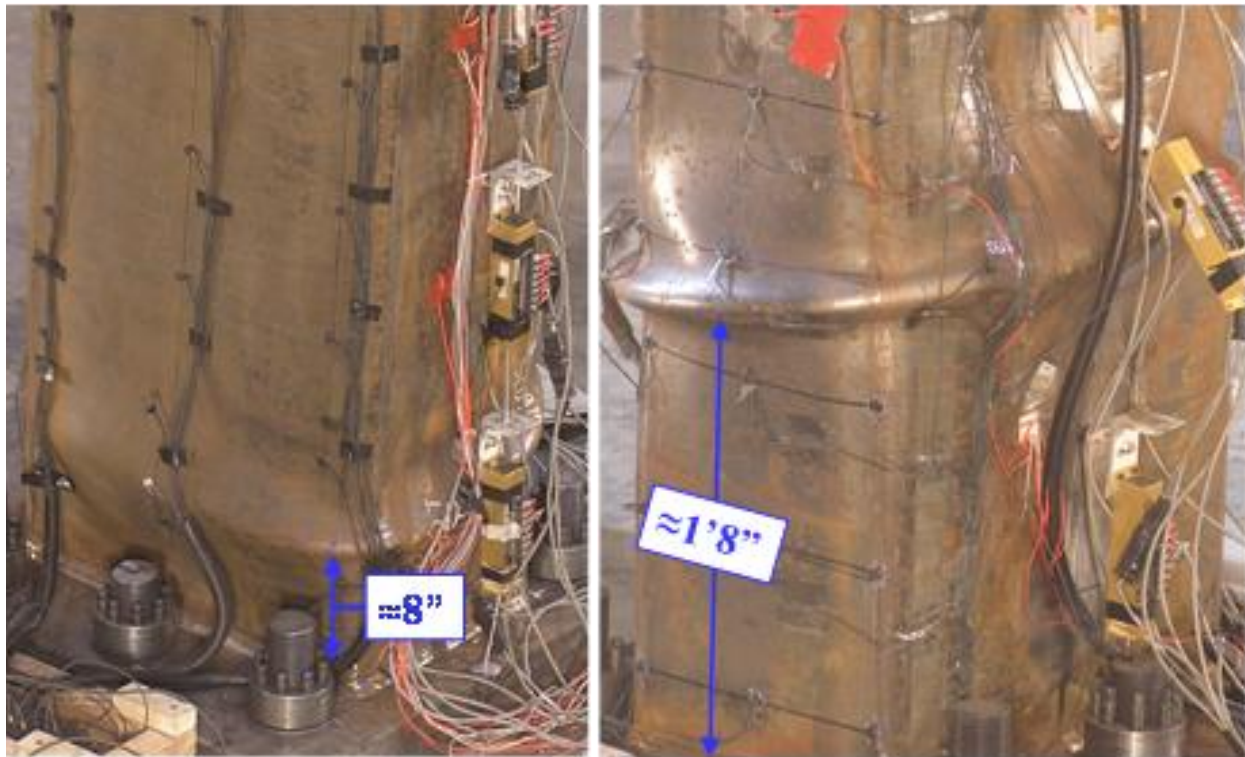


Figure 4.9. Average at 1' 6" and 2' 6" from the base of the transverse strains and stresses measured during the concrete casting on the 20" face for the 26 feet long RCFTs.

The variability in the strains shown in Figure 4.9 is attributed to the different values of pretension given when the braces were placed. Strains were measured during the concrete casting and until the concrete hardened (3 days), and then the braces were removed; strains kept being measured until the 5th day. As shown in Figure 4.9(b), a small increment of the transverse strains occurred (at about the 73rd hour) when the braces were removed.

4.3.4. Observations during the tests

As discussed previously, braces were placed at the rectangular tubes in order to reduce the expansion due to the wet concrete pressure, except in one specimen (4-Rw-18-5) where the braces were not installed on purpose. As predicted for this non-restrained case, the maximum expansion induced an initial out-of-straightness in the steel walls; this expanded shape was also taken by the concrete once it hardened. Once compressive and bending loads were applied for LC1 through LC4, this initial out-of-straightness grew more rapidly than for other sections, such as the column base, that saw higher bending demands. Thus, it was not surprising that on this non-restrained specimen, deformations during casting led to a higher position of the local buckling during the LC1 through LC4 tests as shown in Figure 4.10(b). The two rectangular specimens shown in Figure 4.10 correspond to the final state of these specimens at the end of the load protocol test, contrasting the effects of the wet concrete pressure in regard to the steel local buckling elevation.



(a) 9-Rs-18-12, restrained for casting

(b) 4-Rw-18-5, non-restrained for casting

Figure 4.10. Local buckling position at the end of the testing

This observation suggests also an effect on the strength, as the local buckling will develop earlier if exists a significant initial out-of-straightness in the steel walls of RCFTs due to manufacturing process, transportation, erection and, particularly in RCFTs, due to the concrete casting. The detrimental effect on the strength is expected to be higher for larger initial imperfections at the end of the casting and hardening of concrete.

4.4. Recommendations to minimize the effects of the wet concrete pressure

In order to control the amount of imperfection and an earlier development of the local buckling, the following recommendations are suggested:

- Limit the maximum transverse stress in rectangular steel tubes during the casting to values below the nominal yielding stress reduced by a safety factor (Ω); a safety factor in the order of 2 is recommended. The maximum expected stress due to the hydrostatic pressure of wet concrete during casting may be estimated by:

$$\sigma_{\max} = \max \left[\left(\frac{2h_c}{b_c + 4h_c} \right) \frac{p \cdot h_c^2}{t^2}, \frac{1}{3} \left(\frac{3b_c + 4h_c}{b_c + 4h_c} \right) \frac{p \cdot h_c^2}{t^2} \right] \leq \frac{F_y}{\Omega} \quad (4.14)$$

- Limit the maximum expansion in the steel tube during the casting to an imperfection no greater than $L/2000$, where L is the inter-story length. The maximum expansion due to the hydrostatic pressure of wet concrete at the pouring may be estimated by:

$$\delta_{\max} = \frac{1}{32} \left(\frac{5b_c + 4h_c}{b_c + 4h_c} \right) \frac{p \cdot h_c^4}{E_s \cdot t^3} \leq \frac{L}{2000} \quad (4.15)$$

The previous limits may be met by satisfying one or more of the following possible solutions:

- Increasing the thickness (t) of the steel tubes or the wall slenderness ratio (h/t).
- Decreasing the amount of hydrostatic pressure (p) by reducing the concrete lift heights.
- Adding temporary stiffeners in those positions where the limitations above are not satisfied. These stiffeners should be placed before the casting and they are recommended to stay in-place for 7 days, when the concrete reaches 80% of the specified f_c' , or when the concrete hardens. The recommended spacing of the temporary stiffeners is no larger than either the column base (b) or the column width (h). The recommended stiffened length is 1/3 of the concrete lift heights. The stiffeners should be placed without adding normal forces to the steel walls, or without inducing inward deformation

In case either stresses or deformations in rectangular CFT cross-sections exceed the recommended limits given by Equations 4.14 and 4.15, the cross-section should be treated as slender type section since this would be susceptible to an earlier local buckling.

CHAPTER 5

BUCKLING CAPACITY

5.1. Introduction

One of the primary goals of this research is the experimental determination and verification of the buckling capacity or critical load of composite CFT columns. This goal is targeted through the first load case (LC1) of the load protocol employed in this project, which consisted of a monotonic downward displacement of the composite specimens with its natural initial imperfection; the load was reversed once the compressive capacity was exhausted.

Although utilizing state-of-the-art equipment and controllers, the experimental measurement of the flexural buckling loads was challenging. Unexpected difficulties were encountered to extract reliable values of the buckling loads due to large initial imperfections and other issues related to the testing system (i.e. frictional forces in the actuators and clevises, system compliance, a limit in the axial capacity, and issues with the control of the DOFs). Thus, successful extraction of the buckling loads required that behavior of the loading system be characterized through integration of data from different sensors and careful processing of the raw data measured directly from the tests. This procedure is described in this Chapter, which is organized as follows:

- Section 5.2 presents a summary of the AISC (2010) Specifications and some theoretical concepts behind the design equations that are specified to calculate the nominal critical load capacity (P_n) of CFT columns. The material and geometric limitations in the specifications are discussed too.
- Section 5.3 shows details of the testing set-up, as well as the raw data measured during the load case LC1. A direct comparison of the maximum axial loads from the raw data collected in the tests is made with the expected axial load from the specifications.
- Section 5.4 discusses some of the unexpected difficulties in the extraction of reliable data for the buckling load of the tested CFT specimens. In this section, the data is evaluated and processed in more detail, and final values of the buckling loads were extracted from this processed data.

- Section 5.6 presents results of computational analysis that aims to calibrate and predict behavior observed during the tests. Calibration of column curves from the models is also documented.
- Section 5.7 shows the results of the measured moment-curvature at the critical cross-section in LC1. From these plots, values of the effective flexural stiffness (EI_{eff}) are extracted and evaluated with the goal of improving the accuracy of the calculations for the buckling critical load.

5.2. Buckling load by the AISC Specifications

In late 2005, the American Institute of Steel Construction issued its most recent Specification for Structural Steel Buildings ANSI/AISC 360-05 (AISC, 2005) and its Seismic Provisions ANSI/AISC 340-05 (AISC, 2005b). The changes for 2005 included the unification of both allowable strength design (ASD) and load and resistance factor design methods (LRFD) for steel (rolled and hollow structural sections), composite members (columns, beams, slabs), and connections. The recent revisions to those editions (AISC, 2010; AISC, 2010b) include a complete revamping of the methodologies for assessing stability of framed structures that include the use of the nominal load approach, new provisions for composite structures (i.e. updated material requirements), and new design provisions for fire.

This section presents a brief summary of Chapter I.2.2 (Design of Composite Members, Axially Loaded Members, and Filled Composite Columns) of the AISC (2010) Specifications.

Analytical computation of the critical load, as recommended by the AISC (2010), assumes the following:

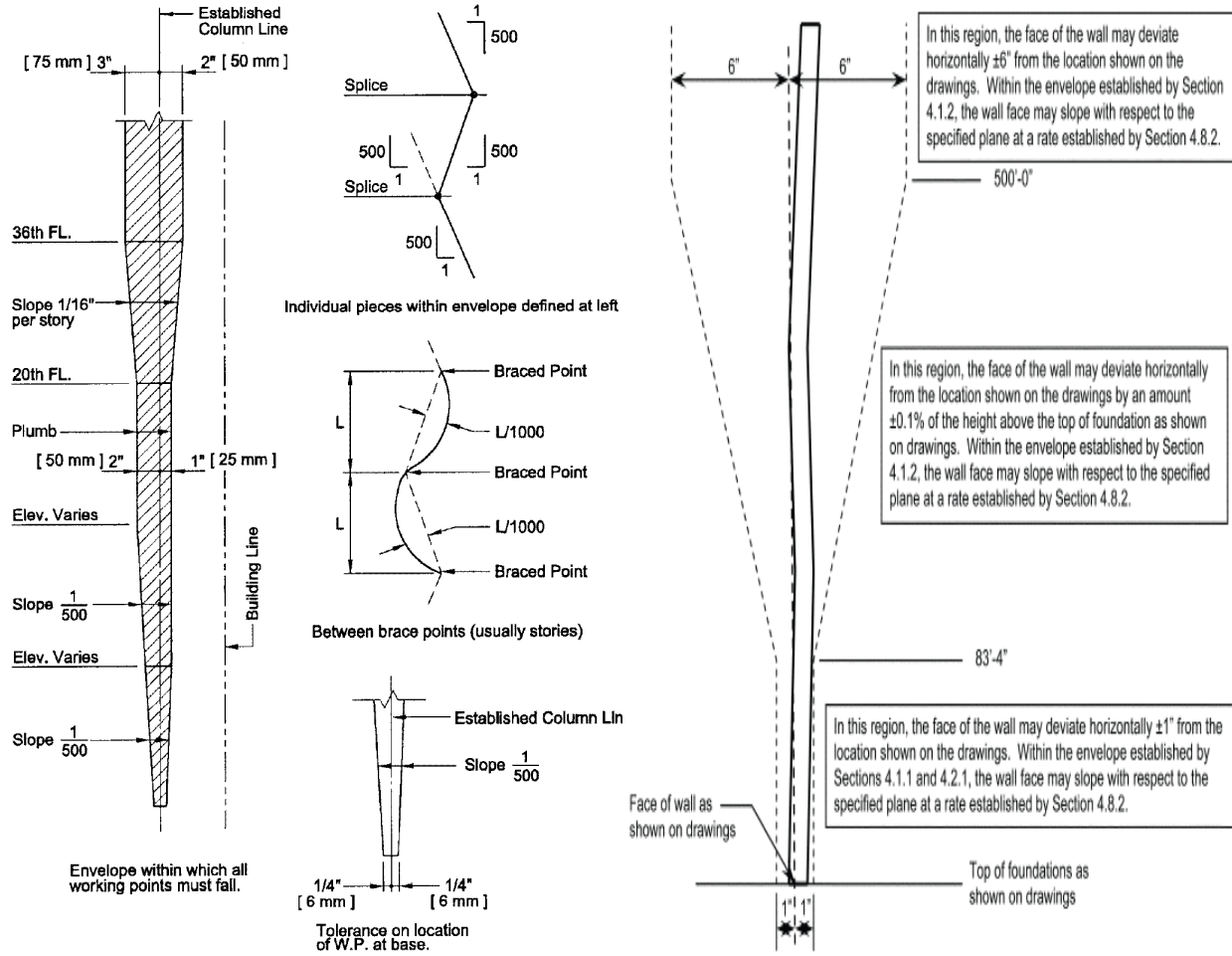
- The compressive capacity of the CFT column shall be determined by the limit state of flexural buckling governing by either inelastic or elastic buckling for short and slender columns, respectively.
- Some cross-section limitations shall be satisfied, such as:

1. Cross-sectional area of the HSS tube shall comprise at least 1 percent of the total composite cross-section; previous specifications did not address sections with 1 to 4 percent steel.
 2. The maximum width-thickness ratio shall not exceed $h/t \leq 2.26\sqrt{E/F_y}$ for RCFTs and $D/t \leq 0.15E/F_y$ for CCFTs. These limits are higher than those for conventional HSS steel-only columns (by 61% and 36%, respectively), and recognize the delay in local buckling due to the steel-concrete contact interaction.
- In addition, some material limitations shall be satisfied, The concrete compressive strength must be higher than 3 ksi and lower than 6 ksi for lightweight weight concrete and 10 ksi for normal concrete, respectively. The lower limit of 3 ksi and the upper limit for lightweight concrete (6 ksi) encourage the use of good quality concrete, while the upper limit of 10 ksi was imposed to restrict the strength calculations related to brittle failure modes. Higher strength concrete is permitted if appropriate testing and analyses are conducted (Commentary AISC, 2005c). These material limitations reflect the range of material properties available from experimental testing (Commentary AISC, 2005c; Ziemian, 2010; Hajjar, 2000; Shanmugam and Lakshmi, 2001; Leon *et al.*, 2005; Goode, 2007).
 - The compression capacity also includes the effects of some initial residual stresses in the steel members resulting from the manufacturing or the welding process. The amount of the accumulated initial residual stresses and its distribution in the steel member may have a wide dispersion. Previous studies, including different cross-section shapes and sizes, different steel types, and different manufacturing process, have confirmed a small reduction on the critical load due to residual stresses (Bjorhovde, 1972; Ziemian, 2010).
 - Last but not least, the element shall not exceed the allowable fabrication and erection tolerances given by the *Standard ASTM A6* (2009) or the *AISC Code of Standard Practice* (AISC, 2005d) for the steel components, and the *Specifications for Tolerances for Concrete Construction and Materials ACI-117* (2006) for the concrete components. The maximum initial out-of-straightness (δ_o) by the Standard ASTM A6 (2009) is limited for hot rolled W shapes to 1/8" for each 10 feet of length (L/960 exactly or L/1000 nominally) or 1 mm for each meter of length (L/1000), and 1/8" for each 5 feet of length (L/480 or L/500 nominally) or 2 mm for each meter of length (L/500) for S, M, C, MC, L, T, Z and HSS shapes. The AISC Code of Standard Practice (AISC, 2005d) allows, as illustrated in Figure 5.1(a), a

maximum out-of-plumbness $\Delta_o = L/500$ (7.13.1.1 in AISC, 2005d), and a maximum out-of-straightness $\delta_o = L/1000$ (6.4.2 in AISC, 2005d). The tolerance on deviations from plumb in ACI-117 (2006) is, as shown in Figure 5.1(b), limited to: (a) 0.3%L (or L/333) if the member length (L) is below 27'9", (b) 1 inch if the member length is between 27'9" and 83'4", (c) L/1000 if the length is between 83'4" and 500', and (d) 6" for element lengths above to 500'. All these Specifications are consequently applicable to composite members and, in particular, for CFTs elements. The final initial imperfections are limited by the imperfection of the steel component plus some possible deformations during the erection and the concrete pouring processes.

Several previous research studies have proved the high influence of the initial imperfection on the buckling load capacity (Timoshenko and Gere, 1972; Bjorhovde, 1972; White and Hajjar, 1997; Ziemian, 2010). Thus, AISC equations E3-2 and E3-3 for the flexural buckling stress on steel members were established (since AISC, 1999) based on the SSRC-P2 column curve (Ziemian, 2010) that accounted for an average initial out-of-straightness of L/1470 observed statistically by Bjorhovde (1972) or L/1500 observed by Fukumoto *et al.* (1983). These design equations were also adapted for composite members since the AISC Specification published in 1999. Thus, imperfections higher than the limits adopted in the AISC Specifications will result in lower capacities of the flexural buckling load.

Unfortunately, there are no analytical equations where the value for the initial imperfection is explicitly expressed. Some Specifications or guidelines have suggested the use of multiple column curves (i.e. EC3 2005, EC4 2004 and CSA 2009) so the dispersion due to the initial imperfection and the manufacturing process can be implicitly accounted in the statistical analysis. A previous methodology that accounted for initial imperfection effects proposed reducing the strength with either a reduction strength factor (ϕ) or a safety factor (Ω). An example of the latter is the CRC column curve (Ziemian, 2010) for steel columns, which has its basis in the tangent modulus theory with a safety factor that depends on the slenderness. Since in practice the straightness and plumbness are controlled and limited by the Standards (i.e. ASTM A6, 2009; AISC, 2005d; ACI-117, 2006), developments of analytical equations with geometric imperfections explicitly expressed are not practical for design purposes.



(a) AISC Code of Standard Practice (AISC, 2005d)

(b) ACI-117 (2006)

Figure 5.1. Column tolerances as specified in the AISC and the ACI Specifications

Thus, nominal compression capacity of a CFT column (P_n) can be calculated as:

$$P_n = \begin{cases} P_o \left(0.658^{\frac{P_o}{P_e}} \right) & \text{if } P_o / P_e \leq 2.25 \\ 0.877 P_e & \text{if } P_o / P_e > 2.25 \end{cases} \quad (5.1)$$

(I2-2, I2-3, AISC-10)

The cross-section compressive strength (P_o) and the Euler load (P_e) are computed by:

$$P_o = \begin{cases} A_s F_y + A_r F_{yr} + C_2 A_c f_c' & \text{for compact sections} \\ A_s F_{cr} + 0.7 f_c' (A_c + A_{sr} E_s / E_c) & \text{for non-compact sections} \end{cases} \quad (5.2)$$

(I2-9, AISC-10)

$$P_e = \frac{\pi^2 E I_{eff}}{(KL)^2} \quad (5.3)$$

(I2-5, AISC-10)

The concrete contribution ($A_c f'_c$) to the compressive strength is affected by the effectiveness coefficient C_2 , classically assumed by the ACI as 0.85 for reinforced concrete members (Section 10.2.7 in ACI-318, 2008). This value was taken by the AISC (2010) for RCFTs but increased to 0.95 for CCFTs, recognizing the higher confinement in circular shapes (Commentary AISC, 2005c; Leon and Aho, 2002). Some research studies (i.e. Sakino *et al.*, 2004; Chang and Mander, 1994, etc) or other specifications (i.e. Eurocode EC-4, 2004; AIJ, 2000) suggest a higher effectiveness for the confined concrete, especially for short columns with low D/t ratios. AISC chose to ignore this effect for simplicity.

Both the critical load and the Euler load depend on the given boundary conditions in the column. For ideal boundary conditions (i.e. “fixed” or “pinned” support), Table 5.2 has been commonly used to get both the theoretical and suggested values of the effective length factor (K), even when in practice this support types are developed only under idealized conditions. The AISC (2005) Specifications has proposed alternative approaches, such as the *direct analysis method (DAM)*, to avoid the use of effective length. However, such approach has not been explored extensively in composite columns in general. For the testing of the columns in this project, ideal boundary conditions will be simulated through a very rigid connection of the base plate to the strong floor at the bottom, and controlled degrees of freedom (DOFs) at the top with the top plate connected to the crosshead. In order to get test data in the slender column range, the control of the DOFs at the top will be mostly as “free” ($K=2$) with input commands in force control holding values of top forces and moments to zero. In some specimens and particular load cases, other boundary conditions may be used and documented accordingly.

Buckled shape of column is shown by dashed line	(a)	(b)	(c)	(d)	(e)	(f)
Theoretical K value	0.5	0.7	1.0	1.0	2.0	2.0
Recommended design value when ideal conditions are approximated	0.65	0.80	1.0	1.2	2.0	2.0
End condition code		Rotation fixed		Translation fixed		
		Rotation free		Translation fixed		
		Rotation fixed		Translation free		
		Rotation free		Translation free		

Figure 5.2. Theoretical and suggested K factors for different BCs (AISC Commentary, 2005)

The flexural effective stiffness (EI_{eff}) in Equation 5.3 also accounts for the contribution of the component materials (steel, reinforcement and concrete). The concrete contribution to the effective stiffness is given by a C_3 coefficient that depends on the structural steel ratio and is related to the influence of cracking and creep on the lateral buckling resistance (Commentary AISC, 2005c; Viest et al., 1997). Thus:

$$EI_{eff} = E_s I_s + E_s I_{sr} + C_3 E_c I_c \quad (5.4)$$

(I2-14, AISC-10)

$$C_3 = 0.6 + 2 \left(\frac{A_s}{A_c + A_s} \right) \leq 0.9 \quad (5.5)$$

(I2-15, AISC-10)

As described in the AISC Commentary (AISC, 2005c), these design equations were calibrated with the available experimental data, and adopted to provide a smooth transition from and to steel-only and concrete-only elements.

Concerning the flexural effective stiffness (EI_{eff}), most specifications concur that this is the summation of the stiffness of each component, with a reduction mostly in the concrete component to account for cracking. Thus, ACI-318 (2008) accounts for the stiffness of steel and 20% of the concrete and a reductive factor β_d for sustained axial loads (Equation 5.6).

$$EI = E_s I_s + \frac{0.2 E_c I_c}{1 + \beta_d} \quad (5.6)$$

(10-23, ACI318-08)

In turn, the Eurocode EC4 (2004) provides two equations. Equation 5.7 is given for the determination of the slenderness (λ) and the elastic critical force (P_n). Equation 5.8, instead, is given for the determination of internal forces on second order analysis; the factor of 0.9 in Equation 5.8 is roughly equivalent to that in the calculation of the effective stiffness used on the Direct Analysis Method (DAM) in the AISC (2010) Specifications for steel members.

$$EI_{eff,I} = E_s I_s + E_s I_{sr} + 0.6 E_c I_c \quad (5.7)$$

(6.40, EC4-04)

$$EI_{eff,II} = 0.9 (E_s I_s + E_s I_{sr} + 0.5 E_c I_c) \quad (5.8)$$

(6.42, EC4-04)

Equation (5.1), which is similar to the one used for steel members in the AISC (2010) Spec., is valid in the inelastic buckling range (when $P_o / P_e \leq 2.25$ or $\lambda = \sqrt{P_o / P_e} = 1.5$), and for a second interval in the elastic buckling range where a reduced Euler load is used. The reductive factor 0.877 in the Euler load for the elastic buckling interval was proposed to account for geometric imperfection effects (White and Hajjar, 1997; Ziemian, 2010). On the other hand, the expression for the inelastic buckling range was obtained by curve fitting experimental data (Bjorhovde, 1972; Ziemian, 2010). Thus, the total reduction factor ($\chi = P_n / P_o$, Equation 5.9) on a column that accounts for initial imperfection, residual stresses, geometric and material nonlinearities and stability effects is illustrated in Figure 5.3.

$$\chi = \frac{P_n}{P_o} = \begin{cases} 0.658^{\lambda^2} & \text{if } \lambda = \sqrt{P_o / P_e} \leq 1.5 \\ 0.877 / \lambda^2 & \text{if } \lambda = \sqrt{P_o / P_e} > 1.5 \end{cases} \quad (5.9)$$

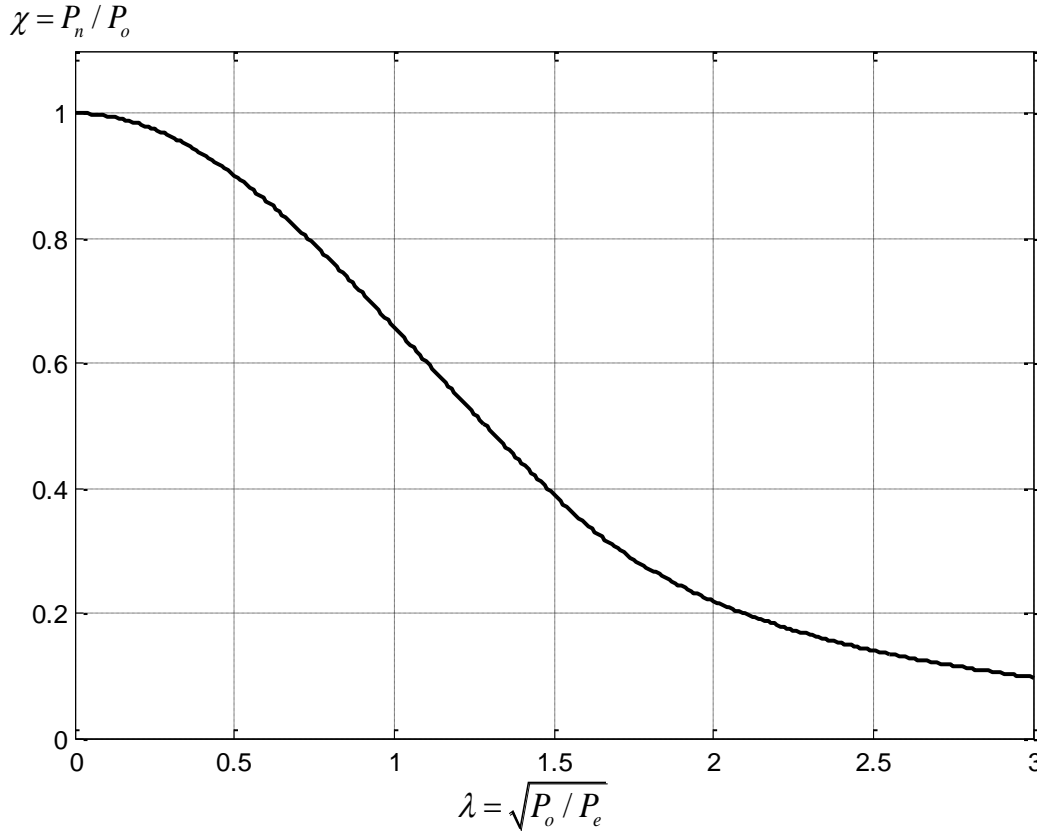


Figure 5.3. Column curve by the AISC (2010) Specifications

5.3. Experimental results from the raw data

As described before, the first load case in all the tests was intended to determine the critical axial load. All the specimens were connected to the strong floor through a fixed connection that restrained the displacements and rotations at the bottom of the column. At the top, most specimens had forces and bending moments controlled by the crosshead, ideally forced to be zero. In other words, the top was controlled as free displacement – free rotation, giving a fixed-free column ($K=2$). Some specimens were also controlled in either free displacement – fixed rotation ($K=1.0$), fixed lateral displacement – free rotation ($K=0.7$), or fixed lateral displacement – fixed rotation ($K=0.5$). Figure 5.4 illustrates all these cases of boundary conditions (BC's), as well as other variables such as the initial out-of-plumbness (Δ_o), the initial out-of-straightness (δ_o), the crosshead induced forces and displacements at the top, and the resultant reactions at the fixed base. As discussed in the following sections, the bending moment at the base (M_2) is the contribution of the first order moments induced by the crosshead (M_1) and the overturning ($F \cdot L$), plus the moment induced by the second order effects ($P \Delta$). Internal bending moments along the length will be influenced by the $P \delta$ effects as well.

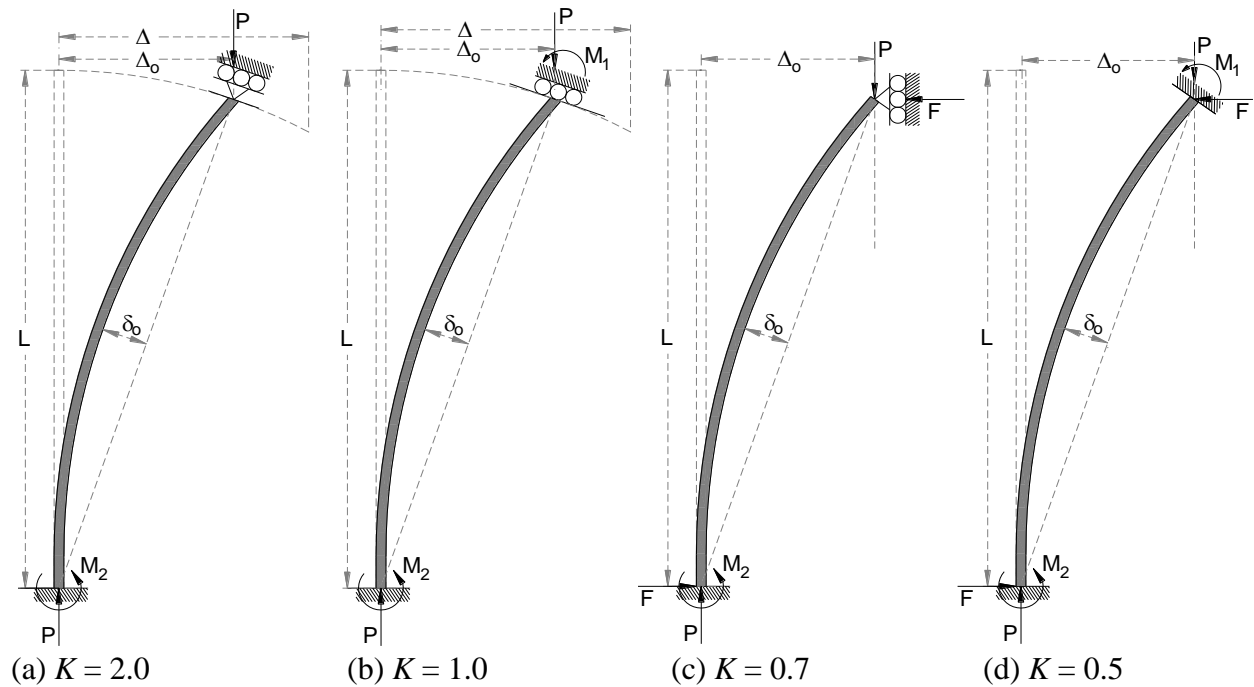


Figure 5.4. Definition of out-of straightness (Δ_o), out-of-plumbness (δ_o), and the different boundary conditions for the buckling load case.

Figure 5.5 illustrate the initial geometric profile at the beginning of LC1 for all specimens; the maximum out-of-straightness (Δ_o) and out-of-plumbness (δ_o) are reported in Table 5.1. The imperfections as shown in Figure 5.5 were measured from the column surveying at the points the string pots were placed, and these discrete measurements are connected assuming linear transition between points to get an approximation of the geometric profile.

Table 5.1 also summarizes the material and geometric properties for each specimen, and the results of the maximum experimental compressive load (P_{exp}) obtained in each LC1 test; this maximum experimental capacity obtained from the raw data is normalized with the squash capacity (P_o , Equation 5.2) and plotted vs. the slenderness parameter λ in Figure 5.6. For these results, the following observations and notes apply:

- The buckling load (P_n) and the slenderness parameter (λ) for each specimen were calculated as described in the AISC (2010) Specifications. These results were obtained based on averaged measured material properties (f'_c , F_y), measured geometric properties (L , Δ_o , δ_o as shown in Figure 5.5), and assumed ideal boundary conditions (K). However, experimental and the analytical buckling loads may have discrepancies due to different assumptions as will be explained in the following section.
- The axial capacity of the crosshead system (1320 kips) was reached before the buckling load on the specimens 3, 5, 7 and 9. In a following section, some extrapolation methodologies will be explored to estimate to buckling critical load of these specimens.
- These results correspond to the fixed-free controlled case ($K=2$), except in specimens 1 and 18 where fixed-fixed BC's were controlled ($K=0.5$). In addition, except for the specimen 1 and 18, the buckling load case started with imperfection at the first step matching the initial imperfection as delivered. The buckling load case with $K=0.5$ for the specimens 1 and 18 (with normalized initial out-of-straightness starting at 0.045% and 0.074%, respectively) was applied later in the load protocol, and thus the normalized imperfection started respectively at 0.711% and 0.196% instead.

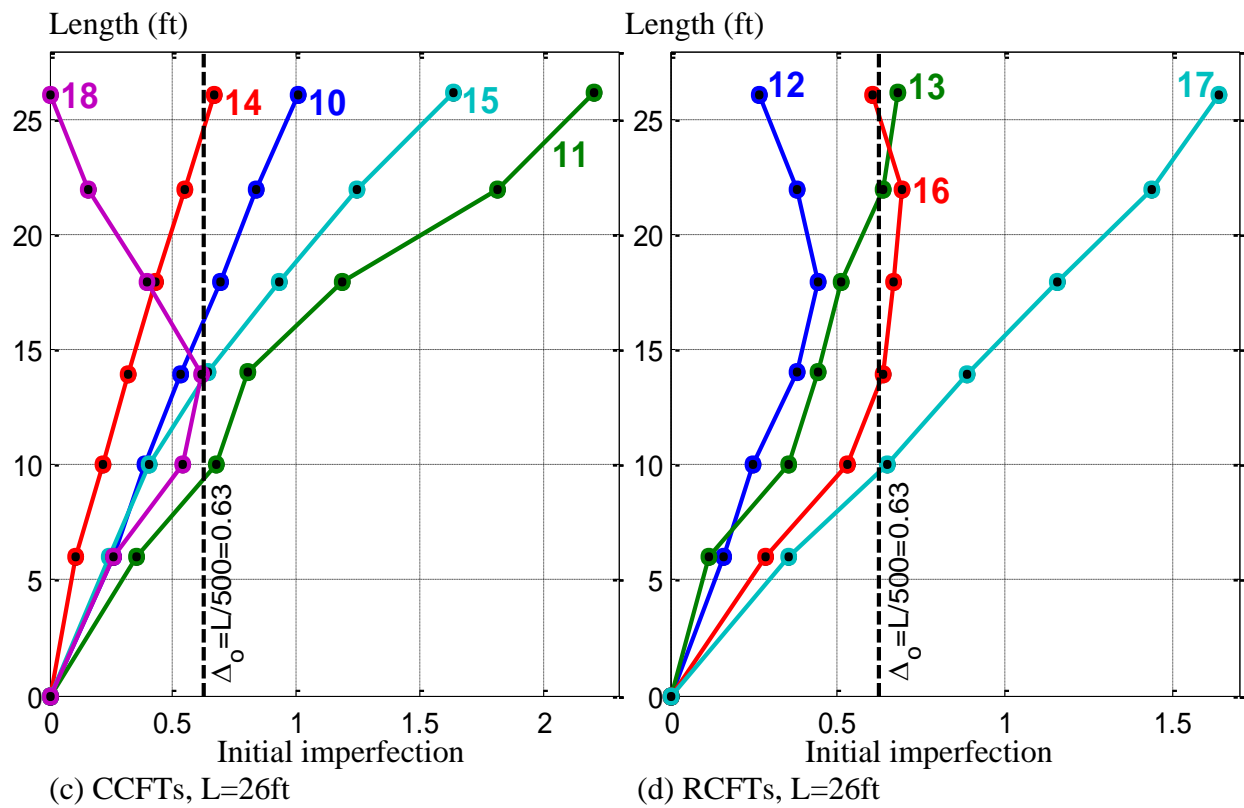
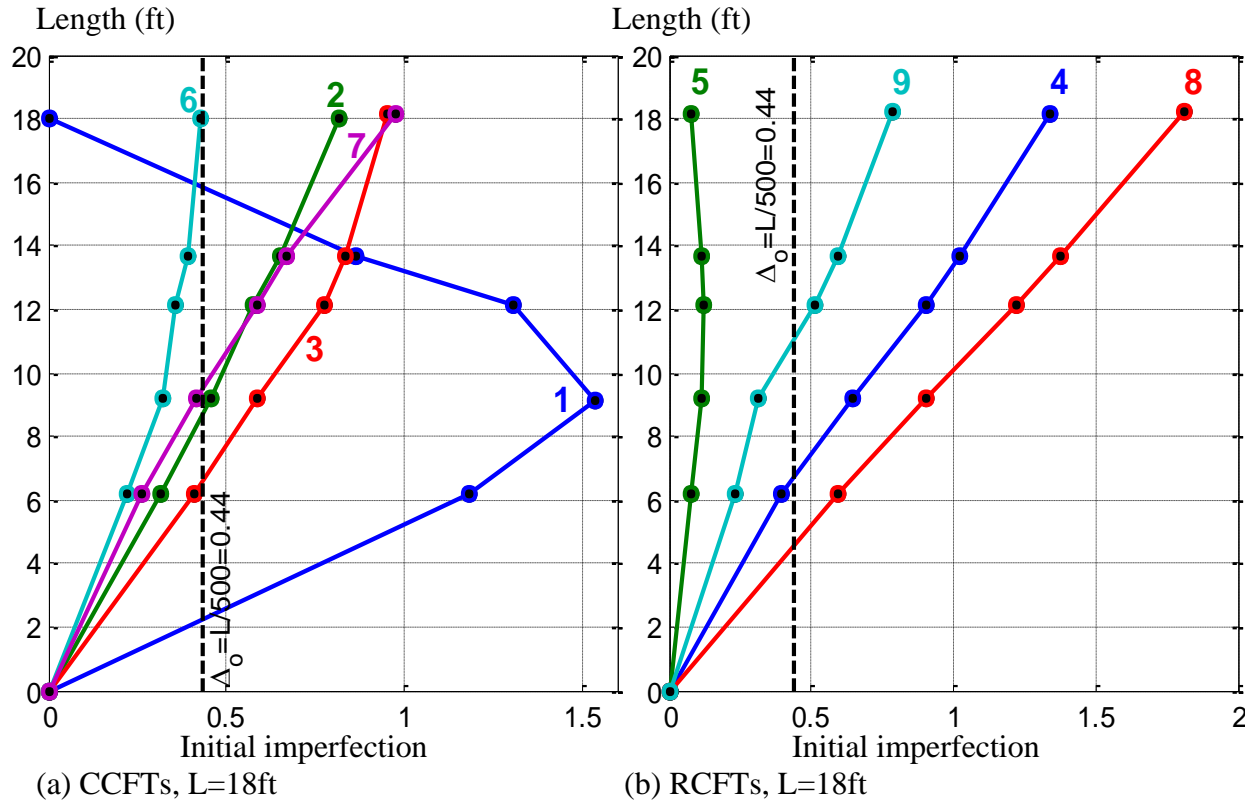


Figure 5.5. Initial profile shape at the beginning of the loading case LC1

Table 5.1. Maximum experimental axial loads obtained from the raw data

Specimen # – name	f_c (ksi)	F_y (ksi)	L (ft, in)	Δ_o/L (%)	δ_o/L (%)	K -	λ -	P_n (kip)	P_{exp} (kip)
1C5-18-5	5.5	55.6	18' 1/2"	0.000	0.711*	0.5	0.90	166	129
18C5-26-12	11.7	55.6	26' 5/8"	0.000	0.196*	0.5	1.51	140	141
2C12-18-5	5.6	48.9	18' 1/2"	0.376	0.035	2	1.55	393	427
6C12-18-12	13.2	48.9	18' 1/2"	0.197	0.049	2	1.90	472	581
10C12-26-5	7.9	48.6	26' 1"	0.322	0.020	2	2.38	207	362
14C12-26-12	11.6	55.5	26' 1 1/2"	0.213	0.023	2	2.72	216	386
3C20-18-5	5.8	47.6	18' 1 1/2"	0.438	0.084	2	1.05	1469	>1320 ⁺
7C20-18-12	13.2	47.6	18' 1 7/8"	0.449	0.039	2	1.30	2190	>1320 ⁺
11C20-26-5	8.1	44.3	26' 2 3/4"	0.700	0.121	2	1.61	992	802
15C20-26-12	11.6	42.5	26' 2"	0.522	0.076	2	1.78	1080	1127
4Rw-18-5	5.9	53.0	18' 2"	0.615	0.029	2	1.38	939	1070
8Rw-18-12	13.3	53.0	18' 2 5/8"	0.828	0.010	2	1.65	1124	961
12Rw-26-5	8.2	58.9	26' 1 1/4"	0.084	0.084	2	2.14	501	791
16Rw-26-12	11.7	55.2	26' 1 1/4"	0.193	0.100	2	2.30	534	1140
5Rs-18-5	5.9	53.0	18' 2"	0.037	0.036	2	0.88	1501	>1320 ⁺
9Rs-18-12	13.3	53.0	18' 2 5/8"	0.360	0.036	2	1.04	2209	>1320 ⁺
13Rs-26-5	8.3	55.5	26' 1 3/4"	0.216	0.030	2	1.35	1199	1320
17Rs-26-12	11.7	55.1	26' 1 1/2"	0.523	0.019	2	1.46	1323	1120

(+) MAST axial capacity (1320 kips) reached before getting the buckling strength. (*) The initial out-of-straightness (δ_o/L) before testing for the specimens 1 and 18 were 0.045% and 0.074%, respectively; the values stated in this table correspond to the out-of-straightness at the beginning of the load case.

As seen in Figure 5.6, the AISC (2010) analytical column curve and some maximum experimental values do not concur. The experimental values below the column curve are either:

- (a) Those specimens (i.e. 3, 5, 7 and 9) where the MAST axial capacity was reached before the buckling load, or
- (b) Those specimens that had a very large initial imperfection (i.e. 1, 8, 11 and 17).

On the other hand, the experimental values above the column curve, which occurs mainly on the specimens with the higher slenderness ($\lambda > 2$), are mainly due to:

- (a) An initial double-curvature deflected shape (i.e. 5, 12 and 16, see Figure 5.5) and
- (b) Parasitic top forces and moments added by the crosshead, which increased the axial capacity (i.e. specimens 10, 12, 14 and 16).

In the next section, more details are discussed about the discrepancies between the experimental and the analytical critical loads.

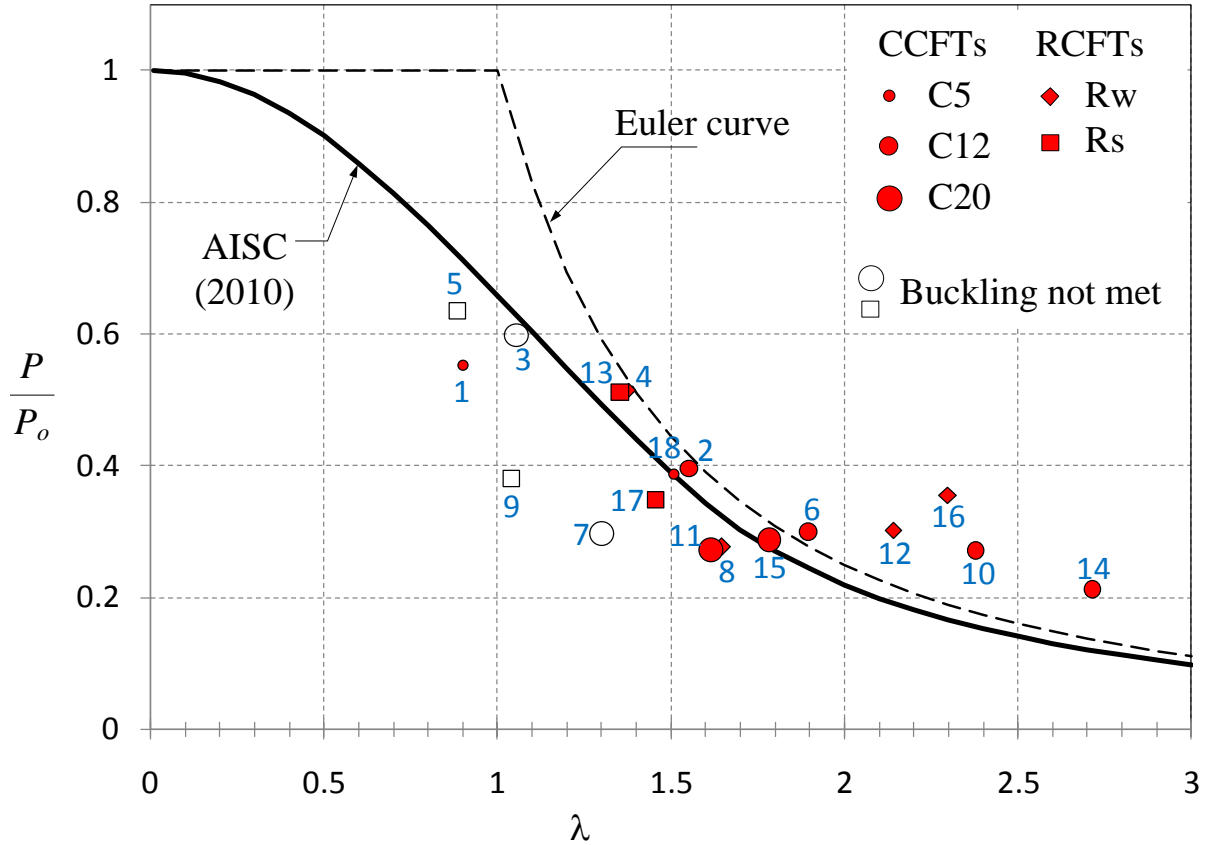


Figure 5.6. Maximum experimental load ratios (P_{exp}/P_o) from the raw data

Note from Table 5.1 that the normalized initial out-of-straightness (δ_o/L) in most specimens before testing was within the limit 1/1000 (or 0.1%) given by the Standards. However, as shown in Table 5.1 and Figure 5.5, the normalized initial out-of-plumbness limit ($\Delta_o/L=1/500=0.2\%$) in the Standards was exceeded in more than the half of the experimental samples.

In real frame structures, the imperfection in out-of-plumbness (Δ_o) may be reduced in the field (only if the out-of-straightness limit is not exceeded) in order to connect these columns with the beam system. In frames with composite CFT columns, the steel components are commonly erected and connected first (which reduces some of the out-of-plumbness), and then the concrete is cast into the steel tubes so it hardens with the shape of the steel columns connected.

In this experimental test program, obtaining the buckling loads with the original imperfections was a more attractive option since:

- (1) The concrete was poured and hardened with the initial imperfection of the steel component after fabrication and transportation.

- (2) No initial stresses were added to either concrete or the steel portions due to adjustments of the imperfections.
- (3) These are the true imperfections for these long and slender columns.
- (4) The analytical calibration for these large imperfections is more challenging and has been less explored in the past.

Unless some calibration is used, the disadvantage of using the initial imperfection without adjustment is the lack of a direct comparison option between the experimental buckling loads and the one obtained from analytical equations calibrated with standard imperfections. In the next section, some methodologies will be discussed to correct and compare experimental results with the analytical predictions.

Figure 5.7 shows the axial force vs. midspan distortion paths (P vs. δ/L) obtained for circular specimens 1C5-18-5 and 18C5-26-12 that were tested as fixed-fixed column ($K=0.5$) and for both all the entire load case and the first loading path. Similarly, the axial force vs. drift paths (P vs. Δ/L) are shown in Figure 5.8 to Figure 5.11 for the CFTs tested as fixed-free cantilever columns ($K=2$). The maximum compression loads (P_{exp}) and the initial imperfection, both reported in Table 5.1, are also included in these figures. Note in Figure 5.7(a) to Figure 5.11(a) that the second buckling load cycle (or higher) of the experimental $P-\Delta$ or $P-\delta$ path tended to go back to the previous peak point and continue along the P-M envelope.

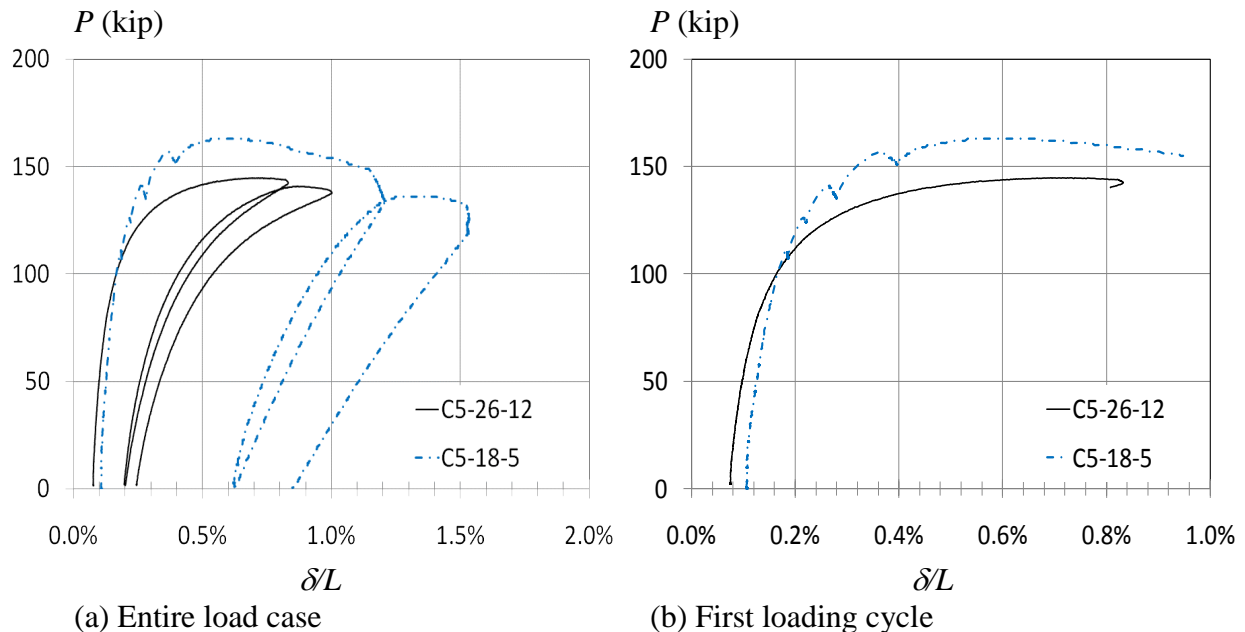


Figure 5.7. Compressive loading vs. midspan distortion for the C5 set of CCFTs

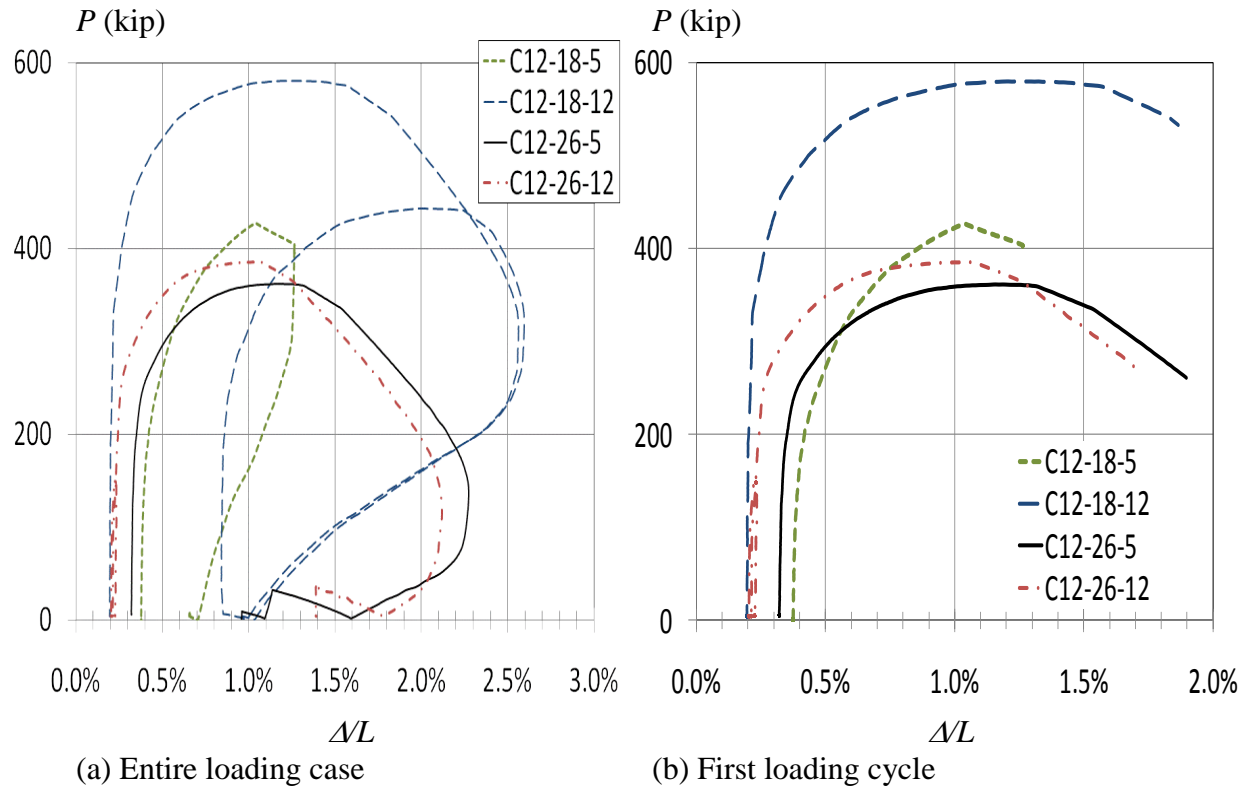


Figure 5.8. Compressive loading vs. Drift for the C12 set of CCFTs

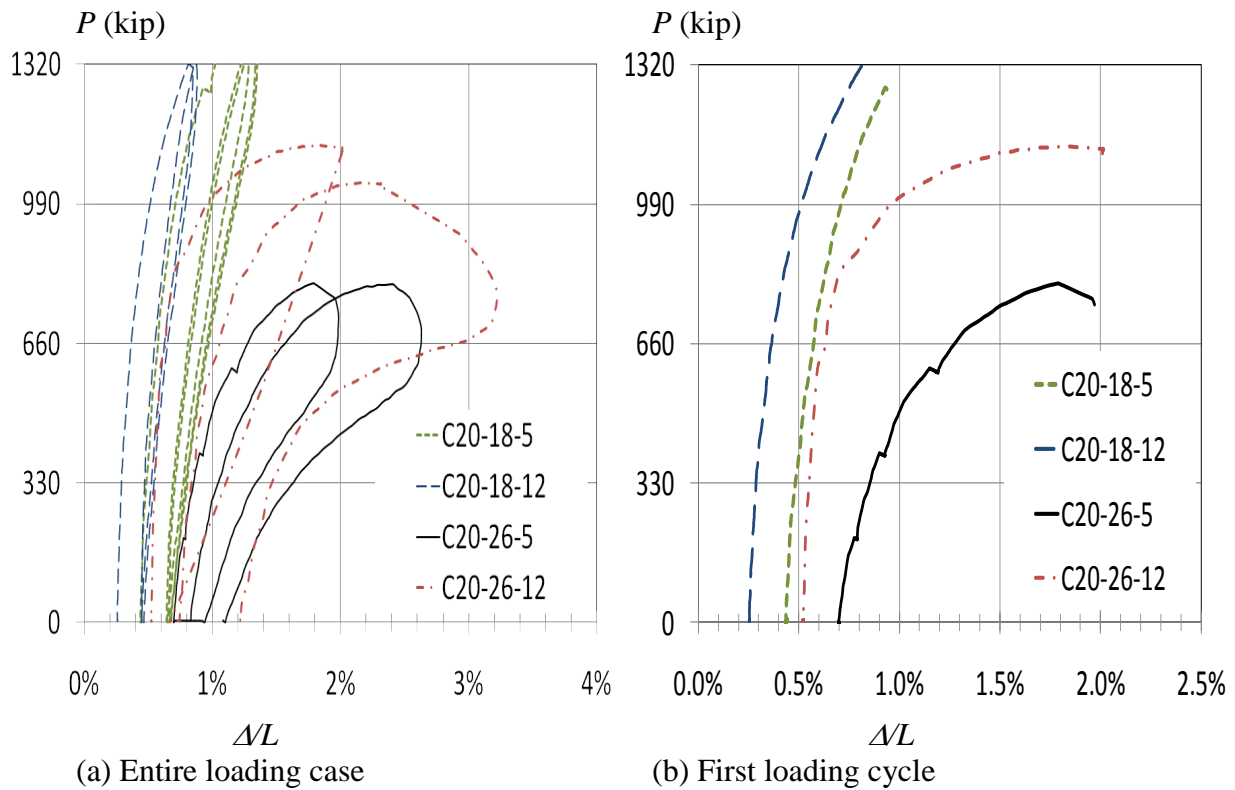


Figure 5.9. Compressive loading vs. Drift for the C20 set of CCFTs

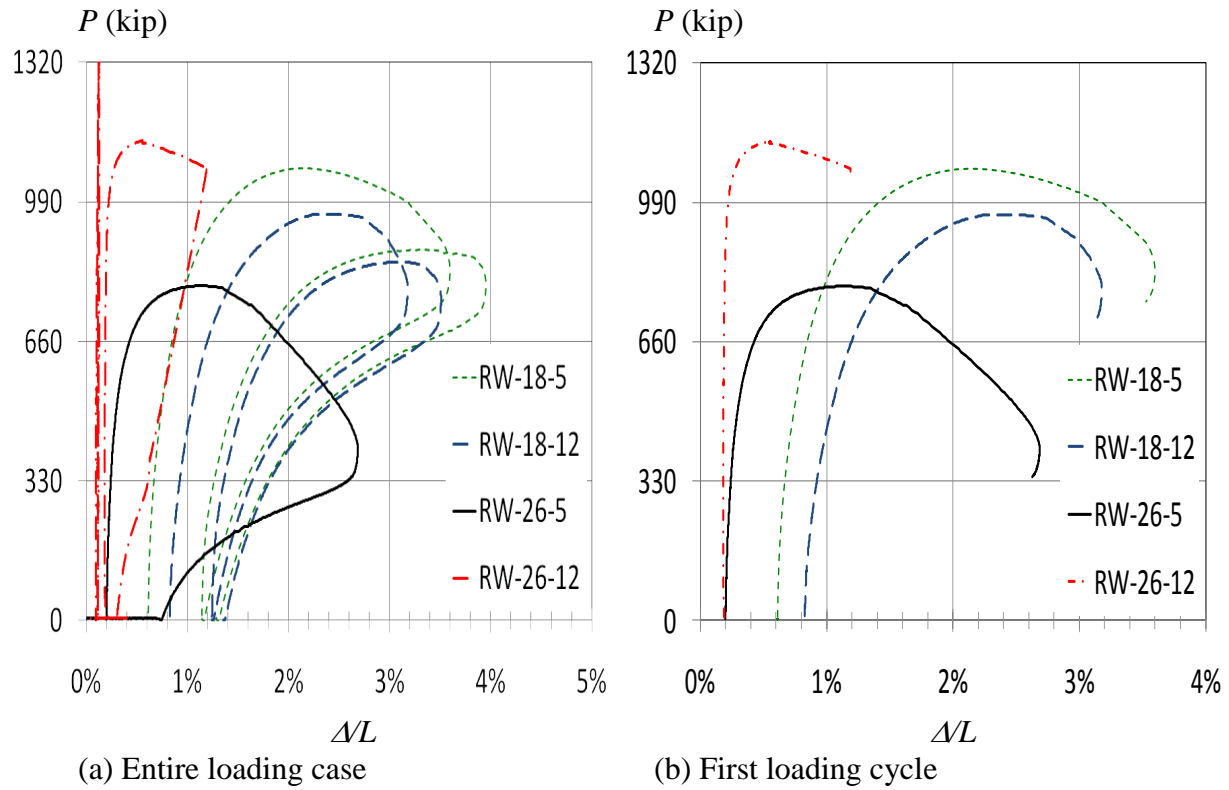


Figure 5.10. Compressive loading vs. Drift for the R_w set of RCFTs

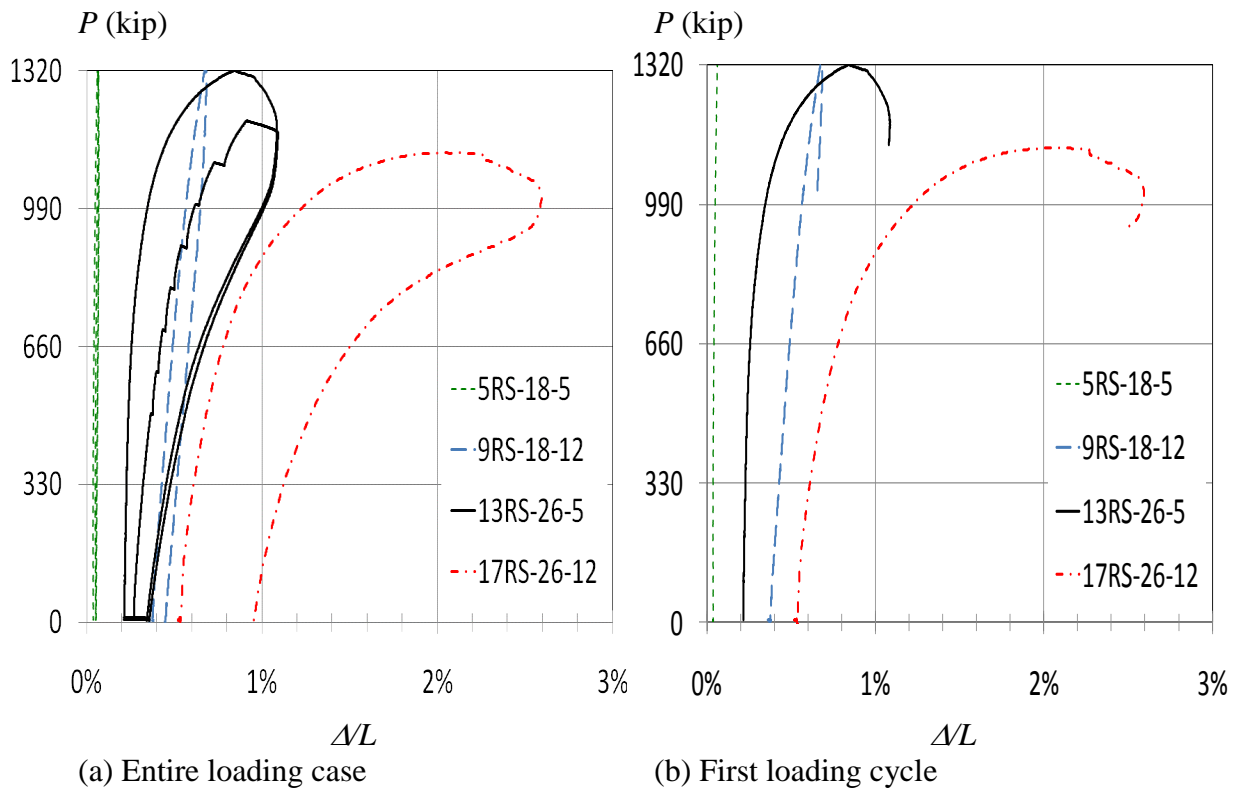


Figure 5.11. Compressive loading vs. Drift for the R_s set of RCFTs

Figure 5.12 shows the axial force vs. midspan moment paths (P vs. M_{CL}) obtained for specimens 1C5-18-5 and 18C5-26-12 tested with double fixed BC's ($K=0.5$). Similarly, the axial force vs. base moment (P vs. M_2) are shown in Figure 5.13 to Figure 5.16 for the CFTs tested with fixed-free BC's ($K=2$). Note in these figures that the moment returns to zero or the initial value when the total axial load was removed. In addition, in those cases when a second buckling load cycle (or higher) was applied, the experimental P-M path tended to go back to the previous peak point and follow the P-M envelope. This tendency is clearly shown in Figure 5.13(a), Figure 5.13(b), Figure 5.14, Figure 5.15(a), Figure 5.15(b) and Figure 5.16(c).

The base moment (M_2) and the midspan moment (M_{CL}) illustrated in these figures were calculated based on equilibrium as the summation of the applied cross-head moments (M_I), the overturning moments ($F \cdot L$) from potential crosshead horizontal forces, and the second order moments due to the initial imperfection. These second order moments, calculated as $P\Delta$ for the base moment (M_2) and as $P\delta$ for the midspan moment (M_{CL}), are the primary contribution to the total moment in this loading case. For the fixed-free ($K=2$) case with a perfect control ($F=0$, $M_I=0$), the base moment (M_2) is equal to just the second order moments due to the initial imperfection ($P\Delta$).

The axial force – bending moment P-M interaction diagrams based on the AISC (2010) Specification obtained for the composite cross-section and the composite beam column (with stability reduction) are also illustrated in Figure 5.12 to Figure 5.16. The maximum compression load from the tests (P_{exp}) and the analytical buckling load from the Specs. (P_n), both reported in Table 5.1, are also illustrated in these figures. However, as clarified below, the experimental moment (total value) and the analytical moment (net value) cannot be compared directly unless they are adjusted so both experimental and analytical show either net or total values. Chapter 6, which is related to P-M interaction diagrams, illustrates adjusted experimental net values that can be directly compared with those obtained analytically.

For design purposes, the P-M interaction diagrams from the Spec. are net values (net M_2) obtained as the total second order moment (M_2) reduced by those moments induced only by the initial imperfections (either $P\Delta$ or $P\delta$). As a consequence, the P-M diagrams from the specifications implicitly account for initial imperfections effects (as well as the steel residual stress), even if the analysis neglect this geometric non-linearity. This approach simplifies substantially the design procedure, since there is no need to include initial geometric imperfections (and residual stresses) in the analysis model. Additional details about analytical P-M interaction diagrams are discussed in Chapter 6.

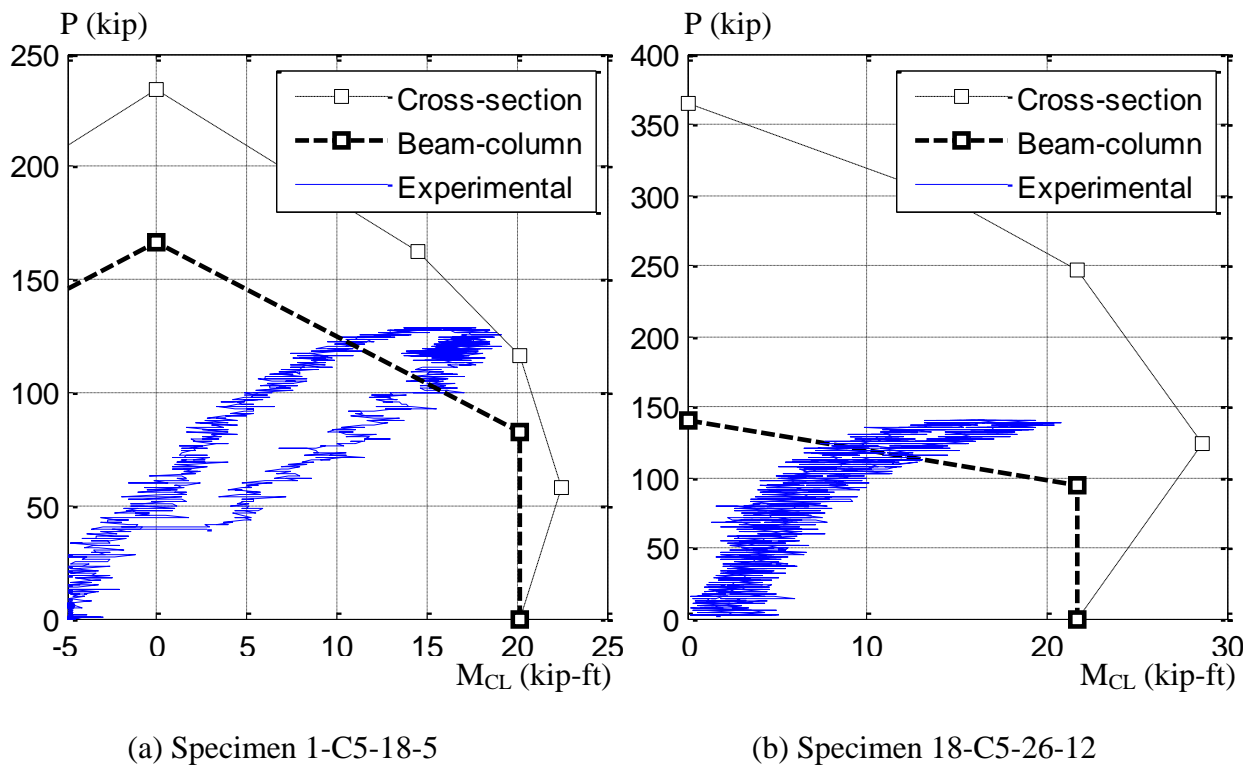


Figure 5.12. Compressive loading vs. midspan moment (P - M_{CL}) for the C5 set of CCFTs

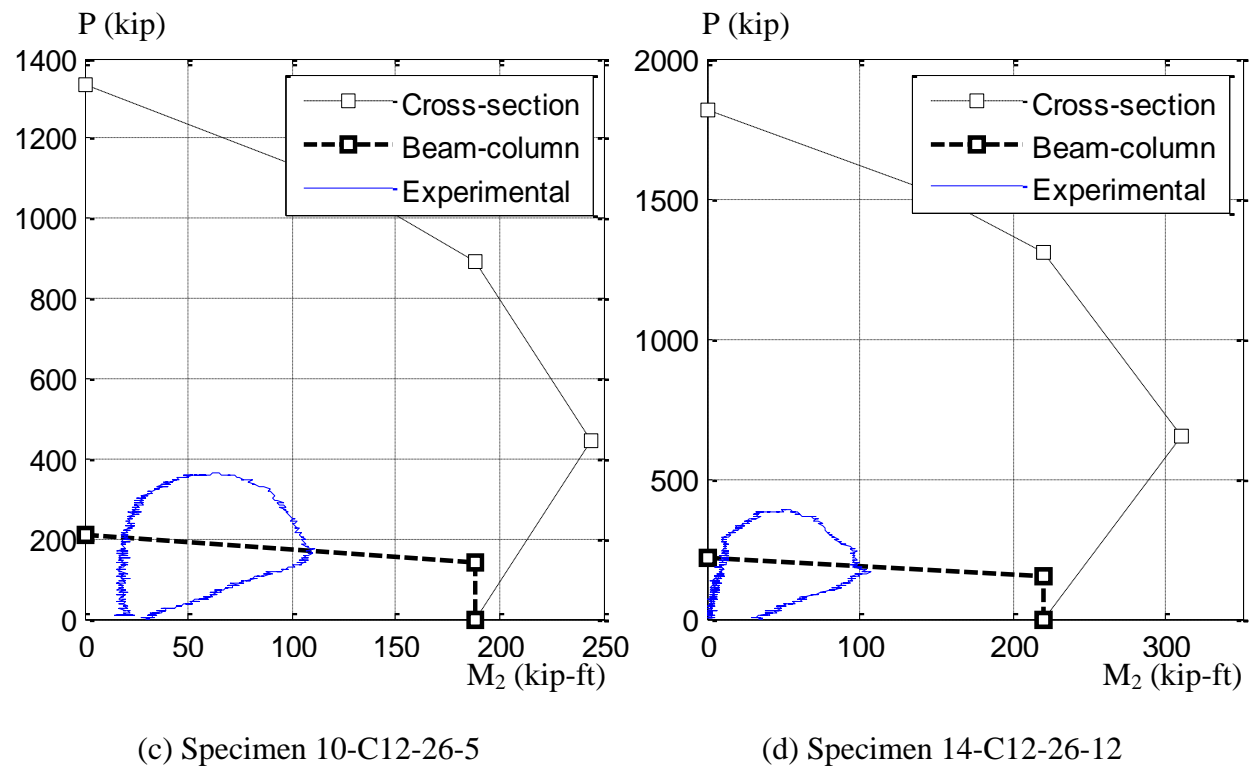
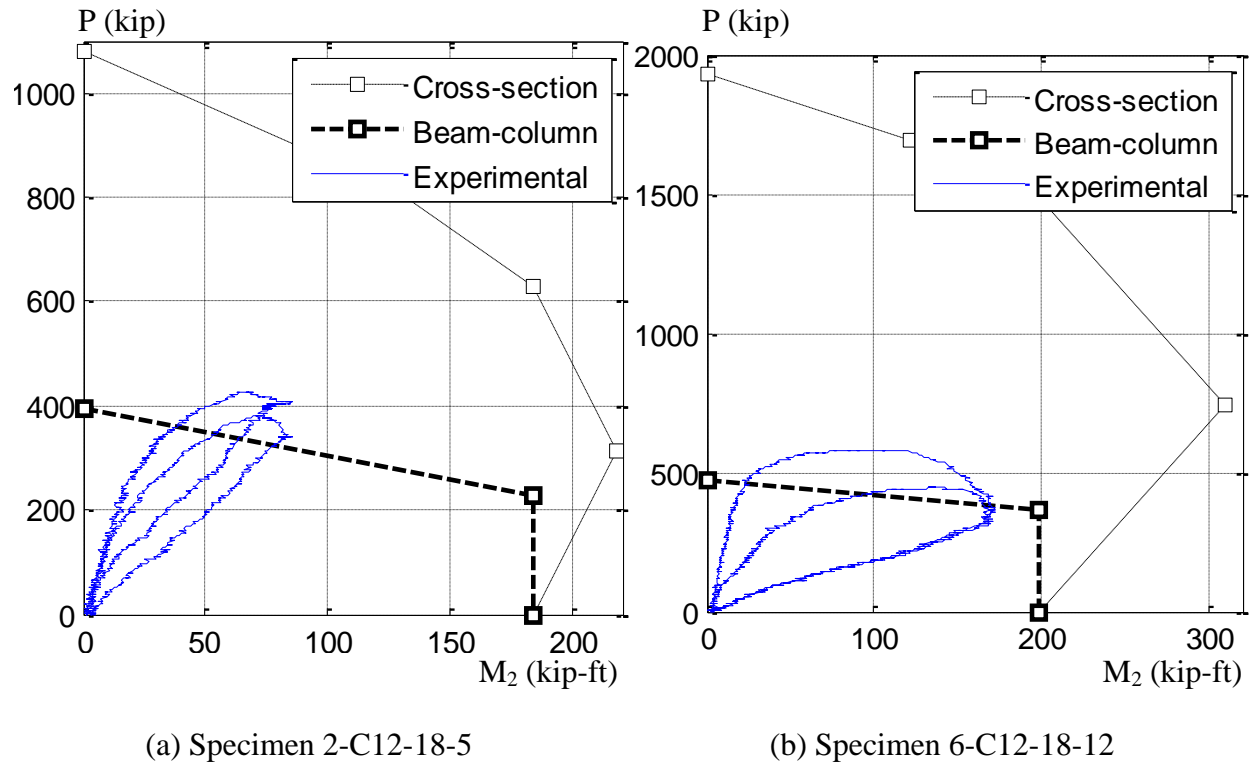
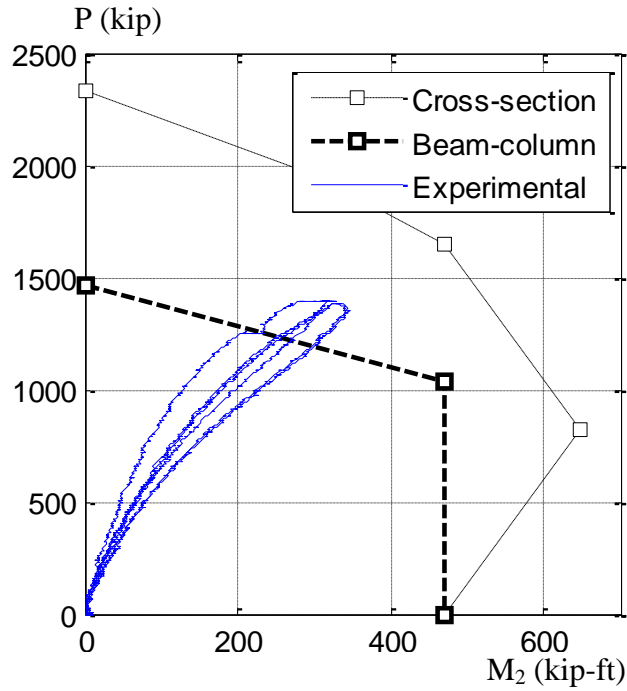
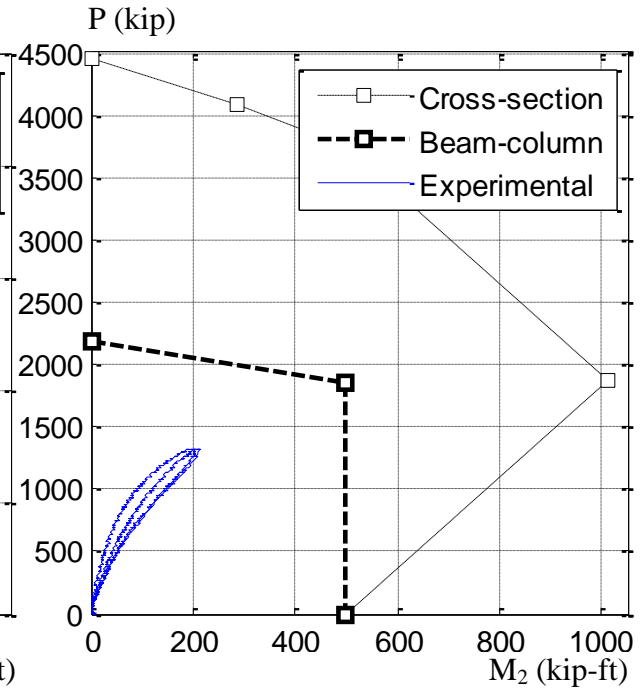


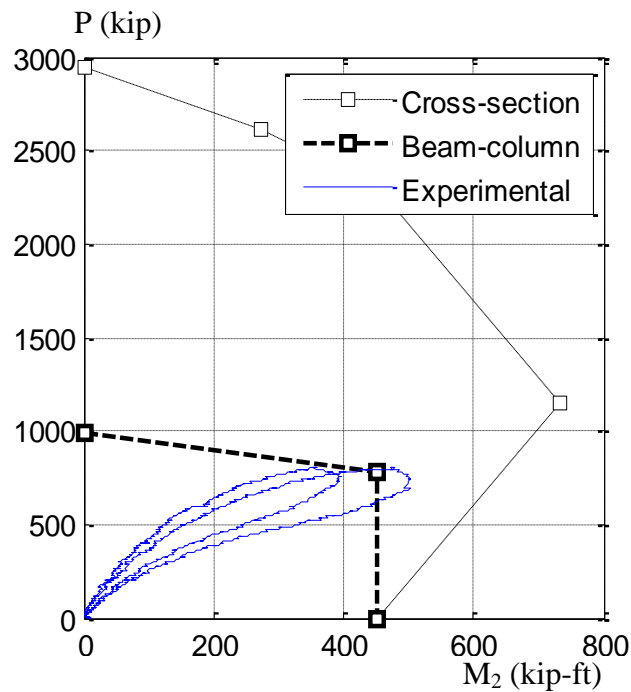
Figure 5.13. Compressive loading vs. base moment (P - M_2) for the C12 set of CCFTs



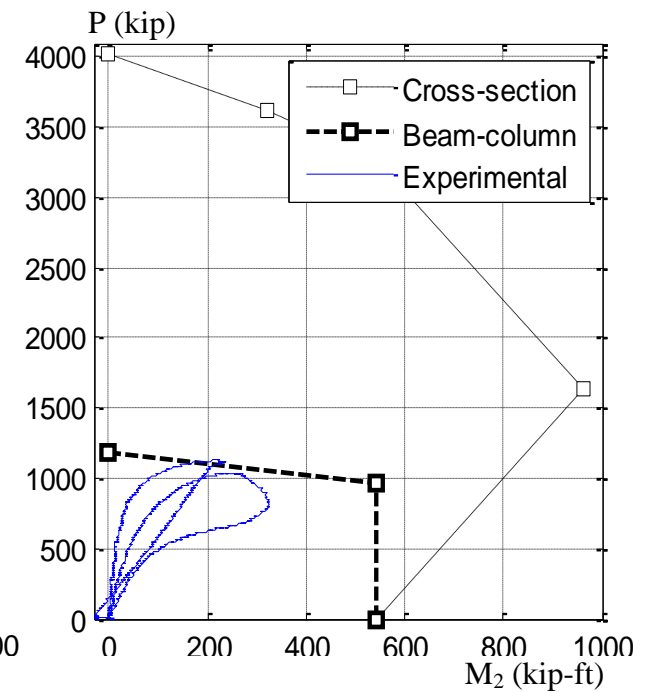
(a) Specimen 3-C20-18-5



(b) Specimen 7-C20-18-12

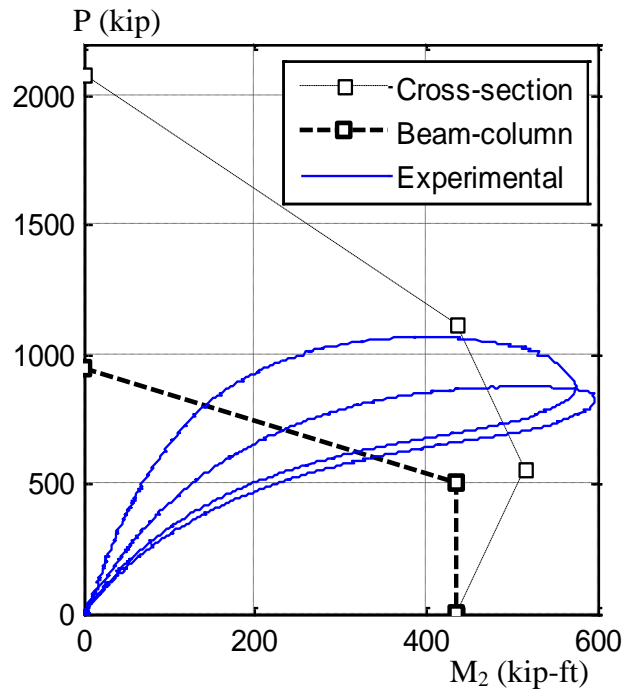


(c) Specimen 11-C20-26-5

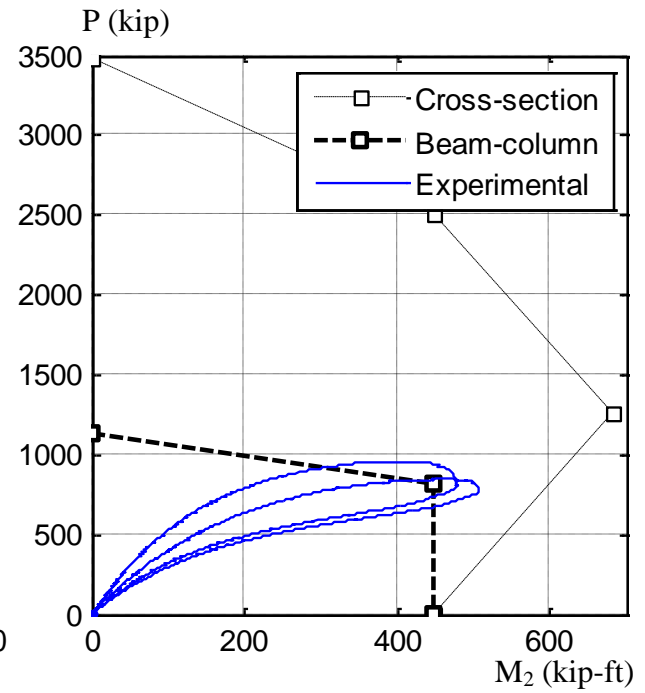


(d) Specimen 15-C20-26-12

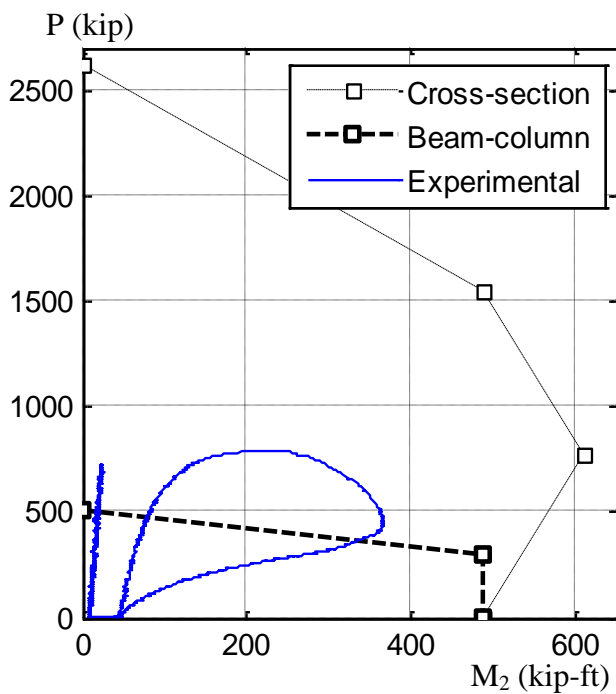
Figure 5.14. Compressive loading vs. base moment (P - M_2) for the C20 set of CCFTs



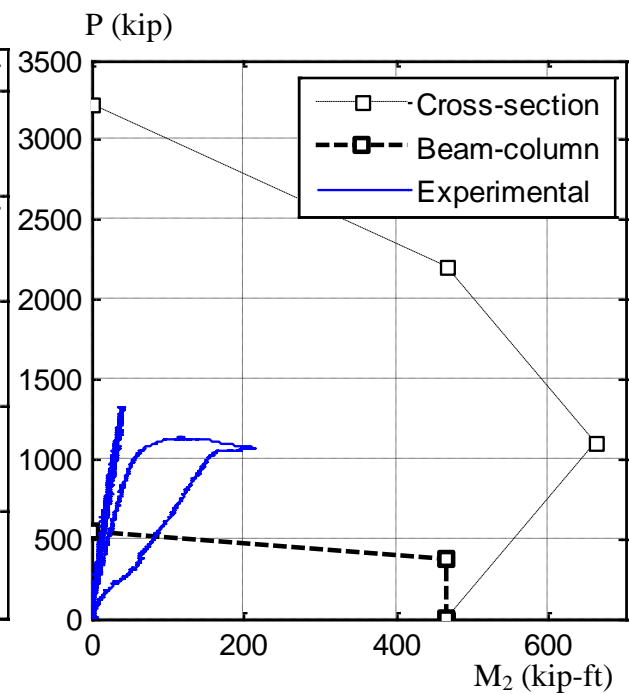
(a) Specimen 4-Rw-18-5



(b) Specimen 8-Rw-18-12

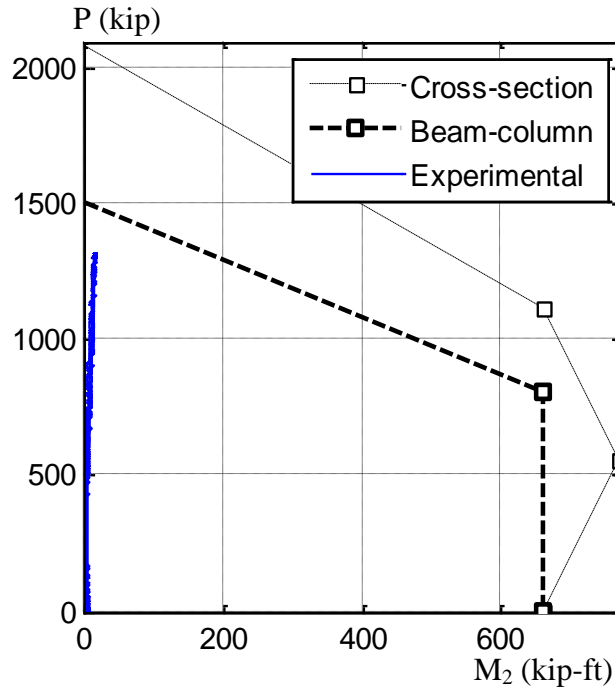


(c) Specimen 12-Rw-26-5

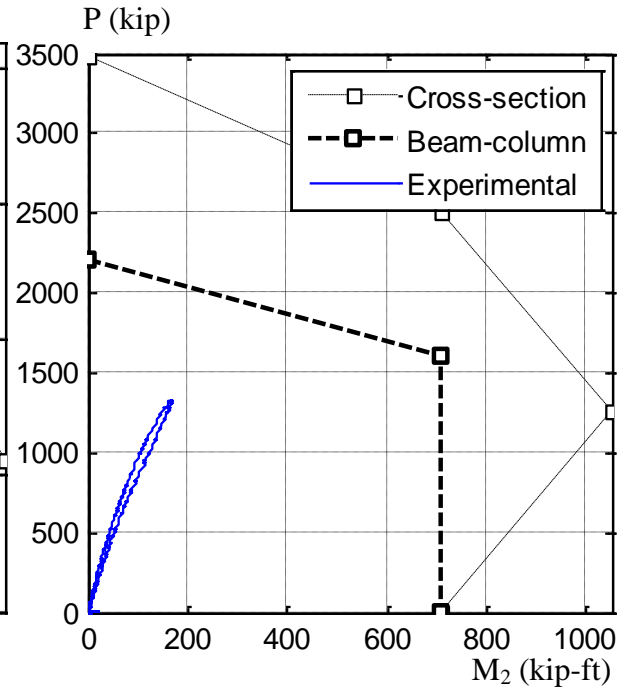


(d) Specimen 16-Rw-26-12

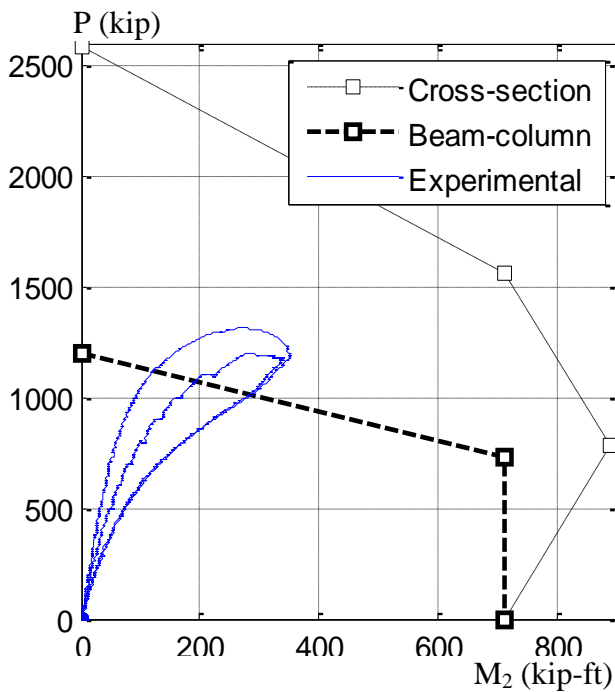
Figure 5.15. Compressive loading vs. base moment (P - M_2) for the Rw set of RCFTs



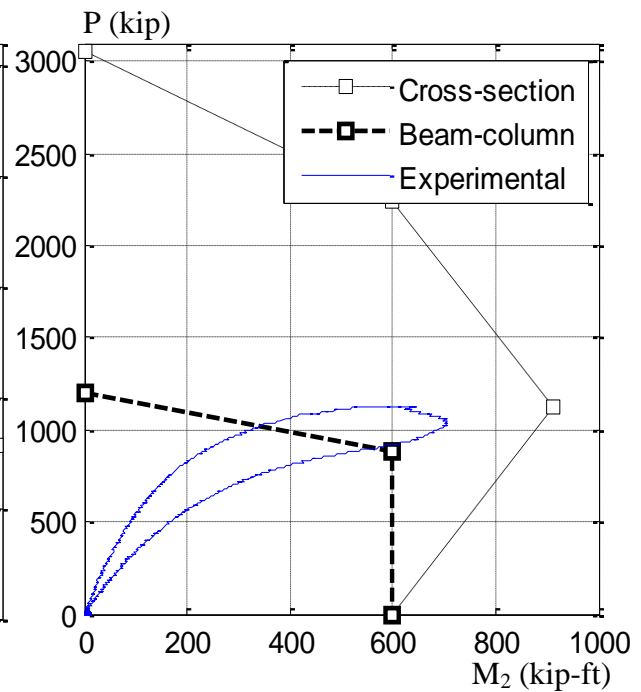
(a) Specimen 5-Rs-18-5



(b) Specimen 9-Rs-18-12



(c) Specimen 13-Rs-26-5



(d) Specimen 17-Rs-26-12

Figure 5.16. Compressive loading vs. base moment (P - M_2) for the Rs set of RCFTs

5.4. Differences between analytical and experimental maximum loads

As mentioned earlier, the main purpose of this load case was a direct measurement of the buckling load for CFT columns. However, as illustrated in Figure 5.6, there were some differences between the analytical and the experimental values. Some of these differences are related to the special characteristics and uncertainties of the CFT specimens, and others are related to the testing setup.

Among the main reasons related to the testing setup that explain differences between the experimental and the analytical maximum axial load capacities are:

- *System compliance.* The crosshead is driven by the MAST system through a controller (*HCC*) that converts input commands of the 6 DOFs at the crosshead center to drive commands for each actuator. The algorithm used by the controller neglects any possible deformation in the system itself, included the crosshead, the connections, and the supports. Tests and finite element analyses conducted for the crosshead have indicated deformations that are not properly accounted by the controller in the computation of the driven commands. This issue makes the axial deformation response calculated by the controller inaccurate and unusable since part of this measured data corresponds to deformation developed in the system and part deformation in the specimens.
- *Friction in the actuator clevises.* The large vertical load actuators have very carefully machined bearings at the clevis pins to eliminate as much of the friction as possible. Tests conducted without any specimens in place indicate that this friction is on the order of 1800 lbs total in each horizontal direction or 900 lbs in each actuator. This is small compared to the lateral load capacity of the system and would be negligible for specimens, such as concrete or masonry walls, that are laterally stiff. However, for slender column specimens as they approach buckling, this level of restraint at the top represents a large proportion of their lateral resistance, so the resulting hysteresis loops appear to have much more energy dissipation than they should. As soon as the load reverses from a peak, this friction needs to be overcome in order to move the specimen in the opposite direction.

- *Lack of perfect control for the DOFs.* As described before, the 6 DOF's at the top for the Specimens 2 to 17 were in vertical displacement control with horizontal forces (F_x , F_y) and top moments (M_x , M_y) in load control such that both forces and moment are kept at zero (fixed base and free top condition, or effective length $K=2$). However, as the system approached the idealized capacity as a fixed-free specimen, the controller began to impose extraneous forces in the opposite direction of motion, and thus increased the maximum load.
- *Limit on axial compressive capacity:* As described earlier, the system is limited to a vertical axial capacity of 330 kip per actuator, or 1320 kip of total capacity. The capacity of some specimens, even when the large slenderness and imperfections, were expected to exceed the capacity of the crosshead.
- Other influencing factors such as a possible inclination of the gravity force with respect to the vertical axis.

Among the main reasons related to the CFT specimens that explain differences between the experimental and the analytical maximum axial load capacities are:

- *Initial imperfections.* The calculation of the critical load in the AISC (2010) assumes that the initial geometric imperfection will be lower than those limits and tolerances ($\Delta_o/L=1/500=0.2\%$ or $\delta_o/L=1/1000=0.1\%$) given by the Standards (i.e. ASTM A6, 2009; AISC, 2005d; ACI-117, 2006). Thus, design equations in the Spec. were tuned and calibrated with geometric imperfection ratios within the tolerances ($\Delta_o/L=1/750$ or $\delta_o/L=1/1500$). As shown in Figure 5.5 and Table 5.1, the initial imperfections were exceeded in most specimens and, for some specimens, the geometric imperfection was significantly larger.
- *Effective stiffness.* The equivalent stiffness (EI_{eff}) as calculated in the AISC (2010) (Equation 5.4) is an approximation of the “true” effective stiffness. Exact calculation of the EI_{eff} is not trivial, since this parameter is highly dependent of the level of cracking and confinement in the concrete, the initial stress or strain field in the steel tube, and even the value of the compressive load in the element.

- *Effective confinement in concrete*: Even though the AISC equations give considerable credit to the circular sections due to confinement, differences were expected in the CFTs buckling capacity due to this parameter.
- Other influencing factors such as the contribution of ignored loads such as the self weight of the specimen, the crosshead and/or the actuators.

The following section gives more details of the previous issues, and how all these were handle in order to extract the more reasonable behavior response of the full-scale and slender CFT specimens tested in this research project.

5.4.1. System compliance

The MAST system, as discussed before, is an assemblage of a “rigid” steel crosshead connected to vertical and horizontal actuators that transfer forces to the strong floor and the L-shaped strong walls. The actuators are pinned connected in both ends to the crosshead and to the strong L-shaped walls and floor through low-friction swivels. The crosshead is driven by a servo-hydraulic control system (HCC). This controller converts the input commands of the 6 DOFs in either displacement or force control (mixed mode) into drive commands for each of the eight actuators; according to the manufacturers, this conversion process accounts for the geometric nonlinearity (<http://nees.umn.edu/facilities/mast.php>). Unfortunately, details in the algorithm of the HCC conversion are not public (Bergson, 2010), and so the overall system compliance is not accurately known.

During the first stages of the data analysis in this research project, an incompatibility between the axial loads and the axial deformations of the CFT specimen was noticed. At this team’s request, an experimental determination of the relative vertical displacement in the crosshead was performed internally by the MAST personnel (Bergson et al., 2010). This test

consisted in driving the crosshead in force control up and down in 3 cycles inducing vertical compression and tension forces on a steel column placed vertically (no out-of-plumbness). The movement crosshead was controlled with the by Z-force DOF (degree of freedom) in force control and all other DOF's in displacement control. The steel column (W12x90, $L = 18'3''$) was put through 3 cycles of compression and tension in the Z direction at ± 750 kips (about 60% of the system axial capacity) with a rate of 2 kip/second; the other DOF's were locked out with the displacement fixed ($\Delta_x = \Delta_y = \theta_x = \theta_y = \theta_z = 0$).

In order to verify the relative vertical displacement measured at each actuator and the computed value at the crosshead center by the controller, a set of eight string pots (with 2 inches of range) connected to the strong floor and to the bottom of the crosshead. Four string pots were located 3 ft. from the center of the crosshead (one on each arm) and the other four were located near the vertical actuators at $8'3''$ from the center of the crosshead (or about $2'3''$ from the center of each actuator). A cross-section of the instrumentation setup is schematically illustrated in Figure 5.17.

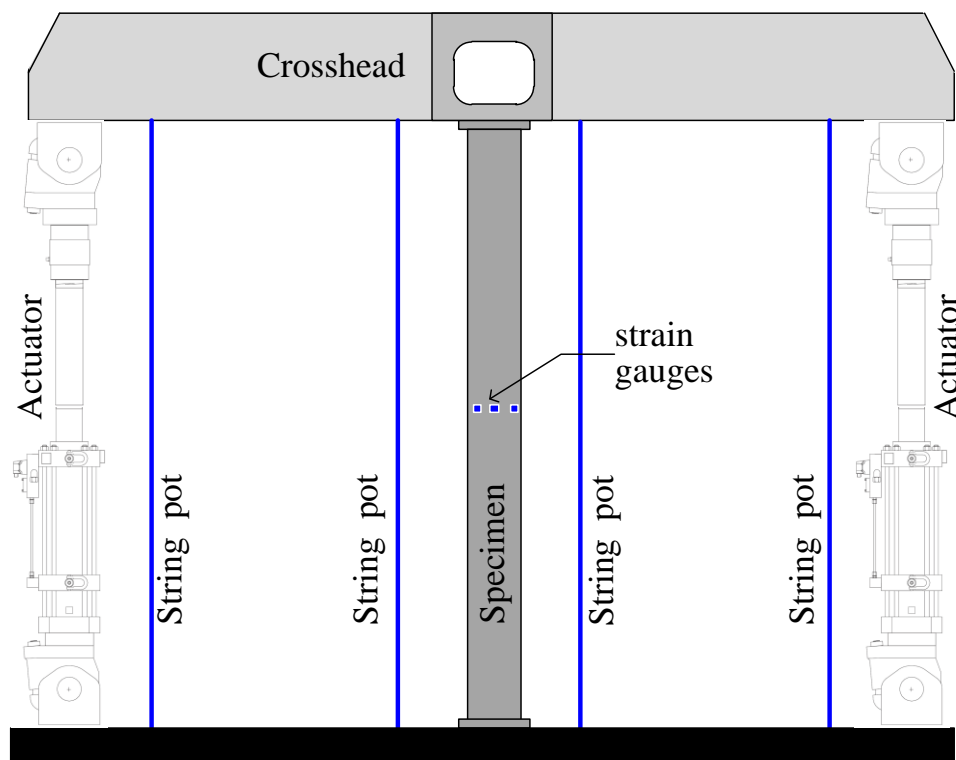


Figure 5.17. Instrumentation setup to verify the crosshead compliance

In addition, a set of six strain gauges were placed in the flanges at the midspan of the steel column. The maximum vertical shortening of the column is calculated then by the product of the average maximum strain (from the six strain gauges) times the column length ($\Delta = \varepsilon L$). Since the column is elastic with the given loading conditions, the expected theoretical shortening is also computed with the mechanic-based equation ($\Delta = PL / EA$); with an axial load $P=750$ kip, a column length $L=18' 3''$, a steel Young's modulus $E=29000$ ksi, and a cross-sectional area $A=55.8$ in², the theoretical maximum shorting results as $\Delta = 0.102$ in. This value is closed to the average shortening of 0.096 in. obtained in the column from the strain gauges.

Table 5.2 summarizes all the downward vertical deflections measured for the crosshead at the time the column is under 750 kip of axial compression force. The data shown in this table is an average of the readings while holding at each peak of the three cycles; the data is consistent between cycles. The measured vertical displacement values from the four actuators, the eight string pots, and the strain gauges are shown in this table; it also shows the global displacement computed by the controller (HCC). The averaged values within cycles for the corresponding point locations along the crosshead are illustrated in Figure 5.18.

As clearly illustrated by Table 5.2 and Figure 5.18, the crosshead has deflections that are not considered in the computed value by the controller, which assumes a rigid plane motion in the calculations. For the particular case of the compliance test presented in this section, the deflection computed by the controller is more than twice the real shortening in the column, with a relative vertical deflection (Δ_r) in the crosshead of 0.11 inches. The MAST team reported as conclusion in this report that the global Z-displacement data computed by the controller does not include the deformation of the crosshead, nor any other system compliance considerations (i.e. force train, swivel bearings, connections, and strong floor/walls).

Table 5.2. Deflections of the compliance test at 750 kips of compression

(a) North-South direction

Cycle	Measurements of the local Z vertical displacement							Global Z displacement computed by Controller
	South			Center	North			
	Actuator	External string pot	Internal string pot	Column	Internal string pot	External string pot	Actuator	
1	0.205	0.158	0.127	0.094	0.118	0.150	0.205	0.205
2	0.205	0.160	0.130	0.096	0.118	0.152	0.205	0.206
3	0.205	0.160	0.130	0.097	0.118	0.152	0.204	0.205

(b) East-West direction

Cycle	Measurements of the local Z vertical displacement							Global Z displacement computed by Controller
	East			Center	West			
	Actuator	External string pot	Internal string pot	Column	Internal string pot	External string pot	Actuator	
1	0.206	0.150	0.120	0.094	0.120	0.178	0.206	0.205
2	0.206	0.148	0.119	0.096	0.119	0.180	0.206	0.206
3	0.206	0.149	0.119	0.097	0.120	0.179	0.206	0.205

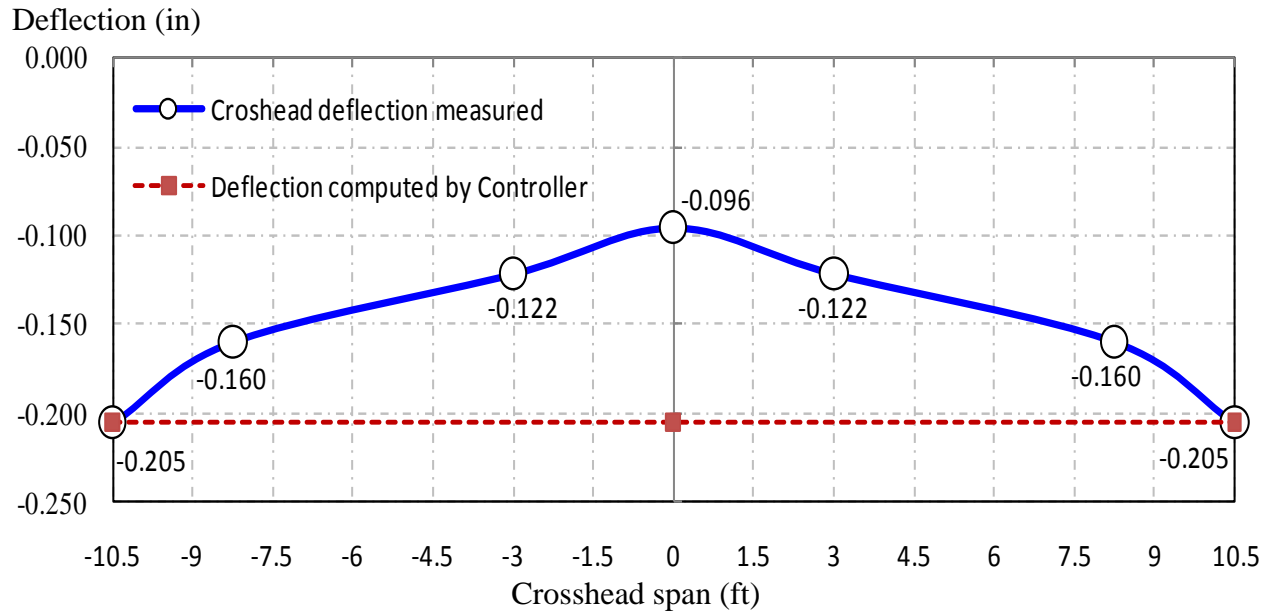


Figure 5.18. Crosshead deflections along the span from averaged measurements in compliance test (relative vertical displacement, $\Delta_r=0.11$ in)

Similar values of crosshead deflections were computed by Dexter (French *et al.*, 2004) through analysis with the finite element method (FEM) of the crosshead with a stiff column attached to the bottom center and under critical loading conditions expected from the actuators. The stress distribution and the displacement shape of four of these critical cases are illustrated in Figure 5.19. This figure also shows the maximum relative crosshead deformation (Δ_r) obtained from the FEM analysis.

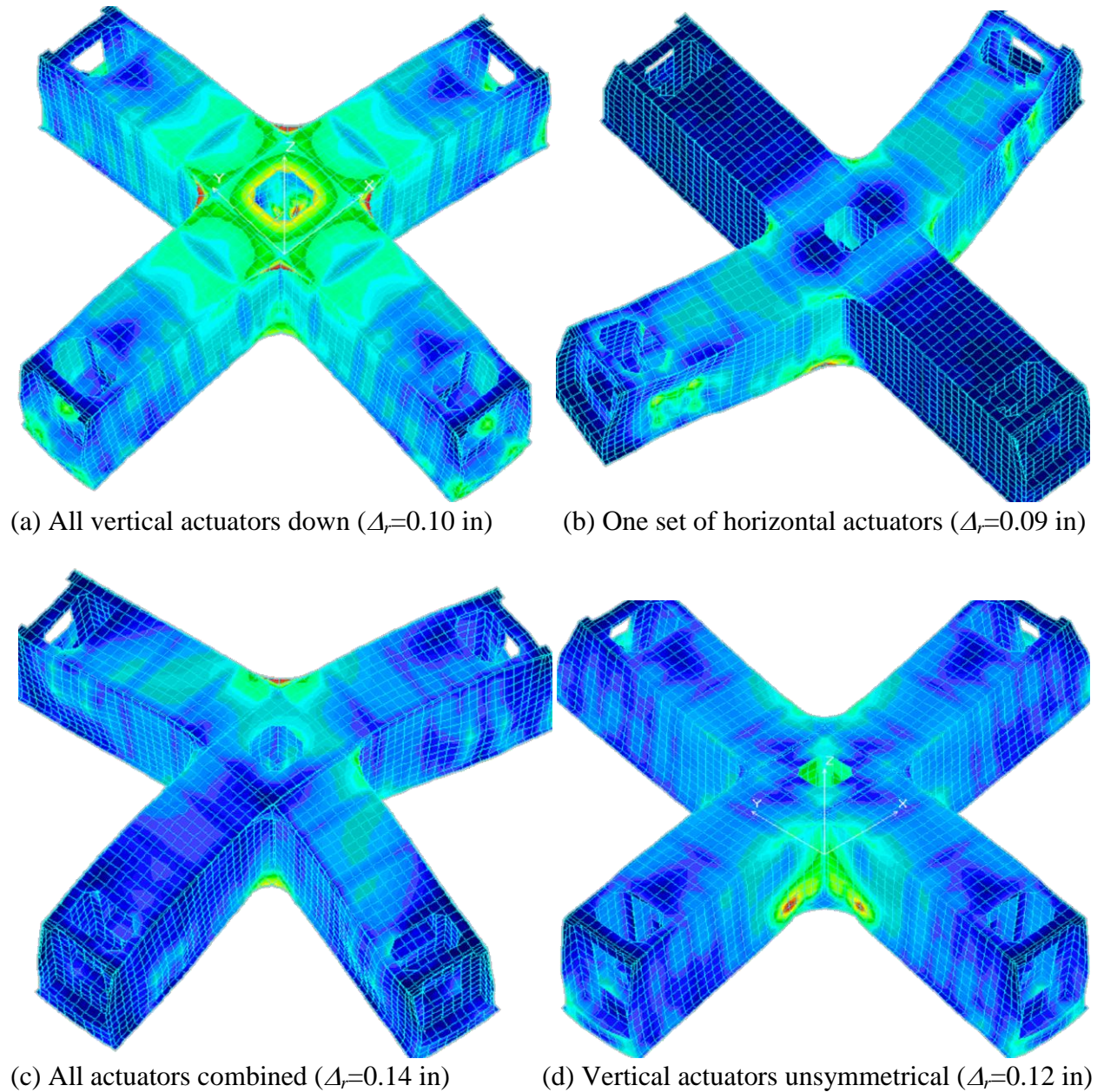


Figure 5.19. FEM analysis for the crosshead under critical conditions

Although the deformation of the crosshead is relatively small (0.15 inches in the worst case), this amount of deflection has a very significant impact on the measured response of the specimen connected to the crosshead. For the compliance test reported herein, the controller reported a global vertical displacement of about twice the real shortening of the specimen.

As shown in Figure 5.20, preliminary analysis on the CFT specimens tested in this research project present fairly similar observations, with an expected axial deformation within 40% to 60% of that computed by the controller based on the measured displacements in the actuators. In this figure, the curve in red is the experimental response reported by the controller, the black curves are extrapolated measurements (maximum end minimum) of the overall shortening based on the LVDT data along the length, and the blue curve is what is calculated from computational analysis. As seen in this figure, the controller is reporting about twice what is expected based on the other measurement channels and the analysis; the shortening computed in the analysis and extrapolated from the LVDT data is consistent. Unfortunately then, there is a difference in the data between the global vertical displacement history and the real axial deformation on the specimens.

The fact that the axial displacement is overestimated by the controller by not extracting the system compliance in the computation makes this measured response unusable. This issue impacts mainly the analytical prediction during the load case LC1, which was driven under incremental axial displacement control with the zero top forces and moments. The measured axial displacement computed by the controller cannot be used neither as input in computational analysis, nor for comparisons with the output shortening response computed in analysis under axial loading.

The impact on the overestimated experimental axial displacement for subsequent load cases is not as critical as in LC1. For the load case LC2 to LC4, the top DOFs were driven under constant axial load control and incremental horizontal displacement control. Therefore, computational analysis can be performed with constant axial load and the target horizontal displacement as input data. The computed axial deformation from the analysis and the measured vertical displacement reported by the controller will not match thought, and the differences can be assumed as the total additional deformation developed in the system.

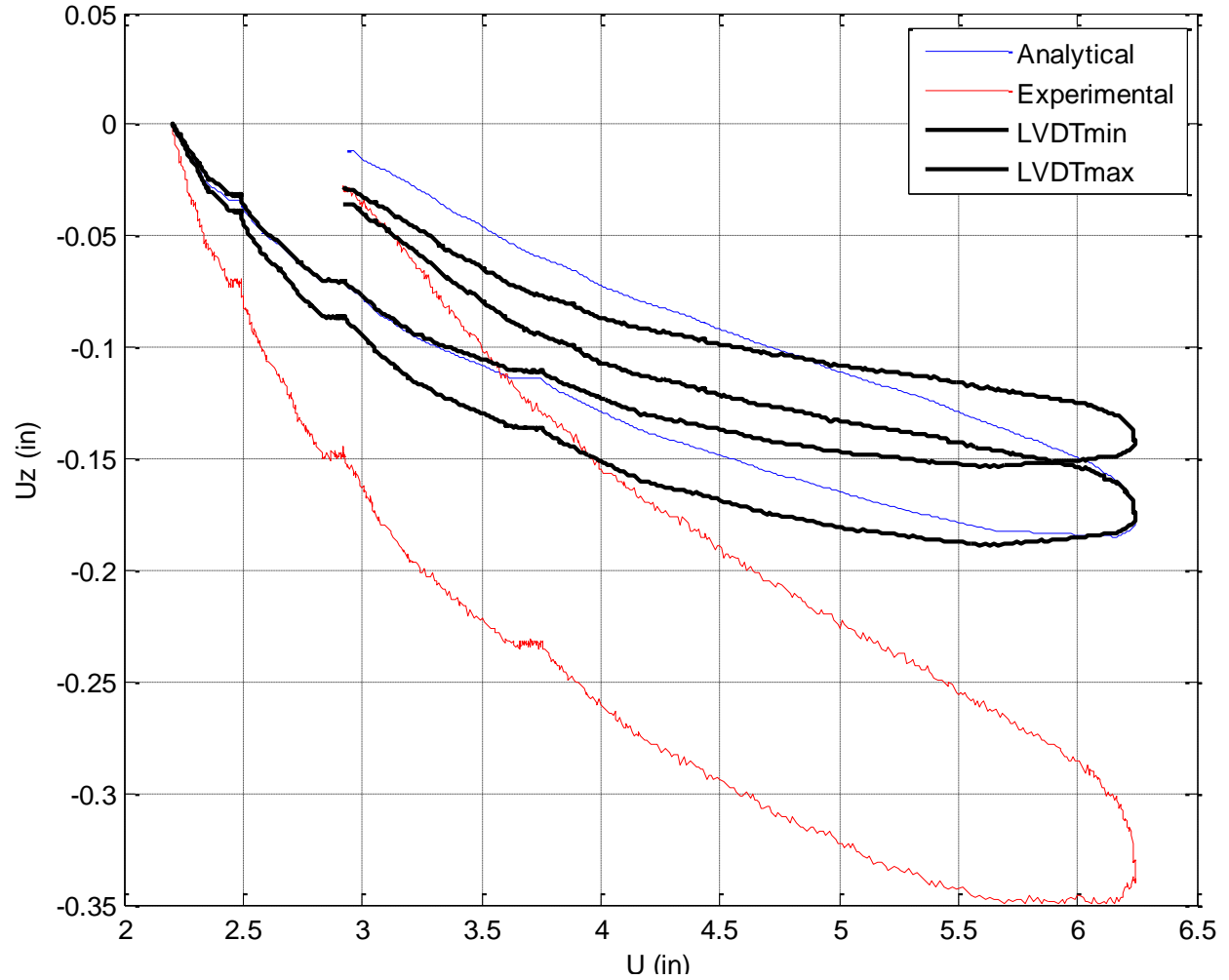


Figure 5.20. Experimental vs. analytical axial-lateral displacement

5.4.2. Frictional forces in the clevises

General features of the MTS actuators used in the MAST system are documented in Chapter 3. These actuators have in both ends swivels with low-friction hydrostatic bearings at the clevis pins that are supposed to eliminate as much of the friction as possible. However, preliminary analysis of the experimental data measured in the CFT specimens suggested the presence of frictional forces that have a significant impact in the weakest specimens.

In order to evaluate how much friction is developed by the system, a test was conducted with driven commands in the crosshead without any connected specimen in place. The crosshead is driven in displacement control with the X and Y displacement and rotation records obtained during the entire loading protocol applied in the Specimen 2C12-18-5.

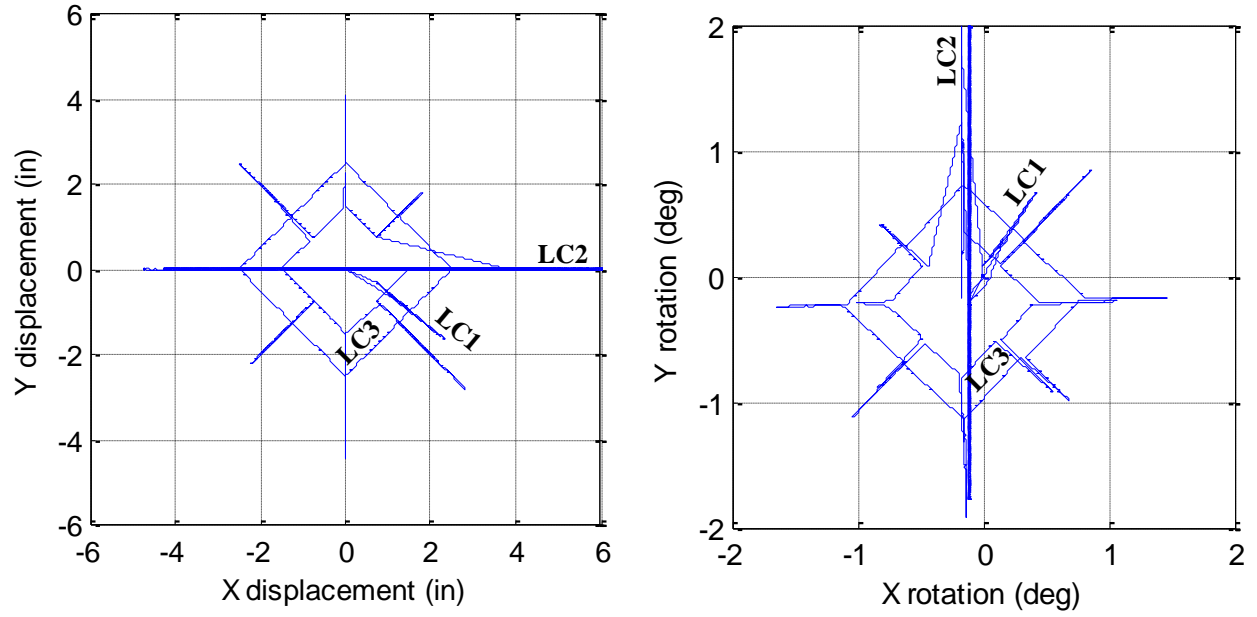
The experimental data response of Specimen 2 during LC1 is reported in this Chapter, while the load cases LC2 and LC3 are documented in more detail in Chapter 6. As summary, Specimen 2 was initially subjected to a pure compression loading (LC1) with a controlled rate of 0.04 inches/min of vertical displacement. In turn, LC2 and LC3 was subjected in constant axial load follow by driven commands to move the top along the X axis (in LC2), and along different probes around the X-Y plane (in LC3); the input commands of lateral motion in both LC2 and LC3 was applied with a rate of 1 inch/min in the X, Y or resultant direction.

The entire top displacement and rotation history recorded in the testing of the specimen 2 (illustrated in Figure 5.19.a) was used as input commands to drive the system without a specimen in place (crosshead and actuators only) and at the same testing rate (0.04 in/min vertically, 0.1 in/min horizontally) without any other specimen element connected to it. The displacement and rotation paths corresponding to each load case in the protocol are labeled in this figure. The forces and moments calculated and reported by the controller of the system only (without any specimen connected) are shown in Figure 5.19.b.

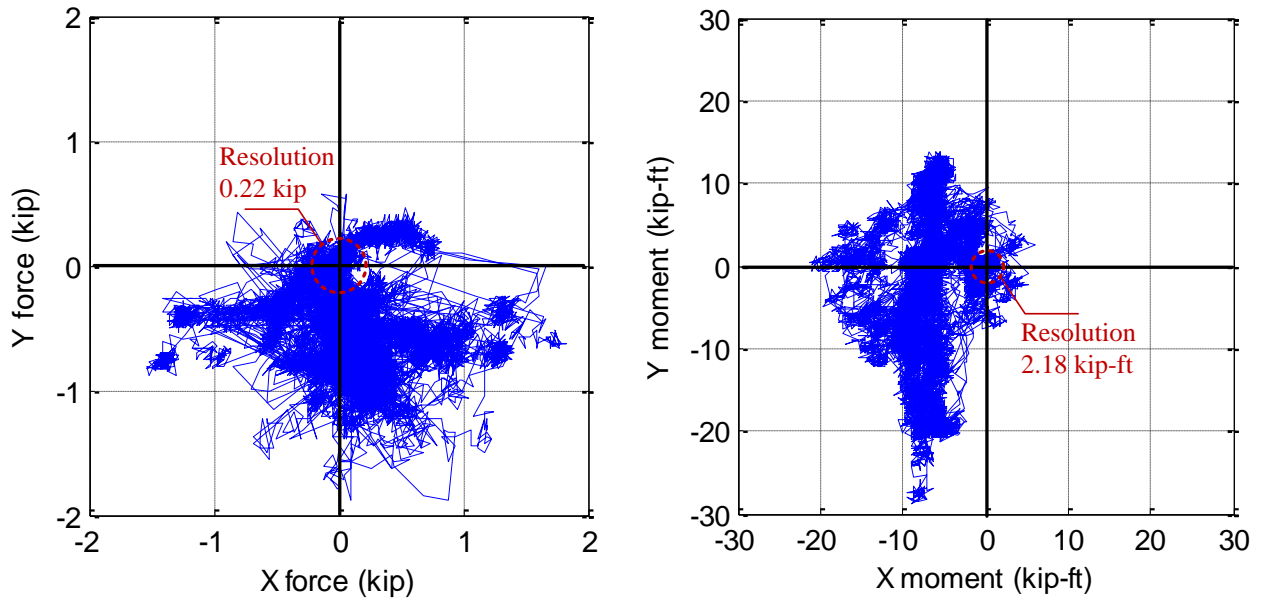
As a side note, the self weight of the crosshead is 94 kips (<http://nees.umn.edu>), and the effective weight in the system (crosshead and tributary weight of actuators) is about 100 kip; during its construction stage, design constraints of the crosshead included a weight limit not to exceed the 100 kip capacity of the crane such that the crosshead could be lifted by the crane (French *et al.*, 2004).

In addition, the expected noise level in the system assuming an effective resolution of 12 bits is about 0.22 kip of lateral force ($880/2^{12}$) and 2.18 kip-ft of top bending moment ($330 \times 27/2^{12}$); thus, forces and moment beyond the noise level are due to friction forces in the clevises.

As observed in Figure 5.19.b, the computed forces and moments (blue path) exceed values expected within the resolution system (red dashed circle), introducing into the system a maximum of 1.875 kip in force and 28.875 kip-ft in moment, and so a moment/force ratio of about 15.4 ft. These lateral frictional forces are small if rigid specimens are tested, but they become significant in very flexible specimens. As an example, the expected base moment with these frictional forces is the order of 33% flexural capacity of the specimen 2C12-18-5.



(a) DOFs controlled at the top



(b) Computed top forces by the controller

Figure 5.21. Data reported by the controller from the empty crosshead test

The 1.8 kip of friction force is equivalent to the inertial force developed in a system of 100 kip of weight that is driven from 1 in/min to the rest condition in an assumed interval of 0.0024 sec; in other words, this is equal to:

$$F = ma = \frac{W}{g} \left(\frac{\Delta V}{t} \right) \approx \frac{100 \text{ kip}}{g} \left(\frac{1 \text{ in/min}}{0.0024 \text{ s}} \right) = 1.8 \text{ kip} \quad (5.10)$$

5.4.3. Initial imperfections

The large initial out-of-plumbness as imperfection in most of the specimens at the beginning of the load case LC1 is another reason that contributes in the differences between the analytical buckling load prediction and the maximum experimental load capacity measured. In the cases with a higher out-of-plumbness as imperfection, the buckling load is reduced as a consequence of a second order component ($P\Delta$) consumed as flexure. This is schematically illustrated in Figure 5.22 with three cases of out-of-plumbness. As shown in this figure, the critical load (P_{cr}) expected for a vertical and straight element ($\Delta_o=0$) is higher than the nominal axial capacities (P_n) for a moderate ($\Delta_o>0$) or a larger ($\Delta_o>>0$) out-of-plumbness. This figure illustrates how the nominal load is reduced (from P_{cr} to P_n) as a consequence of a second order component ($M=P\Delta$) consumed as flexural bending.

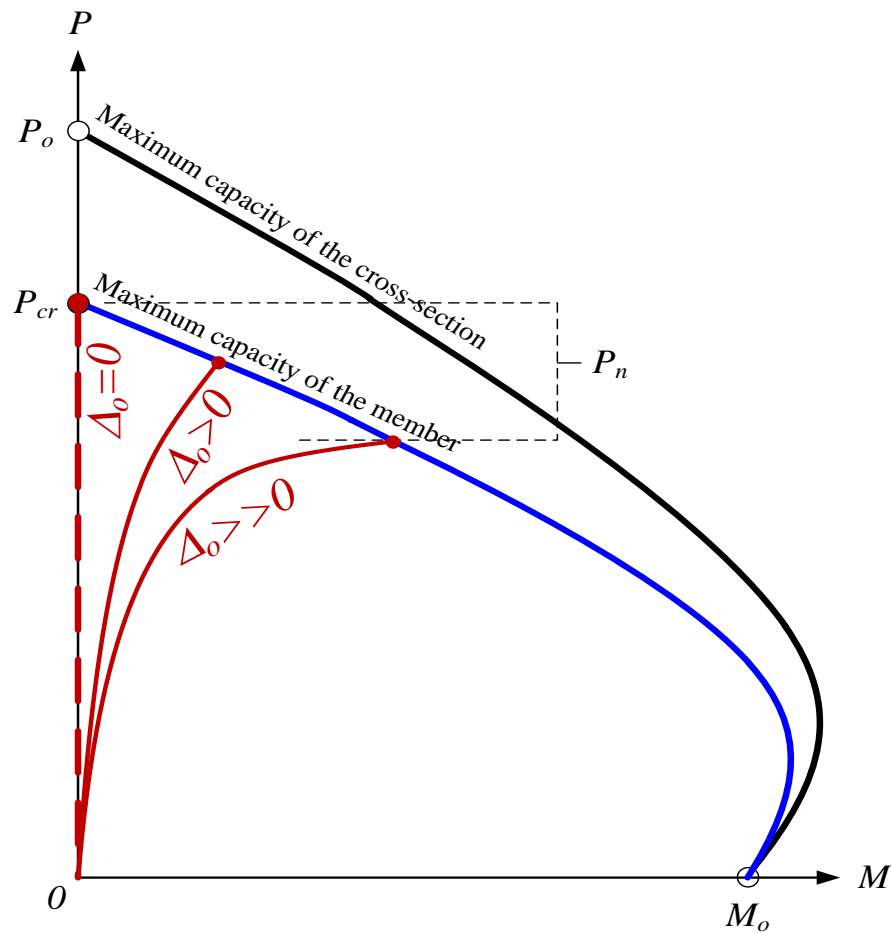


Figure 5.22. Effect of out-of-plumbness on the axial load capacity

However, the critical load can be highly influenced not only by the out-of-plumbness (Δ_o), but also by the out-of-straightness (δ_o) and, in general, by the complex initial deflected shape. Figure 5.23 shows possible variations in the initial deflected shape in cantilever columns taken from ASCE (1997).

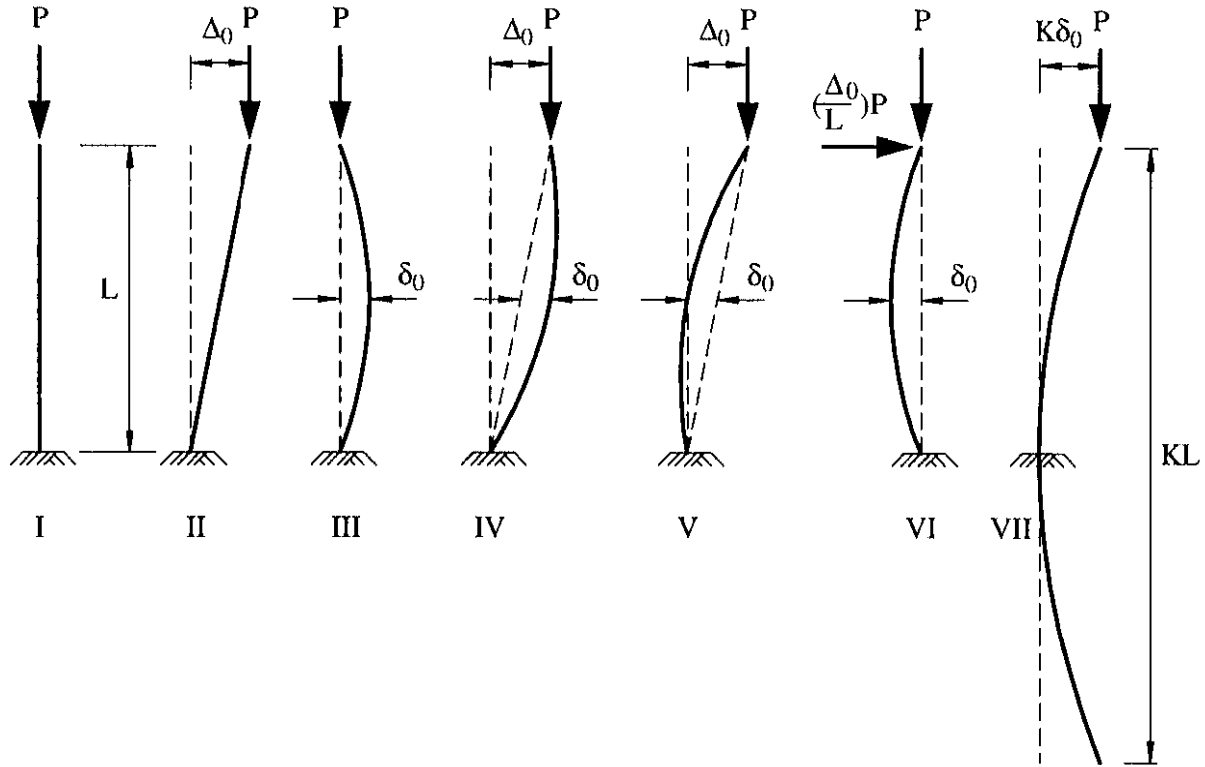


Figure 5.23. Initially imperfect shapes for cantilever columns (ASCE, 1997)

The reduction in the axial capacity due to the out-of-plumbness was illustrated in Figure 5.22. However, as commented above, the expected axial capacity in some cases can be higher under special initial imperfection conditions. This was the case of the Specimens 5, 12 and 16 in this research project. These three specimens have in common the following characteristics:

- (1) The specimens are RCFTs, and their initial imperfection shape is in double curvature as shown in Figure 5.24.
- (2) They have a high out-of-straightness (Δ_o) compared to its out-of-plumbness (δ_o). The ratio δ_o/Δ_o in Specimens 5, 12 and 16 have values of 0.97, 1.00 and 0.52, respectively; the remaining specimens have a ratio below the 0.25 value with an average of 0.11.
- (4) None of these three specimens exceeds the tolerances for imperfection ($\delta_o < L/1000$; $\Delta_o < L/500$) limited in the standards.

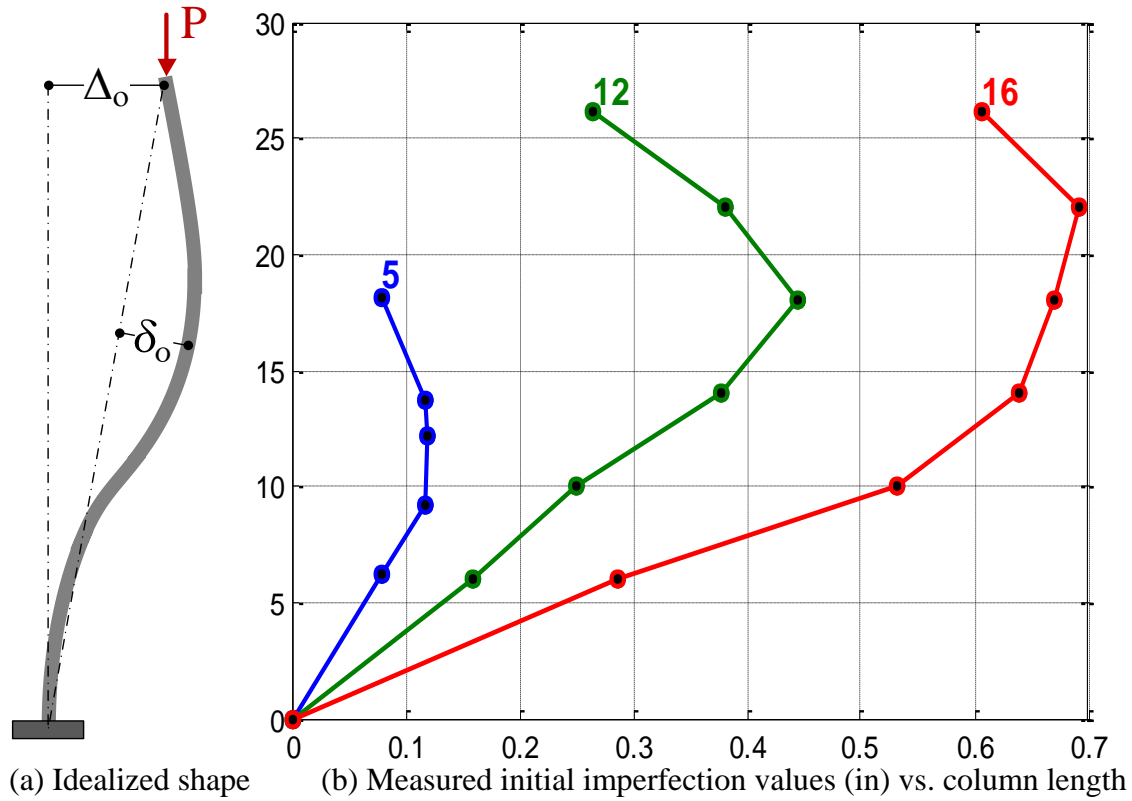


Figure 5.24. Initial deflected shape

It was observed during the tests of these specimens (with the initial shape as shown in Figure 5.24) that the displacement measured by the string pots near the midspan increased initially with a higher rate than the corresponding displacement measured at the column tip. In other words, the deflected shape of these specimens was developed between the buckled shape in Figure 5.4(c) with theoretical $K=0.7$ and the buckle shape in Figure 5.4(a) with $K=2.0$.

For the specimen 12, the second cycle of LC1 was performed with a forced change in the shape from that shown in Figure 5.24(a) or Figure 5.23(IV) to a shape similar to that shown in Figure 5.23(VII). This change of shape was achieved through driving the top in displacement control with no axial load until a target deflected shape as in Figure 5.23(VII) was met, and thus developing an effective length for the second cycle close to as fixed-free or $K=2$. This change of shape also induced a moment at the base as seen in Figure 5.15(b) with no axial load.

The latter adjustment in the initial deflected shape was not performed in the Specimens 5 and 16. In these specimens, a lower effective length factor is more appropriate due to the initial deflected shape as in Figure 5.24(a).

Although specimens 5 and 16 were controlled as base-fixed and top-free ($K=2$), the double curvature as initial shape reduces the effective length ($K<2$) and so the maximum experimental capacity was higher than that expected for the ideal BCs. This behavior type was also observed in the analyses performed by ASCE (1997), where the computed axial strength for the cases III and IV shown in Figure 5.23 were considerably higher than the strength of the cases II, V, VI, VII. This reference does not present effective length factors for each independent imperfection case. However, the following results present a rough estimation of the equivalent K for the imperfection case IV; this case is close to the imperfections shape of specimen 5 and 16.

Advanced analyses of steel columns with all the imperfections cases illustrated in Figure 5.23 are documented in ASCE (1997). The results show different axial load capacities for each imperfection case. This reference concluded that the AISC column curve is not premised on a particular (or unique) set of imperfection parameters, and remarks that the out-of-plumbness (Δ_o) has a more significant effect on the strength than the out-of-straightness (δ_o).

The analyses reported by in ASCE (1997) were calibrated for a cantilever ($K = 2$) steel column of A36 ($F_y = 36$ ksi, $E_s = 29000$ ksi) and a W8x31 cross-section. The length was set such that the slenderness parameter with the latter conditions was equal to one ($\lambda=1$). Thus, the ratio $L/r\pi$ used in the analysis is given by:

$$\left(\frac{L}{r\pi} \right) = \frac{\lambda}{K} \sqrt{\frac{E_s}{F_y}} = \frac{1}{2} \sqrt{\frac{29000}{36}} = 14.191 \quad (5.11)$$

The axial capacity reported for the imperfection case shown in Figure 5.23(IV) is equal to 0.801 times the squashing capacity (P_y). Thus, the equivalent slenderness parameter for the case IV is equal to:

$$\frac{P_n}{P_y} = 0.658^{\lambda^2} = 0.801 \quad \rightarrow \quad \lambda = 0.728 \quad (5.12)$$

Therefore, based on these results, the effective length factor for the case IV is of the order of 1.46 as obtained for the calculation below:

$$K = \frac{\lambda}{L/r\pi} \sqrt{\frac{E_s}{F_y}} = \frac{0.728}{14.191} \sqrt{\frac{29000}{36}} = 1.46 \quad (5.13)$$

Thus, an effective length factor as $K=1.5$ was adopted for the specimens 5 and 16 due to the imperfection shape with double curvature as shown in Figure 5.24(a). The adopted effective length factor presents more appropriate results to account for the initial deflected shape with double curvature as shown in Figure 5.24(a). With the adopted K value, the slenderness parameter (λ) changed from 0.88 to 0.66 for the specimen 5Rs-18-5, and from 2.30 to 1.72 for the specimen 16Rw-26-5 as shown in Table 5.3.

Table 5.3. Experimental buckling loads in specimens with adjusted effective length

Specimen	AISC (2010)			Max. test	ratio
	K	λ	P_n (kip)	P_{exp} (kip)	P_{exp} / P_n
5Rs-18-5	1.5	0.66	1731	1320 ⁺	0.76
16Rw-26-12	1.5	1.72	949	1140	1.20

(+) MAST axial capacity (1320 kips) reached before getting the buckling strength

5.4.4. Lack of perfect control of the DOFs

Even though the CFT specimens were controlled during LC1 as fixed-free cantilever columns (idealized as shown in Figure 5.25.a.), it was observed during this load case that the controller began to impose extraneous forces as the system approached the buckling capacity of the specimen. The additional top forces and moments that were imposed in the opposite direction of motion violate the free top condition. As a consequence, the boundary conditions (BCs) changed to a column that can be idealized as shown in Figure 5.25.b. with a fixed-base and lateral and rotational springs at the top. These springs can be calibrated to include forces and moments in the model that increased proportionally to the axial load, or proportionally to the top lateral displacement and rotation.

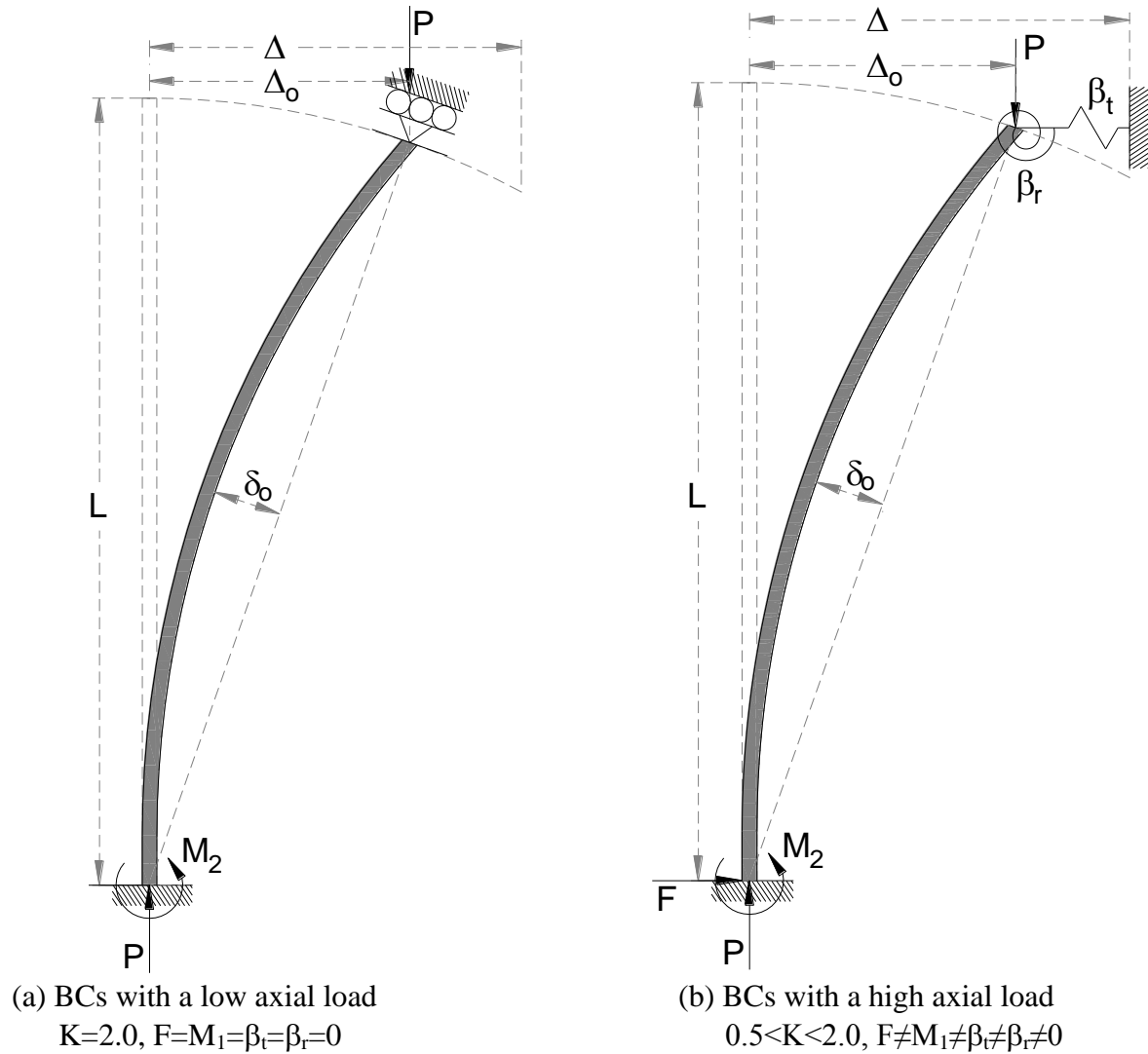


Figure 5.25. Fixed-free and fixed-spring boundary conditions

The amount of additional top forces and moments observed during the tests was significant and, in general, these disturbing top actions started when the vertical force reaches the expected critical load with fixed-free BCs, and increased until the maximum axial load is reached.

Table 5.4 shows a summary of the resultant top forces and moments at the peaks during LC1. As shown in this table, lateral forces (F) and top moments (M_1) exceeded what was expected as noise for both the lateral force (0.22 kip) and moment (2.18 kip-ft), being these additional lateral forces and bending moments larger as the axial load approaches the columns buckling capacity.

Table 5.4. Maximum lateral forces (F_{max}) and top bending moments (M_{1max}) during LC1

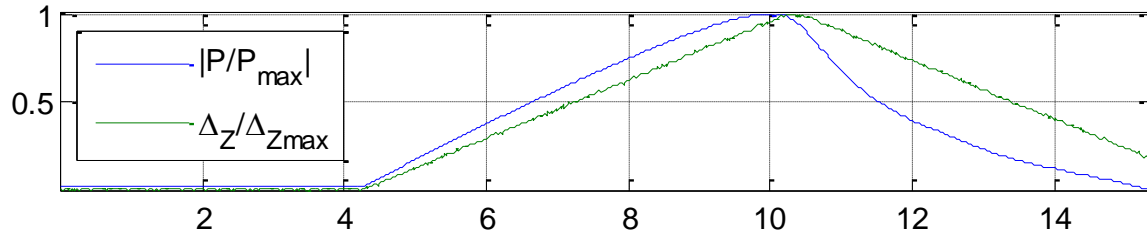
Specimen	Peak gravity force			Peak lateral force			Peak bending moment		
	P_{max} kip	F kip	M_1 kip-ft	P kip	F_{max} kip	M_1 kip-ft	P kip	F kip	M_{1max} kip-ft
2C12-18-5	427	0.54	5.4	370	0.70	5.6	401	0.56	8.1
3C20-18-5	1400	0.18	5.0	1400	0.95	4.6	1160	0.05	18.9
4RW-18-5	1070	0.55	6.9	751	1.20	12.6	752	1.06	14.3
5RS-18-5	1320	0.09	1.0	457	0.27	0.3	1310	0.09	2.3
6C12-18-12	581	1.23	14.2	575	1.54	16.8	574	1.44	18.5
7C20-18-12	1321	0.28	1.2	1198	0.31	4.5	1198	0.31	4.5
8RW-18-12	961	0.66	9.7	671	1.06	9.8	949	0.93	13.2
9RS-18-12	1320	0.08	0.0	1280	0.08	2.9	1280	0.08	2.9
10C12-26-5	362	1.70	11.3	360	1.86	12.2	352	1.78	13.8
11C20-26-5	802	0.58	6.3	525	0.80	8.2	577	0.72	10.3
12RW-26-5	724	0.25	1.0	418	0.44	0.9	451	0.25	2.3
13RS-26-5	1320	0.38	6.7	1310	0.40	8.7	1310	0.40	8.7
14C12-26-12	386	1.39	17.0	373	1.50	18.8	376	1.34	19.4
15C20-26-12	1127	0.99	2.0	1102	2.71	5.5	1080	2.24	10.6
16RW-26-12	1140	1.49	6.1	1050	6.17	2.6	1070	4.04	29.8
17RS-26-12	1120	0.33	0.5	1110	1.24	1.5	1030	0.10	6.0

The relationship among all the collected data was evaluated in order to explore possible interaction between the axial load capacity and other measured response. Thus, a number of the data channels plotted versus time are shown in Figure 5.26 to Figure 5.28 for the Specimens 10C12-26-12, 14C12-26-12 and 15C20-26-12, respectively. These figures include key data on the controller and on the specimens' instrumentation. The responses in time domain plotted in these figures are:

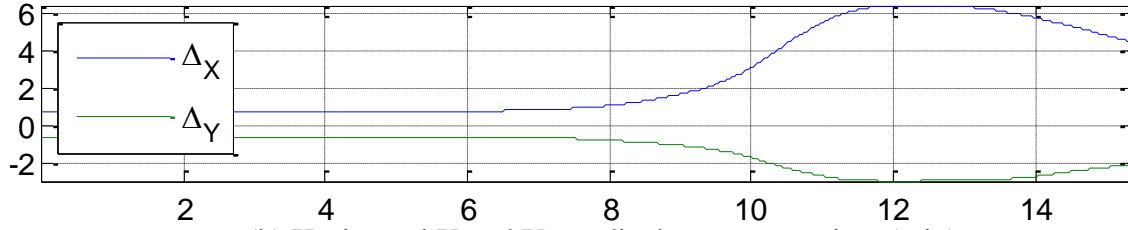
- (a) vertical load and displacement,
- (b) horizontal X and Y top displacements,
- (c) horizontal X and Y top forces,
- (d) top X and Y rotations,
- (e) top X and Y bending moments; and,
- (e) maximum compressive and tensile strains at a cross-section near the base

As illustrated in (c) and (e) of these figures, both forces and moments were able to be controlled and held at zero when the axial force in the specimen was still low, and thus keeping an ideal fixed-free boundary conditions ($K=2$) as illustrated in Figure 5.25.a. However, these figures also show incremental lateral forces and bending moments as the gravity reaches an instability condition, and thus higher axial loads were achieved as these parasitic top forces and moments tended to stabilize the columns. The additional forces and moment at the top essentially changed the boundary conditions similar to those illustrated in Figure 5.25.b.

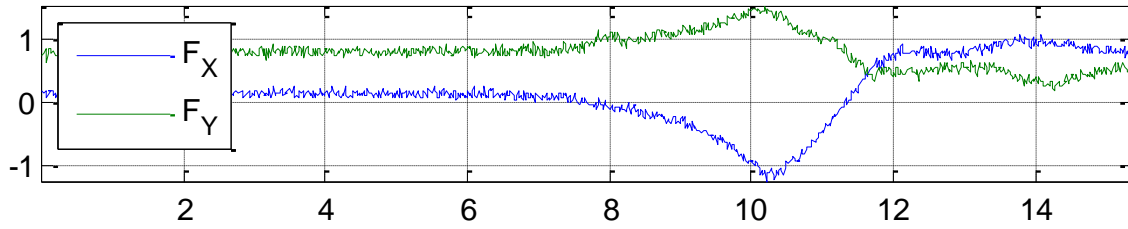
As marked in (e) from Figure 5.26 to Figure 5.28, the maximum compressive and tensile strains at the critical section near the bottom increase proportionally with the axial load. Note that the compressive strain at the critical cross-section reaches a peak value about the same time the controller start adding forces and moments at the top, and eventually this strain response shows and inversion from compression to tension at about the same time the maximum compressive load was reached. Although not necessarily so, the point when the transition of boundary conditions occurs appears to be close to the point where the longitudinal compressive strains reach a peak.



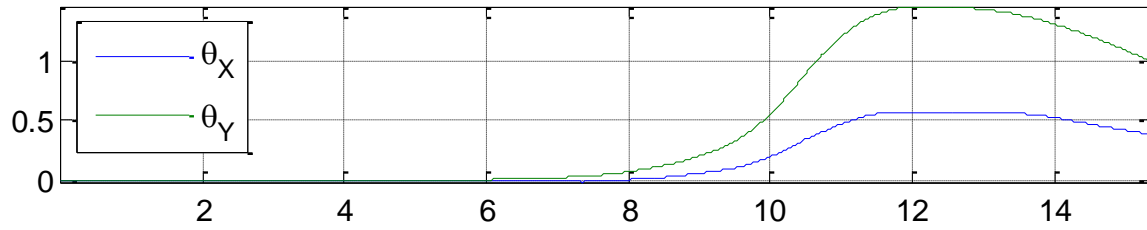
(a) Normalized vertical compression force and displacement vs. time



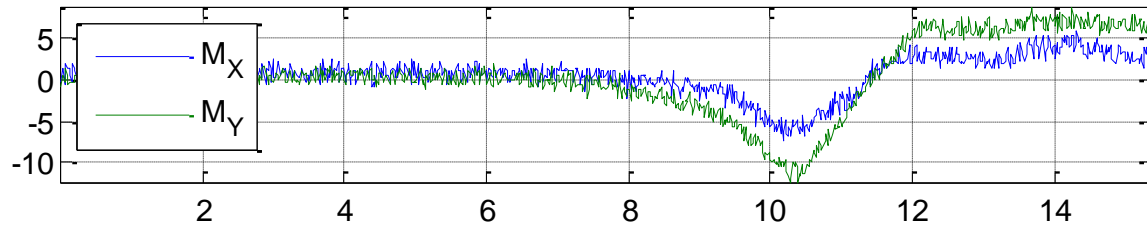
(b) Horizontal X and Y top displacement vs. time (min)



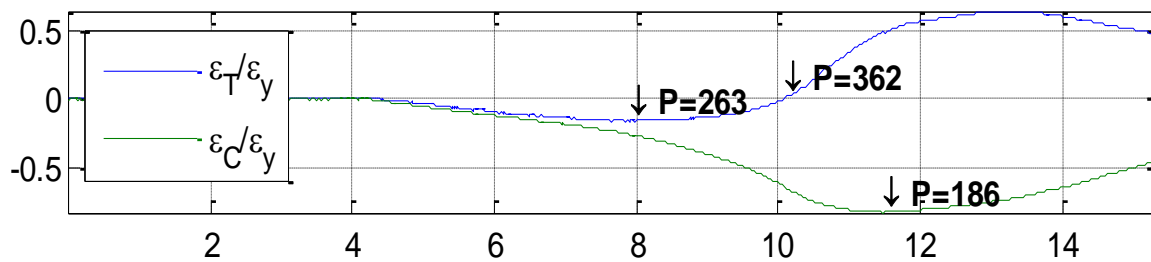
(c) Horizontal X and Y top forces vs. time (min)



(d) X and Y top rotations vs. time (min)

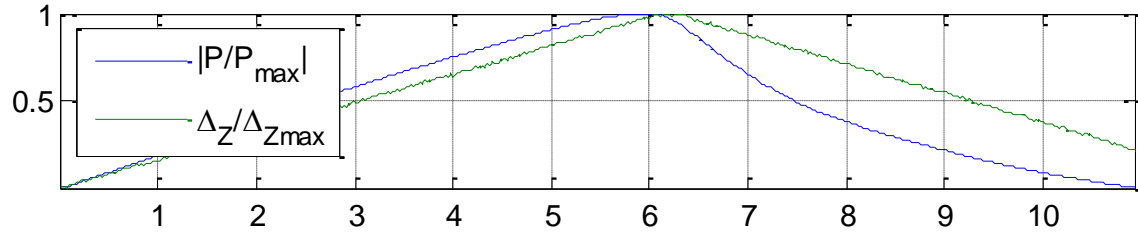


(e) X and Y top moments vs. time (min)

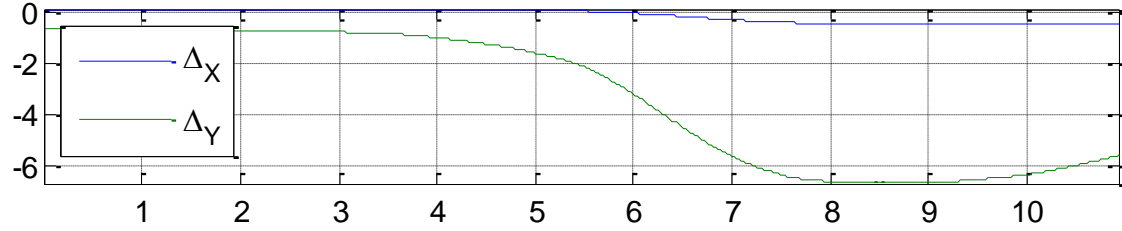


(f) Normalized maximum tensile and compressive strains at 6'' from the base

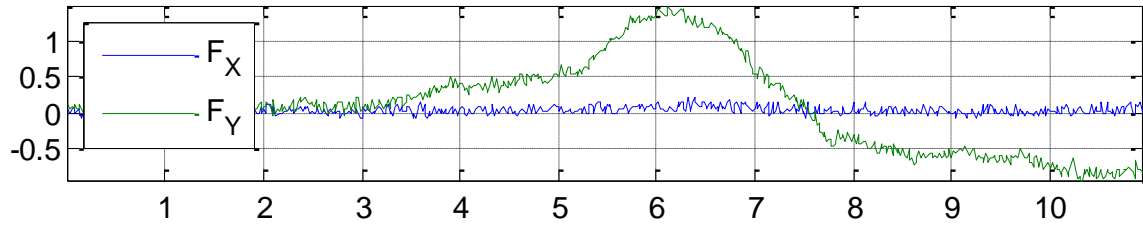
Figure 5.26. Histories of test response for the Specimen 10-C12-26-5



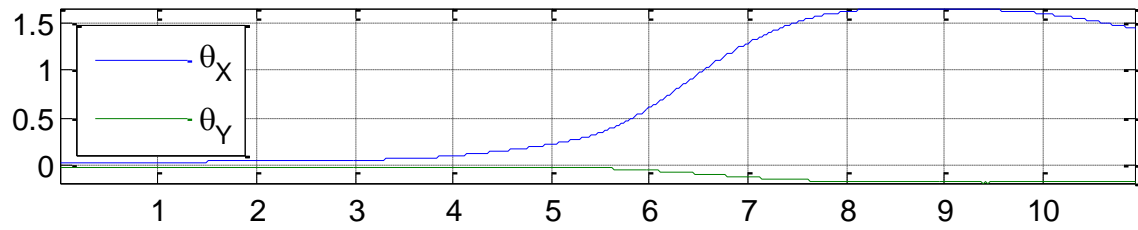
(a) Normalized vertical compression force and displacement vs. time



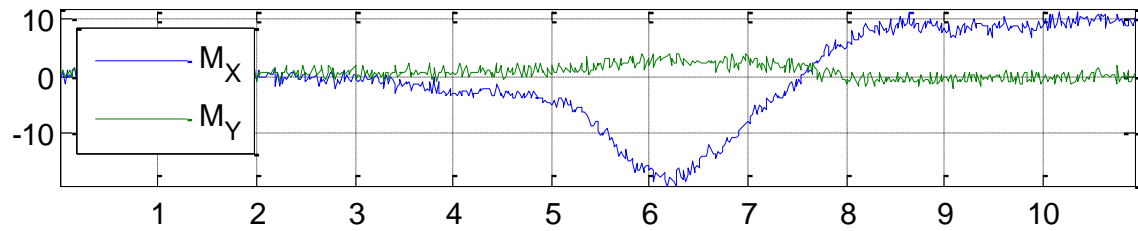
(b) Horizontal X and Y top displacement vs. time (min)



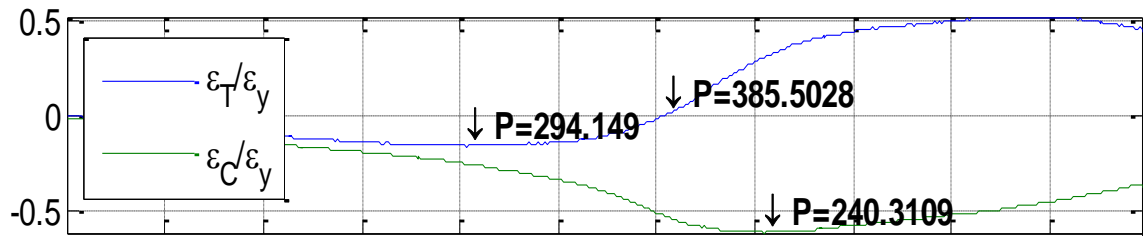
(c) Horizontal X and Y top forces vs. time (min)



(d) X and Y top rotations vs. time (min)

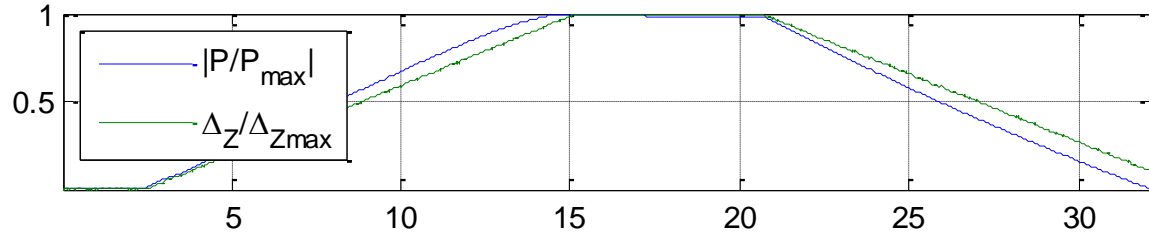


(e) X and Y top moments vs. time (min)

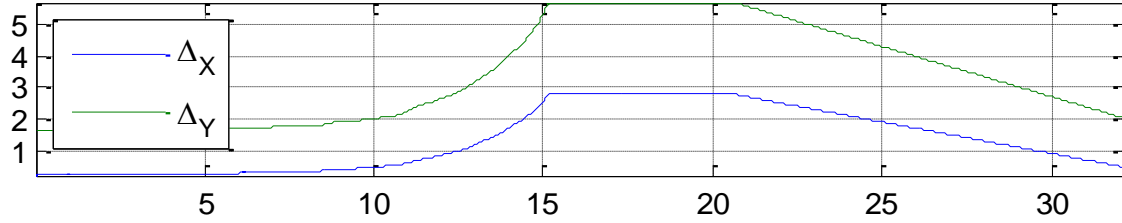


(f) Normalized maximum tensile and compressive strains at 6'' from the base

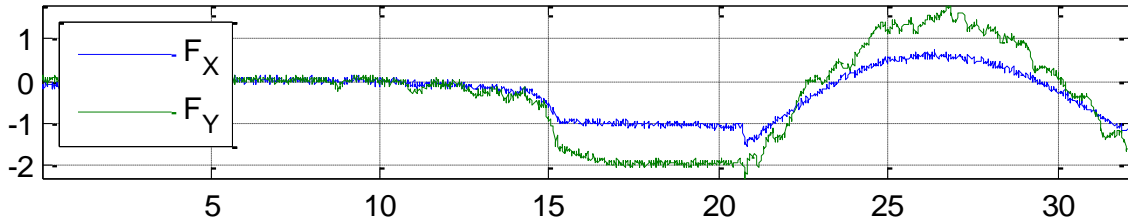
Figure 5.27. Histories of test response for the Specimen 14-C12-26-12



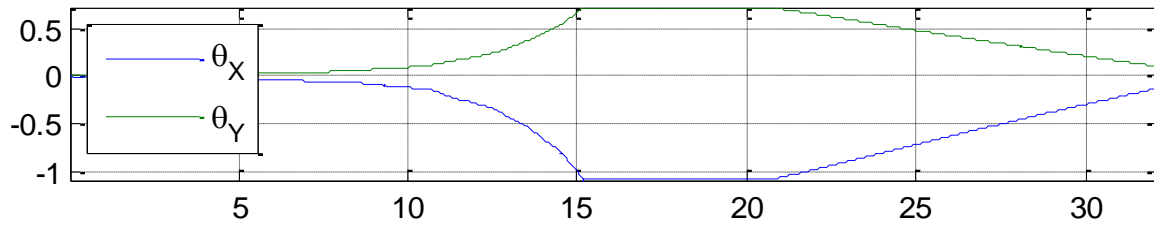
(a) Normalized vertical compression force and displacement vs. time



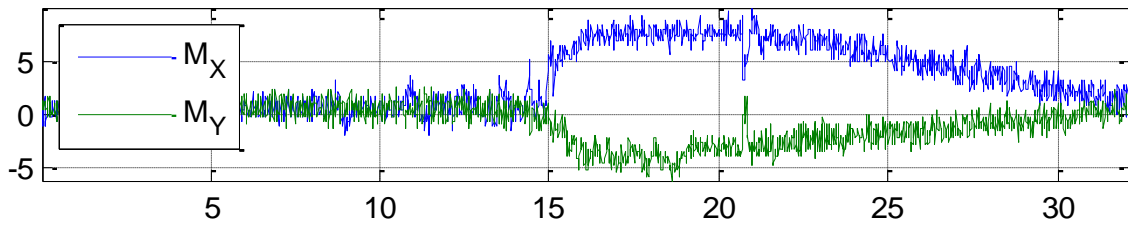
(b) Horizontal X and Y top displacement vs. time (min)



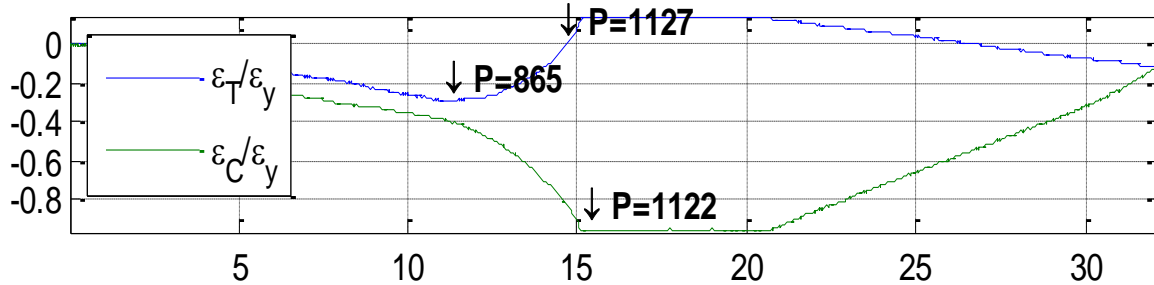
(c) Horizontal X and Y top forces vs. time (min)



(d) X and Y top rotations vs. time (min)



(e) X and Y top moments vs. time (min)



(f) Normalized maximum tensile and compressive strains at 6'' from the base

Figure 5.28. Histories of test response for the Specimen 15-C20-26-12

Figure 5.29 shows the first loading path of the axial load (P) vs. the lateral force (F) obtained for the most slender specimens 10C12-26-5 and 14C12-26-12 during the load case LC1; this experimental response was filtered and smoothed for an ease evaluation. It can be clearly observed in this figure that, again, the lateral force remain low (nominally at zero) with lower axial loads. However, as the specimen approaches the column buckling capacity expected as fixed-free, the lateral force starts increasing appreciably with a higher rate, an eventually exceeding the noise level in lateral force ($880/2^{12} = 0.22$ kip) represented in this figure as the grey area. As indicated in Figure 5.29, the axial load strength related to the point when the control is no longer satisfied (P_{ctrl}) is a better assessment of the nominal critical load capacity (P_n) for the fixed-free column ($K=2$) as predicted by the AISC (2010). At the time perfect control is not longer justifiable, a transition of boundary conditions from those represented on Figure 5.25.a to those on Figure 5.25.b also occurs; beyond this time, the ideal fixed-free boundary conditions are no longer valid, and so the maximum load is now coupled to a system with a lower effective length coefficient ($0.5 < K < 2.0$). As shown in this figure, the final maximum capacity in these two specimens is about 75% higher than the ideal fixed-free case as a consequence of the top lateral forces and moments added by the controller.

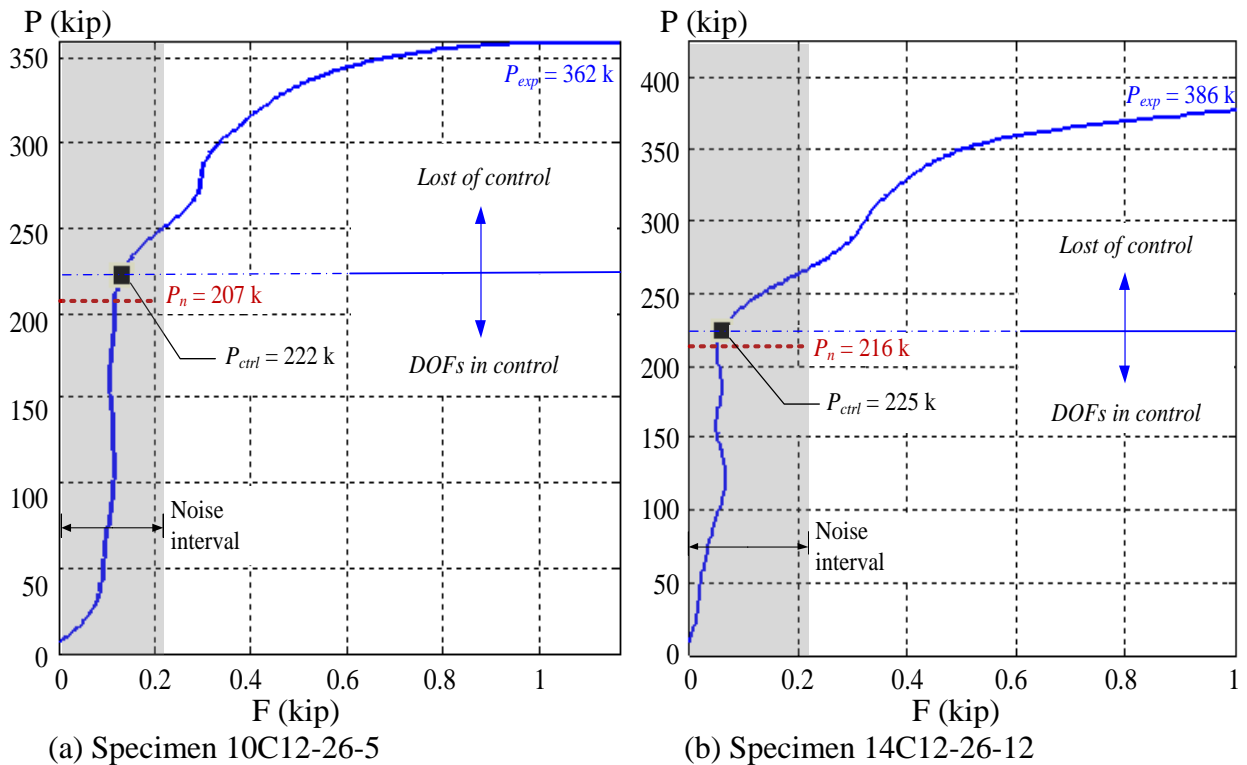


Figure 5.29. Axial force (P) vs. lateral force (F) of the most slender specimens

Similarly to the previous figure, the first loading paths of the axial load (P) vs. the lateral force (F) obtained for all the specimens during LC1 are shown from Figure 5.30 to Figure 5.34. In these plots, the raw data varying within the noise interval is represented by the green signal and its filtered response is represented by the blue smooth curve. As before, these figures show that the system kept control (within the noise level interval) until a certain value of axial load, but then violated the input control commands when disturbing lateral forces were added by the controller with higher axial loads.

From the plots shown in Figure 5.30 to Figure 5.34, approximate axial loads (P_{ctrl}) where the system lost an ideal free-top control were extracted and summarized in Table 5.5 for each specimen. Even though these extracted loads (P_{ctrl}) are still approximate values, they represent the best reasonable experimental measurement of the column with fixed-free ideal boundary conditions.

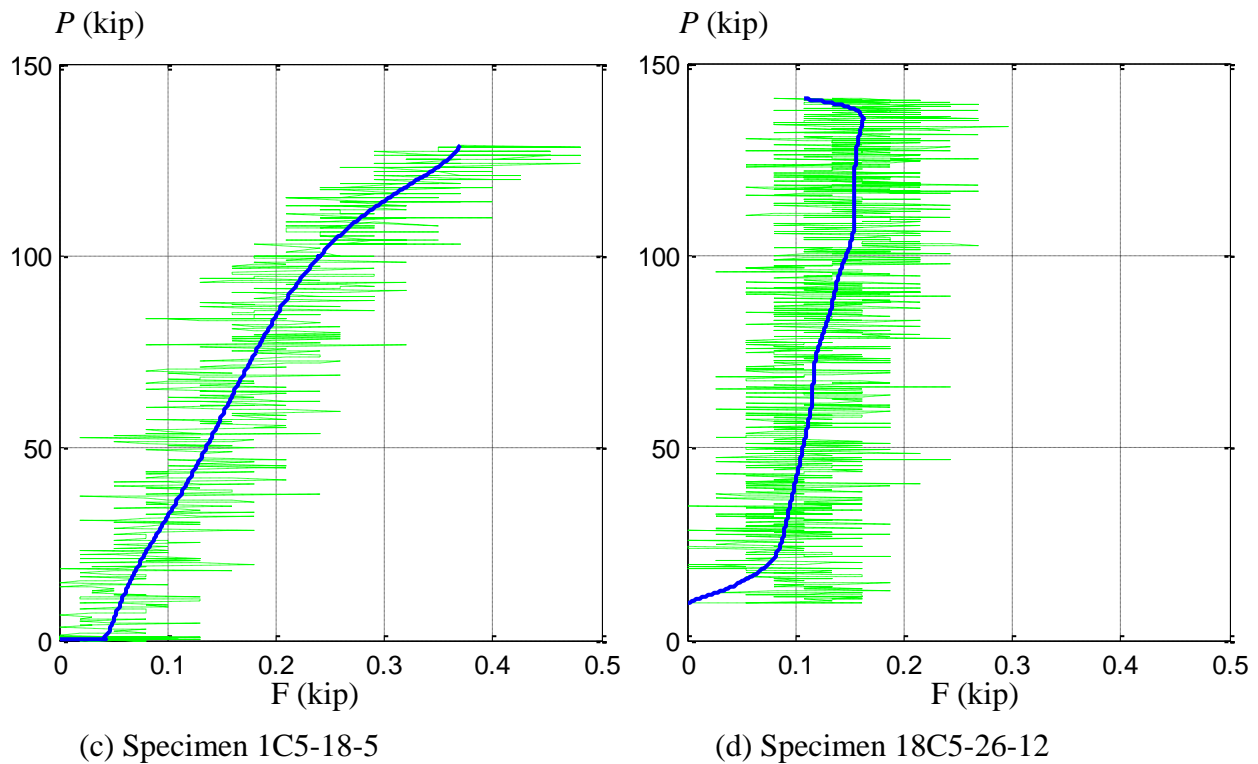
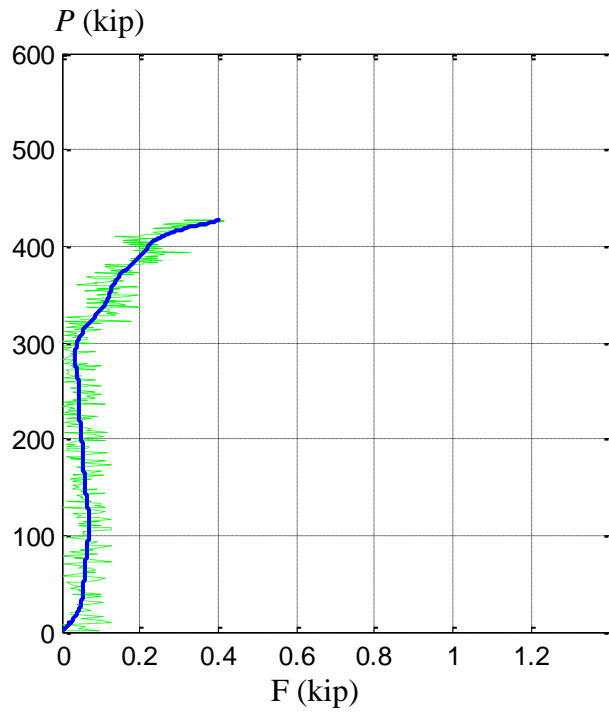
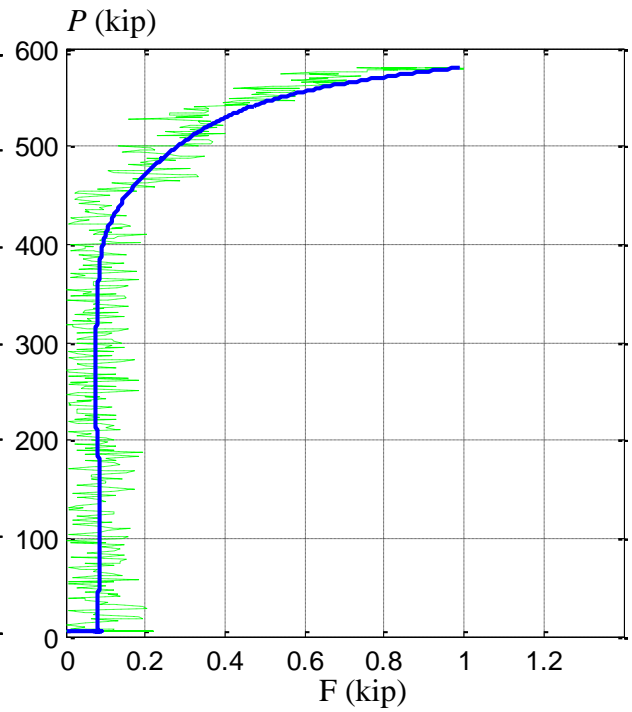


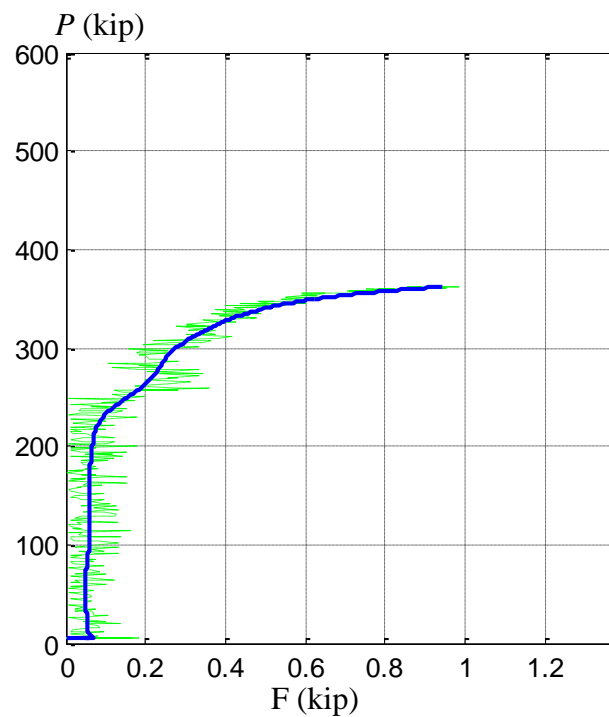
Figure 5.30. Axial force (P) vs. lateral force (F) of the CCFTs with 5.5 in. of diameter



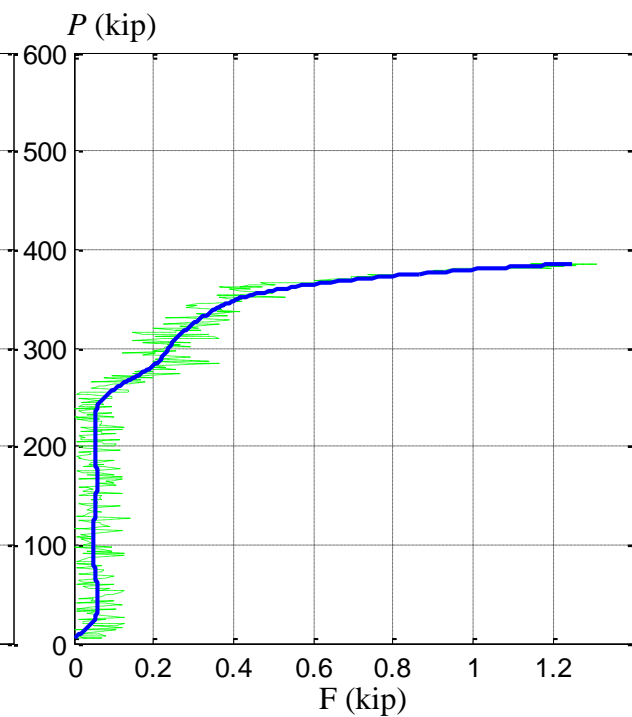
(a) Specimen 2C12-18-5



(b) Specimen 6C12-18-12

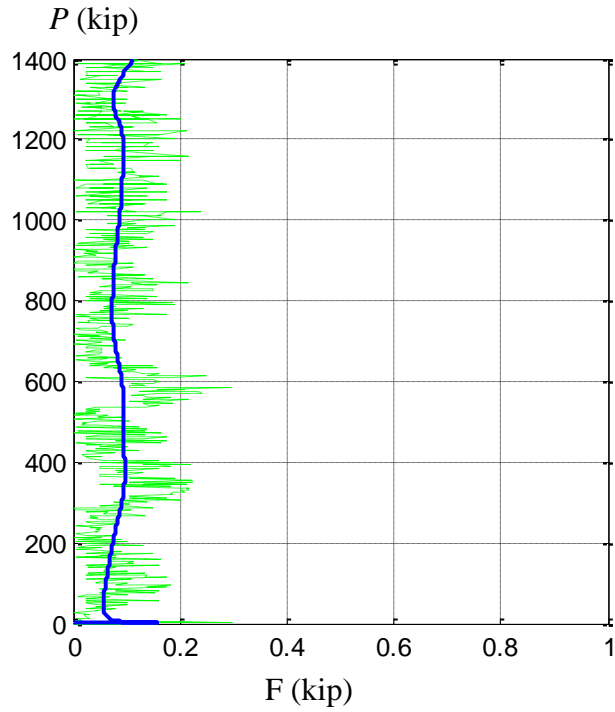


(c) Specimen 10C12-26-5

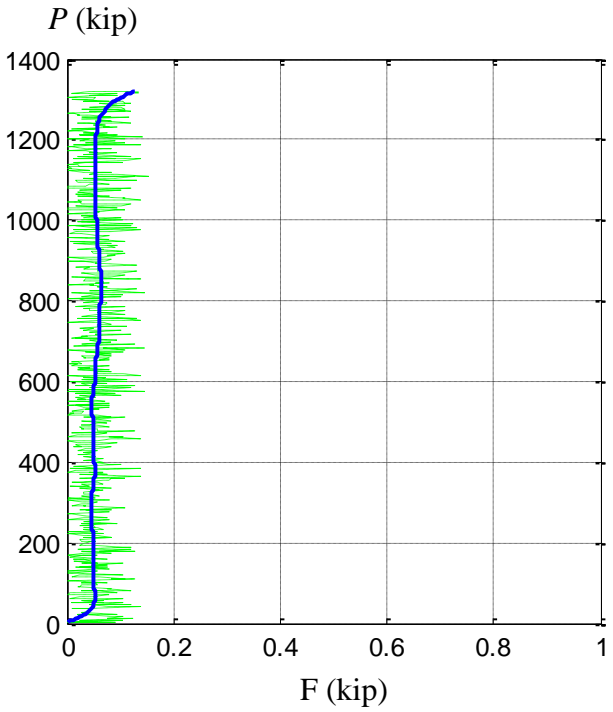


(d) Specimen 14C12-26-12

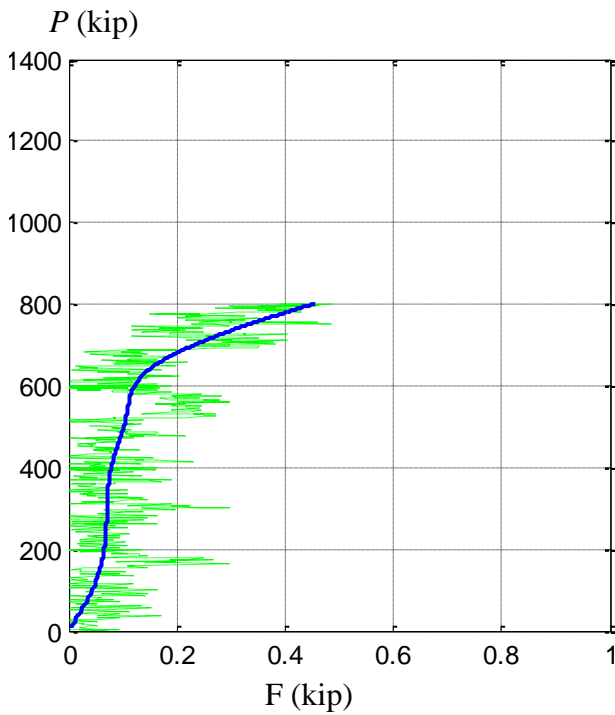
Figure 5.31. Axial force (P) vs. lateral force (F) of the CCFTs with 12.75 in. of diameter



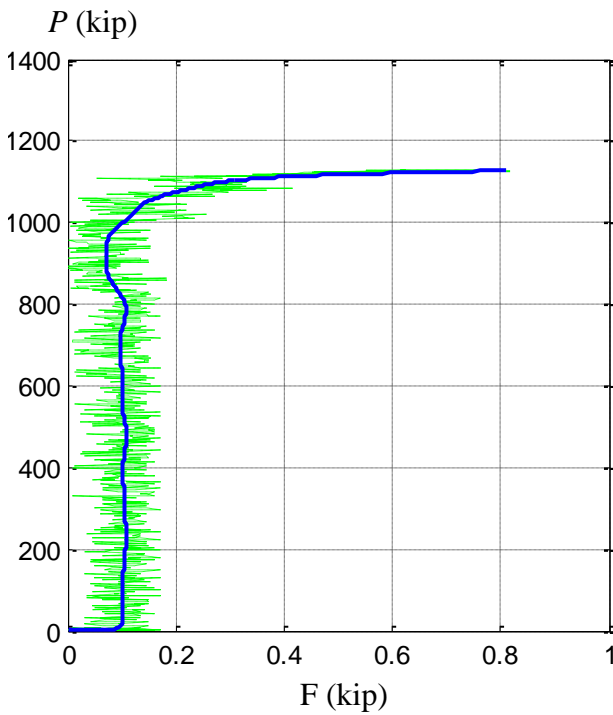
(a) Specimen 3C20-18-5



(b) Specimen 7C20-18-12

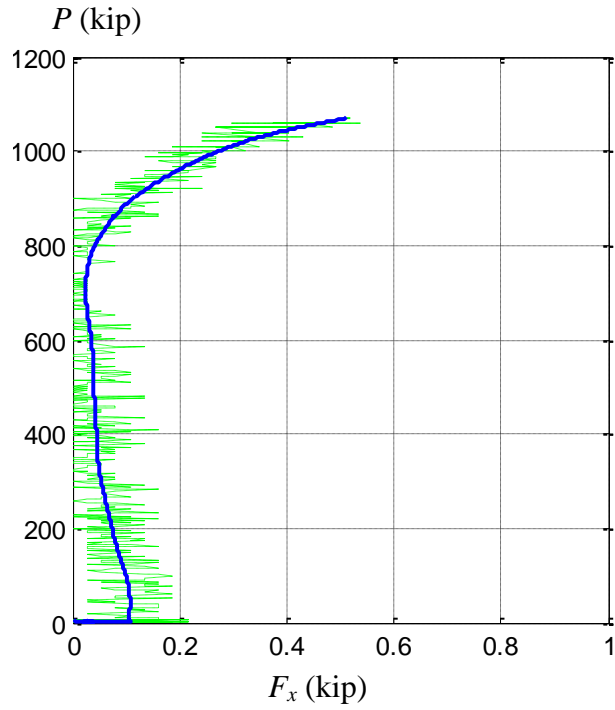


(c) Specimen 11C20-26-5

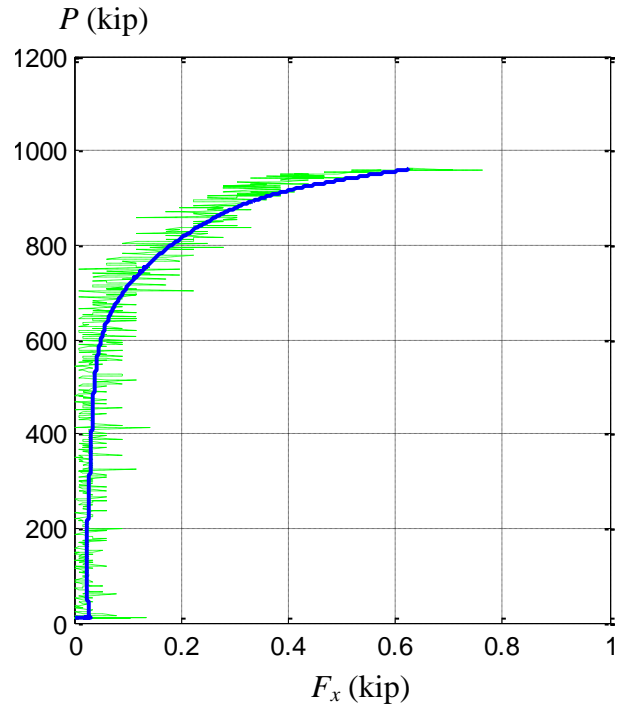


(d) Specimen 15C20-26-12

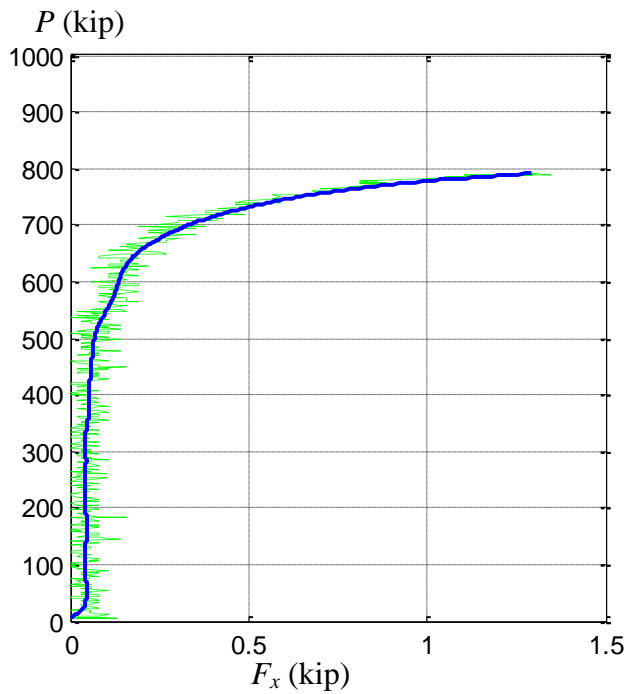
Figure 5.32. Axial force (P) vs. lateral force (F) of the CCFTs with 20 in. of diameter



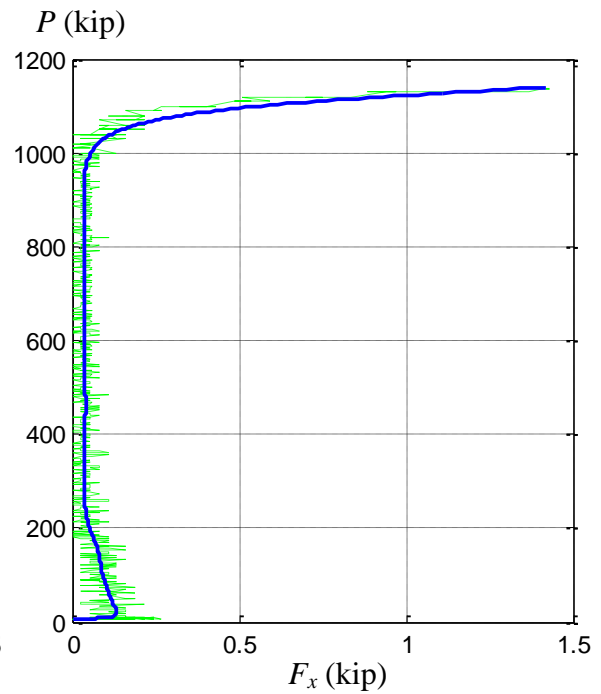
(a) Specimen 4Rw-18-5



(b) Specimen 8Rw-18-12

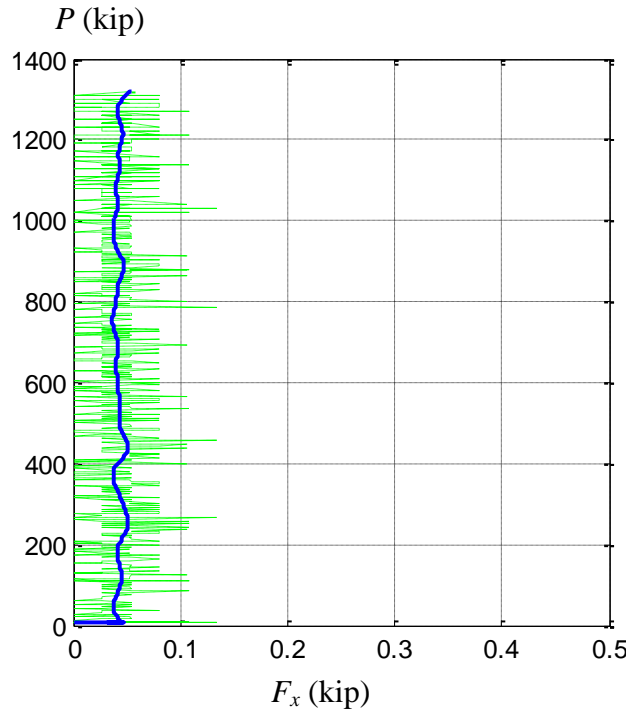


(c) Specimen 12Rw-26-5

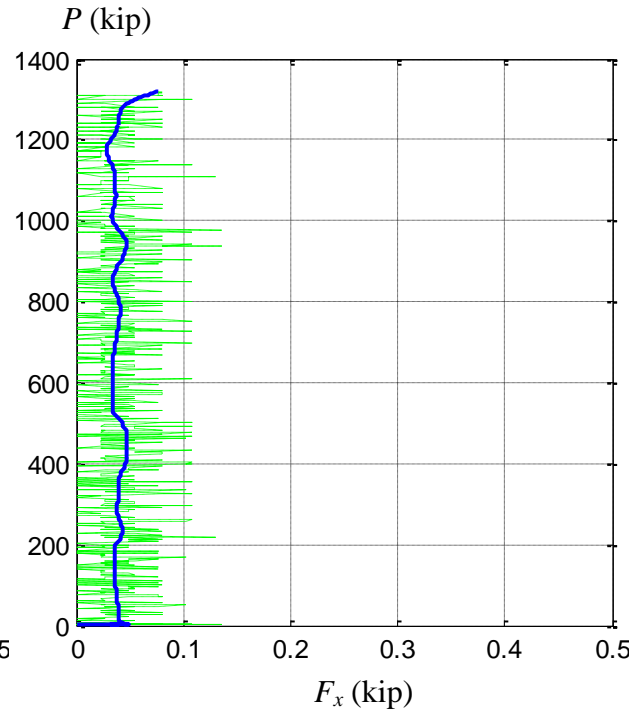


(d) Specimen 16Rw-26-12

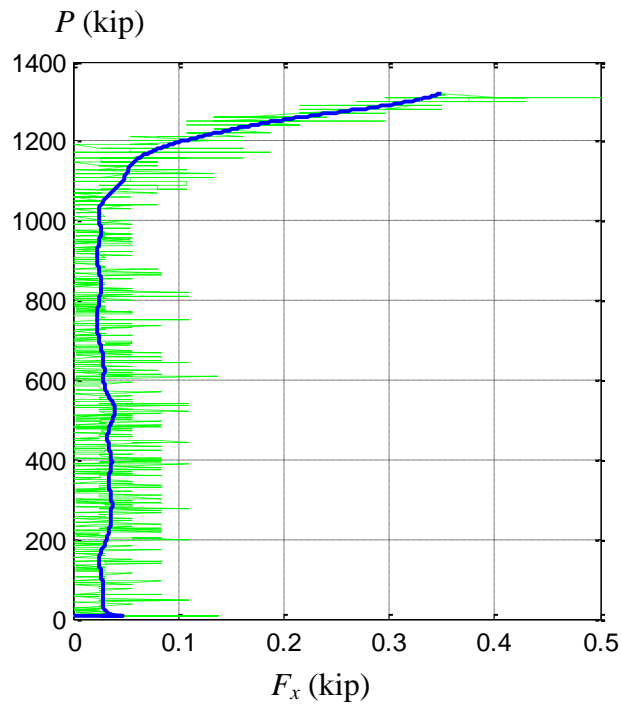
Figure 5.33. Axial force (P) vs. lateral force (F) of the RCFTs oriented in weak axis



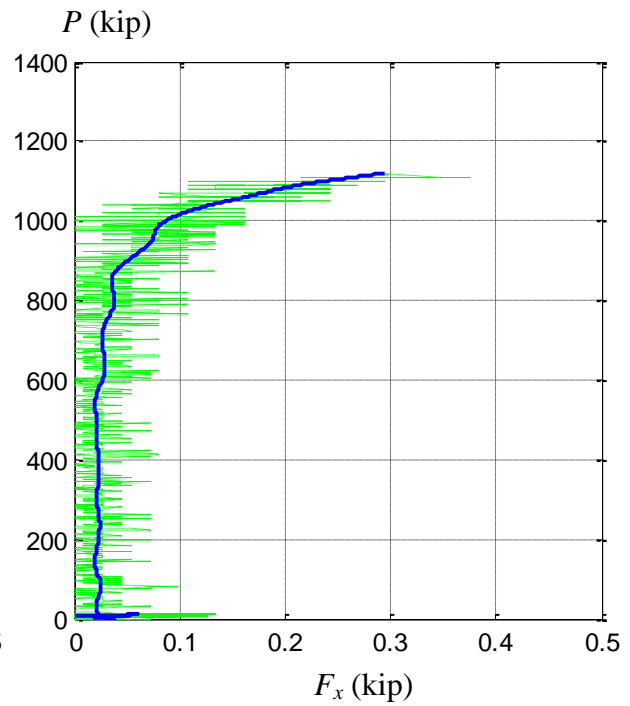
(a) Specimen 5Rs-18-5



(b) Specimen 9Rs-18-12



(c) Specimen 13Rs-26-5



(d) Specimen 17Rs-26-12

Figure 5.34. Axial force (P) vs. lateral force (F) of the RCFTs oriented in strong axis

Table 5.5. Extracted axial loads at the time the system lost ideal control

Specimen	AISC (2010)		Maximum experimental	Maximum controlled	ratio
	λ	P_n (kip)	P_{exp} (kip)	P_{ctrl} (kip)	
1C5-18-5	0.90	166	129	129	0.78
18C5-26-12	1.51	140	141	141	1.00
2C12-18-5	1.55	393	427	400	1.02
6C12-18-12	1.90	472	581	500	1.06
10C12-26-5	2.38	207	362	222	1.07
14C12-26-12	2.72	216	386	225	1.04
3C20-18-5	1.05	1469	1320 ⁺	NA	NA
7C20-18-12	1.30	2190	1320 ⁺	NA	NA
11C20-26-5	1.61	992	802	802	0.81
15C20-26-12	1.78	1080	1127	1100	1.02
4Rw-18-5	1.38	939	1070	950	1.01
8Rw-18-12	1.65	1124	961	961	0.85
12Rw-26-5	2.14	501	791	540	1.08
16Rw-26-12	1.72	949	1140	1000	1.05
5Rs-18-5	0.66	1731	1320 ⁺	NA	NA
9Rs-18-12	1.04	2209	1320 ⁺	NA	NA
13Rs-26-5	1.35	1199	1320	1200	1.00
17Rs-26-12	1.46	1323	1120	1120	0.85

(+) MAST axial capacity (1320 kips) reached before getting the buckling strength

As shown in the Table 5.5, the maximum controlled loads extracted with the approach described previously are much closer in general to the expected nominal load as calculated by the AISC (2010).

However, the experimental P - F path response obtained in some specimens remains in control for the entire load case; the latter is the case of the specimens 3, 5, 7 and 9 where the buckling load was not met (NA) since the test stop at the MAST maximum axial capacity. For these cases, another methodology will be used to extrapolate the buckling load capacity based on the earlier axial load response. This methodology is presented in the following section, and those results complement the values obtained in this section.

5.4.5. Specimens with axial load strength above the MAST capacity

It has been documented in the previous tables that the crosshead ran out of capacity before the buckling loads were reached in the shortest circular specimens with 20 inches diameter (3C20-18-5 and 7C20-18-12) and the shortest rectangular specimens with free translation towards the strong axis (5Rs-18-5 and 9Rs-18-12). In this section, an estimation of the buckling load based on the experimental compressive path obtained during the tests of these specimens is given. In the literature, there are methodologies that aim to estimate the unstable load based on the response with a lower load. Southwell (Horton *et al.*, 1971) noticed that the lateral displacement – axial load ratio (Δ/P or δ/P) keep a linear relationship with the lateral displacement (Δ or δ). He also noticed that the slope of that linear relationship is the inverse value of the buckling load. Similar linear relationships (Horton *et al.*, 1971) were found by Ayrton and Perry ($1/P$ vs. $1/\Delta$), and by Donnell (P vs. P/δ).

In order to calibrate the accuracy of these approaches, these methods were also used in the remaining tests.

The first method, commonly referred as the Southwell plot, was initially developed by Ayrton and Perry in 1886, but later independently rediscovered by Southwell in 1932, and reexamined by Donnell in 1938. Horton *et al.* (1971) present an historical review of this approach in its three available forms (Ayrton-Perry, Southwell and Donnell forms), as well as its derivation and some experimental validation. This method assumes that the first order terms in the series expansion solution derived for columns buckling elastically are predominant (so second order terms are neglected), and thus the axial force and the relative displacements can be represented by a linear relationship, where the elastic critical load is implicitly included (Timoshenko, 1961); a linear relationship will not be exhibit if the second order terms are considerable. This linear relationship can be plotted in different forms, as those illustrated in Figure 5.35 and suggested by Ayrton-Perry ($1/P$ vs. $1/\delta$), Southwell (δ/P vs. δ) or Donnell (P vs. P/δ). From these forms, the elastic buckling load is given by either the inverse of the initial abscissa from the Ayrton-Perry form, the reciprocal of the slope from the Southwell form, or the y-intercept from the Donnell form.

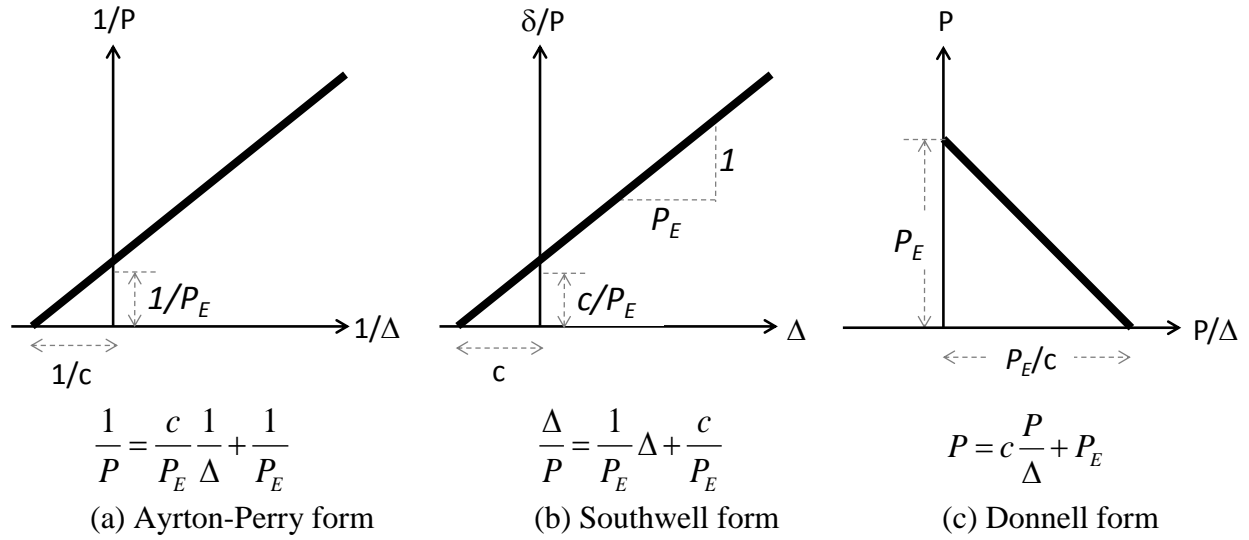


Figure 5.35. Linear relationship in columns with elastic buckling

As mentioned before, the previous approach (from now on just called Southwell or secant approach) is only valid in the elastic buckling range when both forces and displacements keep a linear relationship. Besides, this correlation is held linear only when relative displacements (Δ) are used (no linear with the absolute displacements: $\Delta + \Delta_o$), and thus the effects of the initial imperfection (Δ_o) are not included. Therefore, the application of this method is limited only to the determination of the Euler load (P_E).

The second method proposed in this research is based on the fact that, in either the elastic or the inelastic buckling ranges, the critical load is given when the tangent slope in the P - Δ curve reach zero. Thus, the plot axial force (P) vs. P - Δ tangent ($dP/d\Delta$) is proposed (Figure 5.36.c) for the determination of the buckling load that accounts for the geometric imperfection and the material non-linearities (i.e. yielding in the steel, cracking and crushing in the concrete. Figure 5.36.a). Similar to the Donnell form (Figure 5.36.b), where the secant P - Δ is used for the estimation of the Euler load (P_E), the critical load (P_n) from the tangent form is defined by its y-intercept or when the tangent becomes zero.

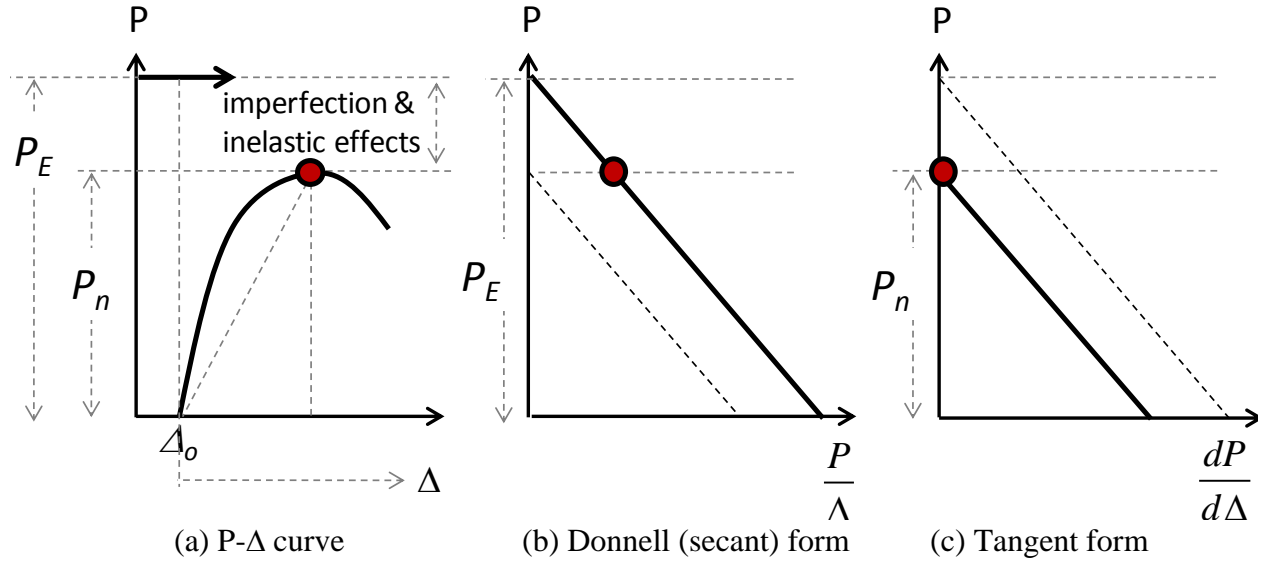
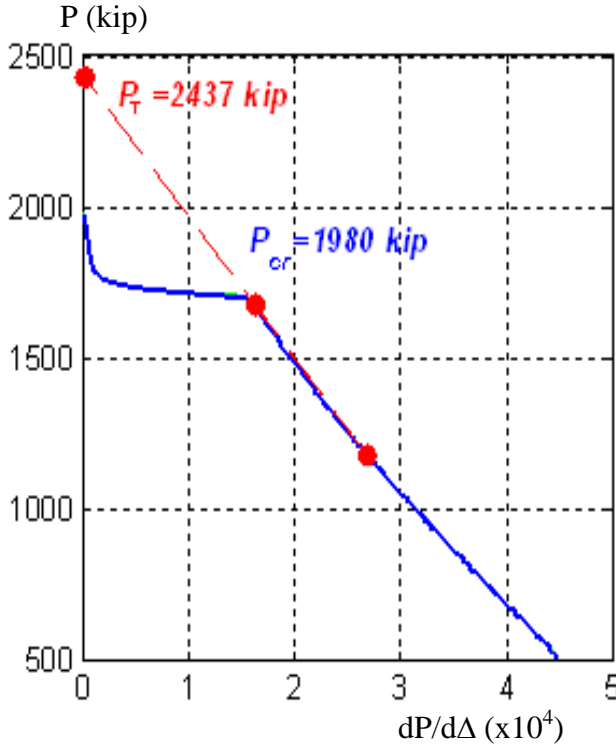
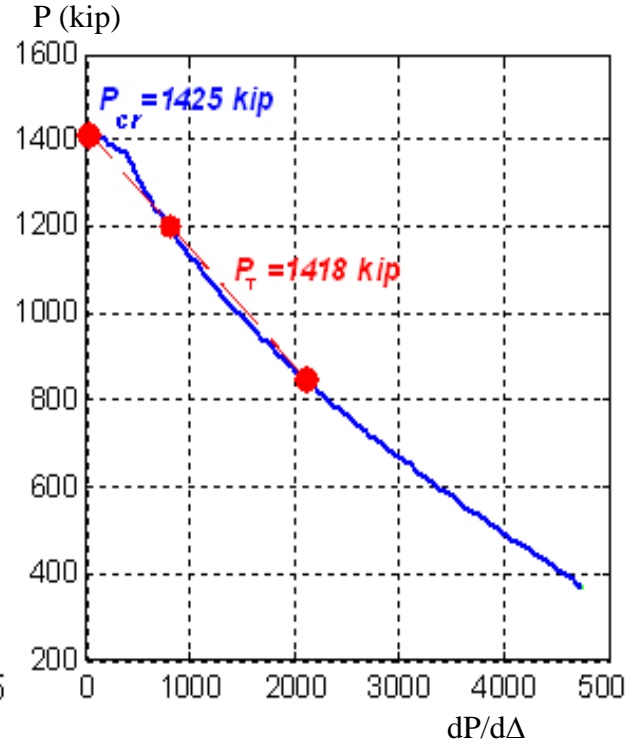


Figure 5.36. Proposed tangent form for elastic and inelastic buckling of columns

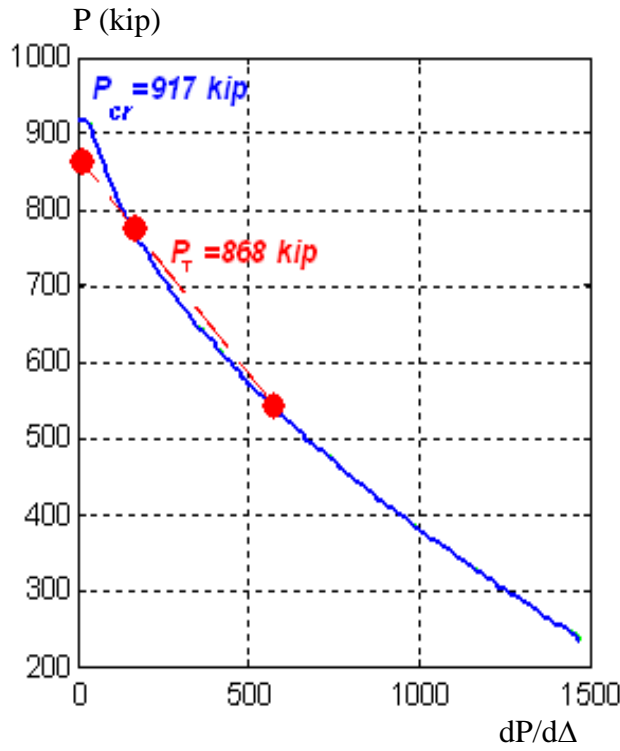
In this approximate method (from now on just called the tangent approach), the relationship P - $dP/d\Delta$ tends to be linear when the column remains elastic (elastic buckling range and low axial loads in the inelastic buckling range). In addition, geometric imperfections are included since the P - Δ slope follows the path defined by the initial imperfection (no matter if it is used relative Δ displacements or absolute $\Delta + \Delta_o$ displacements). As the load increases beyond the elastic limit for short columns within the inelastic buckling range, material nonlinearities (i.e. steel yielding, concrete cracking and crushing) change the tangent and the buckling load estimated linearly. Even if approximate, this method has some advantages over the Southwell plot. Figure 5.37 shows the application of the tangent plot using the analytical results obtained with fiber analysis for a circular CFT column with nominal strength parameters (HSS20x0.25, $F_y=42$ ksi, $f'_c=5$ ksi, $\Delta_o=L/500$) and different slenderness. In these figures, P_{cr} is the buckling load obtained from the analysis represented by the continuous line, and P_T is the estimated load based on the tangent plot defined by two lower loads ($0.6P_{cr}$ and $0.8P_{cr}$) and represented by the dashed line. The prediction of the buckling load based on this method for these cases is reasonable ($<5.5\%$), except for the shortest column ($L=9$ ft, $\lambda=0.49$) shown in Figure 5.37.a.



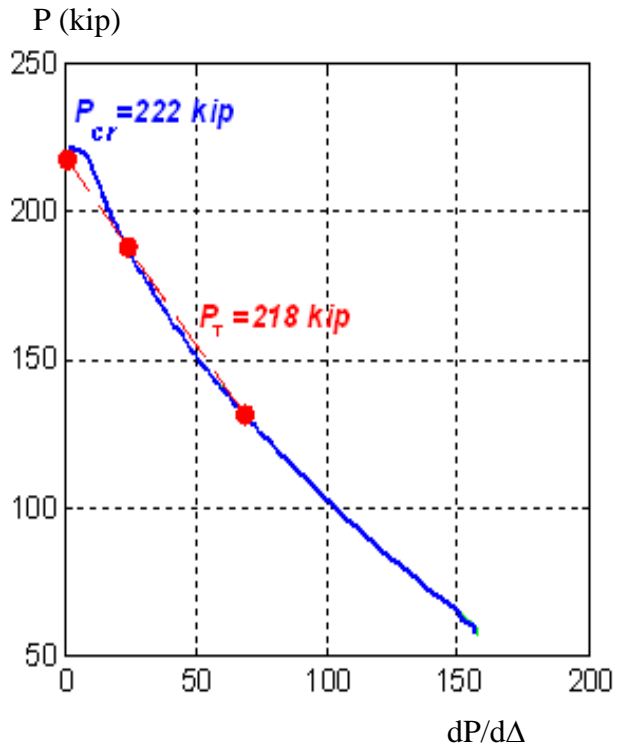
(a) $L = 9$ ft, $\lambda = 0.49$



(b) $L = 18$ ft, $\lambda = 0.97$



(a) $L = 26$ ft, $\lambda = 1.41$



(b) $L = 55$ ft, $\lambda = 2.98$

Figure 5.37. Application of the tangent form on CCFTs with different slenderness

Figure 5.38 shows the influence of the initial imperfection on the analytical results for the mentioned cross-section (CCFT 20x0.25) with a length of $L=18$ ft ($\lambda=0.97$). The initial imperfections selected are $L/250=0.864$ in, $L/500=0.432$ in, and $L/1000=0.216$ in. As seen in this figure, the P - $dP/d\Delta$ curves tends to be linear for low axial loads, but the slope changes when the axial load approaches the instability load. Changes in the slope seem to be lower for larger initial imperfections, where geometric nonlinearities are predominant. The predictions using the tangent form for these three cases are not exact (error<6%), however, the critical load predictions (P_n) with this methodology are more accurate than the predictions obtained with the secant or the Southwell plot that are more related to the Euler load (P_E).

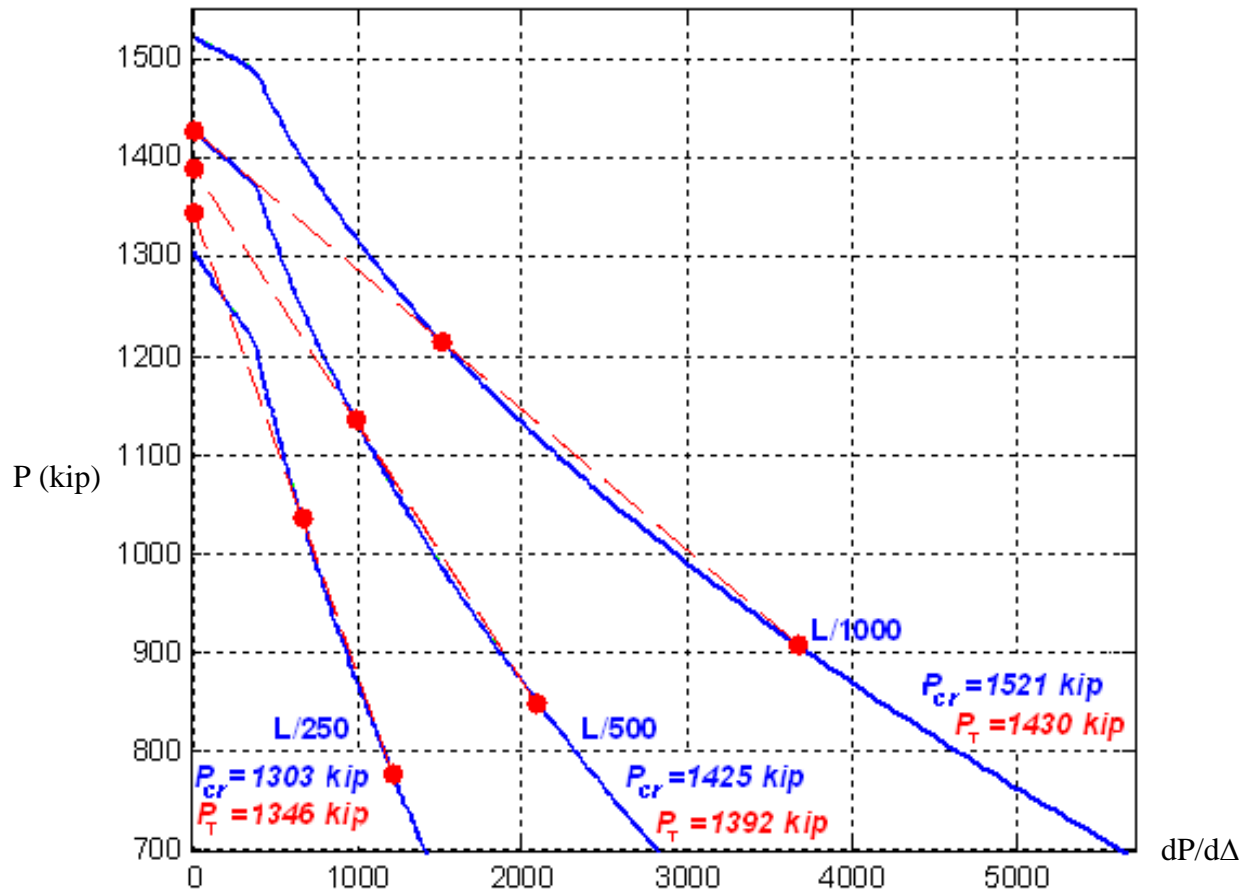


Figure 5.38. Application of the tangent form on a CCFT with different imperfections

As mentioned at the beginning of this section, the application of the secant plot (or Donnell form, variant of the Southwell plot) and the tangent plot (proposed in this research) allows to rough estimate the buckling load for those cases (specimens 3, 5, 7 and 9) when the load history firstly reached the 1320 kip of maximum axial capacity of the testing system.

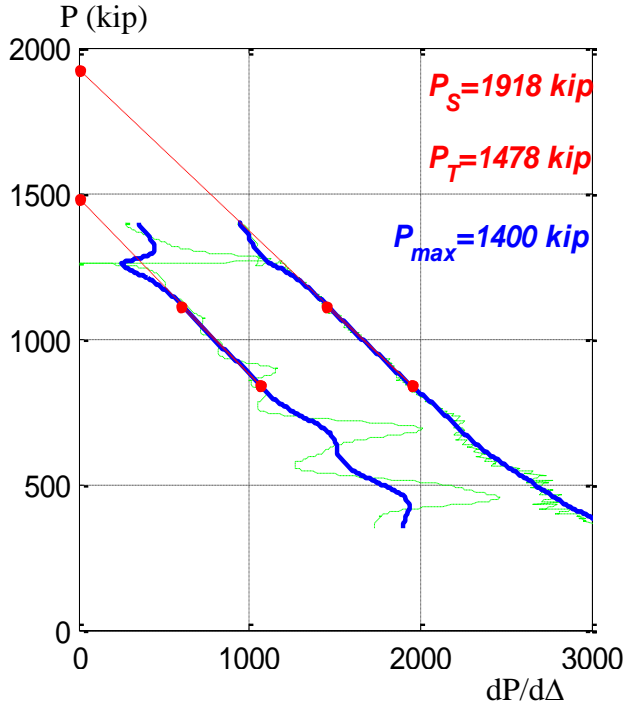
Figure 5.39 shows the results of the application of the secant and the tangent plots for the latter cases (specimens 3, 5, 7 and 9). In this figure, the blue thick lines represent a filtered and smoothed record of the raw data denoted by the green thin lines. Additionally stated in this figure are the maximum load (P_{max}) applied in the test and the y-intercept of the secant plot (P_S , rough estimator of the P_E) and the tangent plot (P_T , rough estimator of the P_n or P_{cr}); the points used for the calculation of the slopes and the extrapolated line to the y-intercept are included in these plots.

As observed in Figure 5.39, the smoothed experimental data do not exhibit a clear linear relation. This may be attributed to the influence of the second order terms in the series expansion solution. Nevertheless, this approach may be seen at a first approach to rough estimate the experimental axial load capacity in these specimens where the buckling instability was not met during the test.

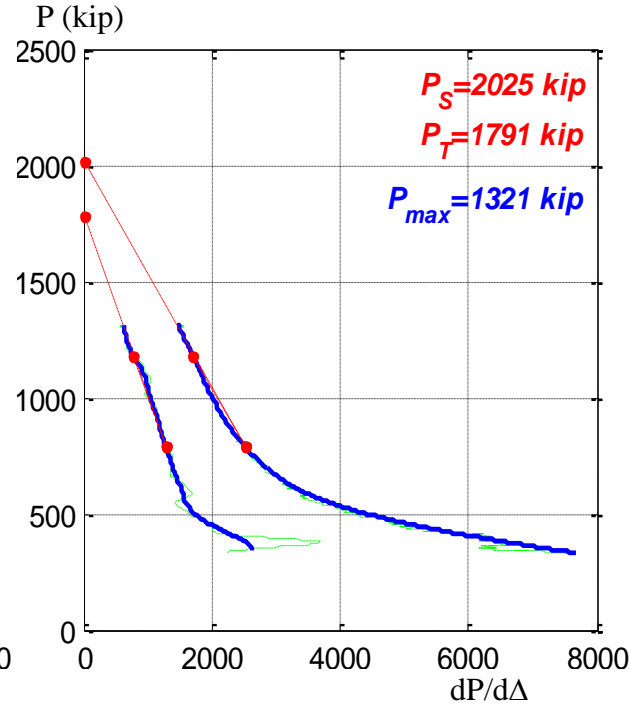
A summary of the buckling load capacities obtained from Figure 5.39 are shown in Table 5.6. In this table, λ and P_n are respectively the slenderness parameter and the buckling capacity calculated with the AISC (2010) Specifications, P_{exp} is the maximum experimental axial load applied on the specimens, P_S is an estimator of the Euler load obtained with the secant plot, and P_T is an estimator of the buckling load capacity (P_n) obtained with tangent plot.

Table 5.6. Summary of the maximum axial loads obtained for the specimens where buckling was not reached in the test

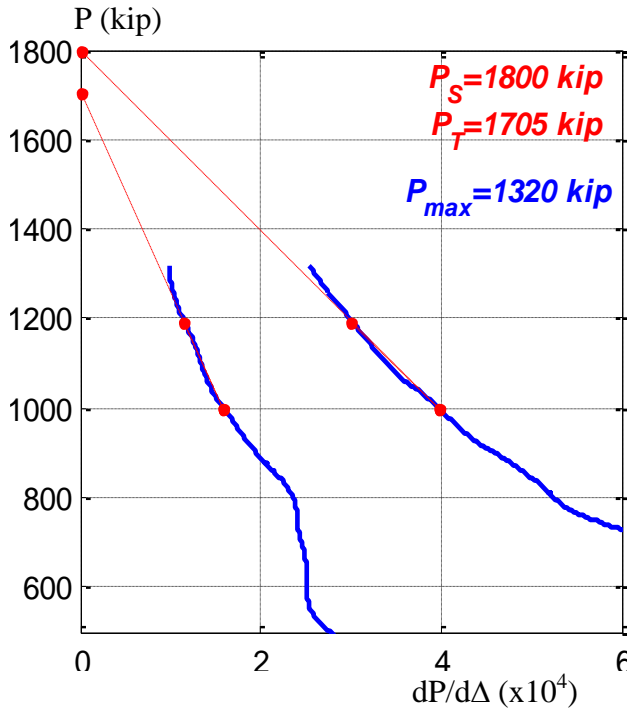
Specimen	AISC (2010)		Tests P_{exp} (kip)	Southwell P_S (kip)	Tangent P_T (kip)	P_T/P_n ratio
	λ -	P_n (kip)				
3C20-18-5	1.05	1469	1320	1918	1478	1.01
7C20-18-12	1.30	2190	1320	2025	1791	0.82
5Rs-18-5	0.66	1731	1320	1800	1705	0.98
9Rs-18-12	1.04	2209	1320	3300	1918	0.87



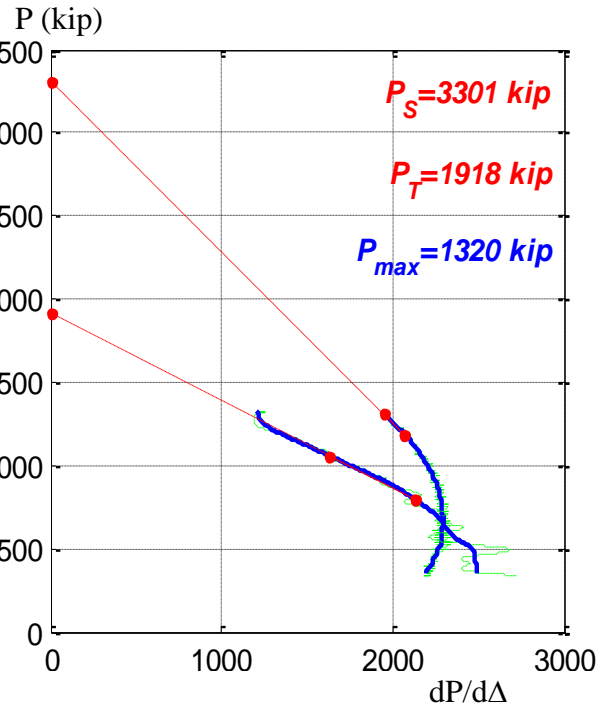
(a) Specimen 3C20-18-5



(b) Specimen 7C20-18-12



(c) Specimen 5Rs-18-5



(d) Specimen 9Rs-18-12

Figure 5.39. Application of the tangent and the secant form on the CCFT specimens that did not buckle with the full compressive capacity of the MAST system

5.5. Experimental buckling loads from processed data

The previous section shows the maximum axial loads obtained for each specimen from the raw data; however, the direct extraction of these results showed significant inconsistencies with analytical results. As a consequence, the source of these inconsistencies were explored and discussed and, when possible, reasonable values of the buckling loads were extracted from the processed data. In this section, the experimental buckling loads extracted for each specimen from the processed data are presented and summarized.

In section 5.4.4, it was observed that the controller lost perfect control by violating the free top control with non-zero forces and moments that increased at about the buckling load of the ideal BCs. Thus, this methodology was used to define the maximum controlled load in each specimen. These extracted loads summarized in Table 5.5, represent the best direct measurement for the column with the ideal support conditions.

The latter methodology cannot be used in those specimens where the MAST capacity was reached before the specimen buckling load (Specimens 3, 5, 7 and 9). Instead, another method presented in section 5.4.5 (called *tangent plot*) was used in order to calculation by extrapolation the axial buckling load value from the measured and available data with lower axial loads. The extrapolated buckling load values are reported in Table 5.6.

In addition, in section 5.4.3 discussed the results of two specimens (5 and 16) that developed a higher load capacity due to an initial imperfection shape in double curvature. For these cases, an effective length factor of $K=1.5$ was adopted to account for these effects as shown in Table 5.3.

Table 5.7 shows a summary of the corrected critical load values that were reported in Table 5.3, Table 5.5 and Table 5.6. The summarized buckling load values shown in Table 5.7 are normalized with its squash capacity (P_o , Equation 5.2) and plotted vs. the slenderness parameter (λ) in Figure 5.39; for comparison purposes, the analytical AISC (2010) column curve and the Euler and plastic limits are also included in this figure.

Table 5.7. Experimental buckling loads from the processed data

Specimen	K	AISC (2010) λ	P_n (kip)	Maximum raw data P_{exp} (kip)	Adjusted critical load P_{cr} , (kip)	ratio P_{cr} / P_n
1C5-18-5	0.5	0.90	166	129	129	0.78
18C5-26-12	0.5	1.51	140	141	141	1.00
2C12-18-5	2.0	1.55	393	427	400 ^a	1.02
6C12-18-12	2.0	1.90	472	581	500 ^a	1.06
10C12-26-5	2.0	2.38	207	362	222 ^a	1.07
14C12-26-12	2.0	2.72	216	386	225 ^a	1.04
3C20-18-5	2.0	1.05	1469	1320 ⁺	1478 ^b	1.01
7C20-18-12	2.0	1.30	2190	1320 ⁺	1791 ^b	0.82
11C20-26-5	2.0	1.61	992	802	802	0.81
15C20-26-12	2.0	1.78	1080	1127	1100 ^a	1.02
4Rw-18-5	2.0	1.38	939	1070	950 ^a	1.01
8Rw-18-12	2.0	1.65	1124	961	961	0.85
12Rw-26-5	2.0	2.14	501	791	540 ^a	1.08
16Rw-26-12	1.5	1.72	949	1140	1000 ^a	1.05
5Rs-18-5	1.5	0.66	1731	1320 ⁺	1705 ^b	0.98
9Rs-18-12	2.0	1.04	2209	1320 ⁺	1918 ^b	0.87
13Rs-26-5	2.0	1.35	1199	1320	1200 ^a	1.00
17Rs-26-12	2.0	1.46	1323	1120	1120	0.85

(+) MAST axial capacity (1320 kips) reached before getting the buckling strength

(a) Experimental axial load given at the instant the controller added significant top forces a moments.

(b) Axial load extrapolated from the tangent plot

Contrary to the values plotted in Figure 5.6, the buckling loads processed in Figure 5.39 are more consistent with the boundary conditions used in the test and with the expected analytical values. The dispersion still observed in Figure 5.39 is due to differences with the initial imperfections.

The next section present results from advanced computational analysis that aims to predict the column response of the CFT specimens.

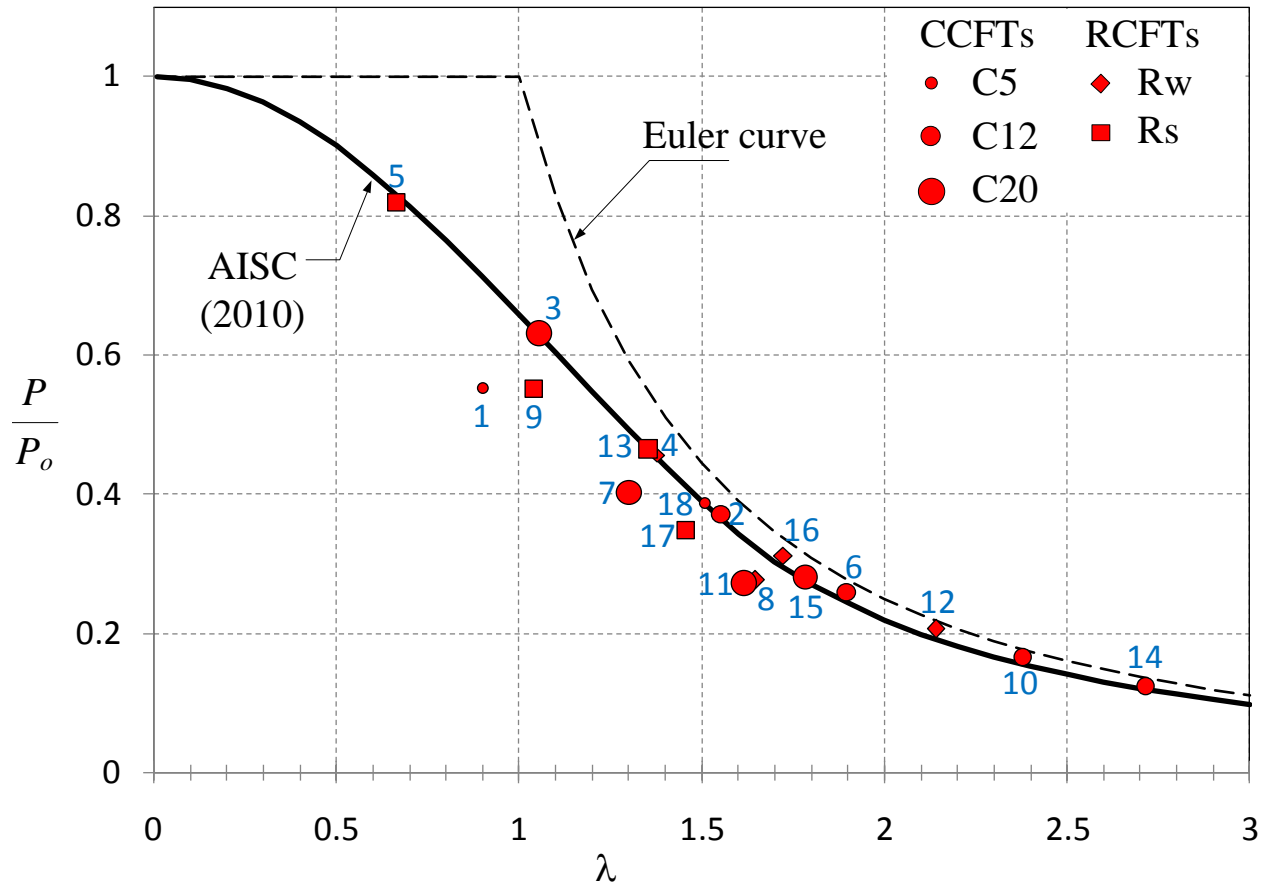


Figure 5.40. Experimental critical load ratios (P_{exp}/P_o) from processed data

5.6. Advanced computational analysis

In order to clarify the differences between the maximum experimental axial capacity and the prediction with the AISC Specification, advanced computational analyses are also performed.

The analyses presented in this section are carried out with the software OpenSees (2010) with a special version compiled by Denavit (2010) that, in addition to the standard OpenSees framework, includes comprehensive constitutive material models and robust 3D distributed-plasticity beam element formulations calibrated and developed by Tort and Hajjar (2007) for RCFTs and Denavit and Hajjar (2010) for CCFTs.

Thus, the specimens tested in this project were modeled with the following characteristics.

- The concrete core was modeled with the Chang and Mander (1994) model as adapted by Tort and Hajjar (2007) for RCFTs and Denavit and Hajjar (2010) for CCFTs.
- The concrete compressive strength used in the analysis corresponds to the measured strength obtained from the test of cylinders at the day of testing; these results are summarized in Chapter 3. The Young's modulus and the tensile strength of the concrete are implicitly calculated in the Chang-Mander model; however, these calculated values are very close to those obtained from the concrete cylinder tests.
- The steel tube was modeled with the Shen *et al.* (1995) model as adapted by Denavit and Hajjar for CCFTs and Tort and Hajjar for RCFTs.
- The steel yield stress, ultimate stress, and the Young's modulus used in the analyses correspond to the measured parameters obtained from the coupon tests. These results are also summarized in Chapter 3.
- The geometric and the cross-section properties (as the member length, thickness and diameter or base and width) correspond to those values measured and summarized in Chapter 3.
- The specimen was subdivided into 6 and 7 sub-members for the specimens with 18 and 26 feet of length, respectively. The integration points are defined at those points where the instrumentation (i.e. string pots, strain gages) was placed along the specimen.

- In addition, the coordinates of the integration points between sub-members correspond to the initial out-of-straightness and out-of-plumbness measured at the surveying. These imperfections were summarized in Table 5.1 and illustrated in Figure 5.5.
- The members were modeled with the mixed 3D finite beam element developed by Denavit and Hajjar for CCFTs and Tort and Hajjar for RCFTs. Since there was no evidence of slip between the concrete and steel surfaces in contact during the test, slip effects were ignored in the analysis.
- The boundary conditions are assumed fixed at the base and free at the bottom, and therefore the effective length factor is $K = 2$.
- In regard to the loading conditions, two sets of considerations were used. The details and results of these two loading conditions are presented below.

5.6.1. Monotonic compression loading with no parasitic forces

Initially, a monotonic compression force was applied until achieving the maximum capacity, followed by the unloading up to zero axial load. This loading condition intended to determine the axial load capacity of the specimens with ideal fixed-free boundary conditions.

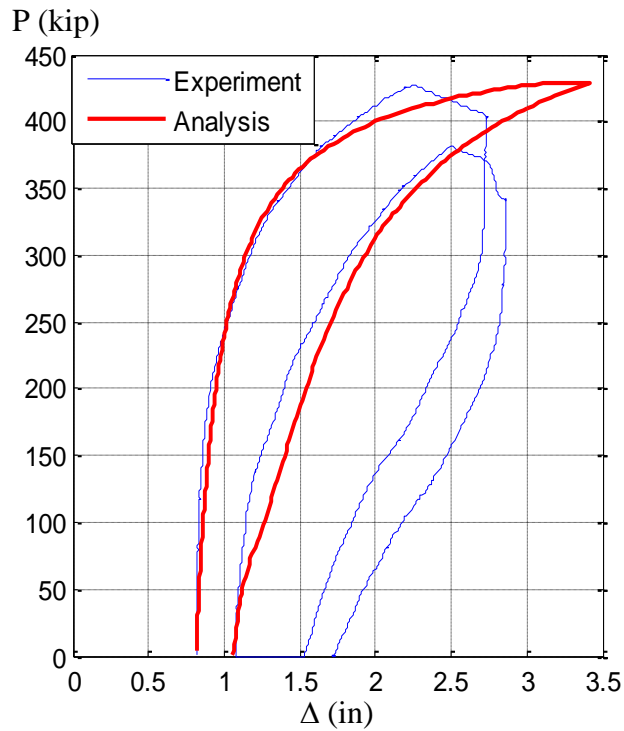
Differences between the experimental and analytical response is expected since:

- The parasitic forces and moments induced by the crosshead when the axial load approaches the buckling capacity are not included in the analysis. Thus, higher differences are expected in the high axial load range; nonetheless, very similar response is expected in the test and the analysis in the lower axial load range.
- Due to the fact that the disturbing forces and moment are not included in the model, and the top is modeled as fixed-free, the applicable effective length factor is equal to $K = 2$ in all the specimens analyzed in this section (specimens 2 to 17).
- There is no limit in the level of axial load in the analysis as occurs in tests which were limited by the MAST capacity of 1320 kip in axial load.
- Since the unloading takes place in the analysis and the test under different conditions (forces, moments, displacements), the descending branch of these responses may not be consistent.
- A second cycle in the analysis is not presented since the residual displacement in the analysis may not correspond to the residual in the test.

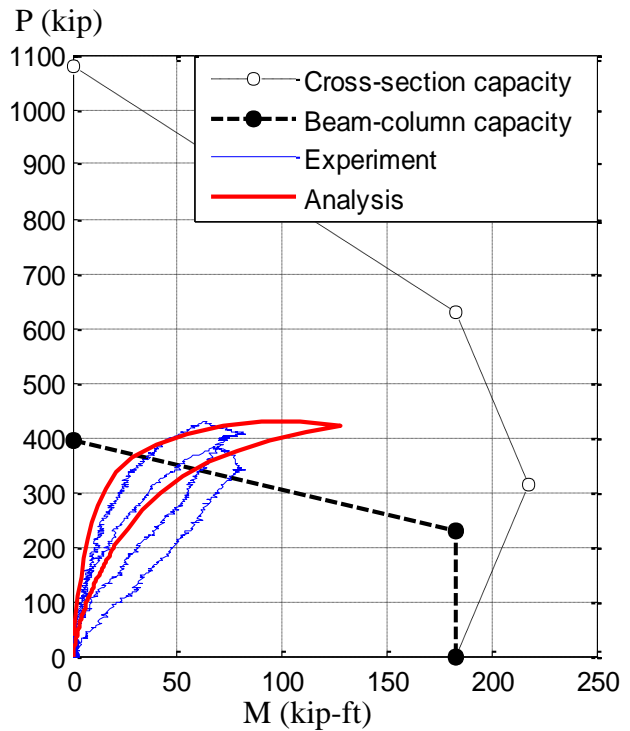
Comparison between the experimental response and the analytical prediction with the characteristics and assumptions stated above are shown from Figure 5.41 to Figure 5.48. The following observations can be made from these figures:

- The analytic prediction follows reasonably the experimental path in the initial range with low axial loads.
- The parasitic forces and moments created by the crosshead near the instability load are the main cause of difference between the analytical and experimental curves in the high axial load range. This is the case of the high-slender specimens 4, 6, 10, 12, 14 and 16, where the analytical prediction predicts consistent the initial response, but start diverging when the load approaches the buckling load. For these specimens, the disturbing forces added by the controller changes the boundary conditions during the test in high axial loads, and so the experimental response ends with a higher axial capacity. In turn, the experimental response ends with the lower load that corresponds to the ideal fixed-free configuration assumed in the model.
- The analytical nominal axial capacity obtained in those specimens where the system ran out of capacity, and thus the specimens did not buckle, is an accurate prediction if the system would have not had such limit and no additional parasitic forces would have been triggered. This is the case of the specimens 3, 5, 7 and 9, where the experimental curves reach the 1320 kip of peak capacity of the system, but the analytical curve keep increasing until the buckling capacity is met.
- Since the analytical and experimental reach the peak load with different conditions (forces, moments, displacements), the descending branch of these responses are not consistent as expected.

Even though there exists some differences in these responses since the model and the test are subjected to different conditions (i.e. the disturbing top forces and moments), the analysis performed in this section presents in some cases a strong correlation in those cases where the controller handled an appropriate control of the top as free. In contrast, a weak correlation is observed in those specimens where the disturbing forces are high compared to its lateral capacity, which is the case of the specimens with the highest slenderness.

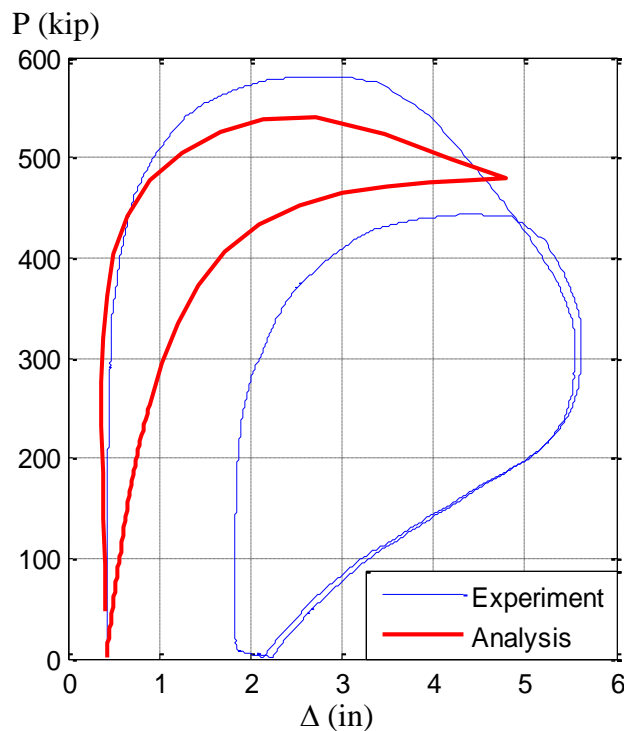


(a) Axial force vs. Top displacement

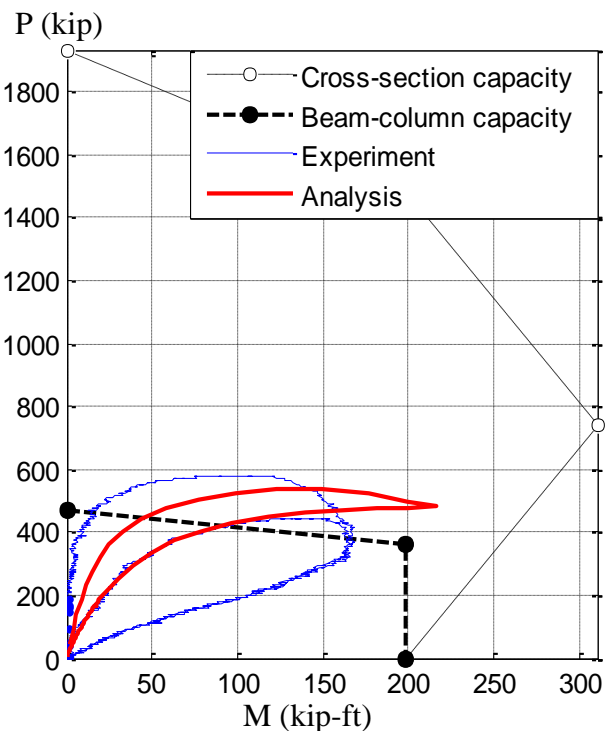


(b) Axial force vs. Base moment

Figure 5.41. Experimental response vs. Analytical prediction for the Specimen 2C12-18-5

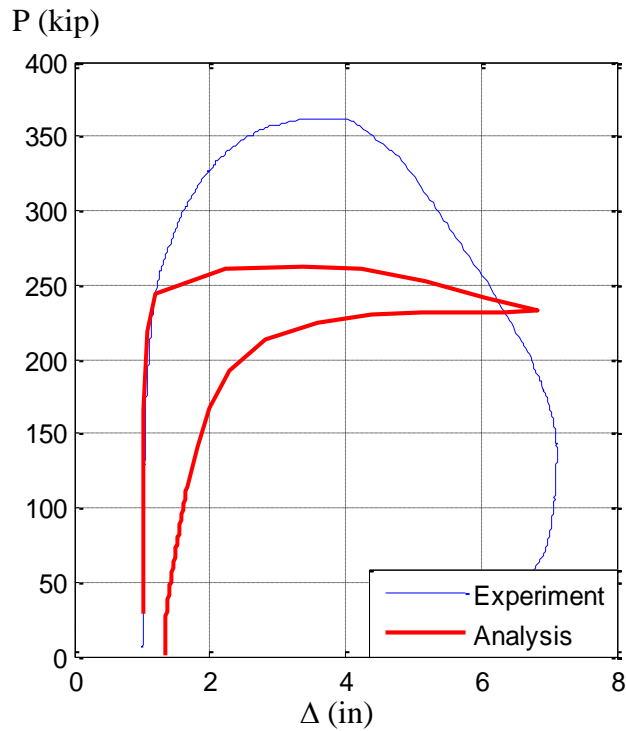


(a) Axial force vs. Top displacement

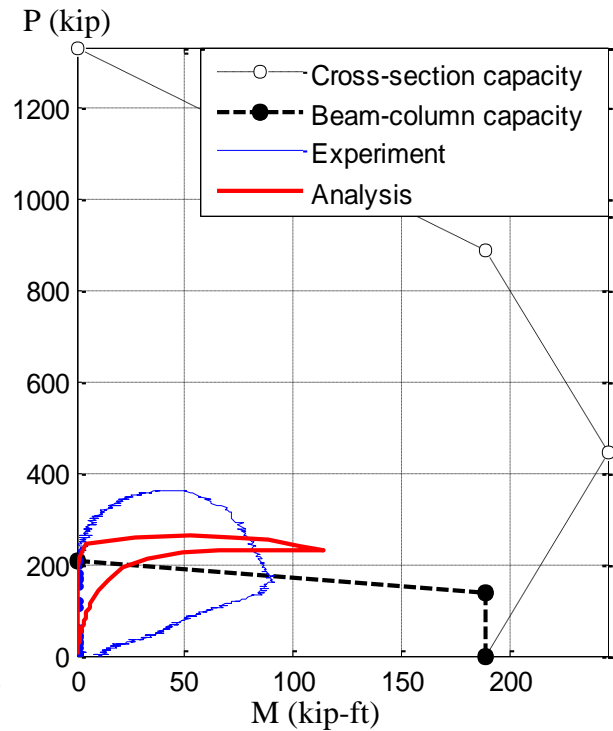


(b) Axial force vs. Base moment

Figure 5.42. Experimental response vs. Analytical prediction for the Specimen 6C12-18-12

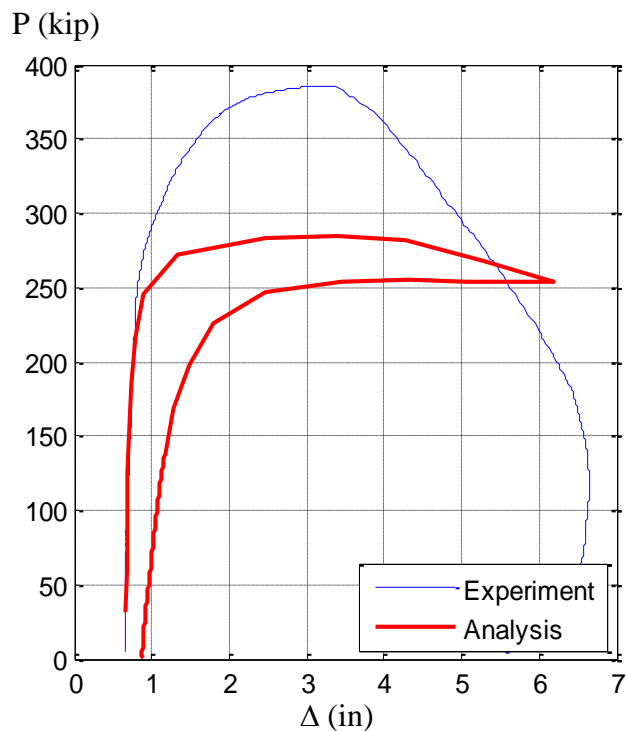


(a) Axial force vs. Top displacement

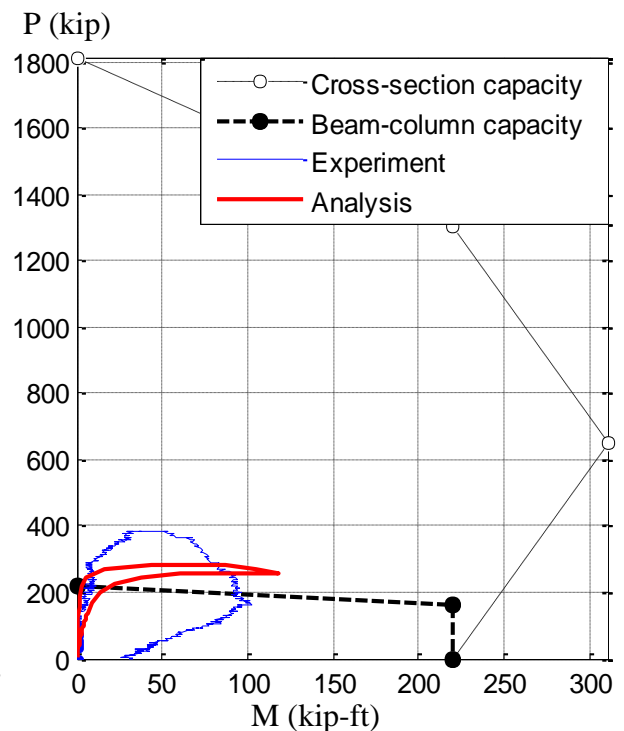


(b) Axial force vs. Base moment

Figure 5.43. Experimental response vs. Analytical prediction for the Specimen 10C12-26-5

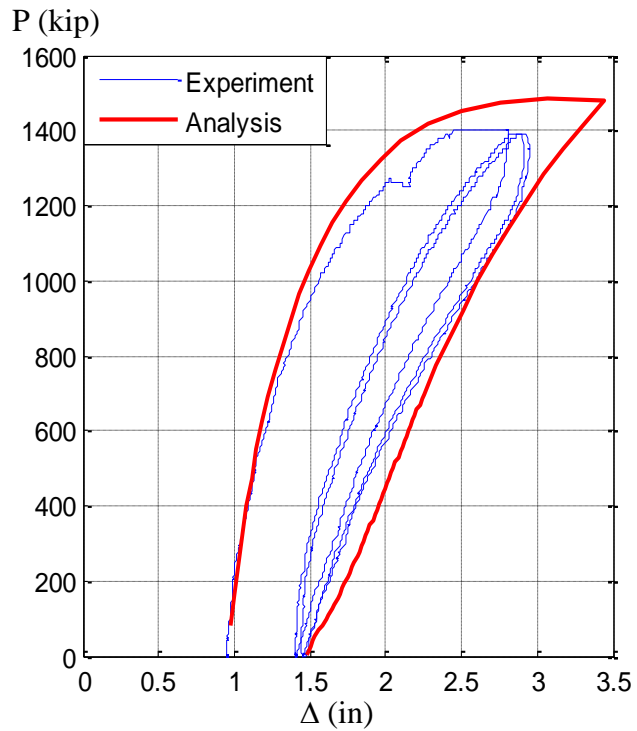


(a) Axial force vs. Top displacement

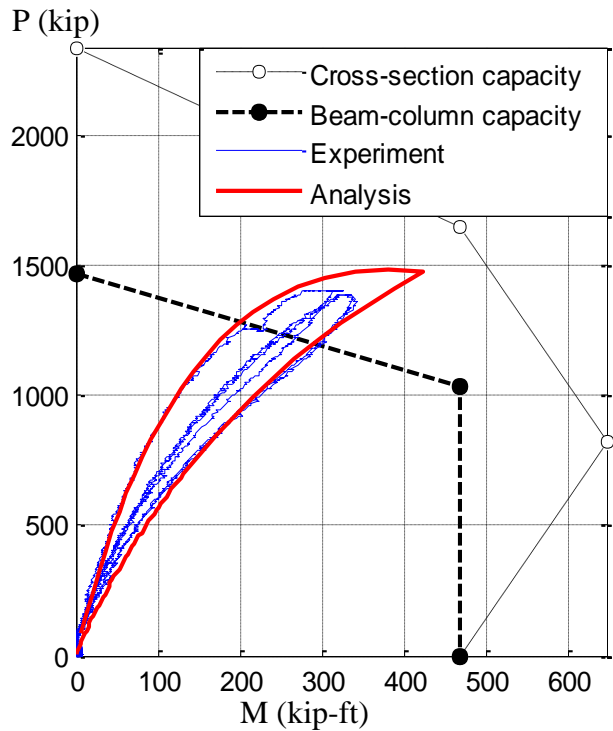


(b) Axial force vs. Base moment

Figure 5.44. Experimental response vs. Analytical prediction for the Specimen 14C12-26-5

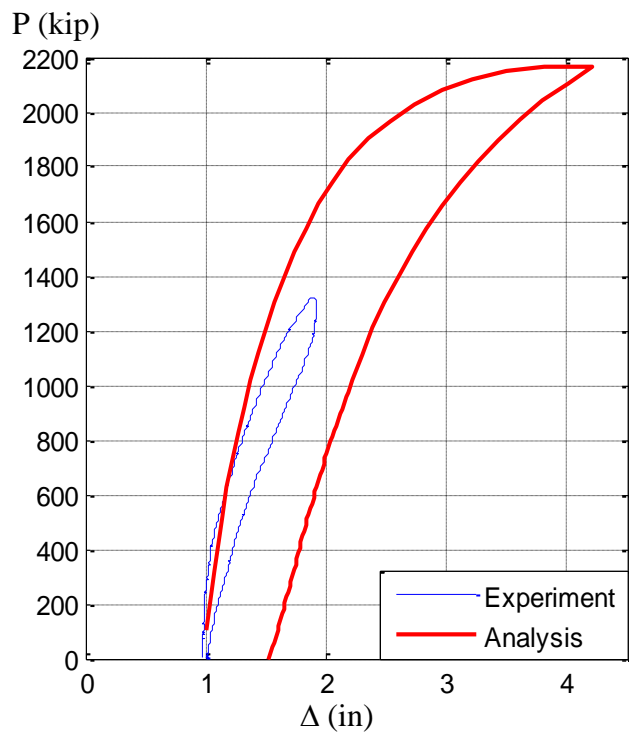


(a) Axial force vs. Top displacement

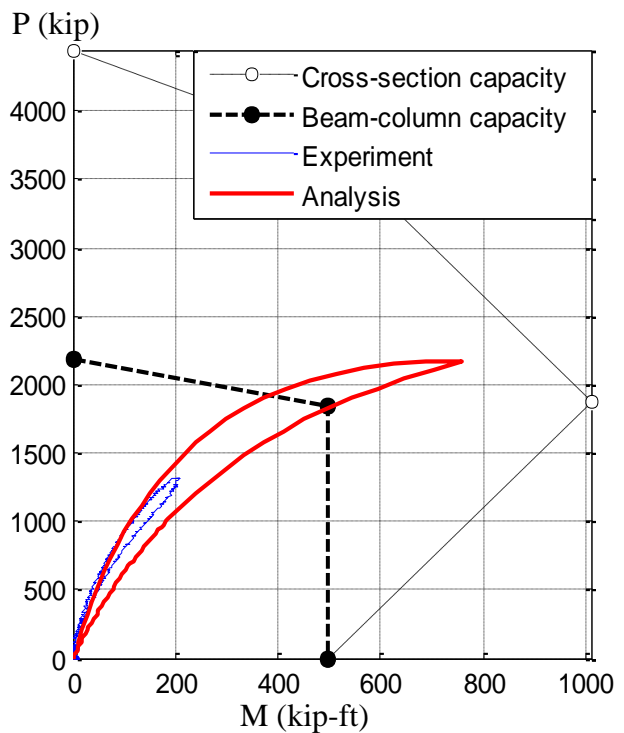


(b) Axial force vs. Base moment

Figure 5.45. Experimental response vs. Analytical prediction for the Specimen 3C20-18-5

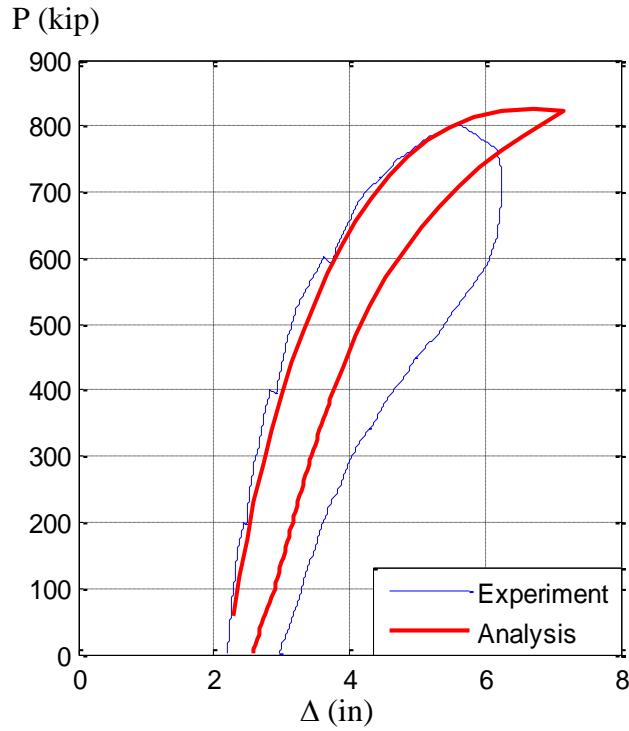


(a) Axial force vs. Top displacement

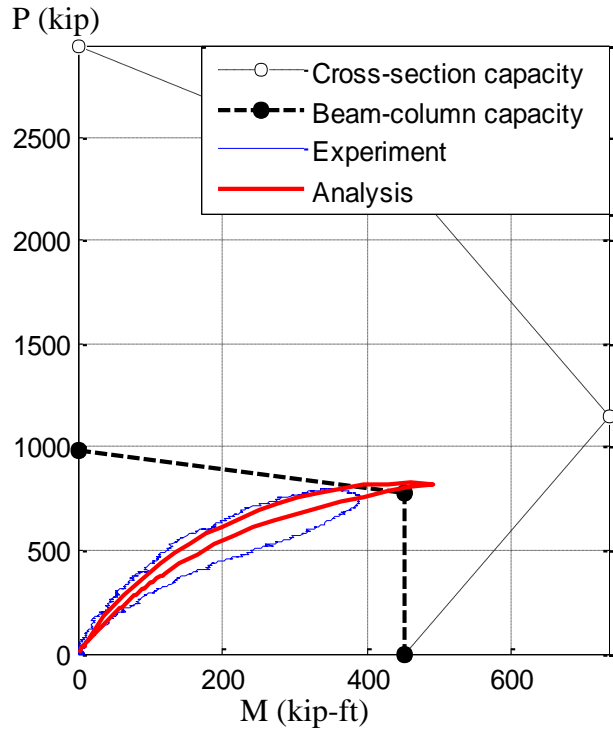


(b) Axial force vs. Base moment

Figure 5.46. Experimental response vs. Analytical prediction for the Specimen 7C20-18-12

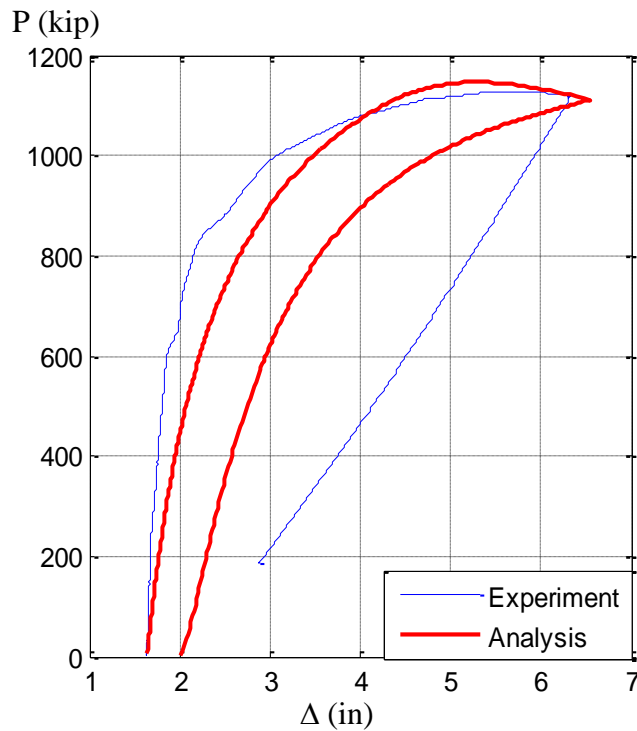


(a) Axial force vs. Top displacement

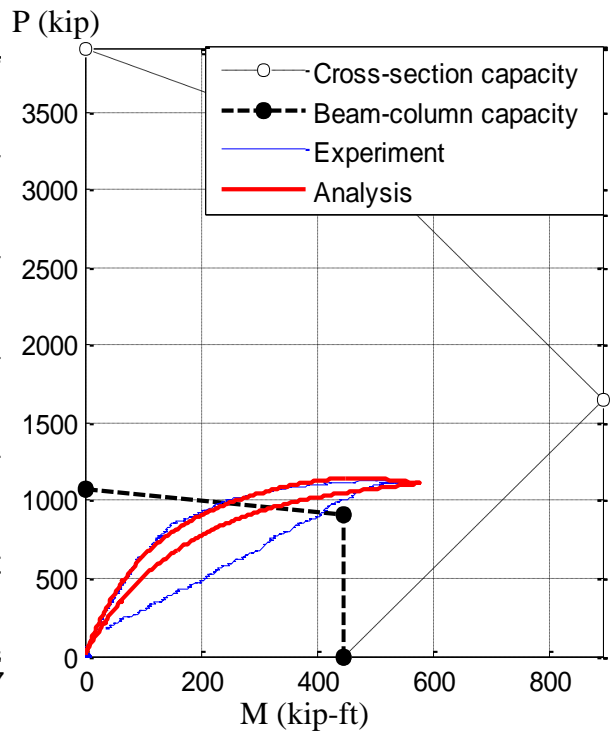


(b) Axial force vs. Base moment

Figure 5.47. Experimental response vs. Analytical prediction for the Specimen 11C20-26-5

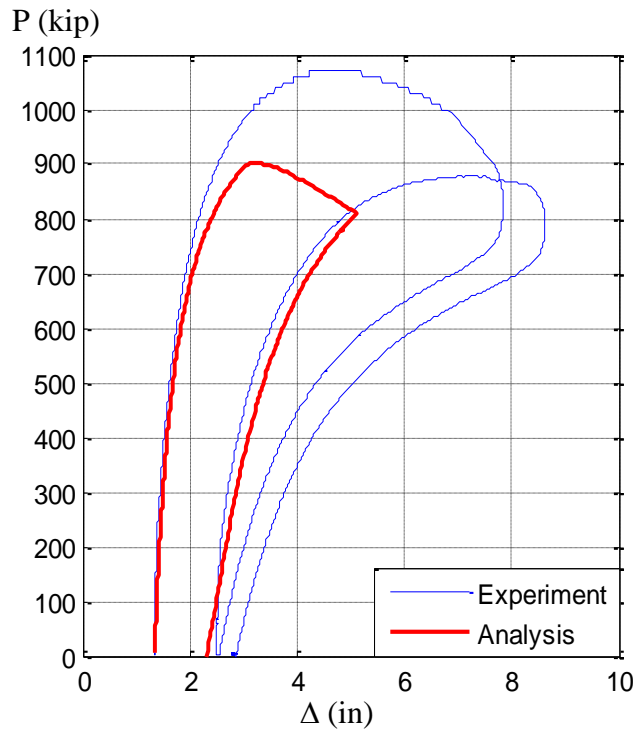


(a) Axial force vs. Top displacement

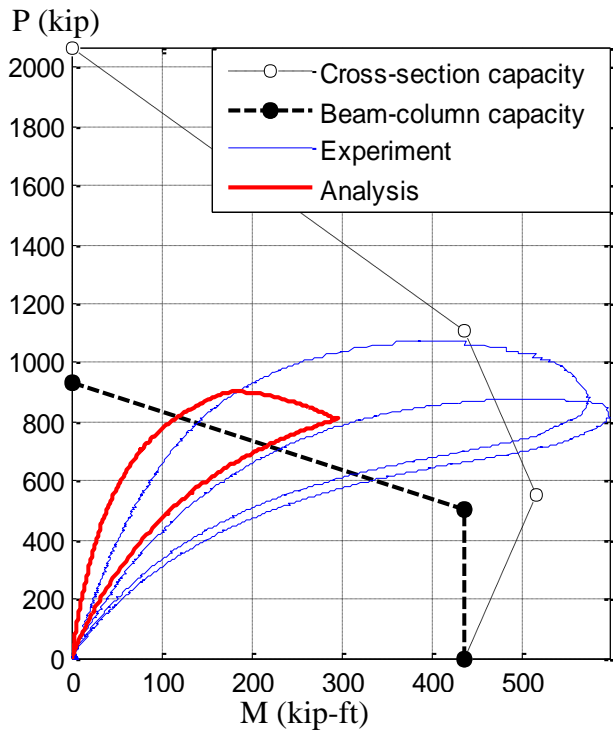


(b) Axial force vs. Base moment

Figure 5.48. Experimental response vs. Analytical prediction for the Specimen 15C20-26-12

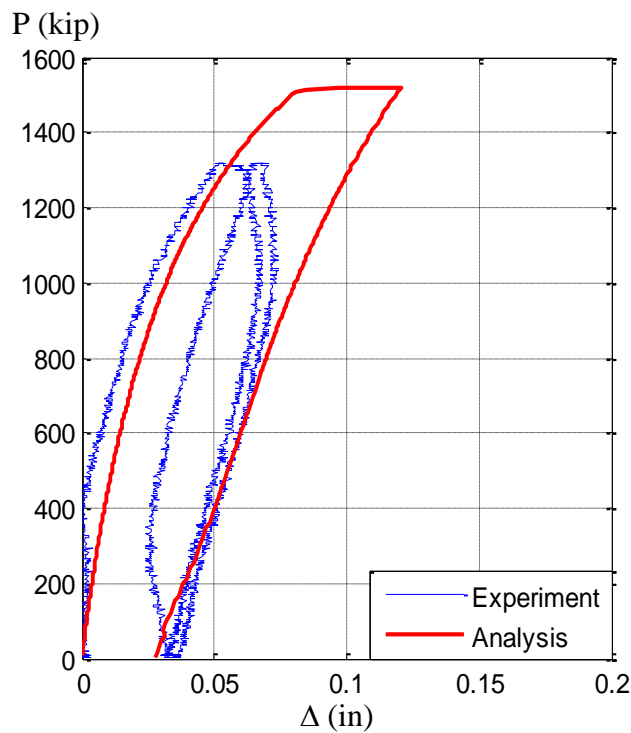


(a) Axial force vs. Top displacement

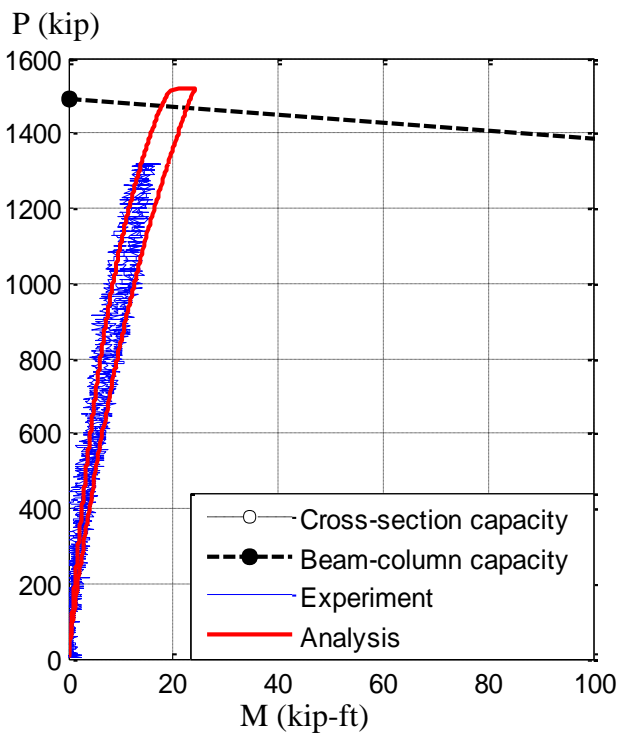


(b) Axial force vs. Base moment

Figure 5.49. Experimental response vs. Analytical prediction for the Specimen 4Rw-18-5



(a) Axial force vs. Top displacement



(b) Axial force vs. Base moment

Figure 5.50. Experimental response vs. Analytical prediction for the Specimen 5Rs-18-5

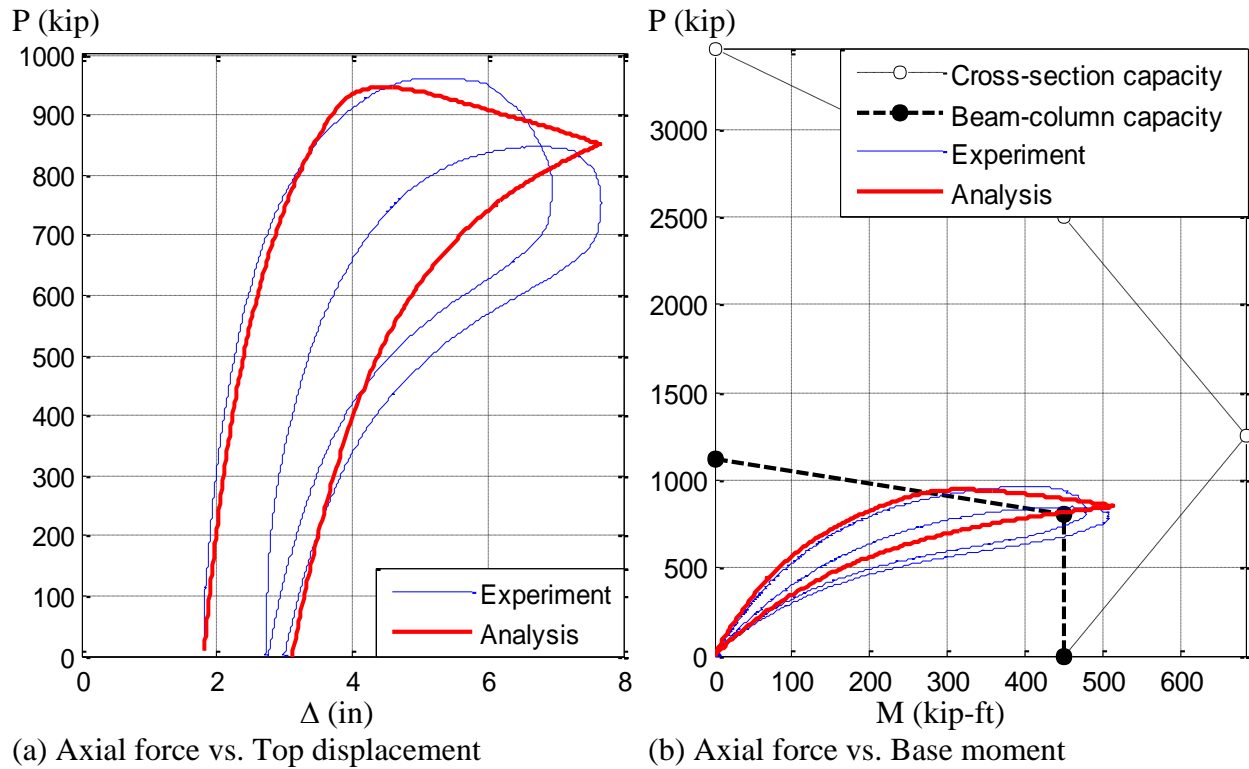


Figure 5.51. Experimental response vs. Analytical prediction for the Specimen 8Rw-18-12

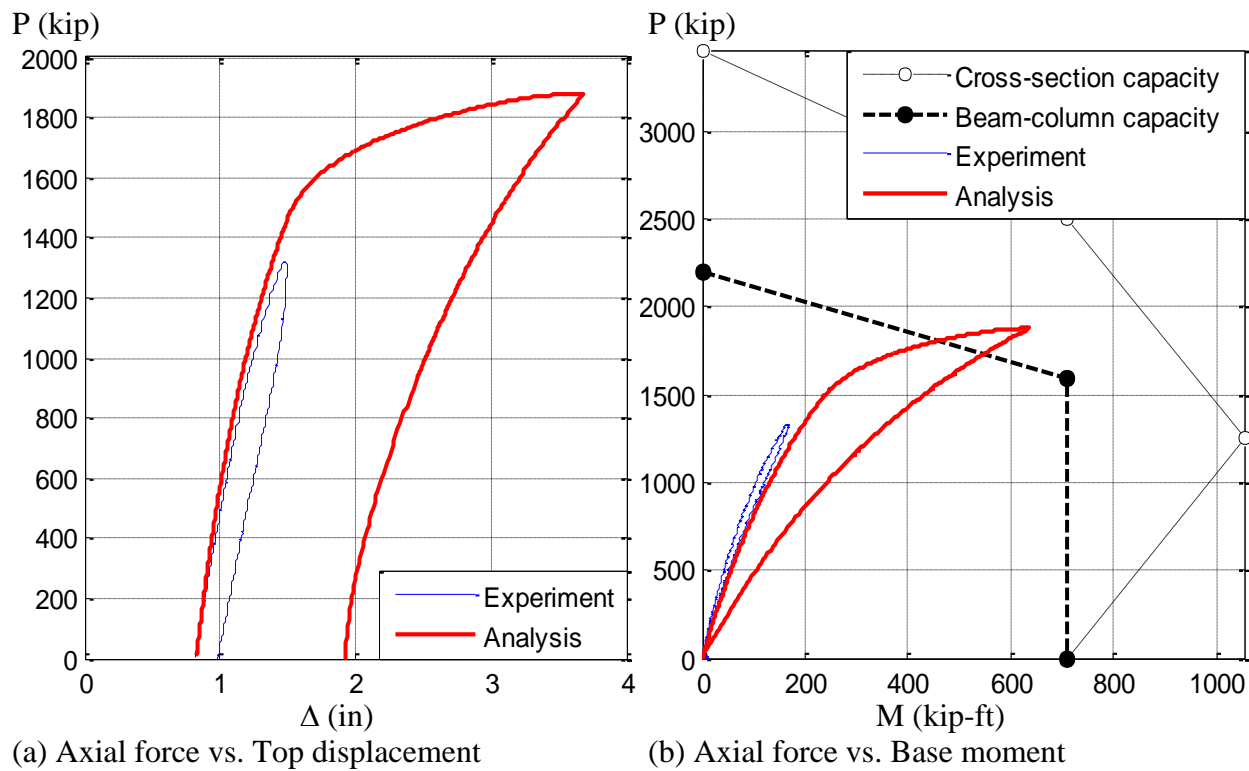


Figure 5.52. Experimental response vs. Analytical prediction for the Specimen 9Rs-18-12

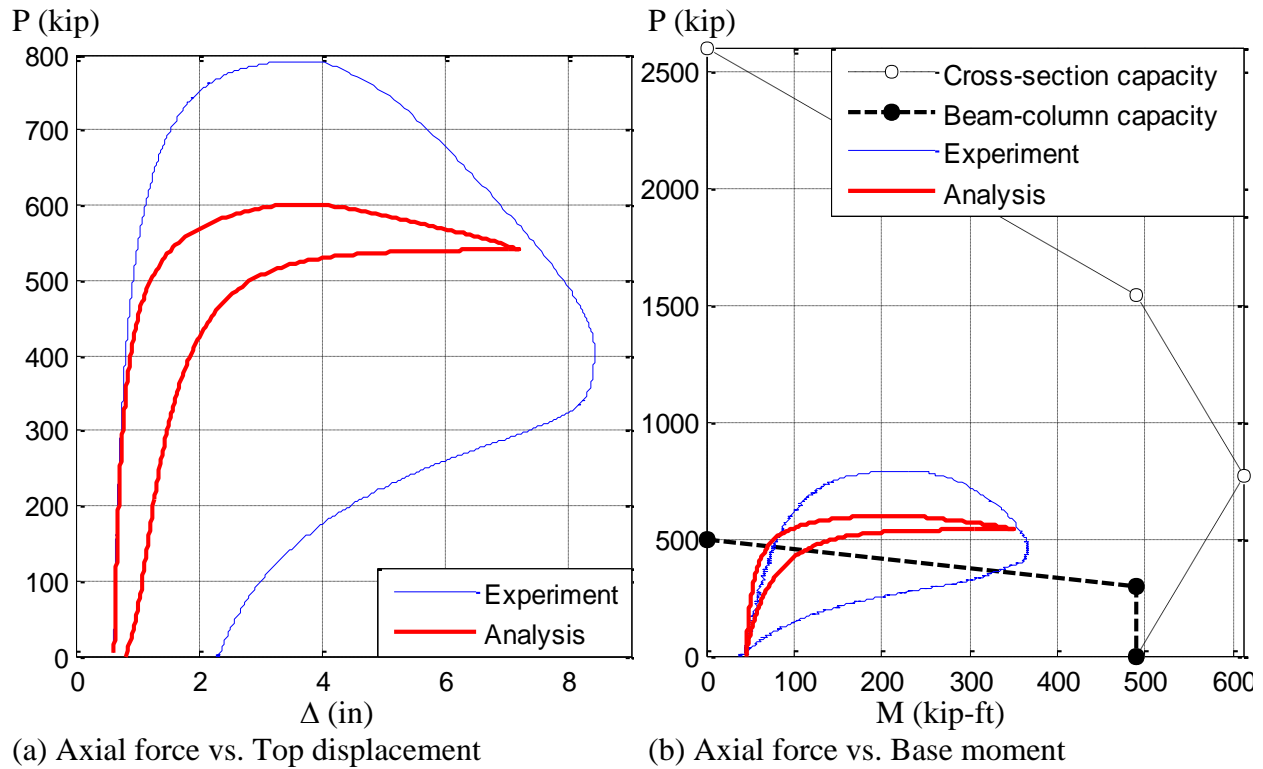


Figure 5.53. Experimental response vs. Analytical prediction for the Specimen 12Rw-26-5

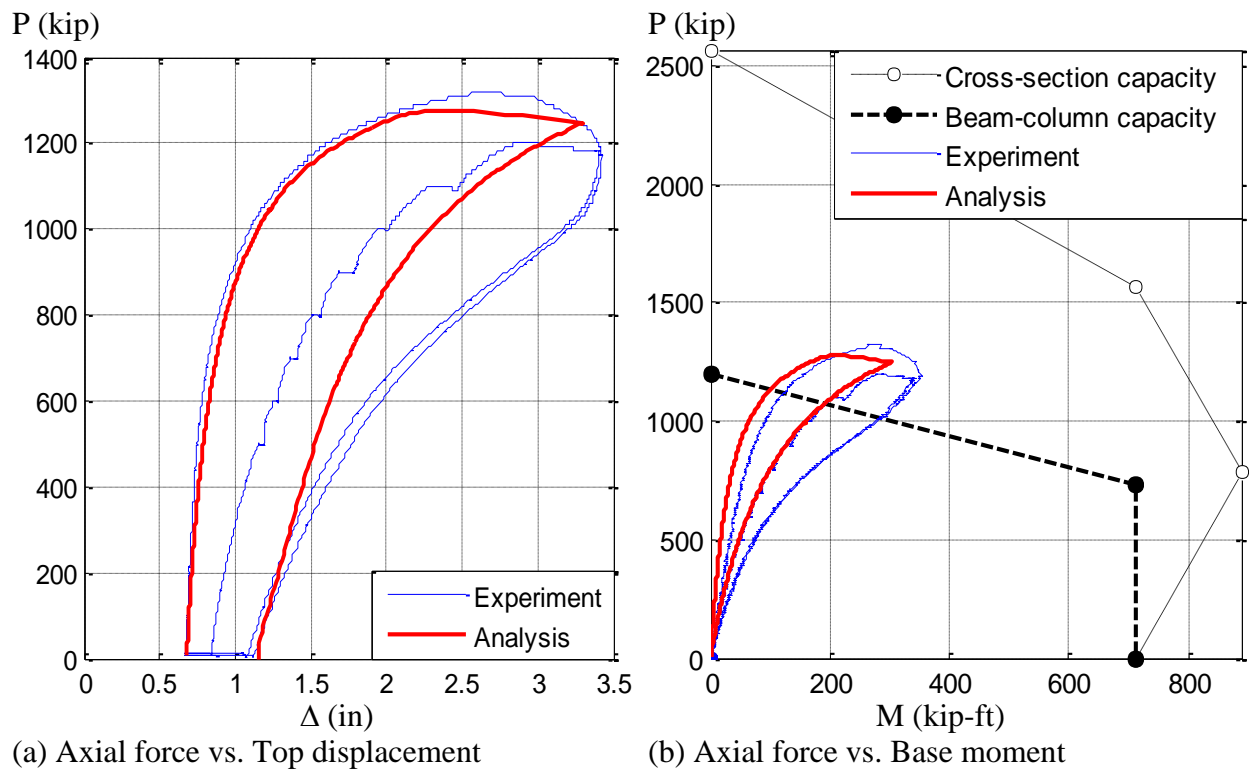


Figure 5.54. Experimental response vs. Analytical prediction for the Specimen 13Rs-26-5

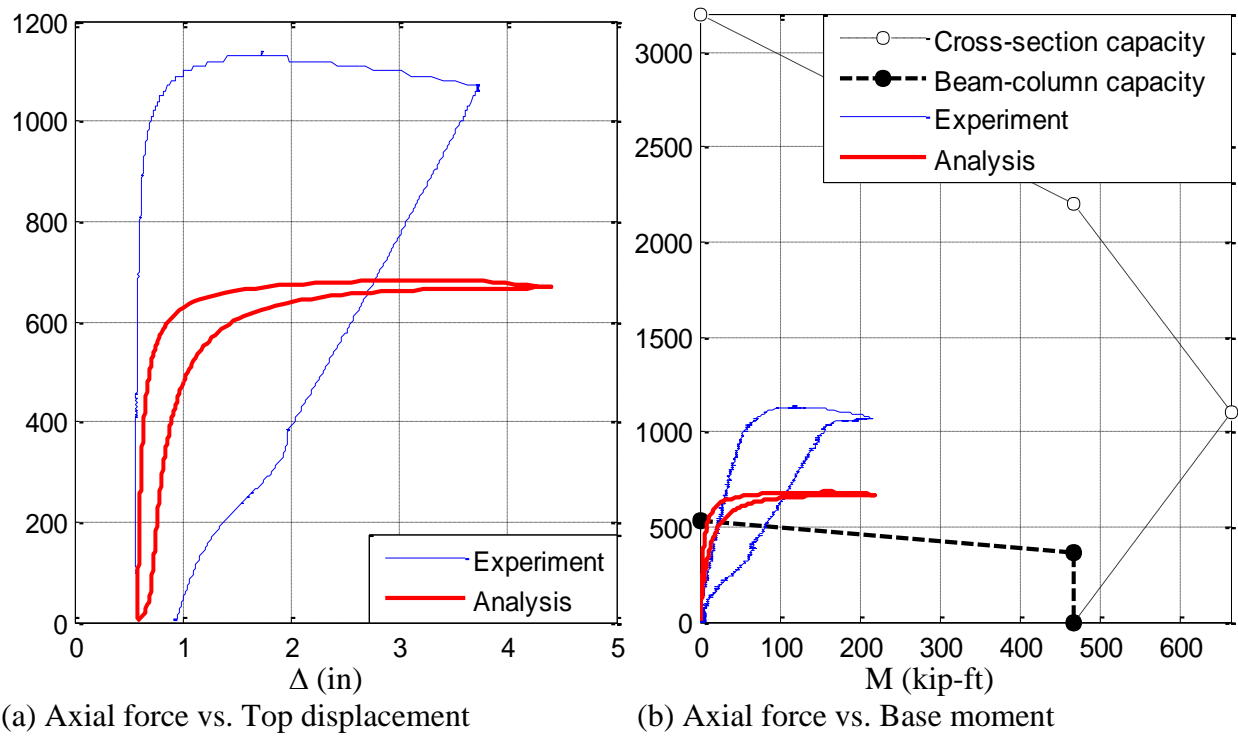


Figure 5.55. Experimental response vs. Analytical prediction for the Specimen 16Rw-26-12

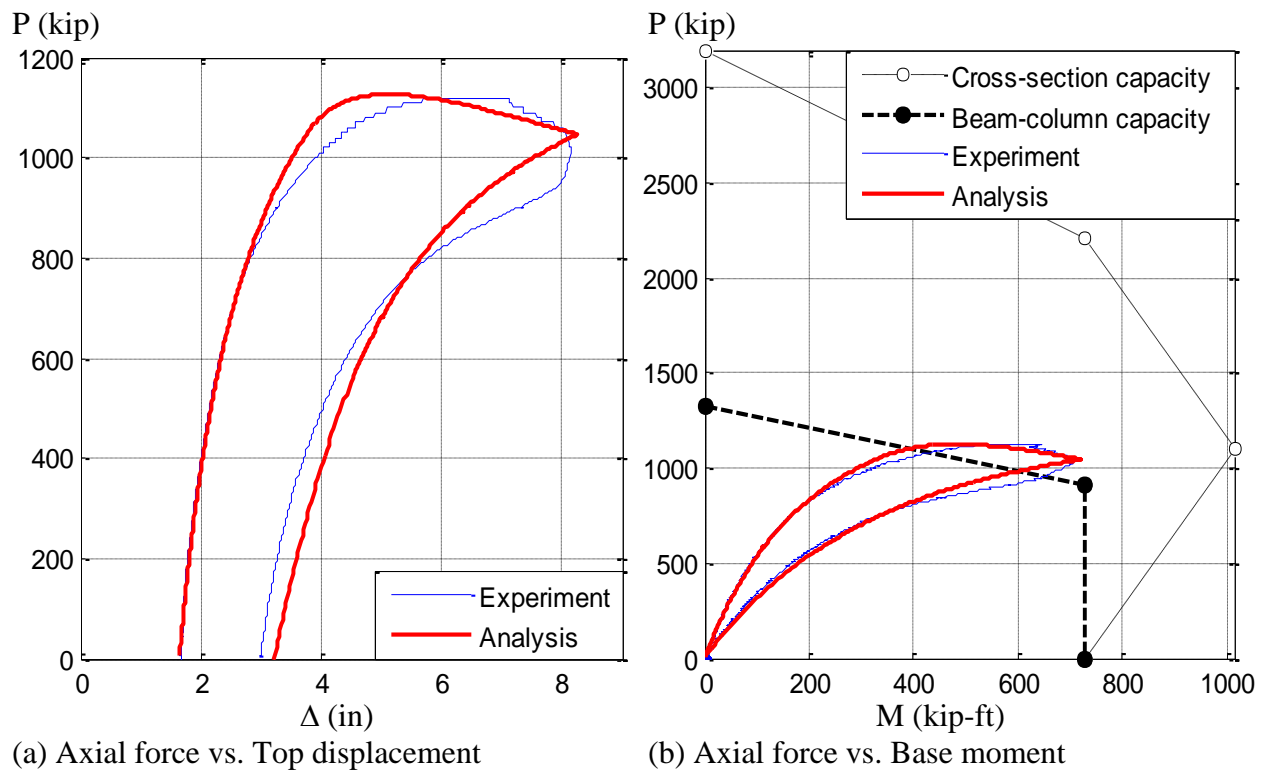


Figure 5.56. Experimental response vs. Analytical prediction for the Specimen 17Rs-26-12

The buckling loads ($E[P_n]$) obtained from this set of computational analyses are summarized in Table 5.8. In this table, the experimental values previously extracted from the raw and processed or adjusted data are also shown. In addition, this table shows the effective length factor (K), the slenderness parameter (λ) and the buckling load (P_n) that is obtained with the AISC (2010) Specifications.

Table 5.8. Buckling loads from computational analysis

Specimen	AISC (2010)			Maximum raw data	Adjusted critical load	Analytical critical load	ratio $E[P_n]/P_n$
	K	λ	P_n (kip)	P_{exp} (kip)	P_{cr} (kip)	$E[P_n]$ (kip)	
2C12-18-5	2.0	1.55	393	427	400 ^a	429.5	1.09
6C12-18-12	2.0	1.90	472	581	500 ^a	540.4	1.14
10C12-26-5	2.0	2.38	207	362	222 ^a	262.2	1.27
14C12-26-12	2.0	2.72	216	386	225 ^a	285.1	1.32
3C20-18-5	2.0	1.05	1469	1320 ⁺	1478 ^b	1486.7	1.01
7C20-18-12	2.0	1.30	2190	1320 ⁺	1791 ^b	2168.7	0.99
11C20-26-5	2.0	1.61	992	802	802	825.3	0.83
15C20-26-12	2.0	1.78	1080	1127	1100 ^a	1146.2	1.06
4Rw-18-5	2.0	1.38	939	1070	950 ^a	901.7	0.96
8Rw-18-12	2.0	1.65	1124	961	961	946.2	0.84
12Rw-26-5	2.0	2.14	501	791	540 ^a	601.1	1.20
16Rw-26-12	2.0	2.30	534	1140	1000 ^a	673.0	1.26
5Rs-18-5	2.0	0.88	1501	1320 ⁺	1705 ^b	1521.0	1.01
9Rs-18-12	2.0	1.04	2209	1320 ⁺	1918 ^b	1877.5	0.85
13Rs-26-5	2.0	1.35	1199	1320	1200 ^a	1275.9	1.06
17Rs-26-12	2.0	1.46	1323	1120	1120	1126.9	0.85

(+) MAST axial capacity (1320 kips) reached before getting the buckling strength

(a) Experimental axial load given at the instant the controller added significant top forces a moments.

(b) Axial load from the tangent plot

As seen in this table, the ratio $E[P_n]/P_n$ still shows some scattering with the Specifications that are still attributed to the dispersion of the initial imperfections; however, these analytical response follows fittingly the AISC column curve as shown in Figure 5.57. This figure shows the slenderness parameter (λ) in the horizontal axis and the predicted buckling load normalized with the squashing capacity (P_o) in the vertical axis. Similarly, Figure 5.58 shows the final experimental and analytical column curves that are obtained, respectively, from the adjusted experimental data and the computational analysis presented in this section. This concluding figure illustrates a reasonable column behavior of the CFT columns, with a relatively low dispersion as a consequence of the variance in each specimen imperfection.

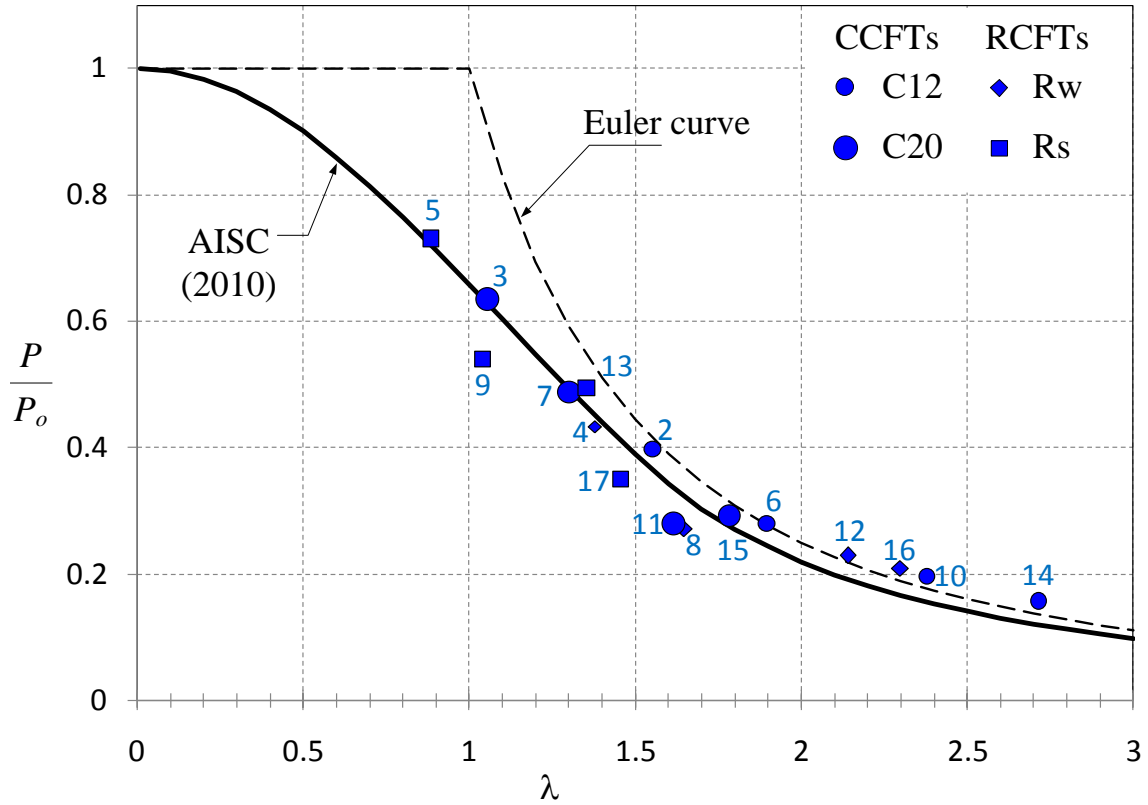


Figure 5.57. Critical load ratios (P_{exp}/P_o) from computational analysis

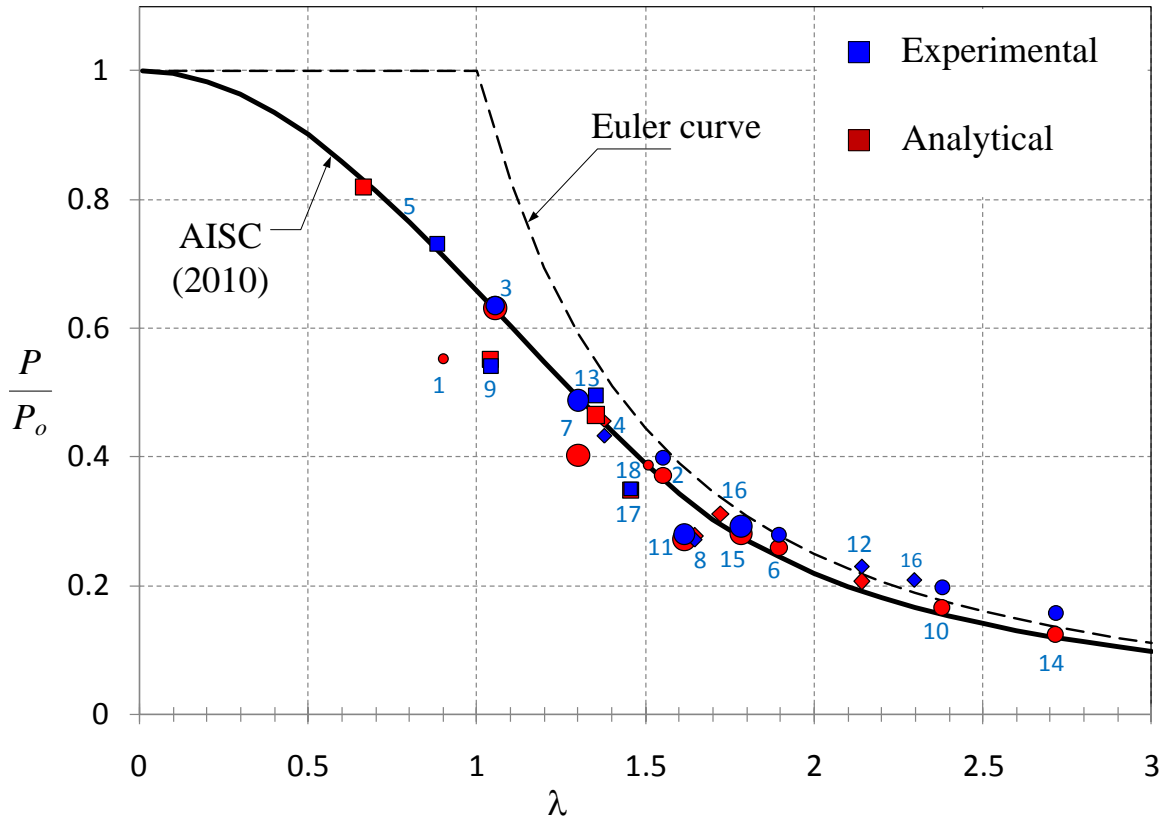


Figure 5.58. Experimental and analytical critical load ratios and AISC column curve

5.6.2. Step-by-step analysis

Except for the loading conditions, the assumptions in this set of analysis are the same to those stated before in 3.6.1. This analysis set intends to follow the same experimental response as collected during this load case LC1.

As reminder, LC1 was performed in CFT specimens with the base fixed and the top controlled by the crosshead with an incremental vertical displacement downward while the lateral forces, bending moments and twisting displacement were fixed to zero; these ideal conditions were considered in the previous analysis set, and still some differences were observed for the output response (axial strength, lateral deflection and base moments). However, as discussed before, the differences are mainly due to a lack of control in the crosshead during the test that modifies the specimen response in high axial load range. Even the resolution noise in lateral force (± 0.22 kip) and bending moment (± 2.18 kip-ft) are considerable in the weakest and the most slender specimens. This is even worst when additional crosshead forces and moments are added to the member.

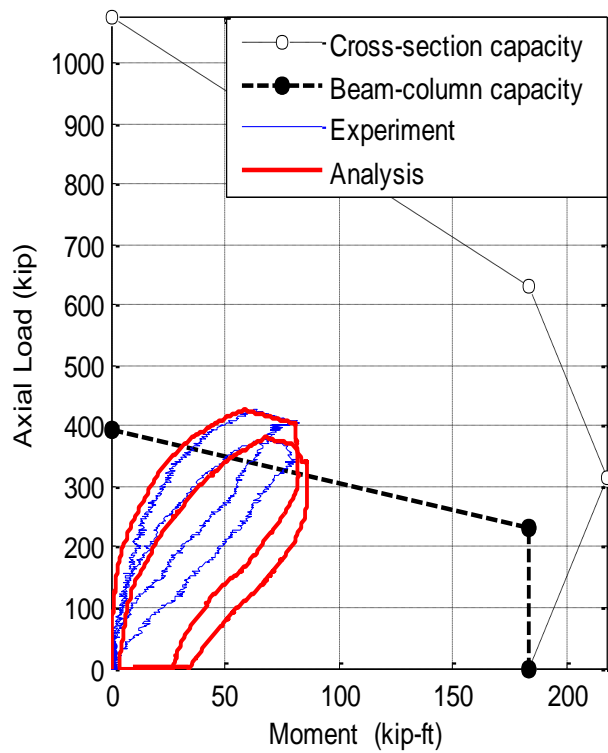
Thus, in this analysis set the top of the column is driven with the displacements and forces recorded during LC1. Unfortunately, the vertical displacement history computed by the controller in the bottom center of the crosshead cannot be applied since it is unknown the contribution on the real shortening in the element and the system compliance (i.e. deformations in the crosshead, force train, swivel bearings and connections). A discussion of the crosshead deflection was made in a previous section in this Chapter, where it was observed that about 40% to 60% of the computed global displacement corresponded to the effective shortening in columns under pure compression placed in the crosshead center; this percentage depends on the axial rigidity and the pressure size, so the assumption of a constant reduction factor for analysis purposes would be inaccurate.

The LVDT data is also useless since the relative shortening was measured only in some segments along the specimen (5 ft at bottom and 1 ft at the top). In addition, the vertical displacement calculated from the strain gauge data may be inaccurate since a considerable amount of strain during this LC1 is due to parasitic moments induced by the crosshead at the top, as well as second order flexure at the base as a consequence of the large out-of-plumbness.

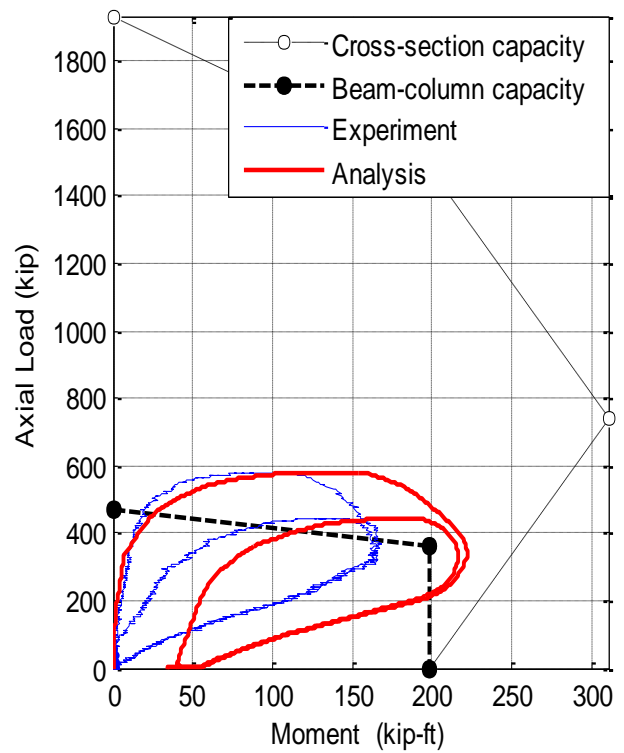
On the other hand, the application of the lateral forces and bending moments coming from the crosshead are not ideal since the level of noise on these histories are still relatively high in the most slender and the weakest specimens. A smoothing process on these stories may alleviate the uneven response, but some inaccuracies may be obtained with a high smoothness.

Based on the above mentioned caveats, the instantaneous vertical force and lateral displacement was chosen as a step-by-step input as loading conditions for the following analysis set; this input data will be useful also during the following load cases (LC2 and LC3). Addition of the lateral displacement is intended to account for the real directionality of the specimen as a consequence of the imperfections and the crosshead forces (frictional and parasitic forces). The critical axial load response cannot be predicted since the instantaneous experimental axial force is applied as input; the latter is a consequence of an over predicted displacement computed by the controller due to the system compliance. However, the inclusion of this input aims to obtain a more accurate overall response such as the base moment.

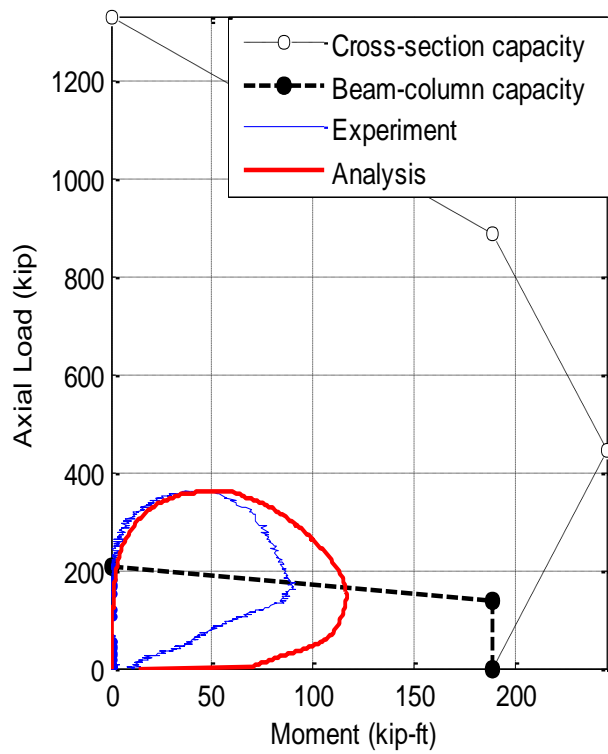
Comparison between the experimental axial force – base moment path and its analytical prediction from these step-by-step analyses with the assumptions previously stated are shown from Figure 5.59 to Figure 5.62. As shown in these figures, the analytical prediction follows reasonably well the experimental P-M path in the loading path. However, the analytical moment predictions after the peak axial load are over predicted compared to those measured in the tests. These additional moments come from additional lateral forces over-predicted in the analysis after the maximum axial load. These additional lateral forces and moments in the post-peak do not vanish during unloading and thus the unloading analytical P-M paths are shifted but parallel to the unloading path in the tests, and they remain as residuals when the total axial load is released.



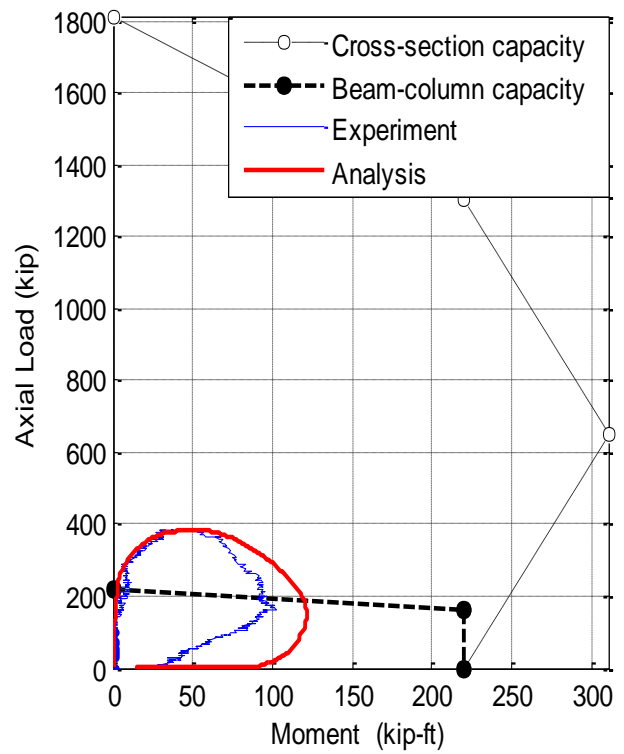
(a) Specimen 2C12-18-5



(b) Specimen 6C12-18-12

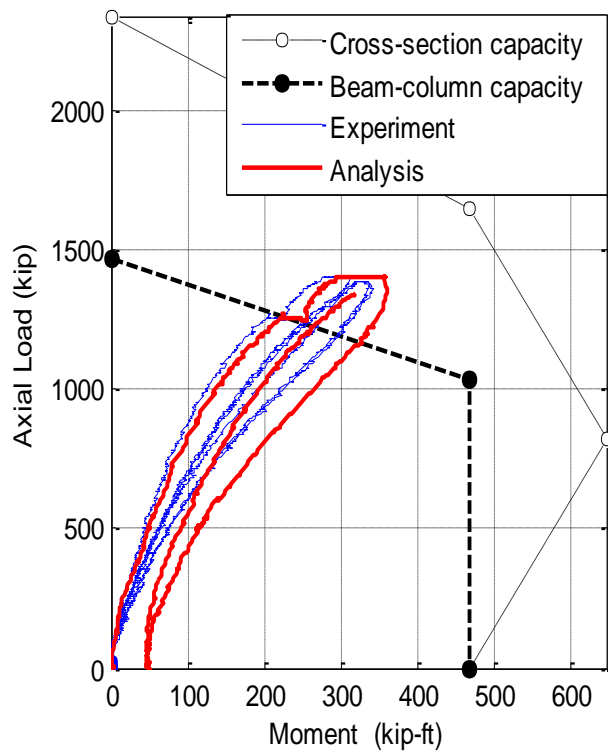


(c) Specimen 10C12-26-5

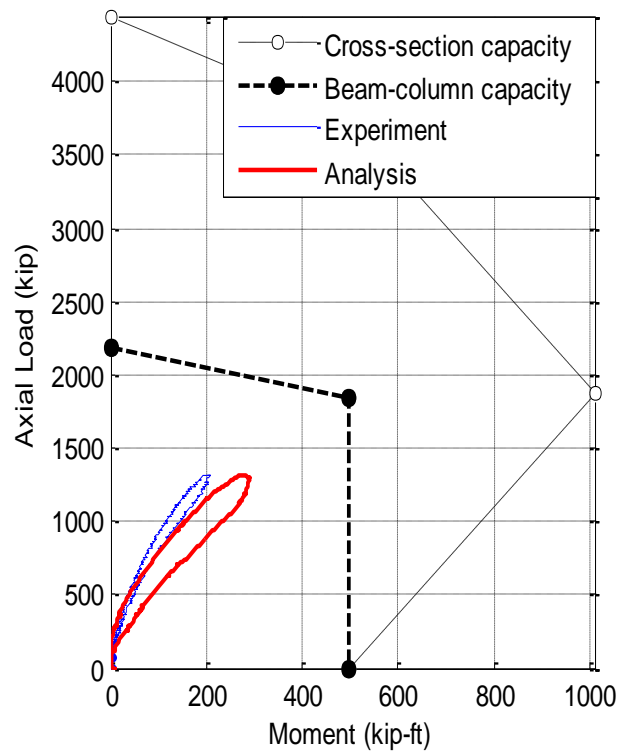


(d) Specimen 14C12-26-12

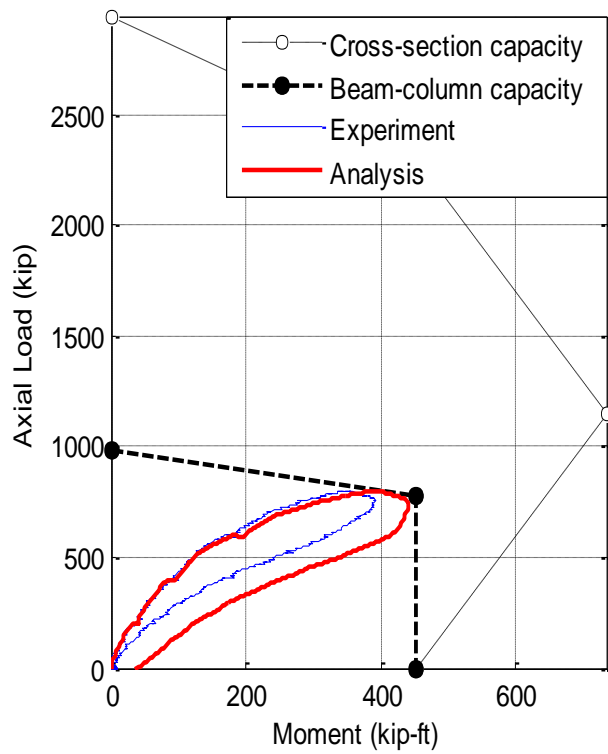
Figure 5.59. Experimental response vs. Analytical prediction for the C12 Specimens



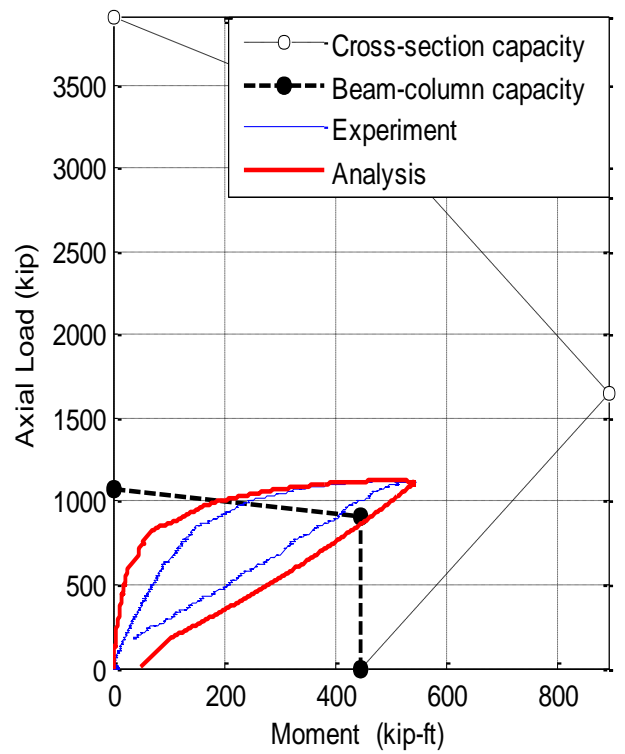
(a) Specimen 3C20-18-5



(b) Specimen 7C20-18-12

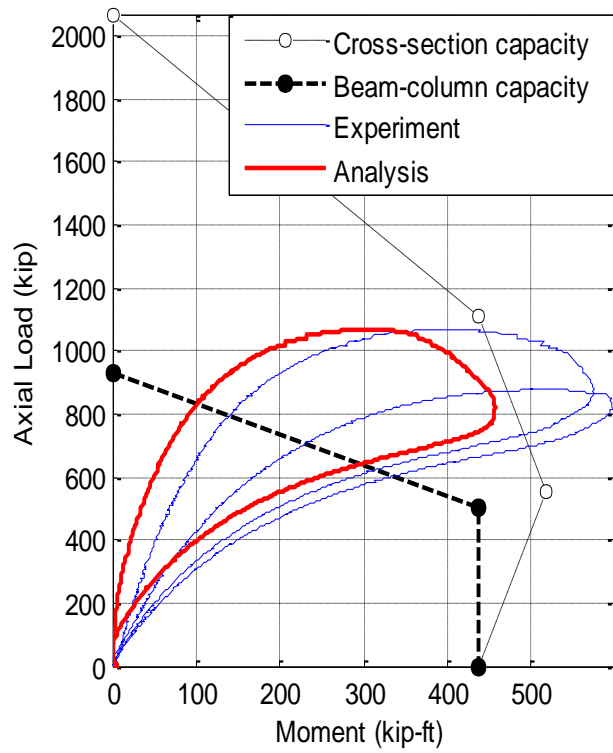


(c) Specimen 11C20-26-5

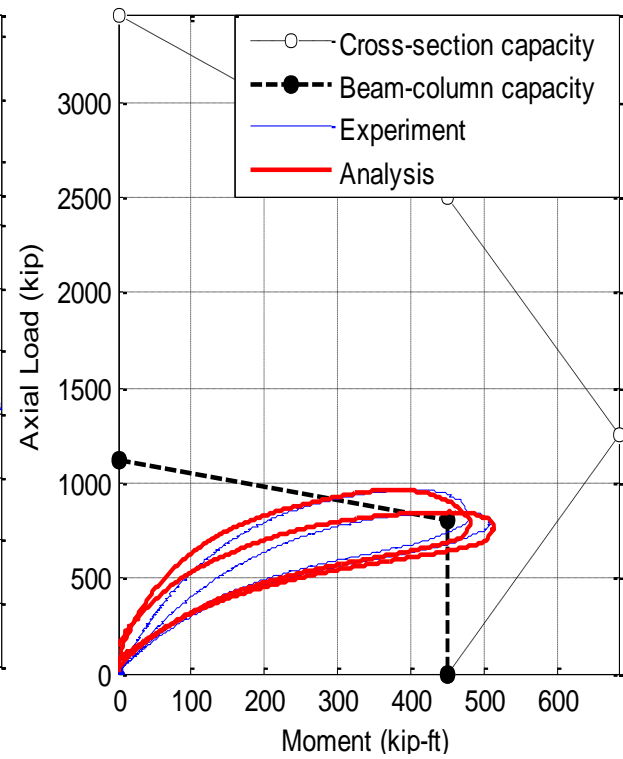


(d) Specimen 15C20-26-12

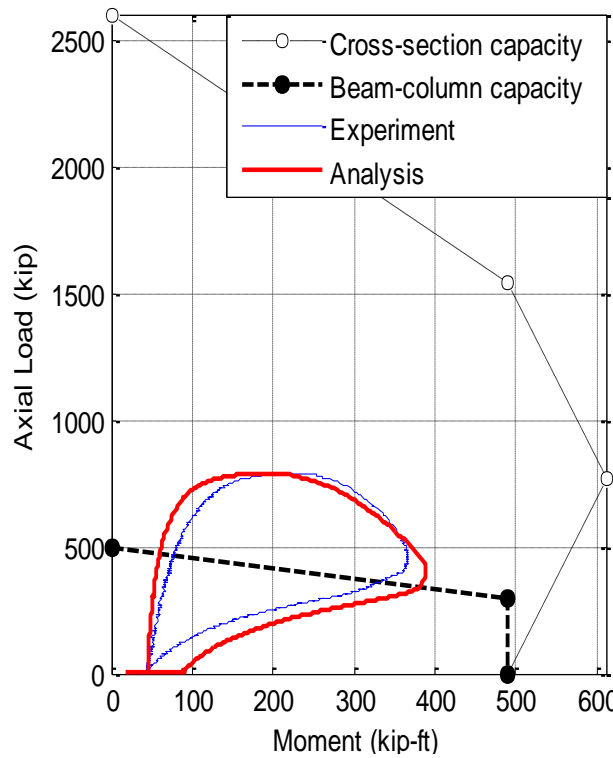
Figure 5.60. Experimental response vs. Analytical prediction for the C20 Specimens



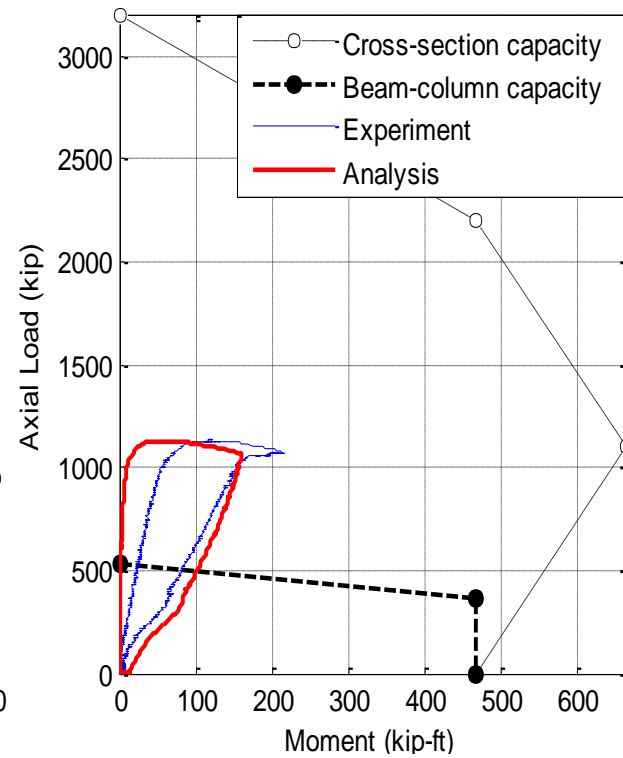
(a) Specimen 4Rw-18-5



(b) Specimen 8Rw-18-12

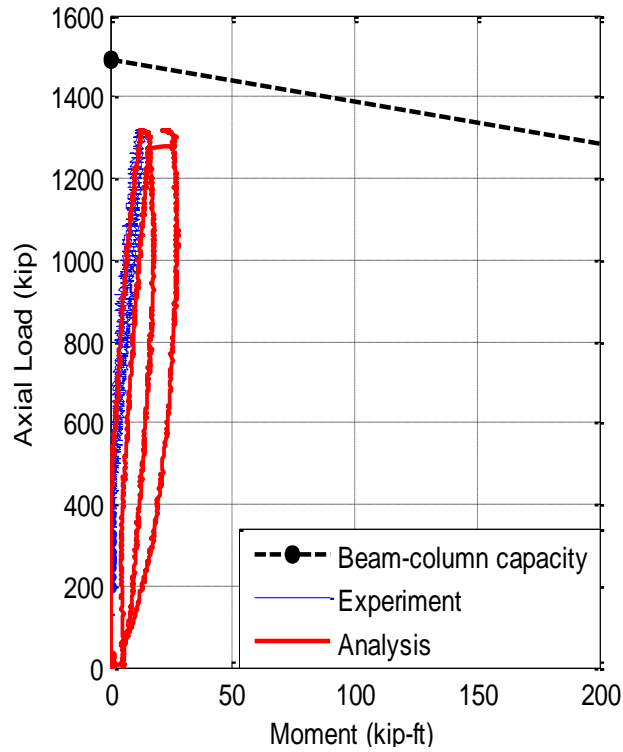


(a) Specimen 12Rw-26-5

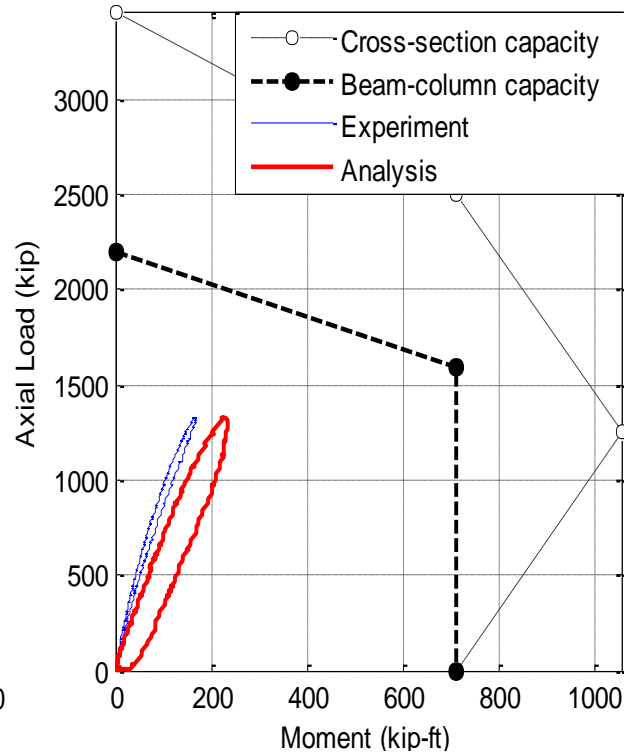


(b) Specimen 16Rw-26-12

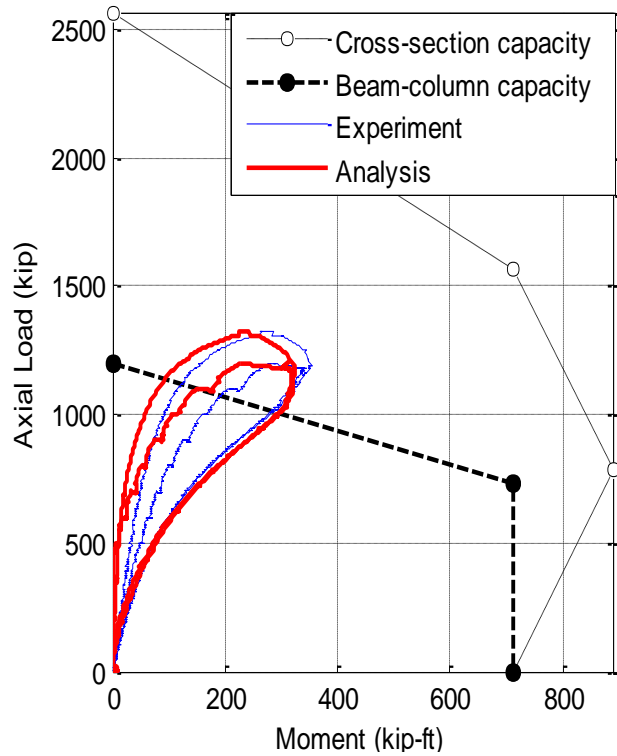
Figure 5.61. Experimental response vs. Analytical prediction for the Rw Specimens



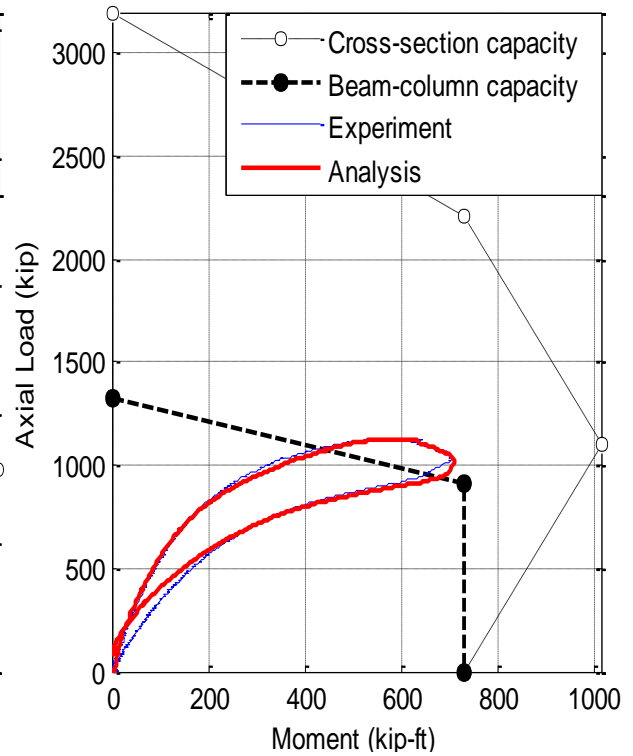
(a) Specimen 5Rs-18-5



(b) Specimen 9Rs-18-12



(a) Specimen 13Rs-26-5



(b) Specimen 17Rs-26-12

Figure 5.62. Experimental response vs. Analytical prediction for the Rs Specimens

5.6.3. Column curves with ideal conditions

The axial load capacity that was obtained in the tests from the processed data was collected and documented in Section 5.5. In Section 5.6.1, buckling load capacities were obtained from computational analysis; both the experimental and analytical responses were illustrated at the end of Section 5.6.1, and the buckling loads show to follow fittingly the column curve of the Specifications. However, the extracted and computed buckling loads presented some dispersion as a consequence of the large distribution of the initial out-of-plumbness and the initial out-of-straightness that was measured in every specimen.

In this section, buckling loads are again computed with the models calibrated in Sections 5.6.1 and 5.6.2. These analyses are performed in cantilever CFT columns with different lengths. Analytical column curves are obtained from these analyses and then compared with the column curve of the AISC (2010) Specifications.

The analyses in this section use the same assumptions that in Sections 5.6.1, except for the material properties and the initial imperfections. Nominal material properties are used for these analyses; in addition, the initial imperfections given in the model are defined by the shape function illustrated in Figure 5.63 this shape-function has been widely used in the calibration of classic stability solutions (i.e. Timoshenko 1961). This function defines the out-of-straightness (δ) through a cosine function that is in terms of the column length (L) and the out-of-plumbness (Δ_o). In these analyses, an out-of plumbness of $KL/1500$ and $KL/1000$ were assumed; since $K=2$, this limits are $L/750$ and $L/500$, respectively. The first value is related to the average imperfection that was used in calibration of the column curve in the AISC Specifications (Bjorhovde 1972; SSRC 1998). The second value is related to the maximum tolerance allowed in the Standards (i.e. ASTM A6, 2009; AISC, 2005d; ACI-117, 2006).

The results of these analyses are illustrated from Figure 5.64 to Figure 5.66. In these figures, the buckling load obtained in the analysis for each column length is plotted vs. the effective length (KL), with blue circles with $KL/1500$ of out of plumbness, and with red circles with $KL/1000$ of out-of-plumbness. The AISC column curve is included in these plots as a continuous black curve, where the cross-section strength (or the maximum axial force when $KL=0$) is calculated with Equation 5.2 and the effective length (KL) from Equation 5.3.

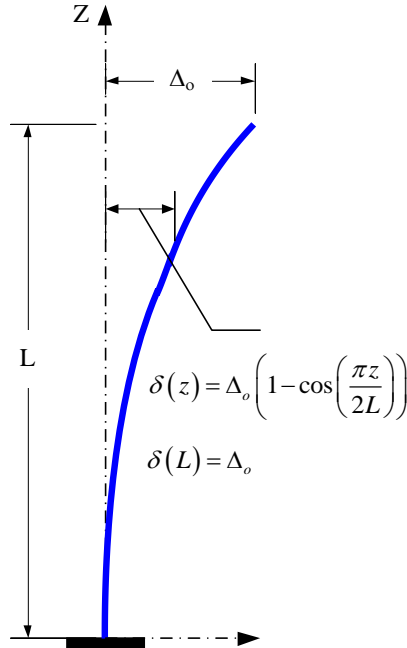
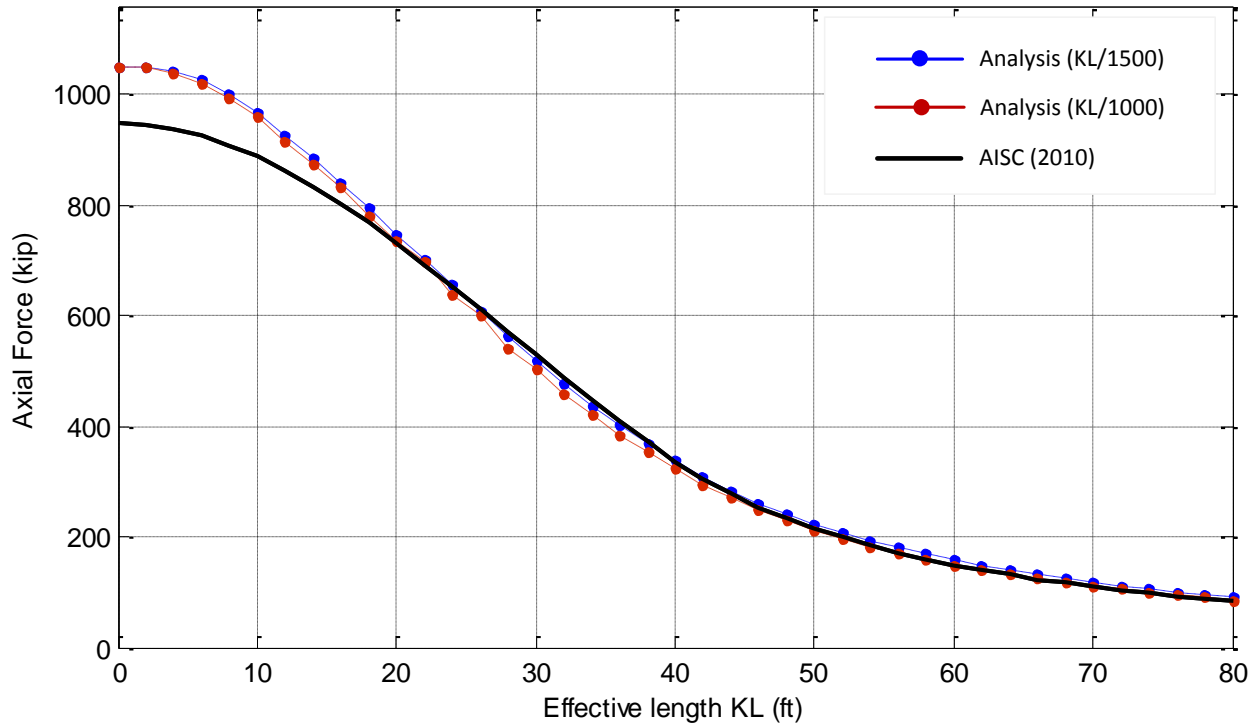


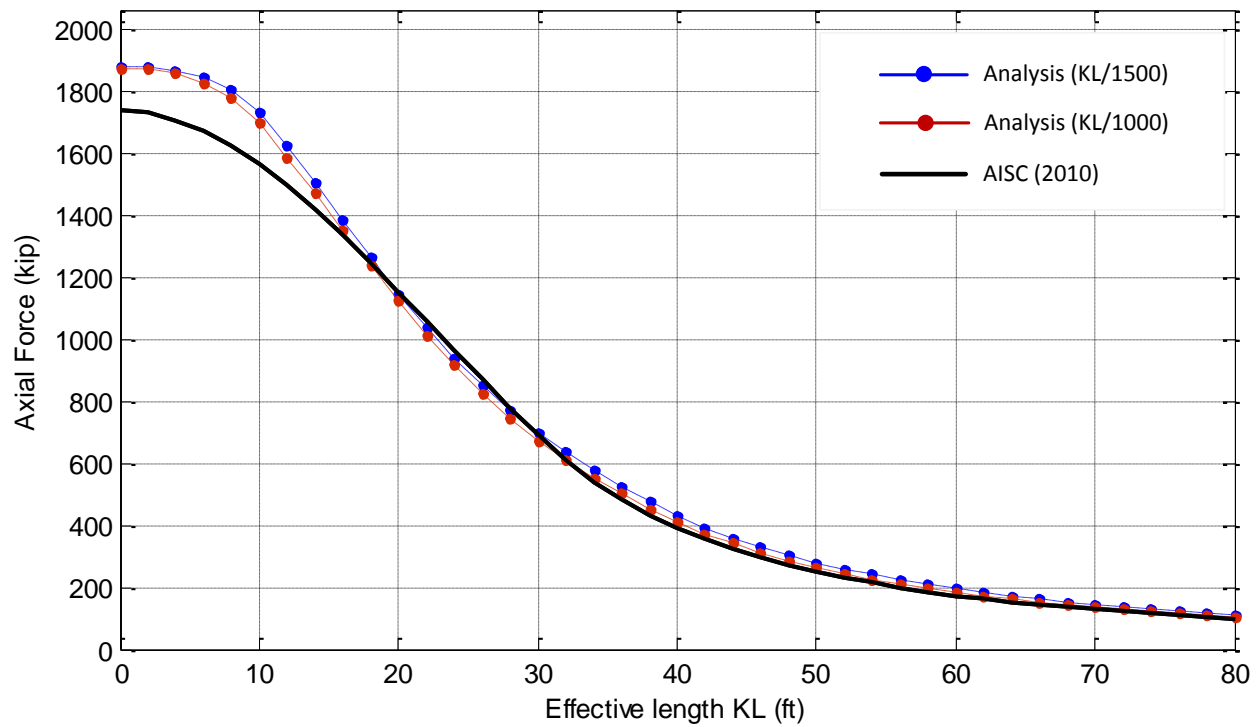
Figure 5.63. Shape function used to represent the initial imperfection

These figures show in general a good fitting of the analytical curves with the column curve of the Specifications. The larger differences are for shorter columns, and they are related to the different confinement effects considerations in the concrete, and different maximum stress and local buckling occurrence in the steel tubes. A confined concrete strength (f_{cc}) that is equal or greater than the concrete strength (f_c') is implicit in the constitutive concrete model and so in the analytical curves, while the Specifications uses a value of $0.95f_c'$ in CCFTs and $0.85f_c'$ in RCFTs. The confinement effects have a much lower impact in the elastic buckling range where the analysis and the Specifications show a good correlation. In addition, the steel model used in the analysis is a curve with smooth transition from the yielding (F_y) to the ultimate stress (F_u); the stress in compression has a softening if the local buckling conditions are met. In turn, the Specifications assumed a stress equal to the yielding stress (F_y) in both tension and compression, and there is no softening due to local buckling. Nevertheless, the column curve of the current AISC Specifications is, in most cases, a lower bound of the analytical results, except for the rectangular column case with the buckling oriented in the weak axis. This is justified by the local buckling occurrence in the analysis that is not considered in the CFT design equations.

The analytical curves with $KL/1500$ ($L/750$) and $KL/1000$ ($L/500$) of out-of-plumbness do not present significant differences. Thus, a column curve calibrated with either imperfection is valid and with negligible practical implications.

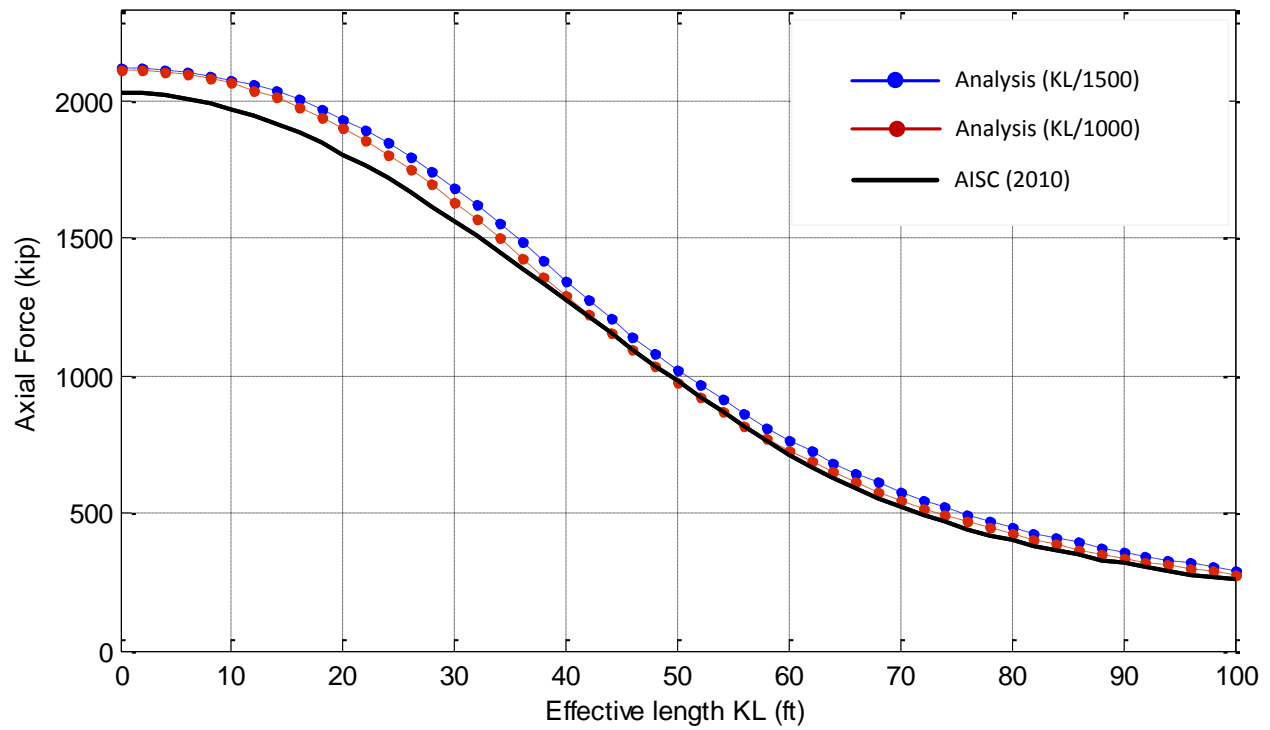


(a) CCFT: $D = 12.75$ " , $t = 0.233$ " , $F_y = 42$ ksi, $f'_c = 5$ ksi

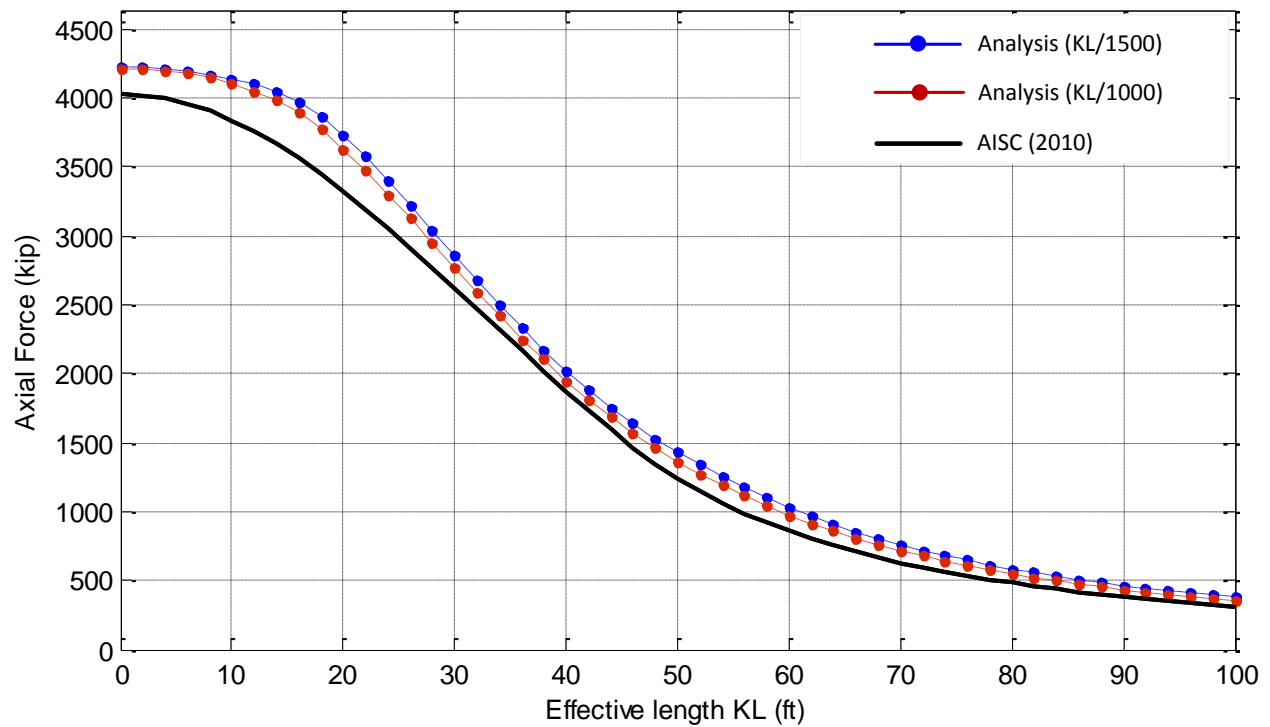


(b) CCFT: $D = 12.75$ " , $t = 0.233$ " , $F_y = 42$ ksi, $f'_c = 12$ ksi

Figure 5.64. Analytical column curves for a CCFT cross-section with 12.75 inches of diameter

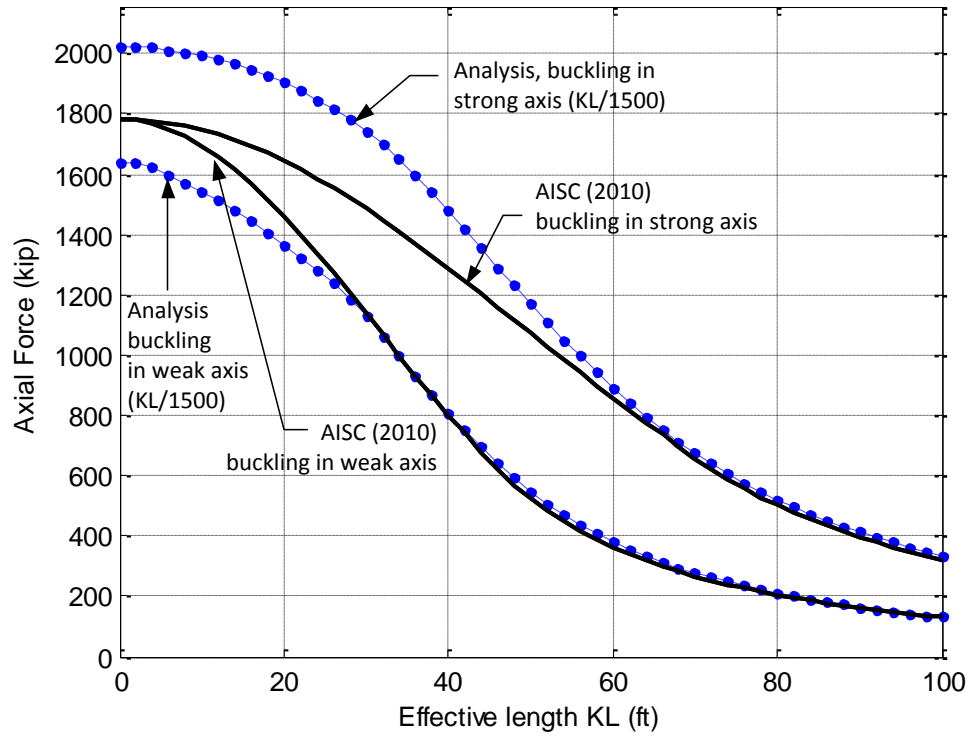


(a) CCFT: $D = 20$ ", $t = 0.233$ ", $F_y = 42$ ksi, $f'_c = 5$ ksi

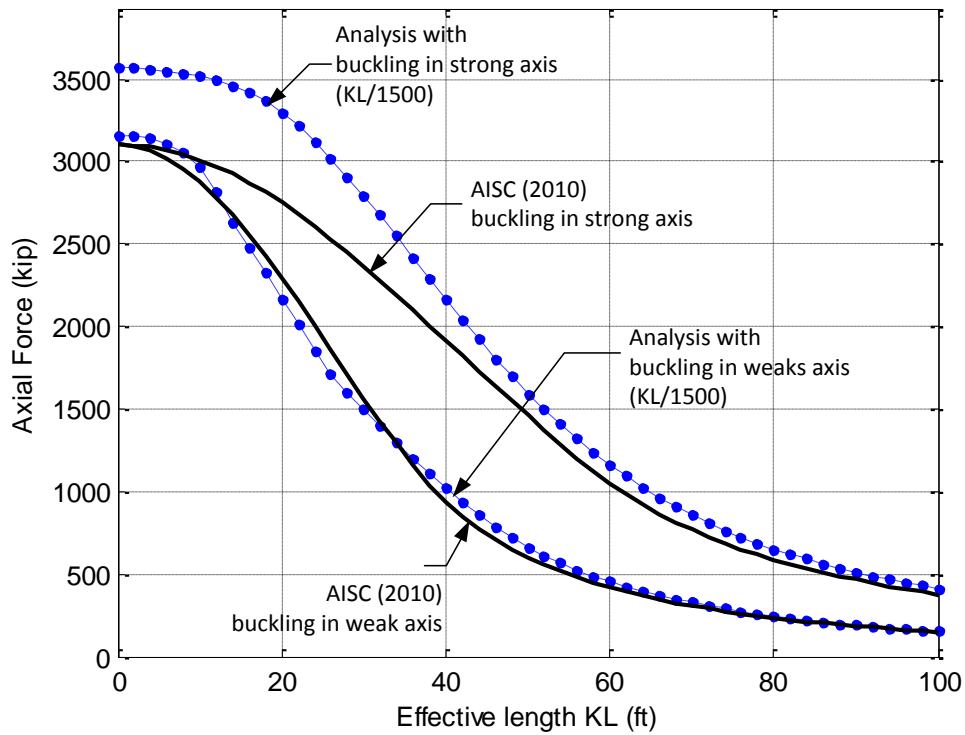


(b) CCFT: $D = 20$ ", $t = 0.233$ ", $F_y = 42$ ksi, $f'_c = 12$ ksi

Figure 5.65. Analytical column curves for a CCFT cross-section with 20 inches of diameter



(a) RCFT: $h = 20"$, $b = 12"$, $t = 0.291"$, $F_y = 46$ ksi, $f'_c = 5$ ksi



(b) RCFT: $h = 20"$, $b = 12"$, $t = 0.291"$, $F_y = 46$, $f'_c = 12$ ksi

Figure 5.66. Analytical column curves for a RCFT cross-section

5.7. Experimental extraction of the effective stiffness

Experimental moment vs. curvature ($M_2-\phi$) response histories at critical cross-sections from the buckling loading case (LC1) are illustrated in Figure 5.67 to Figure 5.71. The experimental moments shown in these figures are computed at the critical cross-section from the member equilibrium with the crosshead data; in turn, the curvature is computed from the strain gauge data placed at the critical cross-section. The critical cross-section is located:

- (a) Near the base for the specimens tested as fixed-free ($K=2$, specimens 2 to 17)
- (b) In the midspan for those specimens tested as fixed-fixed ($K=0.5$, specimens 1 and 18).

Also in these figures, elastic tangent stiffness in the loading (EI_{expL}) and in the unloading (EI_{expU}) branches are also shown, as well as the effective flexural stiffness (EI_{eff}) calculated from the AISC (2010) Specifications and the corresponding experimental-to-analytical ratios. All these values are summarized in Table 5.9. As noted in this table, the coefficient related to the concrete contribution to the total flexural stiffness (C_3) ranges for the 18 CFT specimens between 0.69 and 0.77.

Both tangent stiffness in the loading and the unloading characterize elastic behavior. However, as noted in Figure 5.67 to Figure 5.71, the experimental stiffness values extracted from the unloading show less dispersion than those extracted from the loading branch; the high dispersion in the loading data is a consequence of data issues and calculations with very low data values.

The elastic stiffness extracted from the unloading data varies from 0.73 to 1.62 of the corresponding stiffness obtained with the AISC Specifications, with an average of 1.1 and a standard deviation of 0.20.

More details of these extracted stiffness values in this section for this load case LC1 will be evaluated and discussed integrally with other load cases in Chapter 9.

Table 5.9. Effective flexural stiffness extracted from moment-curvatures during LC1

Specimen	AISC (2010)		Experimental		Ratios	
	C_3	EI_{eff} (kip-in ²)	EI_{expL} (kip-in ²)	EI_{expU} (kip-in ²)	EI_{expL} / EI_{eff}	EI_{expU} / EI_{eff}
1C5-18-5	0.77	341885	302763	405202	0.8856	1.1852
18C5-26-12	0.77	396485	432367	434111	1.0905	1.0949
2C12-18-5	0.74	8509246	8630078	10781215	1.0142	1.2670
6C12-18-12	0.74	10229509	6877299	7923266	0.6723	0.7746
10C12-26-5	0.74	9367575	6956923	8351287	0.7427	0.8915
14C12-26-12	0.74	9803547	11731905	7149629	1.1967	0.7293
3C20-18-5	0.69	40315751	43355559	55151947	1.0754	1.3680
7C20-18-12	0.69	50555345	18228235	54453162	0.3606	1.0771
11C20-26-5	0.69	45410137	35159252	50355301	0.7743	1.1089
15C20-26-12	0.69	49207024	59373195	79799030	1.2066	1.6217
4Rw-18-5	0.75	21081046	21865261	21867369	1.0372	1.0373
8Rw-18-12	0.75	24832498	24983976	27596355	1.0061	1.1113
12Rw-26-5	0.75	22738774	52458353	20996302	2.3070	0.9234
16Rw-26-12	0.75	24214058	33967481	28415197	1.4028	1.1735
5Rs-18-5	0.75	51297809	51297809	51297809	1.0000	1.0000
9Rs-18-12	0.75	62147773	70599870	67194172	1.1360	1.0812
13Rs-26-5	0.75	56209690	62477071	61409086	1.1115	1.0925
17Rs-26-12	0.75	60389479	76290029	68433358	1.2633	1.1332

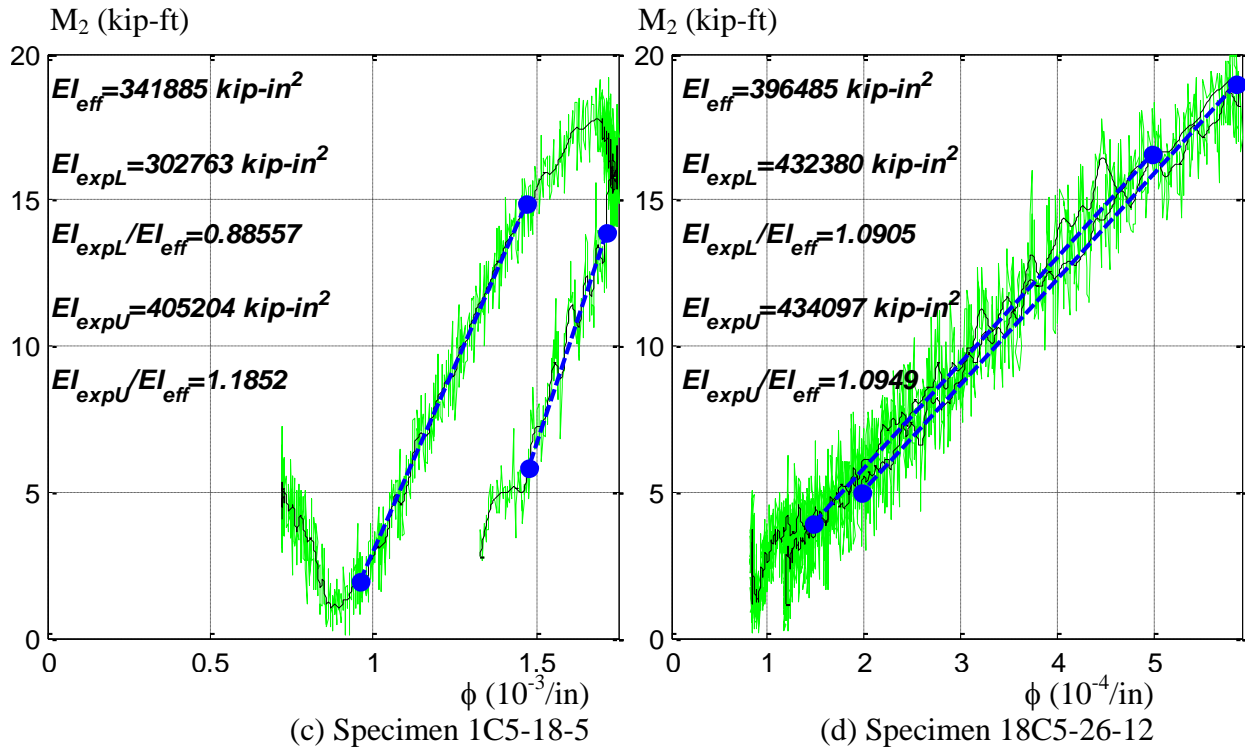


Figure 5.67. Moment-Curvature from LC1 for the C5 set

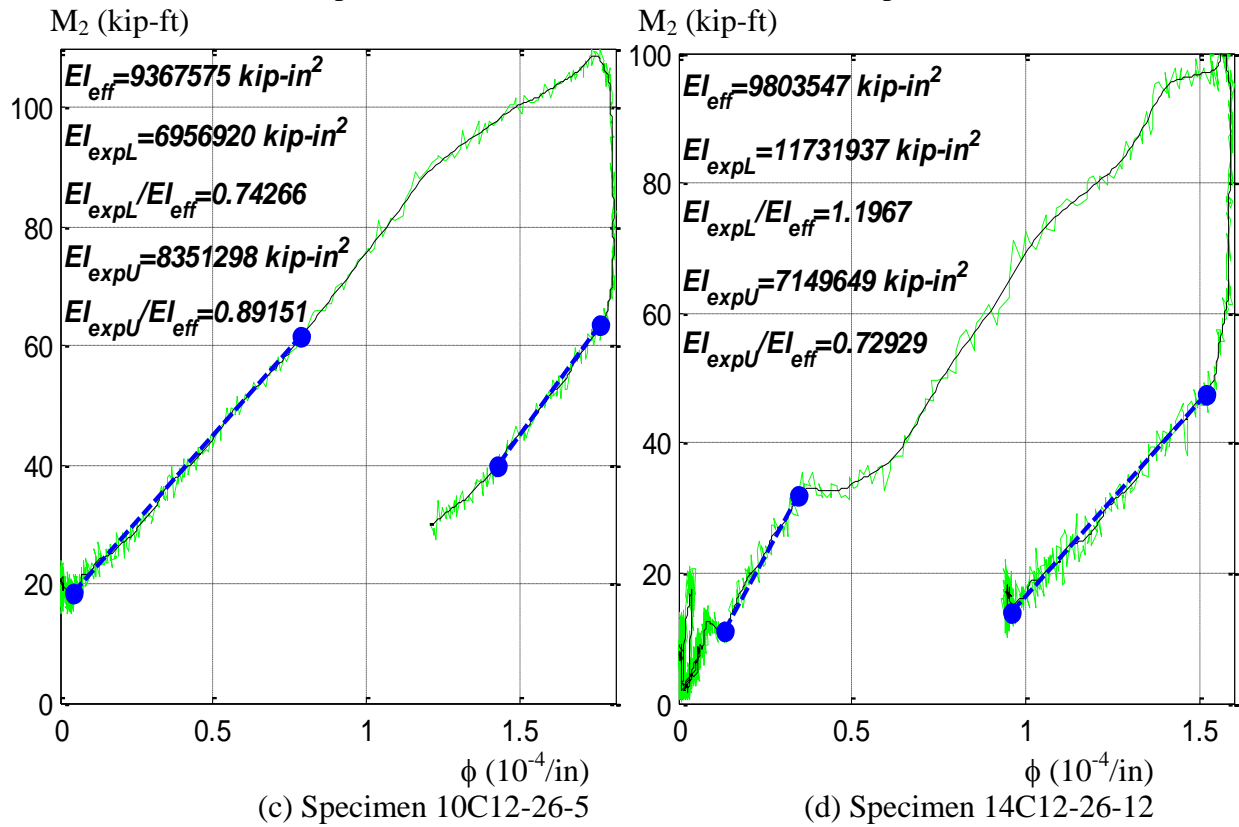
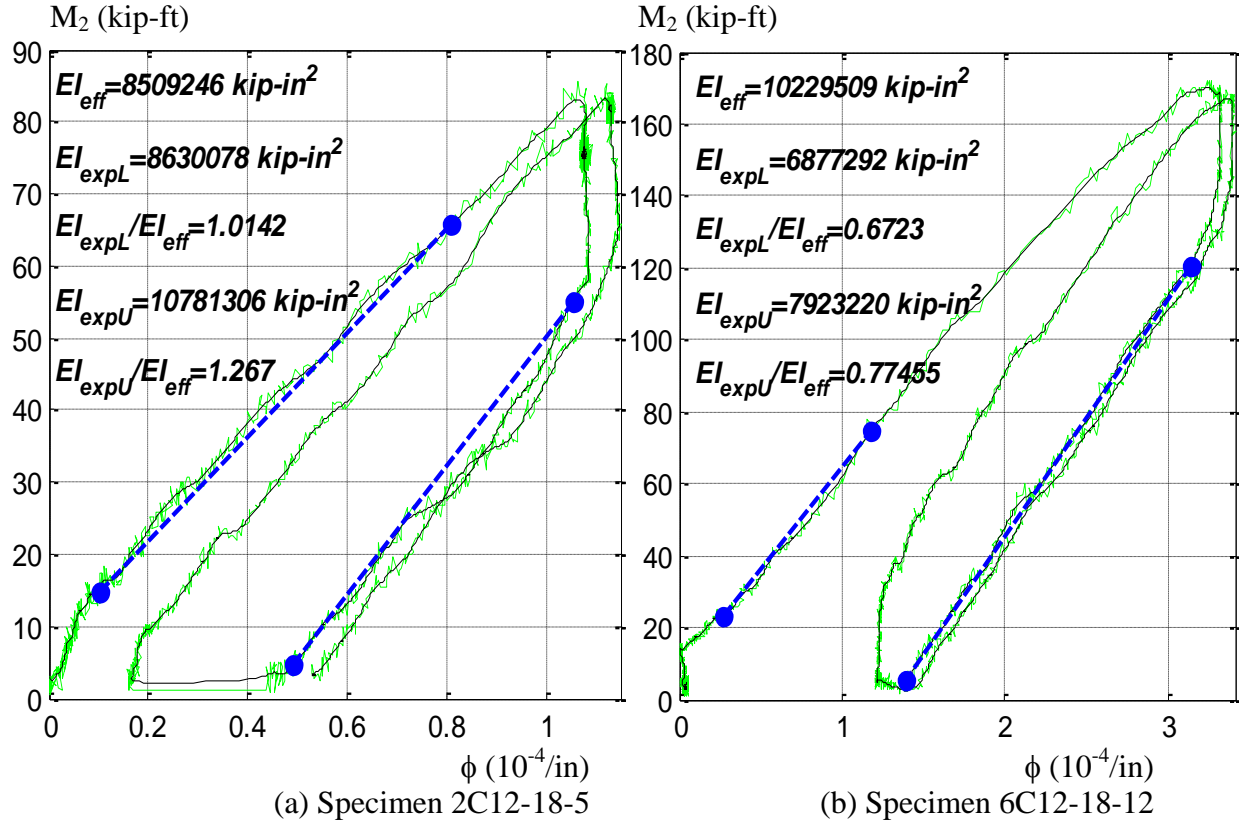


Figure 5.68. Moment-Curvature from LC1 for the C12 set

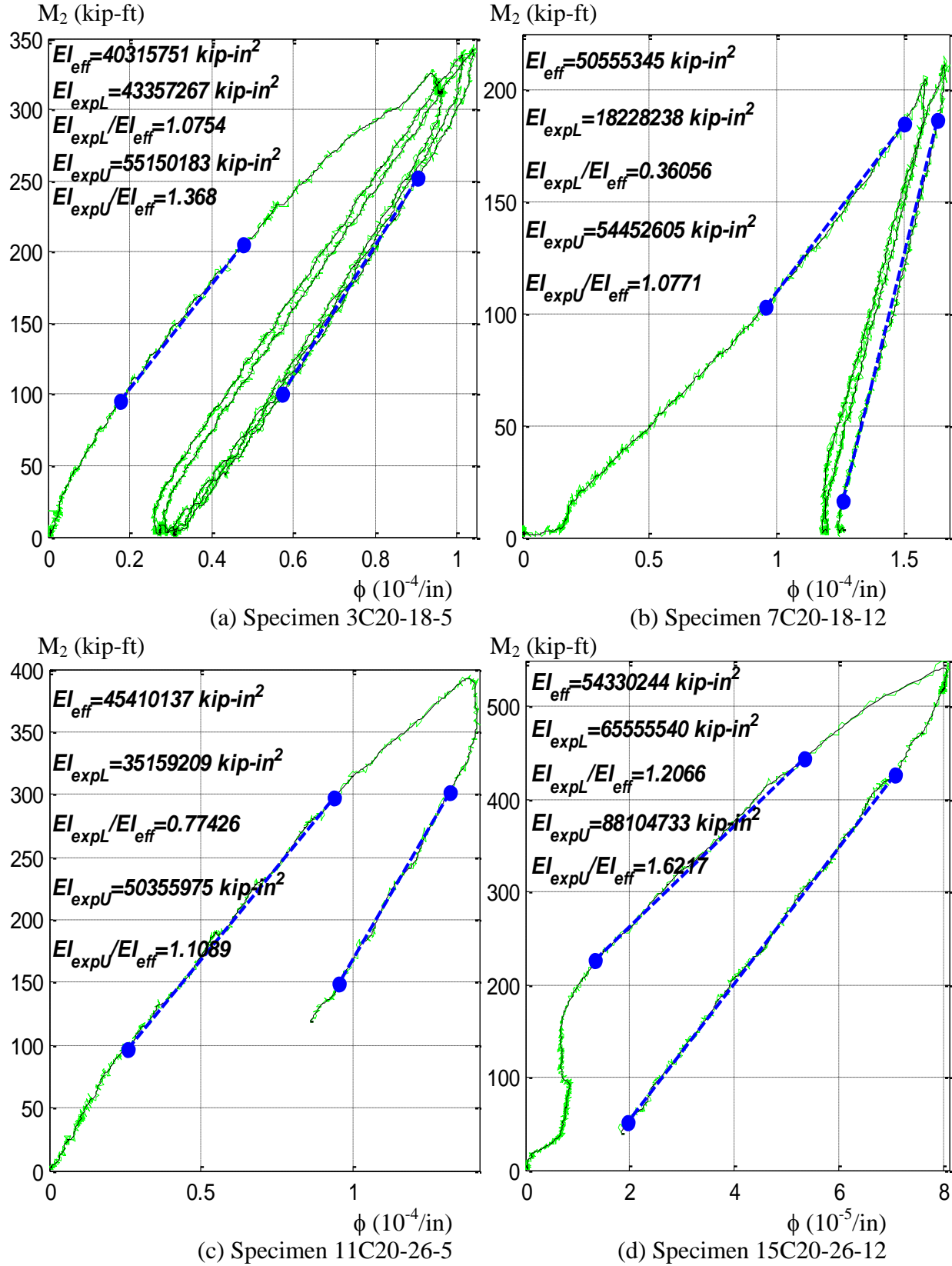


Figure 5.69. Moment-Curvature from LC1 for the C20 set

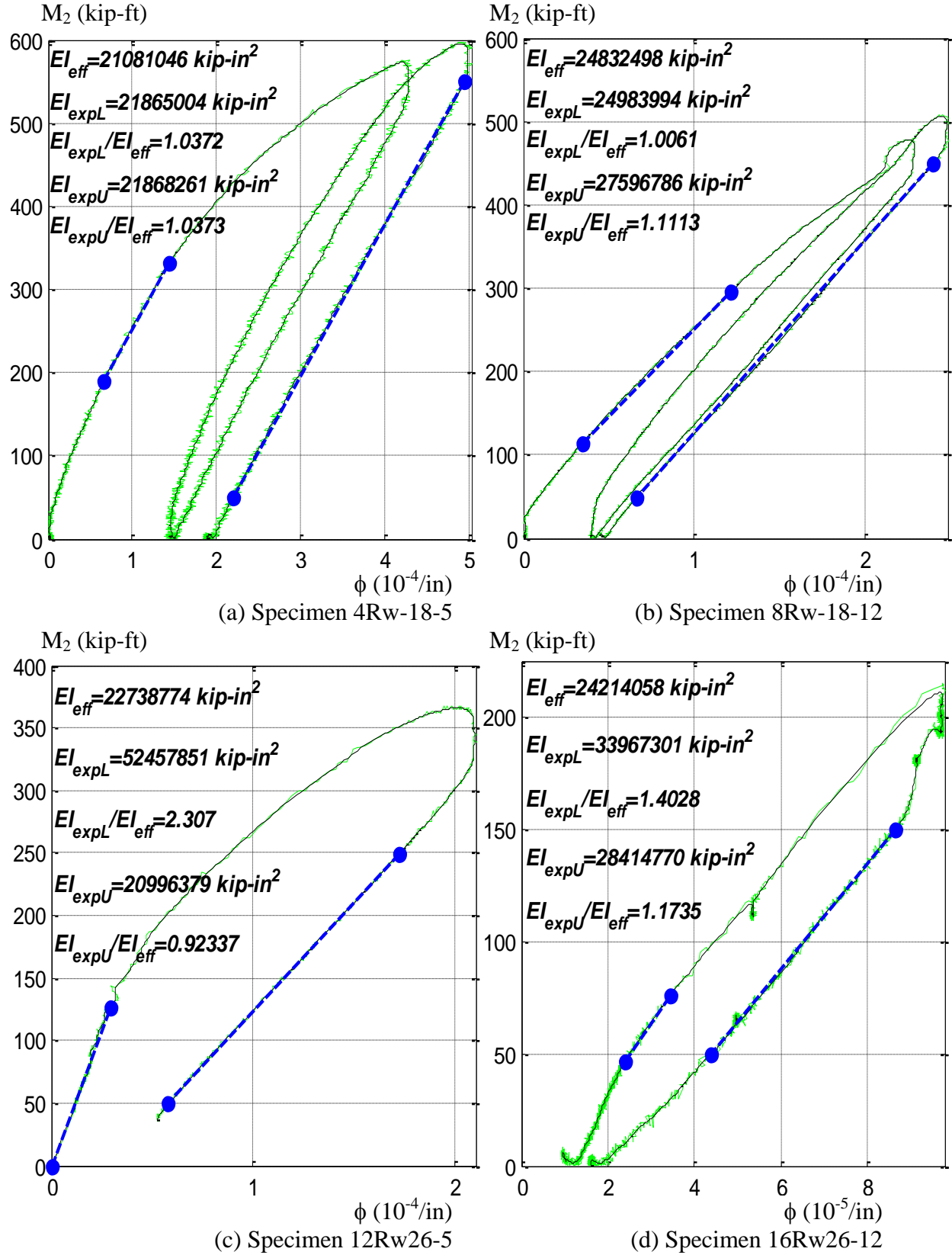


Figure 5.70. Moment-Curvature from LC1 for the Rw set

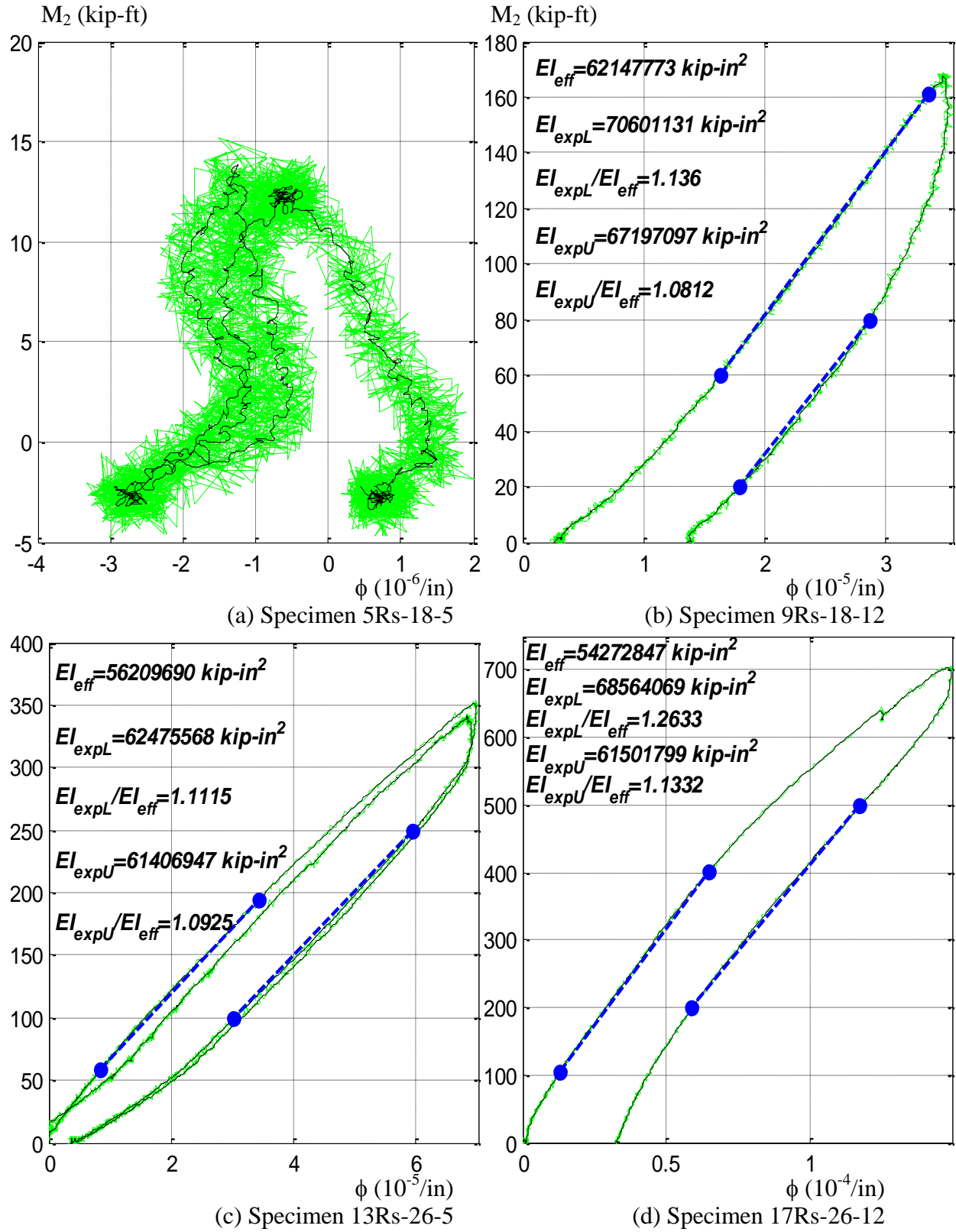


Figure 5.71. Moment-Curvature from LC1 for the Rs set

CHAPTER 6

P-M INTERACTION DIAGRAMS

6.1. Introduction

The main goal of this chapter is the evaluation of the axial load vs. bending moment capacity or P-M interaction diagrams for the CFT beam-columns tested, with emphasis on the stability effects that influence the behavior of slender members.

In order to achieve this goal, the material will be presented as follows:

- Section 6.2 is a brief summary on the determination of interaction P-M interaction diagrams for CFT cross-sections and beam-columns as given in the current AISC (2010) Specifications, as well as some of the theory behind these Specifications.
- Section 6.3 introduces a methodology that discusses the extraction of experimental or analytical values for the maximum axial load vs. bending moment response obtained with an uniaxial and biaxial bending loading as those used in this research project.
- Section 6.4 presents of the experimental test response and the P-M capacity plots extracted from the uniaxial and biaxial tests. The set of P-M experimental points in this section and their comparison with the AISC (2005) prediction are used to calibrate design equations that take into consideration the stability effects in slender beam-columns.
- Section 6.5 presents results from computational analyses that aim to obtain P-M capacities to be used for comparisons with those extracted from the tests. The set of P-M analytical points in this section are also compared with the AISC (2005) prediction.
- Section 6.6 presents a brief review of the main results and the conclusion observed from the evaluation presented in this Chapter.

6.2. P-M interaction diagram by the AISC Specifications

There are two methods allowed in the AISC Specifications (2010) for the determination of the interaction diagrams of composite cross-sections. These methods, first introduced in the 2005 version (AISC 2005a), have been widely used for reinforced concrete sections in the USA, and the ACI-318 code has allowed their use since 1963. These methods are:

(1) *Plastic stress distribution method*: This method, illustrated in Figure 6.1, aims to obtain the ultimate capacity of the cross-section assuming that both steel and concrete have reached their nominal plastic capacity, as there is little remaining strength in the section beyond this point. This method is a simplification of the *strain compatibility method* and assumes either an elastic-perfectly-plastic or fully plastic stress-strain (σ - ϵ) relationship as a material constitutive model for both the steel and concrete. No strain hardening or degradation either in strength or in stiffness is contemplated in this method. The yield stress of the steel in both compression and tension is the nominal F_y . The rectangular compressive block stress assumed for the concrete is taken as having an equivalent stress equal to $0.85f'_c$ (the same that has been given by ACI-318 for reinforced concrete cross-sections) for SRCs and RCFTs. This value is increased to $0.95f'_c$ in CCFTs to account for the superior confinement effect by the circular tube. The contribution of the concrete in tension is neglected. The current AISC procedure does not reduce the size of the compression block to that of an equivalent one as the ACI procedures do (β_1 factor).

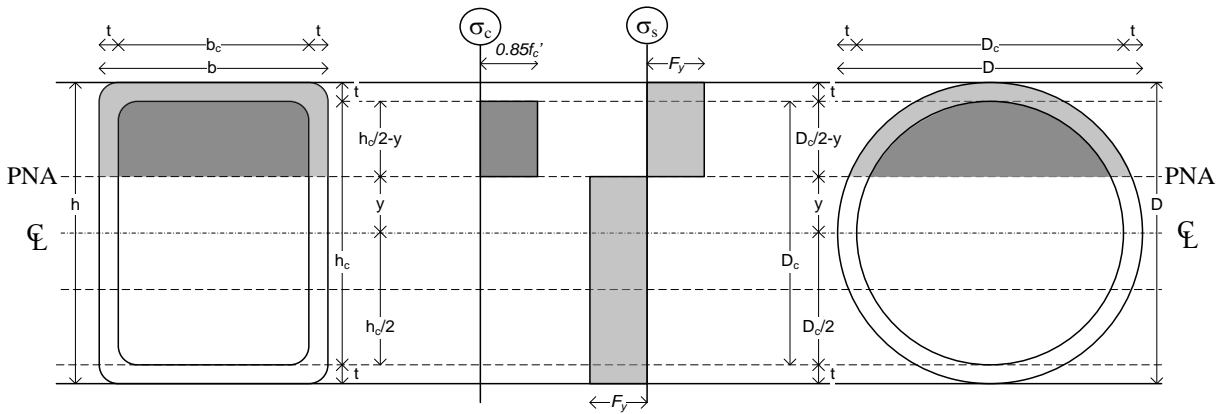


Figure 6.1. Plastic stress distribution method

(2) *Strain compatibility method*: In contrast to the plastic stress distribution method, this approach allows the constitutive material σ - ε models for both the concrete and the steel to be assumed in a more generalized form, as long as they represent the material behavior as supported by experimental tests. The stresses in the cross-section then are defined by the σ - ε model used under the assumption that plane sections remain plane, as shown in Figure 6.2, with an ultimate strain in the concrete of $\varepsilon_c=0.003$. Since any constitutive σ - ε material models validated by tests and analytical investigations are allowed, including models that allow higher ductility due to the confinement effects, the usual strain limit of 0.003 of compression in concrete (ε_c) may be adjusted.

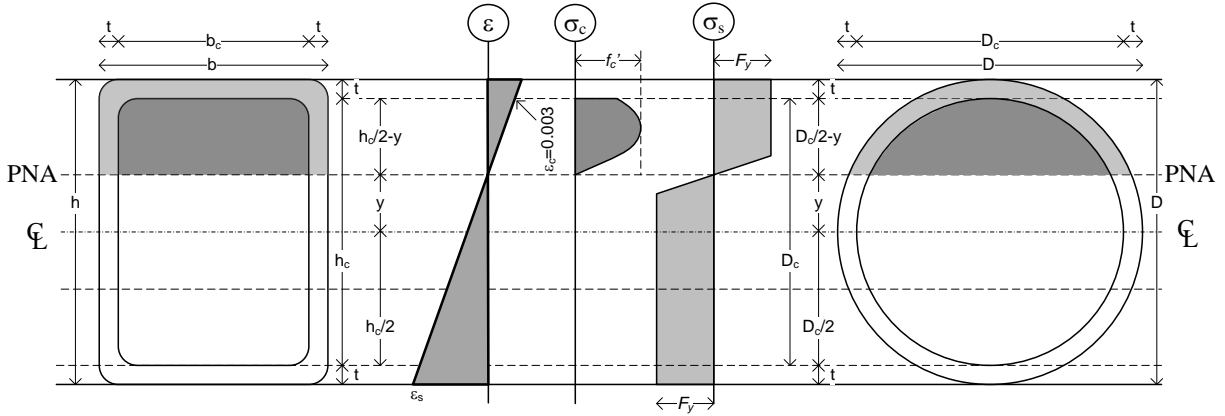


Figure 6.2. Strain compatibility method

A single combination of P and M can be calculated by taking the maximum concrete strain (ε_c), a linear distribution of strains across the section, and the corresponding stresses from the σ - ε material model. By sweeping the position of the neutral axis through the cross section, a set of continuous points of resultant forces and moments (P - M) can be calculated. This set of points are illustrated in Figure 6.3 by the continuous curve, which defines the P - M interaction diagram obtained for the cross-section with the *strain compatibility method* for the case where $\varepsilon_c=0.003$. If elastic-perfectly-plastic or fully-plastic σ - ε behavior is chosen as constitutive material models for both the steel (with F_y as plastic stress) and concrete (with a plastic stress of $0.85f'_c$, or $0.95f'_c$ for CCFTs), the continuous curve obtained with the *strain compatibility method* passes over the AISC (2005) anchor points A-E-C-D-B obtained with the *plastic stress distribution method* assuming key positions of the neutral axis.

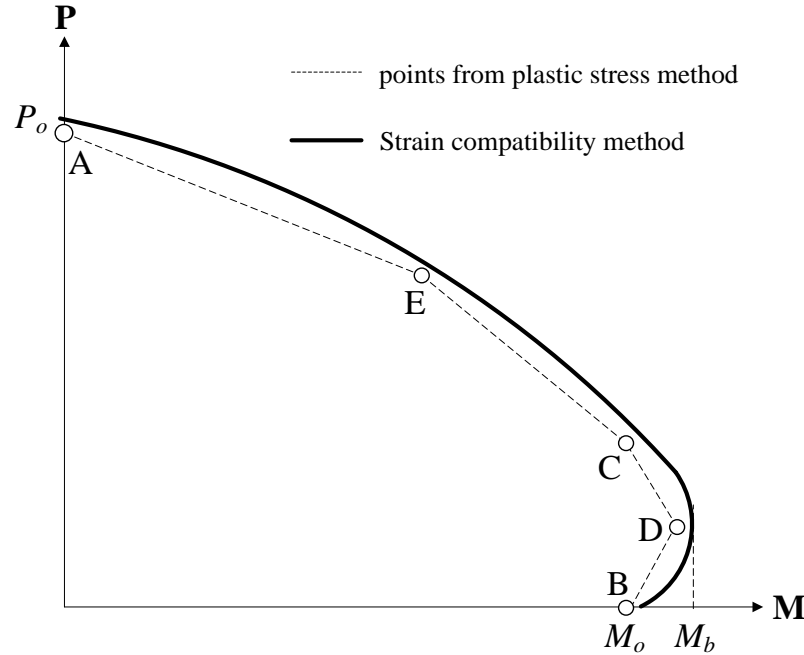


Figure 6.3. *P-M interaction diagrams obtained with the plastic stress method and the strain compatibility method*

Figure 6.4 shows the contribution of the individual materials (steel and concrete) to the overall strength (composite) for three different RCFTs varying from a steel-dominant to a concrete-dominant cross-section using the fully plastic stress method. Note the symmetry of the concrete contribution (with no tensile strength) about a value equal to half of its compression capacity ($P = P_c/2 = 0.85f'_c A_c/2$) and that of the steel about the no axial load line ($P=0$). Figure 6.4.c is a good example of the synergic effects when these materials are combined as evidenced by the increasing axial capacity of the concrete component and the flexural capacity with the steel component. For this composite cross-section, the transition to the fully plastic interaction diagram is shown in Figure 6.5 for the steel component and in Figure 6.6 for the concrete component. Key locations of the plastic neutral axis (PNA) and the compression side (shaded) are shown in these figures as well. In Figure 6.5, the effect of the concrete increases the pure axial capacity by $P_c=0.85f'_c A_c$, while for the balance point this increment is $P_c/2$ of axial load capacity and $0.85f'_c Z_c/2$ of moment capacity; the derivation and components of these expressions are shown in the next section. Figure 4 shows a similar diagram but emphasizing the influence of the steel; in this case, the effect seems to be greater on the bending rather than the axial moment capacity.

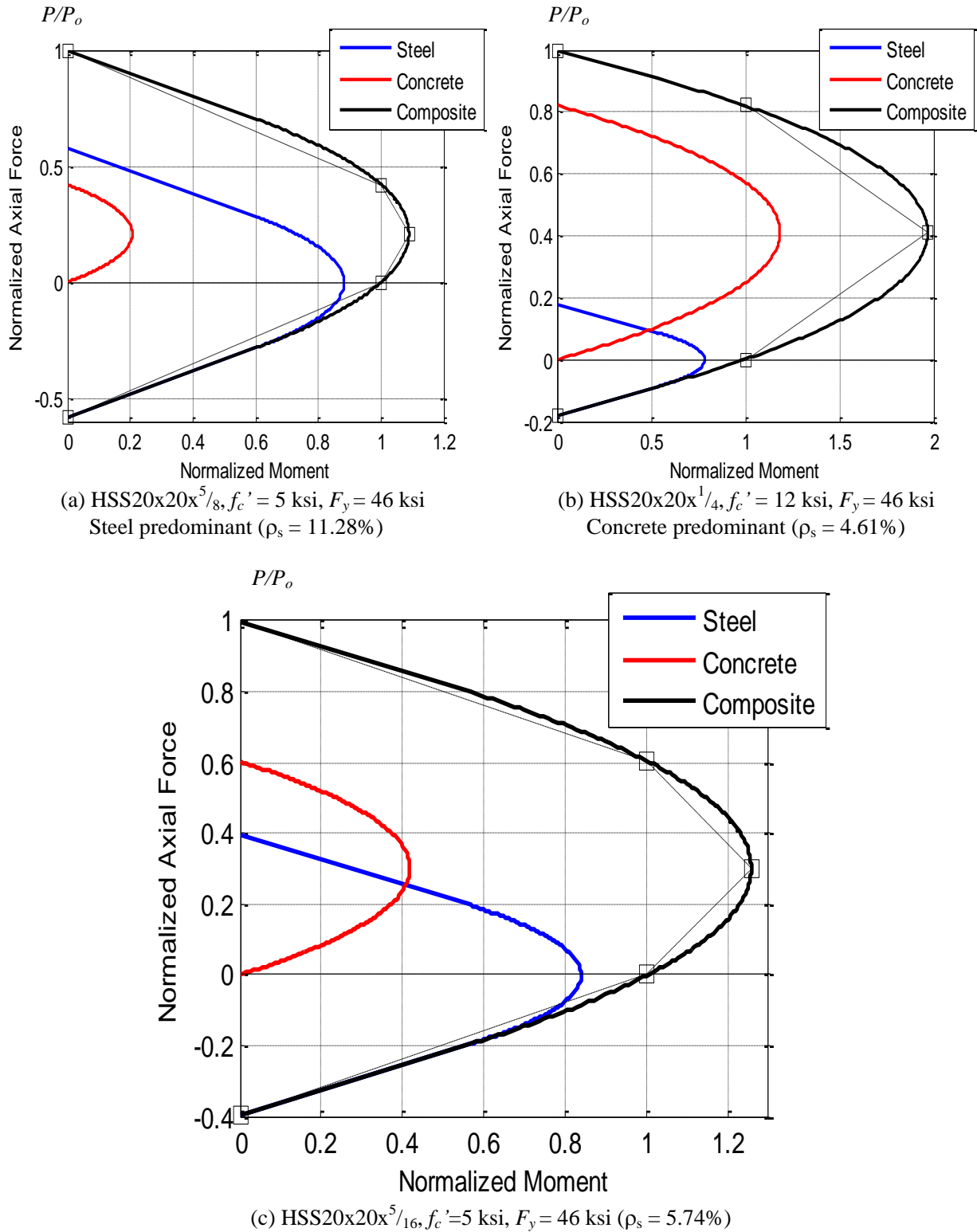


Figure 6.4. Components of the interaction diagram: fully-plastic stress method to RCFTs

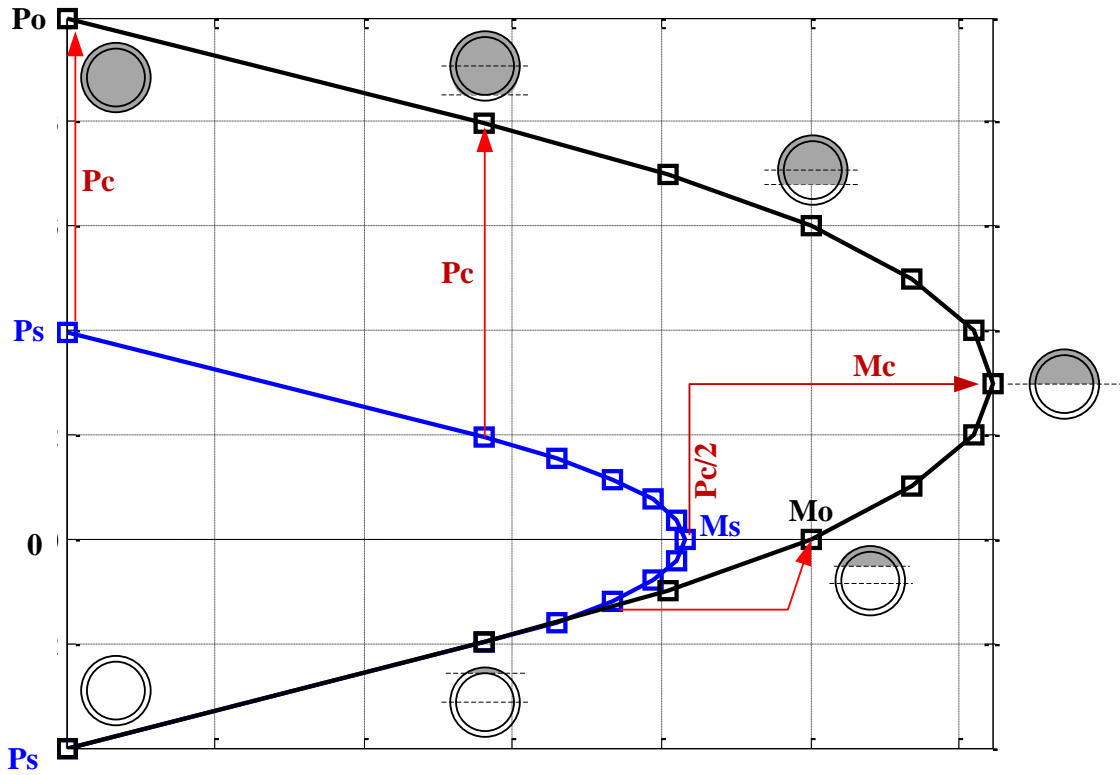


Figure 6.5. Transition of the plastic interaction diagram from the steel component on CFTs

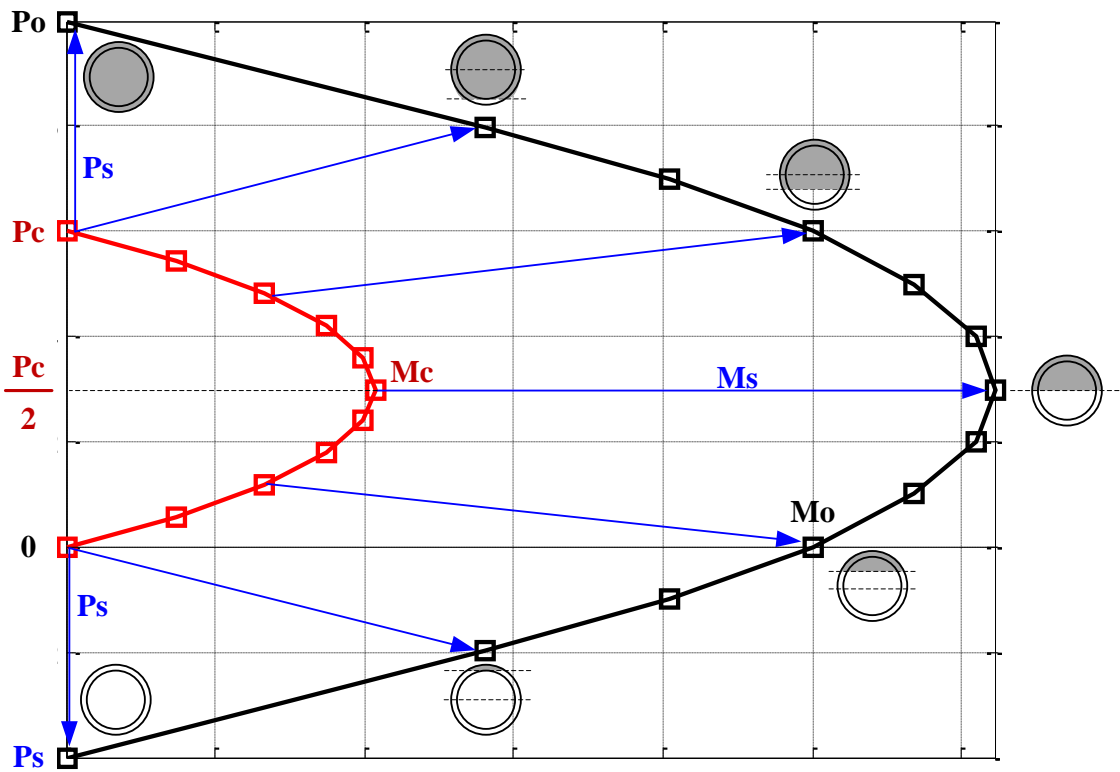


Figure 6.6. Transition of the plastic interaction diagram from the concrete component on CFTs

Based on the *plastic stress distribution method*, simplified equations for characteristic cases on simple cross-sections (symmetric and simple reinforcement distribution) are available in the *AISC Design Examples (2005)*. The characteristic or anchor points for conventional composite cross-sections evaluated by AISC include the following cases:

- Point A is the column case, when there is no bending, and so the cross section is in pure compression. The value of compression P_A is equal to the squash load P_o . As shown in Figure 6.5 and Figure 6.6, for CFTs with no longitudinal reinforcement, this capacity is equal to the superposition of the steel and the concrete capacities.

$$P_A = P_o = P_s + P_c = A_s F_y + C_2 A_c f_c ' \quad (6.1)$$

The coefficient C_2 proposed in AISC (2005) is 0.85 for RCFTs and 0.95 for CCFTs.

- Point B is the beam case when, contrary to the previous case, there is no axial force and the cross-section is in pure bending. The pure bending moment (M_B) is the plastic moment of the cross-section (also referred to as M_o).
- Point D is the balanced case for the beam-column, when both the steel yields and the concrete crushes simultaneously. This point (P_D, M_D) corresponds to the highest plastic bending capacity (M_D) of the cross-section, which occurs when the plastic neutral axis (PNA) is located at the centroidal axis. As shown in Figure 6.5 and Figure 6.6, the strength for CFTs (with no reinforcement) is equal to the concrete capacity axially and the superposition of steel and concrete flexural capacity for flexure.

$$P_D = \frac{P_c}{2} = \frac{C_2 A_c f_c '}{2} \quad (6.2)$$

$$M_D = M_s + M_c = Z_s F_y + \frac{1}{2} Z_c f_c '$$

- As illustrated in Figure 6.5 and Figure 6.6, Point C has mirrored stresses to those of the pure bending point where, after some algebraic operations, it can be shown that this point (P_C, M_C) is defined for CFTs with no reinforcement by the concrete capacity (P_c) and the moment of pure bending capacity (M_B).

$$\begin{aligned} P_C &= P_c = C_2 A_c f_c ' \\ M_C &= M_B \end{aligned} \quad (6.3)$$

- Point E is an optional intermediate case between points A and C. For some cross-sections with certain geometries, the point E is very close (but always above) the straight line between the points A and C. This point E is useful mainly for SRC under weak axis bending and CFTs dominated by the steel contribution, where there is a non-linear transition between the points A and C.

Thus, the union of those characteristic neutral axis locations, or anchor points, by straight lines, as illustrated in Figure 6.7 and Figure 6.8 by the dash-dot multiline A-E-C-D-B or A-C-D-B, defines the P-M interaction diagram obtained for the cross-section with the plastic stress distribution method. For asymmetric or more complex cross-sections, the *strain compatibility method* should be used. Even for that case, however, the overall shape of the interaction diagram does not change significantly from those shown in these figures.

Using either the *plastic stress distribution* or the *strain compatibility* method for the P-M interaction diagram of the cross-section, the axial capacity should be multiplied by a reduction factor (χ) that accounts for the stability effects (i.e. the geometric and material non-linearities, the initial imperfection and the steel residual stresses) on the P-M interaction diagrams of beam columns. The stability reduction factor ($\chi=P_n/P_o$) is calculated for the pure compression condition (Figure 6.7), where the squash load (P_o) at point A is reduced by Equation 5.1 to the critical load (P_n) at the point A_λ . As illustrated in Figure 6.7, the point C obtained with the stress distribution method is also reduced by χ to the points C_λ . In addition, all the calculated points from A to C should be also reduced by the χ factor. Since the reduced balance point D drops outside of the P-M cross-section envelope, the bulge defined by C-D-B is neglected and replaced with a straight line defined by C-B. Thus, the P-M interaction diagram of the beam-column from the plastic stress distribution method is defined by the points A_λ - E_λ - C_λ -D (discontinuous line for the beam-column strength in Figure 6.8), or simply by the bilinear A_λ - C_λ -D interaction diagram (called *P-M Simplified* in the AISC-05 Specifications). As shown in Figure 6.8 (continuous curve for the beam-column strength), the set of points between A and C obtained with the strain compatibility method should be reduced by the stability factor χ to A_λ and C_λ , respectively, and a straight line from D to C_λ (without the bulge) drawn to complete the diagram. The P-M interaction diagram for composite beam-columns is then defined by the shaded area shown on Figure 6.7 and Figure 6.8. Depending on whether LRFD or ASD is used, the P-M envelope

circumscribed by A_λ - C_λ -D then is reduced by the corresponding strength reduction factors ($\phi_c=0.75$, $\phi_b=0.90$) or the safety factors ($\Omega_c=2.00$, $\Omega_b=1.67$) for design purposes. The P-M interaction diagram by the AISC Specifications for composite beam-columns was established based on calibration with previous experimental data (Leon, Kim and Hajjar, 2007).

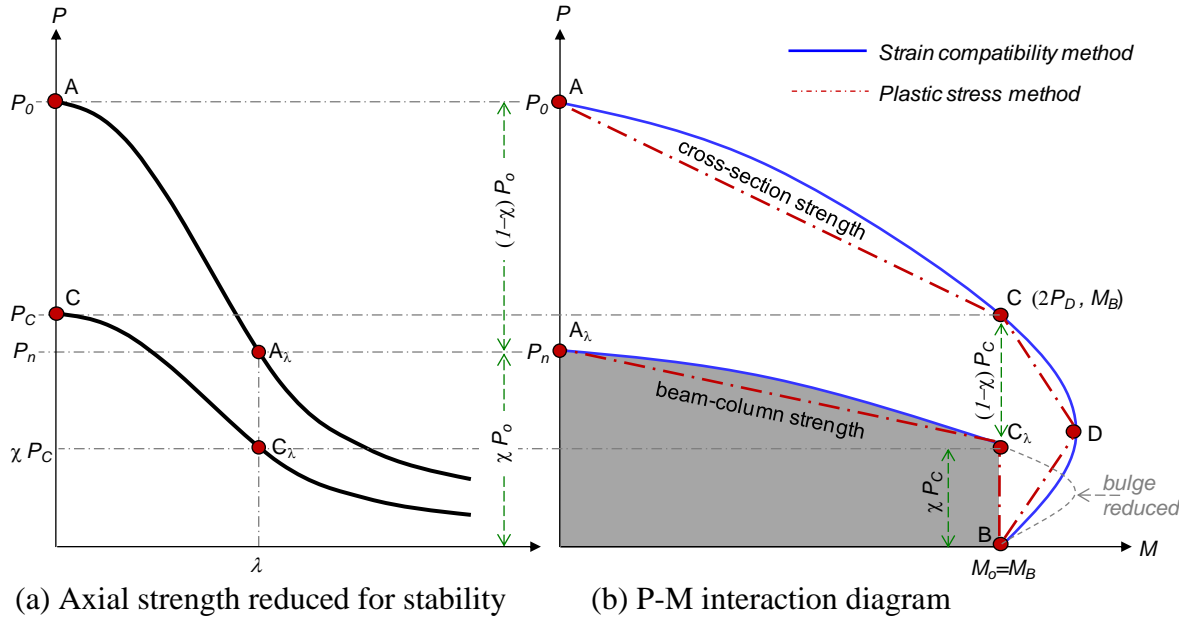


Figure 6.7. Reduction by the AISC (2005) Specifications on the P-M cross-section by the stability effects factor χ to get the P-M strength on composite beam columns

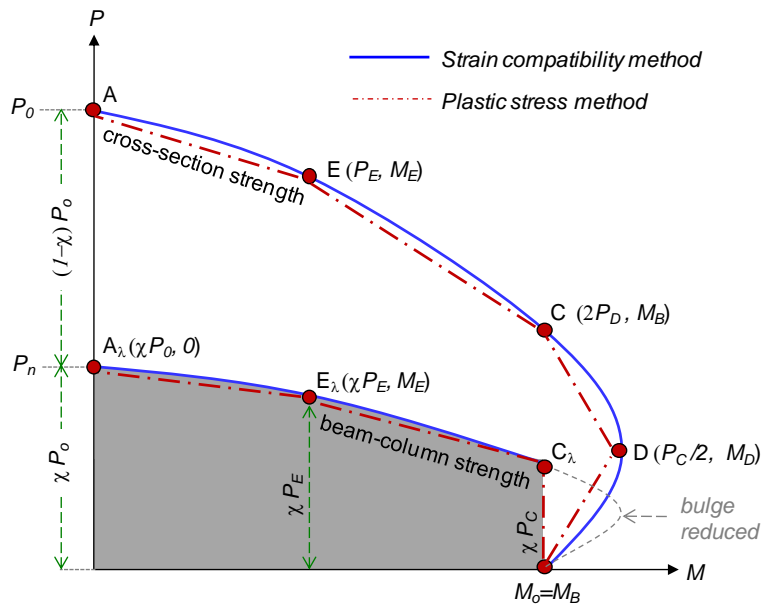


Figure 6.8. P-M interaction diagram for composite cross-sections (stocky columns) and beam columns (reduced by stability effects) by the AISC (2005) Specifications

6.3. Methodology for the determination of the P-M interaction diagram of beam-columns

As illustrated previously, the envelope of the maximum axial-flexural strength of the cross-section only accounts for the material non-linearity (i.e. yielding, strain hardening, residual stresses). However, as the element increases in length, stability effects (or the geometric non-linearities) reduce the beam-column capacity.

The determination of the interaction diagram for a beam-column is defined then by the envelope of its maximum stable capacity when the axial force and flexural bending are acting simultaneously. This maximum stable capacity can be obtained by increasing both the P and M loading components simultaneously (as in path A in Figure 6.9), or increasing one component holding the second one (as in path B in Figure 6.9), or a combination (as in path C in Figure 6.9) until an unstable condition arises (i.e. an abrupt displacement or failure). Figure 1.9 implies load path independency in the determination of the P-M interaction diagram of beam-columns. For reasons associated with controlling the test, holding the gravity load at a constant value and then increasing the bending moment up to the latest stable condition (as either in path B or C in Figure 6.9) was chosen for this research and used for both the experiments and the second-order inelastic analyses. From now, this approach is called the *maximum stable moment method*.

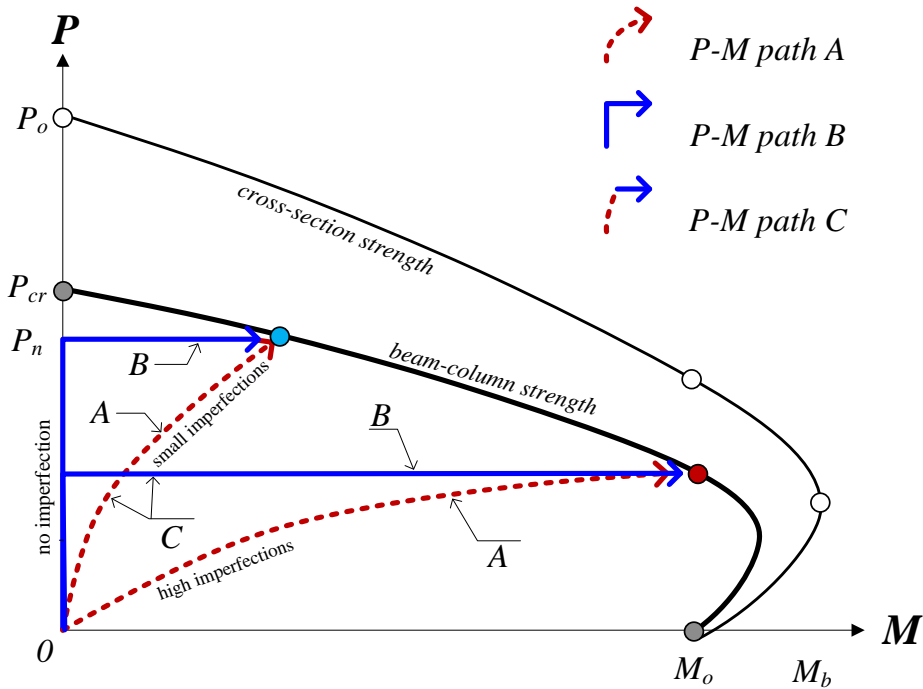


Figure 6.9. P-M paths to approach the beam-column capacity

The *maximum stable moment method* is schematically illustrated in Figure 6.10 and Figure 6.11. Suppose we have straight fixed-free beam-column with a given length, as that illustrated in Figure 6.10 – case 1, with no initial out-of-plumbness and subjected to a constant gravity force (P , between zero and the buckling load P_{cr}). If this beam-column is then subjected to an incremental lateral force F_e , as illustrated in Figure 6.10 – case 2, the base would be subjected to an overturning or first order moment, approximately equal to $F_e L$, plus a second order moment given by $P\Delta_e$. This total second order moment M_{2e} can be resisted elastically by the beam column if the lateral load is relatively low. However, as the lateral force increases, plasticity at the base starts being distributed as concrete cracks and crushes and the steel yields and strain hardens. This plasticity grows due to the overturning moment, and this growth is accelerated by the $P\Delta$ moment. At some point, as shown in Figure 6.10 – case 3, the beam-column runs out of capacity so it cannot carry additional lateral force beyond a peak force F_p . At this peak lateral load, the cross-section may not be fully plasticized, so there is some remaining capacity at the cross-section level. However, the beam-column is in a condition where, given the sustained compression force, a small increment of lateral force would abruptly increase the lateral displacement, resulting in failure. Under a sustained axial load, a stable conditions could be maintained only if the lateral force is decreased by either (a) unloading the lateral force, or (b) shifting the control from load to displacement, which tends to have a reduction on the lateral load with higher displacements as shown in Figure 6.10 – case 4. For the second case, even though the overturning is decreasing in the post-peak range, the $P\Delta$ moment would be increasing at a higher rate such the base moment would eventually reach the cross-section capacity (M_{cs} for the given axial load P).

For the tests carried out in this research, the second case (option (b) above) was used. Thus, given an axial load P on a beam-column with given length L , the maximum safe moment (M_{2p}) is governed by the stability of the element through its maximum capacity to lateral forces (case 3 in Figure 6.10). If this process is repeated with different values of sustained axial forces (P) on a beam-column with the same length (L), the envelope or the interaction diagram axial force – stable moment (P - M_{2p}) can be defined for the beam-column as shown in Figure 6.11 (curve with the label *beam column total strength*). Figure 6.11.b also shows the bending diagram for this fixed-free beam-column (Figure 6.11.a), where the first order moment (FL) and the second order moments ($P\Delta$ and $P\delta$) are illustrated. Figure 6.11.c shows the contribution of the

overturning moment (FL) and the second order moment ($P\Delta$) at the base (critical cross-section for this case) for different values of axial loads (P). In addition, Figure 6.11.c. illustrates the extreme cases for pure bending, when there is no second order moment due to the absence of axial load, and the pure compression case with no imperfections, when there is no capacity for lateral forces because the column force is equal to the buckling load (P_{cr}) of the straight column.

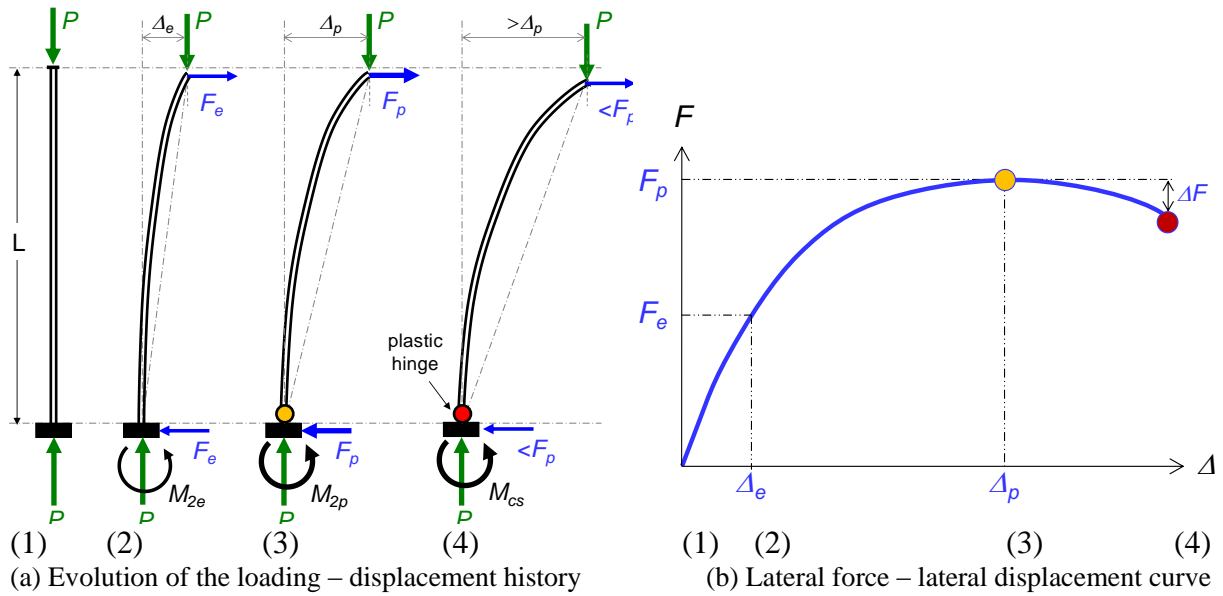


Figure 6.10. Beam column under axial-flexural loading

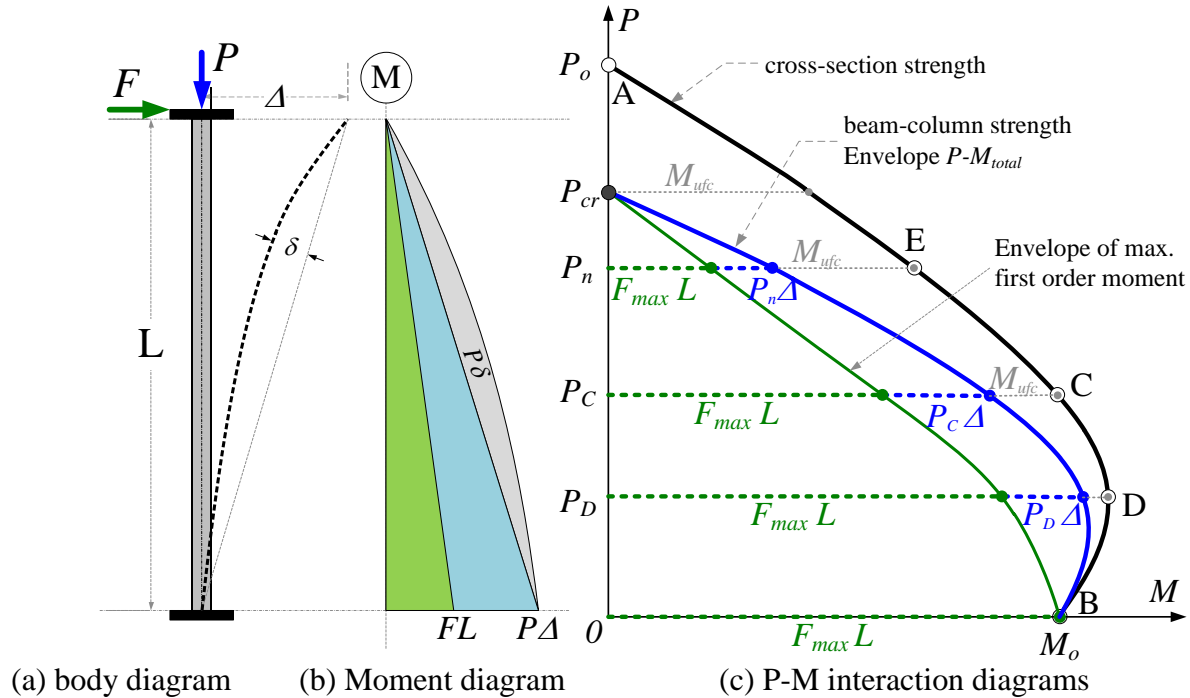


Figure 6.11. Reduction in the P-M interaction diagram to account stability effects

As previously said, the P-M interaction diagram (from the *strain compatibility method*) for a cross section in Figure 6.11.c (continuous black curve A-E-C-D-B) takes into account the material non-linearities (i.e. concrete cracking and crushing, and steel yielding and residual stresses). With the *maximum stable moment method*, the P-M interaction diagram for a beam-column in Figure 6.11.c (continuous blue curve) includes also the geometric nonlinearities. Thus, the stability effects reduced the cross-section capacity for straight beam-columns from P_o to P_{cr} in axial capacity and by M_{ufc} in flexural capacity (Figure 6.11). M_{ufc} is the unusable flexural capacity between the cross-section and the beam column strength due to stability effects, and it is proportional to the axial load.

This approach allows a clear separation of the contributions of the geometric imperfections, taken as the combined effects of Δ_0 (initial out-of-plumbness) and δ_0 (initial out-of-straightness), to the experimental results. Moreover, since these combined effects lead to high moment amplifications as the peak lateral load is approached, the use of the MAST testing system allows for a clear separation of these components, as the forces (P and F) and the displacement (Δ) are tracked independently. It is important to keep in mind that the actual imperfections reported in Chapter 5 (See Figure 5.4) are very different from those used for design purposes by AISC. Thus extreme care will be needed when trying to compare these experimental results to predicted, or design values, given by AISC. This issue is addressed in detail in a following section.

As discussed in Chapter 5, initial imperfections (controlled by tolerances in codes) reduce the axial load capacity on columns. Figure 6.12 is an adjustment of Figure 6.11 that includes the effects of the initial out-of-plumbness. Following the same approach, the axial load P now applied on an element with given length L and initial out-of-plumbness Δ_o . As shown in this figure, the application of the desired axial load follows the P - M_{imp} path indicated with the continuous red line going from zero to the maximum stable capacity P_n - M_{imp} . After this maximum stable condition is reached, the P - M path softens following the beam-column P - M interaction diagram. As defined in Chapter 5, P_n is the nominal pure compression load of the column with a given out-of-plumbness, and P_{cr} is the critical buckling load of a straight column.

Following the load path C in Figure 6.9, the maximum stable capacity can be reached by incrementing the axial load to the target value ($P < P_n$) on the column with the initial imperfection

moment, and then by holding P while moving towards the incipient instability point by increasing F or the lateral displacement. The total capacity following this path C would be the same than that obtained with the path B in Figure 6.9 on the straight column case. Notice that the imperfections reduce the usable moment by consuming some of the available moment. The net, or usable, moment (shaded area in Figure 6.13.a) is then given by the flexural capacity between the total moment and the moment consumed by the initial imperfection. In other words, the net moment is equal to the total stable strength reduced by the moment used by the imperfection (shaded area in Figure 6.13.b). Ideally, with an initial imperfection equal to the maximum tolerable value ($L/750$ to $L/500$ for out-of plumbness, $L/1500$ to $L/1000$ for out-of-straightness), the resultant P - M_{net} interaction diagram should be compatible with the P - M Simplified diagram (A_λ - C_λ -D in Figure 6.8) proposed by the AISC (2005) Specifications.

In this research, the terms P - M_{total} or *total beam-column strength* refer to the maximum strength reduced by the stability of straight elements, and the terms P - M_{net} or *net beam-column strength* refers to the maximum strength reduced by the stability of elements with imperfection.

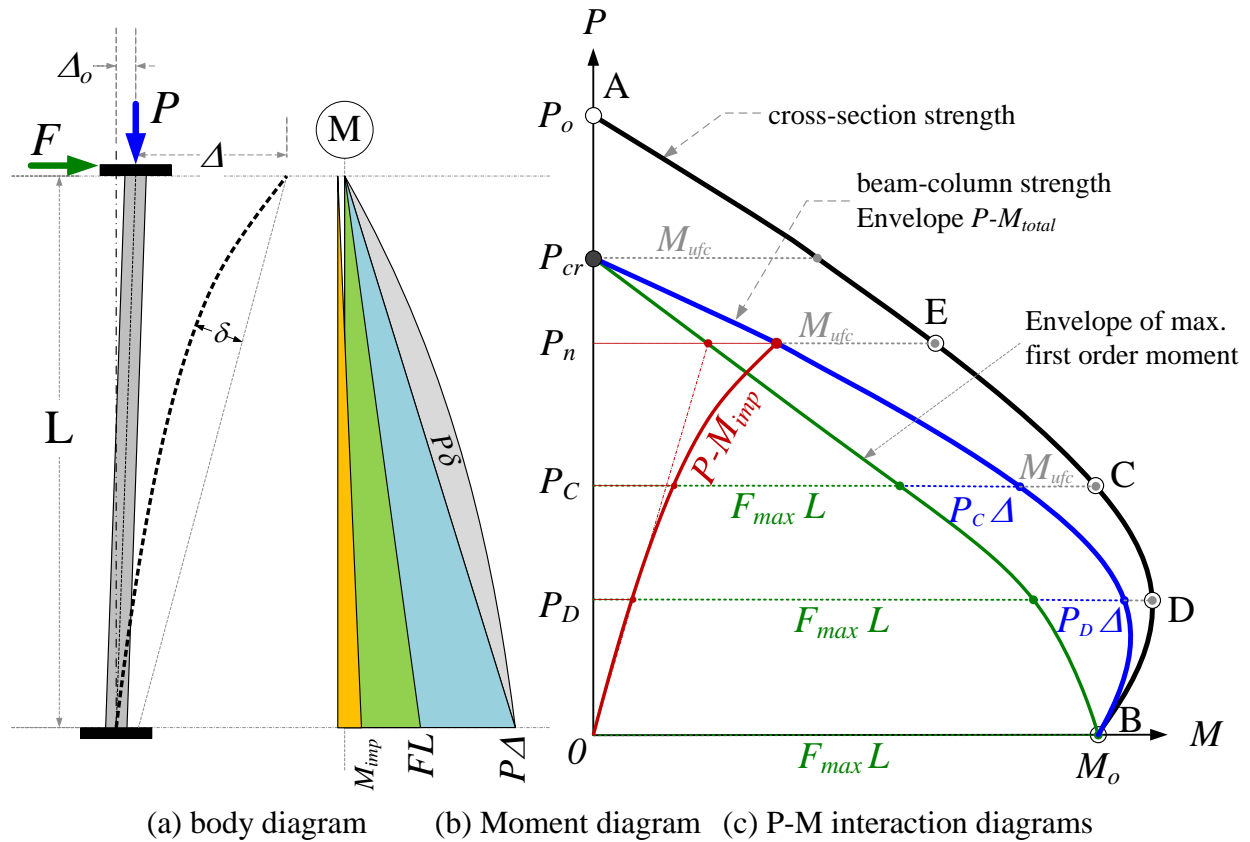


Figure 6.12. Reduction in the P - M interaction diagram to account initial imperfection

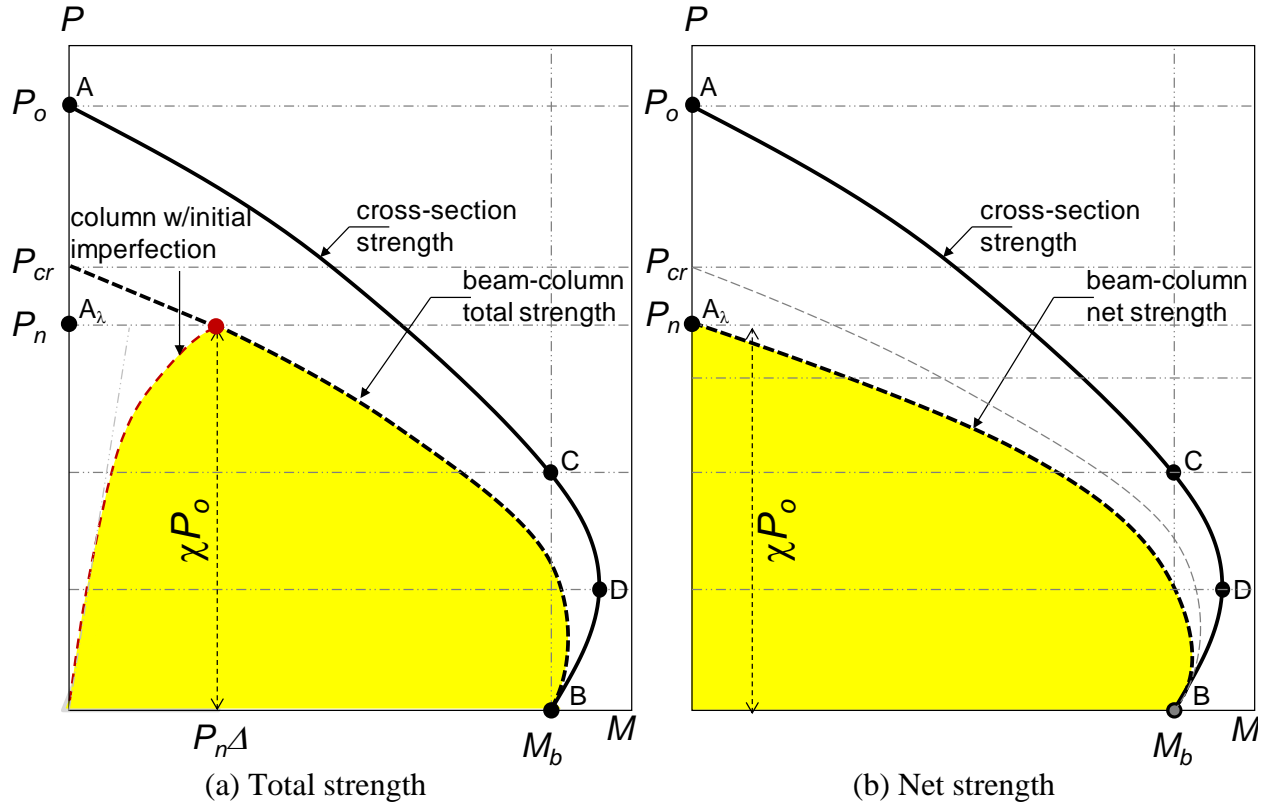


Figure 6.13. Total vs. Net P - M interaction diagrams

The methodology of reducing the total strength by the imperfection effects was originally applied in steel beam-columns to calibrate the interaction equations (H1) of the AISC Specifications (Suroveck-Maleck and White, 2004). The total strength was obtained from second order inelastic analysis on a number of sensitive benchmark frames with straight elements. These analyses, performed by Kanchanalai in 1977 (Suroveck-Maleck and White, 2004), accounted for the spread of yielding and residual stresses (Figure 6.14.a). The effects of the initial imperfection were separately accounted afterward by reducing to the total strength (M_2/M_p), for each level of gravity, the second order imperfection moments of a pinned-pinned column with a given imperfection (Figure 6.14.a). The resultant differences for each level of gravity are net moments (*net* M_2/M_p) where the used up flexure by the imperfection has been removed, and then obtaining the net or available capacity (Figure 6.14.b).

Based on the latter results, Figure 6.15 shows different components of the P-M interaction diagram in steel members. In this figure, the cross section capacity is the curve delineated by the anchor points at unity in both axial force and moment. It also includes the P-M diagram obtained from the second order inelastic analyses of steel beam-columns, and the P-M path from second order inelastic analyses of a steel column. These curves clearly define 4 area components:

- (1) A zone where steel beam-column is unstable due to gravity loads, i.e., the zone above the critical loading P_n (light grey area)
- (2) A region of available flexural capacity in the cross-section but unusable for the beam-column due to member stability effects (dark gray area). Segments 1 and 2 are together the total reduction due to the stability effects.
- (3) A region of flexural capacity consumed by the imperfections (aqua blue area)
- (4) The residual area that is the net P-M capacity in the beam column reduced for stability, residual stress and imperfections (yellow area).

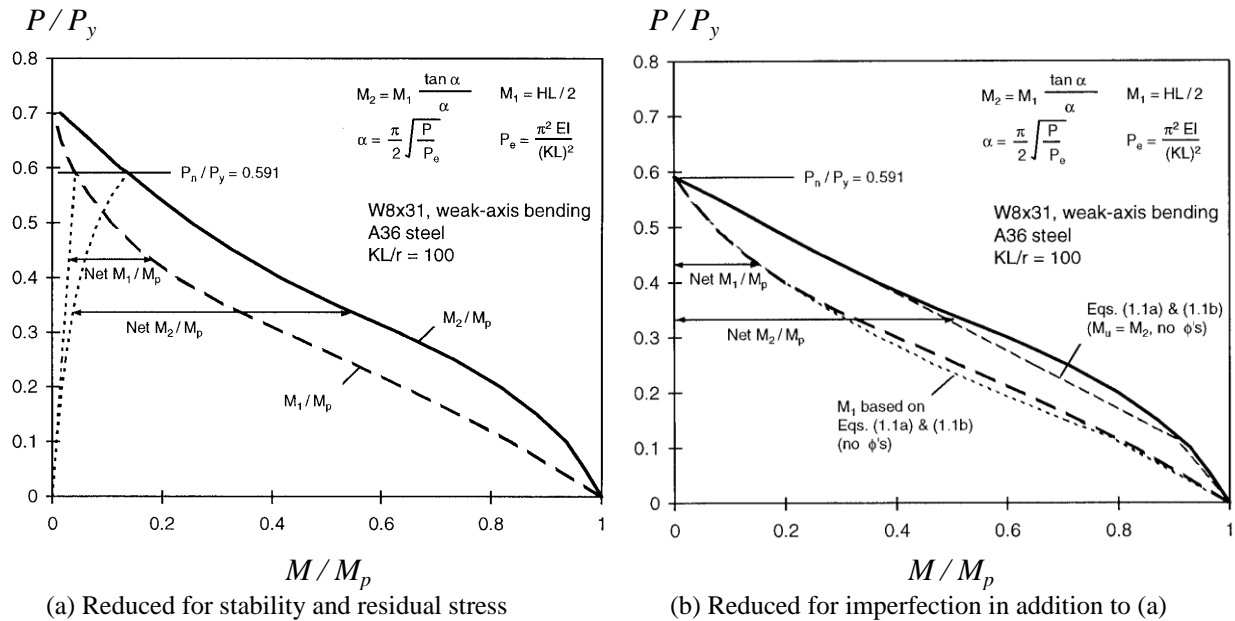


Figure 6.14. P-M interaction diagram used for calibration of steel beam columns (ASCE 1997)

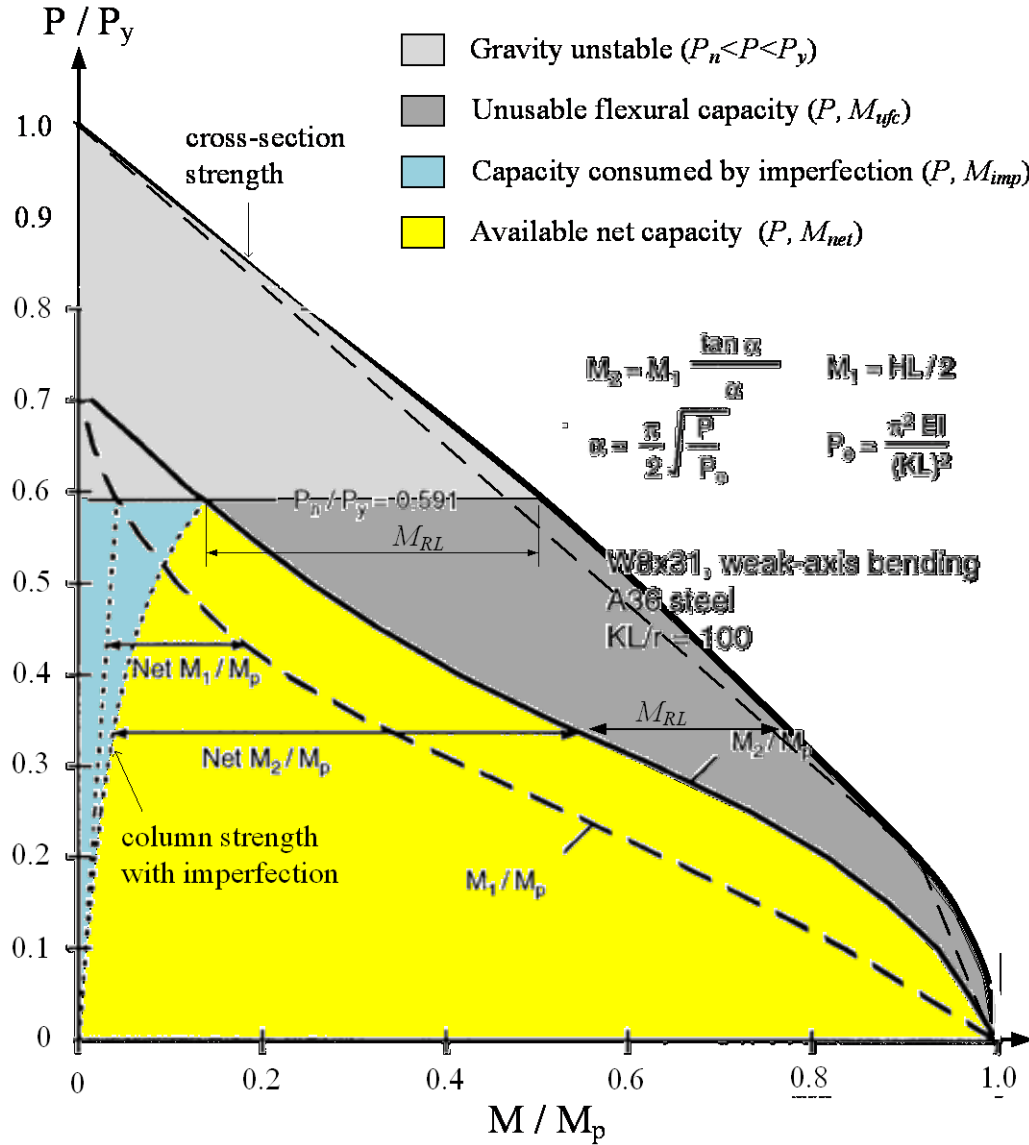


Figure 6.15. Components of the P-M interaction diagram for steel members

The previous components are also identifiable for composite members as illustrated in Figure 6.16, where the net P-M capacity in composite beam-columns is the P-M capacity of the cross-section reduced by the areas of instability due to gravity loading (light grey area) and unusable flexural capacity (dark grey area), as well as the capacity consumed by the initial imperfections (aqua blue area). The bulge that characterizes P-M interaction diagrams of composite members due to the concrete contribution to the strength is also reduced by these unusable areas as well. In Chapter 10, design equations are proposed to obtain the P-M diagram of composite beam columns from the cross-section reduced by the total unusable capacity.

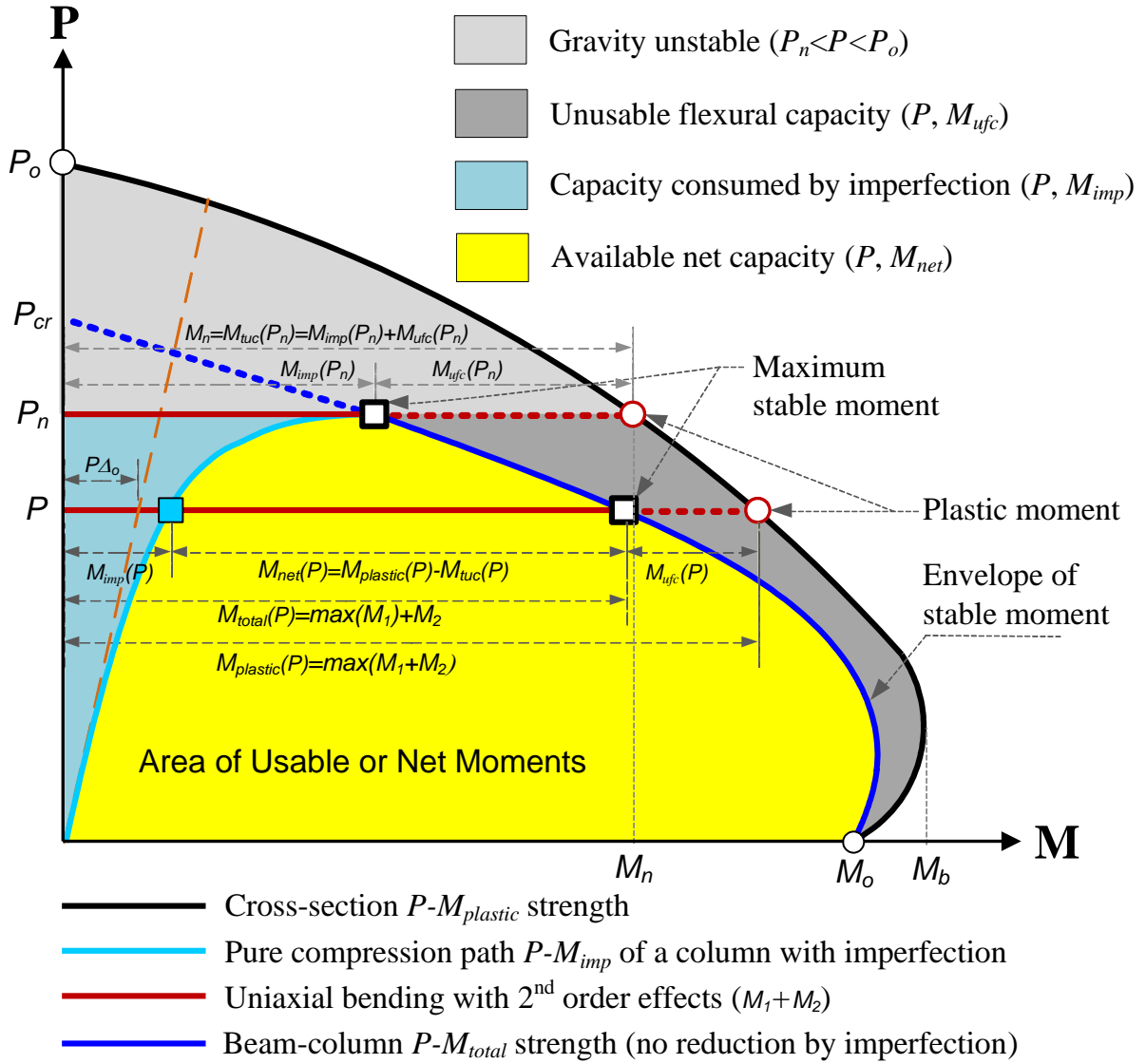


Figure 6.16. Components of the P - M interaction diagram for composite members

6.4. Experimental tests

As previously defined, load cases LC2 and LC3 aimed to extract experimental interaction set of values of the axial load – bending moment (P-M) response so that comparisons could be made to predictions from advanced analytical models and design equations.

Load cases LC2 and LC3 were described in Chapter 3. However, as summary, the specimens in these load cases were under vertical force control with a constant axial load and horizontal displacement control with incremental lateral displacement until a target displacement is met. Thus, uniaxial bending was enforced for LC2 through moving the top of the specimen along one axis (as shown in Figure 6.17), while biaxial bending was used for LC3 by driving the top in the two horizontal axes (as shown in Figure 6.18).

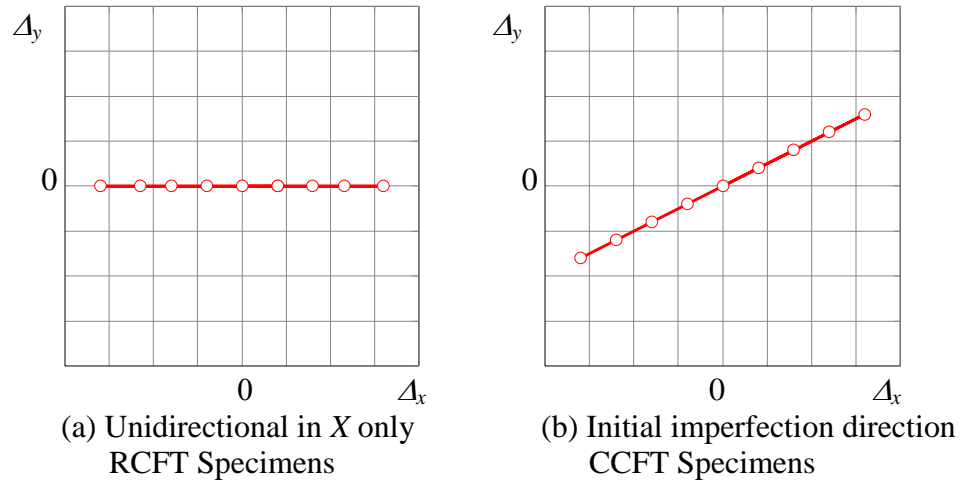


Figure 6.17. Horizontal displacement path at the top during LC2

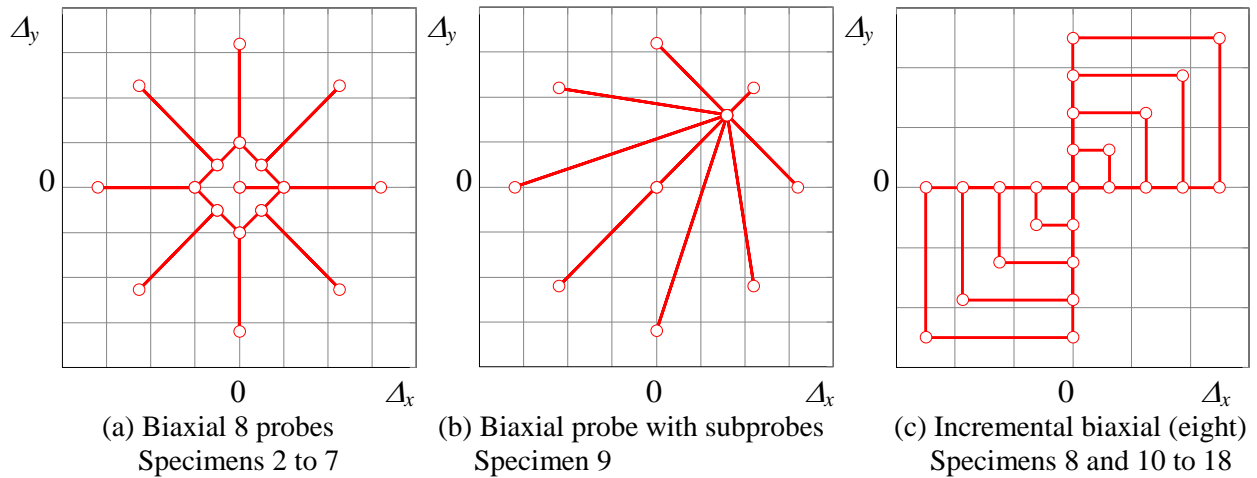


Figure 6.18. Horizontal displacement path at the top during LC3

Table 6.1 summarizes the control of the DOFs at the crosshead during these load cases. In most cases, the top rotations were set as free boundary conditions (or zero moments) and, with the base fixed, the effective length factor in these cases tends to a value of two ($K=2$). In a few cases, the top rotations were controlled also as fixed ($\theta=0$) and so the effective length factor in these cases tends to a value of one ($K=1$). Unless specified as $K=1$ for the cases with fixed rotations, all the results in this section correspond to the default or the top free rotation condition ($K=2$).

Table 6.1. DOFs controlled during LC2 in the CCFT specimens

Load Case	CFT Specimen	Factor K	DOF					
			Force / Displacement			Moment / Rotation		
			X	Y	Z	RX	RY	RZ
LC2	Circular	2	$\Delta_x \rightarrow \Delta_{target}$	$\Delta_y \rightarrow \Delta_{target}$	$F_z = P$	$M_x = 0$	$M_y = 0$	$\theta_z = 0$
	Rectangular	2	$\Delta_x \rightarrow \Delta_{target}$	$\Delta_y = 0$	$F_z = P$	$\theta_x = 0$	$M_y = 0$	$\theta_z = 0$
	Both	1	$\Delta_x \rightarrow \Delta_{target}$	$\Delta_y \rightarrow \Delta_{target}$	$F_z = P$	$\theta_x = 0$	$\theta_y = 0$	$\theta_z = 0$
LC3	Both	2	$\Delta_x \rightarrow \Delta_{target}$	$\Delta_y \rightarrow \Delta_{target}$	$F_z = P$	$M_x = 0$	$M_y = 0$	$\theta_z = 0$
	Both	1	$\Delta_x \rightarrow \Delta_{target}$	$\Delta_y \rightarrow \Delta_{target}$	$F_z = P$	$\theta_x = 0$	$\theta_y = 0$	$\theta_z = 0$

With respect to the uniaxial path in LC2, the motion of the top follows the same axis delineated during the previous load case LC1. Thus, during LC2 the top of rectangular specimens were moved along the X-axis only (with DOFs in Y-axis fixed) as shown in Figure 6.17.a. For circular specimens, both X-axis and Y-axis were moved along the axis delineated by LC1 (or by the axis delineated by the initial imperfection) as schematically illustrated in Figure 6.17.b. The target displacement (Δ_{target}) in some specimens was defined by the peak lateral force, while for others this was a desired level of drift, varying in these cases mostly from 1% to the maximum stroke capacity of the testing system (Δ_{stroke}) and in most cases with increments of 1%.

The explored paths for the top displacement during the biaxial load case LC3 are shown in Figure 6.18.

In order to obtain the P-M interaction surface for specimens 2 to 7, the top was moved as illustrated in Figure 6.18.a along different probes until a peak lateral force in either X or Y was reached. Once the target was met for each probe, the top was moved back and then moved through a diamond path for the following probe with a different angle, and this process repeated around until the diamond path was completed.

For the specimen 9, a path illustrated in Figure 6.18.b was used to obtain also the P-M interaction surface that consisted of different set of probes and sub-probes; similar to the diamond shape path, the top was moved back once the peak force was reached followed by the next sub-probe or a new probe.

For specimens 8 and 10 to 18, the path illustrated in Figure 6.18.c (eight-shape) was used to evaluate the post-peak behavior; this path consisted of an incremental displacement (as percentage of drift) in both X and Y axes until the maximum stroke of the MAST system is achieved.

Table 6.2 recaps the load-displacement conditions imposed in the specimens during LC2 and LC3. In this table, the effective length factor in the direction of motion (K), the gravity load (P), and the motion shapes of the tip imposed by the crosshead are summarized for each specimen. Also, this Table summarizes when the load reversal takes place. As seen in this table, the first half of specimens (from 1 to 9) were run with probes for which reversals in the direction of motion occurs at the peak of the lateral capacity (F_{max}), or when the tangent slope in the force-displacement response becomes zero. For the second half set (specimens 10 to 18), the load reversal occurs at a target drift, starting mostly at $\pm 1\%$ drift and incrementing it in 1% steps up to the max stroke capacity of the MAST system (between 4 to 6% drift).

Table 6.2. Motion shapes of the top, gravity loads, and reversal events at LC2 and LC3

Specimen	LC2				LC3			
	K	P (kip)	Shape	Reversal	K	P (kip)	Shape	Reversal
1C5-18-5	2	15 30	Figure 6.17.a	F_{max} X only	none			
2C12-18-5	2	300 200 100	Figure 6.17.a	F_{max} X only 2 cycles	2	250 150	Figure 6.18.a 8 probes	F_{max}/probe X or Y
3C20-18-5	2	1000 500	Figure 6.17.b	F_{max} X or Y 2 cycles	2	1250 750 250	Figure 6.18.a 16 probes	F_{max}/probe X or Y
4Rw-18-5	2	600 300	Figure 6.17.a	F_{max} X only 2 cycles	2	750 450 150	Figure 6.18.a 8 probes	F_{max}/probe X or Y
5Rs-18-5	2	1000 500	Figure 6.17.a	F_{max} X only	2	750 250	Figure 6.18.a 8 probes	F_{max}/probe X or Y
6C12-18-12	2	300 150	Figure 6.17.b	F_{max} X or Y 2 cycles	2	375 225 75	Figure 6.18.a 8 probes	F_{max}/probe X or Y
7C20-18-12	2	1000 500	Figure 6.17.b	F_{max} X or Y	2	1250	Figure 6.18.a 8 probes	F_{max}/probe X or Y
8Rw-18-12	2	600 300	Figure 6.17.a	F_{max} X only	2	800	Figure 6.18.a 8 probes	F_{max}/probe X or Y
9Rs-18-12	2	1200 400	Figure 6.17.a	F_{max} X only	2	800	Figure 6.18.b 6 main probes	F_{max}/probe X or Y
10C12-26-5	2	200 100	Figure 6.17.b	1 to max @1% drift	2	150 50	Figure 6.18.c	1 to max @1% drift
11C20-26-5	2	600 300	Figure 6.17.b	1 to max @1% drift	2	450 150	Figure 6.18.c	1 to max @1% drift
12Rw-26-5	2	400 200	Figure 6.17.a	1 to max @1% drift	2	300 500	Figure 6.18.c	1 to max @1% drift
13Rs-26-5	2	400 800	Figure 6.17.a	1 to max @1% drift	2	300 500	Figure 6.18.c	1 to max @1% drift
14C12-26-12	2	100 200	Figure 6.17.b	2 to max @2% drift	2	150	Figure 6.18.c	1 to max @1% drift
	1	300 450	Figure 6.17.b	2 to max @2% drift	1	300	Figure 6.18.c	1 to max @1% drift
15C20-26-12	2	400 800	Figure 6.17.b	1 to max @1% drift	2	200 600	Figure 6.18.c	1 to max @1% drift
16Rw-26-12	2	200 400	Figure 6.17.a	1 to max @1% drift	2	300 500	Figure 6.18.c	1 to max @1% drift
17Rs-26-12	2	400 800	Figure 6.17.a	1 to max @1% drift	2	200 600	Figure 6.18.c	1 to max @1% drift
18C5-26-12	1	15 25	Figure 6.17.b	1 to max @1% drift	1	20	Figure 6.18.c	1 to max @1% drift

6.4.1. Uniaxial bending

This section describes the extraction of experimental P-M stable limits obtained during the uniaxial loading cases (LC2). The extracted results are schematically represented in Figure 6.19. In this figure, the cross-section P-M strength calculated with the fully plastic stress method is illustrated by the thin dashed line passing through points A-C-D-B. The P-M strength of the beam-column with reduction due to the stability effects as required by the AISC (2005) are also illustrated by tick dashed line passing through points A_λ - C_λ -B (Simplified P-M). In addition to these analytical capacities for the composite cross-section and beam-column, this figure shows the expected test response. The experimental results included on this plots are:

- (1) The P-M path from the pure compression loading (LC1) up to a given level of gravity force. The second order moment illustrated in this path is developed as a consequence of the initial imperfection. The moment that corresponds to the point when target compression load is reached is represented by the label M_{imp} as a cyan square. As a reminder, this initial second order moments (M_{imp}) corresponds to the experimental initial imperfection, which were not necessarily equal or lower than the maximum allowed imperfections imposed by the codes. As illustrated in Chapter 5 (see figure 5.4), most of the specimens exceeded the limit in out-of-plumbness, and thus care must be taken when interpreting the experimental results vs. a design value that is taken as the result of the tested conditions (i.e. high imperfections, accumulated degradation and damage from previous load cases, and cyclic loading).
- (2) The P-M path from the uniaxial bending loading (LC2) up to a total second order moment at incipient buckling (M_{total}). This moment is illustrated as a blank square in Figure 6.19(a) and is extracted from the uniaxial loading (LC2) at the point where, with a sustained compression load, the maximum lateral force F or the maximum first order moment $M_1 \approx FL$ is reached as shown in Figure 6.19(b). Examples of how these total moments were obtained from the experimental tests during the load case LC2 with reversals at (a) peak load and (b) at target drifts are shown in Figure 6.20. In this figure, the first order, the $P\Delta$ and the total second order experimental moments at the base vs. the lateral displacement are plotted, where the corresponding moments related to the incipient buckling failure are also indicated.

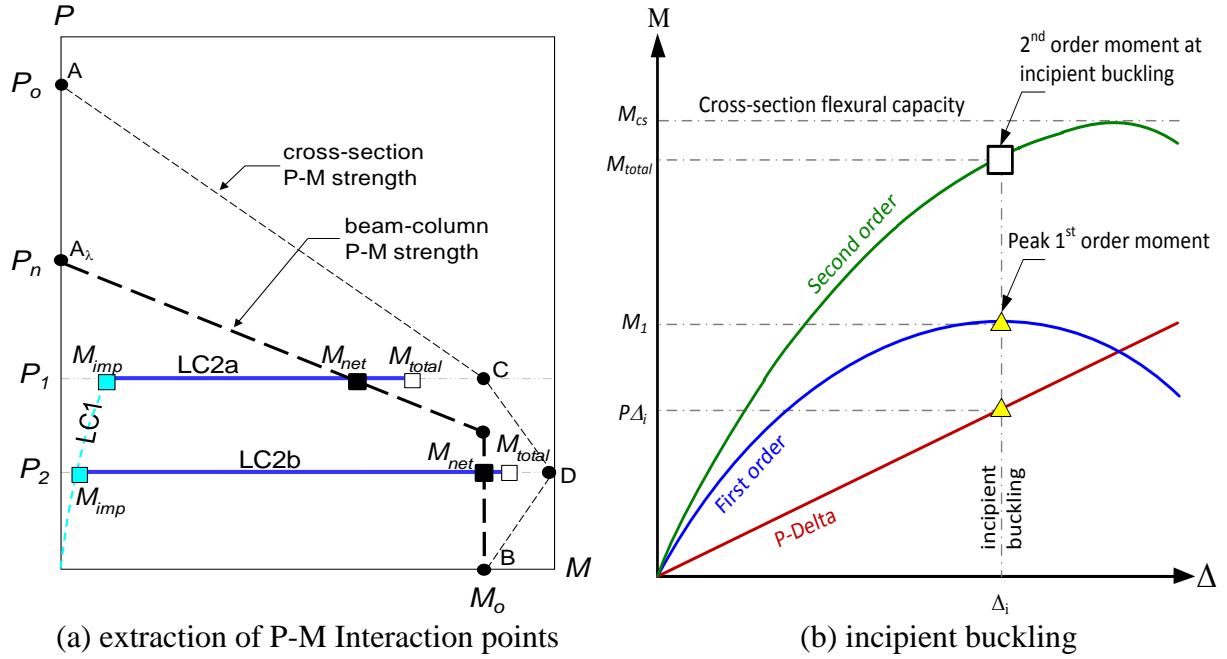


Figure 6.19. Schematic illustration of the extraction of P-M Interaction points from the uniaxial loading (left), and schematic definition of the limit point at the incipient buckling (right)

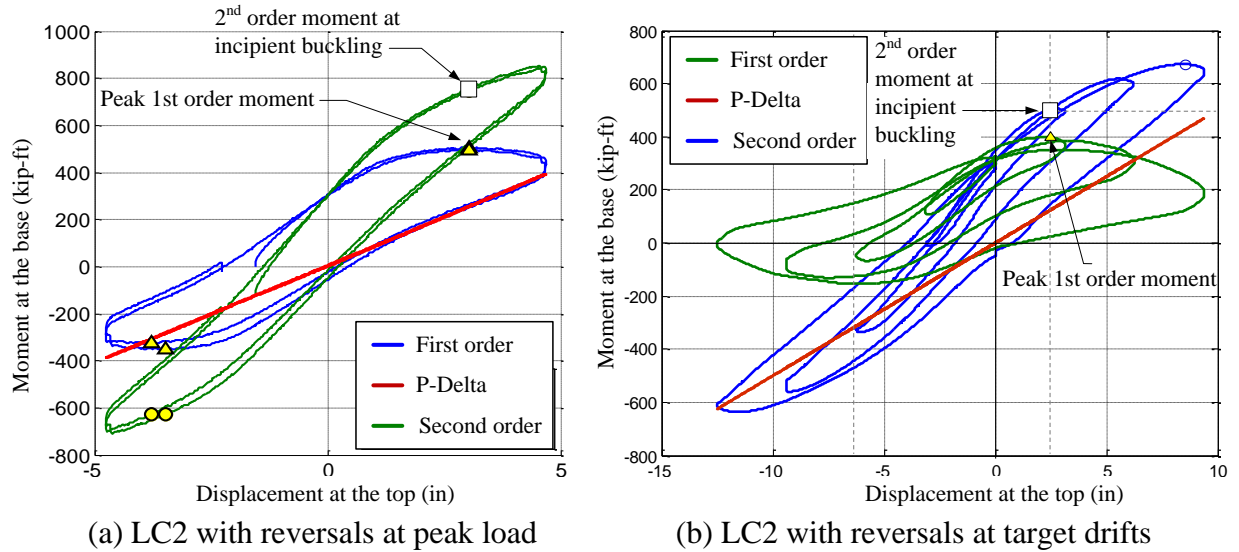


Figure 6.20. Definition of the limit point at the incipient buckling from experimental data

- (3) The net second order moment (M_{net}) accounts for the initial imperfection. This moment is obtained as the total moment due to the maximum overturning strength, minus the moment due to the initial imperfection; in other words: $M_{net} = M_{total} - M_{imp}$. The value of this net moment, represented in the following figures as a black square,

depends on the amount of imperfection in the member. Calibration of the net moments with an ideal imperfection (as $KL/1500$ of initial out-of-plumbness) defines the interaction diagram for beam-columns with stability reduction due to the geometric nonlinearities in non-vertical members.

Figure 6.21 to Figure 6.24 illustrate the experimental axial force – second order moment paths (P - M_2 path) obtained during the pure axial loading case (LC1, cyan line) and the uniaxial bending loading case (LC2, blue lines). From these histories, the moment due to the imperfection (M_{imp} , cyan square), the total usable moment (M_{total} , white squares) and the net usable moment (M_{net} , black squares) are extracted for each case. For comparison purposes, the extracted experimental P-M values are compared with the P-M interaction diagrams obtained with the AISC (2005) Specifications for both the cross-section (thin-black with white circles) and the beam-column with slenderness reduction (thick-black with black circles).

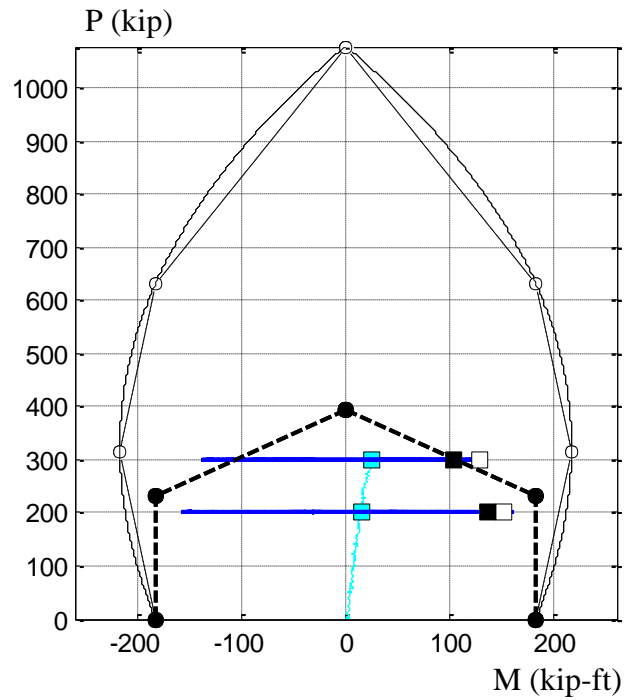
The following points must be made with reference to Figure 6.19 to Figure 6.24:

- Since the reversal of the lateral loading takes place just after passing the peak force, the experimental base moment does not necessarily reach the cross-sectional strength. In other words, the ends of the moment paths at given axial load (blue lines) do not necessarily achieve the cross-sectional P-M (thin line), and so they cannot be directly compared.
- As described before, the total moments (white squares) represent the point of incipient instability due to combined material and geometric nonlinearity for flexure and axial compression loading. These experimental values correspond to the maximum strength to the overturning or first order moments ($\approx FL$), with the corresponding second order moments ($P\Delta$). The amount of the second order moment ($P\Delta$) obviously depends on the total displacement (Δ), which increases from the initial imperfection (Δ_o) to a larger value of Δ when the target gravity (P) is reached (moment used up by imperfections), and then from here to a maximum Δ after the maximum lateral force (F) is reached.
- The net moment (black squares), calculated as the total second order moment (white squares) minus the initial imperfection moment (cyan squares), is the effective moment at the incipient instability of the non-straight composite member due to combined material and geometric nonlinearity for flexure and axial compression loading. This net moment

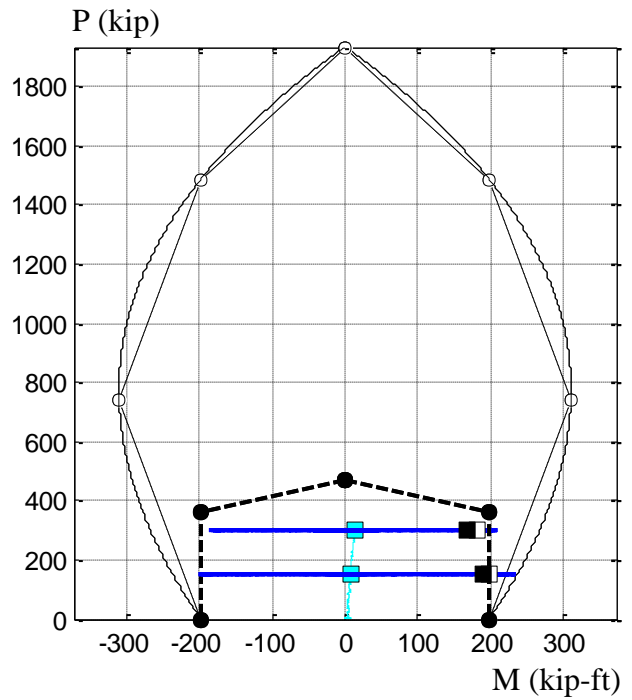
depends primarily on the amount of initial imperfection; thus the net moment tends to be closer to the total moment in straight members; higher reductions occur as the imperfections increase. As intended by AISC (2005) through the P-M interaction diagrams for beam-columns (thick line), the calibration of the net moment within the tolerances allowed in practice construction will delimit the amount of reduction for imperfection.

The results shown from Figure 6.21 to Figure 6.24 are summarized in Table 6.3 and illustrated in Figure 6.25 with normalized values, using the AISC (2005) buckling strength (P_n) for axial loads and the corresponding pure bending strength (M_B) for moments. Since the normalized interaction point P_C/P_n depends on the contribution of the concrete strength in the composite section, which varies for each specimen, the average, the upper bound and the lower bound for this AISC point are shown Figure 6.25. In addition, the normalized values of experimental net moments for each axial load level are also included in Figure 6.25, showing these results for each type of CFT cross-section. Based on these results, the following observations can be highlighted:

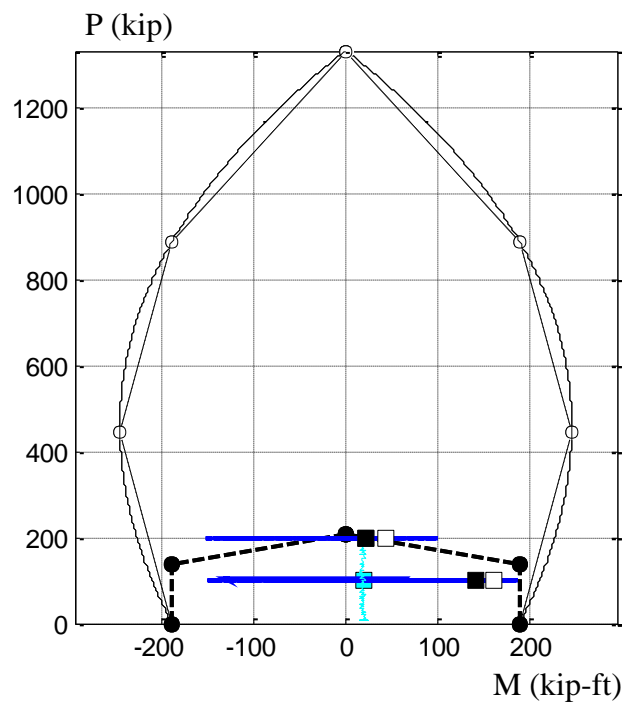
- In general, the experimental net moments are close to the moment predicted by the AISC (2005) Specifications. Excluding some particular cases, the ratio of the experimental net moments over the AISC strength with stability reduction (M_{net}/M_{AISC}) varies from 0.70 to 1.27, with an average of 1.0 and a standard deviation of 0.19 (Table 6.3, Figure 6.25).
- Variability on this ratio is consequence of the simplicity of the AISC approach in keeping constant the moments below the axial force P_C . In addition, the net moments obtained experimentally and illustrated in this section are related to the true imperfection of the specimens that, as mentioned in the previous chapter, there is a significant variability on the imperfections being very small (as in the specimen 5-Rs-18-5) or very large (as in the specimen 17-Rs-26-12).
- As illustrated in Figure 6.25.b, most of the non-slender members had M_{net}/M_{AISC} ratios larger than 1.0 (Figure 6.25.c), while most of the slender specimens had lower ratios than 1.0 (Figure 6.25.d). This behavior suggests a change in the shape of the P-M interaction diagram for beam-columns such that the slenderness is implicit in the moment values, and thus in the P-M shape.



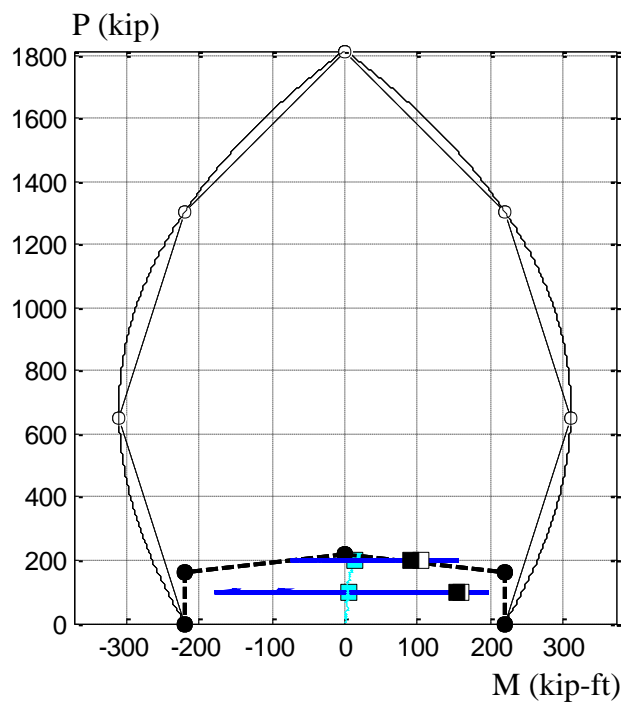
(a) Specimen 2-C12-18-5



(b) Specimen 6-C12-18-12



(c) Specimen 10-C12-26-5



(d) Specimen 14-C12-26-12

Figure 6.21. Extraction of P - M Interaction points from the uniaxial loading LC2 on the circular CFTs with 12.75 inches of diameter.

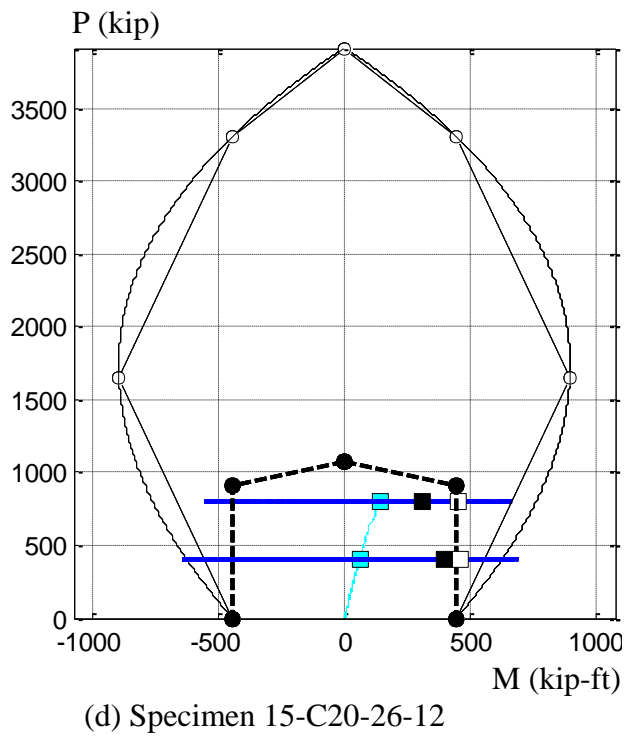
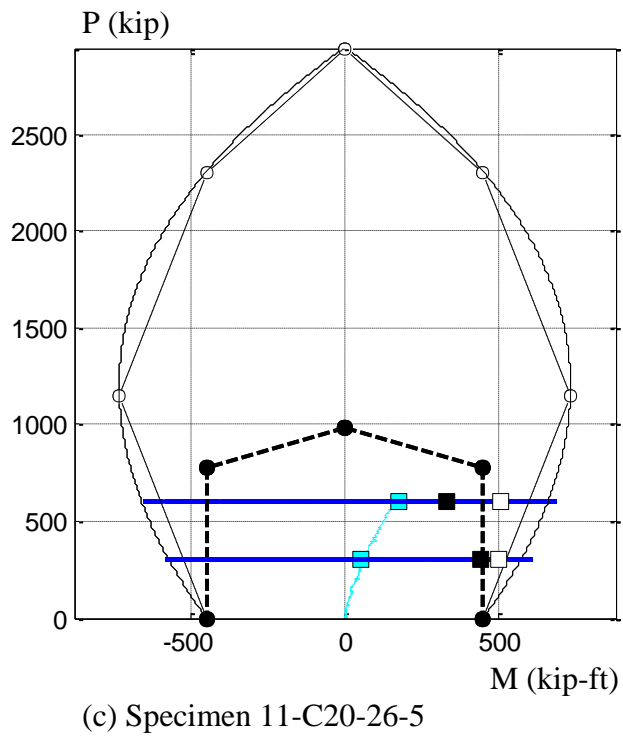
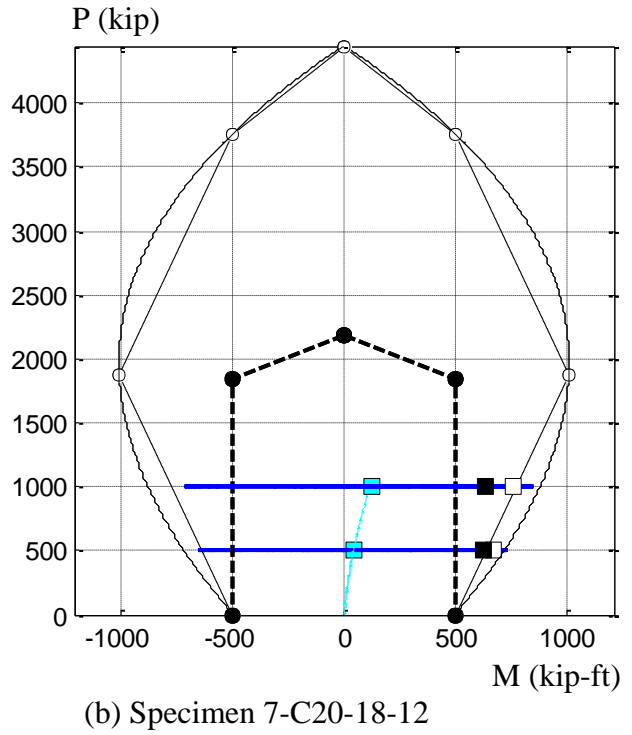
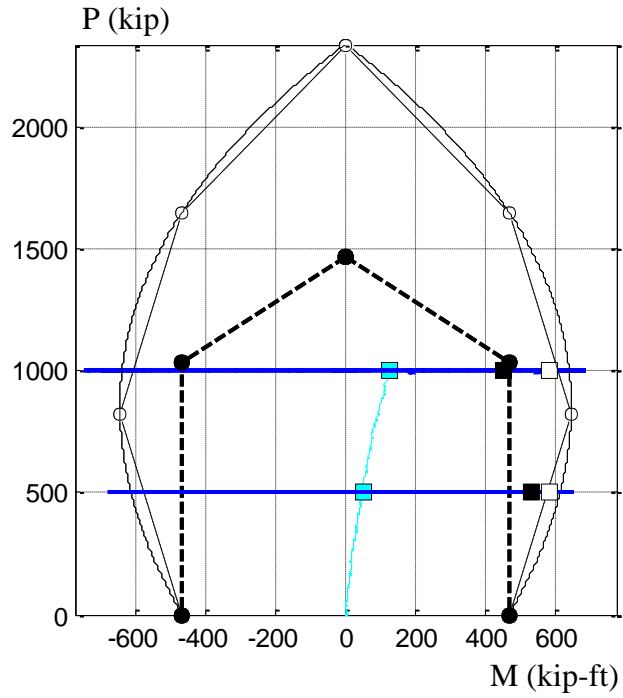
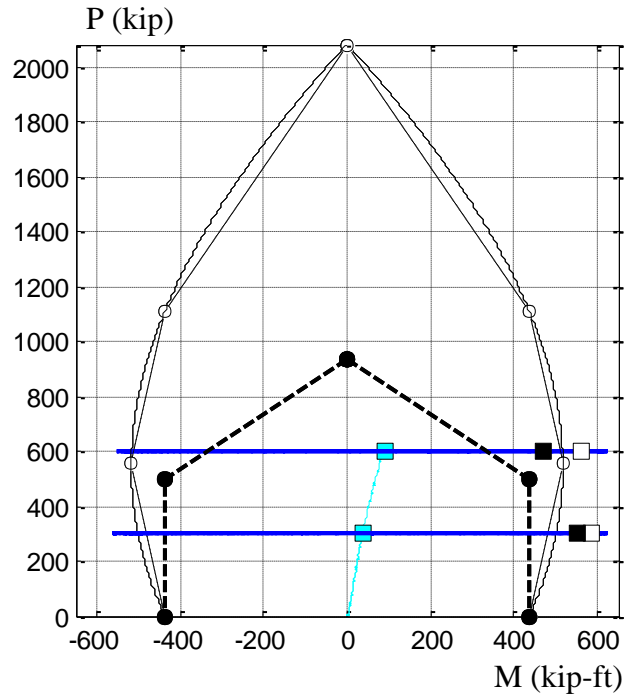
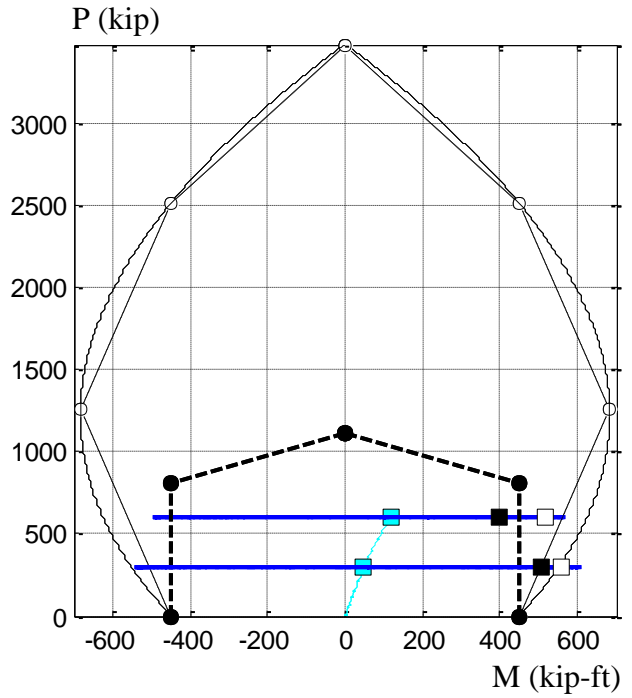


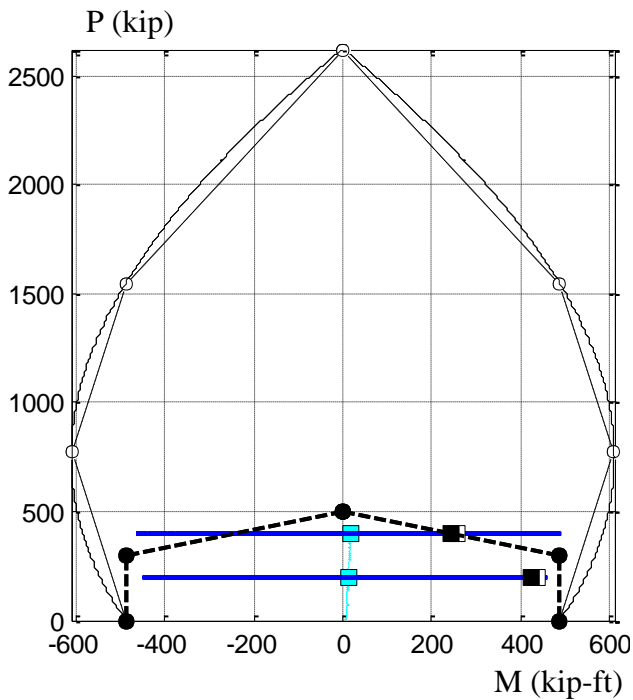
Figure 6.22. Extraction of P - M Interaction points from the uniaxial loading LC2 on the circular CFTs with 20 inches of diameter.



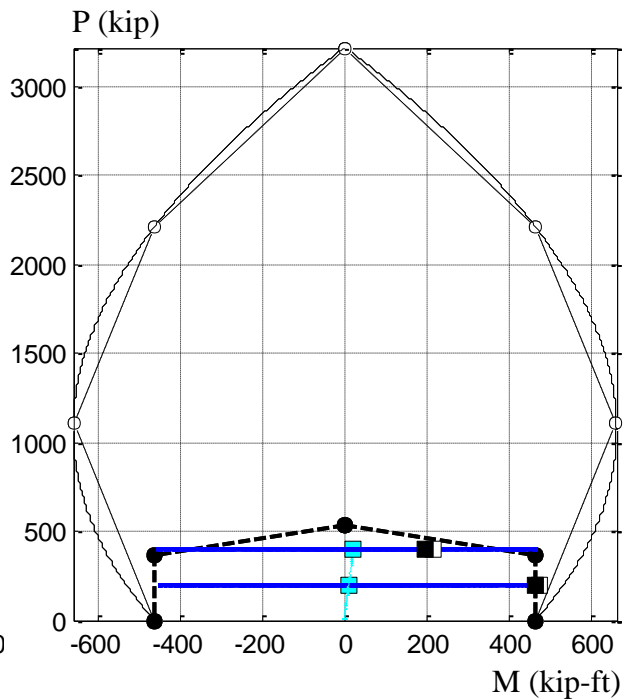
(a) Specimen 4-Rw-18-5



(b) Specimen 8-Rw-18-12

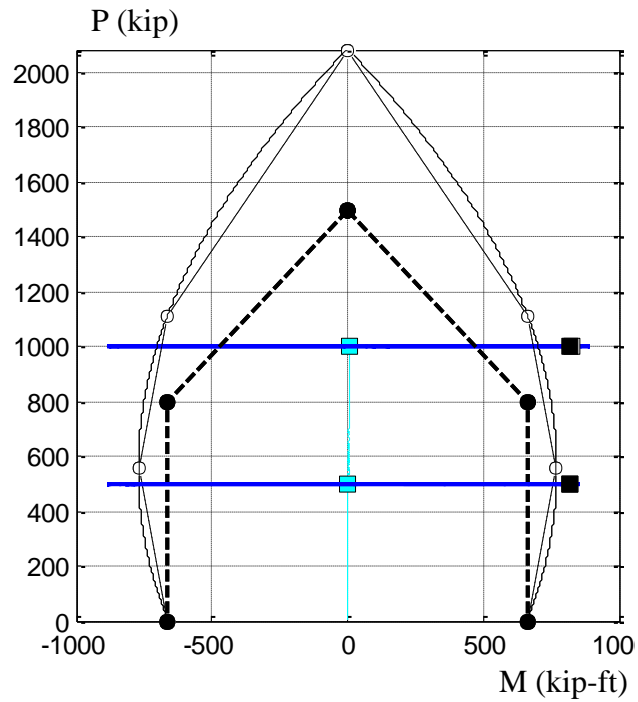


(c) Specimen 12-Rw-26-5

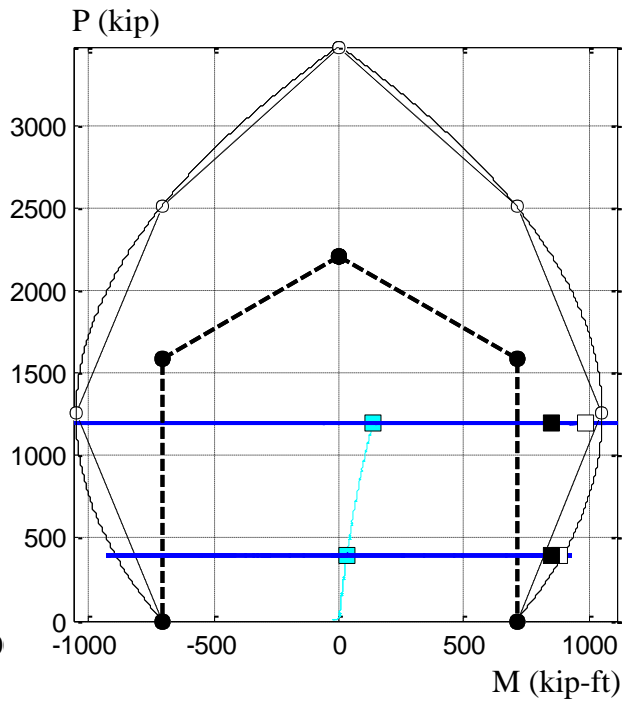


(d) Specimen 16-Rw-26-12

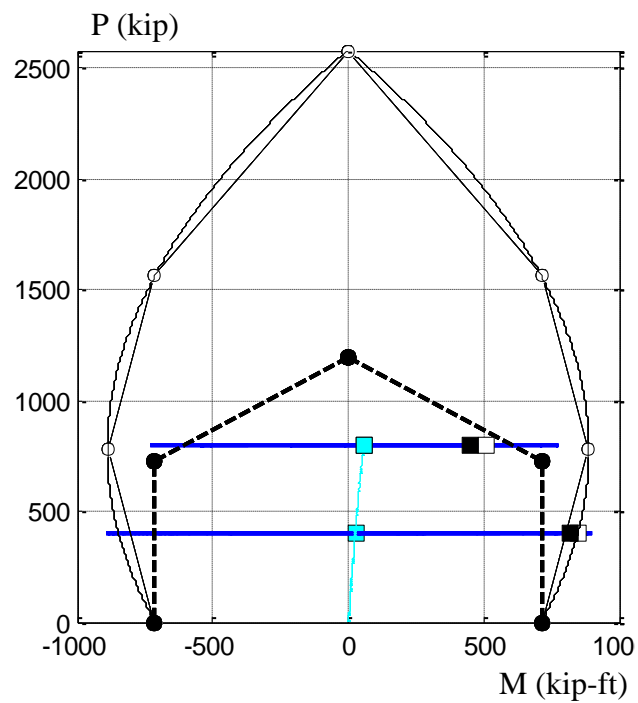
Figure 6.23. Extraction of P - M Interaction points from the uniaxial loading LC2 on the rectangular CFTs oriented in the weak axis



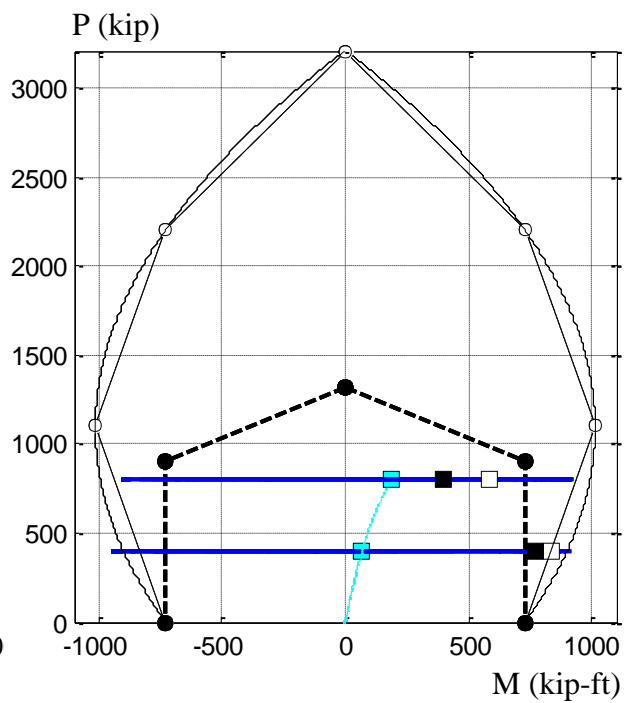
(a) Specimen 5-Rs-18-5



(b) Specimen 9-Rs-18-12



(c) Specimen 13-Rs-26-5

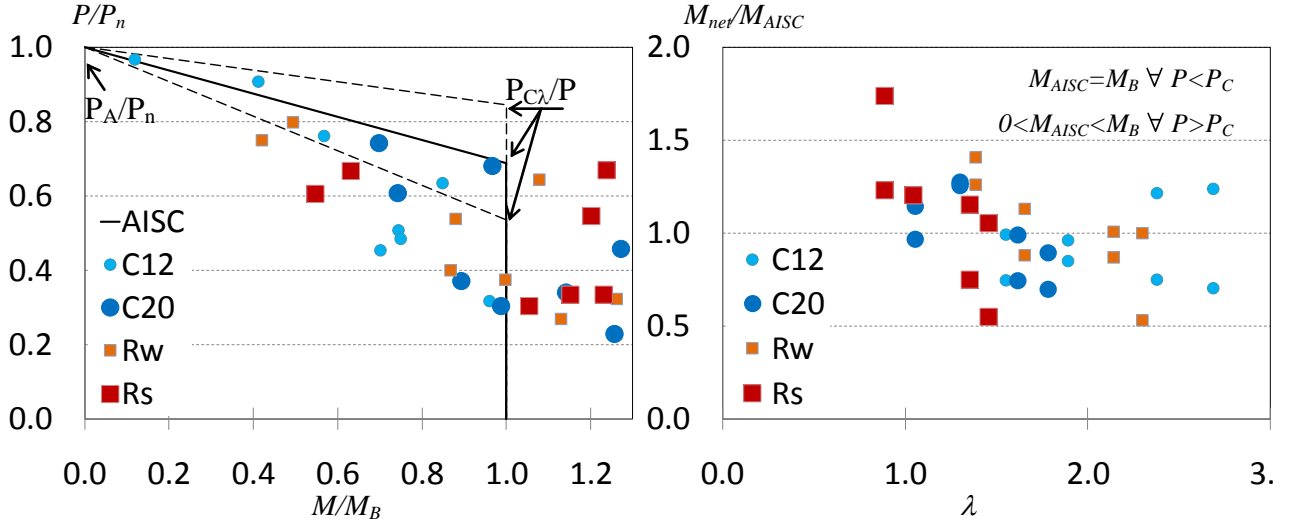


(d) Specimen 17-Rs-26-12

Figure 6.24. Extraction of P - M Interaction points from the uniaxial loading LC2 on the rectangular CFTs oriented in the strong axis

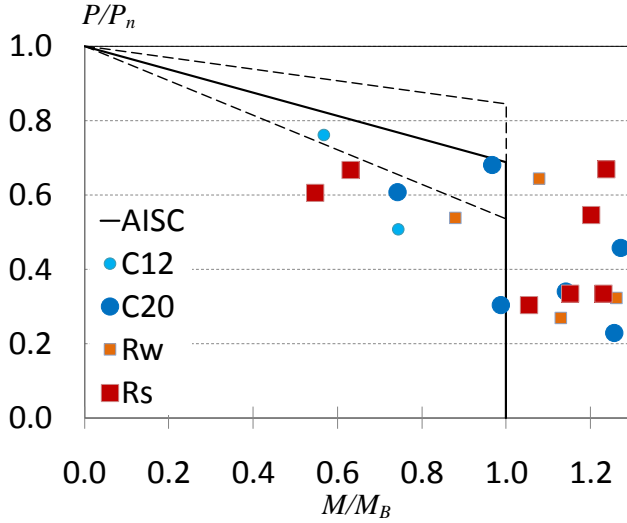
Table 6.3. Summary of extracted P - M interaction points from the uniaxial loading LC2

Specimen	λ	LC	P (kip)	P/P_n	M_{total} (kip-ft)	M_{net} (kip-ft)	M_{AISC} (kip-ft)	M_{net}/M_{AISC}
2C12-18-5	1.55	2a	300	0.76	128.3	104.1	105.1	0.99
		2b	200	0.51	152.3	136.3	183.3	0.74
6C12-18-12	1.89	2a	300	0.63	181.8	168.0	197.8	0.85
		2b	150	0.32	197.9	190.0	197.8	0.96
10C12-26-5	2.38	2a	200	0.97	43.9	22.4	18.5	1.21
		2b	100	0.48	160.5	141.1	188.3	0.75
14C12-26-12	2.69	2a	100	0.45	158.5	154.2	219.9	0.70
		2b	200	0.91	103.3	90.5	73.0	1.24
3C20-18-5	1.06	2a	1000	0.68	581.9	453.4	468.7	0.97
		2b	500	0.34	583.9	535.1	468.7	1.14
7C20-18-12	1.30	2a	1000	0.46	757.9	634.9	498.9	1.27
		2b	500	0.23	669.0	626.7	498.9	1.26
11C20-26-5	1.62	2a	600	0.61	507.2	334.7	451.0	0.74
		2b	300	0.30	499.4	445.3	451.0	0.99
15C20-26-12	1.78	2a	800	0.74	453.0	310.3	445.0	0.70
		2b	400	0.37	457.2	397.5	445.0	0.89
4Rw-18-5	1.38	2a	600	0.64	560.2	470.5	334.2	1.41
		2b	300	0.32	586.7	550.0	436.0	1.26
8Rw-18-12	1.65	2a	600	0.54	516.4	395.9	450.2	0.88
		2b	300	0.27	557.5	508.6	450.2	1.13
12Rw-26-5	2.14	2a	400	0.80	258.7	241.9	240.6	1.01
		2b	200	0.40	438.5	424.7	489.4	0.87
16Rw-26-12	2.30	2a	200	0.38	475.1	465.0	466.2	1.00
		2b	400	0.75	214.4	195.6	370.8	0.53
5Rs-18-5	0.89	2a	1000	0.67	828.8	820.7	472.6	1.74
		2b	500	0.33	817.9	815.7	662.9	1.23
9Rs-18-12	1.04	2a	1200	0.54	990.3	853.1	710.2	1.20
		2b	1200	0.54	990.3	853.1	710.2	1.20
13Rs-26-5	1.35	2a	400	0.33	849.2	821.6	712.9	1.15
		2b	800	0.67	509.9	449.9	602.0	0.75
17Rs-26-12	1.46	2a	400	0.30	835.8	768.4	728.9	1.05
		2b	800	0.60	585.6	398.9	728.9	0.55

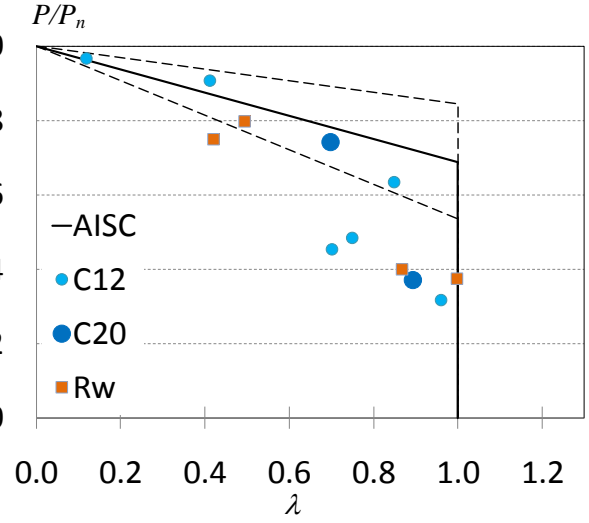


(a) Normalized P-M interaction diagram

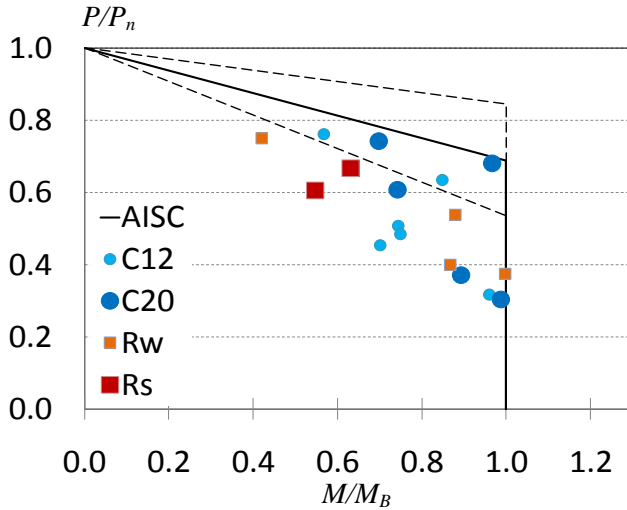
(b) Slenderness vs. the normalized net moment



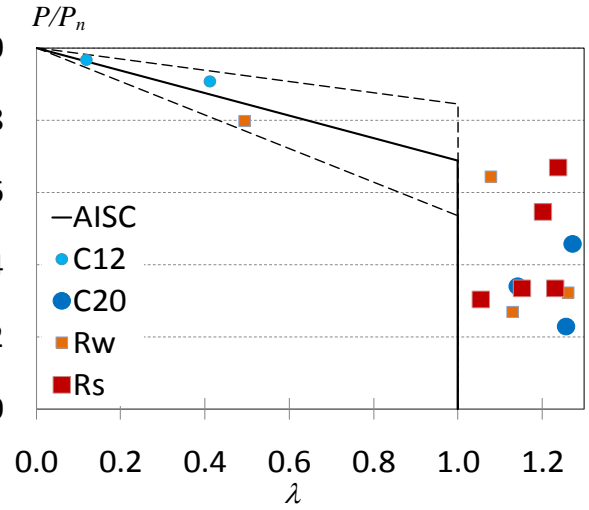
(c) Shorter specimens ($\lambda < 1.7$)



(d) Slender specimens ($\lambda > 1.7$)



(e) $M_{net}/M_{AISC} \leq 1.0$

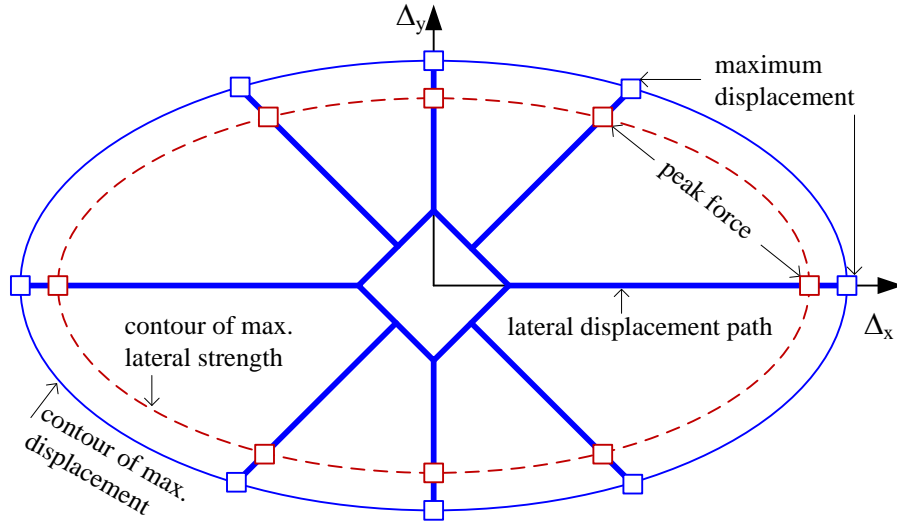


(f) $M_{net}/M_{AISC} > 1.0$

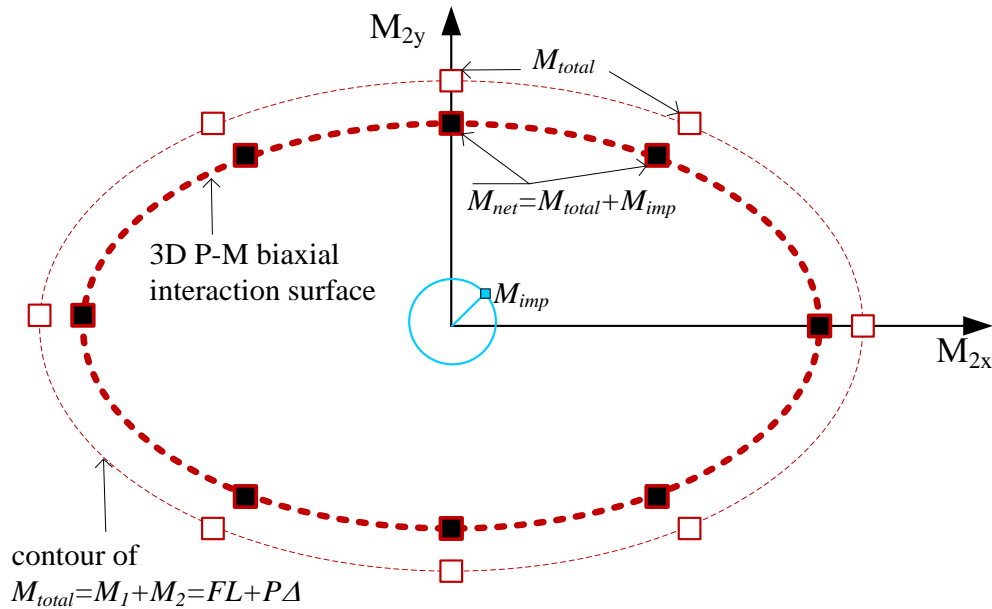
Figure 6.25. Experimental net moments normalized to the AISC strength

6.4.2. Biaxial bending

This section describes the extraction of experimental P-M stable limits obtained during the biaxial loading cases (LC3) illustrated in Figure 6.18. These values are extracted similarly to those extracted for the uniaxial bending case, using the approach that was schematically illustrated in Figure 6.19 for the 2D case. This approach applied to the 3D case is also schematically illustrated in Figure 6.26 for the displacement path shown in Figure 6.18.a.



(a) Determination of the maximum lateral strength with a fixed axial load; its contour delineate the interaction surface in the displacement space.



(b) Determination of the net moments and the interaction surfaces in the moment space

Figure 6.26. Illustration of the interaction surface from the biaxial loading (LC3)

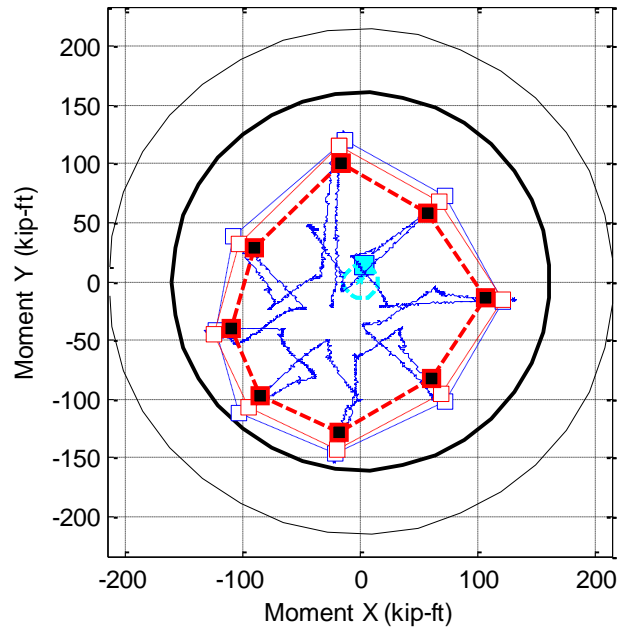
The lateral displacement path of the column tip that was used for specimens 2 to 7 is shown in Figure 6.26.a. In these specimens, the tip was driven through different probes until the maximum lateral strength for each probe was reached. The contour of peak forces delineated by the probes defines an interaction surface in the displacement space.

The experimental results for the second order moments (blue path), the moments due to the imperfection (cyan path – cyan squares), and the extracted net moments (black squares – red dashed line), are shown from Figure 6.27 to Figure 6.31. The P-M interaction diagrams for the cross-section (thin ellipse) and beam-column (thick ellipse) obtained with the AISC (2005) are also shown in these figures. In Figure 6.27 to Figure 6.31, the beam-column interaction diagram (thick ellipse) is the analytical predictor for the experimental net moments (black squares).

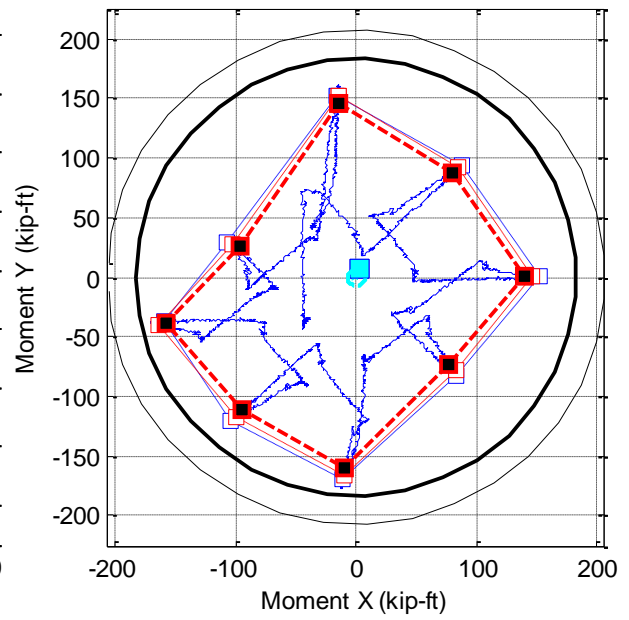
As shown in Figure 6.27 to Figure 6.31, the AISC (2005) prediction of the stability reduction in beam columns presents for some specimens a strong correlation, as in the specimens 3-C20-18-5 and 6-C12-18-12. However, a weak correlation is obtained for the specimens 2-C12-18-5, 4-Rw-18-5 and 5-Rs-18-5. As clearly illustrated in Figure 6.30 and Figure 6.31, the worst prediction occurs in the weak axis of RCFTs; this bad prediction in weak axis of RCFTs is consequence of the accumulation of damage through the progression of the steel local buckling as well as the low confinement in the concrete.

These figures shown in general a relative symmetry in the interaction surfaces, with a trend to a circular surface for the CCFTs and to an elliptical surface for the RCFTs. Based on these experimental results, a future reevaluation of the shape and the size of the AISC interaction surface for slender beam-columns is needed.

The interesting point in comparing the analytical predictor and the experimental values measured is not only in looking at how close or far they are, but also at the in-plane shape due to different axial load levels and due to damage accumulation in the latest loading cases.



(a) $P = 250$ kip



(b) $P = 150$ kip

Figure 6.27. Extraction of P - M Interaction points for the Specimen 2C12-18-5 from LC3

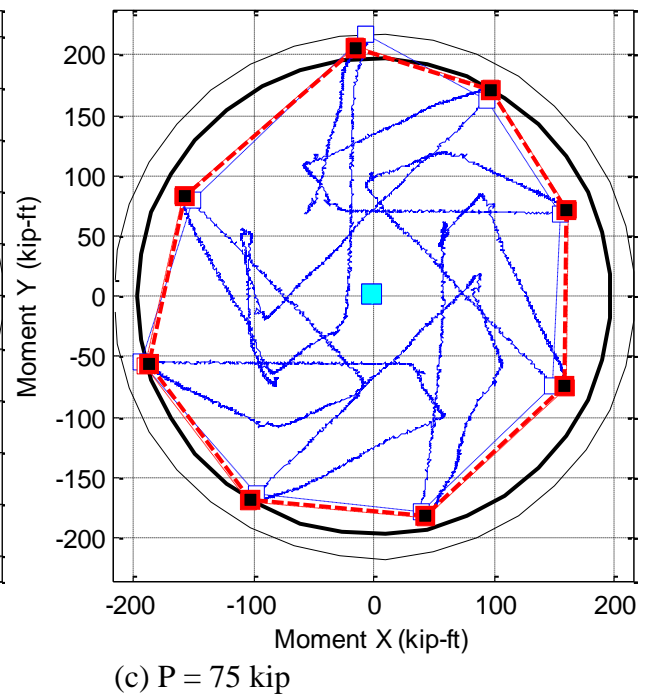
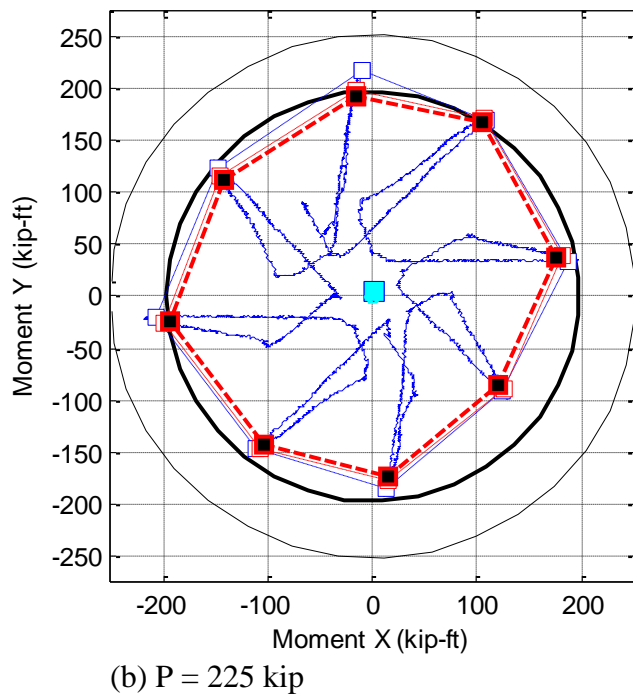
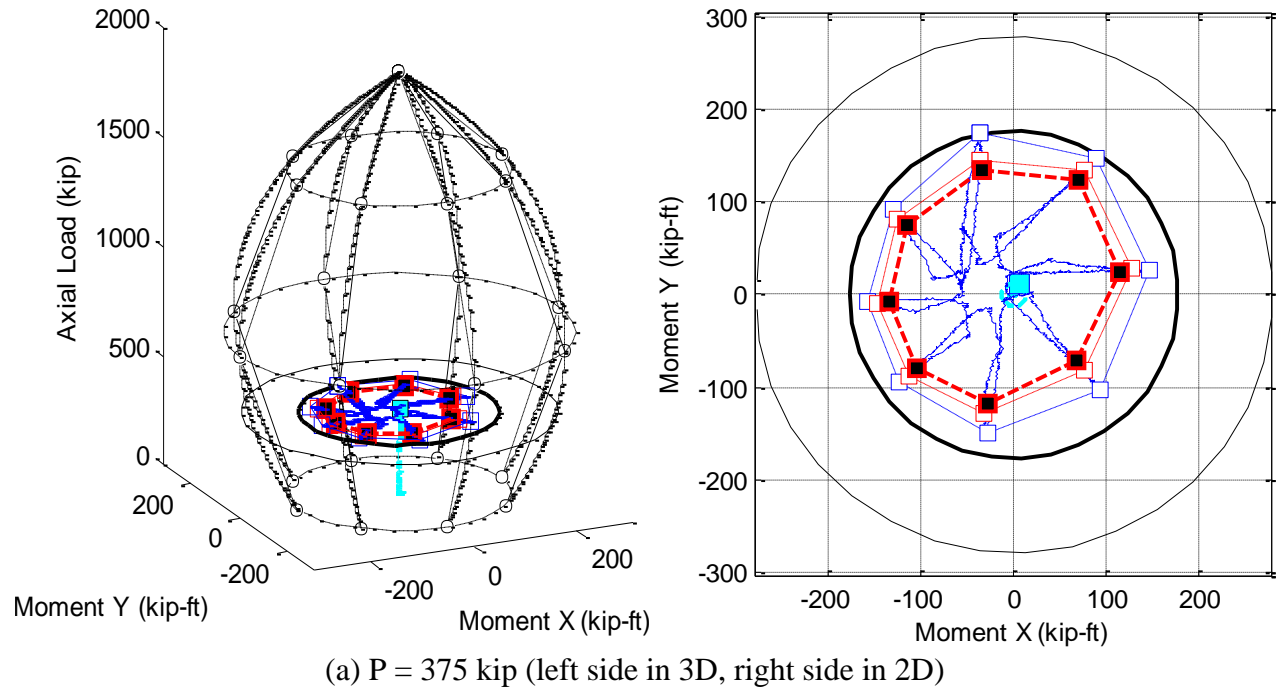


Figure 6.28. Extraction of P - M Interaction points for the Specimen 6C12-18-12 from the biaxial bending loading LC3

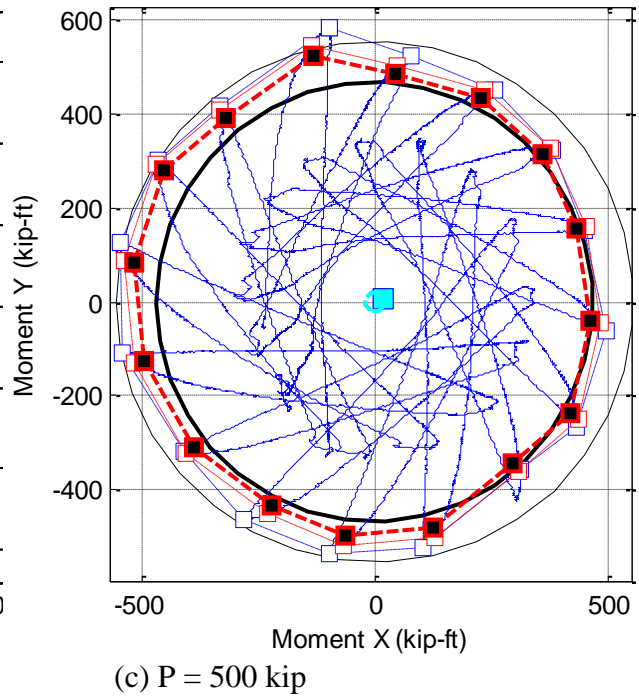
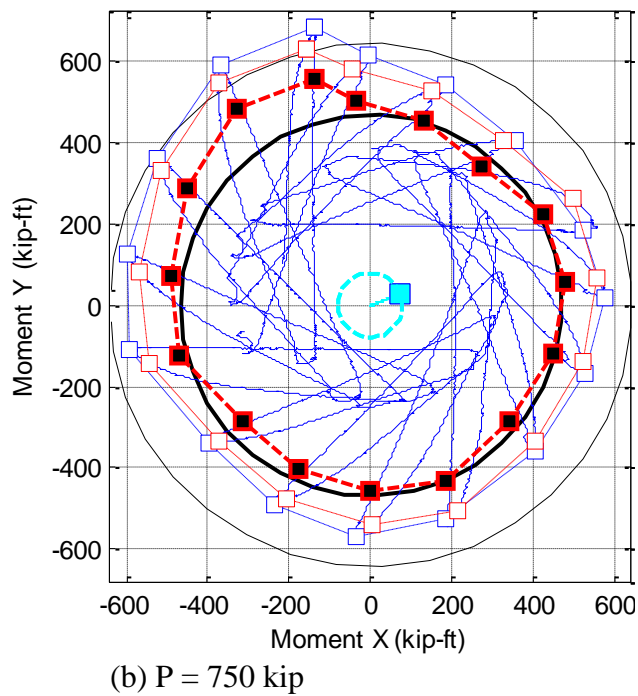
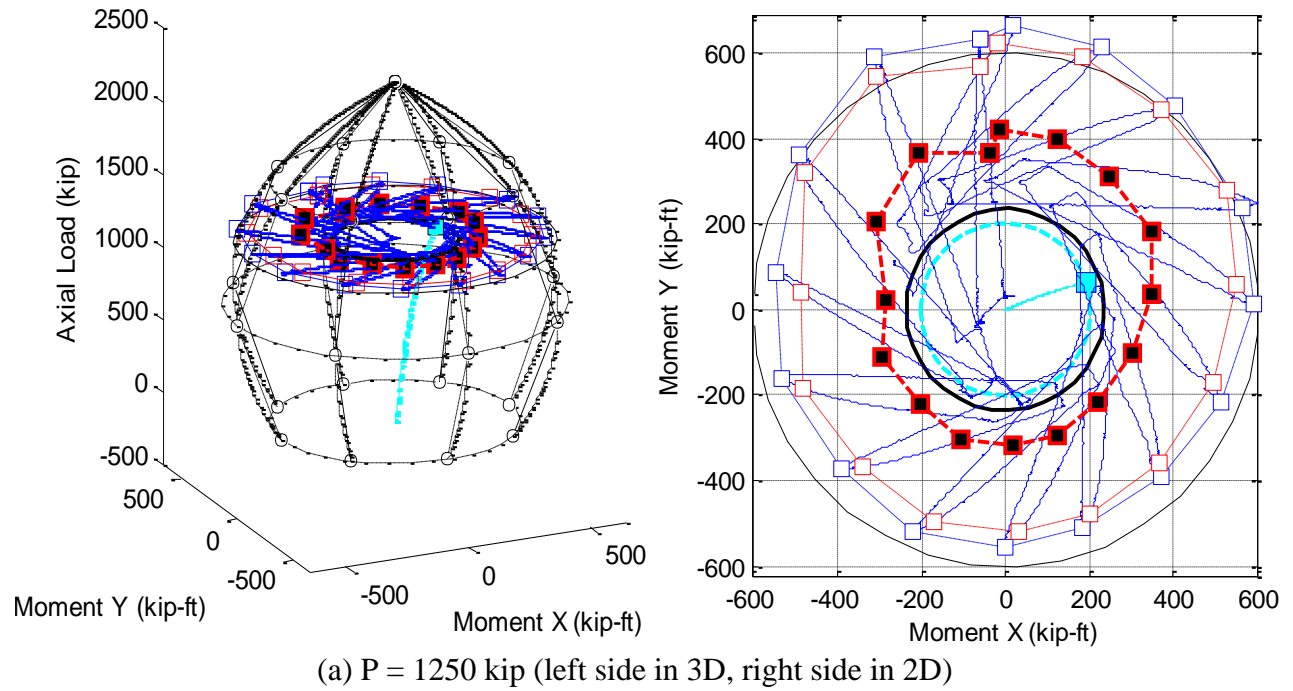


Figure 6.29. Extraction of P - M Interaction points for the Specimen 3C20-18-5 from the biaxial bending loading LC3

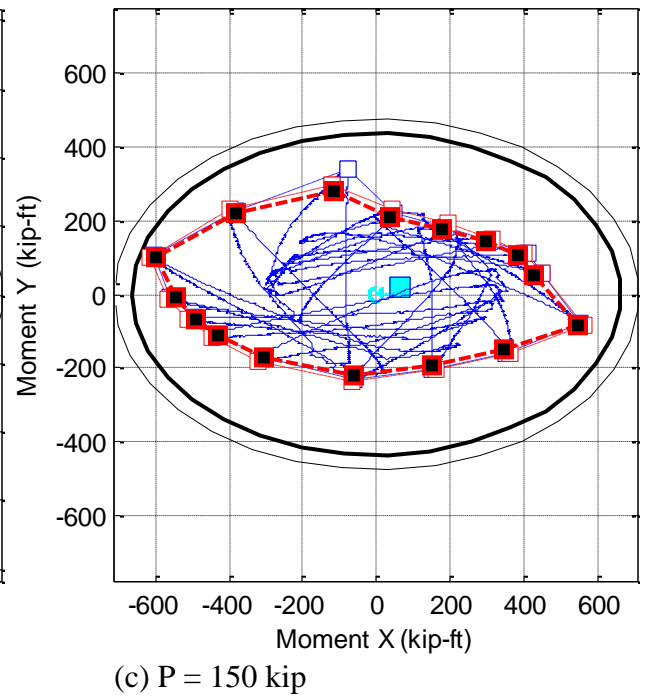
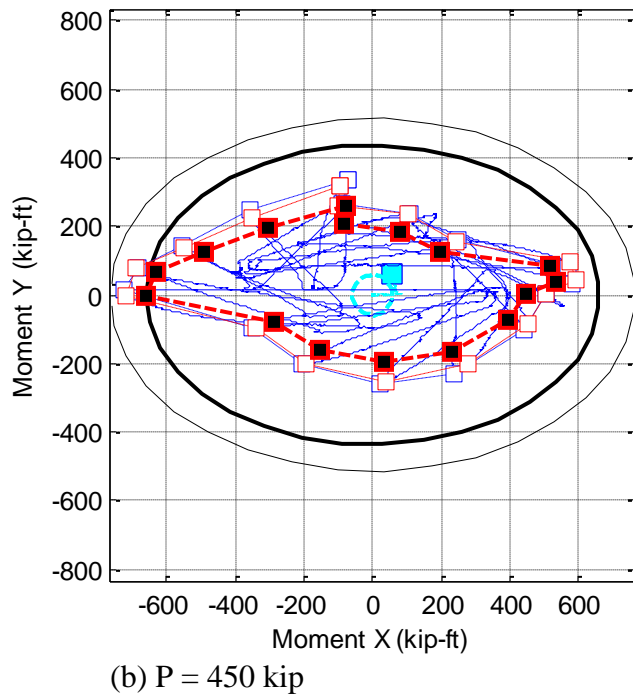
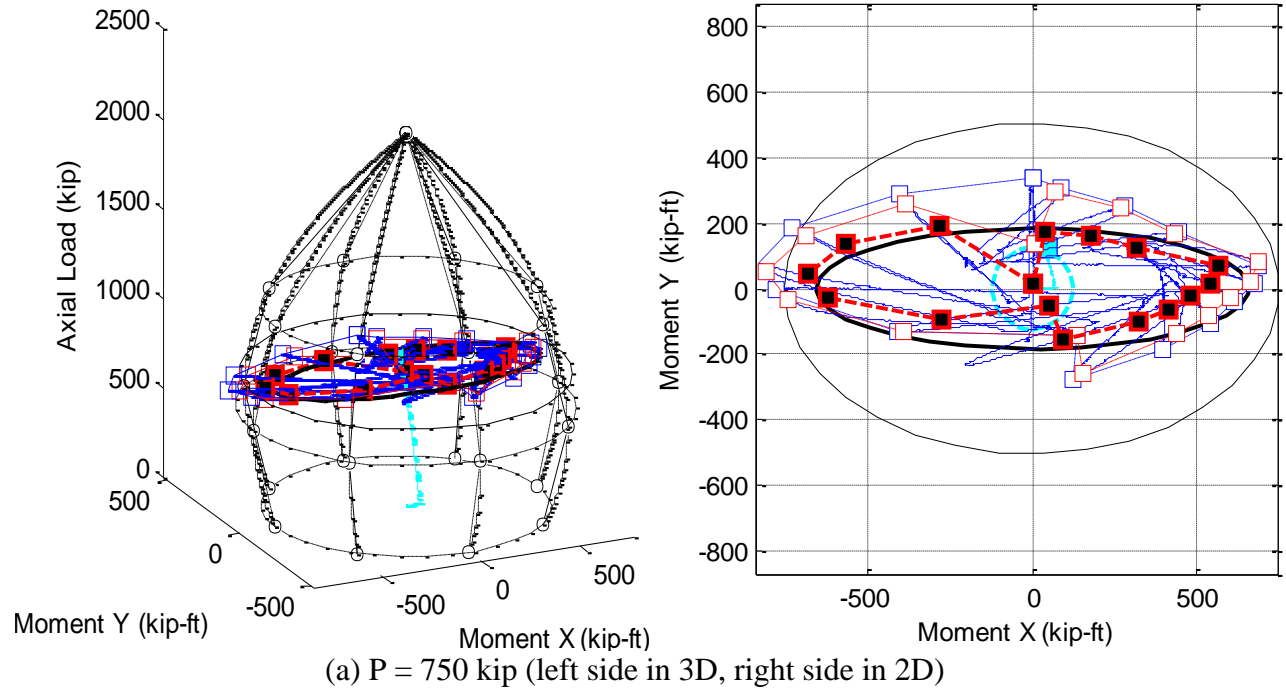


Figure 6.30. Extraction of P-M Interaction points for the Specimen 4Rw-18-5 from the biaxial bending loading LC3

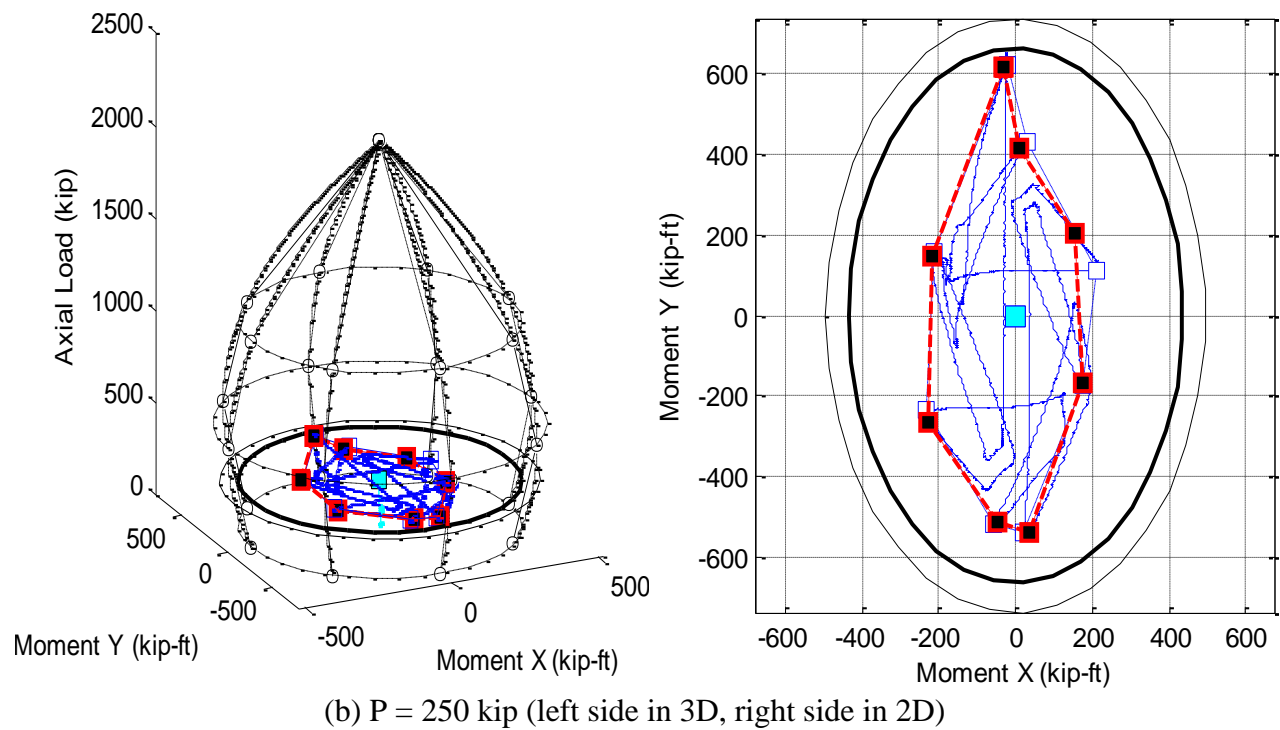
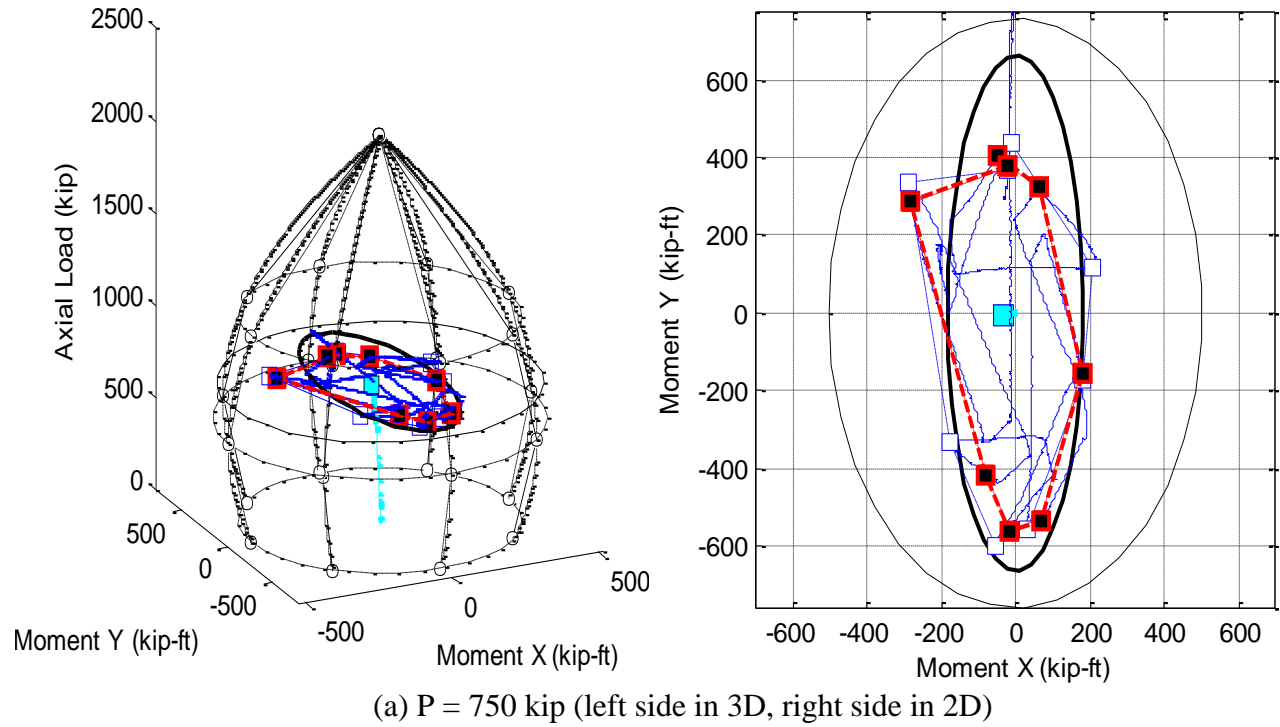


Figure 6.31. Extraction of P-M Interaction points for the Specimen 5Rs-18-5 from the biaxial bending loading LC3

For specimen 9Rs-18-12, the lateral displacement path was similar to that shown in Figure 6.18.b. For this loading case, the maximum lateral strength was identified for each probe and subprobes, indicating its incipient instability due to combined material and geometric nonlinearity. These limit points are shown in Figure 6.32 as black dots, and connecting the limit points from the various subprobes creates experimental interaction surfaces in the displacement space or, with the same limit points, corresponding experimental interaction surfaces can be created in the moment space (Figure 6.33). Each individual interaction surface represents a slice of the biaxial interaction surface at the applied axial load and at the state of the column following the main probe. The applied axial load remained constant throughout all the main probe/sub probe sets, thus the differences in the interaction diagrams can be attributed to the changing state of the specimen as the loading progressed. Addition experimental and analytical investigation of this specimen with this loading case has been discussed with more detail in Denavit *et al.* (2010).

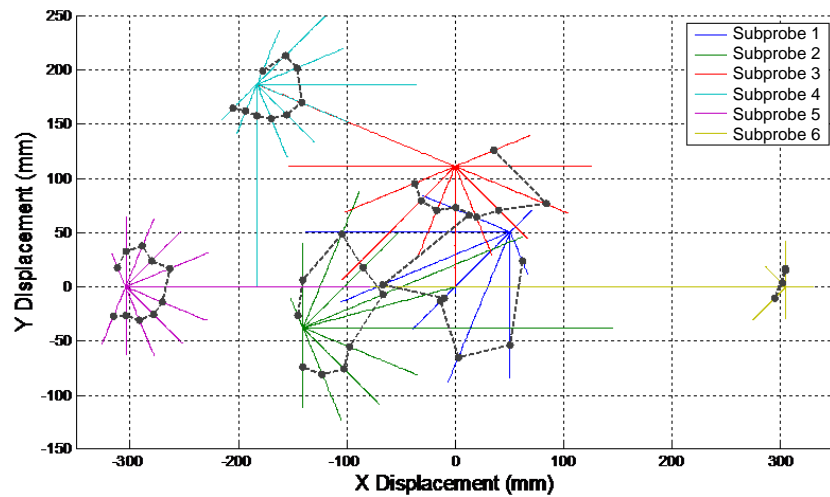


Figure 6.32. Displacement of the beam-column top, Specimen 9Rs-18-12 (Denavit et al., 2010)

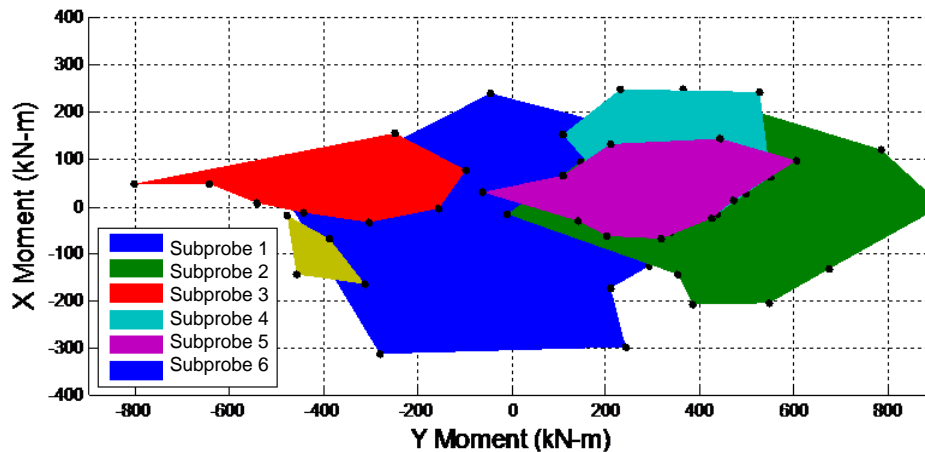


Figure 6.33. Experimental interaction surface (adapted from Denavit et al., 2010)

For specimens 7, 8, and from 10 to 18, the biaxial loading cases (LC3) are like those illustrated in Figure 6.18.c. This loading case aims to reach target values with displacement growing incrementally for each cycle or loop. Extraction of net moments and interaction surfaces are more challenging in this loading case since this was executed in two quadrants only.

The cross-sectional strength (thin ellipse) and the beam-columns strength (thick ellipse), calculated based on the AISC (2005) Specifications, are compared from Figure 6.34 to Figure 6.41 with the biaxial total bending moment (blue path) and the initial imperfection moments.

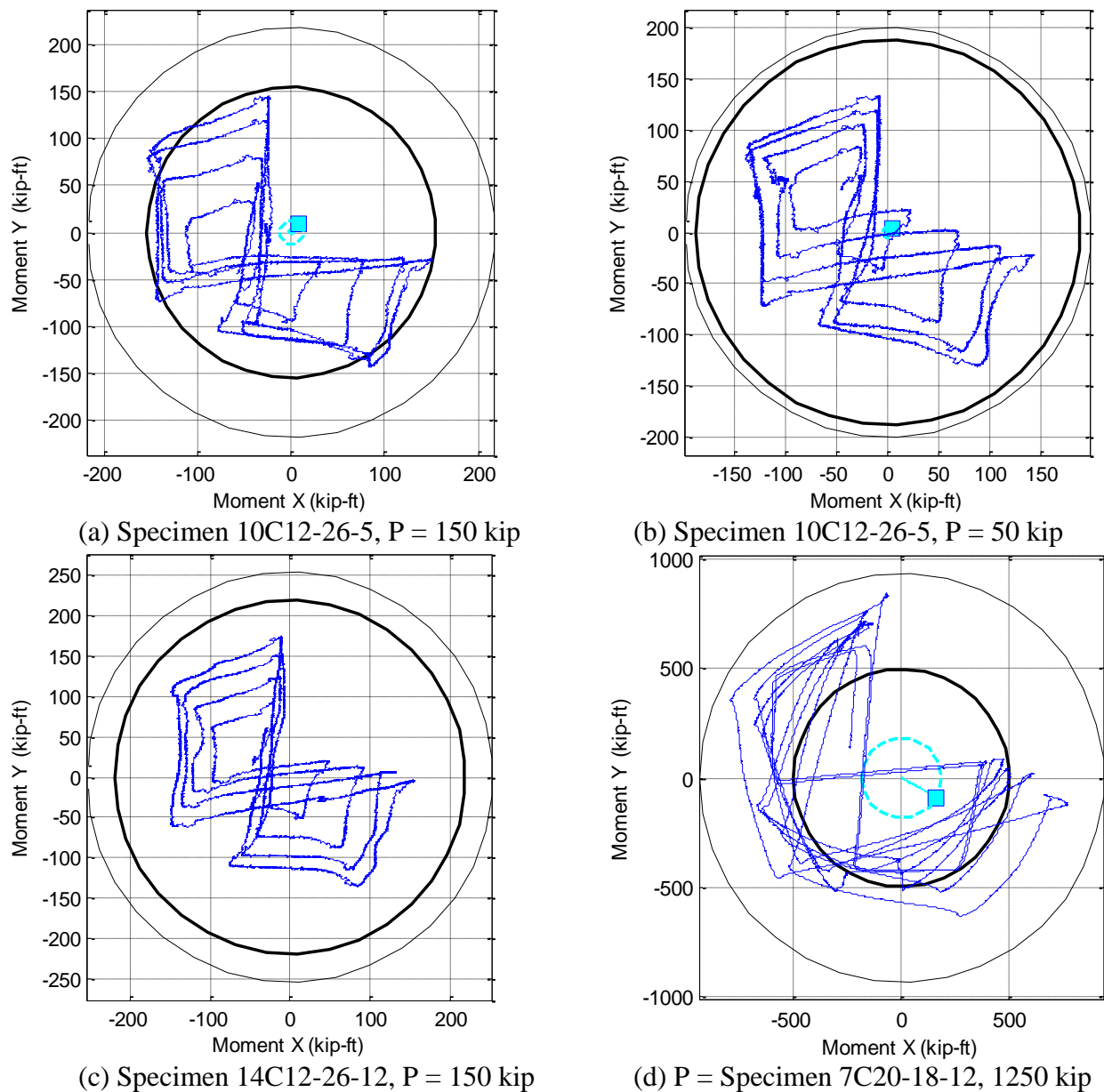
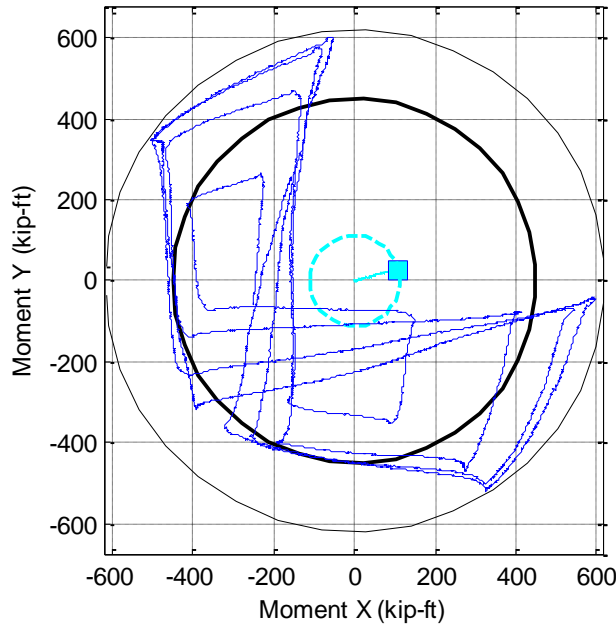
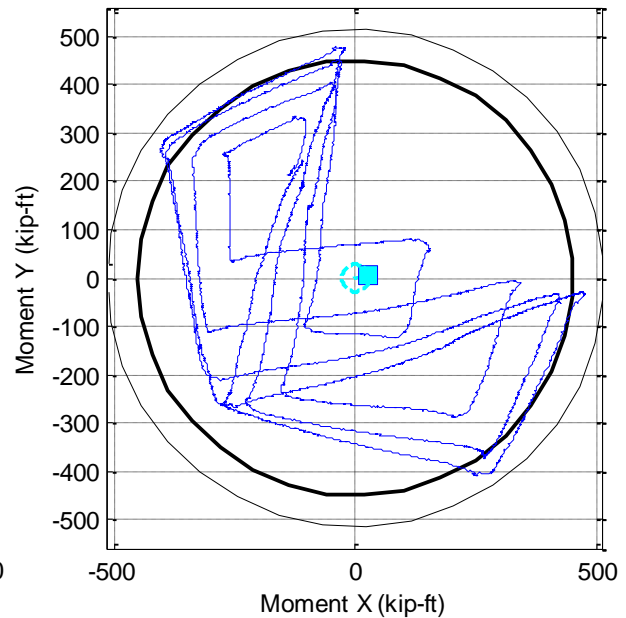


Figure 6.34. Biaxial moment path for the specimens 10-C12-26-5 and 14-C12-26-12 during LC3

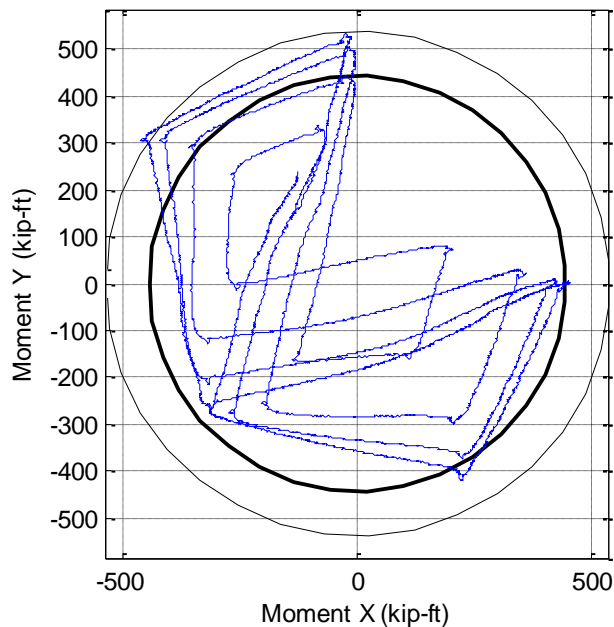
No general conclusions are extracted from these figures, aside from the comment that they appear to reflect reasonable results since the total moment path is inside the cross-sectional strength; there are no points extracted at the case the beam-column passes from a stable to an unstable configuration, and so the beam-column strength is not calibrated from these results.



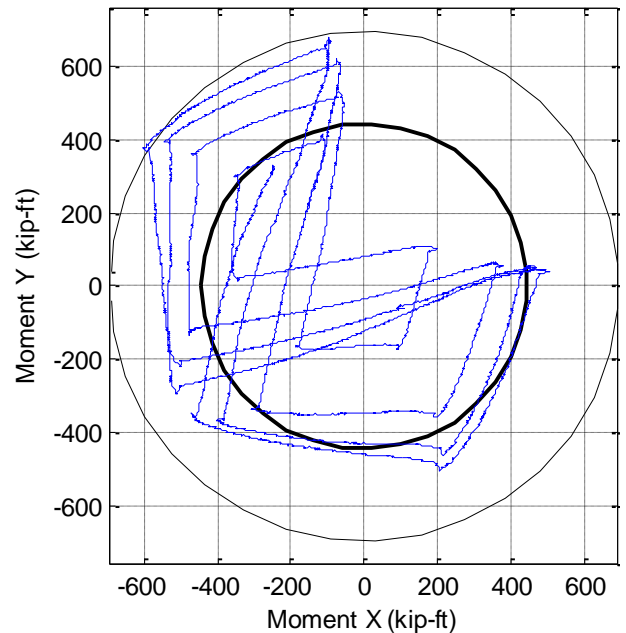
(a) Specimen 11C20-26-5, $P = 450$ kip



(b) Specimen 11C20-26-5, $P = 150$ kip

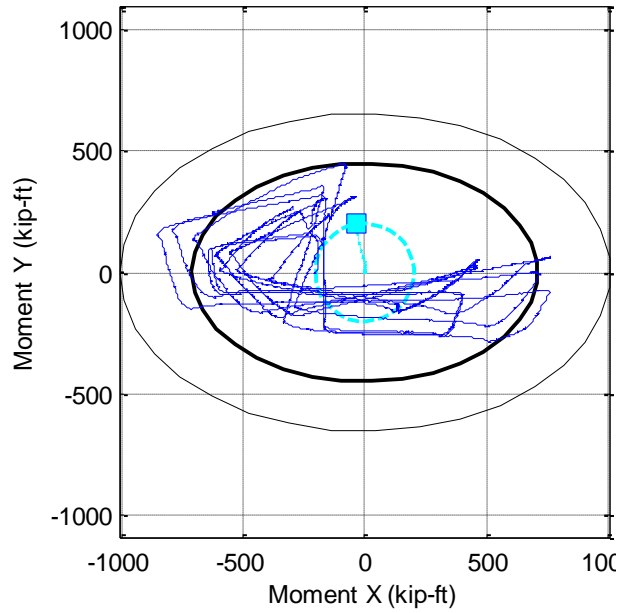


(c) Specimen 15C20-26-12, $P = 200$ kip

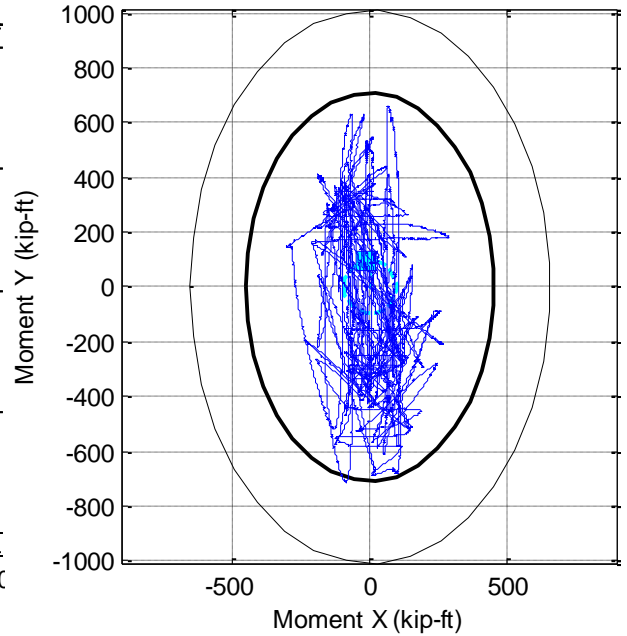


(d) Specimen 15C20-26-12, $P = 600$ kip

Figure 6.35. Biaxial moment path for the specimen 15-C20-26-12 during LC3

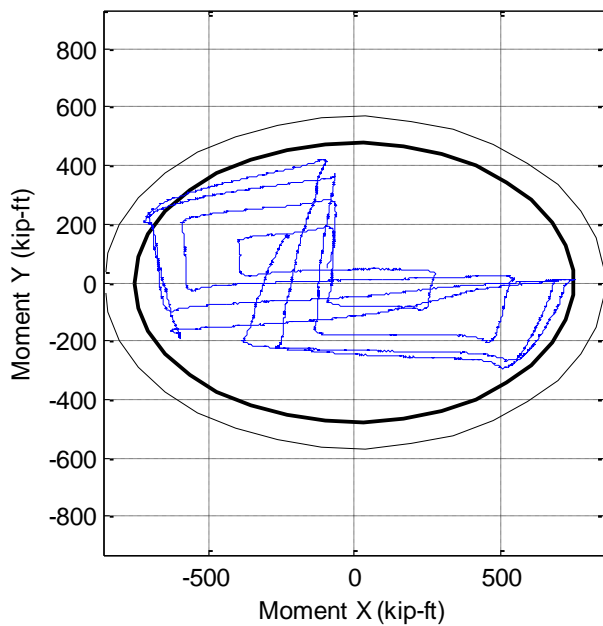


(a) Specimen 8Rw-18-12, $P = 800$ kip

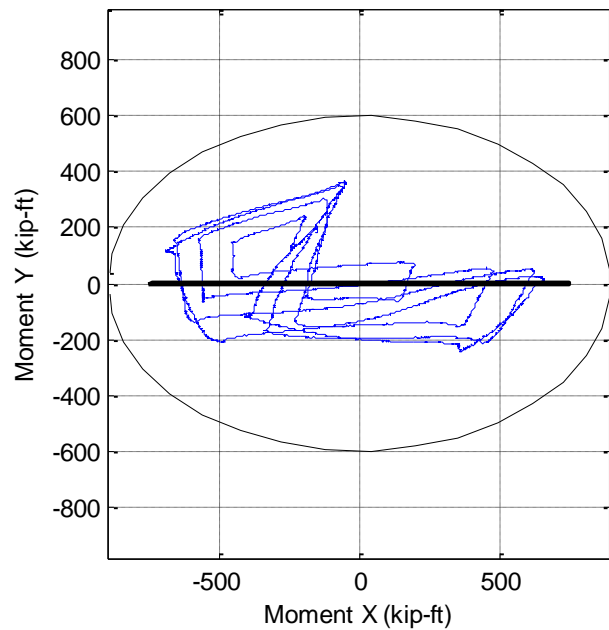


(b) Specimen 9Rs-18-12, $P = 800$ kip

Figure 6.36. Bi-axial moment path for the specimens 8Rw-18-12 and 9Rs-18-12 during LC3



(a) $P = 300$ kip



(b) $P = 500$ kip

Figure 6.37. Bi-axial moment path for the specimen 12-Rw-26-5 during LC3

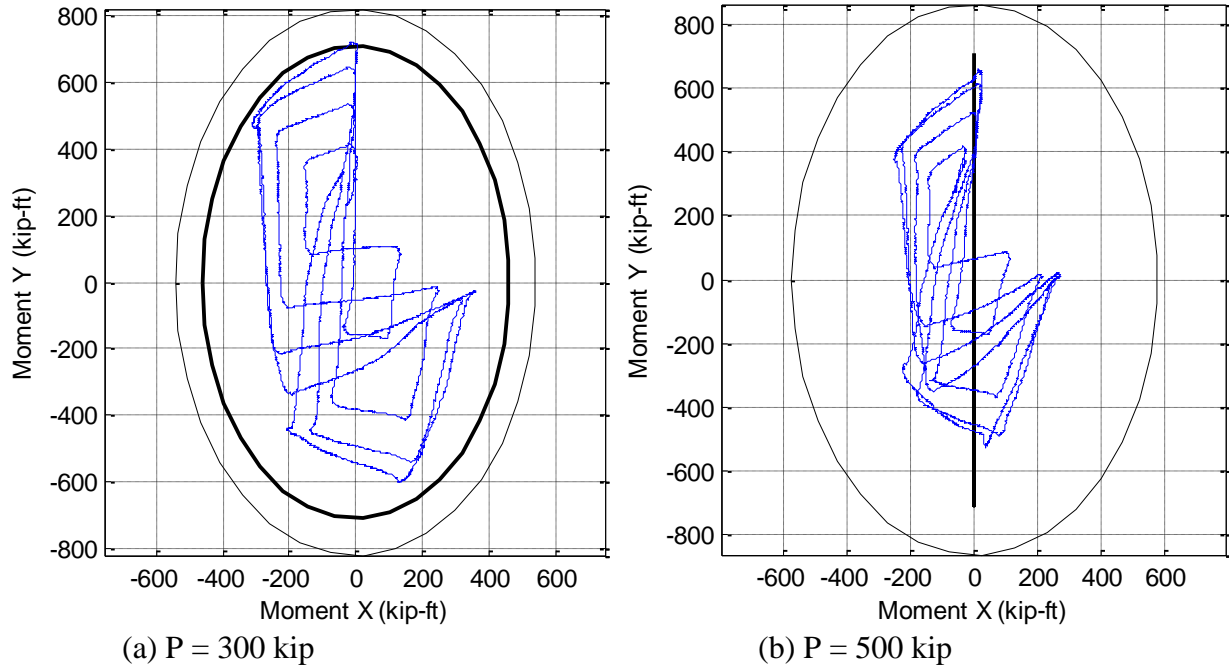


Figure 6.38. Biaxial moment path for the specimen 13Rs-26-5 during LC3

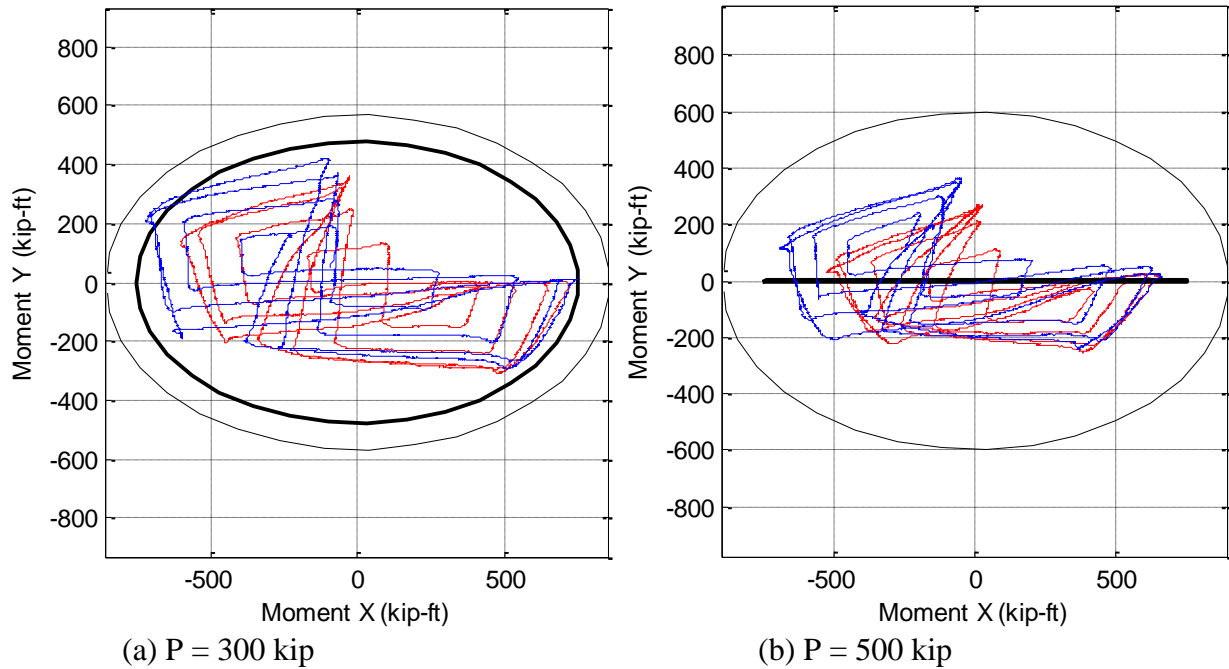
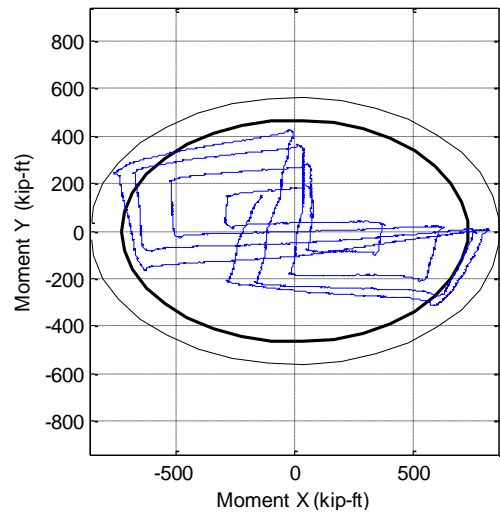
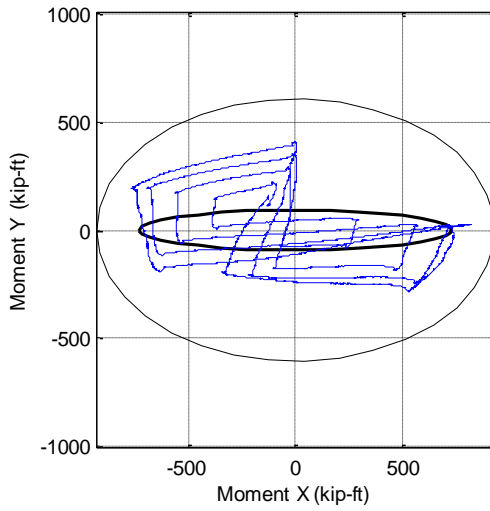


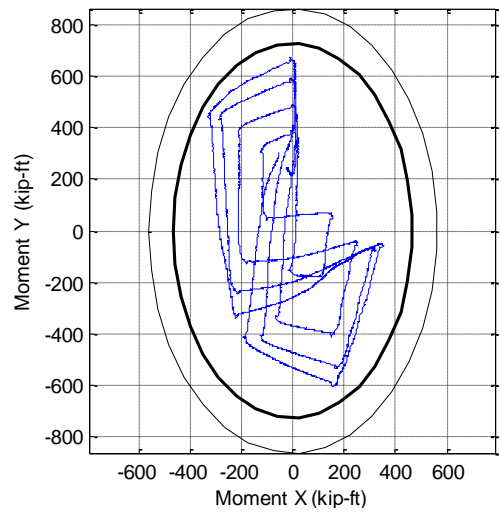
Figure 6.39. Biaxial moment path for the specimens 12-Rw-26-5 (blue path) and 13-Rs-26-5 (red path) during LC3



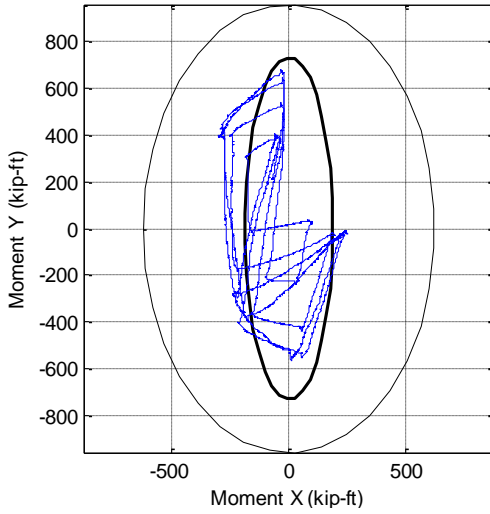
(a) Specimen 16, $P = 300$ kip



(b) Specimen 16, $P = 500$ kip

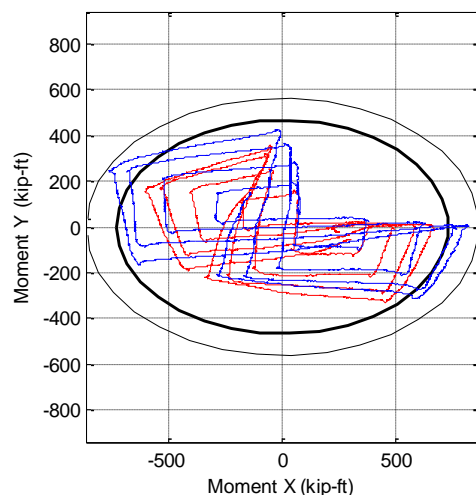


(c) Specimen 17, $P = 300$ kip



(d) Specimen 17, $P = 600$ kip

Figure 6.40. Biaxial moment path for the specimens 16-Rw-26-12 and 17-Rs-26-12 during LC3



(a) $P = 300$ kip

Figure 6.41. Biaxial moment path for the specimens 16-Rw-26-12 (blue) and 17-Rs-26-12 (red)

6.5. Determination of the interaction diagrams using computational analyses

Analytical interaction diagrams can be obtained using the same methodology that was described in section 6.3. In this section, the results of a set of analyses that were developed earlier in this research are presented in the form of P-M interaction diagrams; these diagrams are compared with the P-M diagrams obtained with the AISC Specifications for CFT cross-sections and beam-columns.

The prototypes beam-columns used in these analyses have the following characteristics.

- CCFT cross section (*labeled C20*) is an HSS20x¹/₄ that is filled with concrete of 5 ksi of strength.
- RCFT cross-section (*labeled Rs*) is an HSS20x⁵/₁₆ that is filled with concrete of 5 ksi of strength.
- A length of 18 feet and 26 feet was selected for both cross-section types.
- The members are idealized as straight and inclined cantilever beam-columns with fixed-free boundary conditions ($K=2$) and with an initial out of plumbness of $L/500$.
- The concrete is modeled as (1) with a rigid plastic model (*EPP*) as idealized in the plastic stress distribution method as used in the AISC Specifications, and (2) with the concrete model proposed by *Sakino* as described in Chapter 2. In the rigid plastic model, the plastic stress was assumed as $0.85f_c'$ and $0.95f_c'$ for the RCFT and CCFT cross-sections, respectively.
- Similarly, the steel is modeled as (1) with a rigid plastic model (*EPP*) as idealized in the plastic stress distribution method as used in the AISC Specifications, and (2) with the steel model proposed by *Sakino* model as described in Chapter 2.

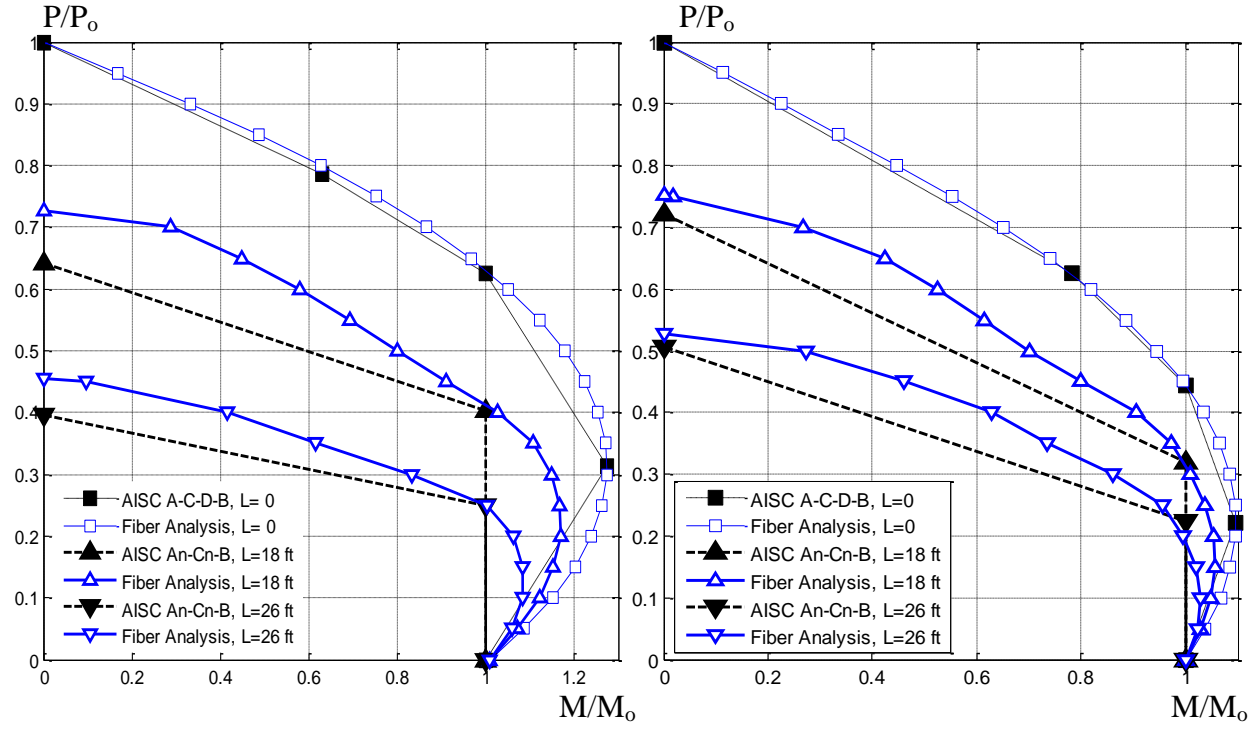
Similarly to the loading path used in the experimental test, these analyses are subjected to a desired initial axial loading (lower than the critical loading) that develops a P-M path, where the moments are used up as a consequence of the initial imperfection; the total imperfection moment is stored as M_{imp} once the target axial loading P is reached. Then, holding the gravity loading, a lateral force at the top is applied and later stopped once the system reaches its maximum lateral strength; at this peak strength, the total moment at the base (M_{total}) in the cantilever beam column is calculated including the peak overturning moment and the corresponding second order $P\Delta$ moment. Finally, the net stable moment (M_{net}) extracted from the

analyses is the difference between the total moment and the moment used up by the imperfection.

The latter process is repeated for different target loads P , and the set of points extracted are used to create the P-M Interaction diagram. Figure 6.42 shows these results with both axial loads and moments normalized with the corresponding pure axial (P_o) and pure bending (M_o) capacity. The corresponding AISC simplified bilinear P-M diagram (AISC A_λ - C_λ -B) proposed for slender beam-columns, as well as the cross-section strength based on fiber analysis and the AISC 2005 Specifications (AISC Interaction A-E-C-D-B) are also compared in these figures.

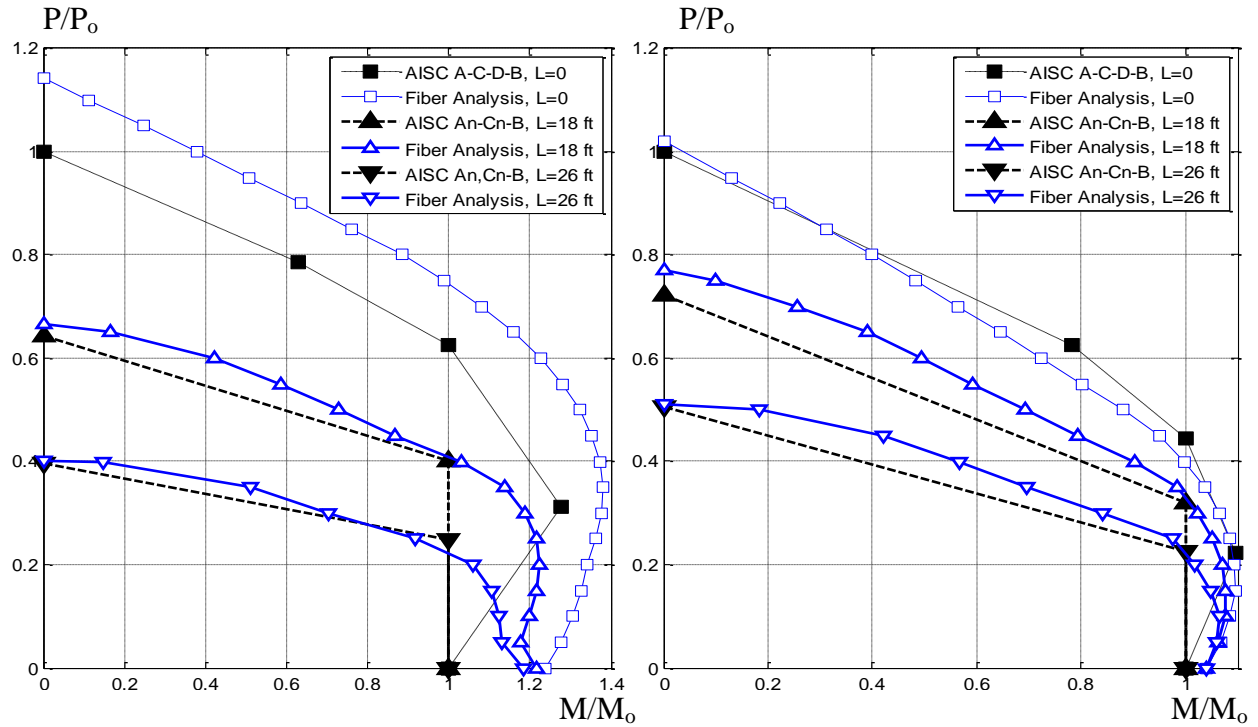
These results expose the following observations:

- The simplified bilinear AISC beam column strength is, for the shorter beam-columns, conservative and a lower bound of the capacity obtained in the analyses. Chapter 5 shows that for short members, the analytical prediction in the buckling load (P_n) is larger than in the AISC Specifications. In addition, the bulge that is developed in the cross-section capacity due to the concrete contribution is kept in short beam-columns.
- However, as the slenderness increases, the unusable flexural capacity due to instability and the imperfection boost up and, as a consequence, the net moment reduces significantly. This reduction will be reflected mainly in the flexural capacity, and the shape may be changed to: (1) a P-M diagram with a small or lacking any bulge, or (2) a diagonal line from the buckling capacity P_n to the pure flexural capacity M_o , or (3) a convex shape. Thus, in slender beam-columns, the AISC prediction may be larger than what is expected based on these models. The latter conclusion was also observed in the experimental data extracted from the tests in section 6.4.
- Confinement effects accounted through the Sakino model induces higher compressive and flexural strength at the cross-section level and for beam-columns, but such compressive over strength vanished for intermediate and slender beam-columns.



(a) C20 section, EPP model

(b) Rs section, EPP model



(c) C20 section, Sakino model

(d) Rs section, Sakino model

Figure 6.42. P-M interaction diagrams for the composite CFT beam columns

6.6. Conclusions

In this chapter, extraction of the axial and flexural capacities from the tests and from some analyses was performed. For the experimental tests, the load cases were selected in the load protocol to obtain a set of P-M points of the interaction diagrams, for both uniaxial bending through LC2 and biaxial bending through LC3. The axial load levels used in the load protocol were applied between the anchor points C_λ and D_λ , interval where the maximum moment is developed in the interaction diagram and the axial loading of columns in practice is very common.

A methodology that has being approved and used in the calibration of steel members in the AISC Specifications (ASCE 1997; SSRC 2010) was discussed and applied in the extraction of axial and flexural capacities for CFT specimens tested and the prototypes analyzed in this project.

The total capacity of the specimens for the given axial load level ($P-M_{total}$) extracted from the tests has implicit the reduction of the unusable flexural capacity due to the instability effects. In addition, the net capacity for the given axial load ($P-M_{net}$) has in addition the reduction of the unusable flexural capacity that is consumed by the imperfections.

The net moments extracted from the test specimens in the shorter specimens drop outside of the bilinear simplified diagram of the AISC for beam-columns, which underestimates the P-M capacities of the shorter specimens around the anchor point at D_λ by assuming a vertical line between the points C_λ -B. The purpose of neglecting the bulge with this vertical line in the AISC Simplified diagram was intended to be conservative through a lower bound, and this simplification was supported by the available experimental data at the time (AISC 2005, Leon and Hajjar 2008).

The shape of the bilinear simplified diagram is less conservative in beam-columns with intermediate slenderness; however, for slender beam-columns (as the specimens tested in this research), the AISC simplified diagram overestimates the net moments capacities and is no longer conservative. The low net moment values are consequence of the substantial flexural capacity that is lost due to the large imperfections that were extracted from LC1. However, many of these points are still unconservative even if the imperfections are neglected. This

unconservative behavior in slender beam-columns suggests a change in the design equations for the calculation of P-M interaction diagrams that serves both short and slender beam columns.

Similar conclusions on the behavior type as described above were observed in both uniaxial and biaxial bending. Extracted total and net moments in some specimens under biaxial bending show circular interaction surfaces in CCFTs and elliptical interaction surfaces in RCFTs. The latter was primarily observed in the earlier probes; however, as the load protocol progresses, the interaction surfaces exhibited reduction in size and changes in shape. This reduction is significant in RCFTs and in the axis related to the weak orientation as a consequence of the progression of large amount of deformation and degradation due to local buckling in the steel and losses of confinement in concrete.

In addition, similar observations and behavior type that was discussed above for the experimental tests were obtained in the computational analysis. Even though more calibration with the computational analysis is needed for slender beam columns, the conclusions stated in this section seems consistent.

Based on the results observed in this section, Chapter 10 proposes design equations that aim in the determination of the P-M interaction diagram for CFT cross-sections and beam-columns. The beam-column capacity as proposed in Chapter 10 includes the unusable capacity due to both stability effects and imperfections.

CHAPTER 7

RESPONSE TO LATERAL FORCES AND EVOLUTION OF THE FLEXURAL RIGIDITY

7.1. Introduction

In Chapter 6, loading cases LC2 and LC3 were used to extract experimental values for the P-M interaction diagrams. In this chapter, these loading cases are used again to evaluate the response of composite CFT beam-columns to lateral forces, as well as the evolution of the flexural rigidity for each specimen through the entire loading protocol. These load cases were explained with detail in Chapter 3 and Chapter 6.

The main purpose of this chapter is the extraction and evaluation of the effective stiffness EI_{eff} associated with these composite members. The evolution of the member stiffness is analyzed with respect to the influence of the applied gravity load and its degradation through the loading protocol. To back track the rigidities, some experimental responses will be evaluated in Section 7.2. Section 7.2.1 presents the lateral force – column drift response obtained for each specimen; the maximum level of drifts reached at the test is highlighted for both the unidirectional loading LC2 and the bidirectional loading LC3. Similarly, Section 7.2.2 presents the moment – curvatures response at the critical cross-section near the base.

Finally, Section 7.3 analyzes the evolution of the effective stiffness (EI_{eff}) extracted from both the lateral force – drift response (presented in Section 7.2.1) and the moment – curvature response (presented in Section 7.2.2). The effective stiffness (EI_{eff}) that was extracted in Chapter 5 from the pure compression loading (LC1) is also included in this analysis.

Finally, Section 7.4 shows the results obtained from computational analysis under the same loading conditions that were applied in LC2 and LC3. The analytical response is also compared with the experimental results.

7.2. Experimental tests

7.2.1. Lateral force – column drift response (F - Δ)

Lateral force (F , kip) vs. Drift (Δ/L , %) curves obtained experimentally for the uniaxial load cases (LC2) are shown in Figure 7.2 through Figure 7.20, and for the biaxial load cases (LC3) in Figure 7.21 through Figure 7.37. The titles of these figures indicate the specimen name, the sustained gravity load on the specimen, and the effective length factor expected based on the controlled boundary conditions. In addition, these figures state the displacement path used (i.e. diamond-shape or eight-shape) and the unloading criterion (i.e. reversal at peak force, or reversal at desired target). All the uniaxial and biaxial load case types are described in Chapters 3 and 5, but as summary, these load cases start when the specimens are moved to zero displacement in both X and Y direction, and then the desired compression load is imposed.

Figure 7.2 to Figure 7.10 show the lateral force – drift response along the axis of motion obtained from the two cycles with the uniaxial loading case (LC2) and reversals at the peak force. This loading case type was applied to the first half of specimens (specimens 1 to 9), and the following observations can be made about these figures:

- Except for Specimen 1, these specimens exhibit a positive stiffness slope until the peak where this slope becomes zero. This peak force is the maximum lateral strength of the beam-column and beyond this point the specimen becomes unstable due to combined material and geometric nonlinearities; the stability of the specimen is maintained beyond the peak since the lateral DOFs are in displacement control. The set of points at where the specimen reaches its maximum lateral capacity were used to obtain experimental values of the interaction diagram as shown in Chapter 5.
- In Specimen 1, the slope is negative since the axial load applied initially was close or exceeded its buckling capacity, and therefore, no additional lateral force could be resisted by the specimen in this condition; again, stability of the specimen is maintained since the lateral DOFs are in displacement control.
- Since few cycles are applied and the peak force was not exceeded, there is little or no strength and stiffness degradation as expected. The drift at the peak depends on the sustained axial load, reaching larger drifts with lower axial load as a consequence of the $P\Delta$ effects.

- During the testing of these specimens, and once the peak lateral force was reached with a speed rate of 1 in/min of lateral motion, the controller was set to “Pause” so new input commands for driving the crosshead in the opposite direction could be input. However, instantaneous with this pause, the lateral force exhibited an instant reduction of the lateral force on the order of 1 to 2 kips, and a similar amount of lateral force reduction once the “Pause” was removed and the specimen driven in the opposite direction. As schematically illustrated in Figure 7.1, a total force relaxation of about 2 to 4 kips was observed at the point of displacement reversals, exhibiting a very stiff response in this pause interval that is likely due to the system friction rather than the specimen rigidity. This relaxation on the lateral force at reversals was also observed in all the types of the uniaxial and the biaxial loading cases (LC2 and LC3).

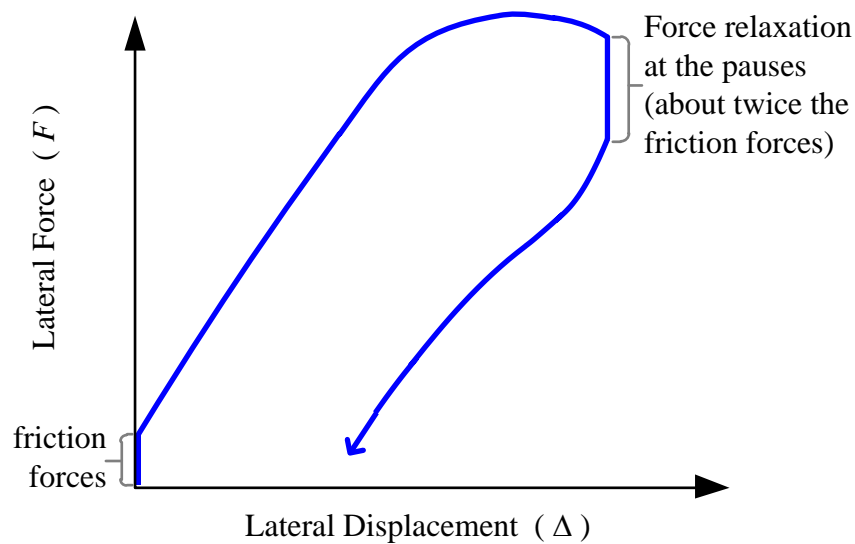


Figure 7.1. Force relaxation at the testing pauses (schematic)

Denavit and Hajjar (2010) accounted for the system friction with rigid-plastic spring at the column tip, with 1 kip of strength and placed at the top in the transverse X and Y directions. The analytical response with these spring elements is similar to the obtained experimental response, but it develops hysteresis loops with higher energy dissipation than that expected without the system friction.

Figure 7.11 to Figure 7.20 show the lateral force – drift cyclic response along the motion axis obtained from the uniaxial loading case (LC2) where the reversals were set at a target drift, mostly 1% of drift increment to the max stroke. This loading case type was applied to the second half of specimens (specimens 10 to 18), and the following notes can be made about these figures:

- In general, all these figures show a good cyclic behavior, especially when the sustained axial load is lower than the axial load at the balance point ($P_{CN}/2$). In these cases, larger drifts were obtained before the maximum peak response was reached. For the cases with higher sustained axial loads, the peak force was met earlier with lower drifts as a consequence of the $P\Delta$ effects.
- Higher degradation is observed for those specimens under high gravity load and when the reversals took place in the post-peak interval at higher drifts.
- As for the previous figures, a very stiff response is exhibited at the reversals as a consequence of the system friction, where the lateral force reduces instantly on the order of 1 to 2 kip.

Figure 7.21 to Figure 7.25 show the lateral force – drift response along the X and Y axis obtained from the biaxial loading case (LC3) where the diamond shape displacement pattern was used. This load case was described in Chapters 3 and 5. As summary, a set of 8 probes (16 probes in Specimen 3) around the specimen were applied. The reversals for each probe were made at the peak force in either the X or Y direction. Between the reversals and the consecutive probe, the specimen was driven back partially and then move along a diamond in order to reduce the amount of testing time. This loading case type was applied in the specimens 2 to 6.

As for the uniaxial case, the peak force at each probe is the maximum lateral strength of the beam-column in a given direction. The set of points at where the specimen reaches its maximum lateral capacity were used to obtain experimental values of the interaction surfaces that were presented in Chapter 5. The following observations can be made about these figures:

- Since the compression loading applied is lower than the buckling capacity, a positive stiffness slope is developed until the peak force is met in either X or Y direction.
- As for the uniaxial case, the drift at the peak depends on the sustained axial load, achieving smaller drifts with higher axial loads as a consequence of the $P\Delta$ effects.

- Since one cycle was applied in each probe and the peak force was not exceeded in either X or Y direction, there is no strength and stiffness degradation observed in the CCFTs. A slight amount of degradation was noted in the RCFTs; this fact validates the interaction surfaces that were obtained in Chapter 5.
- Due to the symmetric shape in CCFTs, similar strength and the stiffness were obtained for both the X and Y direction. However, lower peak strength and lower stiffness were obtained in the weak axis of RCFTs as expected.

Figure 7.26 to Figure 7.36 show the lateral force – drift cyclic response along the X and Y axis obtained from the biaxial loading case (LC3) where the eight-shape displacement pattern was used. This load case is described in Chapters 3 and 5. As summary, reversals were set at a target drift, mostly 1% of drift increment to the max stroke. This loading case type was applied in the specimen 7, 8 and 10 to 18. The following observations can be made about these figures:

- Higher degradation is observed for those specimens under high gravity load and when the reversals took place in the post-peak interval with at higher drifts.
- Due to the symmetric shape in CCFTs, similar strength and the stiffness were obtained for both the X and Y direction. However, lower peak strength and lower stiffness were obtained in the weak axis of RCFTs as expected.
- In these figures, a very stiff response is exhibited at the reversals. In these cases, the change in lateral force with no change in displacement is not only due to the system friction; the main reason for this stiff is due the motion type of this load case. For example, in the first ramp, motion is induced only along the X-axis (holding zero displacement in Y); once the desired drift is reached in the X direction, the controller is set to hold this displacement and then displace the specimen along the Y-axis only the until the desired drift. Here, again, the Y displacement is held and the specimen is driven back to zero displacement in X. Finally, again holding zero displacement in X, the specimen is driven back to zero displacement in Y. This process is then repeated in the negatives X and Y sides, and then both repeated with another target drift. Thus, at the ramps when the specimens is moved in one axis and held in the other, one of the response will exhibit change in force without change in displacement, but without this meaning a

rigid stiffness in the specimens for this interval. Instead, the stiffness of the specimen is related to the part of response when both lateral forces and drifts are changing.

Finally, Figure 7.37 show the lateral force – drift cyclic response along the X and Y axis obtained in the Specimen 9 from the biaxial loading case (LC3) where the probe-subprobe type was used. This load case is described in Chapters 3 and 5. As summary, reversals were set in this loading type at the peaks of lateral strength in either X or Y direction for each probe or subprobe. This load case also aims to obtain the interaction surface and minimizing the testing time. This response also shows lower peak strength and lower stiffness in the weak axis of this RCFT. More details about the post-processing response obtained for this specimen with this load case are presented in Denavit *et al.* (2010).

From all these figures, the slopes at the first unloading path in both positive and negative sides are extracted. These slopes are extracted during the motion ramps in order to avoid the stiff values measured at the pauses as a consequence of the friction in the system. For the RCFT specimens, the stiffness was extracted according to its orientation (stiffness in weak axis for the *Rw* group, and strong axis stiffness for the *Rs* group); this criterion was also used in the biaxial load cases. The stiffness values extracted from these figures are reported in Section 7.3.

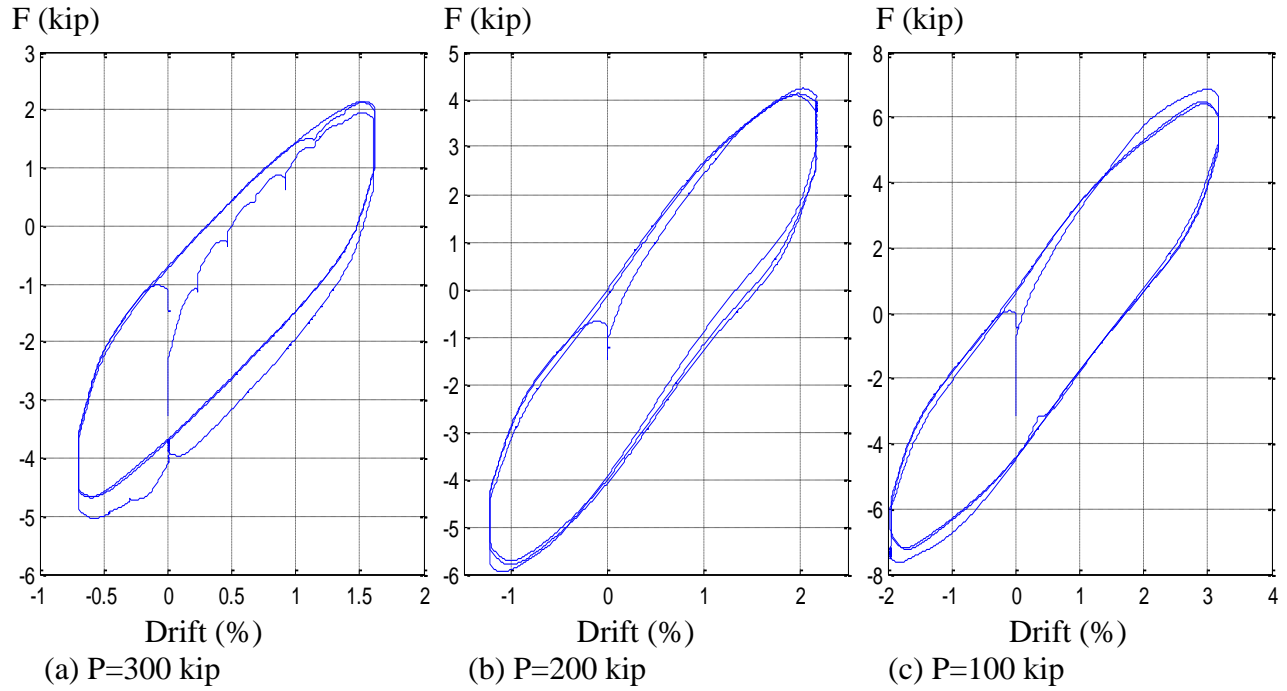


Figure 7.2. Lateral force (F , kip) vs. Drift (Δ/L , %) from the uniaxial load cases (LC2, reversal at peak force) for the Specimen 2C12-18-5

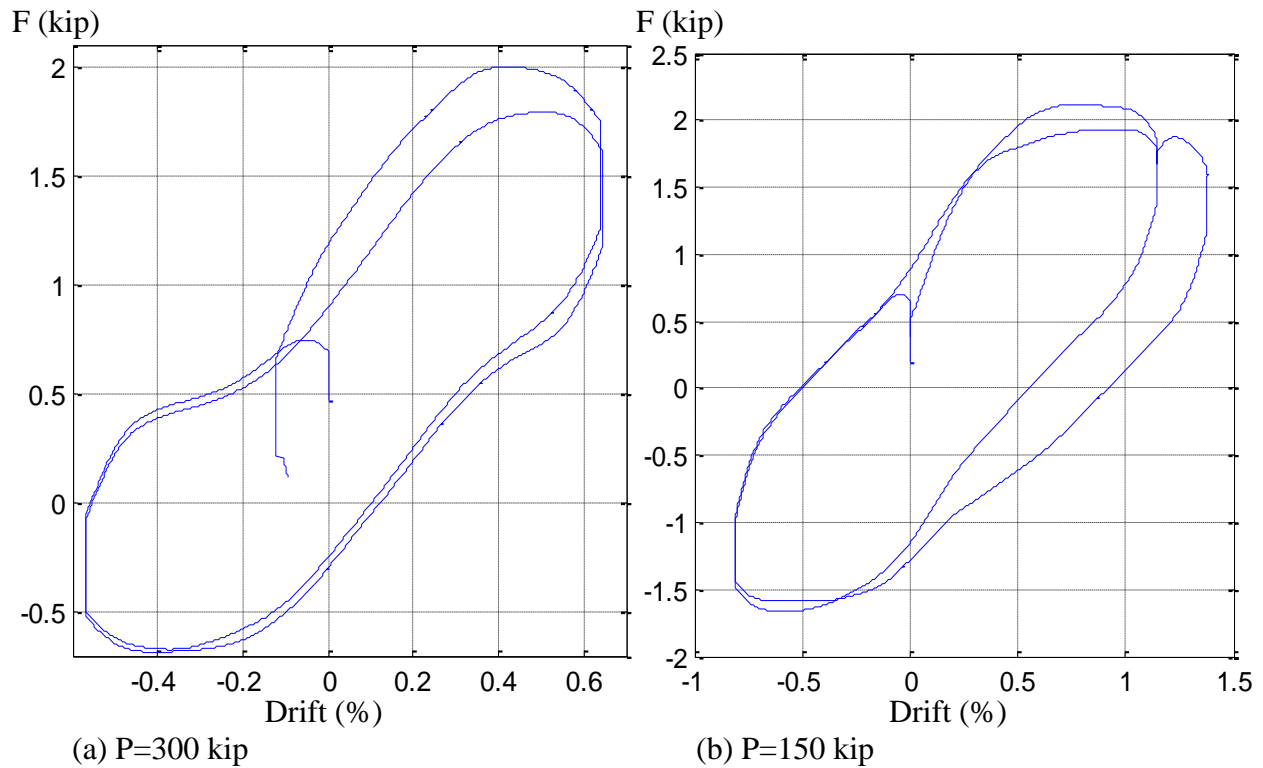


Figure 7.3. Lateral force (F , kip) vs. Drift (Δ/L , %) from the uniaxial load cases (LC2, reversal at peak force) for the Specimen 6C12-18-12

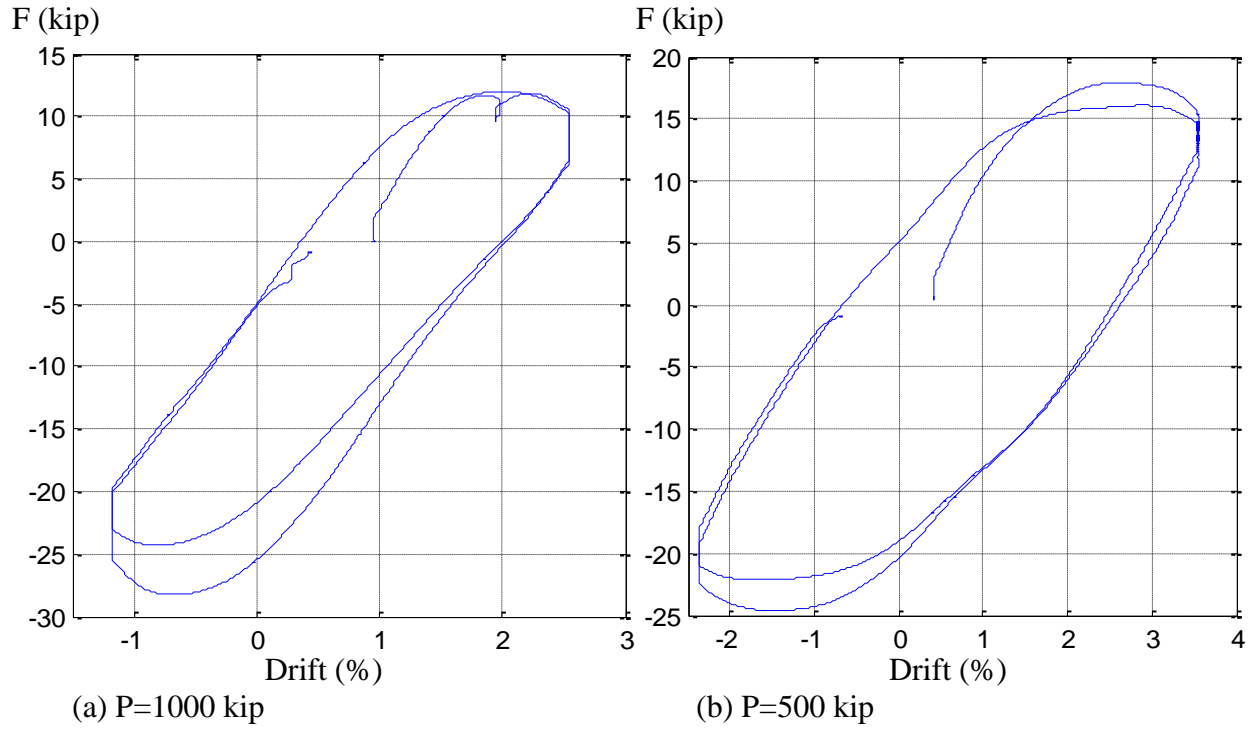


Figure 7.4. Lateral force (F , kip) vs. Drift (Δ/L , %) from the uniaxial load cases (LC2, reversal at peak force) for the Specimen 3C20-18-5

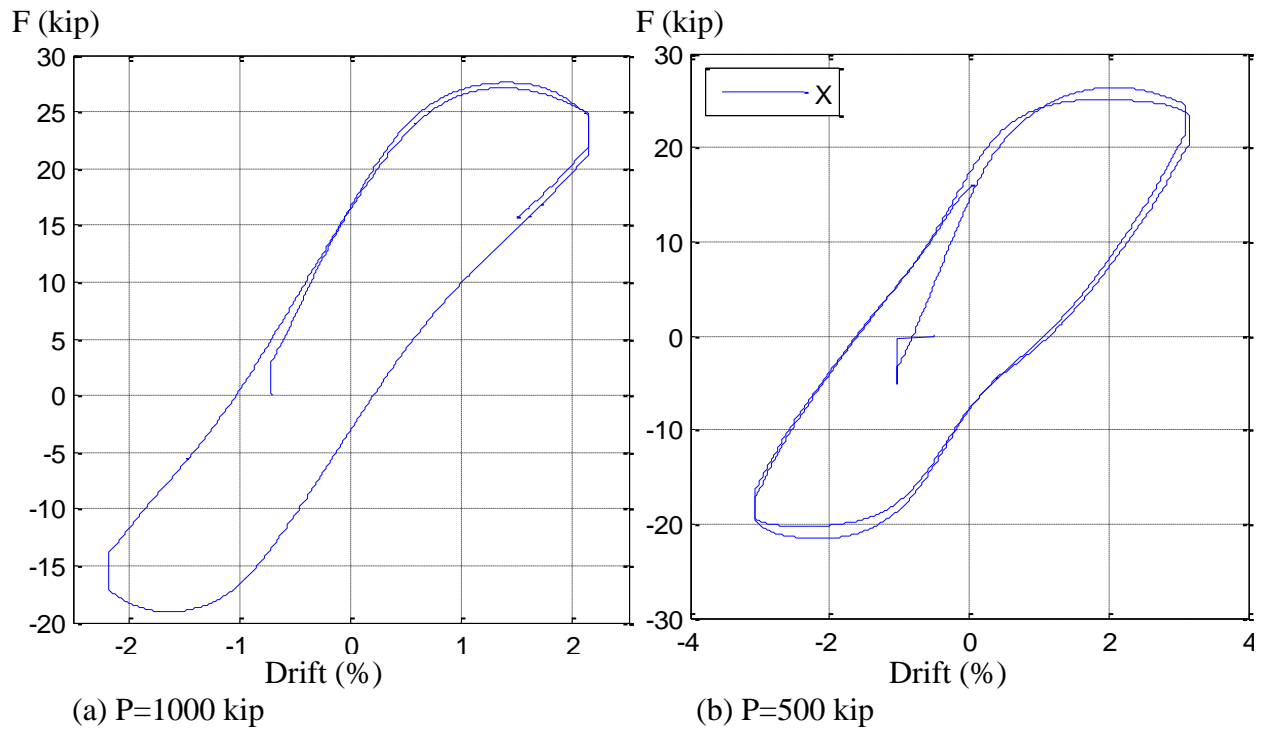


Figure 7.5. Lateral force (F , kip) vs. Drift (Δ/L , %) from the uniaxial load cases (LC2, reversal at peak force) for the Specimen 7C20-18-12

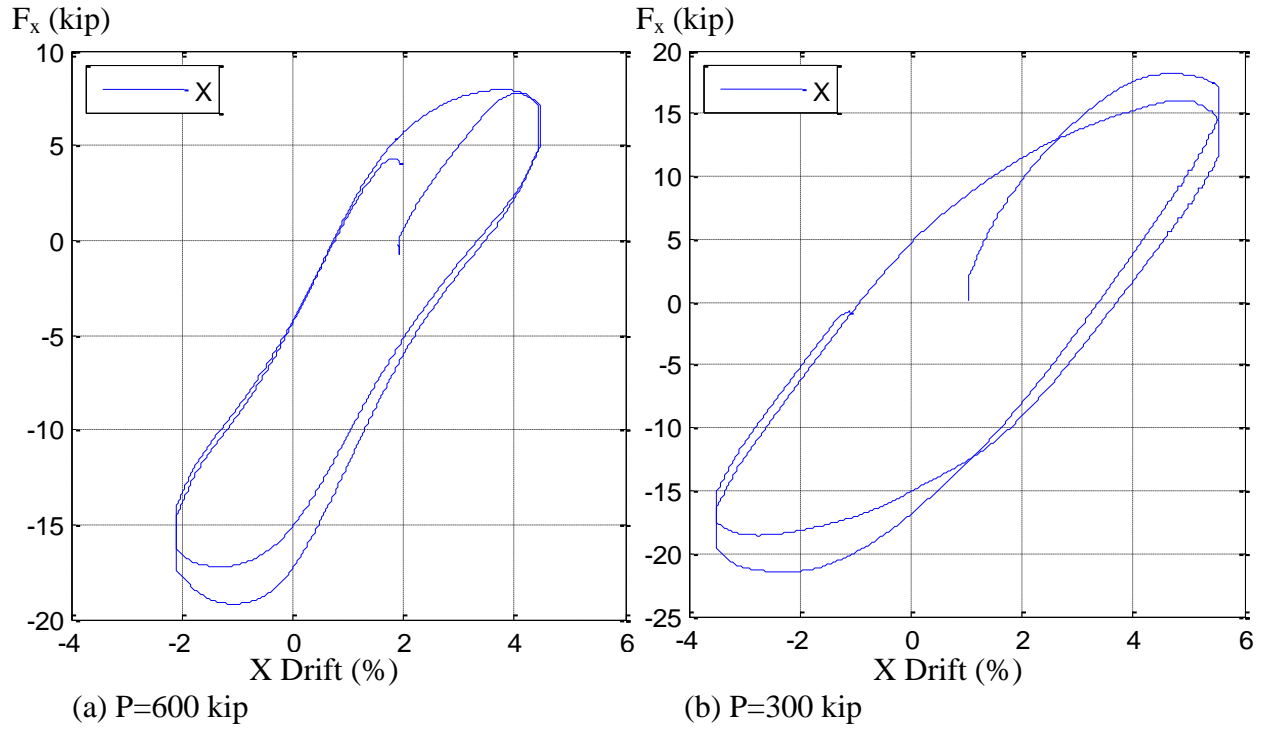


Figure 7.6. Lateral force (F , kip) vs. Drift (Δ/L , %) from the uniaxial load cases (LC2, reversal at peak force) for the Specimen 4Rw-18-5

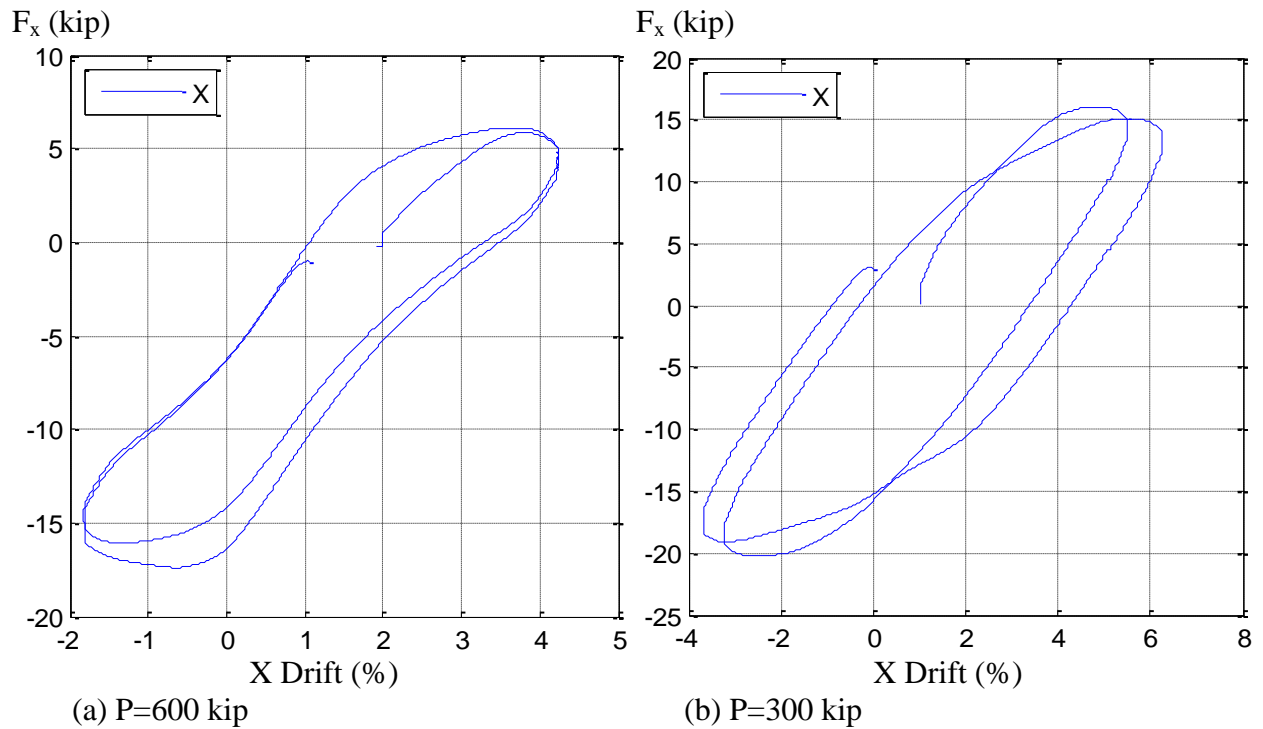


Figure 7.7. Lateral force (F , kip) vs. Drift (Δ/L , %) from the uniaxial load cases (LC2, reversal at peak force) for the Specimen 8Rw-18-12

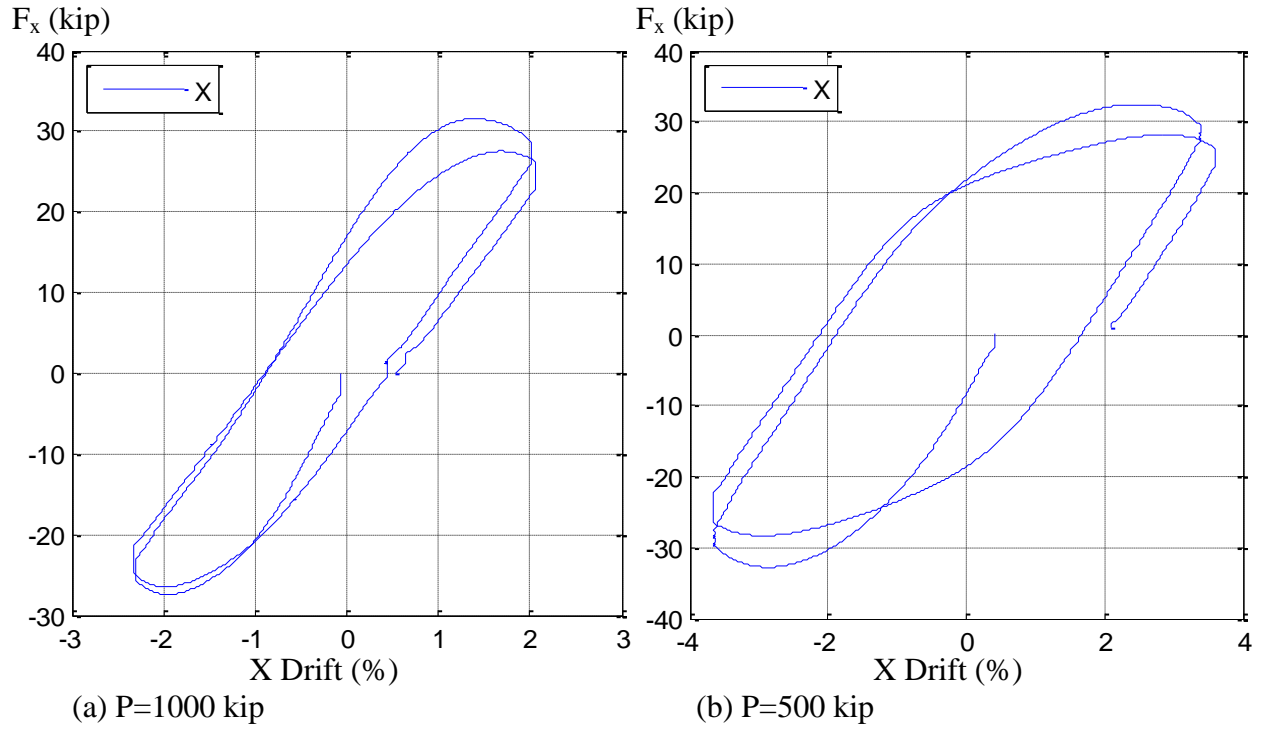


Figure 7.8. Lateral force (F , kip) vs. Drift (Δ/L , %) from the uniaxial load cases (LC2, reversal at peak force) for the Specimen 5Rs-18-5

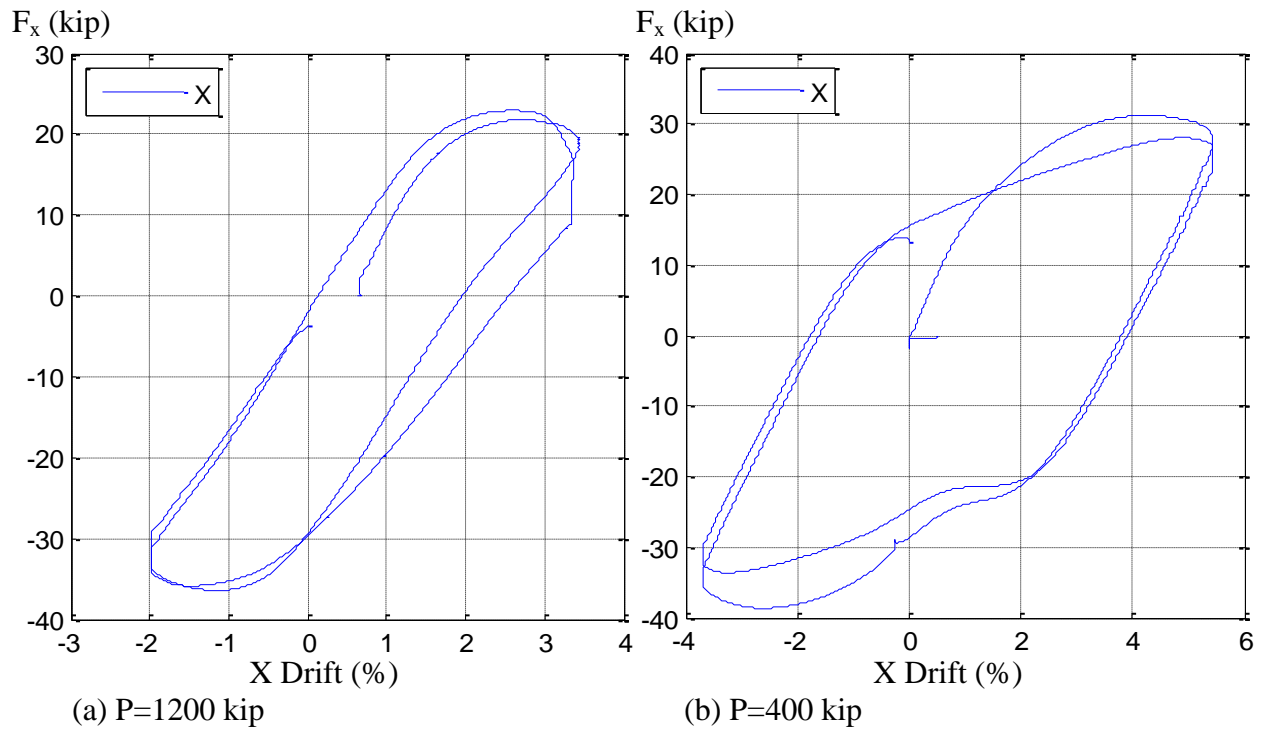


Figure 7.9. Lateral force (F , kip) vs. Drift (Δ/L , %) from the uniaxial load cases (LC2, reversal at peak force) for the Specimen 9Rs-18-12

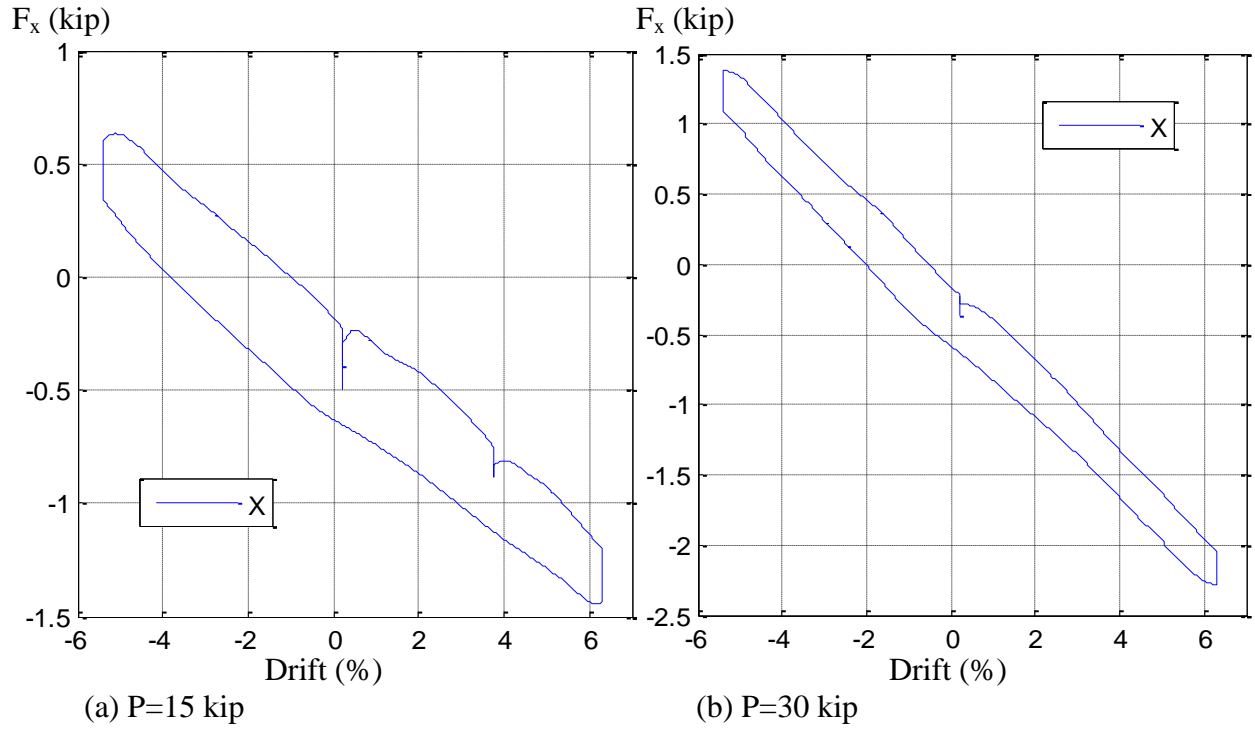


Figure 7.10. Lateral force (F , kip) vs. Drift (Δ/L , %) from the uniaxial load cases (LC2, $K=1$) for the Specimen 1C5-18-5

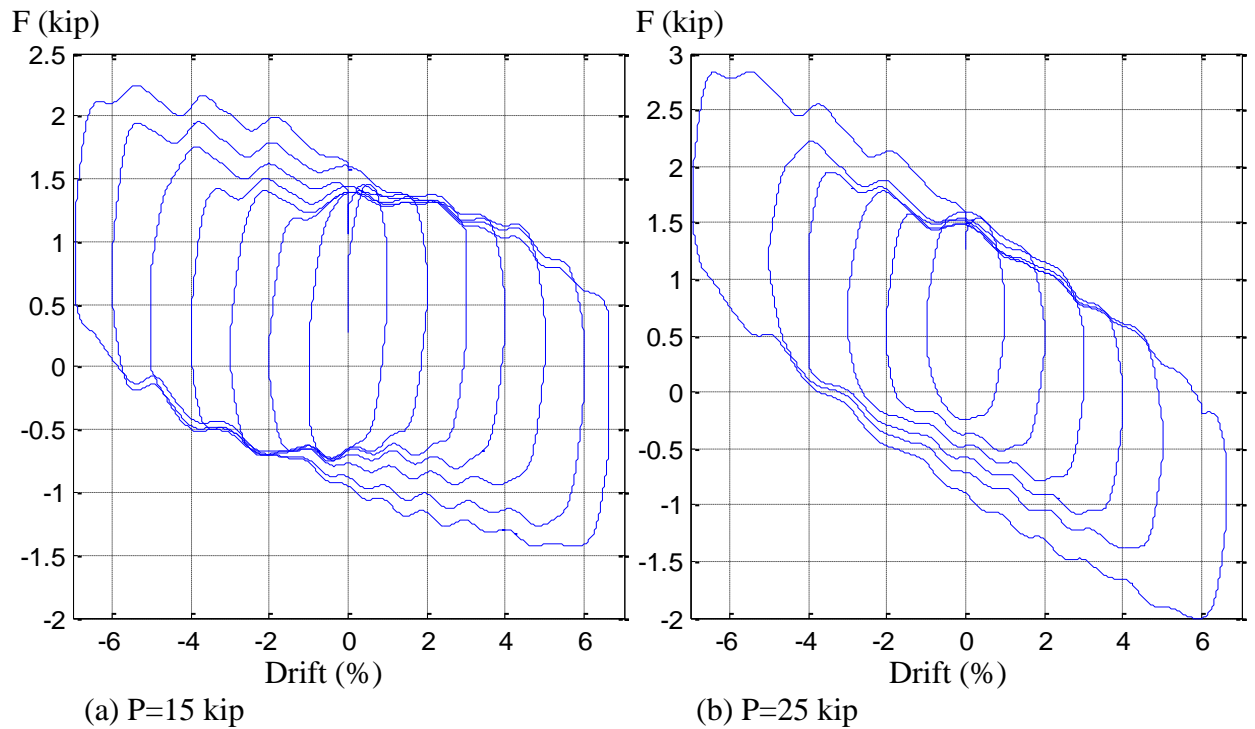


Figure 7.11. Lateral force (F , kip) vs. Drift (Δ/L , %) from the uniaxial load cases (LC2, $K=1$) for the Specimen 18C5-26-12

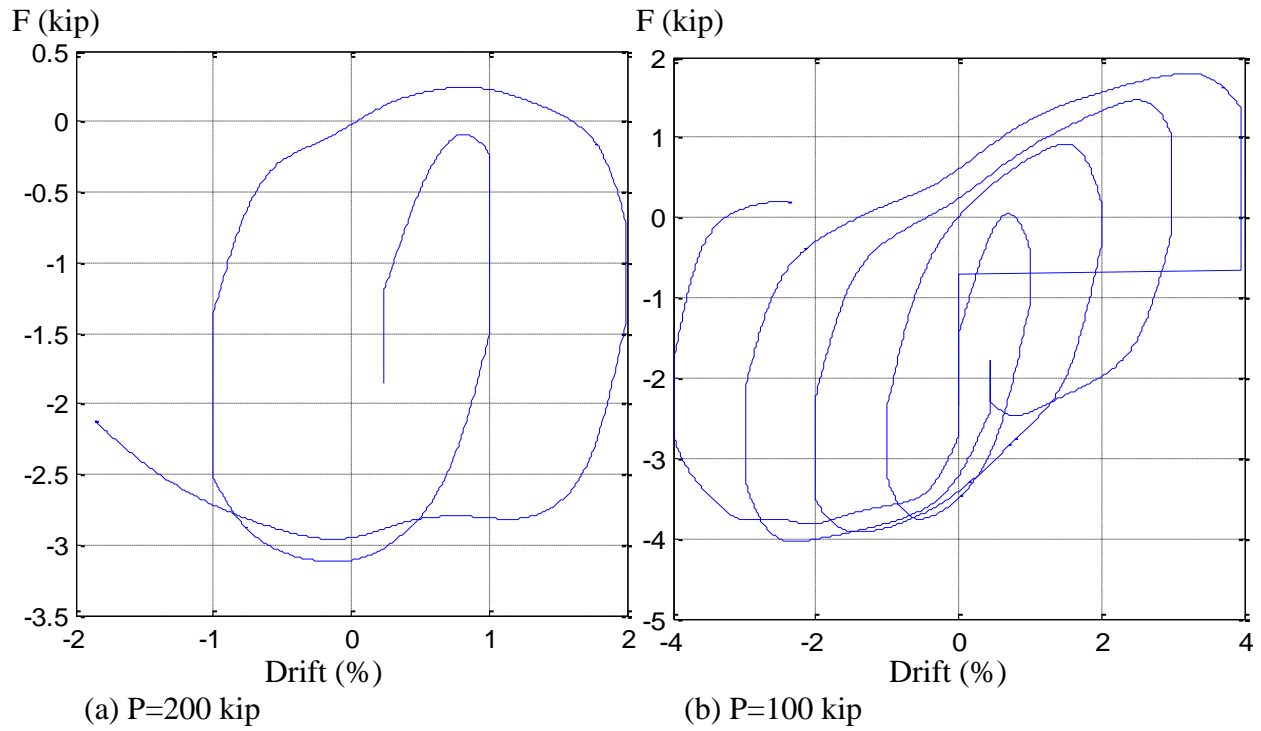


Figure 7.12. Lateral force (F , kip) vs. Drift (ΔL , %) from the uniaxial load cases (LC2, reversal at desired drift) for the Specimens 10C12-26-5

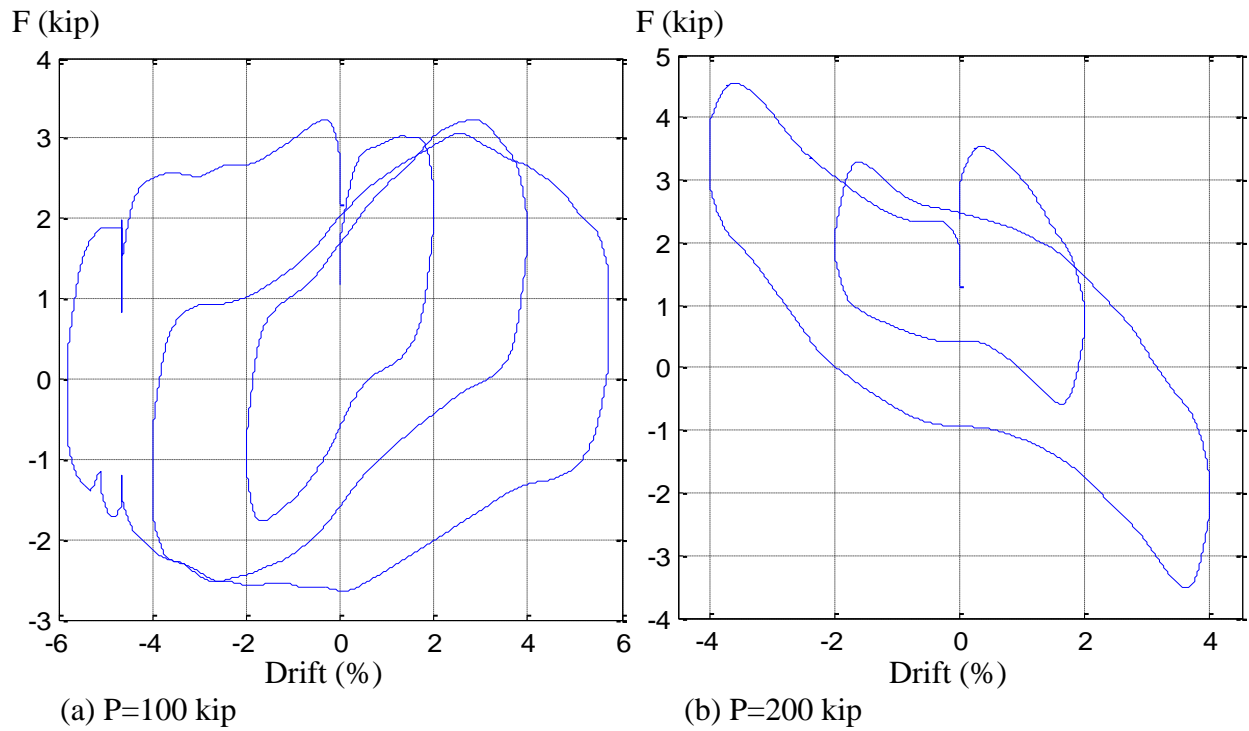


Figure 7.13. Lateral force (F , kip) vs. Drift (ΔL , %) from the uniaxial load cases (LC2, reversal at desired drift) for the specimen 14C12-26-12

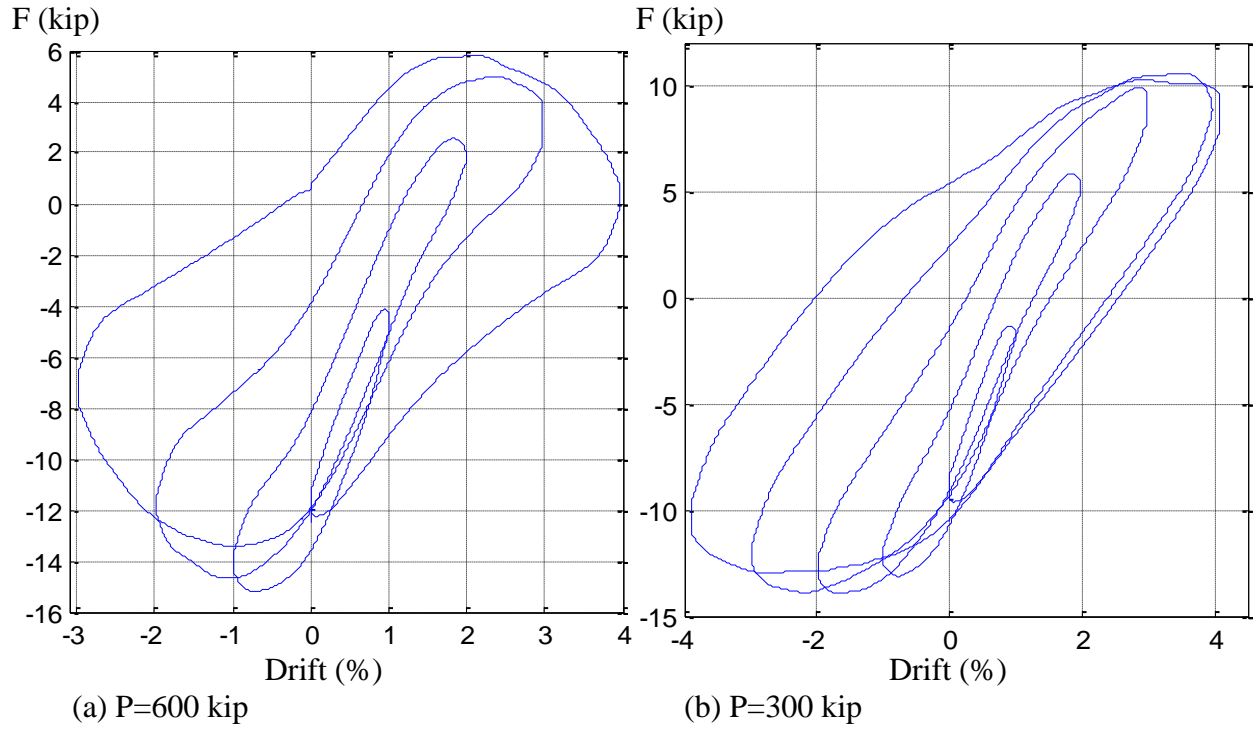


Figure 7.14. Lateral force (F , kip) vs. Drift (ΔL , %) from the uniaxial load cases (LC2, reversal at desired drift) for the Specimen 11C20-26-5

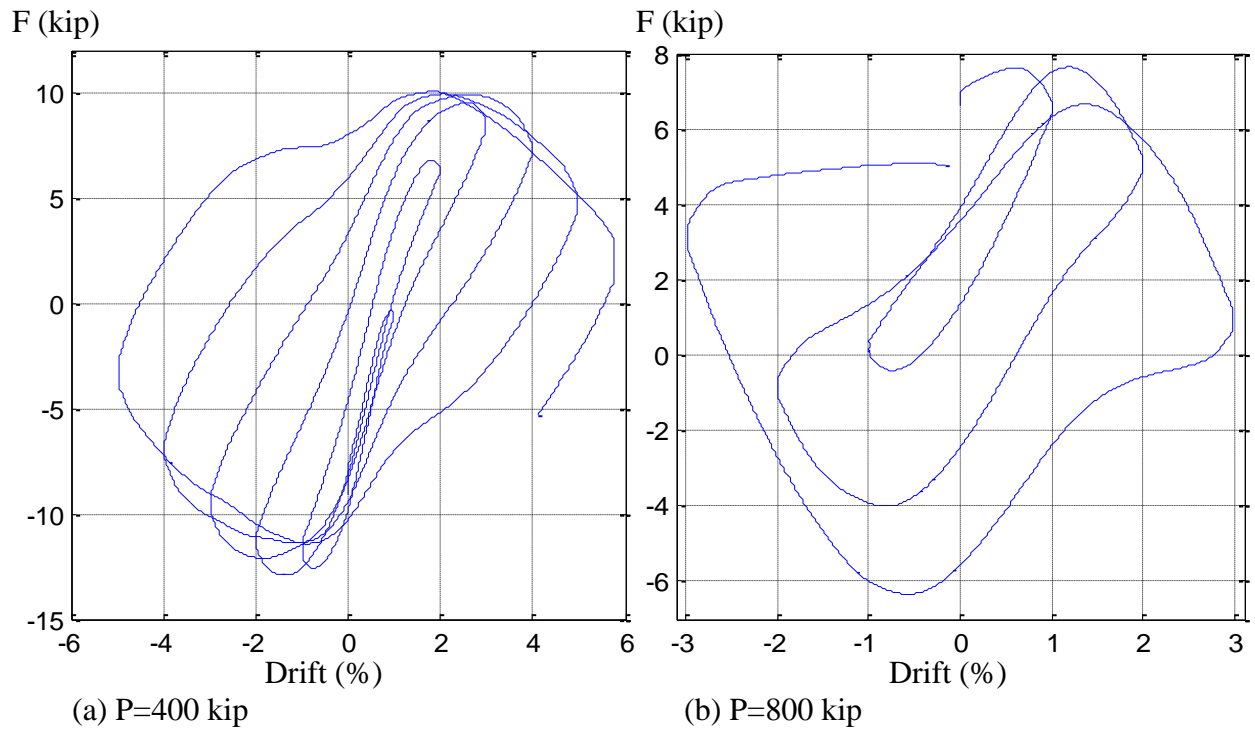


Figure 7.15. Lateral force (F , kip) vs. Drift (ΔL , %) from the uniaxial load cases (LC2, reversal at desired drift) for the Specimen 15C20-26-12

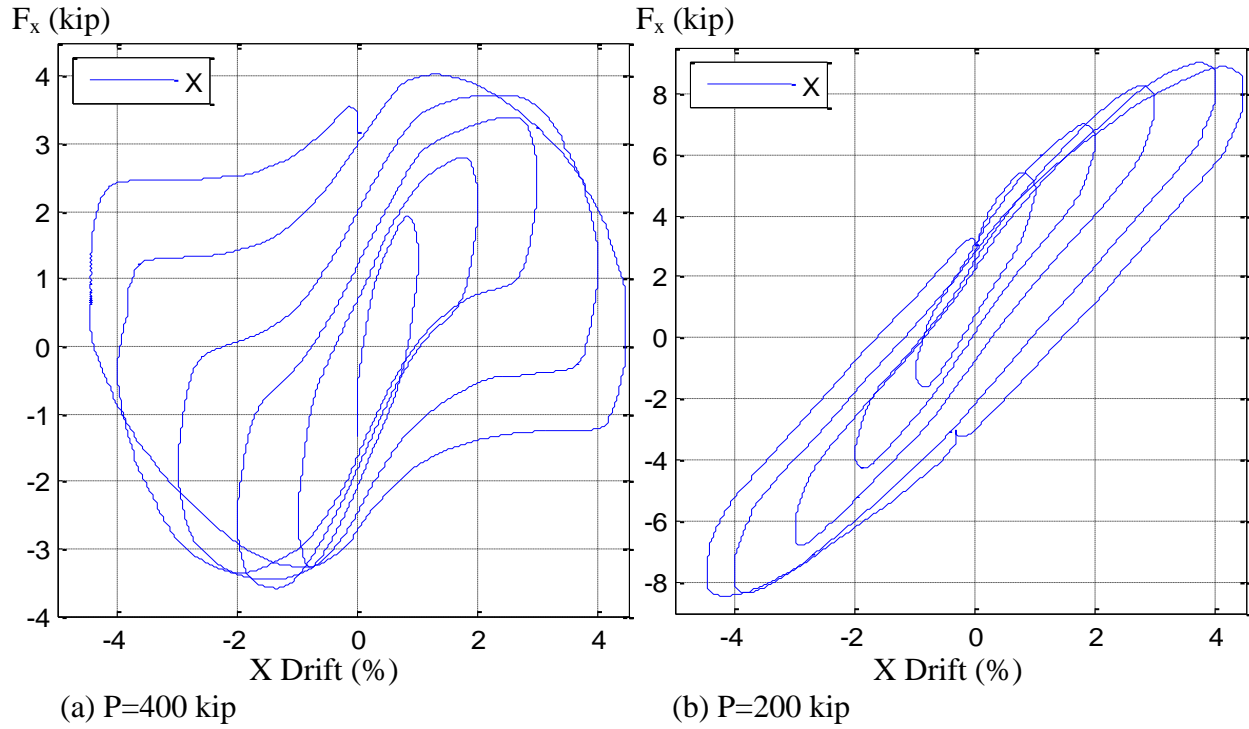


Figure 7.16. Lateral force (F , kip) vs. Drift (ΔL , %) from the uniaxial load cases (LC2, reversal at desired drift) for the Specimen 12Rw-26-5

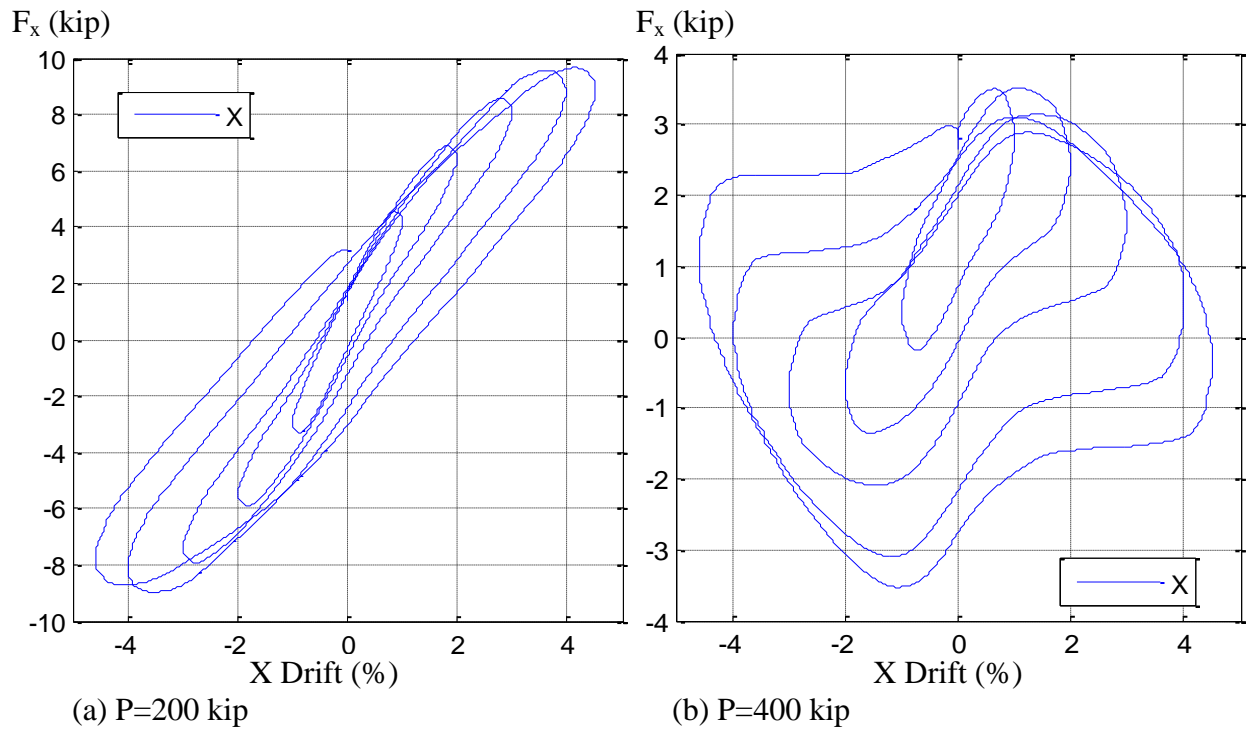


Figure 7.17. Lateral force (F , kip) vs. Drift (ΔL , %) from the uniaxial load cases (LC2, reversal at desired drift) for the Specimen 16Rw-26-12

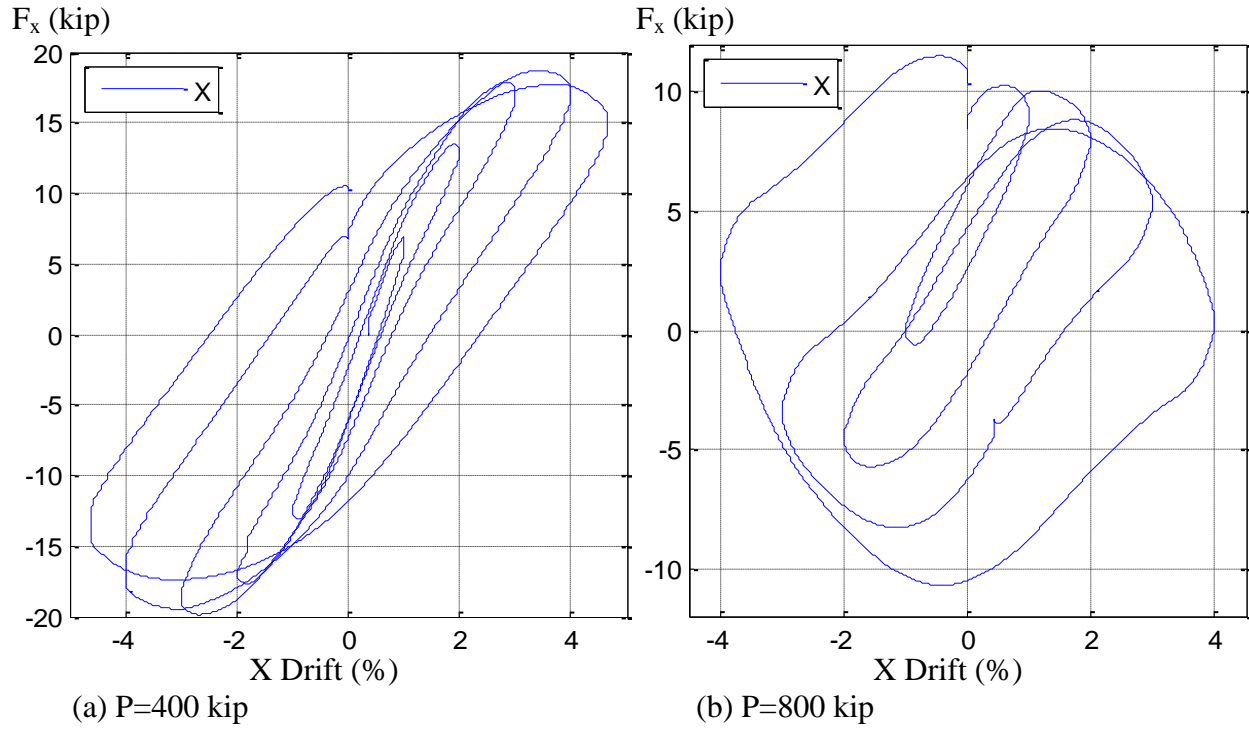


Figure 7.18. Lateral force (F , kip) vs. Drift (ΔL , %) from the uniaxial load cases (LC2, reversal at desired drift) for the Specimen 13Rs-26-5

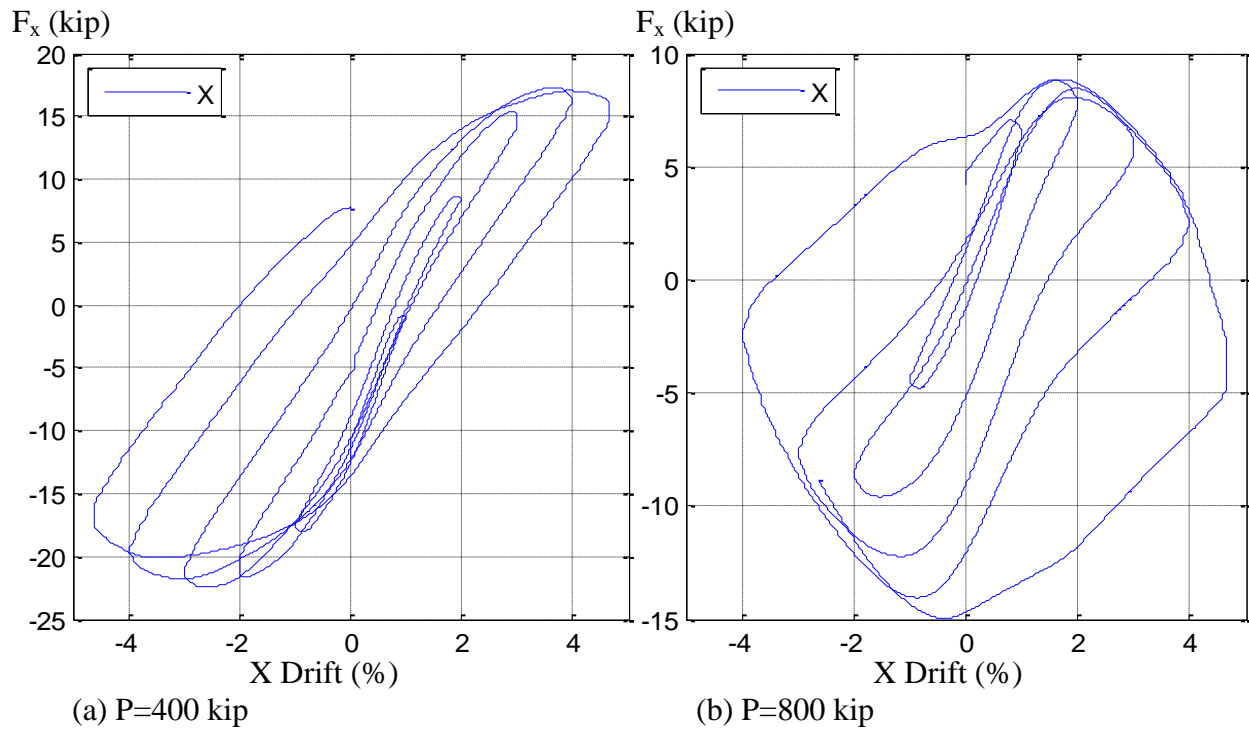


Figure 7.19. Lateral force (F , kip) vs. Drift (ΔL , %) from the uniaxial load cases (LC2, reversal at desired drift) for the Specimen 17Rs-26-12

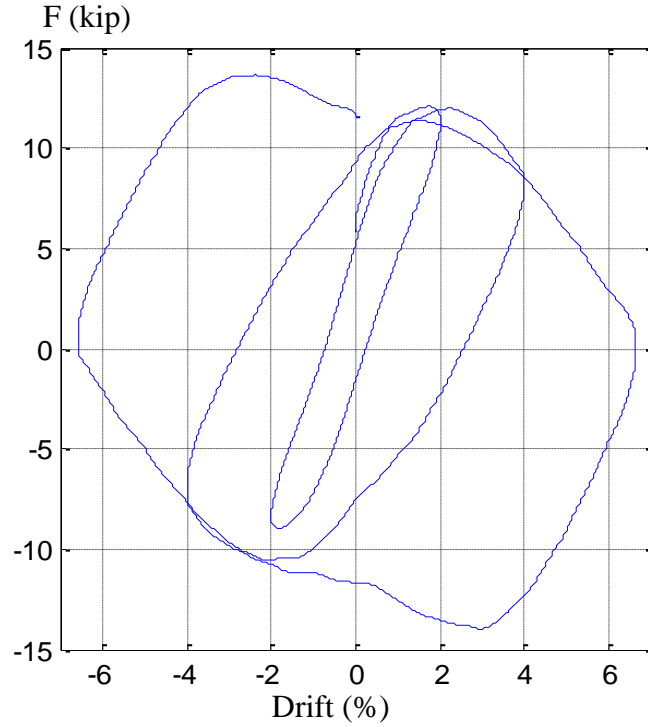


Figure 7.20. Lateral force (F , kip) vs. Drift (ΔL , %) from the uniaxial load case (LC2, $K=1$) for the Specimen 14C12-26-12 ($P=300$ kip)

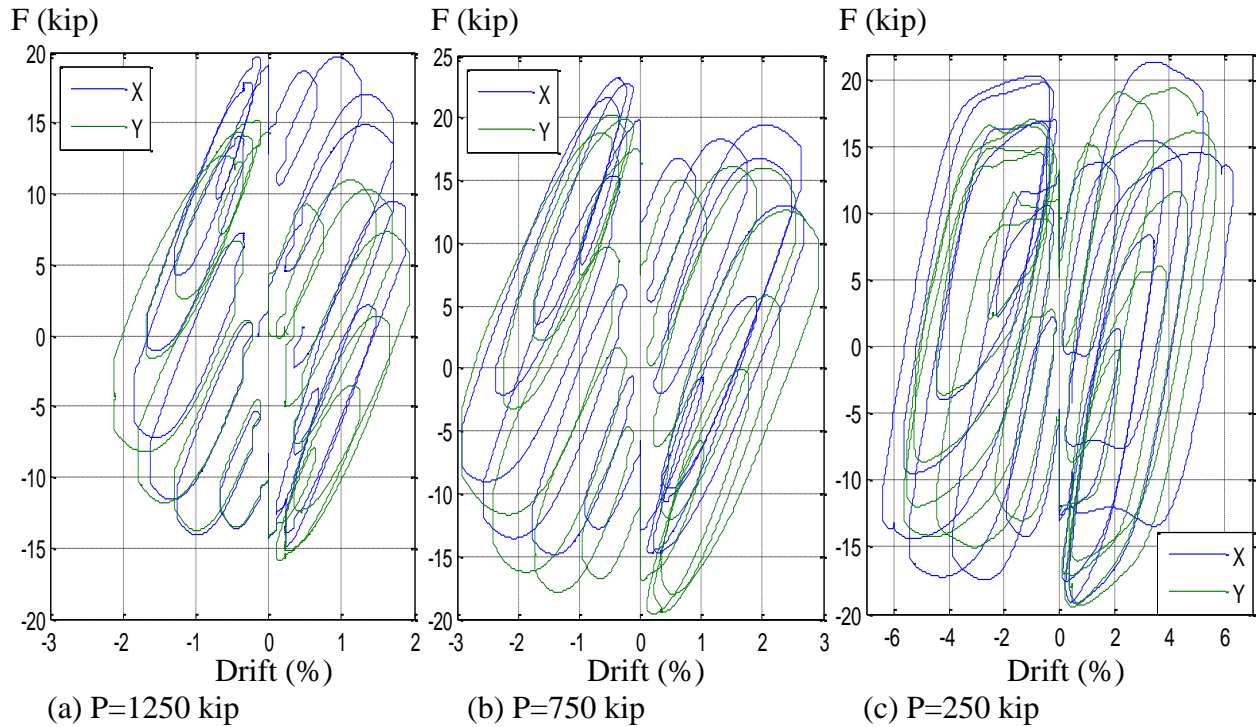


Figure 7.21. Lateral force (F , kip) vs. Drift (ΔL , %) from the biaxial load cases (LC3, diamond-shape) for the Specimen 3C20-18-5

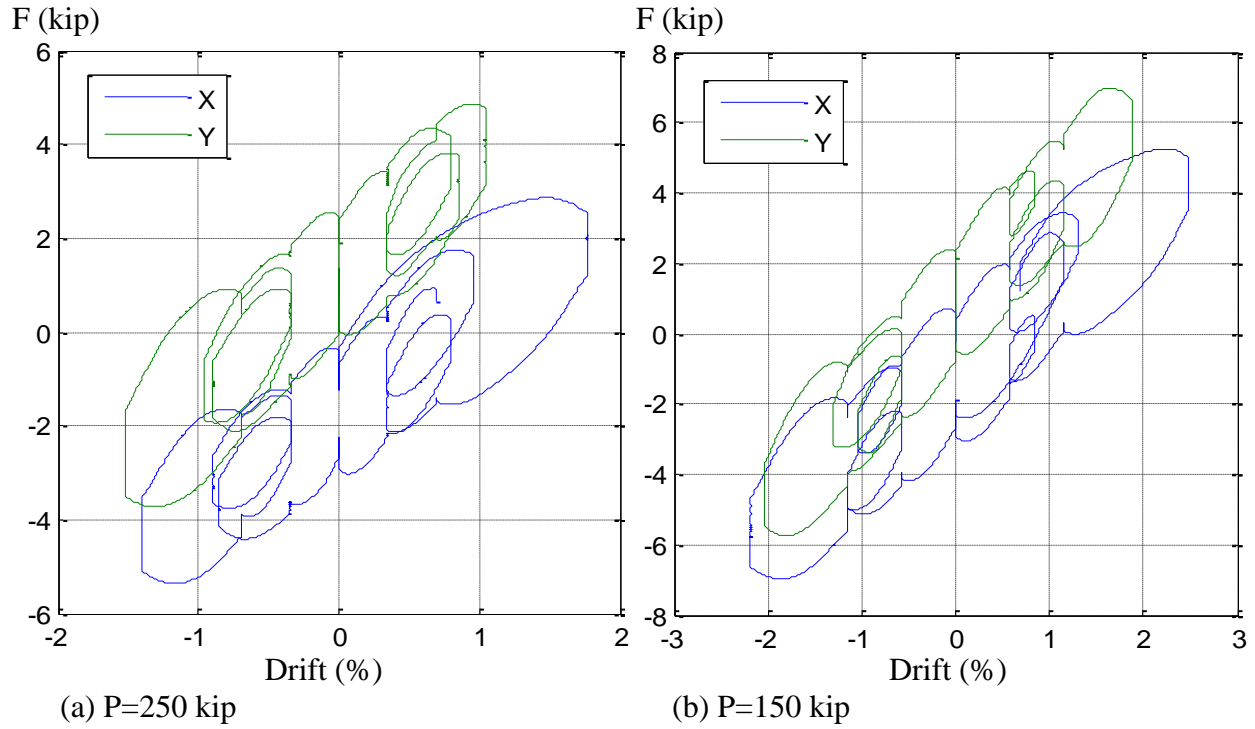


Figure 7.22. Lateral force (F , kip) vs. Drift (ΔL , %) from the biaxial load cases (LC3, diamond-shape) for the Specimen 2C12-18-5

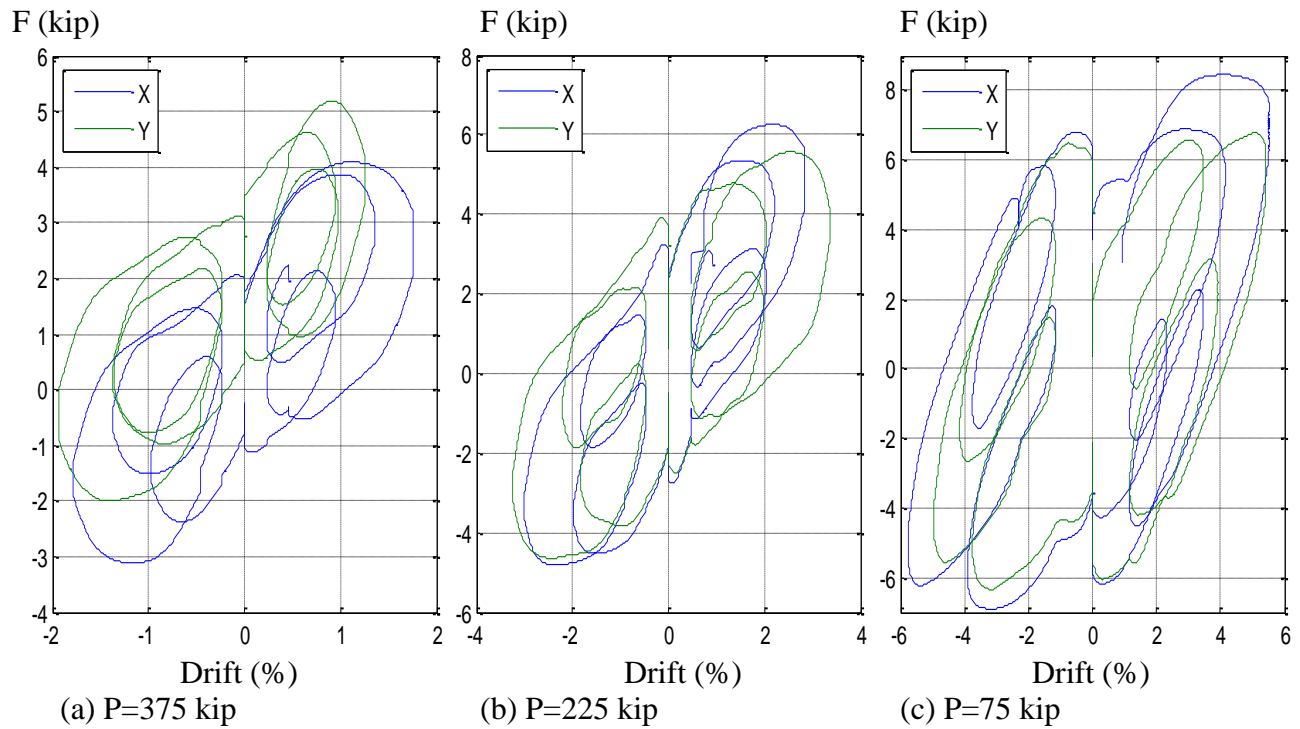


Figure 7.23. Lateral force (F , kip) vs. Drift (ΔL , %) from the biaxial load cases (LC3, diamond-shape) for the Specimen 6C12-18-12

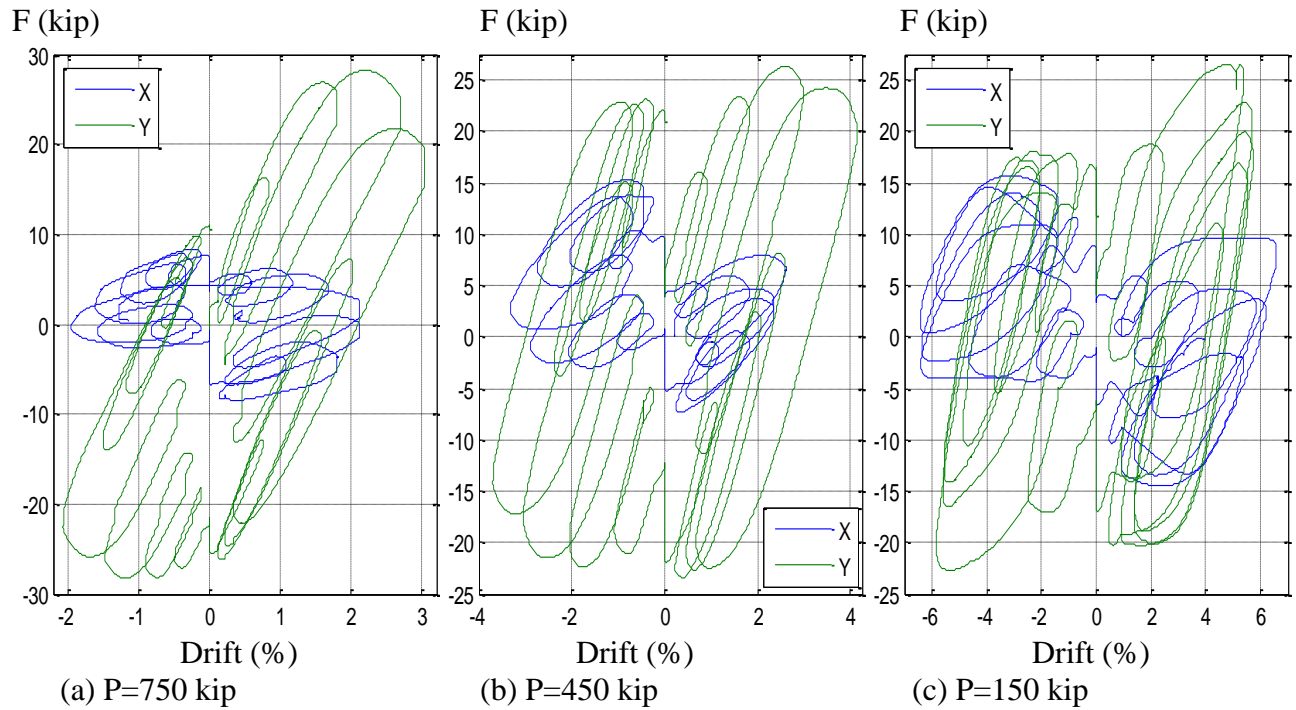


Figure 7.24. Lateral force (F , kip) vs. Drift (ΔL , %) from the biaxial load cases (LC3, diamond-shape) for the Specimen 4Rw-18-5

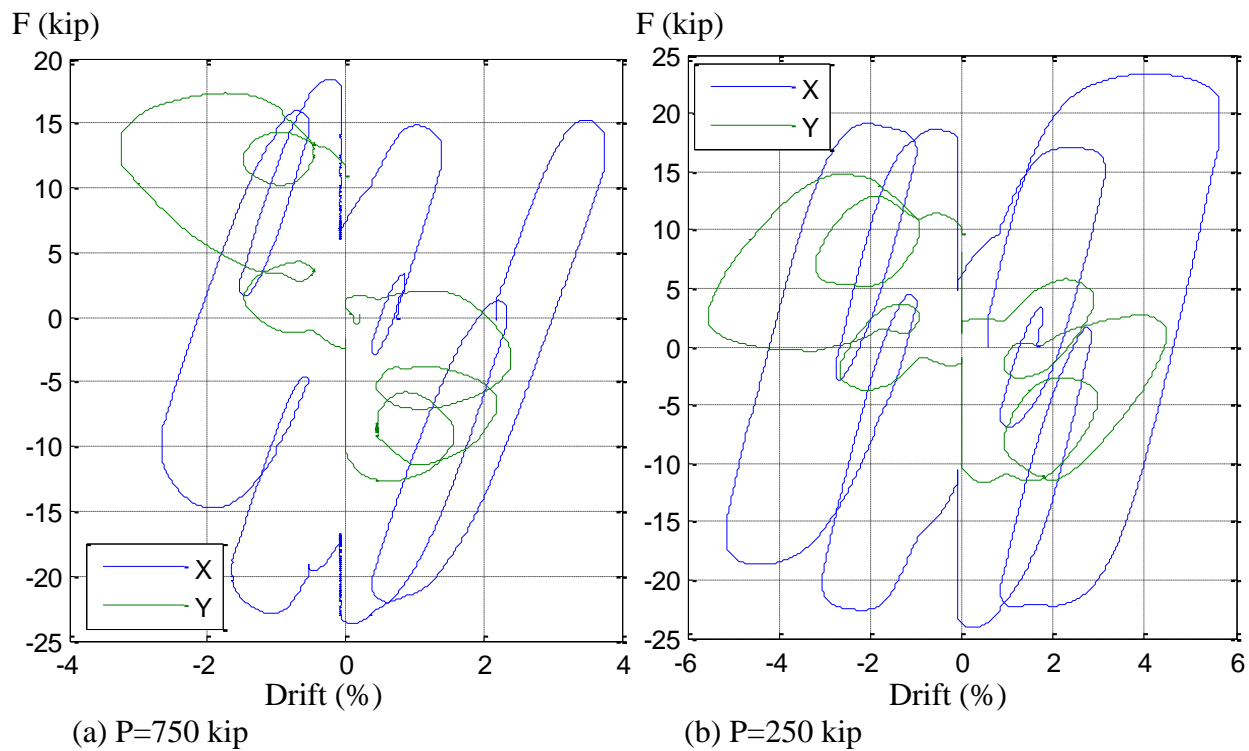
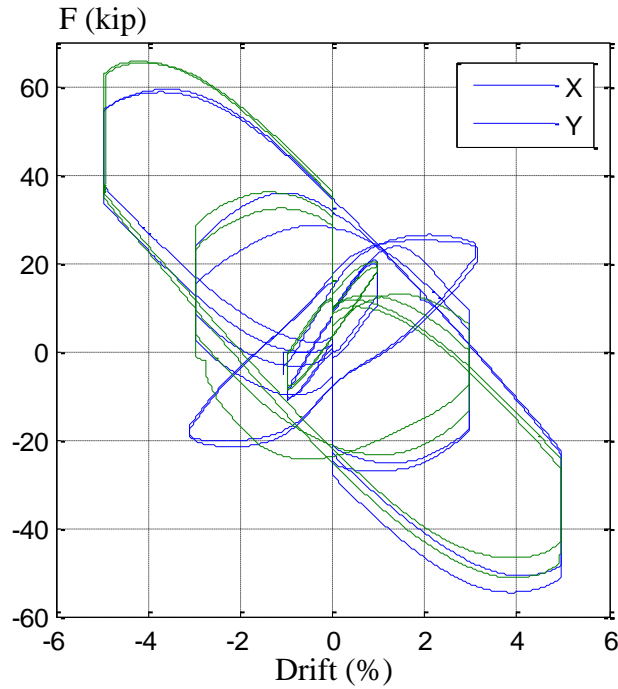


Figure 7.25. Lateral force (F , kip) vs. Drift (ΔL , %) from the biaxial load cases (LC3, diamond-shape) for the Specimen 5Rs-18-5



(a) $P=1250$ kip

Figure 7.26. Lateral force (F , kip) vs. Drift (ΔL , %) from the biaxial load cases (LC3, eight-shape) for the Specimen 7C20-18-12

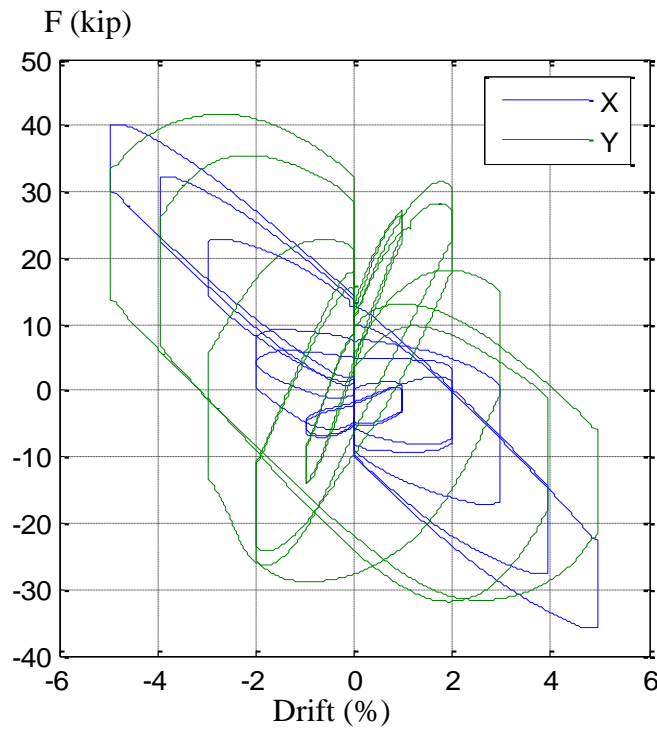


Figure 7.27. Lateral force (F , kip) vs. Drift (ΔL , %) from the biaxial load cases (LC3, eight-shape) for the Specimen 8Rw-18-12 ($P=800$ kip)

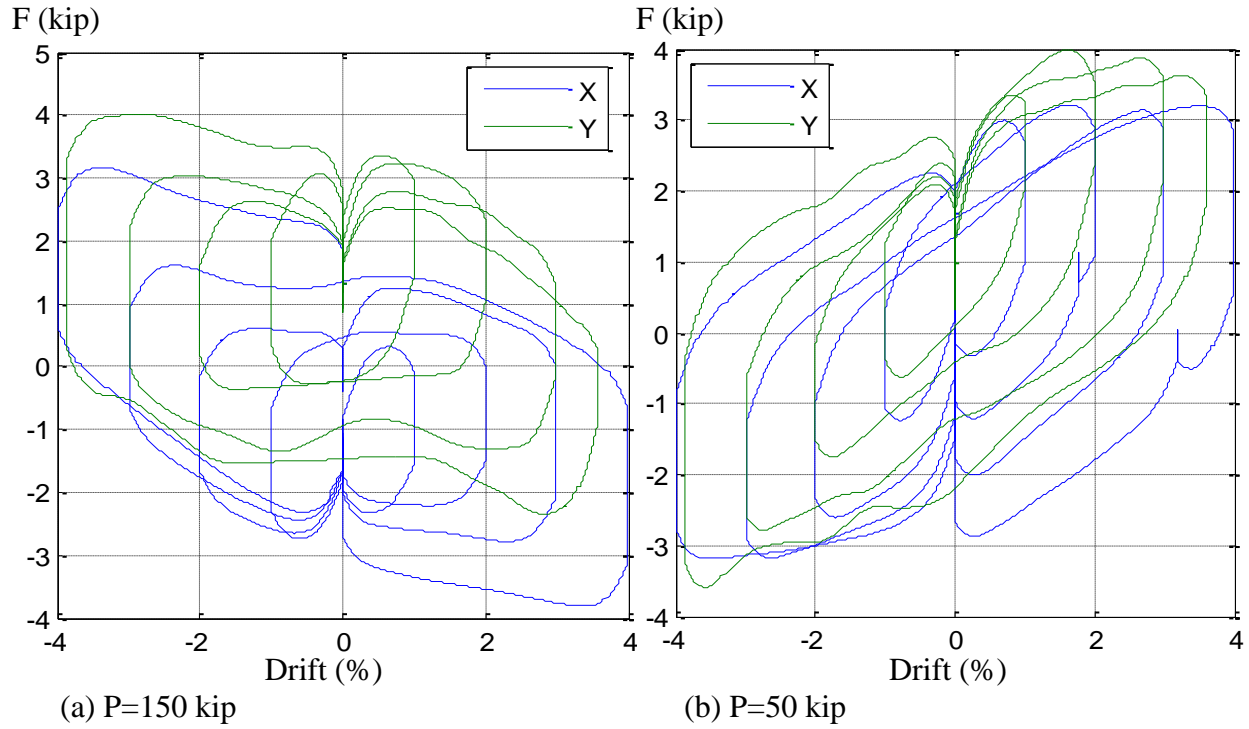


Figure 7.28. Lateral force (F , kip) vs. Drift (ΔL , %) from the biaxial load cases (LC3, eight-shape) for the Specimen 10C12-26-5

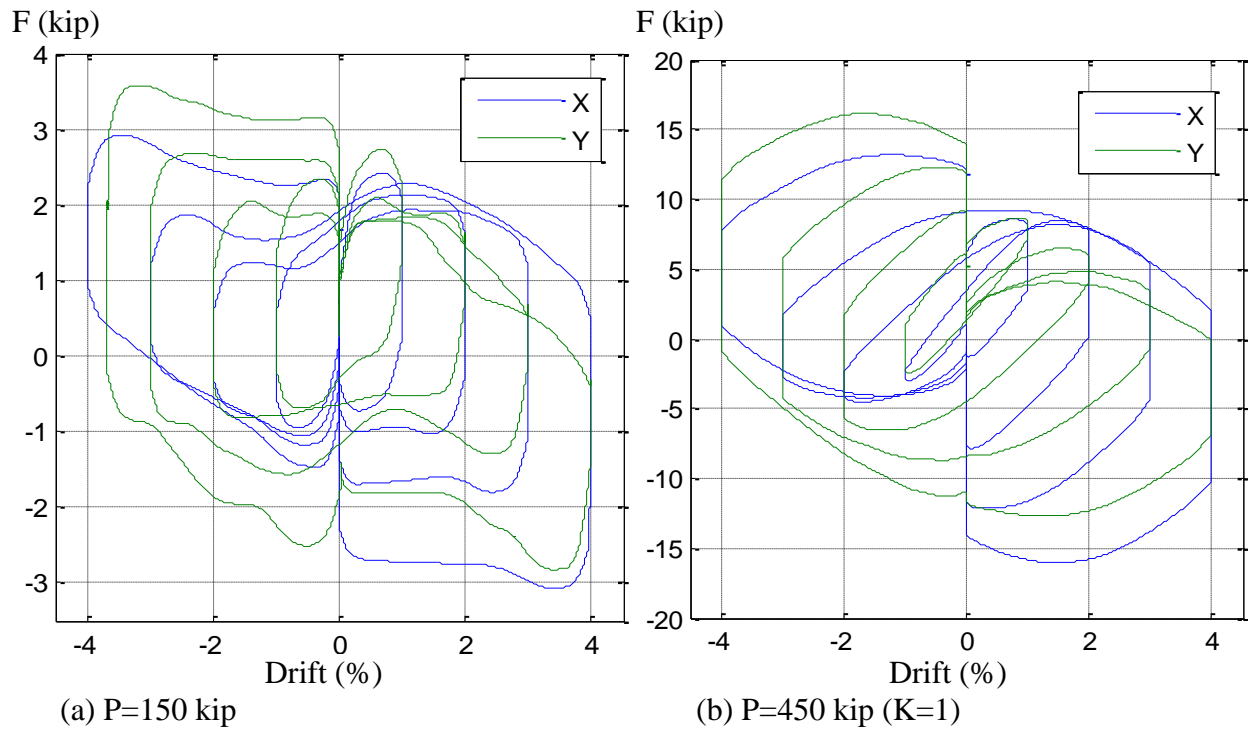


Figure 7.29. Lateral force (F , kip) vs. Drift (ΔL , %) from the biaxial load cases (LC3, eight-shape) for the Specimen 14C12-26-12

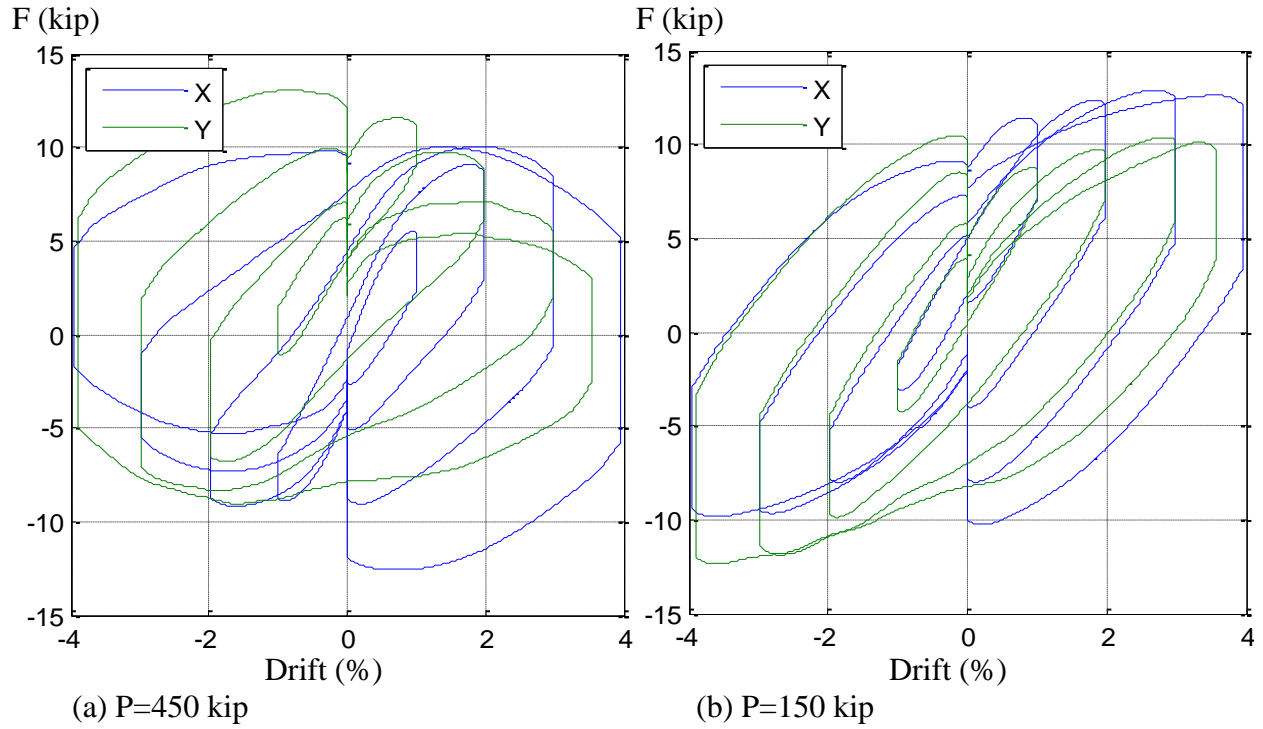


Figure 7.30. Lateral force (F , kip) vs. Drift (Δ/L , %) from the biaxial load cases (LC3, eight-shape) for the Specimens 11C20-26-5

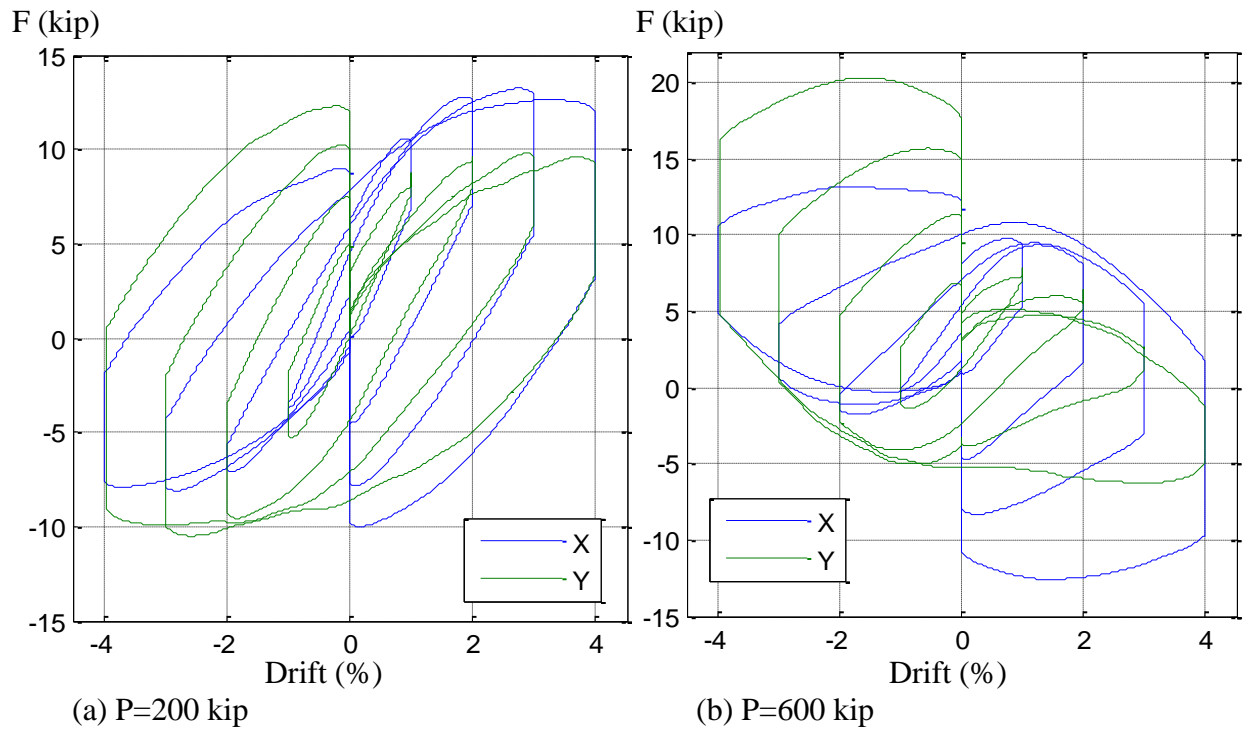


Figure 7.31. Lateral force (F , kip) vs. Drift (Δ/L , %) from the biaxial load cases (LC3, eight-shape) for the Specimen 15C20-26-12

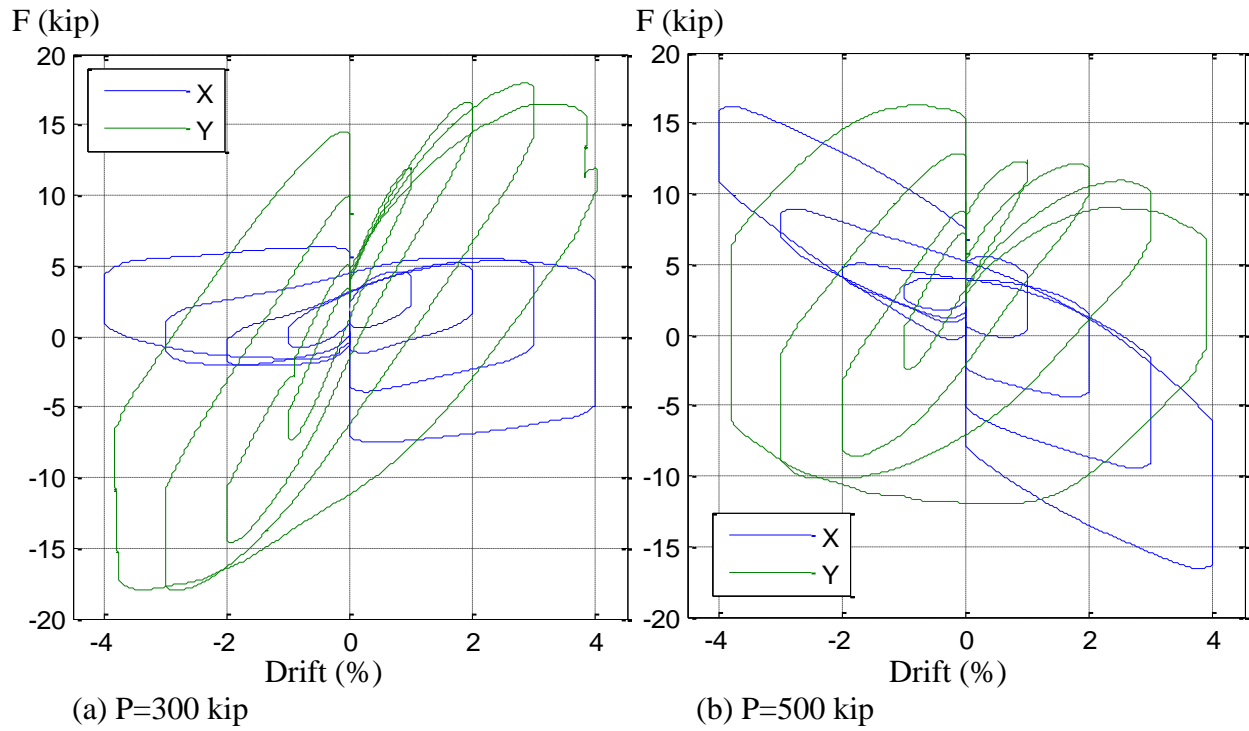


Figure 7.32. Lateral force (F , kip) vs. Drift (ΔL , %) from the biaxial load cases (LC3, eight-shape) for the Specimen 12Rw-26-5

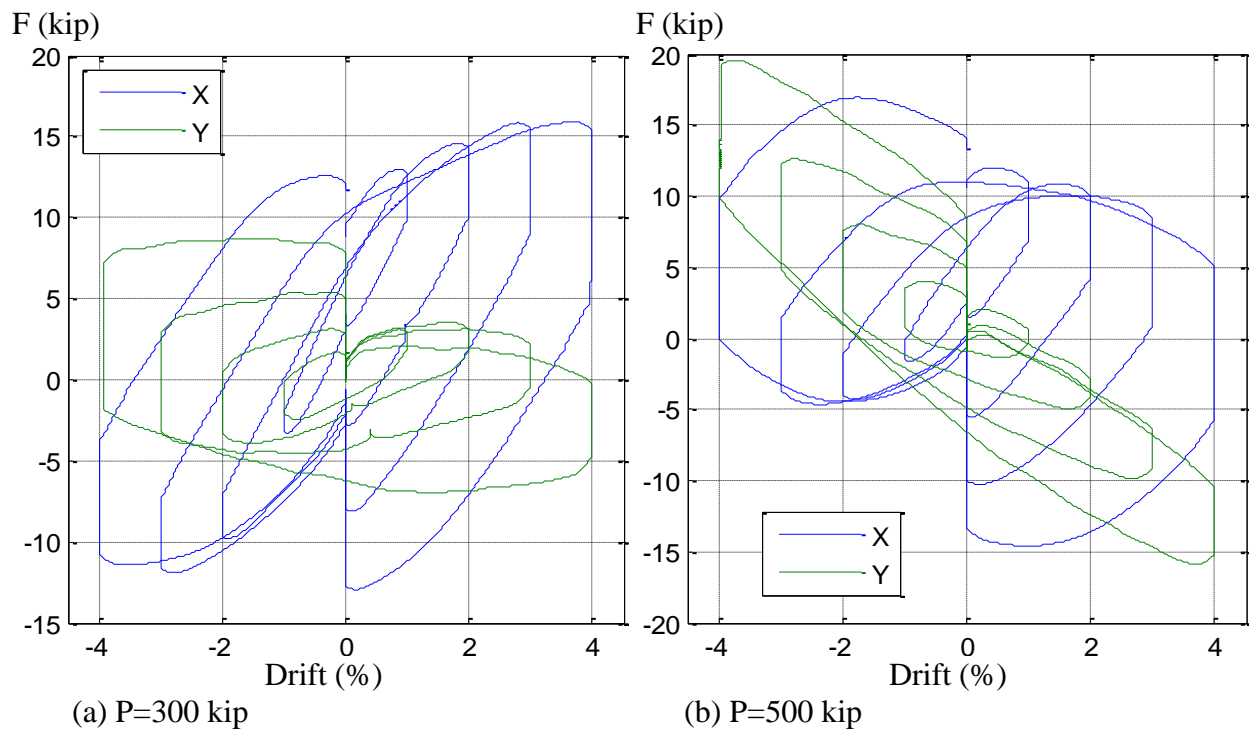


Figure 7.33. Lateral force (F , kip) vs. Drift (ΔL , %) from the biaxial load cases (LC3, eight-shape) for the Specimen 13Rs-26-5

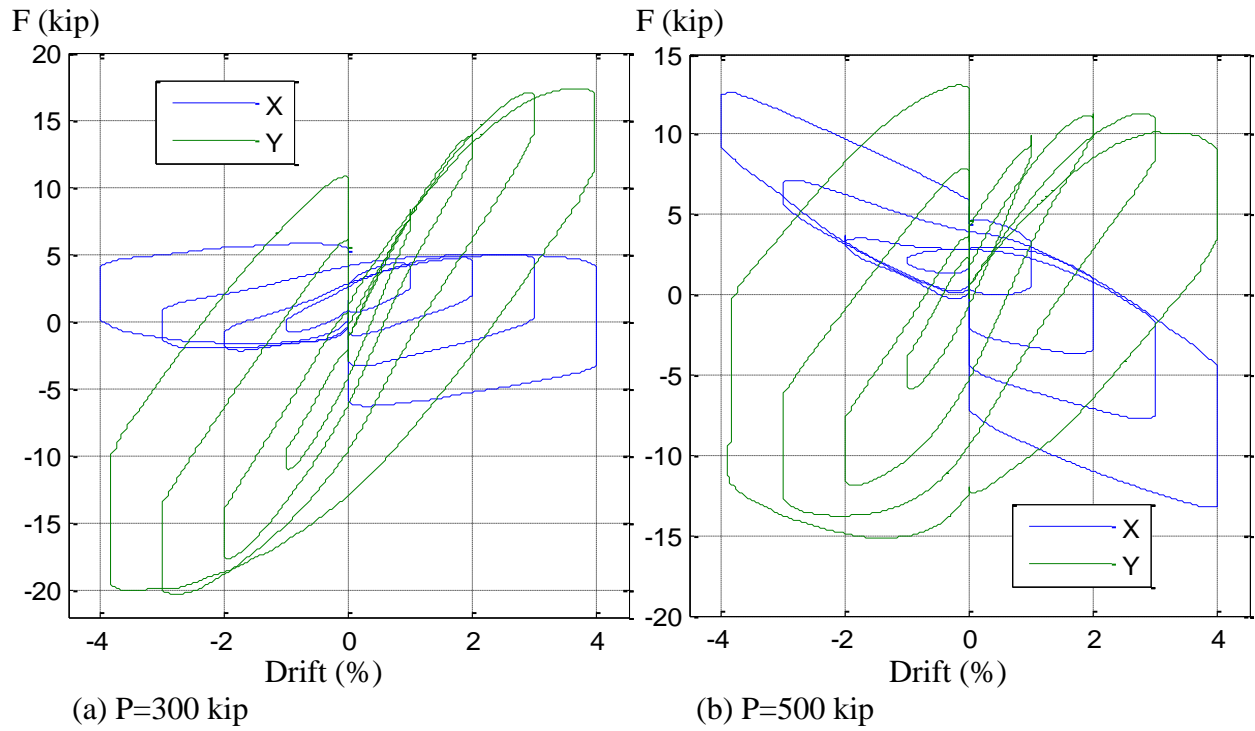


Figure 7.34. Lateral force (F , kip) vs. Drift (ΔL , %) from the biaxial load cases (LC3, eight-shape) for the Specimen 16Rw-26-12

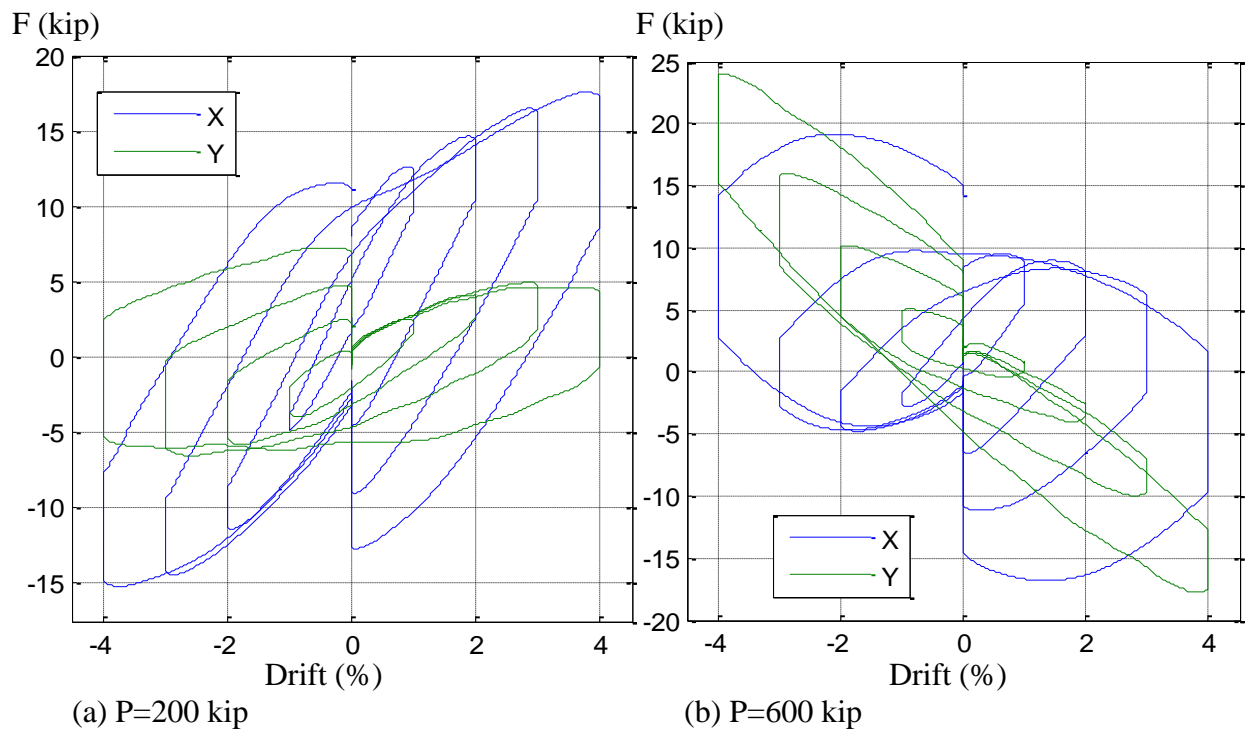


Figure 7.35. Lateral force (F , kip) vs. Drift (ΔL , %) from the biaxial load cases (LC3, eight-shape) for the Specimen 17Rs-26-12

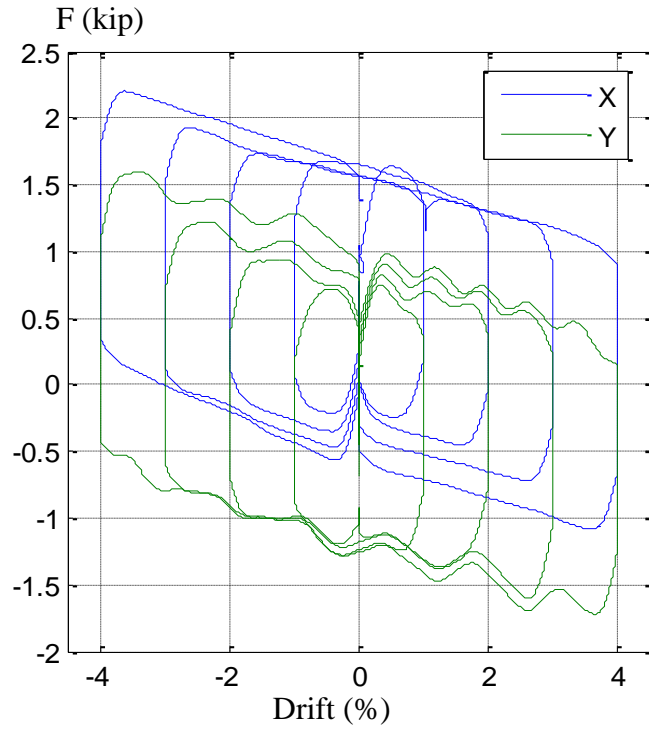


Figure 7.36. Lateral force (F , kip) vs. Drift (ΔL , %) from the biaxial load case (LC3, $K=1$, eight-shape) for the specimens 18C5-26-12 ($P=20$ kip)

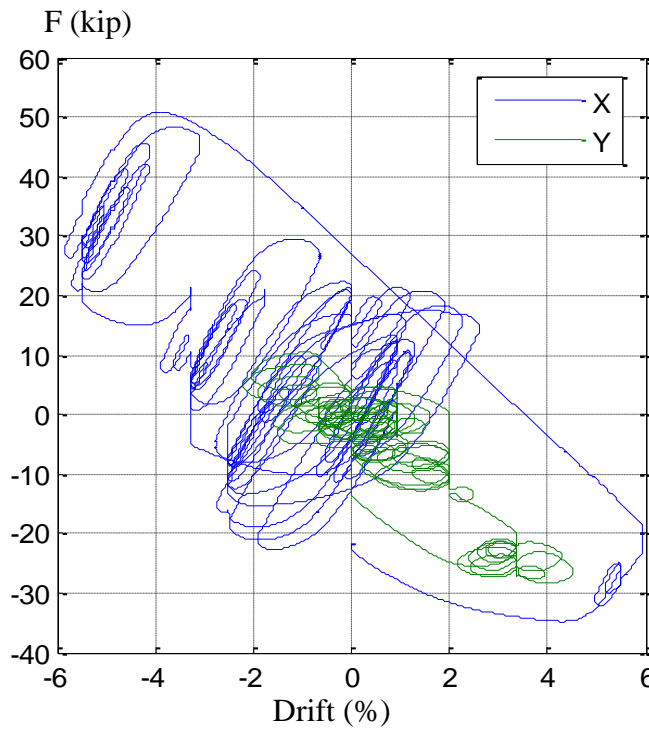


Figure 7.37. Lateral force (F , kip) vs. Drift (ΔL , %) from the biaxial load cases (LC3, probe-subprobe) for the Specimens 9Rs-18-12 ($P=800$ kip)

7.2.2. Moment – curvature response ($M-\phi$)

In this section, the experimental moment-curvature ($M-\phi$) responses for the critical cross-sections near the base of the CFT specimens are presented. For the uniaxial load cases (LC2), the in-plane moment and curvature in the direction of motion are obtained and shown in Figure 7.38 to Figure 7.53. For the biaxial load cases (LC3), the bending moments and cross-section curvatures corresponding to both X and Y directions are presented in Figure 7.54 to Figure 7.66.

The components of the moments at the base are calculated as the top moment components plus the cross product of the arm vector (d) times the force components (F). This is:

$$M = M_{base} = M_{top} + d \times F \quad (7.1)$$

The arm vector (d) defines the distance between the centroid of the column base and the centroid of the column top. The moment at the base thus comprises the first order ($M_{top} + FL$) and the second order moment ($P\Delta$) components.

The curvature (ϕ), on the other hand, is calculated based on the measurements of the three strain gages located near the bottom (6 inches from the base plate). Assuming plane sections always remain plane, the strain at any point of the cross-sections and the corresponding curvatures are estimated based on the three measured values on the plane. Even though these responses were extracted carefully, in few cases (mainly for the latter load cases) the strain gauges were subjected to very large strains as a consequence of the steel local buckling; this fact invalidates the assumption that states that plane sections remain plane.

However, as generally observed in all these figures, the $M-\phi$ curves exhibit good behavior from cycle to cycle within the same load case, with only some minor strength loss and moderate stiffness degradation. In general, the $M-\phi$ response seems consistent, except in few cases where strange slopes (mainly in LC3) are exhibited likely due to high strains as a consequence of the local buckling. In addition, the response from LC3 in some cases is difficult to clarify due to the complexity of these loading types.

Figure 7.38 to Figure 7.45 show the moment – curvature response obtained from the two cycles with the uniaxial loading case (LC2) and reversals at the peak force. As reminder, this

loading case type was applied to the first half of specimens (specimens 1 to 9). Since few cycles are applied and the $M-\phi$ response is limited by the peak lateral force, there is no evidence of accumulated damage (i.e. steel local buckling) and then there is no strength or stiffness degradation in these responses as expected. As a consequence, these responses exhibit a positive stiffness with no softening.

Figure 7.46 to Figure 7.53 show the moment – curvature cyclic response obtained from the uniaxial loading case (LC2) where the reversals were set at a target drift, mostly 1% of drift increment to the max stroke. This loading case type was applied to the second half of specimens (specimens 10 to 18). In general, all these figures show good cyclic behavior with very low degradation and no softening, even when those cases with high compressive load. During this load case, only the specimen 17 exhibited strange slopes as seen in Figure 7.53, likely due to high strains as a consequence of the local buckling.

Figure 7.54 to Figure 7.58 show the moment – curvature response along the X and Y axis obtained from the biaxial loading case (LC3) where the diamond displacement pattern with a set of probes around the specimen was used, and where reversals for each probe were made at the peak lateral force in either X or Y direction. This loading case type was applied in specimens 2 to 6. Since one cycle was applied in each probe and the peak lateral force was not exceeded in either X or Y direction, there is no strength and stiffness degradation observed in CCFTs, slight degradation in the strong axis of RCFTs, and moderate to high degradation in the weak axis of RCFTs. Due to the symmetric shape in CCFTs, similar strength and stiffness were obtained for both the X and Y direction. However, lower moment capacity and lower stiffness were obtained in the weak axis of RCFTs, as expected.

Figure 7.59 to Figure 7.67.a show the moment – curvature cyclic response along the X and Y axis obtained from the biaxial loading case (LC3) where the eight-shape motion with reversals target drifts was used. This loading case type was applied in the specimen 7, 8 and 10 to 18. Contrary to the previous cases, higher degradation is observed for those specimens at large curvatures, mainly in weak axis of RCFTs. Due to the symmetric shape in CCFTs, similar strength and the stiffness were obtained for both the X and Y direction; however, lower capacity and lower stiffness were obtained in the weak axis of RCFTs. In these figures, strange slopes are exhibited due the motion type of this load case in which the top was moved in one longitudinal

direction while holding fixed the other transverse direction, and then switching to the opposite case. The strange slopes can also be attributed to large amount of local buckling deformation (mainly in weak axis of RCFTs) where the “sections remain plain” assumption is perhaps no longer valid.

Finally, Figure 7.67.b shows the moment – curvature cyclic response along the X and Y axis obtained in the Specimen 9 from the biaxial loading case (LC3) where the probe-subprobe type was used. Similar to the other RCFT cases, lower moment capacity and lower stiffness were obtained in the weak axis.

In addition to the $M-\phi$ curves, the experimental flexural stiffness (EI_{exp}) is extracted from these curves as the slope at certain locations. In general these correspond to the unloading region from peak load as that is considered to be the more “elastic” region of the plot. The slope and the selected points for the EI_{exp} are calculated in both the positive and negative sides of the loops. For the RCFT specimens, the stiffness was extracted accordingly to its orientation (stiffness in weak axis for the R_w group, and strong axis stiffness for the R_s group); this criterion was also used in the biaxial load cases. The stiffness values extracted from these figures are reported and analyzed in Section 7.3.

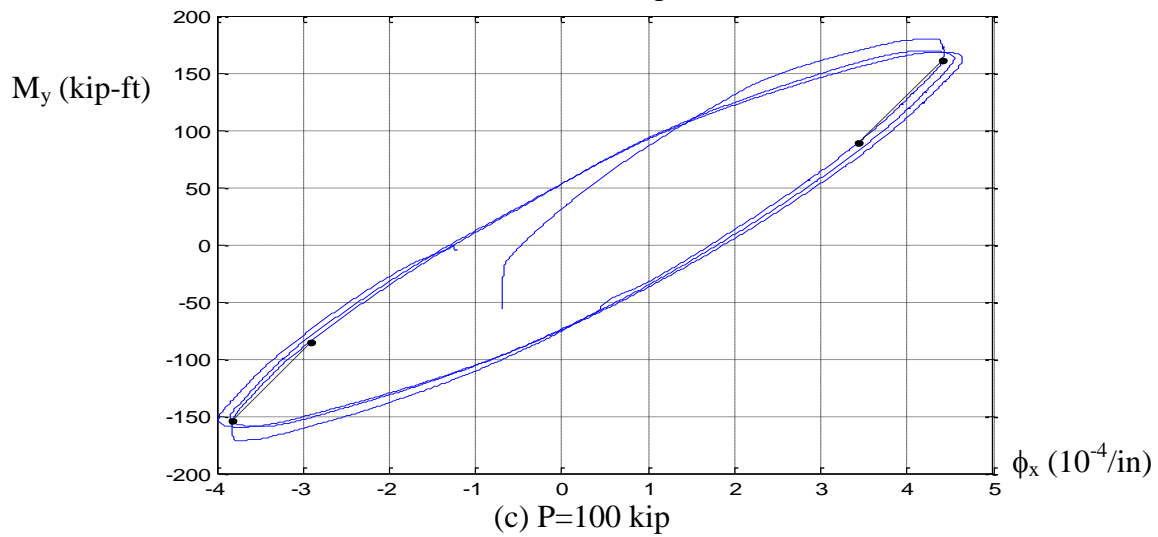
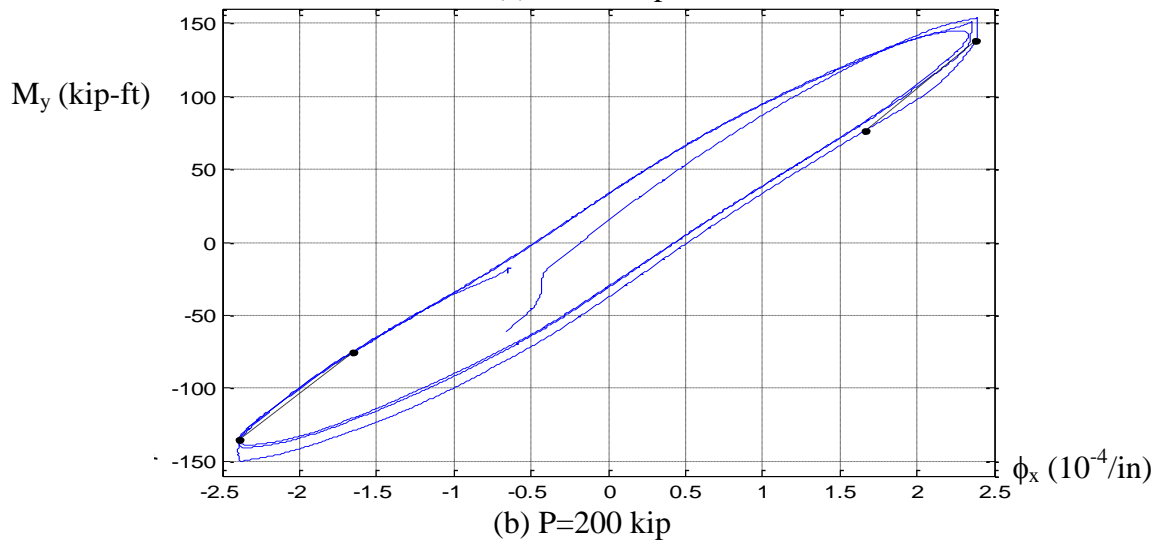
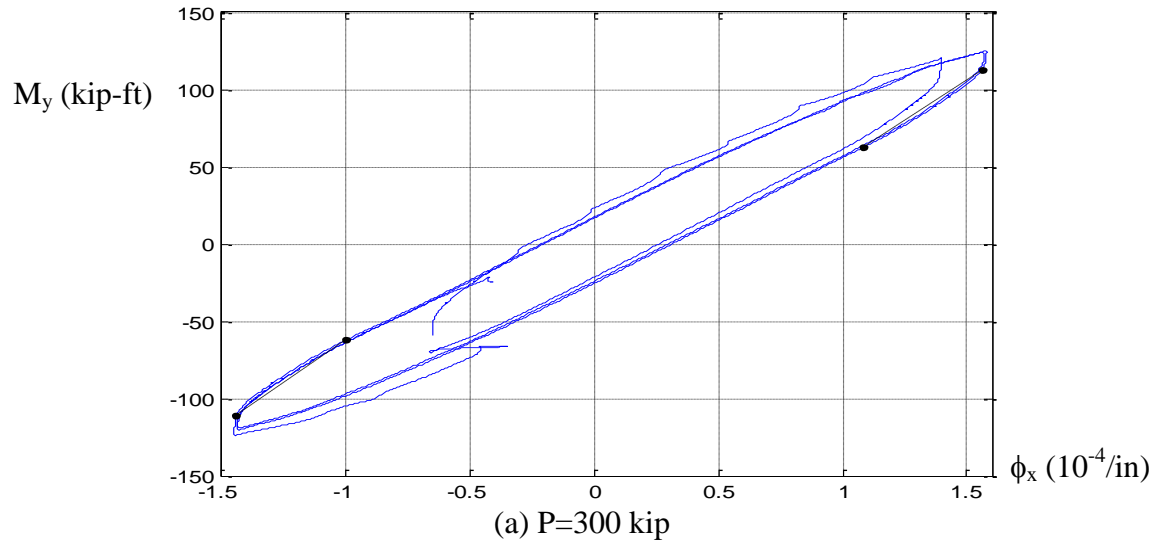
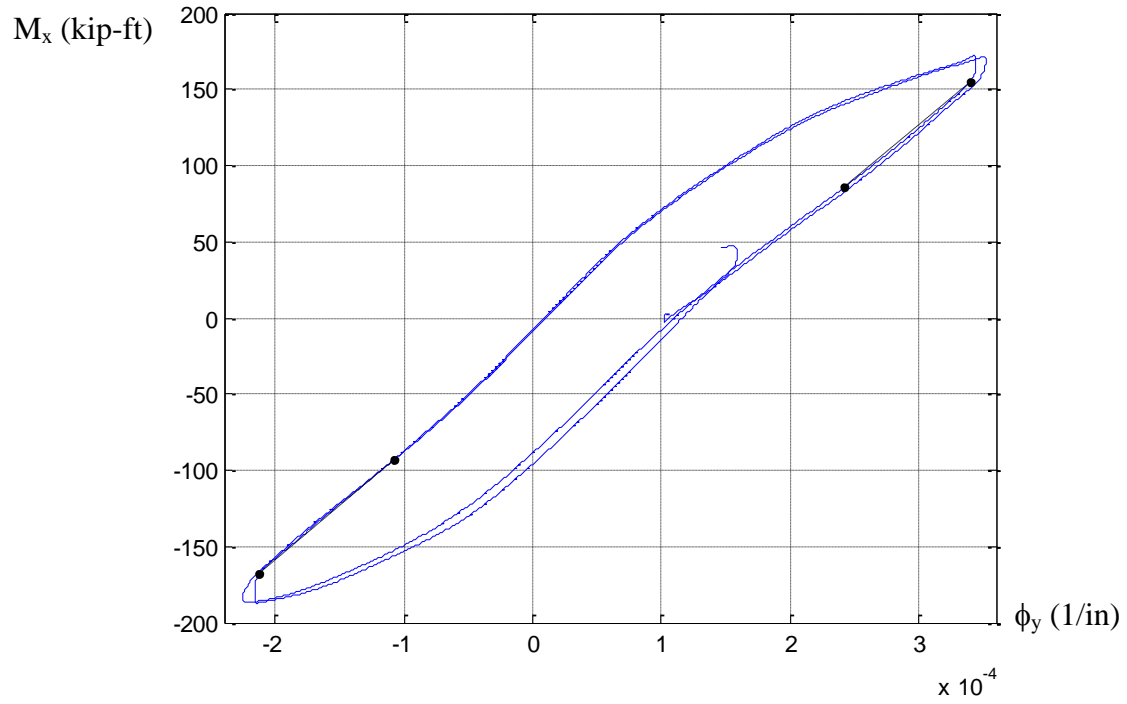
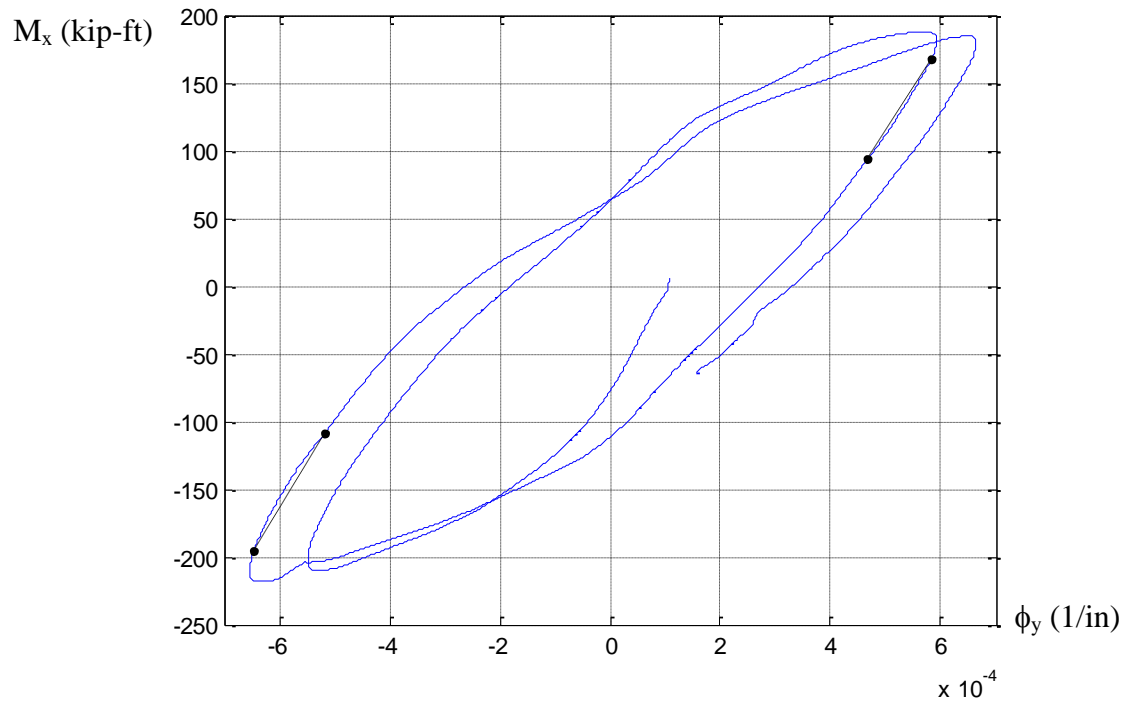


Figure 7.38. Second order moment at the base (M , kip-ft) vs. Curvature (ϕ , 1/in) from the uniaxial load cases (LC2) for the specimen 2C12-18-5

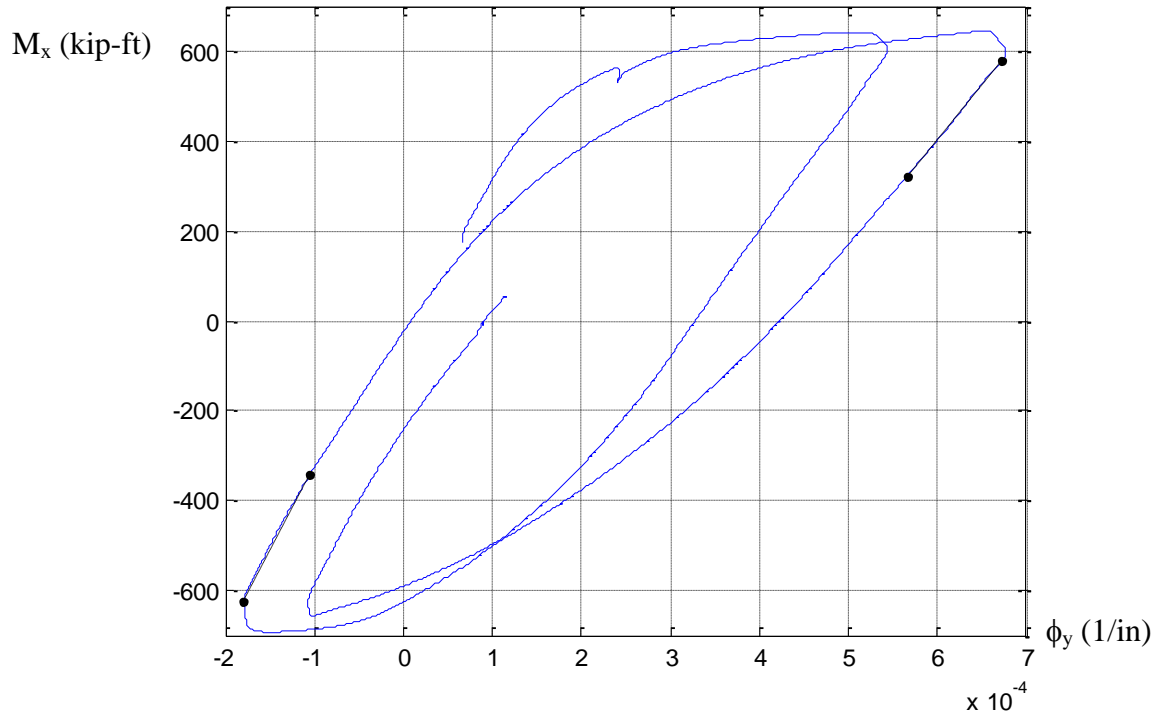


(a) $P=300$ kip

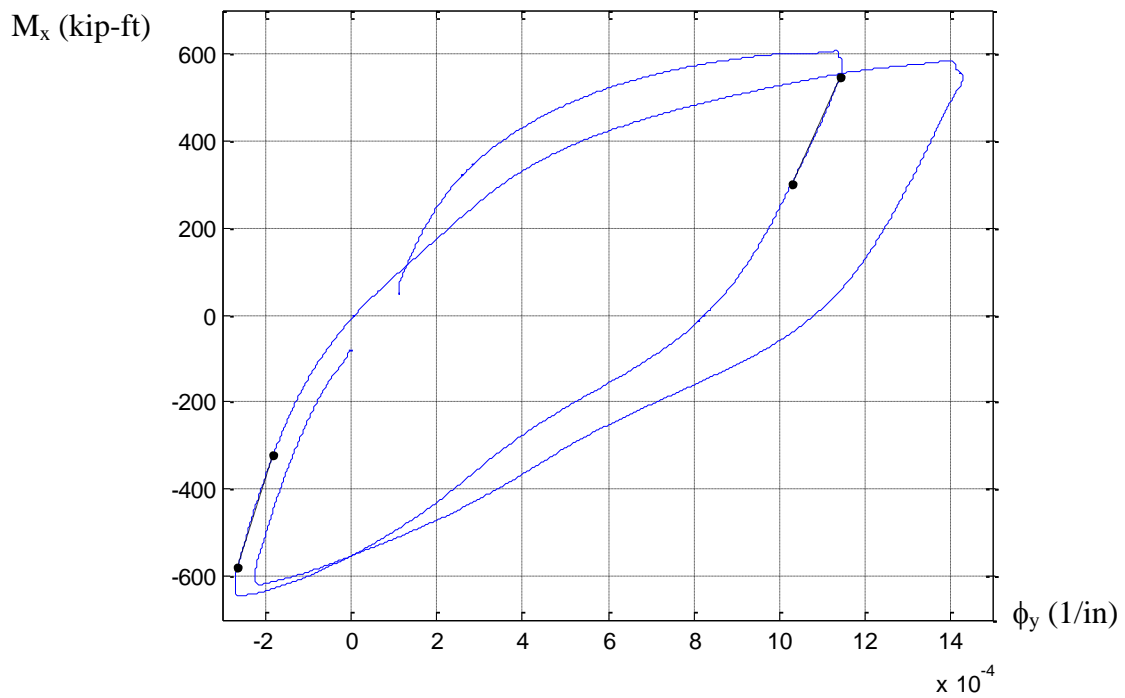


(b) $P=150$ kip

Figure 7.39. Second order moment at the base (M , kip-ft) vs. Curvature (ϕ , 1/in) from the uniaxial load cases (LC2) for the specimen 6C12-18-12



(a) $P=1000$ kip



(b) $P=500$ kip

Figure 7.40. Second order moment at the base (M , kip-ft) vs. Curvature (ϕ , 1/in) from the uniaxial load cases (LC2) for the specimen 3C20-18-5

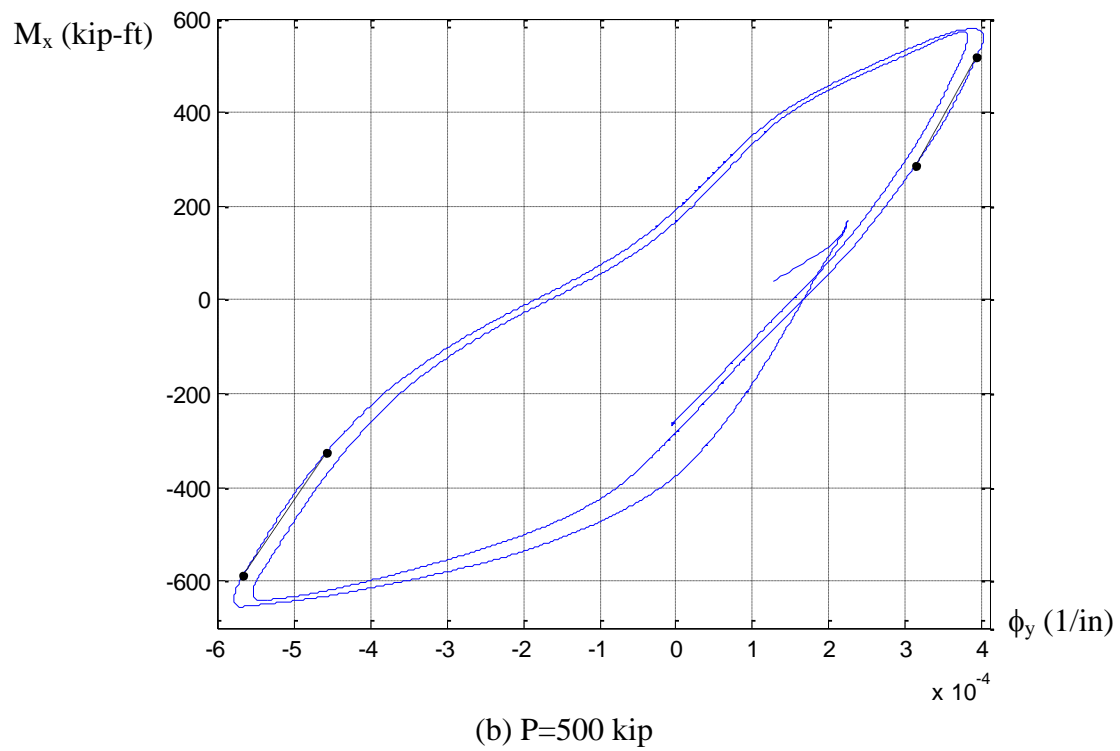
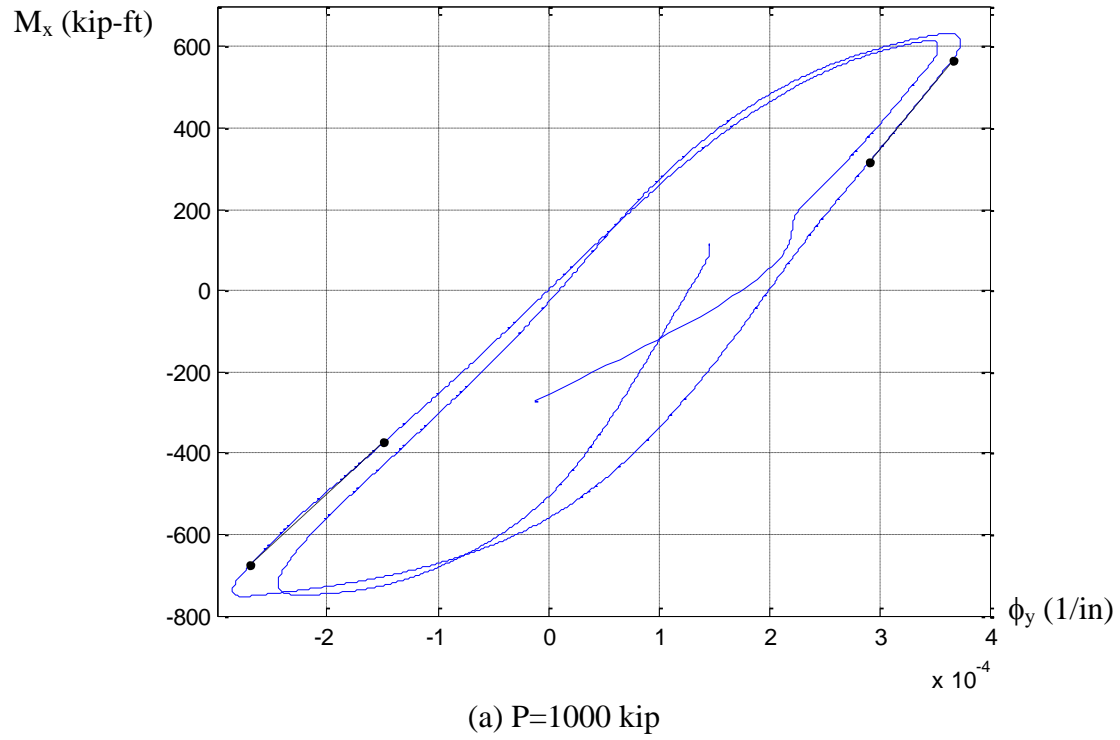
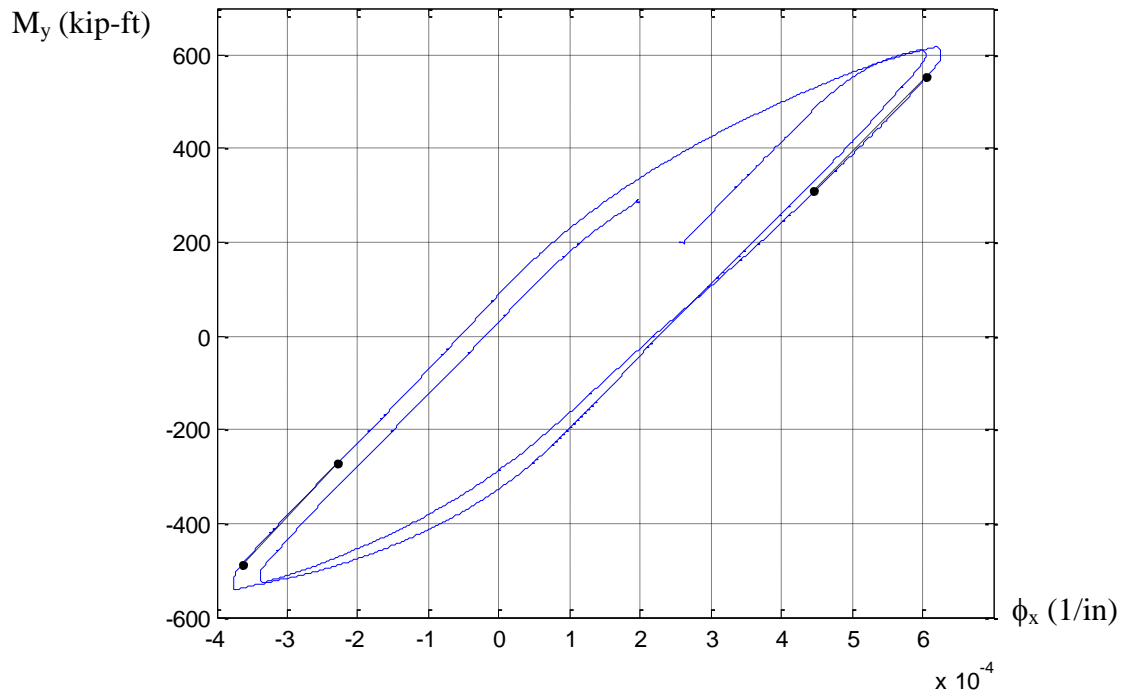
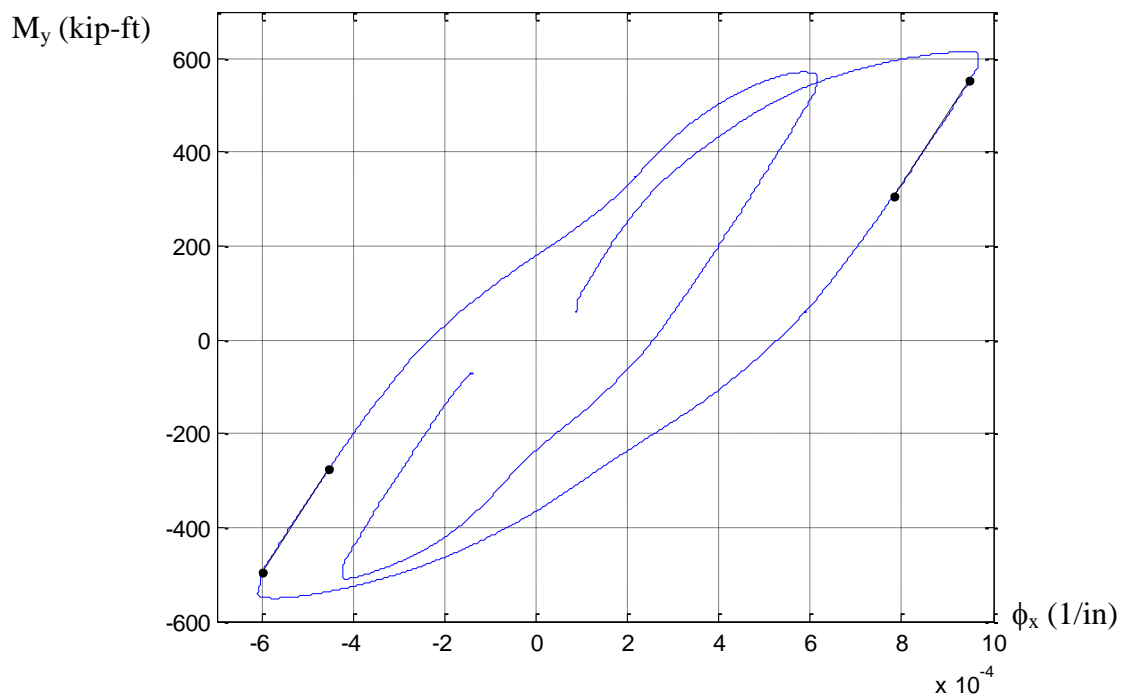


Figure 7.41. Second order moment at the base (M , kip-ft) vs. Curvature (ϕ , 1/in) from the uniaxial load cases (LC2) for the specimen 7C20-18-12

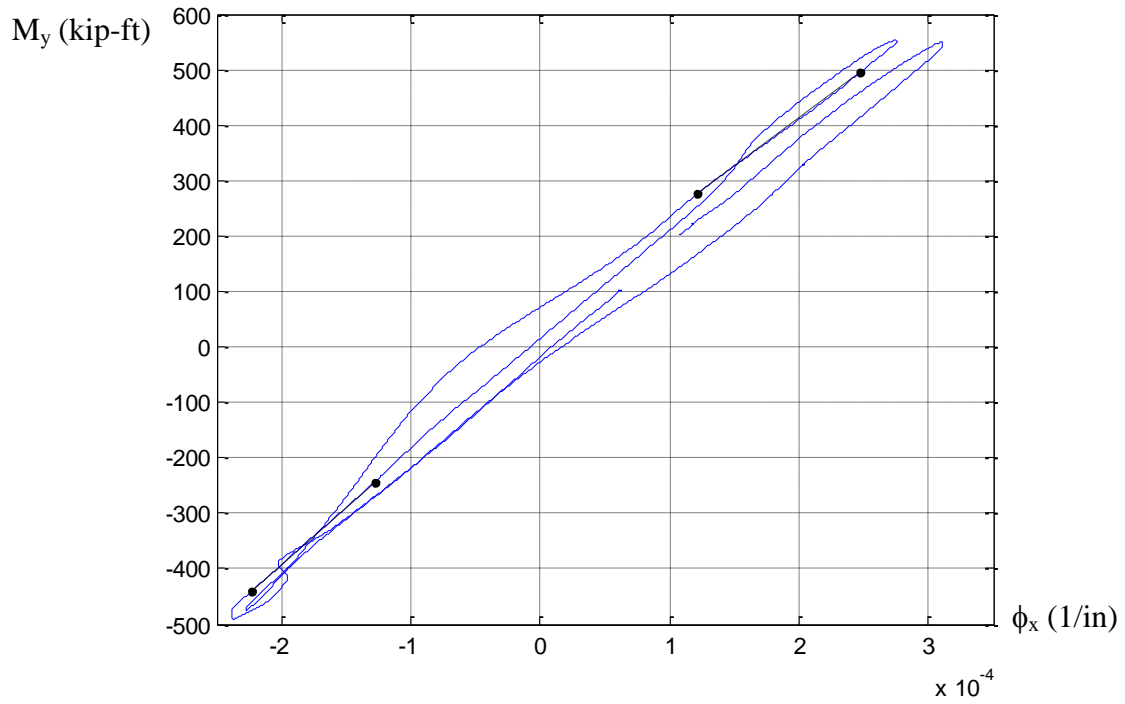


(a) $P=600$ kip

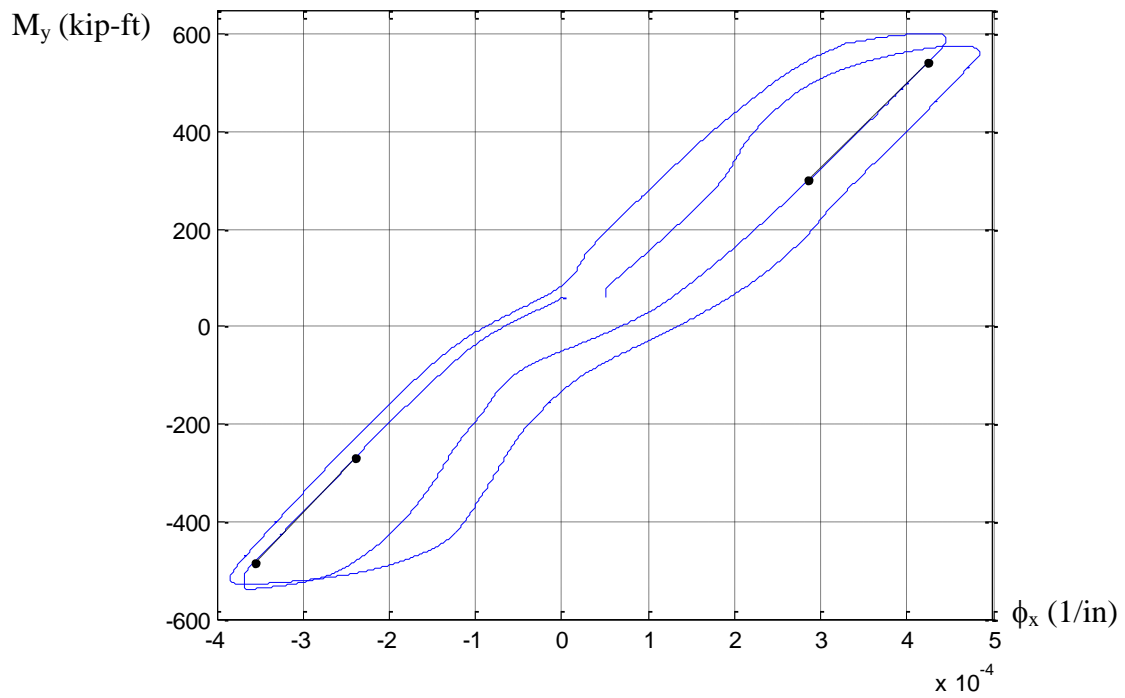


(b) $P=300$ kip

Figure 7.42. Second order moment at the base (M , kip-ft) vs. Curvature (ϕ , 1/in) from the uniaxial load cases (LC2) for the specimen 4Rw-18-5

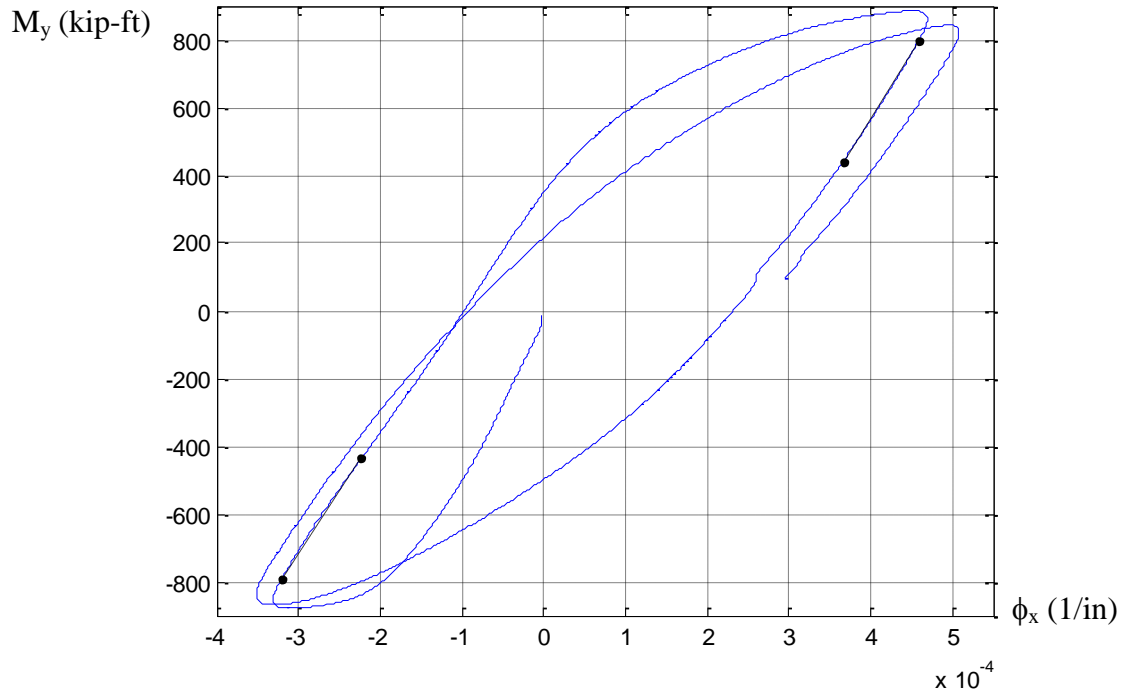


(a) $P=600$ kip

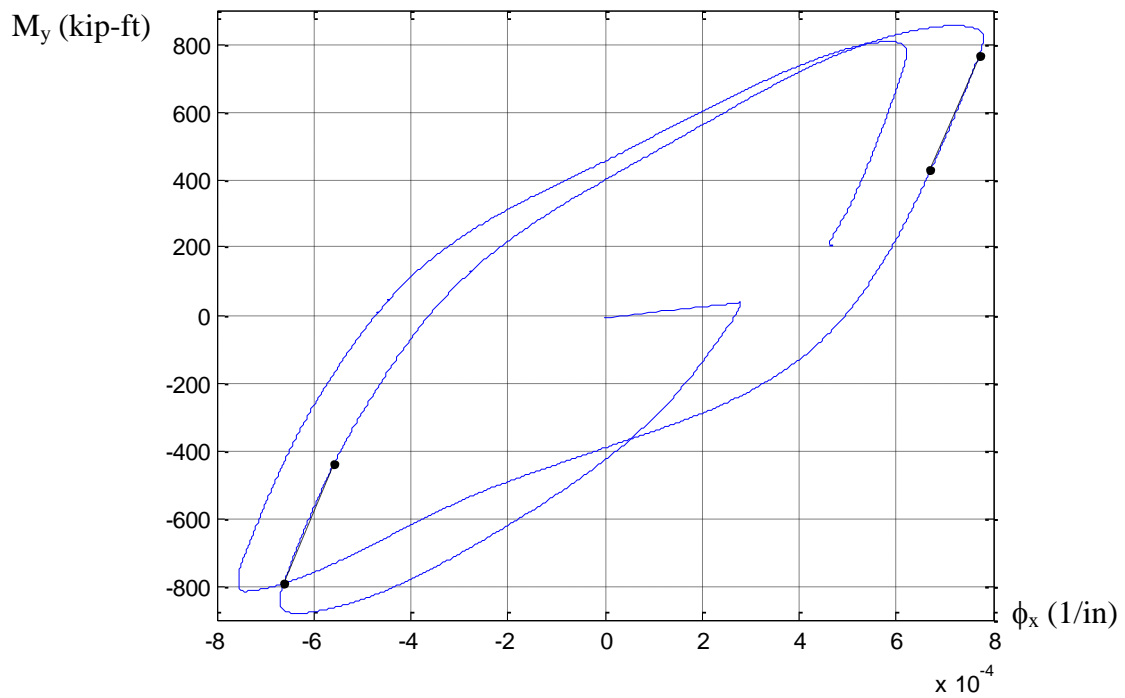


(b) $P=300$ kip

Figure 7.43. Second order moment at the base (M , kip-ft) vs. Curvature (ϕ , 1/in) from the uniaxial load cases (LC2) for the specimen 8Rw-18-12

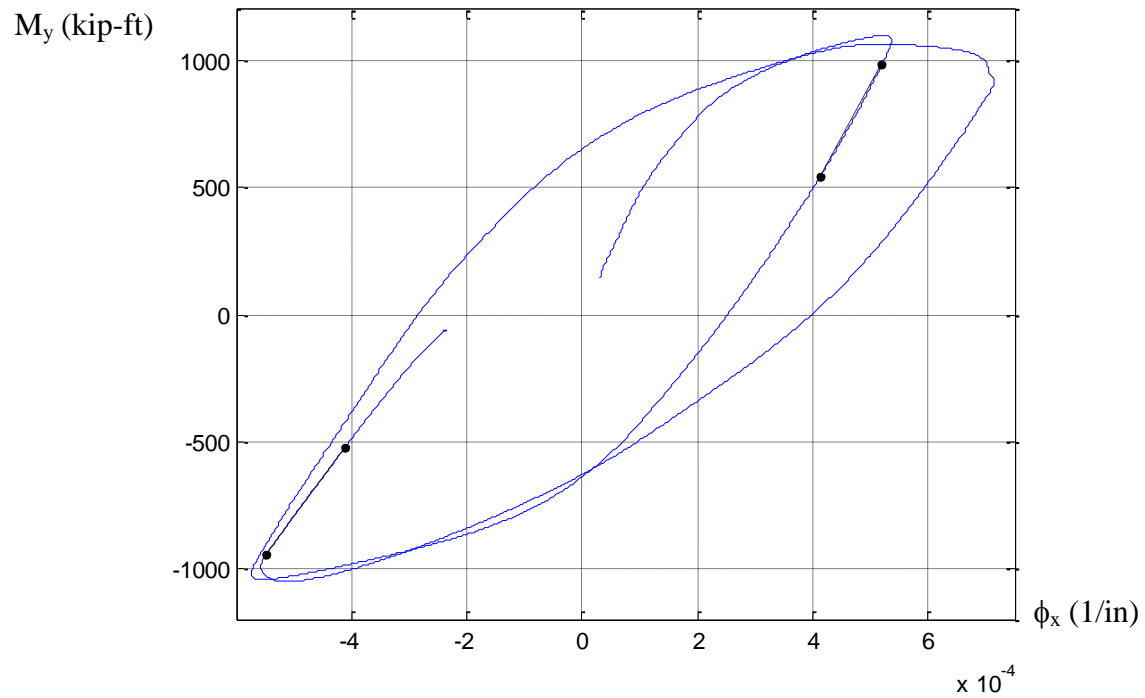


(a) $P=1000$ kip

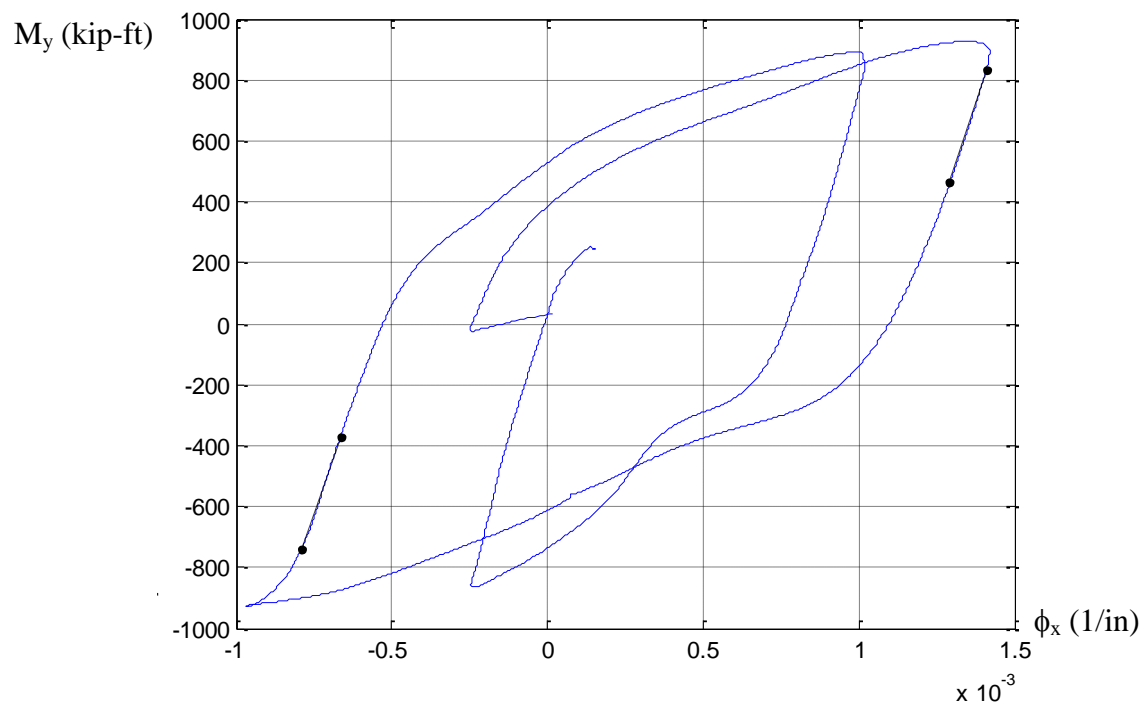


(b) $P=500$ kip

Figure 7.44. Second order moment at the base (M , kip-ft) vs. Curvature (ϕ , $1/\text{in}$) from the uniaxial load cases (LC2) for the specimen 5Rs-18-5

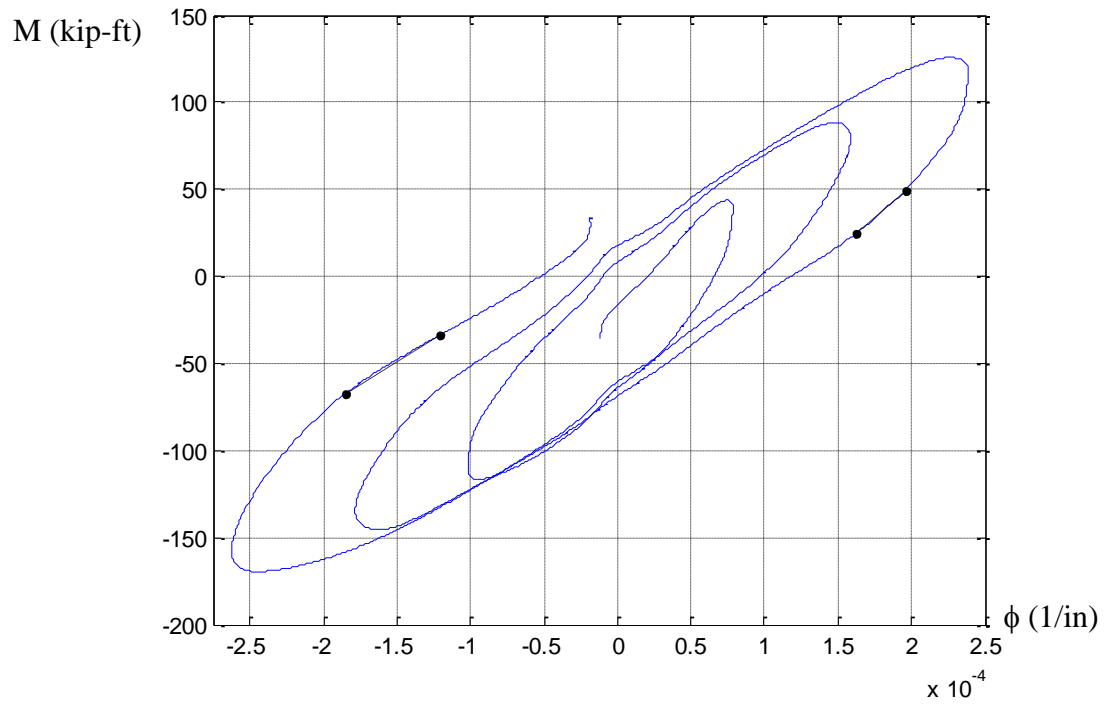


(a) $P=1200$ kip

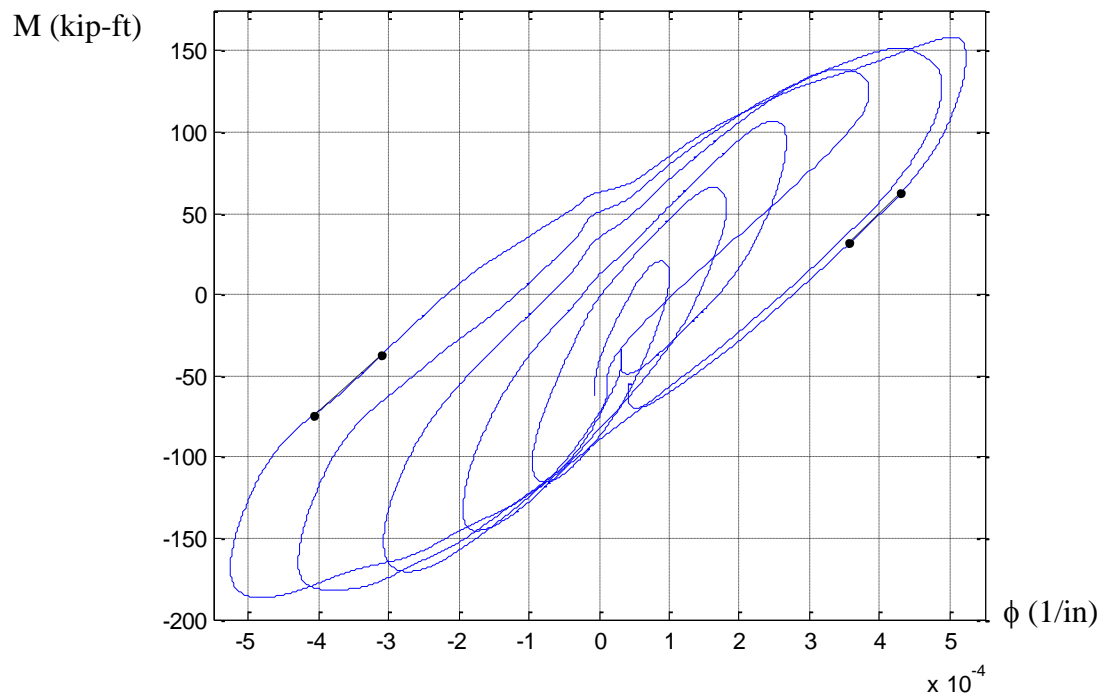


(b) $P=400$ kip

Figure 7.45. Second order moment at the base (M , kip-ft) vs. Curvature (ϕ , 1/in) from the uniaxial load cases (LC2) for the specimen 9Rs-18-12



(a) $P=200$ kip



(b) $P=100$ kip

Figure 7.46. Second order moment at the base (M , kip-ft) vs. Curvature (ϕ , 1/in) from the uniaxial load cases (LC2) for the specimen 10C12-26-5

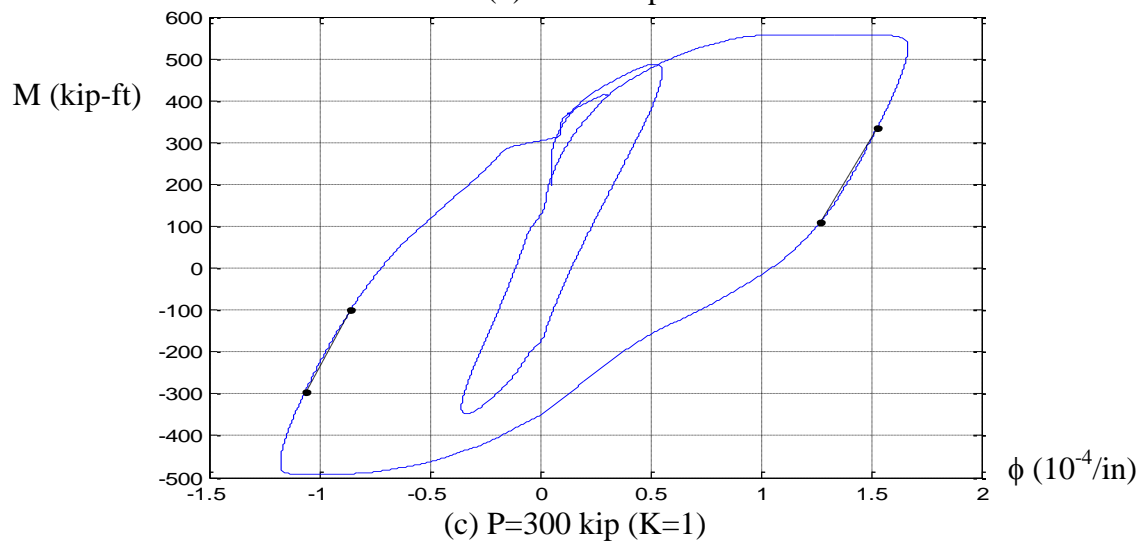
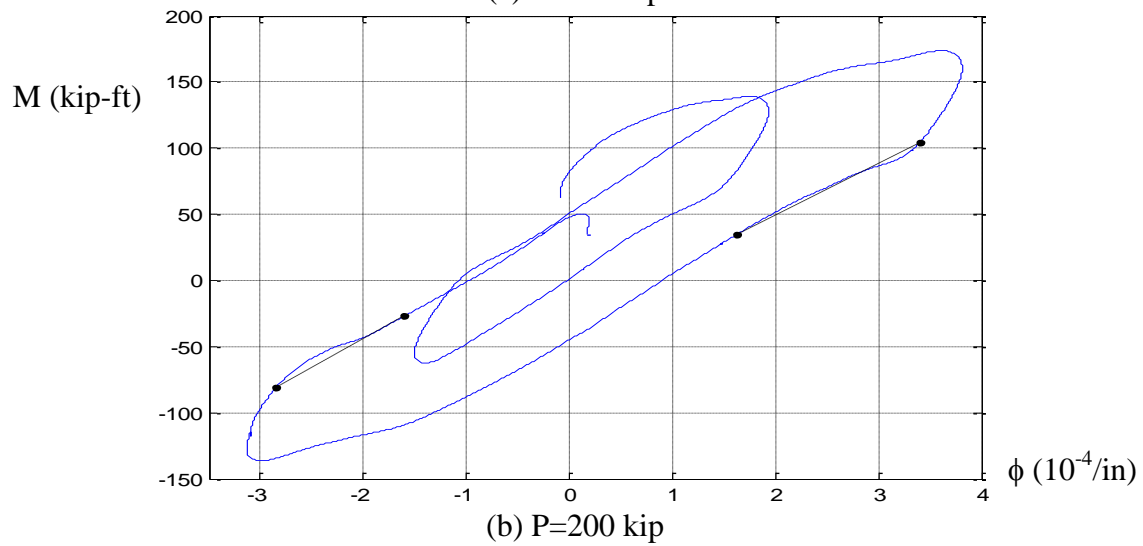
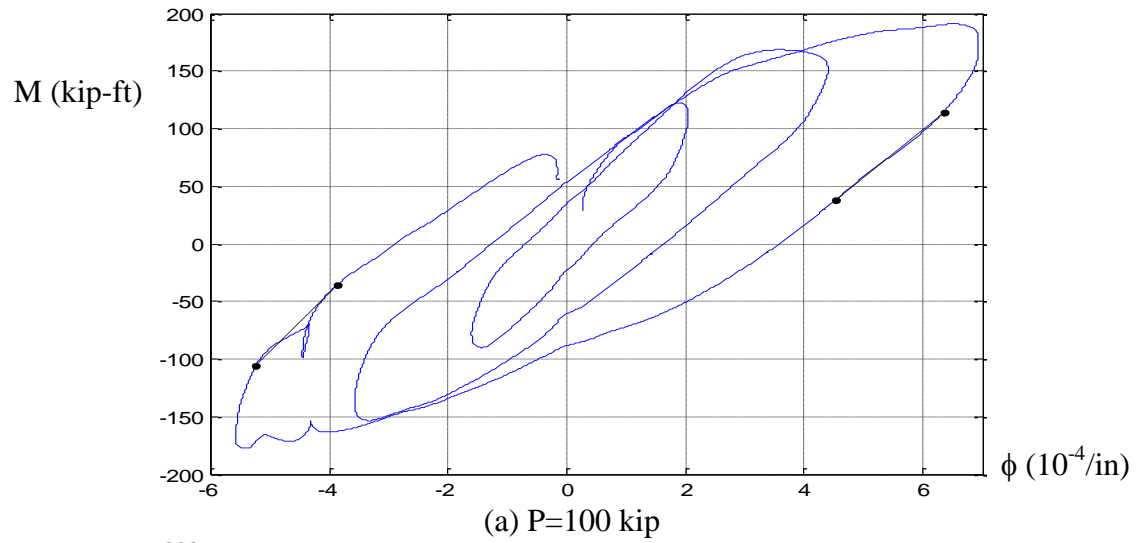
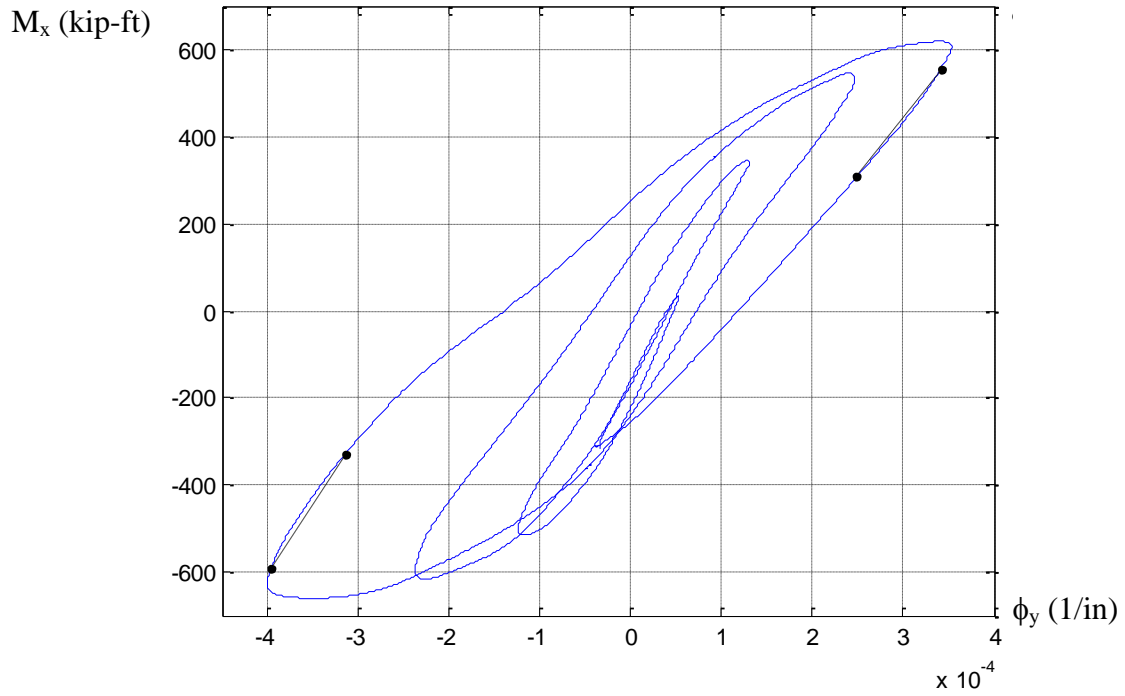
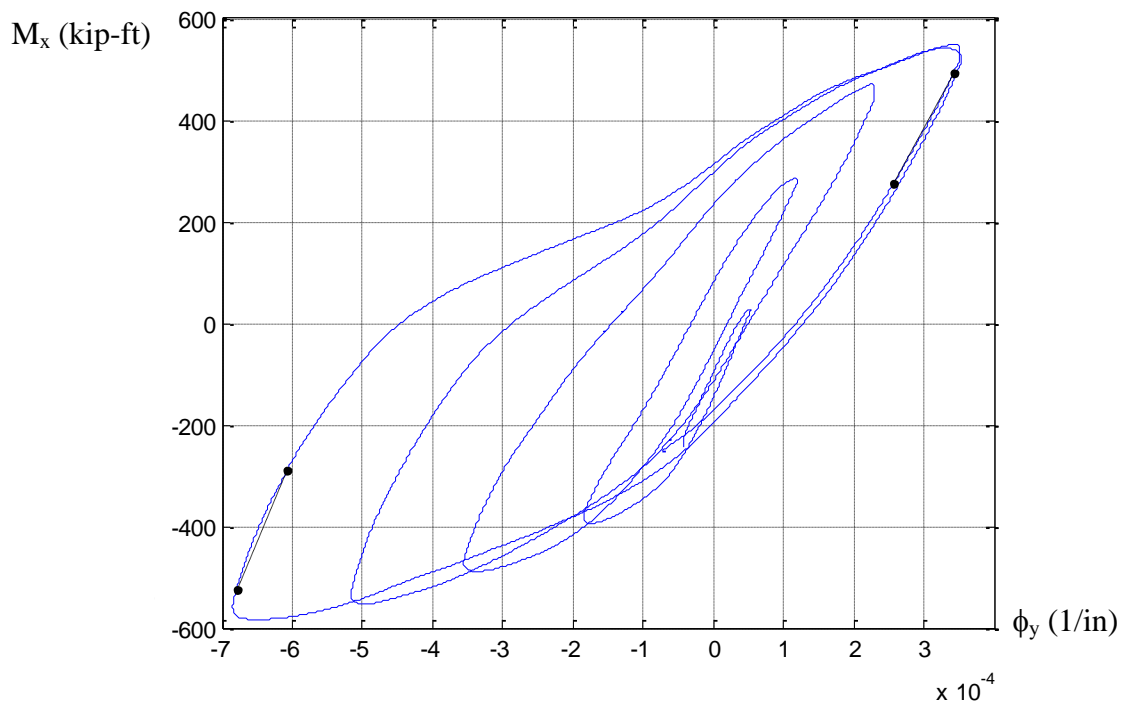


Figure 7.47. Second order moment at the base (M , kip-ft) vs. Curvature (ϕ , $1/\text{in}$) from the uniaxial load cases (LC2) for the specimen 14C12-26-12

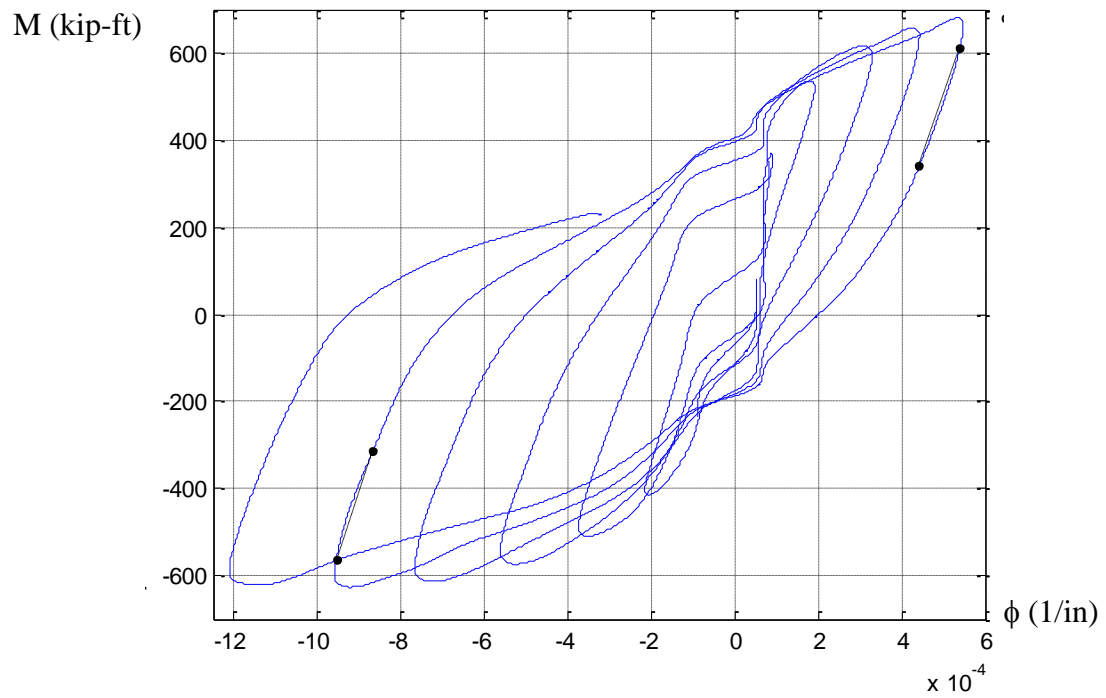


(a) $P=600$ kip

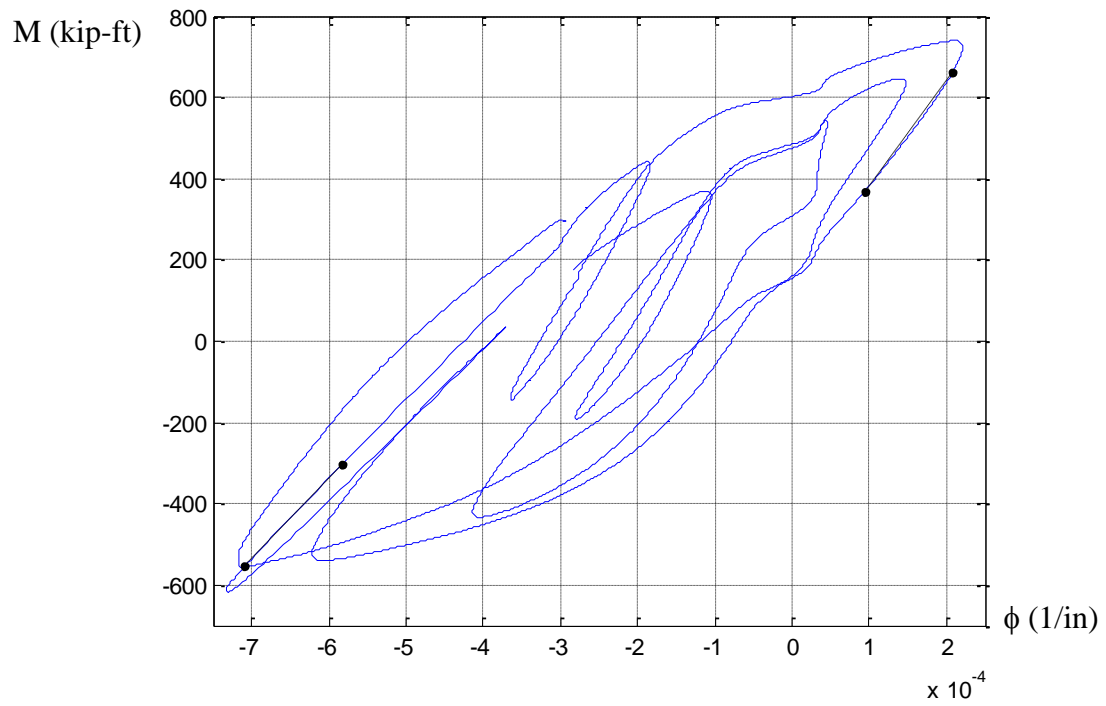


(b) $P=300$ kip

Figure 7.48. Second order moment at the base (M , kip-ft) vs. Curvature (ϕ , 1/in) from the uniaxial load cases (LC2) for the specimen 11C20-26-5

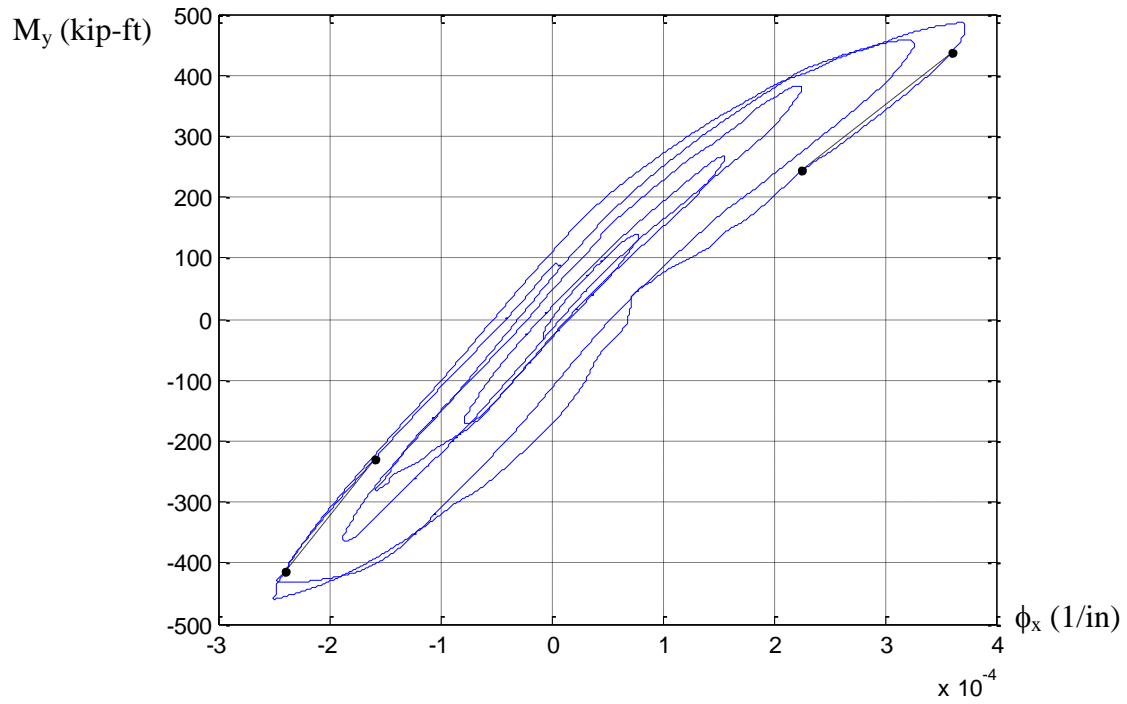


(a) $P=400$ kip

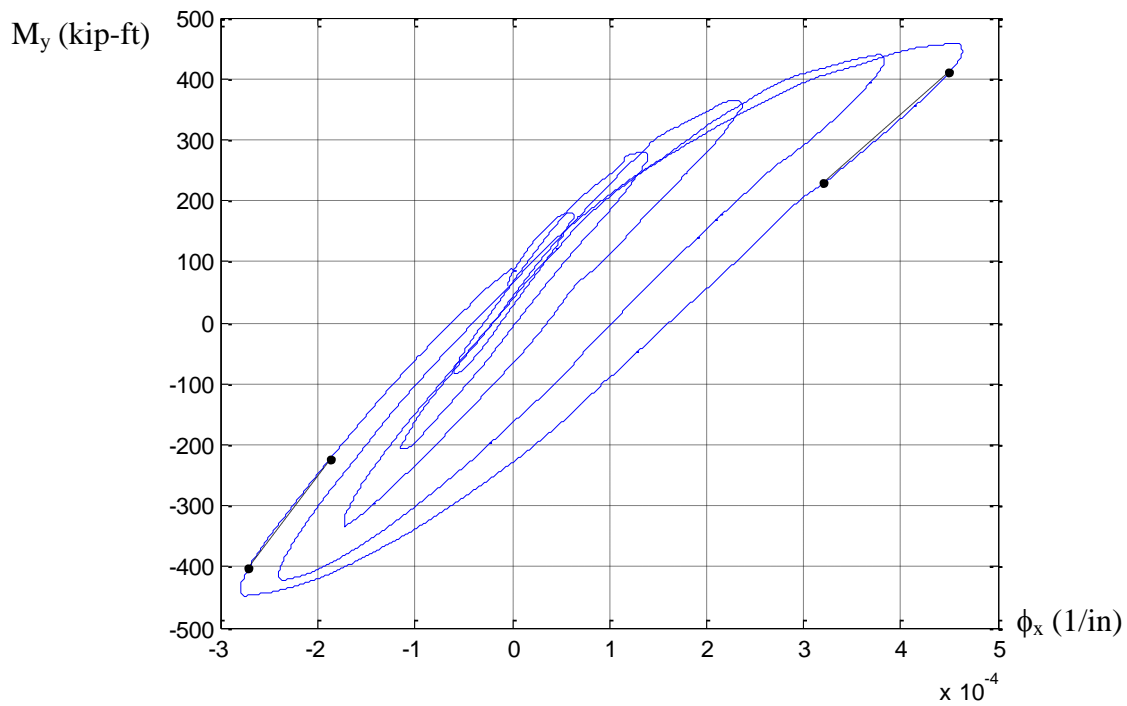


(b) $P=800$ kip

Figure 7.49. Second order moment at the base (M , kip-ft) vs. Curvature (ϕ , 1/in) from the uniaxial load cases (LC2) for the specimen 15C20-26-12

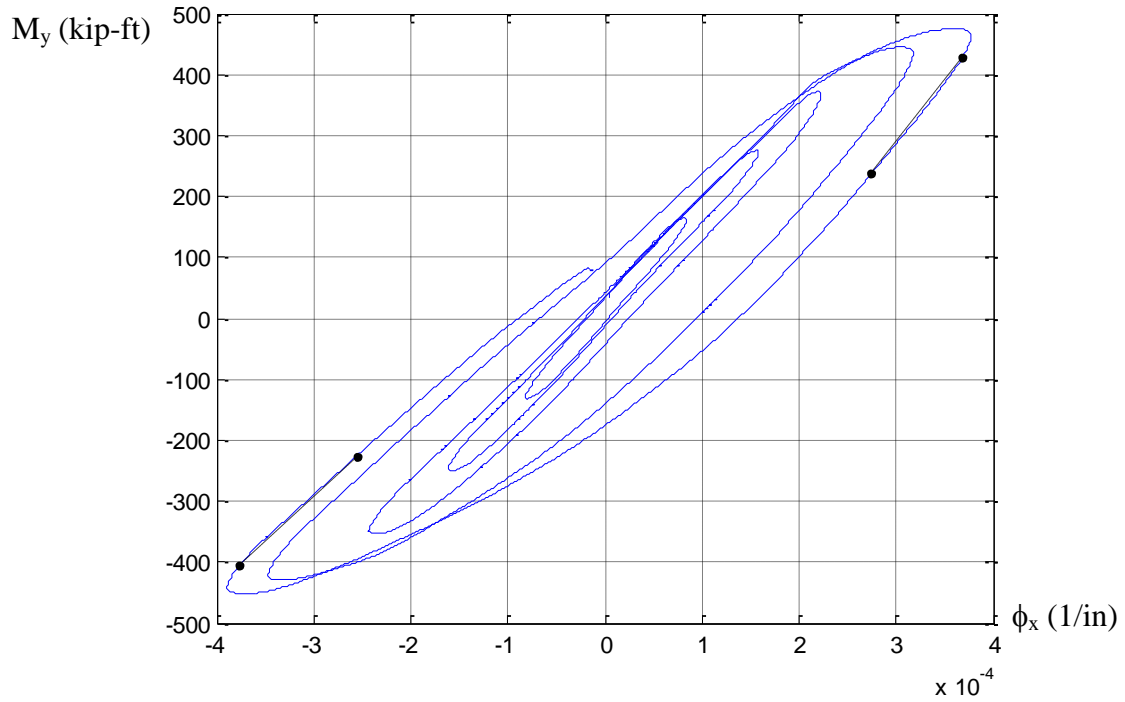


(a) $P=400$ kip

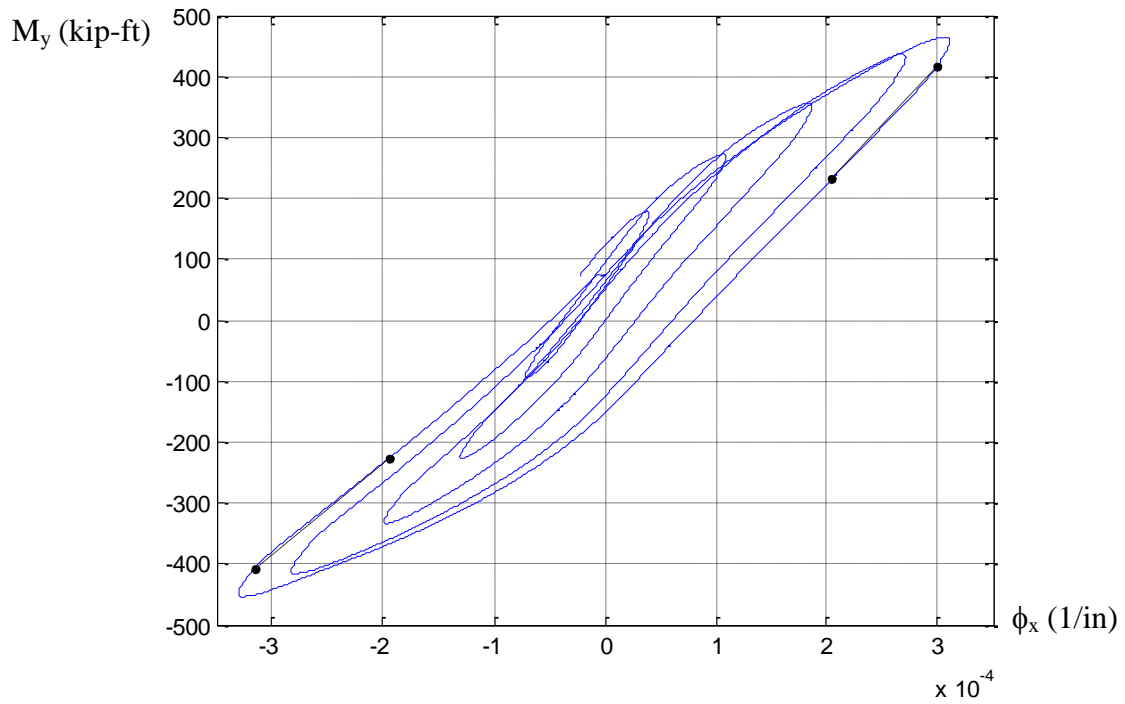


(b) $P=200$ kip

Figure 7.50. Second order moment at the base (M , kip-ft) vs. Curvature (ϕ , 1/in) from the uniaxial load cases (LC2) for the specimen 12Rw-26-5

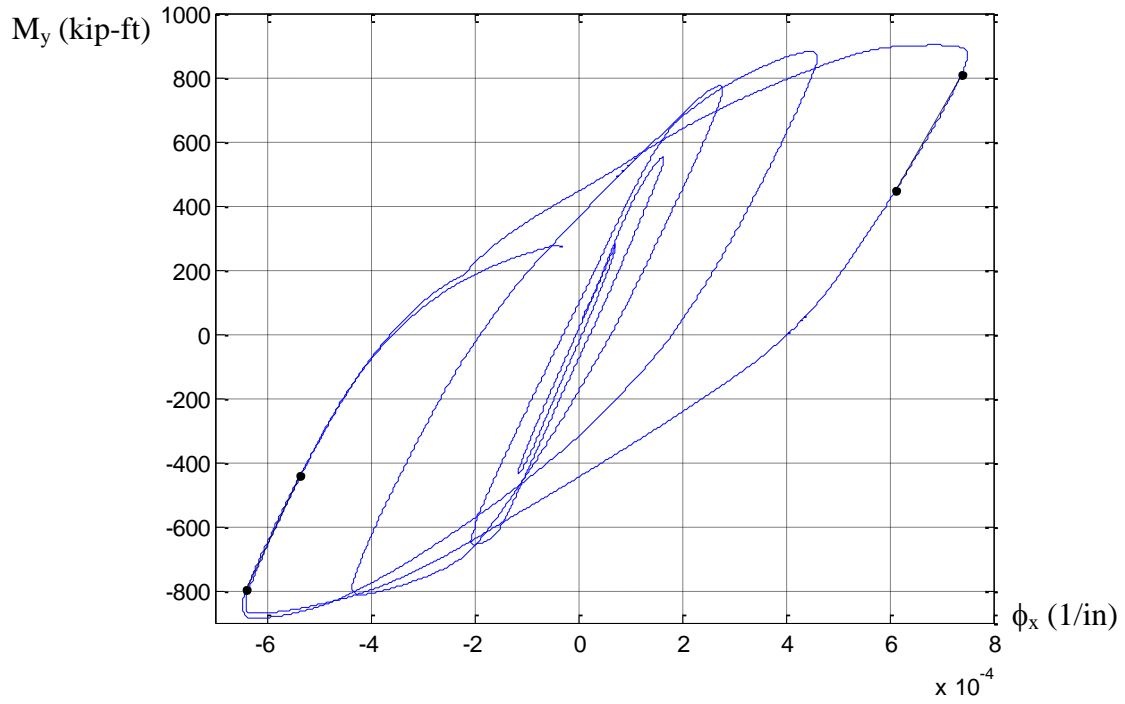


(a) $P=200$ kip

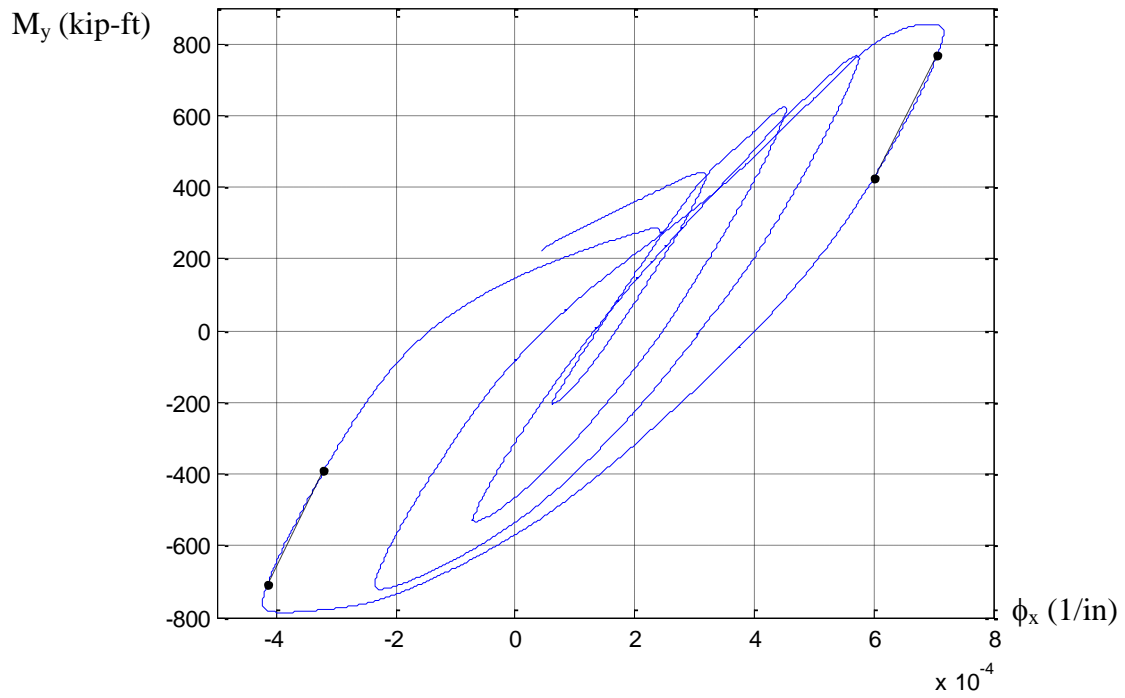


(b) $P=400$ kip

Figure 7.51. Second order moment at the base (M , kip-ft) vs. Curvature (ϕ , $1/\text{in}$) from the uniaxial load cases (LC2) for the specimen 16Rw-26-12

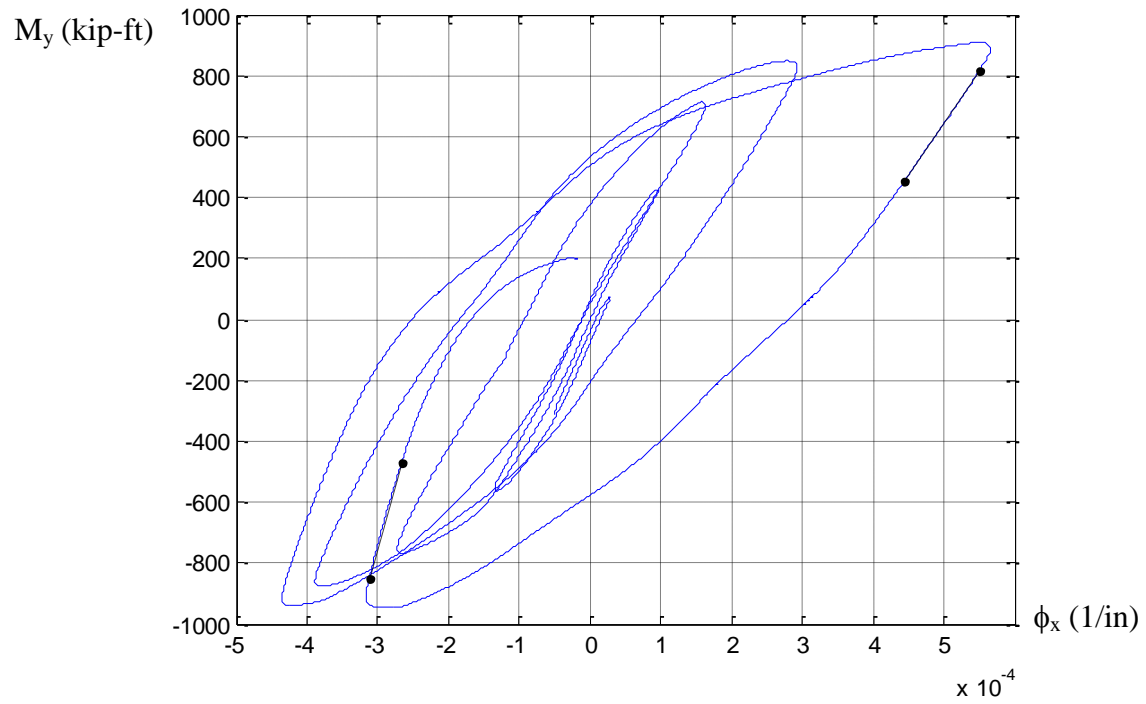


(a) $P=400$ kip

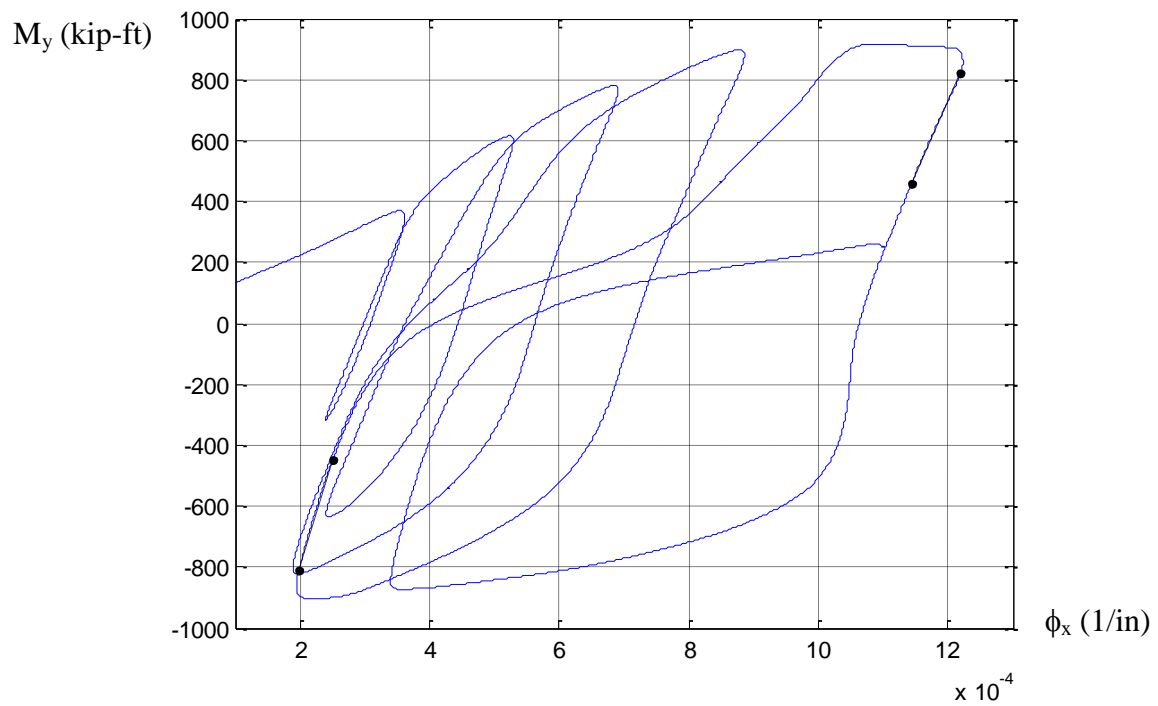


(b) $P=800$ kip

Figure 7.52. Second order moment at the base (M , kip-ft) vs. Curvature (ϕ , 1/in) from the uniaxial load cases (LC2) for the specimen 13Rs-26-5

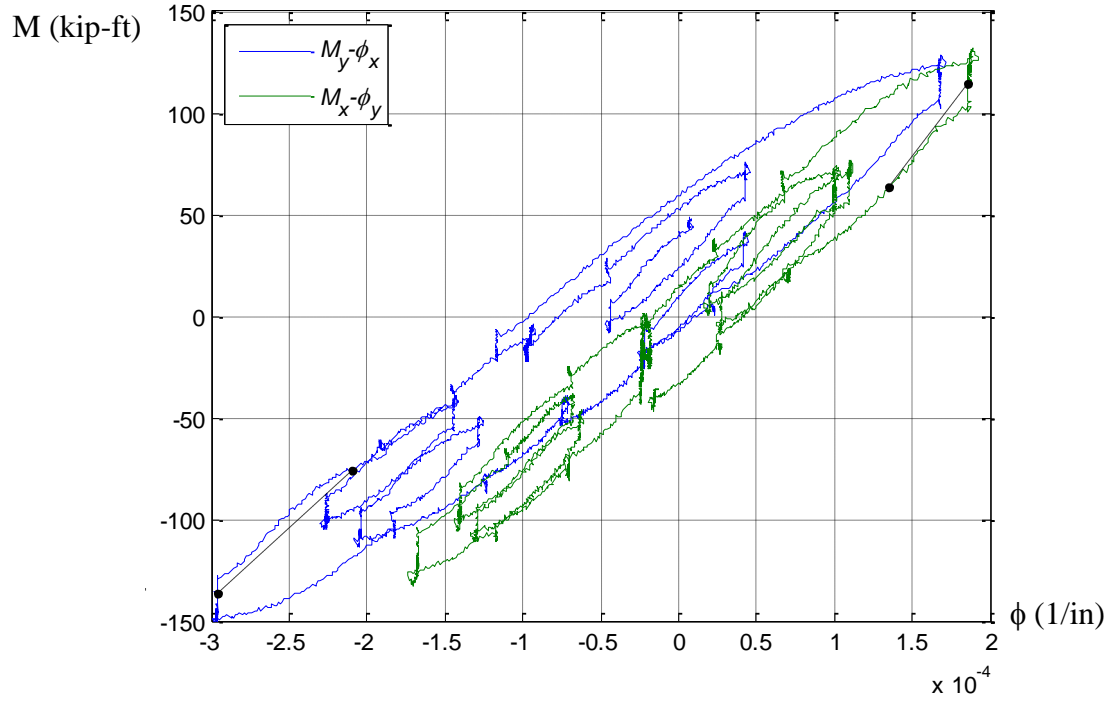


(a) $P=400$ kip

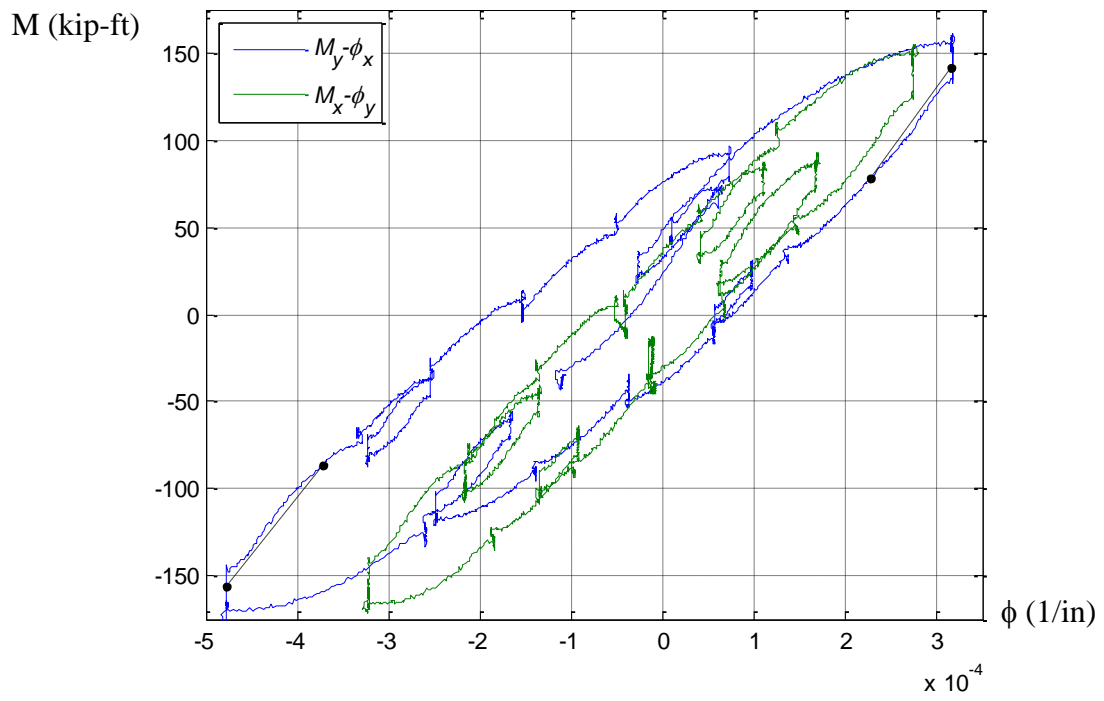


(b) $P=800$ kip

Figure 7.53. Second order moment at the base (M , kip-ft) vs. Curvature (ϕ , 1/in) from the uniaxial load cases (LC2) for the specimen 17Rs-26-12

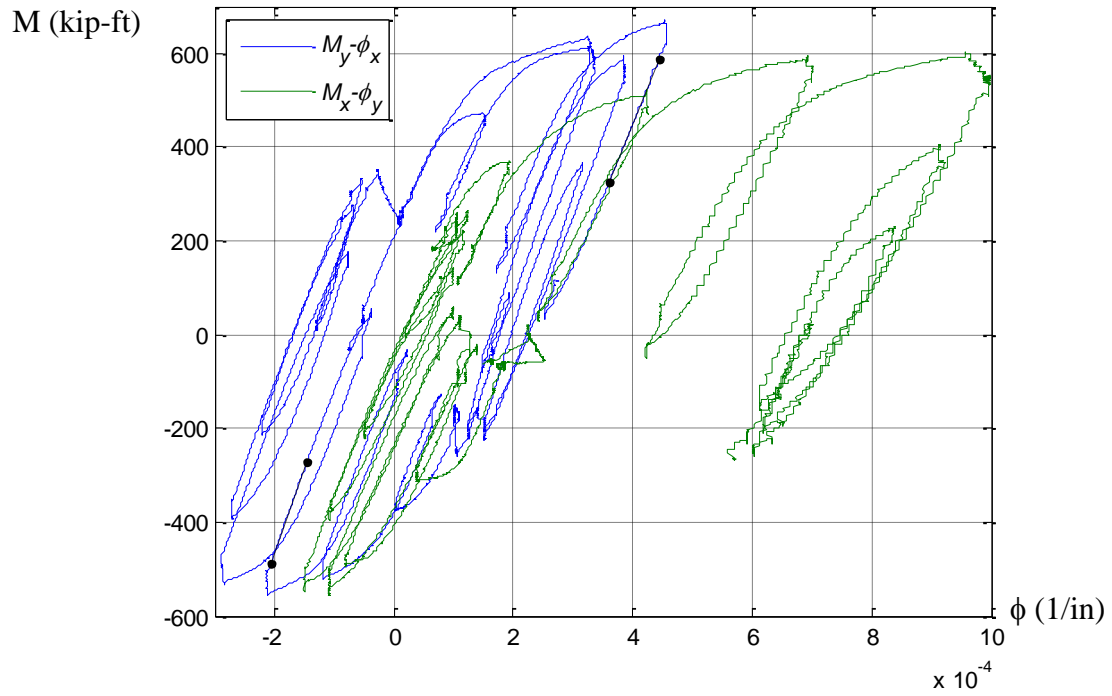


(a) $P=250$ kip

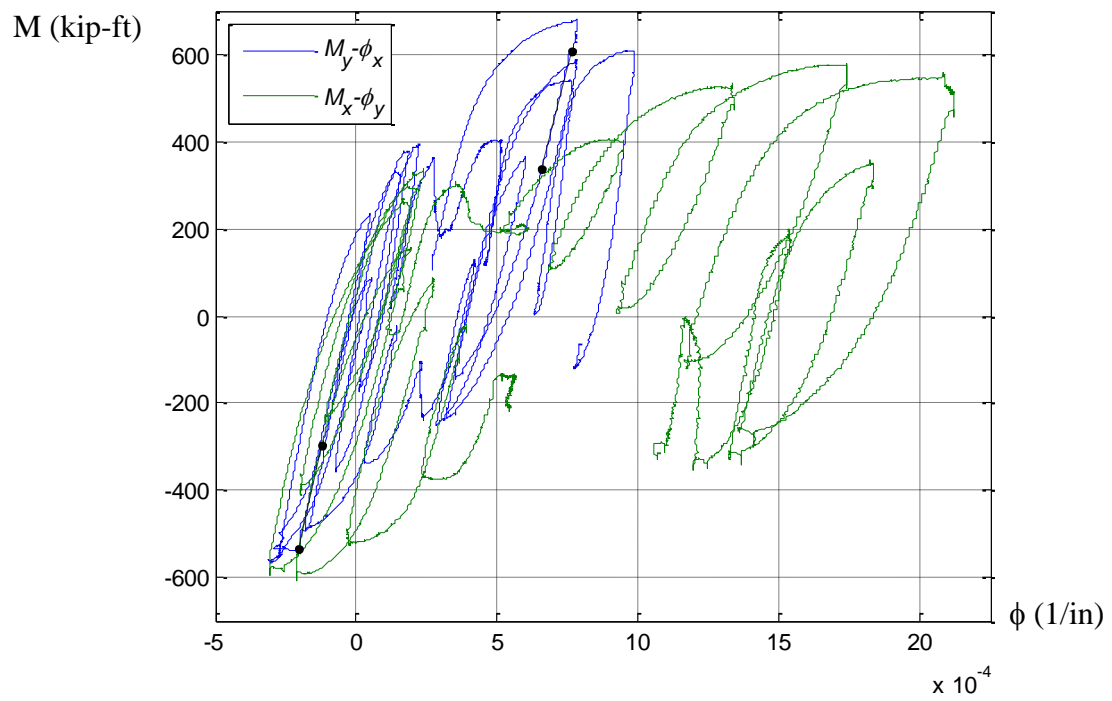


(b) $P=150$ kip

Figure 7.54. Second order moment at the base (M , kip-ft) vs. Curvature (ϕ , 1/in) from the uniaxial load cases (LC2) for the specimen 2C12-18-5



(a) $P=1250$ kip



(b) $P=750$ kip

Figure 7.55. Second order moment at the base (M , kip-ft) vs. Curvature (ϕ , 1/in) from the uniaxial load cases (LC2) for the specimen 3C20-18-5

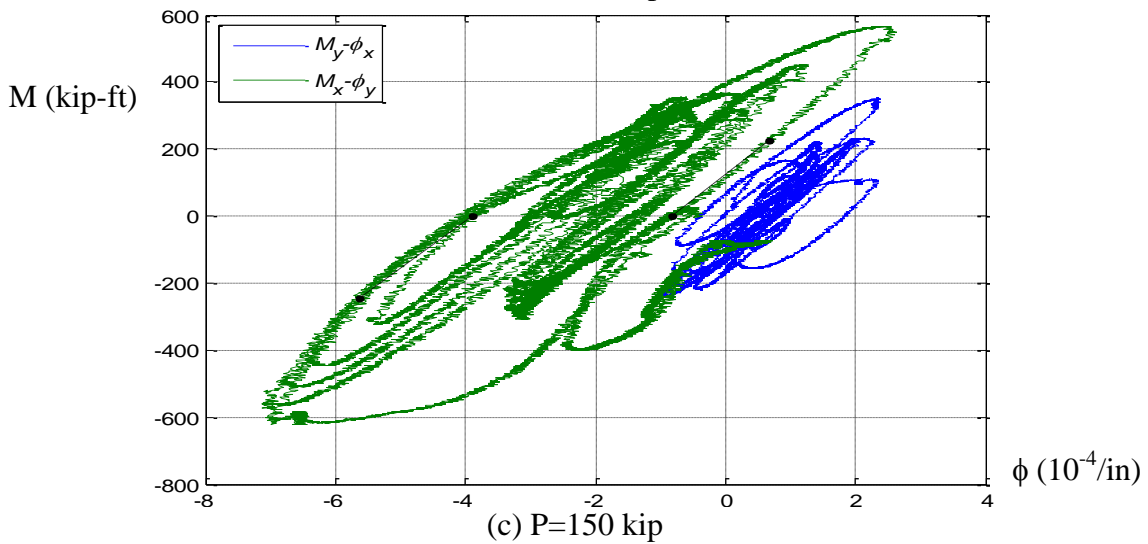
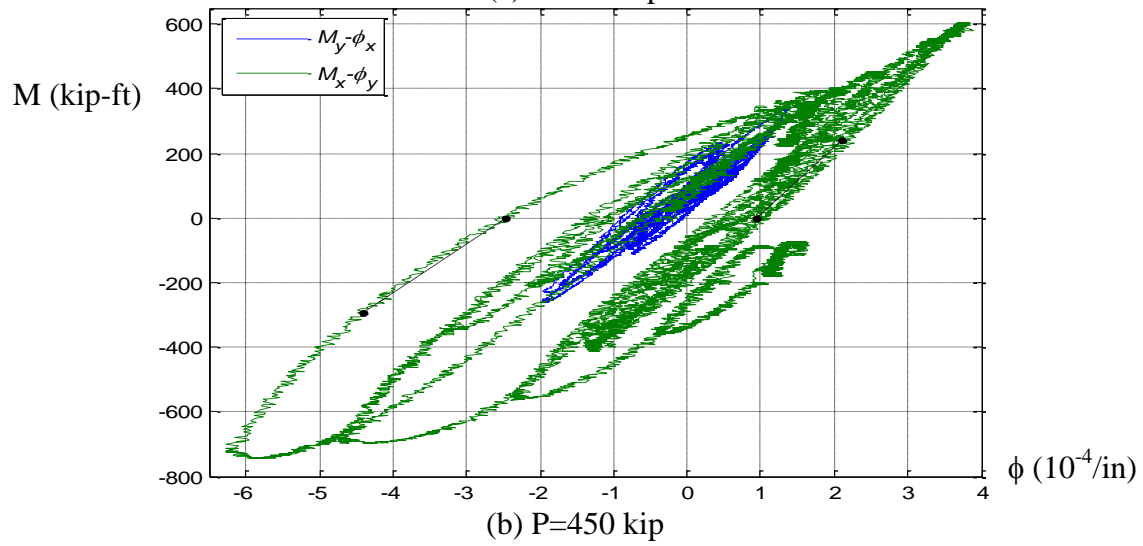
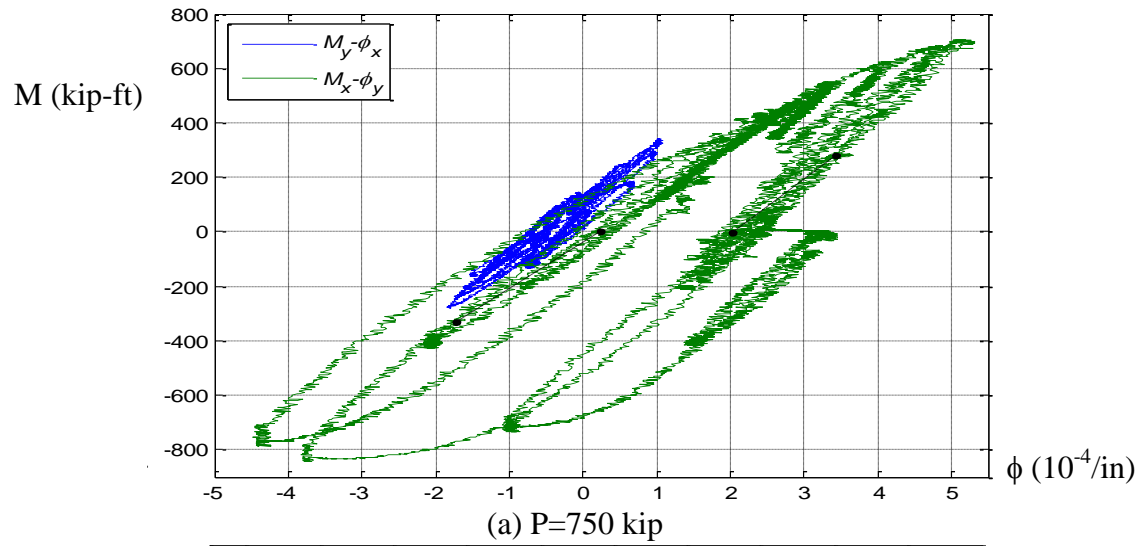
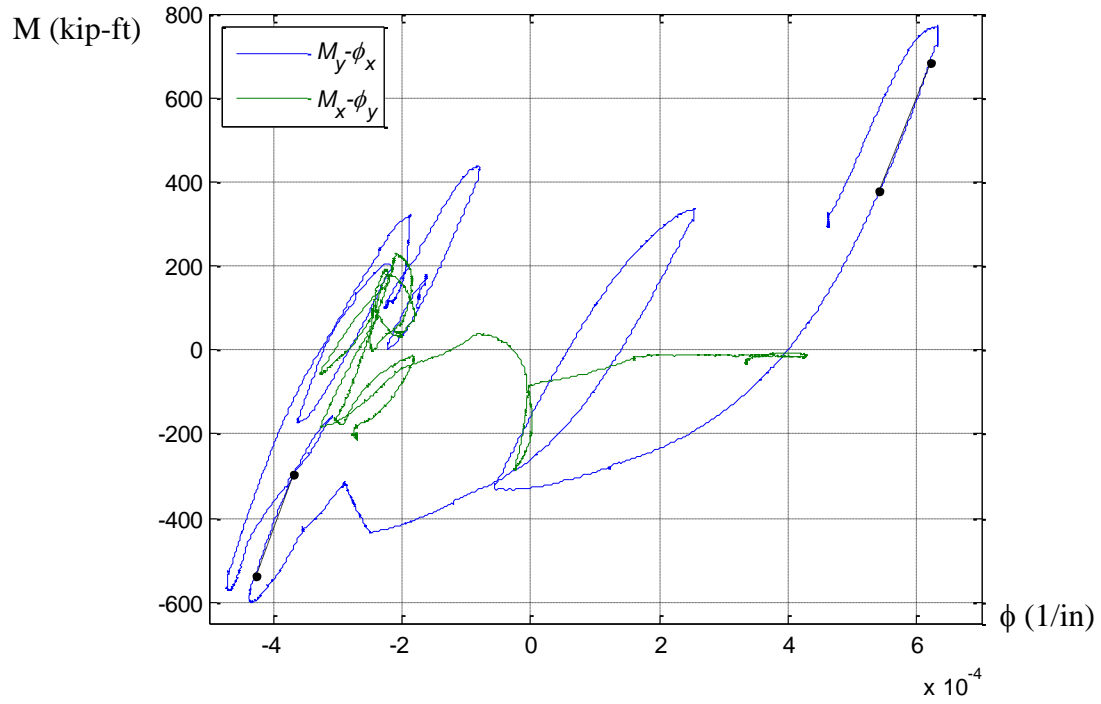
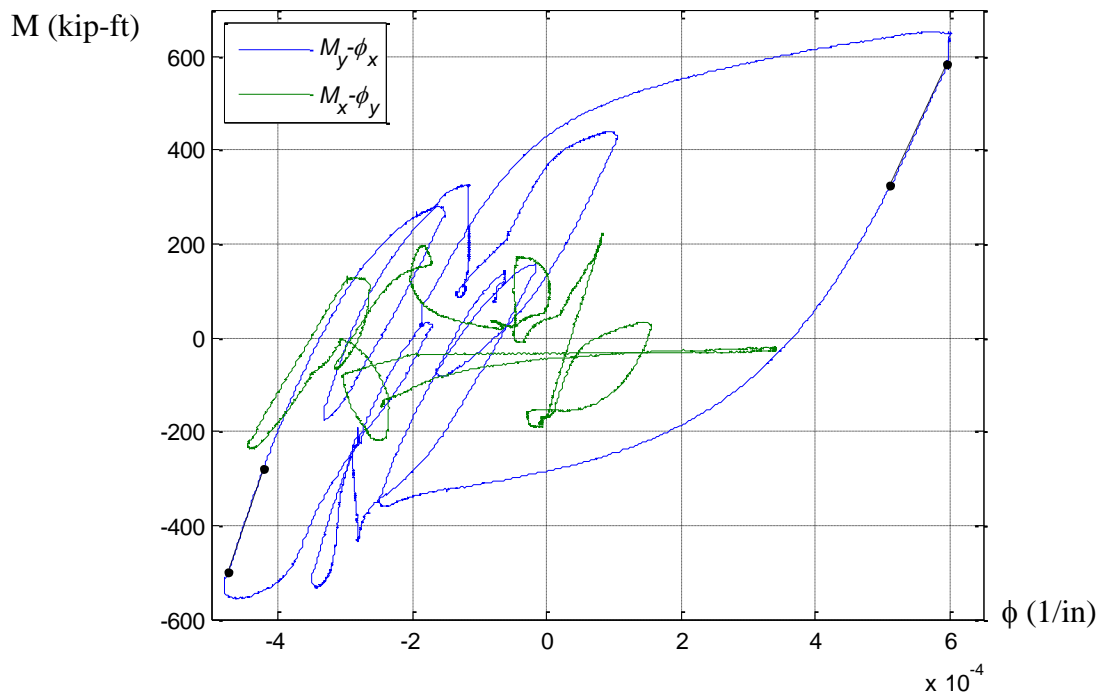


Figure 7.56. Second order moment at the base (M , kip-ft) vs. Curvature (ϕ , 1/in) from the uniaxial load cases (LC2) for the specimen 4Rw-18-5



(a) $P=750$ kip



(b) $P=250$ kip

Figure 7.57. Second order moment at the base (M , kip-ft) vs. Curvature (ϕ , 1/in) from the uniaxial load cases (LC2) for the specimen 5Rs-18-5

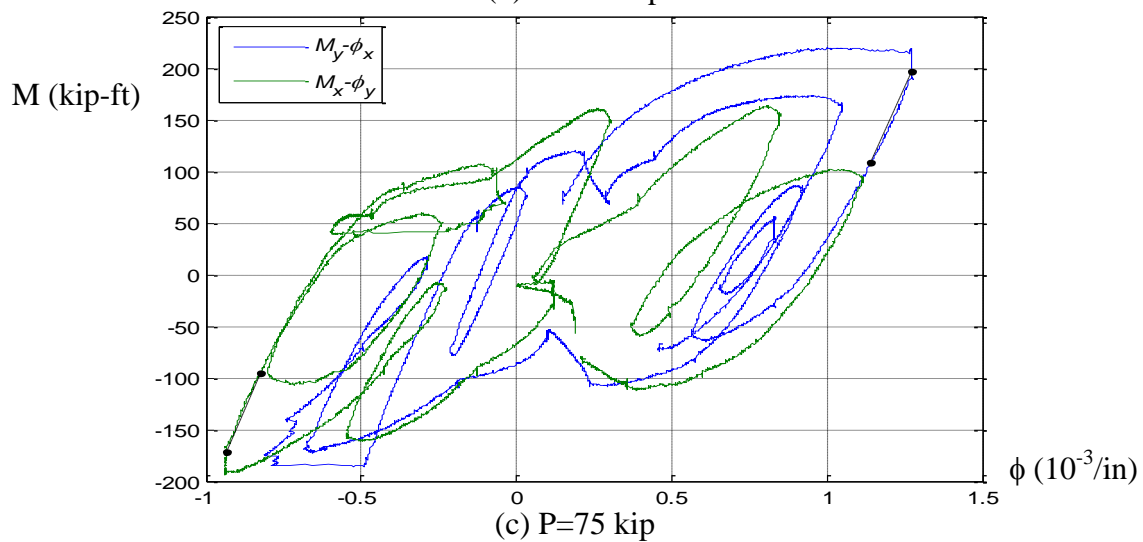
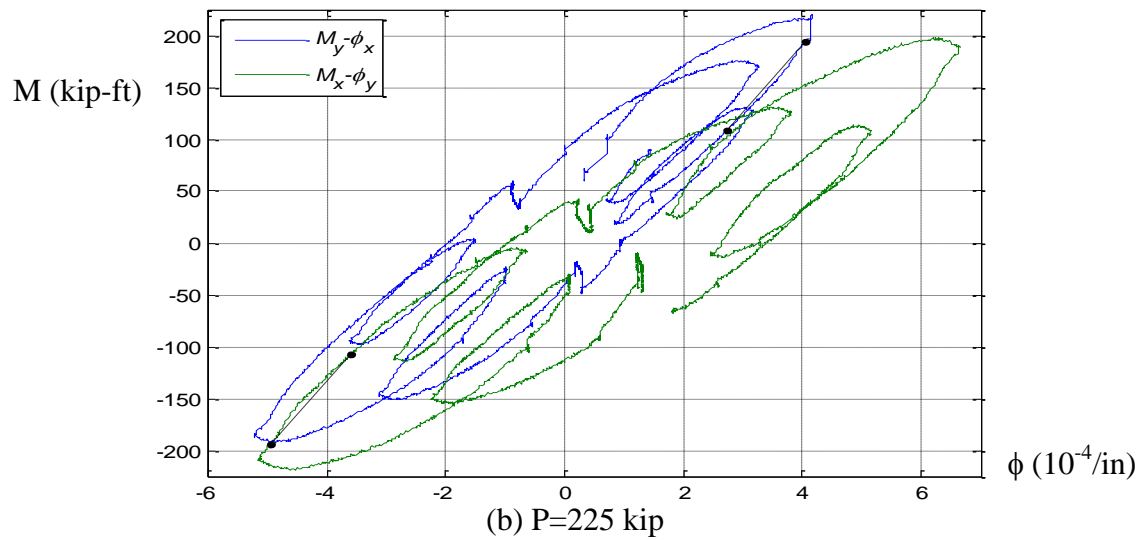
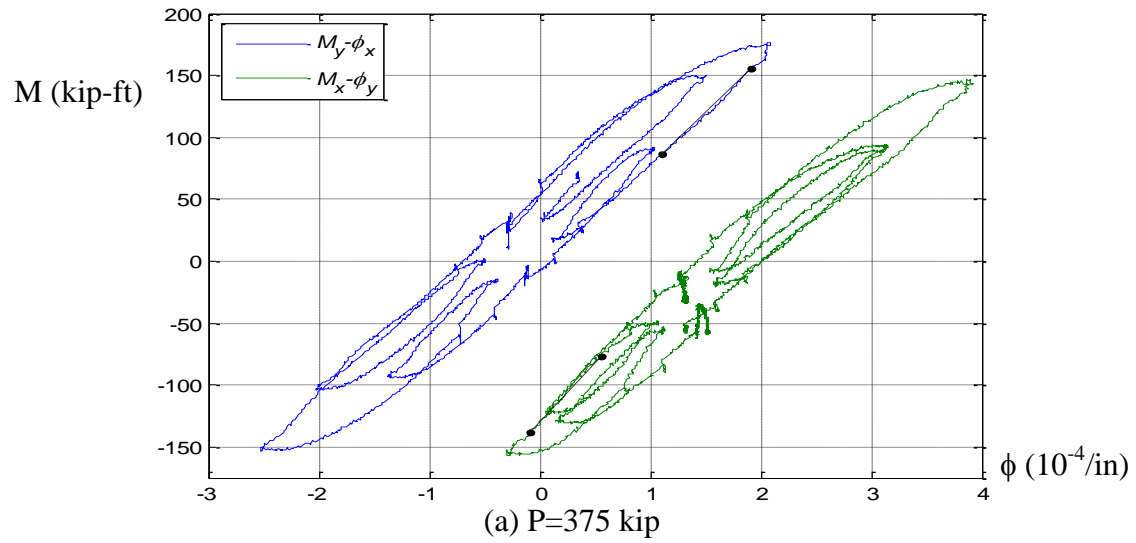
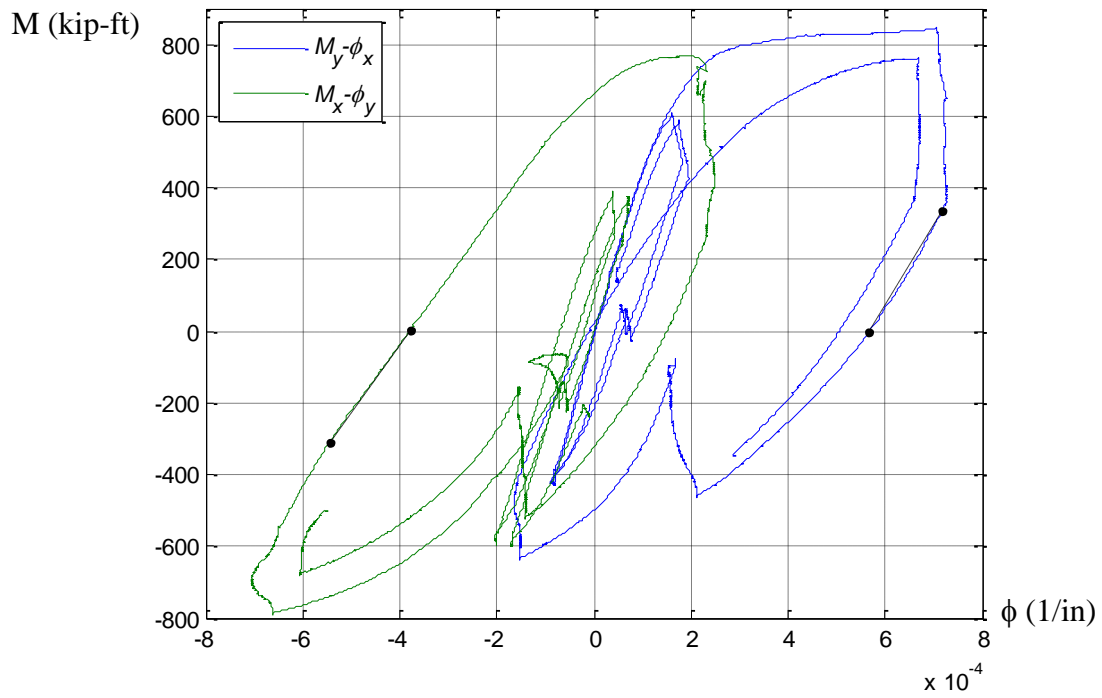
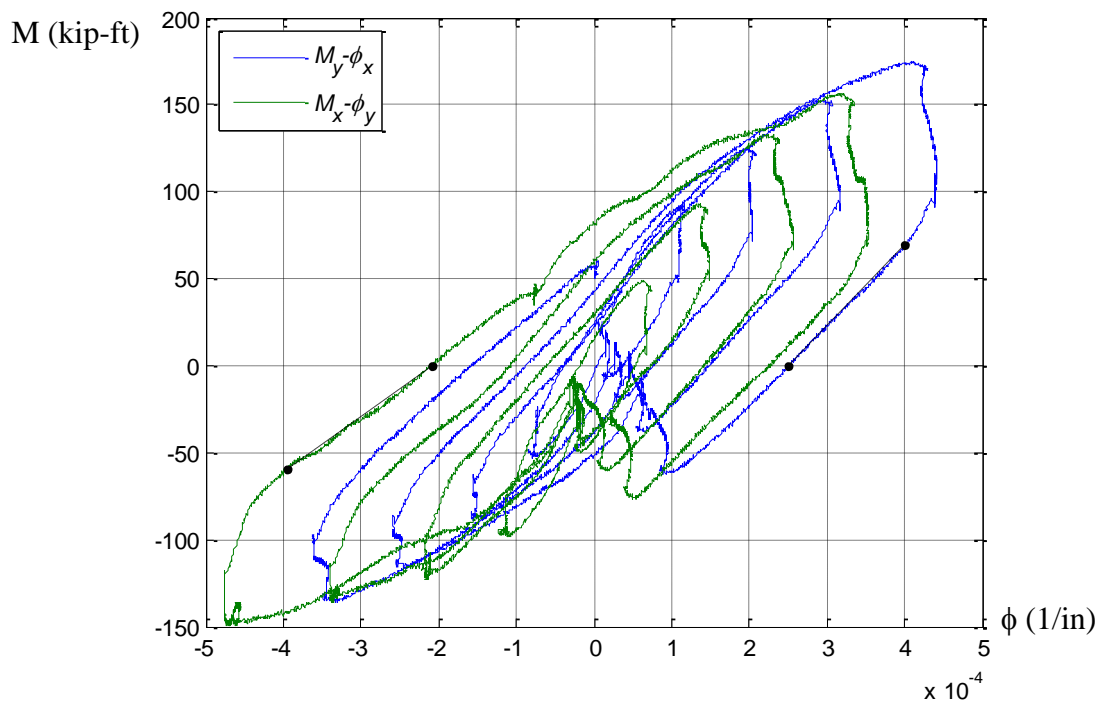


Figure 7.58. Second order moment at the base (M , kip-ft) vs. Curvature (ϕ , $1/\text{in}$) from the uniaxial load cases (LC2) for the specimen 6C12-18-12



(a) 7C20-18-12, $P=1250$ kip



(a) 14C12-26-12, $P=150$ kip

Figure 7.59. Second order moment at the base (M , kip-ft) vs. Curvature (ϕ , 1/in) from the uniaxial load cases (LC2) for the specimen 14C12-26-12 and 7C20-18-12.

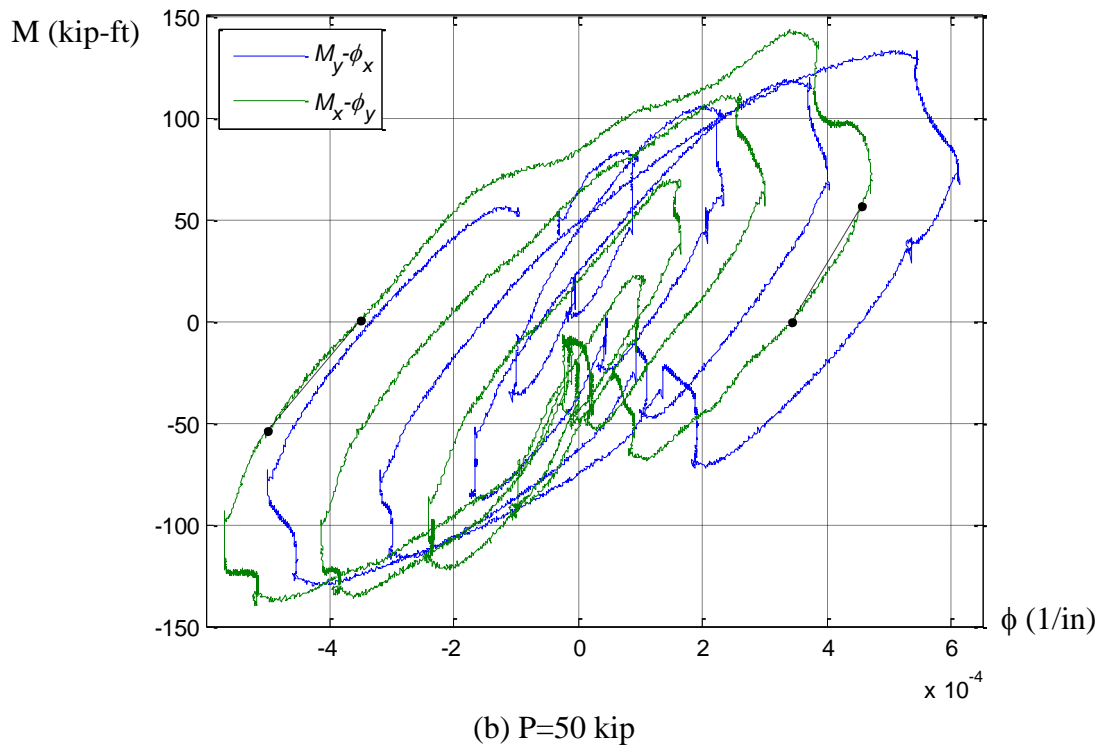
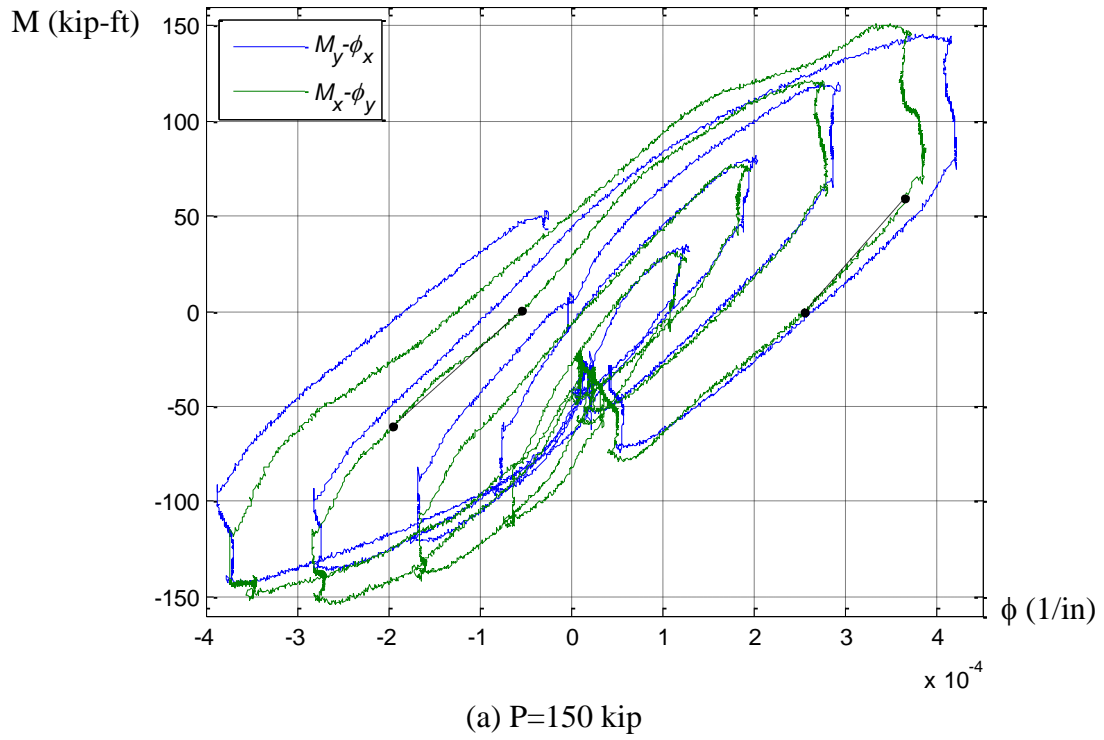
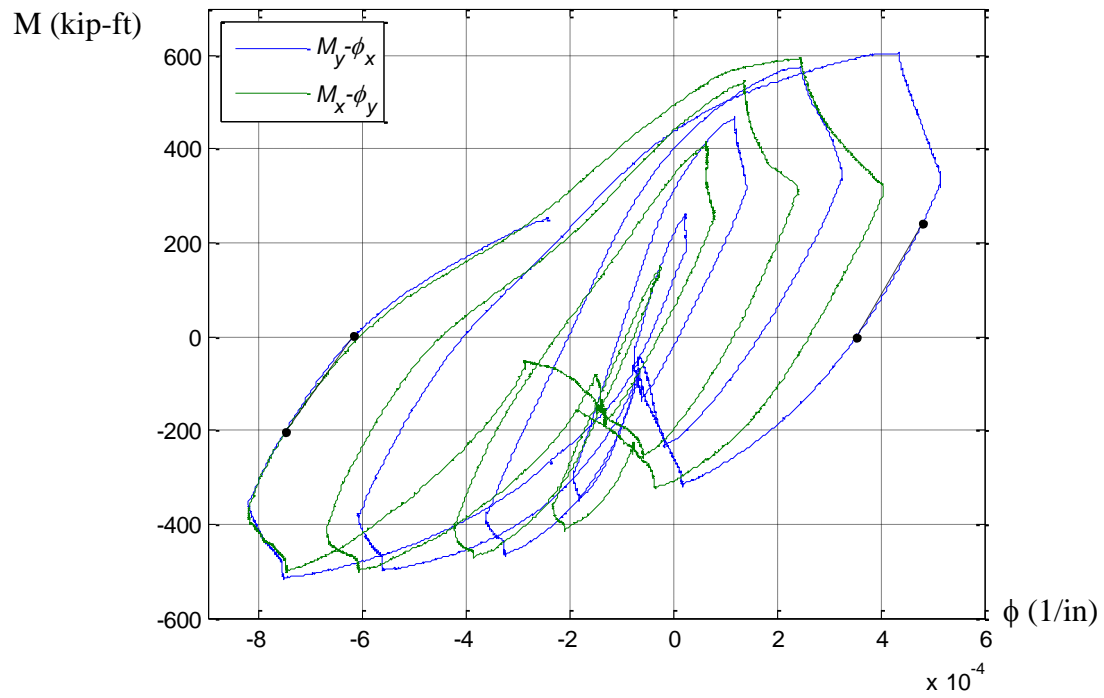
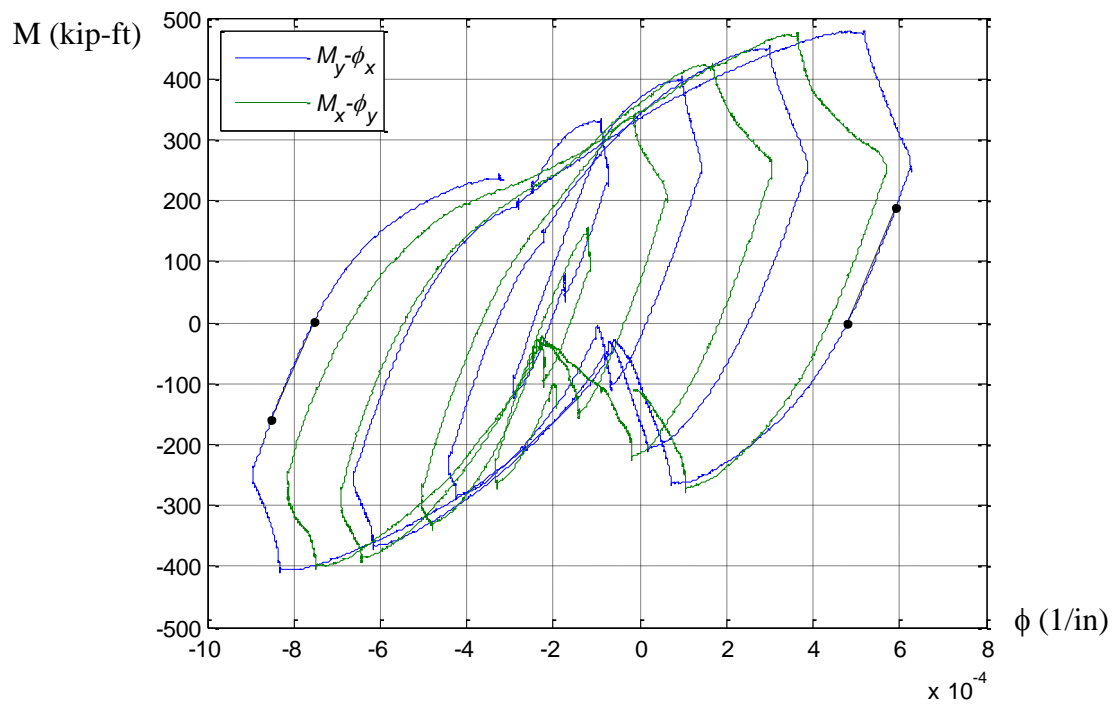


Figure 7.60. Second order moment at the base (M , kip-ft) vs. Curvature (ϕ , 1/in) from the uniaxial load cases (LC2) for the specimen 10C12-26-5

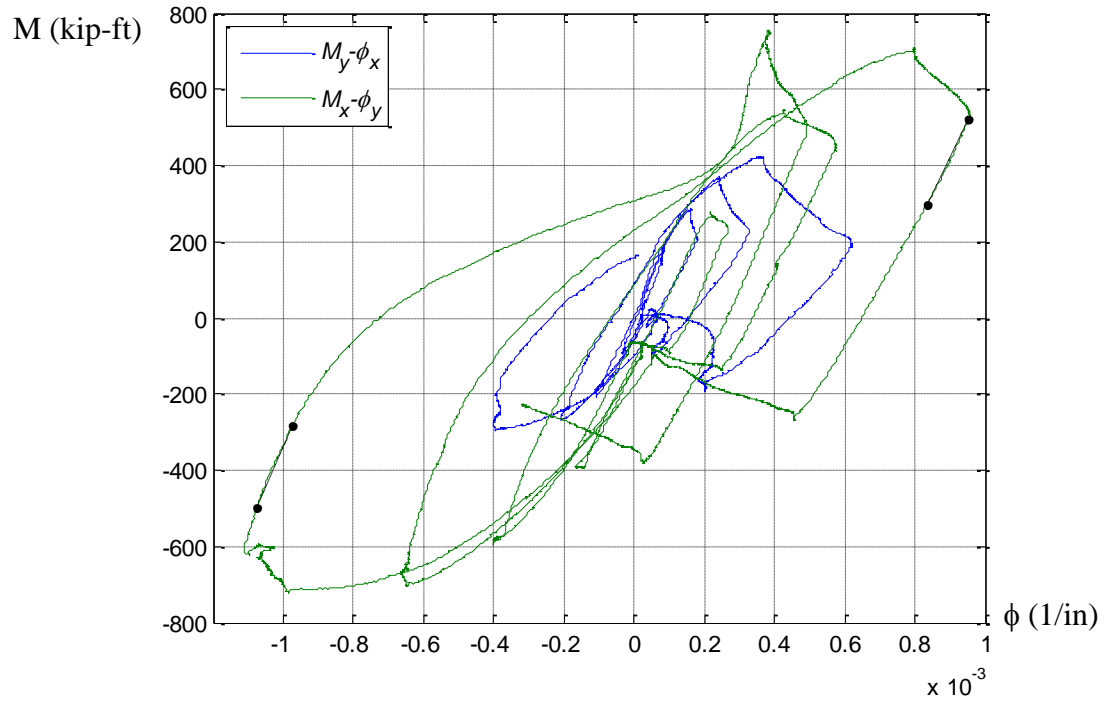


(a) $P=450$ kip

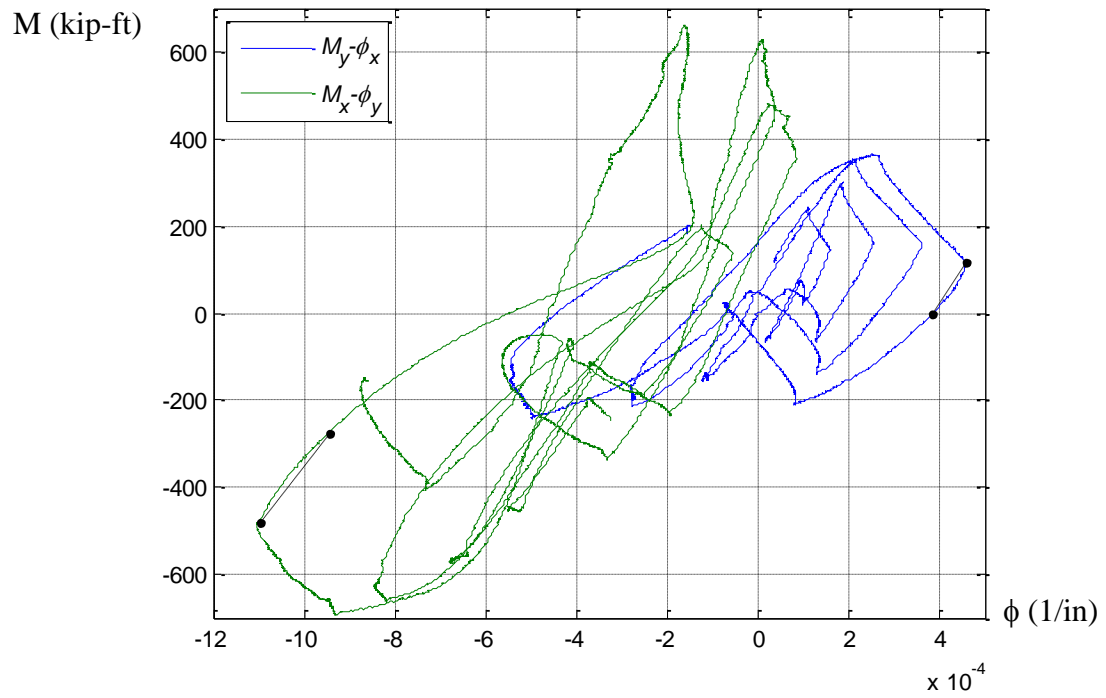


(b) $P=150$ kip

Figure 7.61. Second order moment at the base (M , kip-ft) vs. Curvature (ϕ , 1/in) from the uniaxial load cases (LC2) for the specimen 11C20-26-5

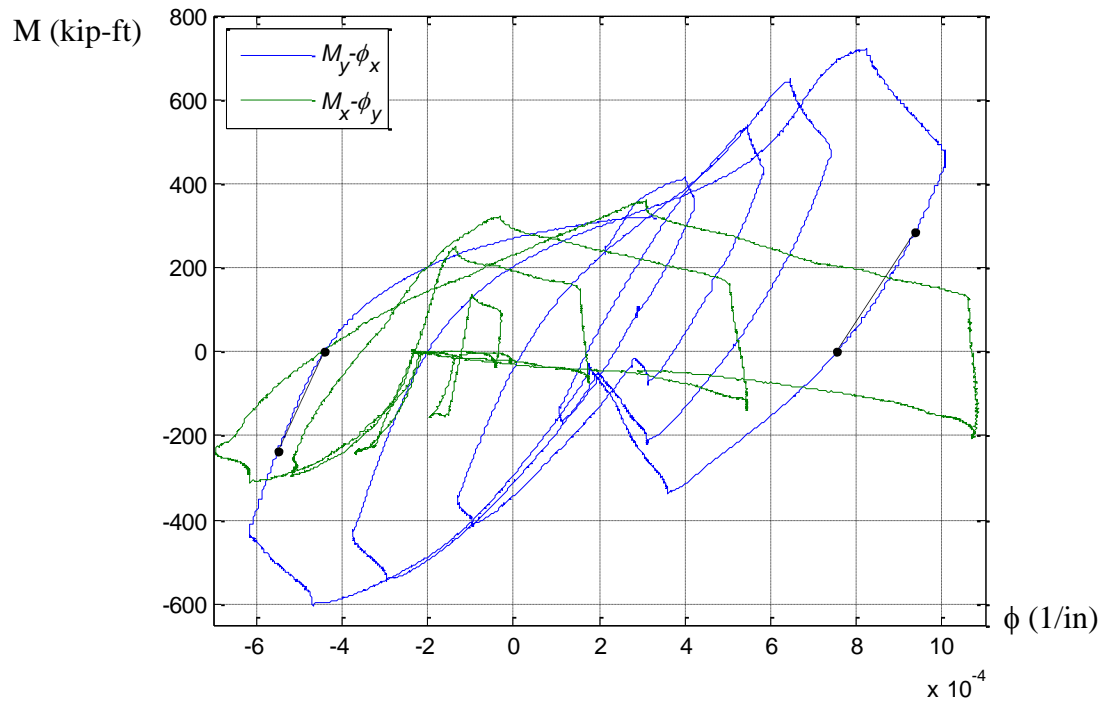


(a) $P=300$ kip

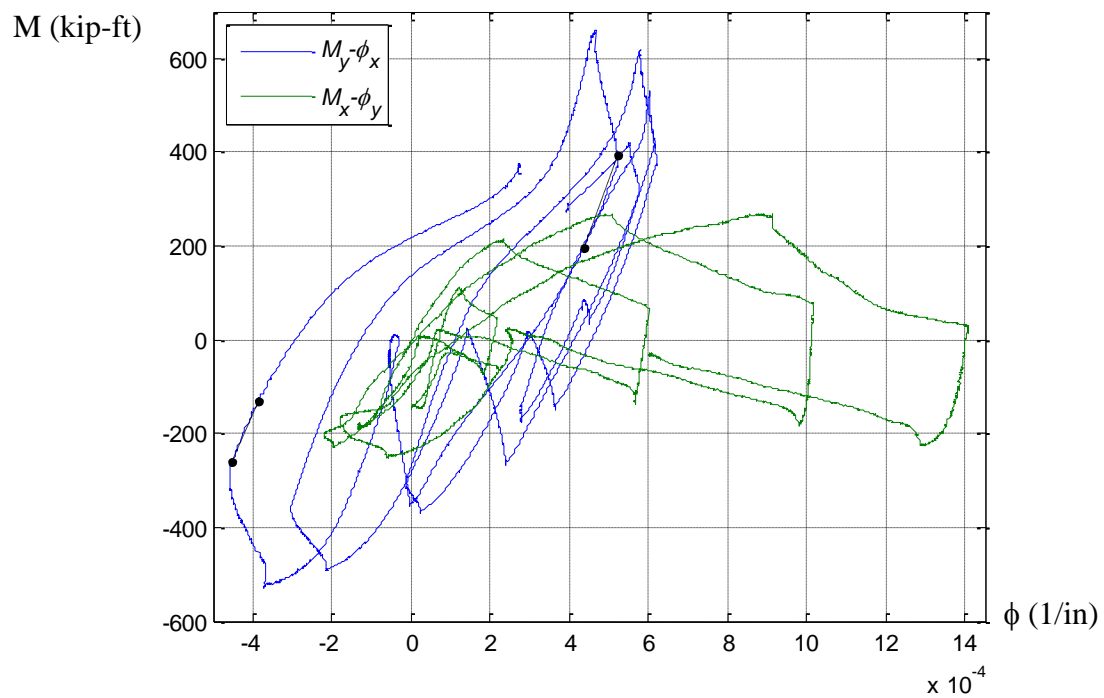


(b) $P=500$ kip

Figure 7.62. Second order moment at the base (M , kip-ft) vs. Curvature (ϕ , 1/in) from the uniaxial load cases (LC2) for the specimen 12Rw-26-5



(a) $P=300$ kip



(b) $P=500$ kip

Figure 7.63. Second order moment at the base (M , kip-ft) vs. Curvature (ϕ , 1/in) from the uniaxial load cases (LC2) for the specimen 13Rs-26-5

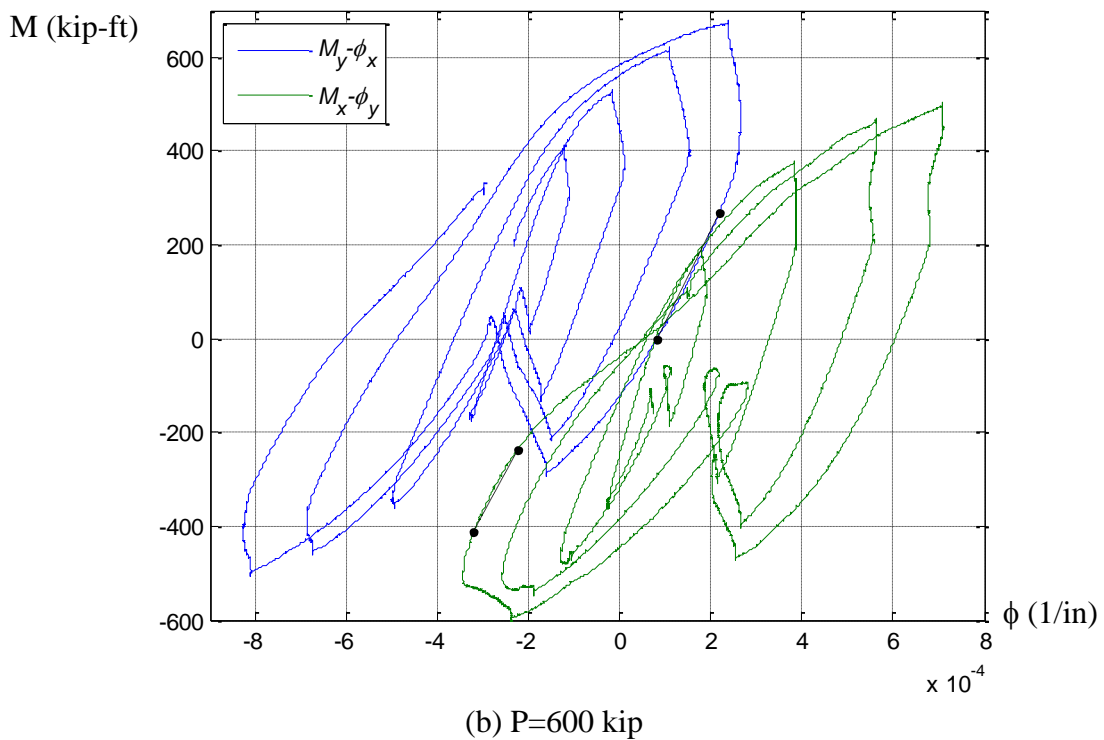
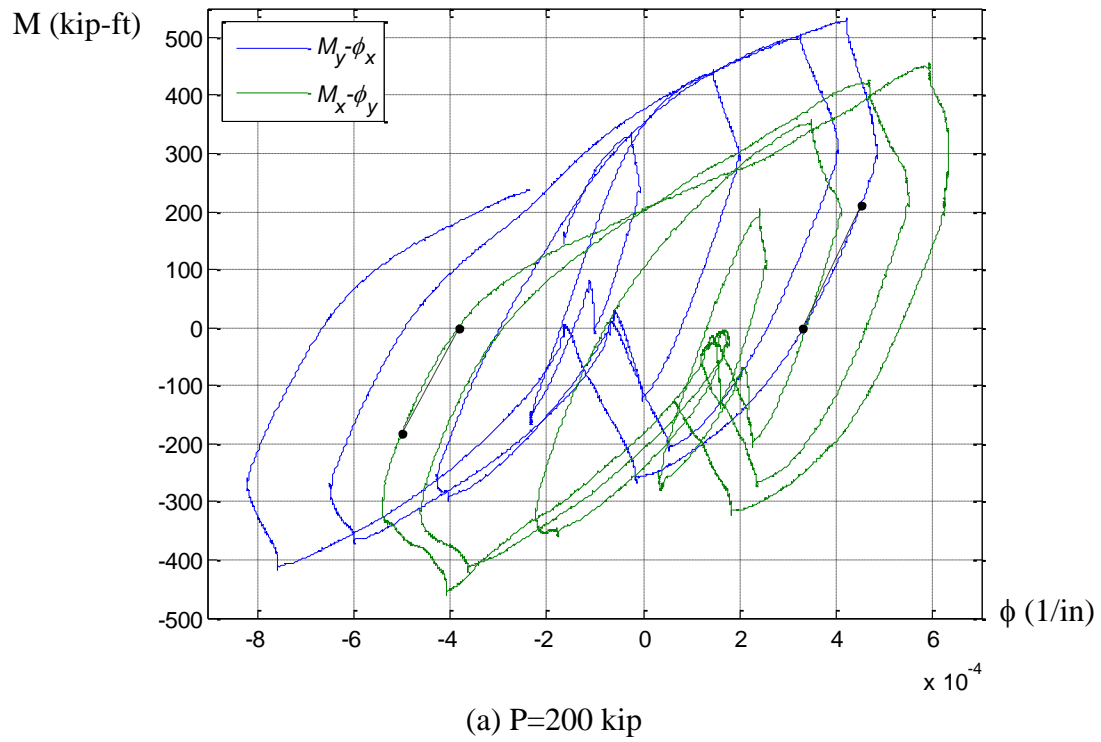


Figure 7.64. Second order moment at the base (M , kip-ft) vs. Curvature (ϕ , 1/in) from the uniaxial load cases (LC2) for the specimen 15C20-26-12

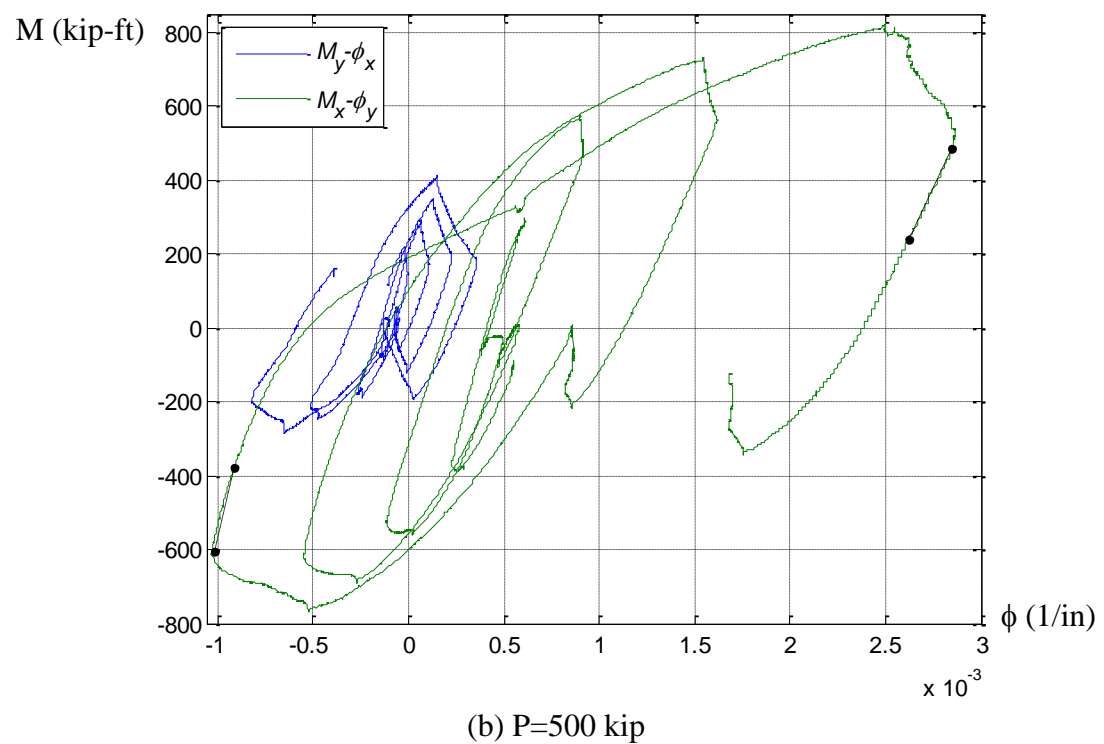
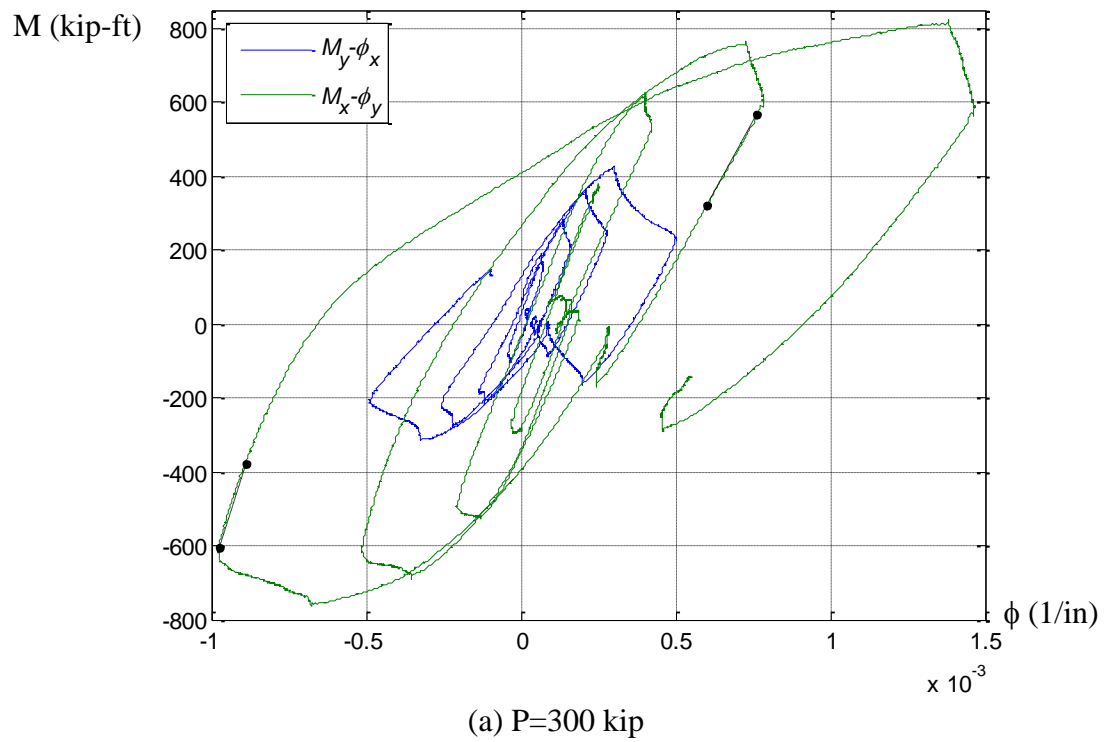
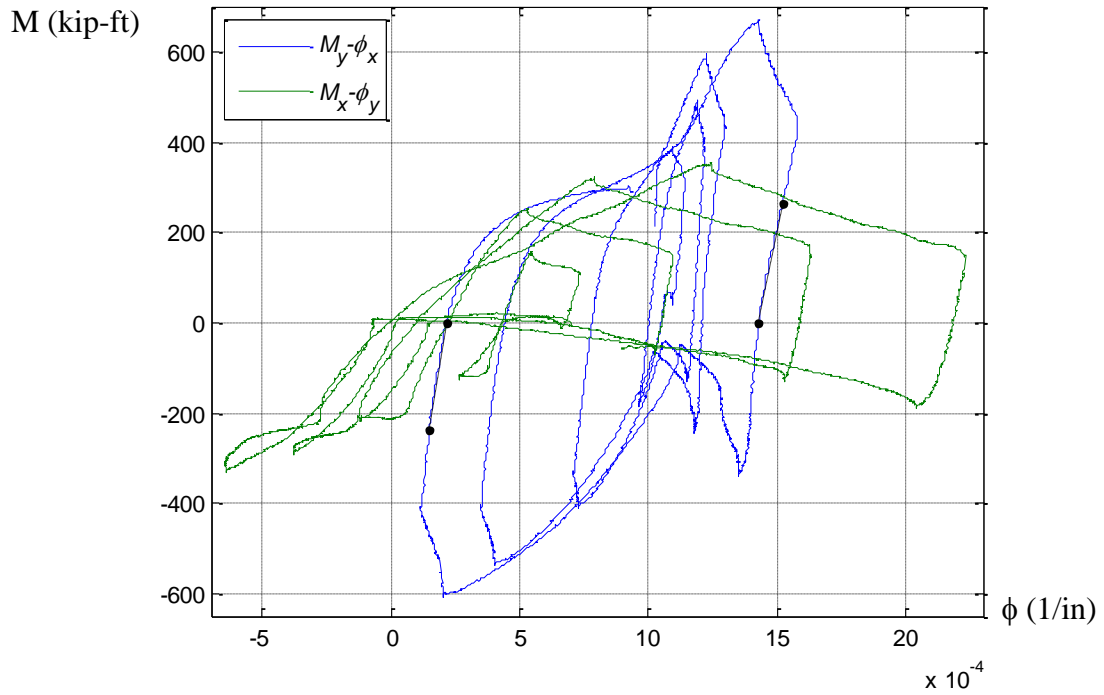
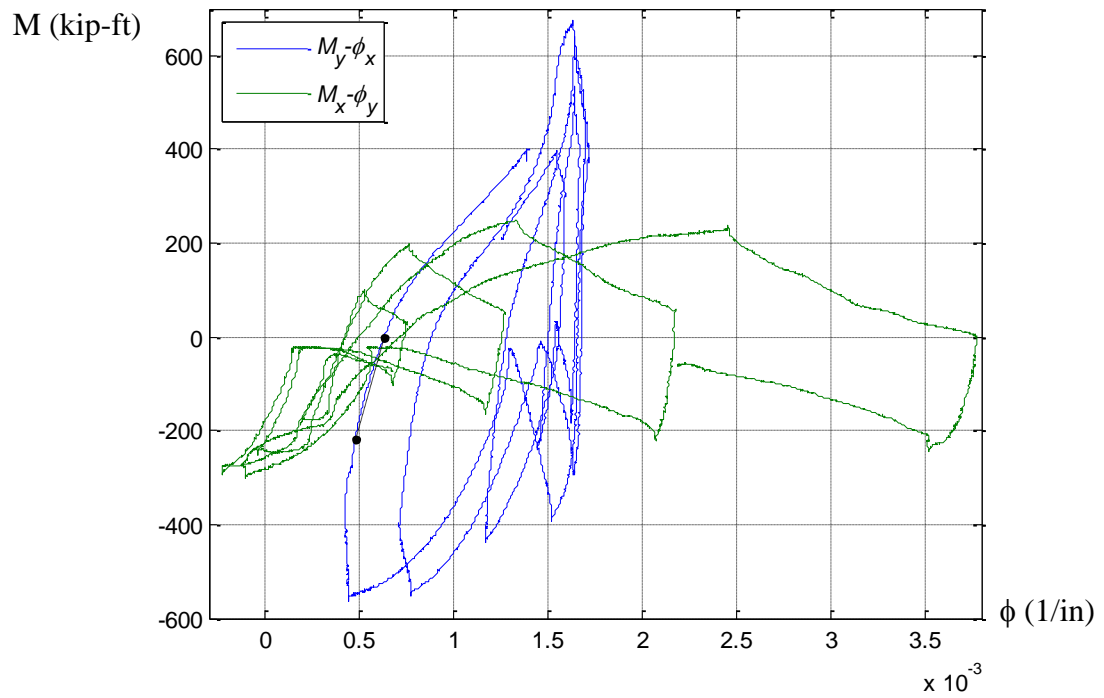


Figure 7.65. Second order moment at the base (M , kip-ft) vs. Curvature (ϕ , 1/in) from the uniaxial load cases (LC2) for the specimen 16Rw-26-12

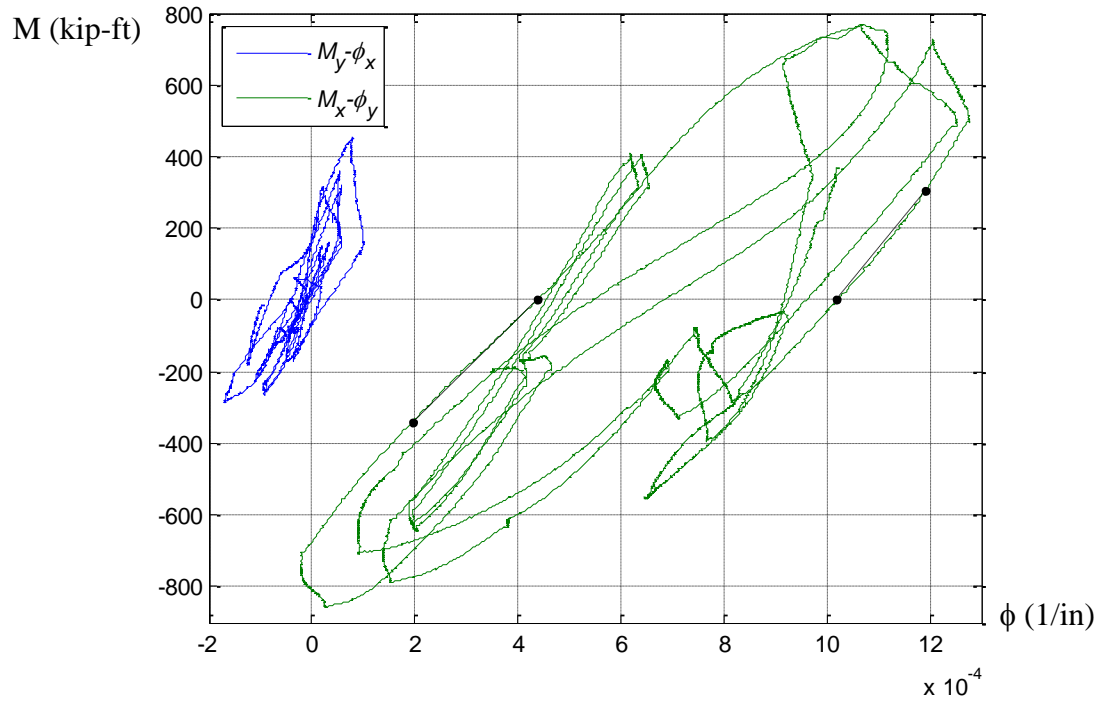


(a) $P=200$ kip

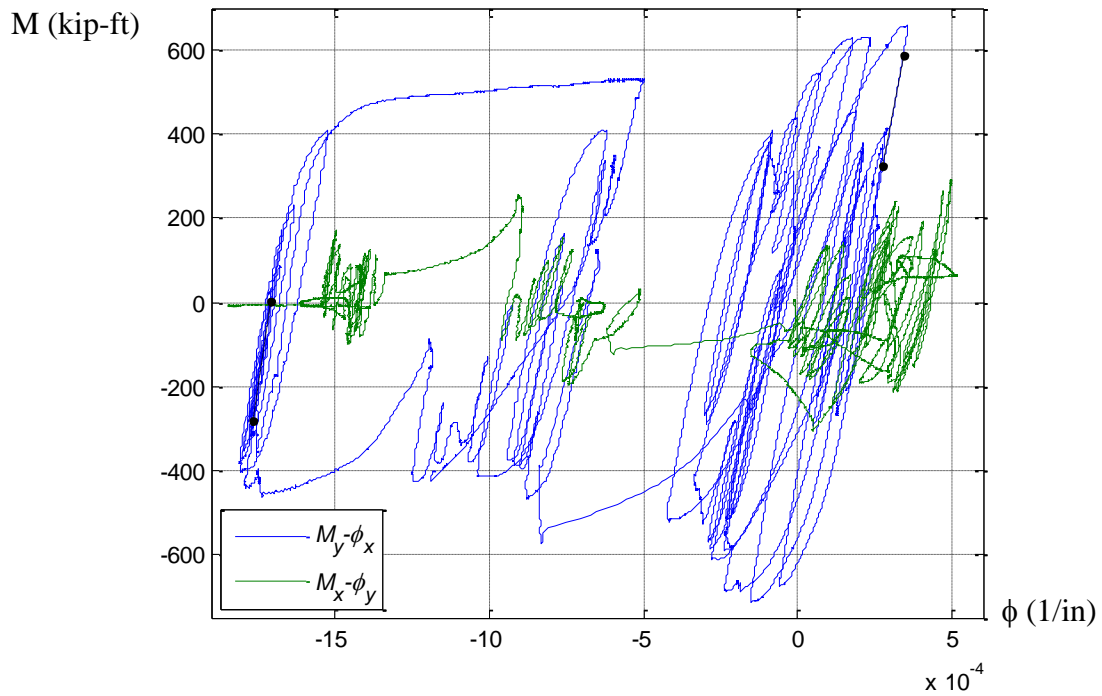


(b) $P=600$ kip

Figure 7.66. Second order moment at the base (M , kip-ft) vs. Curvature (ϕ , 1/in) from the uniaxial load cases (LC2) for the specimen 17Rs-26-12



(a) 8Rw-18-12, $P=800$ kip



(b) 9Rs-18-12, $P=800$ kip

Figure 7.67. Second order moment at the base (M , kip-ft) vs. Curvature (ϕ , 1/in) from the uniaxial load cases (LC2) for the specimens 8Rw-18-12 and 9Rs-18-12

7.3. Evolution of flexural rigidity

The values of the flexural rigidity previously extracted from the tests are analyzed in this section. These values were obtained from the following responses:

- Buckling loads (P_{test}) were obtained from the processed experimental data in Section 5.5, as well as from computational analysis in Section 5.6. Based on this loads, values of the flexural rigidity (EI_{test}) can be calculated with the current design equations by a reverse engineering process with the following equations:

$$EI_{test} = \begin{cases} \left(\frac{KL}{\pi}\right)^2 \cdot \frac{P_o \cdot \log(0.658)}{\log(P_{test} / P_o)} & \text{if } \frac{P_{test}}{P_o} > 0.44 \\ \left(\frac{KL}{\pi}\right)^2 \cdot \frac{P_{test}}{0.877} & \text{if } \frac{P_{test}}{P_o} \leq 0.44 \end{cases} \quad (7.2)$$

The equations are solved for the effective stiffness given that the buckling load is known and equal the buckling capacity obtained in Section 5.5 or 5.6. The rigidities EI_{test} obtained from the experimental processed data shown in Section 5.5 are listed in column (1) of Table 1.1 for the load case LC1. The rigidities obtained from the analytical buckling loads of Section 5.6 are in column (2) of Table 1.1 for the load case LC1.

- Also in Section 5.7, experimental values of the elastic flexural stiffness (EI_{test}) were obtained from the unloading branch from the moment-curvature ($M-\phi$) curves during the pure compression loading case (LC1). Values of the tangent stiffness were extracted then from two selected points ($M_a-\phi_a$, $M_b-\phi_b$) as:

$$EI_{test} = \frac{M_b - M_a}{\phi_b - \phi_a} \quad (7.3)$$

The rigidities EI_{test} obtained from the loading branch of the moment-curvature response are shown in column (3) of Table 1.1 for the load case LC1. In turn, the rigidities obtained from the moment-curvature response from the unloading branch are in column (4) of Table 1.1 for load case LC1.

- In Section 7.2.1, experimental values of the elastic flexural rigidity (EI_{test}) were obtained for the unloading branch from the lateral force – displacement ($F-\Delta$) response of the uniaxial (LC2) and the biaxial (LC3) loading cases (see Figure 7.2 to Figure 7.37). Values of the $F-\Delta$ slope were extracted from two selected points ($F_a-\Delta_a$, $F_b-\Delta_b$), and for both positive and negative sides of the loop.

The EI_{test} extracted from this response is obtained as follows. The second order displacement (Δ_2) in the beam-column is equal to the first order displacement (Δ_1) due to the lateral force in the cantilever member and amplified by a factor (AF) that accounts for the second order effects due to the sustained axial load (P_{test}).

$$\Delta_2 = \Delta_1 \cdot AF = \left(\frac{FL^3}{3EI_{test}} \right) \cdot \left(\frac{1}{1 - \frac{P_{test}}{\pi^2 EI_{test} / (KL)^2}} \right) \quad (7.4)$$

In the previous equation, the first term is the first order displacement of a cantilever member with length (L) under a transverse force (F) and with a flexural rigidity EI_{exp} . The second term, which is equal to $1/(1-P/P_e)$ and where P_e is the Euler load, is the amplification factor that accounts for the second order effects due to the axial force in a member with initial imperfection (W. K. Chen and Lui 1987; Timoshenko 1961). Solving for the flexural rigidity EI_{test} , and writing the final equation in terms of the two extracted force-displacement points ($F_a-\Delta_a$, $F_b-\Delta_b$), the experimental stiffness can be calculated as follows:

$$EI_{test} = \left(\frac{F_b - F_a}{\Delta_b - \Delta_a} \right) \frac{L^3}{3} + \left(\frac{KL}{\pi} \right)^2 P_{test} \quad (7.5)$$

The stiffness EI_{test} obtained from the lateral force – lateral displacement response from the unloading in the positive side is shown in column (1) of Table 1.1 for the load cases LC2 and LC3. In turn, the stiffness obtained from the lateral force – lateral displacement response at the unloading in the negative side is in column (2) of Table 1.1 for the load cases LC2 and LC3.

- Similarly in Section 7.2.2, experimental values of the elastic flexural stiffness (EI_{test}) were obtained from the unloading branch from the moment-curvature ($M-\phi$) curves of the uniaxial (LC2) and the biaxial (LC3) loading cases (see Figure 7.38 to Figure 7.66). Values of the tangent stiffness were extracted from two selected points ($M_a-\phi_a$, $M_b-\phi_b$) as in Equation 7.2, and for both positive and negative sides of the loop.

The rigidities EI_{test} obtained from the moment-curvature response at the unloading in the positive side are shown in column (3) of Table 1.1 for the load cases LC2 and LC3. Also, the rigidities obtained from the moment-curvature response at the unloading in the negative side are listed in column (4) of Table 1.1 for the load cases LC2 and LC3.

The averaged flexural rigidities (EI_{test}) obtained for the same loading case from different responses are shown in the fifth column of Table 1.1. The maximum standard deviation of the averaged stiffness is of the order of 40% the corresponding averaged value.

As seen in Table 1.1, the averaged rigidities range from 0.37 to 0.98 of the summation of the steel ($E_s I_s$) and the concrete ($E_c I_c$) stiffness (gross stiffness), with the highest values in the first load cases and descending for the latter load cases; for the load case LC1 the averaged rigidities vary from 0.70 to 0.98 of the gross stiffness. The steel ($E_s I_s$) and concrete ($E_c I_c$) stiffness are listed in Table 7.2.

In addition, the averaged rigidities range from 0.47 to 1.23 of the effective stiffness (EI_{eff}) calculated with the AISC (2010) Specifications, again being larger for the first load cases and with lower values for the final load cases; for the load case LC1, the averaged rigidities vary from 0.88 to 1.23 of the effective stiffness obtained with the Specifications. The effective stiffness (EI_{eff}) obtained from the AISC (2010) Specifications obtained for each specimen is listed in Table 7.2.

As reminder, the effective stiffness by the AISC (2010) Specifications is given by:

$$EI_{eff} = E_s I_s + C_3 E_c I_c \quad (7.6)$$

where the stiffness coefficient for the concrete in CFTs is equal to:

$$C_3 = \min \left(0.6 + 2 \frac{A_s}{A_s + A_c}, \quad 0.9 \right) \quad (7.7)$$

The final column in Table 1.1 is the calibration of the parameter $C_{3,test}$ obtained from the averaged test rigidities. This parameter is obtained as:

$$C_{3,test} = \frac{EI_{test} - E_s I_s}{E_c I_c} \quad (7.8)$$

Figure 7.68 to Figure 7.71 illustrate the $C_{3,test}$ coefficients obtained from the experimental rigidities and their variation with:

- (a) The gravity load of each load case (P)
- (b) With the sequence during the testing.

These figures also include in dashed line the C_3 coefficients calculated with the AISC (2010) Specifications using Equation 7.7. The C_3 coefficients calculated for each specimen are also listed in Table 7.2, as well as the steel ratio ($\rho_s = A_s / A$) and the slenderness parameter (λ). Table 7.2 also summarizes, for each specimen, the $C_{3,test}$ coefficient obtained from the load case LC1, the average value from the set of load cases LC2, and the average value from the set of load cases LC3.

The comparisons of the evolution of the experimental rigidities or the C_3 coefficients with the gravity load (P) and the loading sequence aim to determine whether or not the rigidity changes are mainly because of the dependency with the sustained axial load or the boundary conditions, or because the degradation due to accumulated damage from previous load cases. Even when contributions are expected from all these causes, these results show a higher impact of the degradation due to the previous loading cases.

Although there is a considerable dispersion of the C_3 coefficients in Figure 7.68 to Figure 7.71, they show in general a higher contribution of the concrete during the first load case LC1, where the $C_{3,test}$ value has an average of 0.81 during LC1 as seen in Table 7.2. This can be attributed to the absence of damage in the concrete during this load case, when cracking and crushing are inexistent or at a minimum.

As the load protocol progresses, the concrete cracking extends and this is reflected in a lower participation of the concrete in the rigidity, where the $C_{3,test}$ value has an average of 0.41 during the load case LC2 and an average of 0.27 during LC3 as seen in Table 7.2. As a consequence of a higher accumulated damage (exhibited as steel local buckling) observed in the RCFTs during the latest load cases, the $C_{3,test}$ values are lower than the corresponding values in the CCFTs. As seen in Table 7.2, the $C_{3,test}$ average coefficients in CCFTs are equal to 0.42 during LC2 and 0.30 during LC3; for the RCFTs, these coefficients are 0.40 during LC2 and 0.25 during LC3.

For the latest load cases (i.e. LC3) in some specimens, the $C_{3,test}$ coefficient resulted in small or trivial values. This indicates a negligible contribution of the concrete to the stiffness as a consequence of a very high damage of the core concrete, as well as in the steel tube.

The effect of the boundary conditions is another factor that has an influence on the value of the C_3 coefficients. For example, Figure 7.68.d illustrates the $C_{3,test}$ values of the Specimen 14C12-26-12 varying with the load sequence. The first set of load cases LC2a, LC2b and LC3 in this specimen were controlled as fixed-free with an effective length factor of $K=2$; however for the second set, the load cases LC2a', LC2b' and LC3a', the DOFs were controlled with fixed top moments or with an effective length factor of $K=1$. The change in boundary conditions in this specimen not only makes it stronger and stiffer, but also increased the concrete contribution on the stiffness by increasing the C_3 coefficient.

Figure 7.72 shows, for each load case set, the variation of the averaged C_3 coefficients presented in Table 7.2 with the steel ratio (ρ) and the slenderness parameter (λ). The dashed line plotted with the steel ratio (ρ) is the C_3 coefficient obtained with the Equation 7.7. In turn, the dashed line plotted with the slenderness parameter (λ) represents the average of the shown data.

The following observation can be highlighted from this figure:

- There seems to be no clear correlation between the C_3 coefficient with either the slenderness parameter (λ) or the steel ratio (ρ).
- Even when the C_3 coefficients calculated with the Equation 7.7 given in the AISC (2010) Specifications present reasonable values with the specimens used, Figure 7.72.a does not show a clear tendency between the steel ratio (ρ) and the contribution of the concrete to the effective stiffness (C_3).
- The dispersion of the C_3 coefficients is higher in the latest load cases, where the standard deviations resulted equal to 0.09 in LC1, 0.14 in LC2 and 0.19 in LC3. The corresponding average C_3 coefficients are 0.81 in LC1, 0.41 in LC2 and 0.27 in LC3.
- As seen in Table 7.2, the lower C_3 coefficients during LC3 correspond to the longer specimens with 26 feet of length, where an average of 0.13 is obtained. For the shorter specimens with 18 feet of length, the averaged C_3 coefficient is similar to the value in LC2 and equal to 0.42.
- Even when the dispersion is considerable, a final average of the coefficient $C_3=0.80$ for the rigidity in the critical load calculation, and $C_3=0.40$ for the rigidity in the lateral response calculation seem appropriate. Thus, the following equations are proposed for the calculation of the effective flexural stiffness of composite CFT members.

For the calculation of the buckling load capacity of CFT columns:

$$EI_{eff} = E_s I_s + 0.80 E_c I_c \quad (7.9)$$

For the lateral and flexural capacity of CFT beam-columns:

$$EI_{eff} = E_s I_s + 0.40 E_c I_c \quad (7.10)$$

Equation 7.10 assumes that only the concrete has a reduction in the stiffness, which is possibly inaccurate once the steel buckles locally (as in the load case LC3). For this case, the equation below is proposed in those cases where the steel is susceptible to buckle locally (as in non-compact or slender steel tube sections).

$$EI_{eff} = 0.85 (E_s I_s + 0.40 E_c I_c) \quad (7.11)$$

The latter expression is equal to the Equation 7.10 reduced by a factor of 0.85. This factor was obtained as the average of the ratio between the experimental stiffness obtained in the load case LC3 and the expected stiffness using the Equation 7.10. This in other words is equal to:

$$\frac{\sum_{n_{LC3}} \frac{EI_{test}}{E_s I_s + 0.40 E_c I_c}}{n_{LC3}} = 0.85 \quad (7.12)$$

where n_{LC3} is the number of data values in the load case LC3 for the average calculation.

Equation 7.9 and 7.11 are similar to the Equations 6.40 and 6.42 in the Eurocode EC-4 (2004) to calculate the effective flexural stiffness. The equations given in the EC-4 are:

For the determination of the slenderness parameter and the elastic critical load:

$$EI_{eff} = E_s I_s + 0.60 E_c I_c \quad (7.13)$$

For the determination of internal forces:

$$EI_{eff} = 0.90 (E_s I_s + 0.50 E_c I_c) \quad (7.14)$$

Similarly, the ACI-318 (2008) proposes a similar Equation (Eq. 10.23) in Section 10.13-5 for the calculation of the elastic critical load on composite cross-sections. This equation is given by:

$$EI_{eff} = E_s I_s + \frac{0.20 E_c I_c}{1 + \beta_d} \quad (7.15)$$

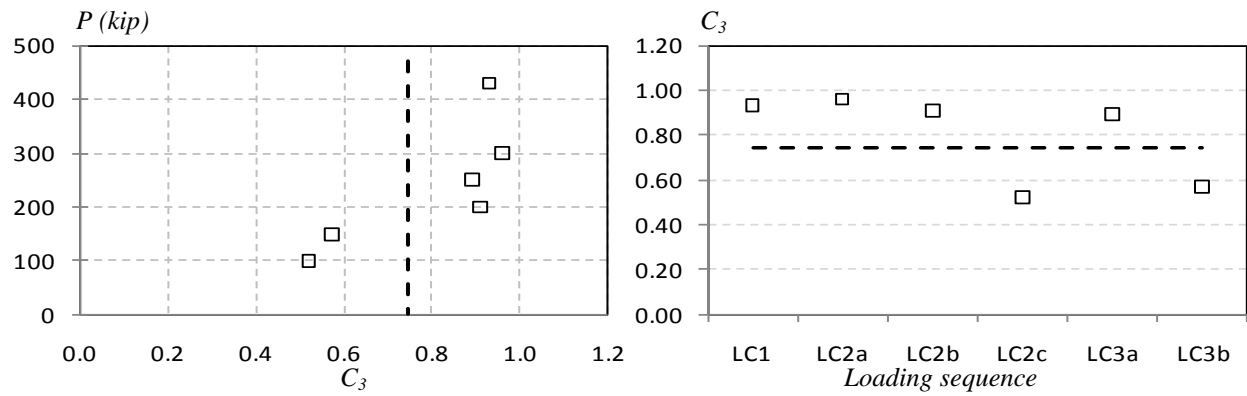
where β_d is a factor that accounts for the reduction of stiffness of columns due to sustained axial load on the concrete. The effective flexural stiffness in Equation 7.15 is used to calculate the Euler load, and this load to obtain the moment amplified to account for the second order effects.

Table 7.1. Flexural rigidity (EI_{exp}) extracted from the measured response

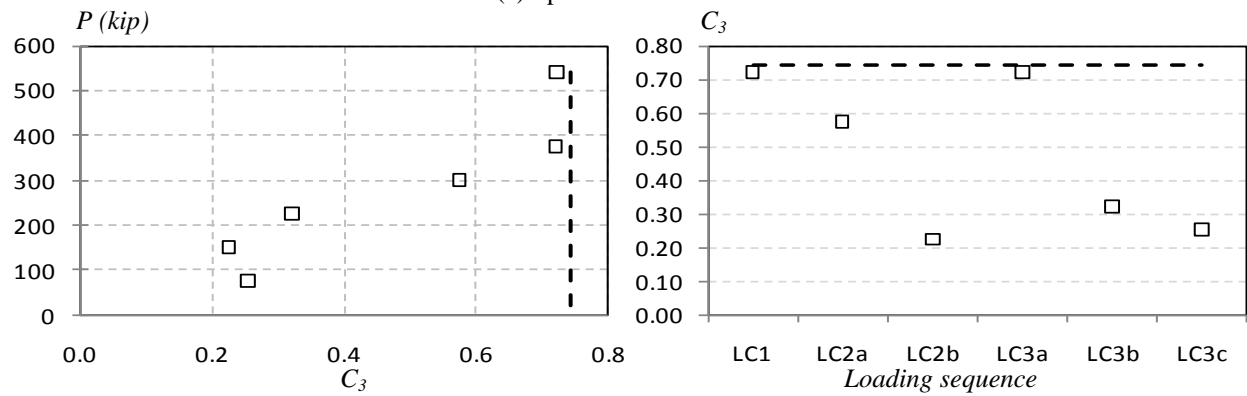
Specimen	Load case	Flexural rigidity (EI_{test} , kip-in ²)					$C_{3,test}$
		(1)	(2)	(3)	(4)	Average	
2C12-18-5	LC1	8664359	9303356	8630078	10781215	9344752	0.93
	LC2a	9216198	9174770	9456473	10044645	9473022	0.96
	LC2b	8214573	8721742	10270089	9830857	9259315	0.91
	LC2c	5961924	6022063	8826942	9227256	7509546	0.52
	LC3a	8817993	9357550	10014835	8493258	9170909	0.89
	LC3b	6637477	7787402	8592190	7935844	7738228	0.57
3C20-18-5	LC1	40868363	41397148	43355559	55151947	45193254	0.86
	LC2a	36539926	40460560	28978702	45355228	37833604	0.61
	LC2b	25837209	23553074	26053844	37289777	28183476	0.27
	LC3a	44385620	42040711	37808655	43108359	41835836	0.75
	LC3b	33732964	34388341	30728484	35634365	33621038	0.46
	LC3c	24611216	19797521	NA	NA	22204369	0.06
4Rw-18-5	LC1	21394262	19803215	21865261	21867369	21232527	0.77
	LC2a	18752228	19762963	18399019	19105014	19004806	0.54
	LC2b	15242456	14649144	17696536	18148225	16434090	0.27
	LC3a	22623966	23034419	24048404	20555444	22565558	0.91
	LC3b	15325346	15508304	15112719	18333789	16070040	0.23
	LC3c	14469864	13067576	17975119	16804843	15579350	0.18
5Rs-18-5	LC1	47350922	53514784	51297809	51297809	50865331	0.74
	LC2a	45886687	48733728	46125586	43818005	46141001	0.57
	LC2b	32862805	32987150	40835491	40879516	36891240	0.24
	LC3a	37450195	39667645	NA	NA	38558920	0.30
	LC3b	30714799	27902549	37222816	50905515	36686420	0.23
6C12-18-5	LC1	10830449	11705549	8877299	8923266	10084141	0.72
	LC2a	9511554	9731319	8486536	8598687	9082024	0.57
	LC2b	5529328	5536487	7657635	8116071	6709880	0.22
	LC3a	9719566	9092469	10185223	11290706	10071991	0.72
	LC3b	7402654	6515300	7804915	7705651	7357130	0.32
	LC3c	5685369	5408503	8105364	8412785	6903005	0.25
7C20-18-12	LC1	49289006	49866585	NA	54453162	51202918	0.71
	LC2a	39420522	43925315	40019720	29933029	38324647	0.41
	LC2b	22232177	25036607	34585845	28770100	27656182	0.16
	LC3a	45663187	47558680	27182290	22605884	35752510	0.35
8Rw-18-12	LC1	21226759	22899853	24983976	27596355	24176736	0.71
	LC2a	18532375	19843051	20839752	24847209	21015597	0.49
	LC2b	14464455	14091215	20870381	21994189	17855060	0.28
	LC3a	18293401	20034043	21470012	16851676	19162283	0.36
9Rs-18-12	LC1	57402005	55759260	70599870	67194172	62738827	0.77
	LC2a	43264029	48709985	49649810	37109611	44683359	0.34
	LC2b	30757122	31345722	38266642	35250470	33904989	0.08
	LC3a	36240571	37111911	48101976	56104082	44389635	0.33

Table 7.1 Flexural rigidity (EI_{exp}) extracted from the measured response (cont.)

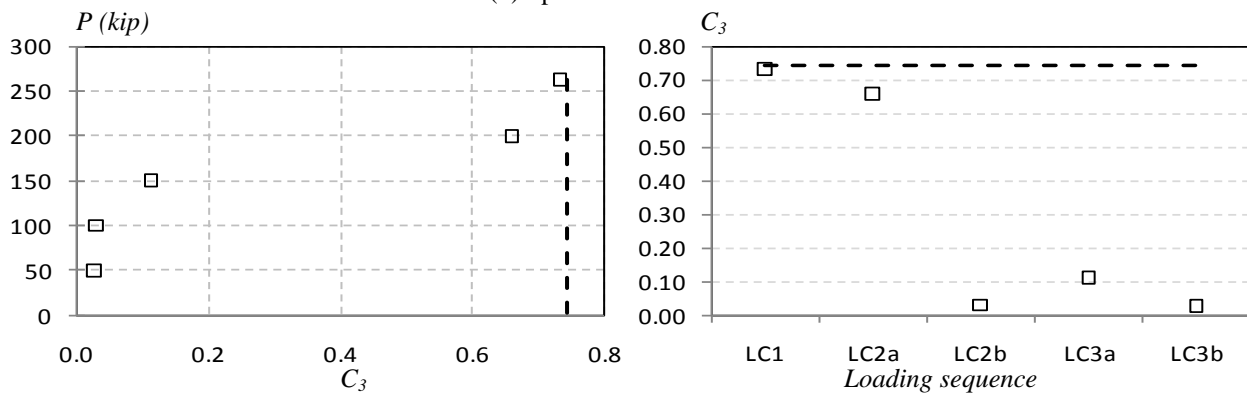
Specimen	Load case	Flexural rigidity (EI_{exp} , kip-in ²)					$C_{3,test}$
		(1)	(2)	(3)	(4)	mean	
10C12-26-5	LC1	10050839	11870855	6956923	8351287	9307476	0.73
	LC2a	9463474	11032586	8881012	6217167	8898560	0.66
	LC2b	5446886	5423381	5053555	5565775	5372399	0.03
	LC3a	NA	NA	6498618	5182598	5840608	0.11
	LC3b	4556513	5468390	5977132	5406009	5352011	0.02
11C20-26-5	LC1	46716942	47783656	45159252	50355301	47503788	0.75
	LC2a	47835489	48123420	32113720	38763853	41709121	0.59
	LC2b	26599637	29680010	30529657	39191667	31500243	0.30
	LC3a	32168268	28123647	22623162	18215771	25282712	0.13
	LC3b	23851474	23682204	20184102	19660375	21844539	0.03
12Rw-26-5	LC1	24487056	27257721	22458353	20996302	23799858	0.84
	LC2a	23031639	29401090	17271928	27119366	24206006	0.87
	LC2b	15264819	14954234	16860130	25572260	18162861	0.37
	LC3a	16065003	17443739	NA	NA	16754371	0.26
13Rs-26-5	LC1	56288316	61193637	62477071	61409086	60342028	0.87
	LC2a	38883271	38040080	38142923	41370730	39109251	0.26
	LC2b	45896274	47532504	38679436	40325189	43108351	0.38
	LC3a	33753334	31690561	28779249	25966352	30047374	0.00
	LC3b	37127812	34547538	27966732	23399982	30760516	0.02
14C12-26-5	LC1	10219232	12948902	11731905	7149629	10512417	0.85
	LC2a	5548725	6096777	5000571	6127449	5693380	0.11
	LC2b	NA	NA	5672096	5207635	5439866	0.07
	LC3a	NA	NA	5571639	4842631	5207135	0.03
	LC2a'	8206163	6296562	10527073	11355253	9096263	0.63
	LC2b'	8145907	7965721	NA	NA	8055814	0.47
	LC3a'	7189101	6172223	NA	NA	6680662	0.26
15C20-26-12	LC1	50120181	52225229	59373195	79799030	60379409	0.96
	LC2a	28064101	26759031	33411347	34078900	30578345	0.24
	LC2b	42489455	41645216	30891355	23832967	34714748	0.34
	LC3a	26849740	25180584	21212423	18545955	22947176	0.06
	LC3b	35773410	39749660	23708060	21828052	30264796	0.24
16Rw-26-12	LC1	25507350	25518127	28967481	28415197	27102039	0.96
	LC2a	15479360	15848960	24377613	17780768	18371675	0.33
	LC2b	20175973	19838826	23272748	17860130	20286919	0.47
	LC3a	16775526	17026660	NA	NA	16901093	0.23
	LC3b	NA	NA	NA	NA	NA	NA
17Rs-26-12	LC1	50869066	51182456	76290029	68433358	61693727	0.78
	LC2a	44192966	43610730	40952462	NA	42918720	0.32
	LC2b	48661507	52857239	NA	NA	50759373	0.51
	LC3a	30821872	30523019	34999860	43451489	34949060	0.12
	LC3b	39579656	40299404	NA	17007786	32295615	0.06



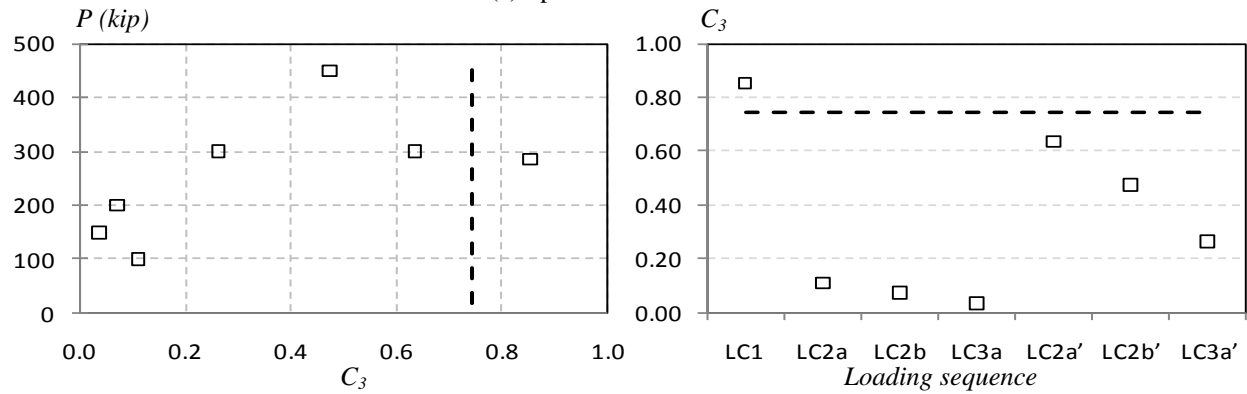
(a) Specimen 2C12-18-5



(b) Specimen 6C12-18-12

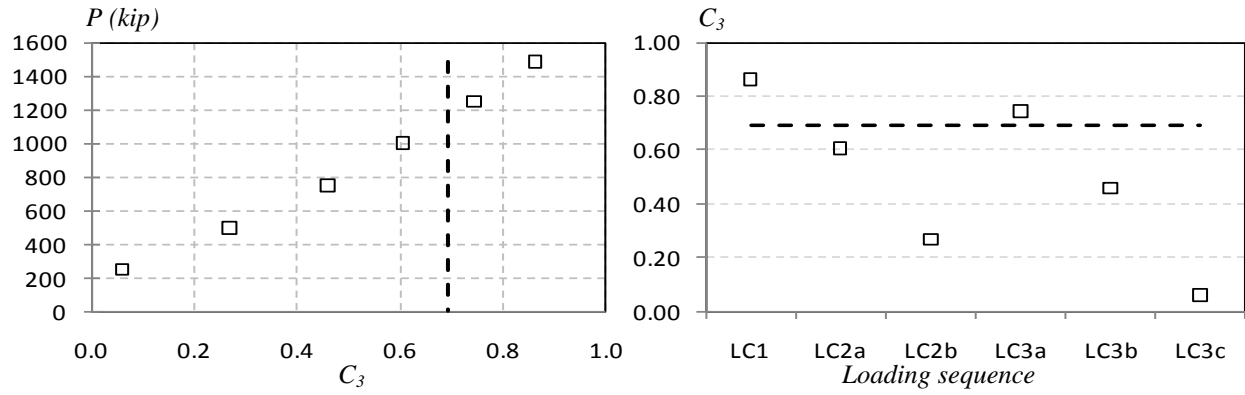


(c) Specimen 10C12-26-5

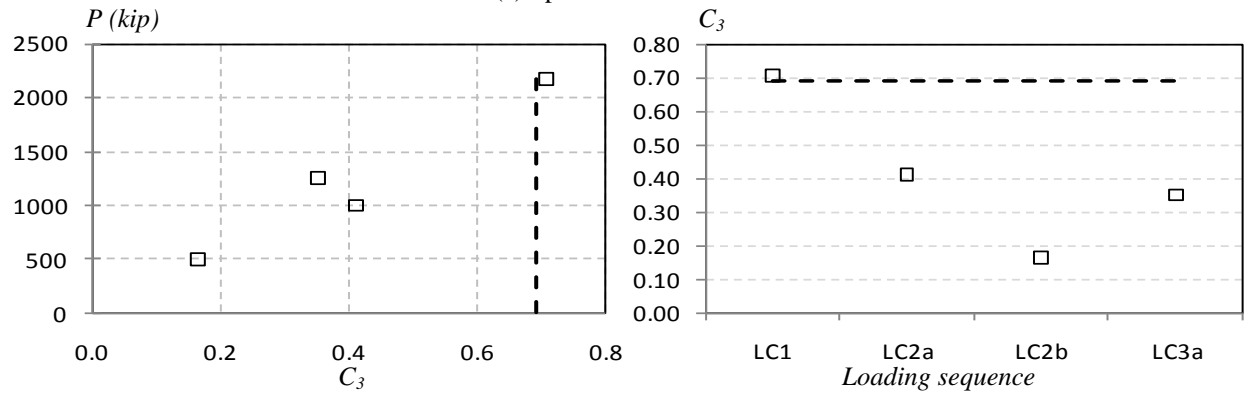


(d) Specimen 14C12-26-12

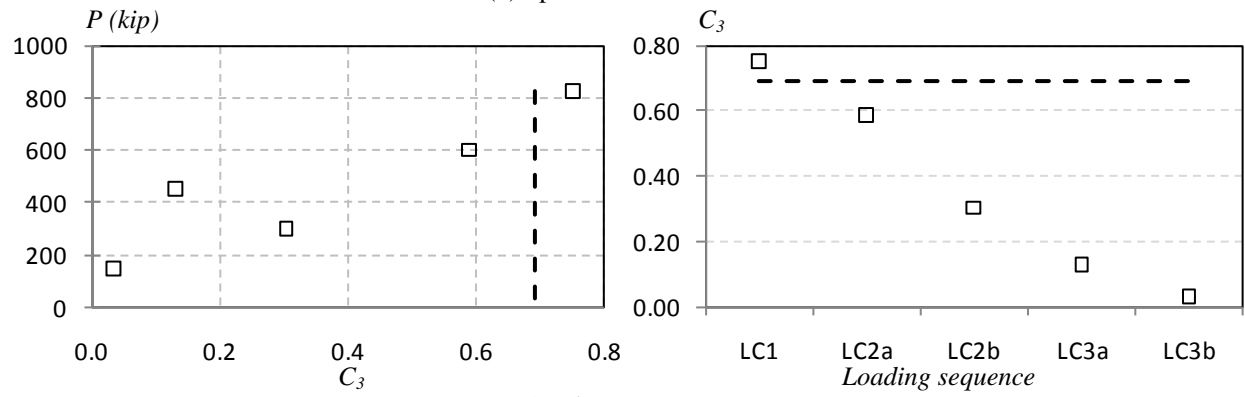
Figure 7.68. Flexural rigidity for the circular specimens with 12 inches of diameter



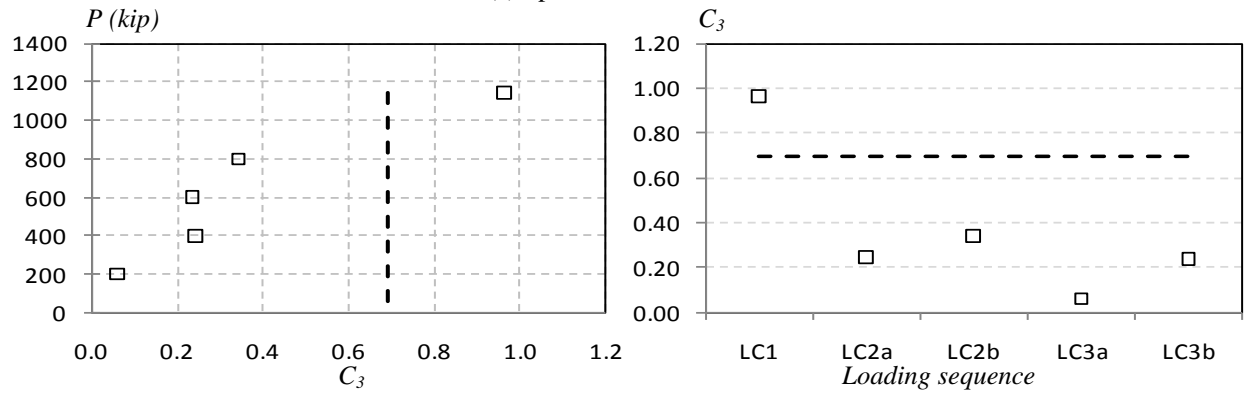
(a) Specimen 3C20-18-5



(b) Specimen 7C20-18-12

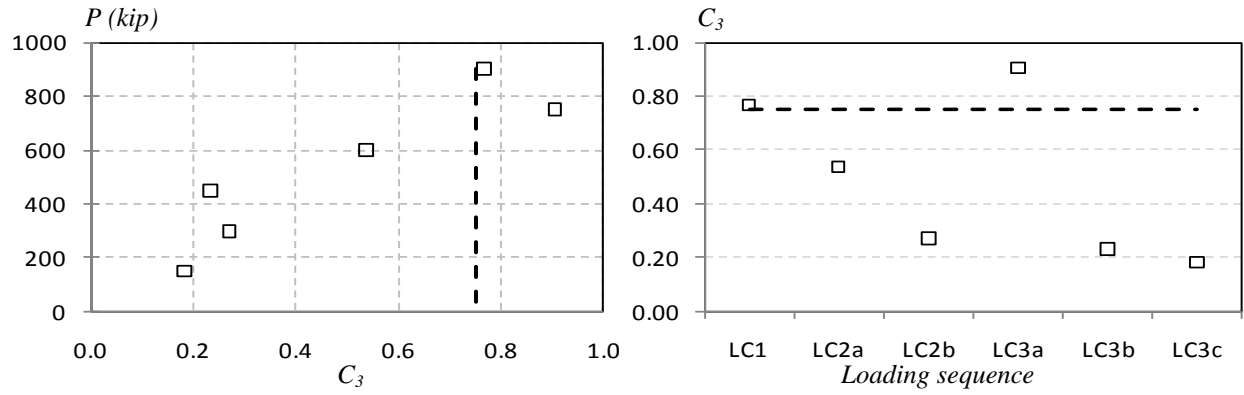


(c) Specimen 11C20-26-5

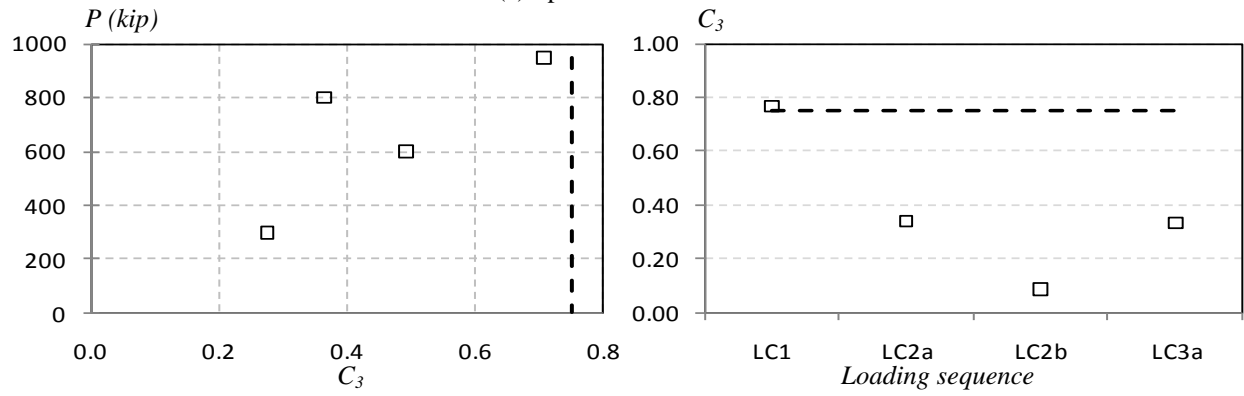


(d) Specimen 15C20-26-12

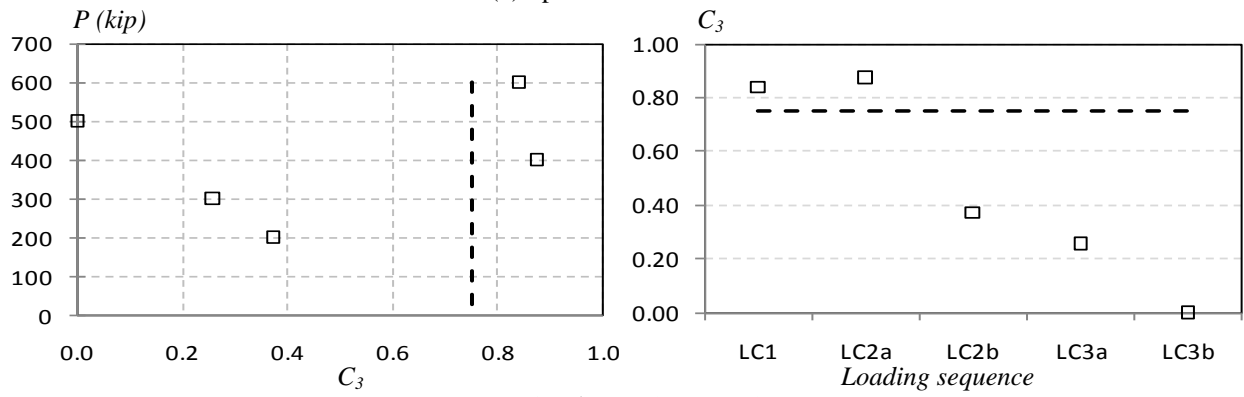
Figure 7.69. Flexural rigidity for the circular specimens with 20 inches of diameter



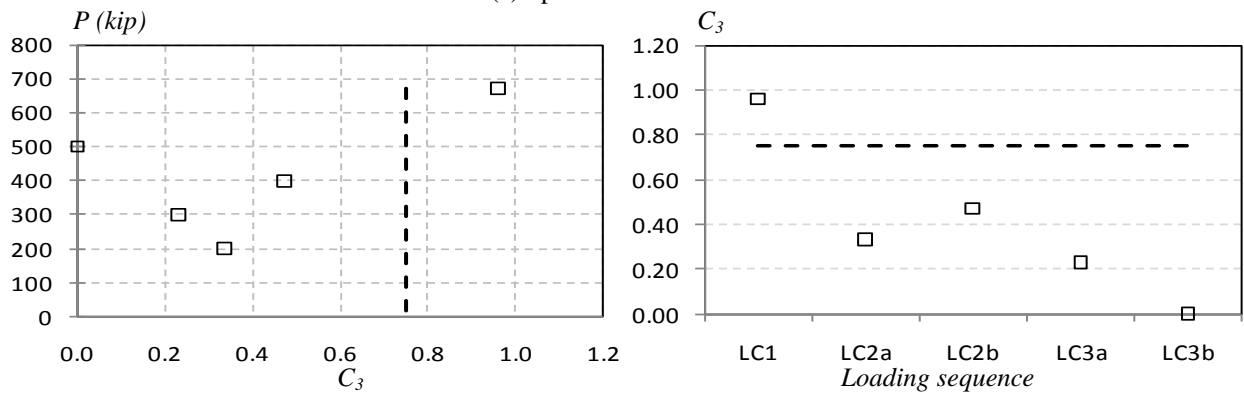
(a) Specimen 4Rw-18-5



(b) Specimen 8Rw-18-12

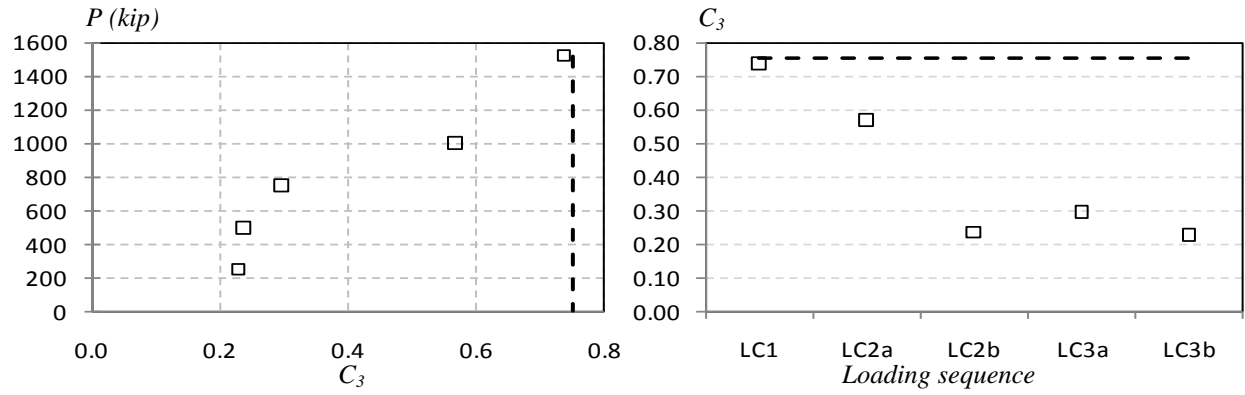


(c) Specimen 12Rw-26-5

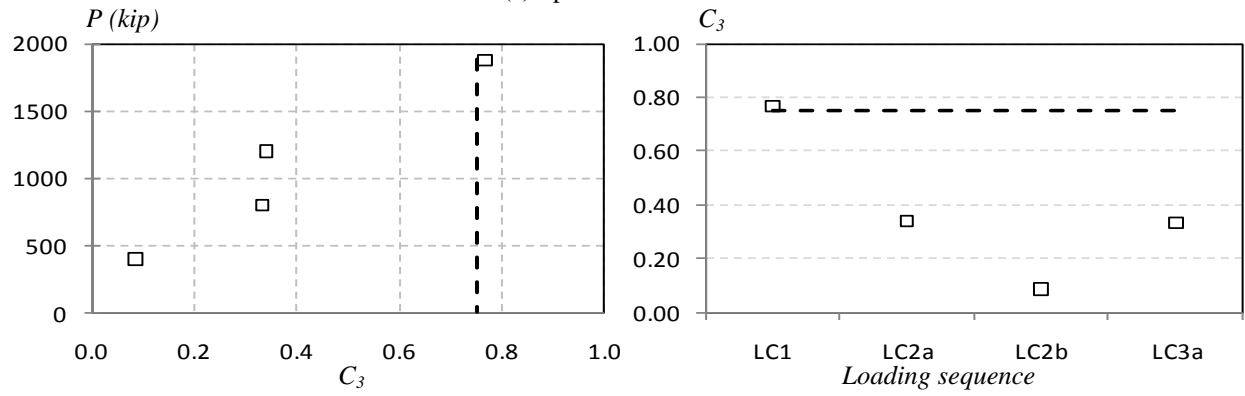


(d) Specimen 16Rw-26-12

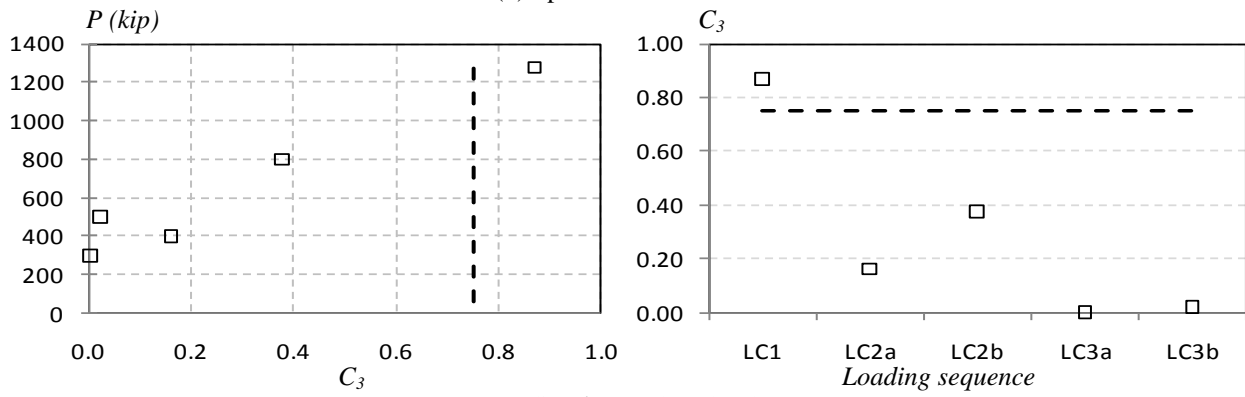
Figure 7.70. Flexural rigidity for the rectangular specimens oriented in the weak axis



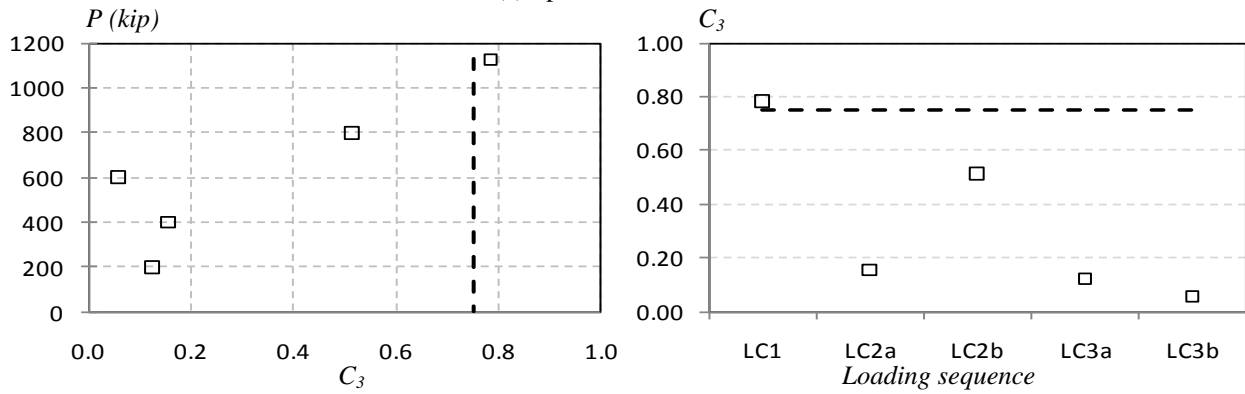
(a) Specimen 5Rs-18-5



(b) Specimen 9Rs-18-12



(c) Specimen 13Rs-26-5



(d) Specimen 17Rs-26-12

Figure 7.71. Flexural rigidity for the rectangular specimens oriented in the strong axis

Table 7.2. Averaged concrete contribution factor ($C_{3,test}$) to the effective stiffness

Specimen	$\rho = A_s/A$	λ	EI_s	EI_c	AISC (2010)		$C_{3,test}$		
					EI_{eff}	C3	LC1	LC2	LC3
2C12-18-5	7.2%	1.55	5185068	4470840	8509246	0.74	0.93	0.80	0.73
3C20-18-5	4.6%	1.05	20529095	28588714	40315751	0.69	0.86	0.44	0.42
4Rw-18-5	7.6%	1.38	13831863	9635036	21081046	0.75	0.77	0.40	0.44
5Rs-18-5	7.6%	0.88	30331694	27866490	51297809	0.75	0.74	0.40	0.26
6C12-18-5	7.2%	1.90	5185068	6784500	10229509	0.74	0.72	0.40	0.43
7C20-18-12	4.6%	1.30	20529095	43383374	50555345	0.69	0.71	0.29	0.35
8Rw-18-12	7.6%	1.65	13831863	14621168	24832498	0.75	0.71	0.38	0.36
9Rs-18-12	7.6%	1.04	30331694	42287399	62147773	0.75	0.77	0.21	0.33
10C12-26-5	7.2%	2.38	5212352	5588550	9367575	0.74	0.73	0.34	0.07
11C20-26-5	4.6%	1.61	20676817	35735893	45410137	0.69	0.75	0.45	0.08
12Rw-26-5	7.6%	2.14	13677296	12043795	22738774	0.75	0.84	0.62	0.26
13Rs-26-5	7.6%	1.35	30002047	34833113	56209690	0.75	0.87	0.32	0.01
14C12-26-5	7.2%	2.72	4983488	6482718	9803547	0.74	0.85	0.32	0.15
15C20-26-12	4.6%	1.78	20516373	41453636	49207024	0.69	0.96	0.29	0.15
16Rw-26-12	7.6%	2.30	13702743	13970803	24214058	0.75	0.96	0.40	0.23
17Rs-26-12	7.6%	1.46	29988613	40406411	60389479	0.75	0.78	0.42	0.09
Average (all the CFTs)							0.81	0.41	0.27
Average (CCFTs)							0.82	0.42	0.30
Average (RCFTs)							0.80	0.40	0.25
Average (CFTs with 18 feet of length)							0.78	0.42	0.42
Average (CFTs with 26 feet of length)							0.84	0.40	0.13

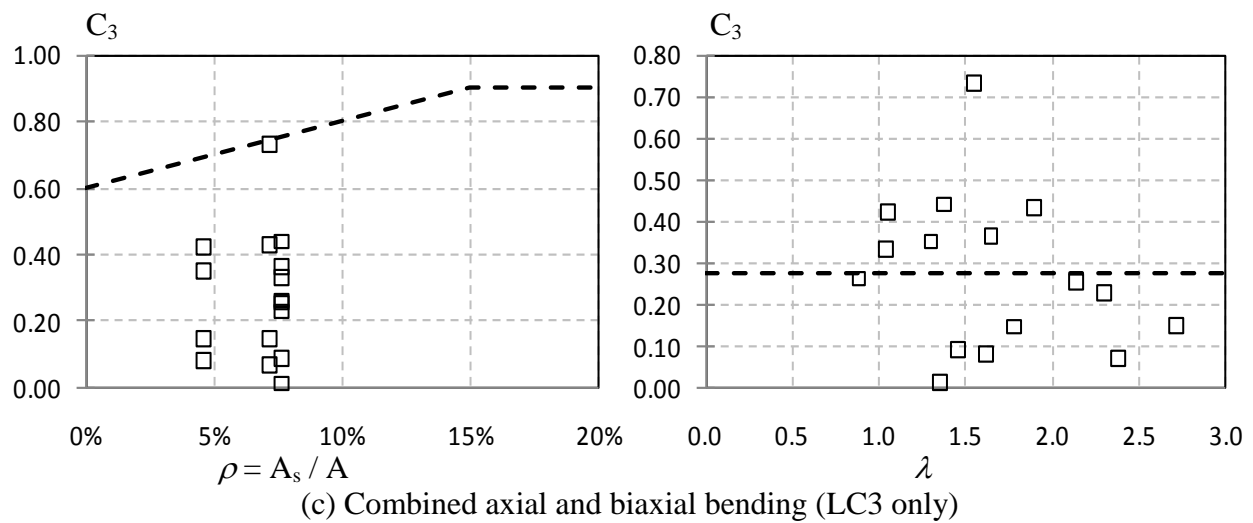
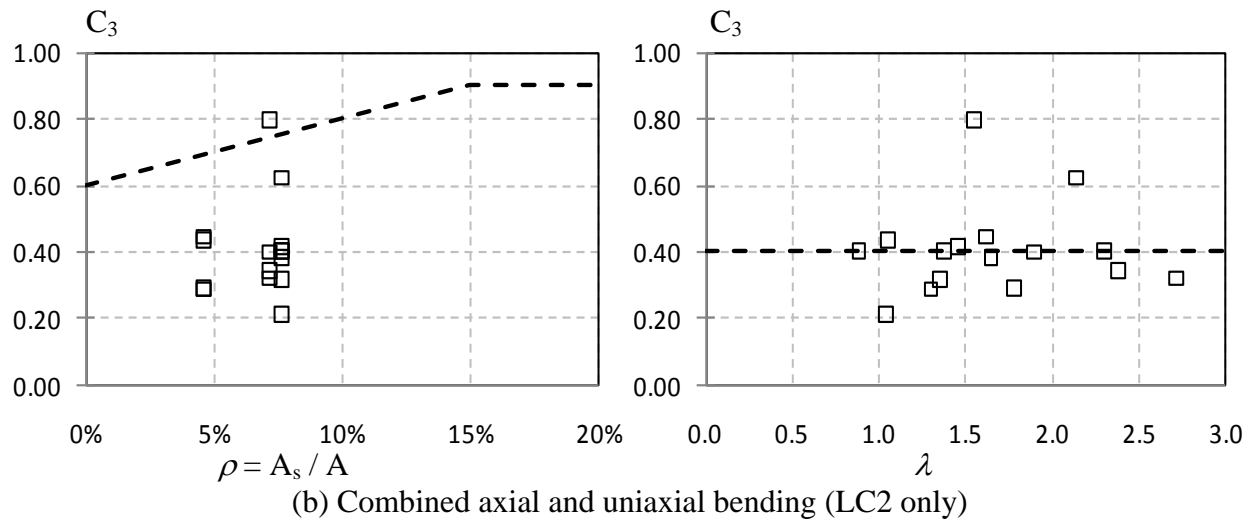
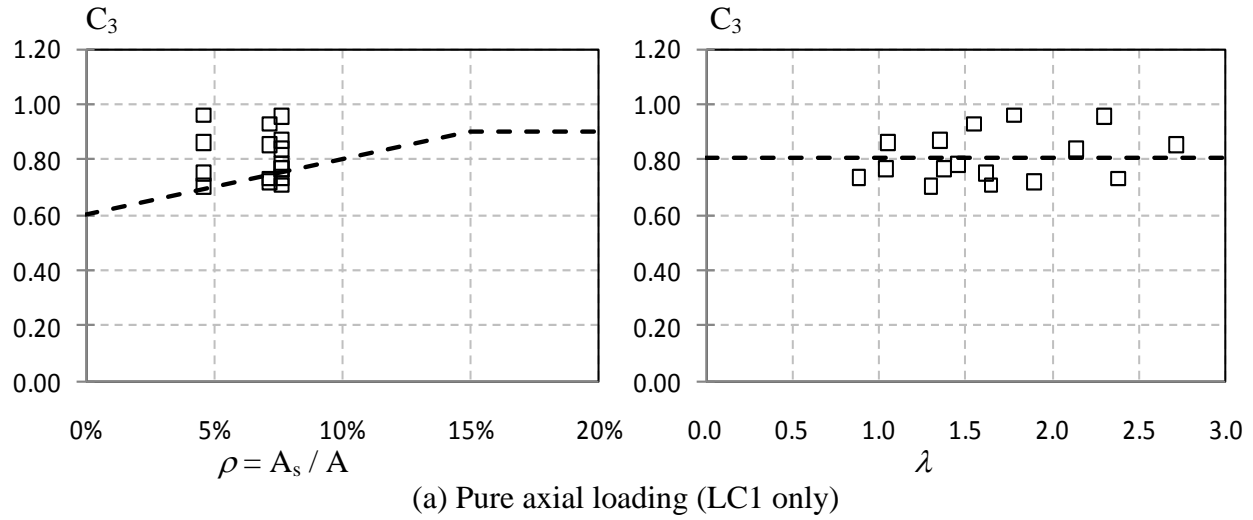


Figure 7.72. Average of the C_3 parameter obtained for each specimen (squares) and for all the specimens (dashed line)

7.4. Advanced computational analysis

In this section, advanced computational analyses are performed for the calibration of the material and element models and contrast the experimental and the analytical responses.

The analyses presented in this section are carried out with the software OpenSees (2010) with a special version compiled by Denavit (2010) that, in addition to the standard OpenSees framework, includes comprehensive constitutive material models and robust 3D distributed-plasticity beam element formulations calibrated and developed by Tort and Hajjar (2007) for RCFTs and Denavit and Hajjar (2010) for CCFTs.

Thus, the specimens are modeled with the following characteristics.

- The geometric and the cross-section properties (as the member length, thickness and diameter or base and width) correspond to those values measured and summarized in Chapter 3.
- The specimen was subdivided into 6 and 8 sub-members for the specimens with 18 and 26 feet of length, respectively. The integration points are defined at those points where the instrumentation (i.e. string pots, strain gages) was placed along the specimen.
- In addition, the coordinates of the integration points between sub-members correspond to the initial out-of-straightness and out-of-plumbness measured at the surveying. These imperfections were summarized in Table 5.1 and illustrated in Figure 5.5.
- The members are modeled with the mixed 3D finite beam element developed by Denavit and Hajjar for CCFTs and Tort and Hajjar for RCFTs. Since there was no evidence of significant slip between the concrete and steel surfaces in contact during the test, slip effects were ignored in the analysis.
- The boundary conditions are assumed fixed at the base and free at the bottom, and therefore the effective length factor is $K = 2$.

- The top DOFs of the members are driven as in the tests; this is with the same compression force and horizontal X and Y displacement and X and Y rotations that were recorded during the uniaxial load cases (LC2). Consideration of the step-by-step lateral displacement is intended to account for the real directionality of the specimen.
- The concrete compressive strength used in the analysis corresponds to the measured strength obtained from the test of cylinders at the day of testing; these results are summarized in Chapter 3. The Young's modulus and the tensile strength of the concrete are implicitly calculated in the Chang-Mander model; however, these calculated values are very close to those obtained from the concrete cylinder tests.
- The concrete core was modeled with the Chang and Mander (1994) model as adapted by Tort and Hajjar (2007) for RCFTs and Denavit and Hajjar (2010) for CCFTs.
- The steel yield stress, ultimate stress, and the Young's modulus used in the analyses correspond to the measured parameters obtained from the coupon tests. These results are also summarized in Chapter 3.
- The steel tube was modeled with the Shen *et al.* (1995) model as adapted by Denavit and Hajjar for CCFTs and Tort and Hajjar for RCFTs. The only modification in the original steel models is the strain that corresponds to the initiation of the local buckling. The local buckling strains that are calibrated and presented in Chapter 8 are used in these analyses instead of the values obtained with the original formulation. This change has a minor effect in the CCFTs since the Equation proposed by Denavit and Hajjar (2010) and the one proposed in Chapter 8 do not have a significant difference. However, higher differences are obtained in the RCFTs, in which the strain given by Tort and Hajjar (2007) predicts a very early development of the local buckling as seen in Figure 7.73.a; the experimental results in RCFTs indicate a later occurrence of the local buckling, which is more reasonable predicted by the proposed equation in the Chapter 8 for RCFTs as illustrated by Figure 7.73.b.

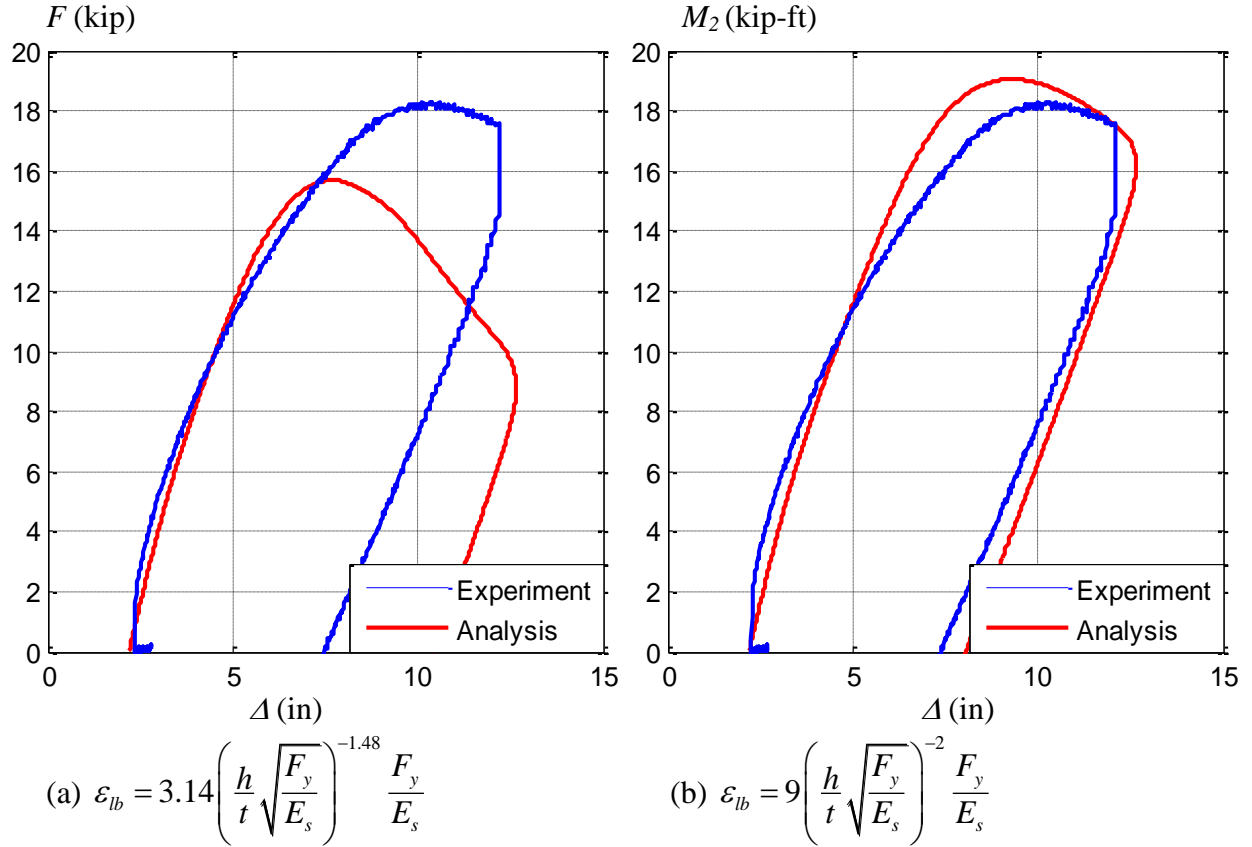


Figure 7.73. Experimental vs. Analytical response with a different initiation of steel local buckling for the Specimen 4Rw-18-5 during the first loading cycle in LC2b

The analyses presented in this section are performed in a fresh model at the beginning of the first uniaxial load case LC2a, but with continuous step-by-step response until the end of the uniaxial loading case (LC2b or LC2c). This assumption ignores possible damages developed during LC1 in these analyses; however, no significant damage (i.e. steel local buckling) was observed from the outside during the load case LC1. The continuous step-by-step consideration during the LC2 intends to consider accumulated damage within this uniaxial loading case, in which at least 60% of the tested specimens buckle locally. Future analyses with the entire load protocol, from LC1 to LC4, are recommended to calibrate the effective accumulated damage within load cases.

Comparisons of the experimental response with the analytical prediction are shown from Figure 7.76 to Figure 7.91. The compared selected responses are:

- (i) The lateral force vs. the top displacement (F - Δ)
- (ii) The base moment vs. the top rotation (M_2 - θ).

As shown in Figure 7.76 to Figure 7.91, the analytical prediction (strength, deformation and stiffness) in general follows reasonably well the experimental response, in some cases with a high correlation and in others with a weak correlation. In addition, the following observation can be noted from these figures:

- With respect to the stiffness, the larger difference between the analytical and the experimental response is observed at the start of motion and mainly on the load reversals. During the testing, pauses were made between ramps in order to introduce the new input commands to drive the crosshead to the next target displacement; pauses were also helpful for taking photos and explore for possible damages on the exterior of the specimen (i.e. local buckling). However, right immediately the system stopped and holds on pause (in lateral displacement control and in vertical force control), the lateral force reported by the controller drops an amount of dF with values around 1 to 2 kip, as observed experimentally with the variation of time in Figure 7.74. This reduction of the lateral force is attributed to the frictional forces that vanish when the system is in pause. As seen in Figure 7.74, the amount of frictional forces decreases again when the specimen is moved in the opposite direction, and so the jump in lateral force at the each reversals (total pause) is about twice the amount of frictional forces ($2dF$) developed in the system (with a total about 2 to 4 kip at reversals). As seen schematically in Figure 7.75, the reduction of the total lateral force at the reversals (or at pauses) show signs of a very high stiffness that does not correspond to the specimen; instead, this is attributed to the accumulation of the system friction within the pause. The relaxation of the lateral force at the displacement pause exposes a significant response difference mainly in those specimens with the higher flexibility, low lateral capacity, and high axial load.
- Concerning the lateral force, and based on the latter discussion, differences between the experimental response in the order of the friction system (about 2 kips) are expected between the analytical and the experimental response. In addition, other factor may impact to increase or decrease such differences such as variability in the material and geometric properties and the assumptions in the structural model. However, the analytical response shows, in general, a well predicted response by the analyses with small differences with respect to the experimental response. Similar observations are applicable to the base moment response that is reasonably well predicted by the analyses.

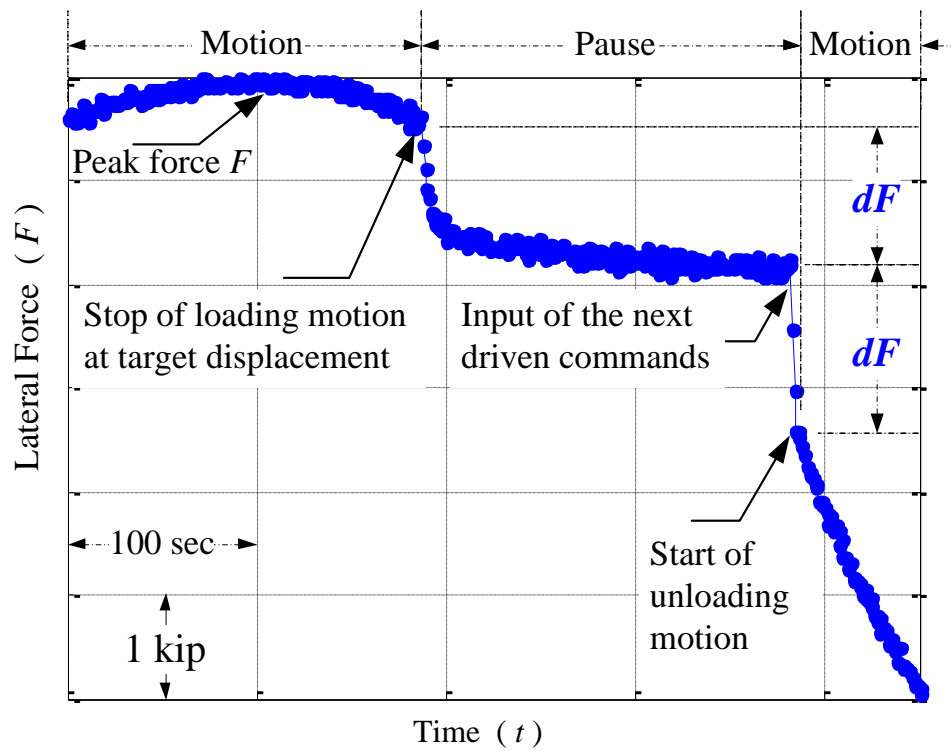


Figure 7.74. Force relaxation with time at the testing pauses (data taken from the Specimen 4Rw-18-5 at the second positive peak in LC2a)

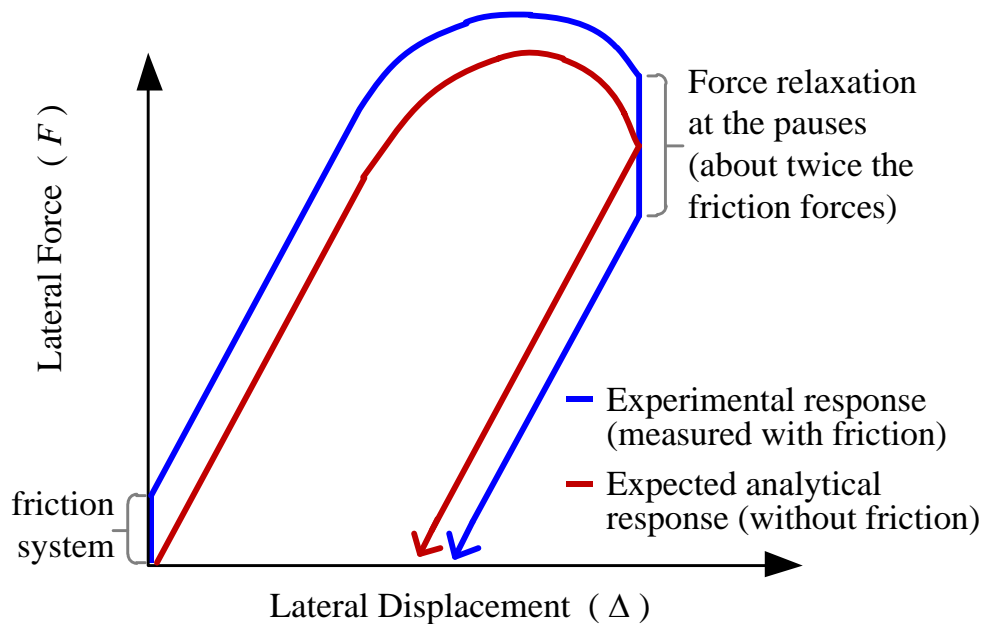
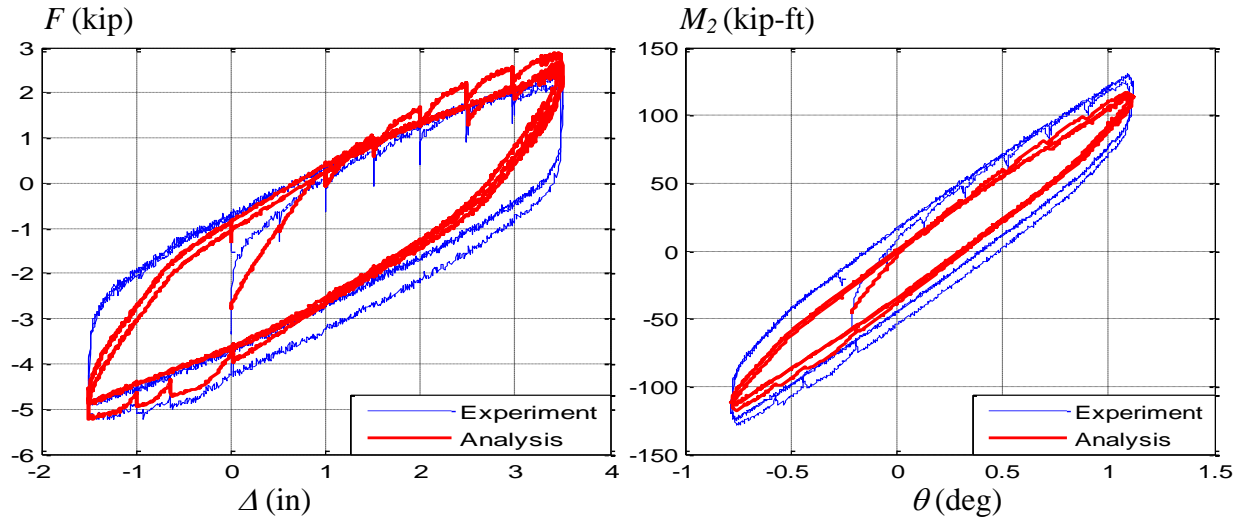
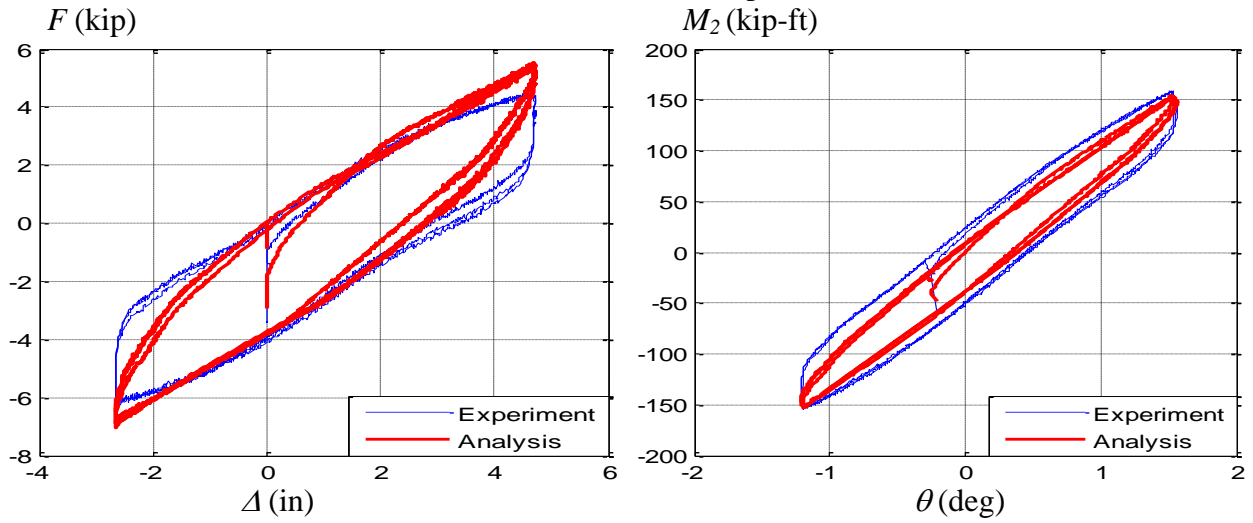


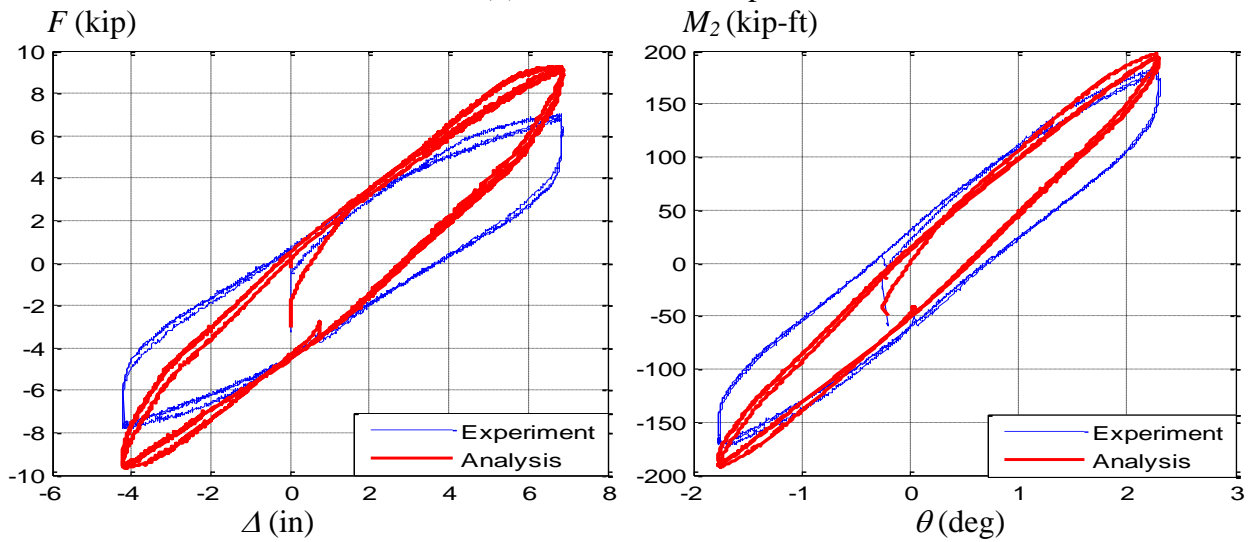
Figure 7.75. Force relaxation at the testing pauses (schematic)



(a) LC2a, $P = 300$ kip

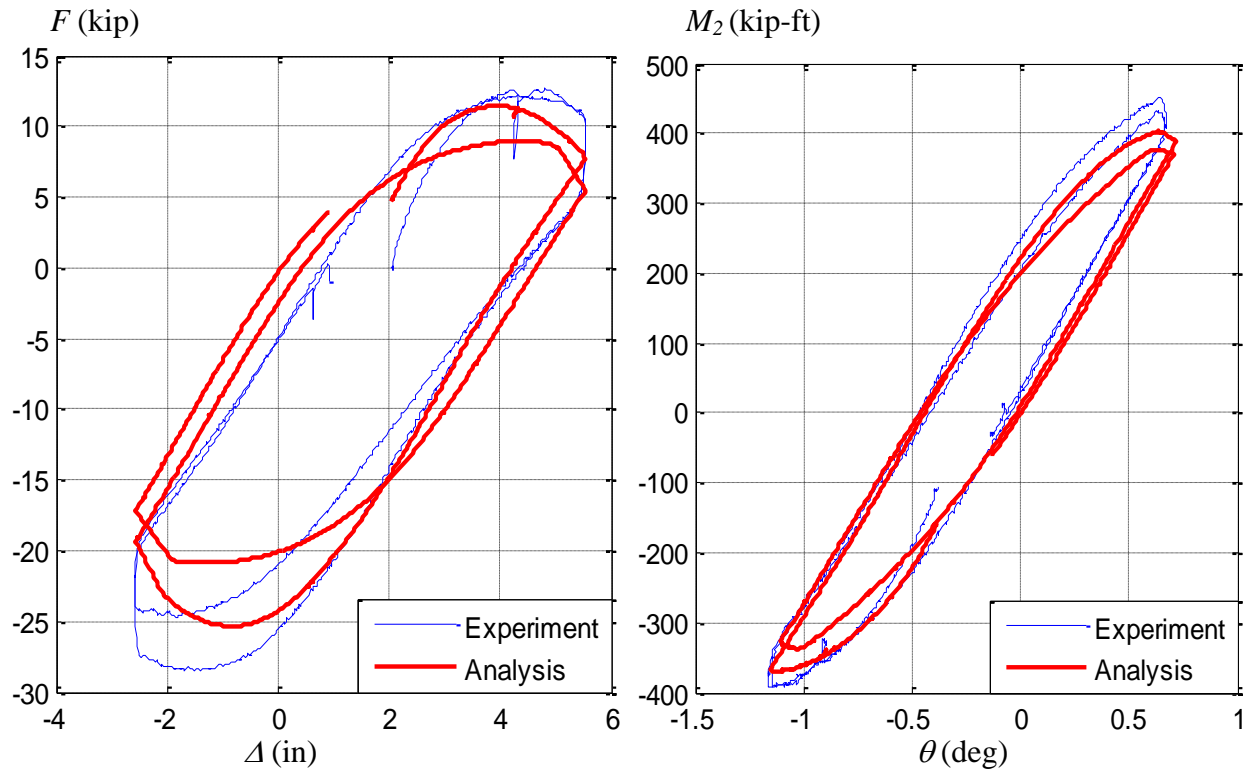


(b) LC2b, $P = 200$ kip

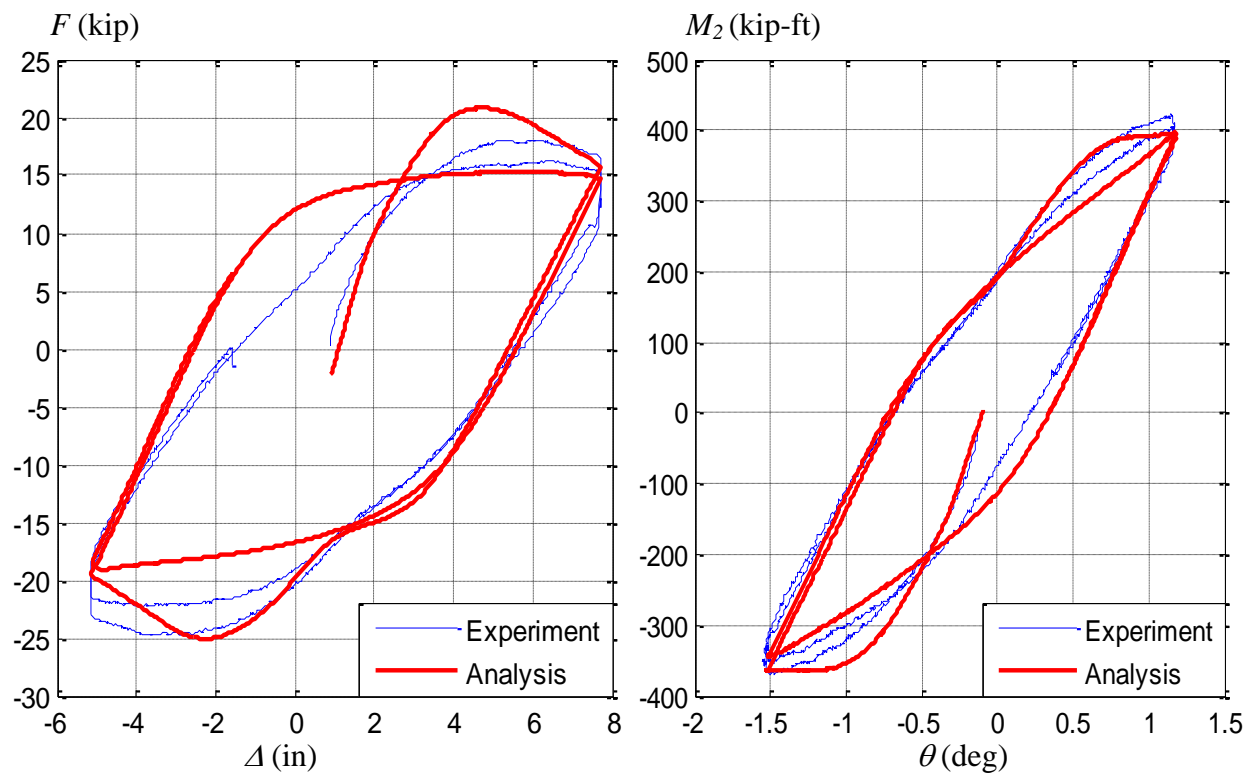


(c) LC2c, $P = 100$ kip

Figure 7.76. Experimental vs. Analytical response for the Specimen 2C12-18-5 during LC2

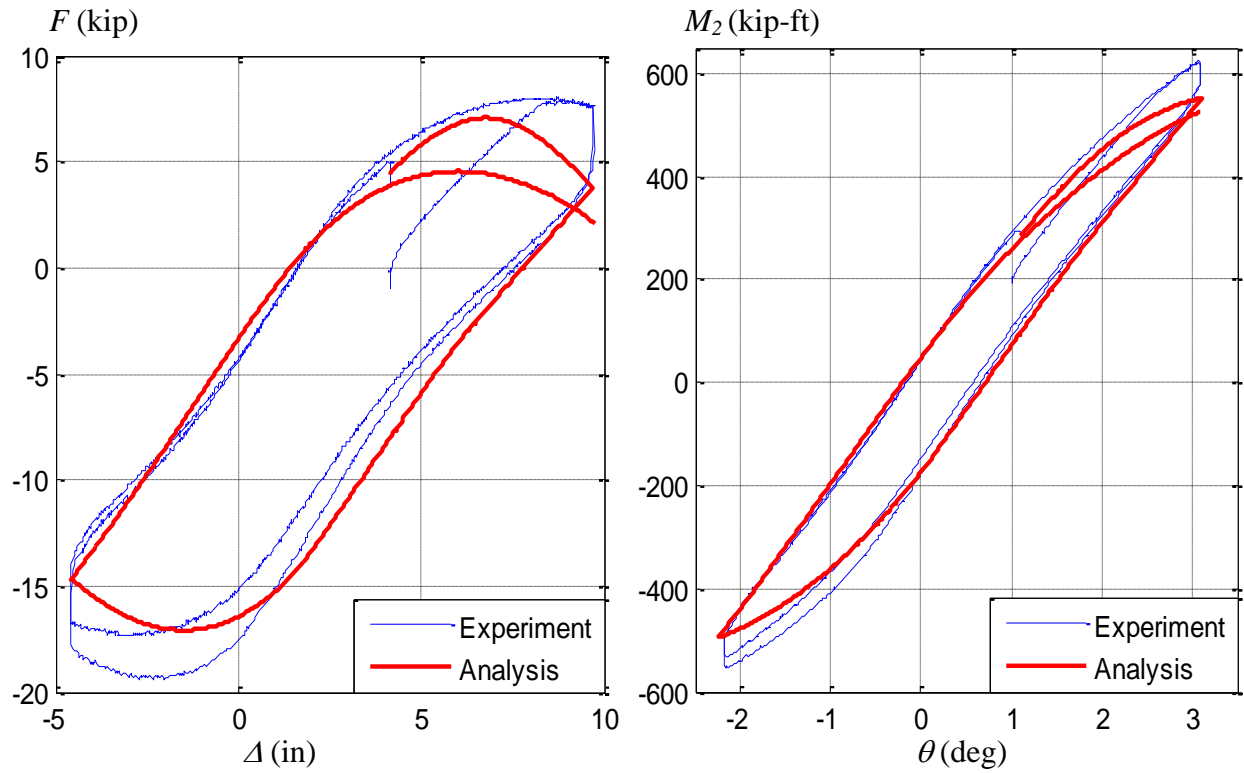


(a) LC2a, $P = 1000$ kip

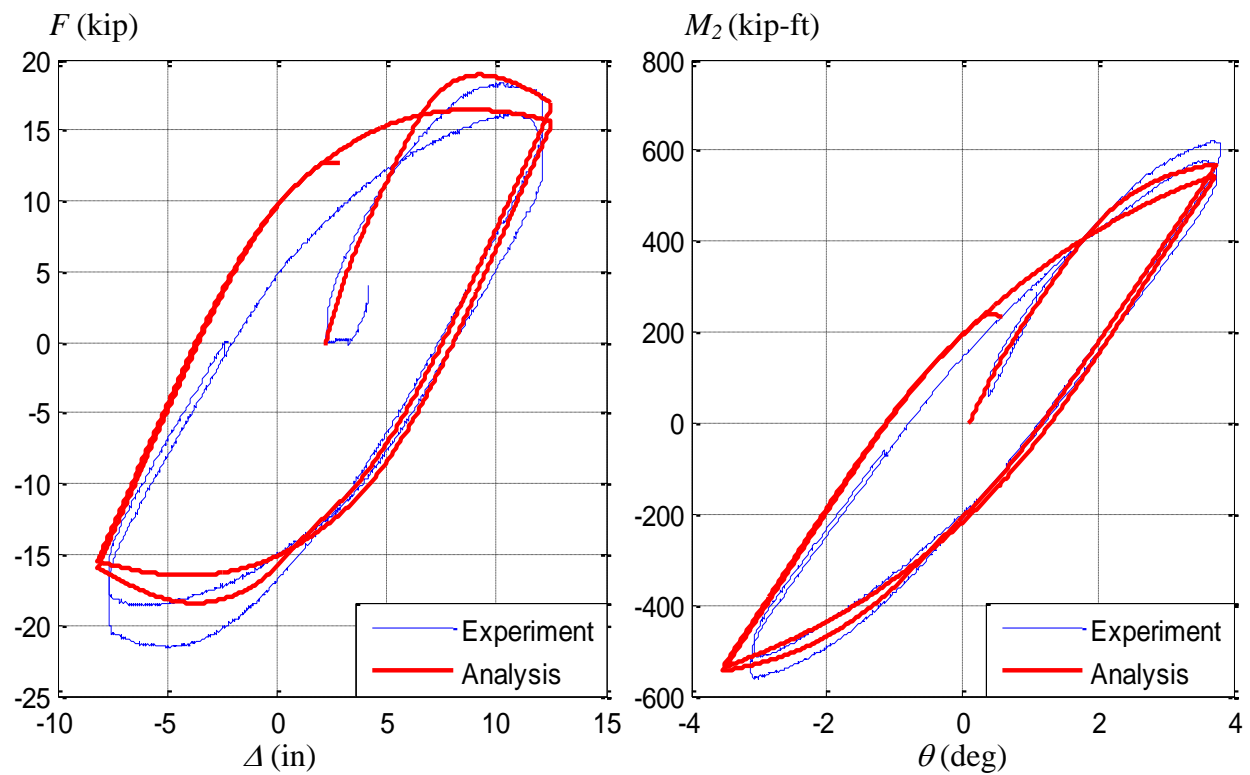


(b) LC2b, $P = 500$ kip

Figure 7.77. Experimental vs. Analytical response for the Specimen 3C20-18-5 during LC2

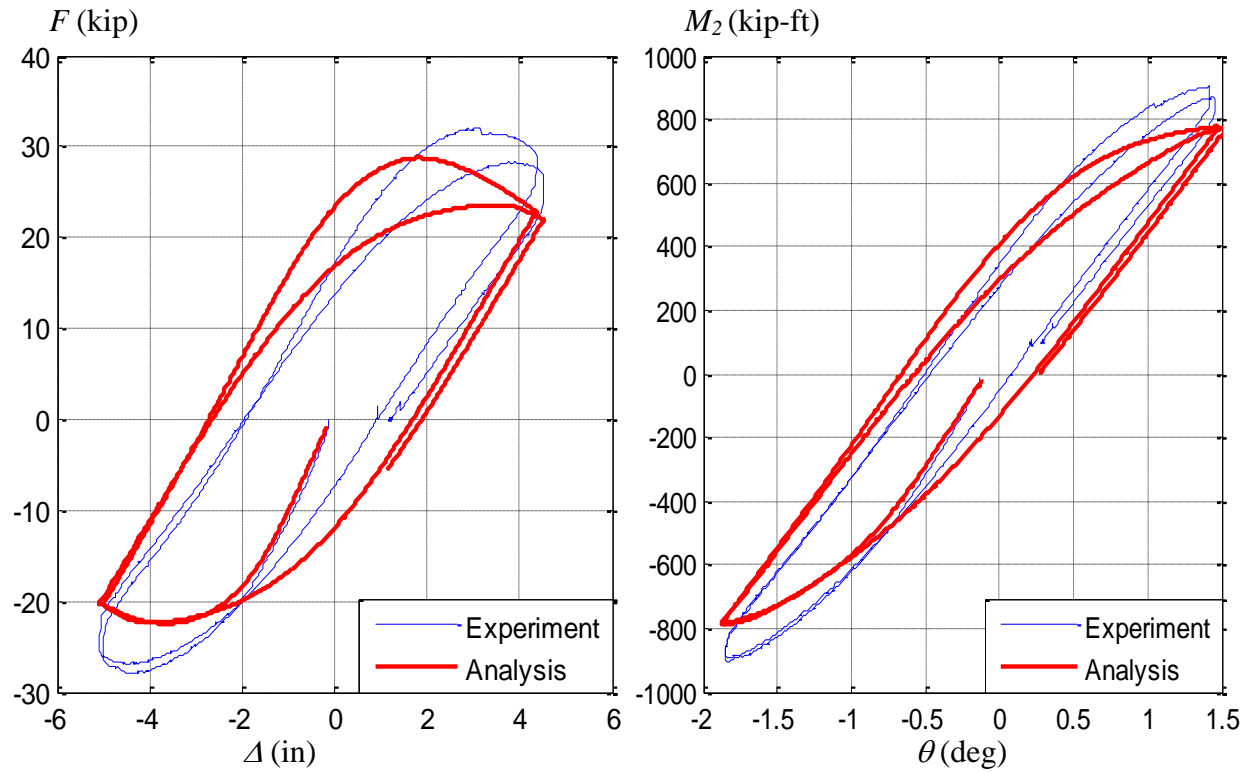


(a) LC2a, $P = 600$ kip

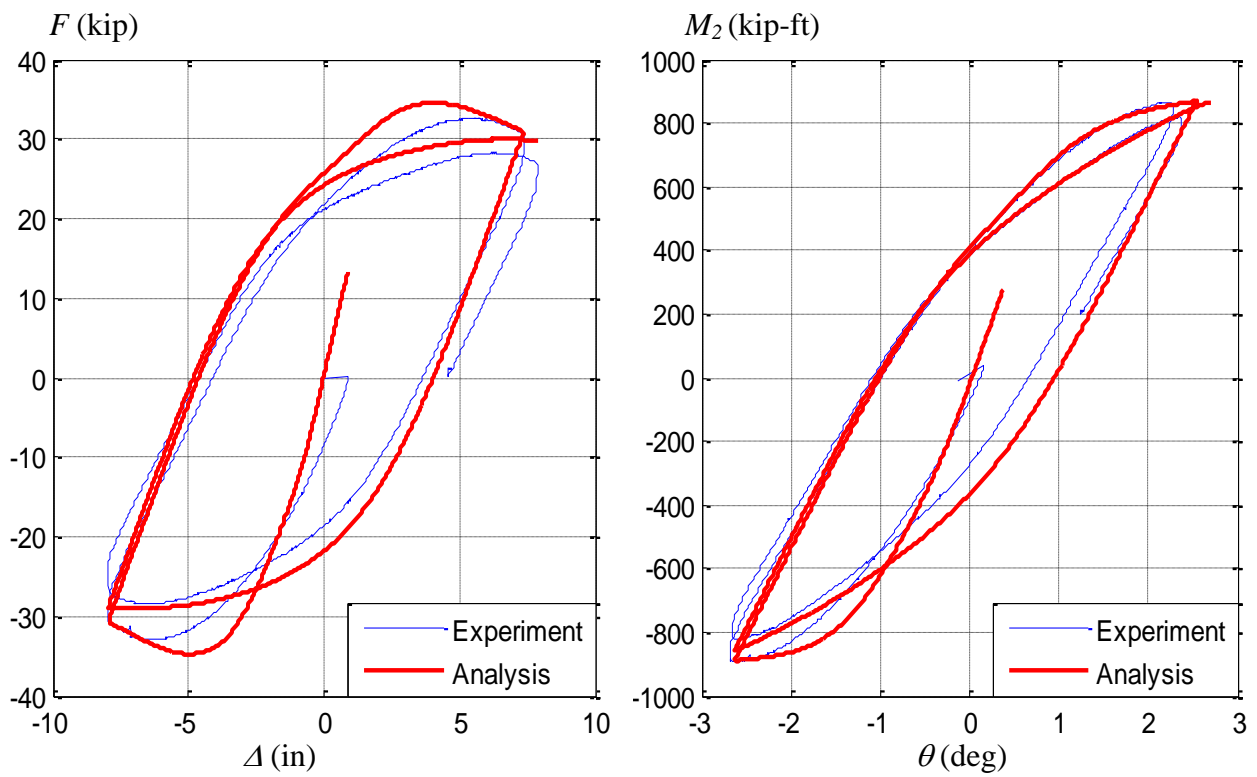


(b) LC2b, $P = 300$ kip

Figure 7.78. Experimental vs. Analytical response for the Specimen 4Rw-18-5 during LC2

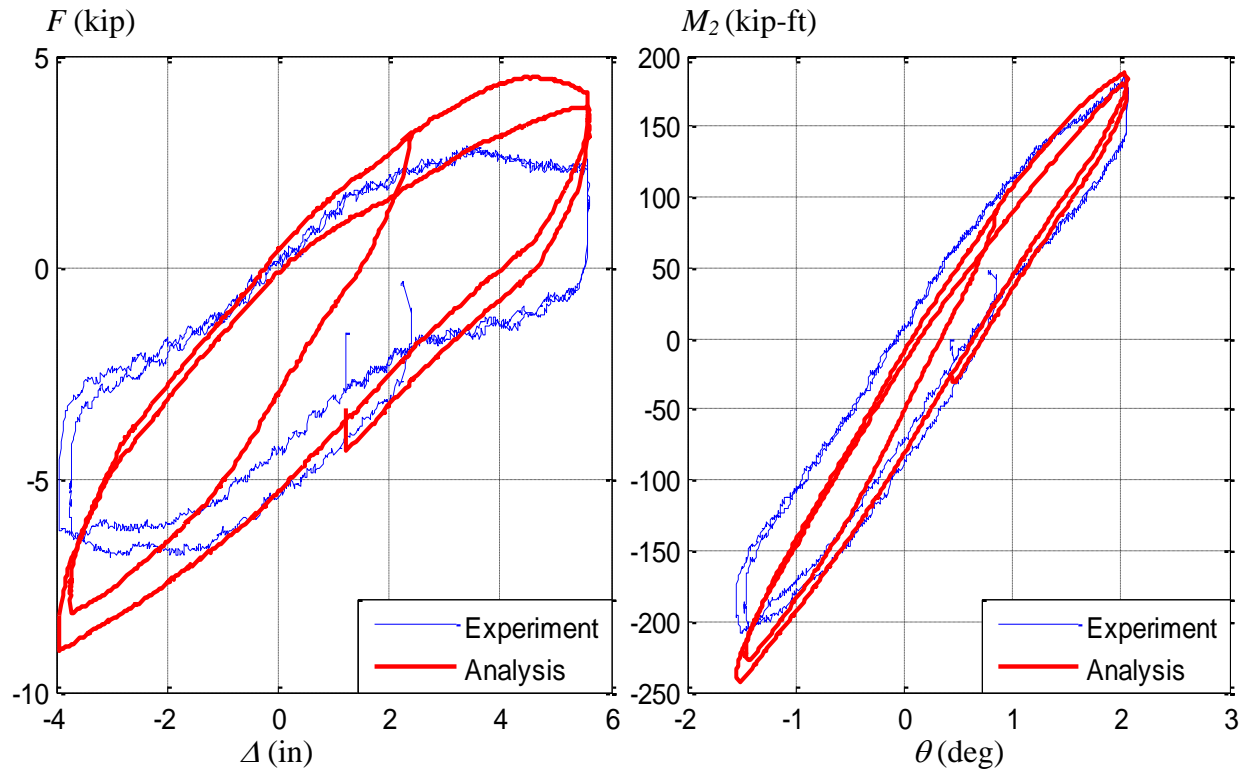


(b) LC2a, $P = 1000$ kip

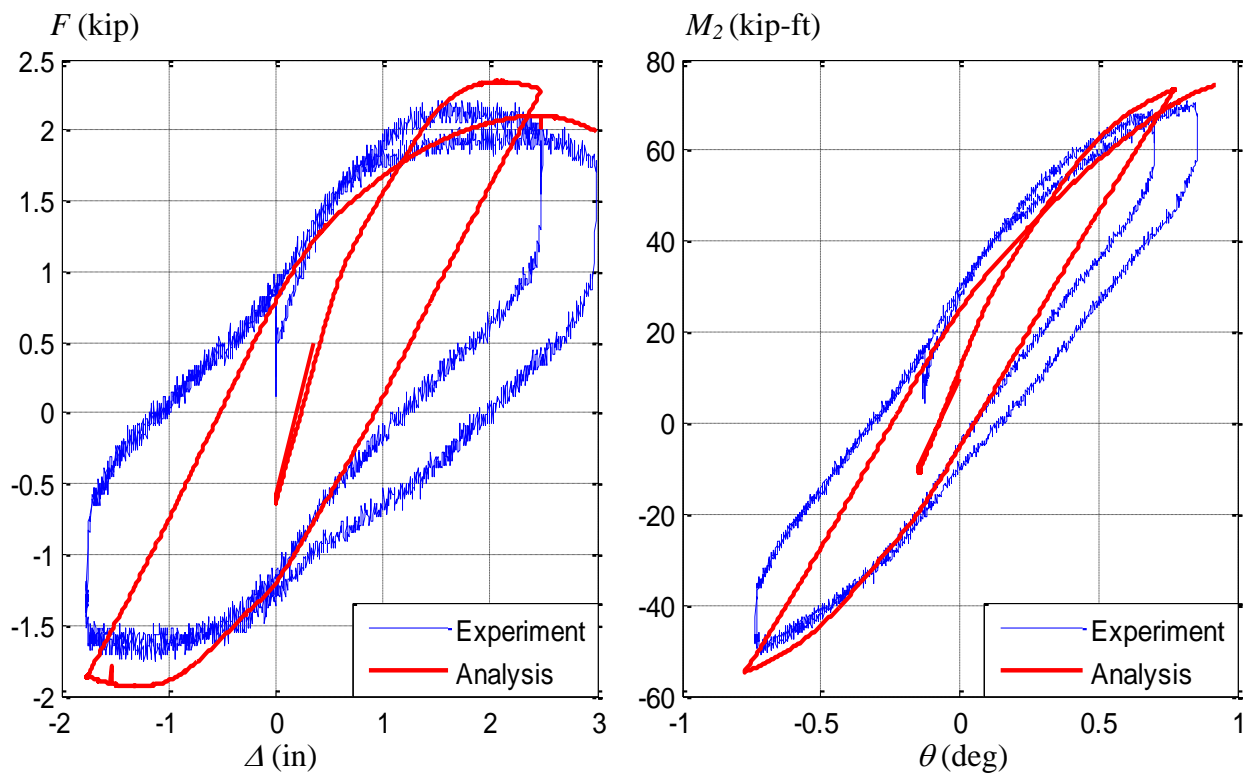


(c) LC2b, $P = 500$ kip

Figure 7.79. Experimental vs. Analytical response for the Specimen 5Rs-18-5 during LC2



(a) LC2a, $P = 300$ kip



(b) LC2b, $P = 150$ kip

Figure 7.80. Experimental vs. Analytical response for the Specimen 6C12-18-12 during LC2

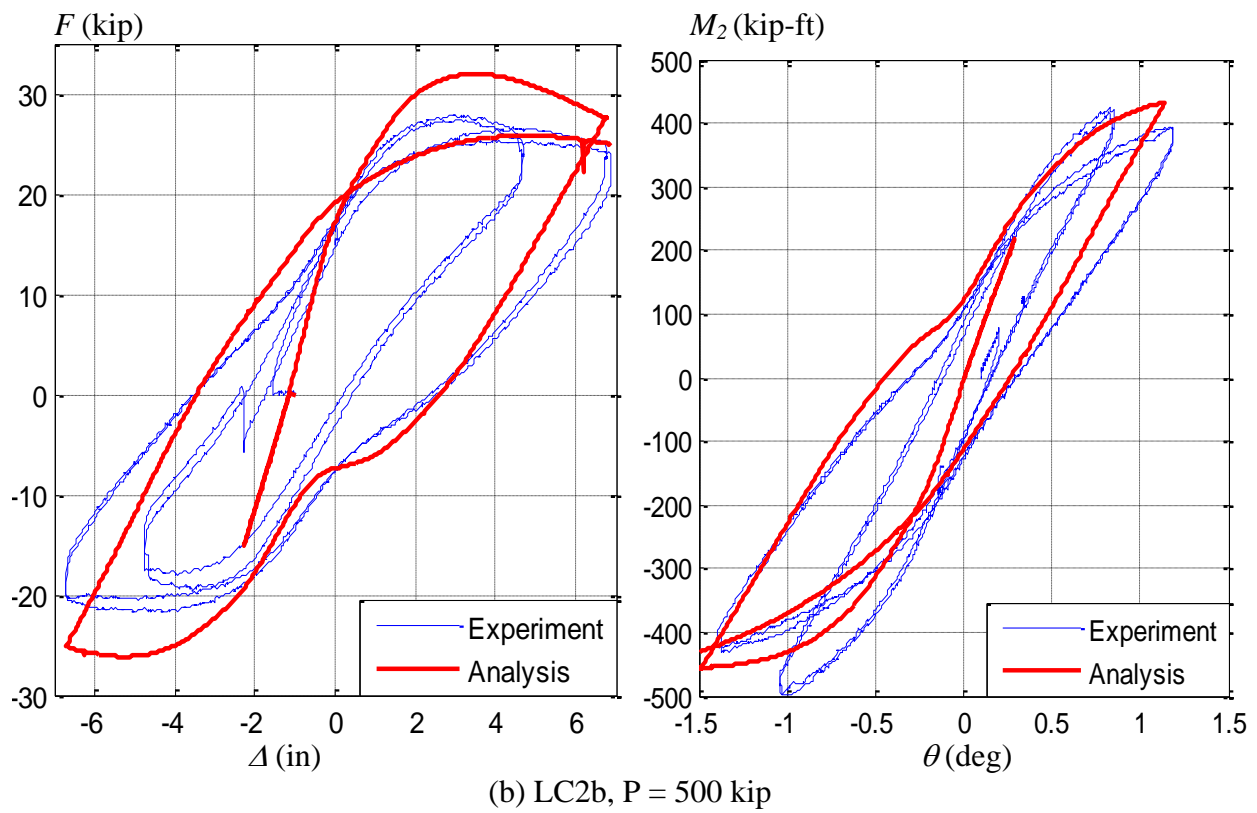
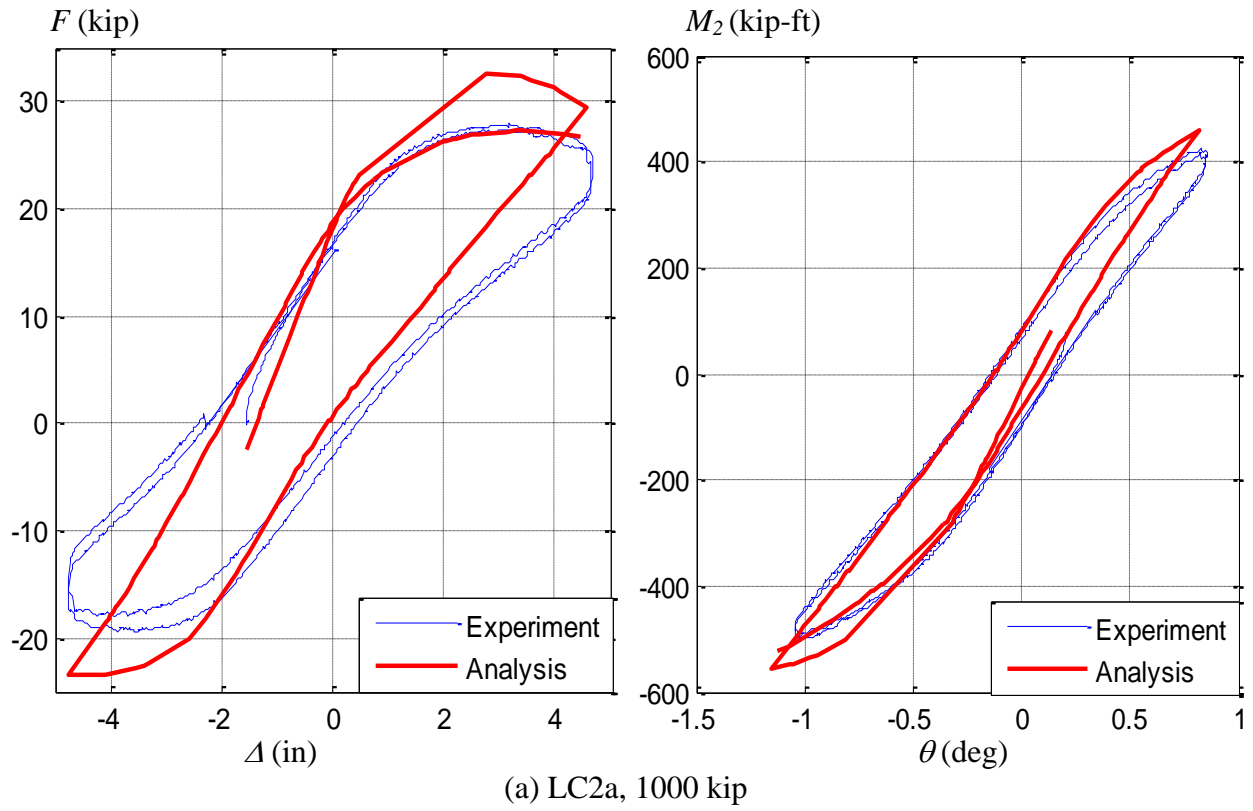
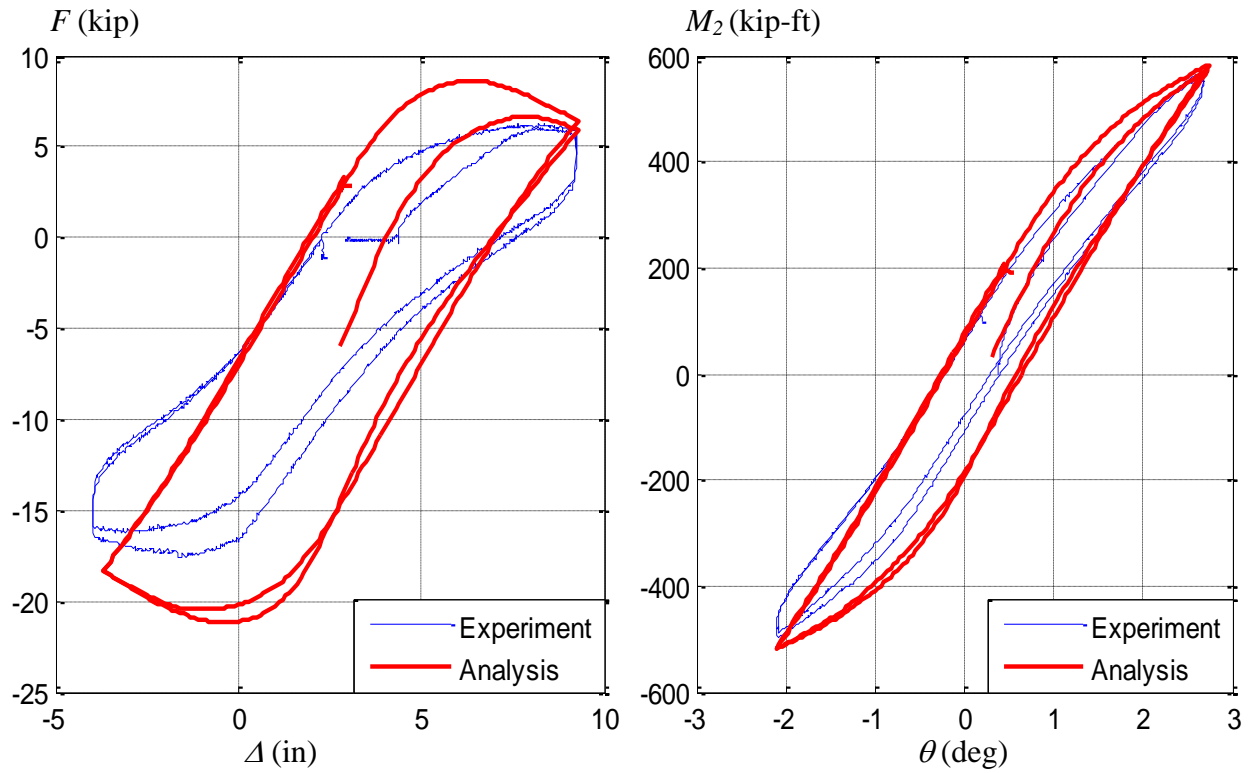
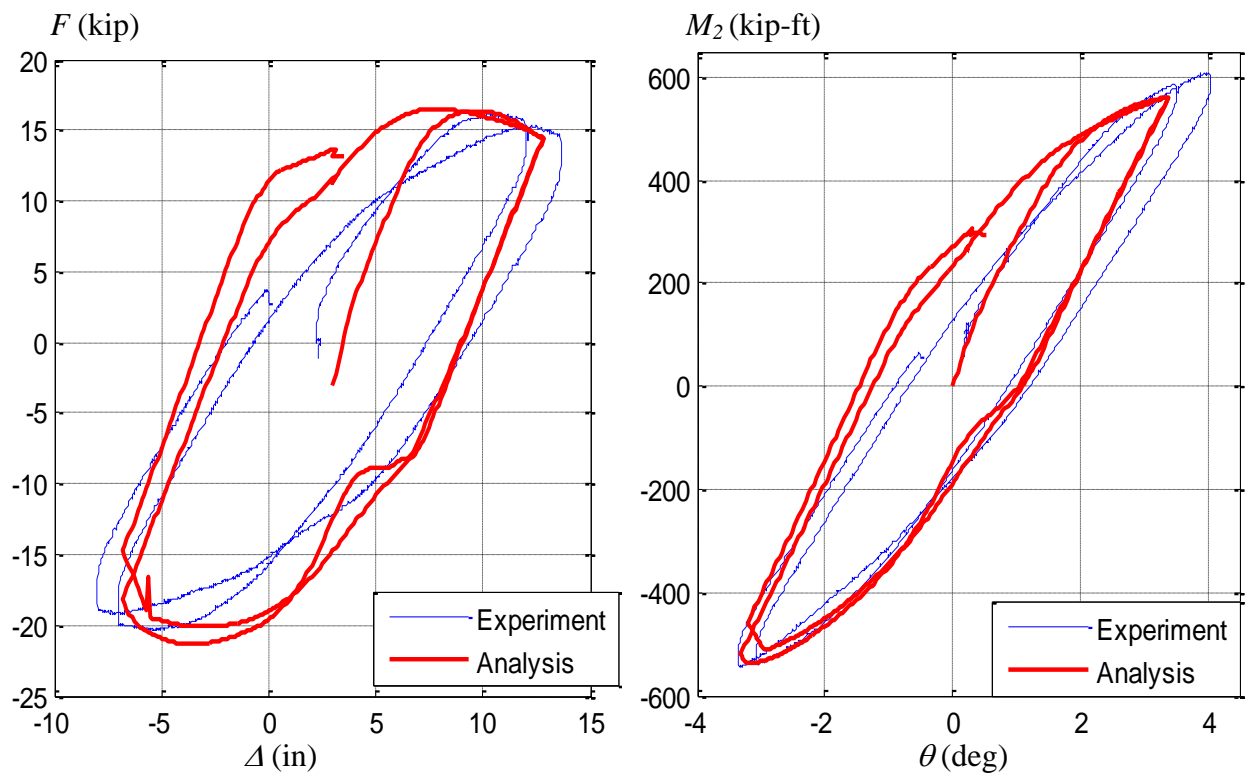


Figure 7.81. Experimental vs. Analytical response for the Specimen 7C20-18-12 during LC2

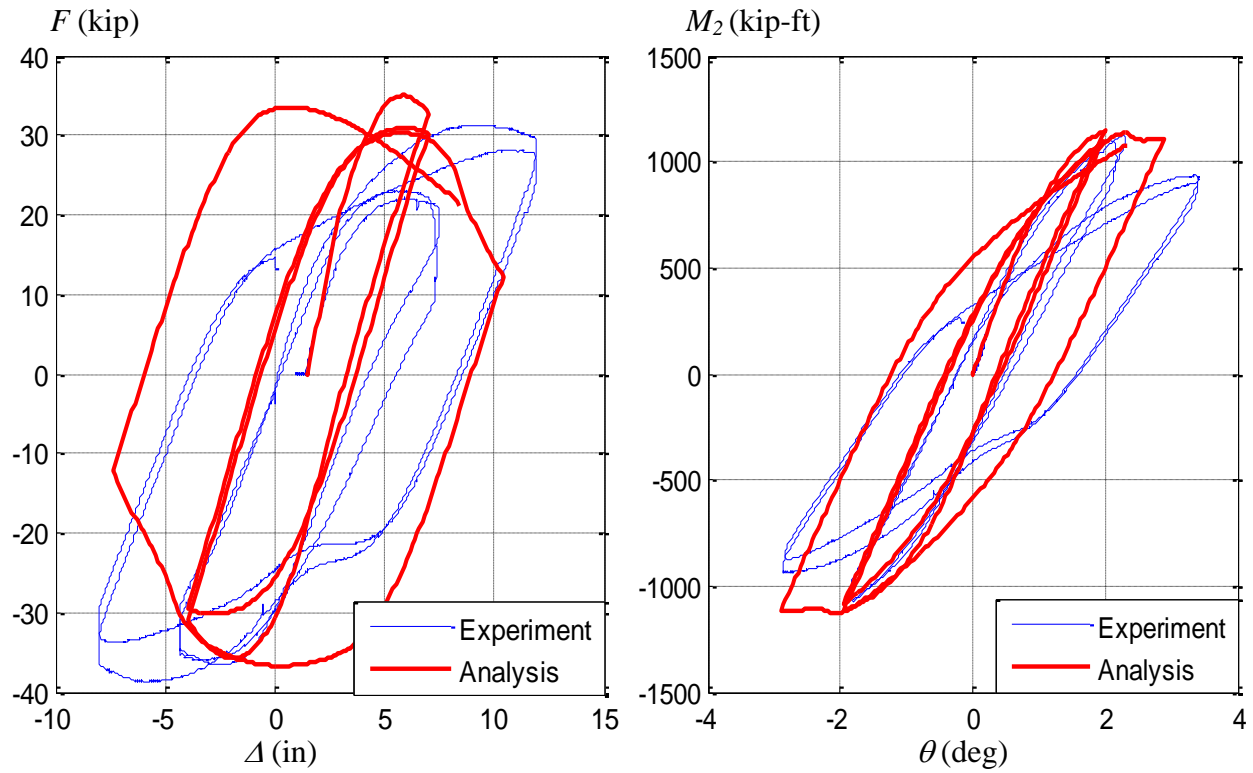


(a) LC2a, $P = 600$ kip

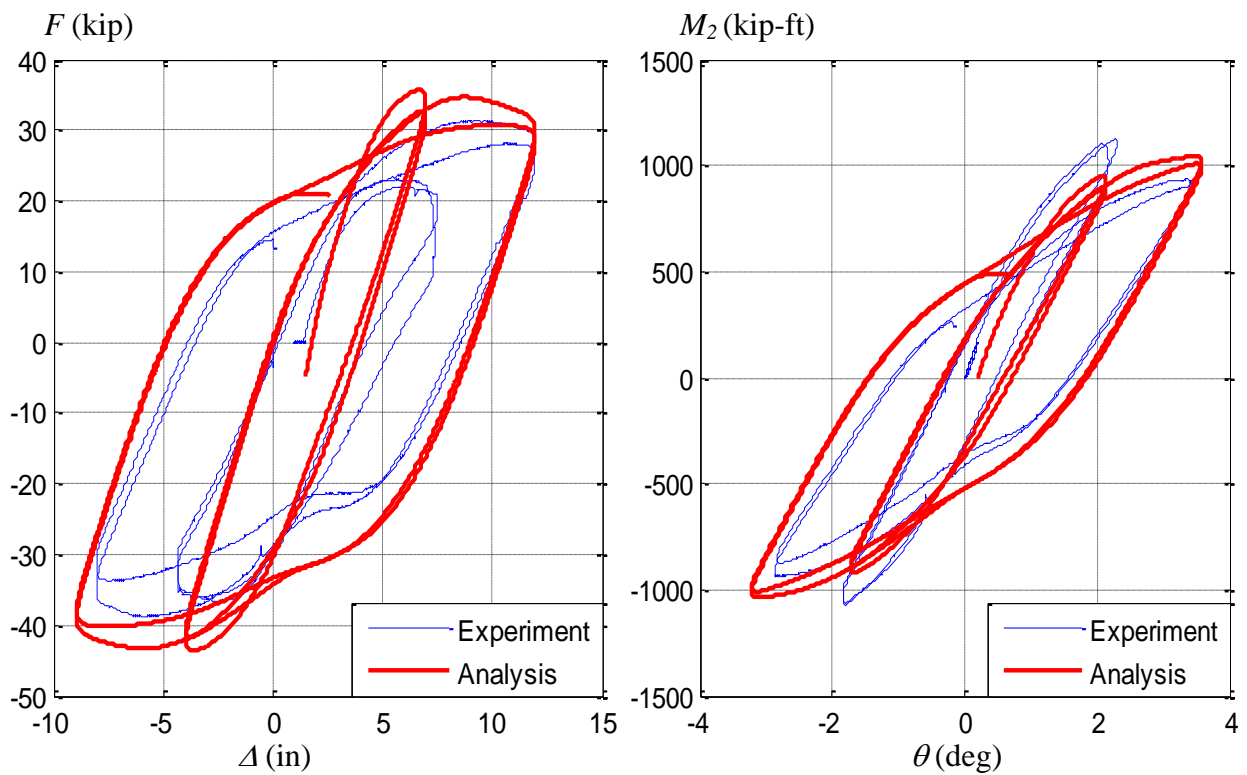


(b) LC2b, $P = 300$ kip

Figure 7.82. Experimental vs. Analytical response for the Specimen 8Rw-18-12 during LC2

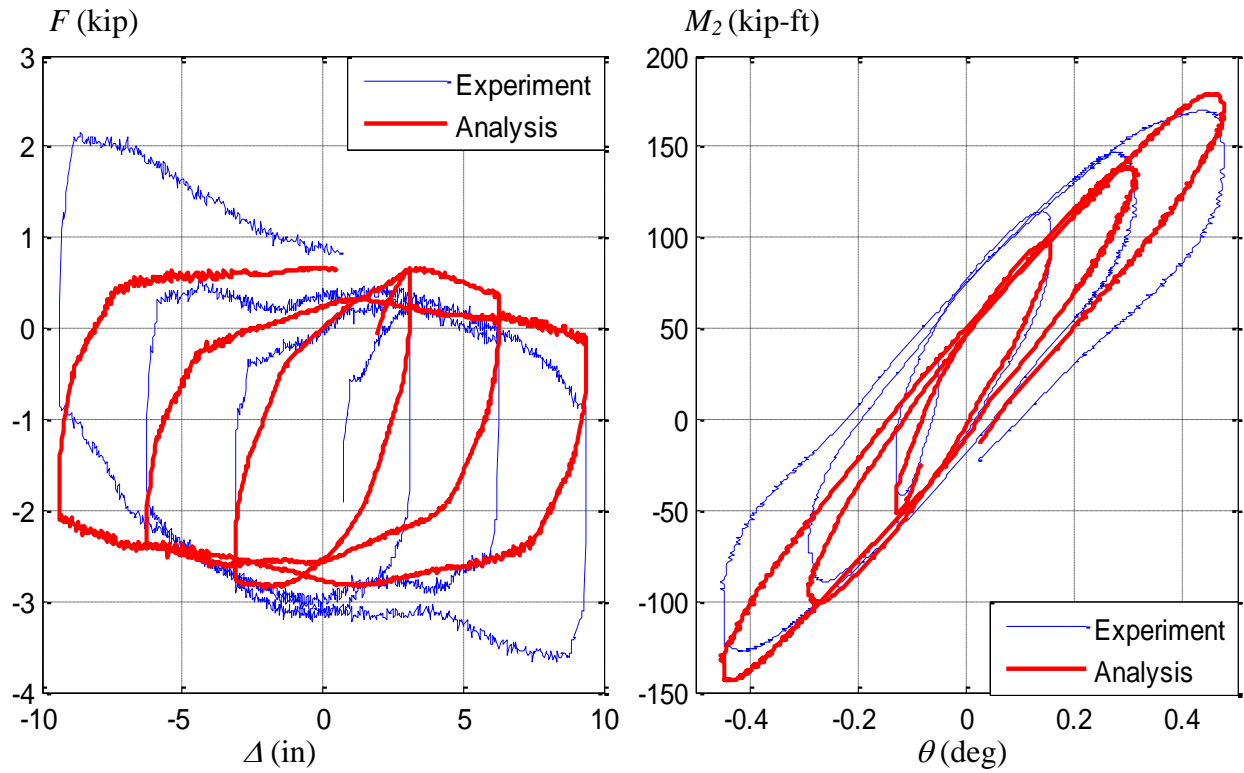


(a) LC2a, $P = 1200$ kip

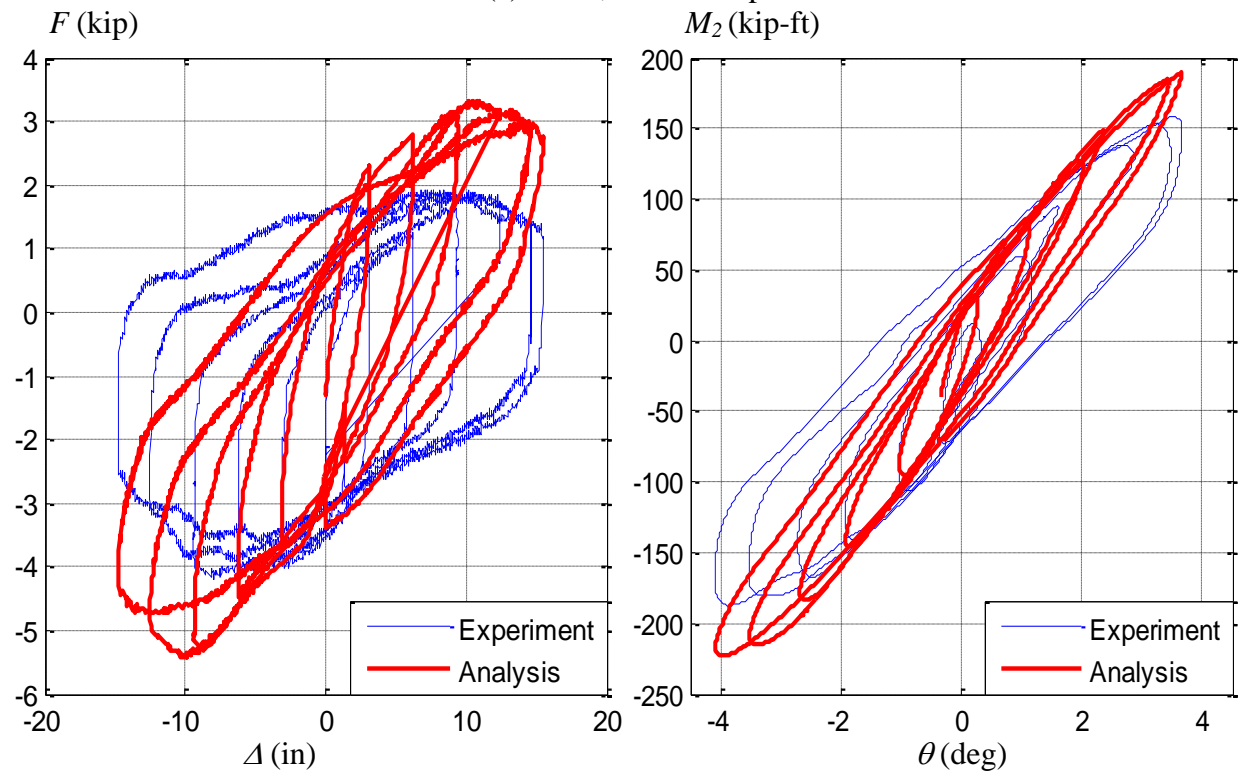


(b) LC2b, $P = 400$ kip

Figure 7.83. Experimental vs. Analytical response for the Specimen 9Rs-18-12 during LC2

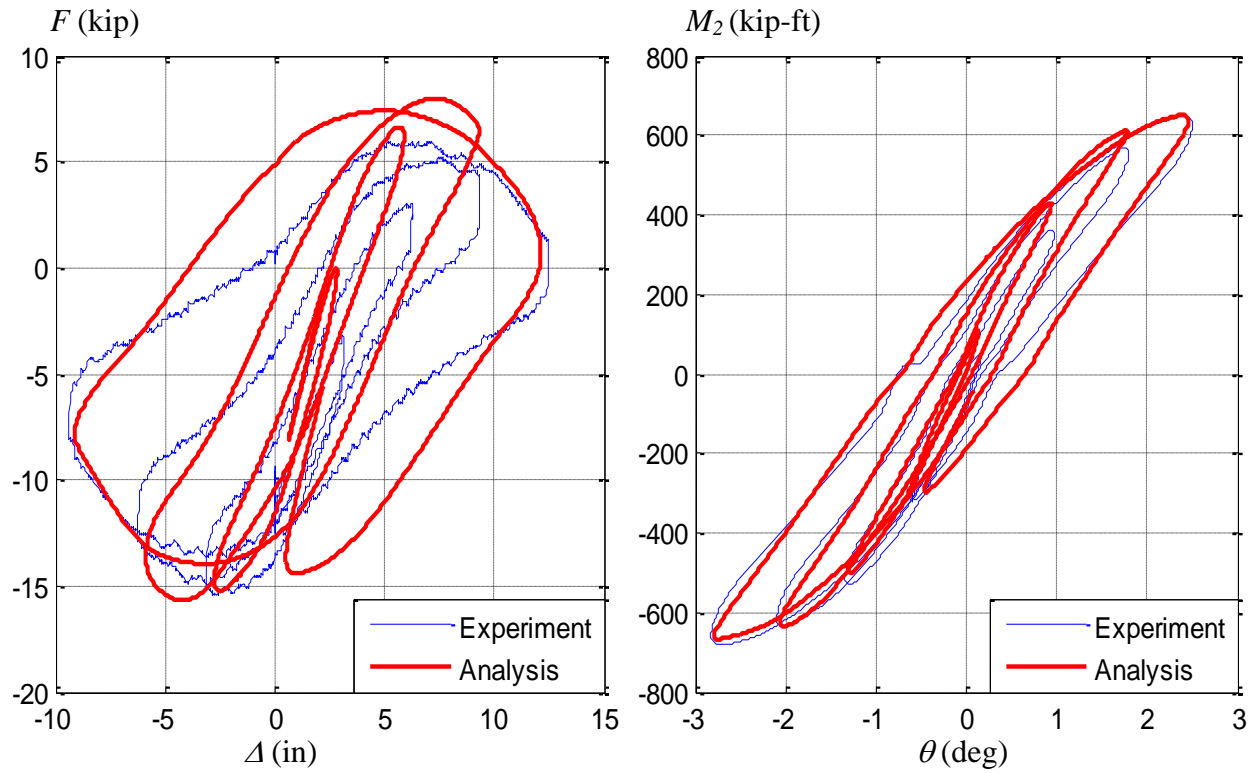


(a) LC2a, $P = 200$ kip

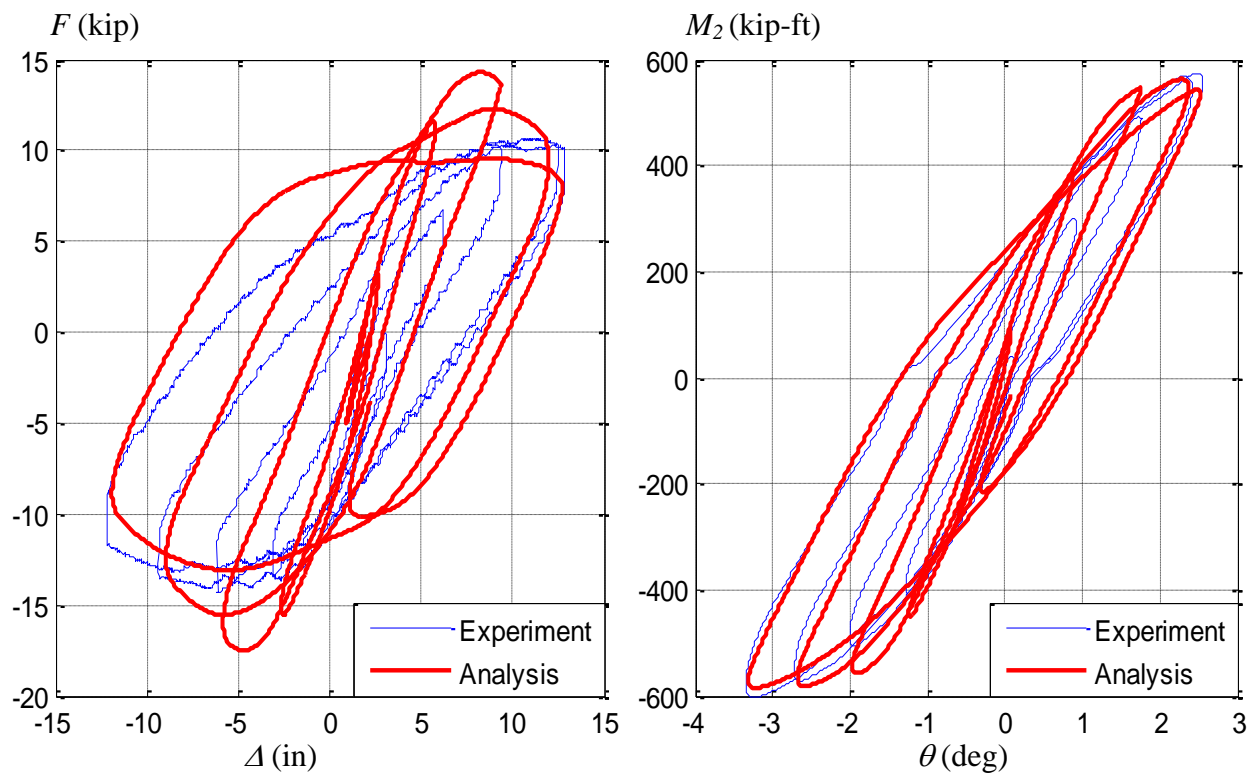


(b) LC2b, $P = 100$ kip

Figure 7.84. Experimental vs. Analytical response for the Specimen 10C12-26-5 during LC2

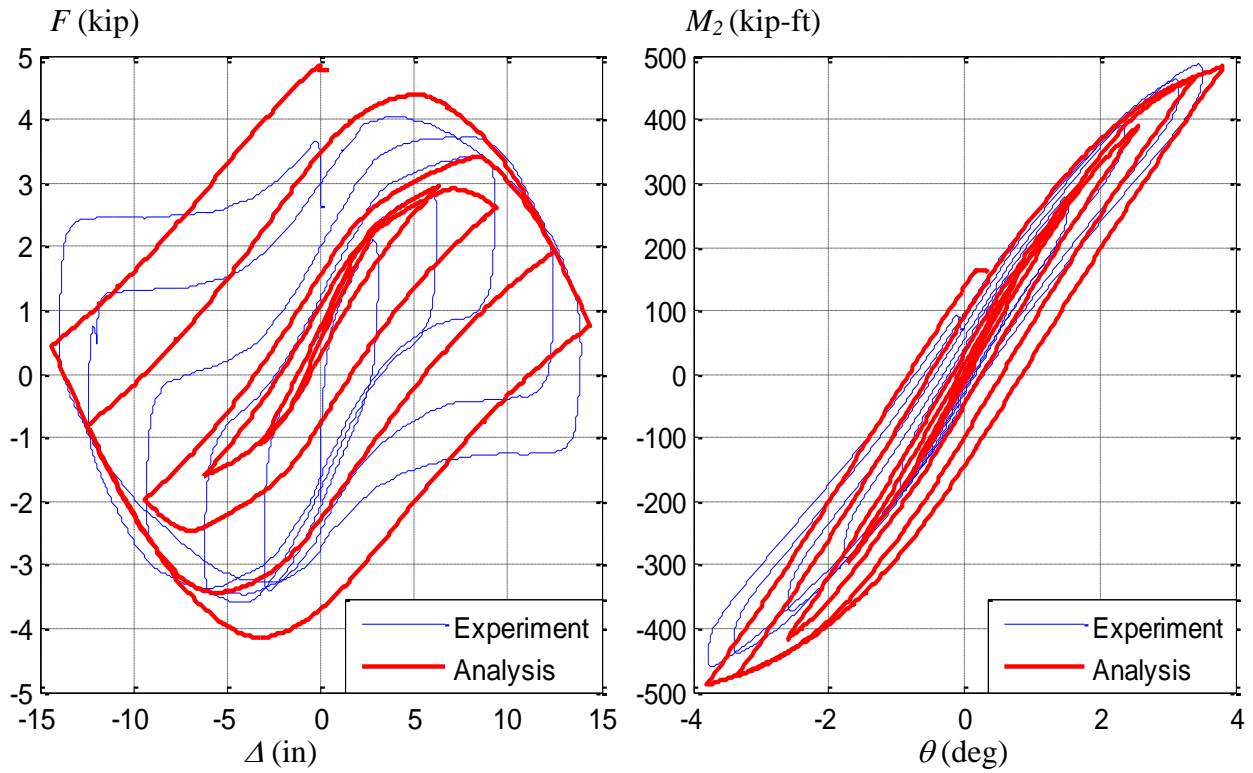


(a) LC2a, $P = 600$ kip

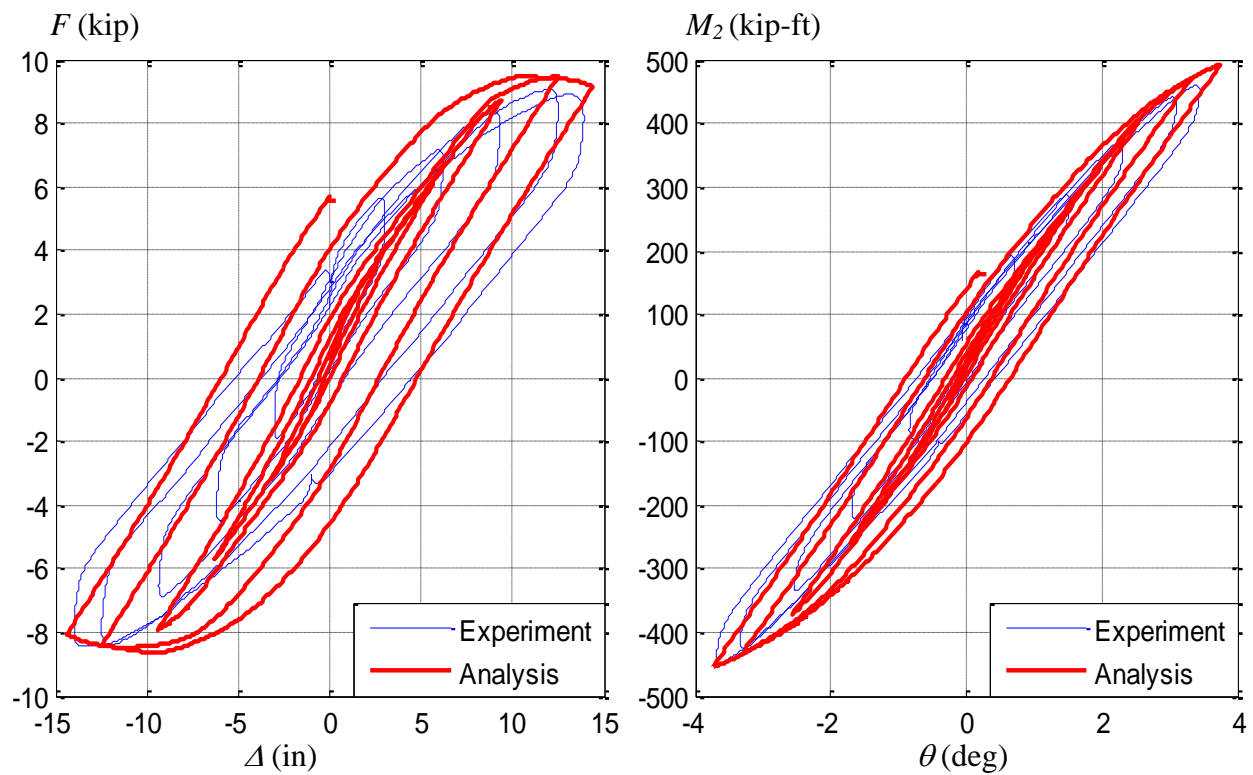


(b) LC2b, $P = 300$ kip

Figure 7.85. Experimental vs. Analytical response for the Specimen 11C20-26-5 during LC2



(a) LC2a, $P = 400$ kip



(b) LC2b, $P = 200$ kip

Figure 7.86. Experimental vs. Analytical response for the Specimen 12Rw-26-5 during LC2

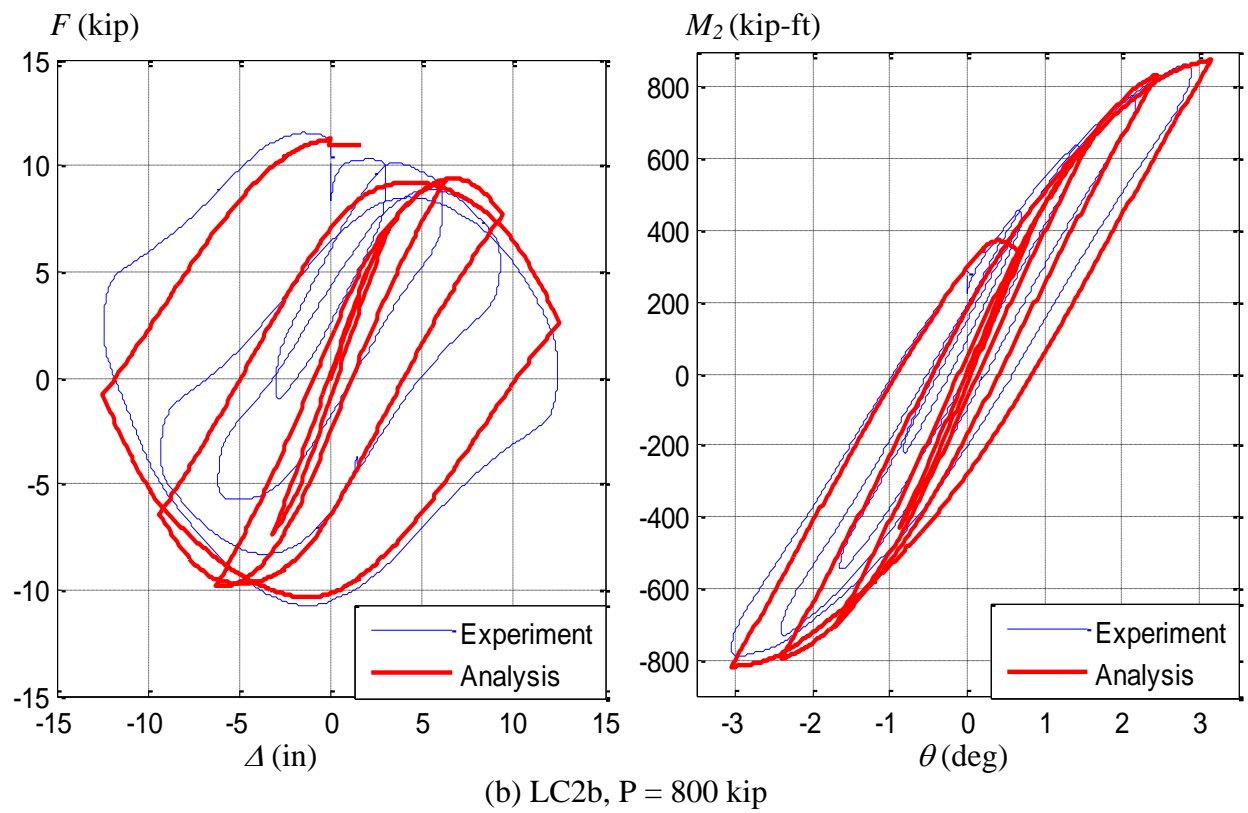
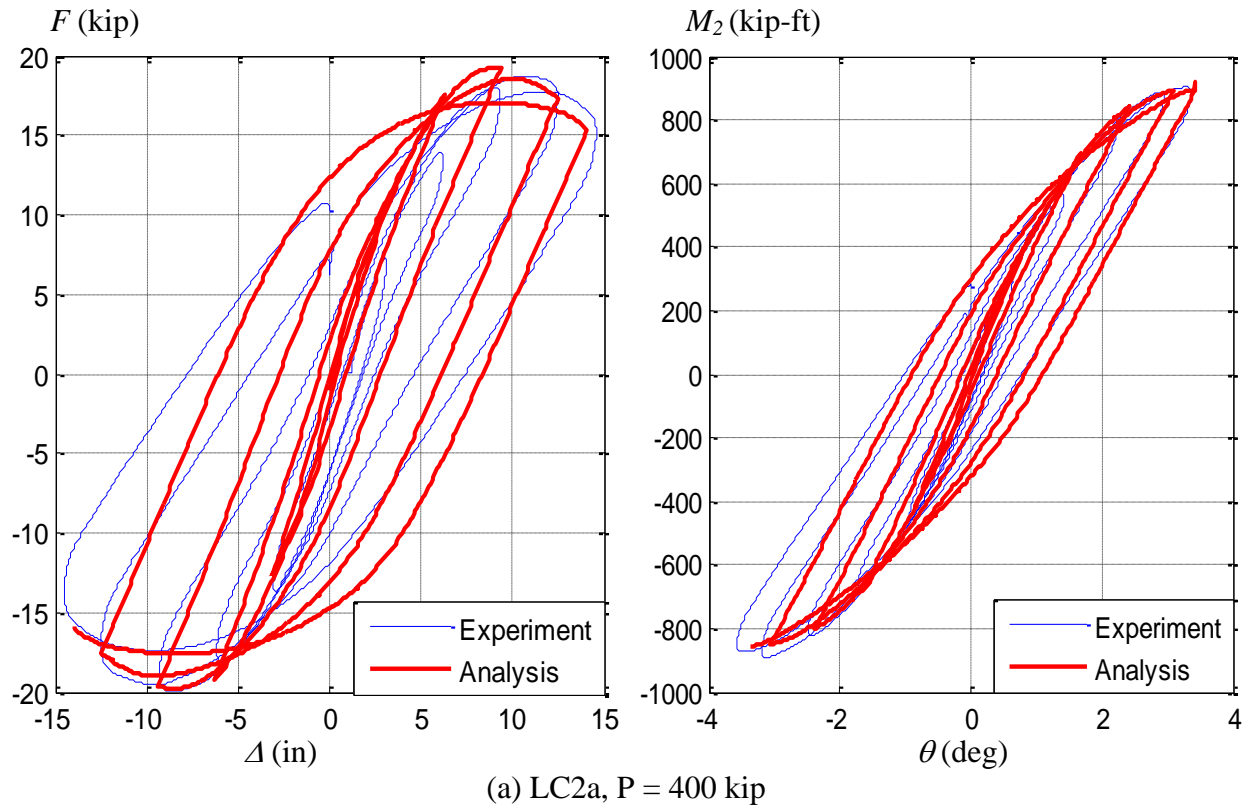
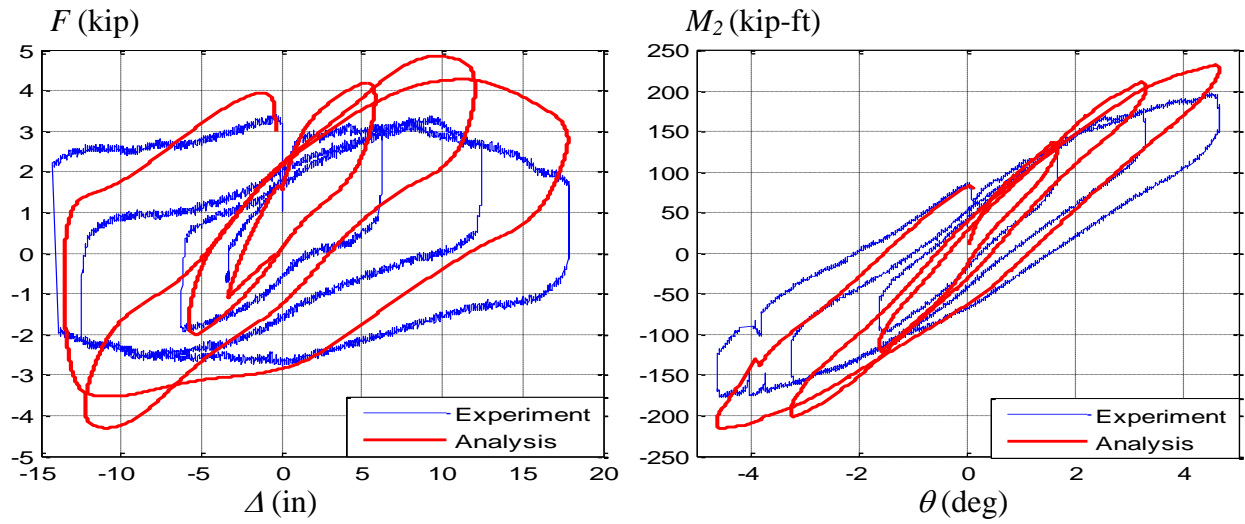
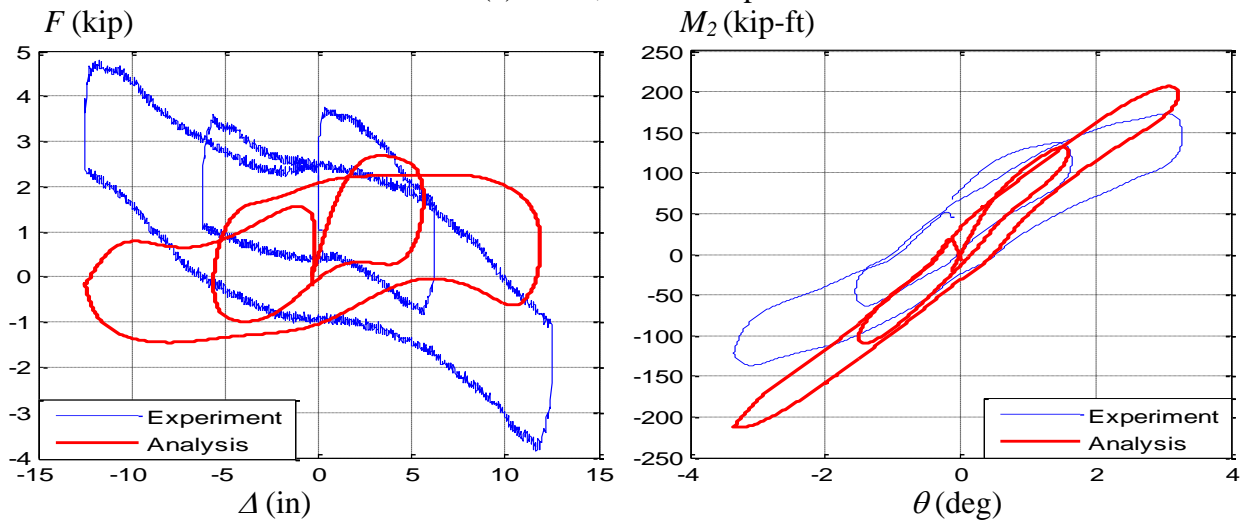


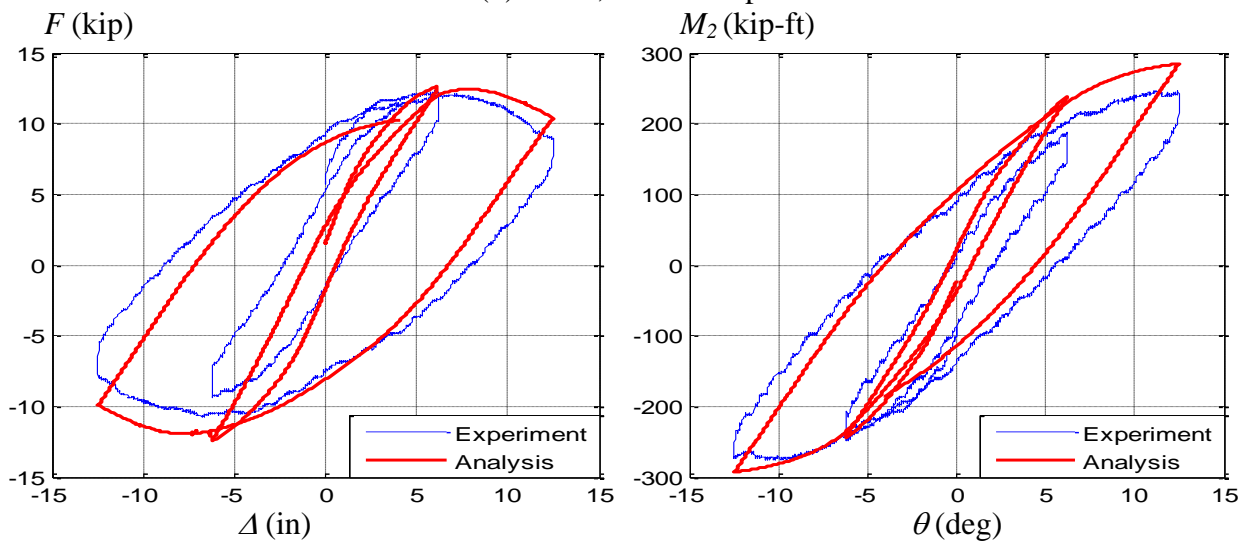
Figure 7.87. Experimental vs. Analytical response for the Specimen 13Rs-26-5 during LC2



(a) LC2a, $P = 100$ kip

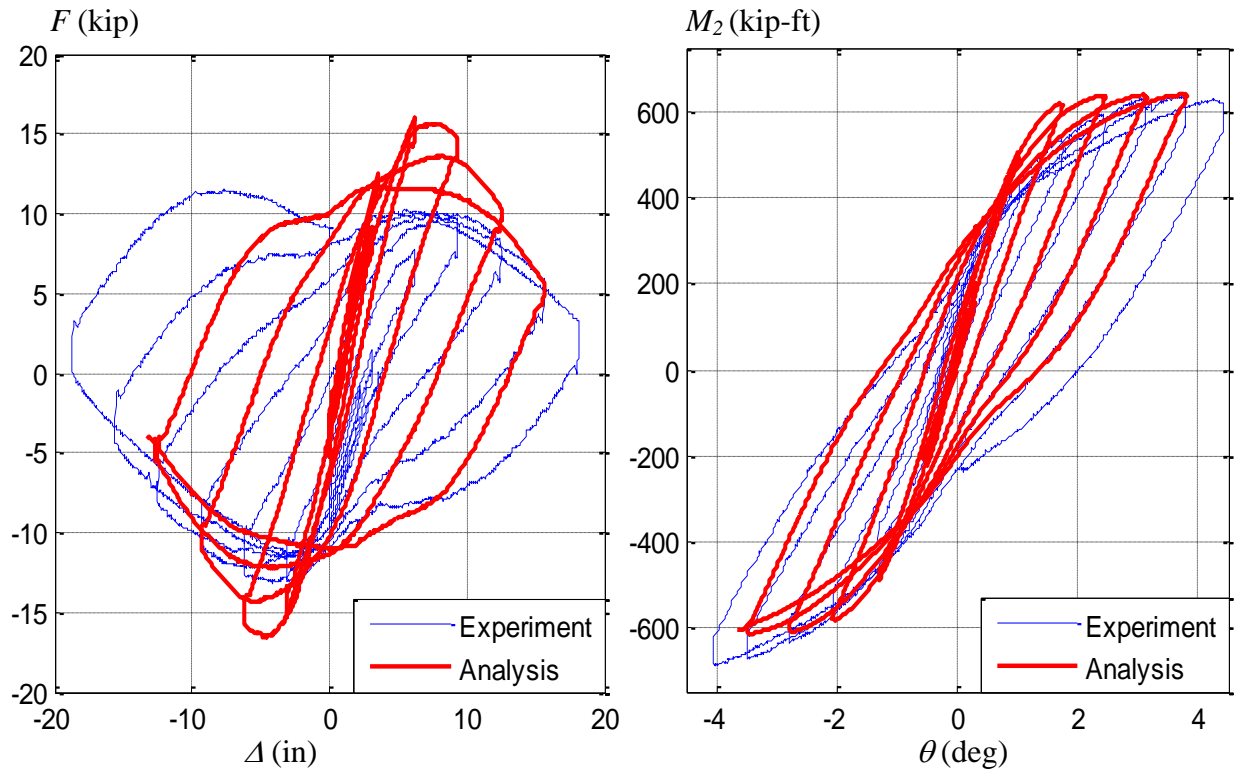


(b) LC2b, $P = 200$ kip

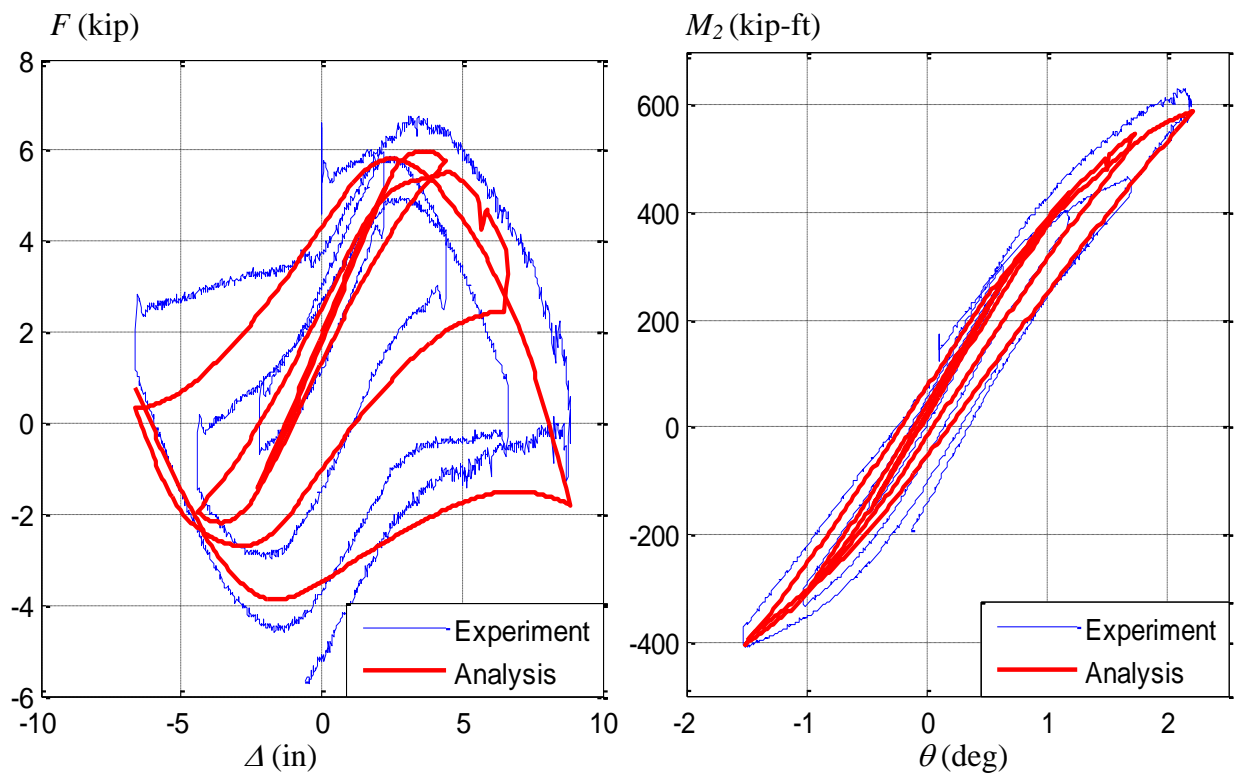


(c) LC2a', $P = 300$ kip, $K = 1$

Figure 7.88. Experimental vs. Analytical response for the Specimen 14C12-26-5 during LC2

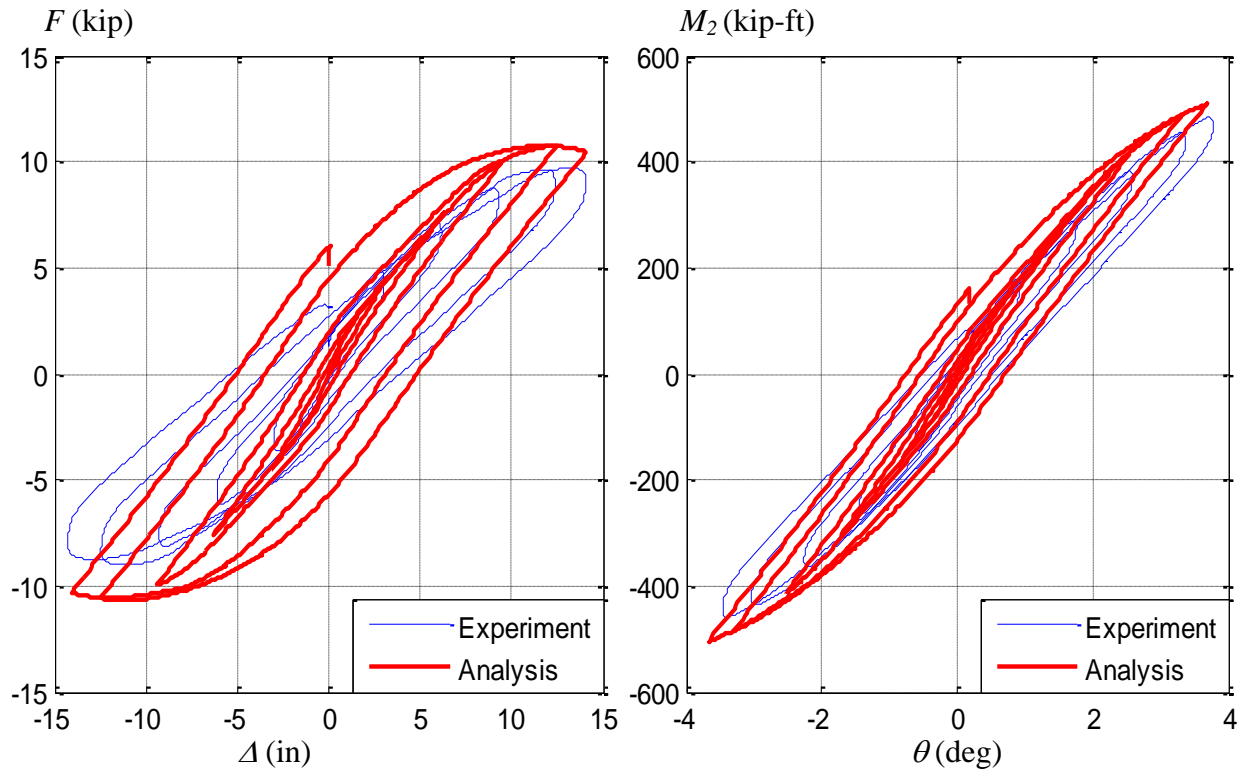


(a) LC2a, $P = 400$ kip

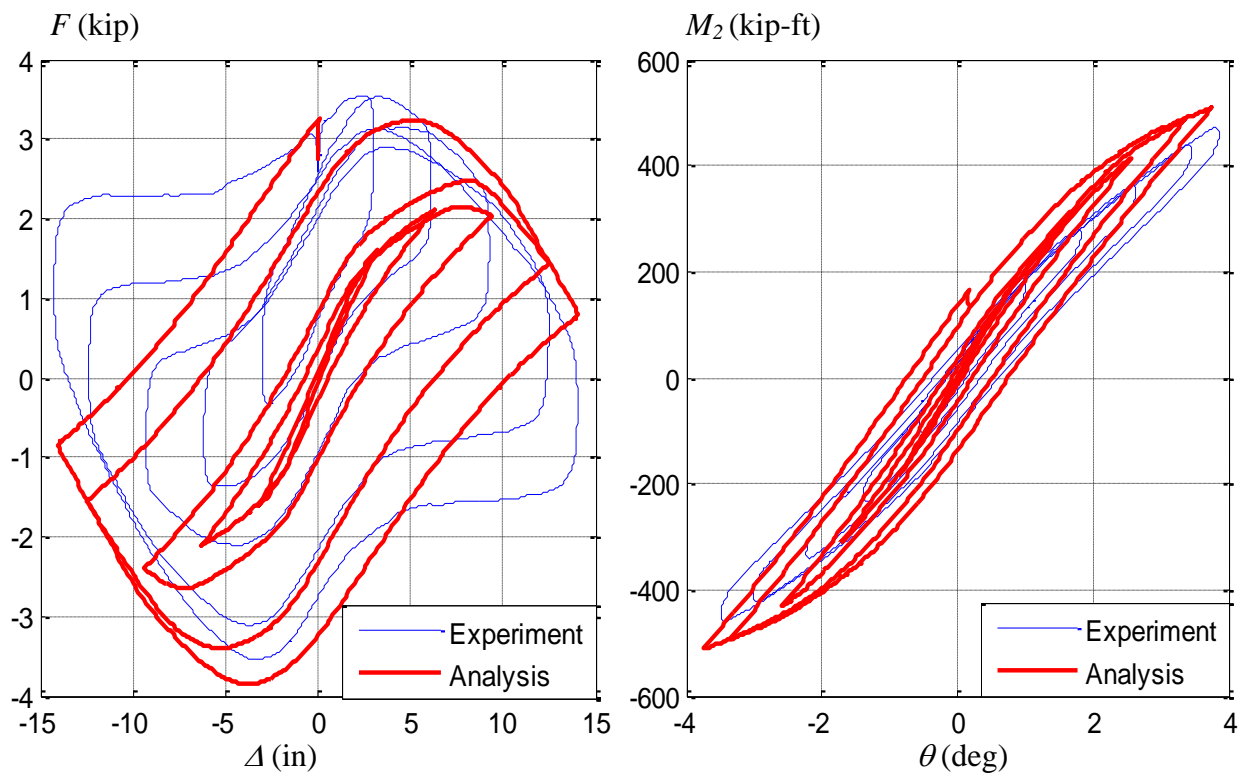


(a) LC2b, $P = 800$ kip

Figure 7.89. Experimental vs. Analytical response for the Specimen 15C20-26-12 during LC2

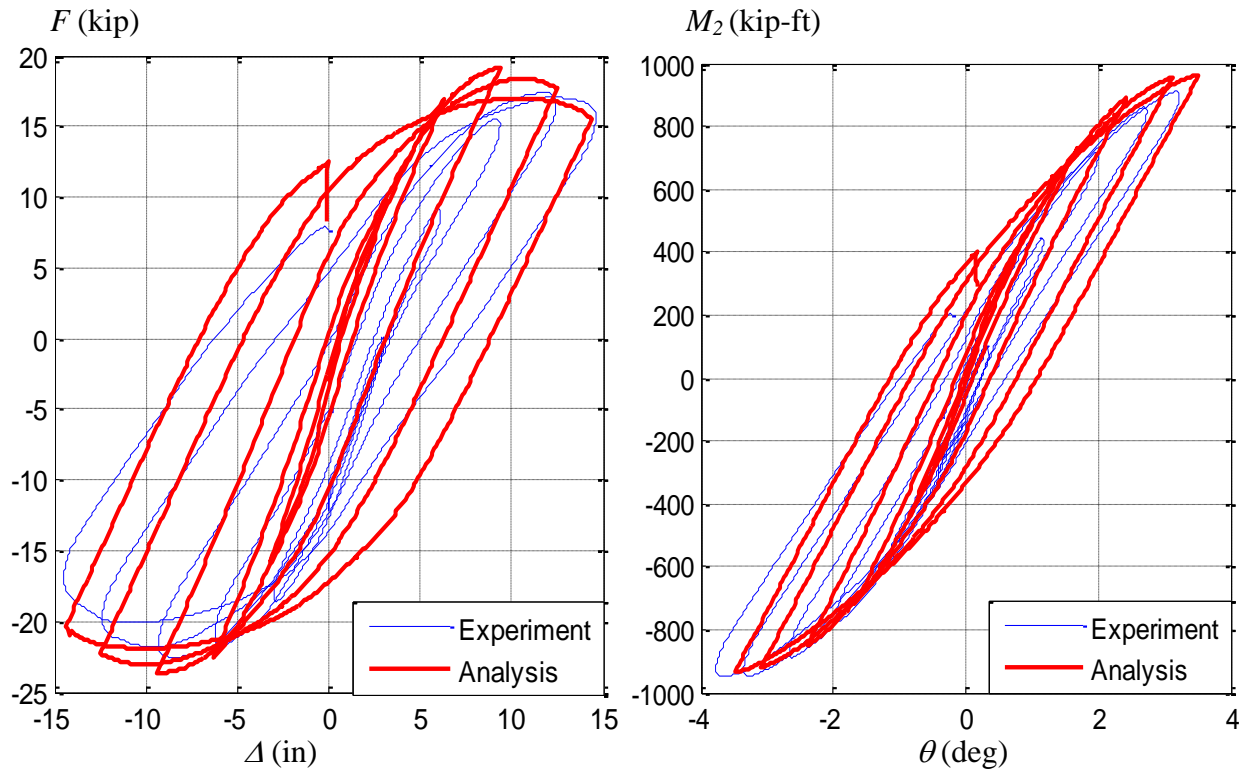


(a) LC2a, $P = 200$ kip

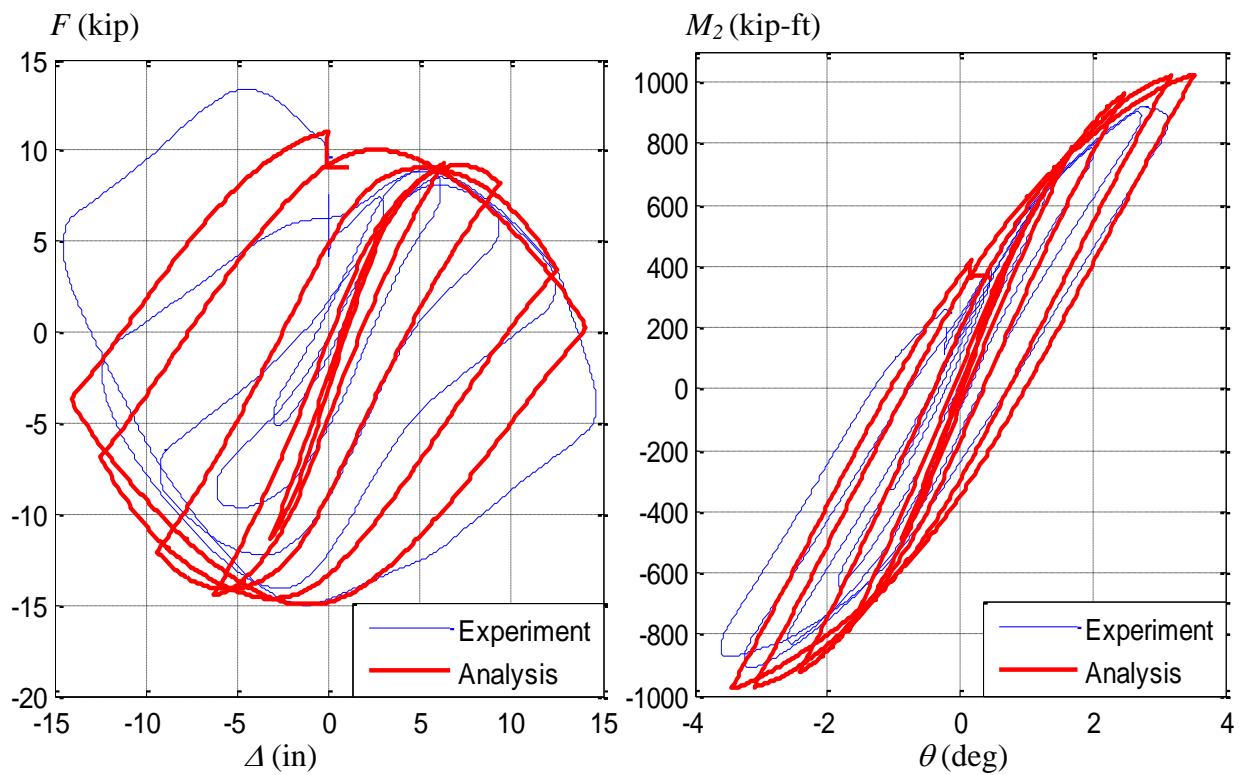


(b) LC2b, $P = 400$ kip

Figure 7.90. Experimental vs. Analytical response for the Specimen 16Rw-26-12 during LC2



(a) LC2a, $P = 400$ kip



(b) LC2b, $P = 800$ kip

Figure 7.91. Experimental vs. Analytical response for the Specimen 17Rs-26-12 during LC2

Computational analyses for the biaxial load case (LC3) were performed for some specimens, and only some selected results are presented in the following figures. The analyses were performed similarly to those in LC2, with the specimens under constant axial load (vertical displacement control) and with the step-by-step experimental story motion for the lateral displacements and the bending rotations (lateral displacement control). These analyses do not account for the accumulated damage developed in the previous load cases (LC1 and LC2). However, even when the accumulated damage from previous loading was ignored in these analyses, the obtained responses seems to be consisted with the measure response from the tests. Consideration of the accumulated damage and the frictional forces of the system are highly recommended for future calibrations.

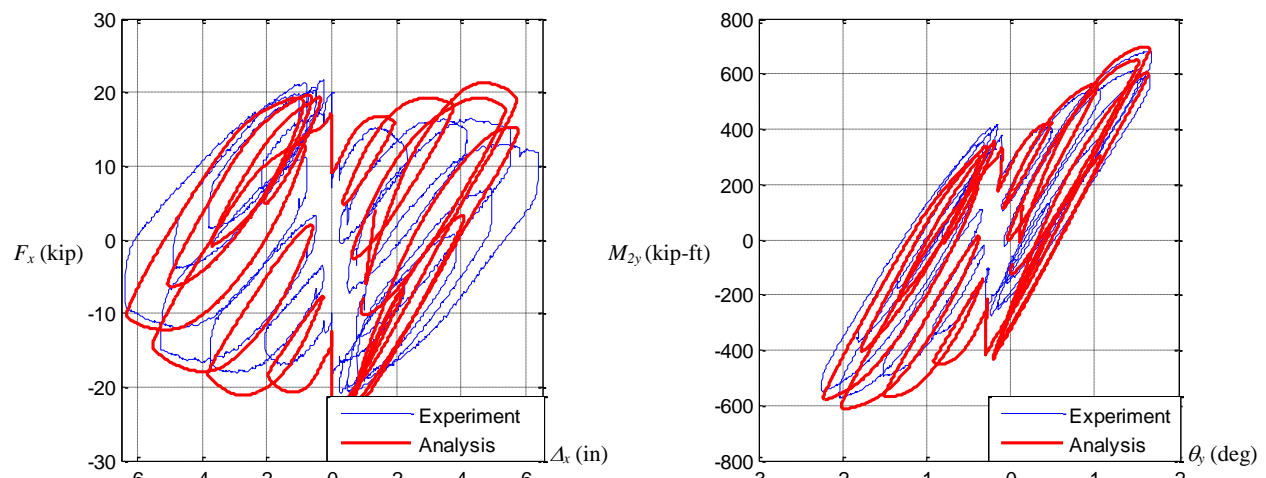


Figure 7.92. Experimental vs. Analytical response for the Specimen 3C20-18-5 during the biaxial load case LC3b ($P=750$ kip, 16 probes around the Specimen)

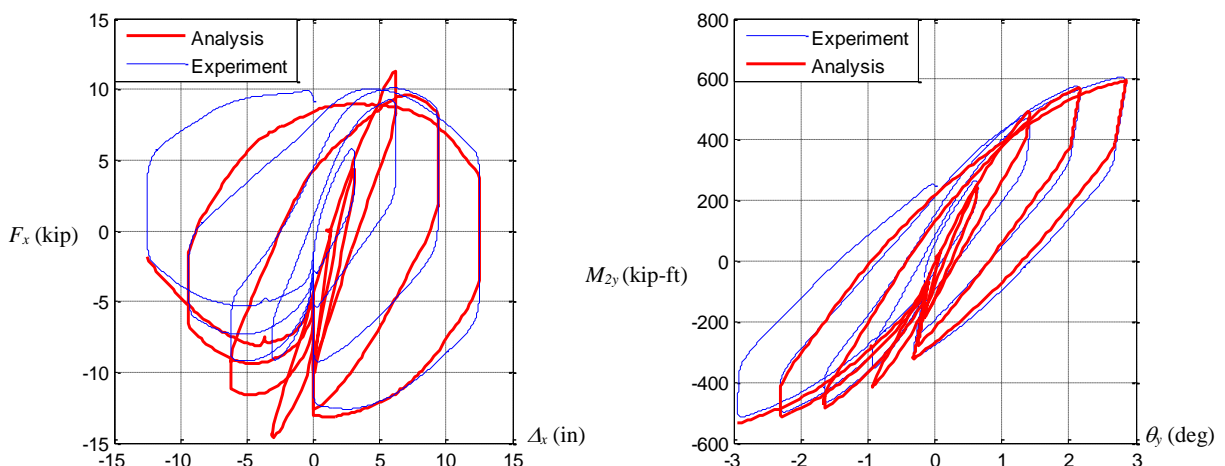


Figure 7.93. Experimental vs. Analytical response for the Specimen 11C20-26-5 during the biaxial load case LC3a ($P=450$ kip, figure eight)

7.5. Conclusions

In this chapter the uniaxial and the biaxial loading cases (LC2 and LC3) were used to evaluate the response to lateral forces of the tested composite CFT specimens. In addition, the evolution of the member stiffness was analyzed with the influence of the applied gravity load, and its degradation through the loading protocol (from LC1 to LC3) with different experimental responses (i.e. the force-displacement path, or the moment-curvature curves, among others). Finally, results obtained from computational analysis under the same loading conditions were shown and compared with the experimental results.

The evaluation of the flexural rigidities extracted from the test results exhibited some variability, mainly as the damage in the concrete core and the steel tubes progressed through the load protocol. Even with this dispersion, interesting results were extracted from the analysis of this data. A brief summary of the observations includes:

- The averaged values of the flexural rigidities extracted from the response during the pure compression loading case (LC1) were very close to the values predicted by the AISC (2005, 2010) Specifications.
- However, the averaged values do not show any proportionality with the steel ratio in the cross-section ($\rho = A_s/A$), as indicated in the AISC Specifications by presenting the C_3 coefficient in terms of the steel ratio. In addition, neither does the slenderness parameter of the column (λ) showed proportional variation with the test data. Instead, a constant averaged coefficient of $C_3 = 0.80$ is proposed for the determination of the buckling load capacity of a CFT column. In other words:

$$EI_{eff} = E_s I_s + 0.80 E_c I_c \quad (7.16)$$

- Similarly, averaged values of the flexural rigidities were also extracted from the response during the uniaxial and biaxial loading cases (LC2 and LC3). This is a unique set of data since this intends to give a simplified equation that approaches the expected rigidity for a beam-column under seismic loading (i.e. combined constant axial load and cyclic uniaxial or biaxial lateral load). As expected, the scatter of the data increased as the damage progressed on the specimen; even with some dispersion is exhibited, the following equations are proposed for the determination of the effective stiffness of a CFT

beam-column under seismic loading, and for the evaluation of lateral and flexural capacity based on frame analysis.

When local buckling is not expected (as in compact cross-sections), the effective flexural capacity may be approached with:

$$EI_{eff} = E_s I_s + 0.40 E_c I_c \quad (7.17)$$

On the other hand, when the steel tube is susceptible to local buckling, the following equation is suggested to obtain the expected effective flexural capacity as:

$$EI_{eff} = 0.85 (E_s I_s + 0.40 E_c I_c) \quad (7.18)$$

Finally in this section, results from the advanced computational analyses were presented in order to enhance the calibration of the material and element models, and compare and contrast the experimental and the analytical responses. In general, the responses obtained from the analyses shows reasonable predictions with respect to the experimental measured responses. However, it was pointed out that additional forces are included in the experimental response as a consequence of the friction forces in the system. The main influence of these frictional forces is an increment of the lateral strength capacity, and a very high unloading stiffness at the reversals. The frictional forces seem to have a higher impact in those specimens with the higher flexibility, low lateral capacity, and high axial load.

CHAPTER 8

EVALUATION OF LIMIT STATES

8.1. Introduction

In this chapter, significant limit states are extracted from the experimental tests. These include limit states that can be directly measured, such as the first yielding in the steel components and some which can only be detected indirectly, such as the steel local buckling and the concrete crushing. In the context of this chapter, “failure” is defined as reaching a limit state, regardless of whether it is associated with an incipient collapse, large loss of load carrying capacity, or large deformations.

In Section 8.2, a discussion on the steel local buckling is presented. The limits on the steel wall-slenderness that have been accepted in the AISC (2010) Specifications to avoid or minimize the local buckling failure are described. Then, the theoretical formulas obtained for the determination of the local buckling of plates are presented. In addition, previous empirical calibrations to characterize the initiation of local buckling are also shown. Finally in this section, the extraction and calibration of the first occurrence of the local buckling within the load protocol in the 18 specimens tested for this project are presented. Based on this calibration, an update of the empirical equations are presented and compared with previous equations; also, wall-slenderness limits to control the local buckling failure that are based on the updated empirical equations are obtained and presented.

In Section 8.3, first occurrence of the steel yielding, concrete crushing and steel local buckling are extracted and indicated in the empirical response obtained within the load protocol.

In Section 8.4, the plastic hinge lengths are determined and presented based on the maximum curvature within the load protocol through the column length.

Section 8.5 shows the post-mortem or forensic analysis of the CFT specimens tested in this project. This analysis is based on a physical review on the steel and concrete

Finally, Section 8.6 presents a brief summary of the main results obtained in this Chapter.

8.2. Local buckling

8.2.1. Introduction

One of the important limit states in steel column and beam-column design is the local buckling of the plate components. Local buckling is defined as a premature failure of a steel member due to the local out-of-plane deformations of, at least, one of the plate components under compressive stresses; this type of failure is controlled by the plate slenderness (λ) often quantified by its width-thickness ratio (D/t , h/t , b/t). This premature failure does not govern on compact cross-sections with low slenderness ratios ($D/t \leq \lambda_p$); compact sections can achieve plastic stresses over the entire cross-section without an evidence of local buckling deformation. This is not the case for non-compact steel sections ($D/t > \lambda_p$), where the plate components are susceptible to buckle locally with lower stresses as illustrated by Figure 8.1.a. In turn, slender steel sections ($D/t > \lambda_r$) can exhibit local buckling failure when only elastic compressive stresses are present. The local buckling failure can be prevented with lower wall slenderness ratios or by adding elements to the plates such that local deformation is reduced by the additional components. Stiffeners plates, encasement, and fillers can be used for this purpose.

The synergy effects on CFT members due to the steel and the concrete interaction were described in Chapter 1. As illustrated in Figure 8.1, one of the benefits of this interaction is the prevention of the inward deflection of the steel plates susceptible to local buckling due to the contact with the rigid concrete. As illustrated in Figure 8.1.b, the points of steel-concrete contact in CFT members restrain the plate components of the steel section in the inward direction, with the plate slenderness reduced as a consequence; this increment in the wall slenderness may change a steel non-compact or a slender section to compact or semi-compact section type if the cross-section is concrete-filled. The fact that the concrete forces the buckling of the tube outward provides two main advantages (Hajjar, 2000):

- When buckling occurs, the distance between the top and bottom flanges of the steel tube increases rather than decreases (as it would without the concrete core). This effect prevents the section modulus from decreasing significantly.
- The concrete tends to spread the local buckling over a larger region, mitigating severe strain concentrations which tend to cause cracking.

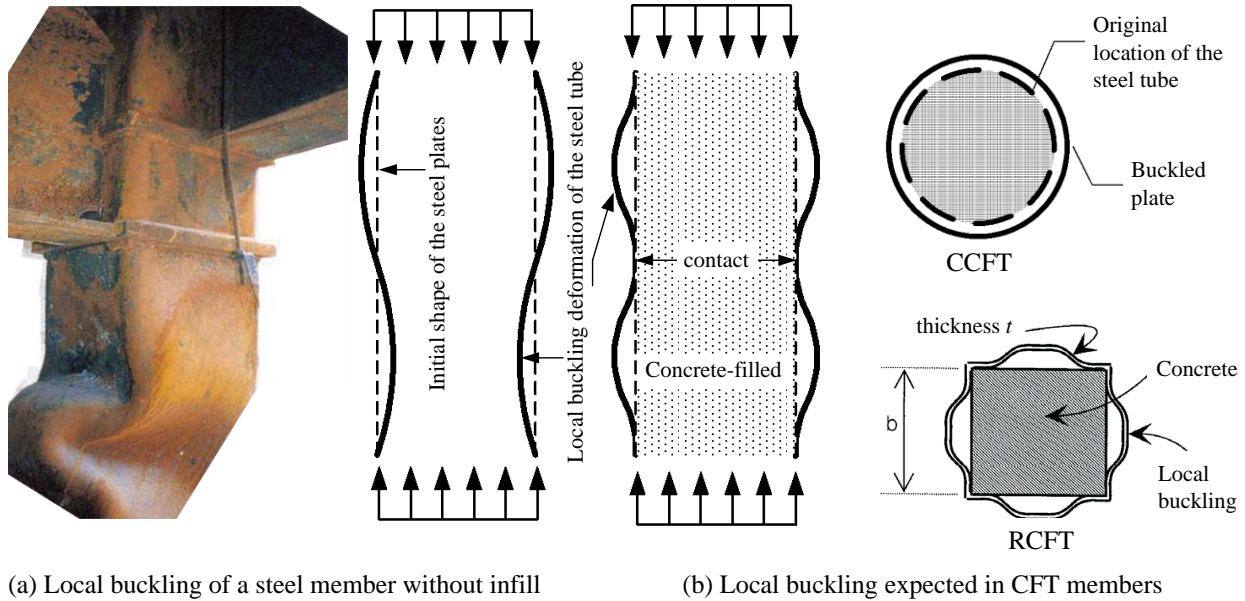


Figure 8.1. Local buckling failure (Leon et al., 2007)

8.2.2. Wall slenderness limits in the AISC Specifications

Although the beneficial effect of the concrete-infill in delaying local buckling in composite members has long been understood and incorporated empirically into design, it was first formally recognized and implemented in the 2005 edition of the AISC Specifications (Leon et al., 2007). In this edition, the limits for composite members were higher than those set for empty tubes classified as compact sections by 36% and 61% for circular and rectangular shapes, respectively. Composite non-compact and slender filled-tubes were recently incorporated in the 2010 edition. Table 8.1 shows a summary in matrix form of the wall-slenderness or width-thickness limits adopted in the AISC (2005) and AISC (2010) for both steel and composite hollow tubes under pure compression and flexure.

The limits shown in Table 8.1 are primarily based in experimental calibrations with tests data of plates under compressive stresses and known geometry and boundary conditions. In addition, they also reflect the application of theoretical derivations of the buckling load capacity with ideal conditions. An example of the later is the change in the format of the limits for circular tubes from one based on $\sqrt{E_s/F_y}$ in the original 1986 LRFD specification to one using E_s/F_y today.

Table 8.1. Wall slenderness limits in the AISC Specifications for steel and composite sections

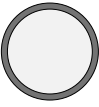

Shape	Type	Section	AISC (2005)		AISC (2010)	
			Compression	Flexure	Compression	Flexure
Circ. HSS 	CFT	Compact λ_p	$\frac{D}{t} \leq 0.15 \frac{E_s}{F_y}$		$\frac{D}{t} \leq 0.15 \frac{E_s}{F_y}$	$\frac{D}{t} \leq 0.09 \frac{E_s}{F_y}$
		Non-compact λ_r	NA		$\frac{D}{t} \leq 0.19 \frac{E_s}{F_y}$	$\frac{D}{t} \leq 0.39 \frac{E_s}{F_y}$
	Steel	Compact λ_p	NA	$\frac{D}{t} \leq 0.07 \frac{E_s}{F_y}$	NA	$\frac{D}{t} \leq 0.07 \frac{E_s}{F_y}$
		Non-compact λ_r	$\frac{D}{t} \leq 0.11 \frac{E_s}{F_y}$	$\frac{D}{t} \leq 0.31 \frac{E_s}{F_y}$	$\frac{D}{t} \leq 0.11 \frac{E_s}{F_y}$	$\frac{D}{t} \leq 0.31 \frac{E_s}{F_y}$
Rect. HSS 	CFT	Compact λ_p	$\frac{b}{t} \leq 2.26 \sqrt{\frac{E_s}{F_y}}$		$\frac{b}{t} \leq 2.26 \sqrt{\frac{E_s}{F_y}}$	$\frac{h}{t} \leq 3.00 \sqrt{\frac{E_s}{F_y}}$
		Non-compact λ_r	NA		$\frac{b}{t} \leq 3.00 \sqrt{\frac{E_s}{F_y}}$	$\frac{h}{t} \leq 7.00 \sqrt{\frac{E_s}{F_y}}$
	Steel	Compact λ_p	NA	$\frac{h}{t} \leq 2.42 \sqrt{\frac{E_s}{F_y}}$ $\frac{b}{t} \leq 1.12 \sqrt{\frac{E_s}{F_y}}$	NA	$\frac{h}{t} \leq 2.42 \sqrt{\frac{E_s}{F_y}}$ $\frac{b}{t} \leq 1.12 \sqrt{\frac{E_s}{F_y}}$
		Non-compact λ_r	$\frac{h}{t} \leq 1.40 \sqrt{\frac{E_s}{F_y}}$ $\frac{b}{t} \leq 1.40 \sqrt{\frac{E_s}{F_y}}$	$\frac{h}{t} \leq 5.70 \sqrt{\frac{E_s}{F_y}}$ $\frac{b}{t} \leq 1.40 \sqrt{\frac{E_s}{F_y}}$	$\frac{h}{t} \leq 1.40 \sqrt{\frac{E_s}{F_y}}$ $\frac{b}{t} \leq 1.40 \sqrt{\frac{E_s}{F_y}}$	$\frac{h}{t} \leq 5.70 \sqrt{\frac{E_s}{F_y}}$ $\frac{b}{t} \leq 1.40 \sqrt{\frac{E_s}{F_y}}$

Table 8.2 shows the classification of the cross-sections of the test specimens according with their width-thickness ratios ($\lambda = D/t$, b/t or h/t) and the wall-slenderness limits specified by the AISC (2010) summarized in Table 8.1. The limits tabulated in Table 8.2 are obtained with nominal strength and stiffness parameters for A500, Gr. B steel; these are 29,000 ksi for the Young's modulus and 42 ksi in the circular tubes and 46 ksi in the rectangular tubes for yield stresses. According to Table 8.2, all the CFT specimens tested are in the compact category for both compression and bending, except for the specimens of the *C20* group with non-compact sections subject to flexure, and the specimens of the *Rw* group with non-compact sections subject to axial compression. As reminder, the “*Rw*” and “*Rs*” labels stand for RCFTs oriented and

tested in the weak and the strong axis, respectively, during the load cases LC1 (pure compression) and LC2 (uniaxial bending).

Table 8.2. Classification of the steel cross-section in terms of the wall slenderness

Group or set	Specimen Name	Steel cross-section	D/t h/t	Compression λ_p λ_r		Uniaxial bending λ_p λ_r		Cross-section classification
C5	1C5-18-5 18C5-26-12	HSS5.563x0.13	45	104	131	62	269	Compact
C12	2C12-18-5 6C12-18-12 10C12-26-5 14C12-26-12	HSS12.75x1/4	55	104	131	62	269	Compact
C20	3C20-18-5 7C20-18-12 11C20-26-5 15C20-26-12	HSS20x1/4	86	104	131	62	269	Non-compact bending
Rw	4Rw-18-5 8Rw-18-12 12Rw-26-5 16Rw-26-12	HSS20x12x5/16	69	57	75	75	176	Non-compact compression
Rs	5Rs-18-5 9Rs-18-12 13Rs-26-5 17Rs-26-12	HSS20x12x5/16	41	57	75	75	176	Compact

8.2.3. Theoretical wall slenderness limits in circular tubes

The theoretical formula for the critical stress at which local buckling occurs in hollow circular tubes under compressive loading is given by the Equation 8.1. However, experimental tests have developed earlier failures with critical stresses around 40 to 60% of this theoretical value (Young and Budynas, 2001). As for similar results for other types of buckling failures, these lower values are attributed to initial imperfections and residual stresses on the plate components.

$$F_{cr} = \frac{E_s}{\sqrt{3}\sqrt{(1-\nu_s^2)}} \frac{2t}{D-t} \quad (8.1)$$

By using a Rayleigh-Ritz method, Bradford *et al.* (2002) derived a closed-form solution for the local buckling stress of thin-walled circular tubes with a rigid infill. The theoretical solution applicable to CCFTs resulted in buckling stresses higher by a factor of $\sqrt{3} = 1.73$ with respect to the stresses derived for steel hollow sections as shown by the Equation 8.2.

$$F_{cr} = \frac{E_s}{\sqrt{(1-\nu_s^2)}} \frac{2t}{D-t} \quad (8.2)$$

As illustrated in Figure 8.2, Bradford *et al.* (2002) calibrated their analytical solution with a limited number of experimental data, where a wall slenderness limit of 125 for tubes with yield stress equal to 250 MPa was proposed for non-compact sections (Equation 8.3). This equation gives a non-dimensional limit as set in Equation 8.4.

$$\lambda = \left(\frac{D}{t} \right) \left(\frac{F_y [MPa]}{250} \right) = 125 \quad (8.3)$$

$$\frac{D}{t} = 125 \left(\frac{250}{F_y [MPa]} \right) \left(\frac{E_s [MPa]}{200,000} \right) = 0.156 \frac{E_s}{F_y} \quad (8.4)$$

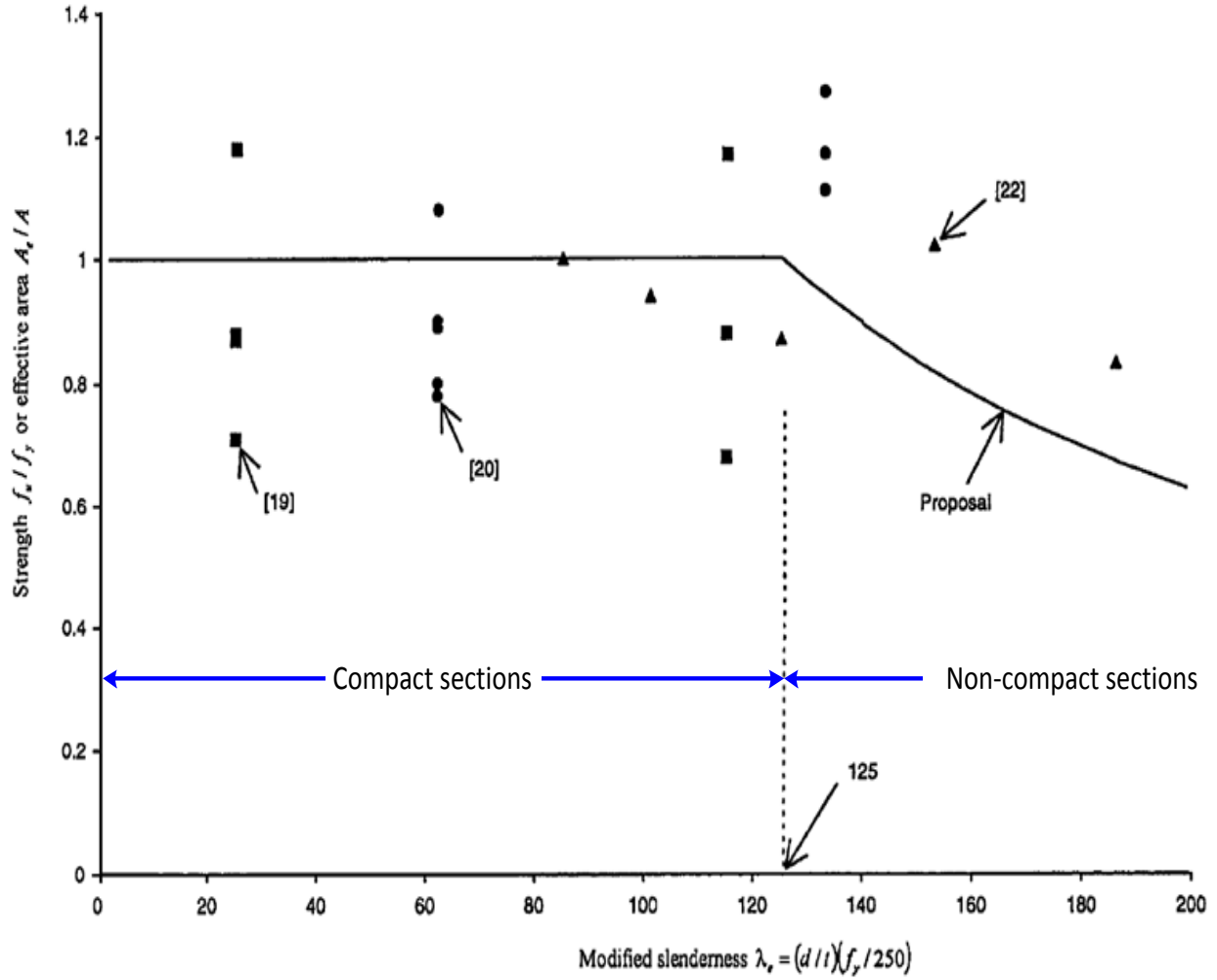


Figure 8.2. Buckling strength calibration of CCFTs by Bradford et al. (2002)

8.2.4. Theoretical wall slenderness limits in rectangular tubes

The analytical solution for rectangular plates under compression and supported along the edges is given by the Equation 8.5 (Young and Budynas, 2001).

$$F_{cr} = k \frac{\pi^2 E_s}{12 \sqrt{(1 - \nu_s^2)} \left(\frac{b}{t}\right)^2} \quad (8.5)$$

When the plate is simply supported along each edge with no out-of-plane restrains, the critical stress can be obtained with $k = 4$ and the corresponding buckling shape is the one shown in Figure 8.1.a. Thus, the theoretical width-thickness limit for steel slender cross-sections can be obtained by letting $F_{cr} = F_y$ and assuming $\nu_s = 0.3$ as in the Equation 8.6.

$$\frac{b}{t} = \sqrt{4 \frac{\pi^2}{12\sqrt{(1-\nu_s^2)}} \frac{E_s}{F_y}} = 1.857 \sqrt{\frac{E_s}{F_y}} \quad (8.6)$$

Calibration to existing data for plates results in lower values than the theoretical limit above since the analytical derivation does not include the initial imperfection effects and residual stresses on the plate components. The calibration with tests data for steel rectangular hollow tubes has led to the limit of $1.40\sqrt{E_s/F_y}$ (SSRC, 1998), which has been adopted in the AISC Specifications.

Uy and Bradford (1996) re-derived Equation 8.5 with different boundary conditions on the edges and with a rigid restraining surface in one side of the plate. The solution with simply supported edges and a rigid restraining surface in one plate is given by the Equation 8.5 with the factor $k=10.3$; previous derivations with similar conditions have resulted in buckling coefficients of 10.67 (Timoshenko and Gere, 1972) and 9.33 (Faxen, 2000). In the AISC (2010), a buckling coefficient of $k=10.0$ was adopted for slender composite cross-sections (Zhang and Varma, 2009), and so assuming $\nu_s=0.3$ and $F_{cr} = F_y$, Equation 8.5 is simplified as in 8.7.

$$F_{cr} = \frac{9E_s}{\left(\frac{b}{t}\right)^2} \rightarrow \frac{b}{t} = 3 \sqrt{\frac{E_s}{F_y}} \quad (8.7)$$

Based on available experimental data and other studies, the limit for non-compact RCFTs in AISC (2005, 2010) was set as $2.26\sqrt{E_s/F_y}$ (Leon *et al.*, 2007).

The previous limits adopted in AISC (2005, 2010) are about 47% higher than the corresponding limits adopted by the Japanese specifications of the AIJ (2001) as shown in Figure 8.3 (Sakino *et al.*, 2004). These limits are given by $2.03\sqrt{E_s/F_y}$ for slender (or type 2) rectangular filled-tubes, and $1.54\sqrt{E_s/F_y}$ for non-compact (or type 1) composite sections.

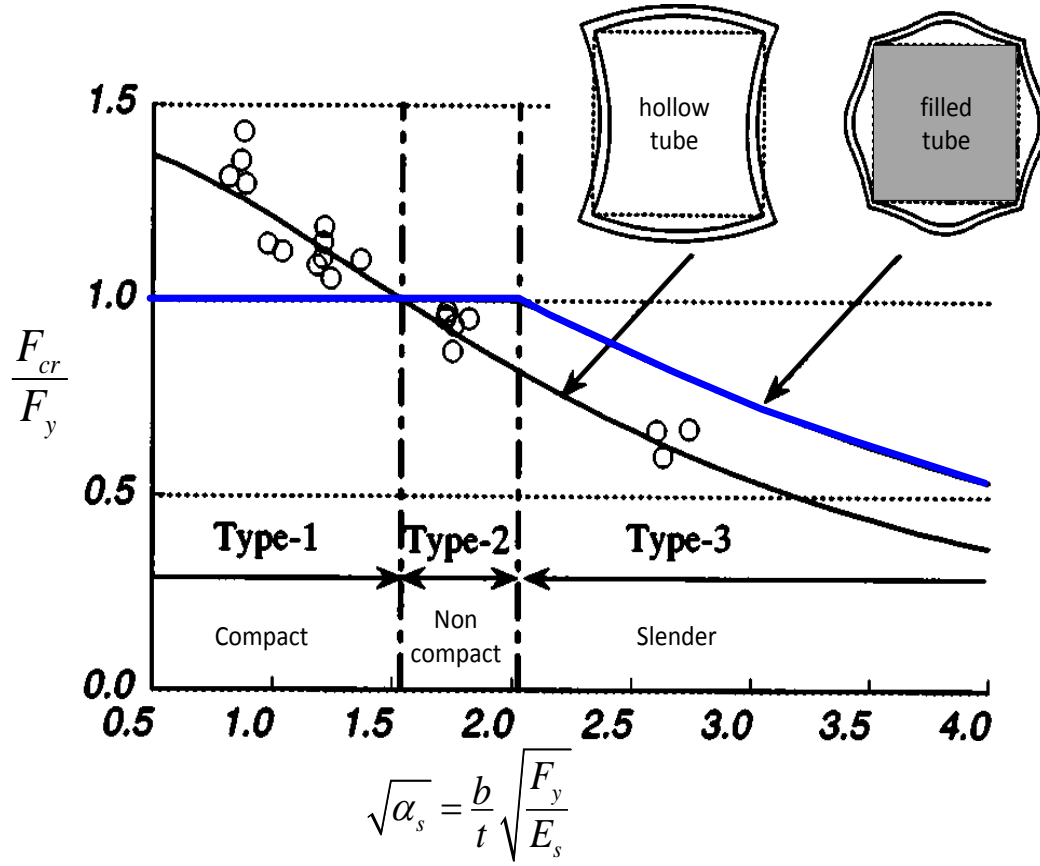


Figure 8.3. Critical stress in hollow and filled rectangular tubes in the AIJ (2001). Figure adapted from Sakino et al. (2004)

8.2.5. Previous empirical calibrations on the initiation of local buckling

The constitutive material models proposed by Sakino *et al.* (2004) for both CCFTs and RCFTs were summarized in Chapter 2. Sakino's model incorporates some of the salient features of CFT members, and one of these features is the initiation of the local buckling and the analytical prediction of the post-buckling response. This model postulates that local buckling in circular tubes is reached at high values of strain, and therefore, local buckling effects can be neglected; this approach is tied to the Japanese design requirements for D/t ratios which basically preclude this failure mode with circular shapes. For RCFTs, in turn, this model assumes that local buckling takes off at a fixed value of strain (ε_{lb}). For RCFTs with compact tubes (or type 1), local buckling develops at a strain ε_{lb} given by the following equation.

$$\varepsilon_{lb} = \left(6.06 \frac{1}{\alpha_s^2} - 0.801 \frac{1}{\alpha_s} + 1.10 \right) \varepsilon_y \quad (8.8)$$

where the factor α_s is defined by:

$$\alpha_s = \left(\frac{b}{t} \sqrt{\frac{F_y}{E_s}} \right)^{\frac{1}{2}} \quad (8.9)$$

According to this model, local buckling occurs at the yield strain ($\varepsilon_{lb} = \varepsilon_y$) for non-compact sections (or type 2), and at a strain within the elastic range for slender sections (or type 1) by.

$$\varepsilon_{lb} = \left(\frac{1}{0.698 + 0.073(h/t)^2 \varepsilon_y} \right) \varepsilon_y \quad (8.10)$$

The previous equations can be rewritten and grouped in terms of the yielding strain (ε_y) and the wall slenderness ratio ($\lambda = h/t$) as:

$$\varepsilon_{lb} = \begin{cases} \left(\frac{6.06}{\lambda^4 \varepsilon_y^2} - \frac{0.801}{\lambda^2 \varepsilon_y} + 1.10 \right) \varepsilon_y & \text{if } \lambda \leq 1.54/\sqrt{\varepsilon_y} \\ \varepsilon_y & \text{if } 1.54/\sqrt{\varepsilon_y} < \lambda < 2.03/\sqrt{\varepsilon_y} \\ \frac{\varepsilon_y}{0.698 + 0.073 \lambda^2 \varepsilon_y} & \text{if } \lambda \geq 2.03/\sqrt{\varepsilon_y} \end{cases} \quad (8.11)$$

As summarized also in Chapter 2, Tort and Hajjar (2007) and Denavit and Hajjar (2010) have calibrated constitutive models for the steel component in RCFTs and CCFTs with experimental data. These references have also proposed the initiation of the local buckling at a strain given by:

$$\varepsilon_{lb} = \begin{cases} 0.214 R^{-1.41} (F_y/E_s) & \text{for CCFT} \\ 3.14 R^{-1.48} (F_y/E_s) & \text{for RCFT} \end{cases} \quad (8.12)$$

where the normalized slenderness factor R is given by:

$$R = \begin{cases} \frac{D}{t} \cdot \frac{F_y}{E_s} & \text{for CCFT} \\ \frac{h}{t} \sqrt{\frac{F_y}{E_s}} & \text{for RCFT} \end{cases} \quad (8.13)$$

The calibration documented by Tort and Hajjar (2007) is based on a fit curve of 23 tests of RCFT columns loaded in monotonic compression. The coefficient of variation of the fitted curve is $R^2=0.61$. This set of collected data and its calibration is shown in Figure 8.4.

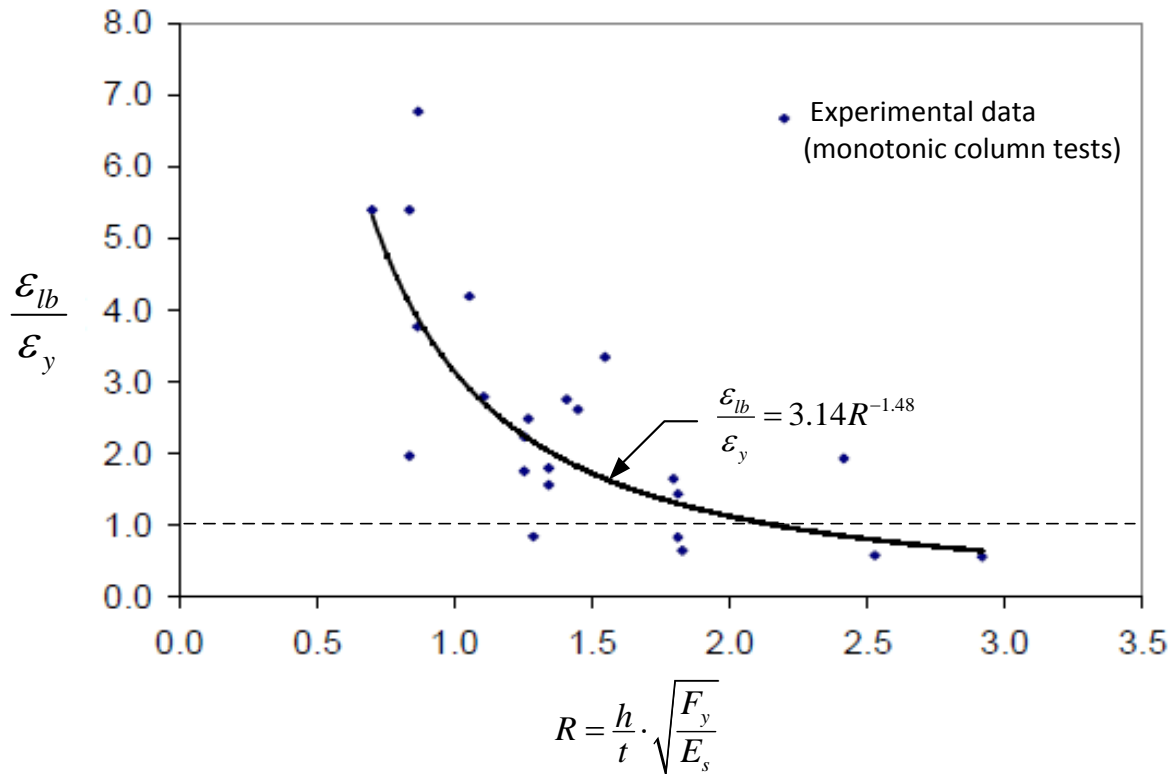


Figure 8.4. Calibration of the strain at local buckling by Tort and Hajjar (2007)

The calibration reported by Denavit and Hajjar (2010) is based on a fit curve of six data tests of CCFT specimens. The coefficient of variation of the fitted curve is $R^2=0.92$. This set of collected data and its calibration is shown in Figure 8.5.

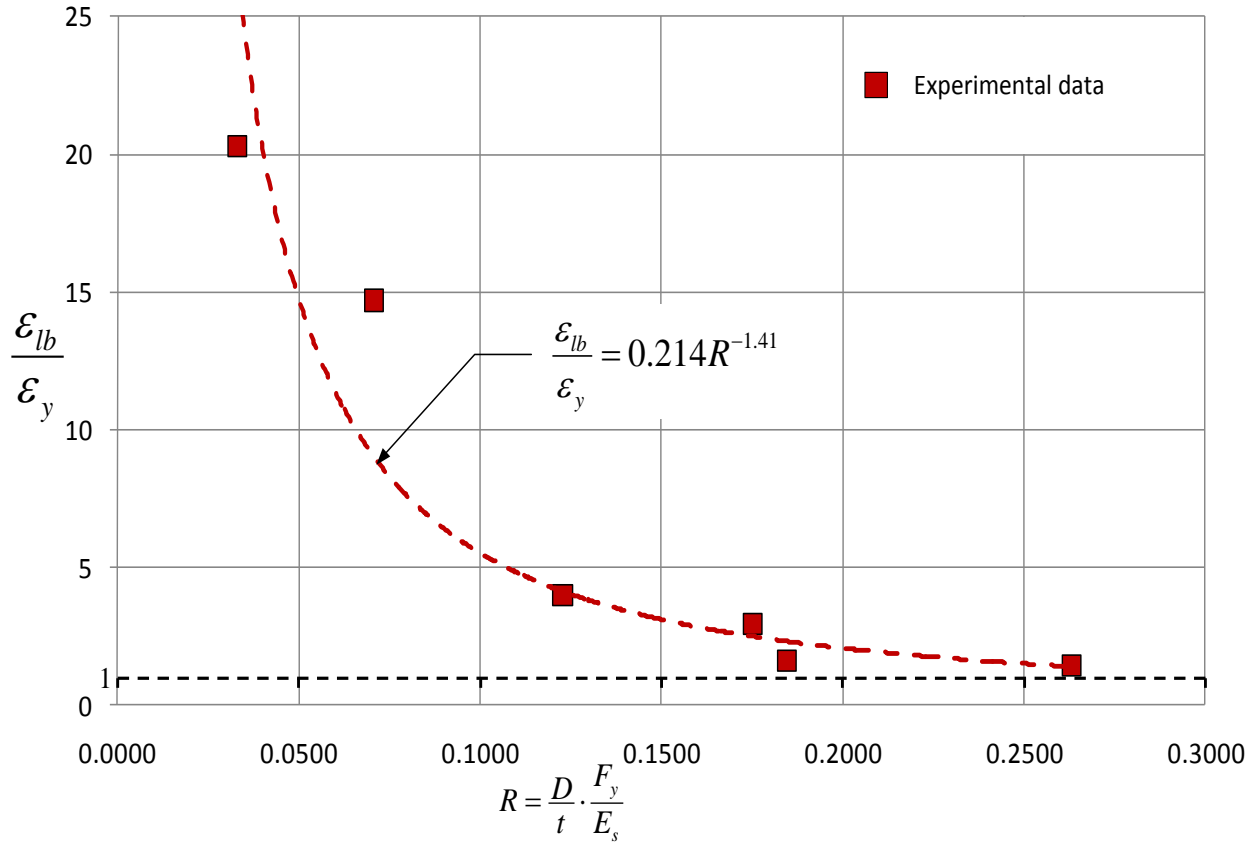


Figure 8.5. Calibration of the strain at local buckling by Denavit and Hajjar (2010)

Equation 8.12 can be rewritten in terms of the yielding strain (ϵ_y) and the wall-slenderness ratio (λ) of the steel tube as shown in Equation 8.14.

$$\epsilon_{lb} = \begin{cases} 0.214\lambda^{-1.41}\epsilon_y^{-0.41} & \text{For CCFTs} \\ 3.14\lambda^{-1.48}\epsilon_y^{0.26} & \text{For RCFTs} \end{cases} \quad (8.14)$$

Equation 8.11 by Sakino *et al.* (2004) and Equation 8.14 by Tort-Hajjar (2007) and Denavit-Hajjar (2010) are plotted in Figure 8.6 with the wall-slenderness ratio ($\lambda = D/t$ or h/t) vs. the strain at occurrence of local buckling normalized with the strain at yielding. The corresponding limiting wall-slenderness ratios (λ_p) in AISC (2005, 2010) for non-compact filled-tubes are marked in this figure. The three calibrated curves and the λ_p limits shown in Figure 8.6

were obtained with nominal strength parameters ($E_s=29000$ ksi, $F_y=42$ ksi for circular tubes, and $F_y=46$ ksi for rectangular tubes).

As observed in Figure 8.6 the two proposed curves for the local buckling strain in RCFTs present very close values. However, the curve by Tort and Hajjar (2007) is a continuous function, while the proposed by Sakino et al. (2004) is a tri-linear curve for the three wall-slenderness types. In addition, this figure shows the non-compact wall-slenderness limits (λ_p) established in AISC (2005, 2010) intersecting the local buckling strain of these calibrations at about one and three times the yielding strain for RCFTs and CCFTs, respectively. Theoretically, the wall slenderness limit for slender sections (λ_r) should correspond to a critical stress equal to yielding stress, or in other words, when the ratio $\varepsilon_{lb}/\varepsilon_y=1$.

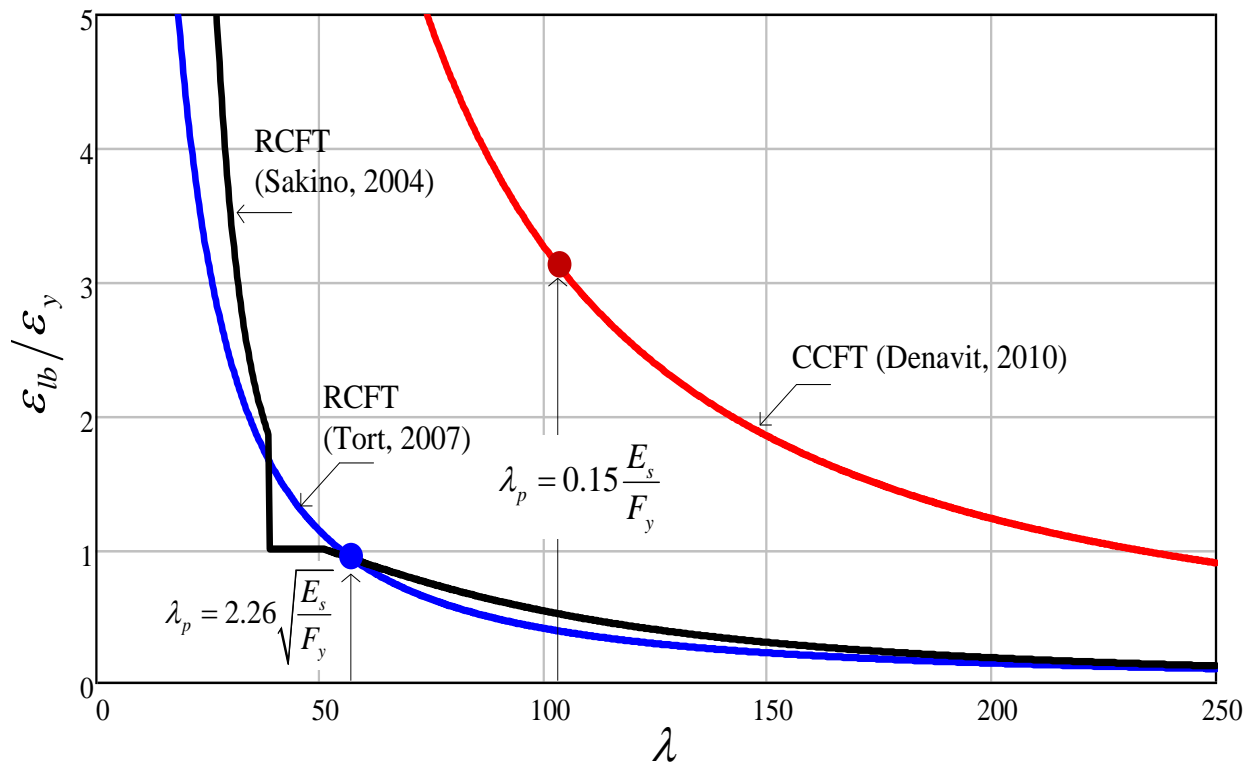


Figure 8.6. Wall-slenderness ratio vs. strain at occurrence of local buckling

The initiation of the local buckling in the stress-strain curves in compression as obtained by the previous equations is also illustrated in Figure 8.7. The stress-strain response measured in coupon tests (with no local buckling allowed) is also included in this figure as a reference. The analytical stress-strain curve is obtained from the corresponding material and geometric properties (i.e F_y , F_u , E_s , D , t) measured from the coupon tests; the samples used in the coupon

tests were taken from the specimens tested in this project. As observed in Figure 8.7, the analytical prediction on the initiation of local buckling is expected at a strain of 0.0130 for the HSS5.563x0.134 tubes, 0.0104 for the HSS12.75x1/4 sections, 0.0056 for the HSS20x1/4 tubes, and 0.0012 for the HSS20x12x5/16 rectangular sections.

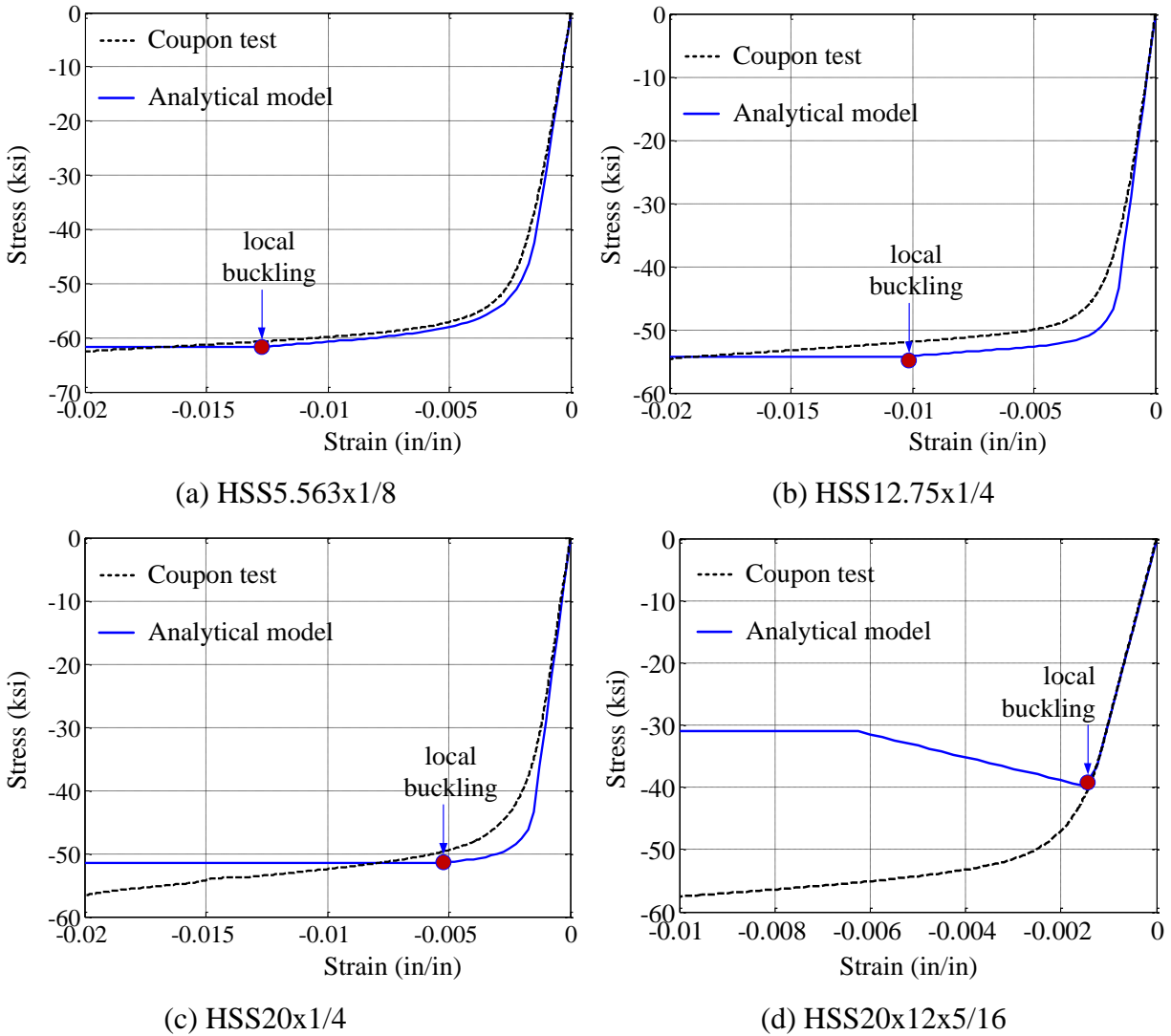


Figure 8.7. Local buckling deformation at the end of the test for the C5 group

8.2.6. Experimental extraction of local buckling from the experimental tests

Accurate calibration of the pre, occurrence and post-local buckling behavior is one of the key parameters in any robust model for member response. As described in Chapter 2 and the previous section, local buckling has been primarily introduced in the steel material constitutive

model. Current models for CFTs (i.e. Sakino *et al.* 2004, Tort and Hajjar 2007, Denavit and Hajjar 2010) have degradation rules once a limit strain in compression is exceeded (ε_{lb}).

This section shows the determination of the local buckling initiation (ε_{lb}) measured in the CFT specimens that are tested in this research project.

Determination of the first occurrence of local buckling during the tests was performed through a physical evaluation of the steel specimens after each major ramp of motion; unfortunately, this evaluation could not be performed within a ramp for safety reasons and time constraints.

In addition, observation of the images captured by the eight still cameras and eight video cameras towards different views and angles of the specimen were monitored during the entire testing; however, local buckling from these images was not clearly visible until the specimen exhibited a relatively large amount of local deformations. Sometimes, even with a physical observation from a very near distance, local buckling was clearly evident unless the steel surface is patted down to feel the local buckling.

Another instrumentation device for tracking possible local buckling occurrence monitored during the entire testing were (a) the out-of-plane coordinates of the LED sensors captured by the Krypton laser camera, and (b) the amount of longitudinal strain from the three strain gauges placed at each cross-section and along the member. As reminder, the strain gauges in each cross-section were placed in the North, South and West external faces of the steel tubes, and along the member (see Chapter 3 for more details about the instrumentation). Assuming that plane sections remain plane, the three discrete points at each cross-section are sufficient to define a plane of strains within the cross-section and, from this strain distribution, the maximum strain in compression and tension can be obtained for each cross-section.

During the load case LC1, a physical observation was performed only at the end of the unloading ramp when a low axial load was sustained. Unfortunately, the inspection was not possible at the maximum peak load for safety reasons. The specimen at this peak axial force tended to drive sideways since the crosshead was set in horizontal force control. However, local buckling during LC1 was not observed from the set of cameras, from direct observation of the specimen from a distant and safe position, or from the out-of-plane LED readings by the Krypton camera.

In addition, the maximum longitudinal strain measured during LC1 for the 18 specimens was lower than the expected ε_{lb} strains calculated with the Equation 8.11 and Equation 8.12 that were discussed in the previous section. From these empirical equations, the expected strains at which local buckling were expected (ε_{lb}) are above five times the yielding strain in the CCFTs, about three times the yielding strain in RCFTs oriented in the strong axis (R_s group), and just above the yielding strain in the RCFTs oriented in the weak axis (R_w group). Only for the latter R_w group, the maximum strain measured at LC1 was quite close to the expected ε_{lb} strains; however, careful analysis of the photographic record and the out-of-plane deformations from the LED readings do not show any evidence of local buckling in these specimens neither at the peak axial load nor at the peak lateral deformation during LC1.

During the subsequent load cases (LC2, LC3 and LC4), physical evaluation of the steel tubes was performed at the end of each principal ramp of motion, especially when local buckling was expected, observed or measured through simultaneous evaluation of the strain gauge data, the Krypton record, and the photographic images. At the time local buckling was first detected, both the load case and the ramp at which this local buckling deformation occurred were documented accordingly. Local buckling does not appear to have occurred in three particular specimens (2C12-18-5, 6-C12-18-12 and 18C5-26-12) for any of the load cases applied.

Based on the ramp motion and the load case reported at the time of testing, a careful examination of the photo images gallery and the out-of-plane coordinate readings from the Krypton data within the ramp was performed in order to get a more accurate time of the first local buckling occurrence. This information was also related with the maximum compressive strain calculated at the nearest cross-section that locally buckled. As noted earlier, the maximum computed strain in the cross-section is computed from three measured strain data within the cross-section assuming plane strain remains plane.

Table 8.3 summarizes, for each specimen, the extracted maximum compressive strain at which the local buckling initially occurred (ε_{lb_test}) within the documented load case, and its normalized value with the yielding strain ($\varepsilon_{lb_test}/\varepsilon_y$). In addition, this table contains wall-slenderness ($\lambda_w = D/t$ or h/t) and its normalized slenderness parameter (R) as defined by the Equation 8.13. The strains reported in this table for the specimens that did not locally buckled correspond to the maximum longitudinal values obtained in the entire load protocol.

Table 8.3. Strain at the first occurrence of local buckling during the testing

SPECIMEN	Load case	Slenderness $\lambda_w = D/t, h/t$	R Eq. 8.13	ε_{lb_test}	$\varepsilon_{lb_test}/\varepsilon_y$
1C5-18-5	LC4	45	0.086	0.0272	14.19
18C5-26-12	NA	45	0.086	0.0052	2.71
2C12-18-5	NA	55	0.092	0.0077	4.57
6C12-18-12	NA	55	0.092	0.0054	3.20
10C12-26-5	LC4	55	0.092	0.0180	10.74
14C12-26-12	LC3c	55	0.105	0.0155	8.10
3C20-18-5	LC2a	86	0.141	0.0083	5.09
7C20-18-12	LC3a	86	0.141	0.0074	4.51
11C20-26-5	LC3a	86	0.131	0.0101	6.61
15C20-26-12	LC2b	86	0.126	0.0093	6.35
4Rw-18-5	LC2a	69	2.938	0.0030	1.64
8Rw-18-12	LC3a	69	2.938	0.0025	1.37
12Rw-26-5	LC3a	69	3.097	0.0026	1.28
16Rw-26-12	LC3a	69	3.000	0.0023	1.21
5Rs-18-5	LC2a	41	1.763	0.0065	3.57
9Rs-18-12	LC2a	41	1.763	0.0058	3.16
13Rs-26-5	LC2a	41	1.804	0.0075	3.92
17Rs-26-12	LC2a	41	1.798	0.0062	3.26

* Local buckling did not occur.

The normalized empirical strains at the initiation of local buckling ($\varepsilon_{lb_test}/\varepsilon_y$) vs. the normalized slenderness parameter (R) are plotted in Figure 8.8 for the CCFT specimens and in Figure 8.9 for the RCFTs. The data used by Denavit and Hajjar (2010) and Tort and Hajjar (2007) in the calibration of the local buckling initiation for CCFTs and RCFTs, respectively, is included in these figures (as red diamonds), as well as their proposed empirical curve-fitting equations (as red dashed curve). The initial local buckling strains determined empirically in the present research project are indicated in Figure 8.8 as blue circles for the CCFTs, and in Figure

8.9 as blue rectangles for the RCFTs; the blank circles in Figure 8.8 indicate those specimens where local buckling did not occur. For reference, the specimen number is also indicated next to the marker.

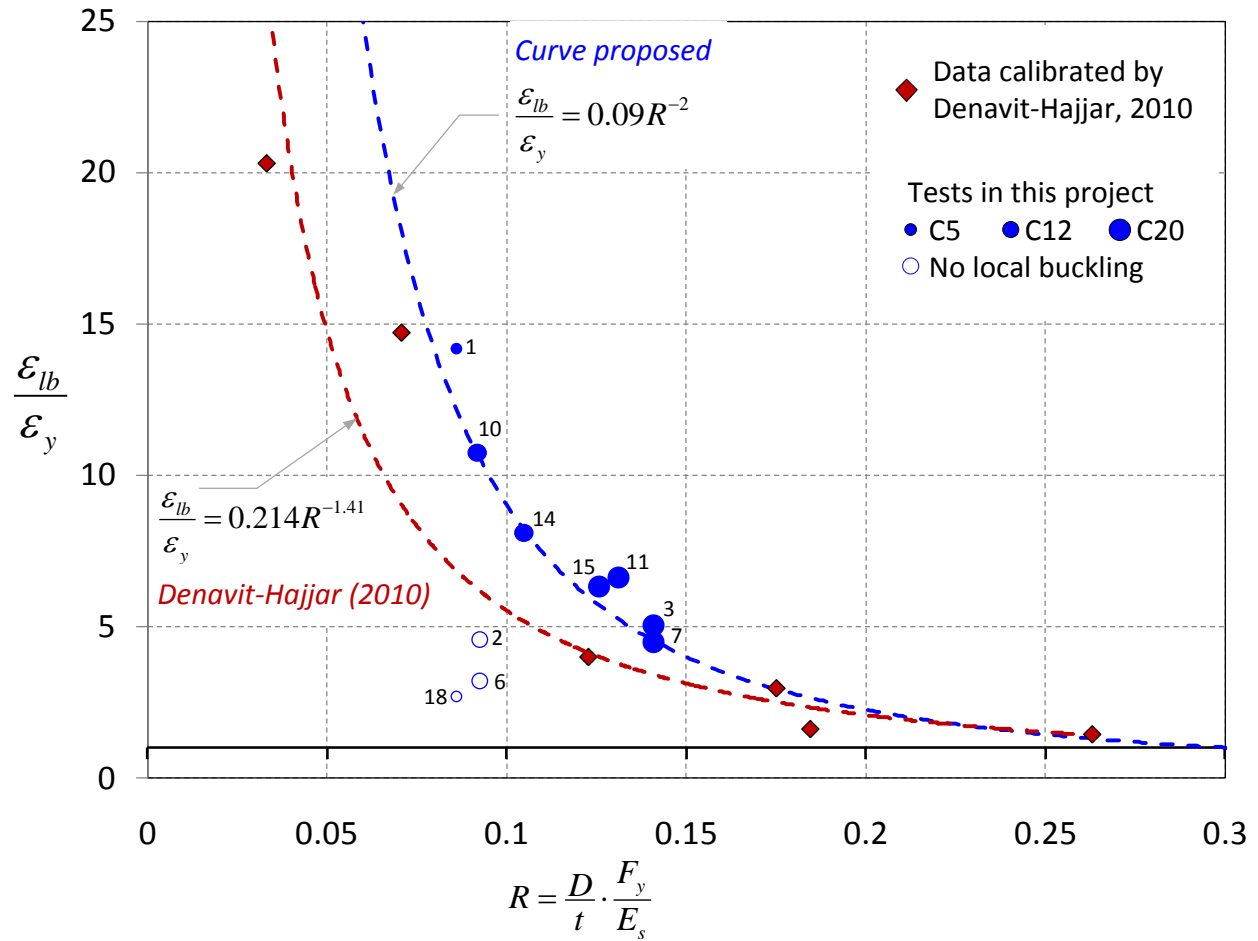


Figure 8.8. Calibration of the local buckling initiation for CCFTs

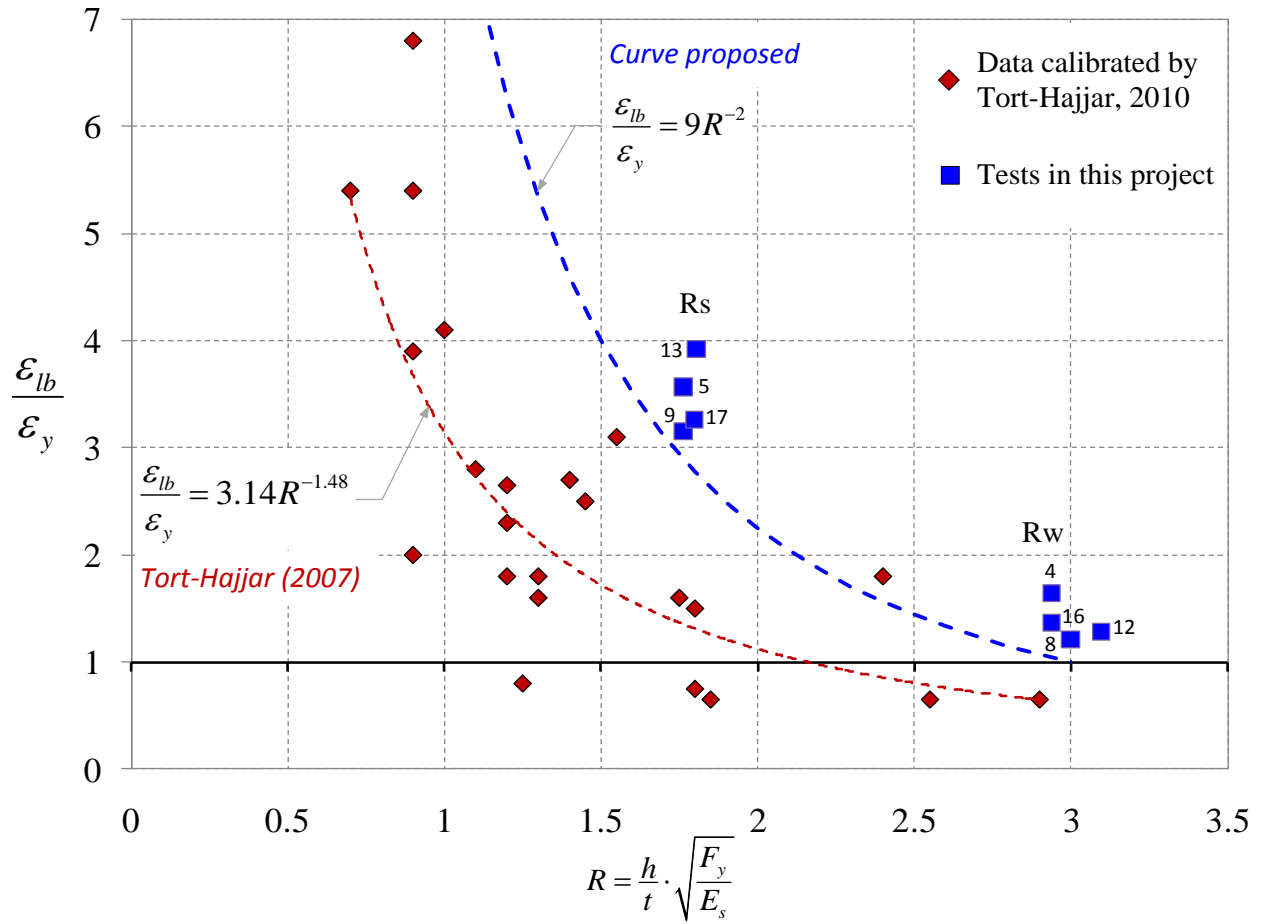


Figure 8.9. Calibration of the local buckling initiation for RCFTs

Based on the empirical data obtained in these tests, an update of empirical equations for the local buckling initiation is proposed. The proposed equations are included in Figure 8.8 and Figure 8.9 as a dashed-blue curve; all the element components are properly labeled in these figures.

$$\epsilon_{lb} = \begin{cases} 0.09 \left(\frac{D}{t} \cdot \frac{F_y}{E_s} \right)^{-2} \frac{F_y}{E_s} = \frac{0.09}{\lambda^2 \cdot \epsilon_y} & \text{for CCFTs} \\ 9 \left(\frac{h}{t} \sqrt{\frac{F_y}{E_s}} \right)^{-2} \frac{F_y}{E_s} = \frac{9}{\lambda^2} & \text{for RCFTs} \end{cases} \quad (8.15)$$

As seen in Figure 8.8 and Figure 8.9, the proposed empirical equations predict lower strains (or conservative) than those extracted in this project, but higher (or unconservative) than those reported in previous empirical data. Differences in CCFT members are not considerable as those differences obtained in the RCFT specimens. The larger dispersion in the RCFTs is a consequence of the large disparity on the initial imperfections of the plate components and some additional outward deformation as a consequence of the hydrostatic pressure of the wet concrete. As noted in the experimental description, the RCFTs tested in this project were braced at critical sections in order to diminish the expansion in the tubes when these were casted. No additional details about these differences are explored, but more exhaustive evaluation of all the available data and their parameters (L , b , d , t , λ_p , λ_r , R , bracing, imperfections, etc.) is highly recommended for future research.

The limits for slender filled tubes (λ_r) are obtained from the empirical calibration equations (Equation 8.14) when the local buckling strain reaches yielding ($\varepsilon_{lb} = \varepsilon_y$ or $\varepsilon_{lb}/\varepsilon_y = 1$). These limits are given by:

$$\lambda_r = \begin{cases} 0.3 \frac{E_s}{F_y} & \text{for CCFTs} \\ 3.0 \sqrt{\frac{E_s}{F_y}} & \text{for RCFTs} \end{cases} \quad (8.16)$$

Limits for non-compact filled tubes (λ_p) from the empirical calibration equations associated to local buckling strains are propose as four times yielding in circular filled tubes ($\varepsilon_{lb}/\varepsilon_y = 4$) and two times yielding in rectangular filled tubes ($\varepsilon_{lb}/\varepsilon_y = 2$); the higher limit in CCFTs is justified by the higher performance of the circular tubes. These limits are:

$$\lambda_p = \begin{cases} 0.15 \frac{E_s}{F_y} & \text{for CCFTs} \\ 2.12 \sqrt{\frac{E_s}{F_y}} & \text{for RCFTs} \end{cases} \quad (8.17)$$

The latter propose ranges aim to establish reliable and consistent limits with the current AISC Specifications. The limits λ_p and λ_r stated above are very close to the limits defined in the AISC (2010) for CFT cross-sections that are shown in Table 8.1.

The limits proposed above for CFTs under both compression and flexure loading that delimits compact, non-compact and slender cross-sections in CFT columns and beam-columns are illustrated in Figure 8.10 and Figure 8.11.

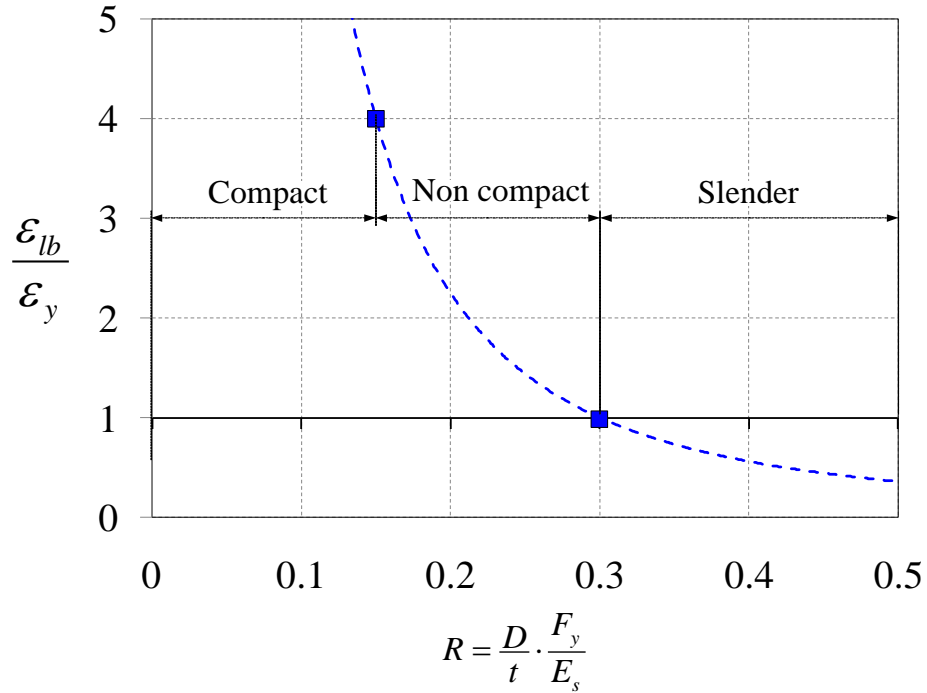


Figure 8.10. Proposed limits for compact, non-compact and slender sections in CCFTs

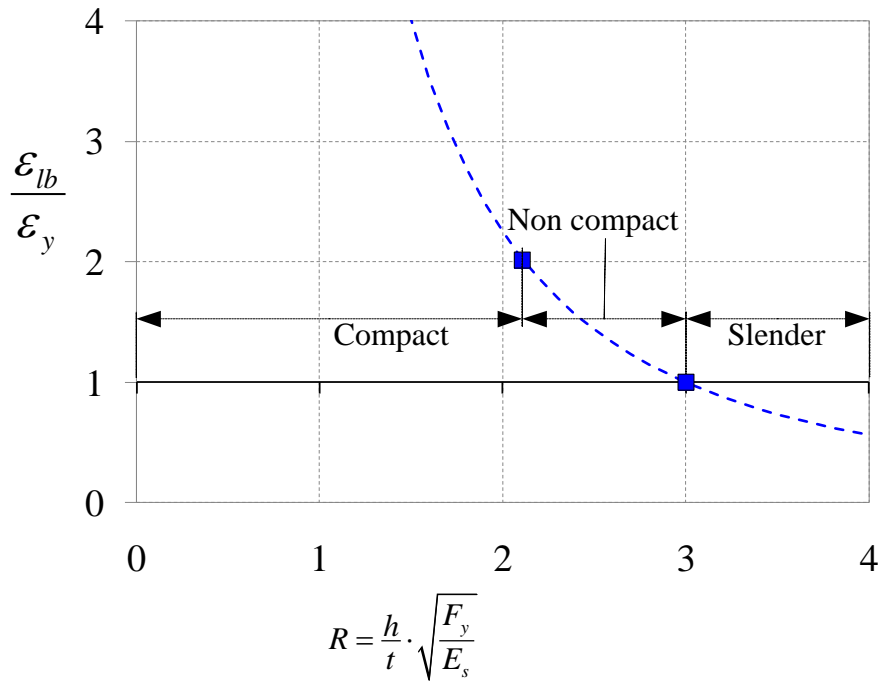
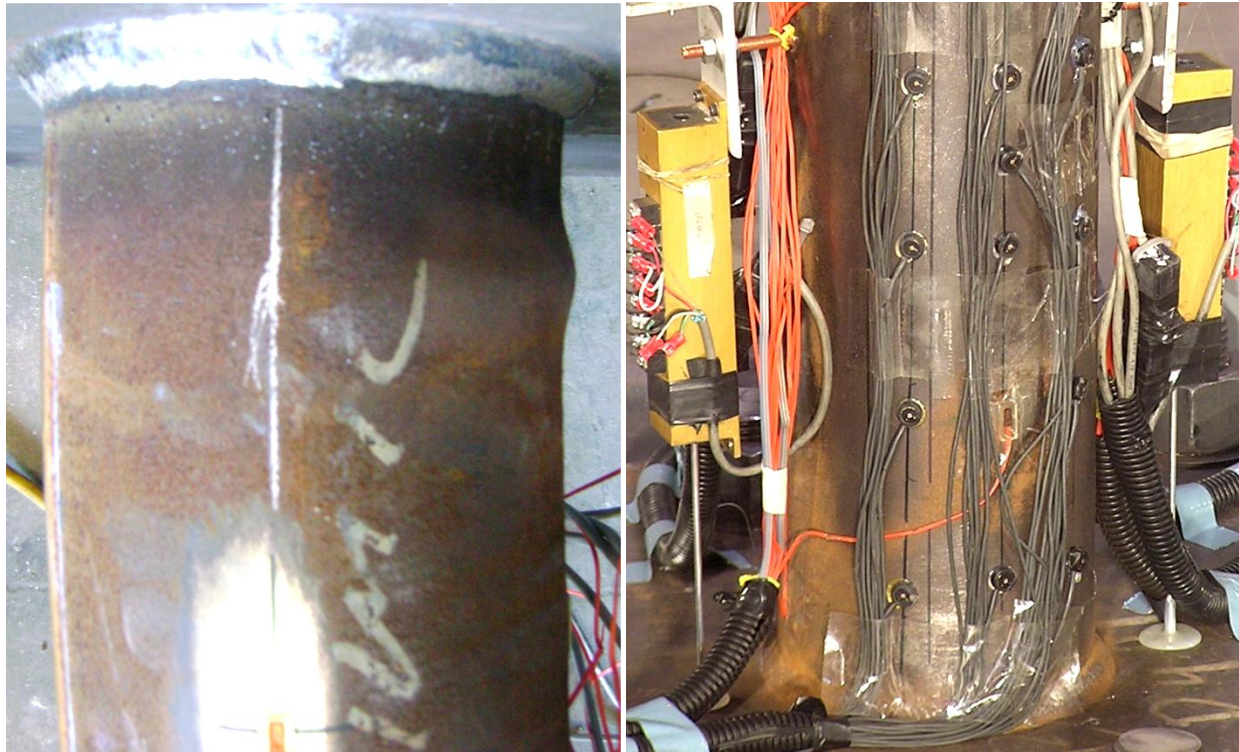


Figure 8.11. Proposed limits for compact, non-compact and slender sections in RCFTs

The results shown above correspond to the initiation of local buckling. However, once local buckling started, the amount of local deformation progressed through the loading protocol. The final local buckling deformation of the 18 CFT specimens tested in this project after completing the load protocol is shown from Figure 8.12 to Figure 8.15. The following observations can be made from these images.

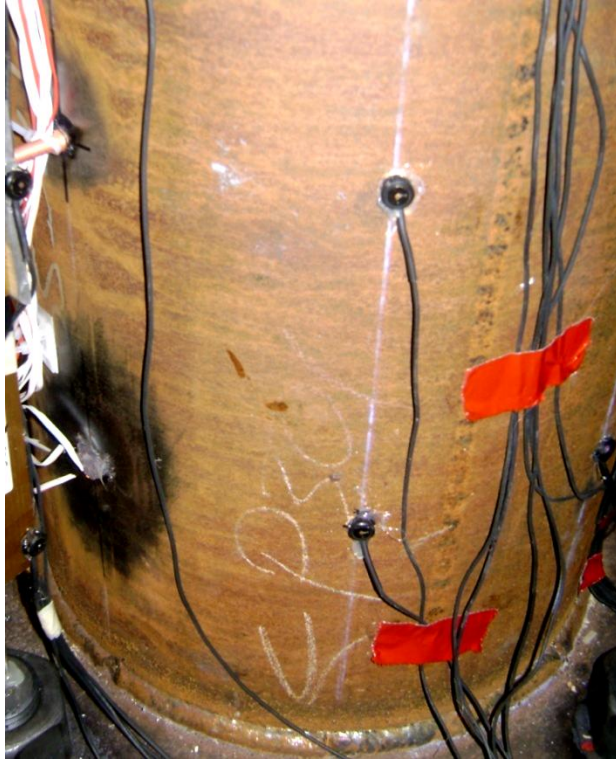
- As a consequence of a low diameter-thickness ratio in the CCFTs with 5.563 and 12.75 inches of diameter (45 and 55, respectively), the amount of local buckling is either low (as in specimens 1, 10, 14) or inexistent (as in specimens 2, 6, and 18). Differences in the final accumulated amount of local buckling in these specimens are due to differences in the strain demands in the applied load protocol.
- As expected due to the shape and the large wall-slenderness ratios, local buckling in RCFTs exhibited a much higher amount of local deformation.
- During LC2, local buckling was developed earlier in RCFTs oriented in weak axis than the RCFTs oriented in strong axis; however, once the LC3 was completed, both weak and strong axis cases exhibited similar amount of local deformation.



(a) 1C5-18-5

(b) 18C5-26-12

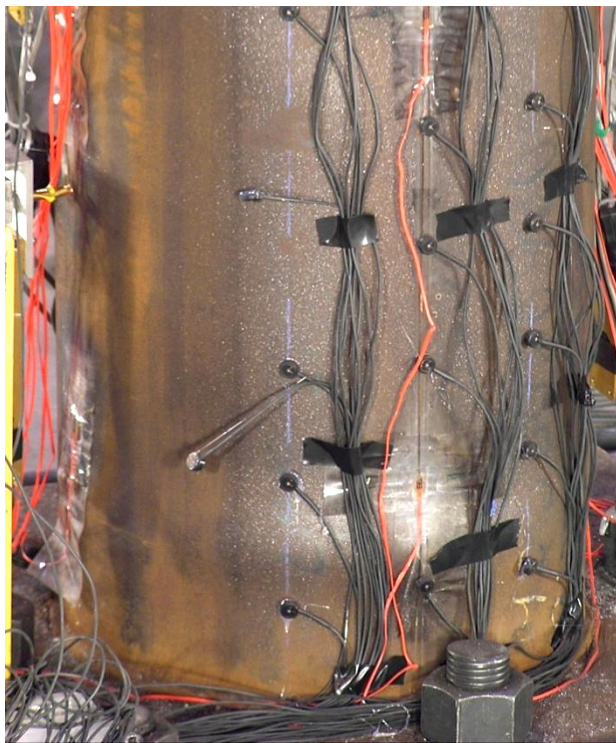
Figure 8.12. Local buckling deformation at the end of the test for the C5 group



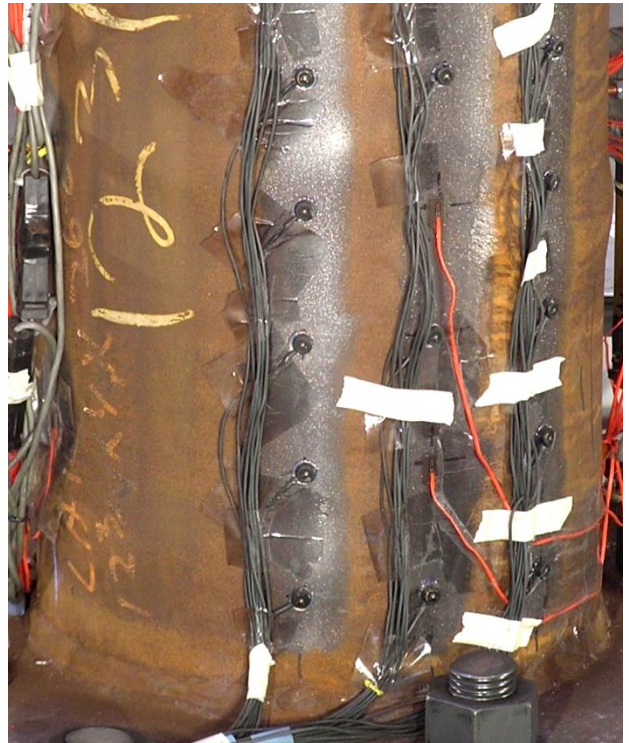
(a) 2C12-18-5



(b) 6C12-18-12



(c) 10C12-26-5

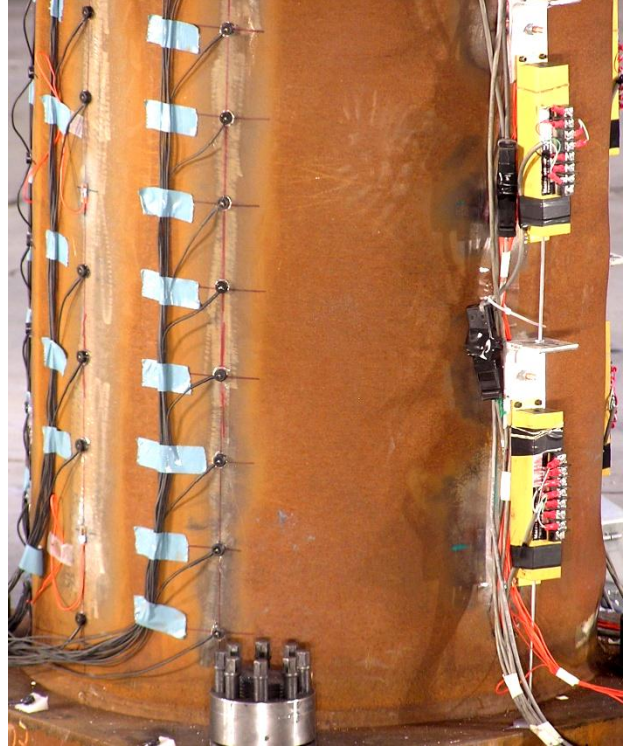


(d) 14C12-26-12

Figure 8.13. Local buckling deformation at the end of the test for the C12 group



(a) 3C20-18-5



(c) 11C20-26-5

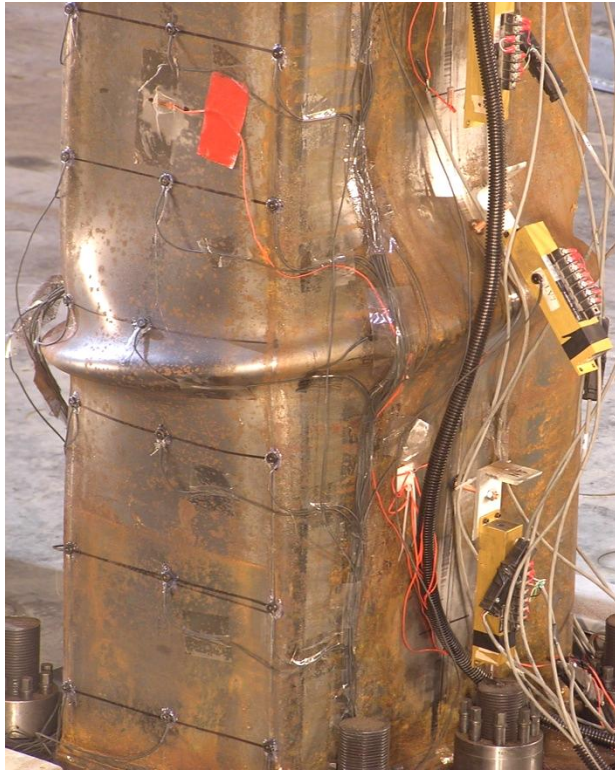


(b) 7C20-18-12



(d) 15C20-26-12

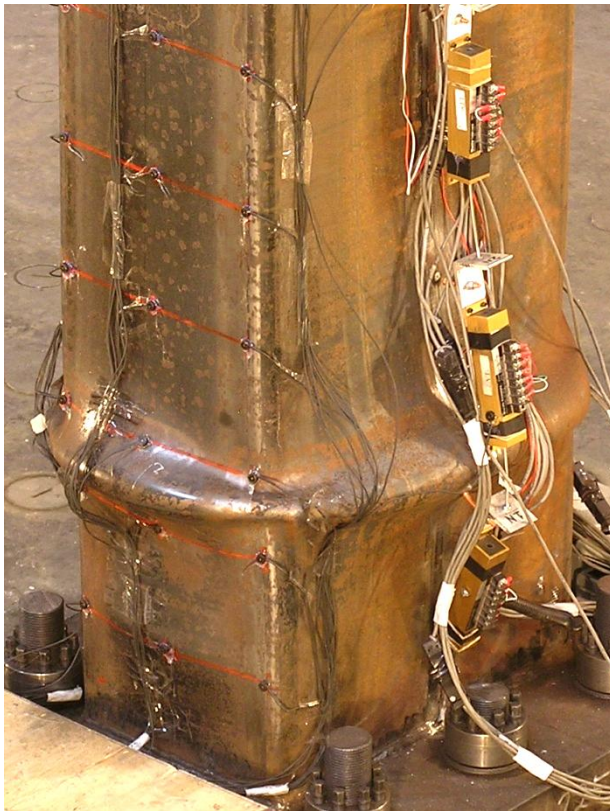
Figure 8.14. Local buckling deformation at the end of the test for the C12 group



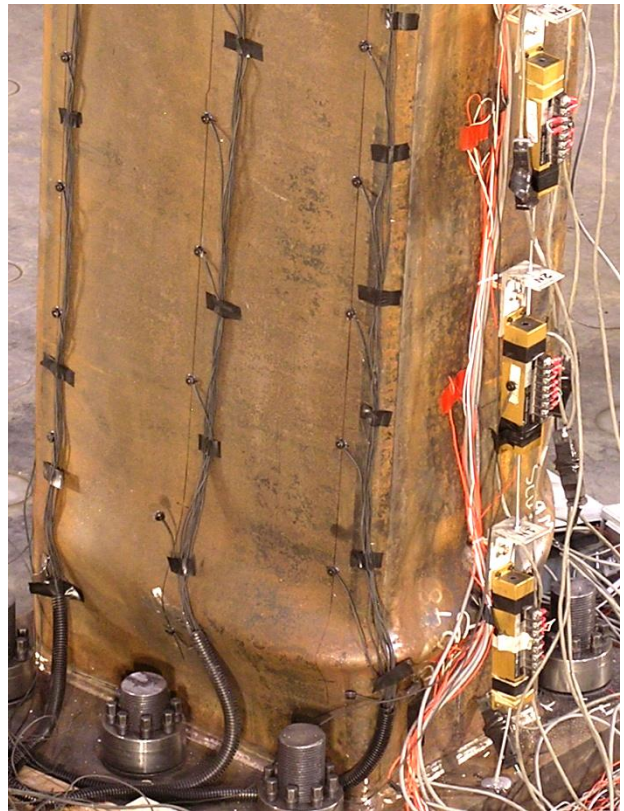
(a) 4Rw-18-5



(b) 5Rs-18-5



(c) 8Rw-18-12

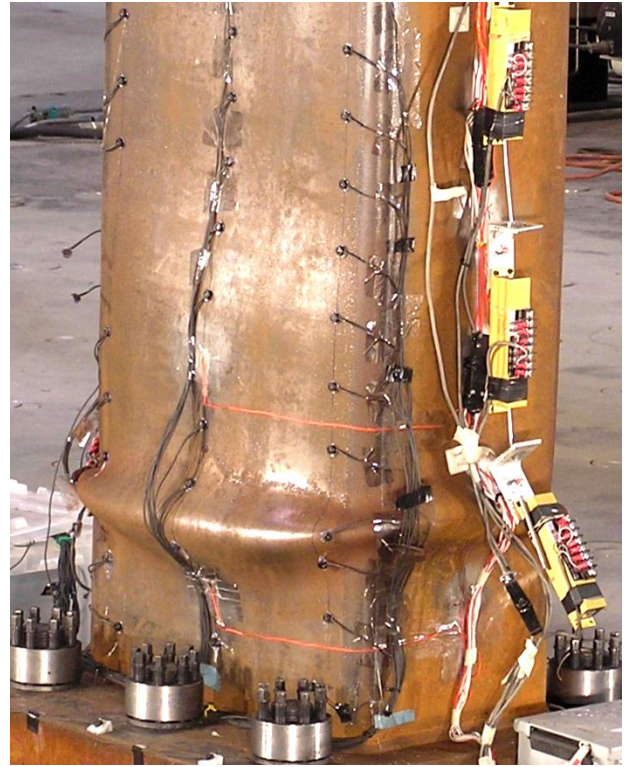


(d) 9Rs-18-12

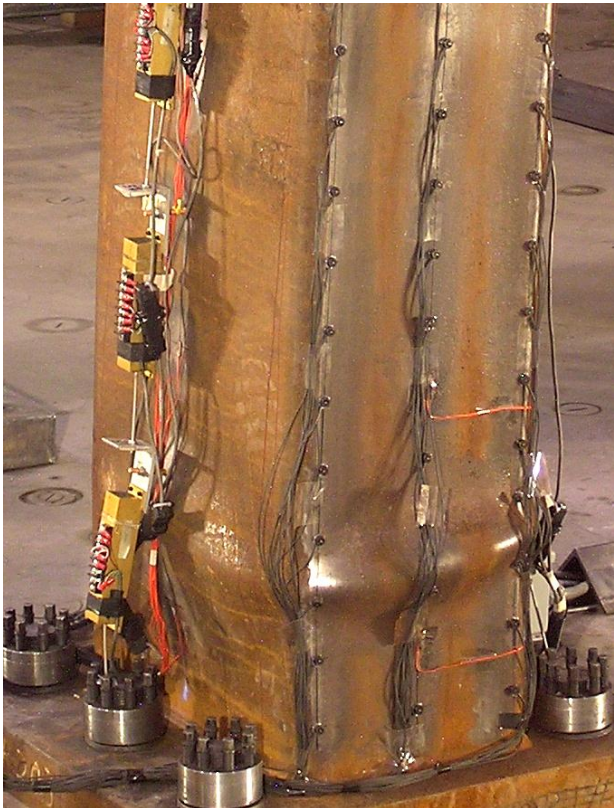
Figure 8.15. Local buckling deformation at the end of the load protocol in RCFTs



(a) 12Rw-26-5



(b) 13Rs-26-5



(c) 16Rw-26-12



(d) 17Rs-26-12

Figure 8.15. Local buckling deformation at the end of the load protocol in RCFTs (cont.)

- Local buckling deformation during the torsional loading (LC4) progressed diagonally in the RCFTs, mainly on their wider plates; this effect can be seen in Figure 8.15.b for the specimen 5Rs-18-5. No out-of-plane deformation was observed due to the torsional loading in the CCFTs.
- Figure 8.15 illustrates differences in the position of the local buckling, being at higher elevation in specimen 4 (which was not braced at the concrete casting, and so wet concrete pressure increased the imperfections of the steel tube), or being at a lower position in specimens 9 or 17 (which were braced to avoid the expansion due to the wet concrete pressure). As commented in Chapter 4, the position of local buckling in height is influenced by the amount and position of initial imperfections of the plate components and the outward deflection created by the hydrostatic pressure of the wet concrete.
- As summarized in Table 8.3, most specimens locally buckled under the load case LC2 (compression with uniaxial bending) and, in few cases, local buckling occurred with higher strain demands during either LC3 (biaxial bending) or LC4 (as in the specimen 1). Specimens 2, 6 and 18 did not exhibit local deformation due to their small D/t ratios and the low demand/capacity ratio.
- The mechanism observed of the local buckling during LC2 is schematically illustrated in Figure 8.16, where the specimen is under constant axial load and cyclic lateral force (in the X direction for the RCFTs and the imperfection direction in CCFTs).

At some point during the first cycle with positive bending (as in Figure 8.16.a), the axial stress in the plate in compression exceeded its buckling capacity, and so deformation was developed in the outward direction. Depending on the concrete strength and the demand of axial stress, the concrete inside likely cracked in the tension side and possibly crushed in the compression side; the concrete in compression may spread the local buckling deformation either completely or partially if the concrete crushed, or remain undamaged if the confined concrete strength was not exceeded.

As shown in Figure 8.16.b, similar behavior is exhibited in the cycle with the negative bending, where the new plate in compression buckled locally if the critical capacity was exceeded. The stresses on the concrete in the compression side start with closing the cracks that were likely developed in the previous cycle, and eventually, spread the local buckling if the crushed capacity is exceeded. On the other hand, the plate that first

buckled in the previous step is now under tension loading in this cycle, and so its local deformation diminishes when the stresses pass from compression to tension; local buckling deformation in the steel tube is totally or partially recovered when the accumulated damage is not significant. The local buckling in the two extreme plates was not necessarily developed in the same elevation due to differences on the axial shortening exhibited in each plate.

As illustrated in Figure 8.16.c, residual local buckling deformation remained in the cross-section at the end of the testing when the bending moment and the axial load is completely removed; the amount of the residual deformation depends on the accumulated damage due to the demand in strain and the number of cycles.

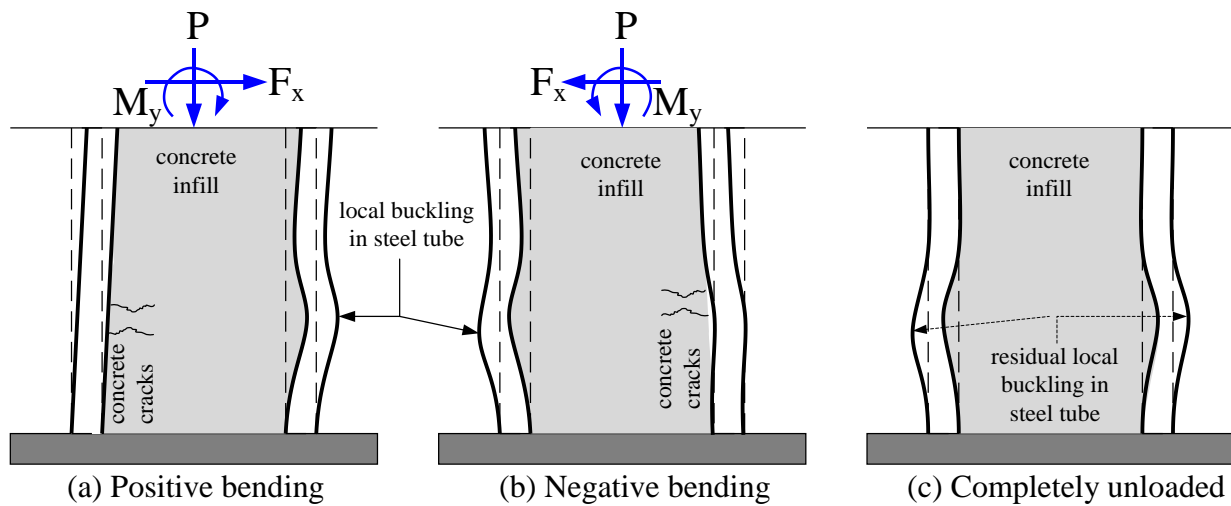


Figure 8.16. Development of local buckling during the load case LC2 (uniaxial bending)

- Differences in the amount and position of local deformation were also observed in the circular tubes filled with different concrete strengths. For those circular tubes filled with high strength concrete, local buckling developed in more than one cross-section as observed in Figure 8.13.d for specimen 14C12-26-12, and in Figure 8.14.c and 8.14d for the specimens 7C20-18-12 and 15C20-26-12, respectively. Multiple locations of local buckling were not observed in tubes filled with normal concrete strength, where local buckling developed only in the critical cross-section.

The effect of multiple cross-sections with local buckling in the circular tubes filled with high strength concrete is attributed to the effective distribution of the surfaces in contact as a consequence of the higher rigidity in high strength confined concrete.

Tubes filled with lower concrete strengths and lower confinement cracked and crushed earlier with lower loading, and when this occurs, the concrete spread the steel local buckling as illustrated in Figure 8.17.a. With a higher load, the damaged zone in both the steel and concrete increases in size.

In contrast, tubes with large D/t ratios and filled with high strength concrete may develop earlier local buckling without significant damage in the concrete. When this occurs, the steel tends to develop inward deflection near the local buckling, but this is restraint by the contact with the rigid concrete. With a higher load, the steel may exhibit additional outward local buckling deflection as illustrated schematically in Figure 8.17.b in different cross-sections until the concrete crushes; at this moment, all the developed local deformations in the steel and concrete increase in size with additional loading.

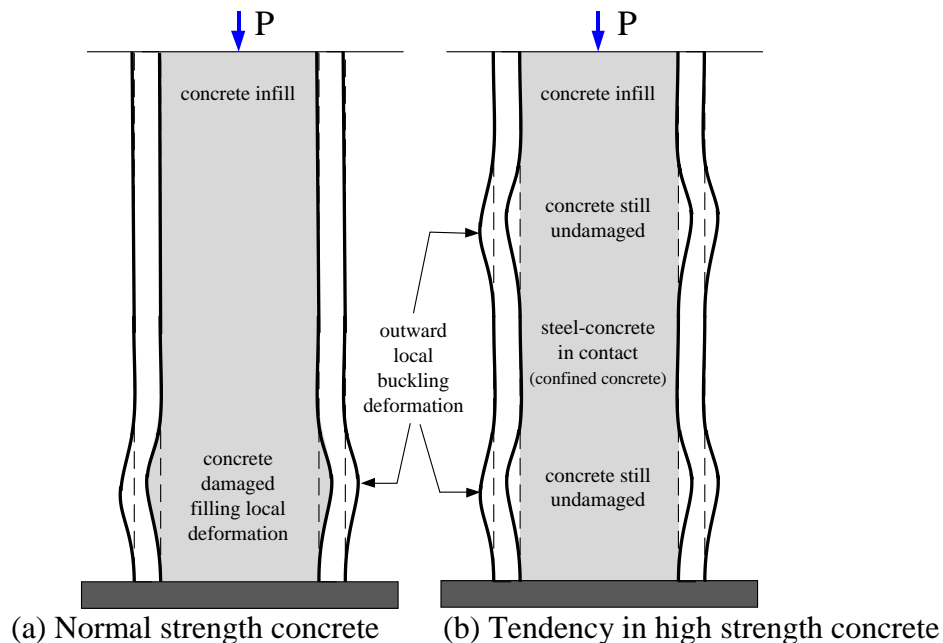


Figure 8.17. Local buckling mechanism in CCFTs with normal and high strength concrete infill

Recall that in these specimens, there are not shear studs or any other anchorage element to maintain the steel and concrete together; the concrete was poured inside the tubes and hardens with the given shape, and so they were barely in contact at the beginning of the test. The steel-concrete surfaces in contact develop frictional forces in the longitudinal and transverse direction, a negligible adhesion force when the steel-concrete surfaces have a tendency to separate in the normal direction, and a rigid (or hard) normal contact when they remain connected.

8.3. Identification of limits states

At the time of the testing in each specimen, several measured responses were monitored simultaneously. These observed responses included media records (as photo or videos) and data records (measurements from the entire instrumentation). The strain gages were monitored in order to identify in which load case the first yielding occurs, and from these then focus on the first occurrence of local buckling. The first occurrence of local buckling was discussed in detail in Section 8.2.

In this section, limit states are identified on the experimental response of the 18 CFT specimens tested in this project. The identification of these limit states is extracted from the history of the maximum compressive and tensile strains in the critical cross-section that is assumed as a plane section.

Due to the fixed-free boundary conditions ($K=2$) most commonly used to control the specimens, the strain gauges near the base were primarily the ones that registered the maximum compressive and tensile strain values. In those specimens controlled as fixed-fixed (specimen 1, 2 and 14, $K=1$), high values of strains were also measured at the cross-section near the top.

The maximum strains within the cross-section are calculated based on the three strain gages placed at the external walls in each -section by assuming linear distribution of the strains on the plane section. Table 8.4 summarizes the maximum compression (ϵ_{sc}) and tension (ϵ_{st}) strains normalized with the yielding strain (ϵ_y) of the steel tube that are obtained within the load cases LC1 and LC2; the slenderness parameter (λ) is also included in this table.

Table 8.4. Summary of the maximum strains measured within load cases LC1 and LC2

Specimen	λ	yielding strain ϵ_y	Max. strain at LC1		Max. strain at LC2		
			Compr. $\epsilon_{sc} / \epsilon_y$	Tension $\epsilon_{st} / \epsilon_y$	LC	Compr. $\epsilon_{sc} / \epsilon_y$	Tension $\epsilon_{st} / \epsilon_y$
2C12-18-5	1.55	0.0017	-0.7381	+0.2122	2a 2b 2c	-0.8125 -1.0147 -1.4894	+0.3974 +0.8545 +2.0765
6C12-18-12	1.90	0.0017	-1.5442	+1.0979	2a 2b	-1.6407 -2.3145	+1.1250 +3.1218
10C12-26-5	2.38	0.0017	-0.8163	+0.6374	2a 2b	-1.3459 -1.3413	+1.1311 +1.6038
14C12-26-12	2.72	0.0019	-0.6334	+0.5423	2a 2b 2a'	-1.6952 -1.0877 -18.2914	+2.9580 +1.4985 +23.7483
3C20-18-5	1.05	0.0016	-1.1980 *	+0.1052 *	2a 2b	-5.0858 -8.4683	+3.2817 +9.1744
7C20-18-12	1.30	0.0016	-1.6437 *	+0.6311 *	2a 2b	-4.0674 -4.4842	+11.0385 +3.4073
11C20-26-5	1.61	0.0015	-1.2717	+0.6220	2a 2b	-2.8421 -3.7748	+2.8270 +5.7679
15C20-26-12	1.78	0.0015	-0.9629	+0.1459	2a 2b	-7.3937 -5.9857	+9.1846 +2.6146
4Rw-18-5	1.38	0.0018	-2.2599	+1.0828	2a 2b	-2.6593 -2.9297	+1.5236 +3.9463
8Rw-18-12	1.65	0.0018	-1.0486	+0.8309	2a 2b	-1.0545 -0.8888	+1.3744 +3.8448
12Rw-26-5	2.14	0.0020	-0.6158	+0.6549	2a 2b	-0.9258 -1.0534	+1.5511 +1.9691
16Rw-26-12	2.30	0.0019	-0.7143	+0.1934	2a 2b	-0.8387 -0.8293	+2.1103 +1.7897
5Rs-18-5	0.88 *	0.0018	-0.5005 *	+0.0000 *	2a 2b	-3.7856 -4.5089	+1.8376 +6.0907
9Rs-18-12	1.04 *	0.0018	-0.6521 *	+0.0440 *	2a 2b	-5.6490 -7.0915	+2.7935 +11.8765
13Rs-26-5	1.35	0.0019	-0.8074	+0.1098	2a 2b	-4.0516 -5.4449	+5.6221 +4.3356
17Rs-26-12	1.46	0.0019	-1.1020	+0.5400	2a 2b	-3.3302 -8.9447	+7.9362 +16.692
1C5-18-5	0.90	0.0019	-3.7576	+1.3323	2a 2b 4a	-0.4626 -0.5243 -14.1877	0.1443 0.2484 13.1320
18C5-26-12	1.50	0.0019	-1.2666	0.4470	2a 2b	-1.2659 -1.3076	3.6680 3.4100

Note: (*) The system did not buckle since the system reaches and reverses at the maximum axial capacity (1320 kip).

The limit states identified in this section correspond to:

- First yielding in compression (ε_{yc}) and tension (ε_{yt}) on the steel tube: These limit states are identified when the corresponding maximum compressive and tensile strains in the outside of the steel cross-section reach the yielding strain ($\varepsilon_{yc} = \varepsilon_{yt} = F_y / E_s$) calculated by the Hooke's law. The yield stress and the Young's modulus are obtained from the coupon tests presented in Chapter 3 and Appendix A.
- Concrete crushing (ε_{cc}): This limit state is calculated with an interpolation of the measured strains on the steel cross-section. Since a plane section hypothesis is assumed, the maximum strains in the concrete are the same than the maximum strains in the inside of the steel tube. Thus, crushing concrete was identified when the maximum compressive strain reach a certain strain value (ε_{cc}). This crushing strain was assumed as:

$$\varepsilon_{cc} = \frac{2}{E_c} F_c = \begin{cases} \frac{2}{E_c} f'_c & \text{for RCFTs} \\ \frac{2}{E_c} \left(f'_c + \frac{1.56 F_y t}{D - 2t} \right) & \text{for CCFTs} \end{cases} \quad (8.18)$$

The latter equation is the tangent stiffness of the concrete attributed to Hognestad (Park and Paulay 1975). For CCFTs, the confinement is accounted by the term in parenthesis as proposed by Sakino *et al.* (2004)

- Initiation of local buckling in the steel tube: This limit state is identified when the corresponding maximum compressive strain in the outside of the steel cross-section reaches the local buckling strain (ε_{lb}) calculated by the empirical equations (Eq. 8.14) that are calibrated in Section 8.2. These equations are:

$$\varepsilon_{lb} = \begin{cases} 0.09 \left(\frac{D}{t} \cdot \frac{F_y}{E_s} \right)^{-2} \frac{F_y}{E_s} = \frac{0.09}{\lambda^2 \cdot \varepsilon_y} & \text{for CCFTs} \\ 9 \left(\frac{h}{t} \sqrt{\frac{F_y}{E_s}} \right)^{-2} \frac{F_y}{E_s} = \frac{9}{\lambda^2} & \text{for RCFTs} \end{cases} \quad (8.19)$$

Again, the geometric and material properties used are those measured and reported in Chapter 3 and Appendix A.

Figure 1.18 to Figure 1.35 show, for each specimen, two of the key responses with the first occurrences of the any of the limit states. The key responses selected are any two of the following:

- $P-M_2$ path during LC1. When a limit state is achieved while the CFT column was under the pure compression loading, the axial force vs. the base moment is plotted, as well as the corresponding exceeded limit or limits; this response is not shown in those cases where no limit was exceeded during this load case.
- $F-\Delta$ path during LC2. During the uniaxial loading case with the CFT specimen under constant axial load and cyclic lateral displacement (LC2), the resultant lateral force vs. the resultant lateral displacement in the direction of the motion is plotted. Similarly, the response values at the exact instant the limit states are suppose to be exceeded are indicated on these figures.
- $P-\Delta_z$ path. The axial force vs. the axial displacement response was chosen only for specimen 1 since the uniaxial and biaxial load cases (LC2 and LC3) were not used in this specimen; instead, pure compression loading (LC1) and a repetition of this (LC4) was applied to this specimen, which was controlled as fixed-fixed ($K=1$).

The following observations can be highlighted from these figures:

- As theoretically expected, inelastic buckling failure occurred in the specimens 1, 3, 4, 7, 17 and 18, which all have a slenderness parameter under the 1.5 limit ($\lambda < 1.5$). This fact is confirmed by Figures 22-23, 26, 33-35 (a), where the buckling load was reached in LC1 with yielding in compression on the steel tube and/or crushing on the concrete core. However, inelastic buckling failure also occurs in specimens 6, 8 and 11, which slenderness parameters are among 1.5 and 1.9. This failure type is attributed, as discussed in Chapter 5, to the change of the top boundary conditions as a consequence of the frictional forces and lack of control in the system. The support changes in these specimens tend to reduce the effective length factor K under the 1.5 limit, and so within the inelastic buckling range.

- On the other hand, the elastic flexural buckling failure is achieved in the slender CFT specimens ($\lambda > 1.5$). This is confirmed for specimens 2, 10, 12, 14, 15 and 16, where the buckling load was reached in LC1 without yielding on the steel tube or without crushing on the concrete core.

Specimens 5 and 7, with slenderness parameter of 0.88 and 1.04 respectively, are exempted from this trend since the system ran out of axial capacity (1320 kip), and so hence yielding did not occur. In addition, the slender parameter in Specimen 13 ($\lambda=1.35$) is close to the 1.5 limit and then either elastic or inelastic buckling can govern in this case.

- The strains of the first local buckling (ε_{lb}) occurrence in the steel tube shown in these figures are calculated with Equations 8.14 or 8.19, both derived from the data calibration. However, the values obtained with these equations are a lower bound of the true local buckling strains reported (see Figure 8.8 and Figure 8.9). Due to the latter, the local buckling may have occurred earlier than reported in these figures. This is the case of the Specimen 4 and 8, where local buckling during LC1 is not reported in Section 8.2, but calculated with Equation 8.20 to be within LC1.
- As seen in these figures, the occurrence sequence of the evaluated limit states starts in general with yielding in the steel tube in compression and then in tension, follows by crushing in the concrete core, and finally with local buckling in the steel tube in the CCFTs and the RCFTs oriented in the strong axis; due to a high wall-slenderness ratio in the RCFTs oriented in the weak axis, the local buckling in these specimens occurred right after yielding and before concrete crushing.

This sequence is result of the strain values associated to each limit states, which ranges between 0.0015 to 0.002 for steel yielding, and around 0.003 to 0.004 for the concrete crushing. In turn, the steel local buckling occurs at strain values above 0.0023 in RCFTs-weak axis, 0.0058 in RCFTs-strong axis, and above 0.0074 in CCFTs.

First occurrence of compression yielding over tension yielding is due to the compressive axial load (P) sustained on the specimens.

As discussed in Section 8.2 and observed in Figures 8.26 to 8.32, RCFTs oriented in the weak axis are more susceptible to developed local buckling right after the steel yields in compression, and right after the concrete crushing in the RCFTs strong axis oriented.

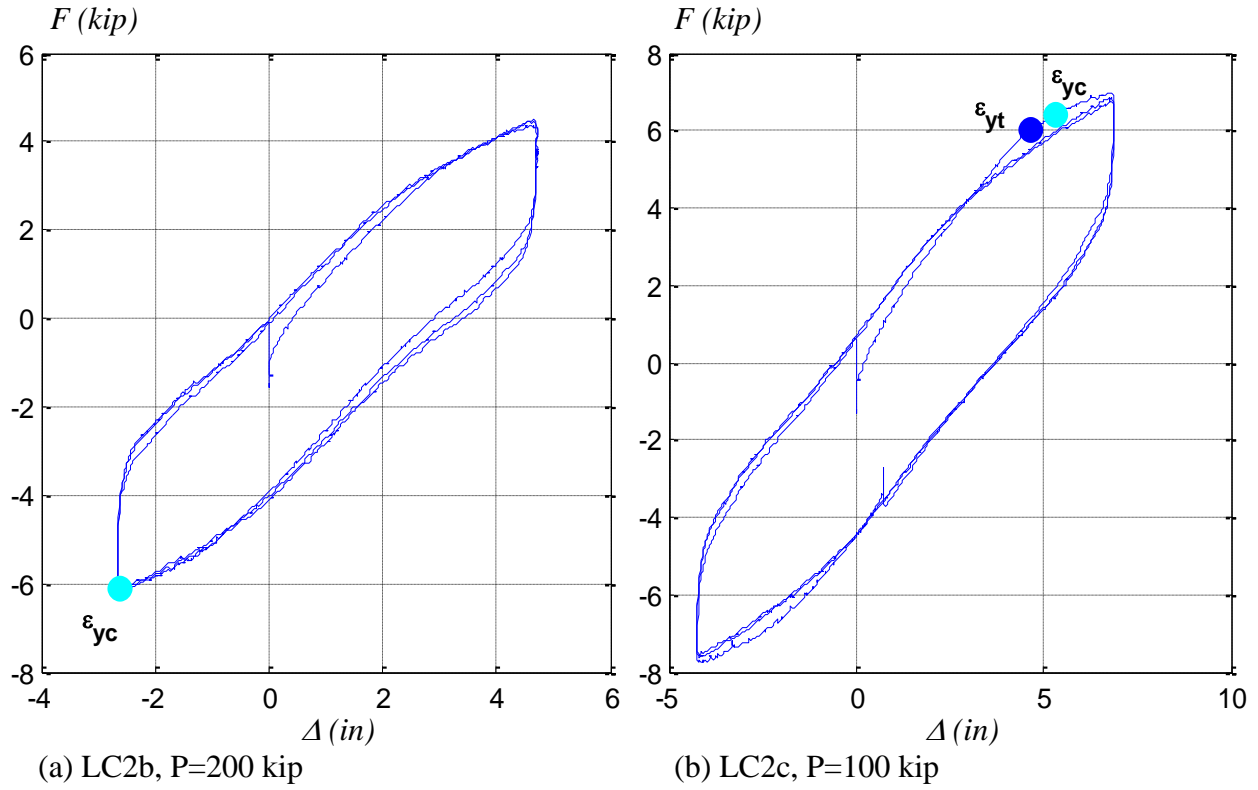


Figure 8.18. Occurrence of limit states in the specimen 2C12-18-5

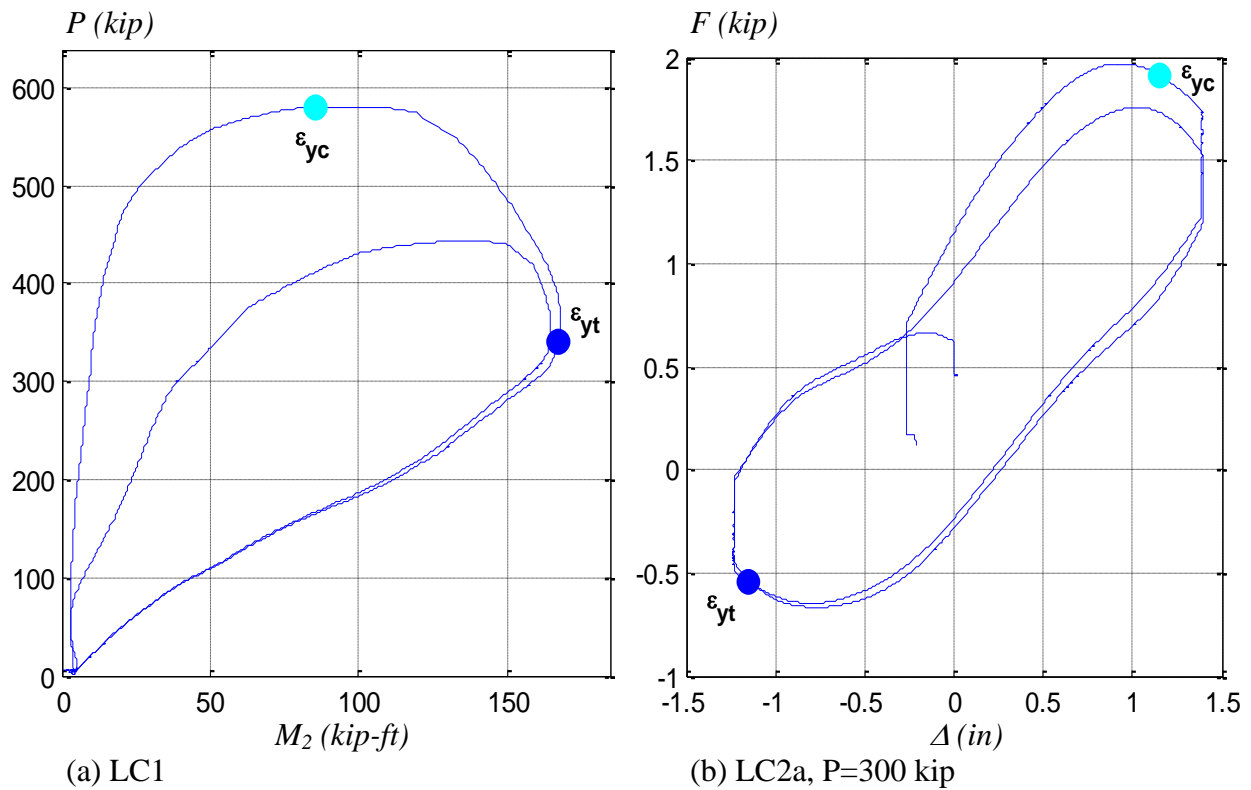


Figure 8.19. Occurrence of limit states in the specimen 6C12-18-12

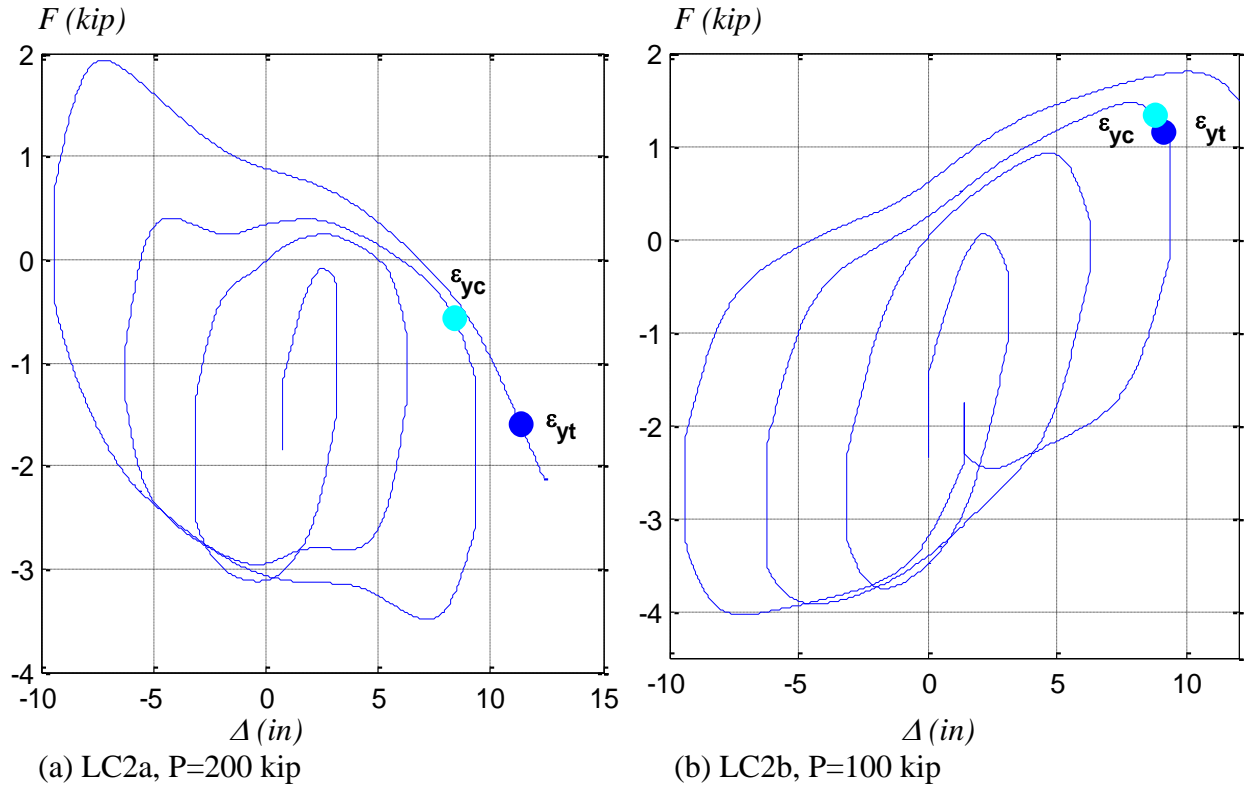


Figure 8.20. Occurrence of limit states in the specimen 10C12-26-5

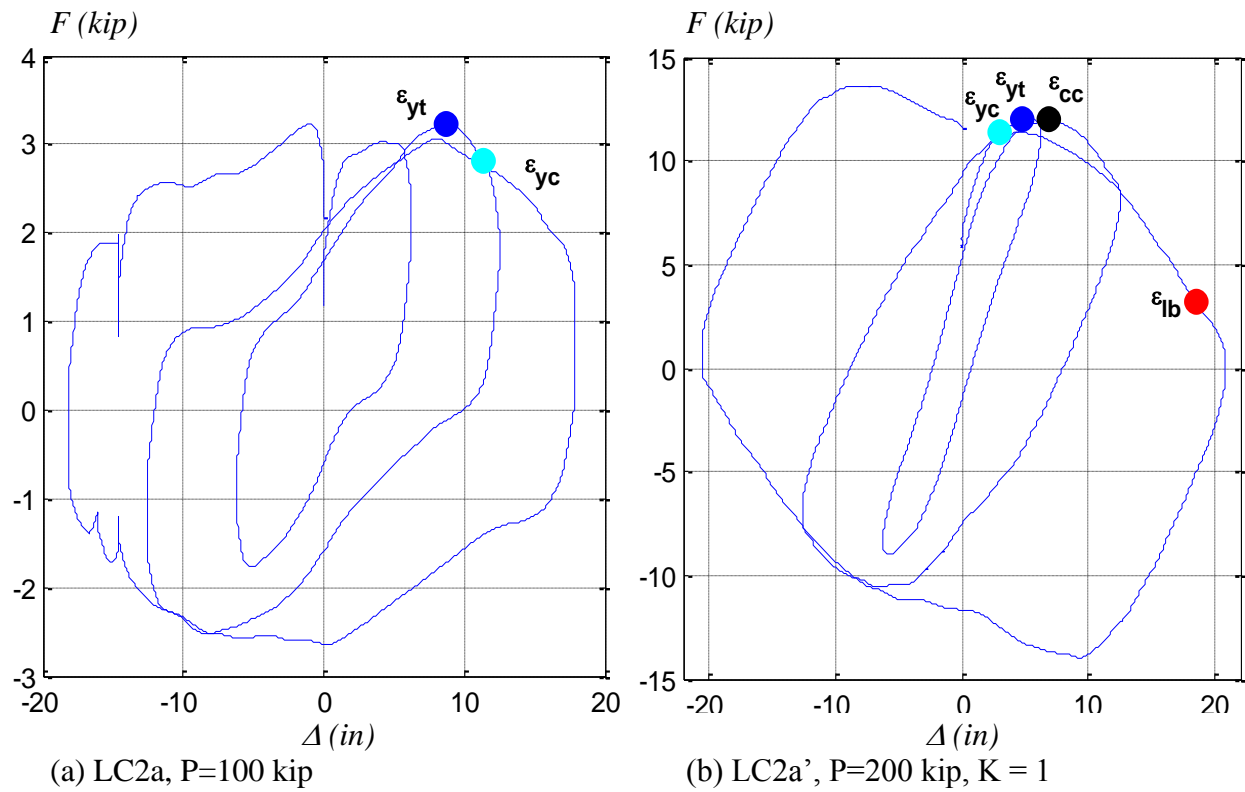


Figure 8.21. Occurrence of limit states in the specimen 14C12-26-12

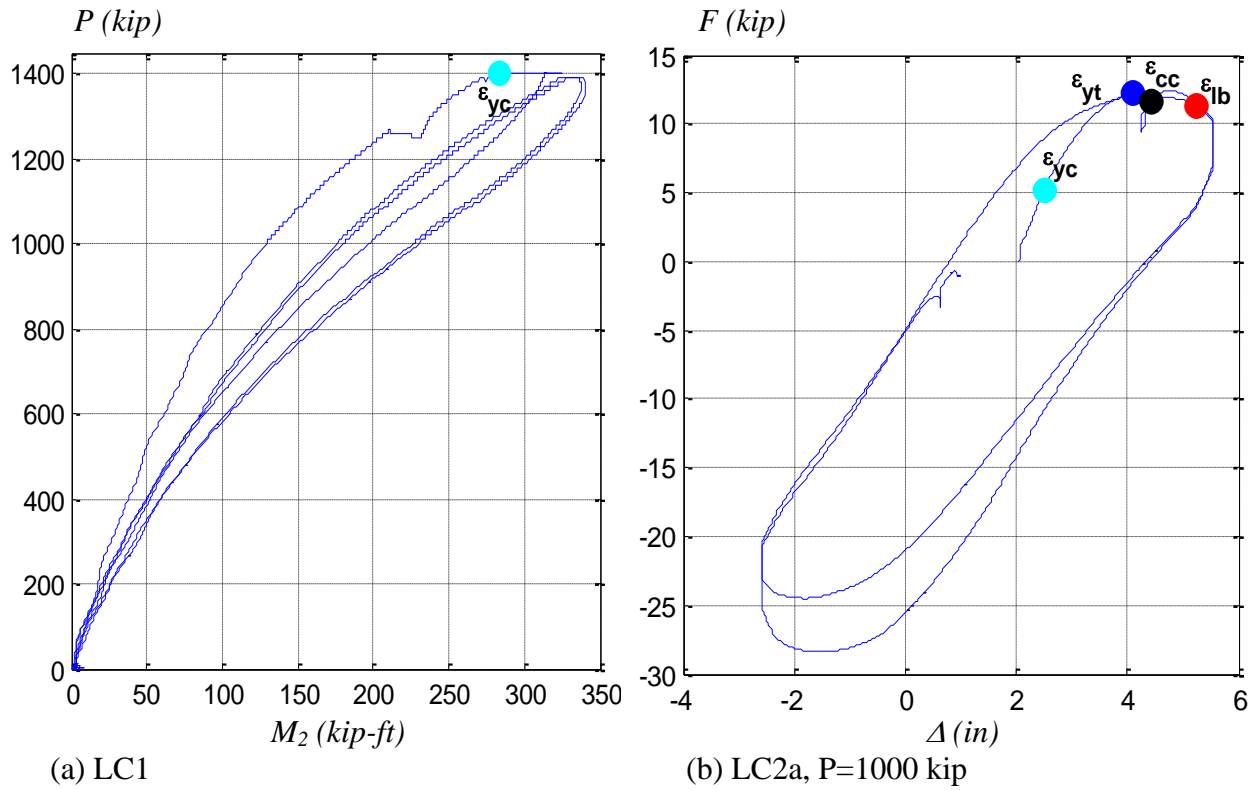


Figure 8.22. Occurrence of limit states in the specimen 3C20-18-5

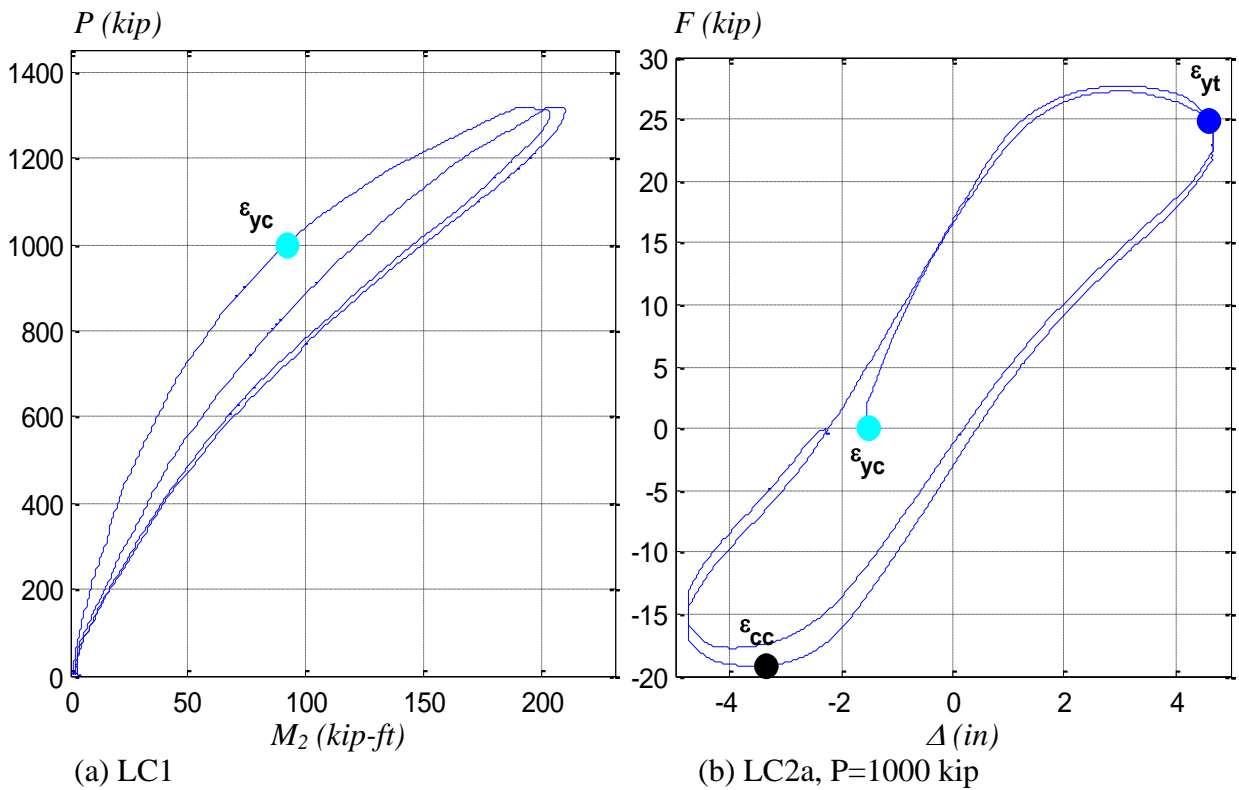


Figure 8.23. Occurrence of limit states in the specimen 7C20-18-12

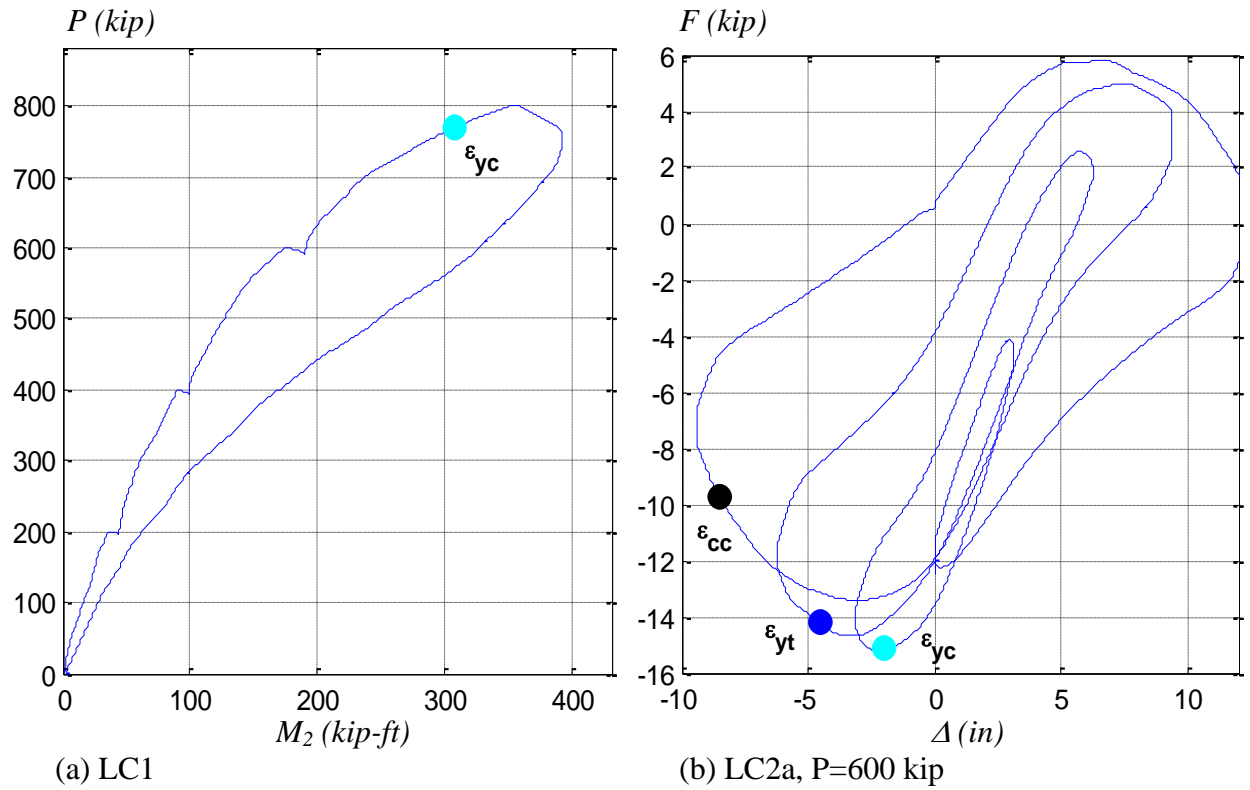


Figure 8.24. Occurrence of limit states in the specimen 11C20-26-5

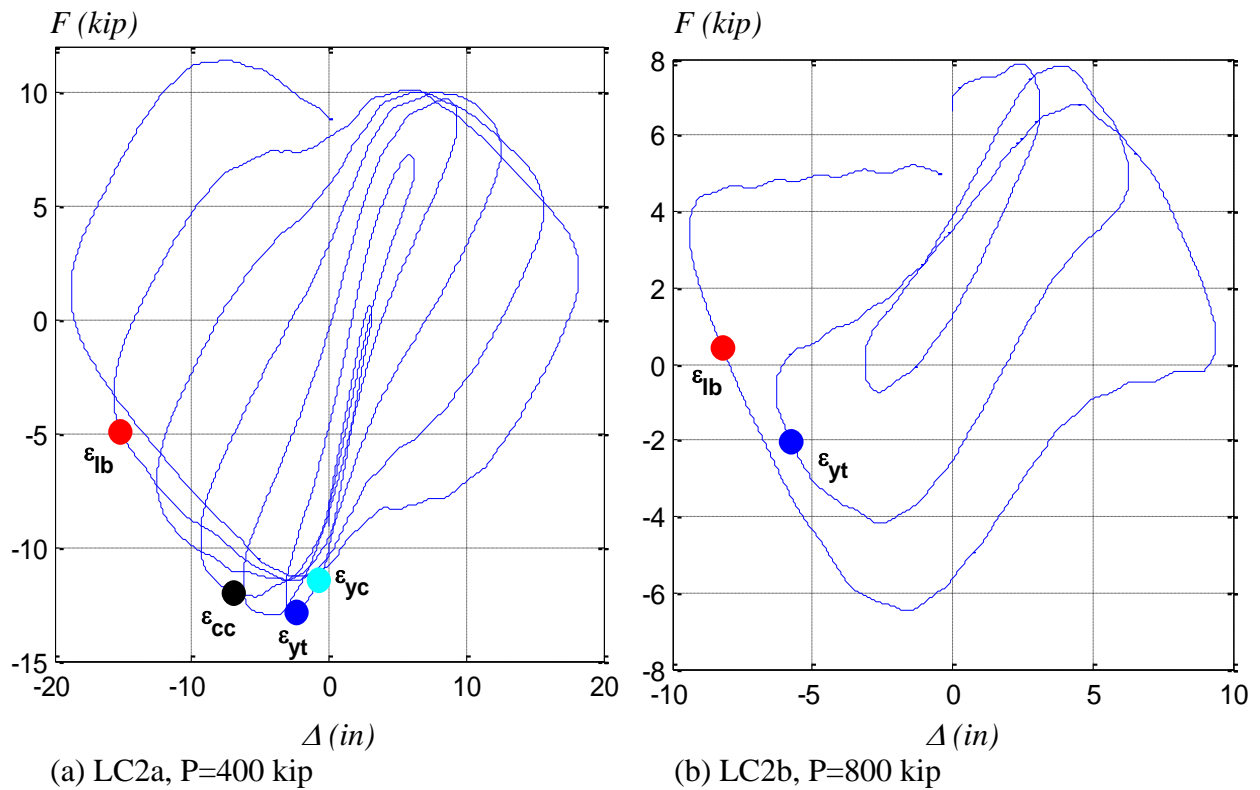


Figure 8.25. Occurrence of limit states in the specimen 15C20-26-12

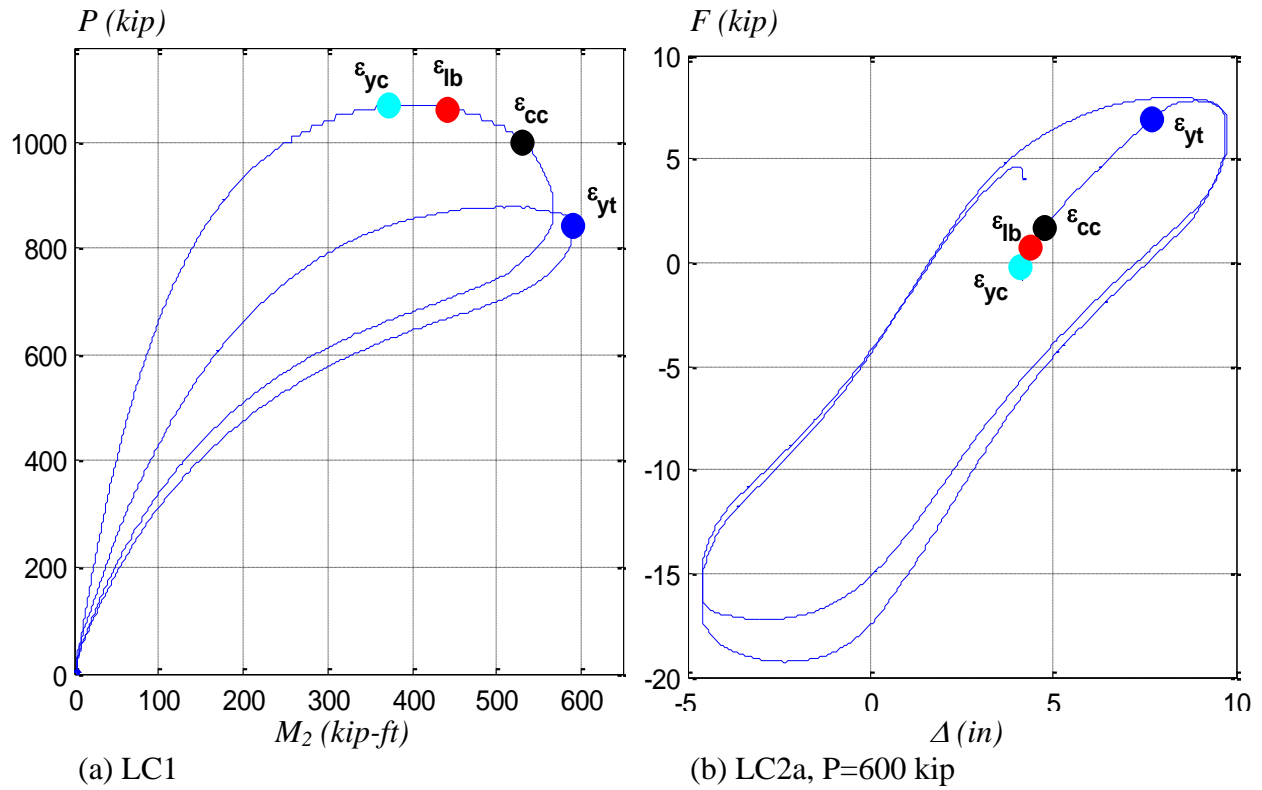


Figure 8.26. Occurrence of limit states in the specimen 4Rw-18-5

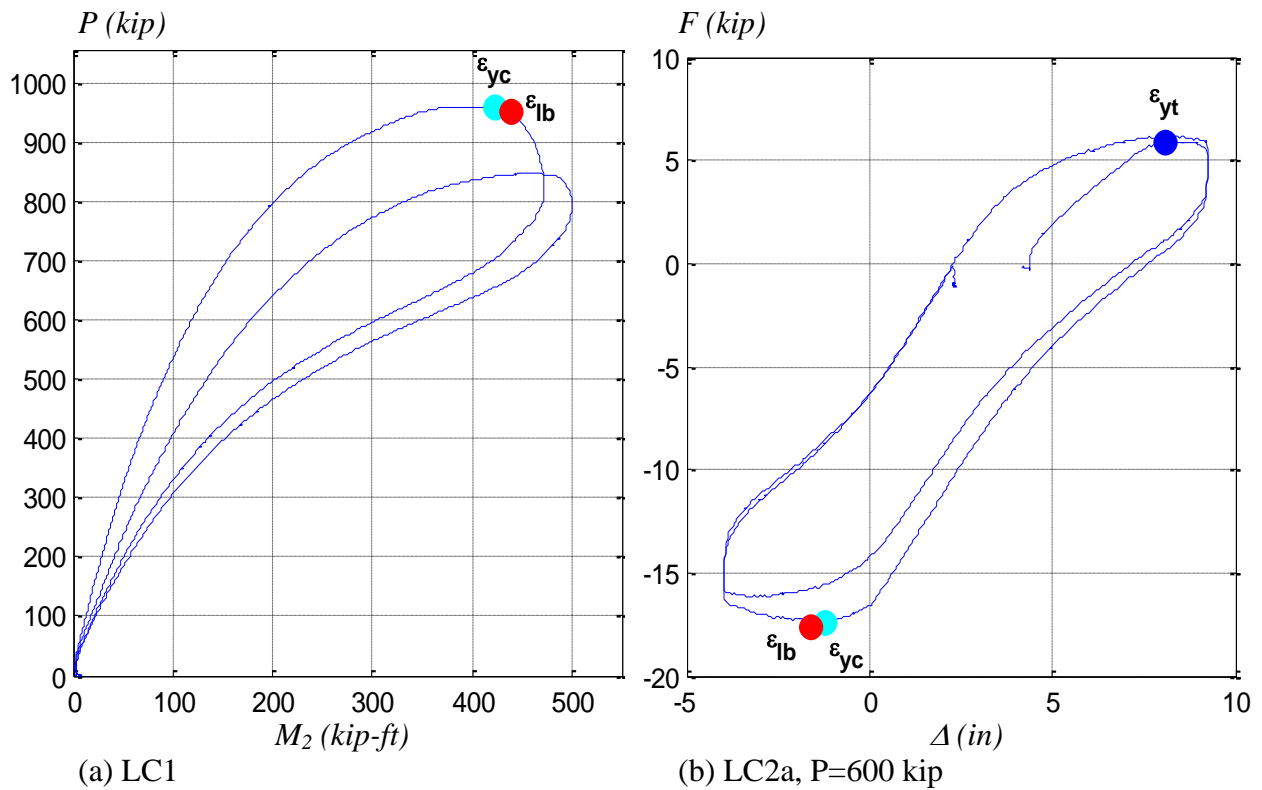
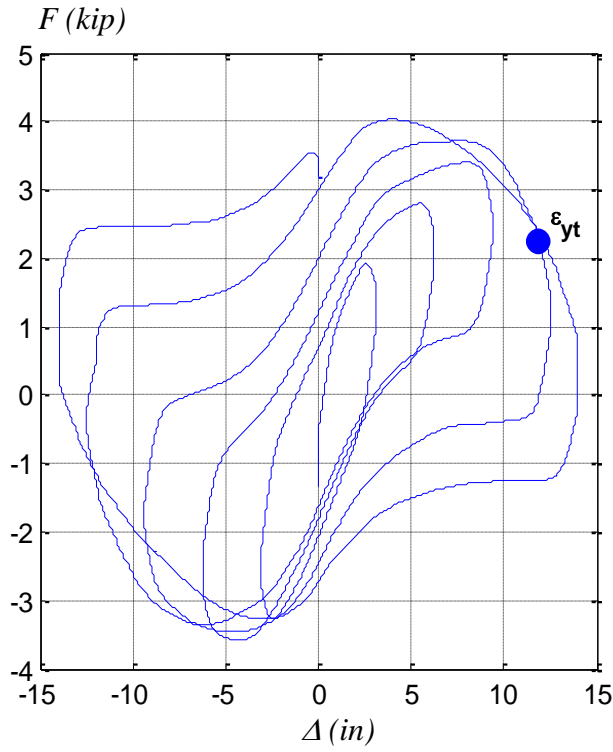
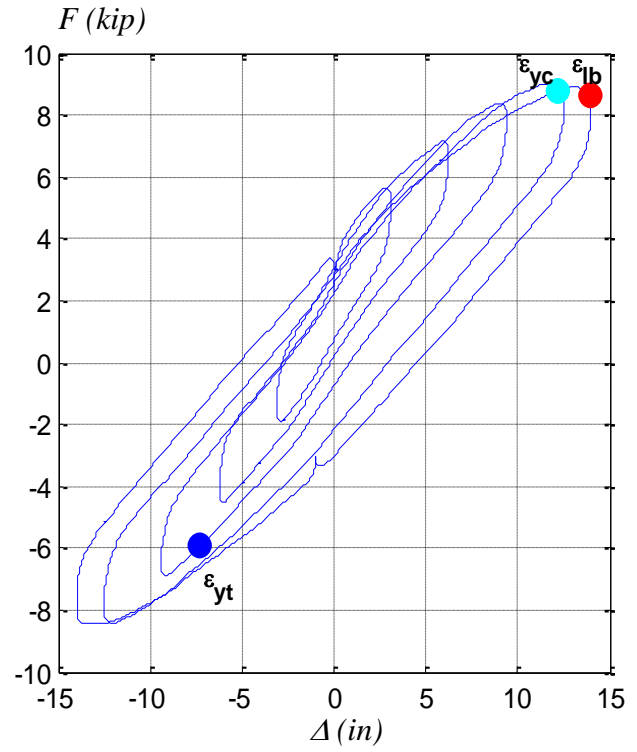


Figure 8.27. Occurrence of limit states in the specimen 8Rw-18-12

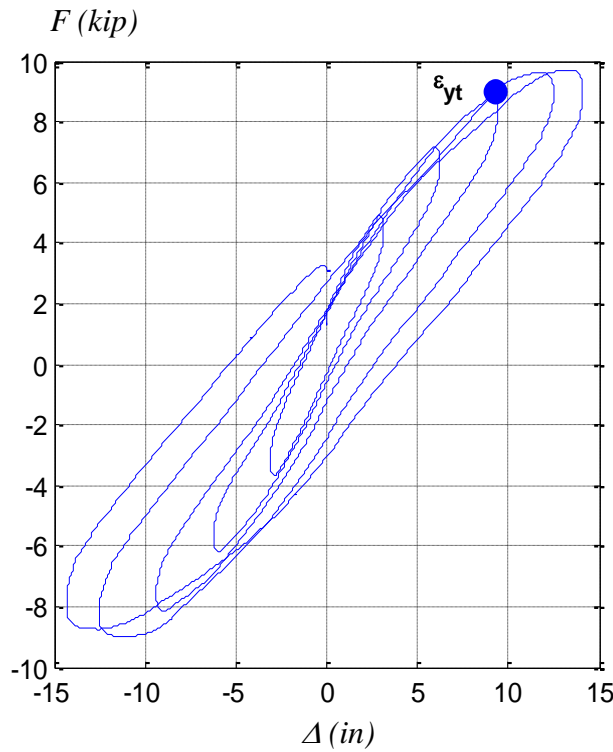


(a) LC2a, P=400 kip

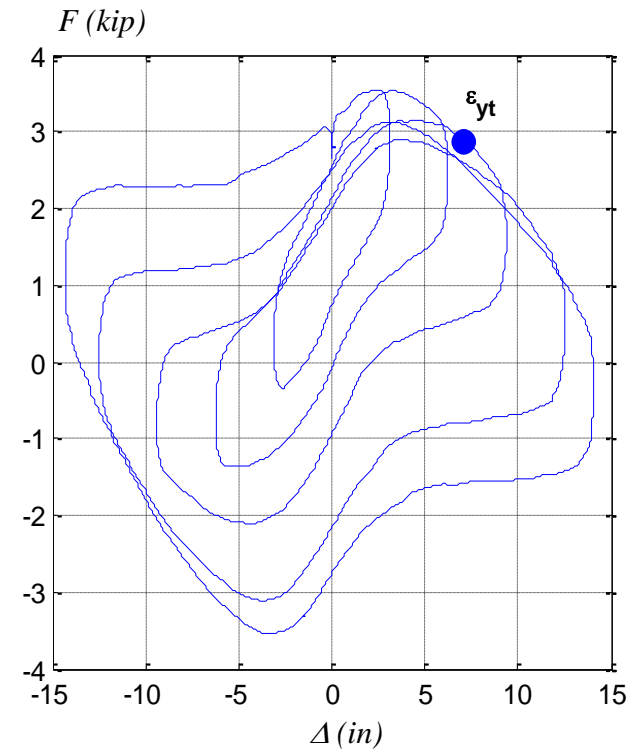


(b) LC2b, P=200 kip

Figure 8.28. Occurrence of limit states in the specimen 12Rw-26-5



(a) LC2a, P=200 kip



(b) LC2b, P=400 kip

Figure 8.29. Occurrence of limit states in the specimen 16Rw-26-12

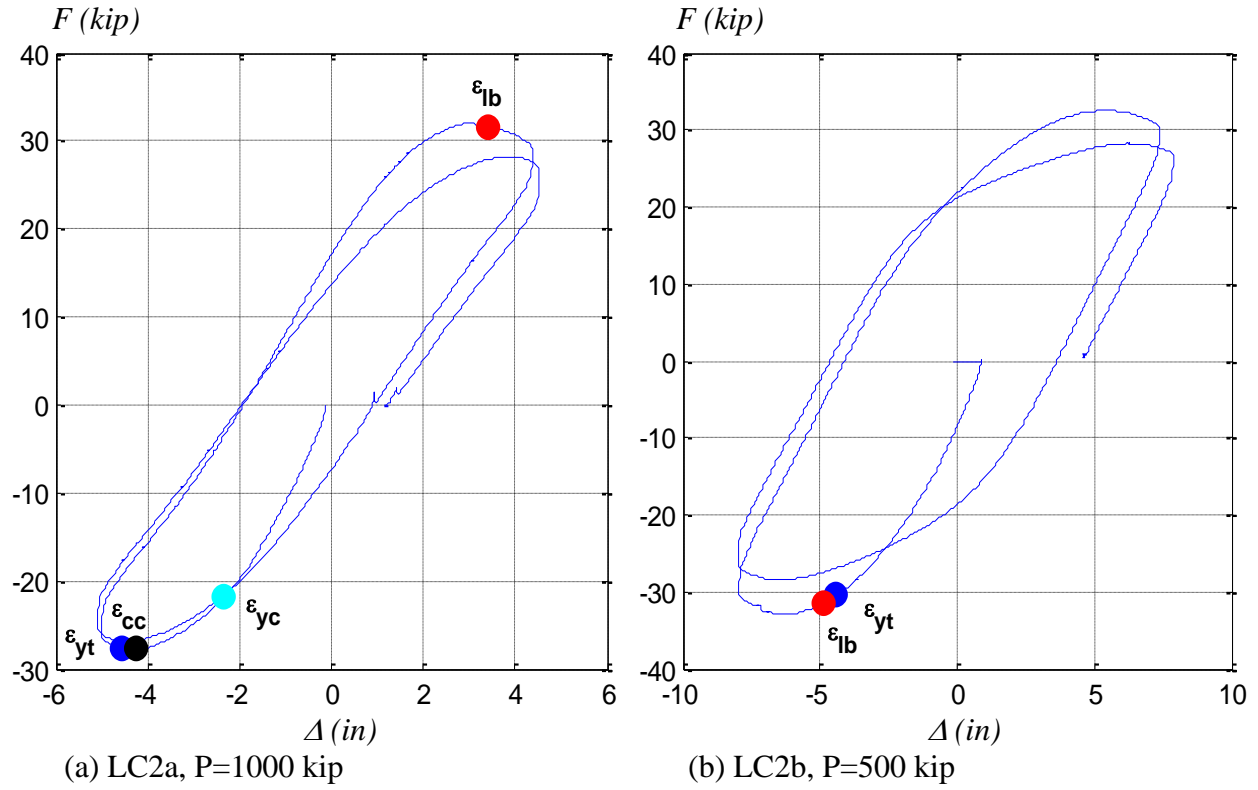


Figure 8.30. Occurrence of limit states in the specimen 5Rs-18-5

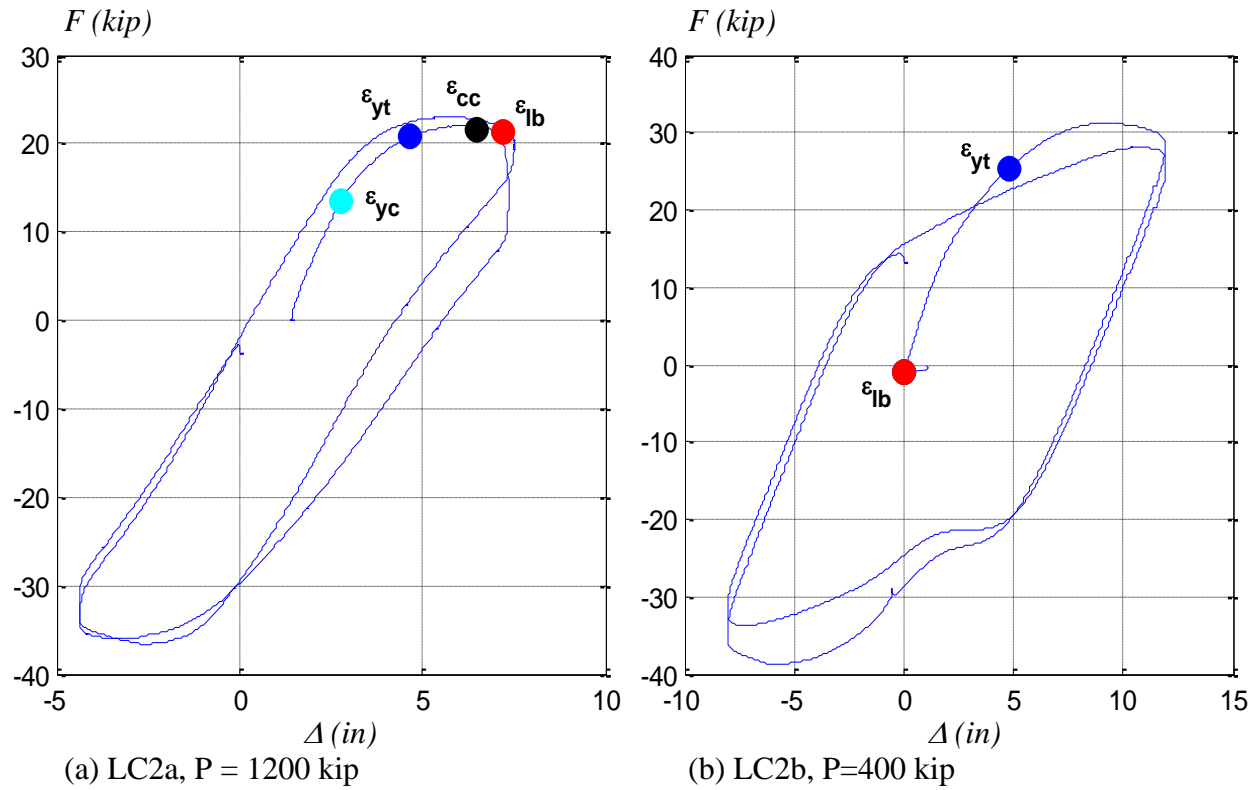
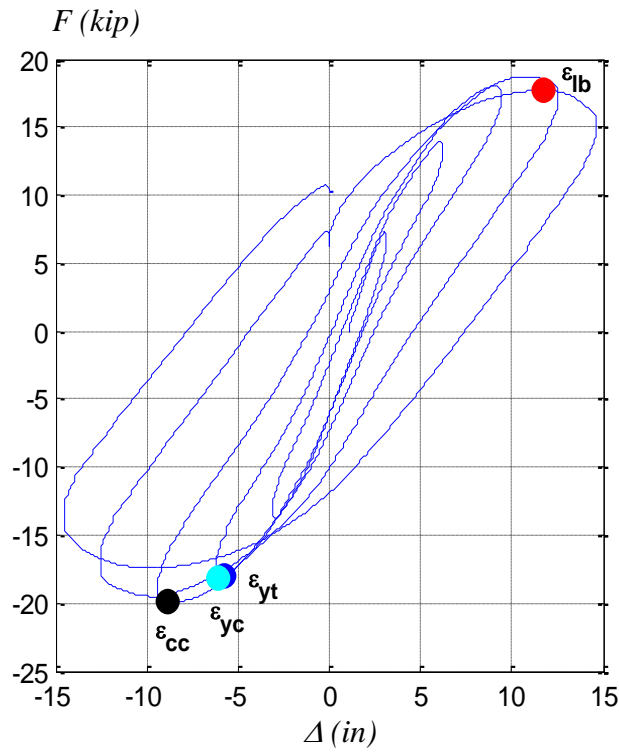
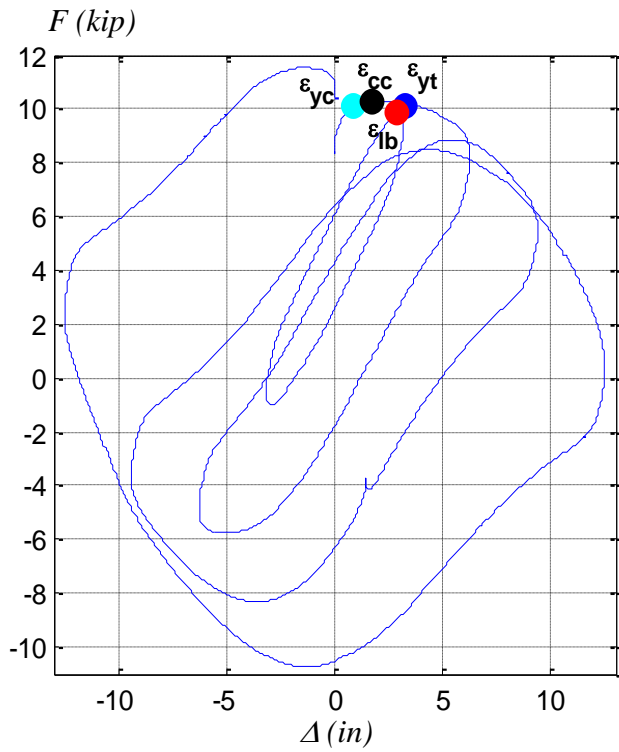


Figure 8.31. Occurrence of limit states in the specimen 9Rs-18-12

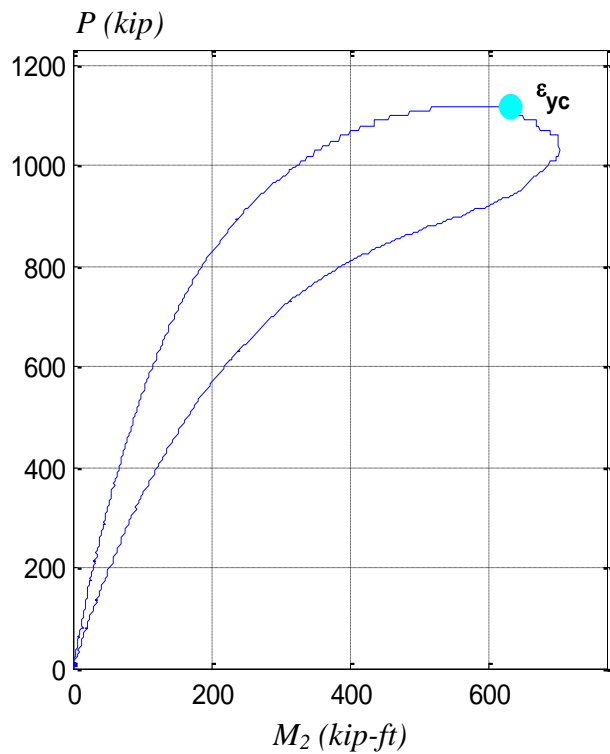


(a) LC2a, $P = 400$ kip

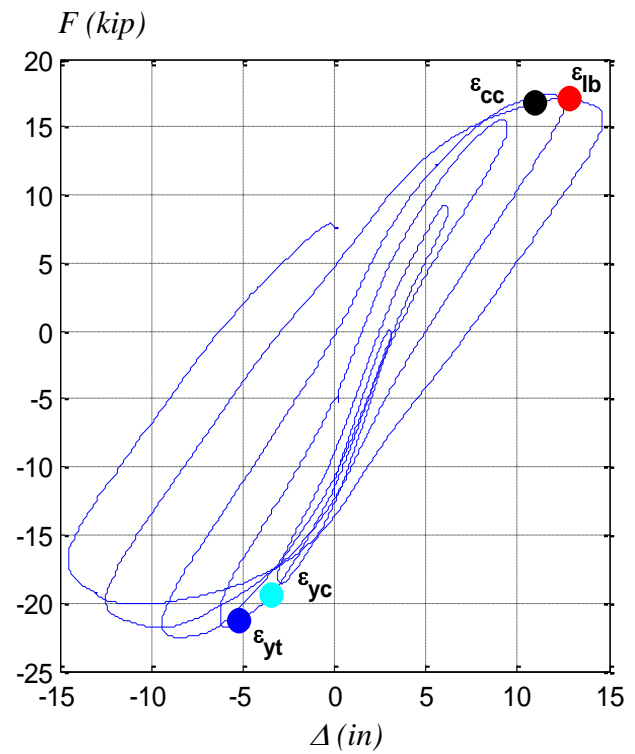


(b) LC2b, $P=800$ kip

Figure 8.32. Occurrence of limit states in the specimen 13Rs-26-5



(a) LC1



(b) LC2a, $P=400$ kip

Figure 8.33. Occurrence of limit states in the specimen 17Rs-26-12

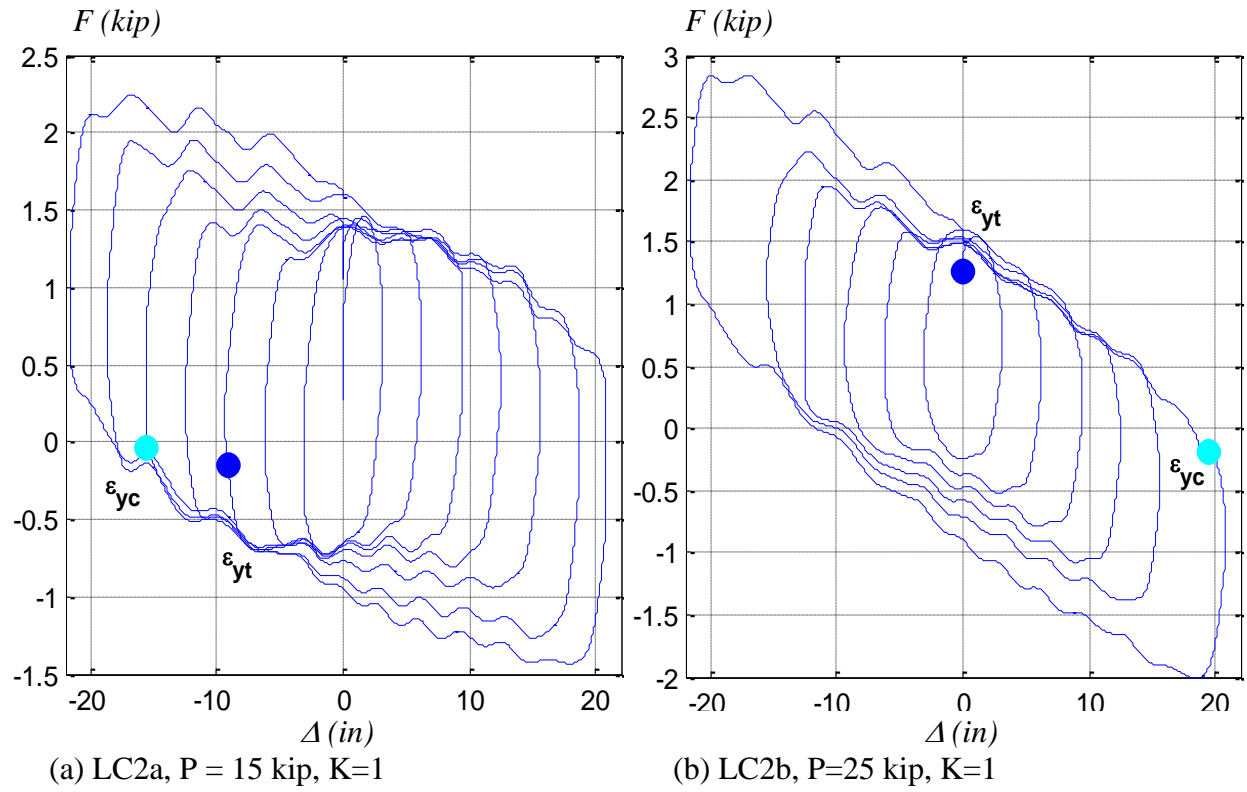


Figure 8.34. Occurrence of limit states in the specimen 18C5-26-12

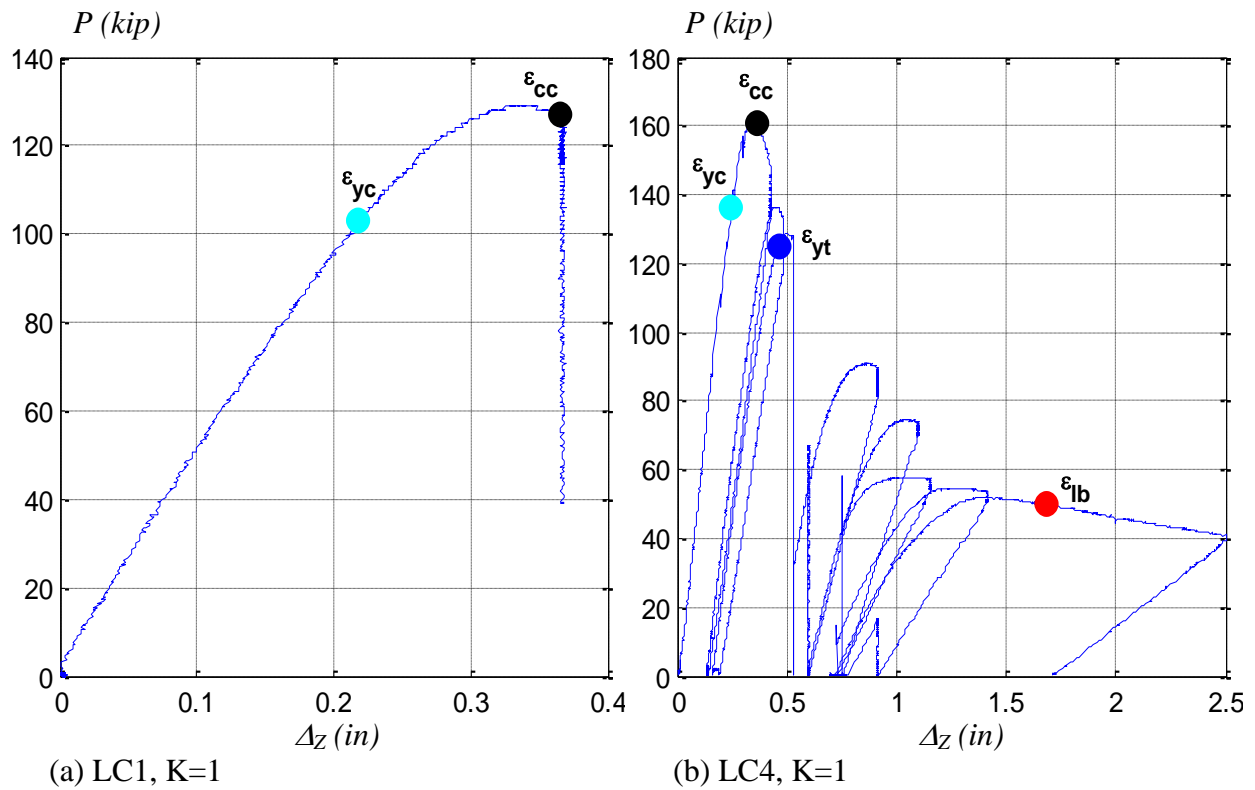


Figure 8.35. Occurrence of limit states in the specimen 1C5-18-5

8.4. Experimental plastic hinge lengths

Experimental determination of the plastic hinge lengths (L_p) may be of interest for calibration of concentrated plasticity models, where the implementation of the plastic hinge length is needed as input data to calculate in the analysis the plastic rotations and the rotation ductility. The plastic hinge length is defined, as illustrated in Figure 8.36, as the segment length that exceed either the elastic moment (M_y) or the elastic curvature (ϕ_y).

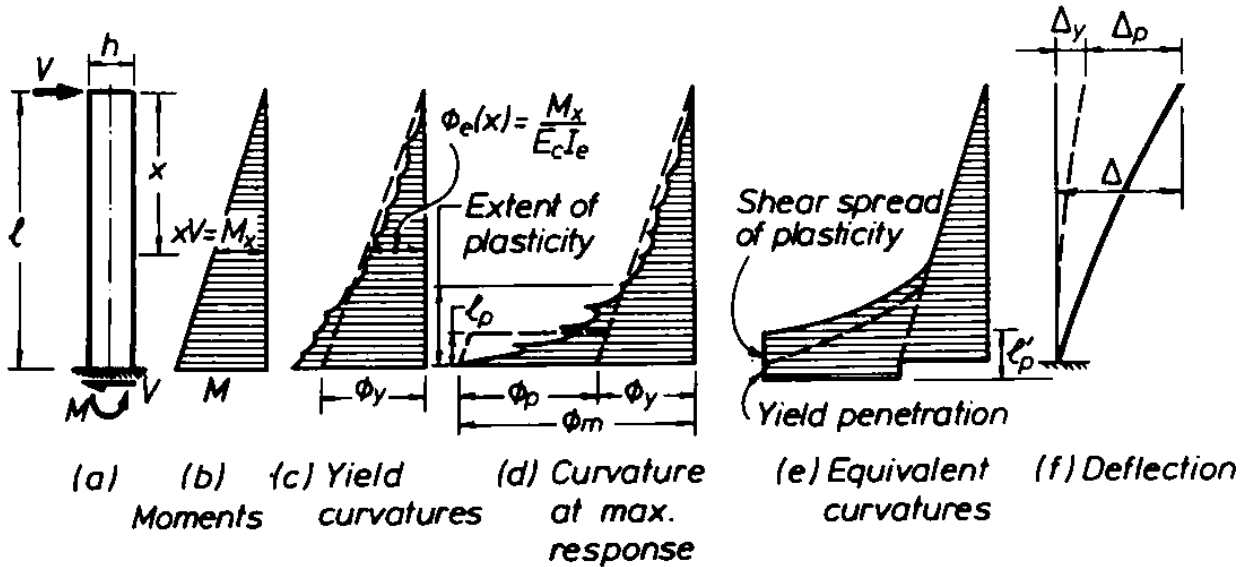


Figure 8.36. Schematic determination of the plastic hinge length (Paulay and Priestley, 1992)

Several empirical and analytical equations obtained for structural steel and reinforced concrete members have been proposed in the literature. Most of the proposed equations relate the plastic hinge length as a function of the effective depth of the cross-section (diameter D in circular shapes or tubes, and h in rectangular shapes or tubes) and the length between the maximum moment and zero.

The plastic hinge length (L_p) can be obtained analytically as illustrated in Figure 8.37 from the linear relation between the member length and its moment distribution. This relationship concludes in an analytical equation that depends on the ratio yielding moment over plastic moment (M_y/M_p). For steel members, this equation can be rewritten as a function of the elastic over the plastic cross-section modulus (S/Z), or the inverse of the shape factor ($1/k_s$).

Thus, the expected plastic hinge with this formula is $0.23L$ for the circular HSS tubes ($k_s=1.3$) and $0.17L$ for the rectangular HSS tubes ($k_s=1.2$).

$$L_p = L \left(1 - \frac{M_y}{M_p} \right) = L \left(1 - \frac{S}{Z} \right) = L \left(1 - \frac{1}{k_s} \right) \quad (8.20)$$

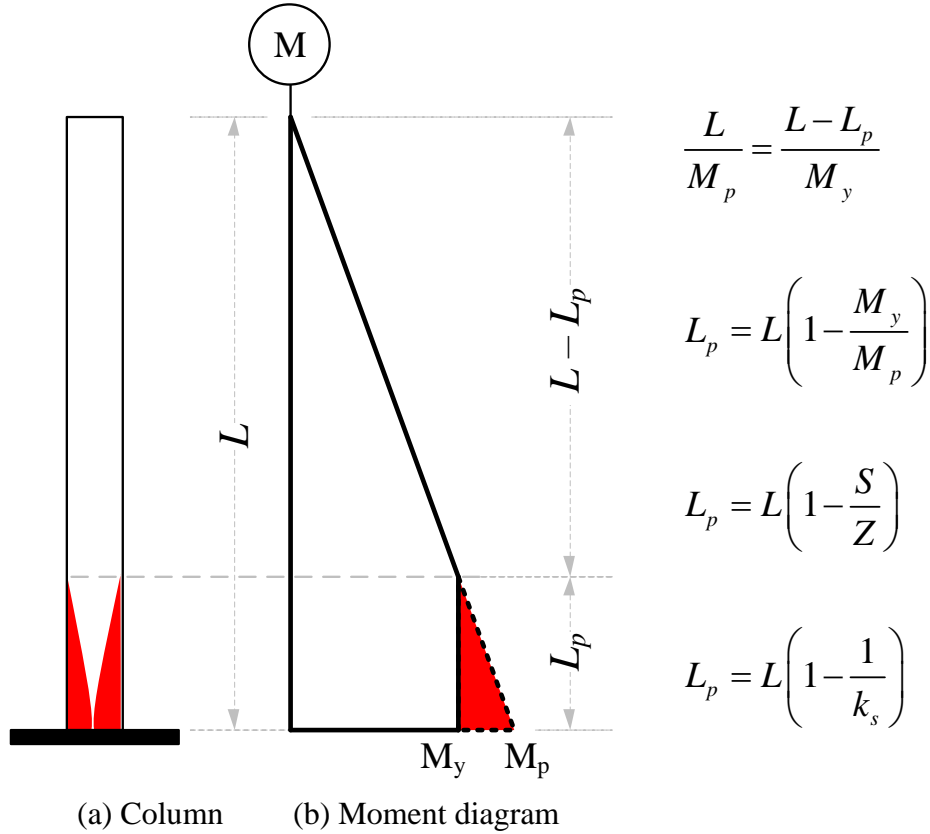


Figure 8.37. Derivation of the plastic hinge length in a cantilever beams

The empirical Equation 8.21 was proposed by Sawyer (Paulay and Priestley, 1992) to obtain the plastic hinge length of concrete members, where D is the effective depth and L is the distance between maximum and zero moment (equal to the member length in cantilever members). This equation assumes a ratio of yielding moment over plastic or ultimate moment equal to $M_y/M_p=0.85$, and a plastic extension of $1/4$ of the effective depth (D).

$$L_p = 0.25D + 0.075L \quad (8.21)$$

Even though it is not the main goal of this project to perform a comprehensive study on plastic hinge lengths, the redundancy in the instrumentation permits a first rough estimation of the plastic hinge length for CFT members. In this project, the curvature approach from the experimental instrumentation and the physical observation of the spread of damage in the exterior tube are used as a first approach to handle the hinge length determination.

For this purpose, the curvatures extracted from the strain gauges data along the column length are illustrated from Figure 8.39 to Figure 8.43. As reminder, three strain gauges were placed in the exterior wall of steel tube at the north, south and west faces and at different cross-section locations along the specimens. Assuming that plane sections remain plane, the three values in each cross-section are used to compute the strain in the east face. The strain values placed in each cardinal direction are then used to compute the X (north-south) and Y (east-west) curvatures for each cross-section. The values illustrated in these figures correspond to the absolute values of the X and Y curvatures in the cross-sections along the member at the instant of maximum top deflection during the load case stated in the captions. The selected load cases in these plots correspond to the latest case in the load history with high curvatures and consistent strain gauge data. Strain data in some latest cases may not be reliable (mainly near the member bottom) due to saturated measurements or detached strain gauges as a consequence of excessive local buckling. Note that the calculated absolute X and Y curvatures in these figures are represented by discrete points that are connected with smooth dashed lines; this curvature variation with the length may not correspond to the true distribution, specially at near the member top where a low density of strain gauges through the length were placed.

Figure 8.39 to Figure 8.43 also illustrate with a thick dash line rough values of the estimated curvature in the CFT cross-section corresponding to the yielding occurrence in the steel component (ϕ_y). As schematically illustrated in Figure 8.38.b, an accurate determination of the yield curvature (ϕ_y) in composite cross-sections under axial force (P) and moment (M) depends on the effective axial loading (P_s) and bending moment (M_s) on the steel component. Alternatively, the yield curvature (ϕ_y) can be estimated in composite beam-columns with the total P and M loading on the composite member but with effective axial (EA_{eff}) and flexural (EI_{eff}) rigidities; both later cases are quite complicate since some key variables (P_s , M_s , EA_{eff}) are unknown.

For beams under pure bending ($P=0$), the yield curvature is simplified as shown in Equation 8.22 and illustrated in Figure 8.38.a; the yield curvature in beam columns varies from zero in pure axial loading to the upper limit given by the value in pure bending.

$$\phi_y \approx \frac{2\varepsilon_{sy}}{D} = \frac{2}{D} \frac{F_y}{E_s} \quad (8.22)$$

In the previous equation, D is the depth of the cross-section related to the bending axis. This is equal to the diameter D in CCFTs, to the height h in RCFTs with strong axis bending, and to the base b in RCFTs with weak axis bending

As a first pass, the upper limit of the yield curvature (ϕ_y) as computed with Equation 8.22 is selected as the limit between the elastic and the plastic ranges. This assumption is contrasted with the fact that the limit is compared with the X and Y measured curvature instead of the maximum curvature. The estimated limits are illustrated from Figure 8.39 to Figure 8.43 with the thick-dash vertical lines. Thus, the experimental plastic hinge lengths are defined as the segment length that exceeds the given limits.

With this approach, the experimental plastic hinge lengths (L_p) extracted from Figure 8.39 to Figure 8.43 are summarized in Table 8.5. This table also shows estimated values of the plastic hinge lengths (L_p) calculated with Equation 8.20 using the steel properties and with Equation 8.21 derived for concrete members. As noted in this table, plastic hinge lengths extracted from the tests present, in general, show values between the analytical predictions with Equations 8.20 and 8.21, but closer to the prediction using the steel tube properties (Equation 8.20).

According to the experimental data evaluated in this project, despite all the simplifications and assumptions involved in this section, the analytical prediction using the shape factors of the steel tube component (Equation 8.20) gives a reasonable prediction of the plastic hinge length for composite CFT members.

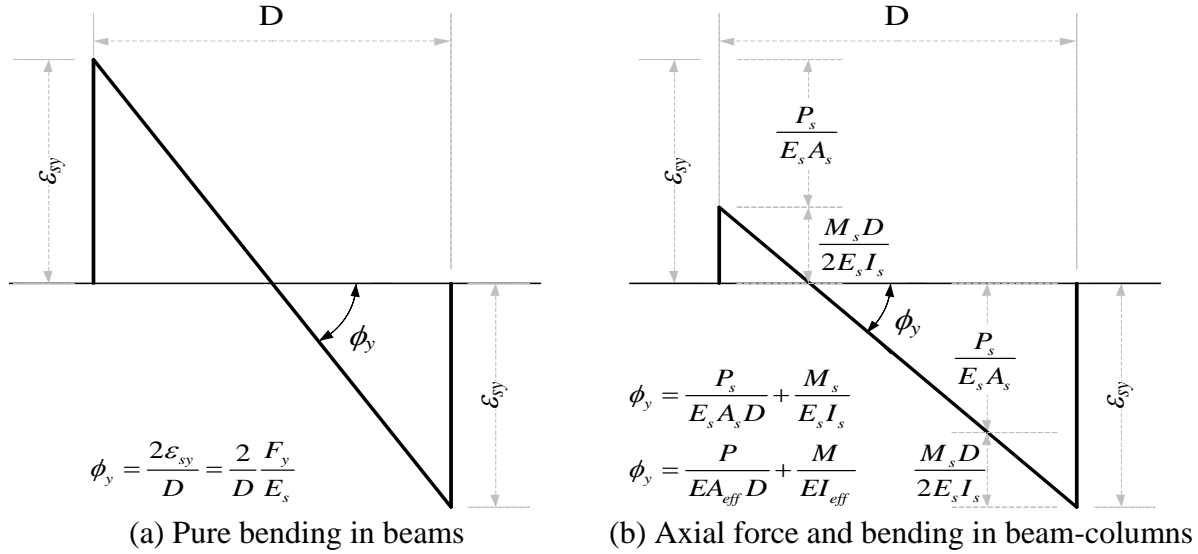
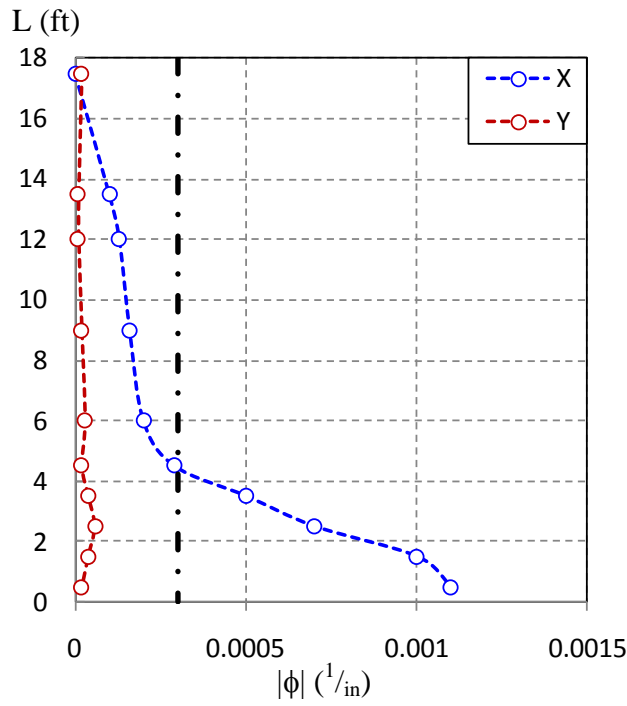


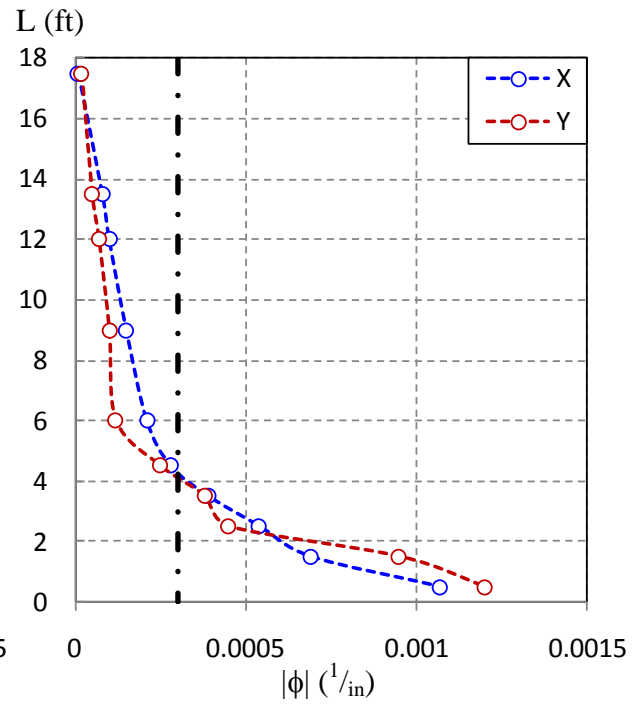
Figure 8.38. Computation of the yield curvature in the cross-section

Table 8.5. Summary of extracted plastic hinge length

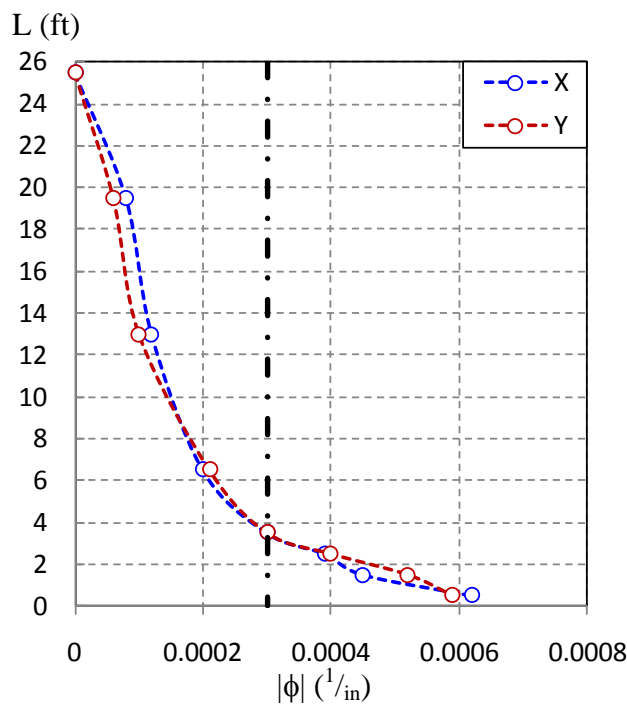
Specimen	D/t	ϕ_y (1/in) Eq. 7.6	ϕ_u (1/in) Tests	L_p (ft) Tests	L_p (ft) Eq. 8.20	L_p (ft) Eq. 8.21
1C5-18-5	45	0.0007	0.0007	--	4.15	1.5
18C5-26-12			0.0010	3.0	6.00	2.1
2C12-18-5	55	0.0003	0.0011	4.0	4.15	1.6
6C12-18-12			0.0012	4.0	4.15	1.6
10C12-26-5			0.0006	4.0	6.00	2.2
14C12-26-12			0.0006	4.0	6.00	2.2
3C20-18-5	86	0.0002	0.0013	2.0	4.15	1.8
7C20-18-12			0.0008	4.0	4.15	1.8
11C20-26-5			0.0006	6.0	6.00	2.4
15C20-26-12			0.0005	6.0	6.00	2.4
4Rw-18-5	69	0.0002	0.0006	4.0	3.00	1.6
8Rw-18-12			0.0030	3.0	3.00	1.6
12Rw-26-5			0.0007	3.0	4.33	2.2
16Rw-26-12			0.0004	4.5	4.33	2.2
5Rs-18-5			0.0011	3.0	3.00	1.8
9Rs-18-12			0.0012	2.5	3.00	1.8
13Rs-26-5			0.0005	4.0	4.33	2.4
17Rs-26-12			0.0009	5.0	4.33	2.4



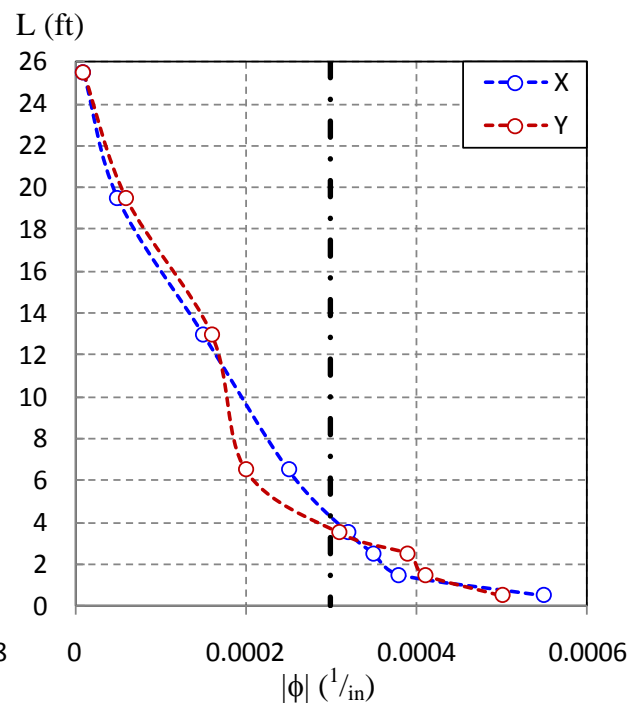
(a) 2C12-18-5, LC3b



(b) 6C12-18-5, LC3c

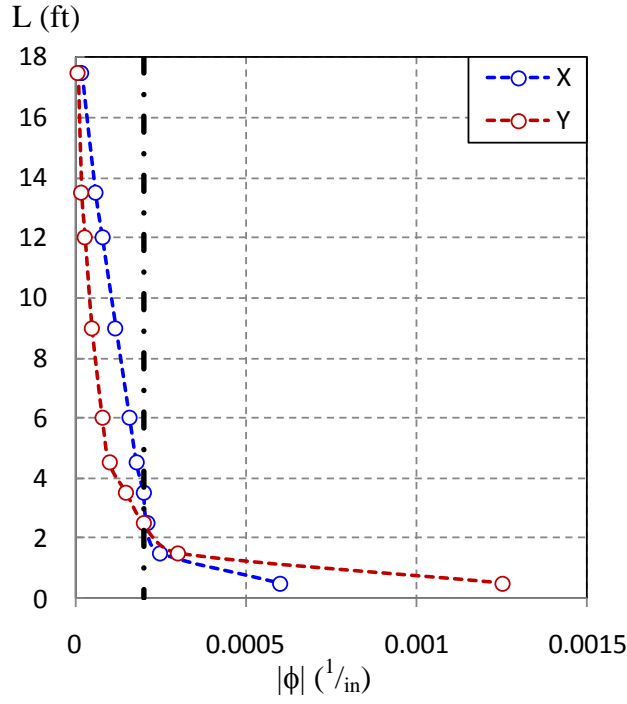


(c) 10C12-18-5, LC3b

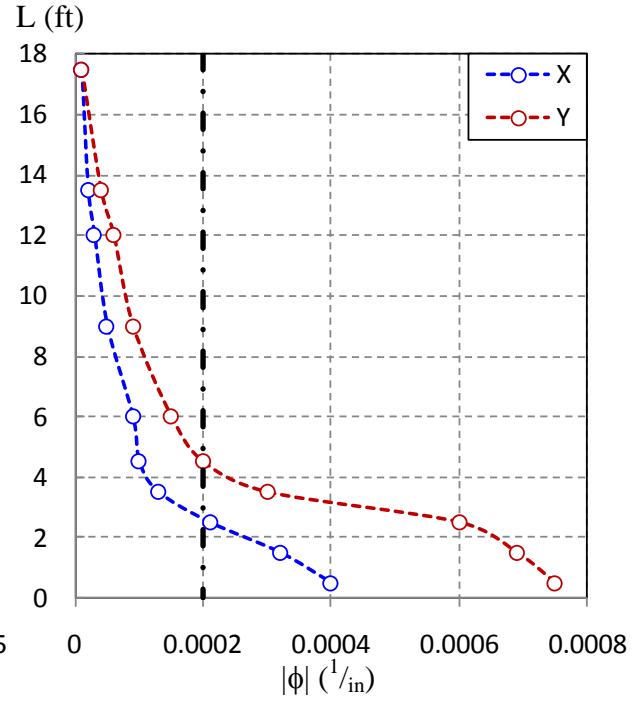


(d) 14C12-18-5, LC3a

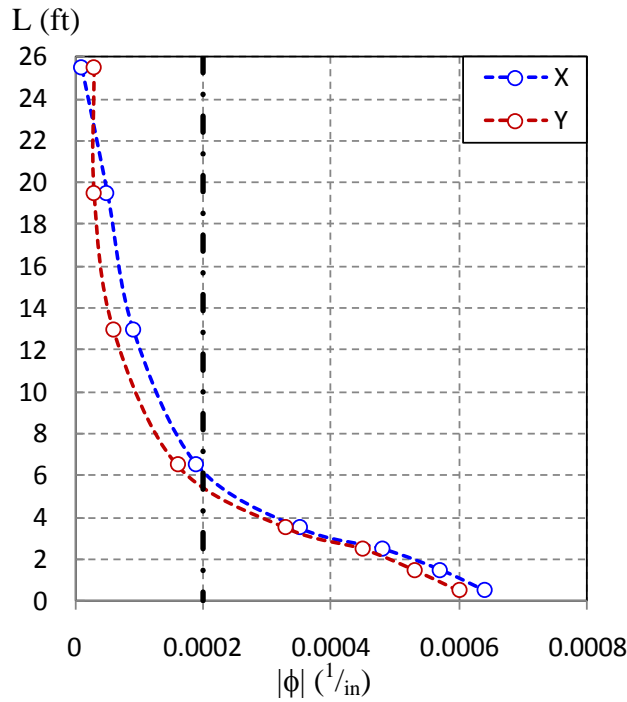
Figure 8.39. Curvatures vs. length at the peak displacement



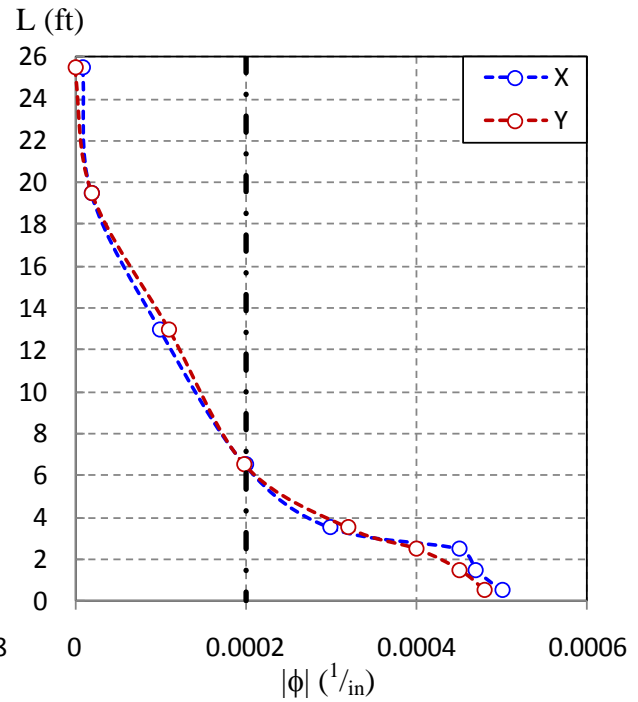
(a) 3C20-18-5, LC3c



(b) 7C20-18-12, LC2

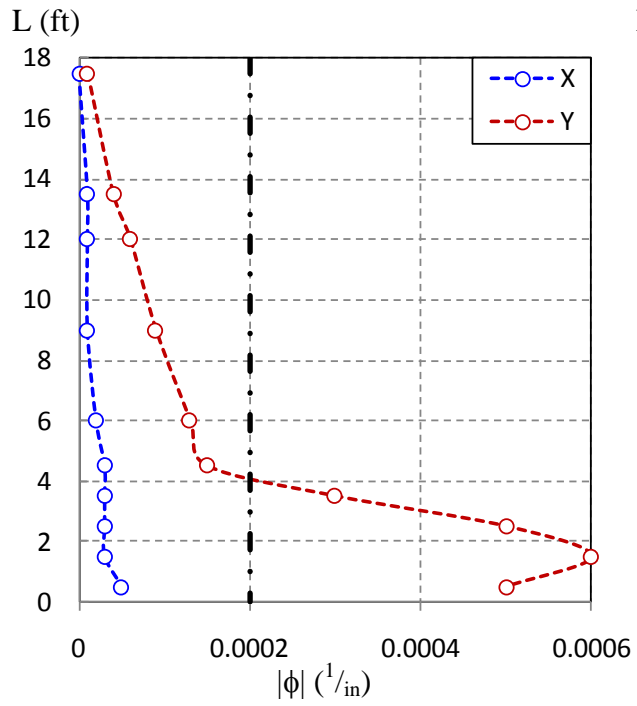


(c) 11C20-18-5, LC4

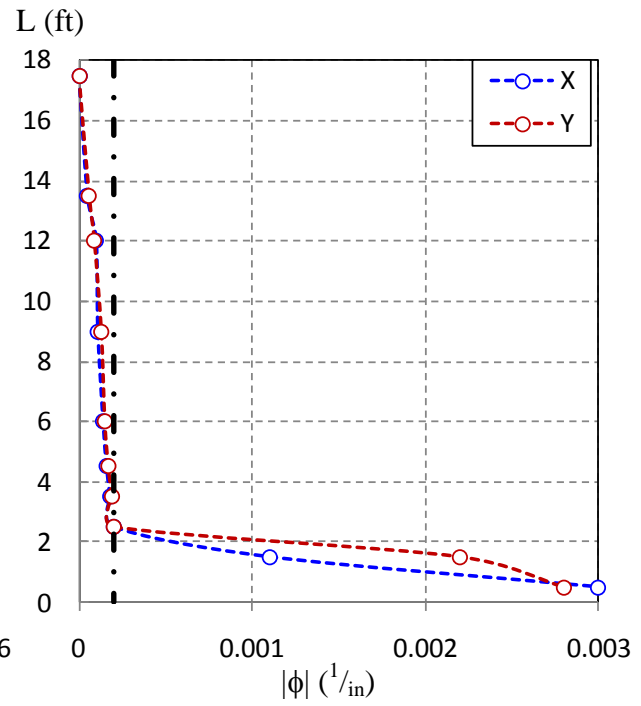


(d) 15C20-26-12, LC4

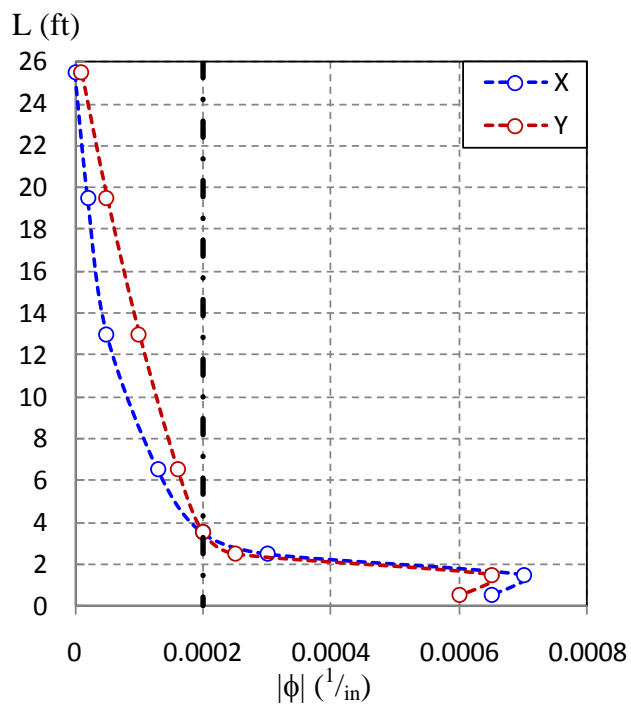
Figure 8.40. Curvatures vs. length at the peak displacement



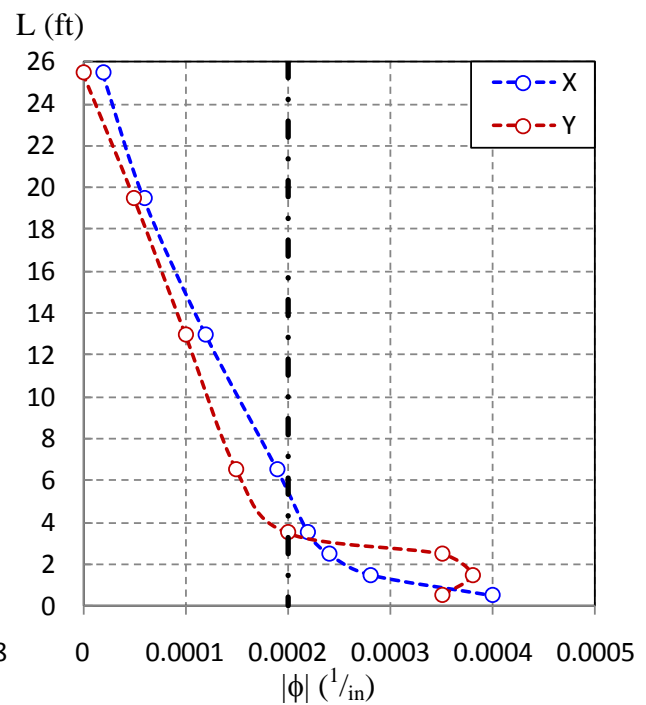
(a) 4Rw-18-5, LC3c



(b) 8Rw-18-12, LC3a

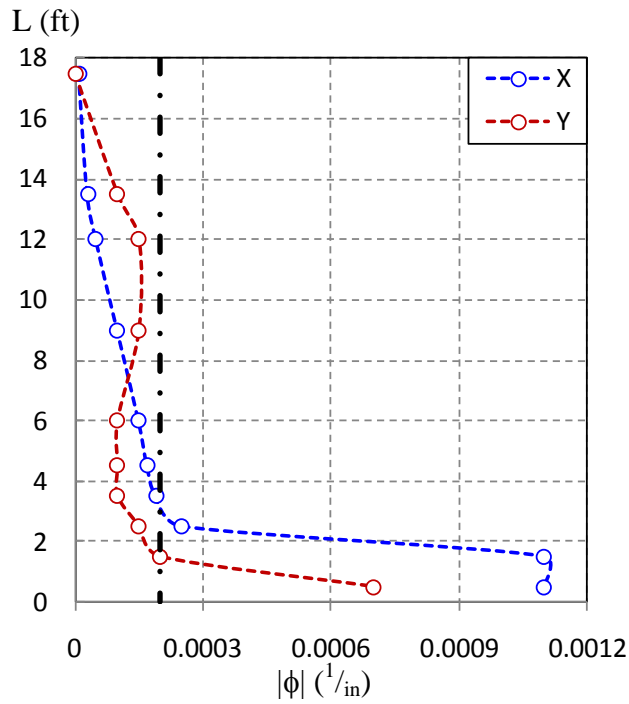


(c) 12Rw-18-12, LC3b

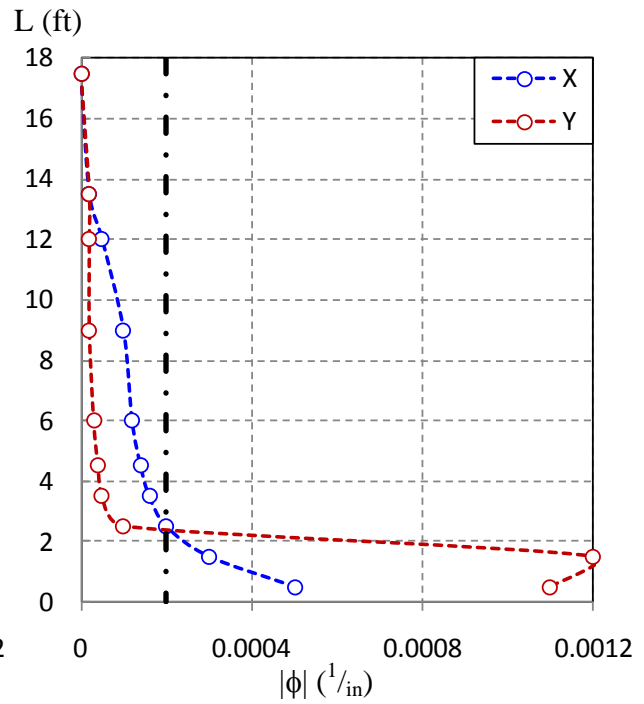


(d) 16Rw-18-12, LC3b

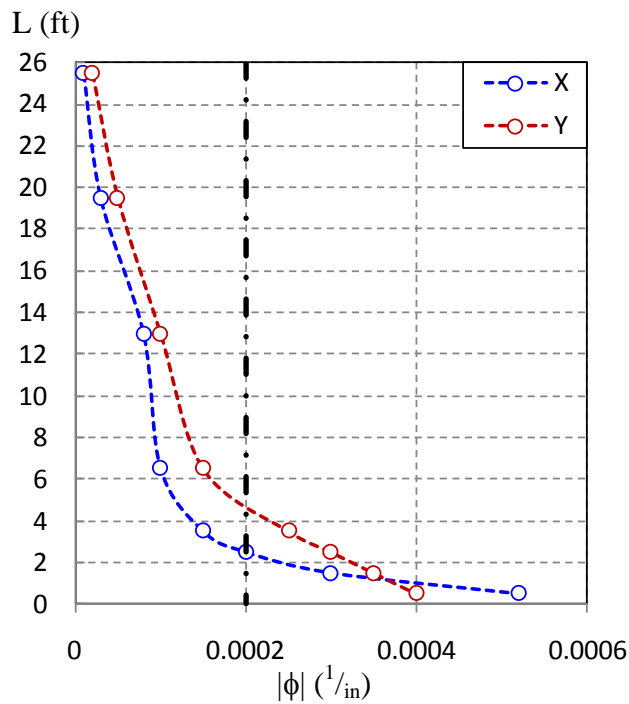
Figure 8.41. Curvatures vs. length at the peak displacement



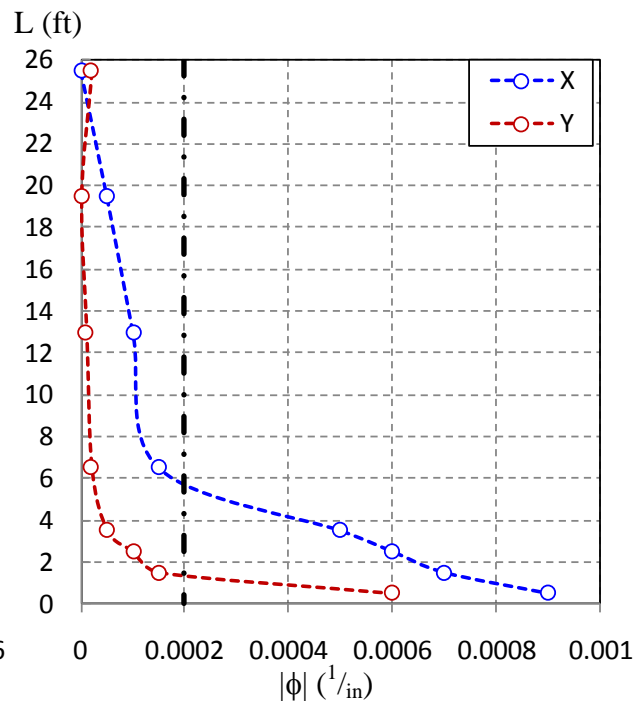
(a) 5Rs-18-5, LC3b



(b) 9Rs-18-12, LC3b



(c) 13Rs-18-12, LC3b



(d) 17Rs-26-12, LC3b

Figure 8.42. Curvatures vs. length at the peak displacement

L (ft)

L (ft)

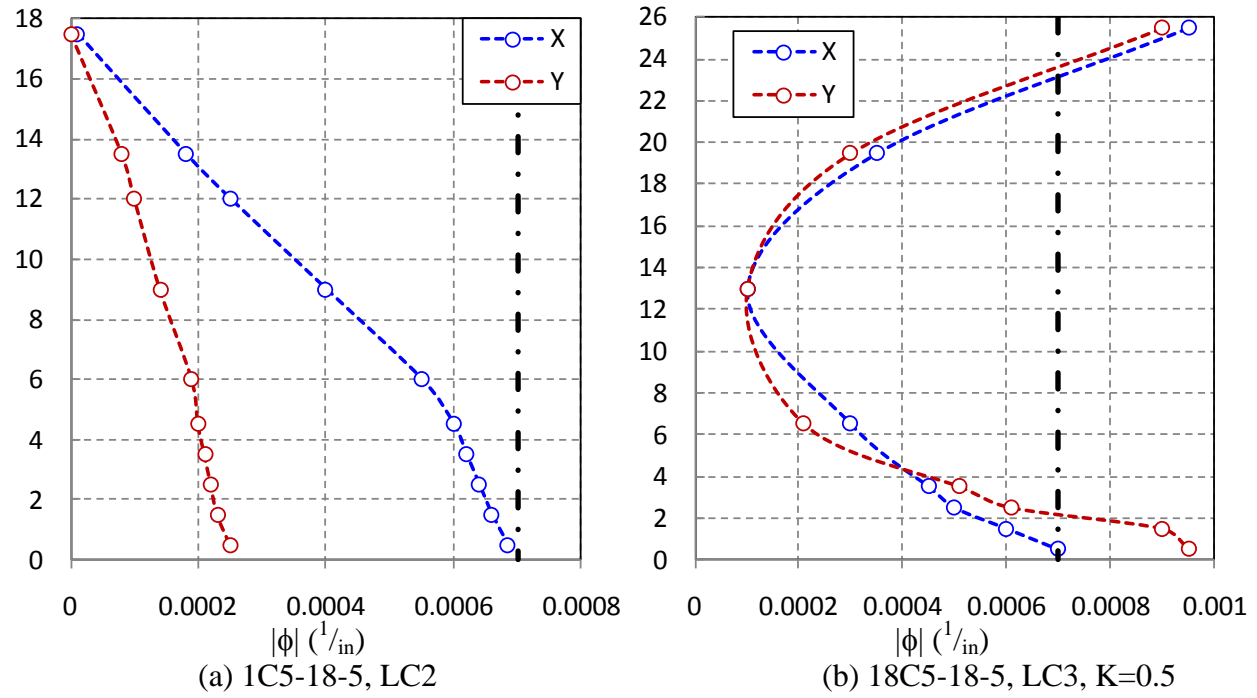


Figure 8.43. Curvatures vs. length at the peak displacement for the Specimens C5

8.5. Postmortem evaluation

At the end of the load protocol, the specimens were disconnected from the crosshead and the strong floor, and were stored in a staging area for a forensic analysis. The postmortem evaluation consisted in cutting the steel tubes at different places along the column. Thus, segments of steel plates were cut and extracted in zones where the highest local buckling deformation was observed (near the base in most cases), and also in those spots where there was no evidence of plasticity or damage (near the top).

Coupon samples were obtained from the steel plates cut in the undamaged areas with the aim of obtaining the steel properties with tension tests. The results obtained from the coupon tests are presented in the Appendix A.

In addition, concrete cores were extracted from the undamaged spots for future corroboration of the concrete properties. The concrete cores extracted, as well as the concrete zone around the exposed area, seemed very healthy and with no evidence of small cracks or voids.

The segments cut in the zone where the highest damage was observed were aimed at determining the concrete condition behind the steel local buckling deformation. Figure 8.44 and Figure 8.45 shows some of the post-mortem photographs taken from specimens 7C20-18-12 and 8Rw-18-12, respectively. When the deformed steel plates were cut and removed, it was observed and confirmed that the highest local buckling deformation was spread by coarse-like pieces of concrete, as shown in Figure 8.44.b, Figure 8.45.c and 8.45d. In addition, small cracks in the concrete were observed superficially in the concrete as shown in Figure 8.44.b and 8.18.c; however, no evidence of concrete-steel slip was observed or noticed. Once the external condition of the concrete was documented, the exploration of deeper cracks was carried out by removing the external surface of the concrete. As shown in Figure 8.44.d and Figure 8.45.e, the concrete cores were found to be highly confined and almost intact, with evidence of additional cracks, voids or similar defects.



(a) Local buckling deformation in steel



(b) Local buckling deformation spread by the concrete

Figure 8.44. Post-mortem images from the specimen 7C20-18-12



(c) Condition of the concrete in the external surface



(d) Condition of the concrete in the interior core

Figure 8.44. Post-mortem images from the specimen 7C20-18-12 (cont.)



(a) Local buckling deformation in steel



(b) Close up to the local buckling in steel



(c) Close up to the concrete deformed shape inside the steel local buckling

Figure 8.45. Post-mortem photos from the specimen 8Rw-18-12



(d) Condition of the concrete in the external surface



(e) Condition of the concrete in the interior core

Figure 8.45. Post-mortem photos from the specimen 8Rw-18-12 (cont.)

8.6. Conclusions

In Section 8.2, a detailed discussion on the steel local buckling was presented. The limits on the steel wall-slenderness that have been accepted in the AISC (2010) Specifications to avoid or minimize the local buckling failure are shown. Then, the theoretical formulas obtained for the determination of the local buckling of plates are presented. In addition, previous empirical calibrations to characterize the initiation of local buckling are also discussed. Finally, in this section, the extraction of the first occurrence of local buckling in the 18 specimens tested for this project is presented.

Based on the empirical data extracted from these tests, an update of empirical equations for the local buckling initiation is proposed for both CCFT and RCFTs. The proposed equation is:

$$\varepsilon_{lb} = \begin{cases} 0.09 \left(\frac{D}{t} \cdot \frac{F_y}{E_s} \right)^{-2} \frac{F_y}{E_s} = \frac{0.09}{\lambda^2 \cdot \varepsilon_y} & \text{for CCFTs} \\ 9 \left(\frac{h}{t} \sqrt{\frac{F_y}{E_s}} \right)^{-2} \frac{F_y}{E_s} = \frac{9}{\lambda^2} & \text{for RCFTs} \end{cases} \quad (8.23)$$

From the empirical calibration equations shown above, an update of limits for slender filled tubes (λ_r) and non-compact tubes are proposed as:

$$\lambda_r = \begin{cases} 0.3 \frac{E_s}{F_y} & \text{for CCFTs} \\ 3.0 \sqrt{\frac{E_s}{F_y}} & \text{for RCFTs} \end{cases} \quad (8.24)$$

$$\lambda_p = \begin{cases} 0.15 \frac{E_s}{F_y} & \text{for CCFTs} \\ 2.12 \sqrt{\frac{E_s}{F_y}} & \text{for RCFTs} \end{cases} \quad (8.25)$$

In Section 8.3, key responses during the load cases LC1 and LC2 were illustrated including first occurrence of the steel yielding in both compression and tension, the concrete crushing and steel local buckling.

In Section 8.4, an analysis on the plastic hinge lengths is presented based on the maximum curvature within the load protocol through the column length. Based in this data analysis, it is recommended to get the plastic hinge length as:

$$L_p = L \left(1 - \frac{M_y}{M_p} \right) = L \left(1 - \frac{S}{Z} \right) = L \left(1 - \frac{1}{k_s} \right) \quad (8.26)$$

The post-mortem or forensic analysis of the CFT specimens tested in this project was presented in Section 8.4. To accomplish this goal, steel segments were cut in the zone where the highest damage was observed. When the deformed steel plates were cut and removed, it was observed and confirmed that the highest local buckling deformation was spread by coarse-like pieces of concrete. No clear evidence of significant concrete-steel slip was observed or noticed when the tubes were cut and open; however, the slip was not monitored or measured during the test, and so this note is based only on the final physical observation on the exposed specimen. Once the external condition of the concrete is reported, the exploration of deeper cracks was carried out by removing the external surface of the concrete. The concrete cores were found to have been highly confined and almost intact.

CHAPTER 9

TORSION

9.1. Introduction

Evaluation of the torsional strength and stiffness of columns has an important role when 3D analysis is performed. For composite columns, the torsional strength (T_n) and rigidity (GJ) have been conservatively assumed as the maximum value obtained for either the steel or the concrete component (the steel commonly governs), or as the superposition of reduced values of these components. The uncertainty in the latter approach resides in the methodology to assess the effective contribution of each component.

Due to the position of the steel tube on the perimeter of the cross-section, it is expected to have a very beneficial effect on the torsional behavior of CFT members. Due to its shape, it is also expected that circular CFT cross-sections will have a much better performance than rectangular CFT cross-sections. In addition, because concrete cracking is much more severe under cyclic than under non-cyclic loading, the contribution of concrete to torsion is expected to be very low under earthquake loading as compared to gravity loading conditions.

Experimental results from the eight CFT specimens that were subjected to torsion are evaluated and discussed in this chapter. This torsional loading case was applied at the end of the load protocol, so these specimens have previous damage, sometimes serious, due to the previous loading cycles (in particular for the RCFTs, where the damage was considerable at this point).

Section 9.2 of this Chapter presents key results and conclusions of previous research studies related to torsional loading. Section 9.3 presents a summary of torsional design approaches given in some codes and specifications. Section 9.4 presents the experimental results obtained from the testing, and section 9.5 describes the calibration with the strength and the stiffness data for CFTs. Section 9.6 presents the conclusions from the observed results.

9.2. Previous studies

9.2.1. Analytical research

Although high torsional strength and rigidity are expected in CFTs, few analytical studies have been focused on the torsional behavior of CFTs. Some of these previous studies are summarized below.

Kitada (1992) reviewed the ultimate strength and ductility of CCFTs and RCFTs under different types of loading, including torsion. According to this study, the ultimate torsional moment of a CFT section is about 1.2 times the sum of the individual torsional resistance of the steel and concrete. This author found that the ultimate torsional moment could be accurately predicted by assuming the ultimate shearing stress of concrete as $0.5f_c'$. As anticipated, CCFTs exhibited a superior ductility and a much larger ultimate torsional moment over the RCFTs.

Han, Yao, and Tao (2007) developed a parametric study to evaluate the behavior of CFTs under pure torsion loads using finite element analysis (FEA). Both the steel tube and concrete core were modeled with eight node brick elements, and the interface between steel tube and concrete core was modeled with contact and Coulomb friction ($\mu=0.6$). Comparison between the FEA and collected empirical results showed good agreement. Formulas for the calculation of the ultimate torsional strength and torsional moment vs. torsional strain curves were developed for circular and square CFTs. As shown in Figure 9.1, the results from the FEA performed by these authors indicate that the steel tube provides the majority of the strength and stiffness of the composite section in torsion; in addition, stresses are concentrated in the corners in square CFTs (even when the corners were modeled with the chamfers rounded), and distributed in circular CFTs with principal stresses at 45° of inclination with respect to the longitudinal axis.

Using the same FE model, similar analyses are presented by Han, Yao, and Tao (2007b) with combined torsional loading (i.e. compression and torsion, bending and torsion, compression, bending and torsion). Comparison between FEA and collected empirical results also showed good agreement. In addition, formulas for the calculation of the ultimate torsional strength and torsional moment vs. torsional strain curves were developed for circular and square CFTs. In this paper, interaction diagrams are presented between different combined loading cases (such as compression and torsion, bending and torsion, compression, bending and torsion) as those illustrated in Figure 9.2.

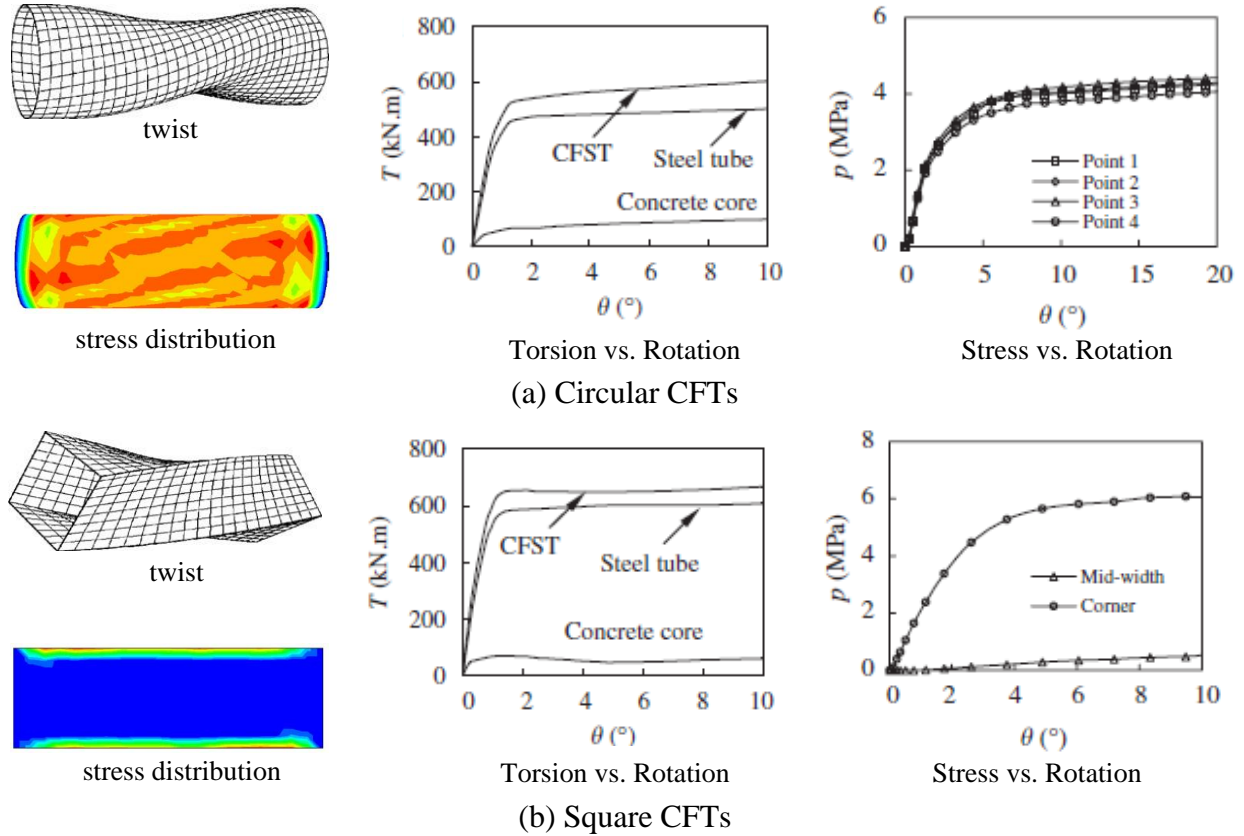


Figure 9.1. Results from FE analysis under pure torsion in CFTs by Han, Yao, and Tao (2007)

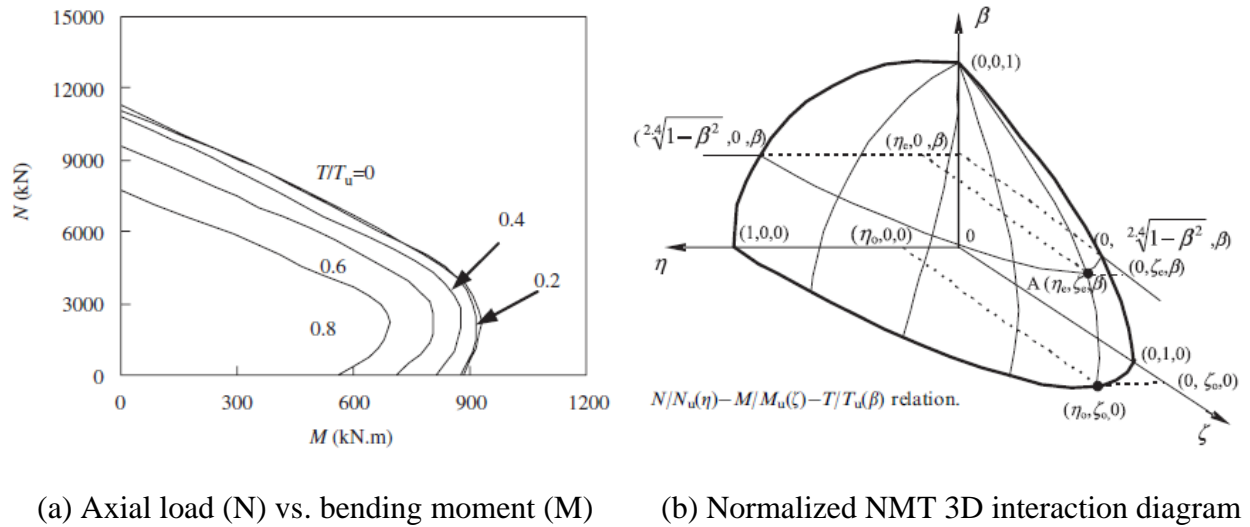


Figure 9.2. Interaction diagrams with torsion in CFTs presented by Han, Yao, and Tao (2007b)

9.2.2. Experimental research

As mentioned in Chapter 2, few experimental research studies have been conducted for composite columns under torsional loads. Some of the experimental studies with torsional loading in CFTs are those reported by Gong (1989), Zhou (1990), Kitada and Nakai (1991), Lee *et al.* (1991), Xu *et al.* (1991), Han and Zhong (1995), and Beck and Kiyomiya (2003). The steel tubes used in all these experimental studies are circular shapes with a maximum 5½ inches of diameter.

Lee *et al.* (1991) tested short CCFTs under monotonic and cyclic torsional loading with and without compression. Results of this study show higher torsional resistance in the CCFTs with higher compression loads.

Xu *et al.* (1991), in contrast, tested short ($L=7D$), medium ($L=13D$) and long ($L=20D$) CCFTs under torsional loading, also with and without compression. Contrary to Lee *et al.*'s results, the ultimate torsional moment resistance decreased with an increase in the axial load ratio, so the highest torsional moment was attained in the pure torsion case. The characteristic failure mechanism was a cracking of the concrete followed by a propagation of the cracks along the length of the tube in a spiral pattern.

Lack of experimental data is evident for rectangular and square CFT specimens under torsional loading. The following section show additional experimental results obtained for both CCFTs and RCFTs under torsional loading.

9.3. Specifications and Codes

There are very few provisions in the available Specifications (i.e. AISC, 2010; ACI, 2008; EC-4, 2004; AIJ, 2001) for design for torsional loads in composite columns. The few provisions concerning torsion in these codes focus mainly on the lateral torsional buckling of composite beams.

For steel beams connected with studs to a concrete slab (inverted U-frame), section 6.4 of the EC-4 (2004) provisions recommends the use of the torsional stiffness of the steel only for the calculation of the critical moment for torsional buckling (M_{cr}). For partially-encased steel beams with encasement reinforcement, the torsional stiffness can be taken as the superposition of the steel and 10% of the concrete stiffness. No other additional torsional provisions are detailed in this EC-4 (2004) document. As complement, the Eurocodes for steel (EC-3, 2004) and concrete (EC-2, 2004) structures give design recommendations for the calculation of torsional strength and stiffness in steel and concrete members, respectively. However, neither full nor partial superposition of the components is recognized for composite members.

The Chapter I of the AISC (2010) Specifications, which focus in composite members, also requires the verification of torsional local buckling for composite beams. The AISC (2005) commentary – Chapter I, mentions that encasement in concrete encased-beams reduce drastically the possibility of lateral-torsional buckling and prevents local buckling of the encased steel. However, the AISC (2010) Specification does not give detailed guidelines of how to incorporate this effect into the calculations.

None of the available provisions above gives recommendations about the torsional strength and torsional rigidity explicitly developed for composite columns. However, the criterion of adopting the maximum capacity (strength or stiffness) between the steel and the concrete component is very common and accepted in practice; design equations for the strength or the stiffness of independent component is well documented in available concrete and steel codes worldwide.

Chapter H in the AISC (2010) Specifications is related to torsion and combined loading in steel members, and section H3.1 is related to HSS cross-sections under torsion. In this section, the nominal torsional strength (T_s) for steel tubes can be calculated as:

$$T_s = F_{crs} \cdot C_s \quad (9.1)$$

where the critical torsional stress of the steel tube depends on the wall slenderness ratio and is limited to $F_{crs} \leq 0.6F_y$.

Approximate equations in a user note for the torsional constant (C_s) are also given in this section. Thus, for round HSS tubes:

$$C_s = \frac{\pi(D-t)^2 t}{2} \quad (9.2)$$

and for rectangular HSS tubes:

$$C_s = 2(b-t)(h-t)t - 4.5(4-\pi)t^3 \quad (9.3)$$

The design torsional capacity is calculated from the nominal strength with a strength reduction factor for torsion equal to $\phi_T = 0.9$ for LRFD design, or with a safety factor for torsion equal to $\Omega_T = 1.67$ for ASD design.

For concrete elements, the design for torsion loading is covered by the section 11.5 in ACI-318 (2008). Torsion may be neglected if the factored torsional moment (T_u) calculated as section 11.5.2 is less than a threshold value given in section 11.5.1. The verification of the minimum concrete cross-section size to avoid cracking and crushing in concrete under torsion is in section 11.5.3. In the same ACI-318 section, equation 11-21 is given for the calculation of the nominal torsional strength of the concrete cross-section; this equation depends only on the lateral reinforcement (diagonal stirrups or ties) and was developed based on the space truss analogy.

9.4. Experimental results

Experimental results from the eight CFT specimens that were subjected to twisting (load case LC4) are evaluated and discussed in this section. As summarized in Table 9.1 (see also Figure 3.21 in Chapter 3), five DOF's for this load case were in displacement control, and the Z vertical DOF was in force control. Thus, both X and Y displacements and rotations were set and fixed at zero displacements and rotations, the Z vertical force was set and fixed at the desired gravity load, and finally, the RZ vertical rotation (or twisting DOF) was moved to the maximum twisting capacity ($\theta_z \approx \pm 10^\circ$) of the crosshead system.

Table 9.1. DOF's controlled during the torsional loading

Step	DOF					
	Force / Displacement			Moment / Rotation		
	X	Y	Z	RX	RY	RZ
1a	$\Delta_x=0$	$\Delta_y=0$	$F_z=0$	$\theta_x=0^\circ$	$\theta_y=0^\circ$	$\theta_z = 0^\circ$
1b	$\Delta_x=0$	$\Delta_y=0$	$F_z=0$	$\theta_x=0^\circ$	$\theta_y=0^\circ$	$\theta_z \rightarrow +10^\circ$
1c	$\Delta_x=0$	$\Delta_y=0$	$F_z=0$	$\theta_x=0^\circ$	$\theta_y=0^\circ$	$\theta_z \rightarrow -10^\circ$
1d	$\Delta_x=0$	$\Delta_y=0$	$F_z=0$	$\theta_x=0^\circ$	$\theta_y=0^\circ$	$\theta_z \rightarrow 0^\circ$
2a	$\Delta_x=0$	$\Delta_y=0$	$F_z=0.2P_o$	$\theta_x=0^\circ$	$\theta_y=0^\circ$	$\theta_z = 0^\circ$
2b	$\Delta_x=0$	$\Delta_y=0$	$F_z=0.2P_o$	$\theta_x=0^\circ$	$\theta_y=0^\circ$	$\theta_z \rightarrow +10^\circ$
2c	$\Delta_x=0$	$\Delta_y=0$	$F_z=0.2P_o$	$\theta_x=0^\circ$	$\theta_y=0^\circ$	$\theta_z \rightarrow -10^\circ$
2d	$\Delta_x=0$	$\Delta_y=0$	$F_z=0.2P_o$	$\theta_x=0^\circ$	$\theta_y=0^\circ$	$\theta_z \rightarrow 0^\circ$

The torsional loading was applied after all the cycles and trials of the buckling loading (LC1) and flexural loading cases (LC2 and LC3) had been completed. Consequently, these experimental torsional results have implicitly incorporated previous damage due to the loading cases LC1 through LC3. At the beginning of the torsional loading, RCFT specimens had higher damage than the CCFTs specimens. This higher damage in RCFTs consisted of a high level of steel local buckling and severe concrete cracking and crushing at the base of the column. However, even with a level of lower damage, CCFTs started the torsional loading tests with some concrete cracks and a low level of steel local buckling as well at the base. It is expected that this initial damage, higher in RCFTs, results in a significant reduction of the experimental torsional stiffness (GJ_{exp}) as compared to the GJ that would be obtained in a brand new specimen.

The torsional load case LC4, with and without axial load, was applied only in the Specimens 1 to 8. The incremental twisting was applied in a full cycle to the maximum twisting

capacity ($\theta_z \approx \pm 10^\circ$). In order to evaluate the effect of the axial force on the torsional strength, the torsional loading was applied without and with compression force on the column. For the cases with axial force, a gravity load of about 20% of the squashing load ($P \approx 0.2P_o$) was selected.

Both torsional moment (T) and twisting angle (θ_z) are measured at the crosshead (top of the column). The main parameters from the available tests data during the torsional loading case are summarized in Table 9.2. As reminder, the ultimate torsional capacity of these CFT specimens was not achieved since, in all cases, the system reached the maximum twisting capacity that varies between 9° to 10° ; for specimen 7, the pure torsion test was stopped at 7.56° to avoid a failure in the connections that were not designed for torsion above 500 kip-ft. Table 9.2 also shows the steel capacity to resist torsion (T_s) as obtained with the AISC (2010) Specifications with the Equation 1.1, with the torsional constant C_s obtained with Equation 1.2 for round HSS and with Equation 1.3 for rectangular HSS. This torsional capacity of the steel component was obtained with the steel parameters obtained from the coupon tests. Even though the ultimate torsional capacity of the composite section was not achieved, the results in Table 9.2 indicate that the torsional strength at the maximum measured torsional deformation exceeded the ultimate torsional capacity of the steel component with values ranging from 1.16 to 1.56; the latter results suggest a participation of the concrete component to the torsional capacity of the composite section. Calibration of the concrete participation is discussed in the following section.

Table 9.2. Summary of results from torsional loading

Specimen	Axial load	Values at twisting stroke		C_s (in ³)	T_s (kip-ft)	T_{exp} / T_s
	P_{exp} (kip)	T_{exp} (kip-ft)	θ_z (deg)	Eq. 1.2 & 1.3	Eq. 1.1	ratio
1C5-18-5	0	19	9.05	5.8	16	1.20
2C12-18-5	0	182	9.66	57.3	140	1.32
	250	197				1.43
6C12-18-12	0	181	10.01	57.3	140	1.32
	380	214				1.56
3C20-18-5	0	439	9.67	143.0	340	1.30
	500	495				1.47
7C20-1812	0	445	7.56 *	143.0	340	1.32
4Rw-18-5	0	439	9.73	134.2	356	1.23
	700	437				1.23
5Rs-18-5	0	436	9.68	134.2	356	1.22
	700	415				1.16
8Rw-18-12	0	458	9.43	134.2	356	1.28

Note: (*) Pure torsion test in Specimen 7 was stopped at 7.56° of twisting rotation.

The torsional moment – twisting angle (T - θ_z) curves obtained experimentally are shown from Figure 9.3 to Figure 9.6. From these figures, the following observations can be noticed:

- Note that the maximum torsion obtained in the test corresponds to the reached value at the instant where the system ran out of twisting capacity (about $\theta_z \approx \pm 10^\circ$), or when the loading test stopped earlier with a lower twisting angle. However, in any case the ultimate torsion capacity was obtained, except in the specimen 1 where the torsion – rotation history exhibited an unexpected response.
- There was a minor effect on the torsional strength and stiffness due to either the change in concrete strength ($f_c' = 5$ ksi vs. $f_c' = 12$ ksi) and the compression load ($P = 0$ vs. $P \approx 0.2P_o$).
 - The increment of the torsional strength for CCFTs with high strength concrete ($f_c' = 12$ ksi) did not exceed 9% of the strength obtained for normal strength concrete ($f_c' = 5$ ksi). Because of higher damage in the concrete inside the rectangular steel tubes, this increment did not exceed 5% in the RCFTs.
 - On the other hand, the increment of the torsional strength with gravity load ($P \approx 0.2P_o$) on CCFT's varies from 8% to 18% of the strength obtained without gravity ($P = 0$), while no increment was achieved for the RCFTs.
 - In regard to the stiffness, no significant differences are noticeable for either the use of high or normal concrete strength or the compression load level.
- The torsion-twisting curves (T - θ_z) have a noticeable non-linear behavior.

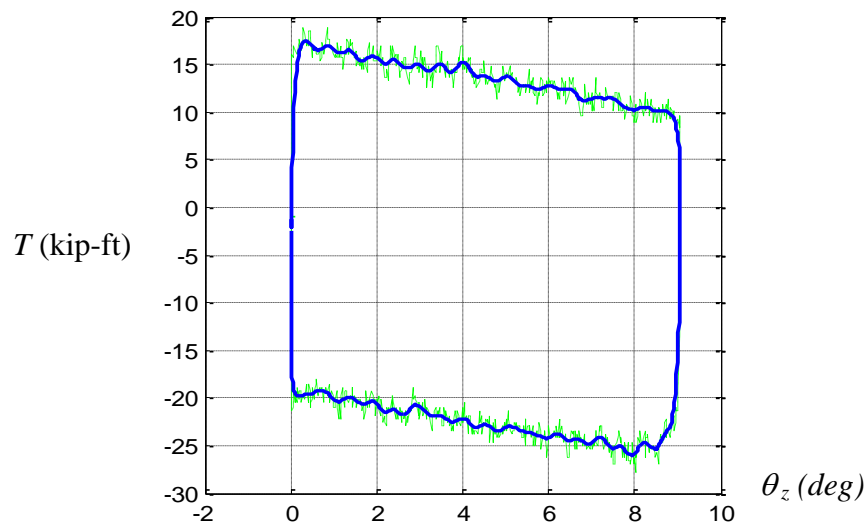


Figure 9.3. Torsional loading vs. twisting angle (T - θ_z) of the Specimen 1C5-18-5 with $P=0$. The blue curve is a filtered and smoothed response of the raw data included in green.

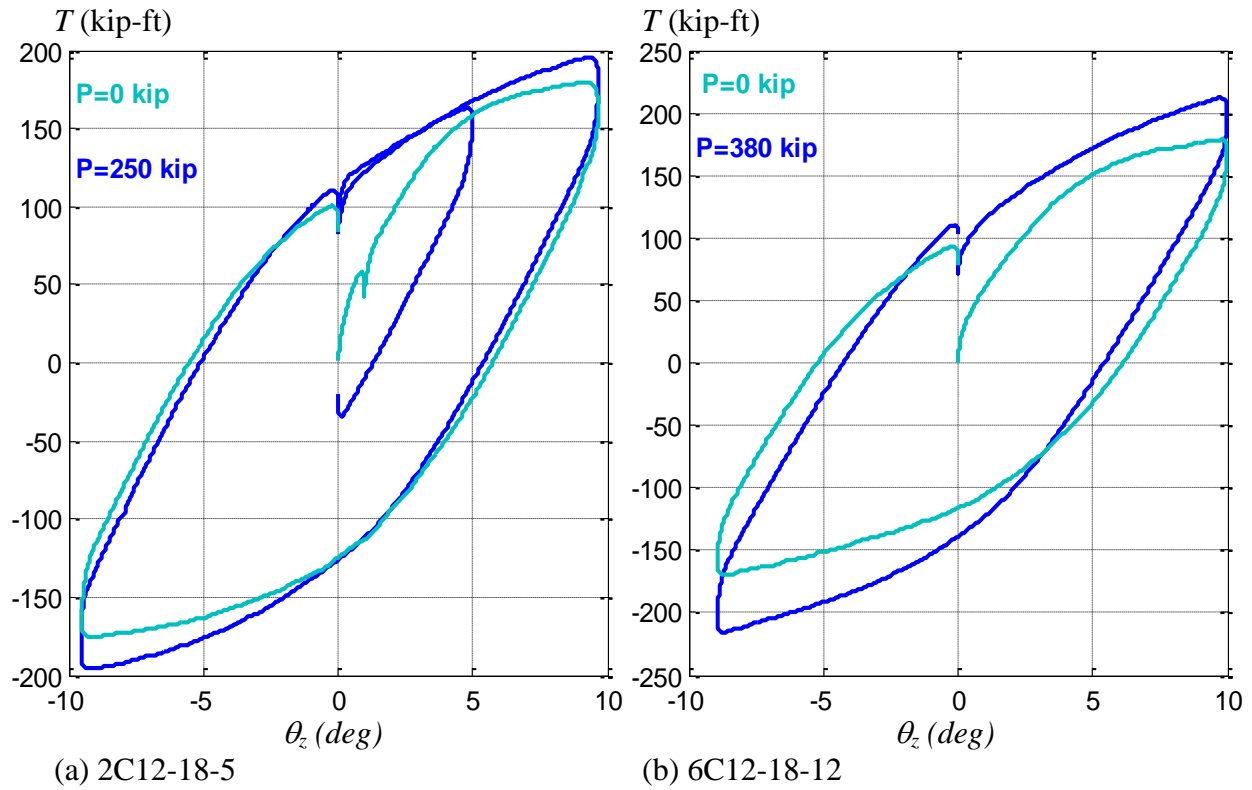


Figure 9.4. Torsional loading vs. twisting angle for the Specimens 2C12-18-6 and 6C12-18-12

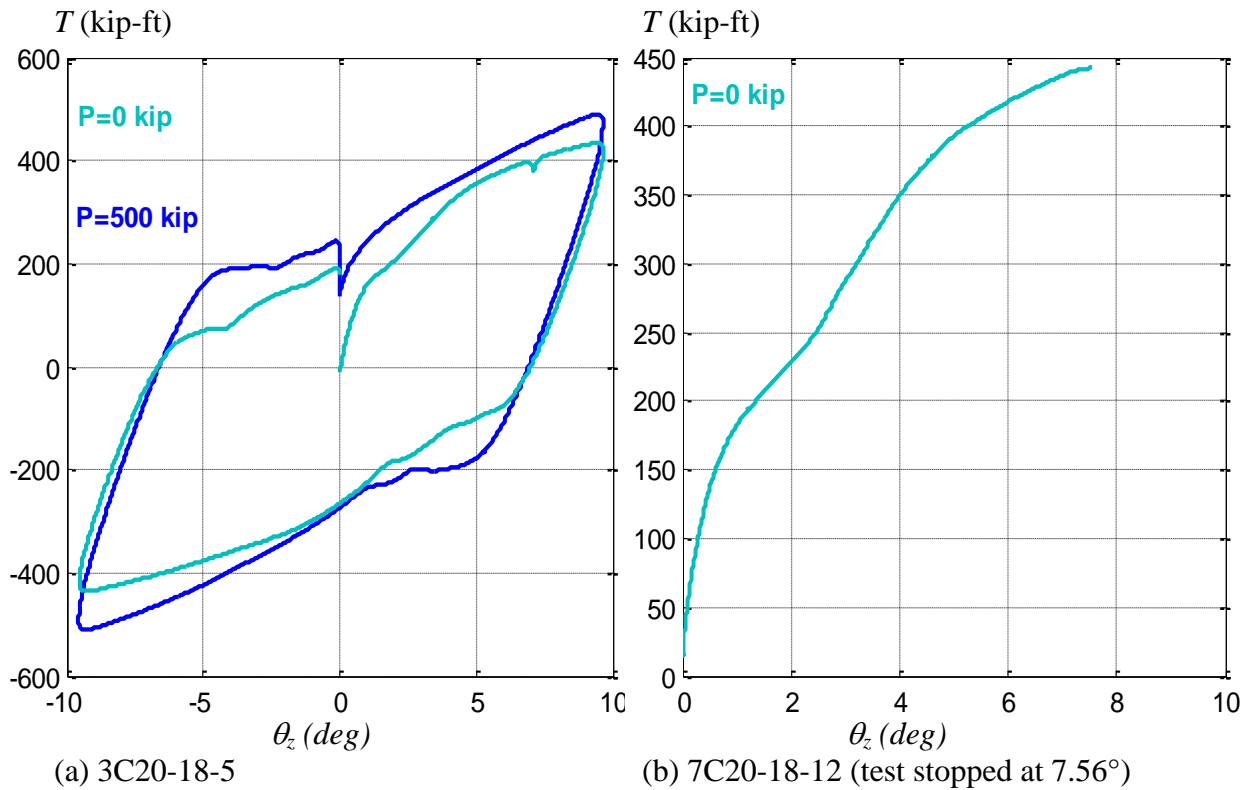


Figure 9.5. Torsional loading vs. twisting angle for the Specimens 3C20-18-5 and 7C20-18-12

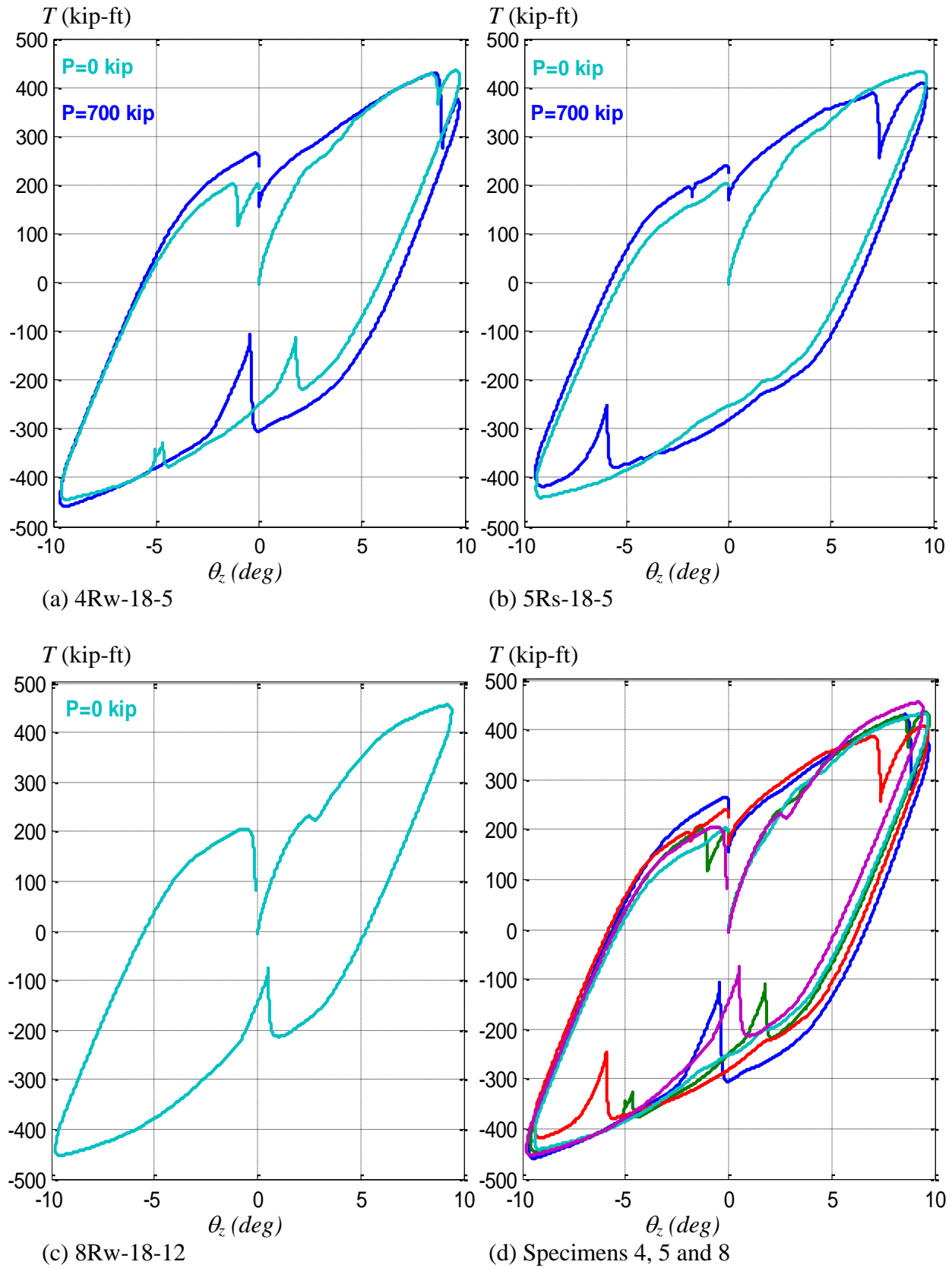


Figure 9.6. Torsional loading vs. twisting angle (T - θ) obtained for the Specimens 4, 5 and 8

9.5. Calibration of the experimental data

The analytical solutions for circular and non circular shafts under torsion are well documented in several textbooks on strength of materials (i.e. Timoshenko and Gere, 1972, Budynas, 1999). However, as mentioned before, theoretical solutions for composite CFT members under torsion have not been totally covered.

In this section, an attempt to calibrate simplified equations to calculate the torsional capacity and torsional rigidity of CFT cross-section with the available experimental data and based on the theoretical solutions are presented. In the following equations, the subscripts “s” and “c” will stand for the steel and the concrete components, respectively.

The material properties needed in torsional loading are the shear modulus for the steel (G_s) and the concrete (G_c), and these are obtained based on the corresponding Young's modulus (E) and the Poisson ratio (ν). Standard Poisson ratio values for the steel ($\nu_s=0.3$) and concrete ($\nu_c=0.2$) are assumed, while the Young's Modulus (E_s , E_c) are taken from the material tests previously documented. Then:

$$G_c = \frac{E_c}{2(1+\nu_c)} \quad (9.4)$$

$$G_s = \frac{E_s}{2(1+\nu_s)} \quad (9.5)$$

Concerning the geometric properties in CCFTs, the polar moment of inertia for the circular concrete cross-section (J_c) and the steel hollow tube (J_s) of diameter (D) and thickness (t) can be obtained by (Young and Budynas 2001):

$$J_c = \frac{\pi(D-2t)^4}{32} \quad (9.6)$$

$$J_s = \frac{\pi D^4}{32} - J_c \quad (9.7)$$

For thin circular steel tubes (or with large D/t ratios), the equation above can be approximated as (Young and Budynas 2001):

$$J_s \approx \frac{\pi D^3 t}{4} \quad (9.8)$$

In RCFTs, the torsion constants for the rectangular concrete cross-section (J_c) and the steel rectangular hollow tube (J_s) can be obtained in terms of the larger side (h, h_c), the shorter side (b, b_c) and the thickness (t) of the steel tube (Young and Budynas 2001):

$$J_c \approx h_c b_c^3 \left(\frac{1}{3} - 0.21 \frac{b_c}{h_c} \left(1 - \frac{1}{12} \left(\frac{b_c}{h_c} \right)^4 \right) \right) \quad (9.9)$$

$$J_s = \frac{2t^2 (h-t)^2 (b-t)^2}{ht + bt - 2t^2} \quad (9.10)$$

9.5.1. Torsional capacity

An accurate calibration of the ultimate torsional strength with the experimental data obtained in this project is challenging since, as a reminder, the maximum torsion strength reported for each test correspond to the torsion when the system ran out of twisting capacity. In addition, as shown in the previous figures, the torsion – twisting response exhibited a non-linear behavior that makes subjective any determination of the elastic and the ultimate torsional capacity. However, conservatively, the nominal maximum torsion is calibrated with the strength related to the maximum twisting stroke. This calibration will provide simple equations that aim to estimate reasonable and conservative values of the nominal twisting capacity.

Thus, the nominal torsional capacity of the CFTs is assumed as the superposition of the torsion capacities of both the steel component (T_s) and the concrete component ($\alpha_T T_c$) as described by the following equation:

$$T_n = T_s + T_c = 0.6F_y C_s + \alpha_T f'_c C_c \quad (9.11)$$

where the factors C_s and C_c are the torsional constant for the steel component (see Equation 9.2 and 9.3) and the concrete component. The critical torsional stress in the steel is taken as 60% of the yielding stress.

The elastic torsional strength (T_s) for circular steel HSS tubes can be approximated as:

$$T_s \approx 0.6F_y \left(\frac{\pi \cdot D \cdot t (D - 3t)}{2} \right) \quad (9.12)$$

The term in parenthesis in the previous equation is a better approximation of the torsional constant (C_s) for the round HSS tube than that given in the AISC (2010) Specifications and reproduced in Equation 9.2.

Similarly, the elastic torsional capacity (T_s) for rectangular steel HSS tubes can be approximated to:

$$T_s \approx 0.6F_y \left[2(b-t)(h-t)t - 3.86t^3 \right] \quad (9.13)$$

The term $3.86t^3$ in the previous equation takes into account the rounded chamfers at the corners in rectangular HSS sections. The term in brackets in the previous equation is a better approximation of the torsional constant (C_s) for the round HSS tube than that given in the AISC (2010) Specifications and reproduced in Equation 9.2.

The two equations above are similar to that given in the AISC (2010) Specifications for HSS tubes (see Equation 9.1).

For the concrete component, the torsional capacity of the circular section is given by:

$$T_c \approx \alpha_T f'_c \left(\frac{\pi (D - 2t)^3}{16} \right) \quad (9.14)$$

The torsional capacity of rectangular concrete section is:

$$T_s \approx \alpha_T f'_c \left[\frac{b_c^2 h_c}{3 \left(1 + 0.6095 \frac{b_c}{h_c} + 0.8865 \left(\frac{b_c}{h_c} \right)^2 - 1.8023 \left(\frac{b_c}{h_c} \right)^3 + 0.91 \left(\frac{b_c}{h_c} \right)^4 \right)} \right] \quad (9.15)$$

Calibration of the participation factor (α_T) for the concrete component in the torsional capacity of the CFT composite member can be extracted by assuming that this capacity (T_n) is equal (or at least very close) to the maximum experimental value (T_{exp}) at the system twisting stroke (given in Table 9.2). Thus:

$$\alpha_T = \frac{T_{exp} - 0.6F_y C_s}{f'_c C_c} \quad (9.16)$$

Table 9.3 shows the results of the calibration as stated above. In this table, the participation factor of concrete in torsion (α_T) was obtained with the Equation 9.16, and using the material properties measured from the material tests reported in Chapter 3 and Appendix A. As seen in Table 9.3, the α_T factor varies in pure tension from 0.11 to 0.26 for CCFTs, and from 0.18 to 0.33 for the RCFTs; for combined torsion and compression, this α_T factor varies from 0.19 to 0.35 in CCFTs, and from 0.18 to 0.33 in RCFTs. The average values obtained for each case are summarized in Table 9.4; these averaged factors are used to get the expected torsional capacity $E(T_n)$ of the composite CFT cross section presented in Table 9.4, which predicts the experimental capacity within a 10% of error.

Table 9.3. Calibration for the torsional capacity of CFTs

Specimen	P_{exp} (kip)	T_{exp} (kip-ft)	θ_z (deg)	C_s (in ³)	C_c (in ³)	α_T	T_s (kip-ft)	$E(T_n)$ (kip-ft)	$E(T_n)/T_{exp}$
1C5-18-5	0	19	9.05	5.6	29.5	0.24	16	18	0.95
2C12-18-5	0	182	9.66	56.2	364.0	0.26	137	166	0.91
	250	197				0.35		180	0.91
6C12-18-12	0	181	10.01	56.2	364.0	0.11	137	200	1.10
	380	214				0.19		236	1.10
3C20-18-5	0	439	9.67	141.3	1463.5	0.15	336	457	1.04
	500	495				0.22		513	1.04
7C20-18-12	0	445	7.56 *	141.3	1463.5	0.07 *	336	610	1.37 *
4Rw-18-5	0	439	9.73	134.2	507.0	0.33	356	418	0.95
	700	437				0.33		418	0.96
5Rs-18-5	0	436	9.68	134.2	507.0	0.24	356	439	1.01
	700	415				0.18		439	1.06
8Rw-18-12	0	458	9.43	134.2	679.2	0.18	356	496	1.08

Note: () Pure torsion test in Specimen 7 was stopped at 7.56° of twisting rotation*

Table 9.4. Effectiveness factor (α_T) of the concrete in the torsion capacity

Torsion case	CCFTs	RCFTs
Pure torsion	0.17	0.25
Combined Torsion and Compression	0.25	0.25

Even though a limited number of data is presented, these results indicate the following tendencies:

- The axial load has a higher impact in CCFTs than in RCFTs.
- The participation of the concrete on the torsion capacity of the composite section is higher in RCFTs than in CCFTs. This is attributed to a higher interlock between the concrete and the steel shape that is developed in RCFTs.
- In addition, the participation of the concrete on the torsion capacity of the composite section is lower with higher strength concrete.

9.5.2. Torsional rigidity

The definition of torsional rigidity or elastic torsional stiffness (GJ) can also be found in any strength of materials textbook (i.e. Timoshenko and Gere, 1972, Budynas, 1999). In general, this stiffness can be calculated as:

$$GJ = \frac{T \cdot L}{\theta_z} \quad (9.17)$$

where L is the total column length between supports, T is the torsional moment for the fixed-free boundary conditions typically used, and θ_z is the total twisting angle (in radians) between the supports, varying from zero at the fixed base to a maximum value at the top.

The previous equation can be rewritten as below in order to get the torsional rigidity from the experimental torsion – twisting response.

$$GJ_{exp} = \frac{\Delta T \cdot L}{\Delta \theta_z} = \frac{(T_2 - T_1) \cdot L}{\theta_{z2} - \theta_{z1}} \quad (9.18)$$

The latter expression is related to the slope of the torsion – twisting (T - θ_z) curve. However, as shown in Figure 9.3 to Figure 9.6, the torsion-twisting response has a noticeable non-linear behavior. The experimental secant stiffness is highly dependent on the definition of

the ultimate point. In addition, the experimental tangent stiffness (calculated with Equation 9.18) also depends on the interval where the tangent is evaluated.

This behavior is clearly illustrated in Figure 9.7, which shows the progression of the tangent stiffness (GJ_{exp}) obtained with Equation 9.18 from the experimental torsion-twisting curve ($T-\theta_z$) for the specimen 7C20-18-12 in pure torsion ($P=0$). This figure shows nominal values of the torsional rigidities obtained for both the steel tube (G_sJ_s) and the concrete core (G_cJ_c) using Equations 9.4 to 9.7.

As for the torsional capacity, the torsional rigidity data is calibrated assuming the full stiffness of the steel component, and partial stiffness of the concrete component. This is reasonable due to the fact that the concrete loses stiffness once this component develops cracking. Thus, the contribution of the concrete to the torsional rigidity of the composite element can be obtained from the experimental rigidity of the CFTs using Equation 9.18, and the expected rigidities of the steel and the concrete components using Equations 9.4 to 9.7. The latter can be expressed as:

$$\beta_T = \frac{GJ_{eff} - G_sJ_s}{G_cJ_c} \quad (9.19)$$

The concrete participation factor to the CFT rigidity computed with Equation 9.19 is also shown in Figure 9.7. This figure shows the progression of the tangent rigidity, which starts with the full contribution of the concrete (Figure 9.7.a), but later reduces as this cracks (Figure 9.7.b and Figure 9.7.c), until eventually this component vanishes completely (Figure 9.7.d) at about 30% of maximum torsion achieved. Beyond this point, the tangent torsional rigidity is even lower than the steel rigidity and there is no contribution of the concrete.

T (kip-ft)

T (kip-ft)

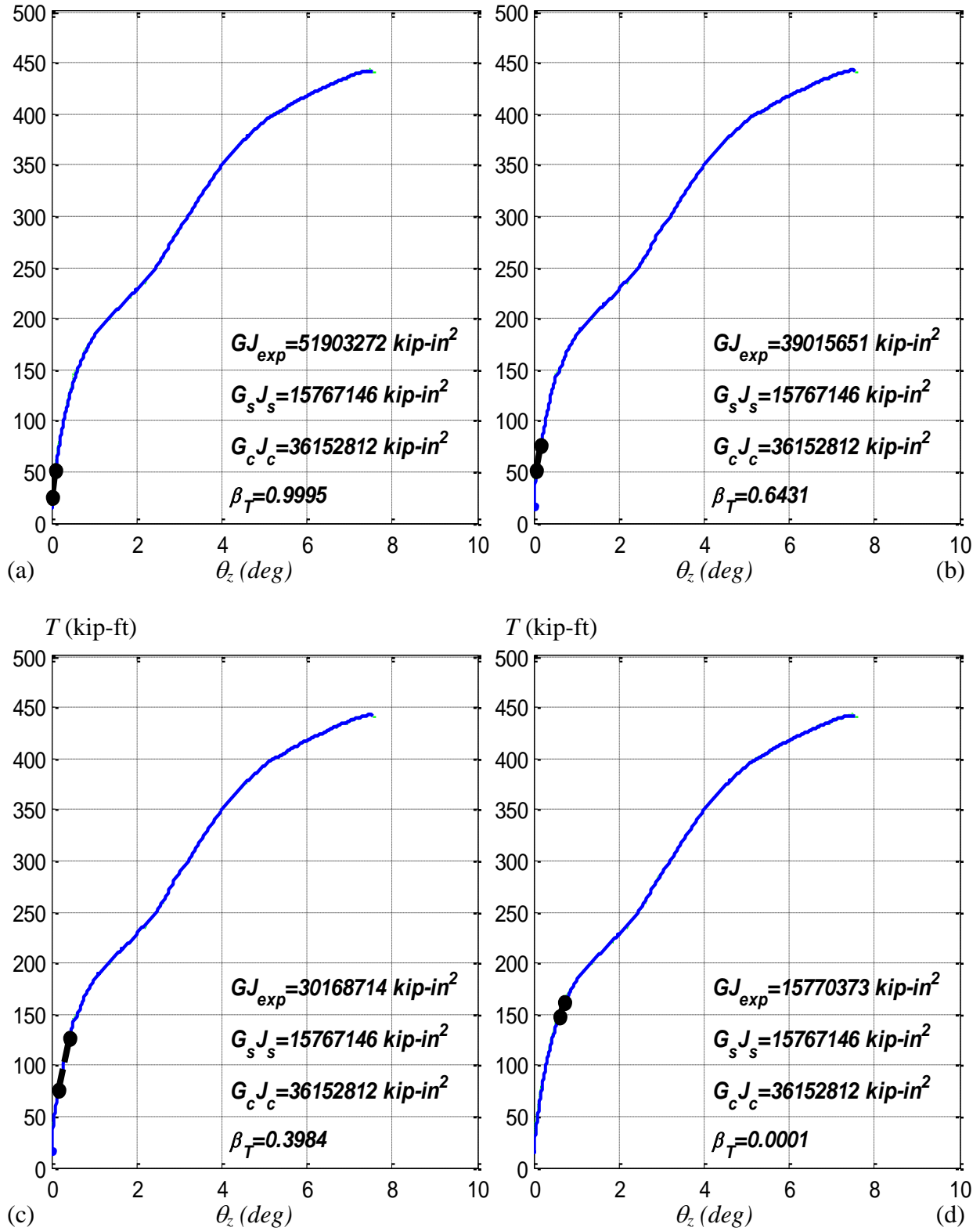


Figure 9.7. Change of the tangent torsional stiffness (GJ_{exp}) in Specimen 7 ($P=0 \text{ kip}$)

Experimental determination of the elastic torsional stiffness in the earlier range of the loading path may include some inaccuracies due to the high noise content when both torsion and twisting are being measured at small values. The elastic and a tangent stiffness can accurately be obtained in the unloading path with Equation 9.18, and earlier in the unloading branch to avoid the Bauschinger effect. Since the $T-\theta_z$ is a non-linear curve, the value of the tangent stiffness depends on where this is evaluated. What is interesting in the experimental determination of the torsional stiffness is the evaluation of the relative contribution of the concrete and the steel to this parameter. Due to a higher strength and the ideal position in the cross-section, the steel component is expected to be the main source of torsional stiffness. Thus, the effective elastic torsional stiffness (GJ_{eff}) of the composite CFT cross-section can be obtained based on the superposition of the elastic steel stiffness and the concrete stiffness (Equation 9.19). The reduction factor β_t accounts for the initial cracking state in the concrete.

Experimental determination of the effectiveness factor for the concrete in torsion (β_t) can be obtained by equating the experimental GJ_{exp} (Equation 9.2) and the effective GJ_{eff} (Equation 9.3) torsional rigidities. The value for this β_t factor depends if the elastic, a secant, or a tangent torsional stiffness is used in the calculation. Figure 9.8 to Figure 9.13 show the $T-\theta_z$ curves and the calculated experimental elastic and tangent torsional stiffness, as well as the corresponding effectiveness factor of the concrete torsion (β_t). All these values are also summarized in Table 9.5. As seen on this table, the effectiveness factor of the concrete in torsion (β_t) it is related to the steel ratio ($\rho_s=A_s/A$), so the higher ρ_s the higher β_t . In addition, β_t depends on the cross-section shape, with values for RCFTs being about one third of the factor for CCFTs. Finally, the ratio of tangent-to-elastic stiffness obtained from the tests is about one half. The tangent value is closer to that we can expect under cyclic load reversals (i.e. earthquake), while the elastic value is more appropriate for use under sustained loads with few or none cycles or wind loads. The equations in Table 9.6 are proposed to estimate the β_t factor for different conditions.

Table 9.5. Experimental torsional stiffness

Specimen (#-SD-L- f_c)	Torsional Stiffness	GJ_{exp} (kip)	G_sJ_s (kip-ft)	G_cJ_c (deg)	β_t
2-C12-18-5	Non-cyclic	5911136	4004254	3725700	0.5118
	Cyclic	5061556			0.2838
2-C12-18-5	Non-cyclic	6016097	4004254	3725700	0.5400
	Cyclic	5057319			0.2826
6-C12-18-12	Non-cyclic	7020025	4004254	5653750	0.5334
	Cyclic	5182661			0.2084
6-C12-18-12	Non-cyclic	6990648	4004254	5653750	0.5282
	Cyclic	5530714			0.2700
3-C20-18-5	Non-cyclic	26520067	15767146	23823929	0.4513
	Cyclic	20299414			0.1902
3-C20-18-5	Non-cyclic	27429138	15767146	23823929	0.4895
	Cyclic	22441338			0.2801
4-Rw-18-5	Non-cyclic	17430909	11003678	31370173	0.2049
	Cyclic	14478774			0.1108
4-Rw-18-5	Non-cyclic	17100976	11003678	31370173	0.1944
	Cyclic	16084750			0.1620
5-Rs-18-5	Non-cyclic	16175255	11003678	31370173	0.1649
	Cyclic	14174017			0.1011
5-Rs-18-5	Non-cyclic	17334775	11003678	31370173	0.2018
	Cyclic	15574941			0.1457
8-Rw-18-12	Non-cyclic	16879515	11003678	47604237	0.1234
	Cyclic	14274249			0.0687

Table 9.6. Equations to estimate the effectiveness factor of the concrete in torsional stiffness

Torsional Stiffness	Effectiveness factor of the concrete in torsional stiffness	
	CCFTs	RCFTs
Non-cyclic loads	$\beta_t = \left[2 \left(\frac{A_s}{A} \right) + 0.4 \right] \leq 1$	$\beta_t = \frac{1}{3} \left[2 \left(\frac{A_s}{A} \right) + 0.4 \right] \leq \frac{1}{3}$
Cyclic	$\beta_t = \frac{1}{2} \left[2 \left(\frac{A_s}{A} \right) + 0.4 \right] \leq \frac{1}{2}$	$\beta_t = \frac{1}{6} \left[2 \left(\frac{A_s}{A} \right) + 0.4 \right] \leq \frac{1}{6}$

(9.20)

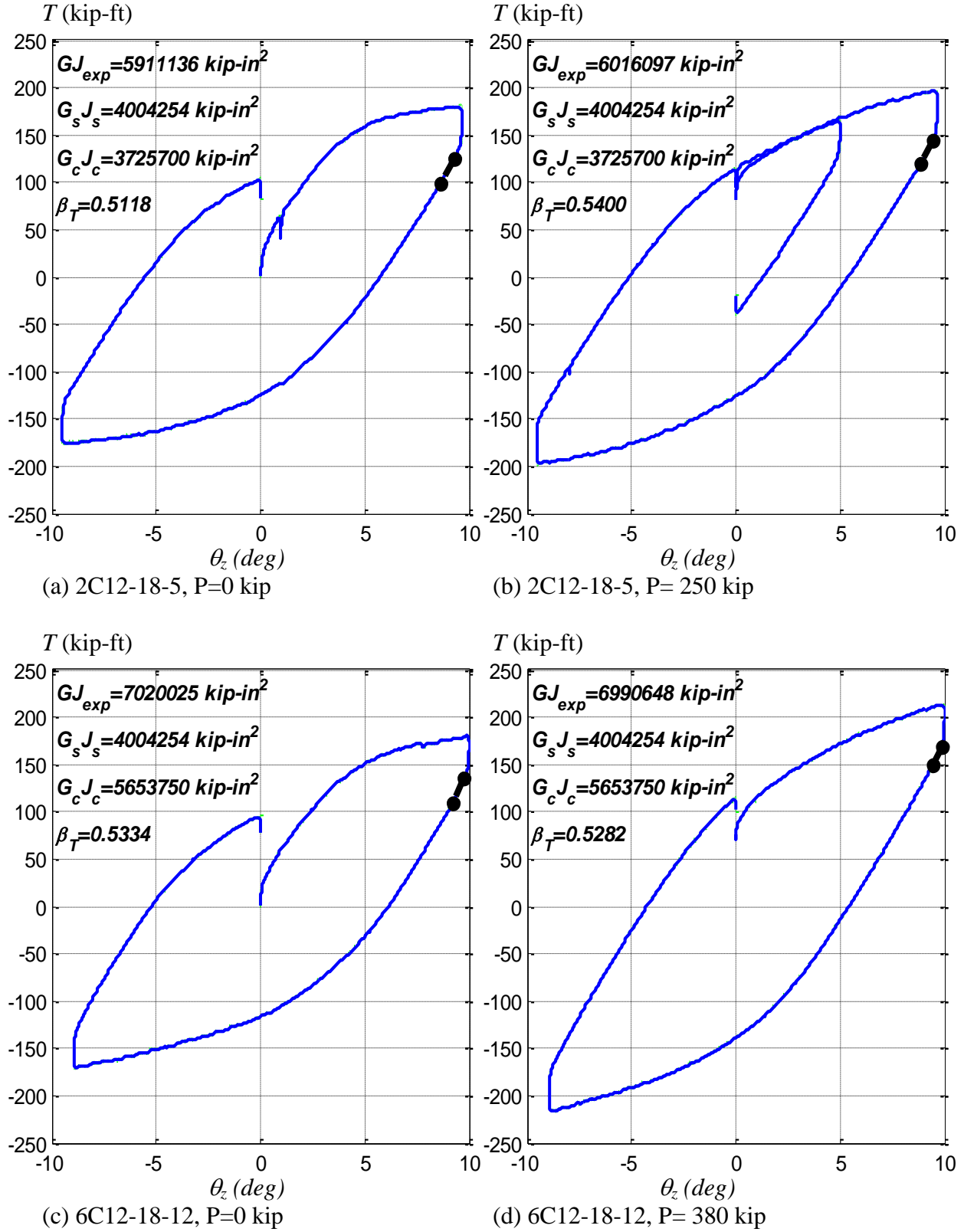


Figure 9.8. Elastic torsional stiffness for the Specimens 2C12-18-5 and 6C12-18-12

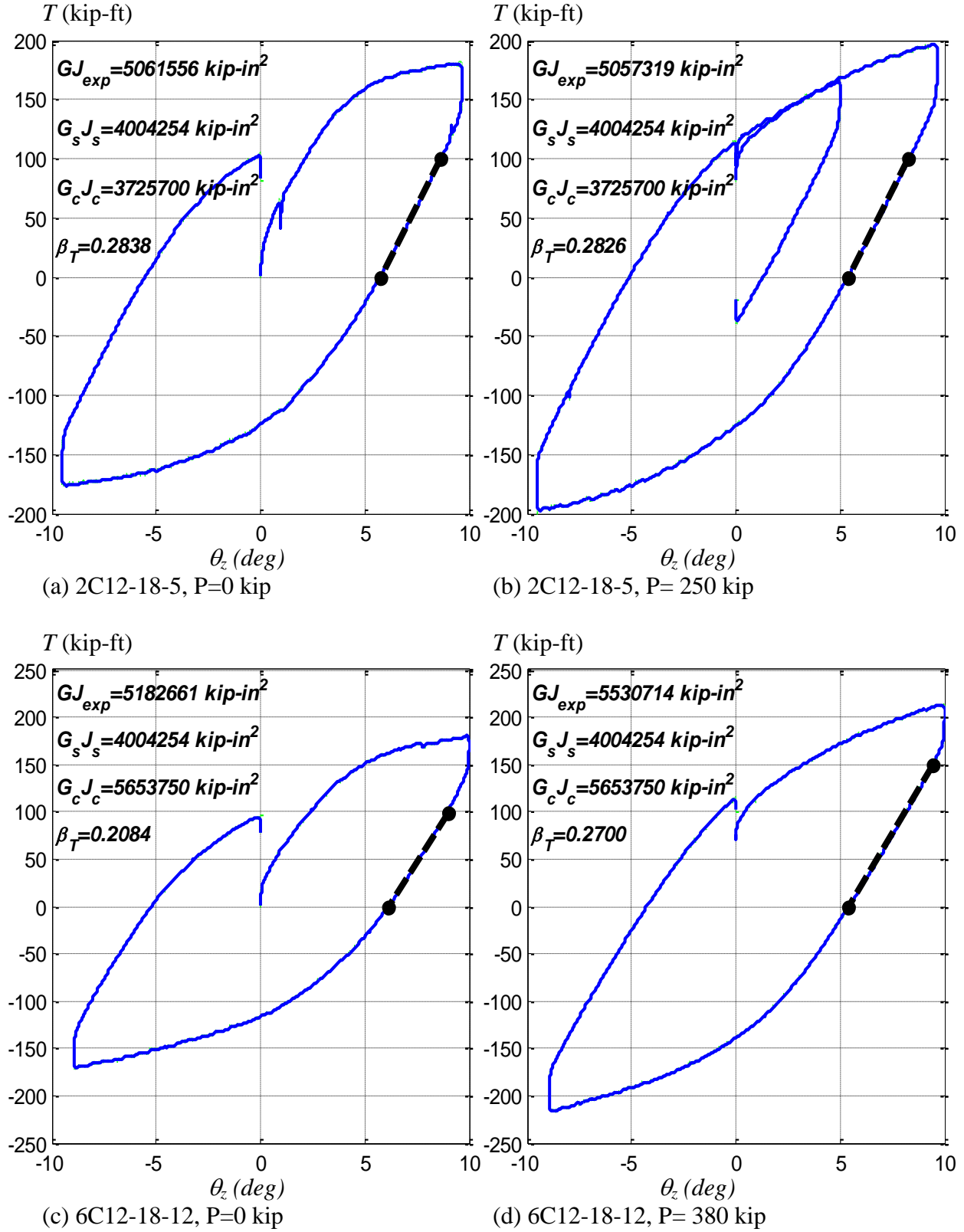


Figure 9.9. Tangent torsional stiffness for the Specimens 2C12-18-5 and 6C12-18-12

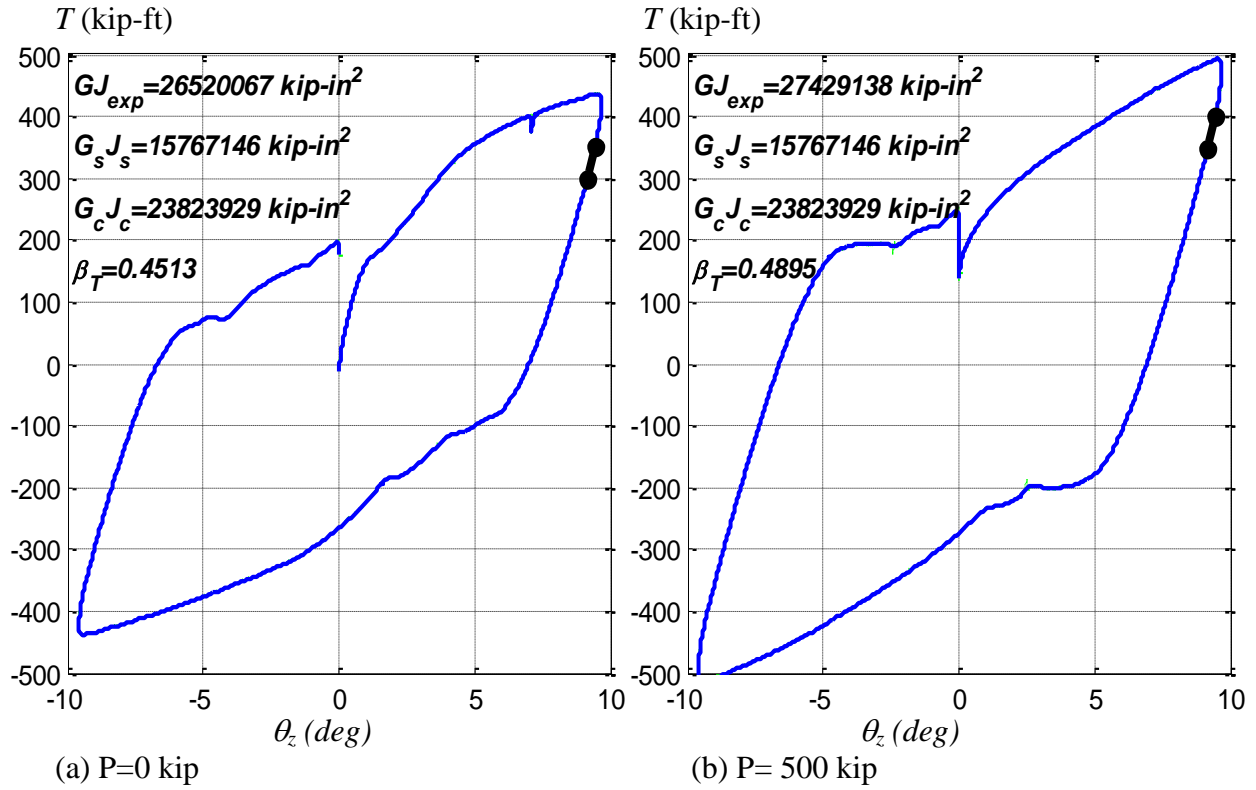


Figure 9.10. Elastic torsional stiffness for the Specimen 3C20-18-5

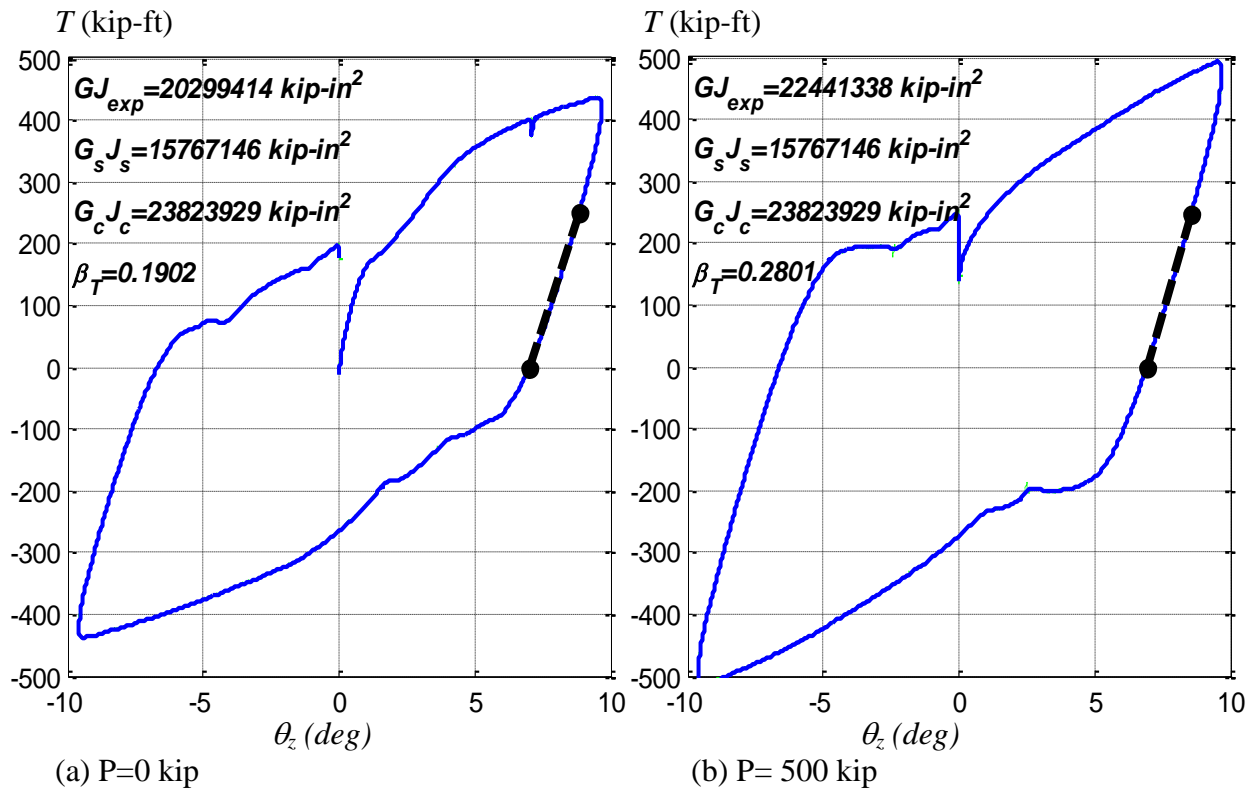


Figure 9.11. Tangent torsional stiffness for the Specimen 3C20-18-5

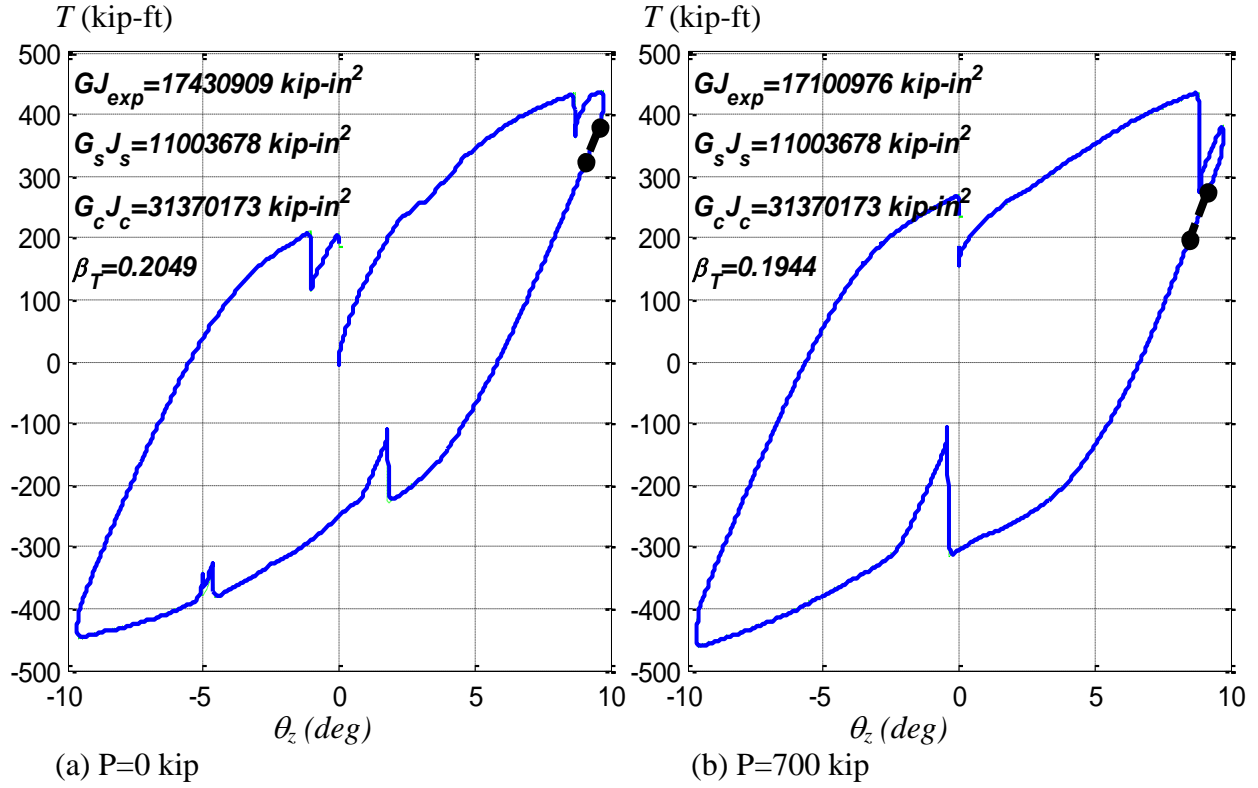


Figure 9.12. Elastic torsional stiffness obtained for the Specimen 4Rw-18-5

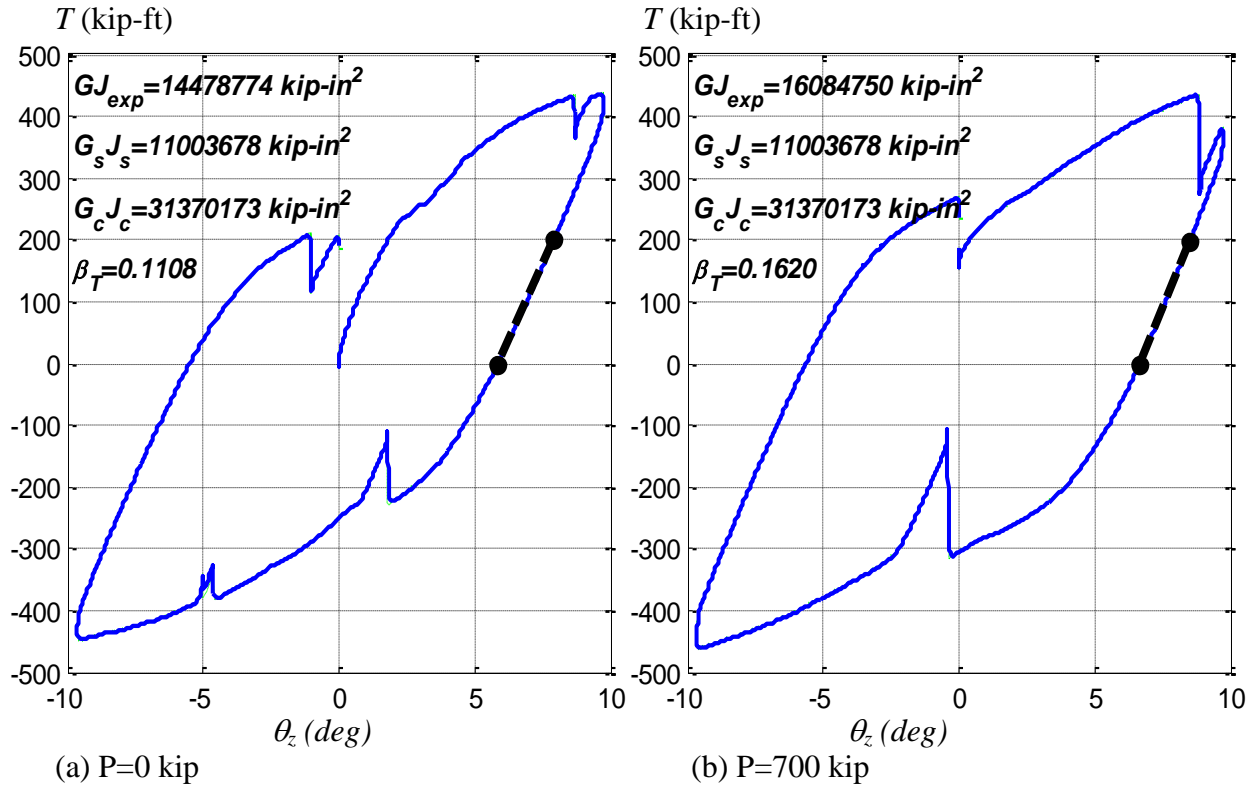


Figure 9.13. Tangent torsional stiffness obtained for the Specimen 4Rw-18-5

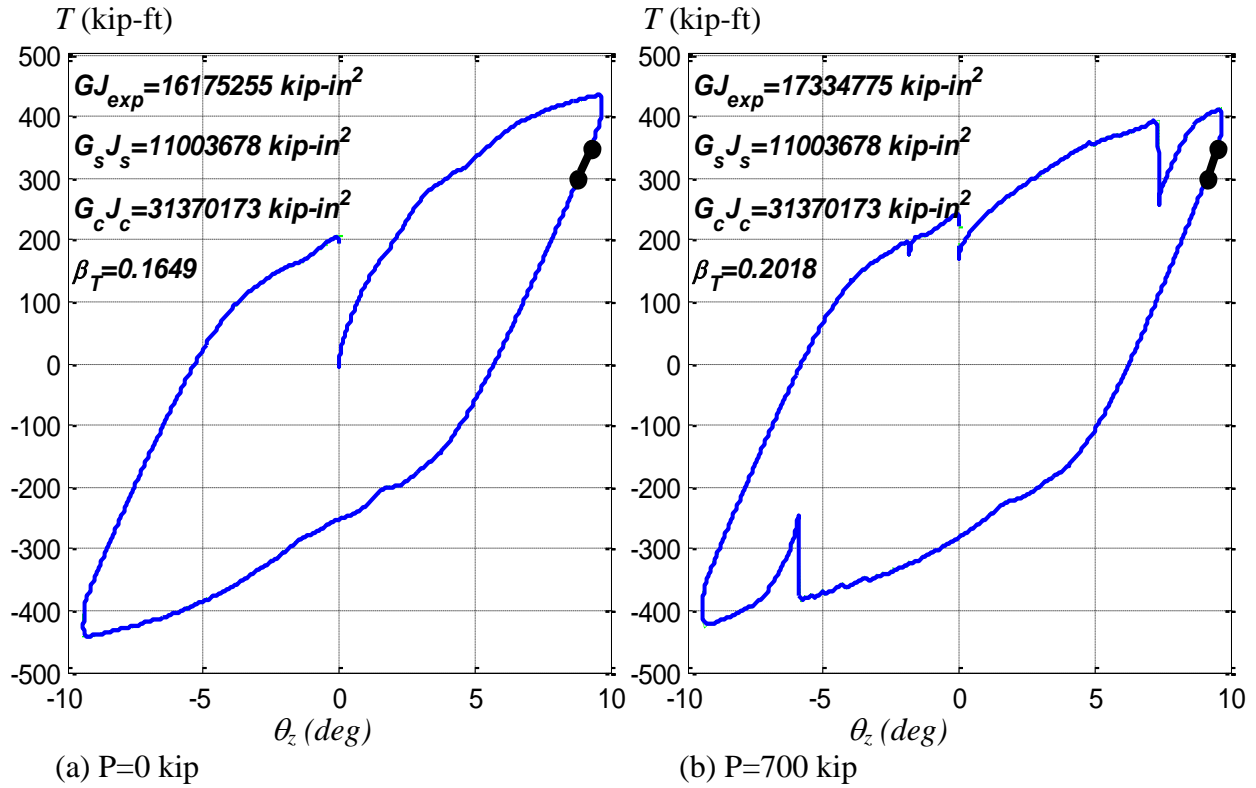


Figure 9.14. Elastic torsional stiffness obtained for the Specimen 5Rs-18-5

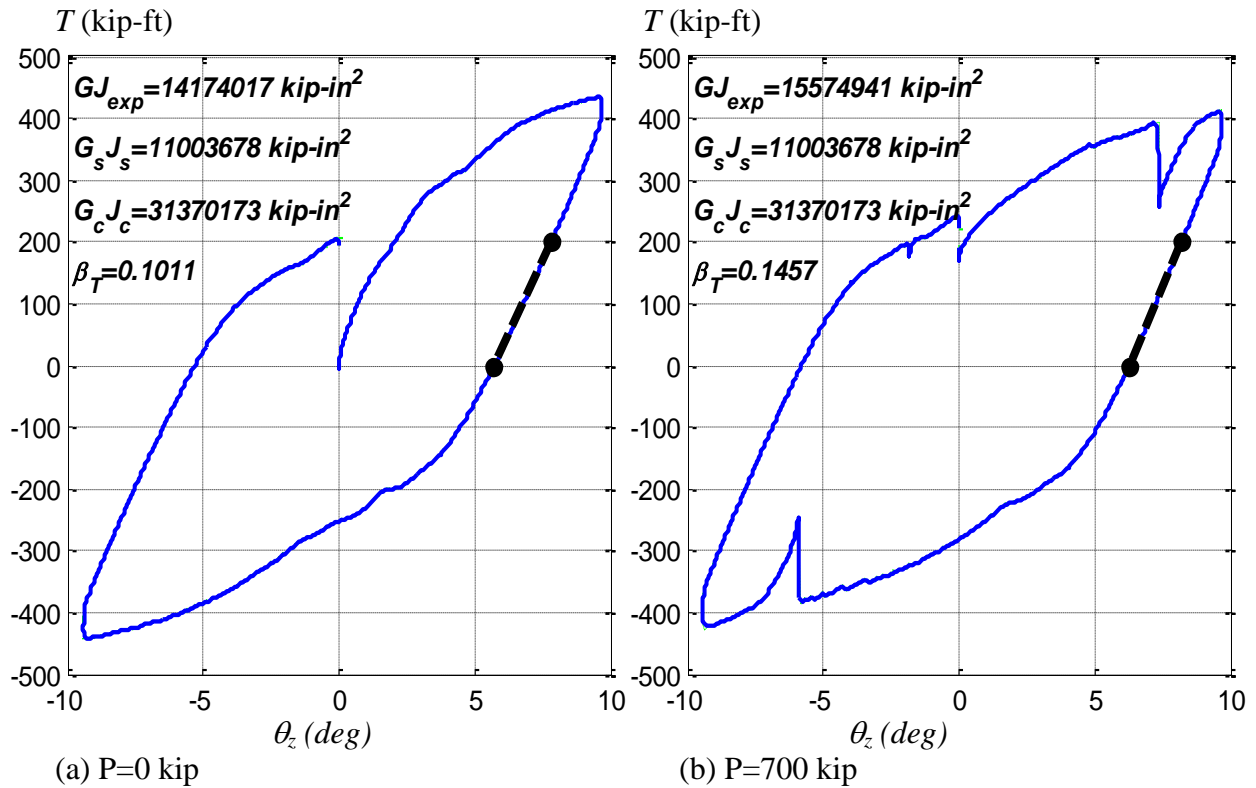


Figure 9.15. Tangent torsional stiffness obtained for the Specimen 5Rs-18-5

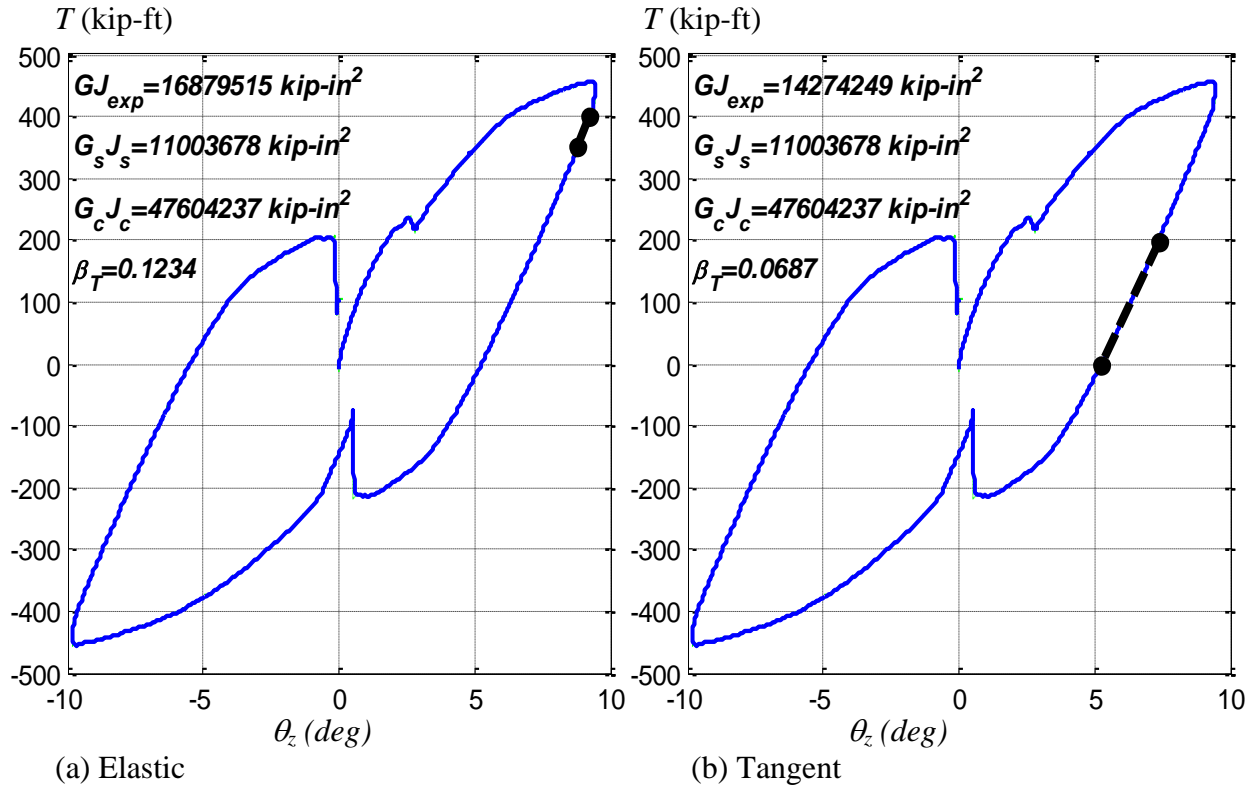


Figure 9.16. Torsional stiffness obtained for the Specimen 8Rw-18-12 ($P=0$)

9.6. Conclusions

As pointed out in this chapter, the torsional strength and stiffness capacity have been explored in a few studies of CFT members. The amount of experimental data for torsional loading is still limited, and most of the available data is related with circular tubes, short members, and small cross-sections. In addition, design codes developed for composite member do not provide enough guidance to calculate neither the torsional strength nor the rigidity of composite members. However, these capacities are well documented in steel or reinforced concrete elements.

This experimental project aims to provide more data of CFT under torsional loading. The specimens used in this project filled gaps with the current available data since full-scale CCFT and RCFT specimens (with larger cross-sections, and lengthy and slender members) were tested under pure torsion and under torsion with combined axial load.

The experimental torsional response obtained from the tests of the CFT specimens points out the following behavior.

- The results indicate a partial contribution of the concrete to both the torsional capacity and the torsional rigidity. Both the strength and the stiffness contributions were calibrated with the test data and design equations developed for torsion.
- The strength response under torsion and combined axial load was slightly higher than the strength obtained in pure torsion only in CCFTs; due to a high damage accumulation in RCFTs, the torsion capacity with and without compression was very similar to the pure torsion capacity.
- As a result of the rectangular shape, the concrete contribution in torsional capacity is slightly higher in RCFTs attributed to the interlock interaction between the concrete surfaces and the steel surfaces in contact. However, the torsional stiffness is slightly higher in CCFTs due to a better performance in circular cross-section shapes; and an earlier local buckling damage in RCFTs, which is less severe in CCFTs.

Assuming full contribution of the steel component and partial contribution of the concrete component, design equations are proposed to estimate both the torsional strength capacity and the torsional rigidity for non-cyclic and cyclic loading. These design equations predict reasonable values of the torsion strength and torsion stiffness.

CHAPTER 10

PROPOSE METHODOLOGY FOR THE STRENGTH CALCULATION

10.1. Introduction

The design methodology for the determination of the axial and flexural strength of CFT members proposed in this section is based on:

- (1) the assumption of a plastic stress-distribution for the cross-section strength,
- (2) a reasonable reduction on the capacity due to stability effects for CFT slender members, and
- (3) empirical calibration equations developed in previous chapters

Some equations and parameters in this methodology were adopted from both the current AISC (2010) Specifications and the ACI-318 Code (2008), but with some adjustments based on the results of this research and the latest knowledge on CFT member behavior. These modifications intend to both provide a smooth transition from all-concrete to all-steel sections (and vice versa) and increase the accuracy of the calculated axial and flexural capacity of CFT cross-sections and members as compared to current codes.

This section summarizes a methodology to calculate the:

- axial strength of CFT cross-sections (based in the plastic stress method),
- axial and flexural interaction for CFT cross-sections,
- axial strength of CFT columns,
 - CFTs incorporating a compact steel section, and
 - CFTs incorporating non-compact or slender steel plates,
- axial and flexural interaction for CFT beam-columns
 - CFTs incorporating a compact steel section, and
 - CFTs incorporating non-compact or slender steel plates.

Recommendations to minimize the effects of wet concrete in construction of RCFTs are included in Chapter 4. In addition, equations for the calculation of the torsional strength and the torsional stiffness of CFT cross-sections are included in Chapter 9. No additional details about these topics are included in this Chapter.

10.2. Material and geometric properties

The methodology for the determination of the cross-section strength is based on the following assumptions:

- For simplicity, the plastic stress distribution method was adopted in the derivations of the cross-section strength. From this computed capacity, the beam-column strength is estimated. If desired or possible, the cross-section strength obtained in this simplified fashion can be replaced by the more exact capacity obtained with the strain compatibility method.
- The equations developed with the plastic stress method do not include the longitudinal reinforcing bars. However, the equations can be easily modified to include rebar in the cross-section. The contribution of the rebar to the strength depends on the amount and distribution of this reinforcement in the concrete section.
- The steel cross-section satisfies the requirements for compact sections, and therefore, they can develop a fully plastic stress state as assumed with the plastic stress method. Thus the plastic stress in the steel is assumed as F_y for both compression and tension. Since a fully plastic distribution in slender cross-sections cannot be developed due an earlier failure by local buckling, the strength for this case should be conservatively obtained based on an elastic stress distribution.
- The equations developed for CFT cross-sections based on the plastic stress method neglect the low contribution of the concrete in tension, and adopt an equivalent block in the compression zone with a plastic stress (F_c) given by the Equation 10.1 for RCFTs and by the Equation 10.2 for CCFTs.

$$F_c = 0.85f_c' \quad (10.1)$$

$$F_c = 0.85f_{cc} = 0.85 \left(f_c' + \frac{1.558F_y t}{D_c} \right) \quad (10.2)$$

The coefficients 0.85 in these equations are adopted from section 10.2.7.1 in ACI-318 (2008). The second term in Equation 10.2 was proposed by Sakino *et al.* (2004) in order to account for the confinement effects provided by the circular steel component. This term increases the concrete compressive stress with higher values of the yield stress (F_y) and thickness (t) of the steel component, and with lower values of the concrete core diameter ($D_c=D-2t$).

Alternatively, the peak stress (f_{cc}) of CCFTs can be obtained as proposed by Chang and Mander (1994) as:

$$F_c = 0.85 f_{cc} = 0.85 f_c' \left(-1.254 + 2.254 \sqrt{1 + \frac{7.94 f_l}{f_c'}} - 2 \frac{f_l}{f_c'} \right) \quad (10.3)$$

where the confinement pressure (f_l) in CCFTs proposed by Denavit and Hajjar (2010) is:

$$f_l = \left(0.138 - 0.00174 \frac{D}{t} \right) \frac{2F_y}{D/t - 2} \geq 0 \quad (10.4)$$

If the strain compatibility method is used, stress-strain curves from analytical or experimental curves can be adopted. However, peak stresses on the concrete in compression of about f_c' for RCFTs and f_{cc} for CCFTs as illustrated in Figure 2.13 are recommended. Confinement effects can be included in the stress-strain curves for plain concrete as recommended by Sakino *et al.* (2004), Tort and Hajjar (2007), Denavit and Hajjar (2010).

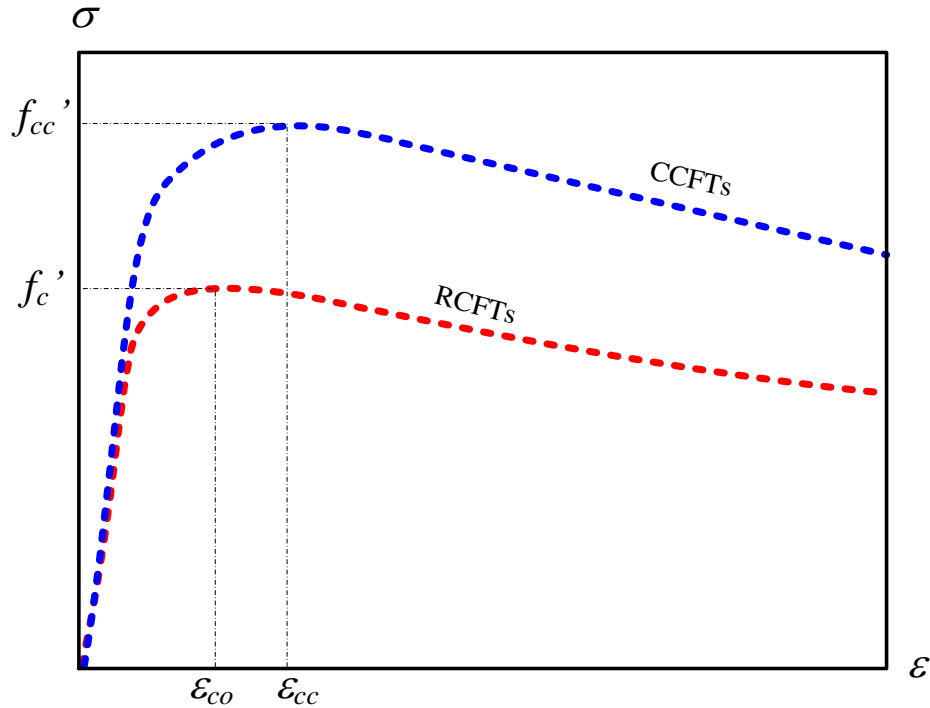


Figure 10.1. Stress-strain (σ - ϵ) curves that are typically applicable to CFTs

The subscripts “_s” and “_c” in this section stand for the steel and the concrete component. The subscripts “_o” refers to the pure strength capacities of the composite cross-section, and the subscripts “_b” is related to the capacity at the balance point or at the maximum moment.

The notation used for geometric dimensions is shown in Figure 10.2, and equations for the calculation of geometric properties (area, plastic section modulus, and moment of inertia) of the concrete and the steel components are summarized in Table 10.1. For HSS cross-sections, the geometric properties of the steel tube can also be taken from the AISC Manual; small differences are possible for the moment of inertia (I_s) and the plastic modulus (Z_s) since the equations in Table 10.1 do not consider the radius of the fillets.

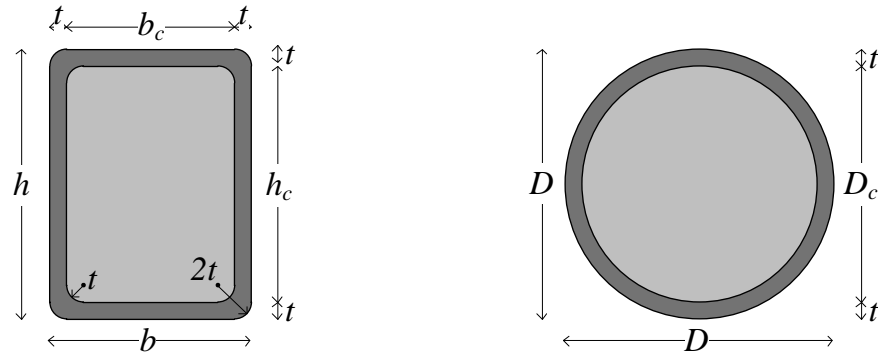


Figure 10.2. Notation in geometric dimensions for RCFTs and CCFTs

Table 10.1. Geometric properties for CFTs

RCFTs:	CCFTs:
$h_c = h - 2t$ $b_c = b - 2t$	$D_c = D - 2t$
$r_s \approx 2t$ $r_c = r_s - t = t$	
$A_c = b_c h_c - (4 - \pi)r_c^2$	$A_c = \frac{\pi D_c^2}{4}$
$A_c = b_c h_c - 0.8584t^2$	
$A_s = bh - (4 - \pi)r_s^2 - A_c$	$A_s = \pi D^2/4 - A_c$
$A_s = bh - b_c h_c - 2.5752t^2$	$A_s = \pi(D - t)t$
$Z_c = \frac{b_c h_c^2}{4}$	$Z_c = \frac{D^3}{6}$
$Z_s = \frac{bh^2}{4} - Z_c$	$Z_s = \frac{D^3}{6} - Z_c$
$I_c = \frac{b_c h_c^3}{12}$	$I_c = \frac{\pi D_c^4}{64}$
$I_s = \frac{bh^3}{12} - I_c$	$I_s = \frac{\pi D^4}{64} - I_c$

10.3. Axial strength of CFT cross-sections based on the plastic stress method

The axial capacity of the composite cross-section (P_o) is the superposition of the axial strength of each component. For CFT cross-sections consisting of only a steel tube and concrete infill, the axial capacity is then:

$$P_o = P_s + P_c \quad (10.5)$$

Since the tensile strength of the concrete is ignored, the tensile strength of the composite CFT member (T_o) is the contribution of the steel component only. The negative sign in Equation 10.5 indicates tension, and this is related to the tensile strength of CFTs without reinforcement.

$$T_o = -P_s \quad (10.6)$$

Based on the plastic stress method, as illustrated in Figure 10.3, each strength component is given by:

$$P_s = A_s F_y \quad (10.7)$$

$$P_c = A_c F_c \quad (10.8)$$

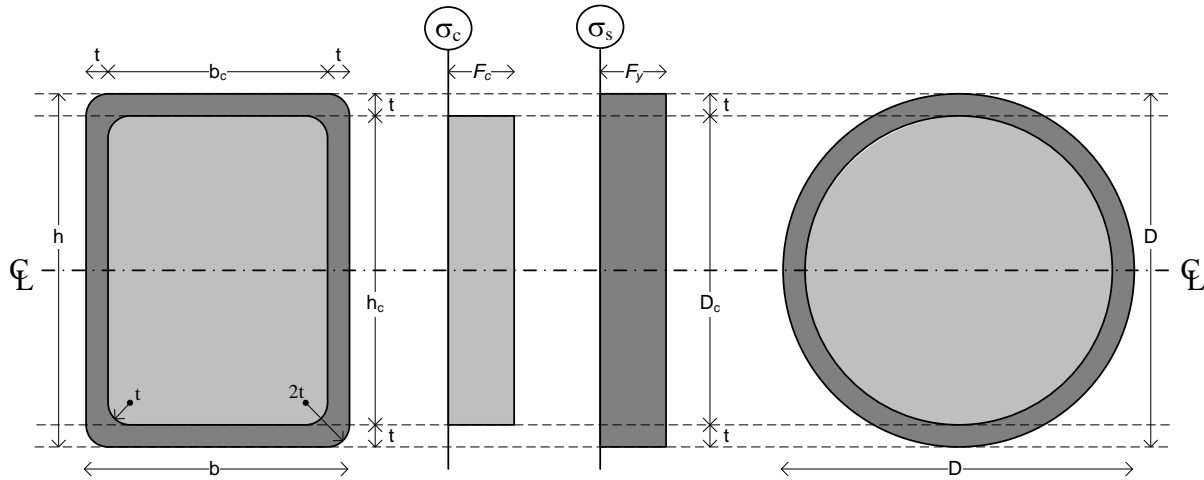


Figure 10.3. Plastic stress distribution of CFTs in pure compression

10.4. Axial and flexural strength of CFT cross-sections based on the plastic stress method

Figure 10.4 illustrates the plastic stress distribution in the steel and the concrete in compression for a given position of the PNA (y) with respect to the centroidal axis of the cross-section. This diagram of stresses is valid for any position of the PNA within the concrete section, or between $-h_c/2 < y < h_c/2$ for RCFTs and between $-D_c/2 < y < D_c/2$ for CCFTs.

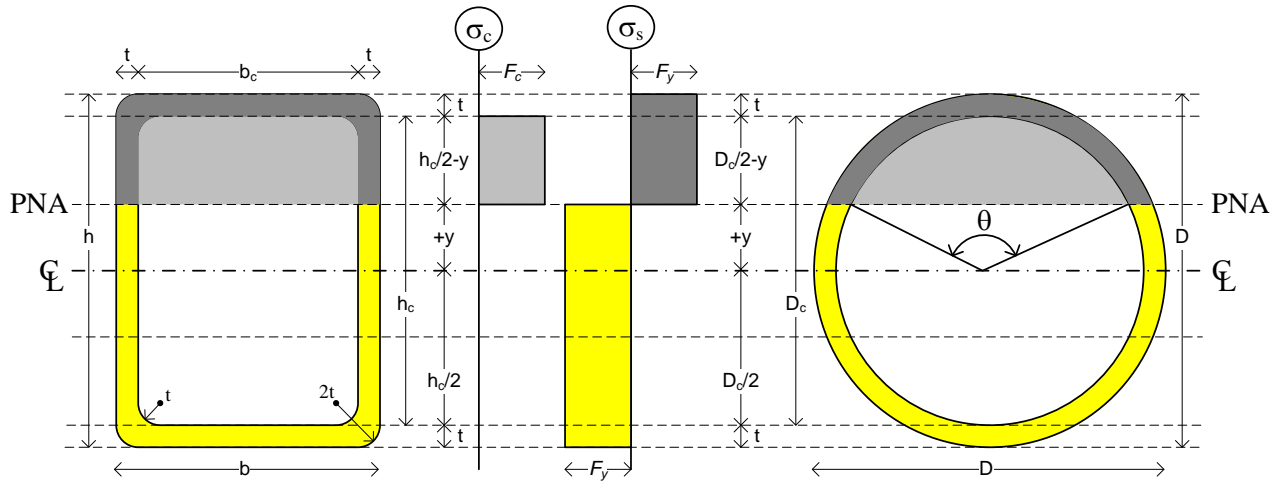


Figure 10.4. Plastic stress distribution for a given position of the PNA

Based on the plastic stress method, different points of the P-M interaction diagrams can be obtained for the cross-section by assuming the value of “ y ” within the concrete section. A more general formulation, in the form of continuous functions $[P_{cs}(y), M_{cs}(y)]$ that depend on the PNA position (y), is derived next. Figure 10.5 shows with the continuous line the interval where the continuous functions $[P_{cs}(y), M_{cs}(y)]$ are valid. In this figure, different positions of the PNA position are schematically illustrated for a CCFT cross-section highlighting in gray the zone in compression in both the steel and concrete portions. As shown in this figure, the limits of the continuous functions are defined for the cases when the PNA is at both ends of concrete section. However, the P-M diagram of the cross-section can be completed by calculating the pure compression ($P_o = P_s + P_c$) and pure tension ($T_o = -P_s$) points. The transition at the end of the continuous functions and these pure axial capacities, illustrated as the discontinuous lines in Figure 10.5, can be assumed to be linear for purposes of design.

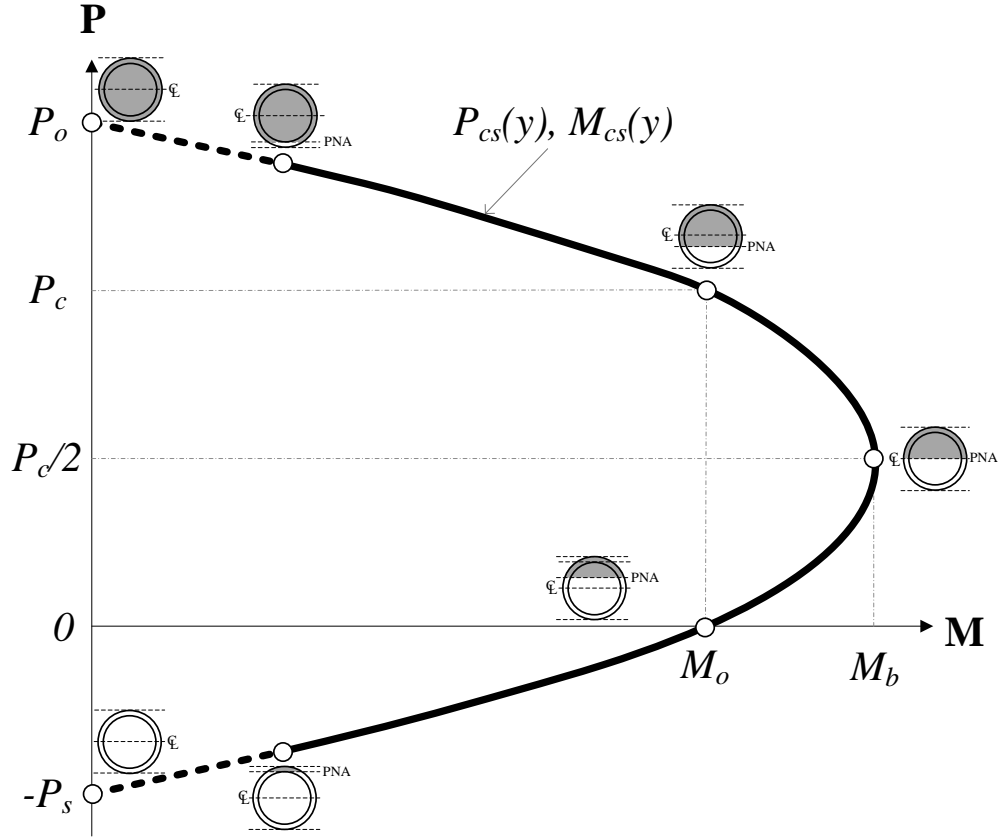


Figure 10.5. *P-M interaction diagram for a CFT cross-section based on the plastic stress method*

As seen from Figure 10.5, the P-M interaction diagram for the cross-section is symmetric about the case when the PNA is located at the centroidal axis (or the balance point). At this PNA position, the flexural capacity (M_b) is maximum because of the superposition of the pure bending strength of the steel component ($Z_s F_y$) and the bending of half cross-section of the concrete component ($Z_c F_c/2$). Since the tensile and compressive strength of the steel cancel each other in this PNA position, the corresponding axial strength is equal to half the strength of the concrete component ($P_b = P_c/2$). Due to the symmetry on the P-M cross-section, the moment M_o is the same at $P=0$ and $P=P_c$. (Roik and Bergmann 1992) (Roberto T Leon and Jerome F Hajjar 2008) documented that simplifications of strength equations are possible through stress superposition of different cases. They illustrated that, after some simplifications, the position of the PNA for the pure bending strength case ($P=0$, $M=M_o$, at y_o) with a negative value is coupled to the pure flexural strength and an axial strength equal to only the strength of the concrete component ($P=P_c$, $M=M_o$, at y_o).

The continuous function $P_{cs}(y)$ that defines the axial compressive strength in terms of the position of the PNA (y) varying within the concrete cross-section in RCFTs is given by:

$$P_{cs}(y) = \left(\frac{h_c}{2} - y \right) b_c F_c - 4ytF_y \quad \forall \quad -\frac{h_c}{2} < y < \frac{h_c}{2} \quad (10.9)$$

The continuous function $P_{cs}(y)$ for the axial compressive strength of CCFTs in terms of the position of the PNA is given by:

$$P_{cs}(y) = (\theta(y) - \pi) K_s + (\theta(y) - \sin \theta(y)) K_c \quad \forall \quad 0 < \theta(y) < 2\pi \quad (10.10)$$

where the angle $\theta(y)$ that defines the position of the PNA varying within the concrete cross-section is:

$$\theta(y) = 2 \cos^{-1} \left(\frac{2y}{D_c} \right) \quad \forall \quad -\frac{D_c}{2} < y < \frac{D_c}{2} \quad (10.11)$$

and the concrete parameter K_c and the steel parameter K_s are:

$$K_c = \frac{D_c^2}{8} F_c \quad (10.12)$$

$$K_s = \frac{D^2 - D_c^2}{2} F_y \quad (10.13)$$

The continuous function $M_{cs}(y)$ for the flexural capacity for CFTs, as a function of the PNA position within the concrete cross-section, is defined as the superposition of the steel and concrete flexural capacities.

$$M_{cs}(y) = Z_s(y) F_y + \frac{1}{2} Z_c(y) F_c \quad (10.14)$$

The proposed continuous functions for the plastic section modulus of the steel $Z_s(y)$ and the concrete $Z_c(y)$ components also depend on the position of the PNA within the concrete cross-section, as well as the corresponding plastic modulus about the centroidal axis that are tabulated

in Table 10.1. Since the tension strength is neglected in the concrete component, only half of the plastic cross-section is taken into account in the equations for the concrete plastic modulus. Thus, the continuous equations for the plastic section modulus in RCFTs are:

$$Z_c(y) = Z_c - b_c y^2 \quad (10.15)$$

$$Z_s(y) = Z_s - 2t y^2 \quad (10.16)$$

The corresponding plastic section modulus equations for CCFTs are:

$$Z_c(y) = Z_c \sin\left(\frac{\theta}{2}\right)^3 \quad (10.17)$$

$$Z_s(y) = Z_s \sin\left(\frac{\theta}{2}\right) \quad (10.18)$$

The proposed continuous functions passes over the key points mentioned before. At the balance point, the PNA is located at $y=0$, and then the corresponding strength from the continuous functions reduces to:

$$P_b = \frac{P_c}{2} \quad (10.19)$$

$$M_b = Z_s F_y + \frac{1}{2} Z_c F_c \quad (10.20)$$

The positions of the PNA at any point within the concrete cross-section at a desired axial or flexural capacity can be obtained from the continuous functions by any numerical method (i.e. bisection). Alternatively, for RCFTs, the position of the PNA (y_i) at a given axial load (P_i) can be obtained as:

$$y_i = \frac{P_c / 2 - P_i}{4t F_y + b_c F_c} \quad (10.21)$$

The PNA position in RCFTs with pure bending strength case ($P_i = 0$) can be calculated as:

$$y_o = \frac{P_c / 2}{4t F_y + b_c F_c} \quad (10.22)$$

The angle (θ_o) related to the position of the PNA for the pure bending strength in CCFTs can be estimated with the equation below adapted from the AISC (2005) Specifications:

$$\theta_o \approx \frac{0.2K_c - K_s}{0.68K_c} + \sqrt{\frac{(0.2K_c + K_s)^2 + 3.4K_cK_s}{0.68K_c}} \quad (10.23)$$

Alternatively, the following approximate equations can also be used to estimate the angle related to the position of the PNA for the pure bending strength case.

$$\theta_o \approx 2 \sec^{-1} \sqrt{\frac{K_s}{K_c} + 1} \quad (10.24)$$

$$\theta_o \approx \left(\frac{5\pi K_s}{K_c} \right)^{1/4} \quad (10.25)$$

The PNA position for at the pure bending strength (y_o) can be calculated from θ_o as:

$$y_o = \frac{D_c}{2} \cos\left(\frac{\theta_o}{2}\right) \quad (10.26)$$

The exact value for θ_o , however, is that which satisfies equilibrium of axial forces within the cross-section. In general, y_o of the PNA and the pure bending strength $M_o = M_{cs}(y_o)$ can be obtained by solving for $P_{cs}(y_o) = 0$.

$$M_o = M_{cs}(y_o) \quad \because \quad P_{cs}(y_o) = 0 \quad (10.27)$$

As a check, the same flexural strength (M_o) and an axial strength equal to the strength of the concrete component (P_c) should be obtained with the negative value “ $-y_o$ ”.

$$M_o = M_{cs}(-y_o) \quad \& \quad P_{cs}(-y_o) = P_c \quad (10.28)$$

The cross-section capacity can be obtained with the continuous functions with a set of points (from 1 to N) within the concrete zone, complemented with the pure compression and tension capacities (0 and N+1). Thus, the P-M interaction diagram can be constructed with the N+2 computed set of points. As an example, the polygonal interaction diagram with the design equation in AISC (2005) can be obtained with the continuous functions with a set of 5 points; this set of points arranged in vector format is shown below.

$$i = \begin{bmatrix} 0 \\ 1 \\ 2 \\ 3 \\ 4 \end{bmatrix} = \begin{bmatrix} A \\ C \\ D \\ B \\ T \end{bmatrix} ; \quad y = \begin{bmatrix} -h/2 \\ -y_o \\ 0 \\ y_o \\ h/2 \end{bmatrix} ; \quad P_{cs} = \begin{bmatrix} P_o \\ P_c \\ P_c/2 \\ 0 \\ -P_s \end{bmatrix} = \begin{bmatrix} P_A \\ P_C \\ P_D \\ 0 \\ T_o \end{bmatrix} ; \quad M_{cs} = \begin{bmatrix} 0 \\ M_o \\ M_b \\ M_o \\ 0 \end{bmatrix} = \begin{bmatrix} 0 \\ M_C \\ M_D \\ M_B \\ 0 \end{bmatrix}$$

The polygonal interaction diagram will turn into a smoother P-M interaction curve if more points are included and calculated with the continuous functions, mainly in the bulge zone where the PNA positions varies within $\pm y_o$ and the corresponding axial capacities varies proportionally between 0 and P_c . A second example of a smoother P-M interaction diagram with a set of 13 total points arranged in vector format is shown below.

$$i = \begin{bmatrix} 0 \\ 1 \\ 2 \\ 3 \\ 4 \\ 5 \\ 6 \\ 7 \\ 8 \\ 9 \\ 10 \\ 11 \\ 12 \end{bmatrix} ; \quad y = \begin{bmatrix} -h/2 \\ -h_c/2 \\ -y_o \\ -3y_o/4 \\ -y_o/2 \\ -y_o/4 \\ 0 \\ y_o/4 \\ y_o/2 \\ 3y_o/4 \\ y_o \\ h_c/2 \\ h/2 \end{bmatrix} ; \quad P_{cs} = \begin{bmatrix} P_o \\ P_{cs}(y_1) \\ P_c \\ P_{cs}(y_3) \\ P_{cs}(y_4) \\ P_{cs}(y_5) \\ P_c/2 \\ P_{cs}(y_7) \\ P_{cs}(y_8) \\ P_{cs}(y_9) \\ 0 \\ P_{cs}(y_{11}) \\ -P_s \end{bmatrix} = \begin{bmatrix} P_A \\ P_1 \\ P_C \\ \approx 7P_c/8 \\ \approx 3P_c/4 \\ \approx 5P_c/8 \\ P_D \\ \approx 3P_c/8 \\ \approx P_c/4 \\ \approx P_c/8 \\ 0 \\ P_{11} \\ T_o \end{bmatrix} ; \quad M_{cs} = \begin{bmatrix} 0 \\ M_{cs}(y_1) \\ M_o \\ M_{cs}(y_3) \\ M_{cs}(y_4) \\ M_{cs}(y_5) \\ M_b \\ M_{cs}(y_7) \\ M_{cs}(y_8) \\ M_{cs}(y_9) \\ M_o \\ M_{cs}(y_{11}) \\ 0 \end{bmatrix} = \begin{bmatrix} 0 \\ M_{cs1} \\ M_C \\ M_{cs3} \\ M_{cs4} \\ M_{cs5} \\ M_D \\ M_{cs7} \\ M_{cs8} \\ M_{cs9} \\ M_B \\ M_{cs11} \\ 0 \end{bmatrix}$$

Figure 10.6 illustrates the interaction diagrams assembled from the sets of P-M points of the two previous examples. As a reminder, the subscripts *A*, *B*, *C*, and *D* refer to the anchor points in the AISC interaction diagram. The subscripts *c* and *s*, as indicated in this chapter, refer to the concrete and steel component, respectively, and the subscript *b* refers to the balance point. P_o and T_o are the pure compression and tension capacities of the composite cross-section, respectively, and y_o is the PNA position at the pure bending case ($P=0$, $M=M_o$).

As shown above, the equations $P(y)$ and $M(y)$ for the axial and flexural capacities, respectively, are functions of the PNA position defined by the variable y . The interaction diagram is then populated by the pairs of axial strength (P_i) and bending moments (M_{csi}) calculated for the i^{th} position y_i , points that were represented in vectorial form.

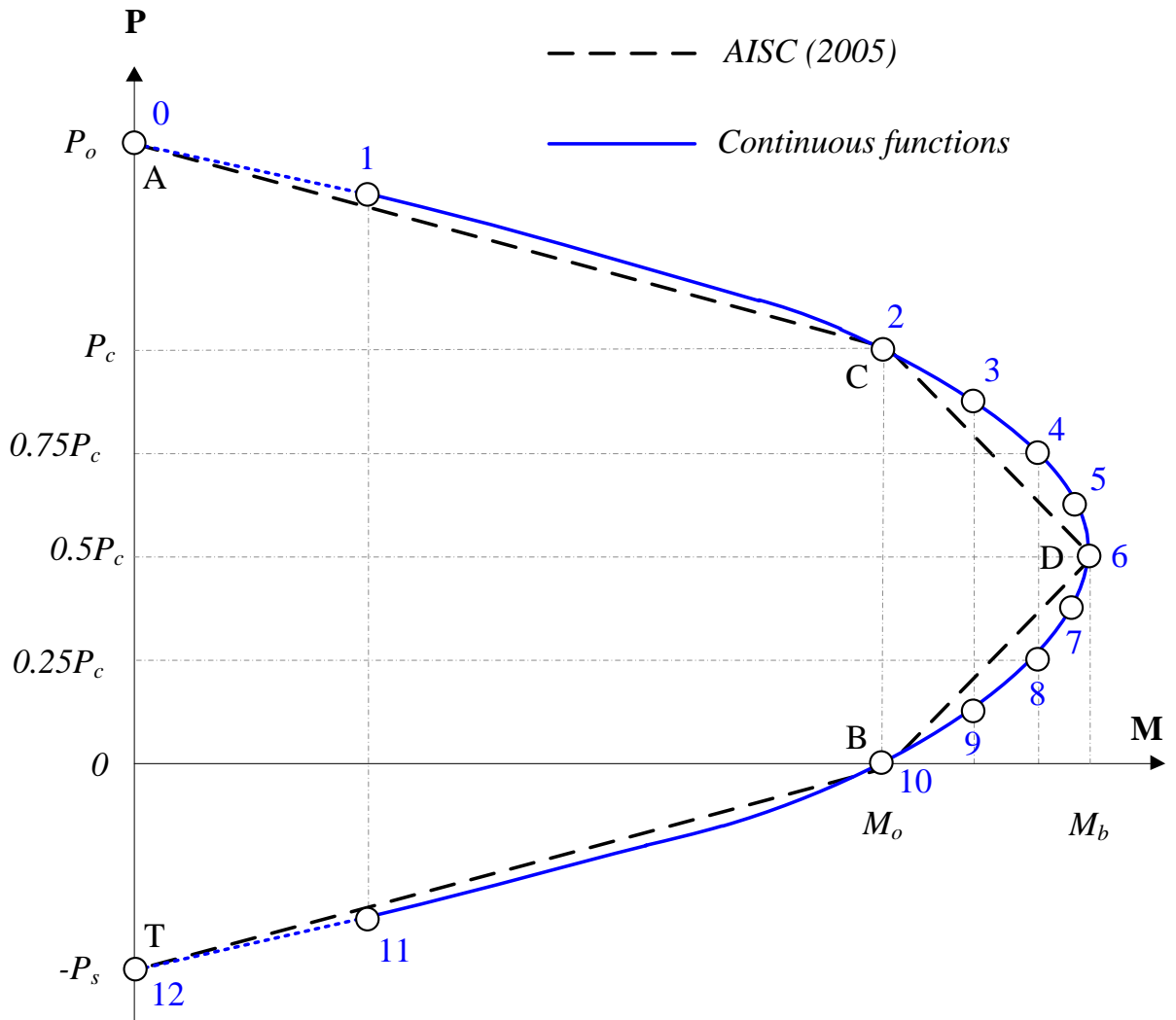


Figure 10.6. Interaction diagram from a set of P - M points for the cross-section capacity

10.5. Axial strength of CFT columns

The critical load (P_n) reduced by the stability effects can be obtained with the current AISC (2010) Specifications given by:

$$P_n = \begin{cases} 0.658^{\frac{P_o}{P_e}} P_o & \text{if } P_e/P_o > 0.44 \\ 0.877 P_e & \text{if } P_e/P_o \leq 0.44 \end{cases} \quad (10.29)$$

Equation 10.42 was proposed by Tide (1985) based on the empirical curve proposed by Bjorhovde (1973), and has been adopted by the AISC Specifications for steel member and composite members. The reduction factor 0.877 to the Euler load (P_e) in the elastic buckling interval accounts for initial imperfection, which is not considered by the Euler formulation. Both parts of this equation accounts for a nominal initial imperfection of $KL/1500$, where KL is the effective buckling length.

The slenderness parameter λ for composite members is given by:

$$\lambda = \sqrt{\frac{P_o}{P_e}} \quad (10.30)$$

The squash load (P_o) is defined by the Equation 4. The Euler load, as a function of the effective flexural stiffness (EI_{eff}) and the effective length (KL) is:

$$P_e = \frac{\pi^2 EI_{eff}}{(KL)^2} \quad (10.31)$$

The effective flexural stiffness (EI_{eff}) of a composite member for the calculation of the Euler load is the superposition of the steel rigidity ($E_s I_s$) and the concrete rigidity of the cracked section ($E_c I_{cr} = \kappa E_c I_c$). In Chapter 7 this equation was calibrated for pure compression loading as:

$$EI_{eff} = E_s I_s + 0.80 E_c I_c \quad (10.32)$$

10.6. Axial and flexural strength of CFT beam-columns

The approach proposed for getting the interaction diagram for beam columns consists in obtaining, for different values of axial forces (P), the available net moment (M_{bc}) through the reduction of the cross-sectional plastic moment (M_{cs}) by the total unusable moment (M_{tum}). The total unusable moment calculated in this approach intends to include those moments consumed by a nominal initial imperfection (M_{imp}) and the unusable flexural capacity moments between the stable and plastic capacities (M_{ufc}). All these parameters are indicated schematically in Figure 10.7.

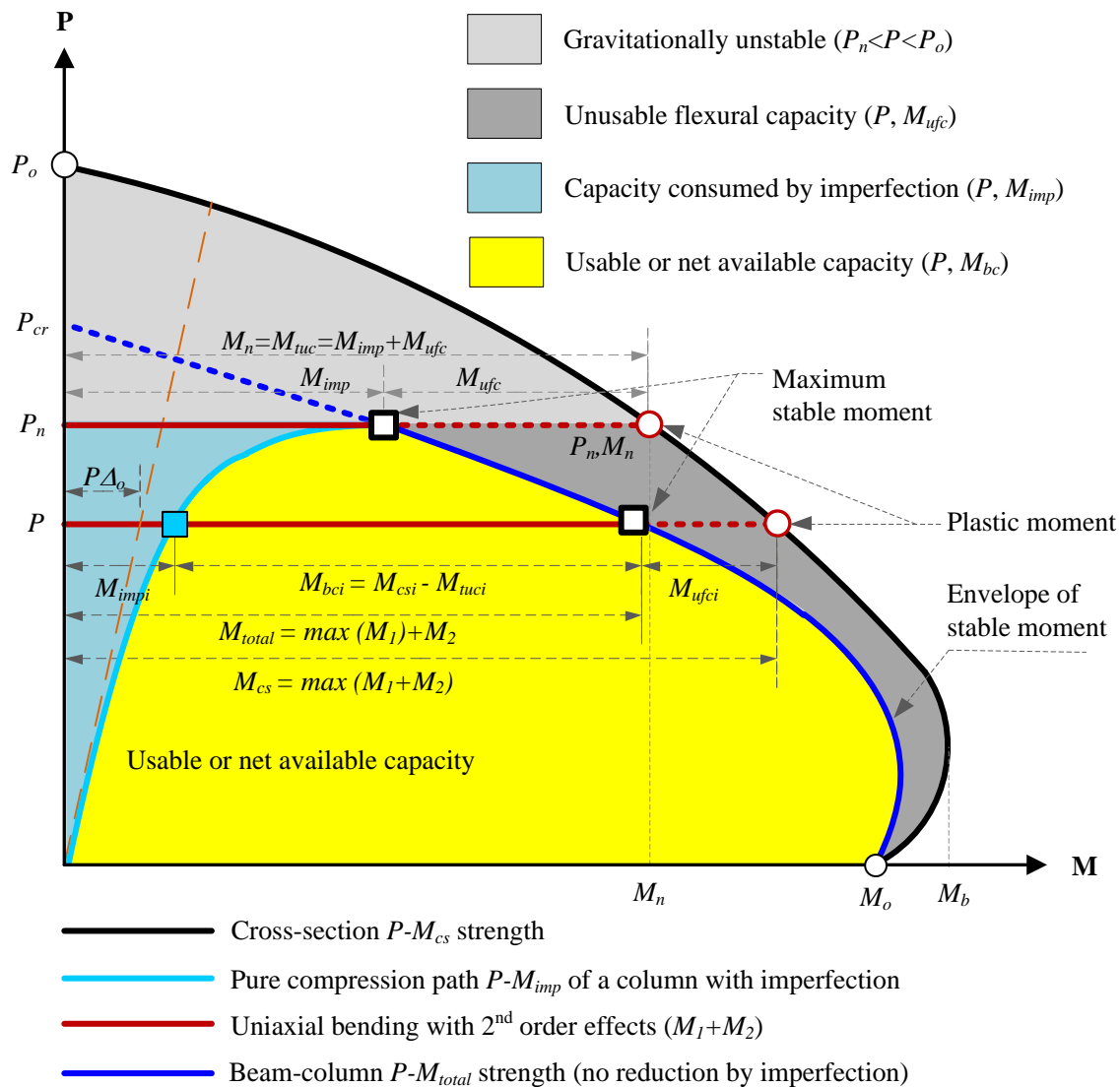


Figure 10.7. Schematic representation of the P-M components in slender CFT members

Figure 10.7 illustrates schematically the axial-moment capacity available in the cross-section ($P-M_{cs}$), which can be calculated based on either the plastic stress method (as described in a previous section with the continuous functions) or the strain compatibility method. For a straight and plumb pin-ended column, an increase in the effective length (KL) will result in the inability to reach the full plastification of the cross-section, as the P-M capacity is reduced by stability. The resultant beam column strength is also illustrated in Figure 10.7 (curve $P-M_{total}$). The area between the P-M cross-section strength and the P-M beam-column strength defines an *unusable capacity* in the member due to instability.

Additionally, Figure 10.7 shows the axial-moment path ($P-M_{imp}$) of a column in pure compression with given effective length (KL) and a nominal imperfection (Δ_o). This load path delimits the maximum stable axial load (P_n) and the moments consumed as a consequence of the imperfection (M_{imp}). The slender member cannot exceed axial loads above P_n , and thus the P-M capacity above this limit is *gravitationally unstable*. In addition, the member spends part of the available capacity due to the imperfections that is no longer available for the member. This *consumed capacity by imperfection* can be estimated by multiplying the first order moment ($P\Delta_o$) by the amplification factor due to second order effects.

$$M_{impi} = P_i \cdot \Delta_o \left(\frac{1}{1 - P_i / P_e} \right) \quad \forall \quad 0 < P_i < P_n \quad (10.33)$$

Besides M_{imp} , another unavailable capacity for the beam-column is the one previously defined as the “unusable flexural capacity (M_{ufc}), which is a partial loss of the plastic capacity due to the slenderness effects. Thus, the usable or net available capacity (M_{bc}) of a slender beam-column is then the residual area after this is reduced, parting from the plastic capacity, by the areas defined as: (1) gravitationally unstable, (2) unusable flexural capacity, and (3) consumed by imperfection; this usable or net capacity area is illustrated in Figure 10.7 in yellow, and is represented by the following equation:

$$M_{bci} = M_{csi} - M_{ufci} - M_{impi} \quad \forall \quad 0 < P_i < P_n \quad (10.34)$$

where the subscript “ i ” refers to the i^{th} vector position for which the same axial strength (P_i) and the flexural capacities (M_{bci} , M_{csi} , M_{ufci} , M_{impi}) are used. The moment M_{csi} is the plastic flexural capacity of the cross-section related to i^{th} axial capacity (P_i) obtained with either the plastic stress

method or the strain compatibility method. M_{impi} is the flexural capacity consumed by the imperfection when the i^{th} axial capacity (P_i) is applied; this used up capacity can be estimated with the Equation 10.33. M_{ufci} is the unused flexural capacity due to the slenderness related to i^{th} axial capacity (P_i).

The information in Figure 10.7 is again illustrated with less detail in Figure 10.8.a, where the net capacity lies in the middle part (its natural form). These areas components can be rearranged for convenience at different positions. As illustrated in Figure 10.8.b, both the *imperfection* and the *unusable* reductive capacities are arranged in the left side, and then grouped into the “*total unusable capacity*” as shown in Figure 10.8.c. Both flexural components of the total unusable capacity (M_{impi} and M_{ufci}) vary proportionally with the axial capacity (P_i), and their summation goes from the origin point ($P=0, M=0$) to the maximum point ($P=P_n, M=M_n$). The moment M_n is the flexural strength of the cross-section coupled to the critical load (P_n). Assuming that both P - M_{tuc} path and P - M_{imp} path are proportional to each other, the total unstable capacity can be then estimated amplifying the imperfection moment (M_{impi} , Equation 10.34) by the ratio M_n / M_{imp} . After some simplifications, the initial imperfection (Δ_o) is cancelled and the equation is reduced to:

$$M_{tuci} = M_{impi} \cdot \frac{M_n}{M_{imp}} = M_n \frac{P_i (P_n - P_e)}{P_n (P_i - P_e)} \quad (10.35)$$

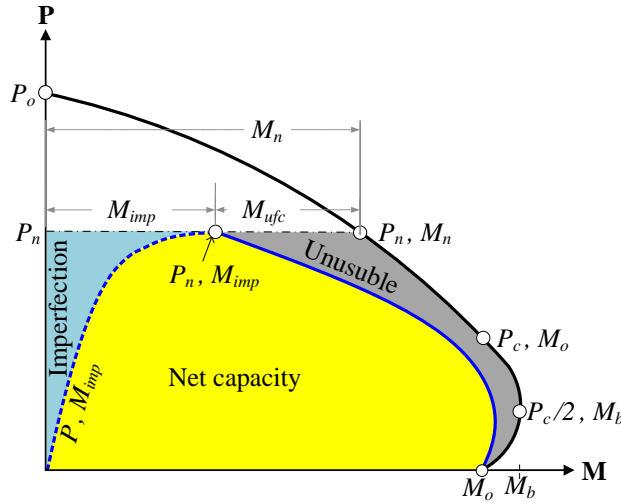
and thus, the net beam-column flexural capacity for the given axial load is given by:

$$M_{bci} = M_{csi} - M_{tuci} = M_{csi} - M_n \left(\frac{P_i (P_n - P_e)}{P_n (P_i - P_e)} \right) \quad (10.36)$$

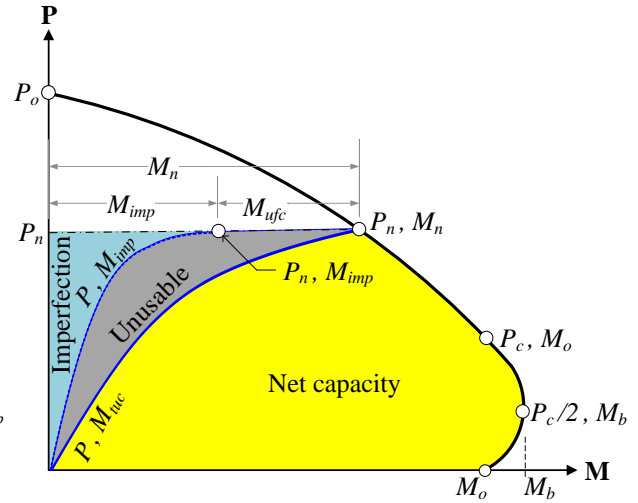
As illustrated in Figure 10.8.d, the final usable or net moment capacity for the i^{th} axial capacity (P_i) between 0 and P_n is equal to.

$$M_{bci} = \begin{cases} 0 & \text{if } P_i \geq P_n \\ M_{csi} - M_{tuci} & \text{if } 0 < P_i < P_n \\ M_{csi} & \text{if } P_i \leq 0 \end{cases} \quad (10.37)$$

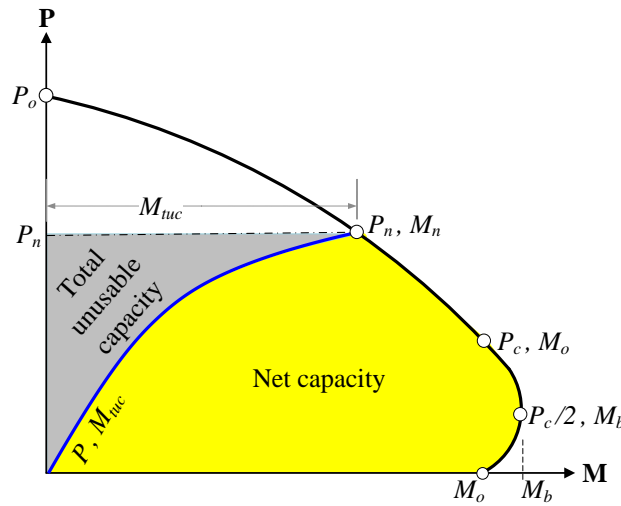
This equation is consistent with its limits since the net moment is equal to zero at the nominal critical load, and equal to M_o at the pure bending loading.



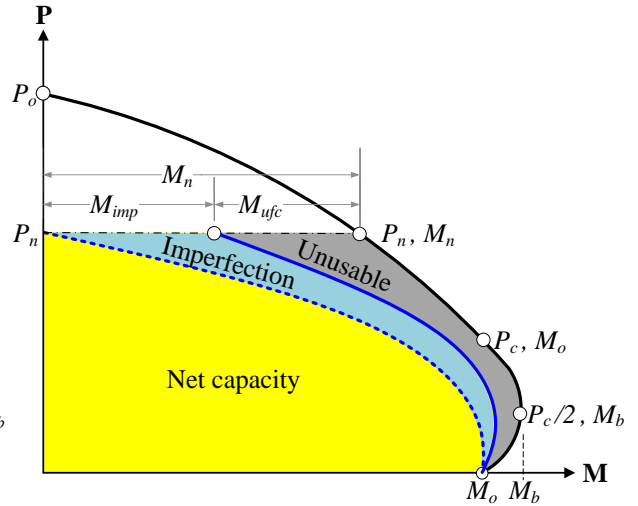
(a) *Natural form*
Net capacity in the middle



(b) *Precontrol form*
Net capacity at the right



(c) *Control form*
Net capacity at the right



(d) *Final form*
Net capacity at the left

Figure 10.8. Schematic representation of the capacity components in different arrangements

10.7. Axial and flexural strength of CFT cross-sections with non-compact steel tubes

The previous section derived equations to calculate the axial and flexural capacity of CFT cross-sections are based on the full plastic stress distribution approach. This hypothesis is strictly valid only if the steel tube is a compact section.

The present section aims to derive equations for the calculation of the axial and flexural strength of CFT cross-sections with non-compact or slender steel tubes.

10.7.1. Wall slenderness limits for steel sections in CFTs

As discussed in Chapter 8, empirical equations for the local buckling initiation were proposed based on the empirical data obtained in these tests. These equations are given by:

$$\varepsilon_{lb} = \begin{cases} 0.09 \left(\frac{D}{t} \cdot \frac{F_y}{E_s} \right)^{-2} \frac{F_y}{E_s} = \frac{0.09}{\lambda^2 \cdot \varepsilon_y} & \text{for CCFTs} \\ 9 \left(\frac{h}{t} \sqrt{\frac{F_y}{E_s}} \right)^{-2} \frac{F_y}{E_s} = \frac{9}{\lambda^2} & \text{for RCFTs} \end{cases} \quad (10.38)$$

The limits for slender filled tubes (λ_r) are obtained from the empirical calibration equations (Equation 10.30) when the local buckling strain reaches yielding ($\varepsilon_{lb} = \varepsilon_y$ or $\varepsilon_{lb}/\varepsilon_y = 1$). These limits are given by:

$$\lambda_r = \begin{cases} 0.3 \frac{E_s}{F_y} & \text{for CCFTs} \\ 3.0 \sqrt{\frac{E_s}{F_y}} & \text{for RCFTs} \end{cases} \quad (10.39)$$

Limits for non-compact filled tubes (λ_p) from the empirical calibration equations associated to local buckling strains are propose as four times yielding in circular filled tubes ($\varepsilon_{lb}/\varepsilon_y = 4$) and two times yielding in rectangular filled tubes ($\varepsilon_{lb}/\varepsilon_y = 2$); the higher limit in CCFTs is justified by the higher performance of the circular tubes. These limits are:

$$\lambda_p = \begin{cases} 0.15 \frac{E_s}{F_y} & \text{for CCFTs} \\ 2.12 \sqrt{\frac{E_s}{F_y}} & \text{for RCFTs} \end{cases} \quad (10.40)$$

The latter propose ranges aims in getting reliable and consistent limits with the current AISC Specifications. The limits λ_p and λ_r stated above are very close to the limits defined in Chapter I of the AISC (2010) for CFT cross-sections.

The previous equations and limits take into account the local buckling in the steel tube given that this is restrained by the concrete in the inward direction, but free to buckle locally in the outward direction.

10.7.2. Interaction diagram for CFTs with slender section

As commented before, local buckling is a premature failure of the element caused by the buckling of one of the plate components that integrates the cross-section. Slender plates are susceptible to buckle locally with elastic compressive stresses, and so the upper bound of a slender plate (or lower bound in a non-slender plate) is when the compressive critical stress equals the yield stress and the wall-slenderness ratio is equal to λ_r .

Figure 10.9 illustrates the distribution of the expected stresses in CFT cross-sections with a slender steel cross-section that is susceptible to buckle locally. The stresses are assumed elastic-perfectly-plastic in the steel in tension, elastic in the steel in compression with a maximum value equal to the yielding stress; the concrete contribution in tension is neglected and, for simplicity, the stresses in compression are assumed linear elastic. In this figure, the distribution of stresses is shown for different positions (y) of the elastic neutral axis (ENA) with respect to the centroidal axis of the cross-section, which is applicable when the ENA position is within the concrete section.

The corresponding compressive elastic stress in the concrete (F_c) at the time local buckling occurs depends on the corresponding strains (ε) in the cross-section. In the current AISC (2010) Specifications, this compressive stresses in the concrete has been adopted linear elastic with a maximum stress assumed as a constant and equal to $0.70f_c'$, where the concrete compressive strength is limited between 3 and 10 ksi. This $0.70f_c'$ of max stress in the concrete (at the steel compressive yielding) is conservative under certain conditions, but it may become unconservative when the CFT section is composed by high strength concrete or low strength steel. To evaluate the latter, the maximum compressive stress when the steel yields can be obtained based on the geometric and material properties and the available models. Adopting the model proposed by Hognestad (Park and Paulay 1975) for plain concrete as:

$$f_c(\varepsilon) = f_c' \left(\frac{2\varepsilon}{\varepsilon_c} - \left(\frac{\varepsilon}{\varepsilon_c} \right)^2 \right) \quad (10.41)$$

Since the strain at the concrete when the steel yields is equal to $\varepsilon = \varepsilon_y(1 - 2t/H)$, and assuming that the strain at the crushing is $\varepsilon_c = 2f_c'/E_c$, the equation above can be rewritten as:

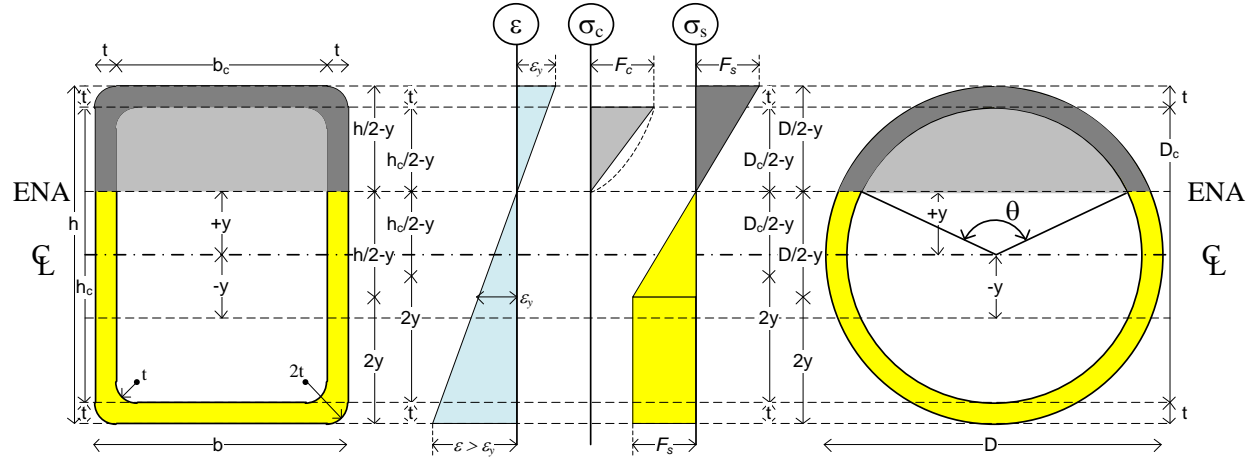
$$F_{ce} = f_c' \left(\frac{E_c \varepsilon_y}{f_c'} \left(1 - \frac{2t}{D} \right) - \left[\frac{E_c \varepsilon_y}{2f_c'} \left(1 - \frac{2t}{D} \right) \right]^2 \right) \leq 0.85 \quad (10.42)$$

where D is the total depth of the steel cross-section.

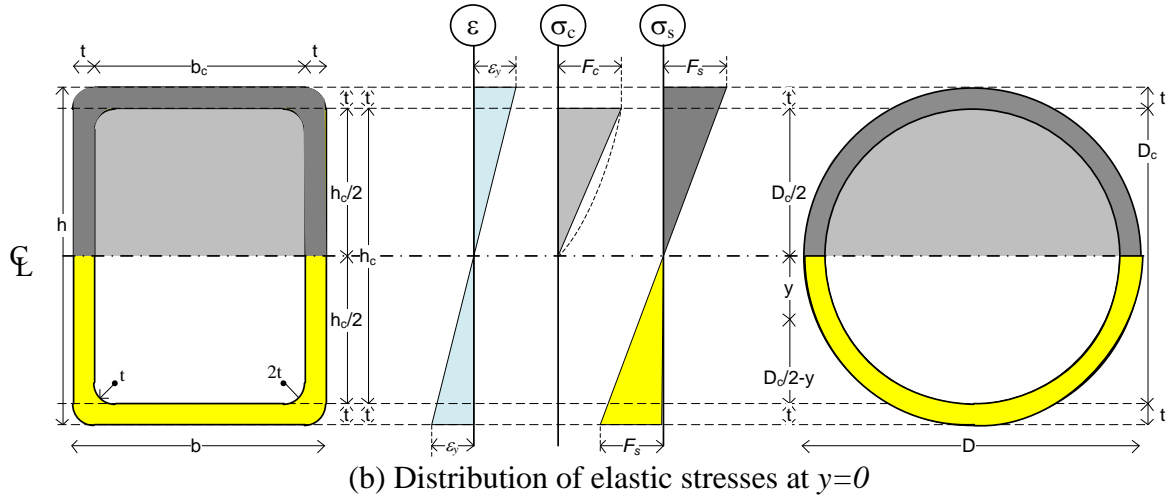
The term in parenthesis in the equation above tends to decrease, even below the 0.7 value, for high strength concrete and lower steel yielding strains. On the other hand, with low strength concrete and high strength steel, this term may be higher, and so this term is limited to 0.85 as in the compact cross-sections.

Equation 10.42 is adopted to calculate the maximum compressive stress (F_c) when the steel yield. This equation takes into account the geometric and material properties in the CFT cross-section and the strain distribution when the steel yields as illustrated in Figure 10.9.

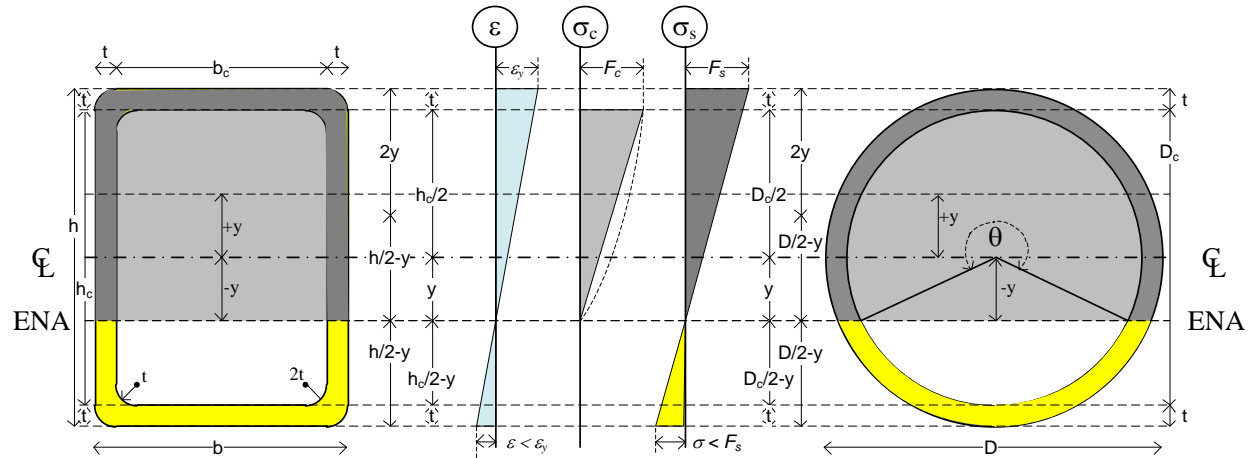
For CCFT cross-sections with non-compact steel tubes, no additional strength is considered in the concrete due to confinement effects. This hypothesis assumes that non-compact steel tubes may provide a very low confinement to the concrete infill, and so Equation 10.42 is valid for both RCFTs and CCFTs.



(a) Distribution of elastic stresses between " $t/2 < y \leq h_c/2$ " in RCFTs or " $t/2 < y \leq D_c/2$ " in CCFTs



(b) Distribution of elastic stresses at $y=0$



(c) Distribution of elastic stresses between " $-h_c/2 \leq y \leq 0$ " in RCFTs or " $-D_c/2 \leq y \leq 0$ " in CCFTs

Figure 10.9. Stress distribution in a CFT cross-section composed by a slender tube ($\lambda = \lambda_r$), assuming that local buckling achieves when steel yields in compression

Based on the stress distribution shown in Figure 10.9, the interaction diagram P-M can be obtained by varying the position of the neutral axis (ENA) under these assumptions. As illustrated in Figure 10.10, the resultant interaction diagram can be accurately delineated by the union of four anchor points. These points can be obtained with the equations below for RCFTs. For CCFTs, the anchor points can be approximately obtained by substituting the steel dimensions b and h for the diameter D , and the concrete dimensions b_c and h_c for D_c . In these calculations, the maximum stress in the steel is assumed as: $F_s = 0.7F_y$ (assuming a residual stress of $0.3F_y$). The maximum stress in concrete F_c can be calculated by Eq. 10.42. Thus, the anchor points are given by the following cases:

(1) *Pure compression*: For the pure compression case ($M_y=0$), the axial capacity for both RCFTs and CCFTs is:

$$P_{oe} = A_s F_s + A_c F_{ce} \quad (10.43)$$

(2) *Maximum moment capacity*: The maximum moment capacity is obtained when the neutral axis is located at the centroidal axis ($y=0$) as shown in Figure 10.9.b. The axial and flexural capacities at this point for both RCFTs and CCFTs are given by:

$$P_{be} = \frac{A_c F_{ce}}{4} \quad (10.44)$$

$$M_{be} = S_s F_s + \frac{S_c}{2} F_{ce} \quad (10.45)$$

(3) *Pure bending* ($P_y=0$): The pure flexure capacity can be estimated with the expression below:

$$M_{oe} \approx M_{be} - \left(\frac{4}{3} t y_o^2 F_y + \frac{b_c y_{oe}^2}{3} F_{ce} \right) \quad (10.46)$$

The position of the ENA at the pure bending point (y_o) can be approximated as:

$$y_{oe} \approx \frac{A_c F_{ce}}{2(8tF_s + b_c F_{ce})} \quad (10.47)$$

(4) *Pure tension*: For the pure tension case ($M_y=0$), the axial capacity is:

$$P_{te} = -A_s F_s \quad (10.48)$$

The negative sign is used for tensile forces as convention

The interaction P-M strength of a CFT cross-section with a slender steel tube ($\lambda = \lambda_r$) can be approximated by lines passing over the previous anchor points as shown by the dashed line in Figure 10.10. In this figure, the P-M interaction diagram for compact sections ($\lambda > \lambda_p$) is included as reference.

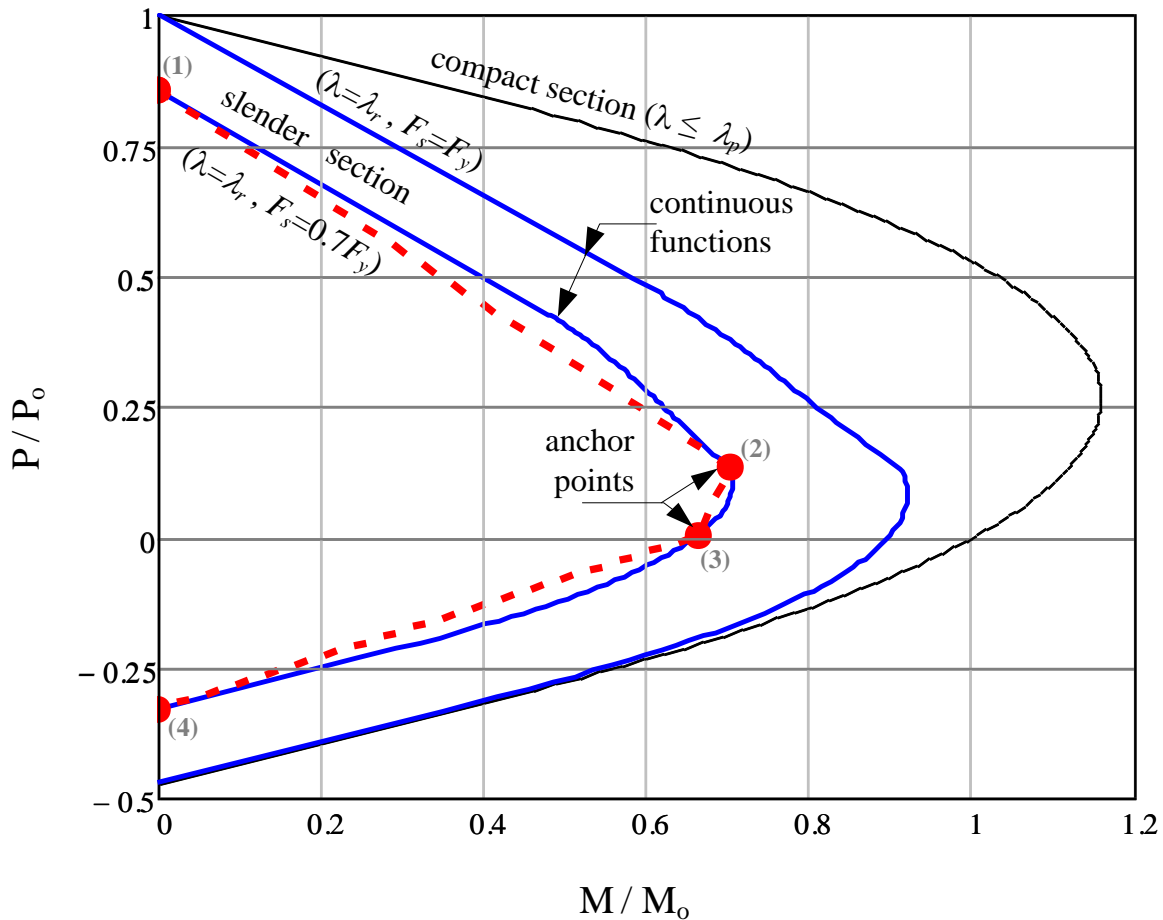


Figure 10.10. Schematic P-M interaction diagram for a CFT with slender steel cross-section which wall slenderness ratio equals λ_r

The equations above are developed assuming the steel buckle locally when the compressive stress reaches the yielding stress (with or without residual stress), or the wall slenderness λ is equal to λ_r . As recommended by the AISC (2010), linear interpolation between the elastic ($\lambda = \lambda_r$) and the plastic ($\lambda \leq \lambda_p$) cases can be used to obtain the axial and flexural capacity of CFT cross-sections when the steel tube is a non-compact section ($\lambda_p < \lambda < \lambda_r$).

Table 10.1 gives a summary of the equations needed to calculate the axial and flexural capacity (anchor points 1, 2 and 3 of Figure 10.10) in CFT cross-sections with compact, non-compact or slender steel section. The equations with the steel compact were derived in section 10.8.4, and the equations related with the slender section were commented previously in this section. The equations for CFT cross-sections with a non-slender steel section are just linear interpolation of the two previous cases, and the P-M interaction diagram is the union of the final interpolated points.

Table 10.2. Equations to calculate the axial and flexural capacity (anchor points 1, 2 and 3) in CFT cross-sections with compact, non-compact or slender steel section

Point	Compact sections $\lambda \leq \lambda_p$	Non-compact sections $\lambda_p < \lambda < \lambda_r$	Slender sections $\lambda = \lambda_r$
(1)	$P_{op} = A_s F_y + A_c F_c$	$P_o = P_{op} - \frac{(\lambda - \lambda_p)}{(\lambda_r - \lambda_p)} (P_{op} - P_{oe})$	$P_{oe} = A_s F_s + A_c F_{ce}$
(2)	$P_{bp} = \frac{A_c F_c}{2}$	$P_b = P_{bp} - \frac{(\lambda - \lambda_p)}{(\lambda_r - \lambda_p)} (P_{bp} - P_{be})$	$P_{be} = \frac{A_c F_{ce}}{4}$
	$M_{bp} = Z_s F_y + \frac{Z_c}{2} F_c$	$M_b = M_{bp} - \frac{(\lambda - \lambda_p)(M_{bp} - M_{be})}{(\lambda_r - \lambda_p)}$	$M_{be} = S_s F_s + \frac{S_c}{2} F_{ce}$
(3)	$M_{op} \approx M_{bp} - 2y_o^2 t F_y - \frac{b_c y_o^2 F_{cp}}{2}$	$M_o = M_{op} - \frac{(\lambda - \lambda_p)(M_{op} - M_{oe})}{(\lambda_r - \lambda_p)}$	$M_{oe} \approx M_{be} - \frac{4}{3} y_{oe}^2 t F_y - \frac{b_c y_{oe}^2 F_{ce}}{3}$
	$y_o \approx \frac{A_c F_c}{2(4tF_y + b_c F_c)}$		$y_{oe} \approx \frac{A_c F_{ce}}{2(8tF_s + b_c F_{ce})}$

CFT cross-section with wall slenderness ratios above the limit λ_r may not be recommended to use in practice due to the following reasons:

- The confinement in the steel tube is lower as the thickness reduces (or the wall slenderness ratio grows). Then, the concrete will tend to behave as plain concrete.
- The concrete will need longitudinal and transverse reinforcement to compensate the low confinement provided by a slender steel tube. The additional reinforcement may complicate the construction process in small tubes and their connections.

- Local buckling will occur very early within the elastic response, and no additional capacity may be carried on due to the poor capacity in the unconfined concrete and the steel locally buckled.
- As shown in Figure 10.11, the reduction of the CFT cross-section capacity with tubes from compact ($\lambda \leq \lambda_p$) to slender ($\lambda = \lambda_r$) sections is significant, and this reduction will increase much higher in slender members with a large total unusable capacity as a consequence of the stability effects.

The P-M interaction diagram for the CFT with slender tube illustrated in the previous figure has not been reduced for the stability effects. In order to account for the length effects, the methodology described in Section 10.6 can be used by reducing the total unusable capacity to the cross-section strength as stated in Equation 10.37, but with a linear transition to the point (P_n, M_n) as illustrated in Figure 10.11.

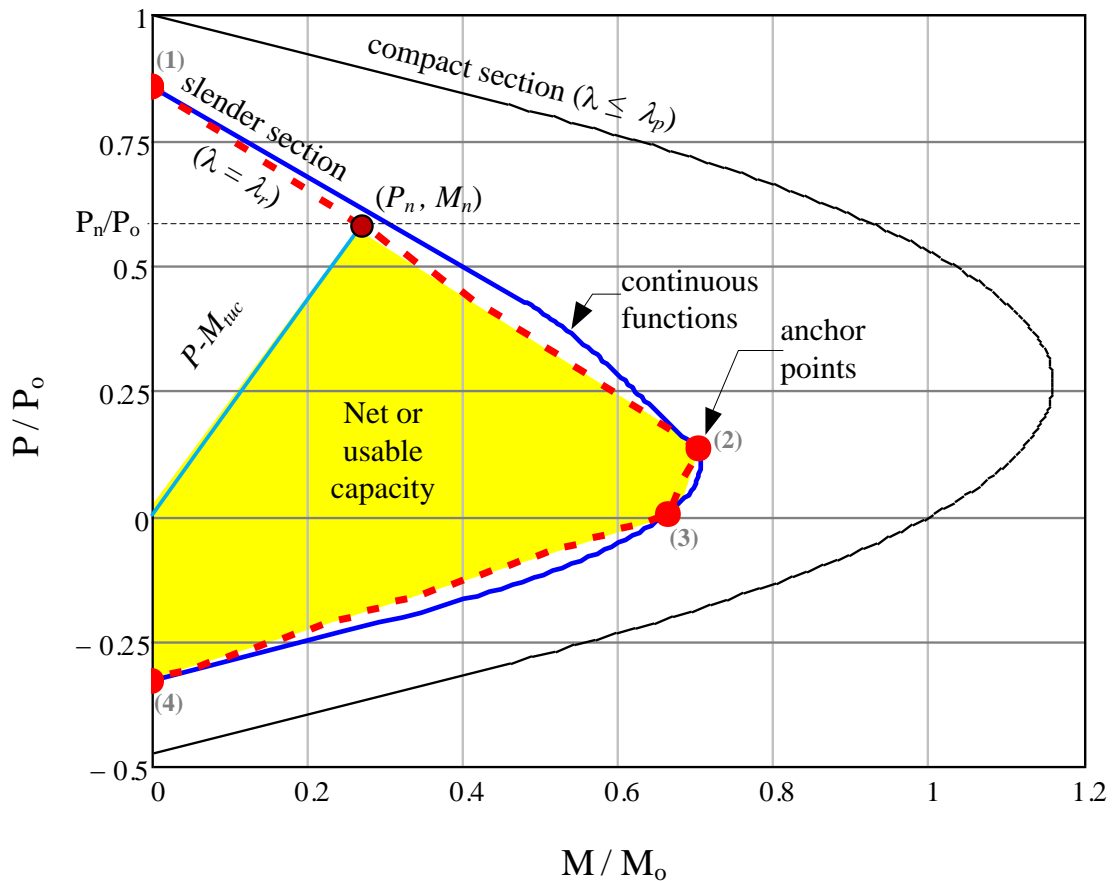


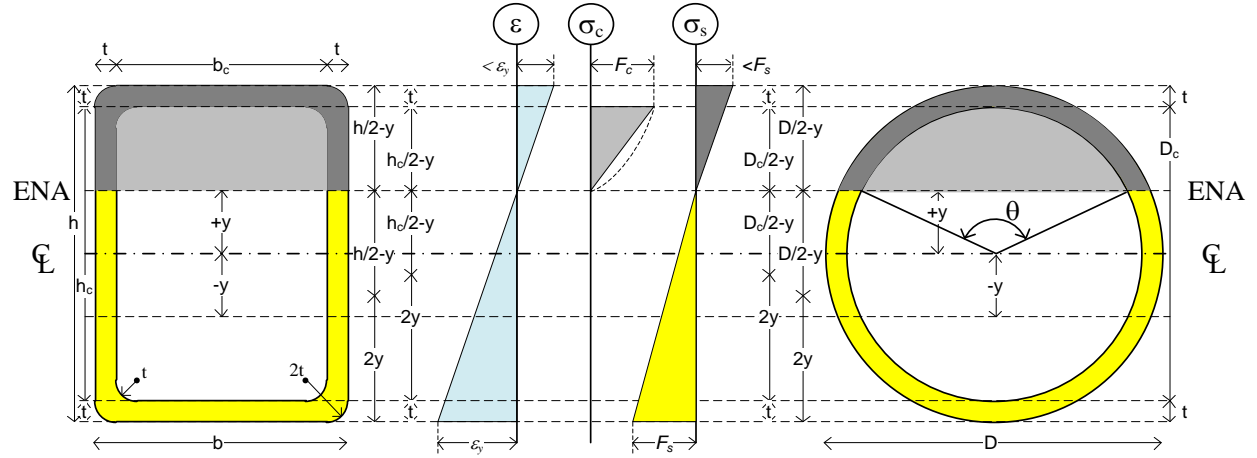
Figure 10.11. Schematic net or usable capacity in a CFT with slender steel cross-section which wall slenderness ratio equals λ_r

10.7.3. Interaction surface at the first steel yielding

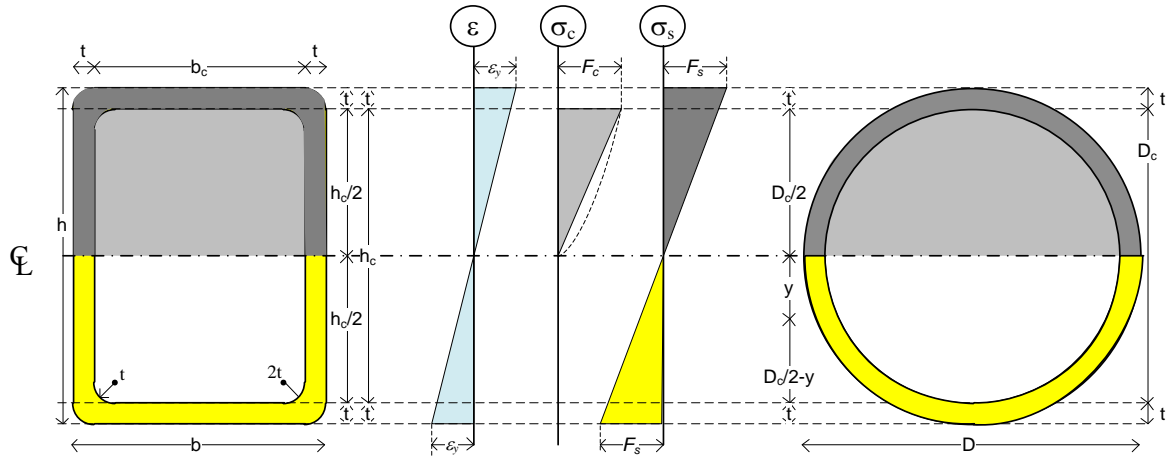
Similarly to the previous section, this section discusses the interaction surface of CFT cross-sections when the steel tube reaches a first yielding in either compression or tension. Figure 10.12 illustrates the distribution of elastic stresses in the steel tube and the concrete in compression for different positions (y) of the elastic neutral axis (ENA) with respect to the centroidal axis of the cross-section. These free-body diagrams of elastic stresses are valid for the ENA position within the concrete section, and they assume that the maximum stress in the steel tube (either in tension or compression) is equal to an effective elastic stress given as $F_s = 0.7F_y$ if the residual stress of $F_r = 0.3F_y$ is assumed. The maximum stress in concrete F_c can be calculated by Equation 10.42.

Based on the stress distribution shown in Figure 10.12, the interaction diagram P-M can also be obtained by varying the position of the neutral axis (ENA) under these assumptions. The cases related to elastic local buckling (Figure 10.9.b and c) and first steel yielding in compression (Figure 10.12.b and c) exhibit the same elastic stress distribution, and then the equations previously developed within this range (ENA below the centroidal axis) are identical.

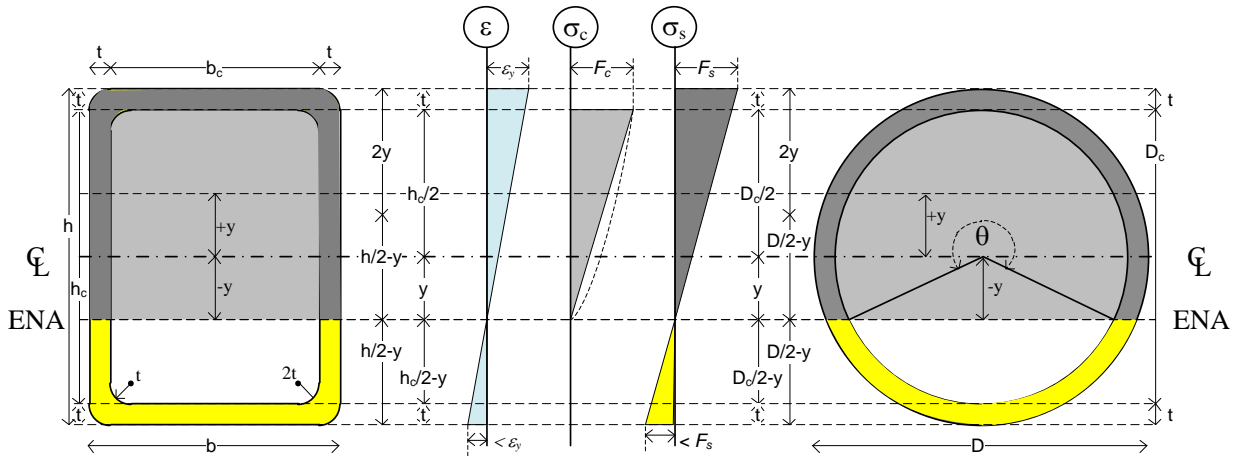
As illustrated in Figure 10.13, the resultant interaction diagram can be approximately delineated by only the two lines connecting three anchor points. The equations for these points are not included in this section, but these are equal to the points 1, 2 and 4 developed in the previous section for both RCFTs and CCFTs. Curves of P-M diagrams at first yielding related to different values of the ENA position are shown in Figure 10.13 with the label “*continuous functions*” with and without assumed residual stresses. In this figure, the P-M interaction diagram obtained with the plastic stress method is also included as reference.



(a) Distribution of elastic stresses between " $t/2 < y \leq h_c/2$ " in RCFTs or " $t/2 < y \leq D_c/2$ " in CCFTs



(b) Distribution of elastic stresses at $y=0$



(c) Distribution of elastic stresses between " $-h_c/2 \leq y \leq 0$ " in RCFTs or " $-D_c/2 \leq y \leq 0$ " in CCFTs

Figure 10.12. Elastic stress distribution in a CFT cross-section related to the first yielding (either compression or tension) in the steel tube

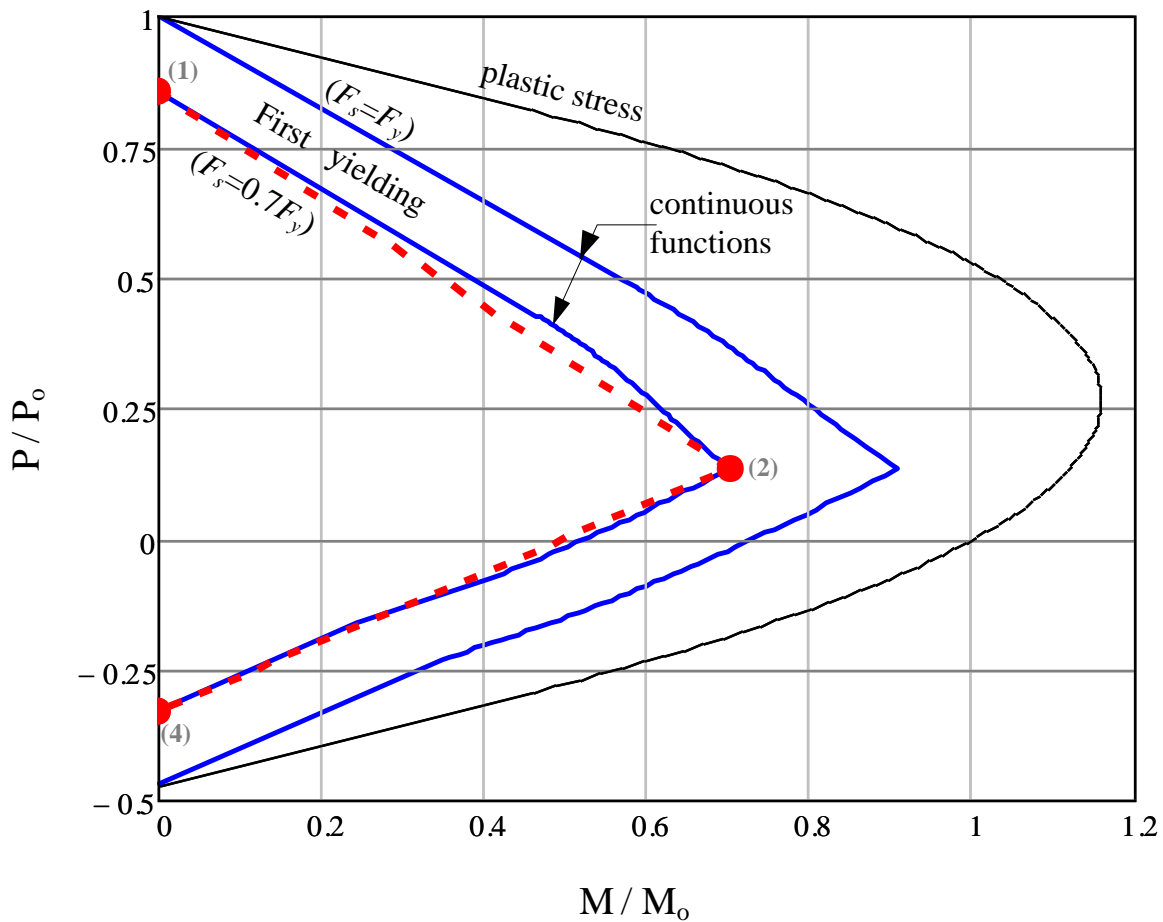


Figure 10.13. Schematic P - M interaction diagram for a CFT with first yielding in the steel tube

10.8. Application examples

The following section includes some application examples of the methodology proposed in this section for the calculation of the axial and flexural capacity of given CFT cross-sections, columns and beam-columns. Geometric and material properties, notes and the calculations are stated in the examples. The first two examples are related with the calculation of the axial and flexural capacities of a CCFT and a RCFT with compact steel tubes. Similarly, the third example is related to the strength calculation of a RCFT with a non-compact steel tube. The cross-section and the beam column capacities are obtained in all the cases.

Example 1

Determination of the capacity of a CCFT member

(subscripts s and c stand for steel and concrete, respectively)

Geometry of the HSS steel cross-section

$$D = 20\text{ in}$$

$$t = 0.233in$$

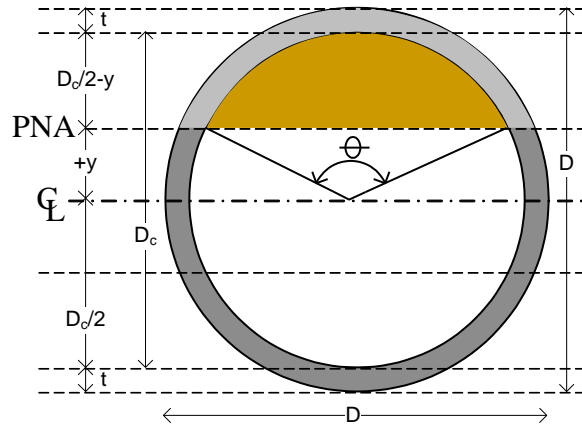
Geometry of the concrete cross-section

$$D_c = D - 2 \cdot t = 19.53in$$

Steel properties

$$F_y = 42 \text{ ksi}$$

$$E_s = 29000ksi$$



Note: Equation for E_c can be replaced by experimental values or any other applicable equation (i.e. ACI 363 for HSC)

Concrete properties

$$f_c = 5 \text{ ksi}$$

$$E_{c_ACI363} = 40ksi \cdot \sqrt{\frac{f_c}{psi}} + 1000ksi = 3828.43ksi$$

$$E_c = 57 \cdot ksi \cdot \sqrt{\frac{f_c}{psi}} = 4030.51 ksi$$

; ACI 318-08, 8.5.1

$$F_c = 0.85 \left(f_c + \frac{1.56 F_y \cdot t}{D_c} \right) = 4.91 \text{ ksi}$$

; Equivalent compressive stress

Steel section classification: compact steel section

$$\lambda = \frac{D}{t} = 85.84$$

$$\lambda_p = 0.15 \frac{E_s}{F_y} = 103.57$$

$$\lambda_r = 0.3 \frac{E_s}{F_y} = 207.14$$

Calculation of the geometric properties

Note: The steel geometric properties can be replaced by those given in the AISC Manual.

$$A_c = \frac{\pi \cdot D_c^2}{4} = 299.69 \text{ in}^2$$

$$I_c = \frac{\pi \cdot D_c^4}{64} = 7147.18 in^4$$

$$Z_c = \frac{D_c^3}{6} = 1242.29 \text{ in}^3$$

$$A_s = \frac{\pi \cdot D^2}{4} - A_c = 14.47 \text{ in}^2$$

$$I_s = \frac{\pi \cdot D^4}{64} - I_c = 706.8 \text{ in}^4$$

$$Z_s = \frac{D^3}{6} - Z_c = 91.05 \text{ in}^3$$

Calculation of pure axial capacity of the cross-section

$$\begin{aligned}
 P_s &= A_s \cdot F_y = 607.71kip && ; \text{ steel contribution} \\
 P_c &= A_c \cdot F_c = 1472.76kip && ; \text{ concrete contribution} \\
 P_o &= P_c + P_s = 2080.47kip && ; \text{ compressive capacity of the CFT cross-section} \\
 T_o &= -P_s = -607.71kip && ; \text{ tension capacity of the CFT cross-section}
 \end{aligned}$$

Calculation flexural capacity at the balance point

$$\begin{aligned}
 M_s &= Z_s \cdot F_y = 318.66ft \cdot kip && ; \text{ steel contribution} \\
 M_c &= \frac{Z_c}{2} \cdot F_c = 254.37ft \cdot kip && ; \text{ concrete contribution} \\
 M_b &= M_c + M_s = 573.03ft \cdot kip && ; \text{ flexural capacity of the CFT cross-section at the balance point}
 \end{aligned}$$

Calculation of the P-M capacity of the cross-section

Note: The given continuous functions are valid with the PNA position (y) within the concrete section

$$-\frac{D_c}{2} \leq y \leq \frac{D_c}{2} \quad \frac{D_c}{2} = 9.767in$$

The PNA position "y" depends on theta

$$\theta(y) = 2 \cdot \arccos\left(\frac{2y}{D_c}\right) \quad \text{or} \quad y(\theta) = \frac{D_c}{2} \cdot \cos\left(\frac{\theta}{2}\right)$$

For convenience, some constants for concrete and the steel are given by:

$$\begin{aligned}
 K_s &= (D - t) \cdot t \cdot F_y = 193.44kip && ; \text{ steel component} \\
 K_c &= \frac{D_c^2 \cdot F_c}{8} = 234.4kip && ; \text{ concrete component}
 \end{aligned}$$

Axial capacity of the cross-section

$$P(y) = (\theta(y) - \pi) \cdot K_s + (\theta(y) - \sin(\theta(y))) \cdot K_c$$

Flexural capacity of the cross-section

$$\begin{aligned}
 Z_s(y) &= Z_s \cdot \sin\left(\frac{\theta(y)}{2}\right) && ; \text{ steel component} \\
 Z_c(y) &= Z_c \cdot \sin\left(\frac{\theta(y)}{2}\right)^3 && ; \text{ concrete component} \\
 M(y) &= Z_s(y) \cdot F_y + \frac{Z_c(y)}{2} \cdot F_c && ; \text{ flexural capacity of the CFT cross-section at any position of the PNA}
 \end{aligned}$$

The pure bending capacity (M_o) is given at " y_o " such that $P(y_o)=0$.

This angle theta for the PNA position can be approximately by the following equations:

$$\theta_{o1} = \frac{0.2K_c - K_s}{0.68K_c} + \frac{\sqrt{(0.2K_c + K_s)^2 + 3.4K_c \cdot K_s}}{0.68K_c} = 1.97$$

$$y(\theta_{o1}) = 5.41in$$

$$P(y(\theta_{o1})) = 18.46kip$$

$$\theta_{o2} = 2 \cdot asec\left(\frac{K_s}{K_c} + 1\right) = 1.982$$

$$y(\theta_{o2}) = 5.35in$$

$$P(y(\theta_{o2})) = 25.39kip$$

$$\theta_{o3} = \left(\frac{5 \cdot \pi \cdot K_s}{K_c}\right)^{\frac{1}{4}} = 1.9$$

$$y(\theta_{o3}) = 5.69in$$

$$P(y(\theta_{o3})) = -17.89kip$$

By trial and error, a more accurate value of " y_o " may be obtained:

Note: The axial capacity is in compression side from " y_o " to " $h_c/2$ "

$$y_o = 5.5503in \quad P(y_o) = 0kip$$

$$-\frac{D_c}{2} = -9.77in < y < y_o = 5.55in$$

Then, the pure bending capacity of the cross-section is:

Check that " y_o " is within the concrete:

$$M_o = M(y_o) = 403.92kip \cdot ft$$

$$-\frac{h_c}{2} \leq y \leq \frac{h_c}{2} \quad \frac{D_c}{2} = 9.767in$$

Checking that at " $-y_o$ " the capacities are equal to P_c and M_o

$$\begin{aligned} y_o = 5.55in \quad P(-y_o) &= 1472.76kip & M(-y_o) &= 403.92kip \cdot ft \\ P_c &= 1472.76kip & M_o &= 403.92kip \cdot ft \end{aligned}$$

Note: The balance point is obtained at:

$$y_b = c \quad P(y_b) = 736.38kip \quad M(y_b) = 573.03kip \cdot ft$$

As stated before, the balance point is also defined by:

$$\frac{P_c}{2} = 736.38kip \quad ; \text{ half of the concrete axial strength}$$

$$M_s + M_c = 573.03kip \cdot ft \quad ; \text{ Steel and concrete flexural strength about the center}$$

The anchor points A to D of the P-M interaction diagram as in the current AISC (2010) are then:

$$P_{aisc} = \left(P_o \quad P_c \quad \frac{P_c}{2} \quad 0 \right)^T \quad P_{aisc}^T = (2080 \quad 1473 \quad 736 \quad 0)kip$$

$$M_{aisc} = (0 \quad M_o \quad M_b \quad M_o)^T \quad M_{aisc}^T = (0 \quad 404 \quad 573 \quad 404)kip \cdot ft$$

Calculation of P-M capacities with the continuous functions

Definition of a vector "y_c" that varies from "y_o" to "h_c/2"

$$size = 18$$

$$i = 1..(size - 1)$$

$$incr = \left[\frac{\left(y_o + \frac{D_c}{2} \right)}{size - 2} \right]$$

$$y_{c_i} = -\frac{D_c}{2} + (i - 1) \cdot incr$$

Calculation of the axial and flexural capacities for all these PNA positions

$$P_{cs_i} = P(y_{c_i})$$

$$M_{cs_i} = M(y_{c_i})$$

Adding the pure compression value

$$y_{c_0} = -\frac{D}{2} \quad P_{cs_0} = P_o \quad M_{cs_0} = 0$$

Summary of results for the cross-section

$$y_c^T = (-10 \ -9.8 \ -8.8 \ -7.9 \ -6.9 \ -5.9 \ -5 \ -4 \ -3.1 \ -2.1 \ -1.2 \ -0.2 \ 0.8 \ 1.7 \ 2.7 \ 3.6 \ 4.6 \ 5.6) \cdot in$$

$$P_{cs}^T = (2080 \ 2080 \ 1881 \ 1760 \ 1641 \ 1522 \ 1400 \ 1276 \ 1149 \ 1021 \ 892 \ 763 \ 633 \ 504 \ 375 \ 248 \ 123 \ 0) \cdot kip$$

$$M_{cs}^T = (0 \ 0 \ 158 \ 243 \ 316 \ 380 \ 436 \ 483 \ 520 \ 548 \ 566 \ 573 \ 570 \ 556 \ 533 \ 499 \ 456 \ 404) \cdot kip \cdot ft$$

Plot of the P-M interaction diagram for the CFT cross-section:

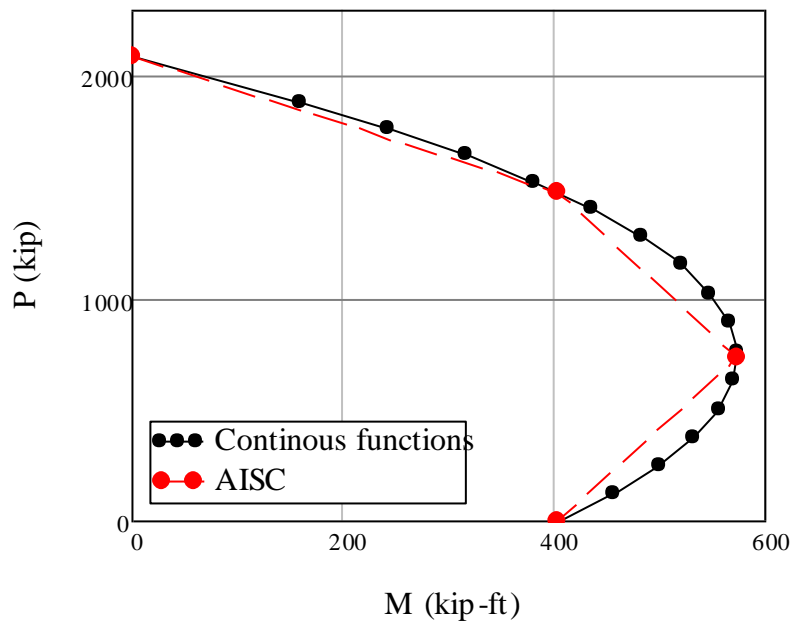


Figure - P-M Cross section strength

Axial strength of a CFT column (reduction for stability)

Column length and effective length coefficient based on the boundary conditions

$$K_{\text{AAA}} = 2 \quad L_{\text{AAA}} = 18\text{ft}$$

Calculations for the axial capacity:

$$EI_{\text{eff}} = E_s \cdot I_s + 0.8 \cdot E_c \cdot I_c = 298379 \text{kip} \cdot \text{ft}^2 \quad ; \text{ effective flexural rigidity}$$

$$P_e = \frac{\pi^2 \cdot EI_{\text{eff}}}{(K \cdot L)^2} = 2272.29 \text{kip} \quad ; \text{ Euler load}$$

$$\lambda_{\text{AAV}} = \sqrt{\frac{P_o}{P_e}} = 0.96 \quad ; \text{ Slenderness parameter}$$

$$P_n = \begin{cases} \frac{P_o}{P_e} \cdot 0.658 & \text{if } \frac{P_o}{P_e} \leq 2.25 \\ 0.877 P_e & \text{otherwise} \end{cases} = 1418.18 \text{kip} \quad ; \text{ Nominal load for the column}$$

$$\chi = \frac{P_n}{P_o} = 0.68 \quad : \text{ ratio beam column / cross-section capacity}$$

Calculation of the PNA position (y_n) when the axial capacity in the cross-section is equal to P_n

check that y_n is within the concrete ($-D_c/2 < y < D_c/2$)

$$y_n = -5.1229 \text{in} \quad -\frac{D_c}{2} = -9.77 \text{in}$$

$$P(y_n) = 1418.18 \text{kip} \quad P_n = 1418.18 \text{kip}$$

Calculation of the P-M capacity of the beam column (reduction due to the stability effects)

K and L given in the previous step are:

$$K = 2 \qquad L = 18ft$$

The column strength capacity (P_n) from the previous step was given at " y_n ":

$$P_n = 1418.18kip \qquad at \qquad y_n = -5.1229in$$

Thus, the cross-section moment (M_n) at the axial capacity (P_n) is given by:

$$M_n = M(y_n) = 428.3kip \cdot ft$$

The cross-section capacities obtained in a previous step are:

$$y_c^T = (-10 \ -9.8 \ -8.8 \ -7.9 \ -6.9 \ -5.9 \ -5 \ -4 \ -3.1 \ -2.1 \ -1.2 \ -0.2 \ 0.8 \ 1.7 \ 2.7 \ 3.6 \ 4.6 \ 5.6) \cdot in$$

$$P_{cs}^T = (2080 \ 2080 \ 1881 \ 1760 \ 1641 \ 1522 \ 1400 \ 1276 \ 1149 \ 1021 \ 892 \ 763 \ 633 \ 504 \ 375 \ 248 \ 123 \ 0) \cdot kip$$

$$M_{cs}^T = (0 \ 0 \ 158 \ 243 \ 316 \ 380 \ 436 \ 483 \ 520 \ 548 \ 566 \ 573 \ 570 \ 556 \ 533 \ 499 \ 456 \ 404) \cdot kip \cdot ft$$

The beam-column axial capacity varies from 0 to P_n

$$P_{bc_i} = \begin{cases} P_{cs_i} & \text{if } P_{cs_i} \leq P_n \\ P_n & \text{otherwise} \end{cases}$$

$$P_{bc}^T = (0 \ 1418 \ 1418 \ 1418 \ 1418 \ 1418 \ 1418 \ 1400 \ 1276 \ 1149 \ 1021 \ 892 \ 763 \ 633 \ 504 \ 375 \ 248 \ 123 \ 0) \cdot kip$$

The moment consumed by imperfection is given by:

$$\Delta_o = \frac{K \cdot L}{1500} = 0.29in \qquad M_{imp_i} = P_{bc_i} \cdot \Delta_o \cdot \left(\frac{1}{1 - \frac{P_{bc_i}}{P_e}} \right) \qquad P_n \cdot \Delta_o \cdot \left(\frac{1}{1 - \frac{P_n}{P_e}} \right) = 90.55kip \cdot ft$$

$$M_{imp}^T = (0 \ 91 \ 91 \ 91 \ 91 \ 91 \ 88 \ 70 \ 56 \ 45 \ 35 \ 28 \ 21 \ 16 \ 11 \ 7 \ 3 \ 0) \cdot kip \cdot ft$$

The total reduction moment for stability is given by:

$$M_{tuc_i} = M_n \cdot \frac{P_{bc_i} \cdot (P_n - P_e)}{P_n \cdot (P_{bc_i} - P_e)}$$

$$M_{tuc}^T = (0 \ 428 \ 428 \ 428 \ 428 \ 428 \ 414 \ 330 \ 264 \ 211 \ 167 \ 130 \ 100 \ 73 \ 51 \ 32 \ 15 \ 0) \cdot kip \cdot ft$$

Then, the available net moment in the beam-column is given by:

$$M_{bc_i} = \begin{cases} M_{cs_i} - M_{tuc_i} & \text{if } P_{cs_i} \leq P_n \\ 0 & \text{otherwise} \end{cases}$$

$$M_{bc}^T = (0 \ 0 \ 0 \ 0 \ 0 \ 0 \ 22 \ 153 \ 256 \ 337 \ 399 \ 443 \ 470 \ 483 \ 482 \ 468 \ 441 \ 404) \cdot \text{kip} \cdot \text{ft}$$

The simplified P-M diagram for the beam column (as in current AISC, 2010) is:

$$P_{aisc_bc} = \chi \cdot (P_o \ P_c \ 0)^T \quad P_{aisc_bc}^T = (1418 \ 1004 \ 0) \text{ kip}$$

$$M_{aisc_bc} = (0 \ M_o \ M_o)^T \quad M_{aisc_bc}^T = (0 \ 404 \ 404) \text{ kip} \cdot \text{ft}$$

Plot of the P-M interaction diagram for the CFT:

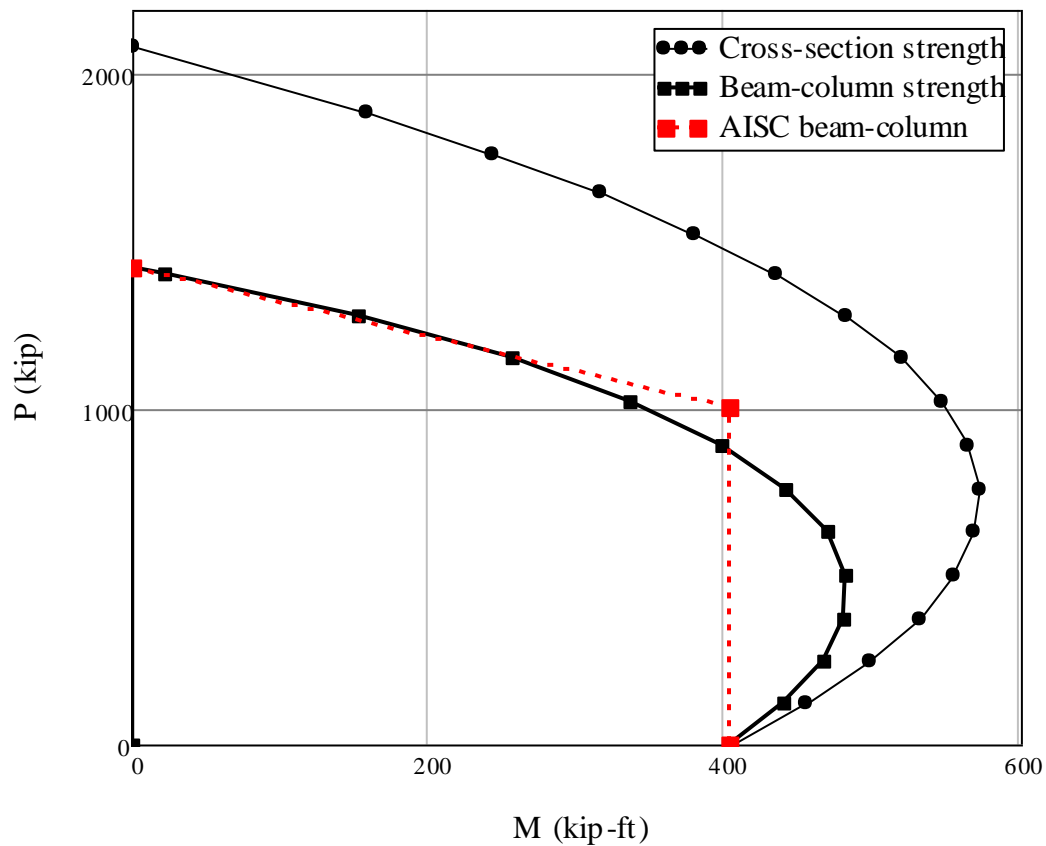


Figure - P-M interaction diagram for a RCFT beam-column

Example 2

Determination of the capacity of a RCFT member (strong axis bending)

(subscript *s* and *c* stand for steel and concrete, respectively)

Geometry of the HSS steel cross-section

$$b = 12 \text{ in}$$

$$h = 20 \text{ in}$$

$$t = 0.291 \text{ in}$$

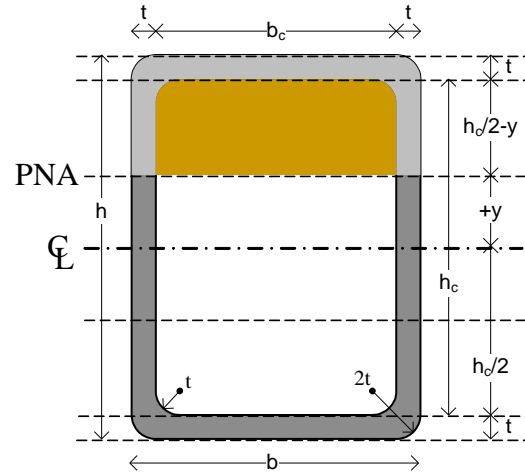
$$r_s = 2 \cdot t = 0.58 \text{ in} \quad ; \text{ external radius}$$

$$r_c = r_s - t = 0.29 \text{ in} \quad ; \text{ internal radius}$$

Geometry of the concrete cross-section

$$b_c = b - 2t = 11.42 \text{ in}$$

$$h_c = h - 2t = 19.42 \text{ in}$$



Steel properties

$$F_y = 46 \text{ ksi}$$

$$E_s = 29000 \text{ ksi}$$

Note: Equation for E_c can be replaced by experimental values or any other applicable equation (i.e. ACI 363 for HSC)

Concrete properties

$$f_c = 5 \text{ ksi}$$

$$E_{c_ACI363} = 40 \text{ ksi} \cdot \sqrt{\frac{f_c}{\text{psi}}} + 1000 \text{ ksi} = 3828.43 \text{ ksi}$$

$$E_c = 57 \text{ ksi} \cdot \sqrt{\frac{f_c}{\text{psi}}} = 4030.51 \text{ ksi}$$

; ACI 318-08, 8.5.1

$$\beta = 0.85$$

; ACI 318-08, 10.2.7.1

$$F_c = \beta \cdot f_c = 4.25 \text{ ksi}$$

; Equivalent compressive stress

Calculation of the geometric properties

$$A_c = b_c \cdot h_c - (4 - \pi) t^2 = 221.64 \text{ in}^2$$

$$A_s = b \cdot h - 4 \cdot (4 - \pi) t^2 - A_c = 18.07 \text{ in}^2$$

$$I_c = \frac{b_c \cdot h_c^3}{12} = 6966.62 \text{ in}^4$$

$$Z_c = \frac{b_c \cdot h_c^2}{4} = 1076.31 \text{ in}^3$$

$$I_s = \frac{b \cdot h^3}{12} - I_c = 1033.38 \text{ in}^4$$

$$Z_s = \frac{b \cdot h^2}{4} - Z_c = 123.69 \text{ in}^3$$

Note: The steel geometric properties can be replaced by those given in the AISC Manual.

Some differences are expected with these equations, mainly for the I_s and Z_s since they are not considering the radius of the fillets

Steel section classification: compact steel section

$$\lambda = \frac{b}{t} = 41.24$$

$$\lambda_p = 2.12 \sqrt{\frac{E_s}{F_y}} = 53.23$$

$$\lambda_r = 3 \cdot \sqrt{\frac{E_s}{F_y}} = 75.33$$

Calculation of pure axial capacity of the cross-section

$$P_s = A_s \cdot F_y = 831.09 \text{kip} \quad ; \text{ steel contribution}$$

$$P_c = A_c \cdot F_c = 941.98 \text{kip} \quad ; \text{ concrete contribution}$$

$$P_o = P_c + P_s = 1773.07 \text{kip} \quad ; \text{ compressive capacity of the CFT cross-section}$$

$$T_o = -P_s = -831.09 \text{kip} \quad ; \text{ tension capacity of the CFT cross-section}$$

Calculation flexural capacity at the balance point

$$M_s = Z_s \cdot F_y = 474.13 \text{ft} \cdot \text{kip} \quad ; \text{ steel contribution}$$

$$M_c = \frac{Z_c}{2} \cdot F_c = 190.6 \text{ft} \cdot \text{kip} \quad ; \text{ concrete contribution}$$

$$M_b = M_c + M_s = 664.73 \text{ft} \cdot \text{kip} \quad ; \text{ flexural capacity of the CFT cross-section}$$

at the balance point

Calculation of the P-M capacity of the cross-section

Note: The given continuous functions are valid with the PNA position (y) within the concrete section

$$-\frac{h_c}{2} \leq y \leq \frac{h_c}{2} \quad \frac{h_c}{2} = 9.709 \text{in}$$

Axial capacity of the cross-section

$$P(y) = \left(\frac{h_c}{2} - y \right) \cdot b_c \cdot F_c - 4 \cdot y \cdot t \cdot F_y$$

Flexural capacity of the cross-section

$$Z_s(y) = Z_s - 2 \cdot t \cdot y^2 \quad ; \text{ plastic section modulus of the steel}$$

$$Z_c(y) = Z_c - b_c \cdot y^2 \quad ; \text{ plastic section modulus of the concrete}$$

$$M(y) = Z_s(y) \cdot F_y + \frac{Z_c(y)}{2} \cdot F_c \quad ; \text{ flexural capacity of the CFT cross-section}$$

The pure bending capacity (M_o) is given at " y_o " such that $P(y_o)=0$. This position is given by:

$$y_o = \frac{\frac{P_c}{2}}{(F_c \cdot b_c + 4 \cdot t \cdot F_y)} = 4.61 \text{ in}$$

By trial and error, a more accurate value of " y_o " may be obtained:

$$y_o = 4.61585 \text{ in} \quad P(y_o) = 0 \text{ kip}$$

Then, the pure bending capacity of the cross-section is:

$$M_o = M(y_o) = 574.11 \text{ kip} \cdot \text{ft}$$

Note: The balance point is obtained at:

$$y_b = c \quad P(y_b) = 471.14 \text{ kip} \quad M(y_b) = 664.73 \text{ kip} \cdot \text{ft}$$

As stated before, the balance point is defined by:

$$\frac{P_c}{2} = 470.99 \text{ kip} \quad ; \text{ half of the concrete axial strength}$$

$$M_s + M_c = 664.73 \text{ kip} \cdot \text{ft} \quad ; \text{ Steel and concrete flexural strength about the center}$$

The anchor points A to D of the P-M interaction diagram as in the current AISC (2010) are then:

$$P_{aisc} = \left(P_o \quad P_c \quad \frac{P_c}{2} \quad 0 \right)^T \quad P_{aisc}^T = (1773 \quad 942 \quad 471 \quad 0) \text{ kip}$$

$$M_{aisc} = \left(0 \quad M_o \quad M_b \quad M_o \right)^T \quad M_{aisc}^T = (0 \quad 574 \quad 665 \quad 574) \text{ kip} \cdot \text{ft}$$

Calculation of P-M capacities with the continuous functions

Definition of a vector " y_c " that varies from " y_o " to " $h_c/2$ "

$$\begin{aligned} size &= 18 \\ i &= 1..(size - 1) \end{aligned} \quad incr = \left[\frac{\left(y_o + \frac{h_c}{2} \right)}{size - 2} \right] \quad y_{c_i} = -\frac{h_c}{2} + (i - 1) \cdot incr$$

Calculation of the axial and flexural capacities for all these PNA positions

$$P_{cs_i} = P(y_{c_i})$$

$$M_{cs_i} = M(y_{c_i})$$

Adding the pure compression value

$$y_{c_0} = -\frac{h}{2} \quad P_{cs_0} = P_o \quad M_{cs_0} = 0$$

Summary of results for the cross-section

$$y_c^T = (-10 \ -9.7 \ -8.8 \ -7.9 \ -7 \ -6.1 \ -5.2 \ -4.3 \ -3.4 \ -2.5 \ -1.7 \ -0.8 \ 0.1 \ 1 \ 1.9 \ 2.8 \ 3.7 \ 4.6) \cdot in$$

$$P_{cs}^T = (1773 \ 1462 \ 1371 \ 1279 \ 1188 \ 1097 \ 1005 \ 914 \ 822 \ 731 \ 640 \ 548 \ 457 \ 366 \ 274 \ 183 \ 91 \ 0) \cdot kip$$

$$M_{cs}^T = (0 \ 264 \ 334 \ 398 \ 455 \ 505 \ 548 \ 585 \ 614 \ 637 \ 653 \ 662 \ 665 \ 660 \ 649 \ 631 \ 606 \ 574) \cdot kip \cdot ft$$

Plot of the P-M interaction diagram for the CFT cross-section:

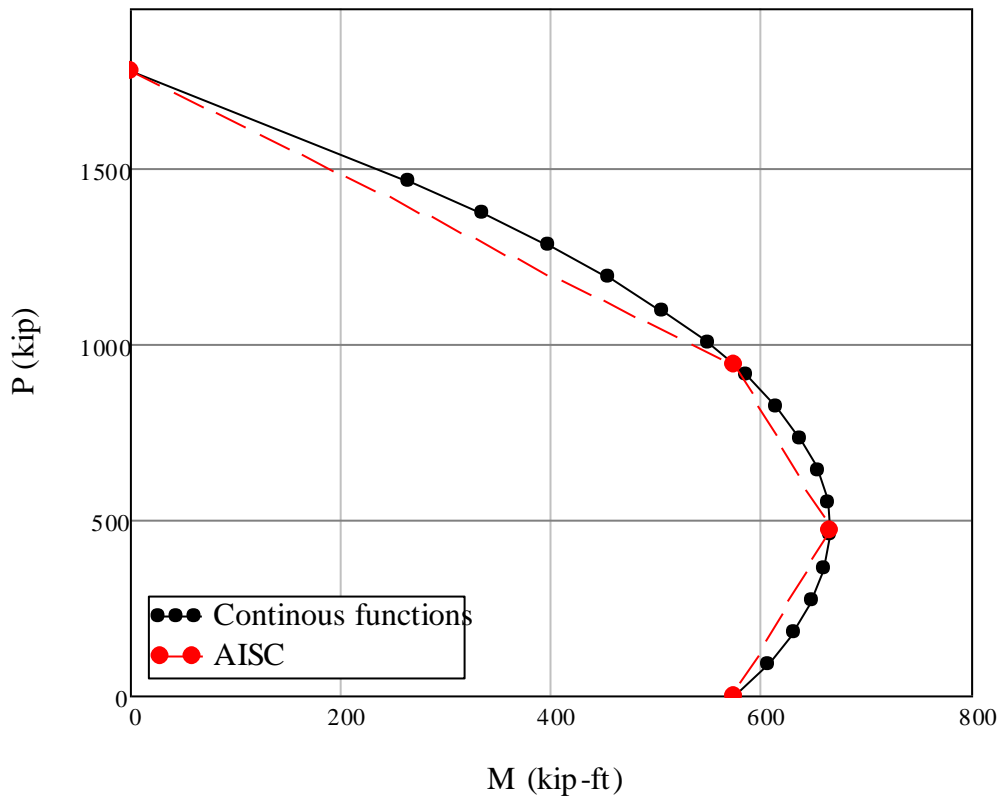


Figure - P-M Cross section strength

Axial strength of a CFT column (reduction due to the stability effects)

Column length and effective length coefficient based on the boundary conditions

$$K_{\text{AAA}} = 2 \quad L_{\text{AAA}} = 18\text{ft}$$

Calculations for the axial capacity:

$$EI_{eff} = E_s \cdot I_s + 0.8 \cdot E_c \cdot I_c = 360205 \text{kip} \cdot \text{ft}^2 \quad ; \text{ effective flexural rigidity}$$

$$P_e = \frac{\pi^2 \cdot EI_{eff}}{(K \cdot L)^2} = 2743.12 \text{kip} \quad ; \text{ Euler load}$$

$$\lambda_{\text{WWW}} = \sqrt{\frac{P_o}{P_e}} = 0.8 \quad ; \text{ Slenderness parameter}$$

$$P_n = \begin{cases} \frac{P_o}{P_e} \cdot 0.658 & \text{if } \frac{P_o}{P_e} \leq 2.25 \\ 0.877 P_e & \text{otherwise} \end{cases} = 1352.8 \text{kip} \quad ; \text{ Nominal load for the column}$$

$$\chi = \frac{P_n}{P_o} = 0.76 \quad ; \text{ ratio beam column / cross-section capacity}$$

Calculation of the PNA position (y_n) when the axial capacity in the cross-section is equal to P_n

$$y_n = \frac{\frac{P_c}{2} - P_n}{(F_c \cdot b_c + 4 \cdot t \cdot F_y)} = -8.64 \text{in} \quad \text{check that } y_n \text{ is within the concrete } (-hc/2 < y < hc/2)$$

$$\frac{h_c}{2} = 9.71 \text{in}$$

$$y_{\text{WWW}} = -8.6377 \text{in} \quad P(y_n) = 1352.8 \text{kip} \quad P_n = 1352.8 \text{kip}$$

Calculation of the P-M capacity of the beam column (reduction due to the stability effects)

The given K and L in the previous step are:

$$K = 2 \qquad L = 18ft$$

The column strength capacity (P_n) from the previous step was given at " y_n ":

$$P_n = 1352.8kip \qquad at \qquad y_n = -8.64in$$

Thus, the cross-section moment (M_n) at the axial capacity (P_n) is given by:

$$M_n = M(y_n) = 347.42kip \cdot ft$$

The cross-section capacities obtained in a previous step are:

$$\begin{aligned} y_c^T &= (-10 \ -9.7 \ -8.8 \ -7.9 \ -7 \ -6.1 \ -5.2 \ -4.3 \ -3.4 \ -2.5 \ -1.7 \ -0.8 \ 0.1 \ 1 \ 1.9 \ 2.8 \ 3.7 \ 4.6) \cdot in \\ P_{cs}^T &= (1773 \ 1462 \ 1371 \ 1279 \ 1188 \ 1097 \ 1005 \ 914 \ 822 \ 731 \ 640 \ 548 \ 457 \ 366 \ 274 \ 183 \ 91 \ 0) \cdot kip \\ M_{cs}^T &= (0 \ 264 \ 334 \ 398 \ 455 \ 505 \ 548 \ 585 \ 614 \ 637 \ 653 \ 662 \ 665 \ 660 \ 649 \ 631 \ 606 \ 574) \cdot kip \cdot ft \end{aligned}$$

The beam-column axial capacity varies from 0 to P_n

$$P_{bc_i} = \begin{cases} P_{cs_i} & \text{if } P_{cs_i} \leq P_n \\ P_n & \text{otherwise} \end{cases}$$

$$P_{bc}^T = (0 \ 1353 \ 1353 \ 1279 \ 1188 \ 1097 \ 1005 \ 914 \ 822 \ 731 \ 640 \ 548 \ 457 \ 366 \ 274 \ 183 \ 91 \ 0) \cdot kip$$

The moment consumed by imperfection is given by:

$$\Delta_o = \frac{K \cdot L}{1500} = 0.29in \qquad M_{imp_i} = P_{bc_i} \cdot \Delta_o \cdot \left(\frac{1}{1 - \frac{P_{bc_i}}{P_e}} \right) \qquad P_n \cdot \Delta_o \cdot \left(\frac{1}{1 - \frac{P_n}{P_e}} \right) = 64.06kip \cdot ft$$

$$M_{imp}^T = (0 \ 64.1 \ 64.1 \ 57.5 \ 50.3 \ 43.8 \ 38.1 \ 32.9 \ 28.2 \ 23.9 \ 20 \ 16.4 \ 13.2 \ 10.1 \ 7.3 \ 4.7 \ 2.3 \ 0) \cdot kip \cdot ft$$

The total reduction moment for stability is given by:

$$M_{tuc_i} = \max \left[M_n \cdot \frac{(P_n - P_e)}{P_n} \cdot \frac{P_{bc_i}}{(P_{bc_i} - P_e)}, M_{imp_i} \right]$$

$$M_{tuc}^T = (0 \ 347 \ 347 \ 312 \ 273 \ 238 \ 207 \ 178 \ 153 \ 130 \ 109 \ 89 \ 71 \ 55 \ 40 \ 25 \ 12 \ 0) \cdot kip \cdot ft$$

Then, the available net moment in the beam-column is given by:

$$M_{bc_i} = \begin{cases} M_{cs_i} - M_{tuc_i} & \text{if } P_{cs_i} \leq P_n \\ 0 & \text{otherwise} \end{cases}$$

$$M_{bc}^T = (0 \ 0 \ 0 \ 86 \ 182 \ 267 \ 342 \ 406 \ 461 \ 507 \ 545 \ 573 \ 593 \ 605 \ 609 \ 605 \ 594 \ 574) \cdot \text{kip} \cdot \text{ft}$$

The simplified P-M diagram for the beam column (as in current AISC, 2010) is:

$$P_{aisc_bc} = \frac{P_n}{P_o} \cdot (P_o \ P_c \ 0)^T \quad P_{aisc}^T = (1773 \ 942 \ 471 \ 0) \text{ kip}$$

$$M_{aisc_bc} = (0 \ M_o \ M_o)^T \quad M_{aisc}^T = (0 \ 574 \ 665 \ 574) \text{ kip} \cdot \text{ft}$$

Plot of the P-M interaction diagram for the CFT:

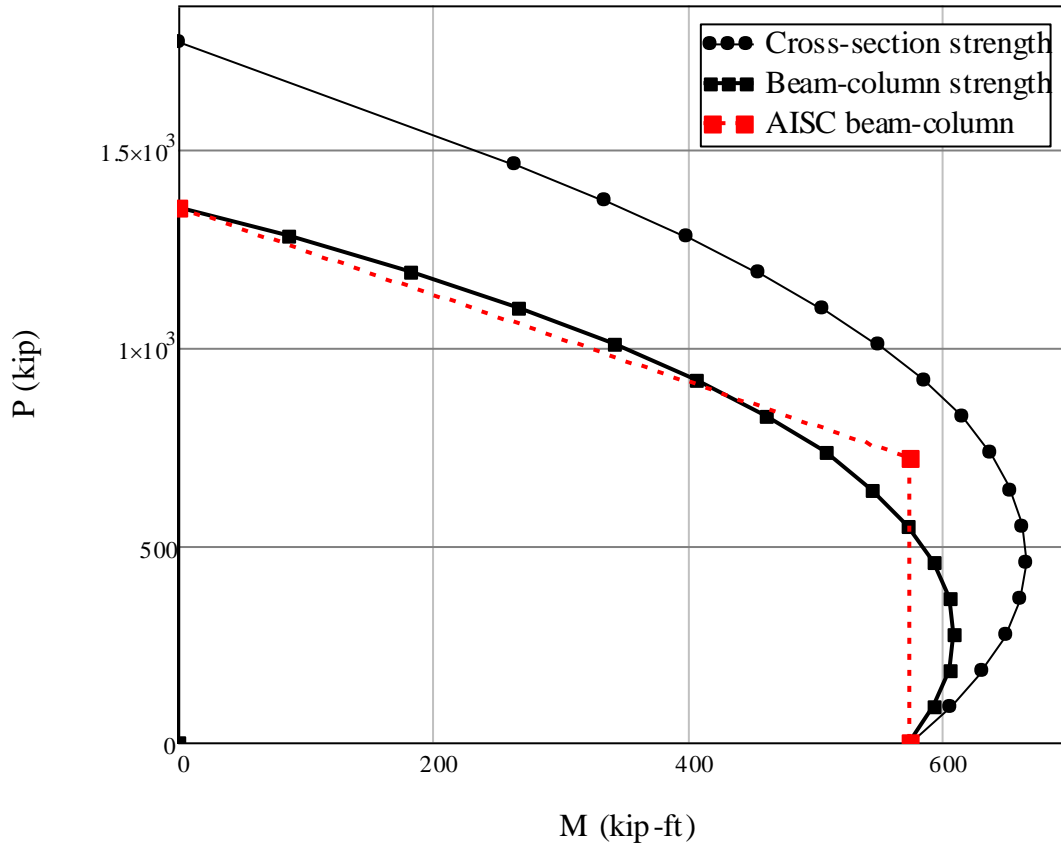


Figure - P-M interaction diagram for a RCFT beam-column

Example 3

Determination of the capacity of a RCFT member (weak axis bending)
(subscript *s* and *c* stand for steel and concrete, respectively)

Geometry of the HSS steel cross-section

$$b = 20in \quad h = 12in \quad t = 0.291in$$

Geometry of the concrete cross-section

$$b_c = b - 2t = 19.42in \quad h_c = h - 2t = 11.42in$$

Steel properties

$$F_y = 46ksi \quad E_s = 29000ksi \quad e_y = \frac{F_y}{E_s} = 0.00159$$

$$F_r = 0.3F_y = 13.8ksi \quad F_s = F_y - F_r = 32.2ksi$$

Steel section classification: non-compact steel section

$$\lambda = \frac{b}{t} = 68.73 \quad \lambda_p = 2.12 \sqrt{\frac{E_s}{F_y}} = 53.23 \quad \lambda_r = 3 \cdot \sqrt{\frac{E_s}{F_y}} = 75.33$$

Concrete properties

$$f_c = 5ksi \quad E_c = 57ksi \cdot \sqrt{\frac{f_c}{psi}} = 4030.51ksi \quad F_{cp} = 0.85f_c = 4.25ksi$$

$$\beta_2 = \min \left[\frac{E_c \cdot e_y}{f_c} \cdot \left(1 - \frac{2t}{b} \right) - \left[\frac{E_c \cdot e_y}{2f_c} \cdot \left(1 - \frac{2t}{b} \right) \right]^2, 0.85 \right] = 0.850 \quad F_{ce} = \beta_2 \cdot f_c = 4.25ksi$$

Calculation of the geometric properties

$$A_c = b_c \cdot h_c - (4 - \pi)t^2 = 221.64in^2$$

$$A_s = b \cdot h - 4 \cdot (4 - \pi)t^2 - A_c = 18.07in^2$$

$$I_c = \frac{b_c \cdot h_c^3}{12} = 2408.76in^4$$

$$I_s = \frac{b \cdot h^3}{12} - I_c = 471.24in^4$$

$$Z_c = \frac{b_c \cdot h_c^2}{4} = 632.88in^3$$

$$Z_s = \frac{b \cdot h^2}{4} - Z_c = 87.12in^3$$

$$S_c = \frac{2I_c}{h_c} = 421.92in^3$$

$$S_s = \frac{2I_s}{h} = 78.54in^3$$

Calculation of pure axial capacity of the cross-section

$$P_{sp} = A_s \cdot F_y = 831.09kip$$

$$P_{se} = A_s \cdot F_s = 581.76kip$$

$$P_{ce} = A_c \cdot F_{ce} = 941.98kip$$

$$P_{cp} = A_c \cdot F_{cp} = 941.98kip$$

$$P_{op} = P_{cp} + P_{sp} = 1773.07kip$$

$$P_{oe} = P_{ce} + P_{se} = 1523.74kip$$

$$P_o = P_{op} - \frac{(\lambda - \lambda_p) \cdot (P_{op} - P_{oe})}{(\lambda_r - \lambda_p)} = 1598.18kip$$

Calculation of flexural capacity at the balance point

$$P_{bp} = \frac{P_{cp}}{2} = 470.99kip$$

$$P_{be} = \frac{P_{ce}}{4} = 235.49kip$$

$$P_b = P_{bp} - \frac{(\lambda - \lambda_p) \cdot (P_{bp} - P_{be})}{(\lambda_r - \lambda_p)} = 305.8kip$$

$$M_{sp} = Z_s \cdot F_y = 333.94ft \cdot kip$$

$$M_{se} = S_s \cdot F_s = 210.75ft \cdot kip$$

$$M_{cp} = \frac{Z_c}{2} \cdot F_{ce} = 112.07ft \cdot kip$$

$$M_{ce} = \frac{S_c}{2} \cdot F_{ce} = 74.72ft \cdot kip$$

$$M_{bp} = M_{cp} + M_{sp} = 446.02ft \cdot kip$$

$$M_{be} = M_{ce} + M_{se} = 285.47ft \cdot kip$$

$$M_b = M_{bp} - \frac{(\lambda - \lambda_p) \cdot (M_{bp} - M_{be})}{(\lambda_r - \lambda_p)} = 333.4ft \cdot kip$$

Calculation of pure bending capacity

$$y_o = \frac{1}{2} \cdot \left(\frac{F_{cp} \cdot A_c}{4 \cdot F_y \cdot t + F_{cp} \cdot b_c} \right) = 3.46in$$

$$y_{oe} = \frac{1}{2} \cdot \left(\frac{F_{ce} \cdot A_c}{8 \cdot F_s \cdot t + F_{ce} \cdot b_c} \right) = 2.99in$$

$$M_{op} = M_{bp} - 2 \cdot y_o^2 \cdot t \cdot F_y - \frac{b_c \cdot y_o^2}{2} \cdot F_{cp} = 378.09kip \cdot ft$$

$$M_{oe} = M_{be} - \frac{4}{3} \cdot y_{oe}^2 \cdot t \cdot F_y - \frac{b_c \cdot y_{oe}^2}{3} \cdot F_{ce} = 251.66kip \cdot ft$$

$$M_o = M_{op} - \frac{(\lambda - \lambda_p) \cdot (M_{op} - M_{oe})}{(\lambda_r - \lambda_p)} = 289.41ft \cdot kip$$

The simplified P-M diagram (as slender section)

$$P_r = (P_{oe} \ P_{be} \ 0)^T \quad P_r^T = (1524 \ 235 \ 0) \cdot kip$$

$$M_r = (0 \ M_{be} \ M_{oe})^T \quad M_r^T = (0 \ 285 \ 252) \cdot kip \cdot ft$$

The simplified P-M diagram (as compact section)

$$P_p = (P_{op} \ P_{bp} \ 0)^T \quad P_p^T = (1773 \ 471 \ 0) \cdot kip$$

$$M_p = (0 \ M_{bp} \ M_{op})^T \quad M_p^T = (0 \ 285 \ 252) \cdot kip \cdot ft$$

The simplified P-M diagram (as compact section)

$$P_{ep} = (P_o \ P_b \ 0)^T \quad P_p^T = (1773 \ 471 \ 0) \cdot kip$$

$$M_{ep} = (0 \ M_b \ M_o)^T \quad M_p^T = (0 \ 285 \ 252) \cdot kip \cdot ft$$

Calculation of the P-M capacity of the cross-section (with continuous functions)

Note: The given continuous functions are valid with

the PNA position (y) within the concrete section

$$-\frac{h_c}{2} \leq y \leq \frac{h_c}{2} \quad \frac{h_c}{2} = 5.709in$$

Axial capacity of the cross-section

$$P(y) = \left(\frac{h_c}{2} - y \right) \cdot b_c \cdot F_{cp} - 4 \cdot y \cdot t \cdot F_y$$

Flexural capacity of the cross-section

$$Zs(y) = Z_s - 2 \cdot t \cdot y^2 \quad ; \text{ plastic section modulus of the steel}$$

$$Zc(y) = Z_c - b_c \cdot y^2 \quad ; \text{ plastic section modulus of the concrete}$$

$$M(y) = Zs(y) \cdot F_y + \frac{Zc(y)}{2} \cdot F_{cp} \quad ; \text{ flexural capacity of the CFT cross-section}$$

The pure bending capacity (M_o) is given at " y_o " such that $P(y_o)=0$.

This position was calculated above as:

$$y_o = 3.46in \quad P(y_o) = 0.15kip$$

Note: The axial capacity is in compression side from " y_o " to " $h_c/2$ "

$$-\frac{h_c}{2} = -5.71in < y < y_o = 3.46in$$

By trial and error, a more accurate

value of " y_o " may be obtained:

$$y_o = 3.46248in \quad P(y_o) = 0kip$$

Check that " y_o " is within the concrete:

$$-\frac{h_c}{2} \leq y \leq \frac{h_c}{2} \quad \frac{h_c}{2} = 5.709in$$

Then, the pure bending capacity of the cross-section is:

$$M_o = M(y_o) = 378.04kip \cdot ft$$

Note: The balance point is obtained at:

$$y_b = 0 \quad P(y_b) = 471.14kip \quad M(y_b) = 446.02kip \cdot ft$$

As stated before, the balance point is defined by:

$$\frac{P_{cp}}{2} = 470.99kip \quad ; \text{ half of the concrete axial strength}$$

$$M_{sp} + M_{cp} = 446.02kip \cdot ft \quad ; \text{ Steel and concrete flexural strength about the center}$$

The anchor points A to D of the P-M interaction diagram as in the current AISC (2010) are then:

$$P_{aisc} = \left(P_{op} \quad P_{cp} \quad \frac{P_{cp}}{2} \quad 0 \right)^T \quad P_{aisc}^T = (1773 \quad 942 \quad 471 \quad 0) \cdot kip$$

$$M_{aisc} = \left(0 \quad M_{op} \quad M_{bp} \quad M_{op} \right)^T \quad M_{aisc}^T = (0 \quad 378 \quad 446 \quad 378) \cdot kip \cdot ft$$

Calculation of P-M capacities with the continuous functions

Definition of a vector " y_c " that varies from " y_o " to " $h_c/2$ "

$$size = 18$$

$$i = 1..(size - 1)$$

$$incr = \left[\frac{\left(y_o + \frac{h_c}{2} \right)}{size - 2} \right]$$

$$y_{c_i} = -\frac{h_c}{2} + (i - 1) \cdot incr$$

Calculation of the axial and flexural capacities for all these PNA positions

$$P_{cs_i} = P(y_{c_i})$$

$$M_{cs_i} = M(y_{c_i})$$

Adding the pure compression value

$$y_{c_0} = -\frac{h}{2}$$

$$P_{cs_0} = P_{op}$$

$$M_{cs_0} = 0$$

Summary of results for the cross-section

$$y_c^T = (-6 \ -5.7 \ -5.1 \ -4.6 \ -4 \ -3.4 \ -2.8 \ -2.3 \ -1.7 \ -1.1 \ -0.6 \ 0 \ 0.6 \ 1.2 \ 1.7 \ 2.3 \ 2.9 \ 3.5) \cdot in$$

$$P_{cs}^T = (1773 \ 1248 \ 1170 \ 1092 \ 1014 \ 936 \ 858 \ 780 \ 702 \ 624 \ 546 \ 468 \ 390 \ 312 \ 234 \ 156 \ 78 \ 0) \cdot kip$$

$$M_{cs}^T = (0 \ 261 \ 296 \ 328 \ 356 \ 380 \ 400 \ 417 \ 430 \ 439 \ 444 \ 446 \ 444 \ 438 \ 429 \ 416 \ 399 \ 378) \cdot kip \cdot ft$$

Plot of the P-M interaction diagram for the CFT cross-section:

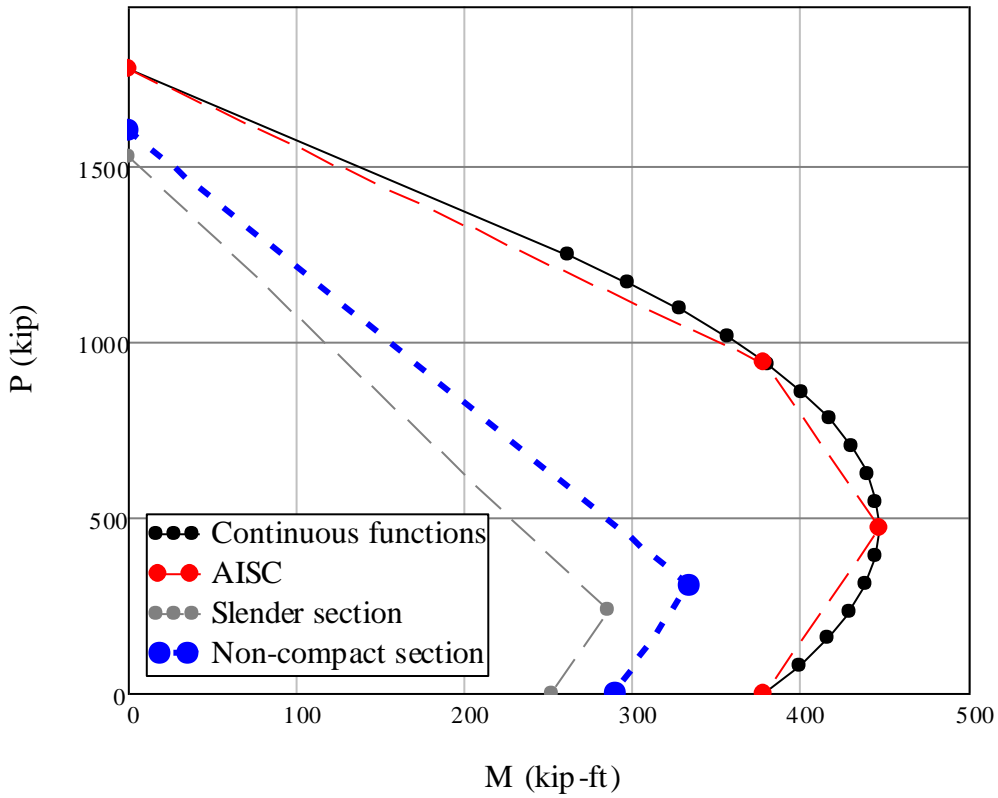


Figure - P-M Cross section strength

Axial strength of a CFT column (reduction due to the stability effects)

Column length and effective length coefficient based on the boundary conditions

$$\underset{\text{AAA}}{K} = 2 \qquad \underset{\text{AAA}}{L} = 18\text{ft}$$

Calculations for the axial capacity:

$$EI_{eff} = E_s \cdot I_s + 0.8 \cdot E_c \cdot I_c = 147491 \text{kip} \cdot \text{ft}^2 \quad ; \text{ effective flexural rigidity}$$

$$P_e = \frac{\pi^2 \cdot EI_{eff}}{(K \cdot L)^2} = 1123.2 \text{kip} \quad ; \text{ Euler load}$$

$$\underset{\text{WWW}}{\lambda} = \sqrt{\frac{P_o}{P_e}} = 1.19 \quad ; \text{ Slenderness parameter}$$

$$P_n = \begin{cases} \frac{P_o}{P_e} \cdot 0.658 & \text{if } \frac{P_o}{P_e} \leq 2.25 \\ 0.877 P_e & \text{otherwise} \end{cases} = 881.02 \text{kip} \quad ; \text{ Nominal load for the column}$$

$$\chi = \frac{P_n}{P_o} = 0.55 \quad ; \text{ ratio beam column / cross-section capacity}$$

Calculation of the PNA position (y_n) when the axial capacity in the cross-section is equal to P_n

$$y_n = -2\text{in} \qquad M_n = M(y_n) = 423.34 \text{kip} \cdot \text{ft} \qquad \text{check that } y_n \text{ is within the concrete} \\ \qquad \qquad \qquad \underset{\text{WWWWW}}{M} = 185 \text{kip} \cdot \text{ft} \qquad \qquad \qquad (-hc/2 < y < hc/2) \qquad \qquad \qquad \frac{h_c}{2} = 5.71\text{in}$$

Calculation of the P-M capacity of the beam column (reduction due to the stability effects)

The given K and L in the previous step are:

$$K = 2 \qquad L = 18ft$$

The column strength capacity (P_n) from the previous step was given at " y_n ":

$$P_n = 881.02kip \qquad at \qquad y_n = -2.in$$

Thus, the cross-section moment (M_n) at the axial capacity (P_n) is given by:

The cross-section capacities obtained in a previous step are:

$$\begin{aligned} y_c^T &= (-6 \ -5.7 \ -5.1 \ -4.6 \ -4 \ -3.4 \ -2.8 \ -2.3 \ -1.7 \ -1.1 \ -0.6 \ 0 \ 0.6 \ 1.2 \ 1.7 \ 2.3 \ 2.9 \ 3.5) \cdot in \\ P_{csi}^T &= (881 \ 881 \ 881 \ 881 \ 881 \ 881 \ 808 \ 734 \ 661 \ 587 \ 514 \ 441 \ 367 \ 294 \ 220 \ 147 \ 73 \ 0) \cdot kip \\ M_{csi}^T &= (0 \ 0 \ 0 \ 0 \ 0 \ 185 \ 204 \ 222 \ 241 \ 259 \ 278 \ 296 \ 315 \ 333 \ 322 \ 311 \ 300 \ 289) \cdot kip \cdot ft \end{aligned}$$

The beam-column axial capacity varies from 0 to P_n

$$P_{bc_i} = \begin{cases} P_{csi_i} & \text{if } P_{csi_i} \leq P_n \\ P_n & \text{otherwise} \end{cases}$$

$$P_{bc}^T = (0 \ 881 \ 881 \ 881 \ 881 \ 881 \ 808 \ 734 \ 661 \ 587 \ 514 \ 441 \ 367 \ 294 \ 220 \ 147 \ 73 \ 0) \cdot kip$$

The moment consumed by imperfection is given by:

$$\Delta_o = \frac{K \cdot L}{1500} = 0.29in \qquad M_{imp_i} = P_{bc_i} \cdot \Delta_o \cdot \left(\frac{1}{1 - \frac{P_{bc_i}}{P_e}} \right) \qquad P_n \cdot \Delta_o \cdot \left(\frac{1}{1 - \frac{P_n}{P_e}} \right) = 98.06kip \cdot ft$$

$$M_{imp}^T = (0 \ 98.1 \ 98.1 \ 98.1 \ 98.1 \ 98.1 \ 69 \ 50.9 \ 38.5 \ 29.5 \ 22.7 \ 17.4 \ 13.1 \ 9.5 \ 6.6 \ 4.1 \ 1.9 \ 0) \cdot kip \cdot ft$$

The total reduction moment for stability is given by:

$$M_{luc}^T = (185 \ 185 \ 185 \ 185 \ 185 \ 185 \ 170 \ 154 \ 139 \ 123 \ 108 \ 93 \ 77 \ 62 \ 46 \ 31 \ 15 \ 0) \cdot kip \cdot ft$$

Then, the available net moment in the beam-column is given by:

$$M_{bc_i} = \begin{cases} M_{csi_i} - M_{tuc_i} & \text{if } P_{cs_i} \leq P_n \\ 0 & \text{otherwise} \end{cases}$$

$$M_{bc}^T = (0 \ 0 \ 0 \ 0 \ 0 \ 0 \ 34 \ 68 \ 102 \ 136 \ 170 \ 204 \ 238 \ 272 \ 276 \ 281 \ 285 \ 289) \cdot \text{kip} \cdot \text{ft}$$

The simplified P-M diagram for the beam column (as in current AISC, 2010) is:

$$P_{aisc_bc} = P_n \cdot (1 \ 0.2 \ 0)^T$$

$$P_{aisc}^T = (1773 \ 942 \ 471 \ 0) \cdot \text{kip}$$

$$M_{aisc_bc} = M_o \cdot (0 \ 0.9 \ 1)^T$$

$$M_{aisc}^T = (0 \ 378 \ 446 \ 378) \cdot \text{kip} \cdot \text{ft}$$

Plot of the P-M interaction diagram for the CFT:

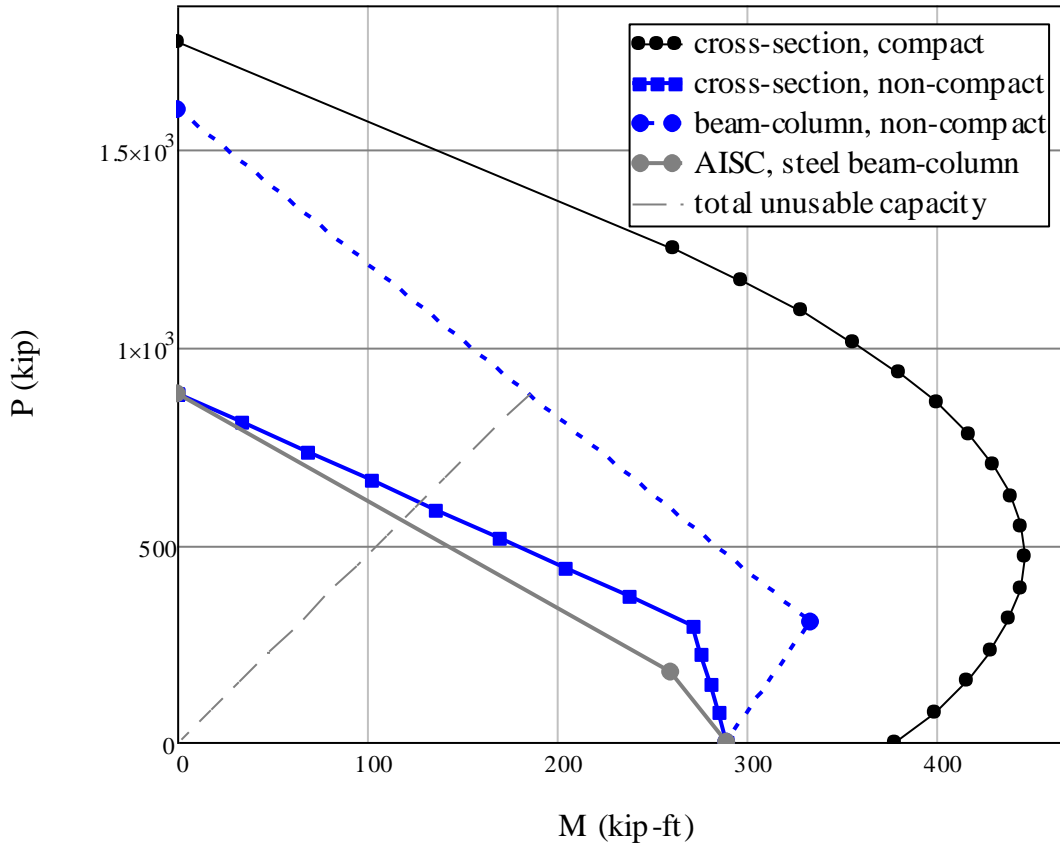


Figure - P-M interaction diagram for a RCFT beam-column

CHAPTER 11

CONCLUSIONS

11.1. Summary and Conclusions

This research presents and discusses the results from a comprehensive experimental program that includes the testing of 18 full-scale concrete-filled steel tube (CFT) specimens. Details about this research project, motivation, objectives, and methodologies used are presented in Chapter 1.

The circular and rectangular CFT specimens selected in this research project are unique since these are the longest and the most slender full-scale CFT members tested worldwide. In addition, these specimens are extensively instrumented, and they are tested under a very complex load protocol using a first class facility as the MAST Laboratory, part of the Network for Earthquake Engineering Simulation (NEES).

The specimen's test matrix was carefully selected to maximize the main features of the MAST Lab Facility and close some gaps found in the available experimental databases. These gaps included very long and slender specimens, large cross-sections with large wall slenderness ratios, and CFTs filled with high-strength concrete. Details about preliminary analytical and experimental studies, as well as the available collected experimental databases are summarized in Chapter 2.

The CFT specimens tested in this research project are extensively and redundantly instrumented, especially in the critical zones where high plasticity demands are expected. Details of the experimental program, the testing facility, testing setup, pretest settings, description of the specimens, the instrumentation, and the load protocol are fully described in Chapter 3.

As discussed in Chapter 3, the CFT specimens are subjected to an extensive load protocol that includes a wide-ranging of load cases that aims to extract many of the relevant characteristics of CFT members. These loading cases pursue to obtain the experimental specimen response under:

- Hydrostatic pressure on the steel tubes when the fresh concrete is poured at the casting process. Results from the analysis of this test data are discussed in Chapter 4.

- Pure compression that aims to determine the experimental axial load capacity of CFT columns accounting for the stability reduction. Results from the analysis of this test data are explored, discussed and analyzed in Chapter 5.
- Uniaxial and biaxial bending combined with compression that aims to determine experimental points of the interaction diagram of CFT beam-columns with stability reduction. These load cases also aim to characterize the stiffness and strength degradation, progression of local buckling, detailed assessment of evolution of damage, plastic hinge lengths, and characterization of different limit states. Results from the analysis of this test data are discussed in Chapters 6 to 8.
- Pure torsion and torsion combined with compression that aims to determine the experimental torsional strength and stiffness of CFT members. Results from the analysis of this test data are discussed in Chapter 9.

Parallel to the experimental study, advanced computational analyses are carried out to calibrate material and element models that characterize the salient features of the observed CFT response, such as steel local buckling and residual stresses, concrete confinement, stability effects, strength and stiffness degradation, among others. The analytical response obtained from the computational analysis was successfully calibrated to reproduce the measured experimental response discussed in Chapters 5 and 7.

Based on the observed behavior, simplified guidelines for the computation of the strength and stiffness parameters for CFT columns and beam-columns are proposed in Chapter 10 for design purposes. This chapter includes determination of the axial and flexural strength for CFT cross-sections and members, integrated with compact and non-compact steel tubes. Examples that illustrate the application of the proposed methodology are included in this Chapter 10.

11.2. Conclusions

As commented above, extensive analyses of computational and experimental data are presented and discussed in this thesis with the aim of improving the prediction of strength, stiffness, deformation capacity, and the overall behavior of slender CFT members. A brief summary of specific conclusions obtained for each loading conditions are presented below.

11.2.1. Wet concrete effects on RCFT members

Since this research intended to test very long CFT specimens, initial deformations on the steel tubes induced by the concrete during casting were contemplated in advanced for the constructions process and the data analysis. For this purpose, stresses and deformations in the steel tube under hydrostatic pressure were evaluated with closed-form analytical solutions and complemented with finite element analysis, as described in Chapter 4. These analytical results indicated that problems would arise in the RCFT specimens, unless the amount of stresses and deformations were limited to low values. For this reason, stiffeners were used during casting of most of the RCFT specimens to control the initial deformations due to the hydrostatic pressure of wet concrete. During the testing of the RCFTs, adverse effects were clear in those specimens that were not stiffened, as the testing started with considerable initial outward deformations on the plates. These side effects consisted in an earlier initiation of the steel local buckling at the elevation where the maximum outward deflection initially occurred as a consequence of the wet concrete pressure. In contrast, there were very low initial deformations on the plates of those specimens that were stiffened properly, and then the local buckling was developed as expected at the critical section (near the base) and as a consequence of the wall-slenderness ratio. Recommendations to minimize the effects of the wet concrete pressures include simplified equations to estimate reasonably the maximum transverse stress and the maximum outward expansion that may occur in a RCFT member at the casting process, values that must not exceed given allowable limits. These are specifically:

$$\sigma_{\max} = \max \left[\left(\frac{2h_c}{b_c + 4h_c} \right) \frac{p \cdot h_c^2}{t^2}, \frac{1}{3} \left(\frac{3b_c + 4h_c}{b_c + 4h_c} \right) \frac{p \cdot h_c^2}{t^2} \right] \leq \frac{F_y}{\Omega} \quad (11.1)$$

$$\delta_{\max} = \frac{1}{32} \left(\frac{5b_c + 4h_c}{b_c + 4h_c} \right) \frac{p \cdot h_c^4}{E_s \cdot t^3} \leq \frac{L}{2000} \quad (11.2)$$

In case either stresses or deformations in rectangular CFT cross-sections exceed the recommended limits above, it is recommended to classify the steel cross-section as slender type section since this would be susceptible to an earlier local buckling.

11.2.2. Nominal axial load capacity of CFT columns

Experimental determination of the nominal axial load capacity on CFT columns was one of the primary goals of this research. The load case used for this purpose (LC1) consisted in driving the crosshead on vertical displacement control downward (*pure compression*), while the top lateral forces and moments are imposed and held at zero in force control (*free top*). However in practice, unexpected difficulties were encountered that made the data analysis very challenging. These difficulties included characterization of the effective confinement in the concrete, the effective flexural stiffness, large dispersion in initial out-of-straightness and out-of-plumbness, among others. In addition, characterization of the system compliance, friction in the system, lack of perfect control for the DOFs, insufficient resolution for flexible specimens, and limits on the system capacity added to the difficulties. Each of these issues is discussed in Chapter 5, and the raw experimental data was then adjusted and processed accordingly. Results from the processed data seem to be more consistent with the expected values than the raw experimental data.

In addition to the processed data, the experimental loading response was also contrasted with the results obtained from non-linear analysis of CFT specimens modeled with fiber elements. The analysis carefully modeled many of the salient features of CFT members such as the confinement effects in the concrete component, as well as the residual stresses and local buckling in the steel component; in addition, they include a very robust hysteretic rules as calibrated by Denavit and Hajjar (2010) and Tort and Hajjar (2007). The results from the computational analysis are consistent with the experimental response data, in some cases with a very strong correlation.

Column curves for CFT columns with ideal boundary conditions (fixed-free, $K=2$) and ideal imperfections (cosine function) are obtained from computational analysis and the calibrated models. These column curves are then compared with the current column curve in the AISC (2010) Specifications. These column curves seem very strong correlated in the elastic critical load range, but with differences in the inelastic buckling load interval. These differences are in general attributed to a higher strength due to the concrete confinement assumed in the computational analysis, and under predicted in the Specifications. In addition for RCFTs with buckling towards the weak axis, the analysis exhibited a lower capacity than in the Specifications

due to an earlier development of the steel local buckling assumed in the model. The results from the computational curves do not exhibit a significant difference between the nominal $KL/1500$ of out-of-plumbness assumed in the development of the steel column curve, and the $KL/2000$ of out-of-plumbness recommended in the direct analysis method of steel members.

11.2.3. P-M interaction diagrams for CFT cross-sections an beam columns

Another main goal of this research project consisted on the determination of experimental set of points of the P-M interaction diagram. For this purpose, some loading cases (LC2 and LC3) were planned with the aim to extract some of these points from the experimental response. These load cases consisted of a constant compression force in load control, while the top is driven laterally in displacement control. The methodology used for the extraction of experimental P-M values of interaction has been previously used for the calibration of the interaction equations for steel members in the AISC Specifications and Eurocodes, using data obtained from second order inelastic analysis of benchmark steel frames. The maximum stable capacity of a beam column is defined by its maximum lateral strength (F_{max}) at which the incipient instability condition arises. Beyond this lateral load capacity, the beam-column is on an unstable condition even when the critical cross-section still has some remaining capacity. Thus, a set of axial load (P) and base moment (M) points related to the instant when the specimen reached the maximum stable capacity (F_{max}) are extracted and compiled as the *total beam-column capacity*. The total capacity as defined above does not incorporate the effects of the initial imperfections. Initial imperfections tends to increase the demand of second order effects, and as a result, the available first order moment capacity is reduced; therefore, the initial imperfections can be included as the difference between the total capacity and that capacity consumed by the imperfections. The resultant P-M points from the previous process are compiled as the *net beam-column capacity*. Theoretically, the net beam-column capacity is the maximum usable P-M capacity in the beam-column, and so the interaction diagrams for the beam-columns are calibrated with this final net response.

The net moments extracted from the test specimens are then compared with the simplified interaction diagram proposed in the AISC (2010) Specifications for composite beam-columns. The following observations were noted from these comparisons:

- In the shorter specimens, the net P-M capacities extracted from the tests drop outside of the bilinear simplified diagram of the AISC for beam-columns, which underestimates the P-M capacities of the shorter specimens around the points C_{λ} -B. The purpose of neglecting the bulge with this vertical line in the AISC Simplified diagram intended to be conservative through a lower bound, and this simplification was supported by the available experimental data at the time.
- The shape of the bilinear simplified diagram turned out to be less conservative in beam-columns with intermediate slenderness; however, for beam-columns with high slenderness, the AISC simplified diagram resulted unconservative with overestimated net capacities.

It must be noted that the net moment capacities obtained from the experiments has a substantial flexural capacity lost due to the large imperfections. Nevertheless, many of these points are still unconservative even if the imperfections are neglected. This unconservative behavior in slender beam-columns suggested a change in the design equations for the calculation of P-M interaction diagrams that serves both short and slender beam columns.

Similar conclusions were observed in both uniaxial and biaxial bending, as well as in the computational analyses. Based on the results reported in Chapter 6 about the total and net P-M capacities extracted for the test data, Chapter 10 proposes design equations that aim in the determination of the P-M interaction diagram for CFT cross-sections and beam-columns. The beam-column capacity as proposed in Chapter 10 takes into account the total unusable capacity lost due to both the stability effects and the imperfections.

11.2.4. Flexural rigidity for CFT members

The evaluation of the flexural rigidities extracted from the test results during the entire load protocol exhibited some variability, mainly as the damage in the concrete core and the steel tubes progressed through the load protocol. Even with this dispersion, interesting results were extracted from the analysis of this data. A brief summary of the observations includes:

- The averaged values of the flexural rigidities extracted from the response during the pure compression loading case (LC1) were very close to the values predicted by the AISC (2005, 2010) Specifications. However, the averaged values does not show any proportionality with the steel ratio in the cross-section ($\rho = A_s/A$), as indicated in the AISC Specifications by presenting the C_3 coefficient in terms of the steel ratio. In addition, neither does the slenderness parameter of the column (λ) showed proportional variation with the test data. Instead, a constant averaged coefficient of $C_3 = 0.80$ was obtained and adopted for the determination of the buckling load capacity of a CFT column. In other words:

$$EI_{eff} = E_s I_s + 0.80 E_c I_c \quad (11.3)$$

- Similarly, averaged values of the flexural rigidities were also extracted from the response during the uniaxial and biaxial loading cases (LC2 and LC3). This is a unique set of data since this intends to give a simplified equation that approaches the expected rigidity for a beam-column under seismic loading (i.e. combined constant axial load and cyclic uniaxial or biaxial lateral load). As expected, the scatter of the data increased as the damage progressed on the specimen; even with some dispersion is exhibited in the averaged test data, the following equations are proposed for the determination of the effective stiffness of a CFT beam-column under seismic loading, and for the evaluation of lateral and flexural capacity based on frame analysis.

When local buckling is not expected (as in compact cross-sections), the effective flexural capacity may be approached with:

$$EI_{eff} = E_s I_s + 0.40 E_c I_c \quad (11.4)$$

On the other hand, when the steel tube is susceptible to local buckling, the following equation is suggested to obtain the expected effective flexural capacity as:

$$EI_{eff} = 0.85 (E_s I_s + 0.40 E_c I_c) \quad (11.5)$$

11.2.5. Steel local buckling in CFT members

Extraction of the first occurrence of local buckling in the 18 specimens tested for this project is presented in Chapter 8. Based on the empirical data extracted from these tests, an update of empirical equations for the local buckling initiation is proposed for both CCFT and RCFTs. The proposed equations are:

For circular concrete filled tubes (CCFTs)

$$\varepsilon_{lb} = 0.09 \left(\frac{D}{t} \cdot \frac{F_y}{E_s} \right)^{-2} \frac{F_y}{E_s} = \frac{0.09}{\lambda^2 \cdot \varepsilon_y} \quad (11.6)$$

For rectangular concrete filled tubes (RCFTs)

$$\varepsilon_{lb} = 9 \left(\frac{h}{t} \sqrt{\frac{F_y}{E_s}} \right)^{-2} \frac{F_y}{E_s} = \frac{9}{\lambda^2} \quad (11.7)$$

From the empirical calibration equations shown above, an update of limits for slender (λ_r) and non-compact (λ_p) filled tubes are proposed as follow:

For circular concrete filled tubes (CCFTs) with slender steel sections

$$\lambda_r = 0.3 \frac{E_s}{F_y} \quad (11.8)$$

For circular concrete filled tubes (CCFTs) with non compact steel sections

$$\lambda_p = 0.15 \frac{E_s}{F_y} \quad (11.9)$$

For rectangular concrete filled tubes (RCFTs) with slender steel sections

$$\lambda_r = 3.0 \sqrt{\frac{E_s}{F_y}} \quad (11.10)$$

For rectangular concrete filled tubes (RCFTs) with non compact steel sections

$$\lambda_p = 2.12 \sqrt{\frac{E_s}{F_y}} \quad (11.11)$$

11.2.6. Plastic hinge length in CFT members

In Section 8.4, an analysis on the plastic hinge lengths is presented based on the maximum curvature within the load protocol through the column length. Based in this data analysis, the equation below proposed for steel sections presented reasonable prediction values of the plastic hinge length.

$$L_p = L \left(1 - \frac{M_y}{M_p} \right) = L \left(1 - \frac{S}{Z} \right) = L \left(1 - \frac{1}{k_s} \right) \quad (11.12)$$

11.2.7. Torsional strength and stiffness of CFT members

The experimental torsional response obtained from the tests of the CFT specimens points out the following behavior.

- The results indicate a partial contribution of the concrete to both the torsional capacity and the torsional rigidity. Both the strength and the stiffness contributions were calibrated with the test data and design equations developed for torsion.
- The strength response under torsion and combined axial load was slightly higher than the strength obtained in pure torsion only in CCFTs; due to a high damage accumulation in RCFTs, the torsion capacity with and without compression was very similar to the pure torsion capacity.
- As a result of the rectangular shape, the concrete contribution in torsional capacity is slightly higher in RCFTs attributed to the interlock interaction between the concrete surfaces and the steel surfaces in contact. However, the torsional stiffness is slightly higher in CCFTs due to a better performance in circular cross-section shapes; and an earlier local buckling damage in RCFTs, which is less severe in CCFTs.

Assuming full contribution of the steel component and partial contribution of the concrete component, design equations are proposed to estimate both the torsional strength capacity and the torsional rigidity for non-cyclic and cyclic loading. These design equations predict reasonable values of the torsion strength and torsion stiffness.

11.2.8. Forensic analysis

The post-mortem or forensic analysis of the CFT specimens tested in this project was presented in Section 8.4. When the deformed steel plates were cut and removed, it was observed and confirmed that the highest local buckling deformation was spread by coarse-like pieces of concrete. No clear evidence of significant concrete-steel slip was observed or noticed when the tubes were cut and open; however, the slip was not monitored or measured during the test, and so this note is based only on the final physical observation on the exposed specimen. Once the external condition of the concrete is reported, the exploration of deeper cracks was carried out by removing the external surface of the concrete. The concrete cores were found to have been highly confined and almost intact.

11.3. Impact and contributions

The present research project is distinctive in many ways. Some points that make this project unique include:

- A comprehensive experimental program that consisted of testing 18 circular and rectangular CFTs, with an extensive and advanced instrumentation, and subjected to a very complex load protocol. All these will make possible to fill many of the gaps found in the experimental CFT databases. These results are expected to become the benchmarks by which future analytical models for composite beam-columns will be evaluated.
- A unique test matrix that includes specimens with very special characteristics, which includes: (1) lengthy and slenderness specimens (the world largest CFT columns and beam columns); (2) the use of the largest and thinnest fabricated HSS cross-section sizes (low width-thickness ratios D/t or h/t); and (3), a wide range of material properties such as high strength concrete. This research will provide much needed data to calibrate material constitutive models and the element models for composite structures.
- Qualitative and quantitative recommendations to evaluate and minimize the effects of the wet concrete pressure in the steel tubes during the pouring. Controlling outward deflections is an important concern mainly in RCFTs, since an earlier failure can be developed if the initial plate deflections are not controlled during the casting process.

- Enhancement of the analytical prediction for strength and deformation capacity of CFT columns and beam-columns with fiber-based or finite-based analysis with respect to:
 - Second order analysis accounting for geometric and material non-linearities
 - Cyclic behavior of beam-columns with strength and stiffness degradation
 - Accumulated damage accounting for effective confinement and local buckling
- Enhancement of the analytical prediction for strength and deformation capacity of CFT columns and beam-columns with simplified design equations, including:
 - Effective flexural (EI_{eff}) and torsional rigidity (GJ_{eff}) for 3D frame analysis
 - Critical load (P_n) and column curves ($P_n-\lambda$) for slender columns
 - P-M interaction diagrams for both cross-sections and beam-columns
- Development of a design procedure for CFT columns with compatible transition from reinforced concrete to steel elements, and vice versa. Also, include some recommendations for design procedure on composite frames with CFT columns subjected to gravity and seismic load conditions.

In summary, this research project provides a unique set of data that can and has been used to verify advanced computational models and provide support for the development of both simplified and advanced analysis techniques for composite CFT members.

In addition, this research study is an effort at (1) developing new fundamental knowledge, (2) improving our understanding of composite beam-column behavior, (3) extending design ranges, (4) providing calibration data, and (5) improving the accuracy of the response prediction on concrete-filled tube members.

The author expects that, based on the results presented in this research project, CFT members experience an immediate increment of the number of applications in practice on the construction of composite and mixed frames systems with CFT members for either constructing new structures or retrofitting old structures.

11.4. Suggested topics for future research studies

The present research study intended to include many of the main parameters that influenced the overall behavior of CFT members subjected to different loading conditions. However, there still exist some uncertainties and unexplored topics that were not included and studied in this project. The list below summarizes some of the topics that may be explored in future research studies.

Suggested topics using the experimental data collected or the results presented in this research:

- Calibration of computational models in cyclic loading using FEA.
- Determination and characterization of the flexural stiffness from computation analysis. This includes both models using fiber elements for the cross-section definition and solid elements (FEA).
- Calibration of the proposed *tangent plot* methodology in other structural members.
- Calibration of the proposed methodology for the calculation of the axial, flexural and torsional capacities of CFT cross-sections, columns and beam-columns.

Suggested topics not evaluated in this research that may require additional testing or analysis:

- Shear strength of CFT cross-sections.
- Shear – Torsion interaction diagrams.
- Lateral torsional buckling of CFT columns and beam-columns.
- Lateral buckling in CFT beams.
- Experimental determination of the slip in the steel-concrete interaction surfaces. In this project, tangential and longitudinal relative slip was neither measured by the instrumentation nor considered in the analysis.
- Calibration of frame analysis that reflects the behavior and salient features of the CFT members observed from the test experiments and the advanced computational analysis.
- Determination of the seismic behavior factors for the different composite structural systems with CFT members.
- Different types of connections of CFT members with other structural elements.

APPENDIX A

MATERIAL PROPERTIES

A.1. On-site concrete filling properties

Table A.1. Concrete mix design used for 5 ksi of nominal strength

MIX ID: MAS5095	Compressive Strength: 5,000 psi at 28-Days	Created On: Jun-26-08	
PROJECT:	MAST Laboratory at the University of Minnesota		
APPLICATION:	Interior Self-Consolidating Concrete		
PLACEMENT:	Pumpable Through a 2" Line		
CEMENT,	(ASTM C 150/TYPE I)	563 lbs. (75%)	2.86 ft ³
FLY ASH,	(ASTM C 618/CLASS F)	187 lbs. (25%)	1.16 ft ³
SAND,	(ASTM C 33)	1,450 lbs. SSD	8.74 ft ³
3/8" GRAVEL,	(MnDOT 3137/CA-80)	1,450 lbs. SSD	8.67 ft ³
WATER,		315 lbs. = 37.8 gal.	5.05 ft ³
ENTRAPPED AIR CONTENT,		3.0 %	0.82 ft ³
			27.30 ft ³
HRWRA,	(ASTM C 494/TYPE F)	45 oz. (6.0 oz/cwt)	
VISCOSITY MODIFYING ADMIXTURE,		45 oz. (6.0 oz/cwt)	
WATER-CEMENTITIOUS RATIO,		0.42	
SPREAD, at point of truck discharge		25.00 in.	
CONCRETE UNIT WEIGHT,		145.2 pcf	
MIX SUITABILITY FACTOR,		31.4	

Table A.2. Concrete mix design used for 12 ksi of nominal strength

MIX ID: MAS12095	Compressive Strength: 12,000 psi at 56-Days	Created On: Jun-26-08	
PROJECT:	MAST Laboratory at the University of Minnesota		
APPLICATION:	Interior Self-Consolidating Concrete		
PLACEMENT:	Pumpable Through a 2" Line		
CEMENT,	(ASTM C 150/TYPE I)	815 lbs. (68%)	4.15 ft ³
SLAG,	(ASTM C 989/GRADE 100)	300 lbs. (25%)	1.69 ft ³
SILICA FUME,	(ASTM C 1240)	85 lbs. (7%)	0.61
SAND,	(ASTM C 33)	1,265 lbs. SSD	7.62 ft ³
3/8" GRAVEL,	(MnDOT 3137/CA-80)	1,271 lbs. SSD	7.60 ft ³
WATER,		300 lbs. = 36.0 gal.	4.81 ft ³
ENTRAPPED AIR CONTENT,		3.0 %	0.82 ft ³
			<u>27.30 ft³</u>
HRWRA,	(ASTM C 494/TYPE F)	120 oz. (10.0 oz/cwt)	
VISCOSITY MODIFYING ADMIXTURE,		36 oz. (3.0 oz/cwt)	
WATER-CEMENTITIOUS RATIO,		0.25	
SPREAD, at point of truck discharge		25.00 in.	
CONCRETE UNIT WEIGHT,		147.9 pcf	
MIX SUITABILITY FACTOR,		38.8	

A.2. Coupon test results

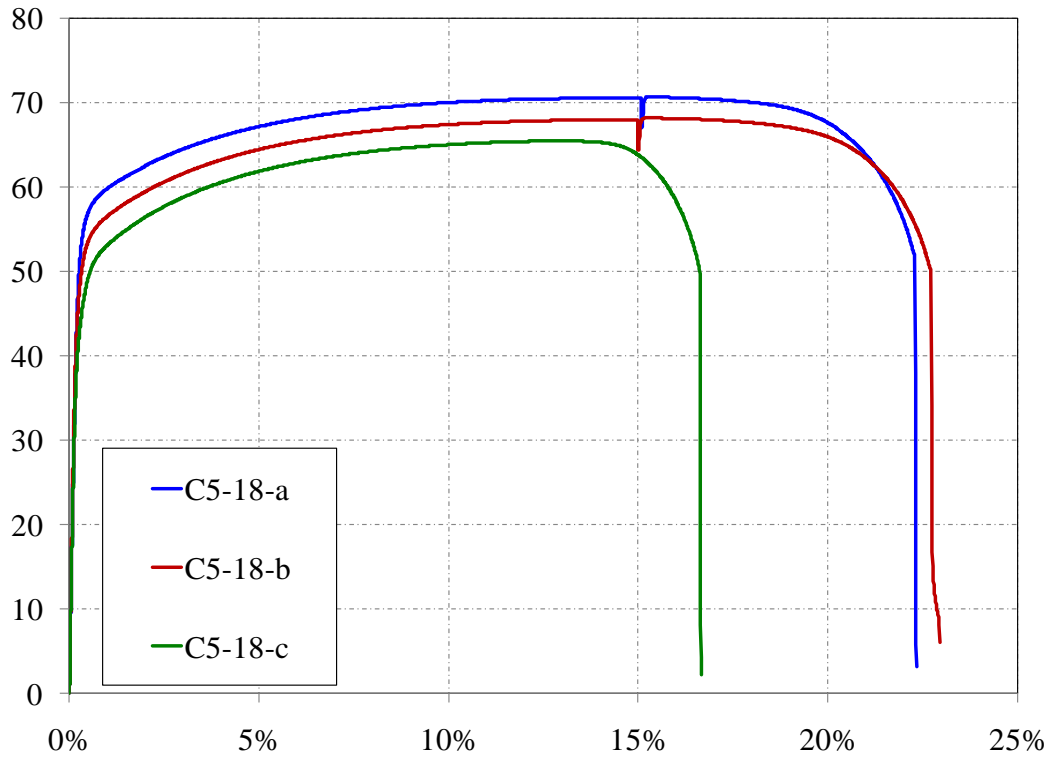


Figure A.1. Coupon tests from the steel corresponding to the Specimens 1 and 18

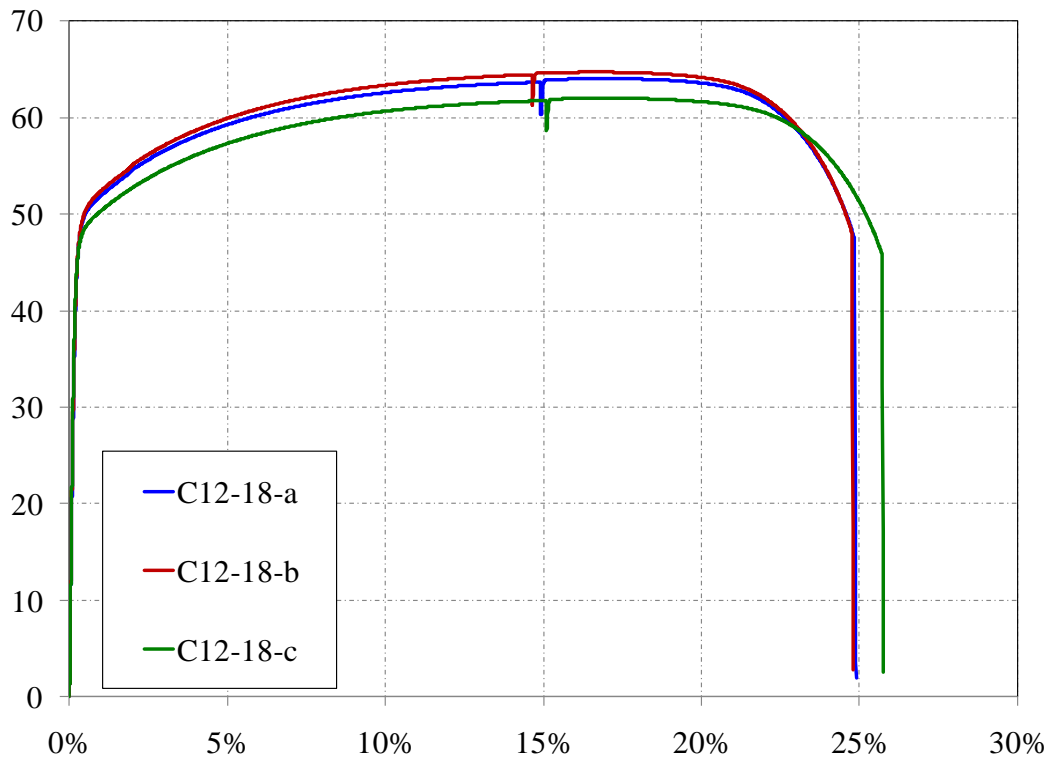


Figure A.2. Coupon tests from the steel corresponding to the Specimens 2 and 6

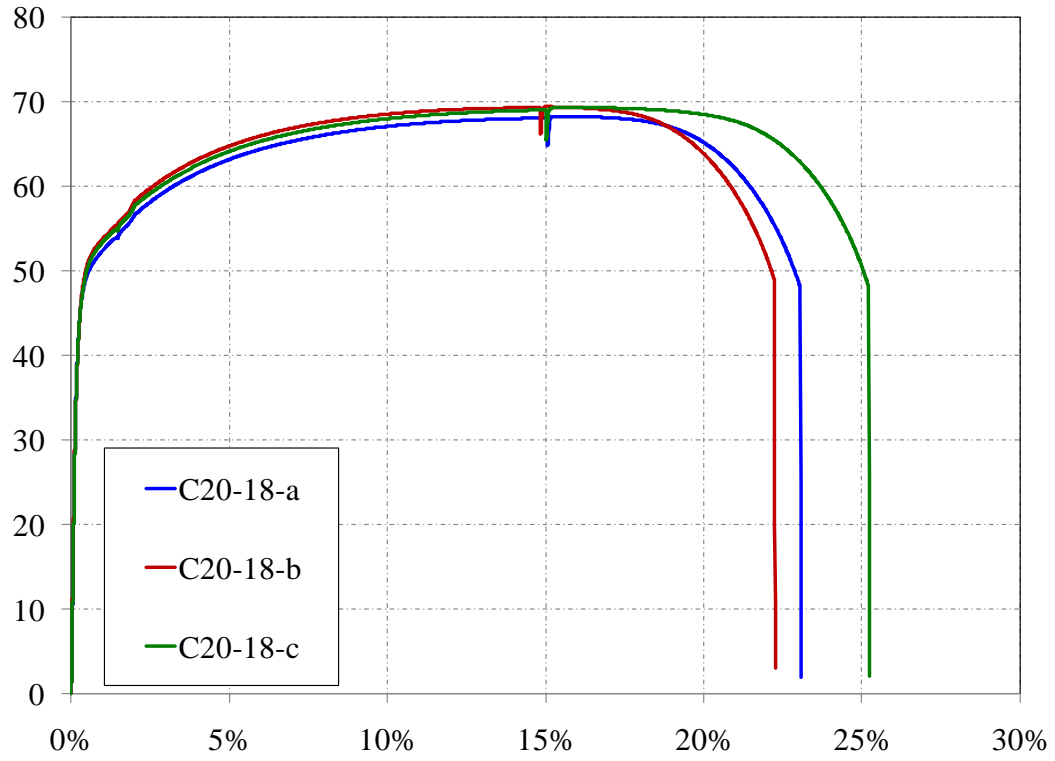


Figure A.3. Coupon tests from the steel corresponding to the Specimens 3 and 7

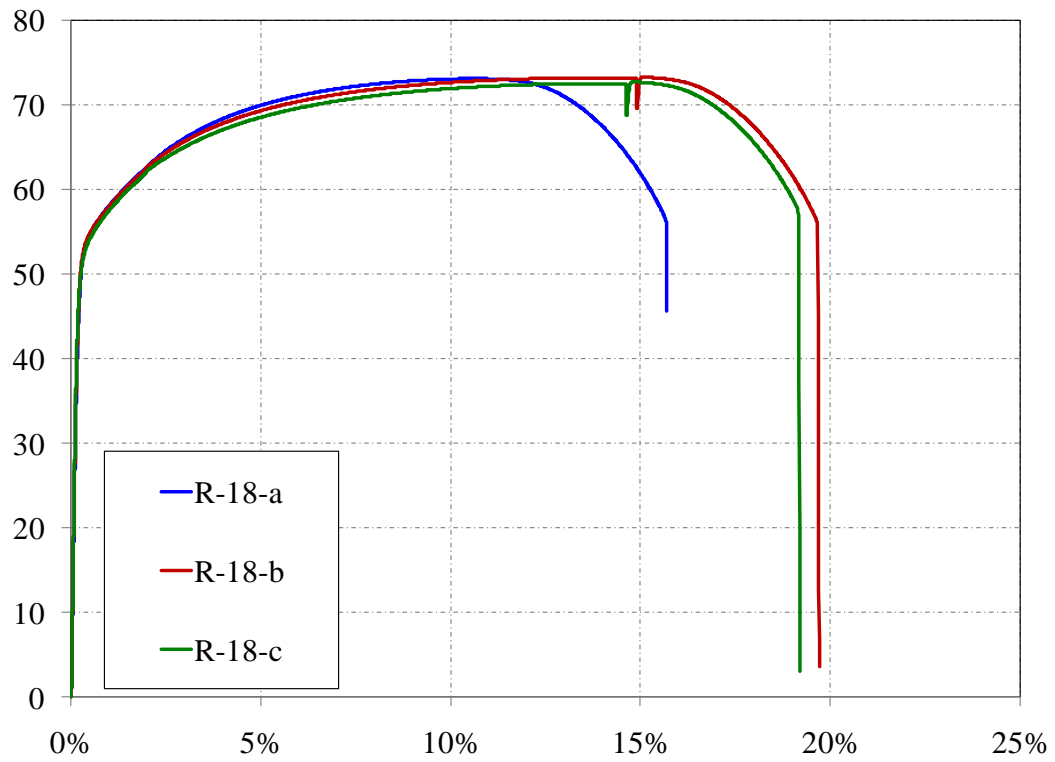


Figure A.4. Coupon tests from the steel corresponding to the Specimens 4, 5, 8 and 9

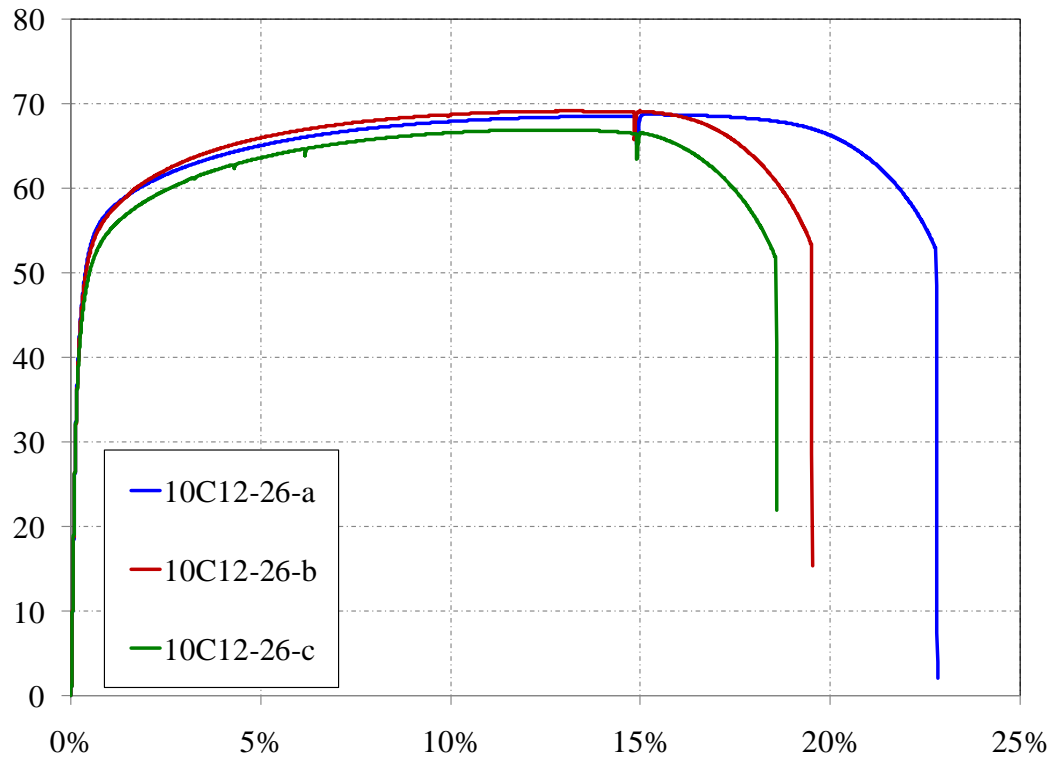


Figure A.5. Coupon tests from the steel corresponding to the Specimen 10

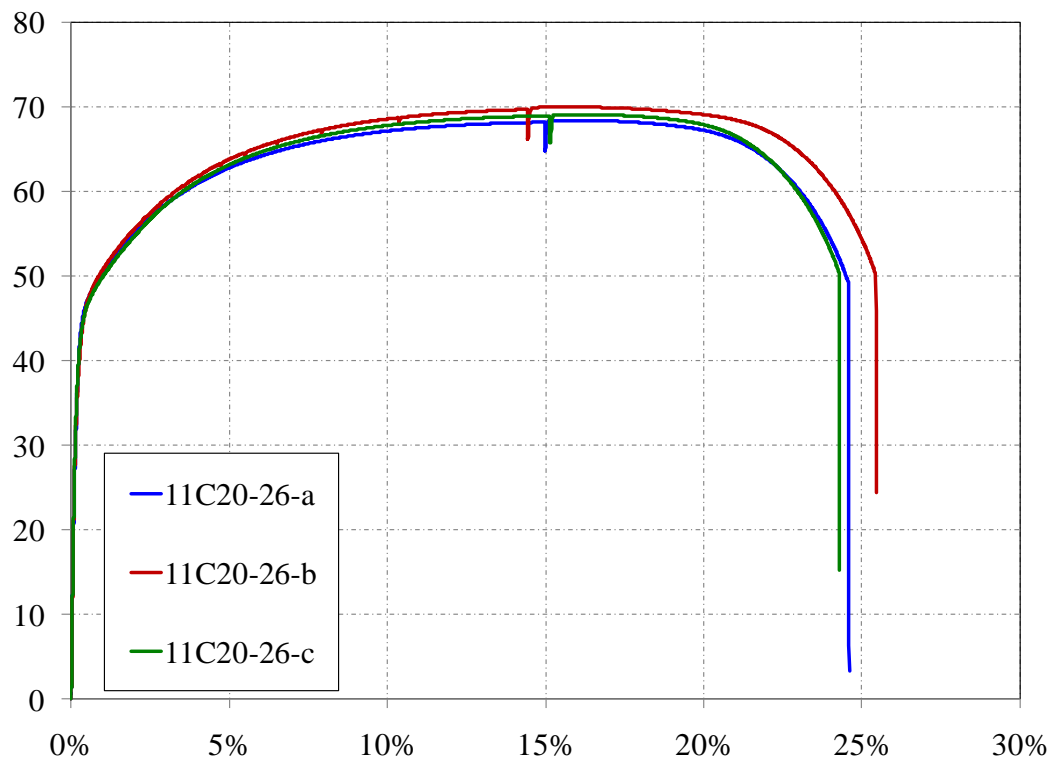


Figure A.6. Coupon tests from the steel corresponding to the Specimen 11

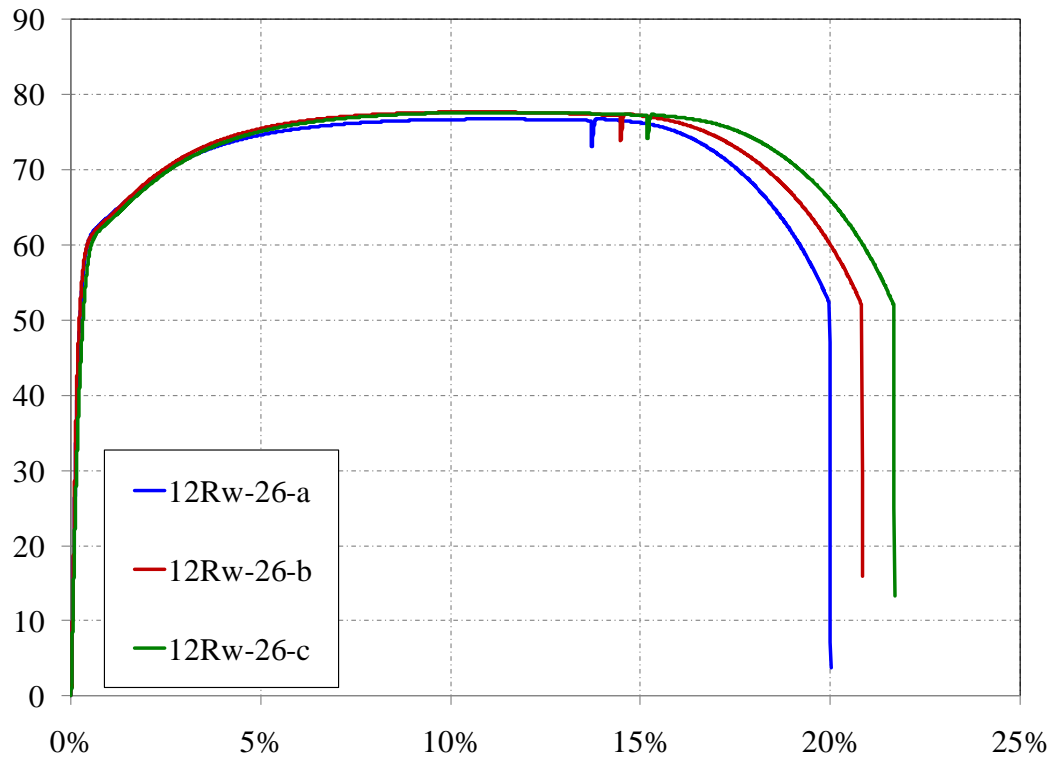


Figure A.7. Coupon tests from the steel corresponding to the Specimen 12

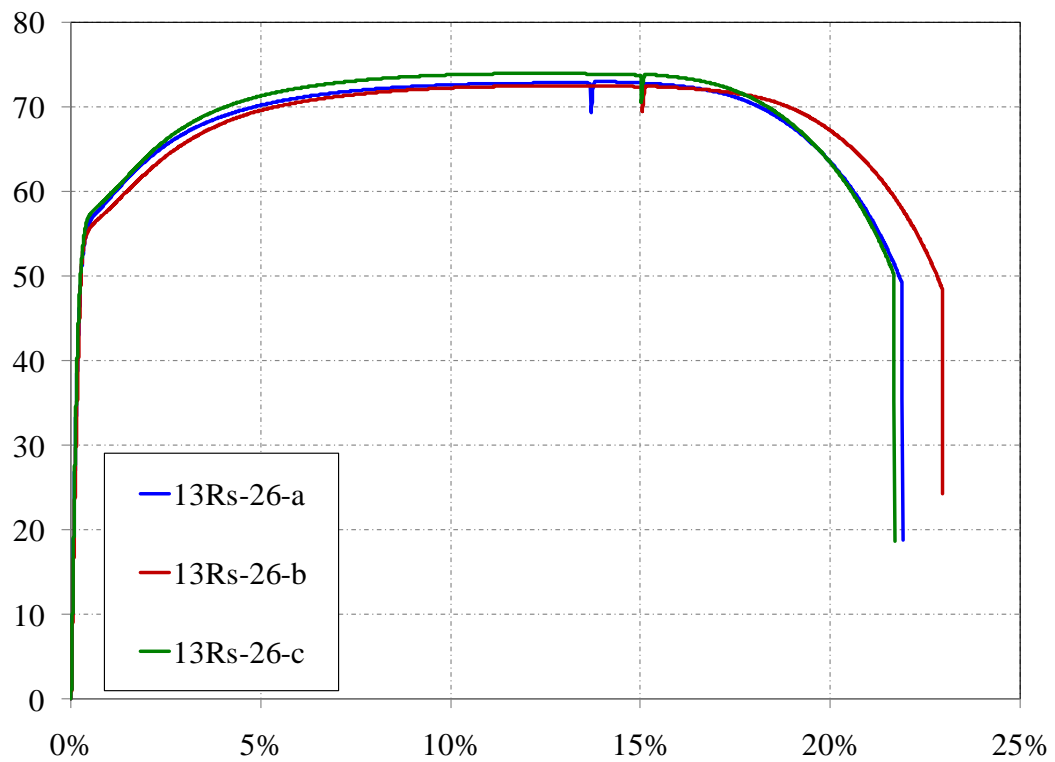


Figure A.8. Coupon tests from the steel corresponding to the Specimen 13

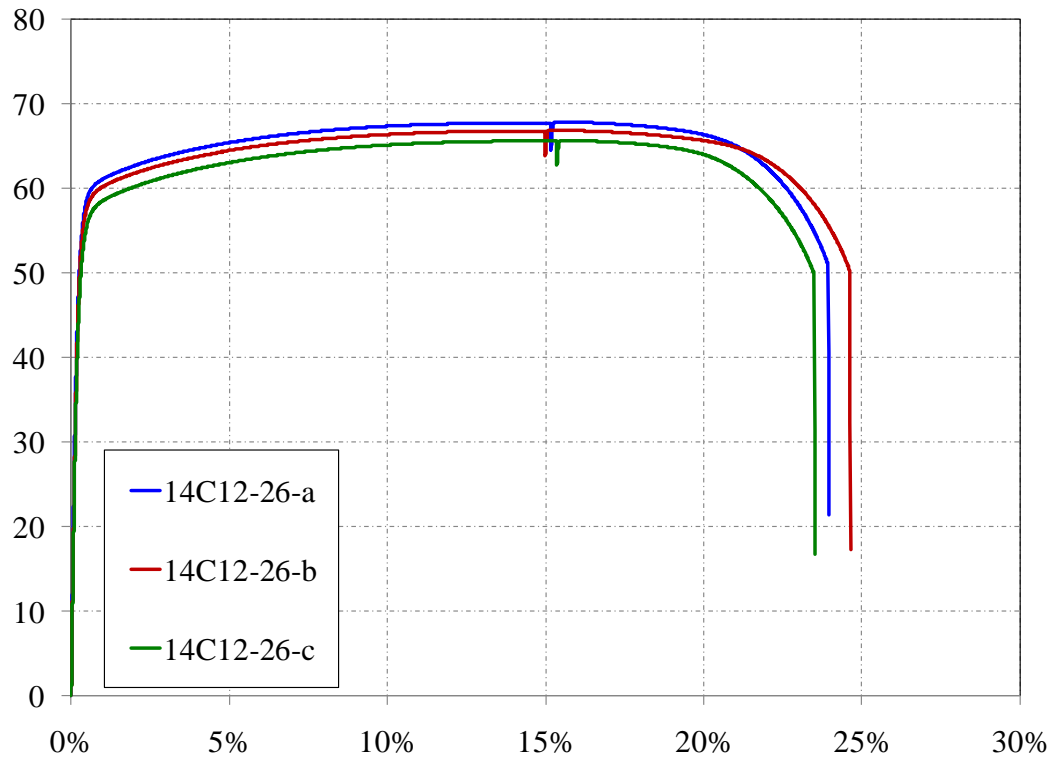


Figure A.9. Coupon tests from the steel corresponding to the Specimen 14

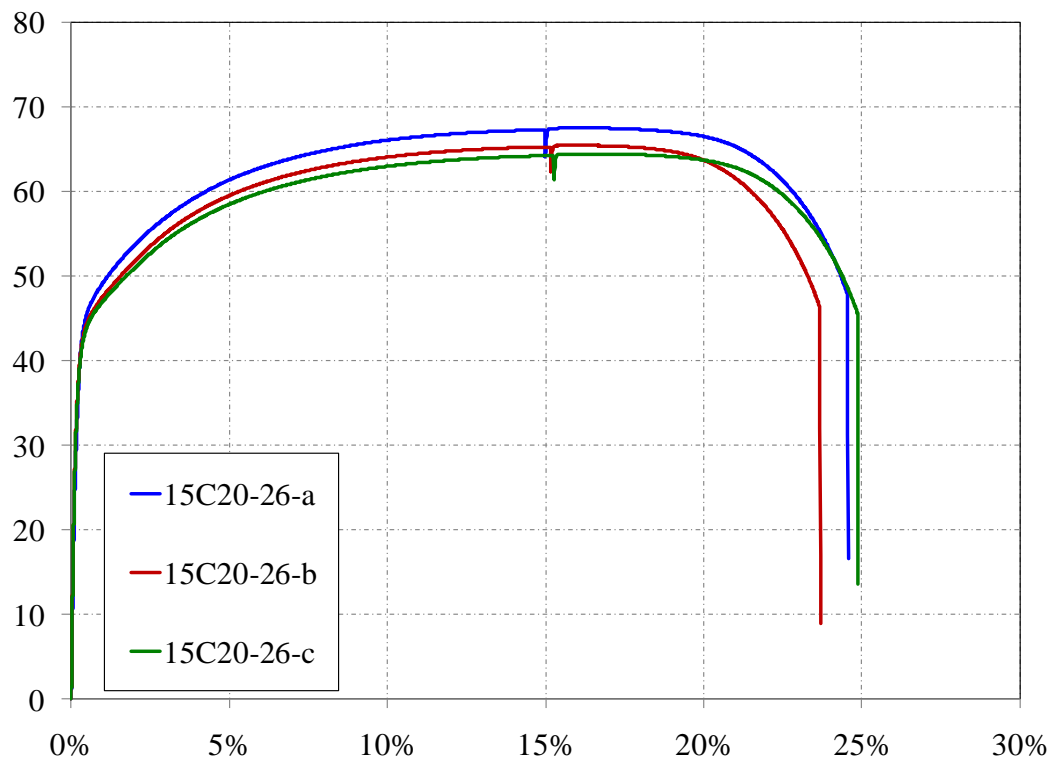


Figure A.10. Coupon tests from the steel corresponding to the Specimen 15

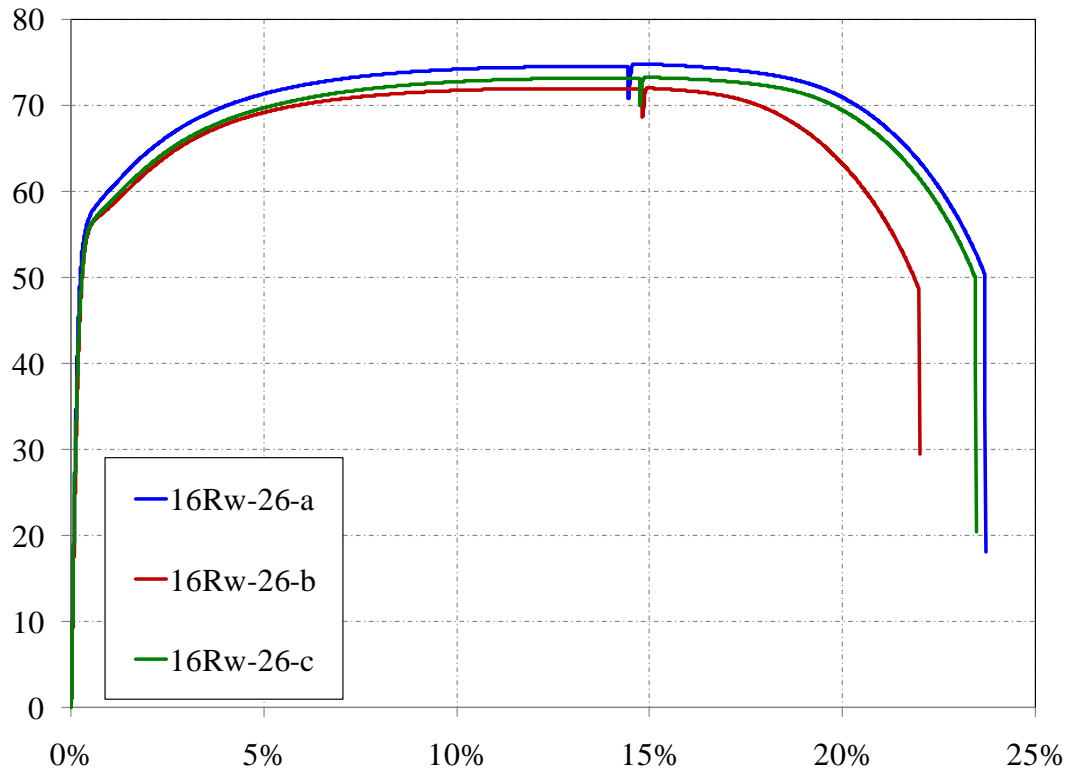


Figure A.11. Coupon tests from the steel corresponding to the Specimen 16

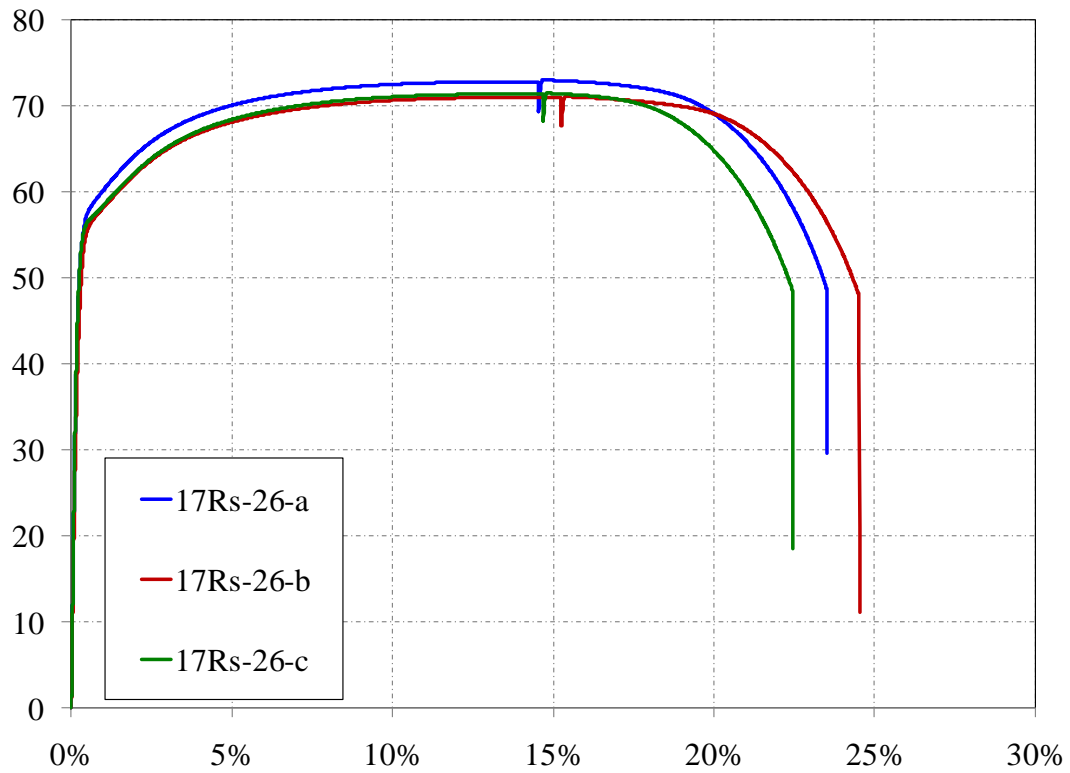


Figure A.12. Coupon tests from the steel corresponding to the Specimen 17

APPENDIX B

EXPERIMENTAL RESULTS

This section gives a brief description and summarizes some parameters for each of the specimens. Besides, this section summarizes the load protocol adopted and shows some of the main experimental results for each CFT specimen and each load case.

B.1. Specimen 1C5-18-5

Description:

- Specimen number: 1
- Composite Cross-section: CCFT
- Steel cross-section: HSS5.563x0.134
- Design concrete strength: 5 ksi
- Design specimen length: 18 ft
- Pouring date: 06/27/2008
- Testing date: 07/29/2008

Parameters:

- Specimen length: 18' 1/2"
- Initial out-of-straightness: $U_{xo} = -1.54'' / U_{yo} = 0.01''$
- Steel yielding stress: $F_y = 55.6$ ksi
- Steel ultimate stress: $F_u = 70.7$ ksi
- Concrete strength at the 28th day: $f_c' = 5.5$ ksi
- Concrete strength at the testing day: $f_c = 5.5$ ksi
- Concrete Young's modulus: $E_c = 5000$ ksi
- Concrete tensile strength: $f_t = 1.1$ ksi

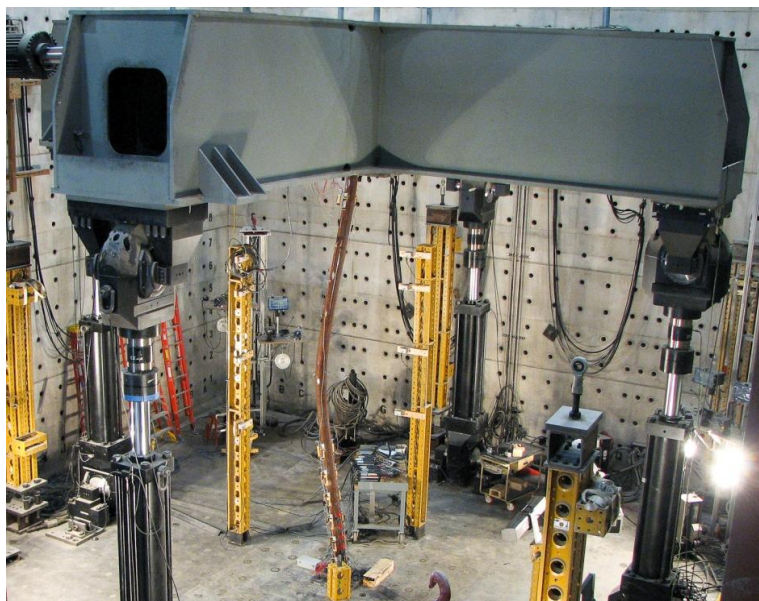


Figure B.1. Specimen 1C5-18-5

Table B.1. Load protocol summary for the specimen 3C20-18-5

LC1 – Proportional loading – several cycles, different eccentricities

Step	DOF						Stop Criterion
	X	Y	Z	RX	RY	RZ	
1	$F_x = 0$	$F_y = 0$	$U_z \downarrow$	$M_x = 0$	$M_y = 0$	$R_z = 0$	max P
2	$F_x = 0$	$F_y = 0$	$U_z \uparrow$	$M_x = 0$	$M_y = 0$	$R_z = 0$	P = 0

LC2a - Cyclic uniaxial lateral displacements with constant compression force ($-F_z = P = 15$ kips). The top was forced to have zero moments.

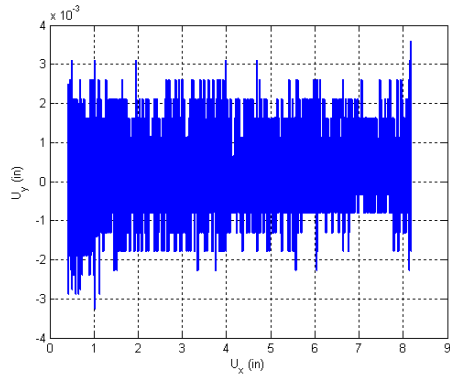
Step	DOF						Stop Criterion
	X	Y	Z	RX	RY	RZ	
1	$U_x \downarrow$	$U_y = 0$	P = 15k	$R_x = 0$	$M_y = 0$	$R_z = 0$	+F peak
2	$U_x \uparrow$	$U_y = 0$	P = 15k	$R_x = 0$	$M_y = 0$	$R_z = 0$	-F peak
3	$U_x \uparrow$	$U_y = 0$	P = 15k	$R_x = 0$	$M_y = 0$	$R_z = 0$	$U_z = 0$

LC2b - Cyclic uniaxial lateral displacements with constant compression force ($-F_z = P = 30$ kips). The top was forced to have zero moments.

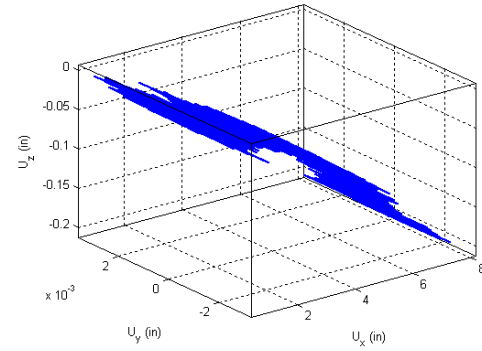
Step	DOF						Stop Criterion
	X	Y	Z	RX	RY	RZ	
1	$U_x \downarrow$	$U_y = 0$	P = 30k	$R_x = 0$	$M_y = 0$	$R_z = 0$	+F peak
2	$U_x \uparrow$	$U_y = 0$	P = 30k	$R_x = 0$	$M_y = 0$	$R_z = 0$	-F peak
5	$U_x \uparrow$	$U_y = 0$	P = 30k	$R_x = 0$	$M_y = 0$	$R_z = 0$	$U_z = 0$

LC4 – Proportional loading – several cycles, different BCs

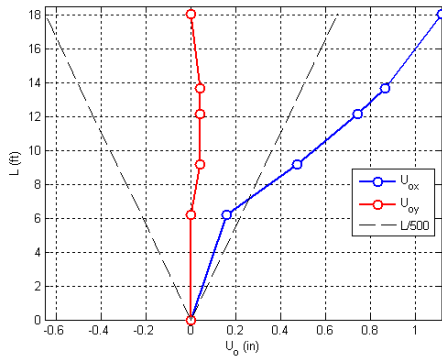
Step	DOF						Stop Criterion
	X	Y	Z	RX	RY	RZ	
1	var	var	$U_z \downarrow$	var	var	$R_z = 0$	max P
2	var	var	$U_z \uparrow$	var	var	$R_z = 0$	P = 0



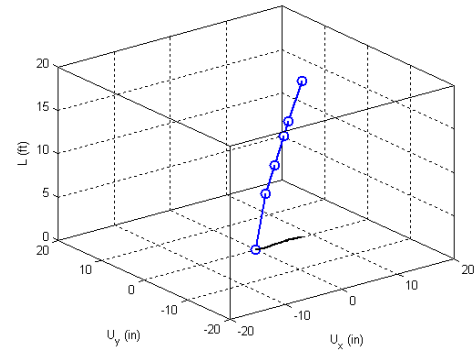
Y displacement vs. X displacement



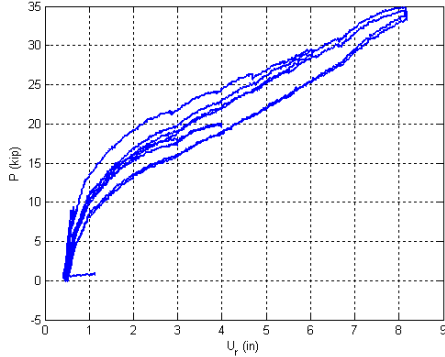
Z displacement vs. X and Y displacement



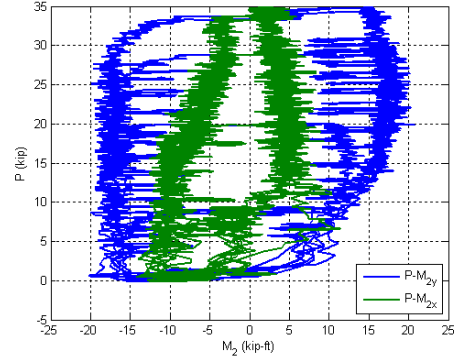
Initial deflected shape



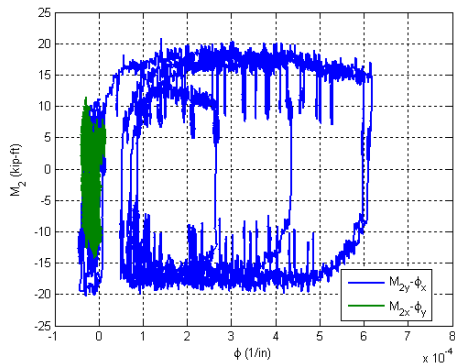
Maximum lateral displacement



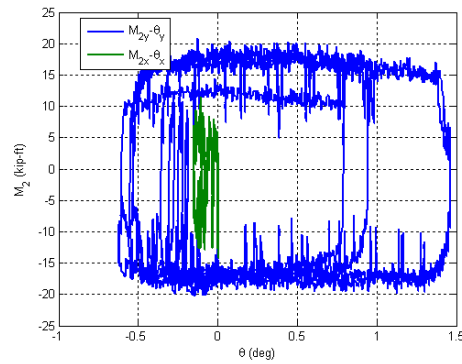
Axial force vs. lateral displacement



Axial force vs. base moments

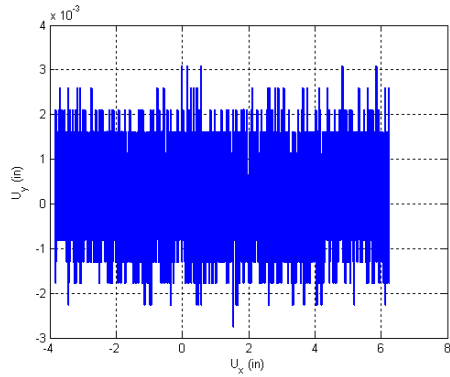


Base moment vs. base curvature

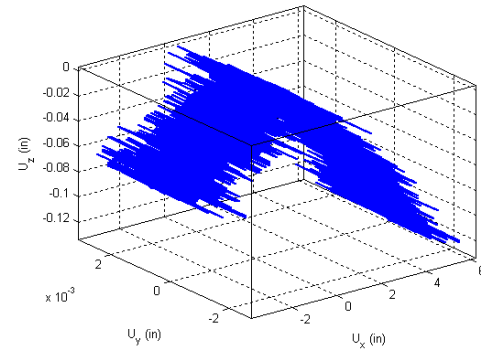


Base moment vs. top rotation

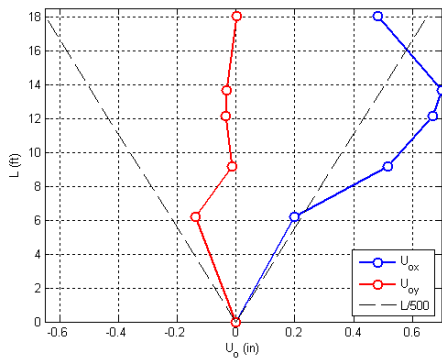
Figure B.2. Experimental results from LC1 in the specimen 1C5-18-5



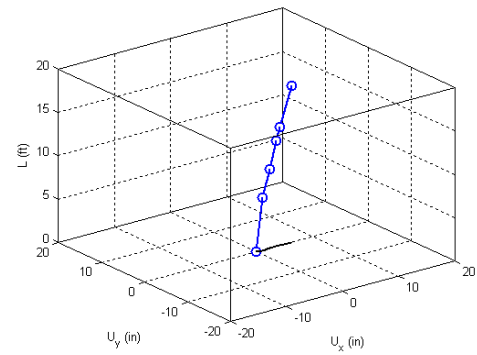
Y displacement vs. X displacement



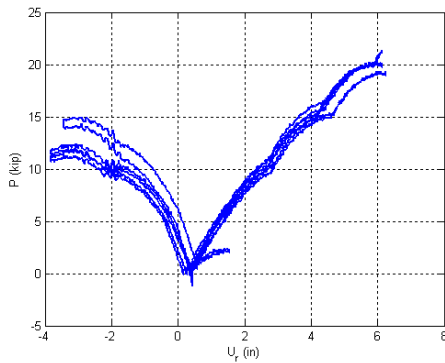
Z displacement vs. X and Y displacement



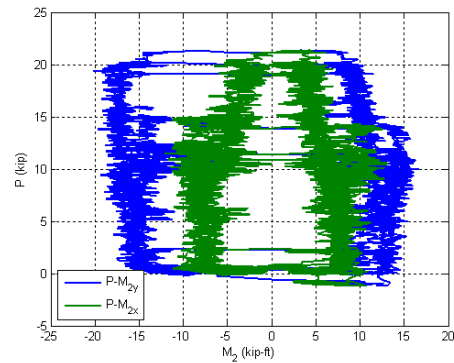
Initial deflected shape



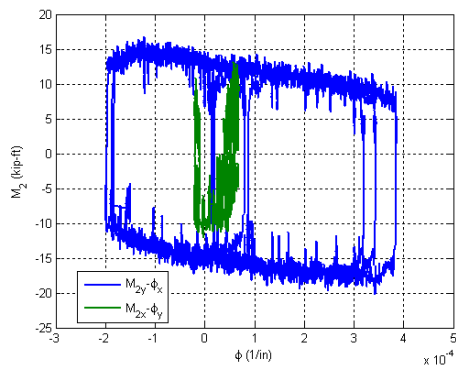
Maximum lateral displacement



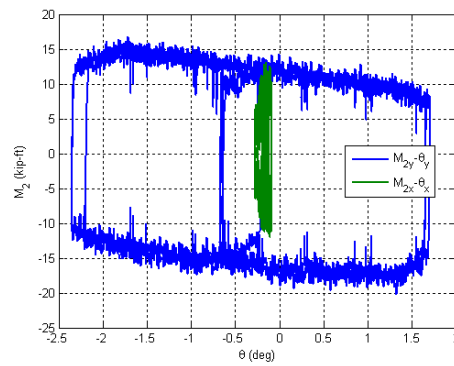
Axial force vs. lateral displacement



Axial force vs. base moments

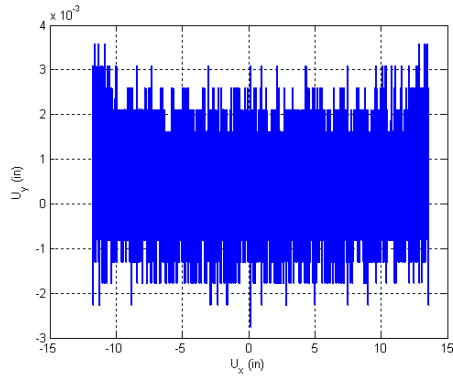


Base moment vs. base curvature

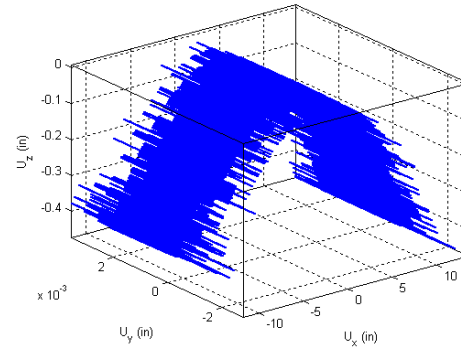


Base moment vs. top rotation

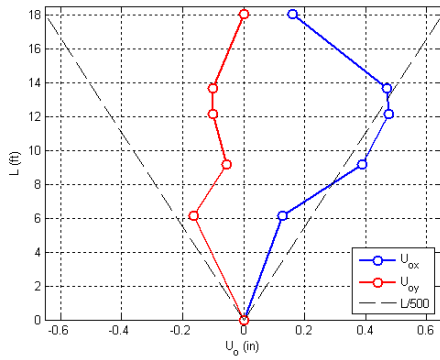
Figure B.3. Experimental results from LC1a in the specimen 1C5-18-5



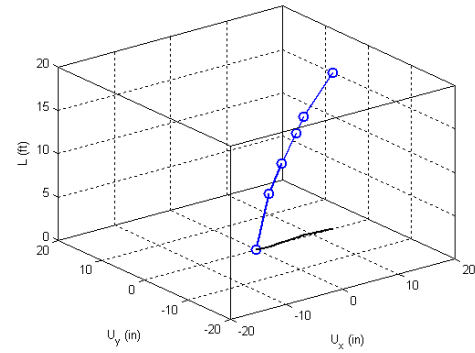
Y displacement vs. X displacement



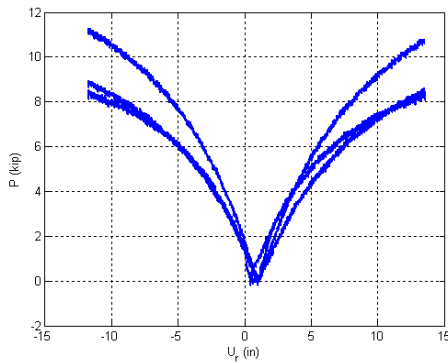
Z displacement vs. X and Y displacement



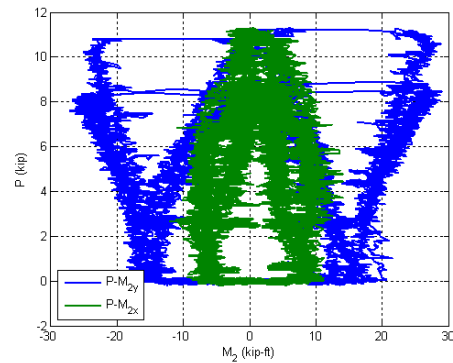
Initial deflected shape



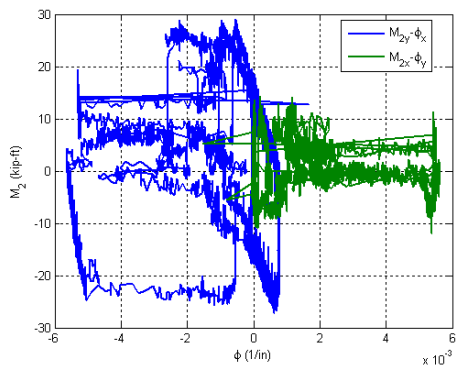
Maximum lateral displacement



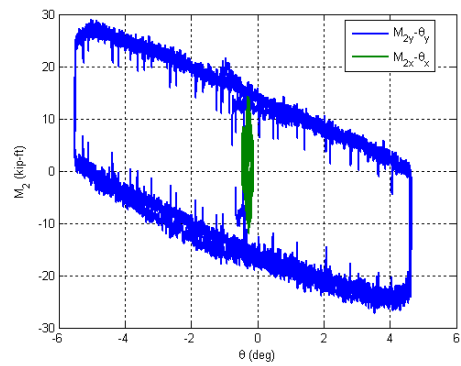
Axial force vs. lateral displacement



Axial force vs. base moments

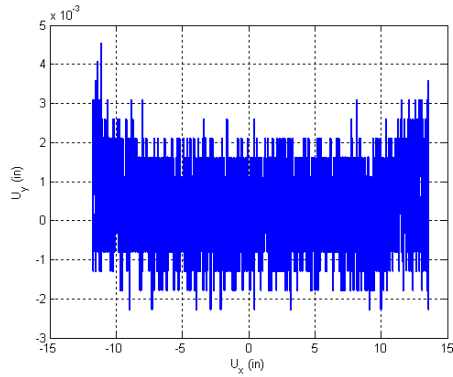


Base moment vs. base curvature

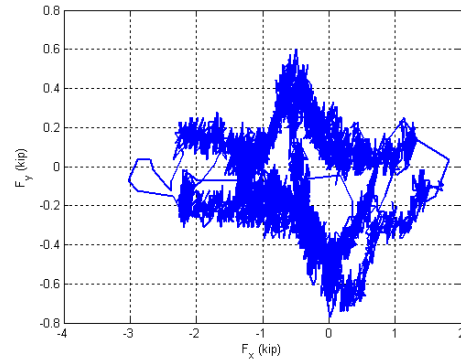


Base moment vs. top rotation

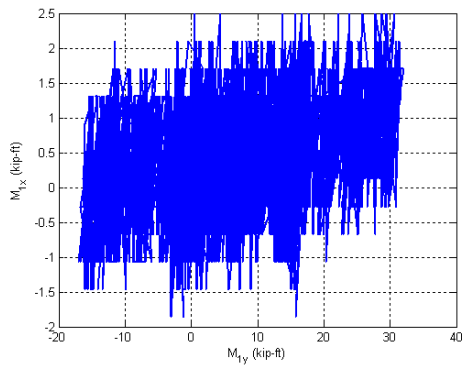
Figure B.4. Experimental results from LC1b in the specimen 1C5-18-5



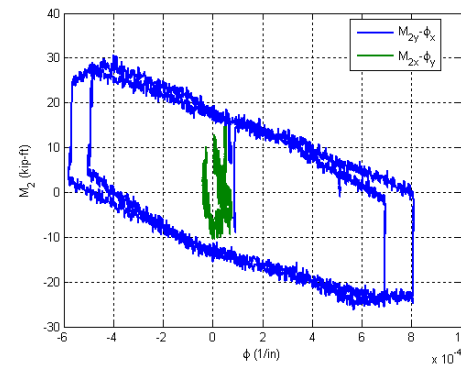
Y Displacement vs. X Displacement



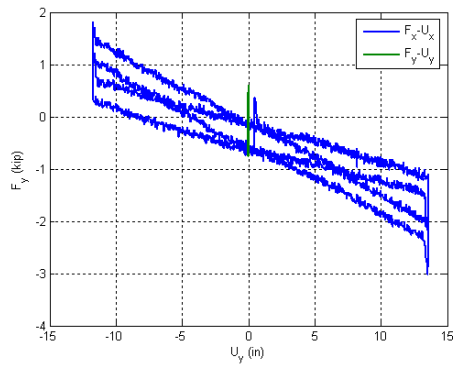
Y Force vs. X Force



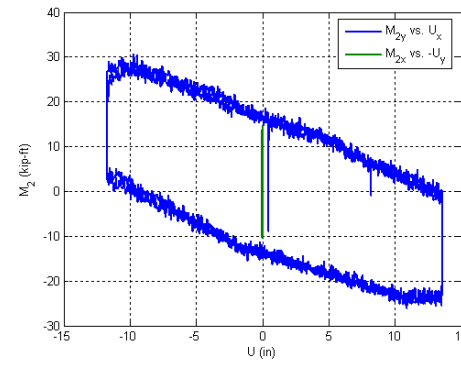
X Moment vs. Y Moment at the top



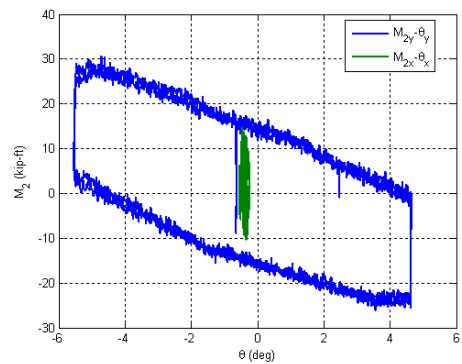
X Moment vs. Y Moment at the base



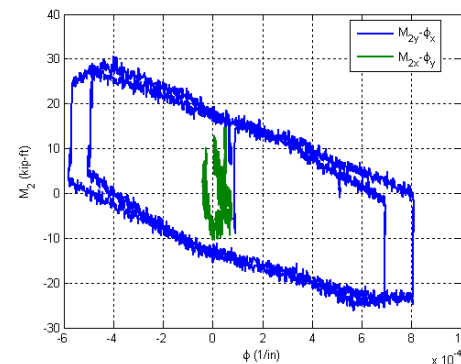
Lateral Force vs. Lateral Displacement



Base Moment vs. Top Displacement

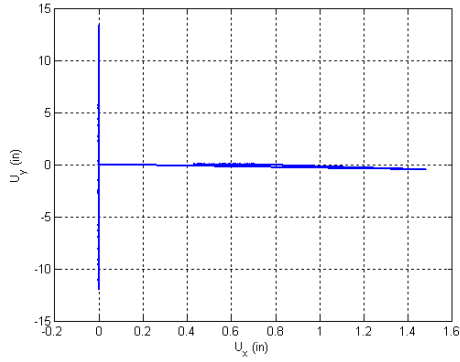


Base Moment vs. Top Rotation

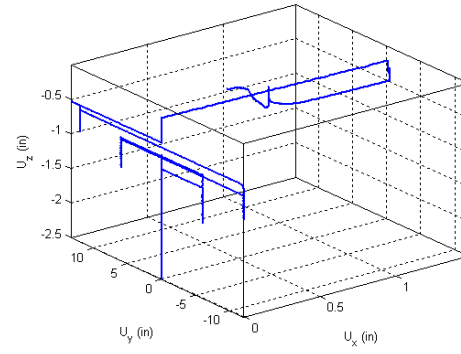


Base Moment vs. Base Curvature

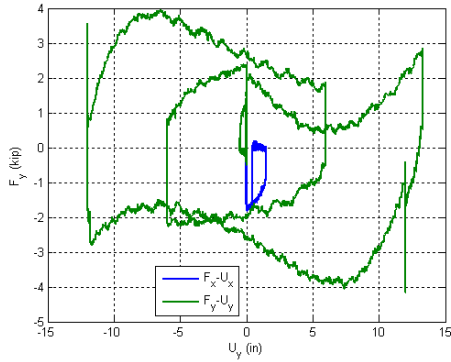
Figure B.5. Experimental results from LC2 in the specimen 1C5-18-5



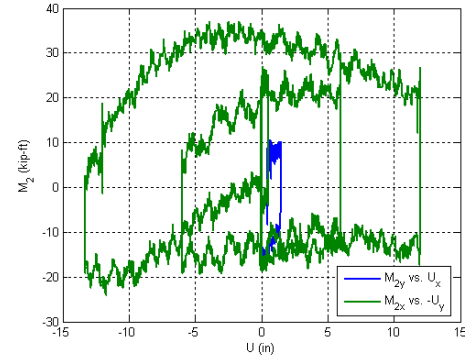
Y displacement vs. X displacement



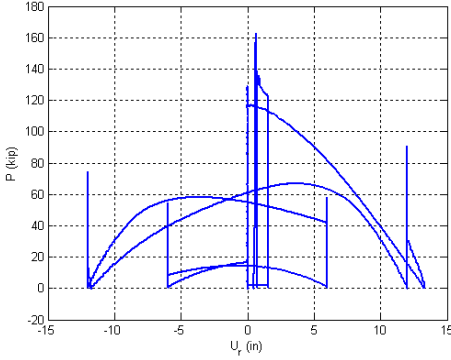
Z displacement vs. X and Y displacement



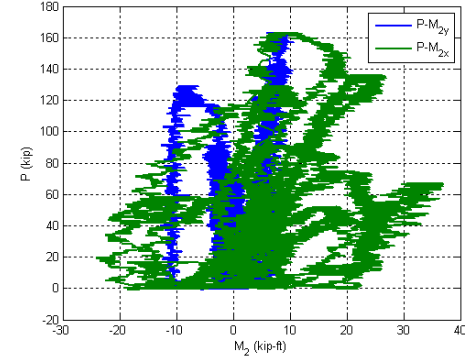
Lateral Force vs. Lateral Displacement



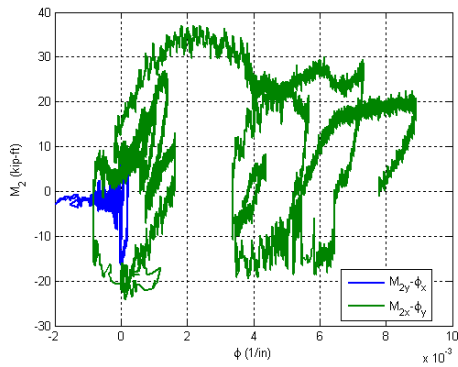
Base Moment vs. Top Displacement



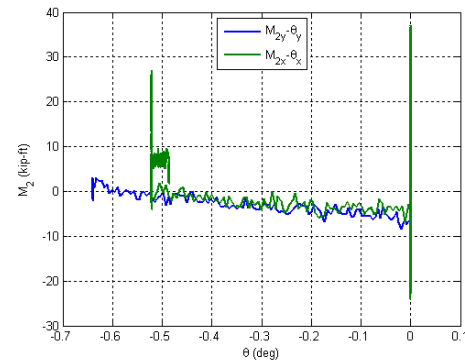
Axial force vs. lateral displacement



Axial force vs. base moments



Base moment vs. base curvature



Base moment vs. top rotation

Figure B.6. Experimental results from LC4 in the specimen 1C5-18-5

B.2. Specimen 2C12-18-5

Description:

- Specimen number: 2
- Composite Cross-section: CCFT
- Steel cross-section: HSS12.75x0.25
- Design concrete strength: 5 ksi
- Design specimen length: 18 ft
- Pouring date: 06/27/2008
- Testing date: 07/29/2008

Parameters:

- Specimen length: 18' 1/2"
- Initial out-of-plumbness: $U_{xo} = 0.75'' / U_{yo} = -0.32''$
- Steel yielding stress: $F_y = 48.9$ ksi
- Steel ultimate stress: $F_u = 64.7$ ksi
- Concrete strength at the 28th day: $f_c' = 5.5$ ksi
- Concrete strength at the testing day: $f_c = 5.6$ ksi
- Concrete Young's modulus: $E_c = 4000$ ksi
- Concrete tensile strength: $f_t = 1.1$ ksi

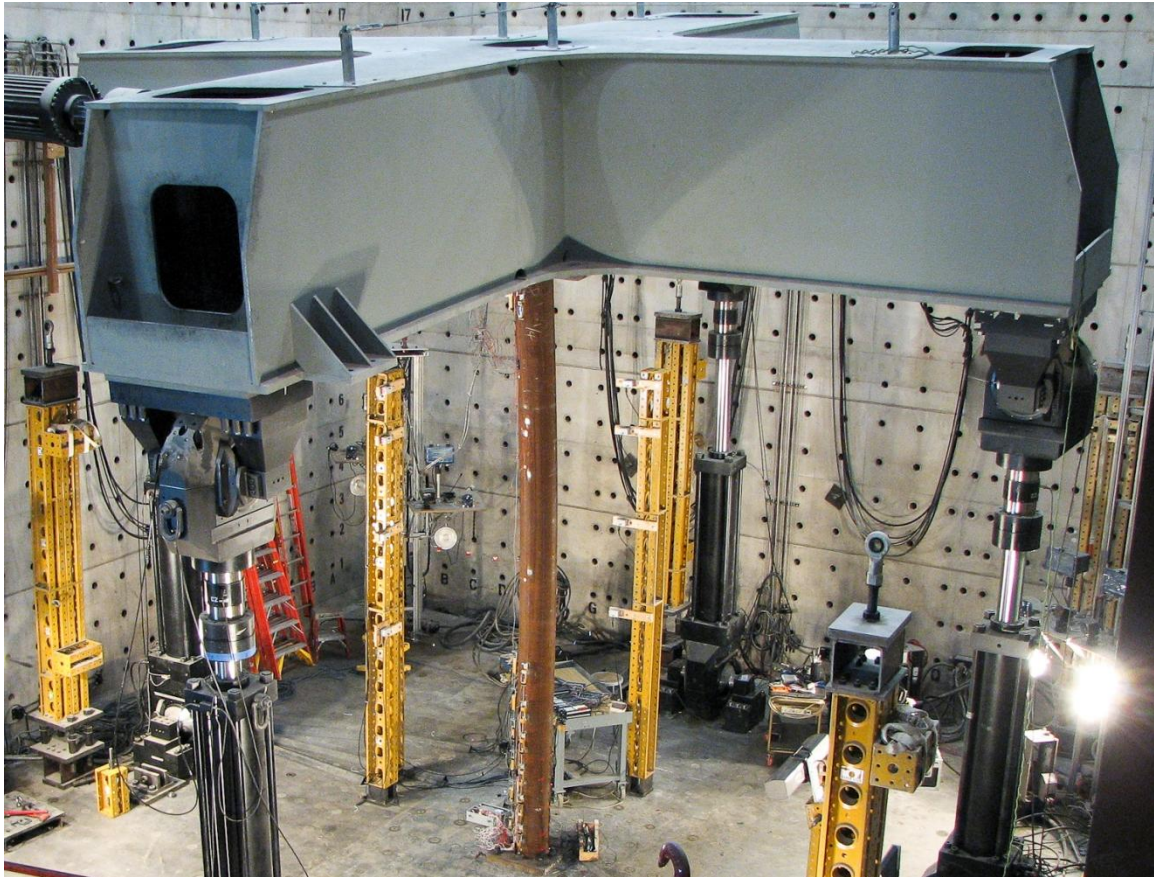


Figure B.7. Specimen 2C12-18-5

Table B.2. Load protocol summary for the specimen 3C20-18-5

LC1 - Incremental compression loading in three cycles until the maximum load is reached. The top is forced to be free at all the time.

Step	DOF						Stop Criterion
	X	Y	Z	RX	RY	RZ	
1	$F_x = 0$	$F_y = 0$	$U_z \downarrow$	$M_x = 0$	$M_y = 0$	$R_z = 0$	max P
2	$F_x = 0$	$F_y = 0$	$U_z \uparrow$	$M_x = 0$	$M_y = 0$	$R_z = 0$	P = 0
3	$F_x = 0$	$F_y = 0$	$U_z \downarrow$	$M_x = 0$	$M_y = 0$	$R_z = 0$	max P
4	$F_x = 0$	$F_y = 0$	$U_z \uparrow$	$M_x = 0$	$M_y = 0$	$R_z = 0$	P = 0

LC2a - Cyclic uniaxial lateral displacements with constant compression force ($-F_z = P = 300$ kips). The top was forced to have zero moments.

Step	DOF						Stop Criterion
	X	Y	Z	RX	RY	RZ	
1	$U_x \downarrow$	$U_y = 0$	P = 300k	$R_x = 0$	$M_y = 0$	$R_z = 0$	+F peak
2	$U_x \uparrow$	$U_y = 0$	P = 300k	$R_x = 0$	$M_y = 0$	$R_z = 0$	-F peak
3	$U_x \downarrow$	$U_y = 0$	P = 300k	$R_x = 0$	$M_y = 0$	$R_z = 0$	+F peak
4	$U_x \uparrow$	$U_y = 0$	P = 300k	$R_x = 0$	$M_y = 0$	$R_z = 0$	-F peak
5	$U_x \uparrow$	$U_y = 0$	P = 300k	$R_x = 0$	$M_y = 0$	$R_z = 0$	$U_z = 0$

LC2b - Cyclic uniaxial lateral displacements with constant compression force ($-F_z = P = 200$ kips). The top was forced to have zero moments.

Step	DOF						Stop Criterion
	X	Y	Z	RX	RY	RZ	
1	$U_x \downarrow$	$U_y = 0$	P = 200k	$R_x = 0$	$M_y = 0$	$R_z = 0$	+F peak
2	$U_x \uparrow$	$U_y = 0$	P = 200k	$R_x = 0$	$M_y = 0$	$R_z = 0$	-F peak
3	$U_x \downarrow$	$U_y = 0$	P = 200k	$R_x = 0$	$M_y = 0$	$R_z = 0$	+F peak
4	$U_x \uparrow$	$U_y = 0$	P = 200k	$R_x = 0$	$M_y = 0$	$R_z = 0$	-F peak
5	$U_x \uparrow$	$U_y = 0$	P = 200k	$R_x = 0$	$M_y = 0$	$R_z = 0$	$U_z = 0$

LC2c - Cyclic uniaxial lateral displacements with constant compression force ($-F_z = P = 100$ kips). The top was forced to have zero moments.

Step	DOF						Stop Criterion
	X	Y	Z	RX	RY	RZ	
1	$U_x \downarrow$	$U_y = 0$	P = 100k	$R_x = 0$	$M_y = 0$	$R_z = 0$	+F peak
2	$U_x \uparrow$	$U_y = 0$	P = 100k	$R_x = 0$	$M_y = 0$	$R_z = 0$	-F peak
3	$U_x \downarrow$	$U_y = 0$	P = 100k	$R_x = 0$	$M_y = 0$	$R_z = 0$	+F peak
4	$U_x \uparrow$	$U_y = 0$	P = 100k	$R_x = 0$	$M_y = 0$	$R_z = 0$	-F peak
5	$U_x \uparrow$	$U_y = 0$	P = 100k	$R_x = 0$	$M_y = 0$	$R_z = 0$	$U_z = 0$

LC3 - Cyclic biaxial lateral displacements (8 probes with diamond shape) with constant compression force ($-F_z = P = 250$ and 150 kips). The top was forced to have zero moments.

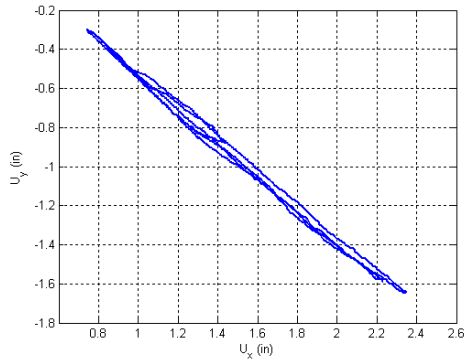
Step	DOF						Stop Criterion
	X	Y	Z	RX	RY	RZ	
1	$U_x \downarrow$	$U_y \downarrow$	$P = 250k$	$M_x = 0$	$M_y = 0$	$R_z = 0$	F peak at each of the 16 probes
2	$U_x \uparrow$	$U_y \uparrow$	$P = 150k$	$M_x = 0$	$M_y = 0$	$R_z = 0$	

LC4a - Cyclic uniaxial lateral displacements with constant compression force ($-F_z = P = 300$ kips). The top was forced to have zero moments.

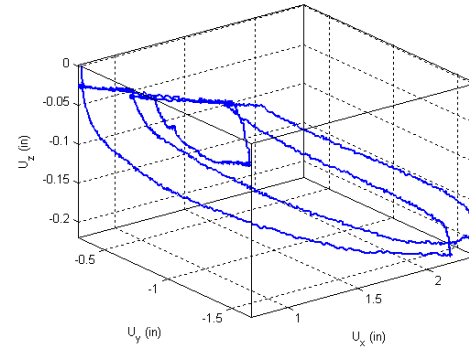
Step	DOF						Stop Criterion
	X	Y	Z	RX	RY	RZ	
1	$U_x \downarrow$	$U_y = 0$	$P = 300k$	$R_x = 0$	$M_y = 0$	$R_z = 0$	+F peak
2	$U_x \uparrow$	$U_y = 0$	$P = 300k$	$R_x = 0$	$M_y = 0$	$R_z = 0$	-F peak
3	$U_x \downarrow$	$U_y = 0$	$P = 300k$	$R_x = 0$	$M_y = 0$	$R_z = 0$	+F peak
4	$U_x \uparrow$	$U_y = 0$	$P = 300k$	$R_x = 0$	$M_y = 0$	$R_z = 0$	-F peak
5	$U_x \uparrow$	$U_y = 0$	$P = 300k$	$R_x = 0$	$M_y = 0$	$R_z = 0$	$U_z = 0$

LC4 - Torsion The top was twisted in displacement control.

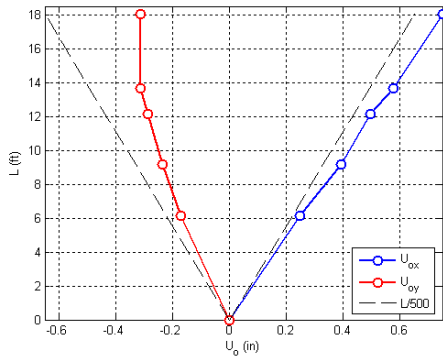
Step	DOF						Stop Criterion
	X	Y	Z	RX	RY	RZ	
1	$U_x = 0$	$U_y = 0$	$P = 0$	$R_x = 0$	$R_y = 0$	$R_z \uparrow$	+/-max. twist
2	$U_x = 0$	$U_y = 0$	$P = 250k$	$R_x = 0$	$R_y = 0$	$R_z \downarrow$	+/-max. twist



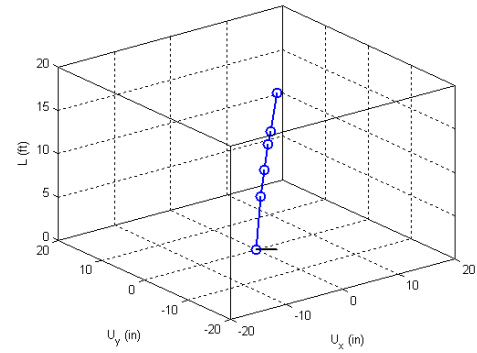
Y displacement vs. X displacement



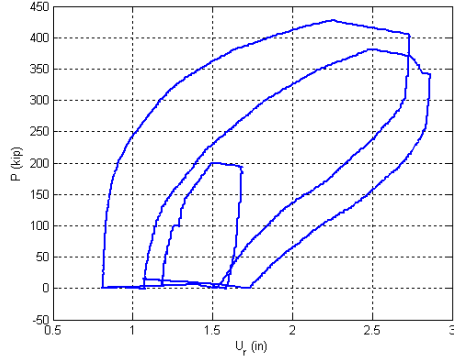
Z displacement vs. X and Y displacement



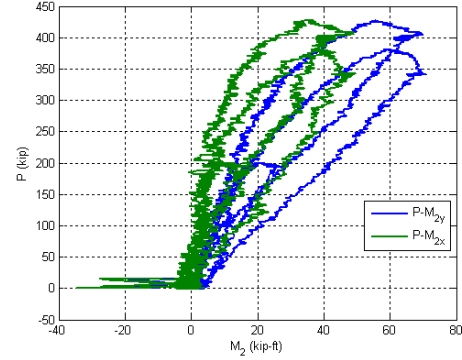
Initial deflected shape



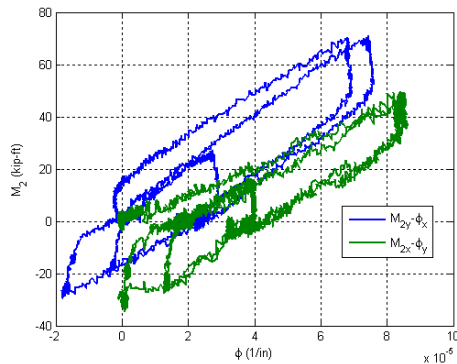
Maximum lateral displacement



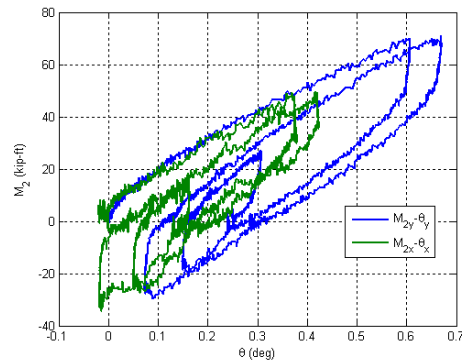
Axial force vs. lateral displacement



Axial force vs. base moments

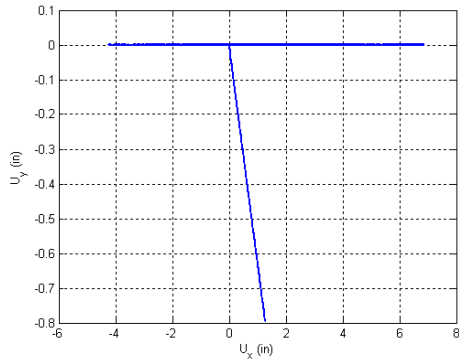


Base moment vs. base curvature

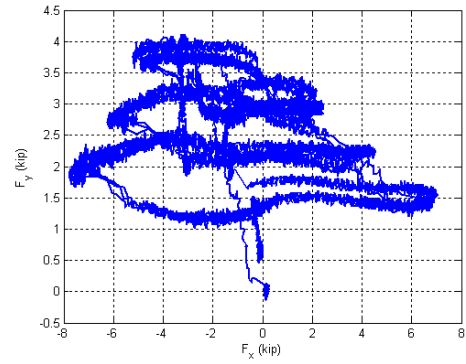


Base moment vs. top rotation

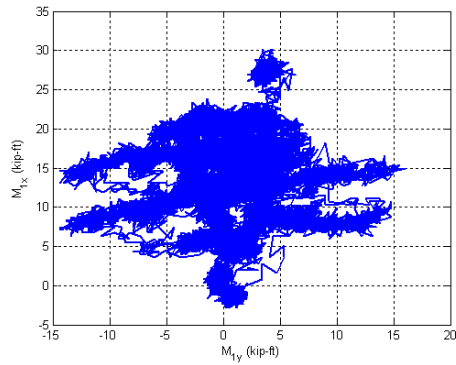
Figure B.8. Experimental results from LC1 in the specimen 2C12-18-5



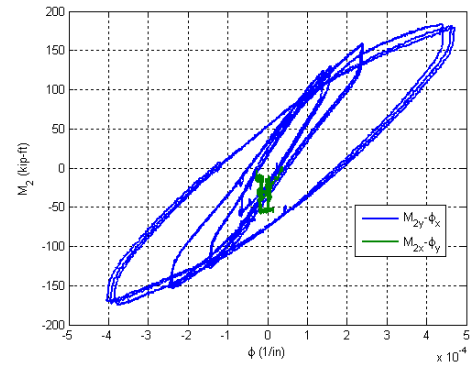
Y Displacement vs. X Displacement



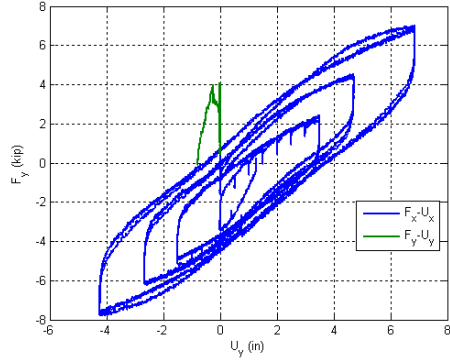
Y Force vs. X Force



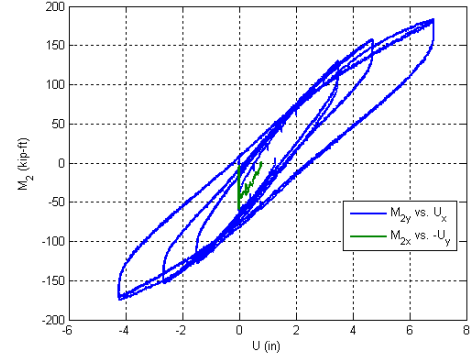
X Moment vs. Y Moment at the top



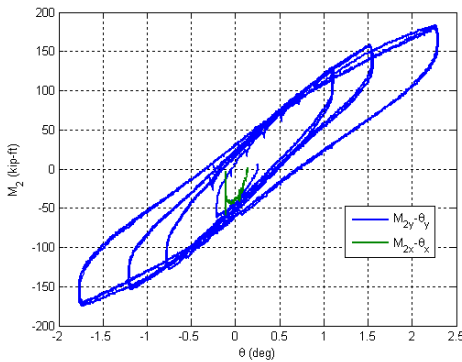
X Moment vs. Y Moment at the base



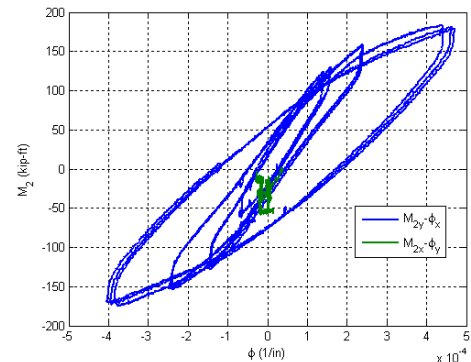
Lateral Force vs. Lateral Displacement



Base Moment vs. Top Displacement

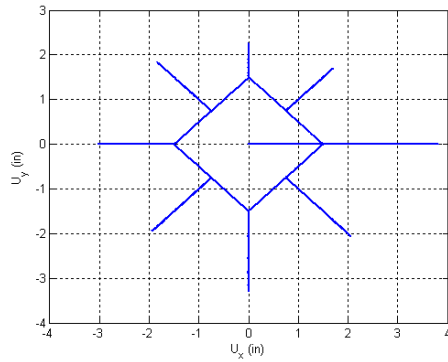


Base Moment vs. Top Rotation

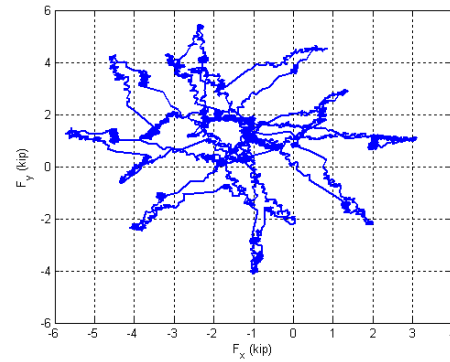


Base Moment vs. Base Curvature

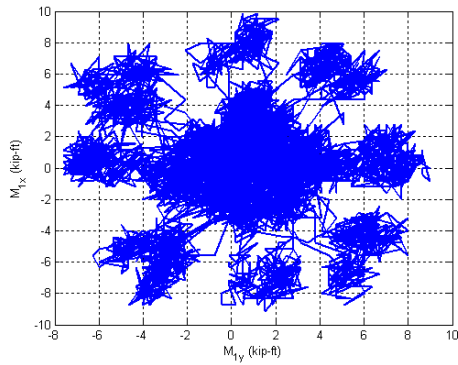
Figure B.9. Experimental results from LC2a in the specimen 2C12-18-5



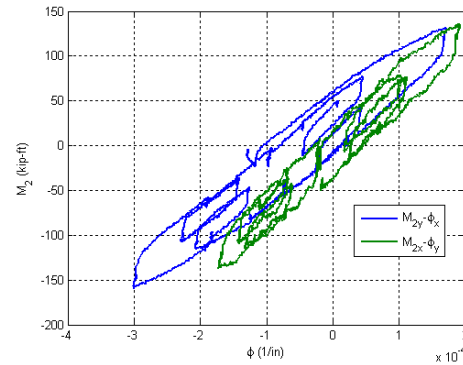
Y Displacement vs. X Displacement



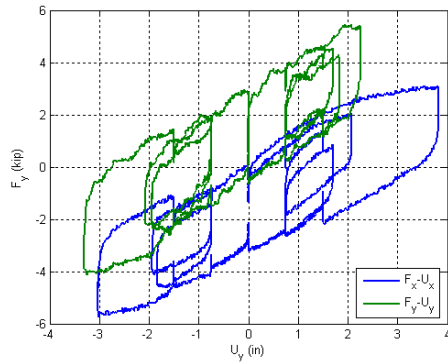
Y Force vs. X Force



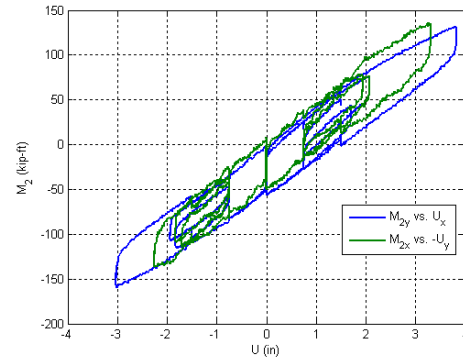
X Moment vs. Y Moment at the top



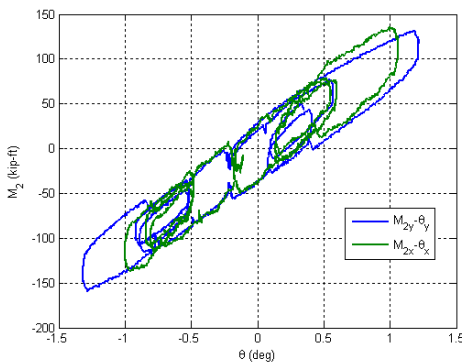
X Moment vs. Y Moment at the base



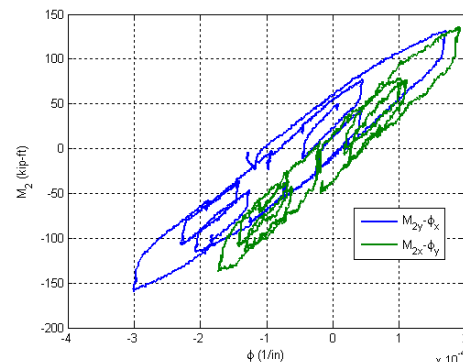
Lateral Force vs. Lateral Displacement



Base Moment vs. Top Displacement

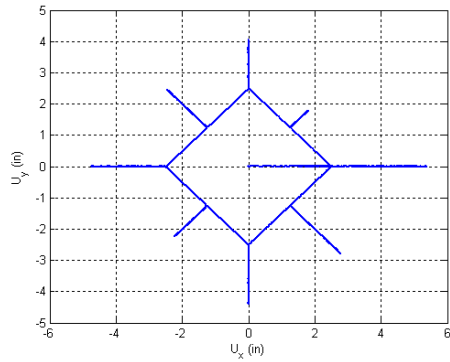


Base Moment vs. Top Rotation

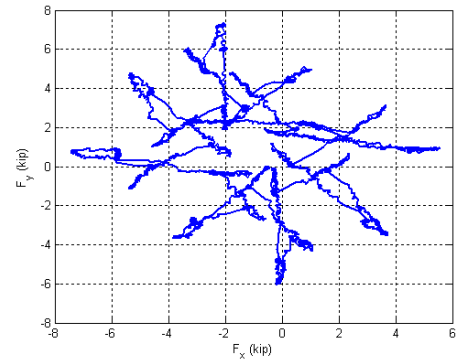


Base Moment vs. Base Curvature

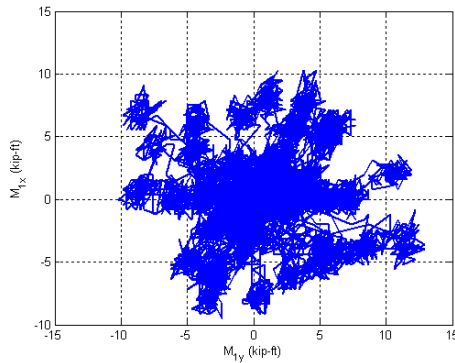
Figure B.10. Experimental results from LC3a in the specimen 2C12-18-5



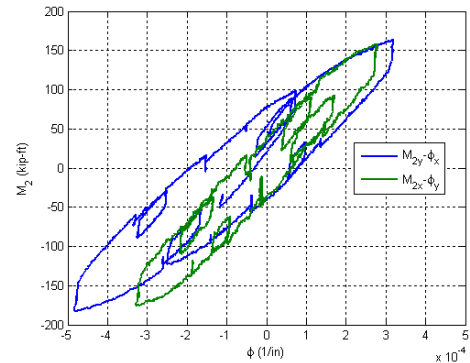
Y Displacement vs. X Displacement



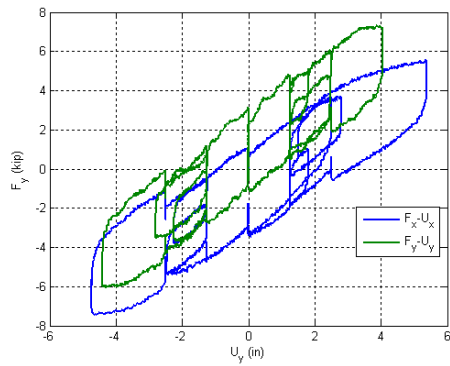
Y Force vs. X Force



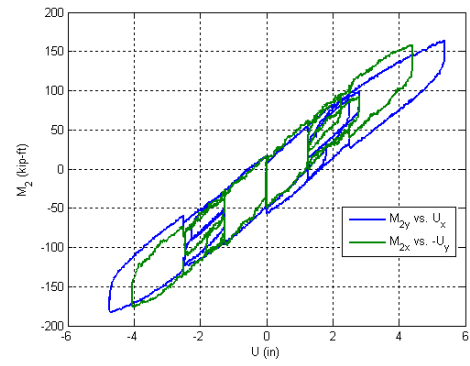
X Moment vs. Y Moment at the top



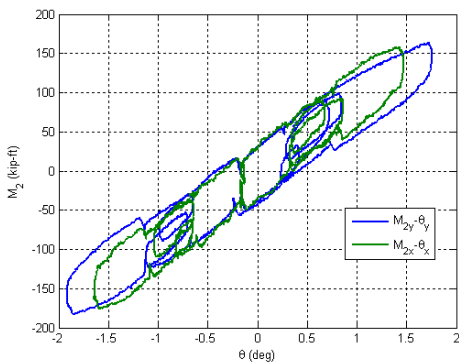
X Moment vs. Y Moment at the base



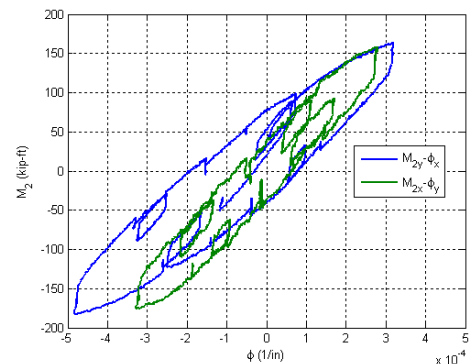
Lateral Force vs. Lateral Displacement



Base Moment vs. Top Displacement

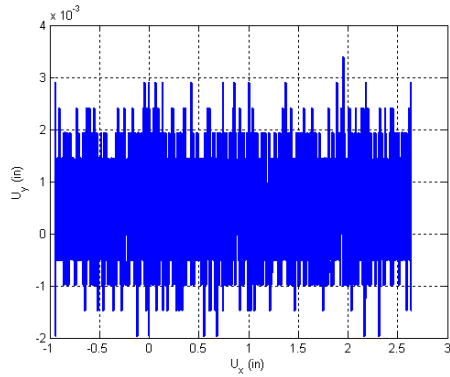


Base Moment vs. Top Rotation

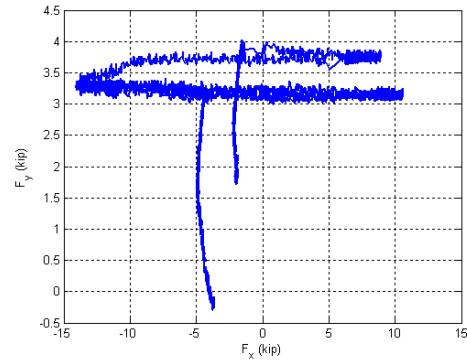


Base Moment vs. Base Curvature

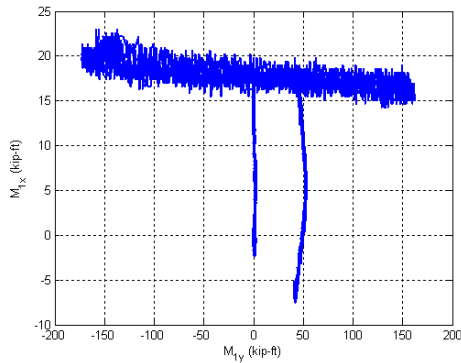
Figure B.11. Experimental results from LC3b in the specimen 2C12-18-5



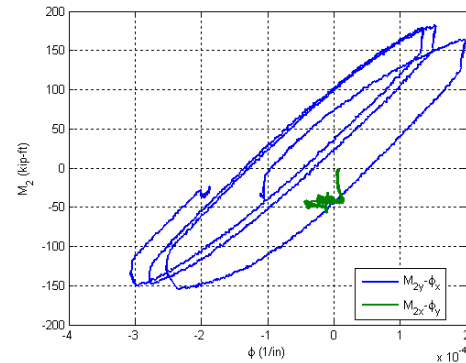
Y Displacement vs. X Displacement



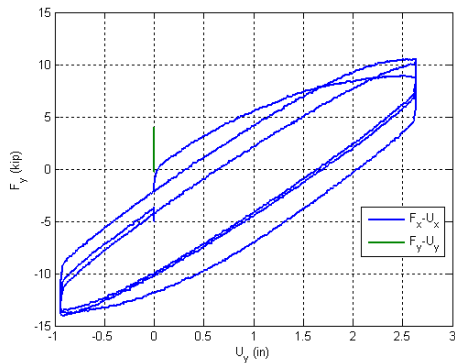
Y Force vs. X Force



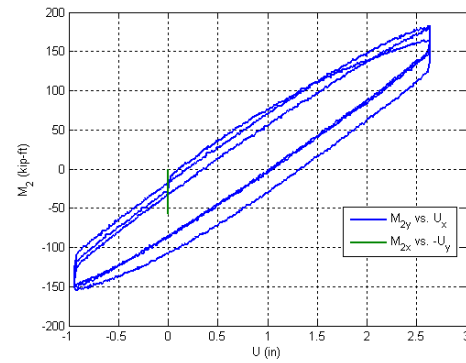
X Moment vs. Y Moment at the top



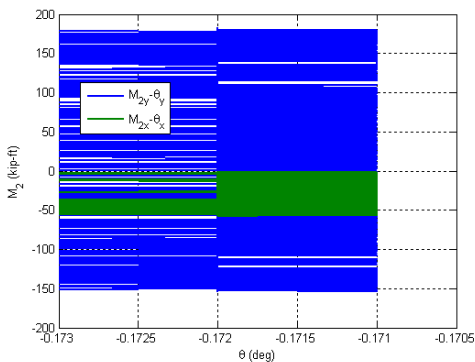
X Moment vs. Y Moment at the base



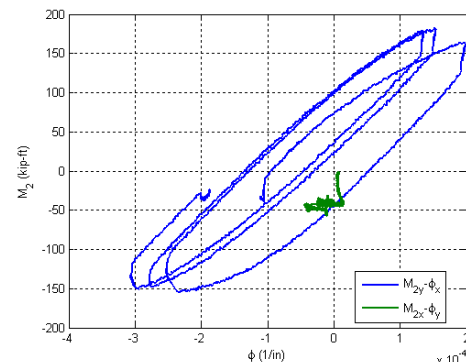
Lateral Force vs. Lateral Displacement



Base Moment vs. Top Displacement

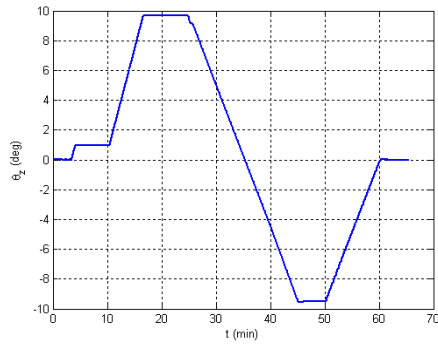


Base Moment vs. Top Rotation

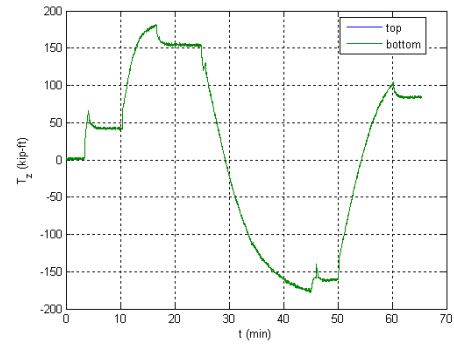


Base Moment vs. Base Curvature

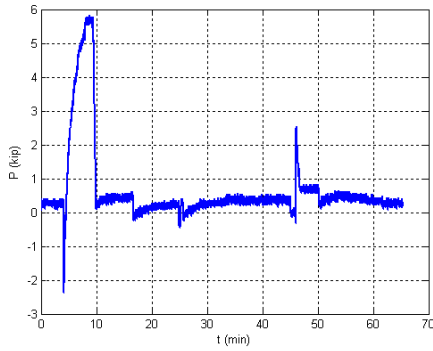
Figure B.12. Experimental results from LC2b in the specimen 2C12-18-5



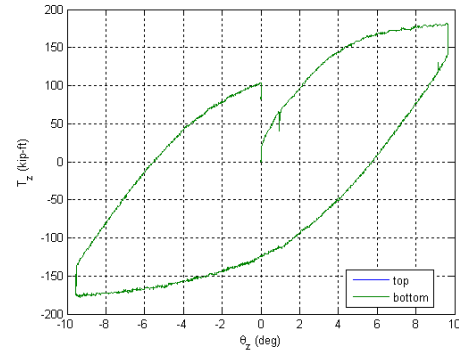
Twisting Angle vs. Time



Torsion Moment vs. Time

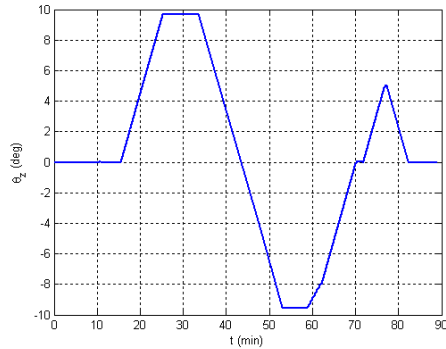


Axial Force vs. Time

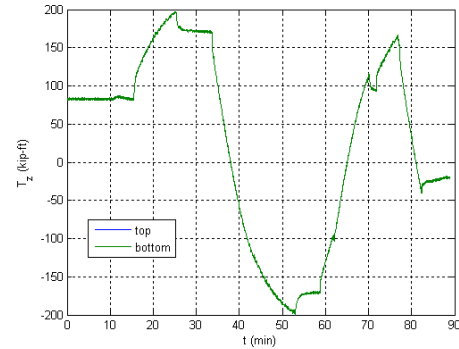


Torsion Moment vs. Twisting Angle

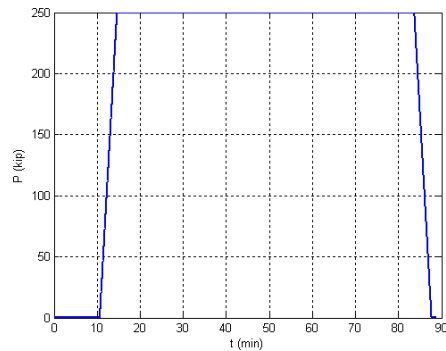
Figure B.13. Experimental results from LC4a in the specimen 2C12-18-5



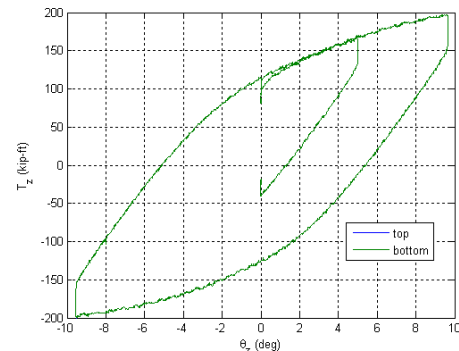
Twisting Angle vs. Time



Torsion Moment vs. Time

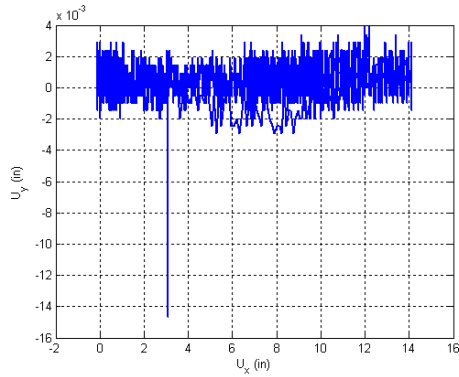


Axial Force vs. Time

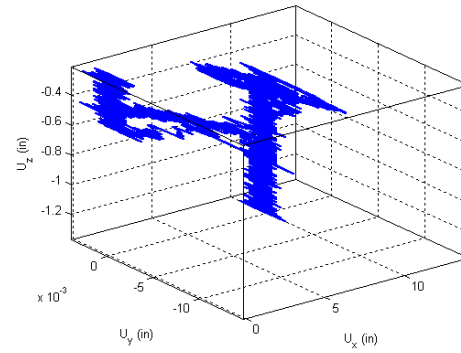


Torsion Moment vs. Twisting Angle

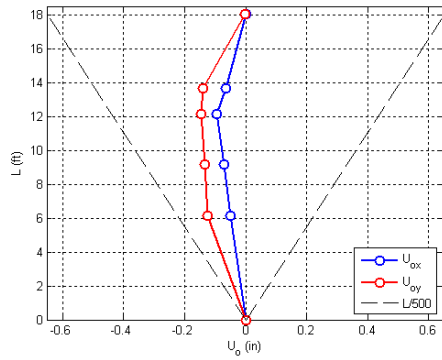
Figure B.14. Experimental results from LC4b in the specimen 2C12-18-5



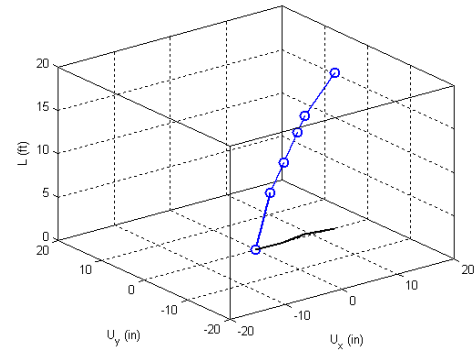
Y displacement vs. X displacement



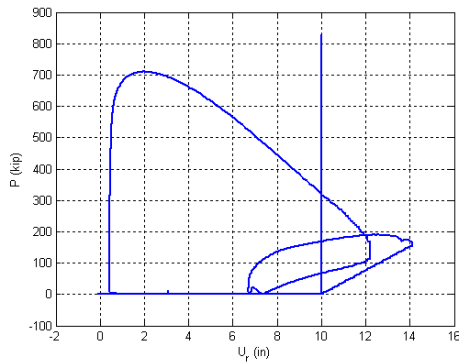
Z displacement vs. X and Y displacement



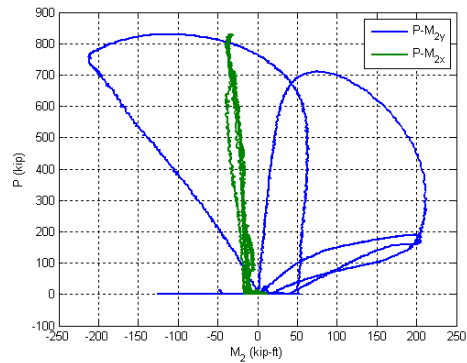
Initial deflected shape



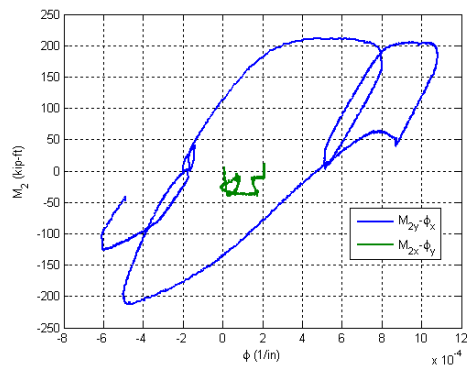
Maximum lateral displacement



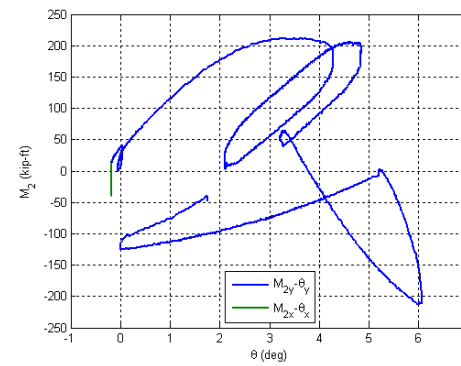
Axial force vs. lateral displacement



Axial force vs. base moments



Base moment vs. base curvature



Base moment vs. top rotation

Figure B.15. Experimental results from LC4c in the specimen 2C12-18-5

B.3. Specimen 3C20-18-5

Description:

- Specimen number: 3
- Composite Cross-section: CCFT
- Steel cross-section: HSS20x0.25
- Design concrete strength: 5 ksi
- Design specimen length: 18 ft
- Pouring date: 06/27/2008
- Testing date: 10/30/2008

Parameters:

- Specimen length: 18' 1 1/2"
- Initial out-of-plumbness: $U_{xo} = 0.40'' / U_{yo} = -0.87''$
- Steel yielding stress: $F_y = 47.6$ ksi
- Steel ultimate stress: $F_u = 68.3$ ksi
- Concrete strength at the 28th day: $f_c' = 5.5$ ksi
- Concrete strength at the testing day: $f_c = 5.8$ ksi
- Concrete Young's modulus: $E_c = 4000$ ksi
- Concrete tensile strength: $f_t = 1.1$ ksi

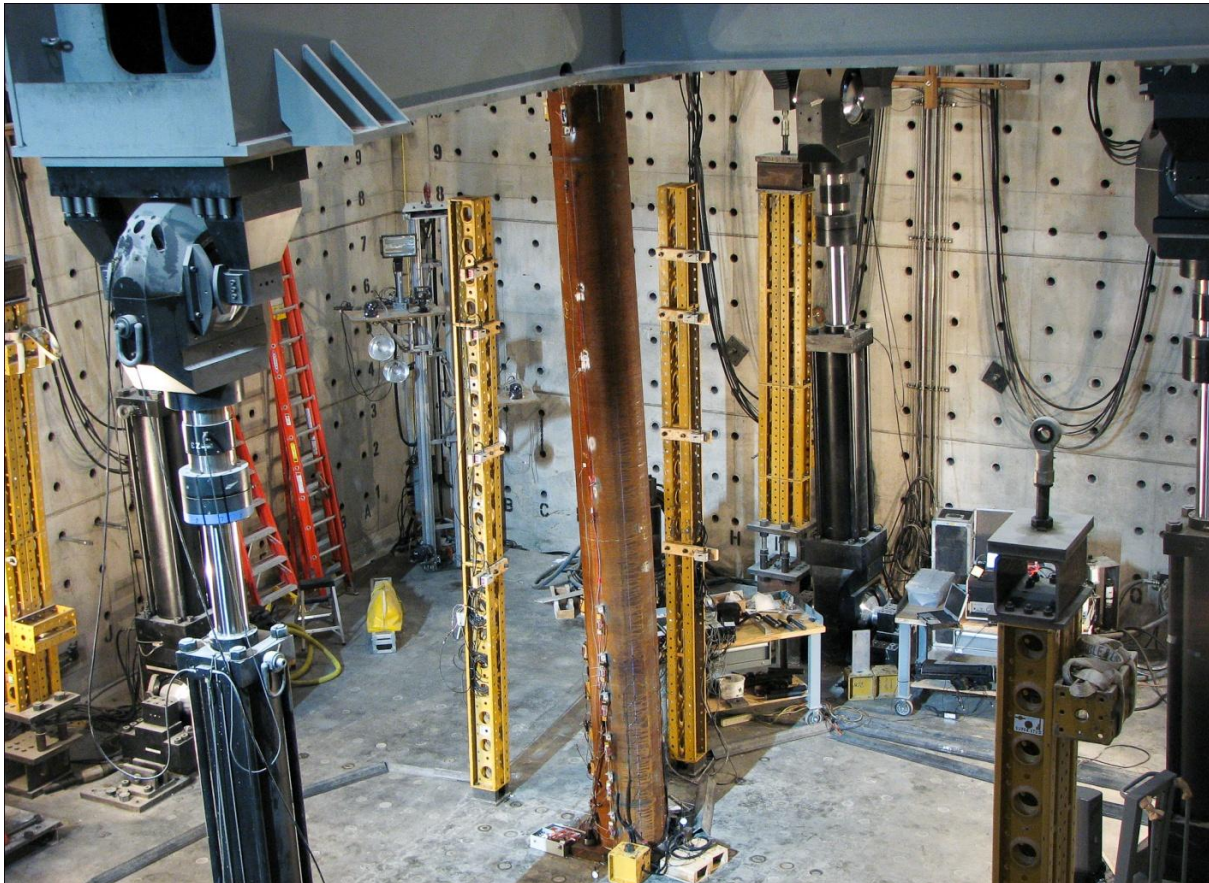


Figure B.16. Specimen 3C20-18-5

Table B.3. Load protocol summary for the specimen 3C20-18-5

LC1 - Incremental compression loading in three cycles until the maximum load is reached. The top is forced to be free at all the time.

Step	DOF						Stop Criterion
	X	Y	Z	RX	RY	RZ	
1	$F_x = 0$	$F_y = 0$	$U_z \downarrow$	$M_x = 0$	$M_y = 0$	$R_z = 0$	max P
2	$F_x = 0$	$F_y = 0$	$U_z \uparrow$	$M_x = 0$	$M_y = 0$	$R_z = 0$	P = 0
3	$F_x = 0$	$F_y = 0$	$U_z \downarrow$	$M_x = 0$	$M_y = 0$	$R_z = 0$	max P
4	$F_x = 0$	$F_y = 0$	$U_z \uparrow$	$M_x = 0$	$M_y = 0$	$R_z = 0$	P = 0
5	$F_x = 0$	$F_y = 0$	$U_z \downarrow$	$M_x = 0$	$M_y = 0$	$R_z = 0$	max P
6	$F_x = 0$	$F_y = 0$	$U_z \uparrow$	$M_x = 0$	$M_y = 0$	$R_z = 0$	P = 0

LC2a - Cyclic uniaxial lateral displacements with constant compression force ($-F_z = P = 1000$ kips). The top was forced to have zero moments.

Step	DOF						Stop Criterion
	X	Y	Z	RX	RY	RZ	
1	$U_x \downarrow$	$U_y \uparrow$	P = 1000k	$M_x = 0$	$M_y = 0$	$R_z = 0$	+F peak
2	$U_x \uparrow$	$U_y \downarrow$	P = 1000k	$M_x = 0$	$M_y = 0$	$R_z = 0$	-F peak
3	$U_x \downarrow$	$U_y \uparrow$	P = 1000k	$M_x = 0$	$M_y = 0$	$R_z = 0$	+F peak
4	$U_x \uparrow$	$U_y \downarrow$	P = 1000k	$M_x = 0$	$M_y = 0$	$R_z = 0$	-F peak
5	$U_x \uparrow$	$U_y \downarrow$	P = 1000k	$M_x = 0$	$M_y = 0$	$R_z = 0$	$U_z = 0$

LC2b - Cyclic uniaxial lateral displacements with constant compression force ($-F_z = P = 500$ kips). The top was forced to have zero moments.

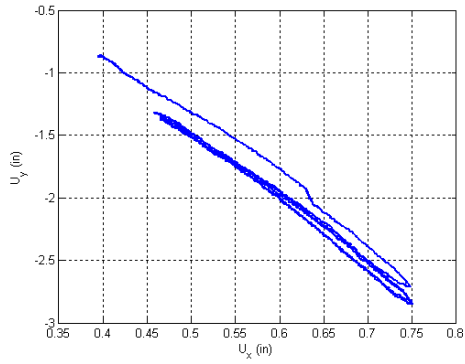
Step	DOF						Stop Criterion
	X	Y	Z	RX	RY	RZ	
1	$U_x \downarrow$	$U_y \uparrow$	P = 500k	$M_x = 0$	$M_y = 0$	$R_z = 0$	+F peak
2	$U_x \uparrow$	$U_y \downarrow$	P = 500k	$M_x = 0$	$M_y = 0$	$R_z = 0$	-F peak
3	$U_x \downarrow$	$U_y \uparrow$	P = 500k	$M_x = 0$	$M_y = 0$	$R_z = 0$	+F peak
4	$U_x \uparrow$	$U_y \downarrow$	P = 500k	$M_x = 0$	$M_y = 0$	$R_z = 0$	-F peak
5	$U_x \uparrow$	$U_y \downarrow$	P = 500k	$M_x = 0$	$M_y = 0$	$R_z = 0$	$U_z = 0$

LC3 - Cyclic biaxial lateral displacements (16 probes with diamond shape) with constant compression force ($-F_z = P = 1250, 750$ and 250 kips). The top was forced to have zero moments.

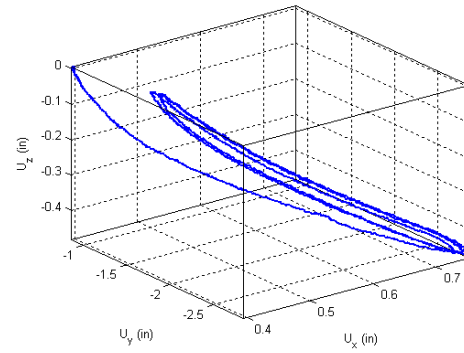
Step	DOF						Stop Criterion
	X	Y	Z	RX	RY	RZ	
1	$U_x \updownarrow$	$U_y \updownarrow$	P = 1250k	$M_x = 0$	$M_y = 0$	$R_z = 0$	F peak at each of the 16 probes
2	$U_x \updownarrow$	$U_y \updownarrow$	P = 750k	$M_x = 0$	$M_y = 0$	$R_z = 0$	
3	$U_x \updownarrow$	$U_y \updownarrow$	P = 250k	$M_x = 0$	$M_y = 0$	$R_z = 0$	

LC4 - Torsion The top was twisted in displacement control.

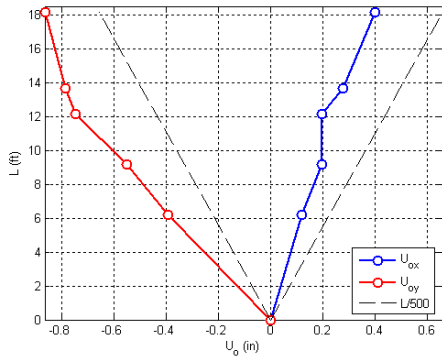
Step	DOF						Stop Criterion
	X	Y	Z	RX	RY	RZ	
1	$U_x = 0$	$U_y = 0$	P = 0	$R_x = 0$	$R_y = 0$	$R_z \updownarrow$	+/-max. twist
2	$U_x = 0$	$U_y = 0$	P = 500k	$R_x = 0$	$R_y = 0$	$R_z \updownarrow$	+/-max. twist



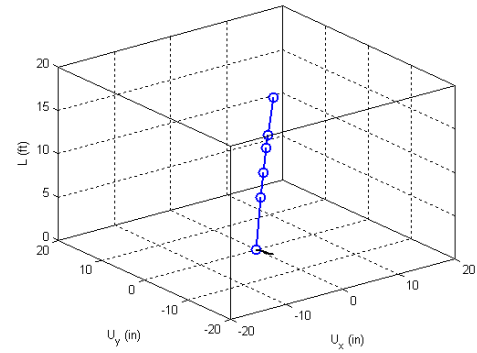
Y displacement vs. X displacement



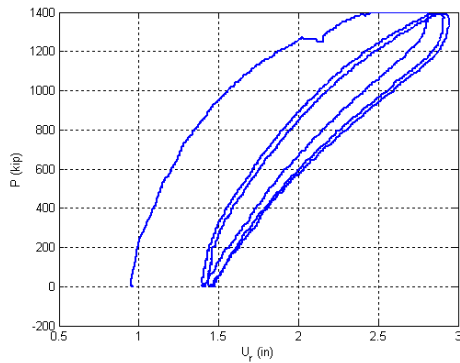
Z displacement vs. X and Y displacement



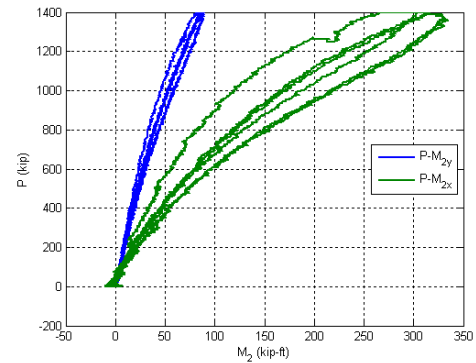
Initial deflected shape



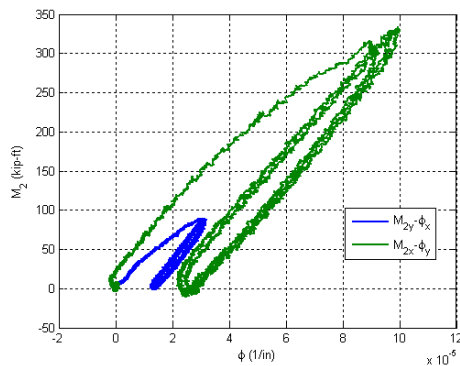
Maximum lateral displacement



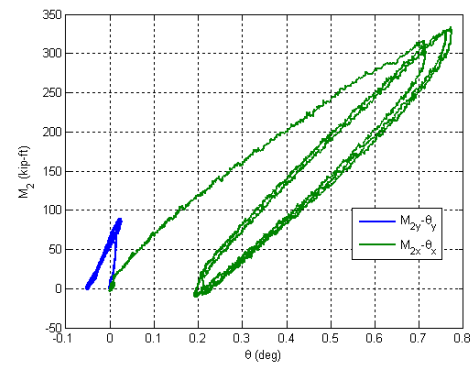
Axial force vs. lateral displacement



Axial force vs. base moments

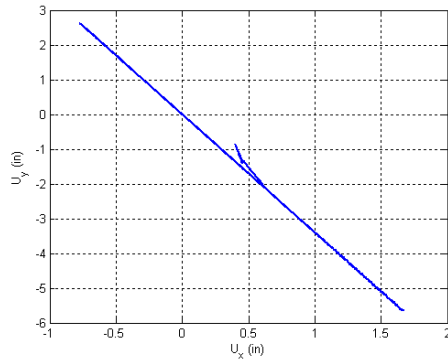


Base moment vs. base curvature

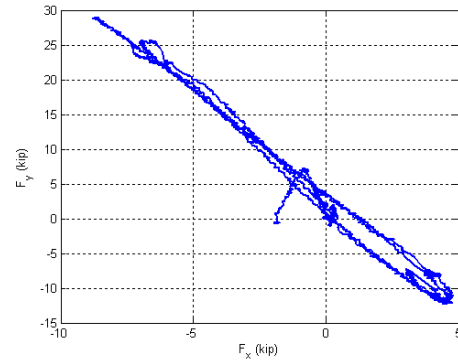


Base moment vs. top rotation

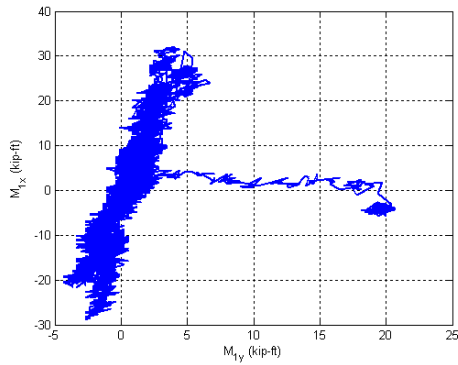
Figure B.17. Experimental results from LC1 in the specimen 3C20-18-5



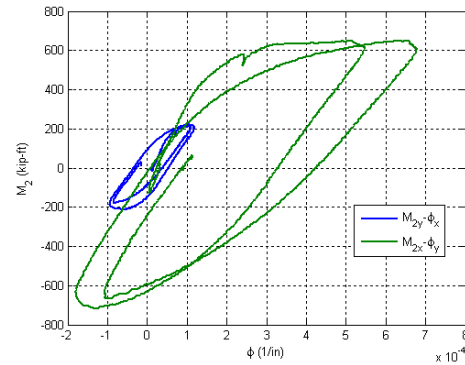
Y Displacement vs. X Displacement



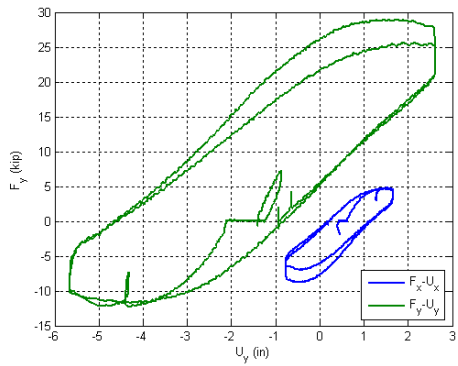
Y Force vs. X Force



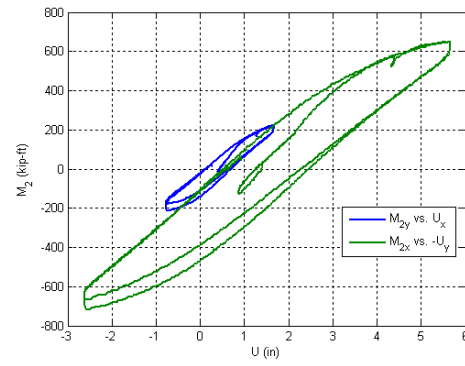
X Moment vs. Y Moment at the top



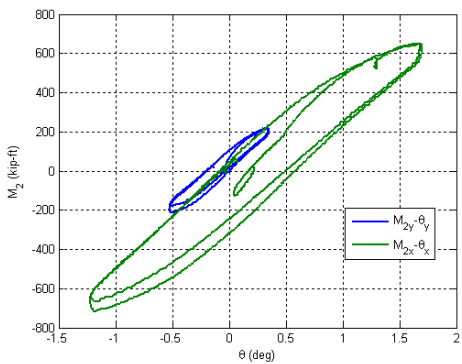
X Moment vs. Y Moment at the base



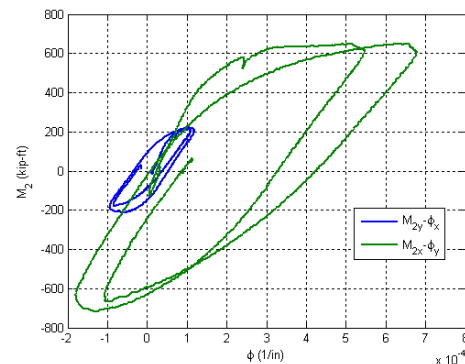
Lateral Force vs. Lateral Displacement



Base Moment vs. Top Displacement

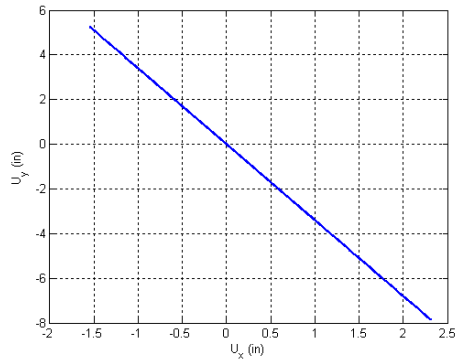


Base Moment vs. Top Rotation

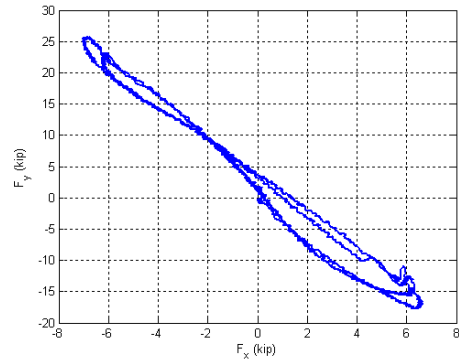


Base Moment vs. Base Curvature

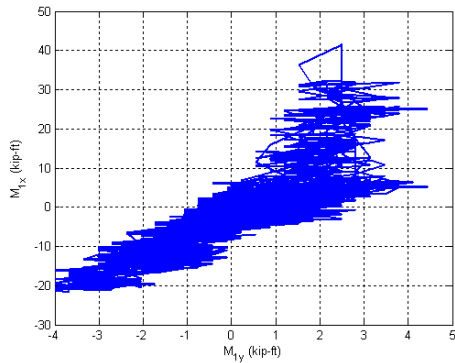
Figure B.18. Experimental results from LC2a in the specimen 3C20-18-5



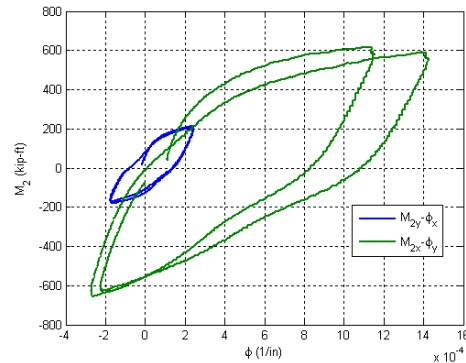
Y Displacement vs. X Displacement



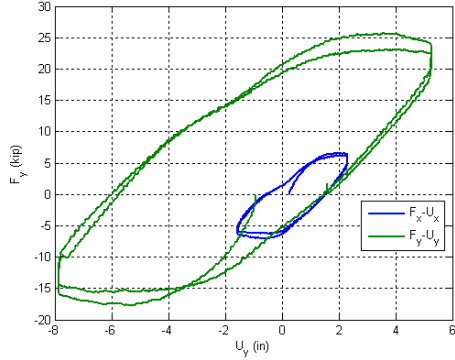
Y Force vs. X Force



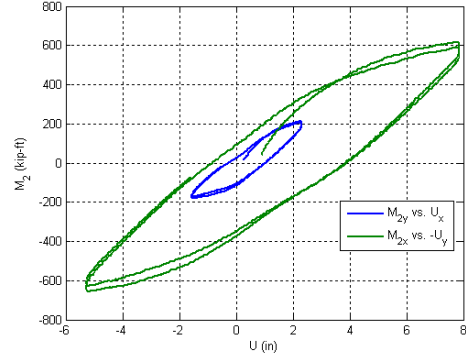
X Moment vs. Y Moment at the top



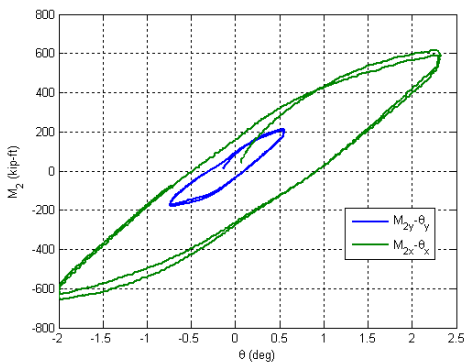
X Moment vs. Y Moment at the base



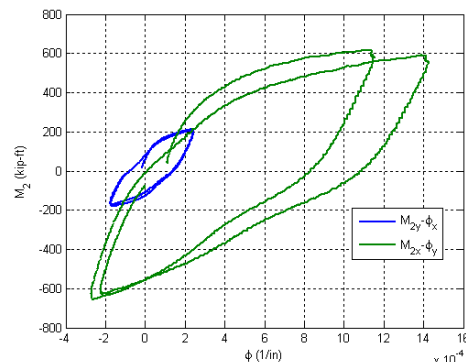
Lateral Force vs. Lateral Displacement



Base Moment vs. Top Displacement

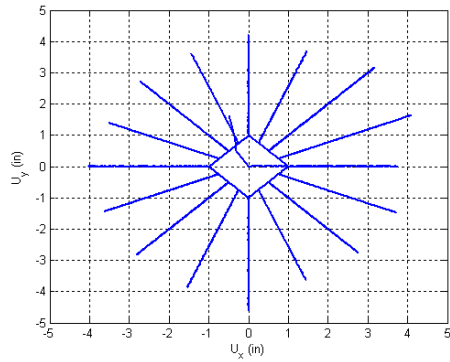


Base Moment vs. Top Rotation

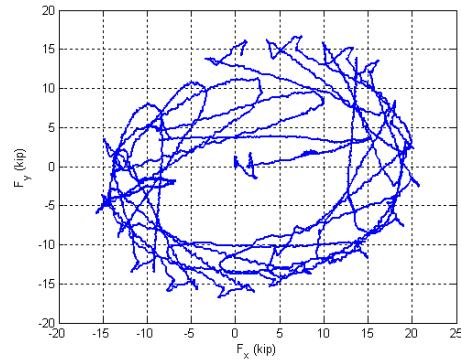


Base Moment vs. Base Curvature

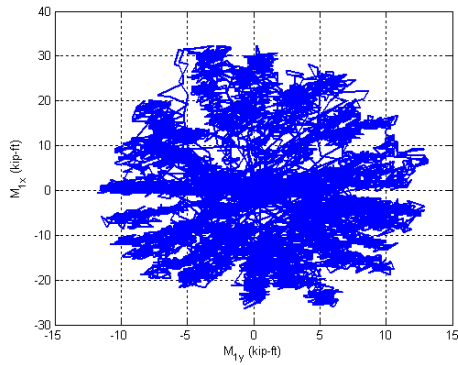
Figure B.19. Experimental results from LC2b in the specimen 3C20-18-5



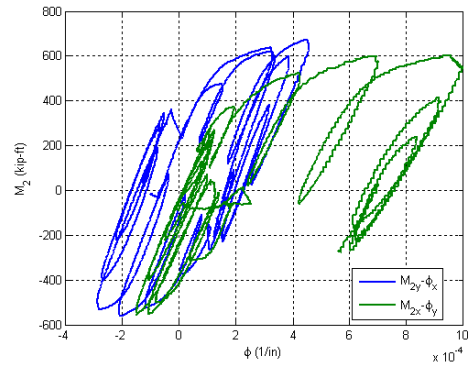
Y Displacement vs. X Displacement



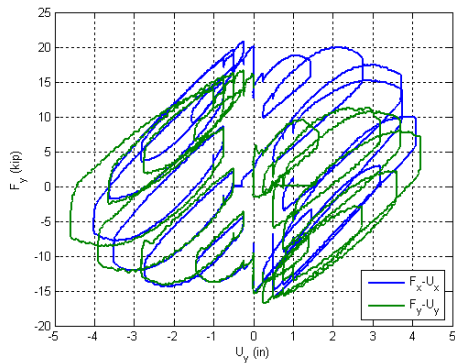
Y Force vs. X Force



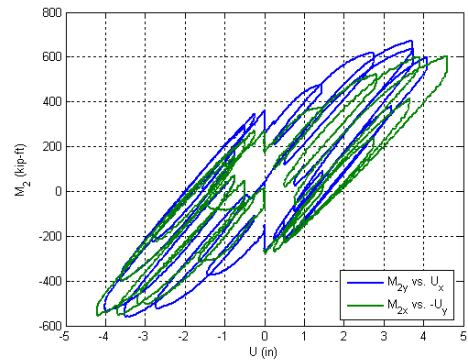
X Moment vs. Y Moment at the top



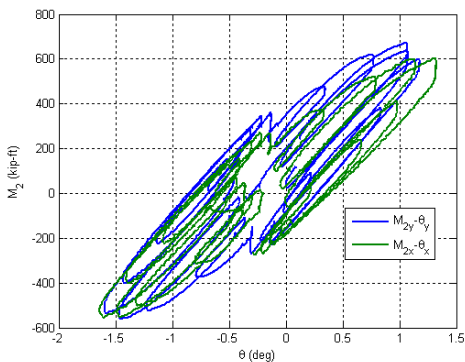
X Moment vs. Y Moment at the base



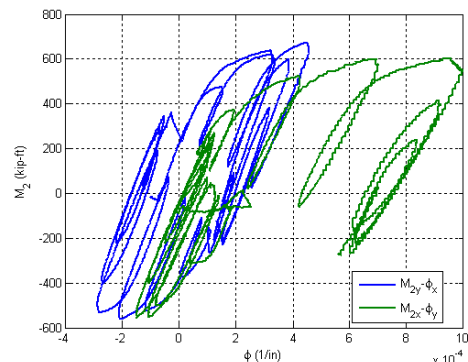
Lateral Force vs. Lateral Displacement



Base Moment vs. Top Displacement

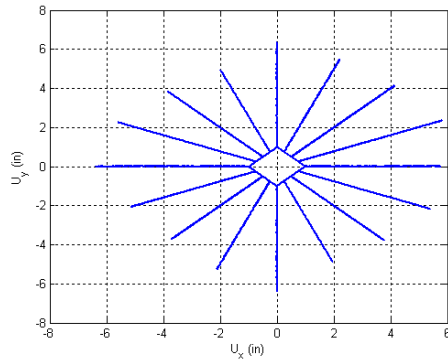


Base Moment vs. Top Rotation

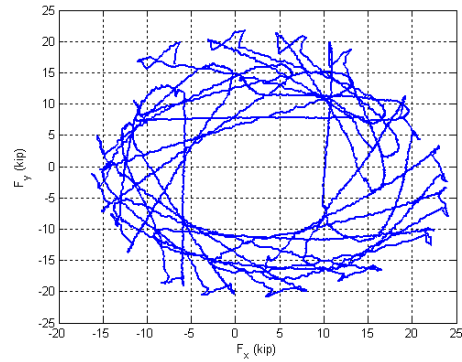


Base Moment vs. Base Curvature

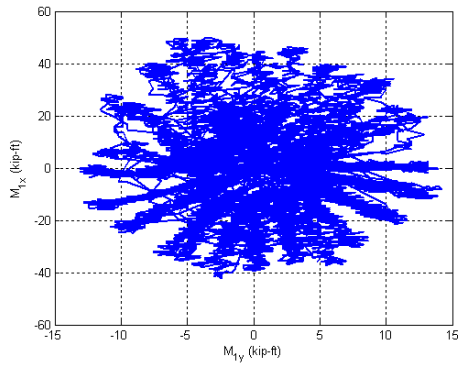
Figure B.20. Experimental results from LC3a in the specimen 3C20-18-5



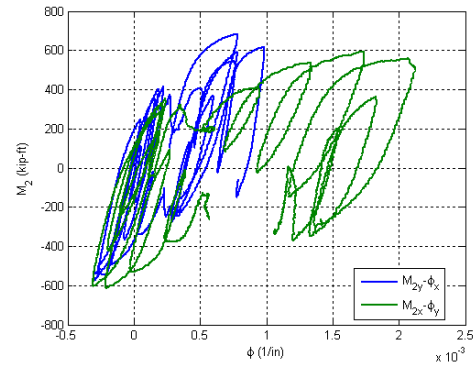
Y Displacement vs. X Displacement



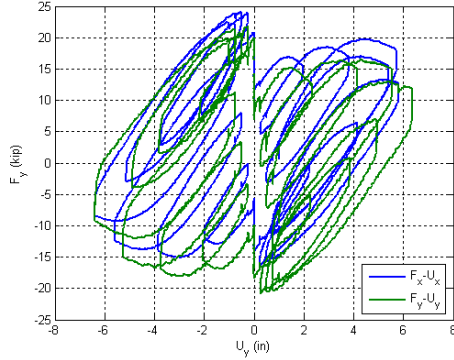
Y Force vs. X Force



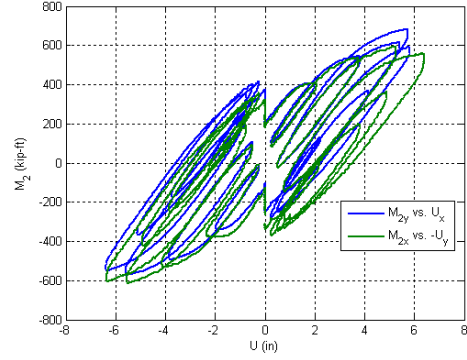
X Moment vs. Y Moment at the top



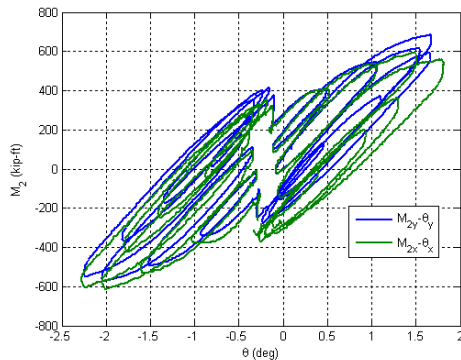
X Moment vs. Y Moment at the base



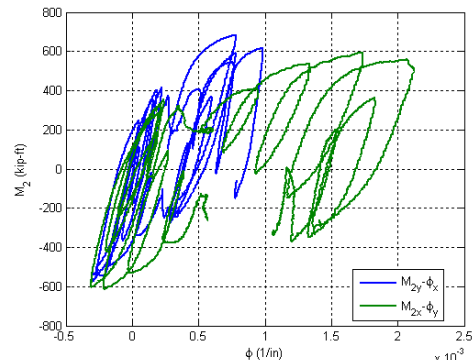
Lateral Force vs. Lateral Displacement



Base Moment vs. Top Displacement

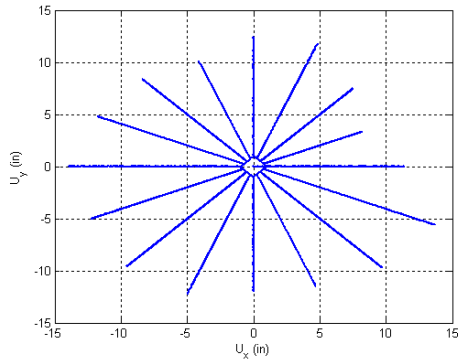


Base Moment vs. Top Rotation

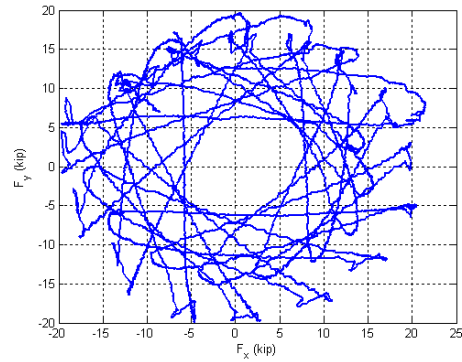


Base Moment vs. Base Curvature

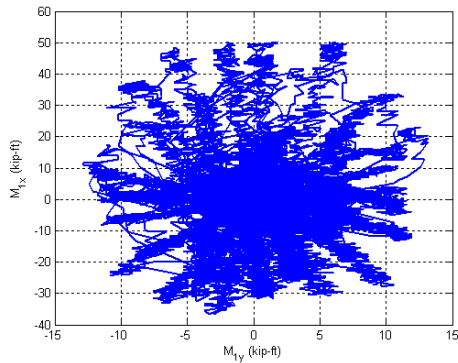
Figure B.21. Experimental results from LC3b in the specimen 3C20-18-5



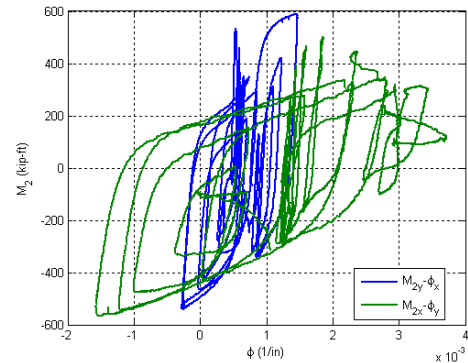
Y Displacement vs. X Displacement



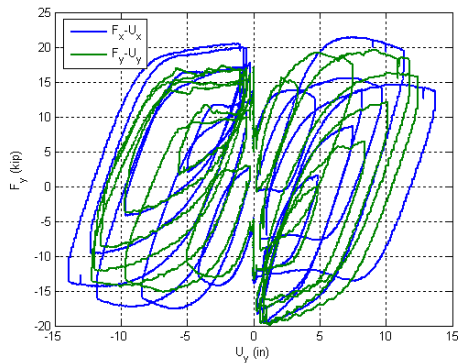
Y Force vs. X Force



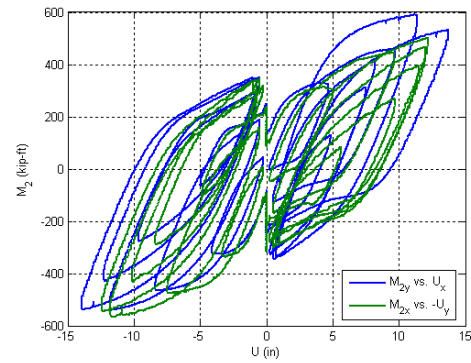
X Moment vs. Y Moment at the top



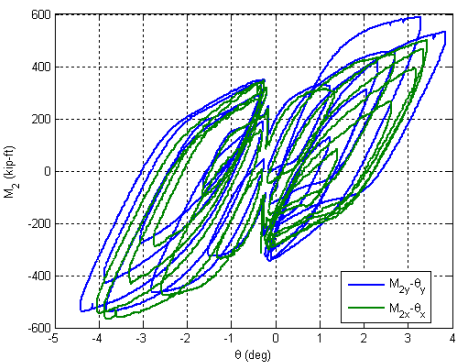
X Moment vs. Y Moment at the base



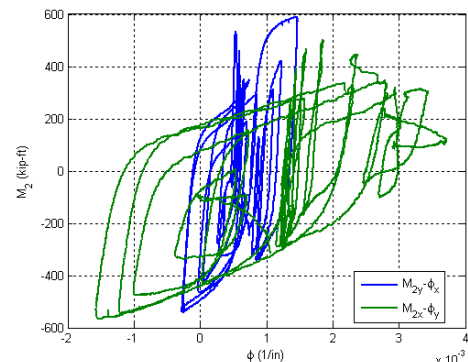
Lateral Force vs. Lateral Displacement



Base Moment vs. Top Displacement

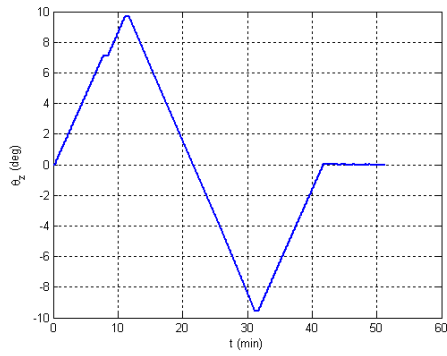


Base Moment vs. Top Rotation

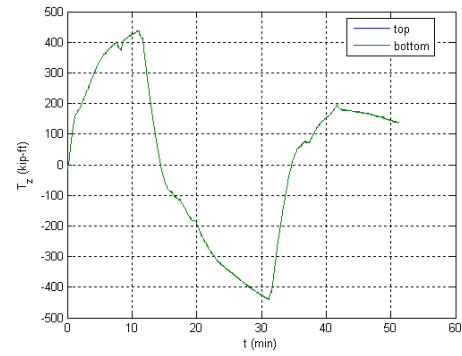


Base Moment vs. Base Curvature

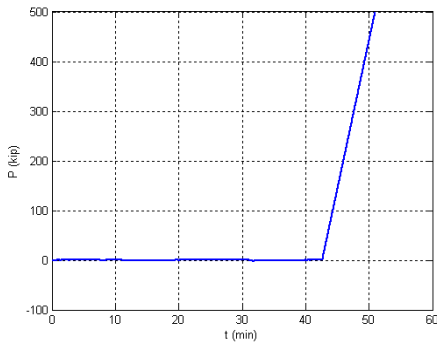
Figure B.22. Experimental results from LC3c in the specimen 3C20-18-5



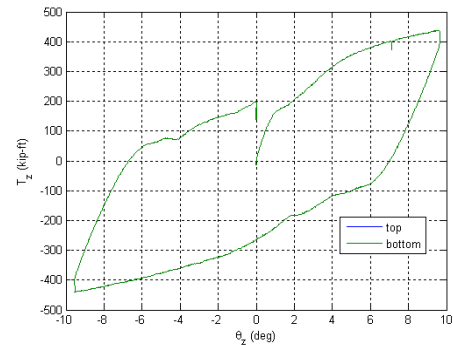
Twisting Angle vs. Time



Torsion Moment vs. Time

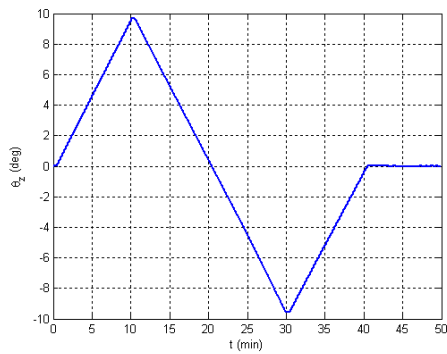


Axial Force vs. Time

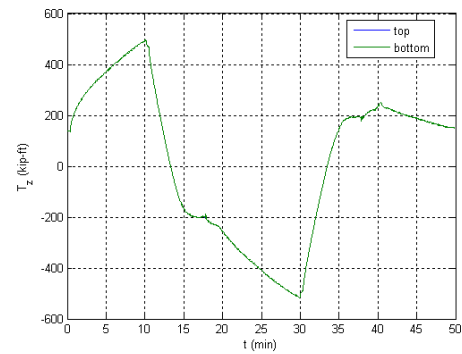


Torsion Moment vs. Twisting Angle

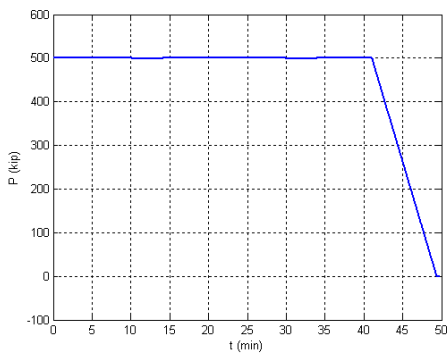
Figure B.23. Experimental results from LC4a in the specimen 3C20-18-5



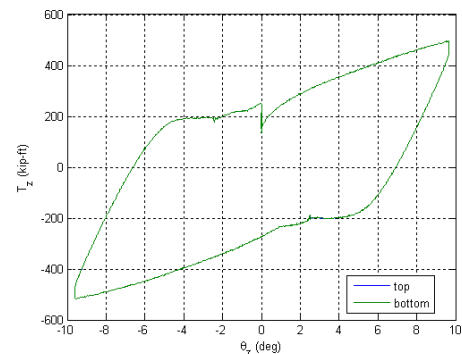
Twisting Angle vs. Time



Torsion Moment vs. Time

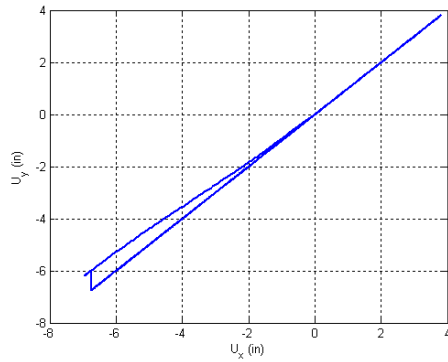


Axial Force vs. Time

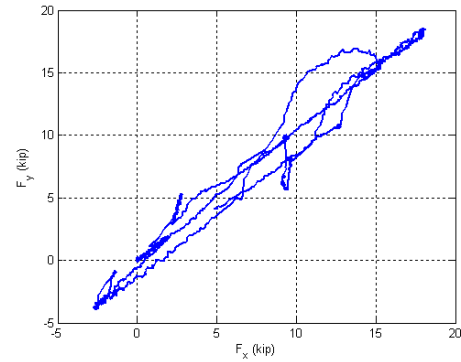


Torsion Moment vs. Twisting Angle

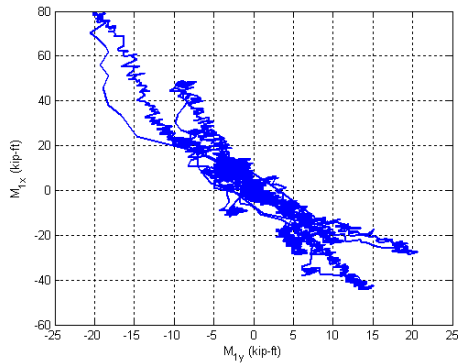
Figure B.24. Experimental results from LC4b in the specimen 3C20-18-5



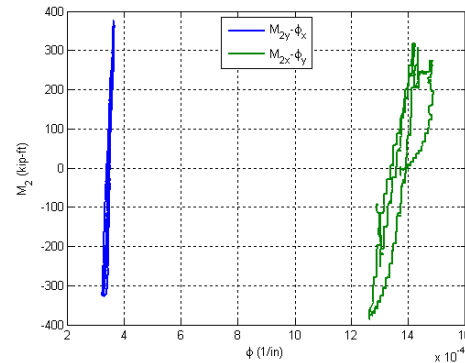
Y Displacement vs. X Displacement



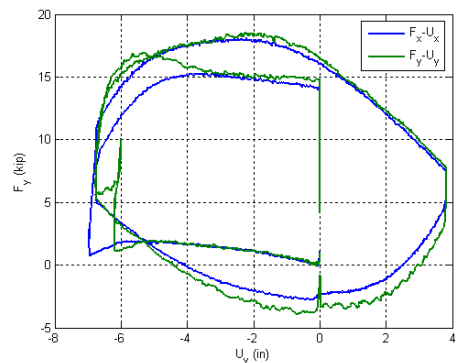
Y Force vs. X Force



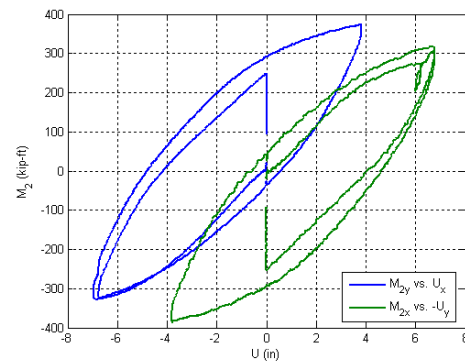
X Moment vs. Y Moment at the top



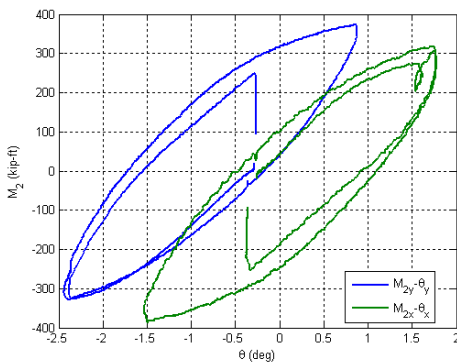
X Moment vs. Y Moment at the base



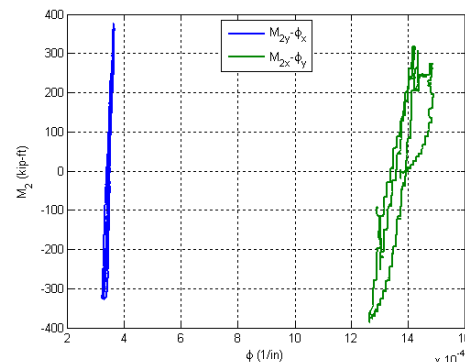
Lateral Force vs. Lateral Displacement



Base Moment vs. Top Displacement



Base Moment vs. Top Rotation



Base Moment vs. Base Curvature

Figure B.25. Experimental results from LC4c in the specimen 3C20-18-5

B.4. Specimen 4Rw-18-5

Description:

- Specimen number: 4
- Composite Cross-section: RCFT
- Steel cross-section: HSS20x12x0.25
- Design concrete strength: 5 ksi
- Design specimen length: 18 ft
- Pouring date: 06/27/2008
- Testing date: 11/12/2008

Parameters:

- Specimen length: 18' 2"
- Initial out-of-plumbness: $U_{xo} = 1.34'' / U_{yo} = 0.20''$
- Steel yielding stress: $F_y = 53.0$ ksi
- Steel ultimate stress: $F_u = 72.8$ ksi
- Concrete strength at the 28th day: $f_c' = 5.5$ ksi
- Concrete strength at the testing day: $f_c = 5.9$ ksi
- Concrete Young's modulus: $E_c = 4000$ ksi
- Concrete tensile strength: $f_t = 1.1$ ksi

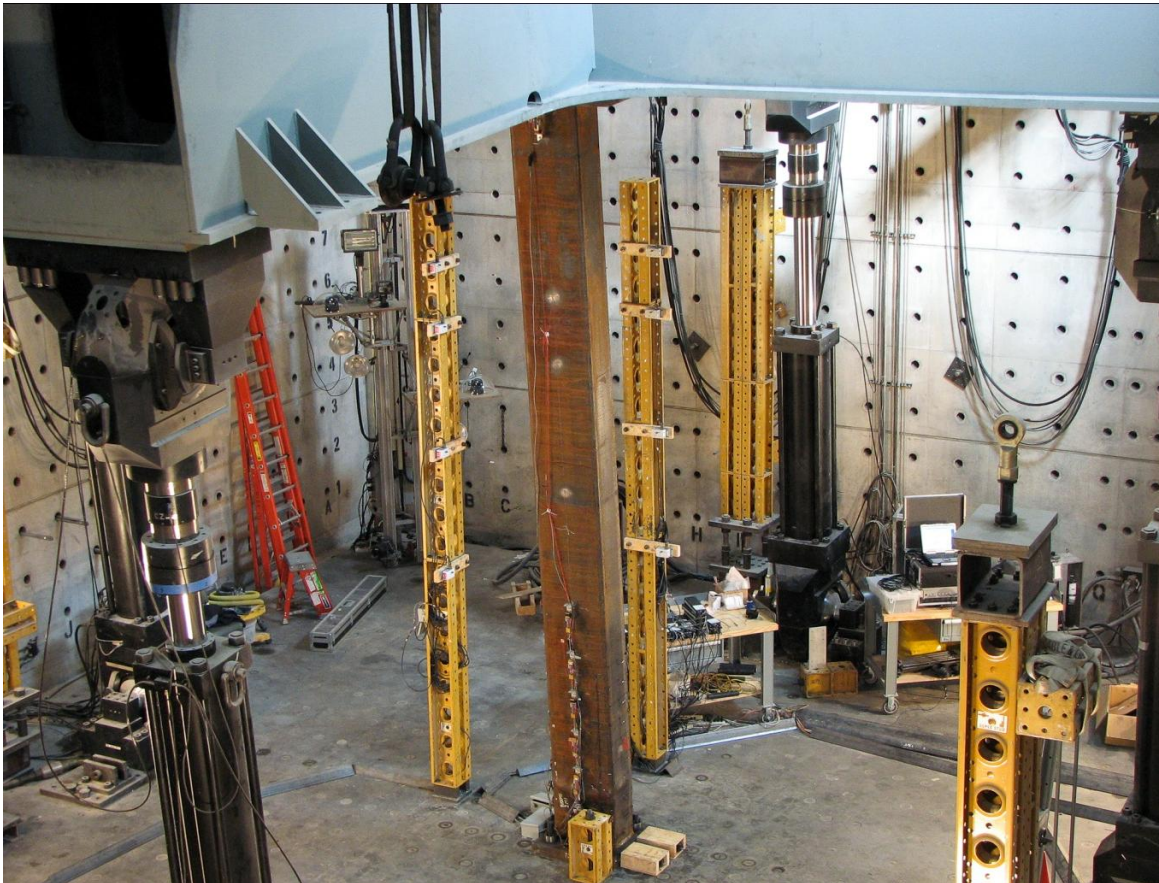


Figure B.26. Specimen 4Rw-18-5

Table B.4. Load protocol summary for the specimen 4Rw-18-5

LC1 - Incremental compression loading in three cycles until the maximum load is reached. The top is forced to be free at X asnd fixed at Y.

Step	DOF						Stop Criterion
	X	Y	Z	RX	RY	RZ	
1	$F_x = 0$	$U_y = 0$	$U_z \downarrow$	$R_x = 0$	$M_y = 0$	$R_z = 0$	max P
2	$F_x = 0$	$U_y = 0$	$U_z \uparrow$	$R_x = 0$	$M_y = 0$	$R_z = 0$	P = 0
3	$F_x = 0$	$U_y = 0$	$U_z \downarrow$	$R_x = 0$	$M_y = 0$	$R_z = 0$	max P
4	$F_x = 0$	$U_y = 0$	$U_z \uparrow$	$R_x = 0$	$M_y = 0$	$R_z = 0$	P = 0

LC2a - Cyclic uniaxial lateral displacements with constant compression force ($-F_z = P = 600$ kips). The top was forced to have zero moments.

Step	DOF						Stop Criterion
	X	Y	Z	RX	RY	RZ	
1	$U_x \downarrow$	$U_y = 0$	P = 600k	$R_x = 0$	$M_y = 0$	$R_z = 0$	+F peak
2	$U_x \uparrow$	$U_y = 0$	P = 600k	$R_x = 0$	$M_y = 0$	$R_z = 0$	-F peak
3	$U_x \downarrow$	$U_y = 0$	P = 600k	$R_x = 0$	$M_y = 0$	$R_z = 0$	+F peak
4	$U_x \uparrow$	$U_y = 0$	P = 600k	$R_x = 0$	$M_y = 0$	$R_z = 0$	-F peak
5	$U_x \uparrow$	$U_y = 0$	P = 600k	$R_x = 0$	$M_y = 0$	$R_z = 0$	$U_z = 0$

LC2b - Cyclic uniaxial lateral displacements with constant compression force ($-F_z = P = 300$ kips). The top was forced to have zero moments.

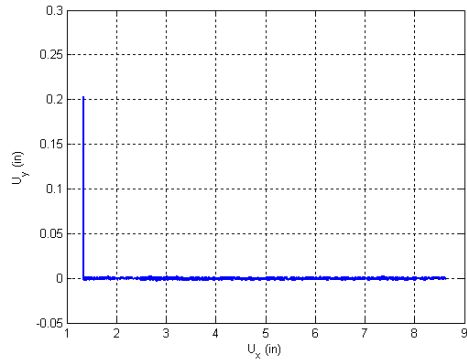
Step	DOF						Stop Criterion
	X	Y	Z	RX	RY	RZ	
1	$U_x \downarrow$	$U_y = 0$	P = 300k	$R_x = 0$	$M_y = 0$	$R_z = 0$	+F peak
2	$U_x \uparrow$	$U_y = 0$	P = 300k	$R_x = 0$	$M_y = 0$	$R_z = 0$	-F peak
3	$U_x \downarrow$	$U_y = 0$	P = 300k	$R_x = 0$	$M_y = 0$	$R_z = 0$	+F peak
4	$U_x \uparrow$	$U_y = 0$	P = 300k	$R_x = 0$	$M_y = 0$	$R_z = 0$	-F peak
5	$U_x \uparrow$	$U_y = 0$	P = 300k	$R_x = 0$	$M_y = 0$	$R_z = 0$	$U_z = 0$

LC3 - Cyclic biaxial lateral displacements (16 probes with diamond shape) with constant compression force ($-F_z = P = 750, 450$ and 150 kips). The top was forced to have zero moments.

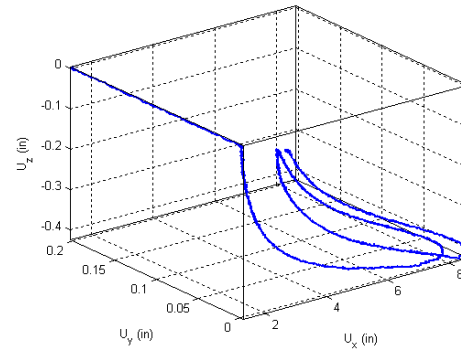
Step	DOF						Stop Criterion
	X	Y	Z	RX	RY	RZ	
1	$U_x \uparrow$	$U_y \uparrow$	P = 750k	$M_x = 0$	$M_y = 0$	$R_z = 0$	F peak at each of the 16 probes
2	$U_x \downarrow$	$U_y \downarrow$	P = 450k	$M_x = 0$	$M_y = 0$	$R_z = 0$	
3	$U_x \downarrow$	$U_y \downarrow$	P = 150k	$M_x = 0$	$M_y = 0$	$R_z = 0$	

LC4 - Torsion The top was twisted in displacement control.

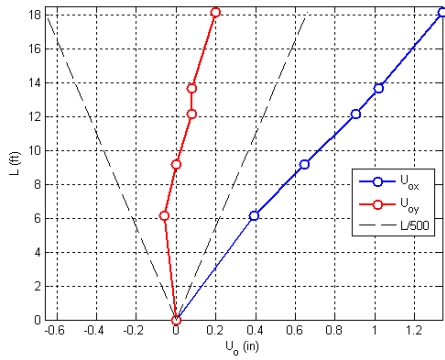
Step	DOF						Stop Criterion
	X	Y	Z	RX	RY	RZ	
1	$U_x = 0$	$U_y = 0$	P = 0	$R_x = 0$	$R_y = 0$	$R_z \downarrow$	+/-max. twist
2	$U_x = 0$	$U_y = 0$	P = 430k	$R_x = 0$	$R_y = 0$	$R_z \uparrow$	+/-max. twist



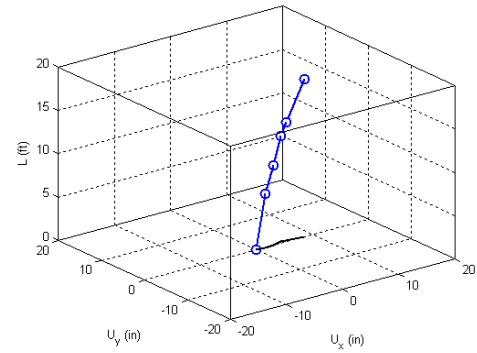
Y displacement vs. X displacement



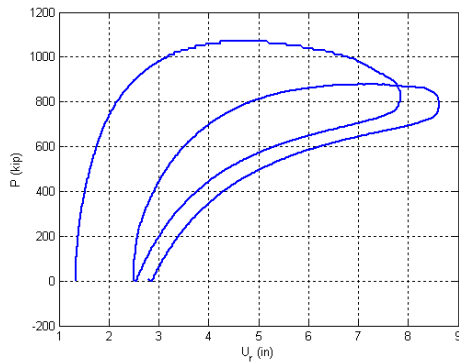
Z displacement vs. X and Y displacement



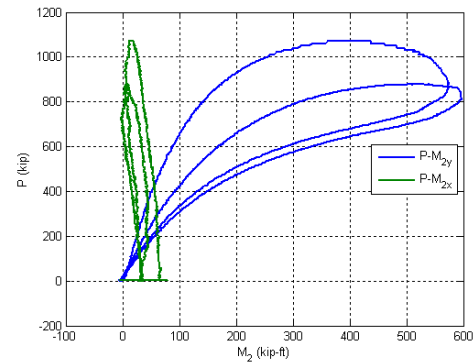
Initial deflected shape



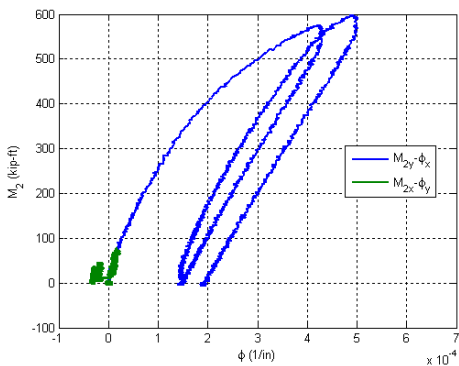
Maximum lateral displacement



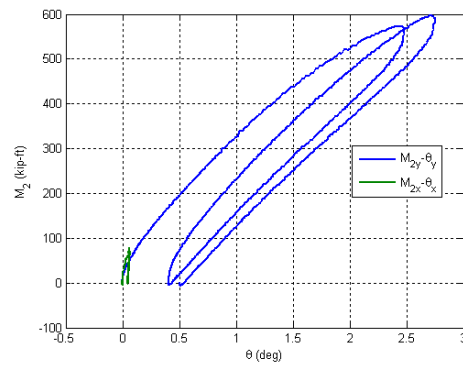
Axial force vs. lateral displacement



Axial force vs. base moments

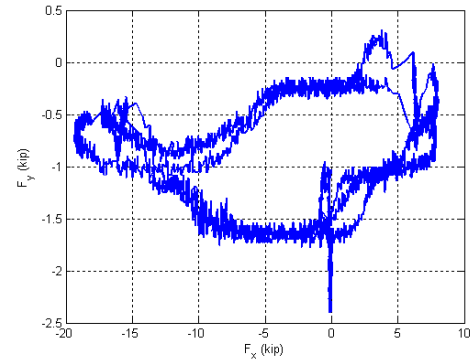
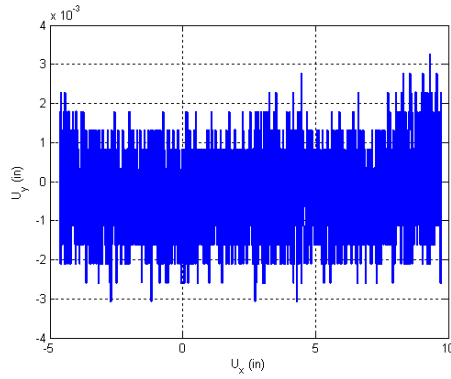


Base moment vs. base curvature

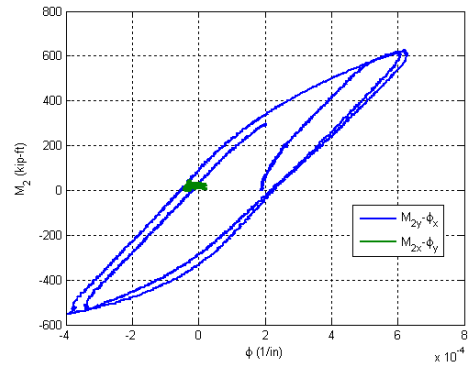
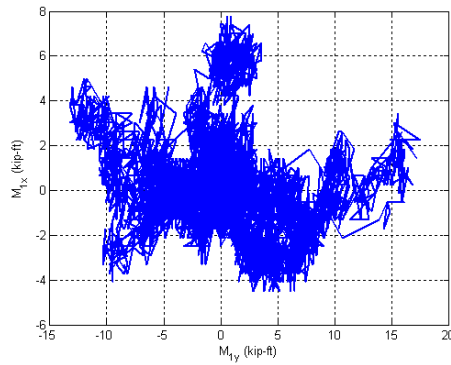


Base moment vs. top rotation

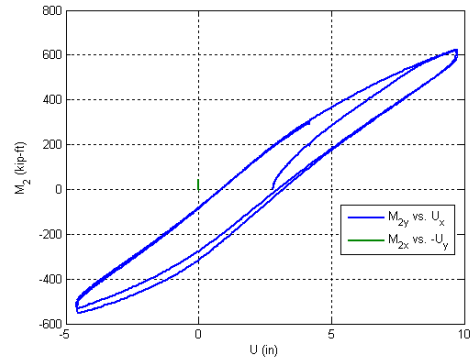
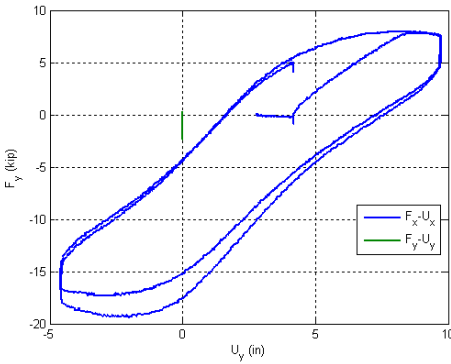
Figure B.27. Experimental results from LC1 in the specimen 4Rw-18-5



Y Displacement vs. X Displacement Y Force vs. X Force

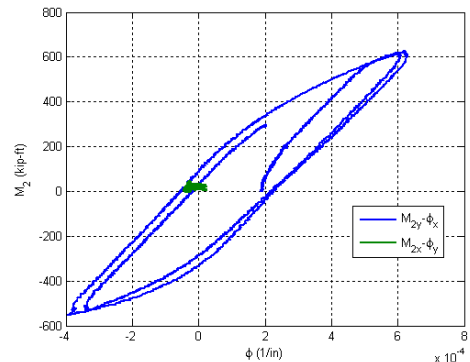
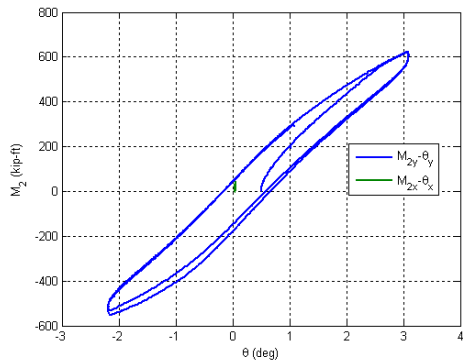


X Moment vs. Y Moment at the top X Moment vs. Y Moment at the base



Lateral Force vs. Lateral Displacement

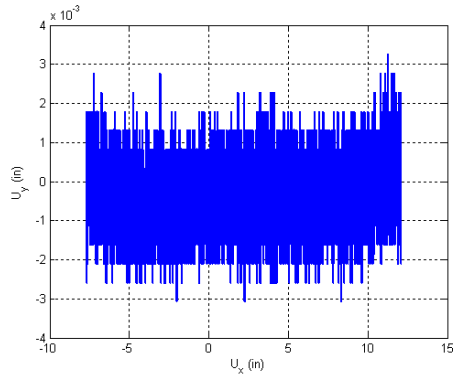
Base Moment vs. Top Displacement



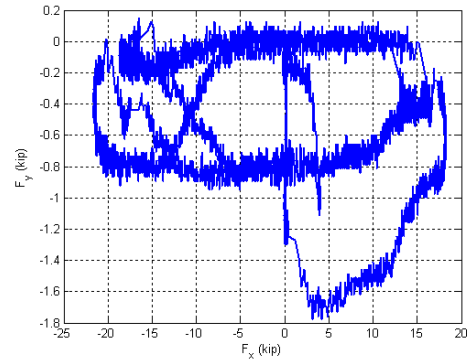
Base Moment vs. Top Rotation

Base Moment vs. Base Curvature

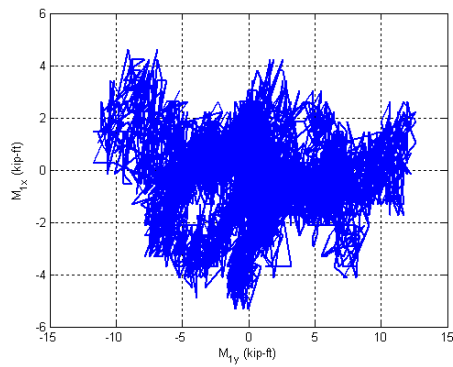
Figure B.28. Experimental results from LC2a in the specimen 4Rw-18-5



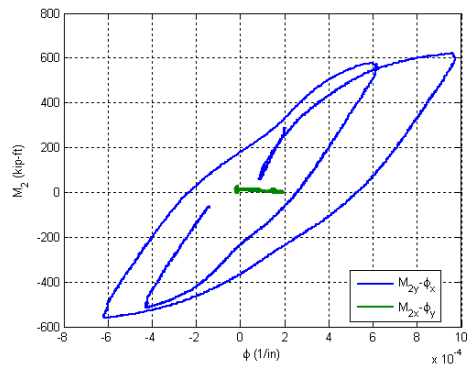
Y Displacement vs. X Displacement



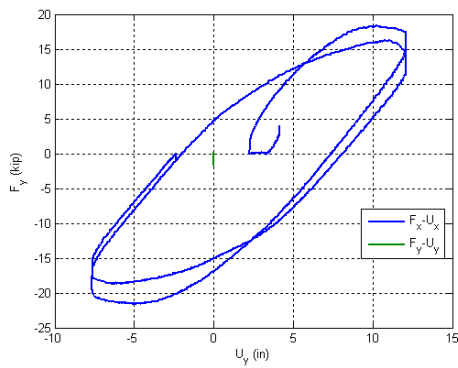
Y Force vs. X Force



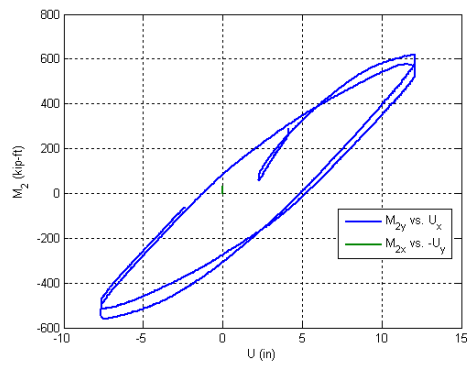
X Moment vs. Y Moment at the top



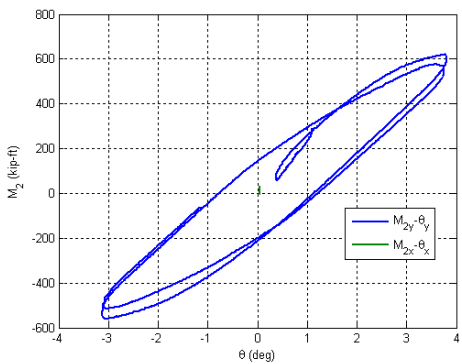
X Moment vs. Y Moment at the base



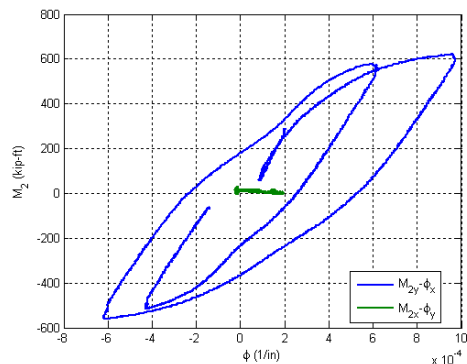
Lateral Force vs. Lateral Displacement



Base Moment vs. Top Displacement

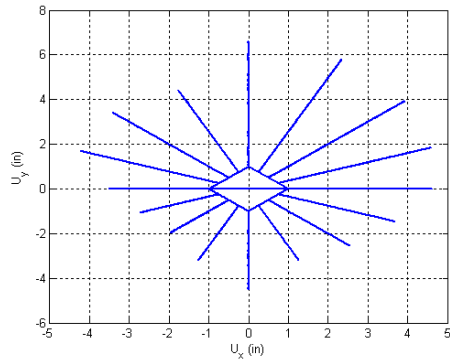


Base Moment vs. Top Rotation

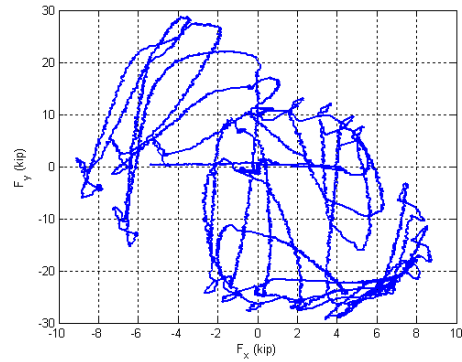


Base Moment vs. Base Curvature

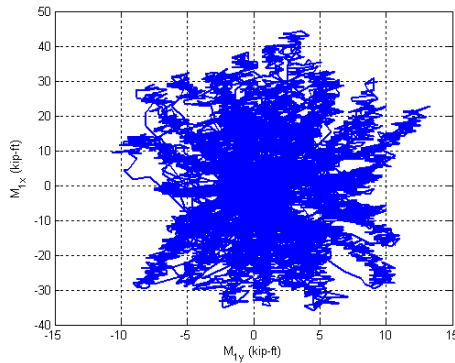
Figure B.29. Experimental results from LC2b in the specimen 4Rw-18-5



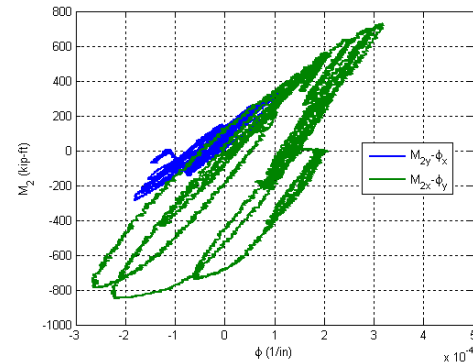
Y Displacement vs. X Displacement



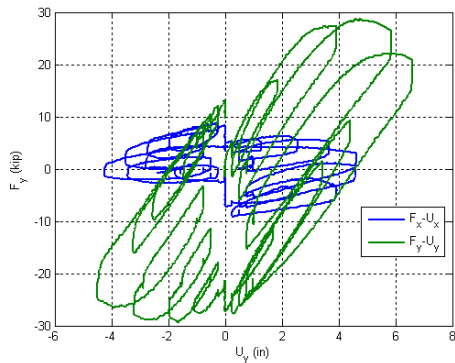
Y Force vs. X Force



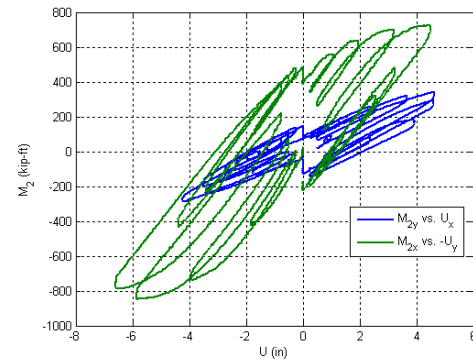
X Moment vs. Y Moment at the top



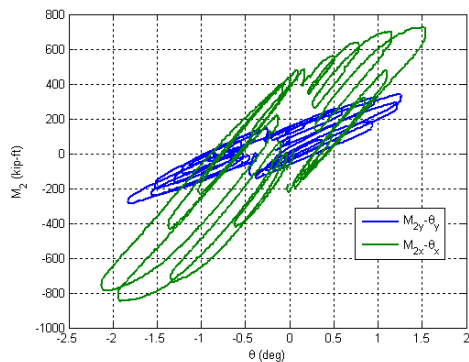
X Moment vs. Y Moment at the base



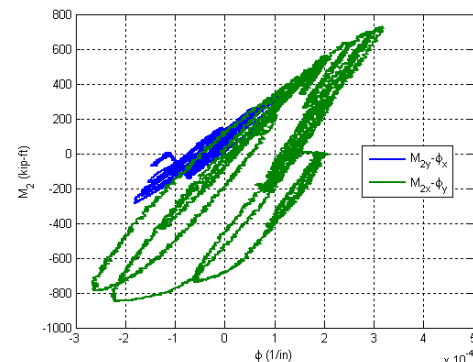
Lateral Force vs. Lateral Displacement



Base Moment vs. Top Displacement

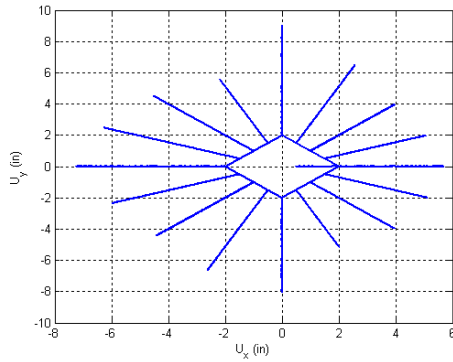


Base Moment vs. Top Rotation

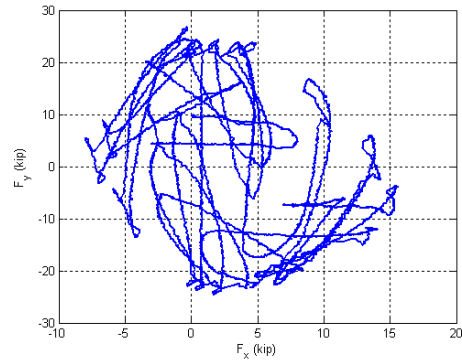


Base Moment vs. Base Curvature

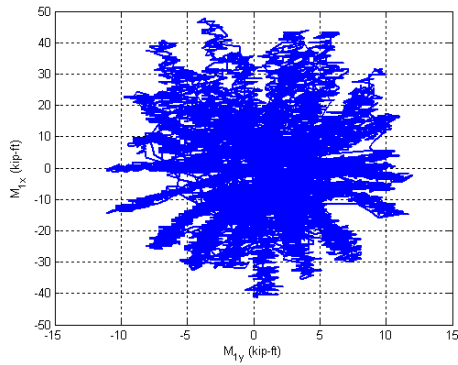
Figure B.30. Experimental results from LC3a in the specimen 4Rw-18-5



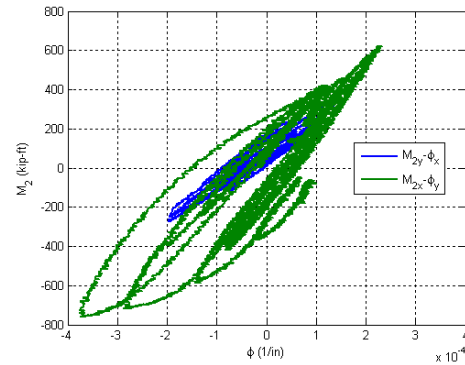
Y Displacement vs. X Displacement



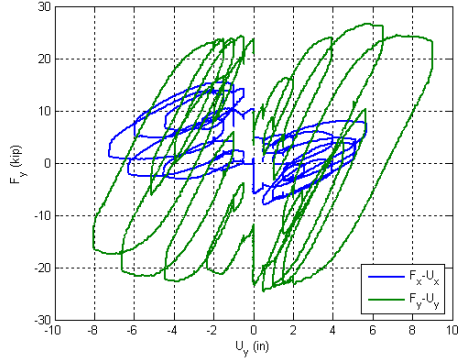
Y Force vs. X Force



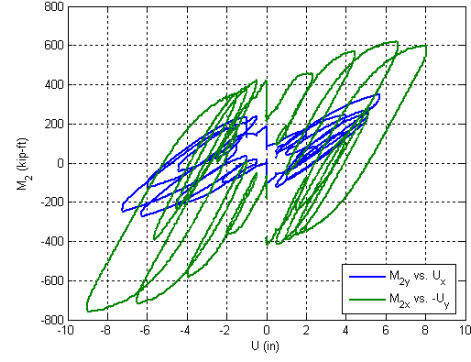
X Moment vs. Y Moment at the top



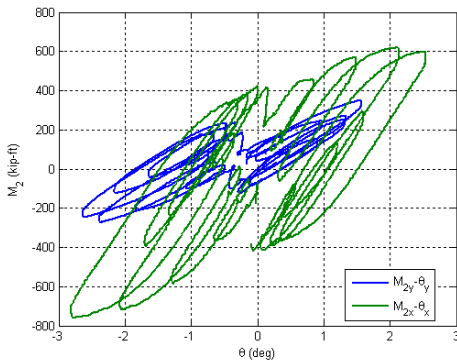
X Moment vs. Y Moment at the base



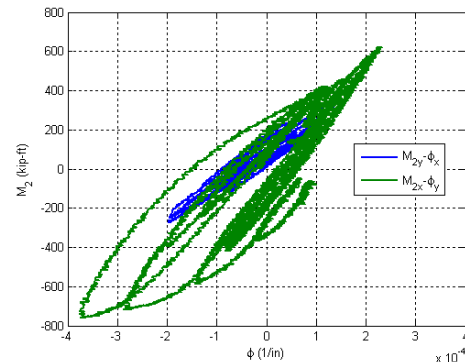
Lateral Force vs. Lateral Displacement



Base Moment vs. Top Displacement

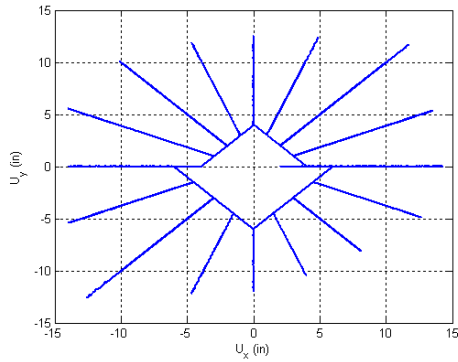


Base Moment vs. Top Rotation

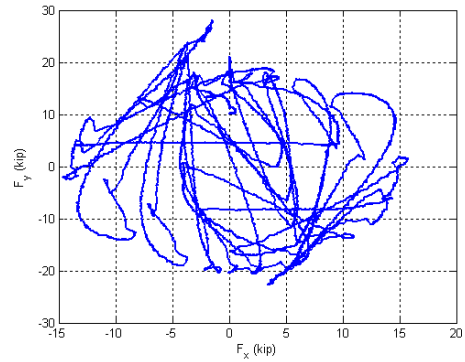


Base Moment vs. Base Curvature

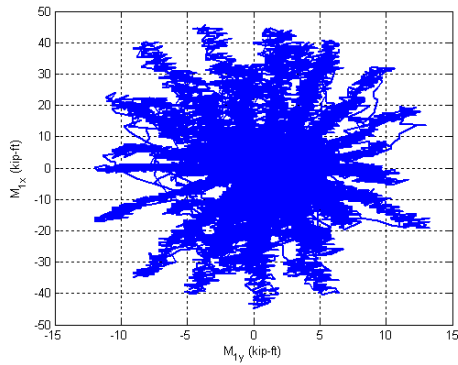
Figure B.31. Experimental results from LC3b in the specimen 4Rw-18-5



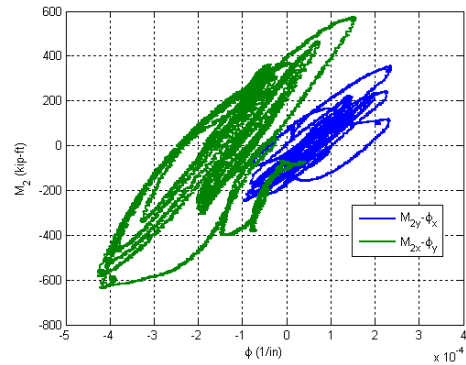
Y Displacement vs. X Displacement



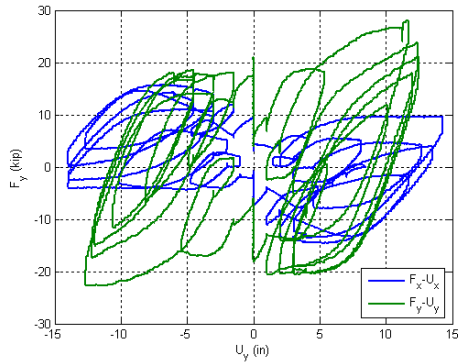
Y Force vs. X Force



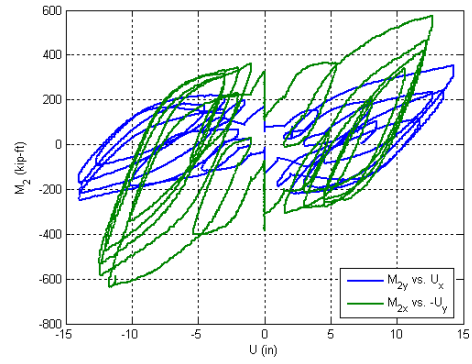
X Moment vs. Y Moment at the top



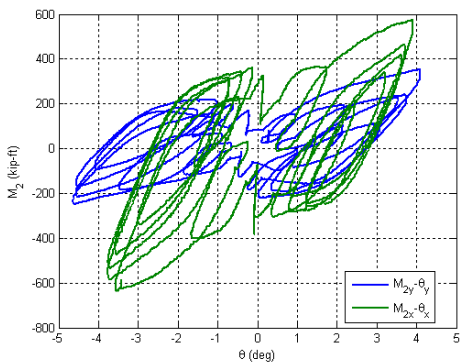
X Moment vs. Y Moment at the base



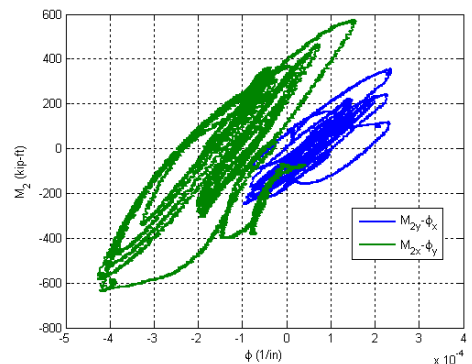
Lateral Force vs. Lateral Displacement



Base Moment vs. Top Displacement

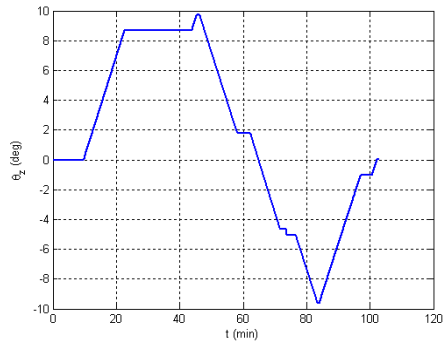


Base Moment vs. Top Rotation

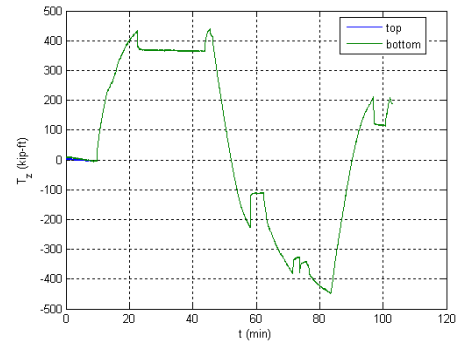


Base Moment vs. Base Curvature

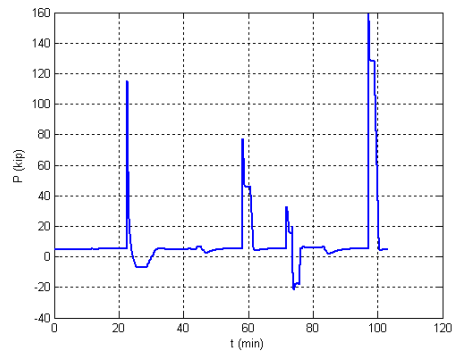
Figure B.32. Experimental results from LC3c in the specimen 4Rw-18-5



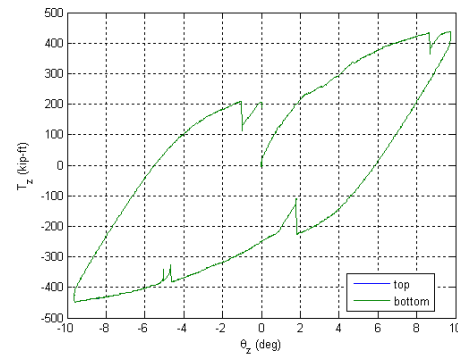
Twisting Angle vs. Time



Torsion Moment vs. Time

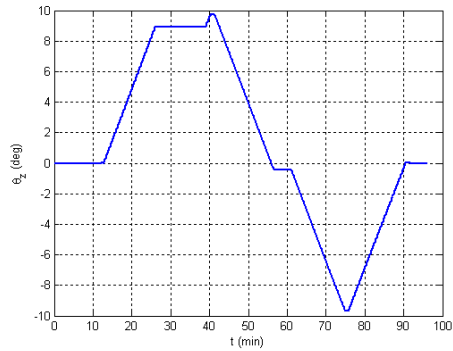


Axial Force vs. Time

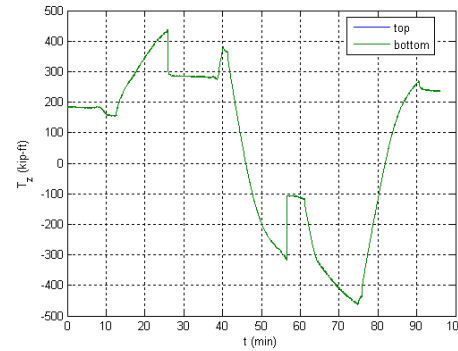


Torsion Moment vs. Twisting Angle

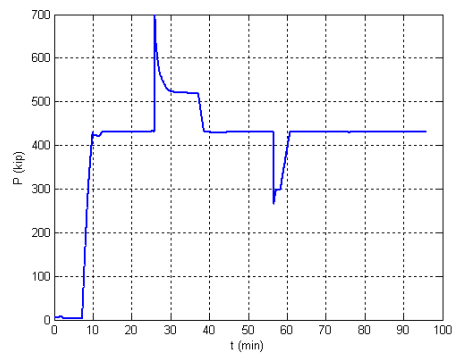
Figure B.33. Experimental results from LC4a in the specimen 4Rw-18-5



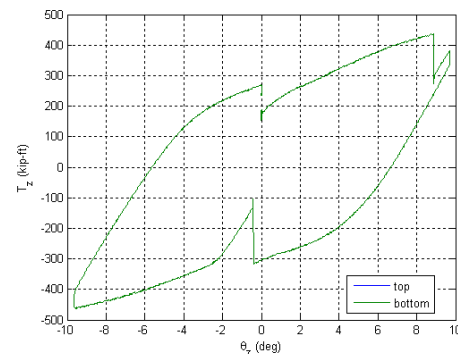
Twisting Angle vs. Time



Torsion Moment vs. Time

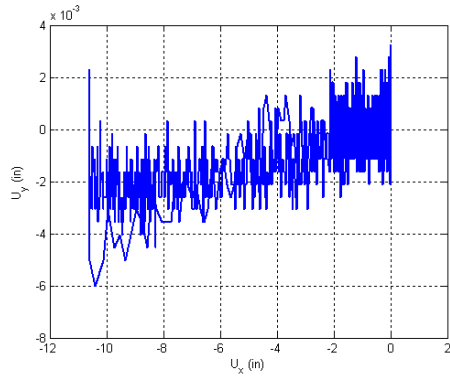


Axial Force vs. Time

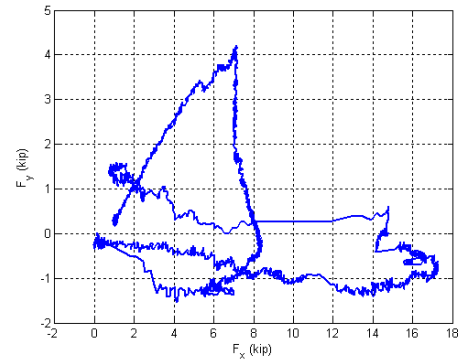


Torsion Moment vs. Twisting Angle

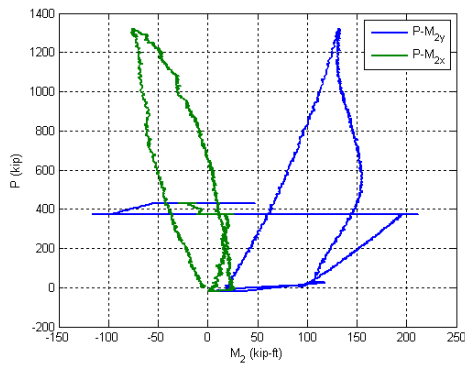
Figure B.34. Experimental results from LC4b in the specimen 4Rw-18-5



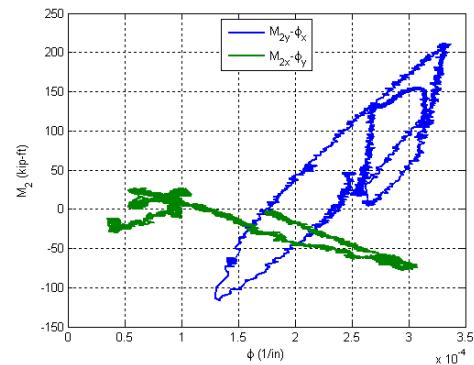
Y Displacement vs. X Displacement



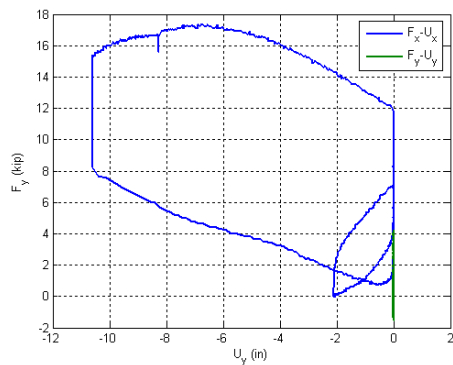
Y Force vs. X Force



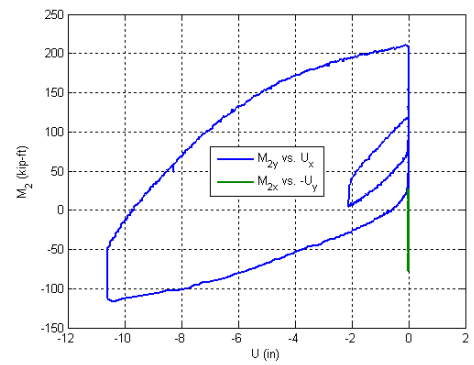
Axial force vs. base moments



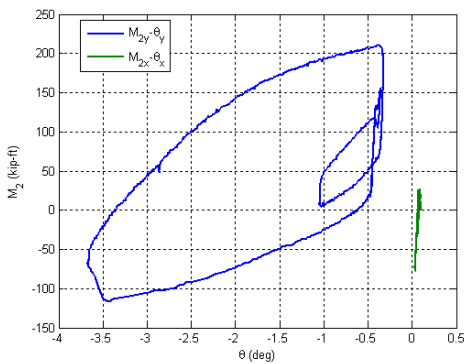
X Moment vs. Y Moment at the base



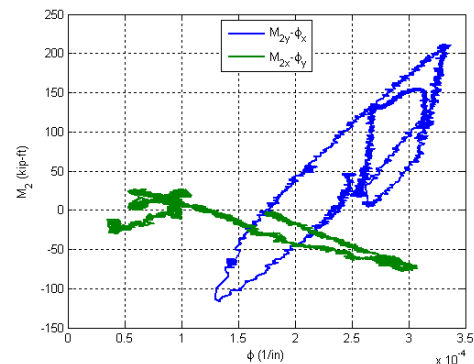
Lateral Force vs. Lateral Displacement



Base Moment vs. Top Displacement



Base Moment vs. Top Rotation



Base Moment vs. Base Curvature

Figure B.35. Experimental results from LC4c in the specimen 4Rw-18-5

B.5. Specimen 5Rs-18-5

Description:

- Specimen number: 5
- Composite Cross-section: RCFT
- Steel cross-section: HSS20x12x0.25
- Design concrete strength: 5 ksi
- Design specimen length: 18 ft
- Pouring date: 06/27/2008
- Testing date: 11/21/2008

Parameters:

- Specimen length: 18' 2"
- Initial out-of-plumbness: $U_{xo} = -0.08'' / U_{yo} = 0.45''$
- Steel yielding stress: $F_y = 53.0$ ksi
- Steel ultimate stress: $F_u = 72.8$ ksi
- Concrete strength at the 28th day: $f_c' = 5.5$ ksi
- Concrete strength at the testing day: $f_c = 5.9$ ksi
- Concrete Young's modulus: $E_c = 4000$ ksi
- Concrete tensile strength: $f_t = 1.1$ ksi

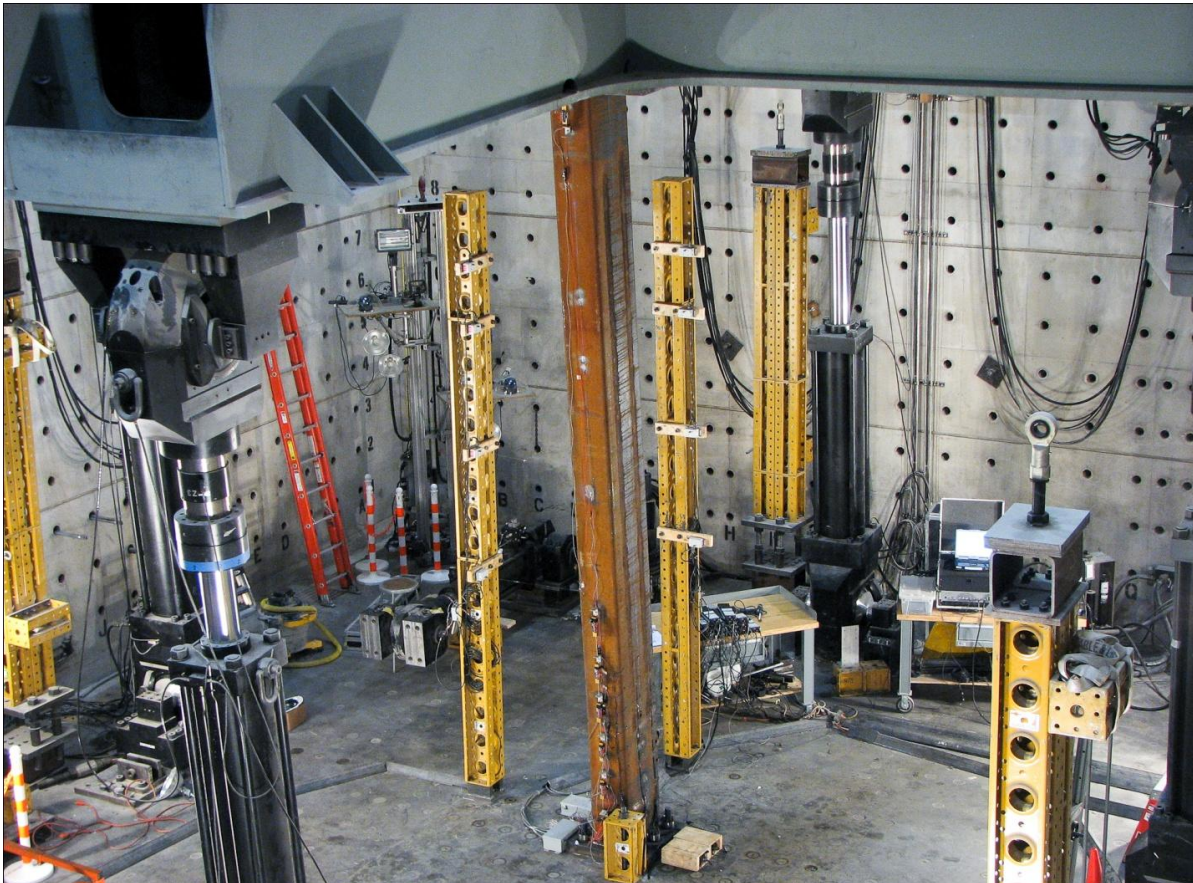


Figure B.36. Specimen 5Rs-18-5

Table B.5. Load protocol summary for the specimen 5Rs-18-5

LC1 - Incremental compression loading in three cycles until the maximum load is reached. The top is forced to be free at X asnd fixed at Y.

Step	DOF						Stop Criterion
	X	Y	Z	RX	RY	RZ	
1	$F_x = 0$	$U_y = 0$	$U_z \downarrow$	$R_x = 0$	$M_y = 0$	$R_z = 0$	max P
2	$F_x = 0$	$U_y = 0$	$U_z \uparrow$	$R_x = 0$	$M_y = 0$	$R_z = 0$	P = 0
3	$F_x = 0$	$U_y = 0$	$U_z \downarrow$	$R_x = 0$	$M_y = 0$	$R_z = 0$	max P
4	$F_x = 0$	$U_y = 0$	$U_z \uparrow$	$R_x = 0$	$M_y = 0$	$R_z = 0$	P = 0

LC2a - Cyclic uniaxial lateral displacements with constant compression force ($-F_z = P = 1000$ kips). The top was forced to have zero moments.

Step	DOF						Stop Criterion
	X	Y	Z	RX	RY	RZ	
1	$U_x \downarrow$	$U_y = 0$	P = 1000k	$R_x = 0$	$M_y = 0$	$R_z = 0$	+F peak
2	$U_x \uparrow$	$U_y = 0$	P = 1000k	$R_x = 0$	$M_y = 0$	$R_z = 0$	-F peak
3	$U_x \downarrow$	$U_y = 0$	P = 1000k	$R_x = 0$	$M_y = 0$	$R_z = 0$	+F peak
4	$U_x \uparrow$	$U_y = 0$	P = 1000k	$R_x = 0$	$M_y = 0$	$R_z = 0$	-F peak
5	$U_x \uparrow$	$U_y = 0$	P = 1000k	$R_x = 0$	$M_y = 0$	$R_z = 0$	$U_z = 0$

LC2b - Cyclic uniaxial lateral displacements with constant compression force ($-F_z = P = 500$ kips). The top was forced to have zero moments.

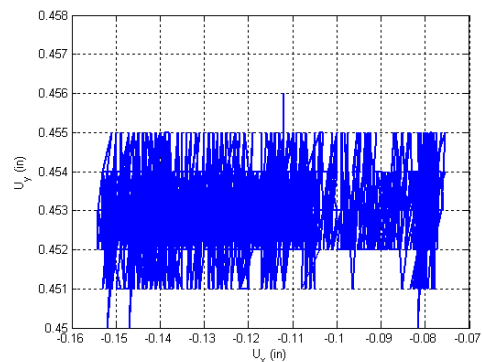
Step	DOF						Stop Criterion
	X	Y	Z	RX	RY	RZ	
1	$U_x \downarrow$	$U_y = 0$	P = 500k	$R_x = 0$	$M_y = 0$	$R_z = 0$	+F peak
2	$U_x \uparrow$	$U_y = 0$	P = 500k	$R_x = 0$	$M_y = 0$	$R_z = 0$	-F peak
3	$U_x \downarrow$	$U_y = 0$	P = 500k	$R_x = 0$	$M_y = 0$	$R_z = 0$	+F peak
4	$U_x \uparrow$	$U_y = 0$	P = 500k	$R_x = 0$	$M_y = 0$	$R_z = 0$	-F peak
5	$U_x \uparrow$	$U_y = 0$	P = 500k	$R_x = 0$	$M_y = 0$	$R_z = 0$	$U_z = 0$

LC3 - Cyclic biaxial lateral displacements (8 probes with diamond shape) with constant compression force ($-F_z = P = 750$ and 250 kips). The top was forced to have zero moments.

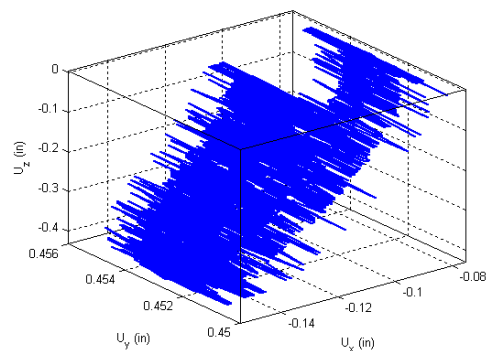
Step	DOF						Stop Criterion
	X	Y	Z	RX	RY	RZ	
1	$U_x \uparrow$	$U_y \uparrow$	P = 750k	$M_x = 0$	$M_y = 0$	$R_z = 0$	F peak at each of the 8 probes
2	$U_x \uparrow$	$U_y \uparrow$	P = 250k	$M_x = 0$	$M_y = 0$	$R_z = 0$	

LC4 - Torsion The top was twisted in displacement control.

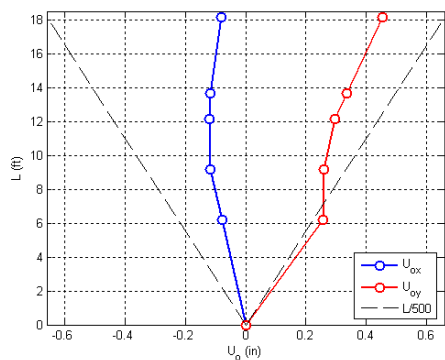
Step	DOF						Stop Criterion
	X	Y	Z	RX	RY	RZ	
1	$U_x = 0$	$U_y = 0$	P = 0	$R_x = 0$	$R_y = 0$	$R_z \uparrow$	+/-max. twist
2	$U_x = 0$	$U_y = 0$	P = 450k	$R_x = 0$	$R_y = 0$	$R_z \uparrow$	+/-max. twist



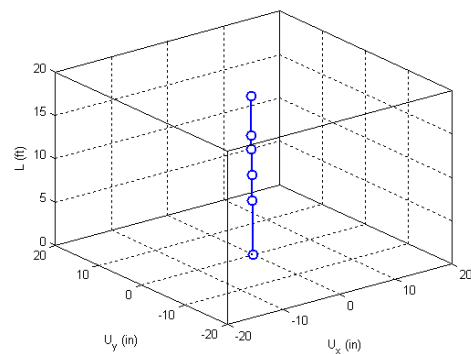
Y displacement vs. X displacement



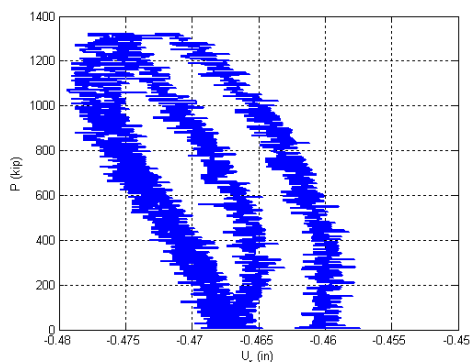
Z displacement vs. X and Y displacement



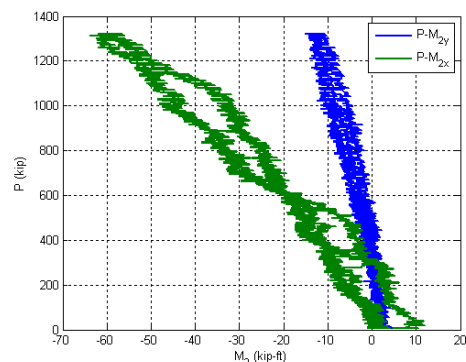
Initial deflected shape



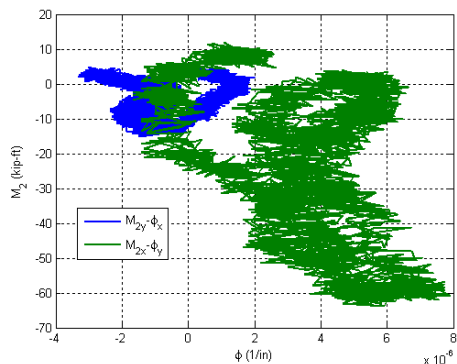
Maximum lateral displacement



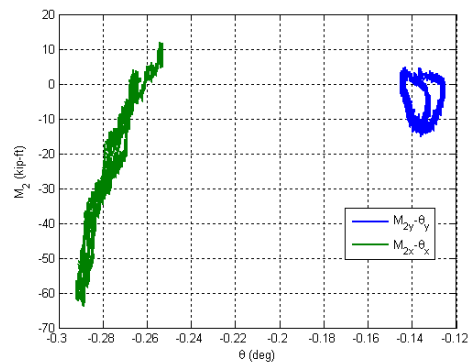
Axial force vs. lateral displacement



Axial force vs. base moments

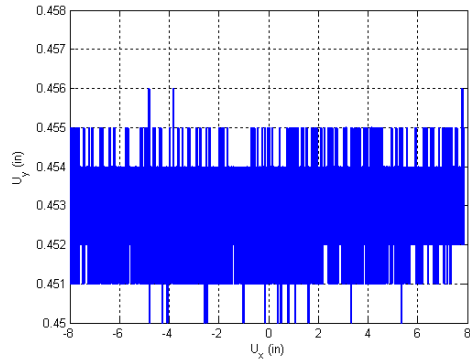


Base moment vs. base curvature

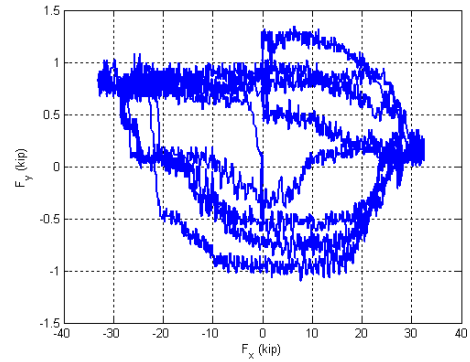


Base moment vs. top rotation

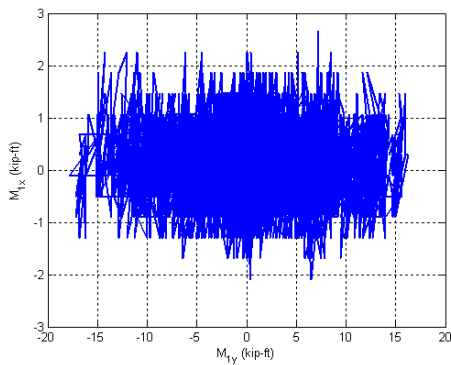
Figure B.37. Experimental results from LC1 in the specimen 5Rs-18-5



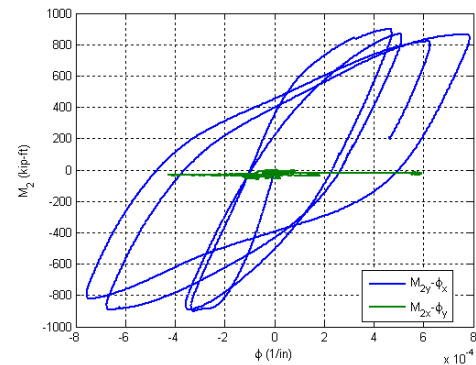
Y Displacement vs. X Displacement



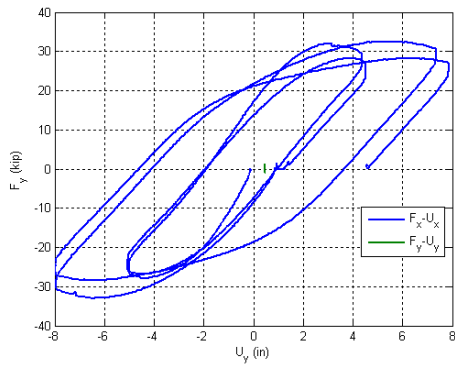
Y Force vs. X Force



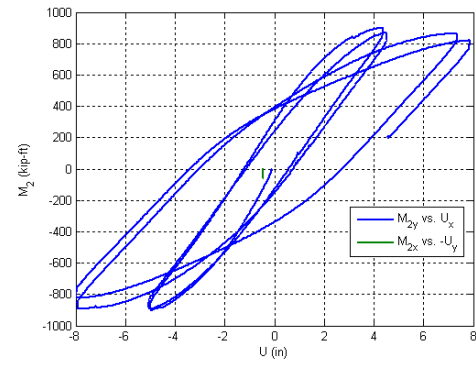
X Moment vs. Y Moment at the top



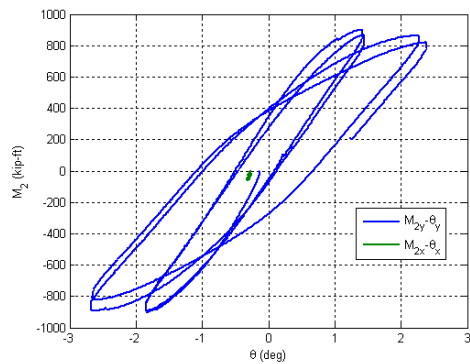
X Moment vs. Y Moment at the base



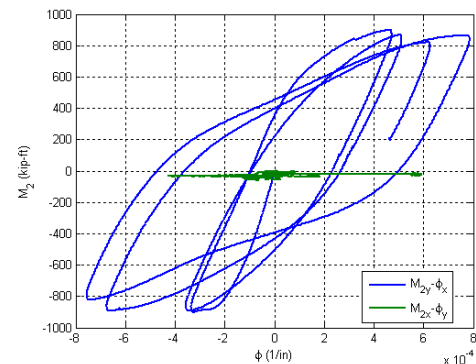
Lateral Force vs. Lateral Displacement



Base Moment vs. Top Displacement

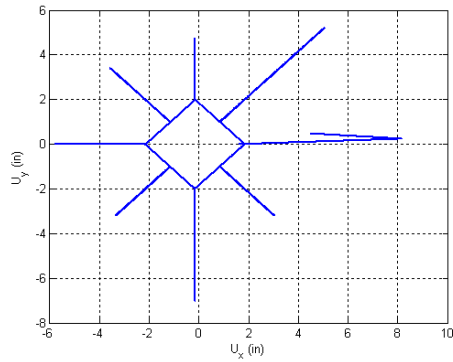


Base Moment vs. Top Rotation

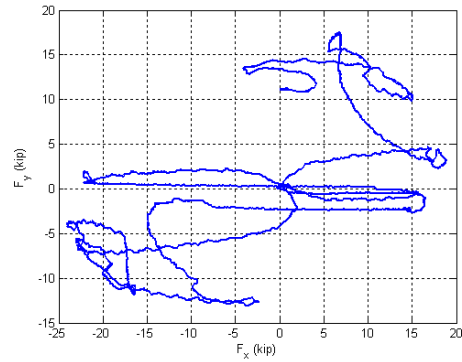


Base Moment vs. Base Curvature

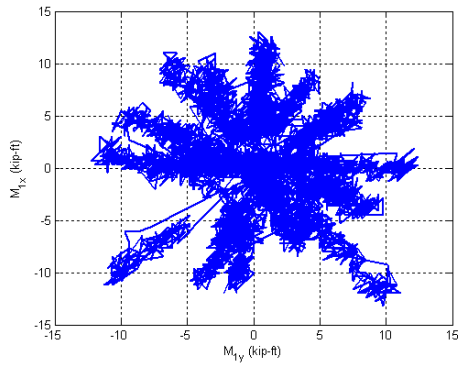
Figure B.38. Experimental results from LC2 in the specimen 5Rs-18-5



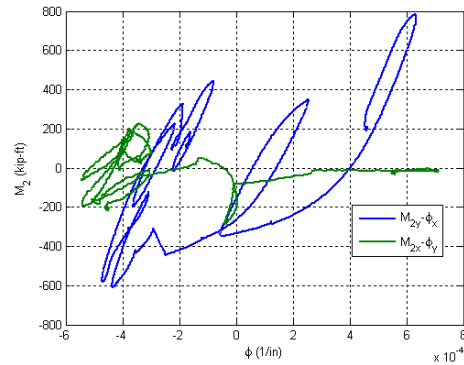
Y Displacement vs. X Displacement



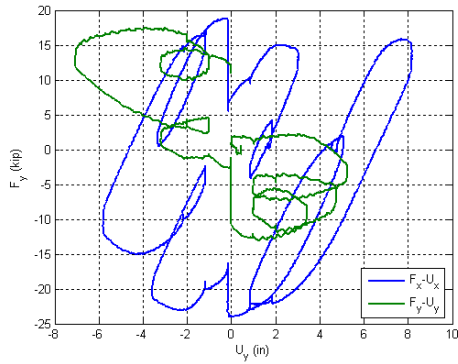
Y Force vs. X Force



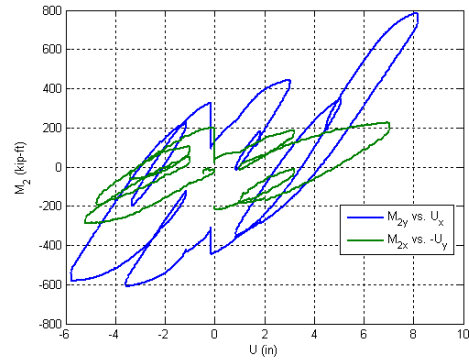
X Moment vs. Y Moment at the top



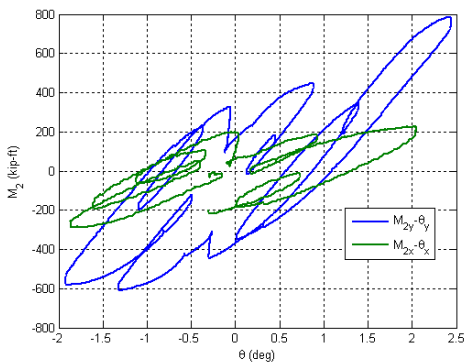
X Moment vs. Y Moment at the base



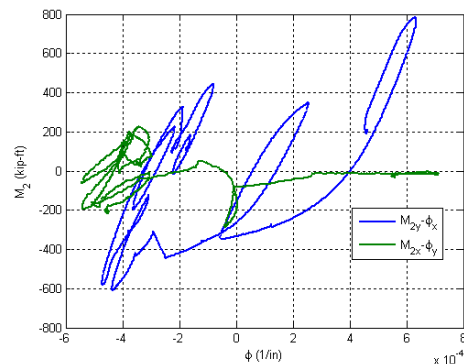
Lateral Force vs. Lateral Displacement



Base Moment vs. Top Displacement

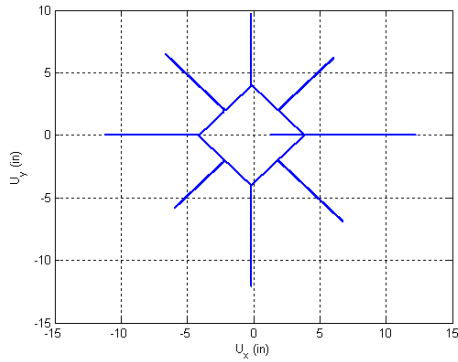


Base Moment vs. Top Rotation

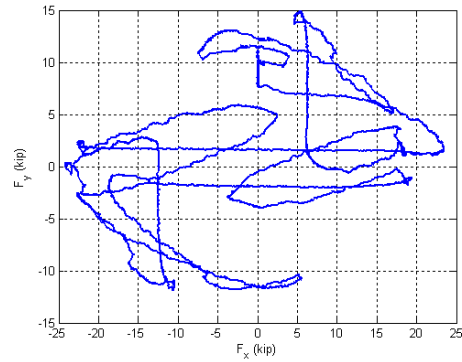


Base Moment vs. Base Curvature

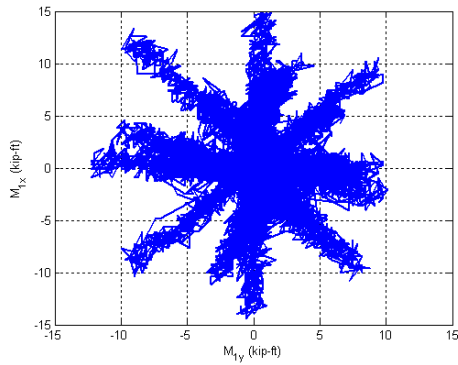
Figure B.39. Experimental results from LC3a in the specimen 5Rs-18-5



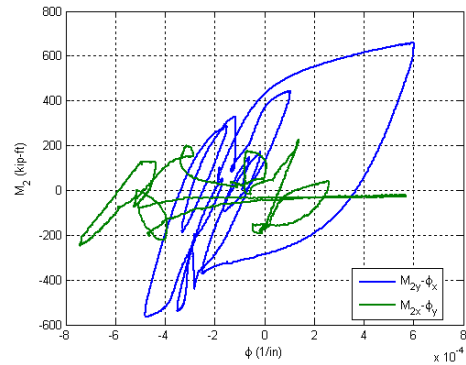
Y Displacement vs. X Displacement



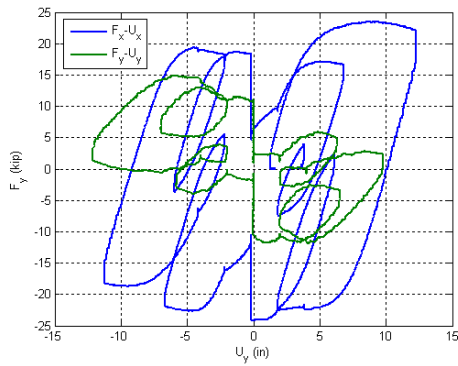
Y Force vs. X Force



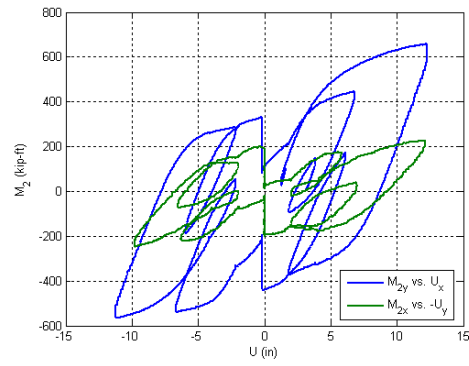
X Moment vs. Y Moment at the top



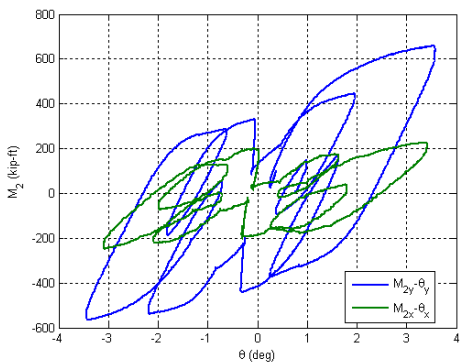
X Moment vs. Y Moment at the base



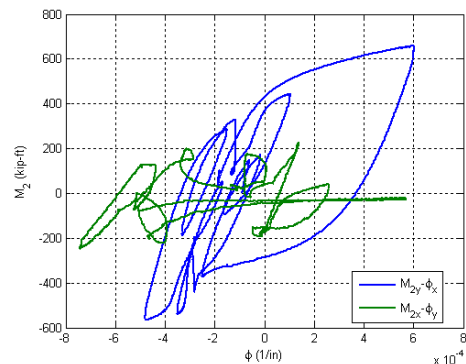
Lateral Force vs. Lateral Displacement



Base Moment vs. Top Displacement

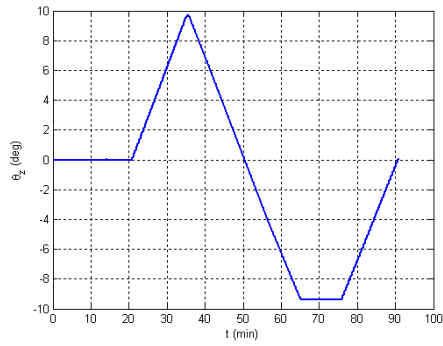


Base Moment vs. Top Rotation

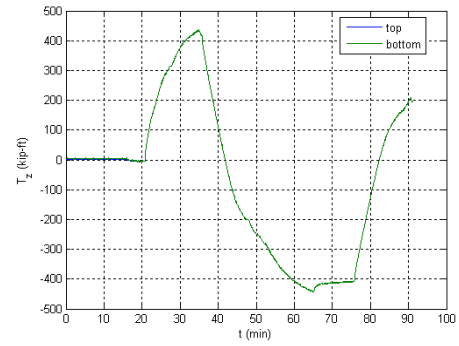


Base Moment vs. Base Curvature

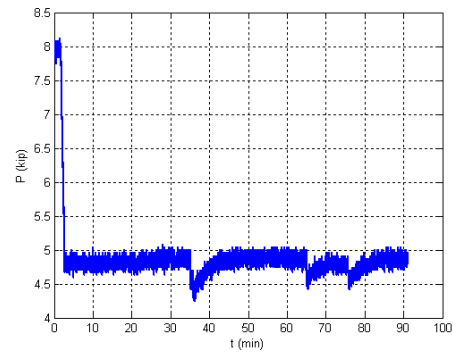
Figure B.40. Experimental results from LC3b in the specimen 5Rs-18-5



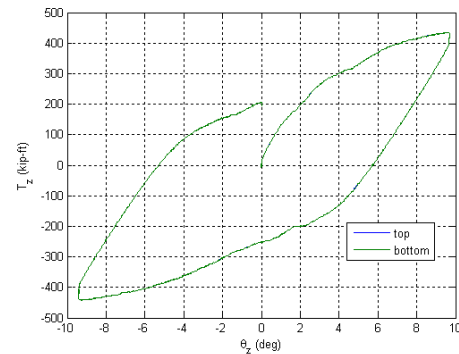
Twisting Angle vs. Time



Torsion Moment vs. Time

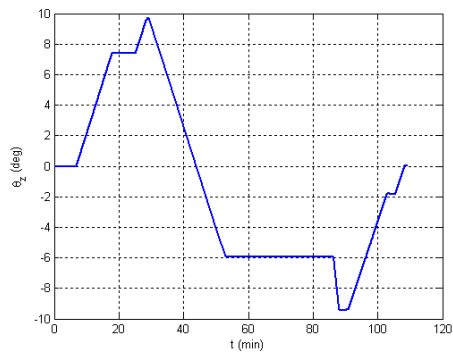


Axial Force vs. Time

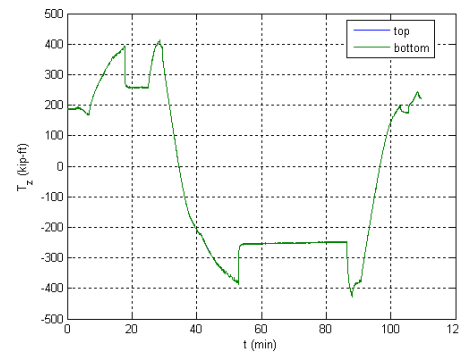


Torsion Moment vs. Twisting Angle

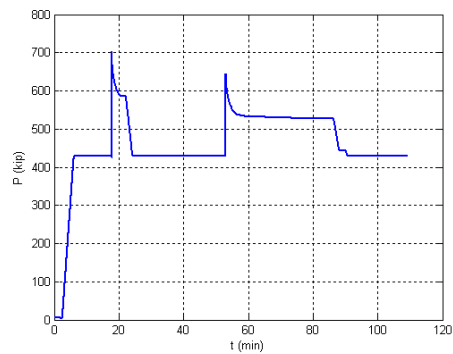
Figure B.41. Experimental results from LC4a in the specimen 5Rs-18-5



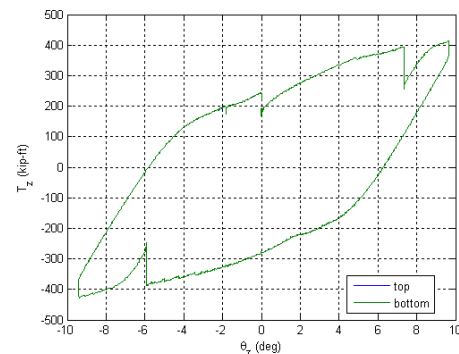
Twisting Angle vs. Time



Torsion Moment vs. Time

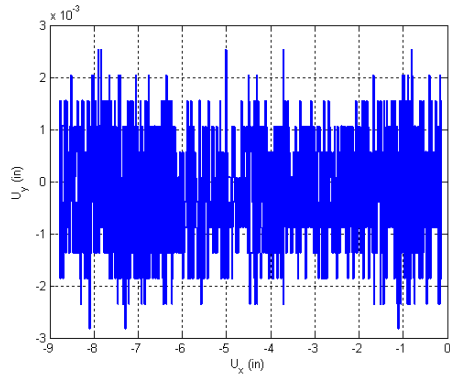


Axial Force vs. Time

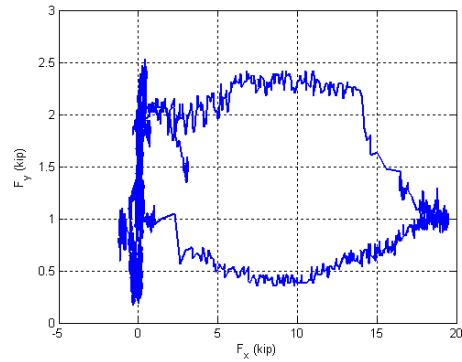


Torsion Moment vs. Twisting Angle

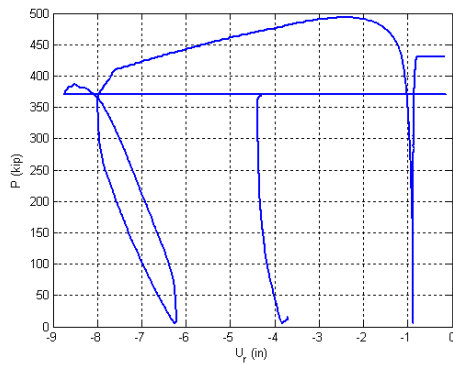
Figure B.42. Experimental results from LC4b in the specimen 5Rs-18-5



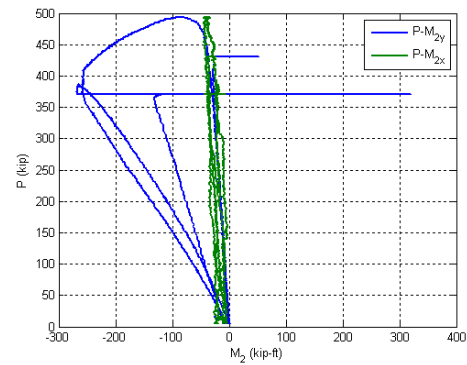
Y Displacement vs. X Displacement



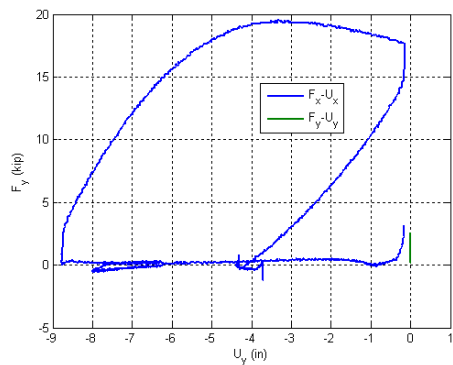
Y Force vs. X Force



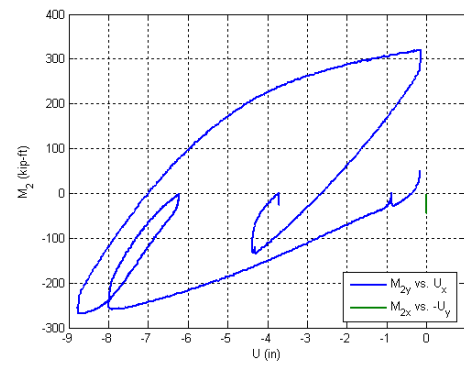
Axial force vs. lateral displacement



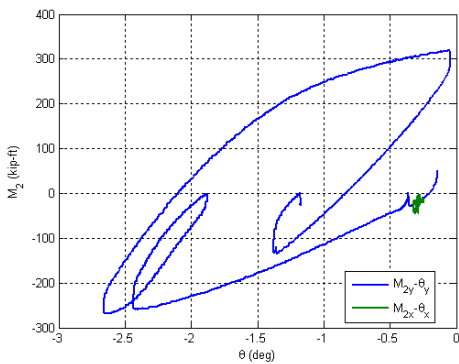
Axial force vs. base moments



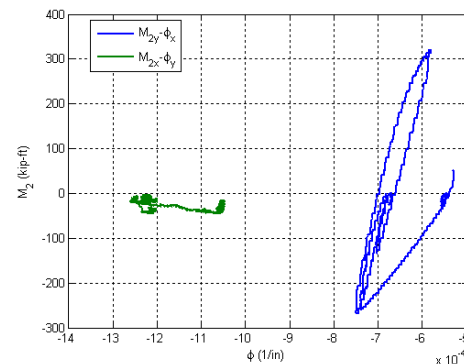
Lateral Force vs. Lateral Displacement



Base Moment vs. Top Displacement



Base Moment vs. Top Rotation



Base Moment vs. Base Curvature

Figure B.43. Experimental results from LC4c in the specimen 5Rs-18-5

B.6. Specimen 6C12-18-12

Description:

- Specimen number: 6
- Composite Cross-section: CCFT
- Steel cross-section: HSS12.75x0.25
- Design concrete strength: 12 ksi
- Design specimen length: 18 ft
- Pouring date: 09/17/2008
- Testing date: 12/04/2008

Parameters:

- Specimen length: 18' 1/2"
- Initial out-of-plumbness: $U_{xo} = 0.36'' / U_{yo} = -0.24''$
- Steel yielding stress: $F_y = 48.9$ ksi
- Steel ultimate stress: $F_u = 64.7$ ksi
- Concrete strength at the 28th day: $f_c' = 12.7$ ksi
- Concrete strength at the testing day: $f_c = 13.2$ ksi
- Concrete Young's modulus: $E_c = 6070$ ksi
- Concrete tensile strength: $f_t = 1.65$ ksi



Figure B.44. Specimen 6C12-18-12

Table B.6. Load protocol summary for the specimen 6C12-18-12

LC1 - Incremental compression loading in three cycles until the maximum load is reached. The top is forced to be free at all the time.

Step	DOF						Stop Criterion
	X	Y	Z	RX	RY	RZ	
1	$F_x = 0$	$F_y = 0$	$U_z \downarrow$	$M_x = 0$	$M_y = 0$	$R_z = 0$	max P
2	$F_x = 0$	$F_y = 0$	$U_z \uparrow$	$M_x = 0$	$M_y = 0$	$R_z = 0$	P = 0
3	$F_x = 0$	$F_y = 0$	$U_z \downarrow$	$M_x = 0$	$M_y = 0$	$R_z = 0$	max P
4	$F_x = 0$	$F_y = 0$	$U_z \uparrow$	$M_x = 0$	$M_y = 0$	$R_z = 0$	P = 0

LC2a - Cyclic uniaxial lateral displacements with constant compression force ($-F_z = P = 300$ kips). The top was forced to have zero moments.

Step	DOF						Stop Criterion
	X	Y	Z	RX	RY	RZ	
1	$U_x \downarrow$	$U_y \uparrow$	P = 300k	$M_x = 0$	$M_y = 0$	$R_z = 0$	+F peak
2	$U_x \uparrow$	$U_y \downarrow$	P = 300k	$M_x = 0$	$M_y = 0$	$R_z = 0$	-F peak
3	$U_x \downarrow$	$U_y \uparrow$	P = 300k	$M_x = 0$	$M_y = 0$	$R_z = 0$	+F peak
4	$U_x \uparrow$	$U_y \downarrow$	P = 300k	$M_x = 0$	$M_y = 0$	$R_z = 0$	-F peak
5	$U_x \uparrow$	$U_y \downarrow$	P = 300k	$M_x = 0$	$M_y = 0$	$R_z = 0$	$U_z = 0$

LC2b - Cyclic uniaxial lateral displacements with constant compression force ($-F_z = P = 150$ kips). The top was forced to have zero moments.

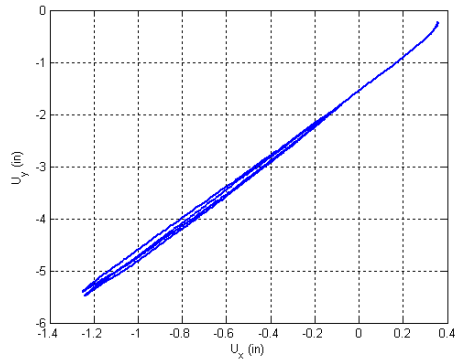
Step	DOF						Stop Criterion
	X	Y	Z	RX	RY	RZ	
1	$U_x \downarrow$	$U_y \uparrow$	P = 150k	$M_x = 0$	$M_y = 0$	$R_z = 0$	+F peak
2	$U_x \uparrow$	$U_y \downarrow$	P = 150k	$M_x = 0$	$M_y = 0$	$R_z = 0$	-F peak
3	$U_x \downarrow$	$U_y \uparrow$	P = 150k	$M_x = 0$	$M_y = 0$	$R_z = 0$	+F peak
4	$U_x \uparrow$	$U_y \downarrow$	P = 150k	$M_x = 0$	$M_y = 0$	$R_z = 0$	-F peak
5	$U_x \uparrow$	$U_y \downarrow$	P = 150k	$M_x = 0$	$M_y = 0$	$R_z = 0$	$U_z = 0$

LC3 - Cyclic biaxial lateral displacements (8 probes with diamond shape) with constant compression force ($-F_z = P = 375, 225$ and 75 kips). The top was forced to have zero moments.

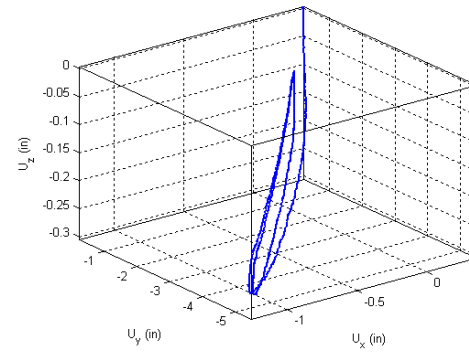
Step	DOF						Stop Criterion
	X	Y	Z	RX	RY	RZ	
1	$U_x \uparrow$	$U_y \uparrow$	P = 375k	$M_x = 0$	$M_y = 0$	$R_z = 0$	F peak at each of the 8 probes
2	$U_x \downarrow$	$U_y \downarrow$	P = 225k	$M_x = 0$	$M_y = 0$	$R_z = 0$	
3	$U_x \downarrow$	$U_y \downarrow$	P = 75k	$M_x = 0$	$M_y = 0$	$R_z = 0$	

LC4 - Torsion The top was twisted in displacement control.

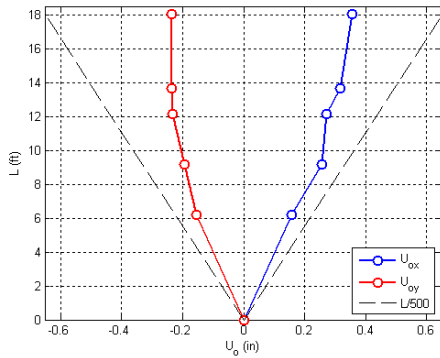
Step	DOF						Stop Criterion
	X	Y	Z	RX	RY	RZ	
1	$U_x = 0$	$U_y = 0$	P = 0	$R_x = 0$	$R_y = 0$	$R_z \uparrow$	+/-max. twist
2	$U_x = 0$	$U_y = 0$	P = 380k	$R_x = 0$	$R_y = 0$	$R_z \downarrow$	+/-max. twist



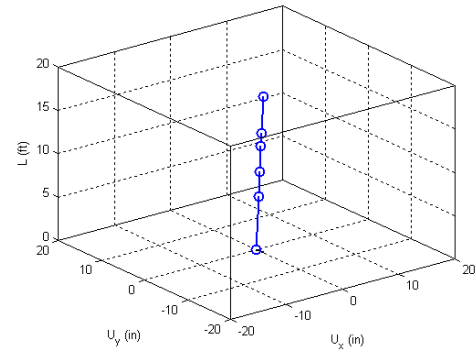
Y displacement vs. X displacement



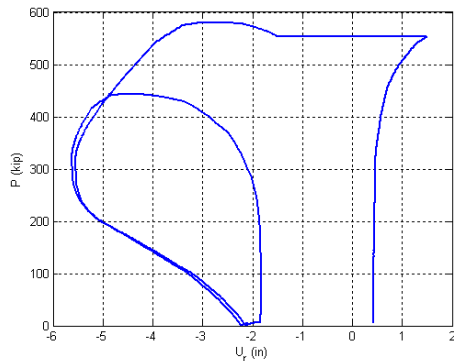
Z displacement vs. X and Y displacement



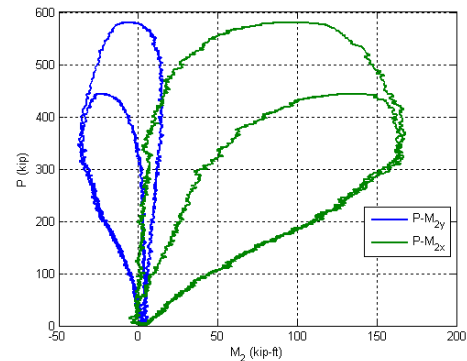
Initial deflected shape



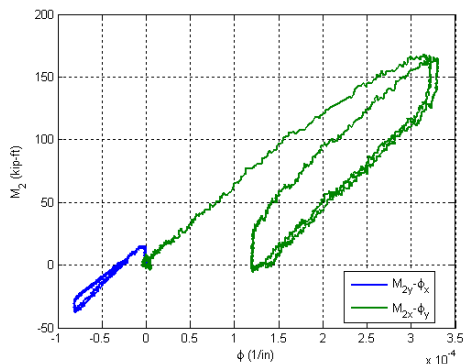
Maximum lateral displacement



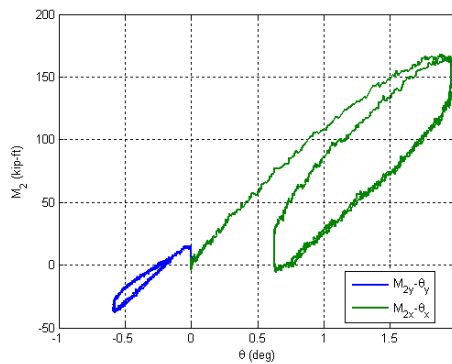
Axial force vs. lateral displacement



Axial force vs. base moments

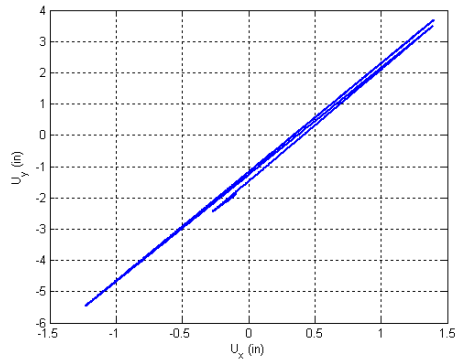


Base moment vs. base curvature

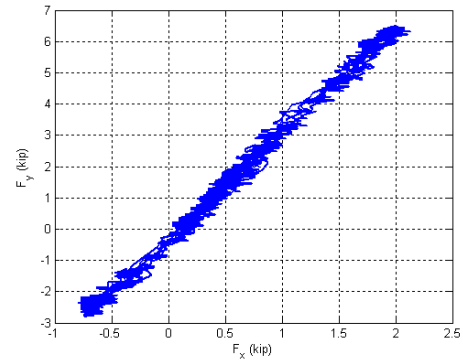


Base moment vs. top rotation

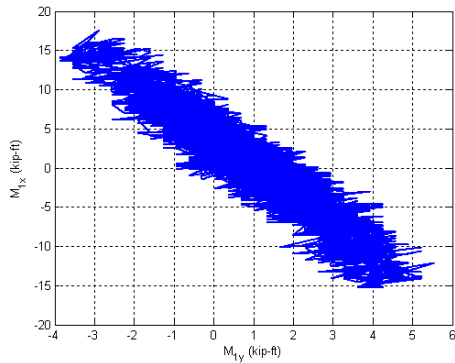
Figure B.45. Experimental results from LC1 in the specimen 6C12-18-12



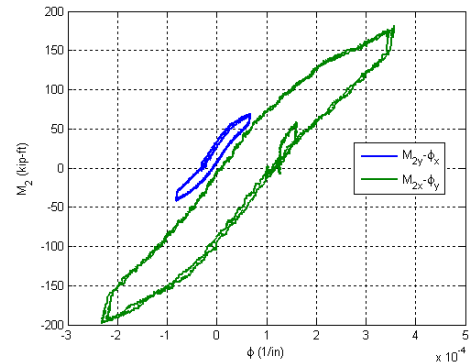
Y Displacement vs. X Displacement



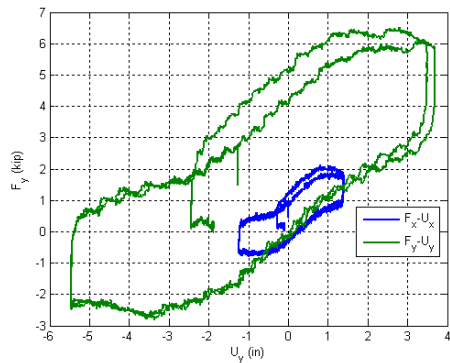
Y Force vs. X Force



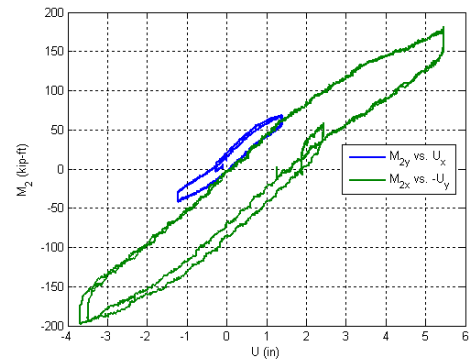
X Moment vs. Y Moment at the top



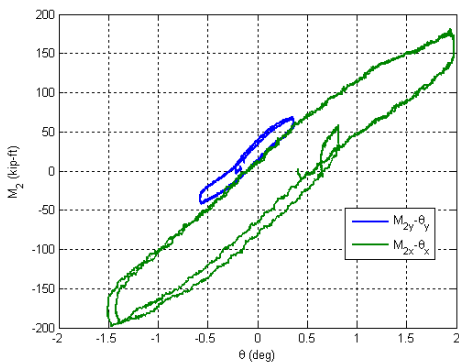
X Moment vs. Y Moment at the base



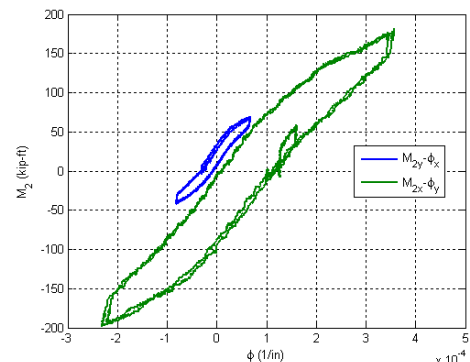
Lateral Force vs. Lateral Displacement



Base Moment vs. Top Displacement

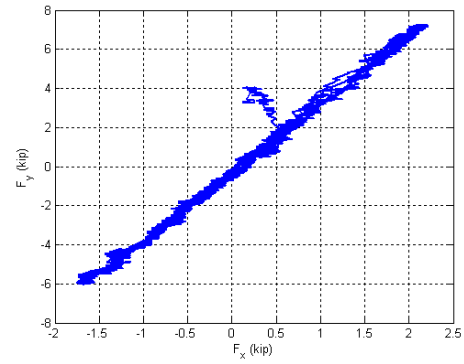
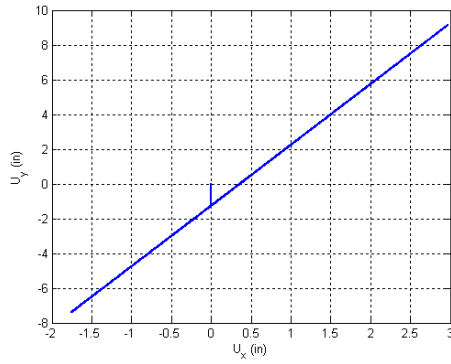


Base Moment vs. Top Rotation

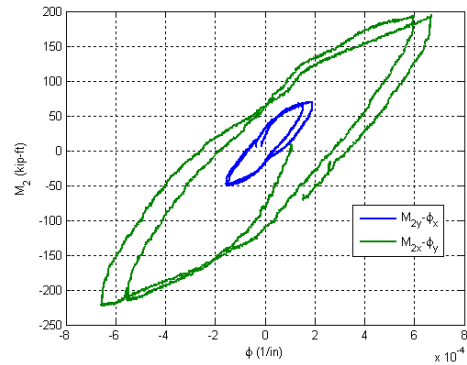
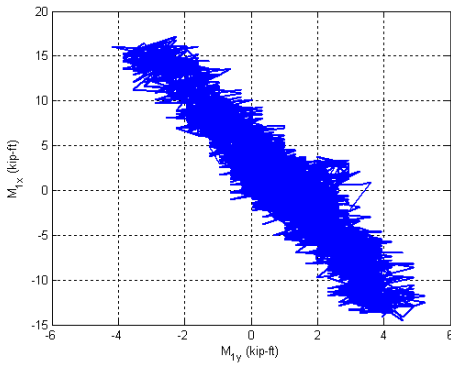


Base Moment vs. Base Curvature

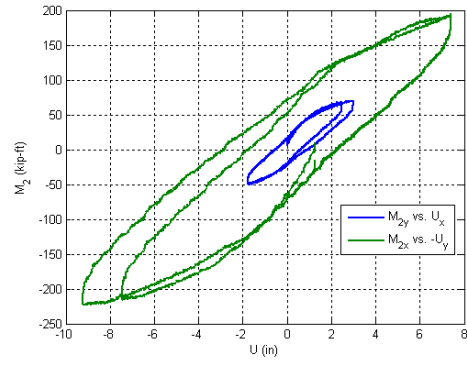
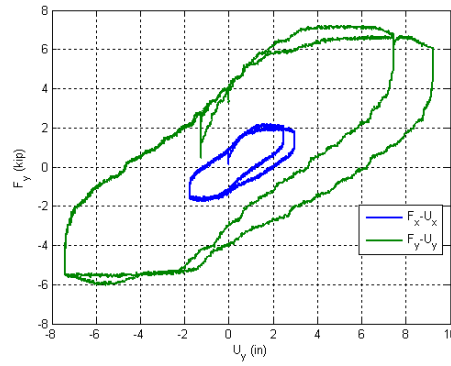
Figure B.46. Experimental results from LC2a in the specimen 6C12-18-12



Y Displacement vs. X Displacement Y Force vs. X Force

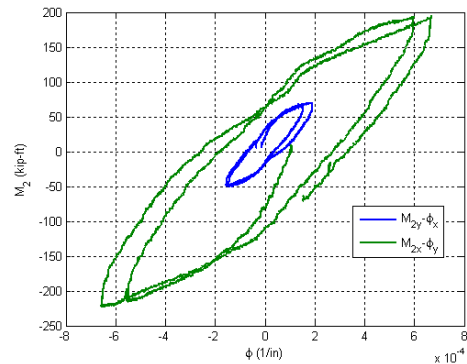
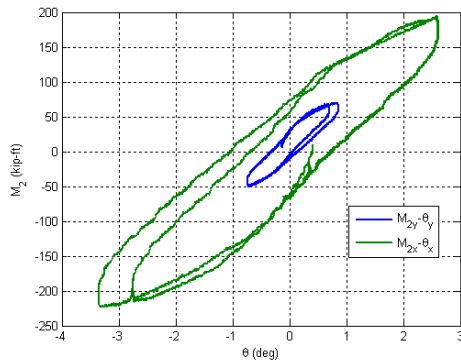


X Moment vs. Y Moment at the top X Moment vs. Y Moment at the base



Lateral Force vs. Lateral Displacement

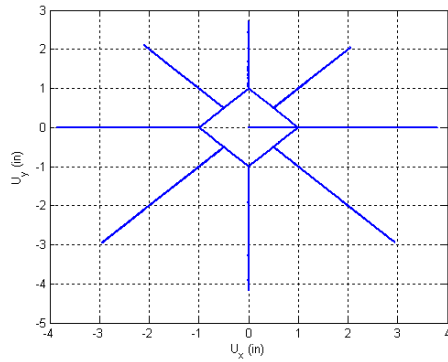
Base Moment vs. Top Displacement



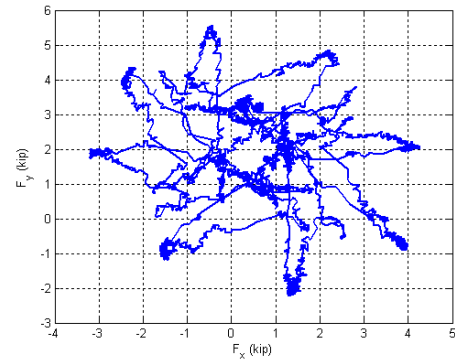
Base Moment vs. Top Rotation

Base Moment vs. Base Curvature

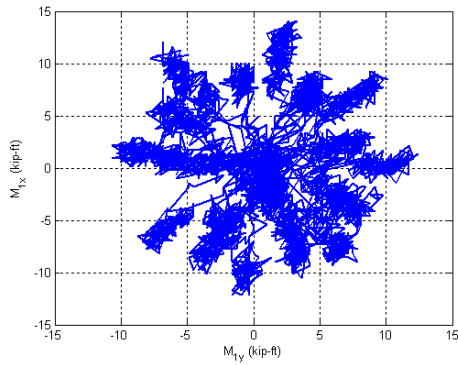
Figure B.47. Experimental results from LC2b in the specimen 6C12-18-12



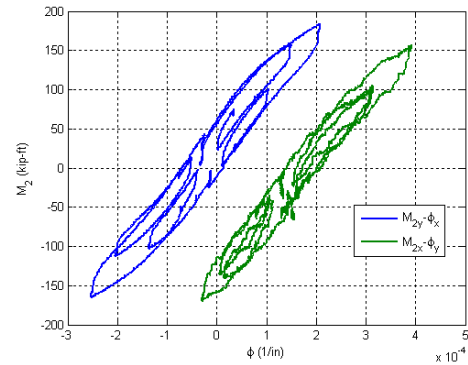
Y Displacement vs. X Displacement



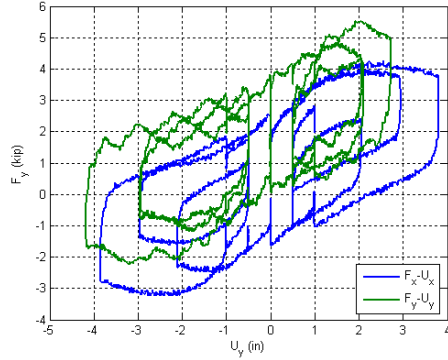
Y Force vs. X Force



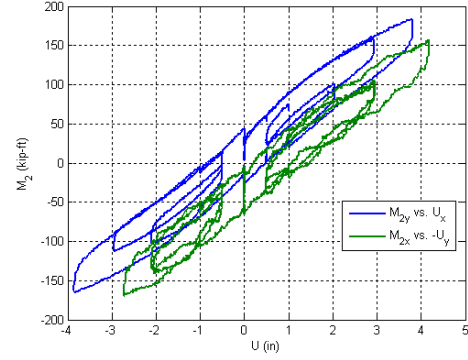
X Moment vs. Y Moment at the top



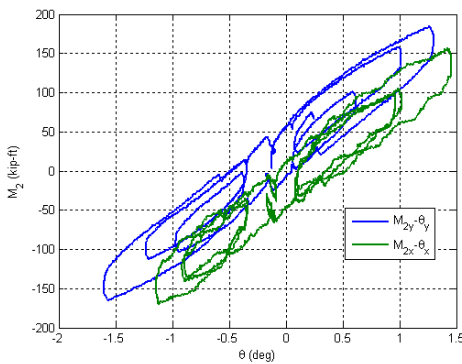
X Moment vs. Y Moment at the base



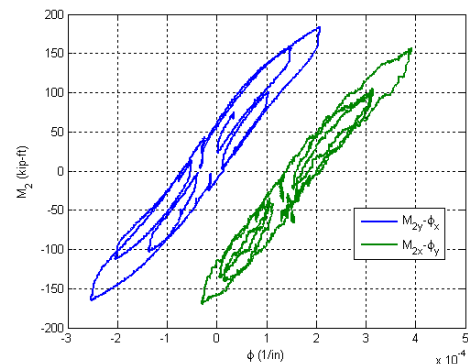
Lateral Force vs. Lateral Displacement



Base Moment vs. Top Displacement

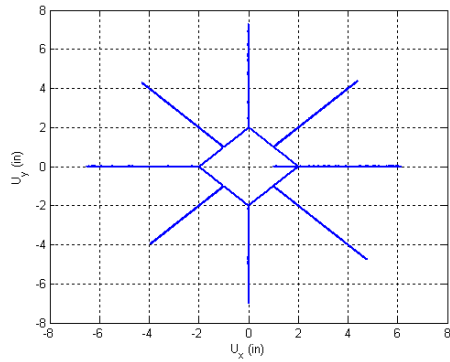


Base Moment vs. Top Rotation

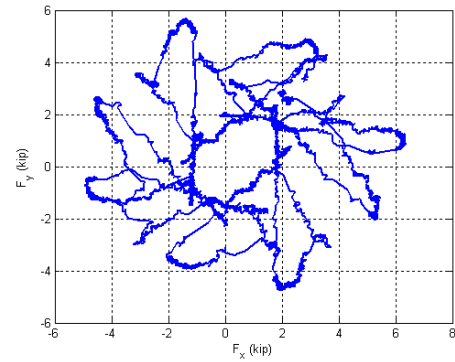


Base Moment vs. Base Curvature

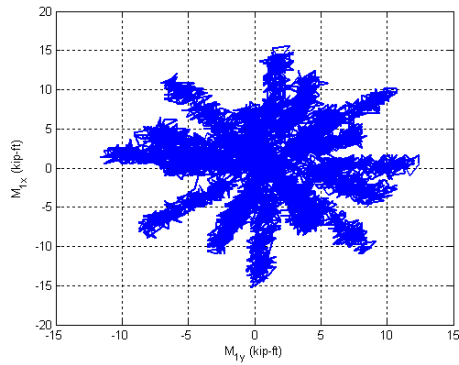
Figure B.48. Experimental results from LC3a in the specimen 6C12-18-12



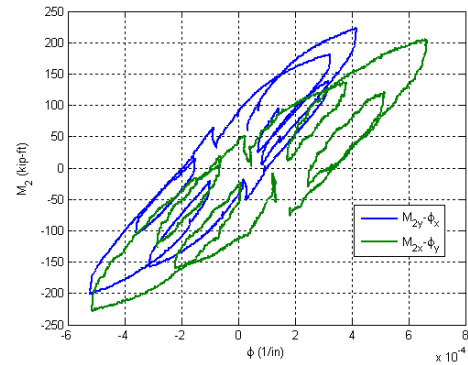
Y Displacement vs. X Displacement



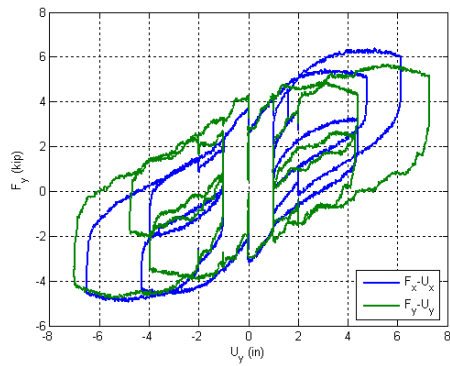
Y Force vs. X Force



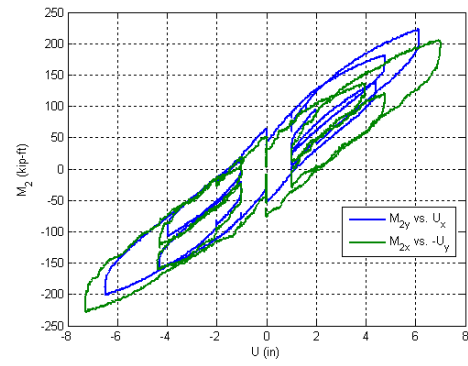
X Moment vs. Y Moment at the top



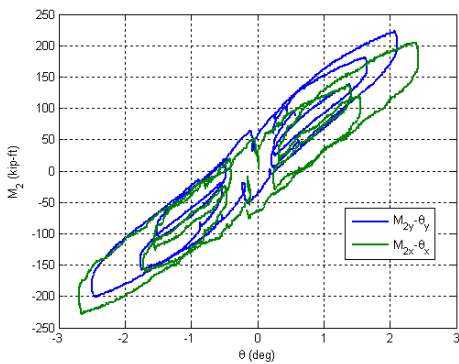
X Moment vs. Y Moment at the base



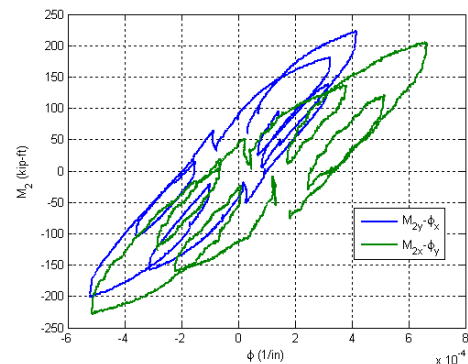
Lateral Force vs. Lateral Displacement



Base Moment vs. Top Displacement

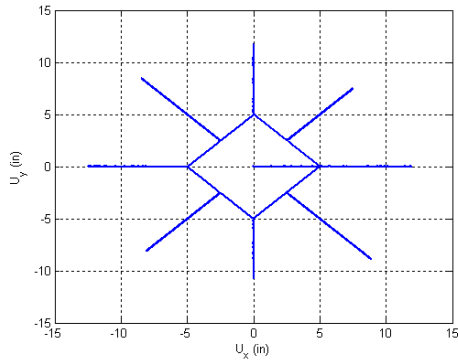


Base Moment vs. Top Rotation

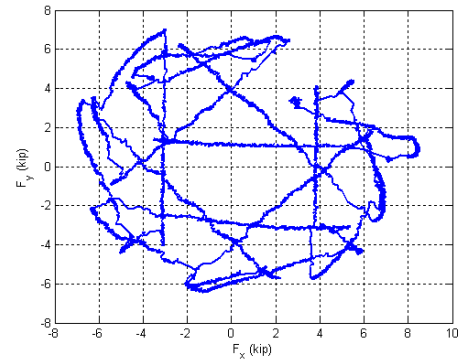


Base Moment vs. Base Curvature

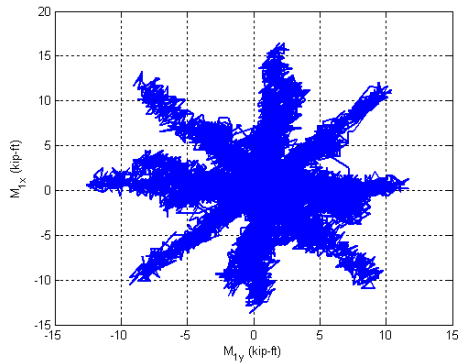
Figure B.49. Experimental results from LC3b in the specimen 6C12-18-12



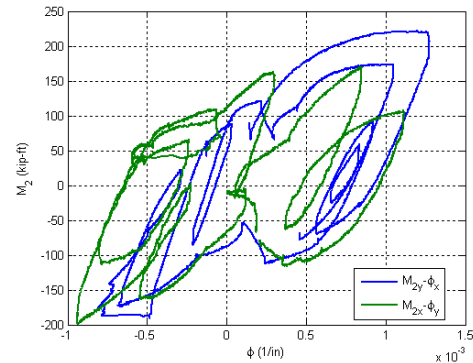
Y Displacement vs. X Displacement



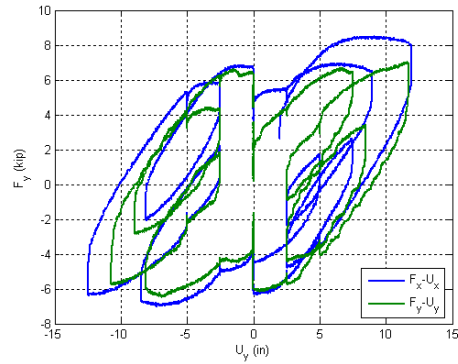
Y Force vs. X Force



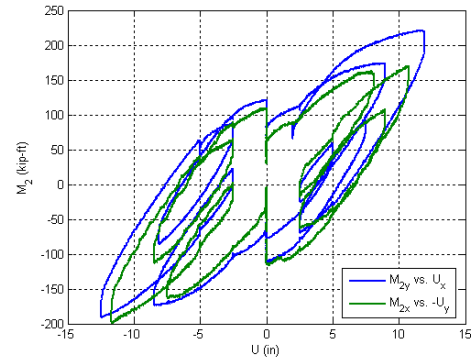
X Moment vs. Y Moment at the top



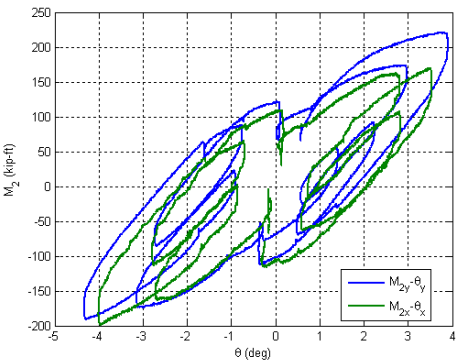
X Moment vs. Y Moment at the base



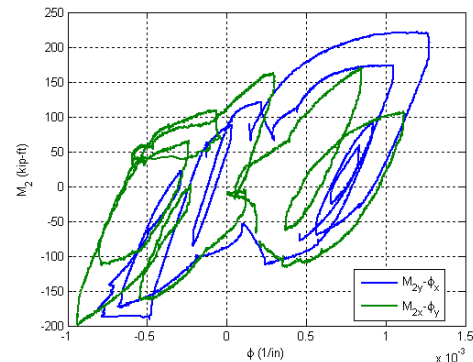
Lateral Force vs. Lateral Displacement



Base Moment vs. Top Displacement

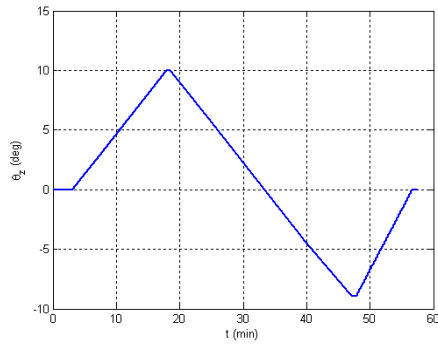


Base Moment vs. Top Rotation

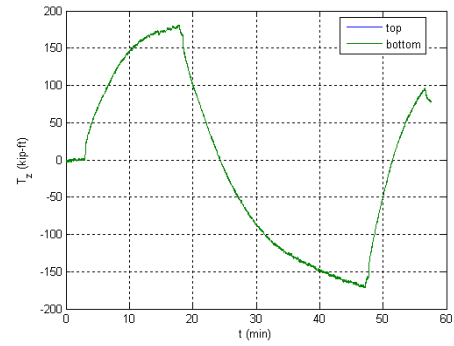


Base Moment vs. Base Curvature

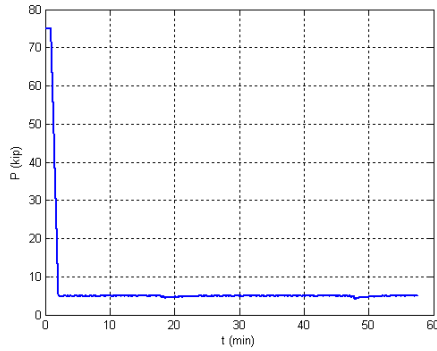
Figure B.50. Experimental results from LC3c in the specimen 6C12-18-12



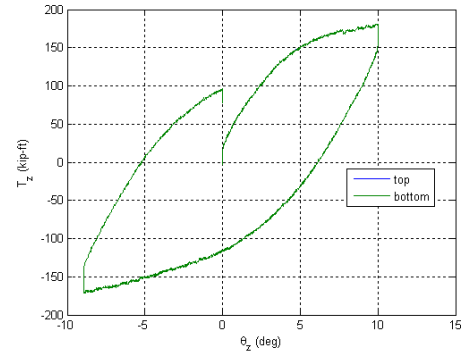
Twisting Angle vs. Time



Torsion Moment vs. Time

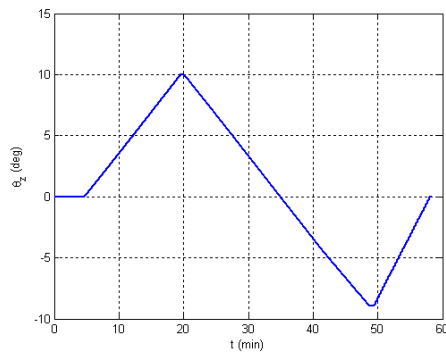


Axial Force vs. Time

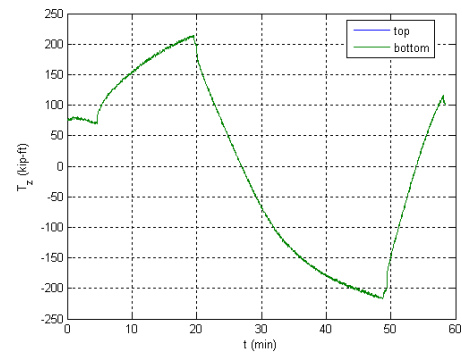


Torsion Moment vs. Twisting Angle

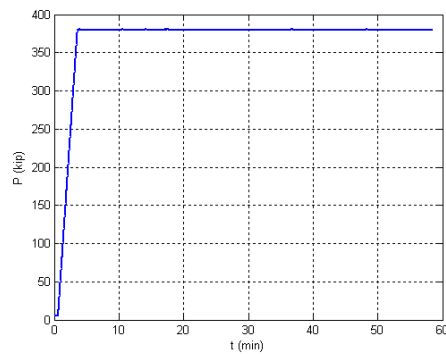
Figure B.51. Experimental results from LC4a in the specimen 6C12-18-12



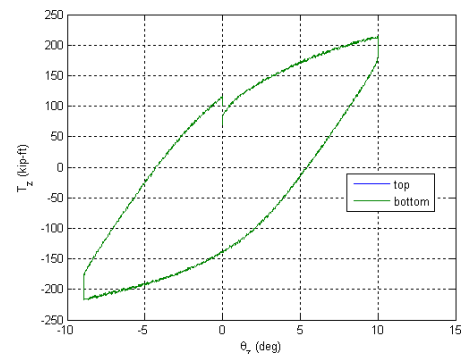
Twisting Angle vs. Time



Torsion Moment vs. Time

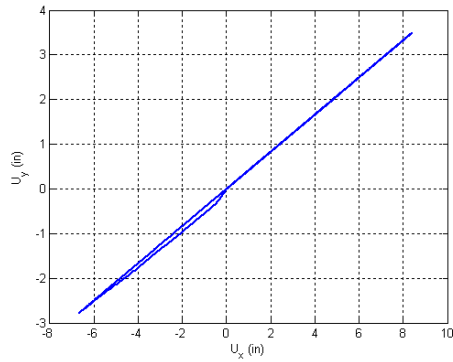


Axial Force vs. Time

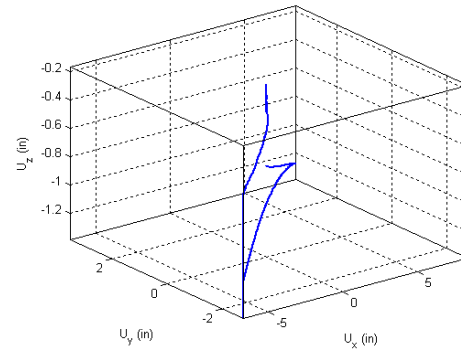


Torsion Moment vs. Twisting Angle

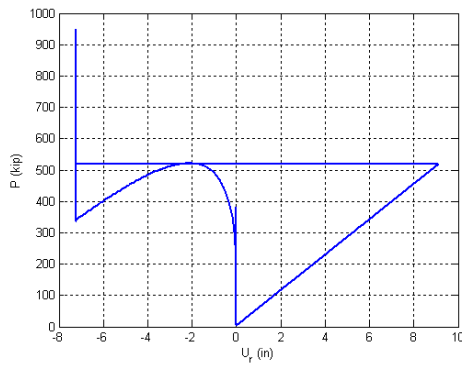
Figure B.52. Experimental results from LC4b in the specimen 6C12-18-12



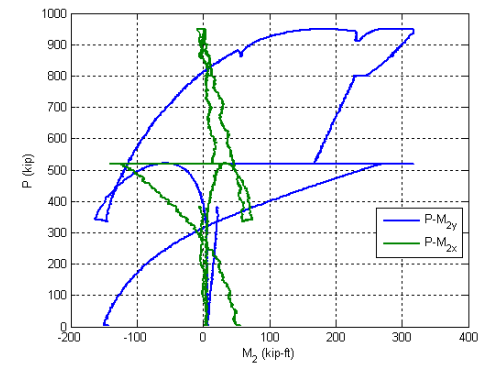
Y displacement vs. X displacement



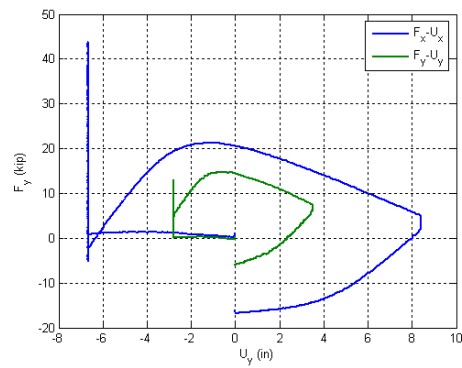
Z displacement vs. X and Y displacement



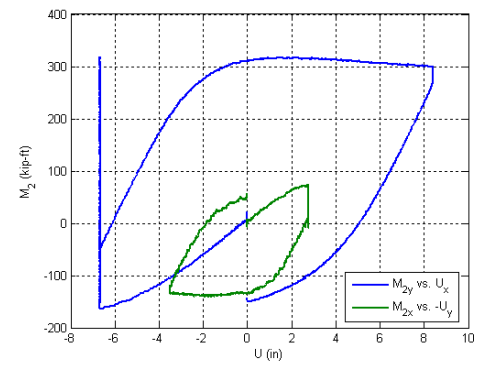
Axial force vs. lateral displacement



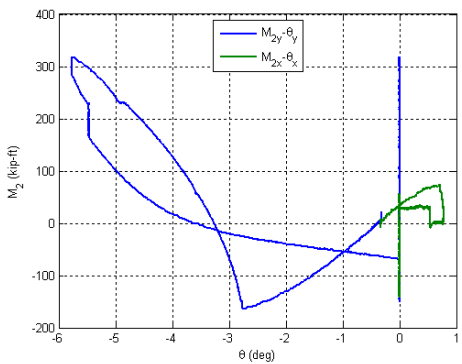
Axial force vs. base moments



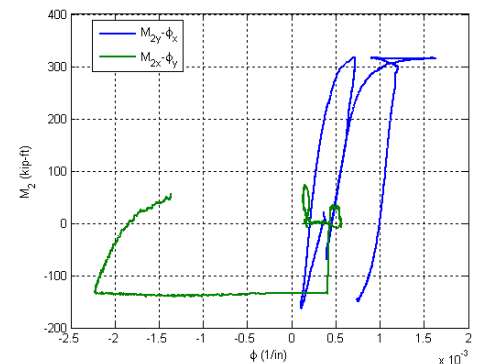
Lateral Force vs. Lateral Displacement



Base Moment vs. Top Displacement



Base Moment vs. Top Rotation



Base Moment vs. Base Curvature

Figure B.53. Experimental results from LC4c in the specimen 6C12-18-12

B.7. Specimen 7C20-18-12

Description:

- Specimen number: 7
- Composite Cross-section: CCFT
- Steel cross-section: HSS20x0.25
- Design concrete strength: 12 ksi
- Design specimen length: 18 ft
- Pouring date: 09/17/2008
- Testing date: 12/10/2008

Parameters:

- Specimen length: 18' 1 7/8"
- Initial out-of-plumbness: $U_{xo} = -0.47'' / U_{yo} = -0.86''$
- Steel yielding stress: $F_y = 47.6$ ksi
- Steel ultimate stress: $F_u = 68.3$ ksi
- Concrete strength at the 28th day: $f_c' = 12.7$ ksi
- Concrete strength at the testing day: $f_c = 13.2$ ksi
- Concrete Young's modulus: $E_c = 6070$ ksi
- Concrete tensile strength: $f_t = 1.65$ ksi

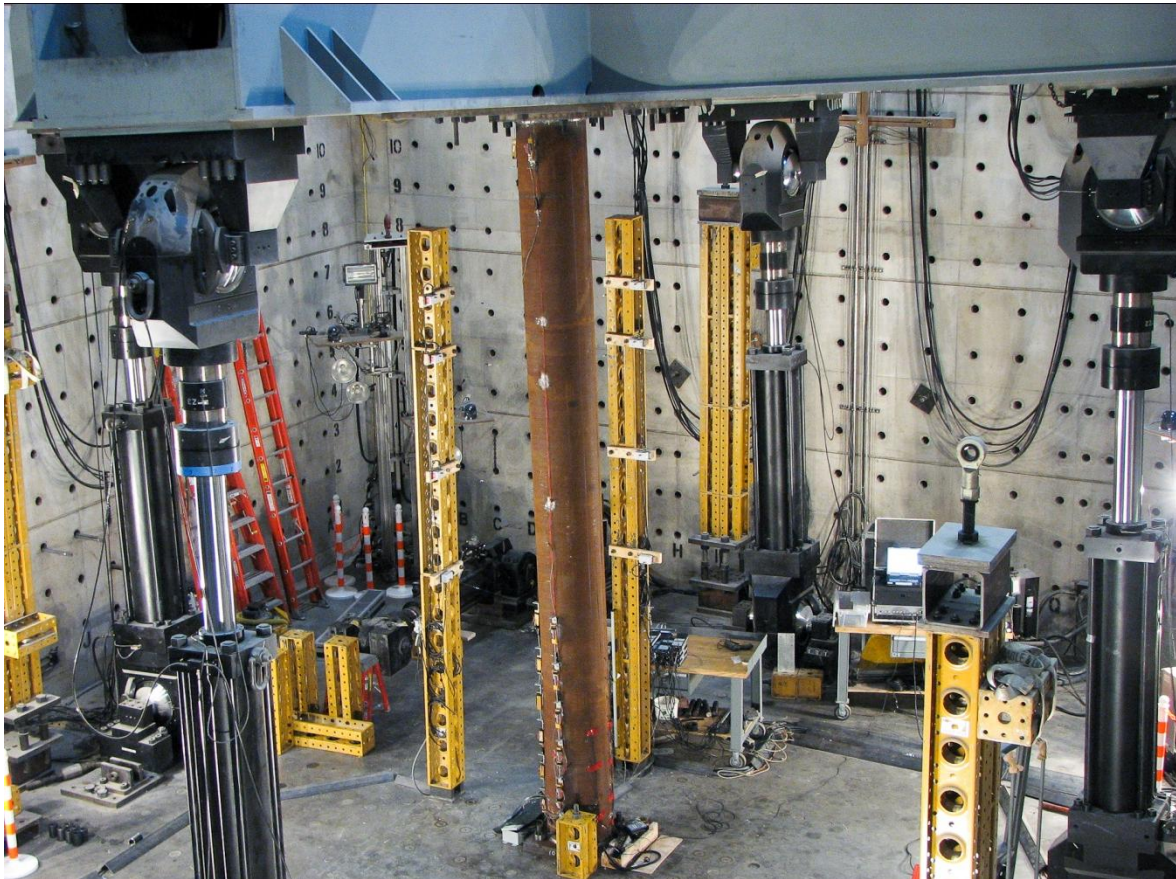


Figure B.54. Specimen 7C20-18-12

Table B.7. Load protocol summary for the specimen 7C20-18-12

LC1 - Incremental compression loading in three cycles until the maximum load is reached. The top is forced to be free at all the time.

Step	DOF						Stop Criterion
	X	Y	Z	RX	RY	RZ	
1	$F_x = 0$	$F_y = 0$	$U_z \downarrow$	$M_x = 0$	$M_y = 0$	$R_z = 0$	max P
2	$F_x = 0$	$F_y = 0$	$U_z \uparrow$	$M_x = 0$	$M_y = 0$	$R_z = 0$	P = 0
3	$F_x = 0$	$F_y = 0$	$U_z \downarrow$	$M_x = 0$	$M_y = 0$	$R_z = 0$	max P
4	$F_x = 0$	$F_y = 0$	$U_z \uparrow$	$M_x = 0$	$M_y = 0$	$R_z = 0$	P = 0

LC2a - Cyclic uniaxial lateral displacements with constant compression force ($-F_z = P = 1000$ kips). The top was forced to have zero moments.

Step	DOF						Stop Criterion
	X	Y	Z	RX	RY	RZ	
1	$U_x \downarrow$	$U_y \uparrow$	P = 1000k	$M_x = 0$	$M_y = 0$	$R_z = 0$	+F peak
2	$U_x \uparrow$	$U_y \downarrow$	P = 1000k	$M_x = 0$	$M_y = 0$	$R_z = 0$	-F peak
3	$U_x \downarrow$	$U_y \uparrow$	P = 1000k	$M_x = 0$	$M_y = 0$	$R_z = 0$	+F peak
4	$U_x \uparrow$	$U_y \downarrow$	P = 1000k	$M_x = 0$	$M_y = 0$	$R_z = 0$	-F peak
5	$U_x \uparrow$	$U_y \downarrow$	P = 1000k	$M_x = 0$	$M_y = 0$	$R_z = 0$	$U_z = 0$

LC2b - Cyclic uniaxial lateral displacements with constant compression force ($-F_z = P = 500$ kips). The top was forced to have zero moments.

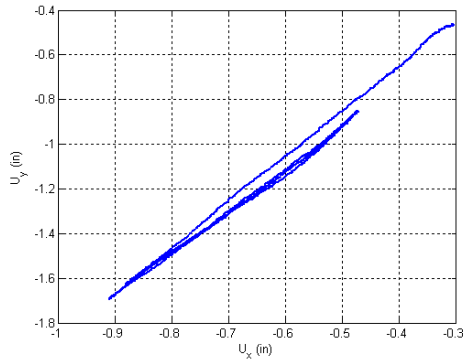
Step	DOF						Stop Criterion
	X	Y	Z	RX	RY	RZ	
1	$U_x \downarrow$	$U_y \uparrow$	P = 500k	$M_x = 0$	$M_y = 0$	$R_z = 0$	+F peak
2	$U_x \uparrow$	$U_y \downarrow$	P = 500k	$M_x = 0$	$M_y = 0$	$R_z = 0$	-F peak
3	$U_x \downarrow$	$U_y \uparrow$	P = 500k	$M_x = 0$	$M_y = 0$	$R_z = 0$	+F peak
4	$U_x \uparrow$	$U_y \downarrow$	P = 500k	$M_x = 0$	$M_y = 0$	$R_z = 0$	-F peak
5	$U_x \uparrow$	$U_y \downarrow$	P = 500k	$M_x = 0$	$M_y = 0$	$R_z = 0$	$U_z = 0$

LC3 - Cyclic biaxial lateral displacements (8 shape) with constant compression force ($-F_z = P = 1250$ kips). The top was forced to have zero moments.

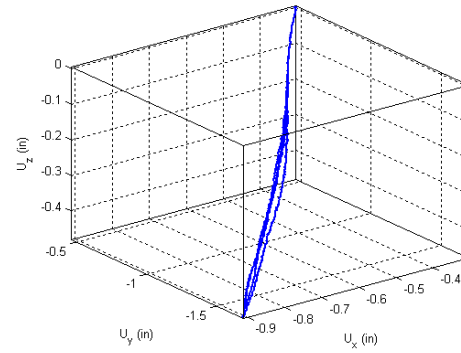
Step	DOF						Stop Criterion
	X	Y	Z	RX	RY	RZ	
1	$U_x \updownarrow$	$U_y \updownarrow$	P = 1250k	$M_x = 0$	$M_y = 0$	$R_z = 0$	+/-1% drift
2	$U_x \updownarrow$	$U_y \updownarrow$	P = 1250k	$M_x = 0$	$M_y = 0$	$R_z = 0$	+/-3% drift
3	$U_x \updownarrow$	$U_y \updownarrow$	P = 1250k	$M_x = 0$	$M_y = 0$	$R_z = 0$	+/-5% drift

LC4 - Torsion The top was twisted in displacement control.

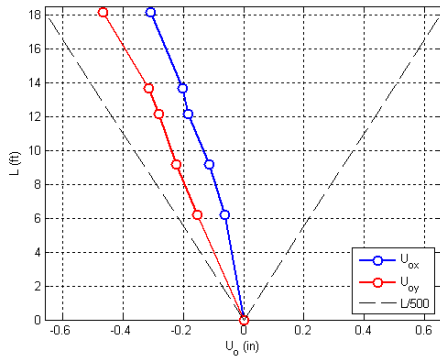
Step	DOF						Stop Criterion
	X	Y	Z	RX	RY	RZ	
1	$U_x = 0$	$U_y = 0$	P = 0	$R_x = 0$	$R_y = 0$	$R_z \updownarrow$	+max. twist



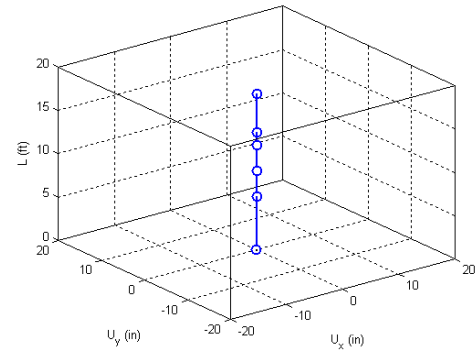
Y displacement vs. X displacement



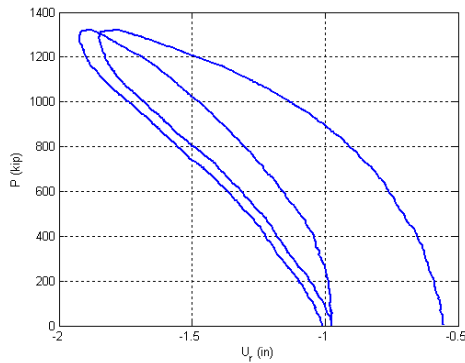
Z displacement vs. X and Y displacement



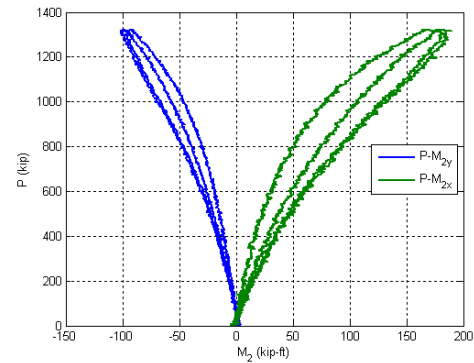
Initial deflected shape



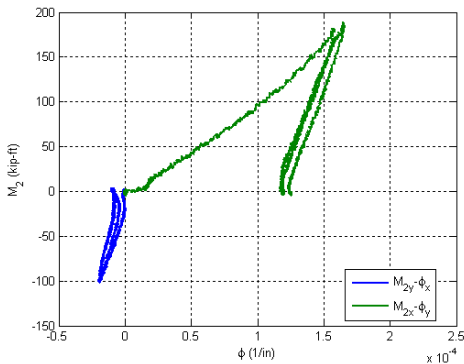
Maximum lateral displacement



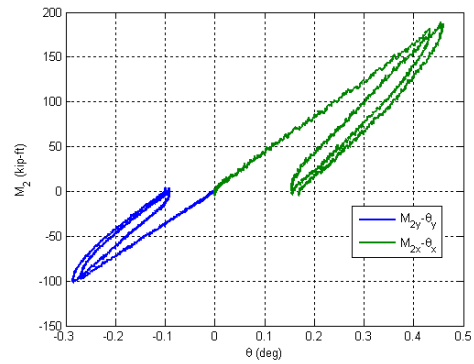
Axial force vs. lateral displacement



Axial force vs. base moments

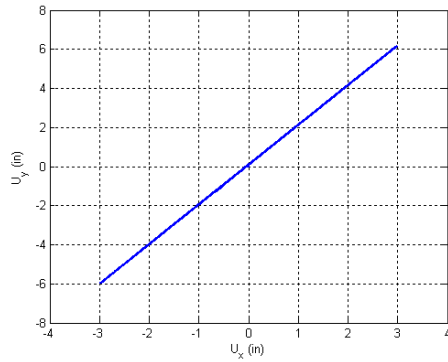


Base moment vs. base curvature

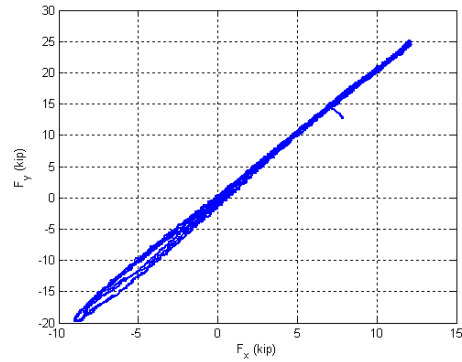


Base moment vs. top rotation

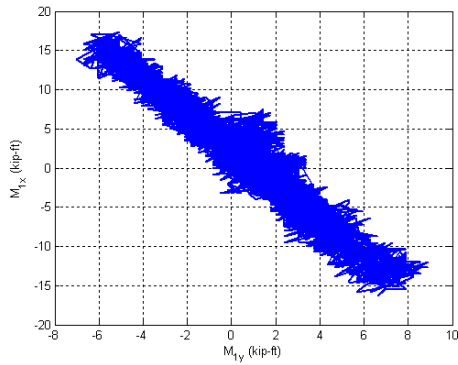
Figure B.55. Experimental results from LC1 in the specimen 7C20-18-12



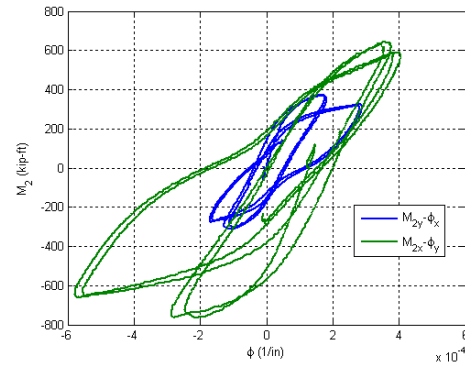
Y Displacement vs. X Displacement



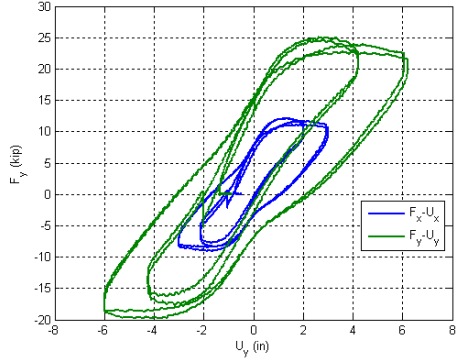
Y Force vs. X Force



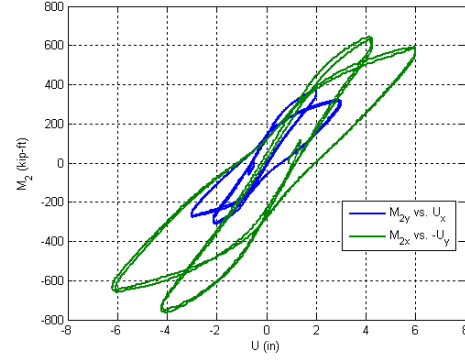
X Moment vs. Y Moment at the top



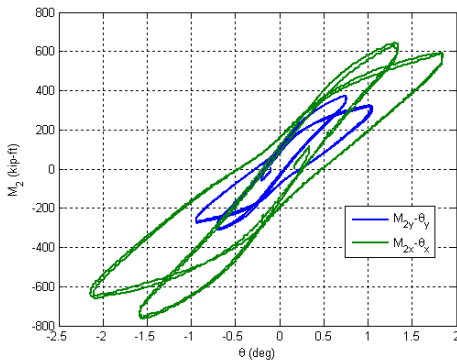
X Moment vs. Y Moment at the base



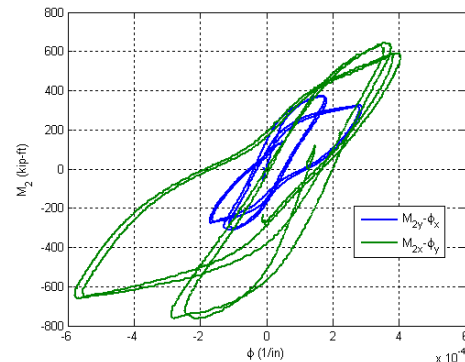
Lateral Force vs. Lateral Displacement



Base Moment vs. Top Displacement

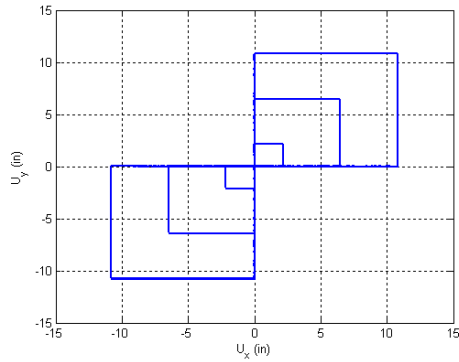


Base Moment vs. Top Rotation

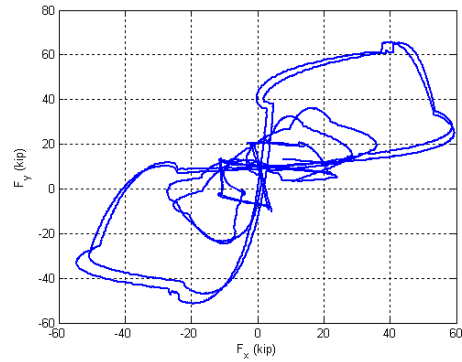


Base Moment vs. Base Curvature

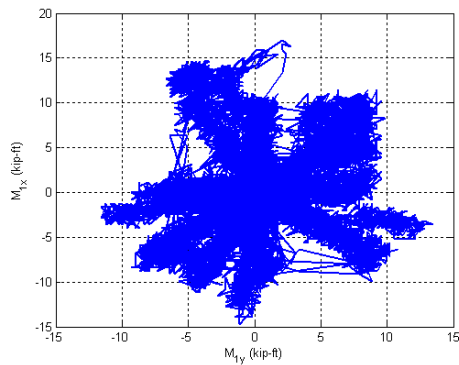
Figure B.56. Experimental results from LC2 in the specimen 7C20-18-12



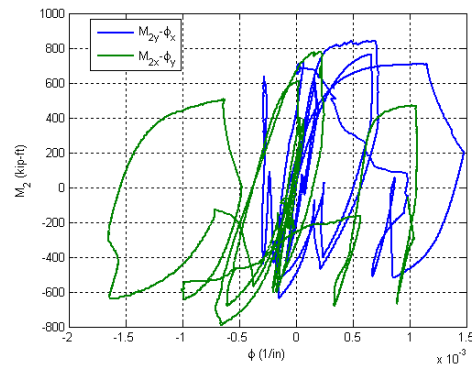
Y Displacement vs. X Displacement



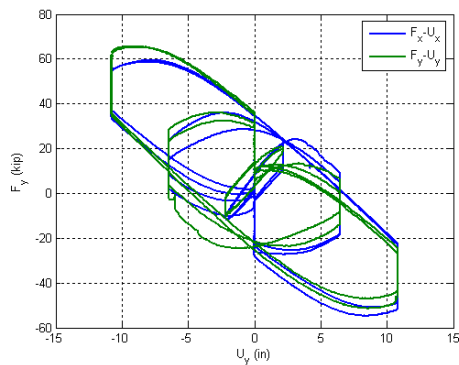
Y Force vs. X Force



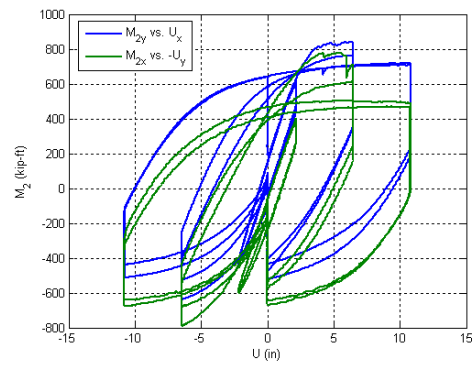
X Moment vs. Y Moment at the top



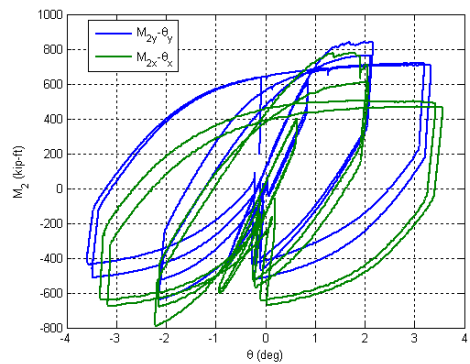
X Moment vs. Y Moment at the base



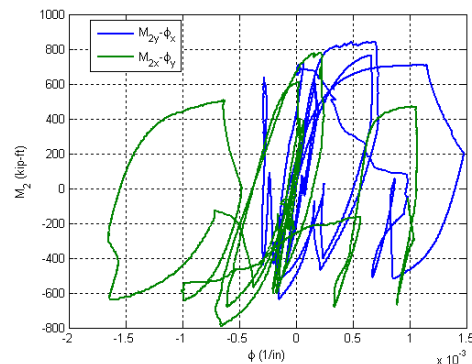
Lateral Force vs. Lateral Displacement



Base Moment vs. Top Displacement



Base Moment vs. Top Rotation



Base Moment vs. Base Curvature

Figure B.57. Experimental results from LC3 in the specimen 7C20-18-12

B.8. Specimen 8Rw-18-12

Description:

- Specimen number: 8
- Composite Cross-section: RCFT
- Steel cross-section: HSS20x12x0.3125
- Design concrete strength: 12 ksi
- Design specimen length: 18 ft
- Pouring date: 09/17/2008
- Testing date: 12/18/2008

Parameters:

- Specimen length: 18' 2 5/8"
- Initial out-of-plumbness: $U_{xo} = 1.81'' / U_{yo} = -0.63''$
- Steel yielding stress: $F_y = 53.0$ ksi
- Steel ultimate stress: $F_u = 72.8$ ksi
- Concrete strength at the 28th day: $f_c' = 12.7$ ksi
- Concrete strength at the testing day: $f_c = 13.3$ ksi
- Concrete Young's modulus: $E_c = 6070$ ksi
- Concrete tensile strength: $f_t = 1.65$ ksi

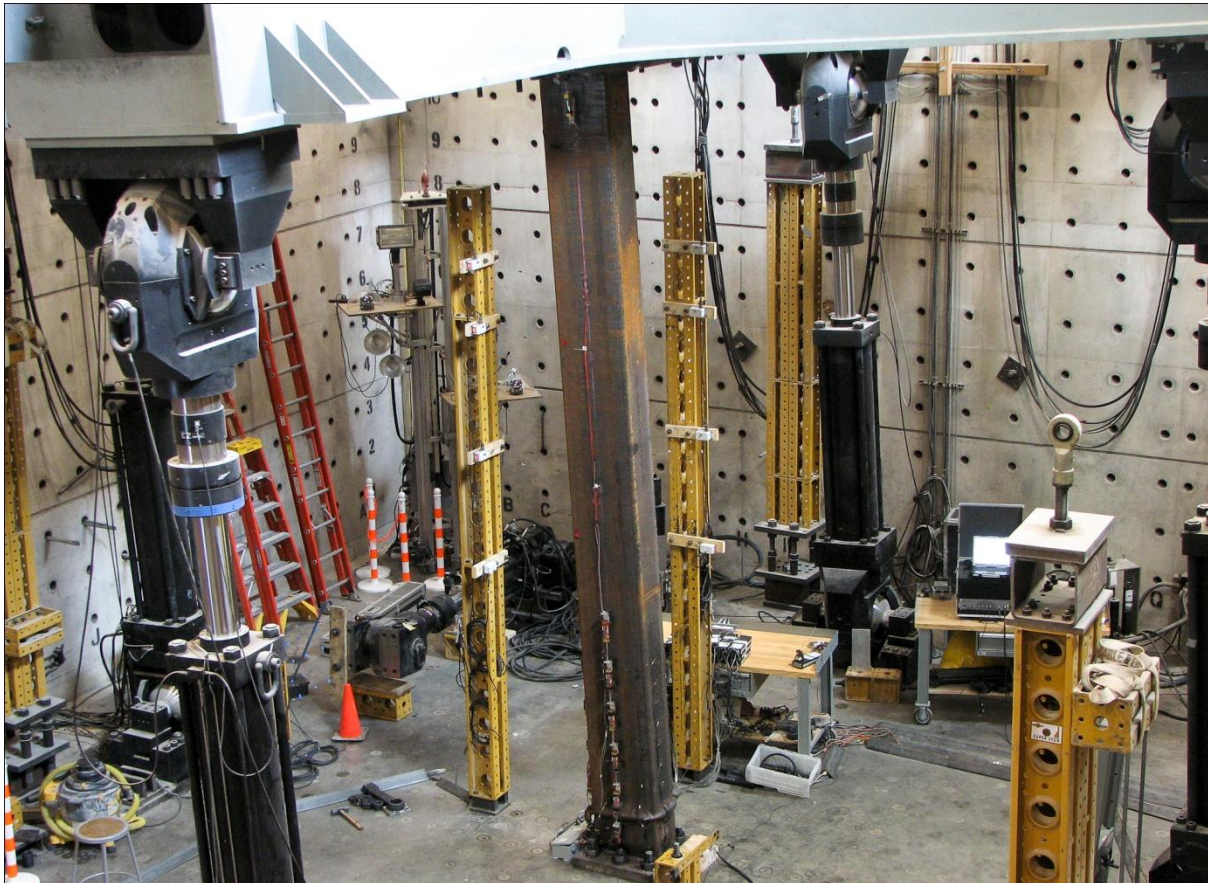


Figure B.58. Specimen 8Rw-18-12

Table B.8. Load protocol summary for the specimen 8Rw-18-12

LC1 - Incremental compression loading in two cycles until the maximum load is reached. The top is forced to be free at X ($K_x=2$) and fixed at Y ($K_y=0.5$).

Step	DOF						Stop Criterion
	X	Y	Z	RX	RY	RZ	
1	$F_x = 0$	$U_y = 0$	$U_z \downarrow$	$R_x = 0$	$M_y = 0$	$R_z = 0$	max P
2	$F_x = 0$	$U_y = 0$	$U_z \uparrow$	$R_x = 0$	$M_y = 0$	$R_z = 0$	P = 0
3	$F_x = 0$	$U_y = 0$	$U_z \downarrow$	$R_x = 0$	$M_y = 0$	$R_z = 0$	max P
4	$F_x = 0$	$U_y = 0$	$U_z \uparrow$	$R_x = 0$	$M_y = 0$	$R_z = 0$	P = 0

LC2a - Cyclic uniaxial lateral displacements with constant compression force ($-F_z = P = 600$ kips). The top was forced to have zero moments in Y and fixed rotation in X.

Step	DOF						Stop Criterion
	X	Y	Z	RX	RY	RZ	
1	$U_x \downarrow$	$U_y = 0$	P = 600k	$R_x = 0$	$M_y = 0$	$R_z = 0$	+F peak
2	$U_x \uparrow$	$U_y = 0$	P = 600k	$R_x = 0$	$M_y = 0$	$R_z = 0$	-F peak
3	$U_x \downarrow$	$U_y = 0$	P = 600k	$R_x = 0$	$M_y = 0$	$R_z = 0$	+F peak
4	$U_x \uparrow$	$U_y = 0$	P = 600k	$R_x = 0$	$M_y = 0$	$R_z = 0$	-F peak
5	$U_x \uparrow$	$U_y = 0$	P = 600k	$R_x = 0$	$M_y = 0$	$R_z = 0$	$U_z = 0$

LC2b - Cyclic uniaxial lateral displacements with constant compression force ($-F_z = P = 300$ kips). The top was forced to have zero moments in Y and fixed rotation in X.

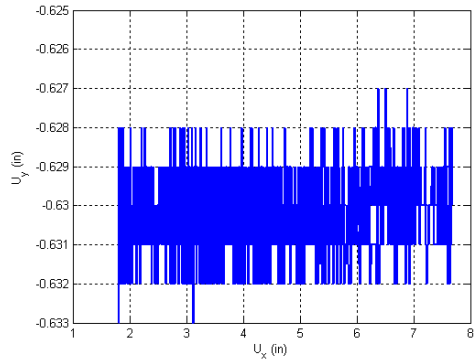
Step	DOF						Stop Criterion
	X	Y	Z	RX	RY	RZ	
1	$U_x \downarrow$	$U_y = 0$	P = 300k	$R_x = 0$	$M_y = 0$	$R_z = 0$	+F peak
2	$U_x \uparrow$	$U_y = 0$	P = 300k	$R_x = 0$	$M_y = 0$	$R_z = 0$	-F peak
3	$U_x \downarrow$	$U_y = 0$	P = 300k	$R_x = 0$	$M_y = 0$	$R_z = 0$	+F peak
4	$U_x \uparrow$	$U_y = 0$	P = 300k	$R_x = 0$	$M_y = 0$	$R_z = 0$	-F peak
5	$U_x \uparrow$	$U_y = 0$	P = 300k	$R_x = 0$	$M_y = 0$	$R_z = 0$	$U_z = 0$

LC3a - Cyclic biaxial lateral displacements (8 shape) with constant compression force ($-F_z = P = 800$ kips). The top was forced to have zero moments.

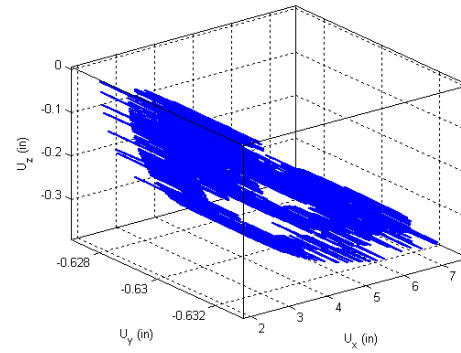
Step	DOF						Stop Criterion
	X	Y	Z	RX	RY	RZ	
1	$U_x \uparrow$	$U_y \uparrow$	P = 800k	$M_x = 0$	$M_y = 0$	$R_z = 0$	+/-1% drift
2	$U_x \downarrow$	$U_y \downarrow$	P = 800k	$M_x = 0$	$M_y = 0$	$R_z = 0$	+/-2% drift
3	$U_x \downarrow$	$U_y \uparrow$	P = 800k	$M_x = 0$	$M_y = 0$	$R_z = 0$	+/-3% drift
4	$U_x \uparrow$	$U_y \downarrow$	P = 800k	$M_x = 0$	$M_y = 0$	$R_z = 0$	+/-4% drift
5	$U_x \uparrow$	$U_y \uparrow$	P = 800k	$M_x = 0$	$M_y = 0$	$R_z = 0$	+/-5% drift

LC4 - Torsion The top was twisted in displacement control.

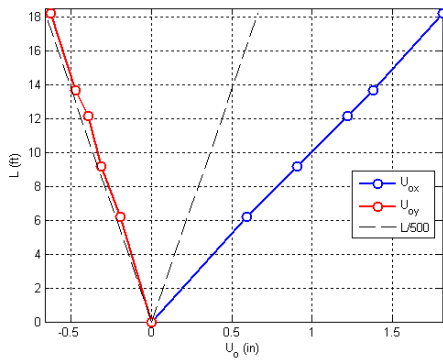
Step	DOF						Stop Criterion
	X	Y	Z	RX	RY	RZ	
1	$U_x = 0$	$U_y = 0$	P = 0	$R_x = 0$	$R_y = 0$	$R_z \uparrow$	+/-max. twist



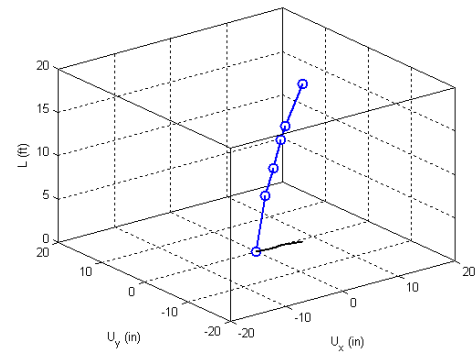
Y displacement vs. X displacement



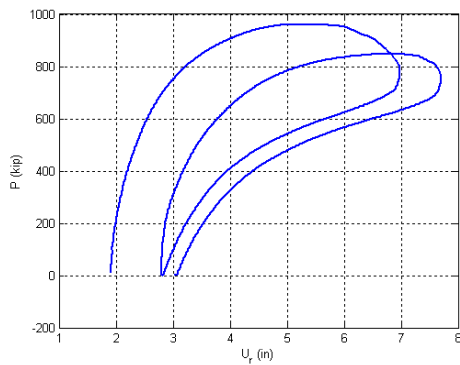
Z displacement vs. X and Y displacement



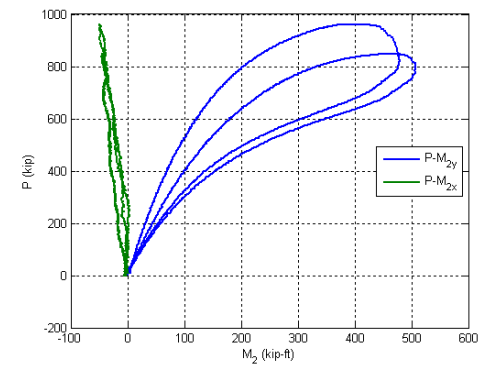
Initial deflected shape



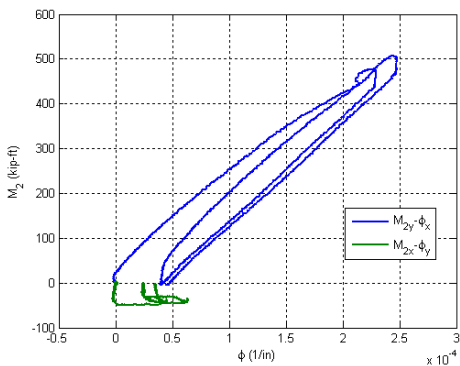
Maximum lateral displacement



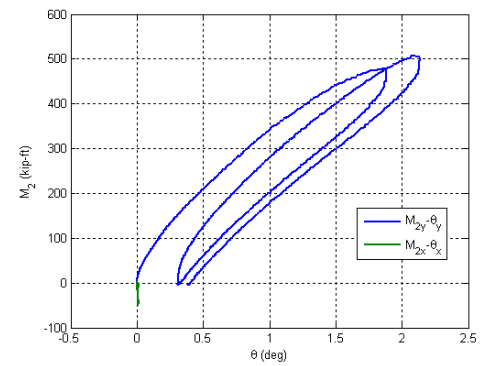
Axial force vs. lateral displacement



Axial force vs. base moments

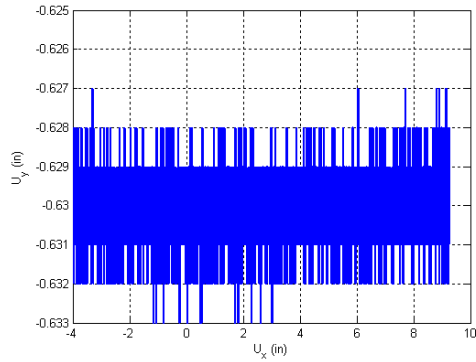


Base moment vs. base curvature

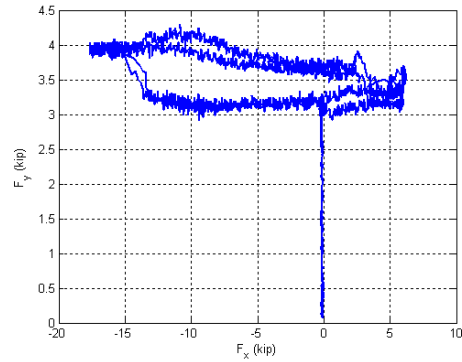


Base moment vs. top rotation

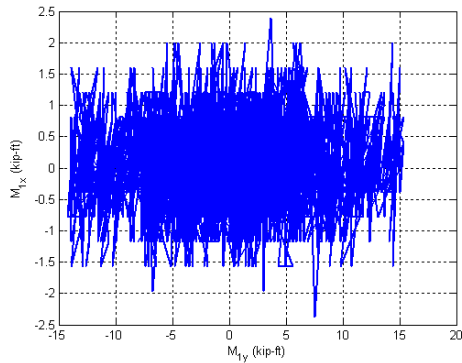
Figure B.59. Experimental results from LC1 in the specimen 8Rw-18-12



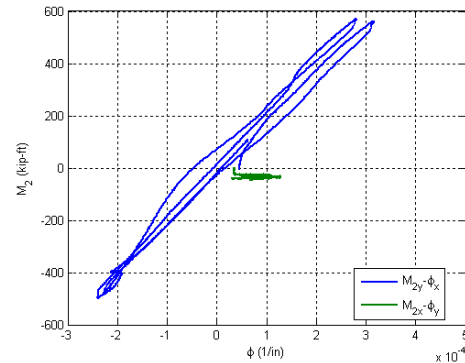
Y Displacement vs. X Displacement



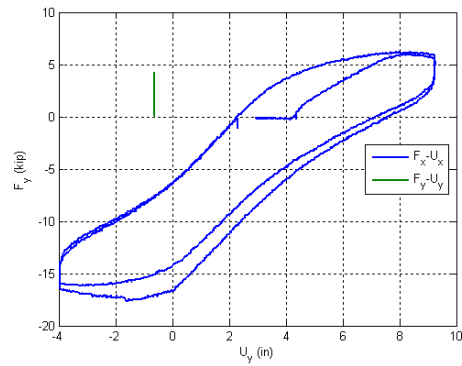
Y Force vs. X Force



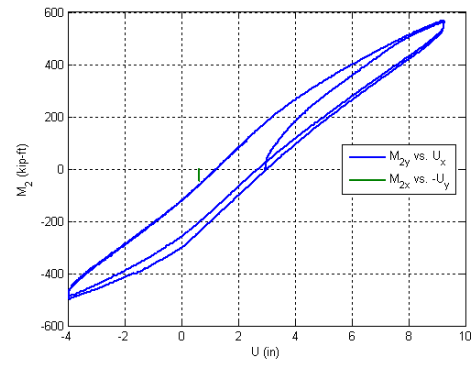
X Moment vs. Y Moment at the top



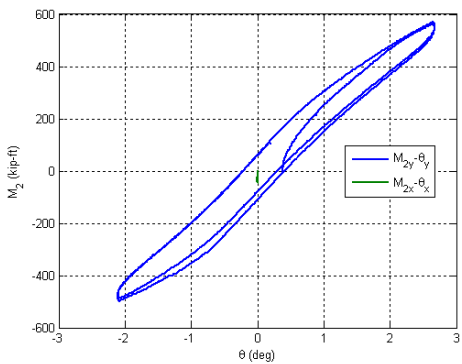
X Moment vs. Y Moment at the base



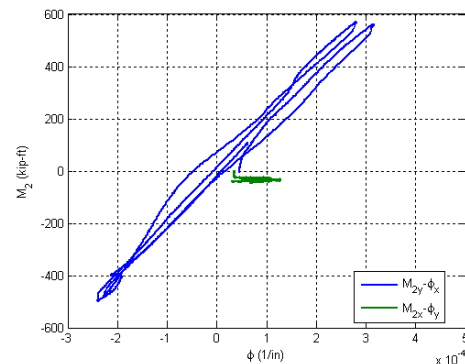
Lateral Force vs. Lateral Displacement



Base Moment vs. Top Displacement

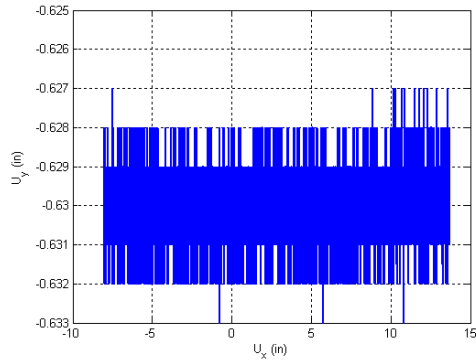


Base Moment vs. Top Rotation

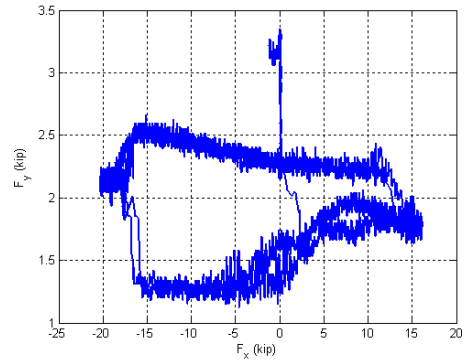


Base Moment vs. Base Curvature

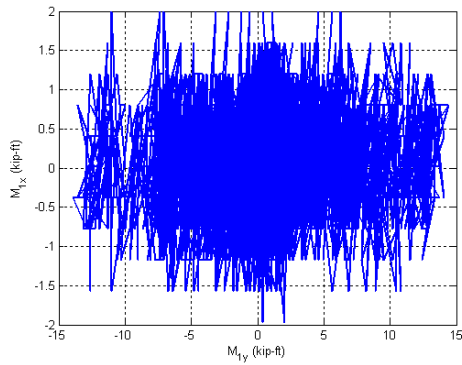
Figure B.60. Experimental results from LC2a in the specimen 8Rw-18-12



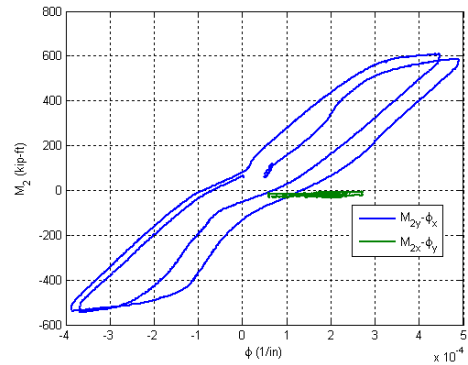
Y Displacement vs. X Displacement



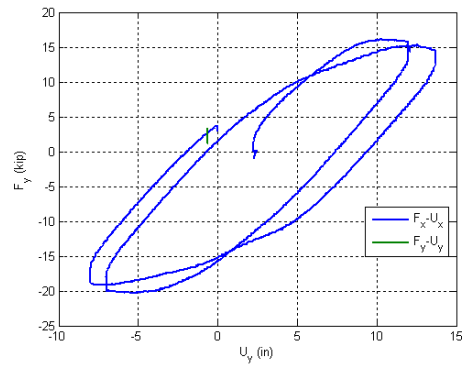
Y Force vs. X Force



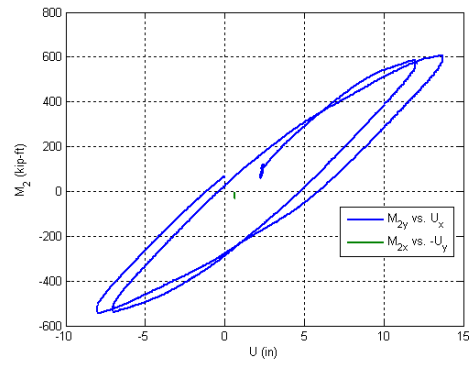
X Moment vs. Y Moment at the top



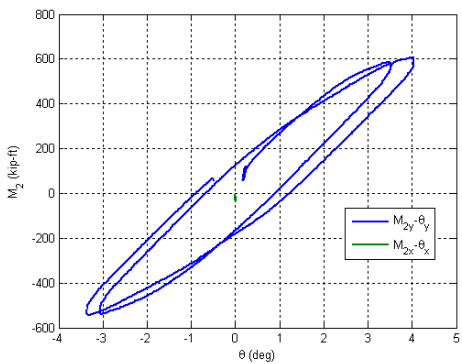
X Moment vs. Y Moment at the base



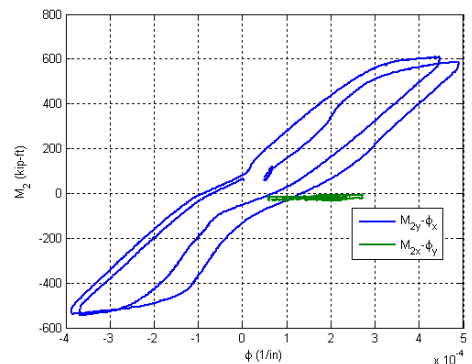
Lateral Force vs. Lateral Displacement



Base Moment vs. Top Displacement

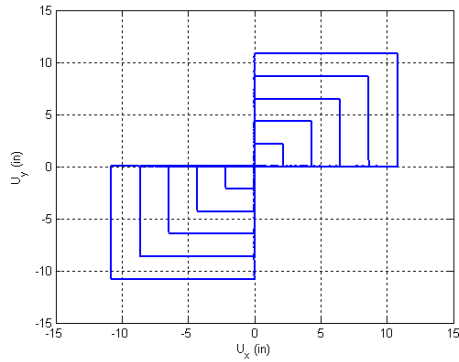


Base Moment vs. Top Rotation

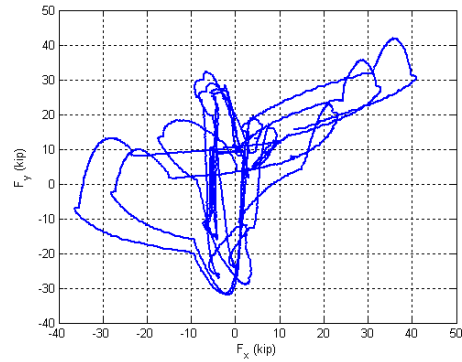


Base Moment vs. Base Curvature

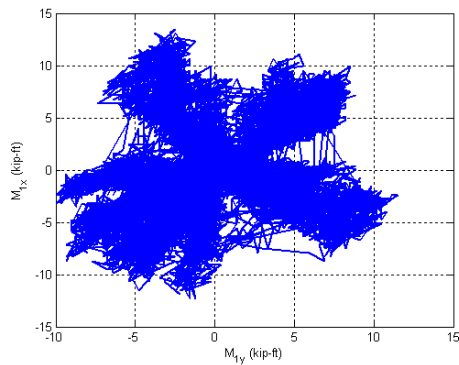
Figure B.61. Experimental results from LC2b in the specimen 8Rw-18-12



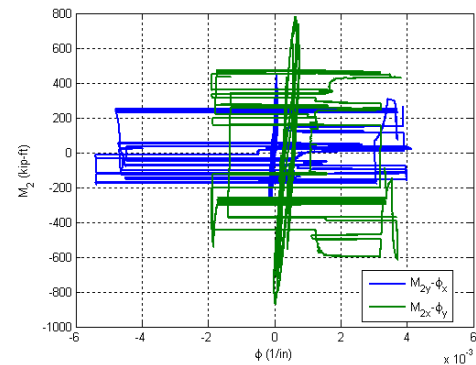
Y Displacement vs. X Displacement



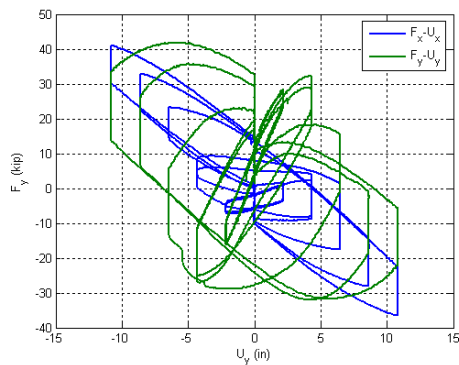
Y Force vs. X Force



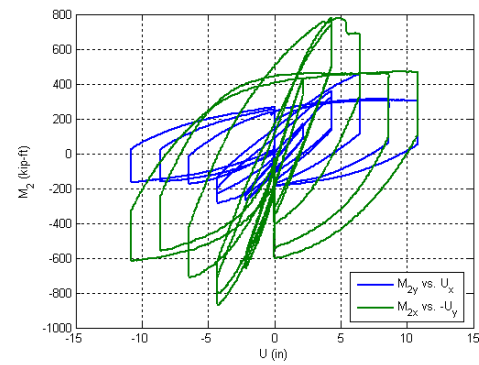
X Moment vs. Y Moment at the top



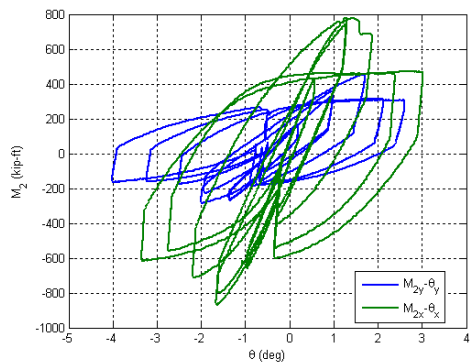
X Moment vs. Y Moment at the base



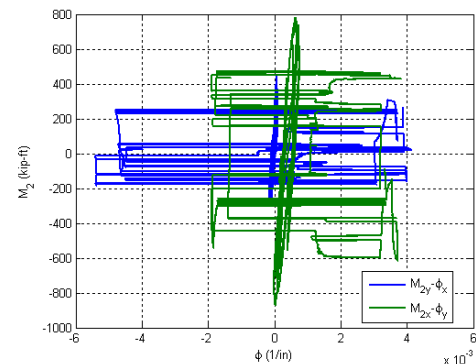
Lateral Force vs. Lateral Displacement



Base Moment vs. Top Displacement

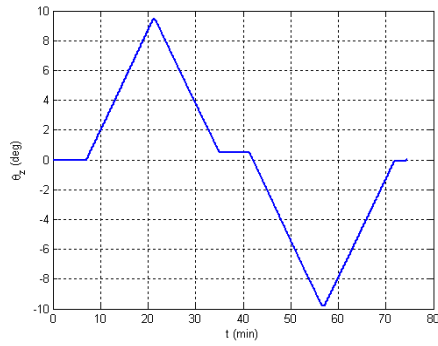


Base Moment vs. Top Rotation

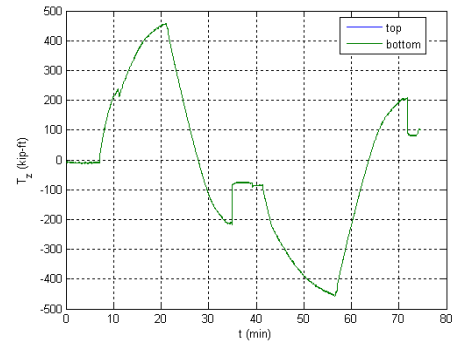


Base Moment vs. Base Curvature

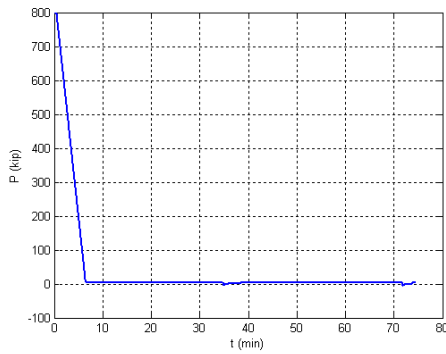
Figure B.62. Experimental results from LC3a in the specimen 8Rw-18-12



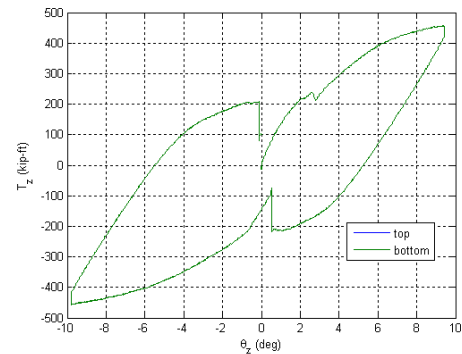
Twisting Angle vs. Time



Torsion Moment vs. Time

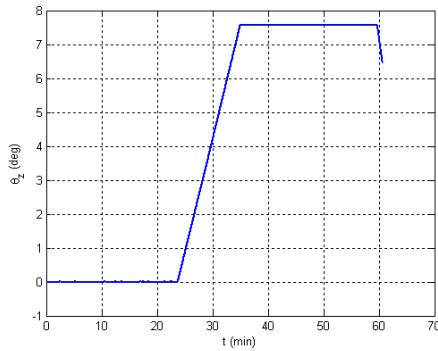


Axial Force vs. Time

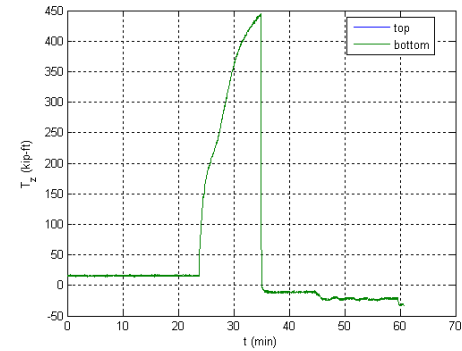


Torsion Moment vs. Twisting Angle

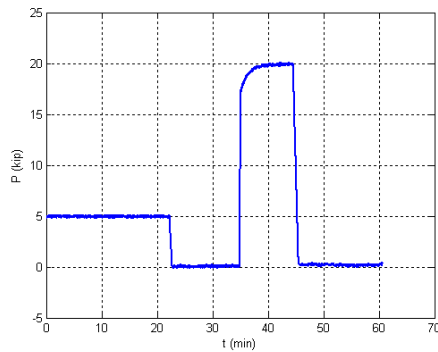
Figure B.63. Experimental results from LC4 in the specimen 8Rw-26-12



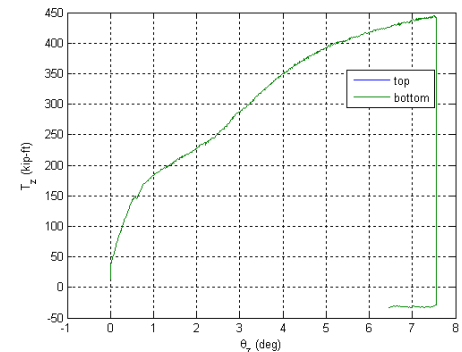
Twisting Angle vs. Time



Torsion Moment vs. Time



Axial Force vs. Time



Torsion Moment vs. Twisting Angle

Figure B.64. Experimental results from LC4 in the specimen 8Rw-18-12

B.9. Specimen 9Rs-18-12

Description:

- Specimen number: 9
- Composite Cross-section: RCFT
- Steel cross-section: HSS20x12x0.3125
- Design concrete strength: 12 ksi
- Design specimen length: 18 ft
- Pouring date: 09/17/2008
- Testing date: 12/29/2008

Parameters:

- Specimen length: 18' 2 5/8"
- Initial out-of-plumbness: $U_{xo} = 0.82'' / U_{yo} = -0.24''$
- Steel yielding stress: $F_y = 53.0$ ksi
- Steel ultimate stress: $F_u = 72.8$ ksi
- Concrete strength at the 28th day: $f_c' = 12.7$ ksi
- Concrete strength at the testing day: $f_c = 13.3$ ksi
- Concrete Young's modulus: $E_c = 6070$ ksi
- Concrete tensile strength: $f_t = 1.65$ ksi

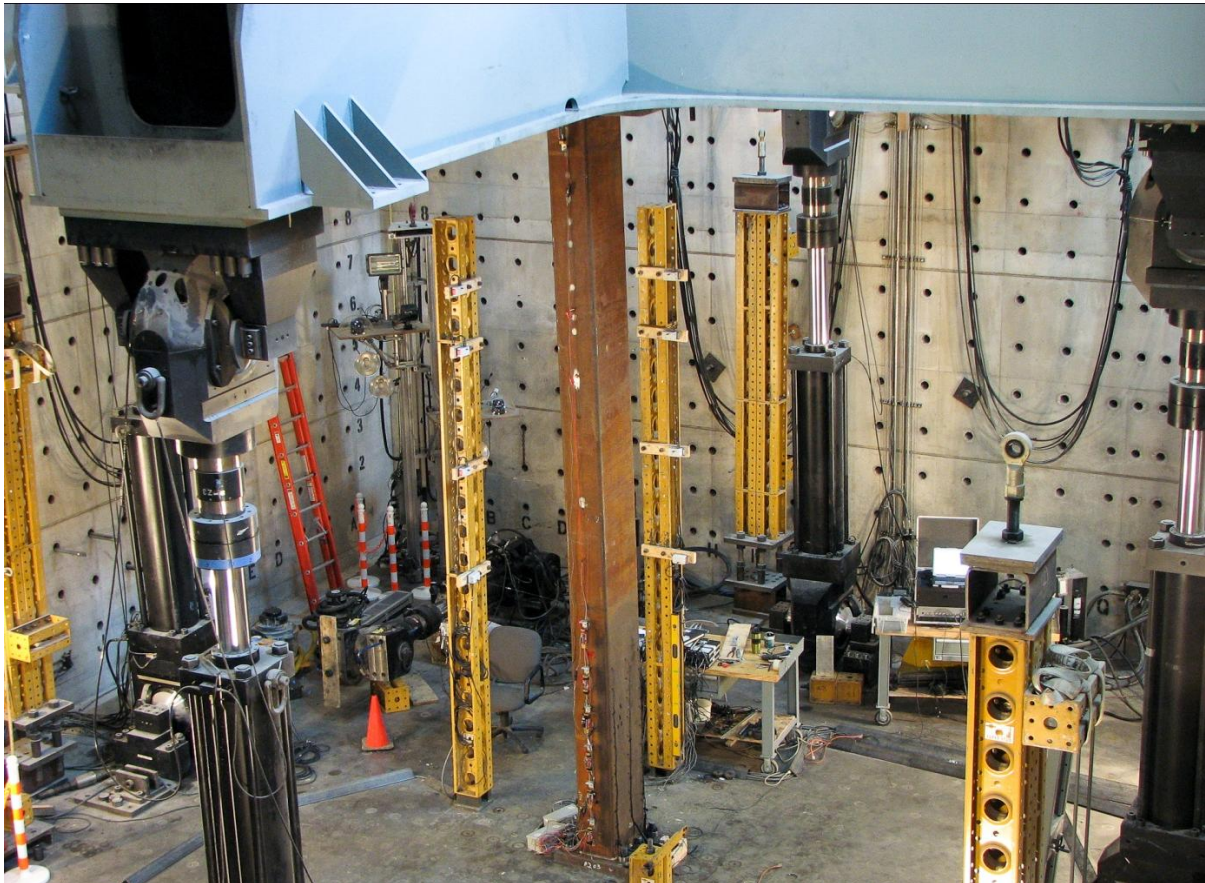


Figure B.65. Specimen 9Rs-18-12

Table B.9. Load protocol summary for the specimen 9Rs-18-12

LC1 - Incremental compression loading in two cycles until the maximum load is reached. The top is forced to be free at X ($K_x=2$) and fixed at Y ($K_y=0.5$).

Step	DOF						Stop Criterion
	X	Y	Z	RX	RY	RZ	
1	$F_x = 0$	$U_y = 0$	$U_z \downarrow$	$R_x = 0$	$M_y = 0$	$R_z = 0$	max P
2	$F_x = 0$	$U_y = 0$	$U_z \uparrow$	$R_x = 0$	$M_y = 0$	$R_z = 0$	P = 0
3	$F_x = 0$	$U_y = 0$	$U_z \downarrow$	$R_x = 0$	$M_y = 0$	$R_z = 0$	max P
4	$F_x = 0$	$U_y = 0$	$U_z \uparrow$	$R_x = 0$	$M_y = 0$	$R_z = 0$	P = 0

LC2a - Cyclic uniaxial lateral displacements with constant compression force ($-F_z = P = 1200$ kips). The top was forced to have zero moments in Y and fixed rotation in X.

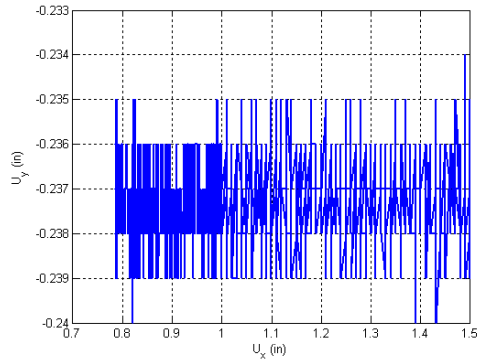
Step	DOF						Stop Criterion
	X	Y	Z	RX	RY	RZ	
1	$U_x \downarrow$	$U_y = 0$	P = 1200k	$R_x = 0$	$M_y = 0$	$R_z = 0$	+F peak
2	$U_x \uparrow$	$U_y = 0$	P = 1200k	$R_x = 0$	$M_y = 0$	$R_z = 0$	-F peak
3	$U_x \downarrow$	$U_y = 0$	P = 1200k	$R_x = 0$	$M_y = 0$	$R_z = 0$	+F peak
4	$U_x \uparrow$	$U_y = 0$	P = 1200k	$R_x = 0$	$M_y = 0$	$R_z = 0$	-F peak
5	$U_x \uparrow$	$U_y = 0$	P = 1200k	$R_x = 0$	$M_y = 0$	$R_z = 0$	$U_z = 0$

LC2b - Cyclic uniaxial lateral displacements with constant compression force ($-F_z = P = 400$ kips). The top was forced to have zero moments in Y and fixed rotation in X.

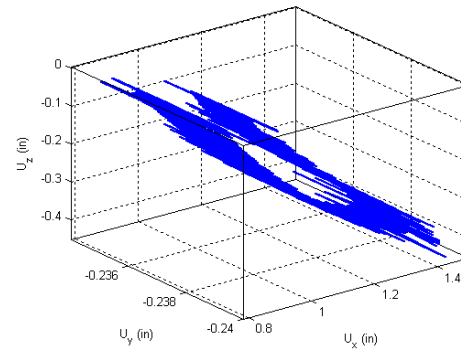
Step	DOF						Stop Criterion
	X	Y	Z	RX	RY	RZ	
1	$U_x \downarrow$	$U_y = 0$	P = 400k	$R_x = 0$	$M_y = 0$	$R_z = 0$	+F peak
2	$U_x \uparrow$	$U_y = 0$	P = 400k	$R_x = 0$	$M_y = 0$	$R_z = 0$	-F peak
3	$U_x \downarrow$	$U_y = 0$	P = 400k	$R_x = 0$	$M_y = 0$	$R_z = 0$	+F peak
4	$U_x \uparrow$	$U_y = 0$	P = 400k	$R_x = 0$	$M_y = 0$	$R_z = 0$	-F peak
5	$U_x \uparrow$	$U_y = 0$	P = 400k	$R_x = 0$	$M_y = 0$	$R_z = 0$	$U_z = 0$

LC3a - Cyclic biaxial lateral displacements with constant compression force ($-F_z = P = 800$ kips), and a set of 6 probes and several subprobes each. The top was forced to have zero moments.

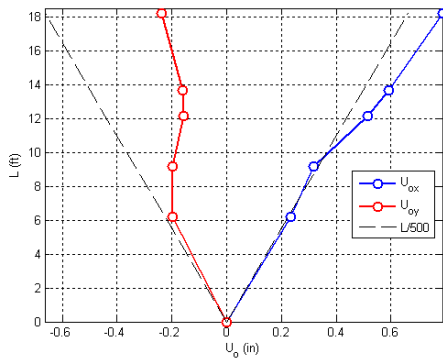
Step	DOF						Stop Criterion
	X	Y	Z	RX	RY	RZ	
1	$U_x \uparrow$	$U_y \uparrow$	P = 800k	$M_x = 0$	$M_y = 0$	$R_z = 0$	Probe 1
2	$U_x \downarrow$	$U_y \downarrow$	P = 800k	$M_x = 0$	$M_y = 0$	$R_z = 0$	Probe 2
3	$U_x \uparrow$	$U_y \downarrow$	P = 800k	$M_x = 0$	$M_y = 0$	$R_z = 0$	Probes 3
4	$U_x \downarrow$	$U_y \uparrow$	P = 800k	$M_x = 0$	$M_y = 0$	$R_z = 0$	Probe 4
5	$U_x \downarrow$	$U_y \downarrow$	P = 800k	$M_x = 0$	$M_y = 0$	$R_z = 0$	Probe 5
6	$U_x \uparrow$	$U_y \uparrow$	P = 800k	$M_x = 0$	$M_y = 0$	$R_z = 0$	Probe 6



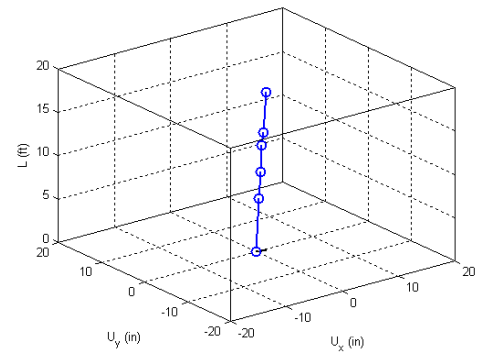
Y displacement vs. X displacement



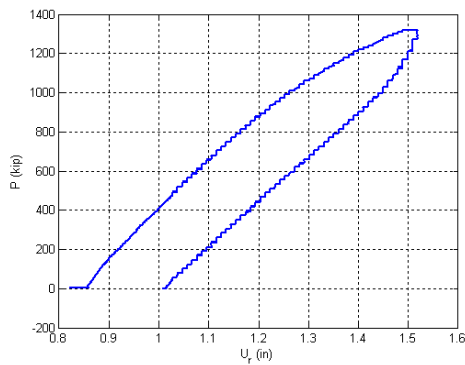
Z displacement vs. X and Y displacement



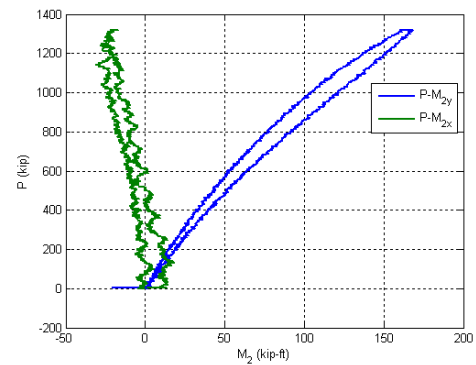
Initial deflected shape



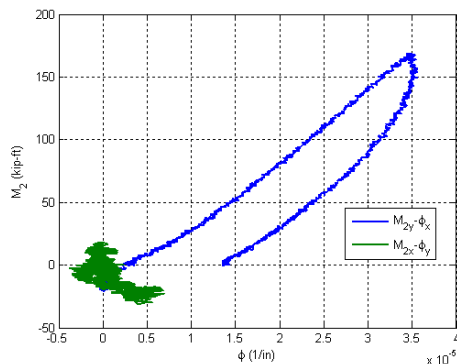
Maximum lateral displacement



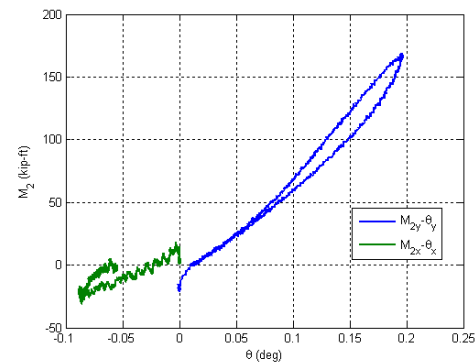
Axial force vs. lateral displacement



Axial force vs. base moments

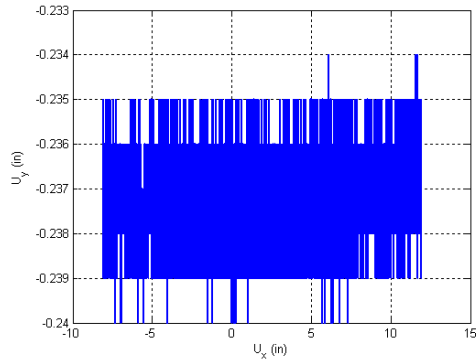


Base moment vs. base curvature

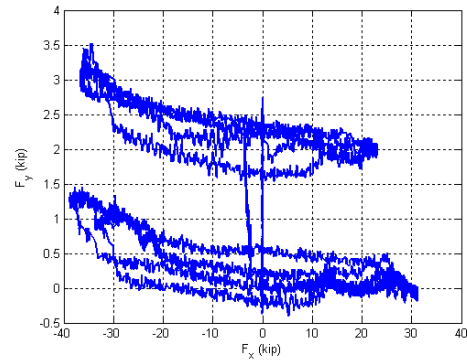


Base moment vs. top rotation

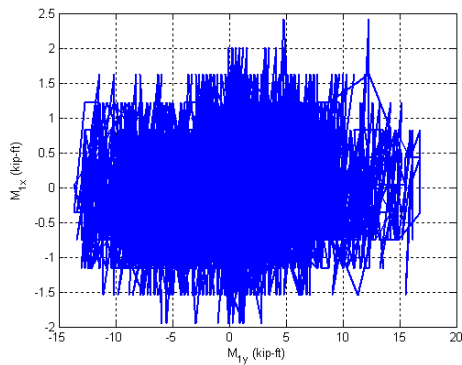
Figure B.66. Experimental results from LC1 in the specimen 9Rs-18-12



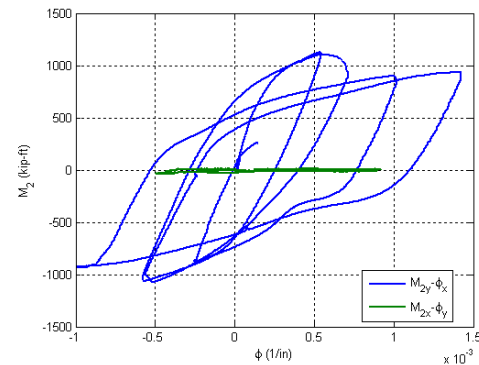
Y Displacement vs. X Displacement



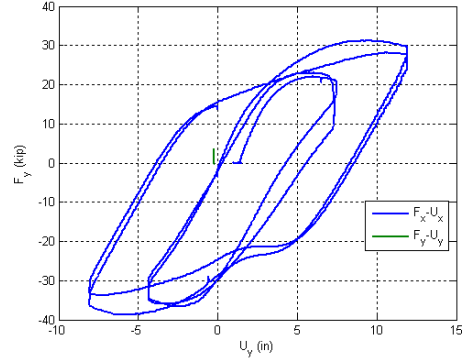
Y Force vs. X Force



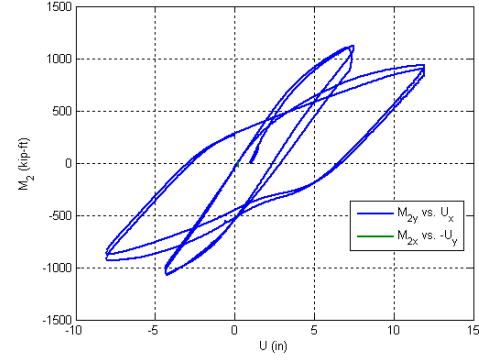
X Moment vs. Y Moment at the top



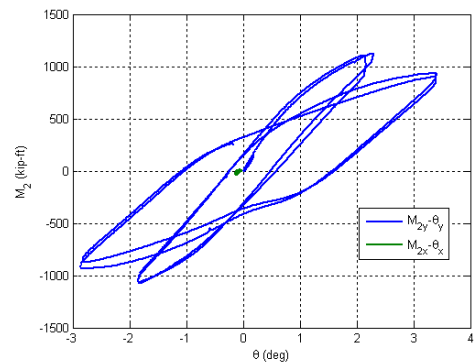
X Moment vs. Y Moment at the base



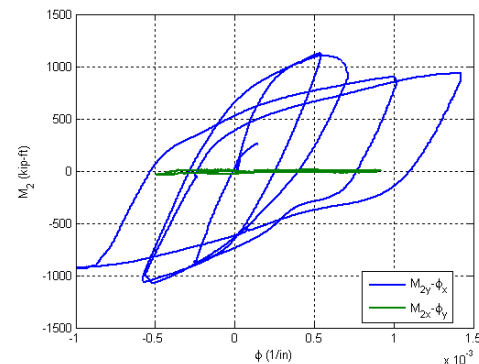
Lateral Force vs. Lateral Displacement



Base Moment vs. Top Displacement

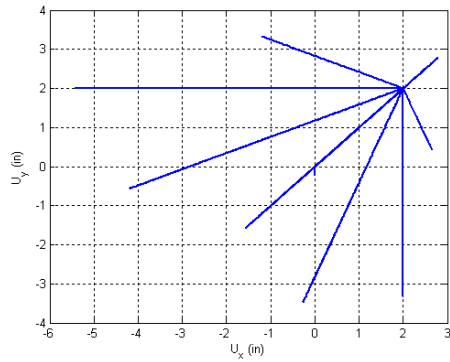


Base Moment vs. Top Rotation

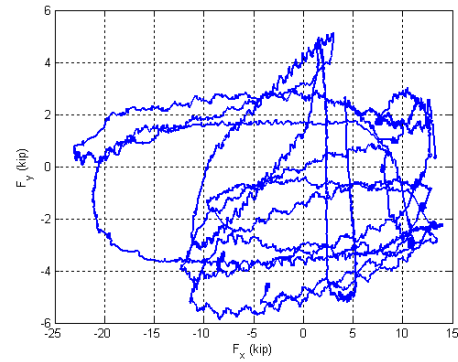


Base Moment vs. Base Curvature

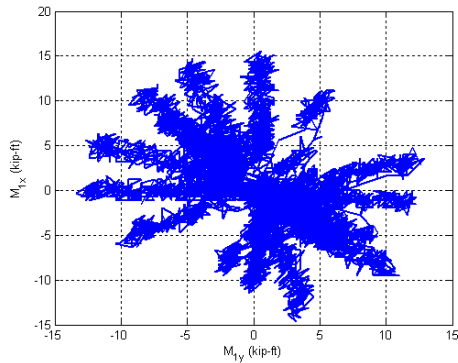
Figure B.67. Experimental results from LC2 in the specimen 9Rs-18-12



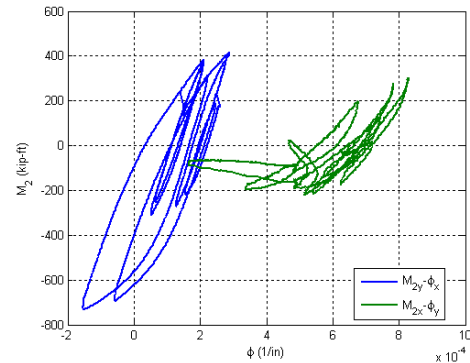
Y Displacement vs. X Displacement



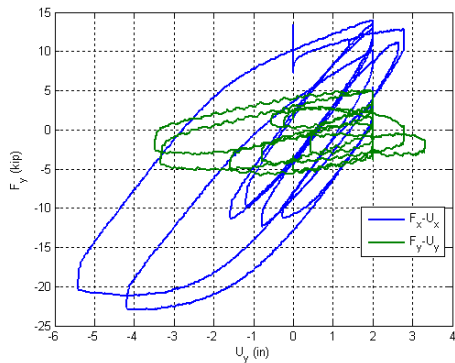
Y Force vs. X Force



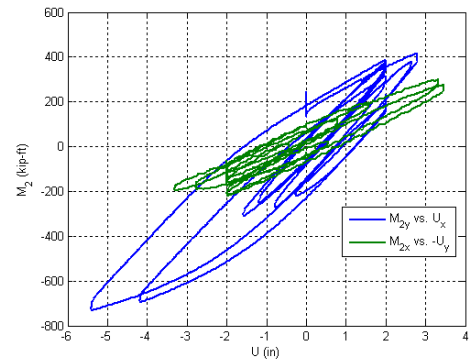
X Moment vs. Y Moment at the top



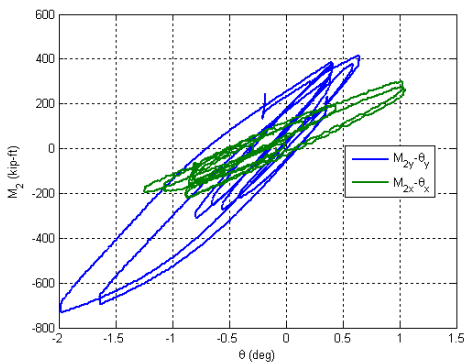
X Moment vs. Y Moment at the base



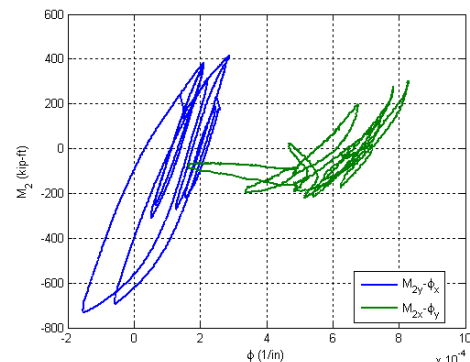
Lateral Force vs. Lateral Displacement



Base Moment vs. Top Displacement

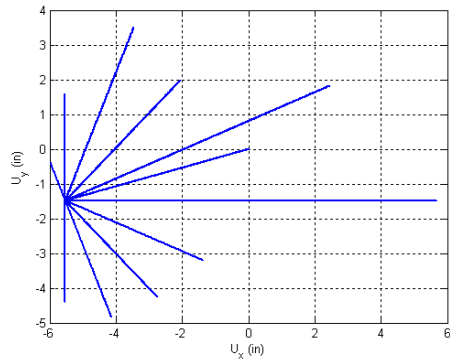


Base Moment vs. Top Rotation

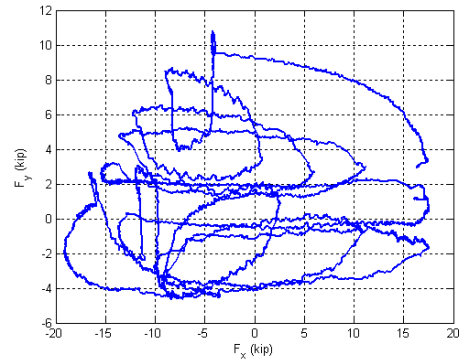


Base Moment vs. Base Curvature

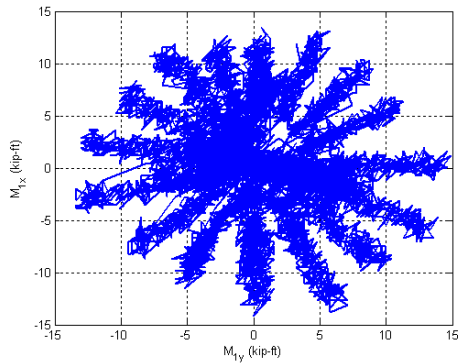
Figure B.68. Experimental results from LC3a in the specimen 9Rs-18-12



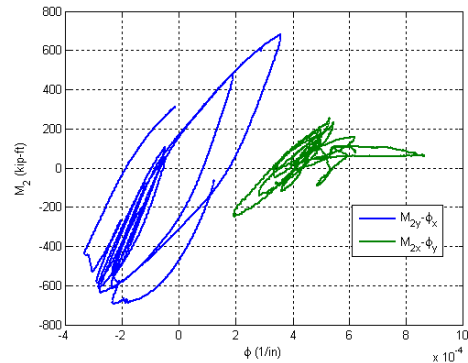
Y Displacement vs. X Displacement



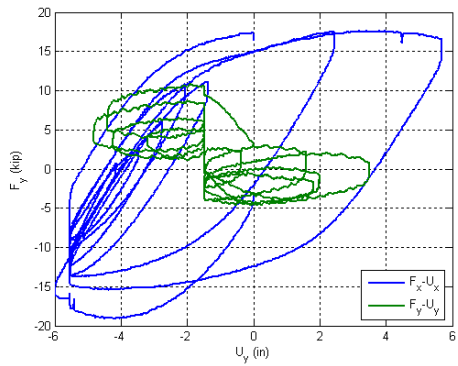
Y Force vs. X Force



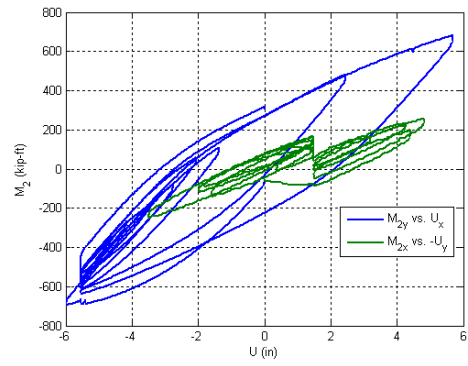
X Moment vs. Y Moment at the top



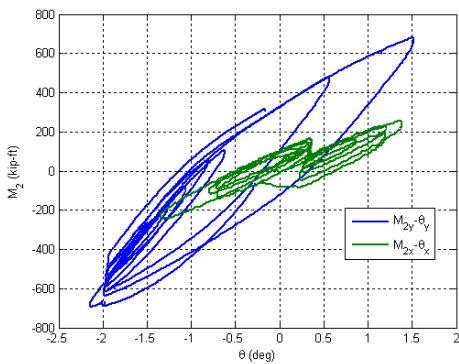
X Moment vs. Y Moment at the base



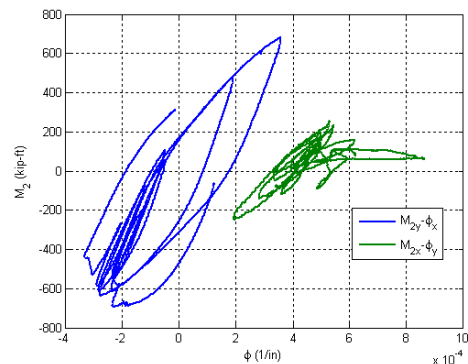
Lateral Force vs. Lateral Displacement



Base Moment vs. Top Displacement

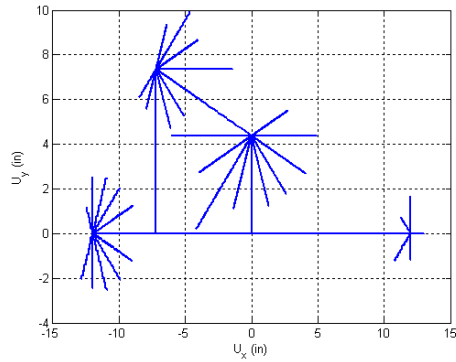


Base Moment vs. Top Rotation

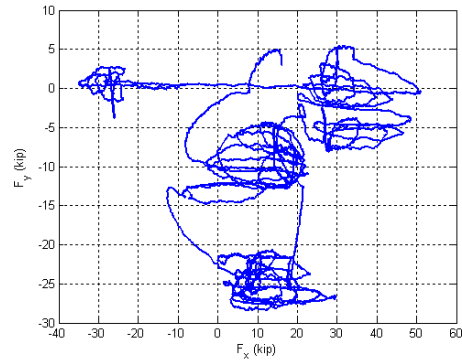


Base Moment vs. Base Curvature

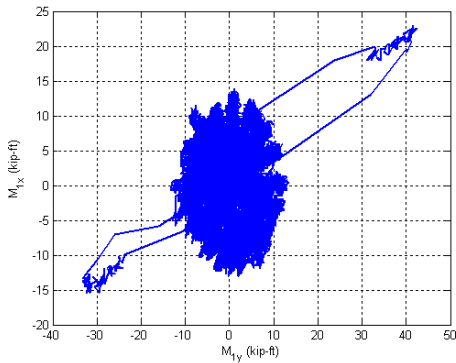
Figure B.69. Experimental results from LC3b in the specimen 9Rs-18-12



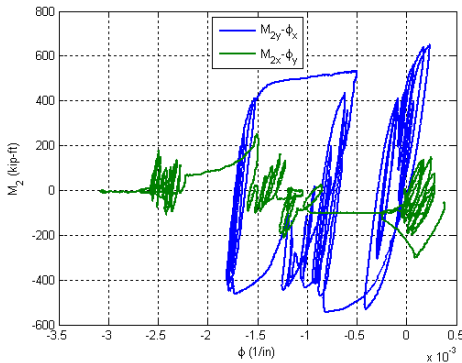
Y Displacement vs. X Displacement



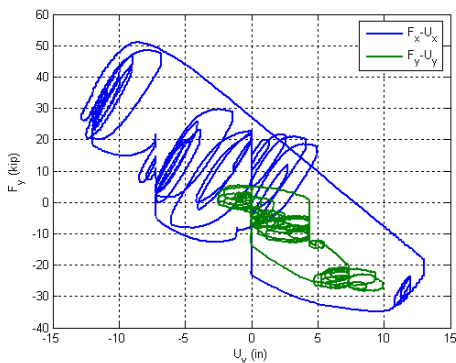
Y Force vs. X Force



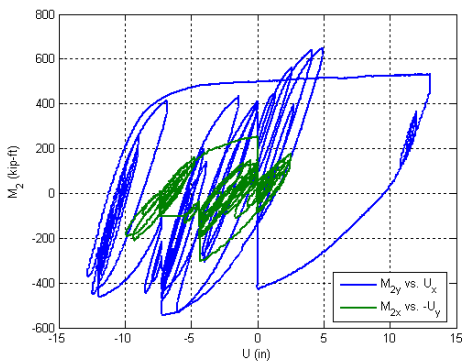
X Moment vs. Y Moment at the top



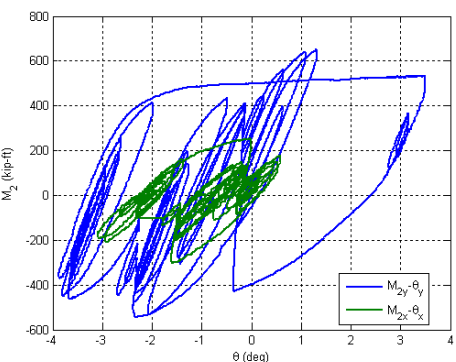
X Moment vs. Y Moment at the base



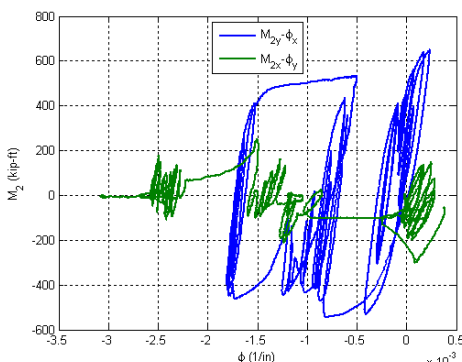
Lateral Force vs. Lateral Displacement



Base Moment vs. Top Displacement



Base Moment vs. Top Rotation



Base Moment vs. Base Curvature

Figure B.70. Experimental results from LC3c in the specimen 9Rs-18-12

B.10. Specimen 10-C12-26-5

Description:

- Specimen number: 10
- Composite Cross-section: CCFT
- Steel cross-section: HSS12.75x0.25
- Design concrete strength: 5 ksi
- Design specimen length: 26 ft
- Pouring date: 03/27/2009
- Testing date: 05/18/2009

Parameters:

- Specimen length: 26' 1"
- Initial out-of-plumbness: $U_{xo} = 0.79'' / U_{yo} = -0.63''$
- Steel yielding stress: $F_y = 48.6 \text{ ksi}$
- Steel ultimate stress: $F_u = 68.1 \text{ ksi}$
- Concrete strength at the 28th day: $f_c' = 7.3 \text{ ksi}$
- Concrete strength at the testing day: $f_c = 7.9 \text{ ksi}$
- Concrete Young's modulus: $E_c = 5000 \text{ ksi}$
- Concrete tensile strength: $f_t = 0.6 \text{ ksi}$

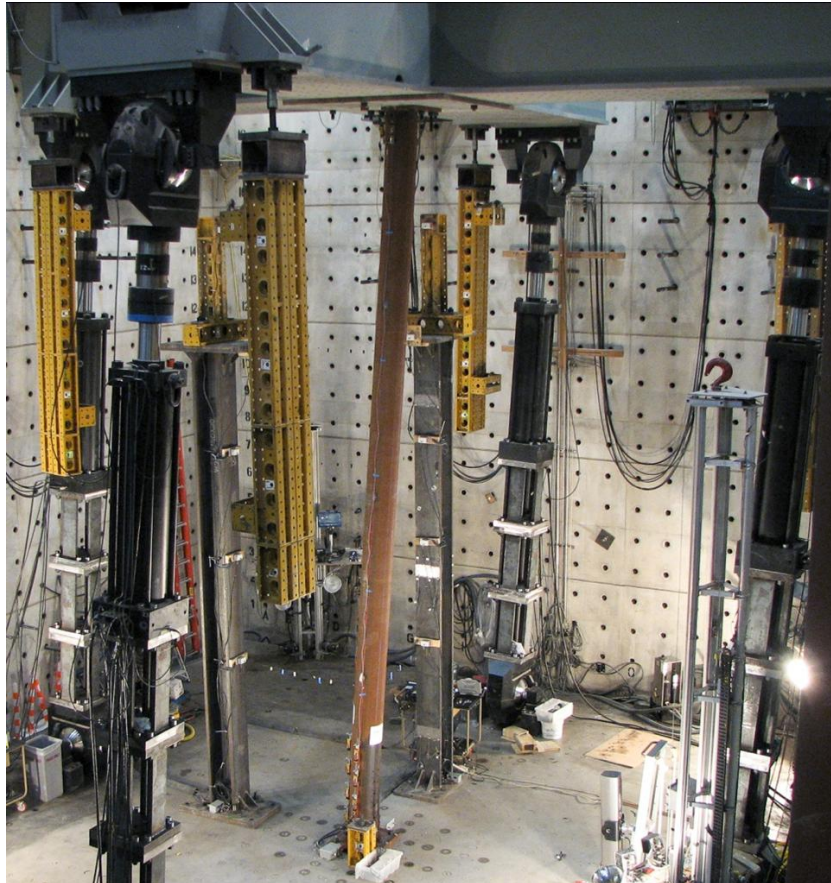


Figure B.71. Specimen C12-26-5

Table B.10. Load protocol summary for the specimen 10C12-26-5

LC1 - Incremental compression loading in two cycles until the maximum load is reached. The top is forced to be free at all the time.

Step	DOF						Stop Criterion
	X	Y	Z	RX	RY	RZ	
1	$F_x = 0$	$F_y = 0$	$U_z \downarrow$	$M_x = 0$	$M_y = 0$	$R_z = 0$	max P
2	$F_x = 0$	$F_y = 0$	$U_z \uparrow$	$M_x = 0$	$M_y = 0$	$R_z = 0$	P = 0
3	$F_x = 0$	$F_y = 0$	$U_z \downarrow$	$M_x = 0$	$M_y = 0$	$R_z = 0$	max P
4	$F_x = 0$	$F_y = 0$	$U_z \uparrow$	$M_x = 0$	$M_y = 0$	$R_z = 0$	P = 0
5	$F_x = 0$	$F_y = 0$	$U_z \downarrow$	$M_x = 0$	$M_y = 0$	$R_z = 0$	P = 200k

LC2a - Cyclic uniaxial lateral displacements with constant compression force ($-F_z = P = 200$ kips). The top was forced to have zero moments.

Step	DOF						Stop Criterion
	X	Y	Z	RX	RY	RZ	
1	$U_x \downarrow$	$U_y \uparrow$	P = 200k	$M_x = 0$	$M_y = 0$	$R_z = 0$	-1% drift
2	$U_x \uparrow$	$U_y \downarrow$	P = 200k	$M_x = 0$	$M_y = 0$	$R_z = 0$	+2% drift
3	$U_x \downarrow$	$U_y \uparrow$	P = 200k	$M_x = 0$	$M_y = 0$	$R_z = 0$	-2% drift
4	$U_x \uparrow$	$U_y \downarrow$	P = 200k	$M_x = 0$	$M_y = 0$	$R_z = 0$	+3% drift
5	$U_x \downarrow$	$U_y \uparrow$	P = 200k	$M_x = 0$	$M_y = 0$	$R_z = 0$	-3% drift
6	$U_x \uparrow$	$U_y \downarrow$	P = 200k	$M_x = 0$	$M_y = 0$	$R_z = 0$	$U_z = 0$

LC2b - Cyclic uniaxial lateral displacements with constant compression force ($-F_z = P = 100$ kips). The top was forced to have zero moments.

Step	DOF						Stop Criterion
	X	Y	Z	RX	RY	RZ	
1	$U_x \downarrow$	$U_y \downarrow$	P = 100k	$M_x = 0$	$M_y = 0$	$R_z = 0$	+/-1% drift
2	$U_x \uparrow$	$U_y \uparrow$	P = 100k	$M_x = 0$	$M_y = 0$	$R_z = 0$	+/-2% drift
3	$U_x \downarrow$	$U_y \downarrow$	P = 100k	$M_x = 0$	$M_y = 0$	$R_z = 0$	+/-3% drift
4	$U_x \uparrow$	$U_y \uparrow$	P = 100k	$M_x = 0$	$M_y = 0$	$R_z = 0$	+/-4% drift
5	$U_x \downarrow$	$U_y \downarrow$	P = 100k	$M_x = 0$	$M_y = 0$	$R_z = 0$	+/-5% drift
6	$U_x \uparrow$	$U_y \uparrow$	P = 100k	$M_x = 0$	$M_y = 0$	$R_z = 0$	$F_z = 0$

LC3a - Cyclic biaxial lateral displacements (8 shape) with constant compression force ($-F_z = P = 150$ kips). The top was forced to have zero moments.

Step	DOF						Stop Criterion
	X	Y	Z	RX	RY	RZ	
1	$U_x \downarrow$	$U_y \downarrow$	P = 150k	$M_x = 0$	$M_y = 0$	$R_z = 0$	+/-1% drift
2	$U_x \uparrow$	$U_y \uparrow$	P = 150k	$M_x = 0$	$M_y = 0$	$R_z = 0$	+/-2% drift
3	$U_x \downarrow$	$U_y \downarrow$	P = 150k	$M_x = 0$	$M_y = 0$	$R_z = 0$	+/-3% drift
4	$U_x \uparrow$	$U_y \uparrow$	P = 150k	$M_x = 0$	$M_y = 0$	$R_z = 0$	+/-4% drift

LC3b - Cyclic biaxial lateral displacements (8 shape) with constant compression force ($-F_z = P = 50$ kips). The top was forced to have zero moments.

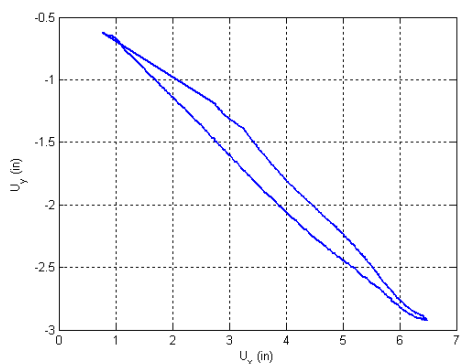
Step	DOF						Stop Criterion
	X	Y	Z	RX	RY	RZ	
1	$U_x \uparrow$	$U_y \uparrow$	$P = 50k$	$M_x = 0$	$M_y = 0$	$R_z = 0$	+/-1% drift
2	$U_x \downarrow$	$U_y \downarrow$	$P = 50k$	$M_x = 0$	$M_y = 0$	$R_z = 0$	+/-2% drift
3	$U_x \uparrow$	$U_y \uparrow$	$P = 50k$	$M_x = 0$	$M_y = 0$	$R_z = 0$	+/-3% drift
4	$U_x \downarrow$	$U_y \downarrow$	$P = 50k$	$M_x = 0$	$M_y = 0$	$R_z = 0$	+/-4% drift

LC4a - Incremental compression loading until the maximum load is reached. The top is forced to have free translation and fixed rotation ($K=1$).

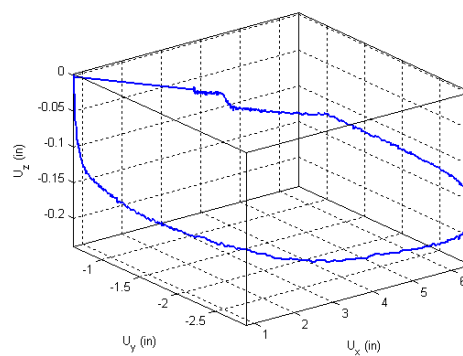
Step	DOF						Stop Criterion
	X	Y	Z	RX	RY	RZ	
1	$F_x \rightarrow 0$	$F_y \rightarrow 0$	$F_z \rightarrow 0$	$M_x = 0$	$M_y = 0$	$R_z = 0$	$F_x=F_y=0$
2	$F_x = 0$	$F_y = 0$	$U_z \downarrow$	R_x	R_y	$R_z = 0$	$P=1000k$
3	$U_x \downarrow$	$U_y \downarrow$	$P=1000k$	R_x	R_y	$R_z = 0$	$U_x=U_y=\max$
4	$U_x \uparrow$	$U_y \uparrow$	$P=1000k$	R_x	R_y	$R_z = 0$	$F_x=F_y=0$
5	$F_x = 0$	$F_y = 0$	$U_z \uparrow$	R_x	R_y	$R_z = 0$	$F_z = P = 0$

LC4b - Cyclic uniaxial lateral displacements (4 corners) with constant compression force ($-F_z = P = 300$ kips). The top is forced to have free translation and fixed rotation ($K=1$).

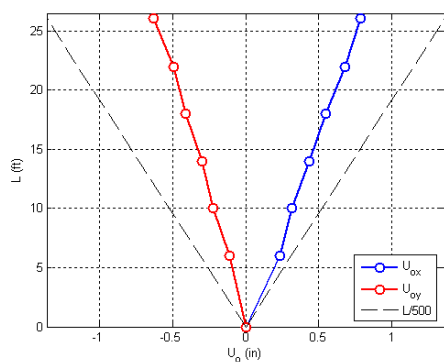
Step	DOF						Stop Criterion
	X	Y	Z	RX	RY	RZ	
1	$U_x = \uparrow$	$U_y \uparrow$	$P = 300k$	R_x	R_y	$R_z = 0$	max stroke
2	$U_x \downarrow$	$U_y \downarrow$	$P = 300k$	R_x	R_y	$R_z = 0$	max stroke
3	$U_x \rightarrow 0$	$U_y \rightarrow 0$	$P = 300k$	R_x	R_y	$R_z = 0$	$U_x=U_y=0$
4	$U_x \uparrow$	$U_y \downarrow$	$P = 300k$	R_x	R_y	$R_z = 0$	max stroke
5	$U_x \downarrow$	$U_y \uparrow$	$P = 300k$	R_x	R_y	$R_z = 0$	max stroke
6	$U_x \rightarrow 0$	$U_y \rightarrow 0$	$P = 300k$	R_x	R_y	$R_z = 0$	$U_x=U_y=0$



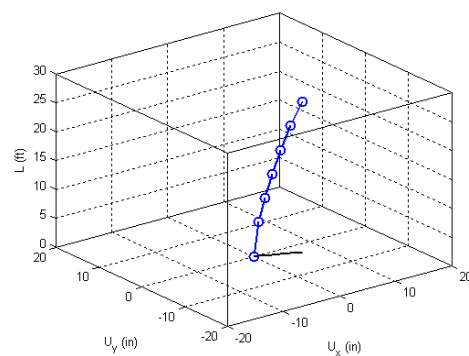
Y displacement vs. X displacement



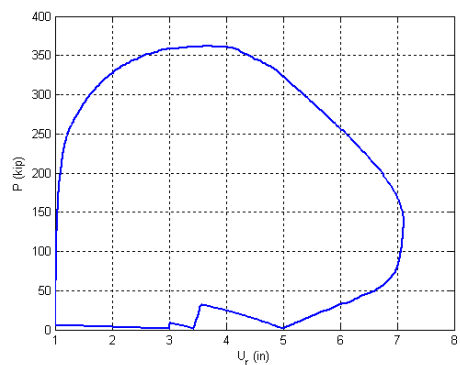
Z displacement vs. X and Y displacement



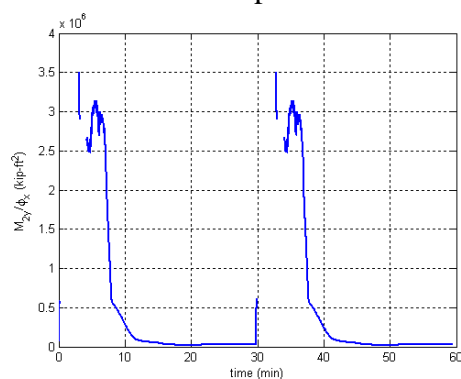
Initial deflected shape



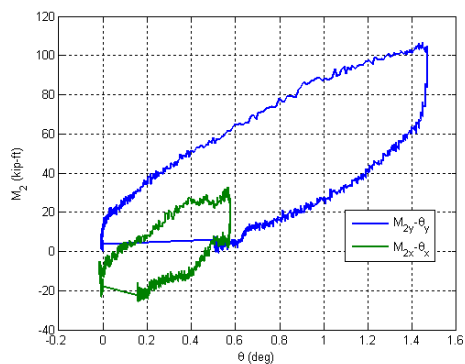
Maximum lateral displacement



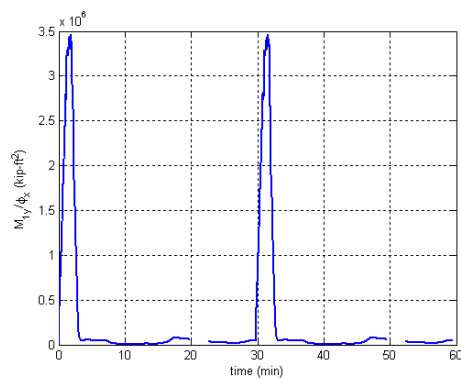
Axial force vs. lateral displacement



Axial force vs. base moments

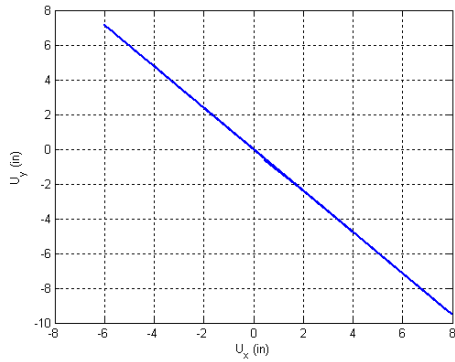


Base moment vs. base curvature

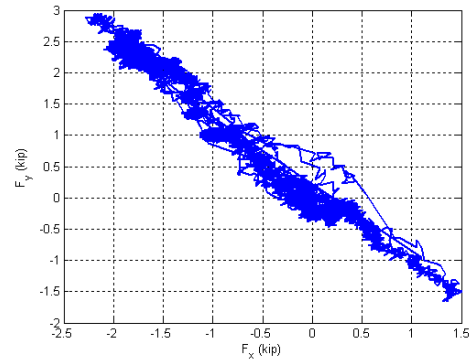


Base moment vs. top rotation

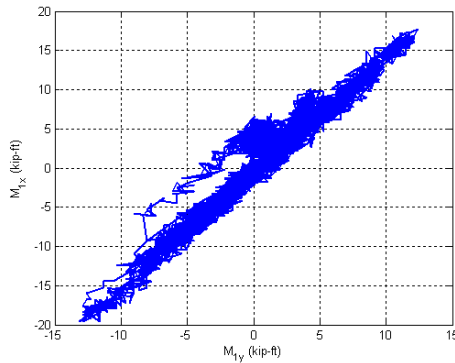
Figure B.72. Experimental results from LC1 in the specimen 10C12-26-5



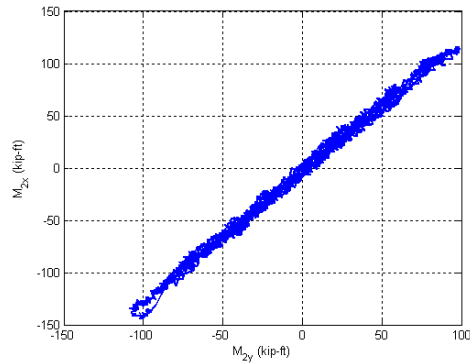
Y Displacement vs. X Displacement



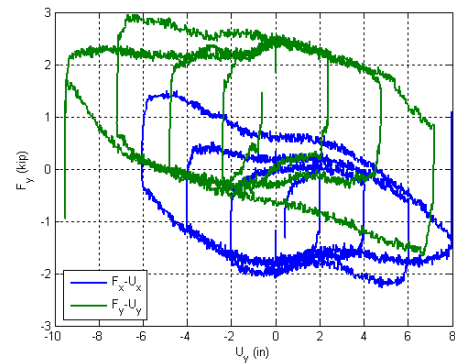
Y Force vs. X Force



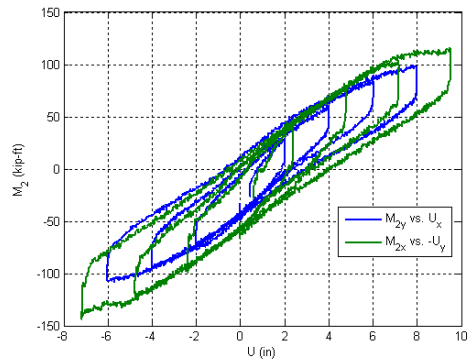
X Moment vs. Y Moment at the top



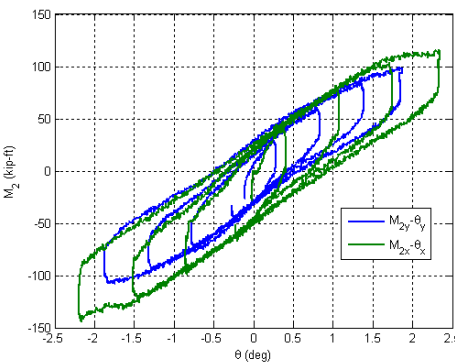
X Moment vs. Y Moment at the base



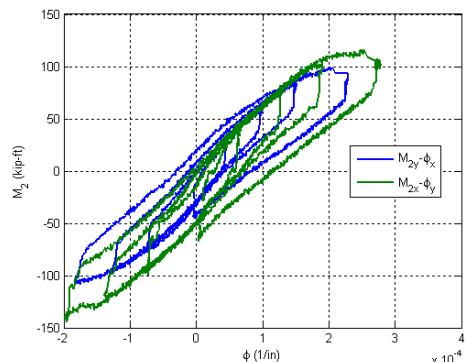
Lateral Force vs. Lateral Displacement



Base Moment vs. Top Displacement

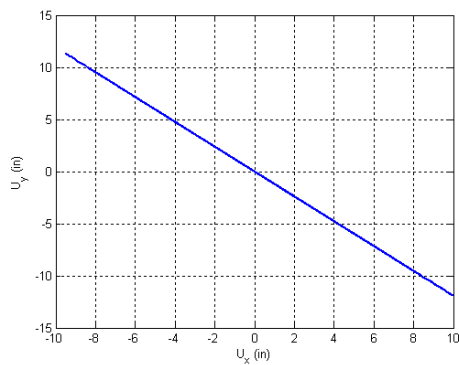


Base Moment vs. Top Rotation

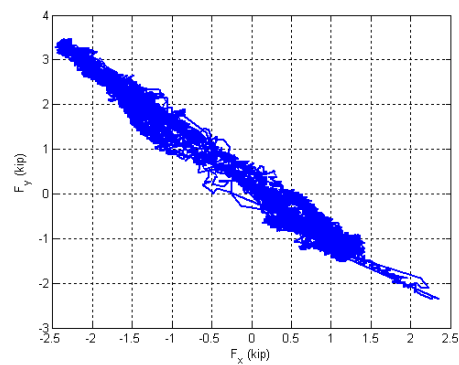


Base Moment vs. Base Curvature

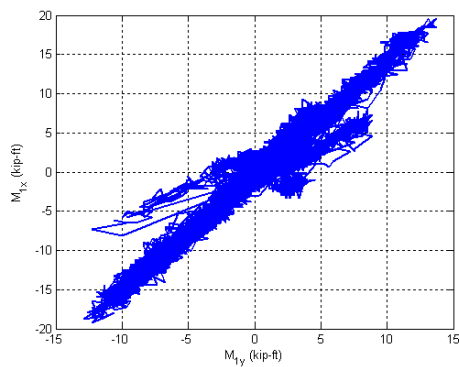
Figure B.73. Experimental results from LC2a in the specimen 10C12-26-5



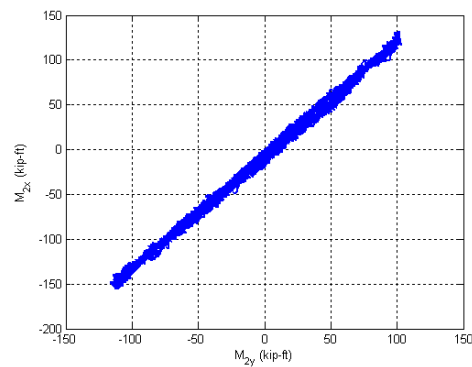
Y Displacement vs. X Displacement



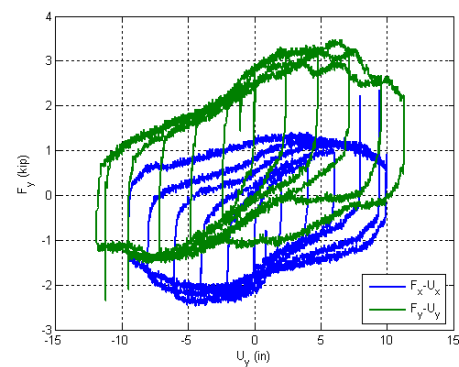
Y Force vs. X Force



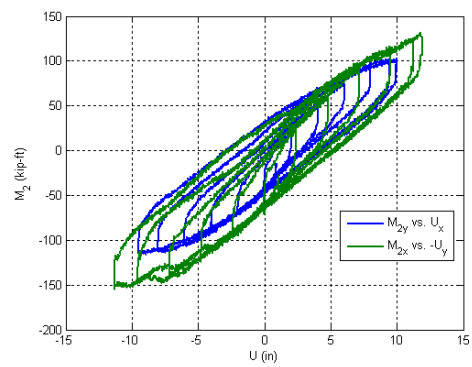
X Moment vs. Y Moment at the top



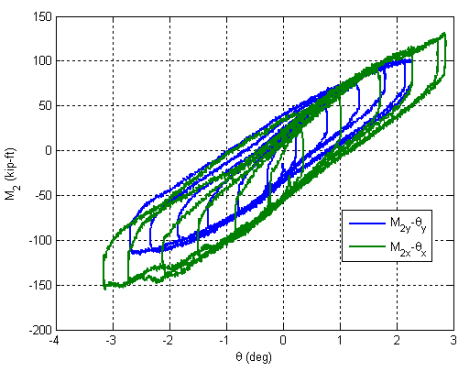
X Moment vs. Y Moment at the base



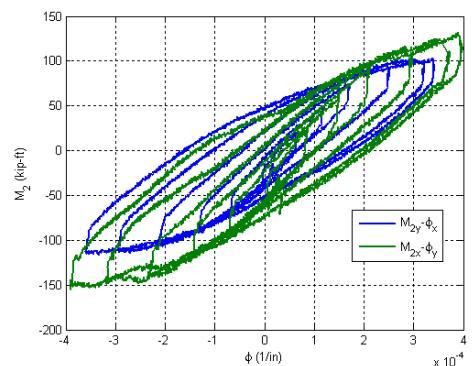
Lateral Force vs. Lateral Displacement



Base Moment vs. Top Displacement

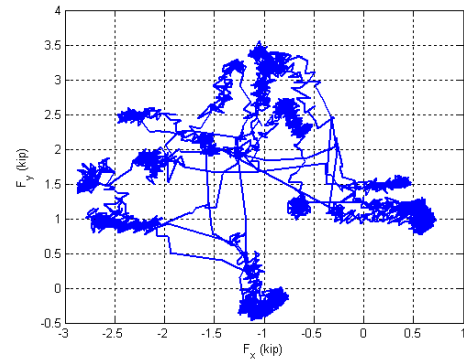
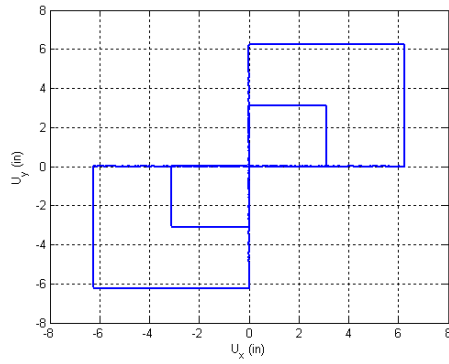


Base Moment vs. Top Rotation

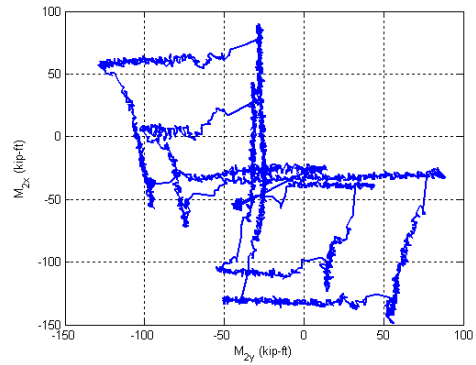
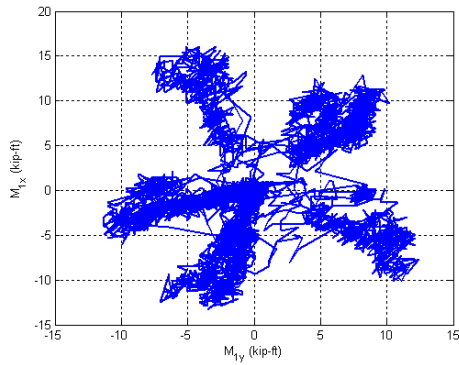


Base Moment vs. Base Curvature

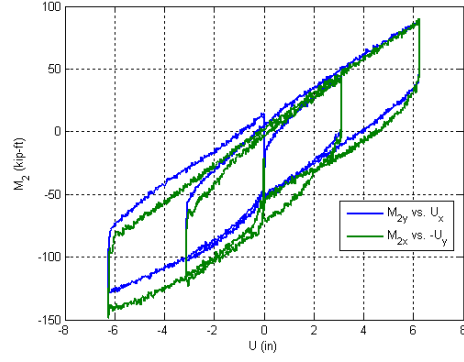
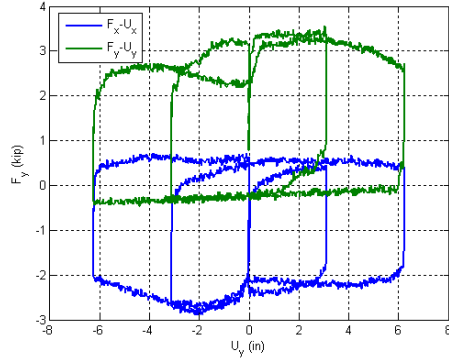
Figure B.74. Experimental results from LC2b in the specimen 10C12-26-5



Y Displacement vs. X Displacement Y Force vs. X Force

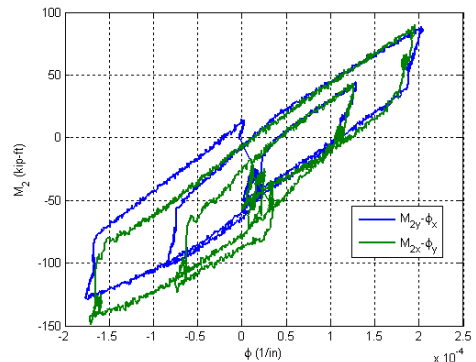
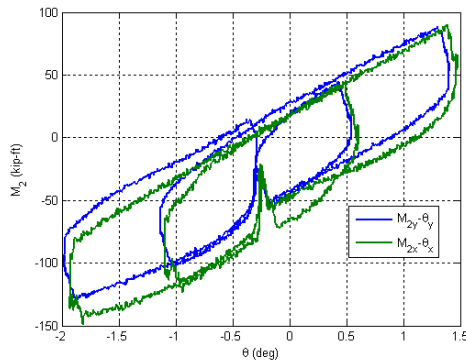


X Moment vs. Y Moment at the top X Moment vs. Y Moment at the base



Lateral Force vs. Lateral Displacement

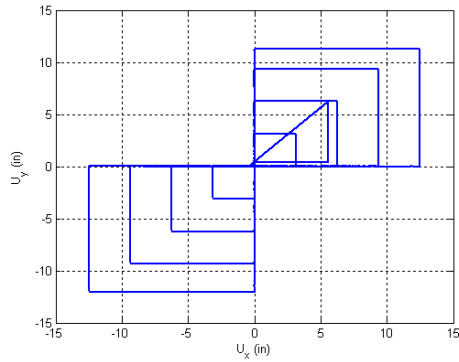
Base Moment vs. Top Displacement



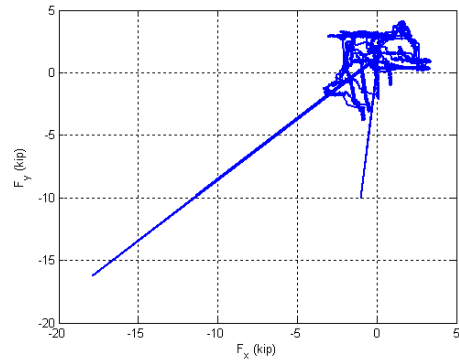
Base Moment vs. Top Rotation

Base Moment vs. Base Curvature

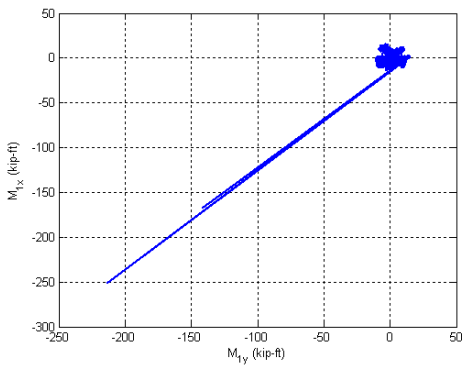
Figure B.75. Experimental results from LC3a in the specimen 10C12-26-5



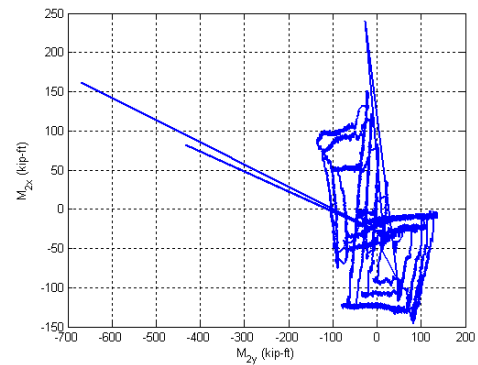
Y Displacement vs. X Displacement



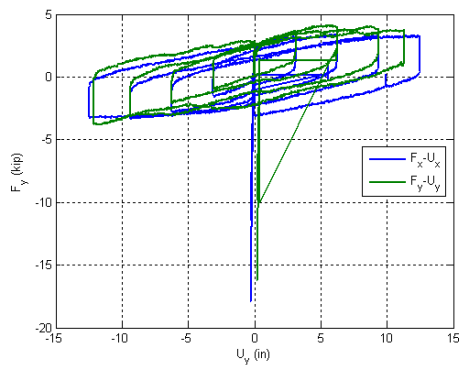
Y Force vs. X Force



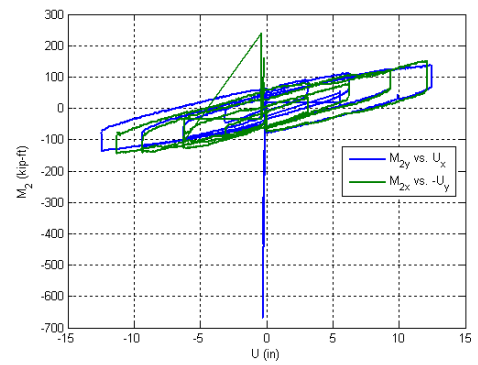
X Moment vs. Y Moment at the top



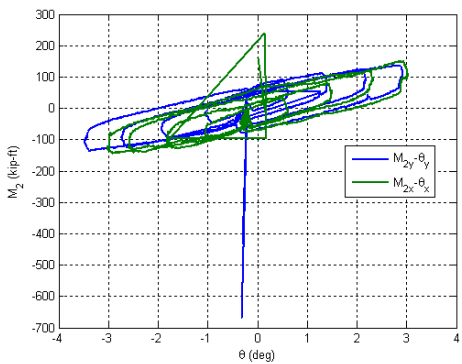
X Moment vs. Y Moment at the base



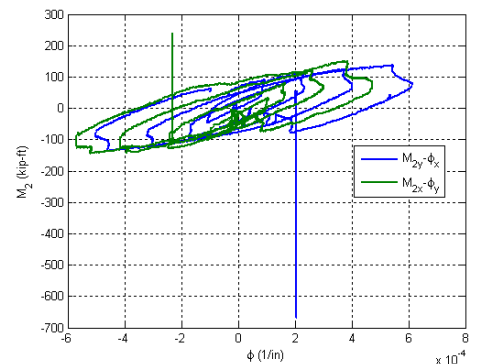
Lateral Force vs. Lateral Displacement



Base Moment vs. Top Displacement

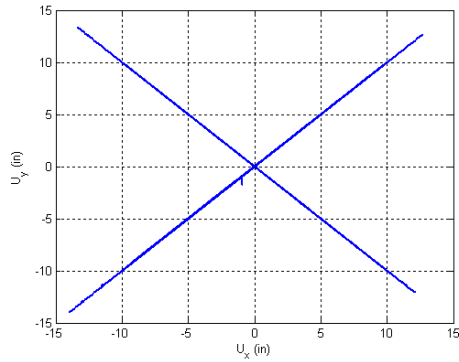


Base Moment vs. Top Rotation

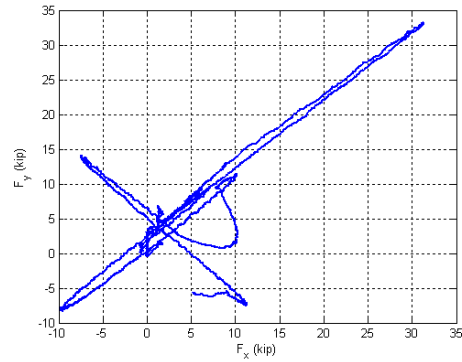


Base Moment vs. Base Curvature

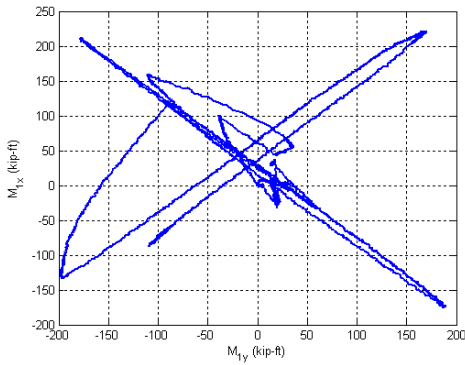
Figure B.76. Experimental results from LC3b in the specimen 10C12-26-5



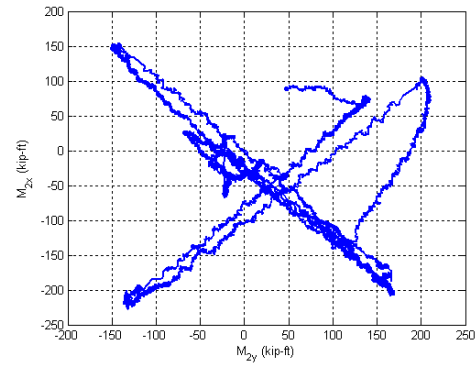
Y Displacement vs. X Displacement



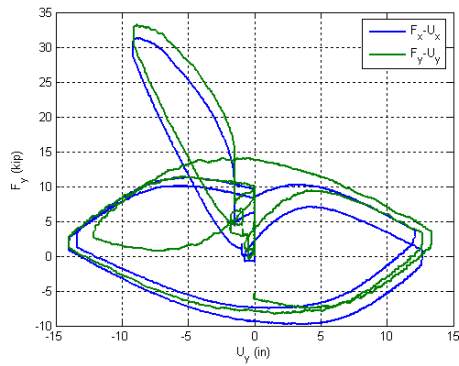
Y Force vs. X Force



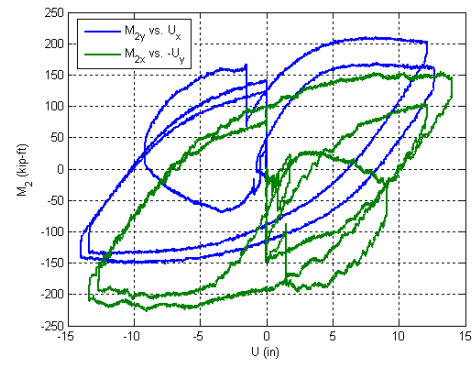
X Moment vs. Y Moment at the top



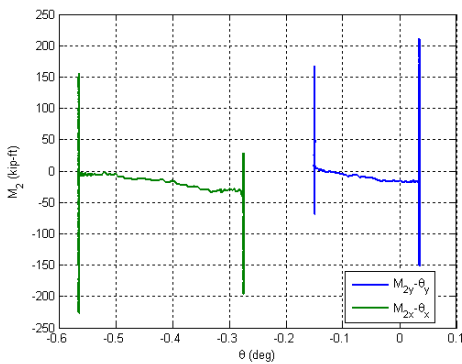
X Moment vs. Y Moment at the base



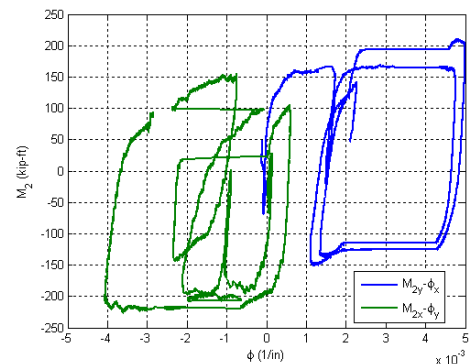
Lateral Force vs. Lateral Displacement



Base Moment vs. Top Displacement



Base Moment vs. Top Rotation



Base Moment vs. Base Curvature

Figure B.77. Experimental results from LC4 in the specimen 10C12-26-5

B.11. Specimen 11C20-26-5

Description:

- Specimen number: 11
- Composite Cross-section: CCFT
- Steel cross-section: HSS20x0.25
- Design concrete strength: 5 ksi
- Design specimen length: 26 ft
- Pouring date: 03/27/2009
- Testing date: 05/28/2009

Parameters:

- Specimen length: 26' 2 3/4"
- Initial out-of-plumbness: $U_{xo} = 0.59'' / U_{yo} = -2.12''$
- Steel yielding stress: $F_y = 44.3$ ksi
- Steel ultimate stress: $F_u = 69.2$ ksi
- Concrete strength at the 28th day: $f_c' = 7.3$ ksi
- Concrete strength at the testing day: $f_c = 8.1$ ksi
- Concrete Young's modulus: $E_c = 5000$ ksi
- Concrete tensile strength: $f_t = 0.6$ ksi

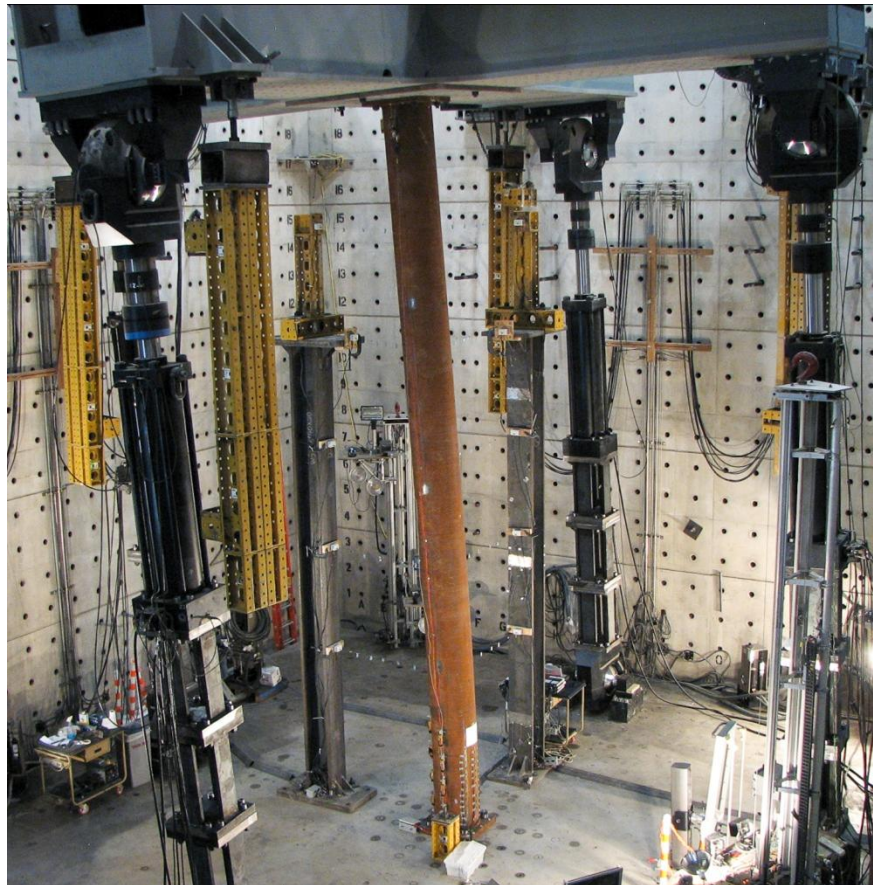


Figure B.78. Specimen 11C20-26-5

Table B.11. Load protocol summary for the specimen 11C20-26-5

LC1 - Incremental compression loading in two cycles until the maximum load is reached. The top is forced to be free at all the time.

Step	DOF						Stop Criterion
	X	Y	Z	RX	RY	RZ	
1	$F_x = 0$	$F_y = 0$	$U_z \downarrow$	$M_x = 0$	$M_y = 0$	$R_z = 0$	max P
2	$F_x = 0$	$F_y = 0$	$U_z \uparrow$	$M_x = 0$	$M_y = 0$	$R_z = 0$	P = 0
3	$U_x \rightarrow U_{xo}$	$U_y \rightarrow U_{yo}$	P = 0	$M_x = 0$	$M_y = 0$	$R_z = 0$	U_{xo}, U_{yo}
4	$F_x \rightarrow 0$	$F_y \rightarrow 0$	P = 0	$M_x = 0$	$M_y = 0$	$R_z = 0$	$F_x=F_y=0$
5	$F_x = 0$	$F_y = 0$	$U_z \downarrow$	$M_x = 0$	$M_y = 0$	$R_z = 0$	max P
6	$F_x = 0$	$F_y = 0$	$U_z \uparrow$	$M_x = 0$	$M_y = 0$	$R_z = 0$	P = 0

LC2a - Cyclic uniaxial lateral displacements with constant compression force ($-F_z = P = 600$ kips). The top was forced to have zero moments.

Step	DOF						Stop Criterion
	X	Y	Z	RX	RY	RZ	
1	$U_x \uparrow$	$U_y \downarrow$	P = 600k	$M_x = 0$	$M_y = 0$	$R_z = 0$	+1% drift
2	$U_x \downarrow$	$U_y \uparrow$	P = 600k	$M_x = 0$	$M_y = 0$	$R_z = 0$	-1% drift
3	$U_x \uparrow$	$U_y \downarrow$	P = 600k	$M_x = 0$	$M_y = 0$	$R_z = 0$	+2% drift
4	$U_x \downarrow$	$U_y \uparrow$	P = 600k	$M_x = 0$	$M_y = 0$	$R_z = 0$	-2% drift
5	$U_x \uparrow$	$U_y \downarrow$	P = 600k	$M_x = 0$	$M_y = 0$	$R_z = 0$	+3% drift
6	$U_x \downarrow$	$U_y \uparrow$	P = 600k	$M_x = 0$	$M_y = 0$	$R_z = 0$	-3% drift
7	$U_x \uparrow$	$U_y \downarrow$	P = 600k	$M_x = 0$	$M_y = 0$	$R_z = 0$	+4% drift
8	$U_x \downarrow$	$U_y \uparrow$	P = 600k	$M_x = 0$	$M_y = 0$	$R_z = 0$	$U_z = 0$

LC2b - Cyclic uniaxial lateral displacements with constant compression force ($-F_z = P = 300$ kips). The top was forced to have zero moments.

Step	DOF						Stop Criterion
	X	Y	Z	RX	RY	RZ	
1	$U_x \uparrow$	$U_y \downarrow$	P = 300k	$M_x = 0$	$M_y = 0$	$R_z = 0$	+1% drift
2	$U_x \downarrow$	$U_y \uparrow$	P = 300k	$M_x = 0$	$M_y = 0$	$R_z = 0$	-1% drift
3	$U_x \uparrow$	$U_y \downarrow$	P = 300k	$M_x = 0$	$M_y = 0$	$R_z = 0$	+2% drift
4	$U_x \downarrow$	$U_y \uparrow$	P = 300k	$M_x = 0$	$M_y = 0$	$R_z = 0$	-2% drift
5	$U_x \uparrow$	$U_y \downarrow$	P = 300k	$M_x = 0$	$M_y = 0$	$R_z = 0$	+3% drift
6	$U_x \downarrow$	$U_y \uparrow$	P = 300k	$M_x = 0$	$M_y = 0$	$R_z = 0$	-3% drift
7	$U_x \uparrow$	$U_y \downarrow$	P = 300k	$M_x = 0$	$M_y = 0$	$R_z = 0$	+4% drift
8	$U_x \downarrow$	$U_y \uparrow$	P = 300k	$M_x = 0$	$M_y = 0$	$R_z = 0$	-4% drift
9	$U_x \uparrow$	$U_y \downarrow$	P = 300k	$M_x = 0$	$M_y = 0$	$R_z = 0$	+ stroke
10	$U_x \downarrow$	$U_y \uparrow$	P = 300k	$M_x = 0$	$M_y = 0$	$R_z = 0$	$U_z = 0$

LC3a - Cyclic biaxial lateral displacements (8 shape) with constant compression force ($-F_z = P = 450$ kips). The top was forced to have zero moments.

Step	DOF						Stop Criterion
	X	Y	Z	RX	RY	RZ	
1	$U_x \uparrow$	$U_y \uparrow$	$P = 450k$	$M_x = 0$	$M_y = 0$	$R_z = 0$	+/-1% drift
2	$U_x \downarrow$	$U_y \downarrow$	$P = 450k$	$M_x = 0$	$M_y = 0$	$R_z = 0$	+/-2% drift
3	$U_x \uparrow$	$U_y \uparrow$	$P = 450k$	$M_x = 0$	$M_y = 0$	$R_z = 0$	+/-3% drift
4	$U_x \downarrow$	$U_y \downarrow$	$P = 450k$	$M_x = 0$	$M_y = 0$	$R_z = 0$	+/-4% drift

LC3b - Cyclic biaxial lateral displacements (8 shape) with constant compression force ($-F_z = P = 150$ kips). The top was forced to have zero moments.

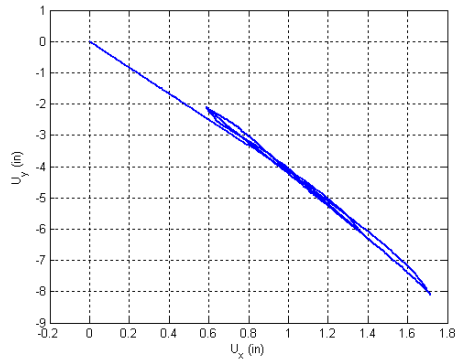
Step	DOF						Stop Criterion
	X	Y	Z	RX	RY	RZ	
1	$U_x \uparrow$	$U_y \uparrow$	$P = 150k$	$M_x = 0$	$M_y = 0$	$R_z = 0$	+/-1% drift
2	$U_x \downarrow$	$U_y \downarrow$	$P = 150k$	$M_x = 0$	$M_y = 0$	$R_z = 0$	+/-2% drift
3	$U_x \uparrow$	$U_y \uparrow$	$P = 150k$	$M_x = 0$	$M_y = 0$	$R_z = 0$	+/-3% drift
4	$U_x \downarrow$	$U_y \downarrow$	$P = 150k$	$M_x = 0$	$M_y = 0$	$R_z = 0$	+/-4% drift

LC4a - Incremental compression loading until the maximum load is reached. The top is forced to be free at all the time.

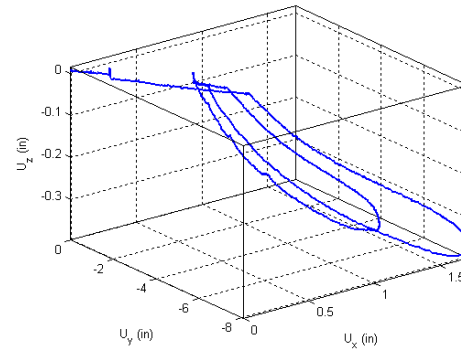
Step	DOF						Stop Criterion
	X	Y	Z	RX	RY	RZ	
1	$F_x \rightarrow 0$	$F_y \rightarrow 0$	$F_z \rightarrow 0$	$M_x = 0$	$M_y = 0$	$R_z = 0$	$F_x=F_y=0$
2	$F_x = 0$	$F_y = 0$	$U_z \downarrow$	$M_x = 0$	$M_y = 0$	$R_z = 0$	$P = 0.8P_{max}$

LC4b - Cyclic uniaxial lateral displacements (4 corners) with constant compression force ($-F_z = P = 300, 375$ and 425 kips). The top is forced to be free at all the time.

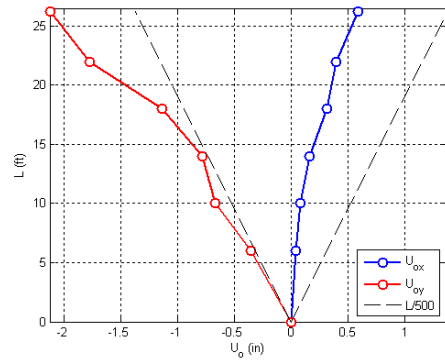
Step	DOF						Stop Criterion
	X	Y	Z	RX	RY	RZ	
1	$U_x \uparrow$	$U_y \uparrow$	$P = 300k$	$M_x = 0$	$M_y = 0$	$R_z = 0$	max stroke
2	$U_x \downarrow$	$U_y \downarrow$	$P = 300k$	$M_x = 0$	$M_y = 0$	$R_z = 0$	max stroke
3	$U_x \rightarrow 0$	$U_y \rightarrow 0$	$P = 300k$	$M_x = 0$	$M_y = 0$	$R_z = 0$	$U_x=U_y=0$
4	$U_x \uparrow$	$U_y \downarrow$	$P = 375k$	$M_x = 0$	$M_y = 0$	$R_z = 0$	max stroke
5	$U_x \downarrow$	$U_y \uparrow$	$P = 425k$	$M_x = 0$	$M_y = 0$	$R_z = 0$	max stroke
6	$U_x \rightarrow 0$	$U_y \rightarrow 0$	$P = 425k$	$M_x = 0$	$M_y = 0$	$R_z = 0$	$U_x=U_y=0$



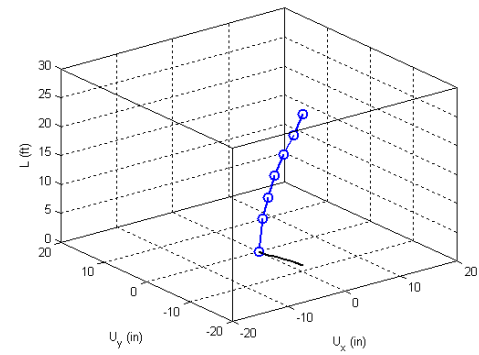
Y displacement vs. X displacement



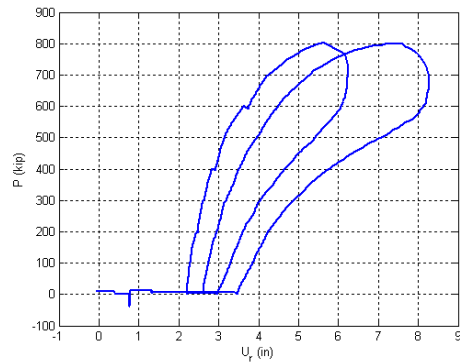
Z displacement vs. X and Y displacement



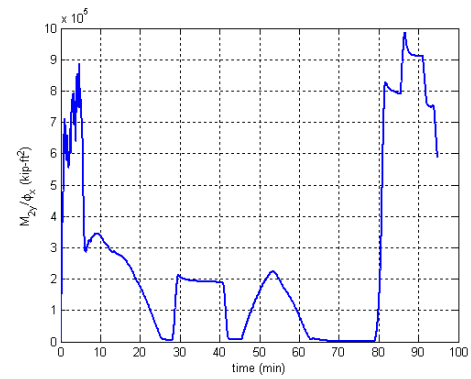
Initial deflected shape



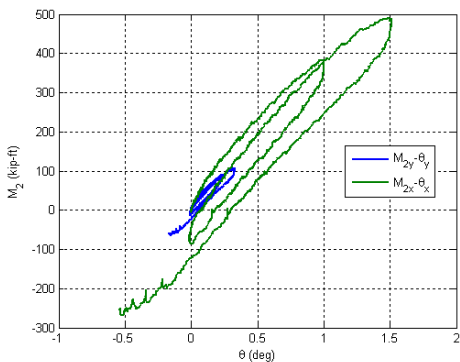
Maximum lateral displacement



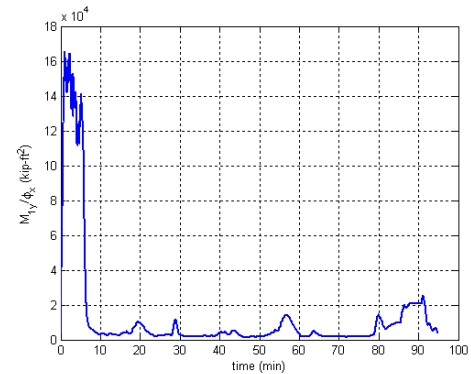
Axial force vs. lateral displacement



Axial force vs. base moments

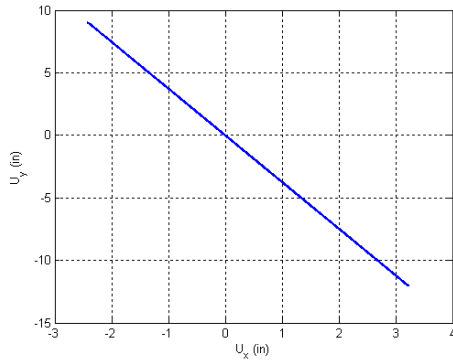


Base moment vs. base curvature

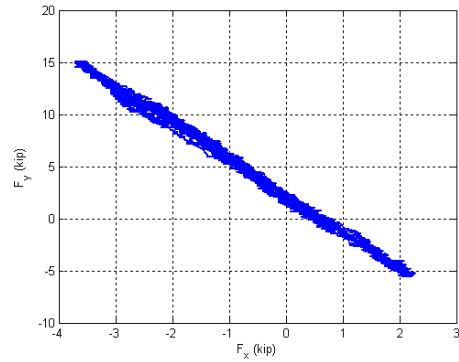


Base moment vs. top rotation

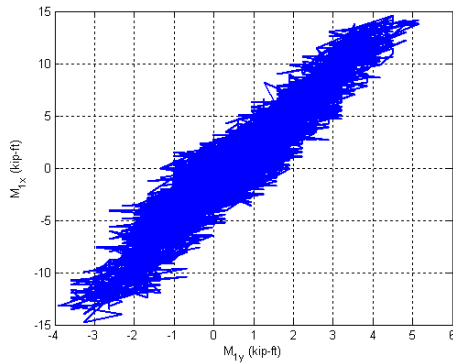
Figure B.79. Experimental results from LC1 in the specimen 11C20-26-5



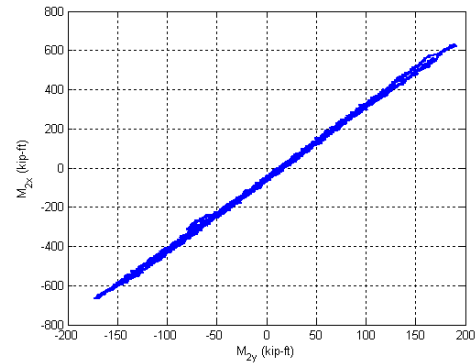
Y Displacement vs. X Displacement



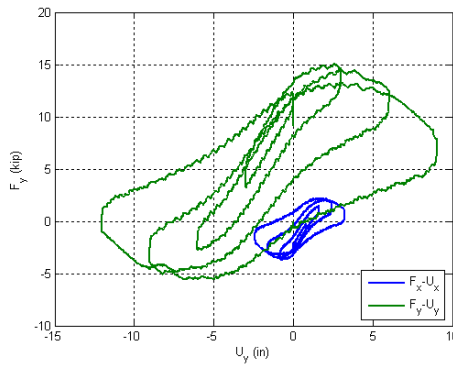
Y Force vs. X Force



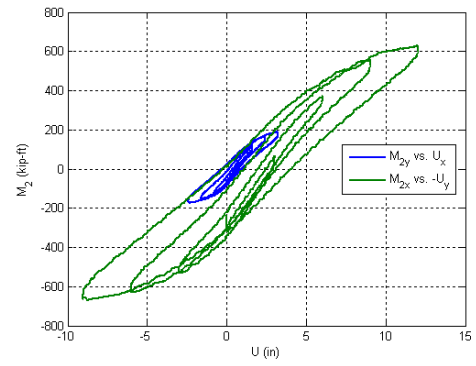
X Moment vs. Y Moment at the top



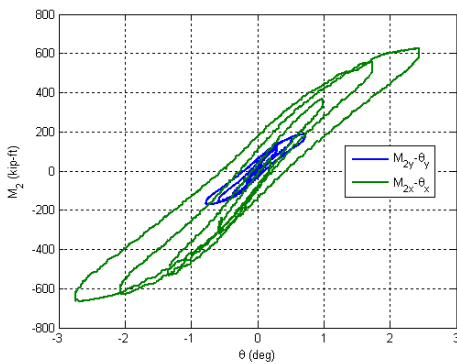
X Moment vs. Y Moment at the base



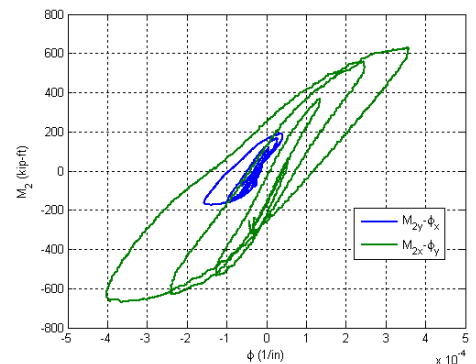
Lateral Force vs. Lateral Displacement



Base Moment vs. Top Displacement

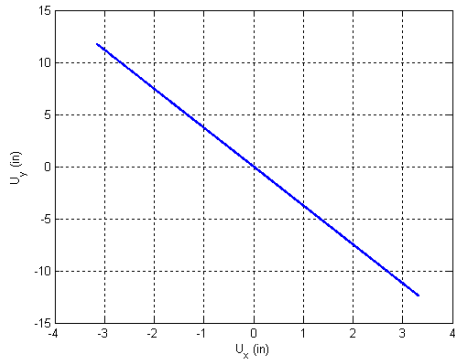


Base Moment vs. Top Rotation

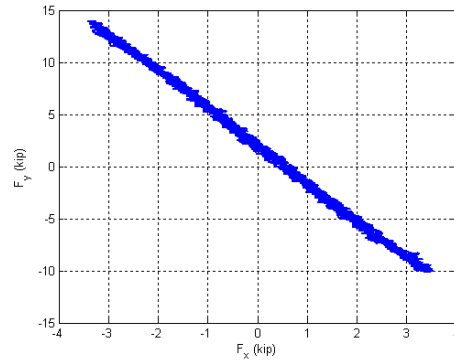


Base Moment vs. Base Curvature

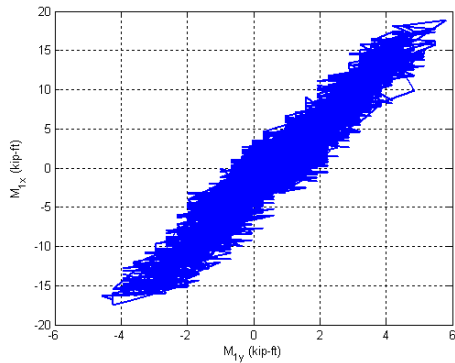
Figure B.80. Experimental results from LC2a in the specimen 11C20-26-5



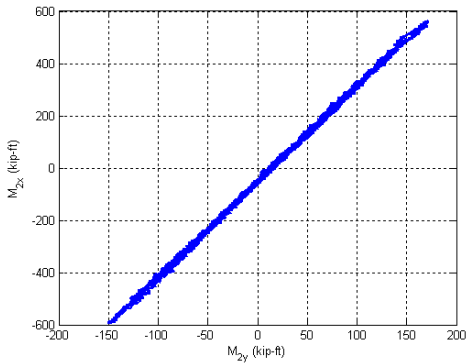
Y Displacement vs. X Displacement



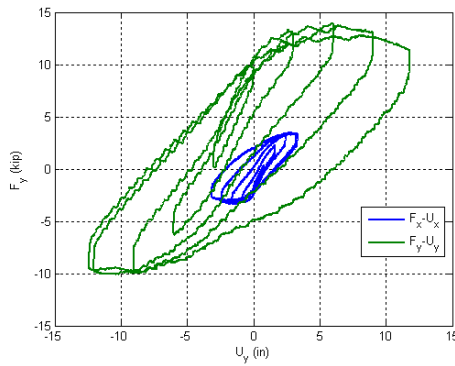
Y Force vs. X Force



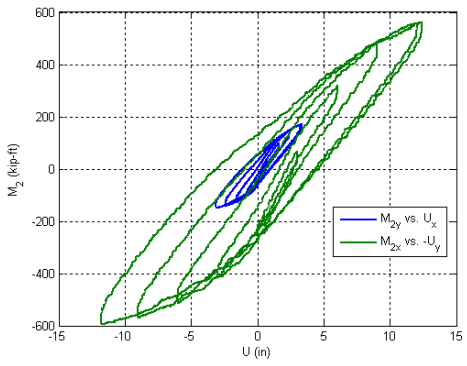
X Moment vs. Y Moment at the top



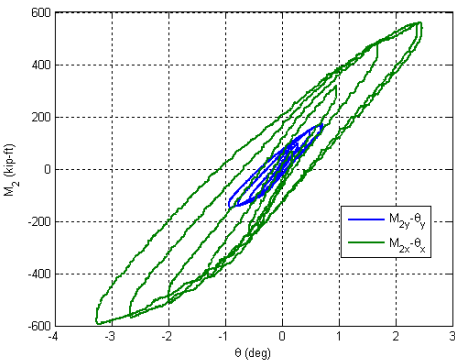
X Moment vs. Y Moment at the base



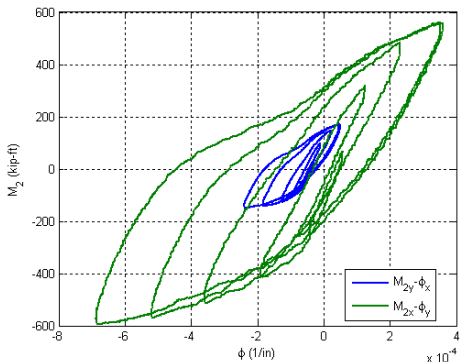
Lateral Force vs. Lateral Displacement



Base Moment vs. Top Displacement

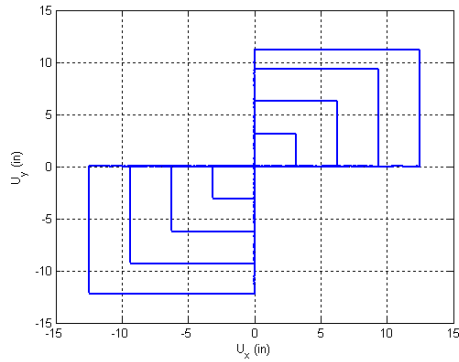


Base Moment vs. Top Rotation

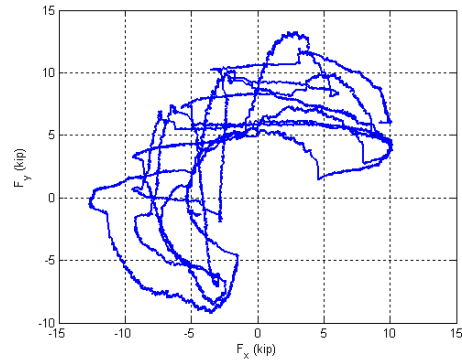


Base Moment vs. Base Curvature

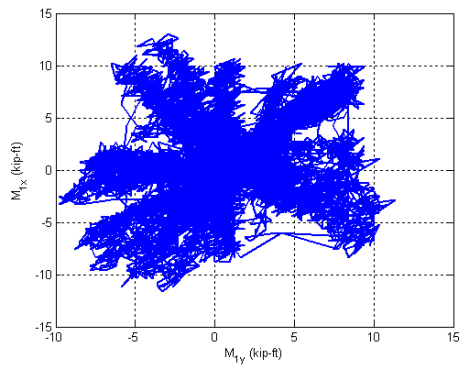
Figure B.81. Experimental results from LC2b in the specimen 11C20-26-5



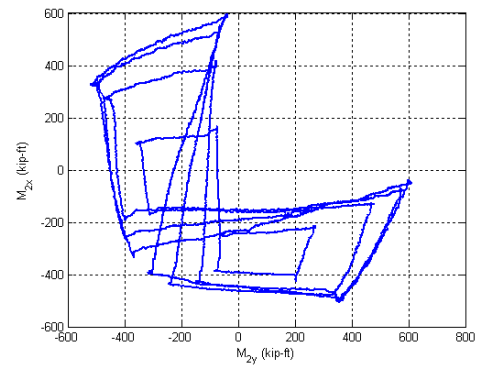
Y Displacement vs. X Displacement



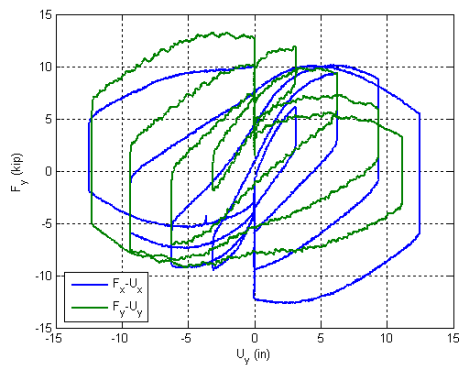
Y Force vs. X Force



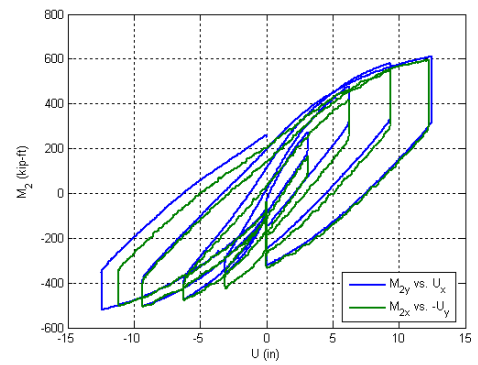
X Moment vs. Y Moment at the top



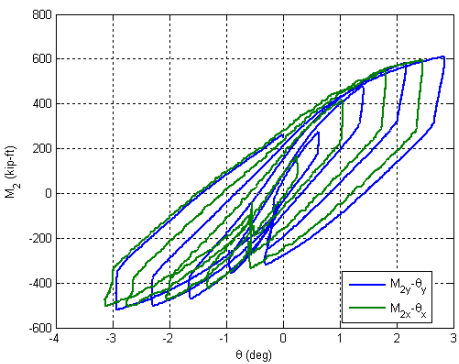
X Moment vs. Y Moment at the base



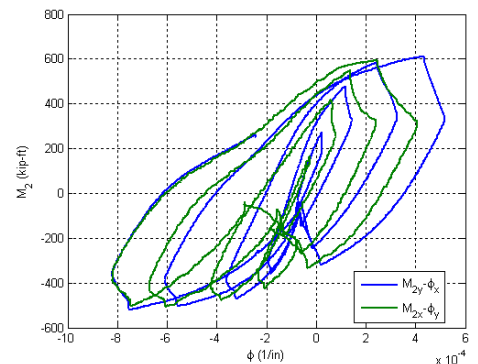
Lateral Force vs. Lateral Displacement



Base Moment vs. Top Displacement

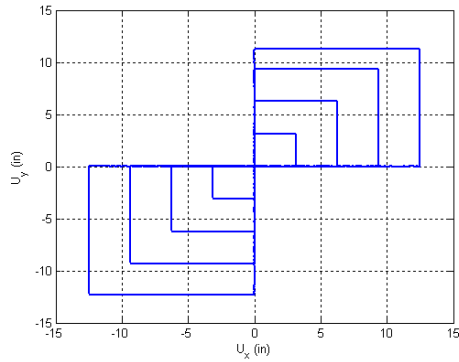


Base Moment vs. Top Rotation

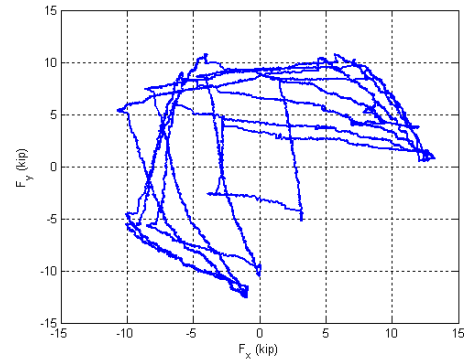


Base Moment vs. Base Curvature

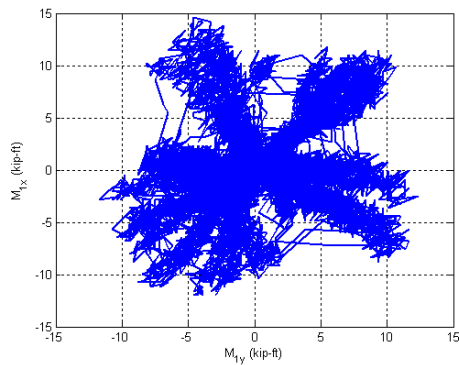
Figure B.82. Experimental results from LC3a in the specimen 11C20-26-5



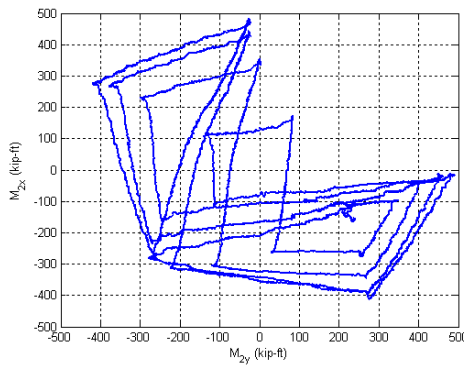
Y Displacement vs. X Displacement



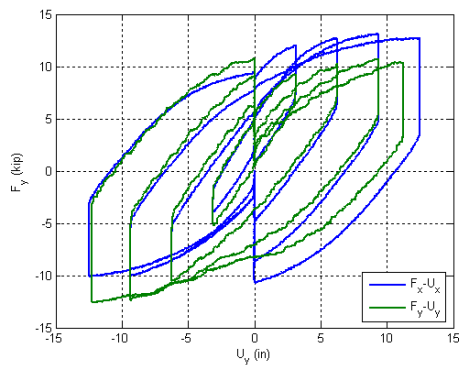
Y Force vs. X Force



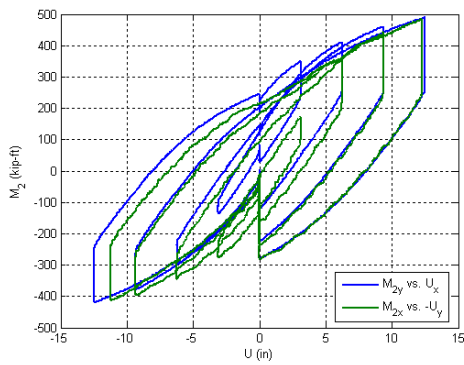
X Moment vs. Y Moment at the top



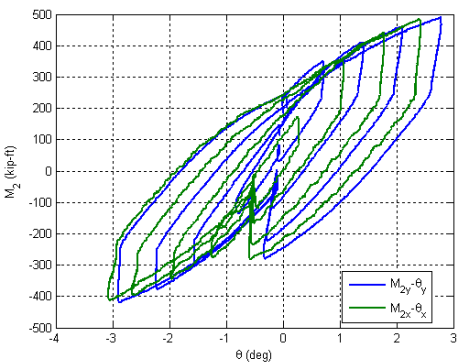
X Moment vs. Y Moment at the base



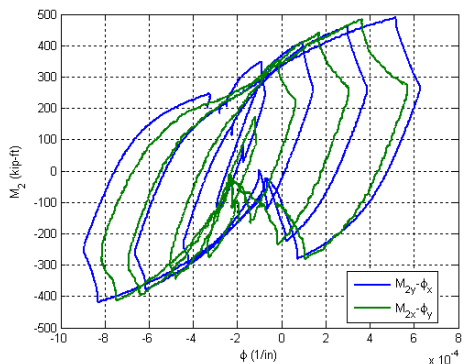
Lateral Force vs. Lateral Displacement



Base Moment vs. Top Displacement

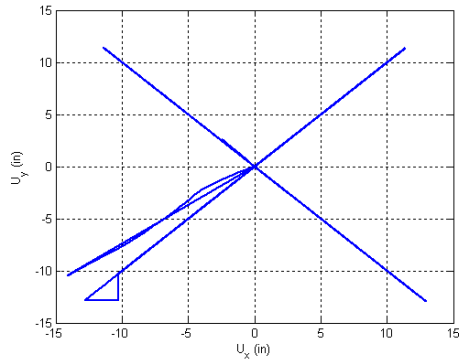


Base Moment vs. Top Rotation

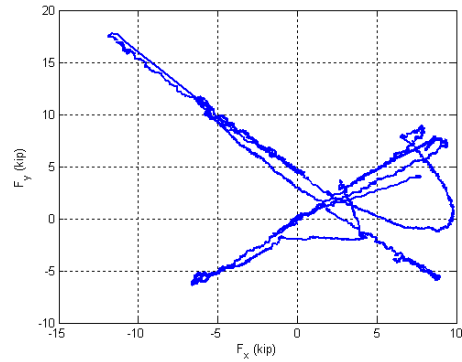


Base Moment vs. Base Curvature

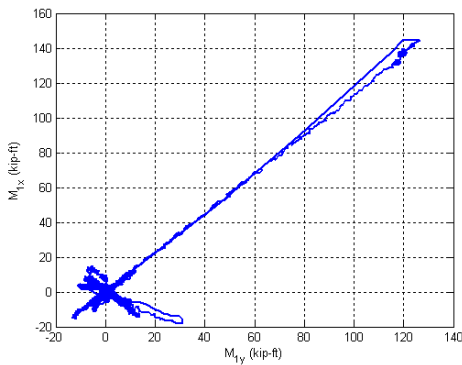
Figure B.83. Experimental results from LC3b in the specimen 11C20-26-5



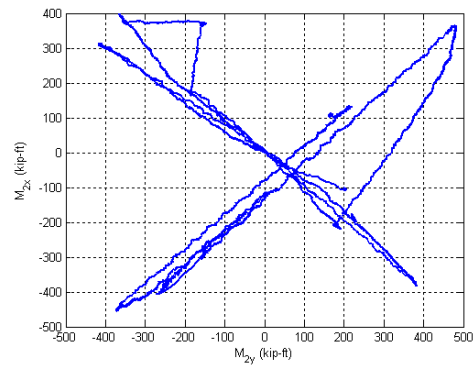
Y Displacement vs. X Displacement



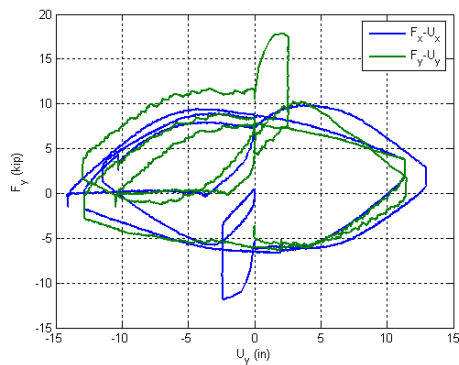
Y Force vs. X Force



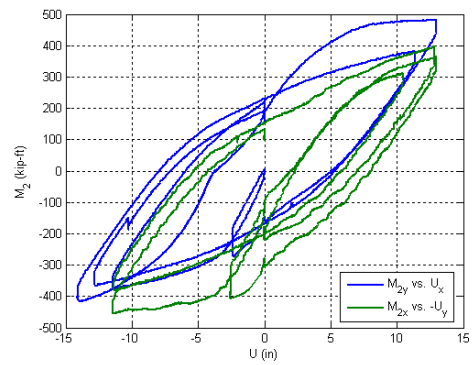
X Moment vs. Y Moment at the top



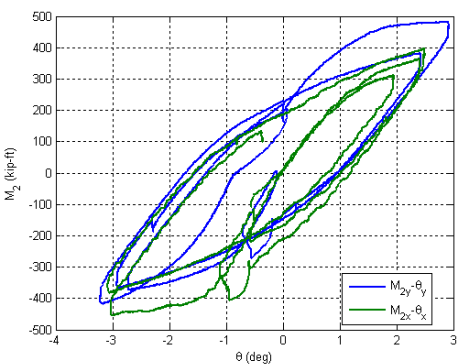
X Moment vs. Y Moment at the base



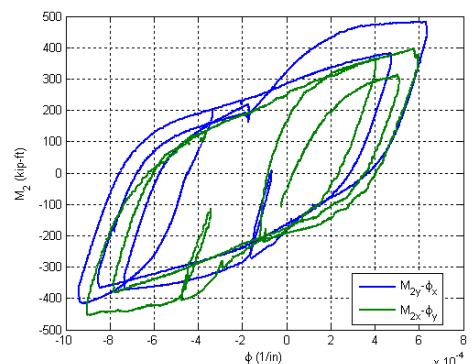
Lateral Force vs. Lateral Displacement



Base Moment vs. Top Displacement



Base Moment vs. Top Rotation



Base Moment vs. Base Curvature

Figure B.84. Experimental results from LC4 in the specimen 11C20-26-5

B.12. Specimen 12Rw-26-5

Description:

- Specimen number: 12
- Composite Cross-section: RCFT
- Steel cross-section: HSS20x12x0.25
- Design concrete strength: 5 ksi
- Design specimen length: 26 ft
- Pouring date: 03/27/2009
- Testing date: 06/04/2009

Parameters:

- Specimen length: 26' 1 1/4"
- Initial out-of-plumbness: $U_{xo} = 0.63'' / U_{yo} = 0.00''$
- Steel yielding stress: $F_y = 58.9$ ksi
- Steel ultimate stress: $F_u = 77.4$ ksi
- Concrete strength at the 28th day: $f_c' = 7.3$ ksi
- Concrete strength at the testing day: $f_c = 8.2$ ksi
- Concrete Young's modulus: $E_c = 5000$ ksi
- Concrete tensile strength: $f_t = 0.6$ ksi

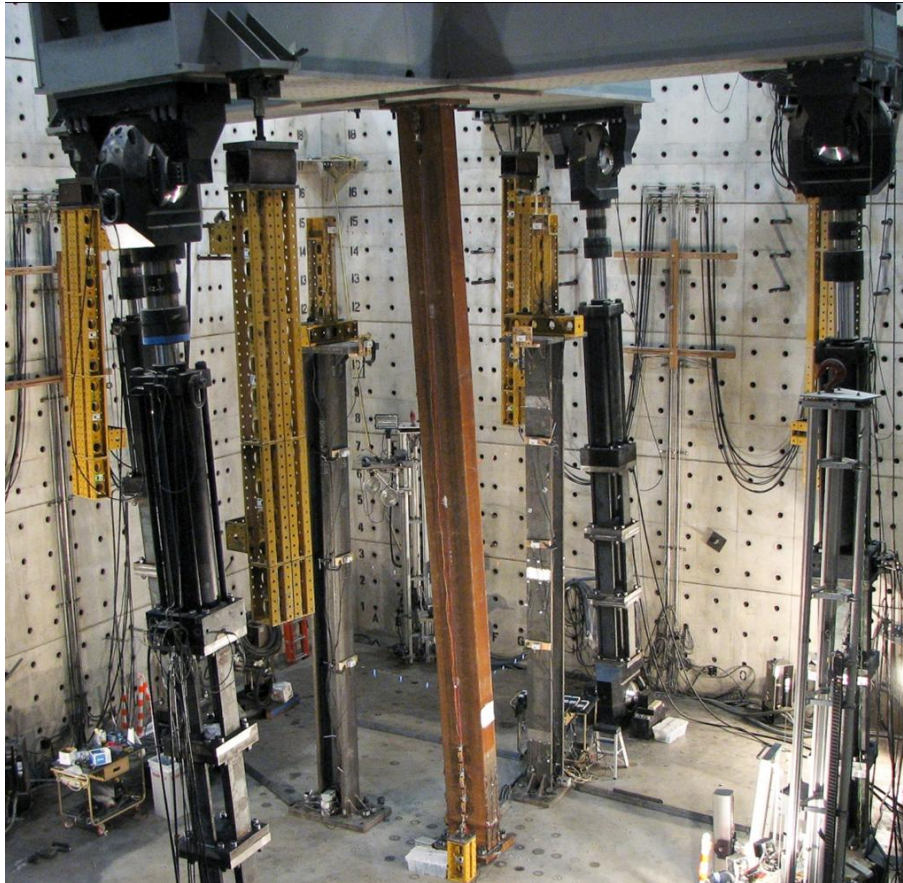


Figure B.85. Specimen 12Rw-26-5

Table B.12. Load protocol summary for the specimen 12Rw-26-5

LC1 - Incremental compression loading in two cycles until the maximum load is reached. The top is forced to be free at X ($K_x=2$) and fixed at Y ($K_y=0.5$).

Step	DOF						Stop Criterion
	X	Y	Z	RX	RY	RZ	
1	$F_x = 0$	$U_y = 0$	$U_z \downarrow$	$R_x = 0$	$M_y = 0$	$R_z = 0$	max P
2	$F_x = 0$	$U_y = 0$	$U_z \uparrow$	$R_x = 0$	$M_y = 0$	$R_z = 0$	P = 0
3	$F_x = 0$	$U_y = 0$	$U_z \downarrow$	$R_x = 0$	$M_y = 0$	$R_z = 0$	max P
4	$F_x = 0$	$U_y = 0$	$U_z \uparrow$	$R_x = 0$	$M_y = 0$	$R_z = 0$	P = 0

LC2a - Cyclic uniaxial lateral displacements with constant compression force ($-F_z = P = 400$ kips). The top was forced to have zero moments in Y and fixed rotation in X.

Step	DOF						Stop Criterion
	X	Y	Z	RX	RY	RZ	
1	$U_x \uparrow$	$U_y = 0$	P = 400k	$R_x = 0$	$M_y = 0$	$R_z = 0$	+1% drift
2	$U_x \downarrow$	$U_y = 0$	P = 400k	$R_x = 0$	$M_y = 0$	$R_z = 0$	-1% drift
3	$U_x \uparrow$	$U_y = 0$	P = 400k	$R_x = 0$	$M_y = 0$	$R_z = 0$	+2% drift
4	$U_x \downarrow$	$U_y = 0$	P = 400k	$R_x = 0$	$M_y = 0$	$R_z = 0$	-2% drift
5	$U_x \uparrow$	$U_y = 0$	P = 400k	$R_x = 0$	$M_y = 0$	$R_z = 0$	+3% drift
6	$U_x \downarrow$	$U_y = 0$	P = 400k	$R_x = 0$	$M_y = 0$	$R_z = 0$	-3% drift
7	$U_x \uparrow$	$U_y = 0$	P = 400k	$R_x = 0$	$M_y = 0$	$R_z = 0$	+4% drift
8	$U_x \downarrow$	$U_y = 0$	P = 400k	$R_x = 0$	$M_y = 0$	$R_z = 0$	-4% drift
9	$U_x \uparrow$	$U_y = 0$	P = 400k	$R_x = 0$	$M_y = 0$	$R_z = 0$	+5% drift
10	$U_x \downarrow$	$U_y = 0$	P = 400k	$R_x = 0$	$M_y = 0$	$R_z = 0$	-5% drift
11	$U_x \downarrow$	$U_y = 0$	P = 400k	$R_x = 0$	$M_y = 0$	$R_z = 0$	$U_z = 0$

LC2b - Cyclic uniaxial lateral displacements with constant compression force ($-F_z = P = 200$ kips). The top was forced to have zero moments in Y and fixed rotation in X.

Step	DOF						Stop Criterion
	X	Y	Z	RX	RY	RZ	
1	$U_x \uparrow$	$U_y = 0$	P = 200k	$R_x = 0$	$M_y = 0$	$R_z = 0$	+1% drift
2	$U_x \downarrow$	$U_y = 0$	P = 200k	$R_x = 0$	$M_y = 0$	$R_z = 0$	-1% drift
3	$U_x \uparrow$	$U_y = 0$	P = 200k	$R_x = 0$	$M_y = 0$	$R_z = 0$	+2% drift
4	$U_x \downarrow$	$U_y = 0$	P = 200k	$R_x = 0$	$M_y = 0$	$R_z = 0$	-2% drift
5	$U_x \uparrow$	$U_y = 0$	P = 200k	$R_x = 0$	$M_y = 0$	$R_z = 0$	+3% drift
6	$U_x \downarrow$	$U_y = 0$	P = 200k	$R_x = 0$	$M_y = 0$	$R_z = 0$	-3% drift
7	$U_x \uparrow$	$U_y = 0$	P = 200k	$R_x = 0$	$M_y = 0$	$R_z = 0$	+4% drift
8	$U_x \downarrow$	$U_y = 0$	P = 200k	$R_x = 0$	$M_y = 0$	$R_z = 0$	-4% drift
9	$U_x \uparrow$	$U_y = 0$	P = 200k	$R_x = 0$	$M_y = 0$	$R_z = 0$	+5% drift
10	$U_x \downarrow$	$U_y = 0$	P = 200k	$R_x = 0$	$M_y = 0$	$R_z = 0$	-5% drift
11	$U_x \downarrow$	$U_y = 0$	P = 200k	$R_x = 0$	$M_y = 0$	$R_z = 0$	$U_z = 0$

LC3a - Cyclic biaxial lateral displacements (8 shape) with constant compression force ($-F_z = P = 300$ kips). The top was forced to have zero moments.

Step	DOF						Stop Criterion
	X	Y	Z	RX	RY	RZ	
1	$U_x \uparrow$	$U_y \uparrow$	$P = 300k$	$M_x = 0$	$M_y = 0$	$R_z = 0$	+/-1% drift
2	$U_x \downarrow$	$U_y \downarrow$	$P = 300k$	$M_x = 0$	$M_y = 0$	$R_z = 0$	+/-2% drift
3	$U_x \uparrow$	$U_y \uparrow$	$P = 300k$	$M_x = 0$	$M_y = 0$	$R_z = 0$	+/-3% drift
4	$U_x \downarrow$	$U_y \downarrow$	$P = 300k$	$M_x = 0$	$M_y = 0$	$R_z = 0$	+/-4% drift

LC3b - Cyclic biaxial lateral displacements (8 shape) with constant compression force ($-F_z = P = 500$ kips). The top was forced to have zero moments.

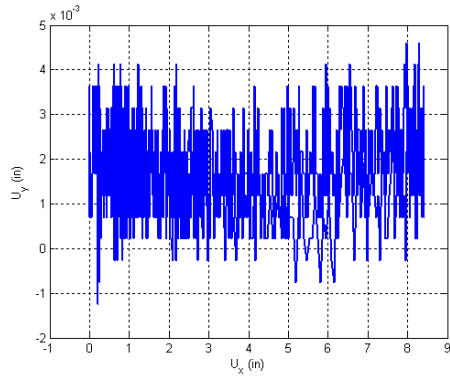
Step	DOF						Stop Criterion
	X	Y	Z	RX	RY	RZ	
1	$U_x \uparrow$	$U_y \uparrow$	$P = 500k$	$M_x = 0$	$M_y = 0$	$R_z = 0$	+/-1% drift
2	$U_x \downarrow$	$U_y \downarrow$	$P = 500k$	$M_x = 0$	$M_y = 0$	$R_z = 0$	+/-2% drift
3	$U_x \uparrow$	$U_y \uparrow$	$P = 500k$	$M_x = 0$	$M_y = 0$	$R_z = 0$	+/-3% drift
4	$U_x \downarrow$	$U_y \downarrow$	$P = 500k$	$M_x = 0$	$M_y = 0$	$R_z = 0$	+/-4% drift

LC4a - Incremental compression loading until the maximum load is reached. The top is forced to be free at all the time.

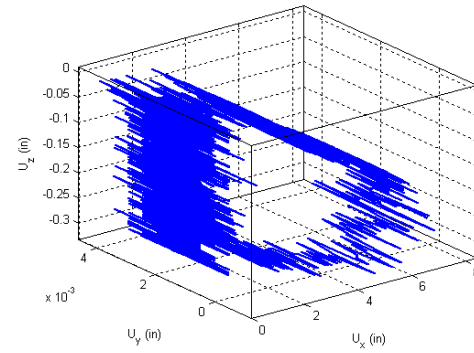
Step	DOF						Stop Criterion
	X	Y	Z	RX	RY	RZ	
1	$F_x \rightarrow 0$	$F_y \rightarrow 0$	$F_z \rightarrow 0$	$M_x = 0$	$M_y = 0$	$R_z = 0$	$F_x=F_y=0$
2	$F_x = 0$	$F_y = 0$	$U_z \downarrow$	$M_x = 0$	$M_y = 0$	$R_z = 0$	$P = P_{max}$

LC4b - Cyclic uniaxial lateral displacements (4 corners) with constant compression force ($-F_z = P = 600$ kips). The top is forced to be free at all the time.

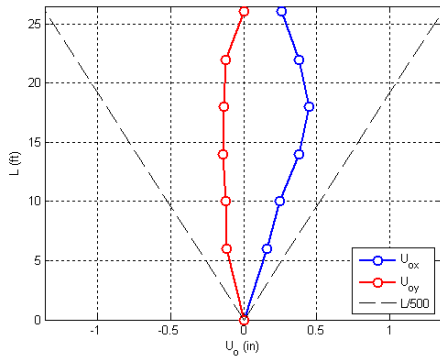
Step	DOF						Stop Criterion
	X	Y	Z	RX	RY	RZ	
1	$U_x \uparrow$	$U_y \uparrow$	$P = 600k$	$M_x = 0$	$M_y = 0$	$R_z = 0$	max stroke
2	$U_x \downarrow$	$U_y \downarrow$	$P = 600k$	$M_x = 0$	$M_y = 0$	$R_z = 0$	max stroke
3	$U_x \rightarrow 0$	$U_y \rightarrow 0$	$P = 600k$	$M_x = 0$	$M_y = 0$	$R_z = 0$	$U_x=U_y=0$
4	$U_x \uparrow$	$U_y \downarrow$	$P = 600k$	$M_x = 0$	$M_y = 0$	$R_z = 0$	max stroke
5	$U_x \downarrow$	$U_y \uparrow$	$P = 600k$	$M_x = 0$	$M_y = 0$	$R_z = 0$	max stroke
6	$U_x \rightarrow 0$	$U_y \rightarrow 0$	$P = 600k$	$M_x = 0$	$M_y = 0$	$R_z = 0$	$U_x=U_y=0$



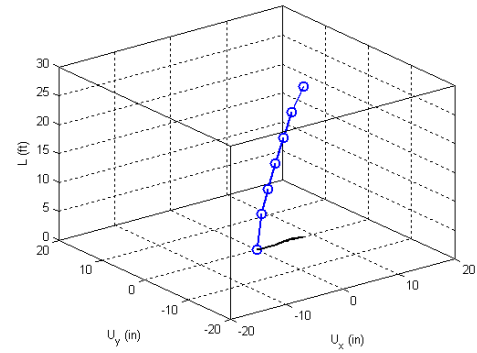
Y displacement vs. X displacement



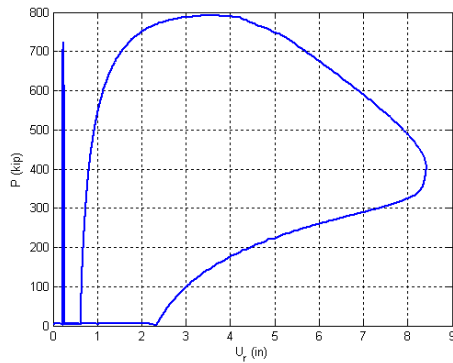
Z displacement vs. X and Y displacement



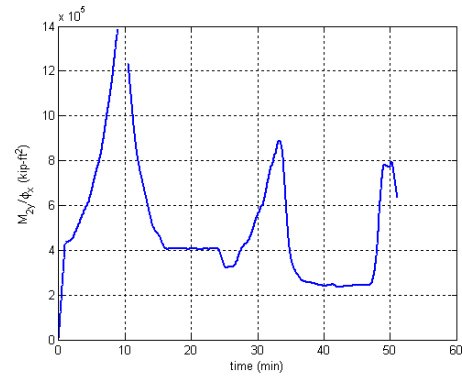
Initial deflected shape



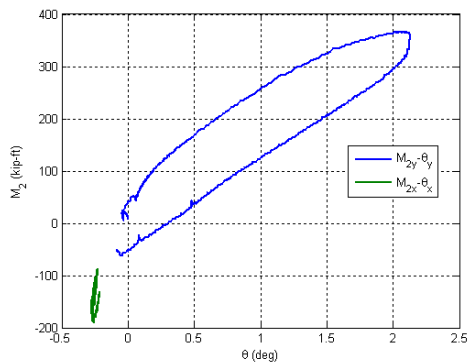
Maximum lateral displacement



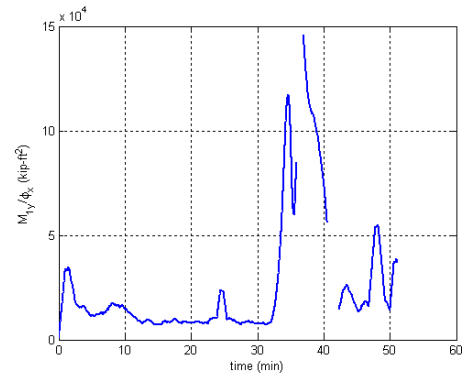
Axial force vs. lateral displacement



Axial force vs. base moments

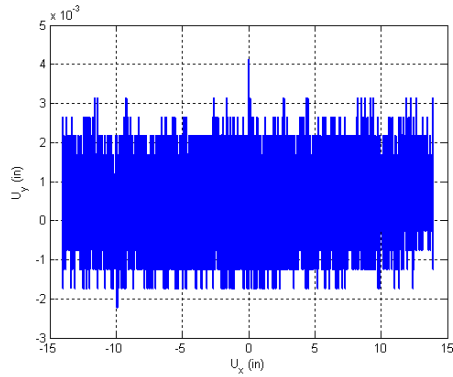


Base moment vs. base curvature

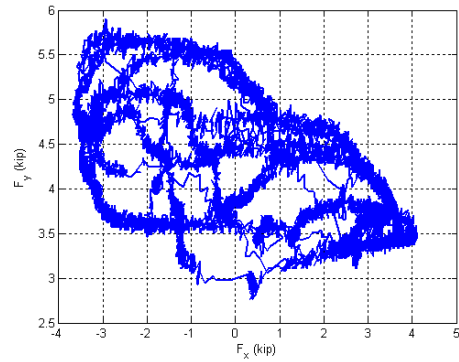


Base moment vs. top rotation

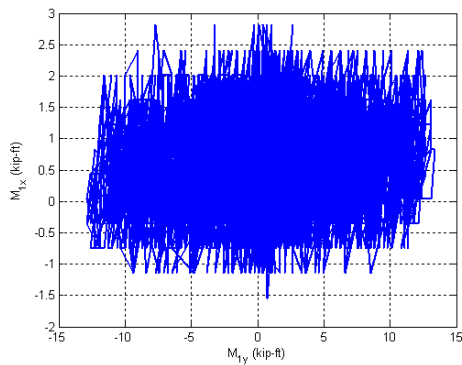
Figure B.86. Experimental results from LC1 in the specimen 12Rw-26-5



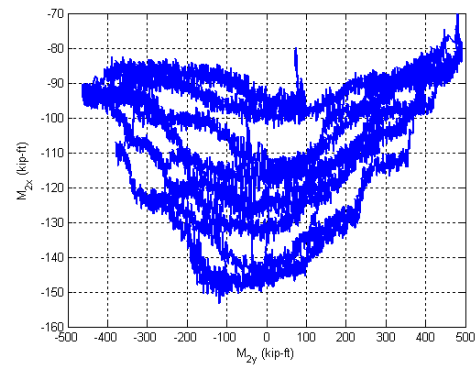
Y Displacement vs. X Displacement



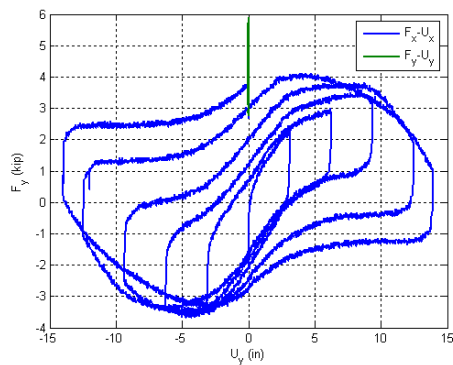
Y Force vs. X Force



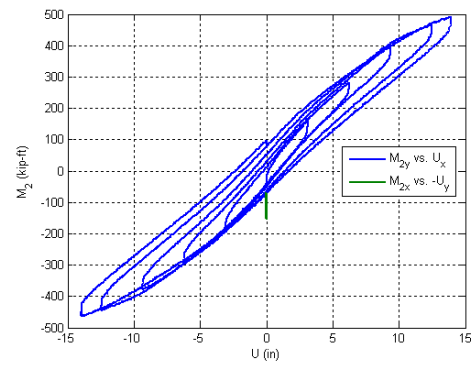
X Moment vs. Y Moment at the top



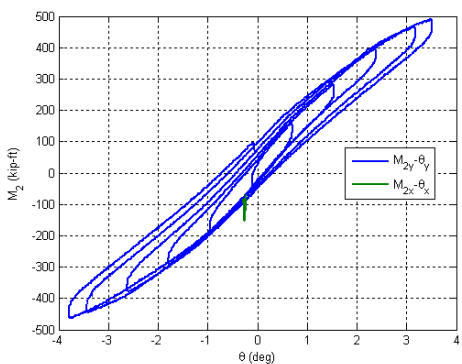
X Moment vs. Y Moment at the base



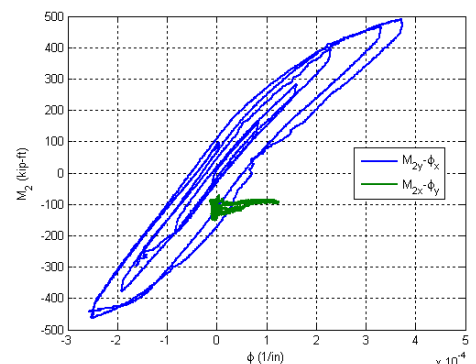
Lateral Force vs. Lateral Displacement



Base Moment vs. Top Displacement

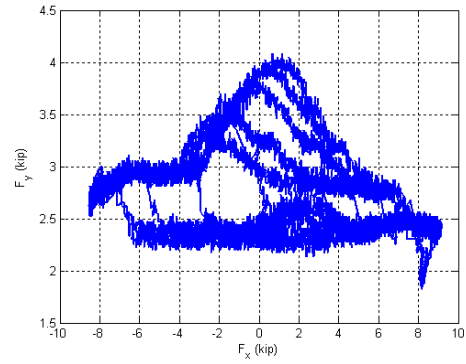
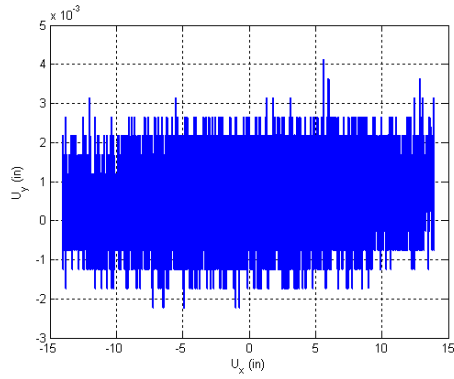


Base Moment vs. Top Rotation

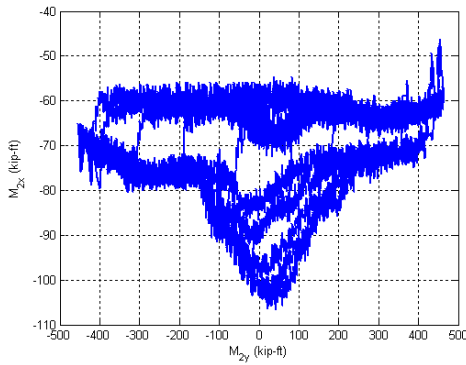
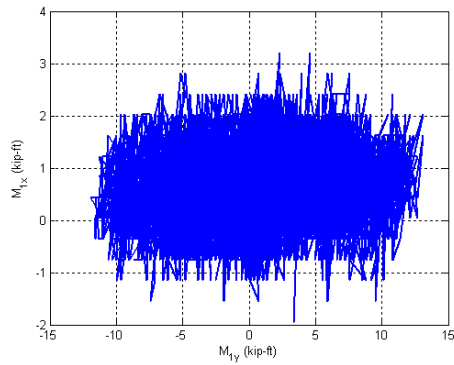


Base Moment vs. Base Curvature

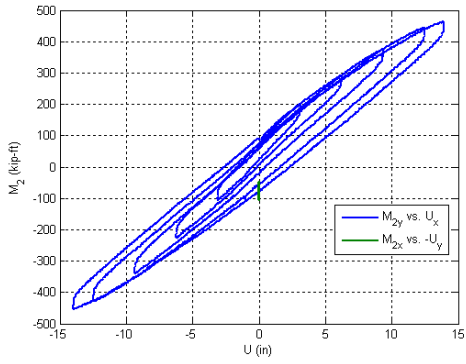
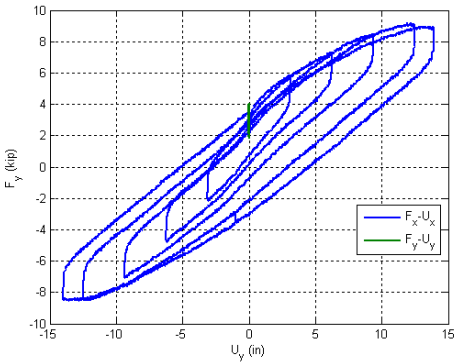
Figure B.87. Experimental results from LC2a in the specimen 12Rw-26-5



Y Displacement vs. X Displacement Y Force vs. X Force

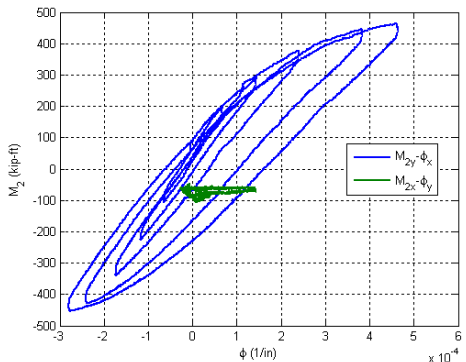
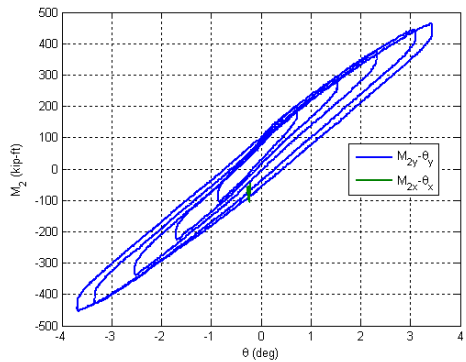


X Moment vs. Y Moment at the top X Moment vs. Y Moment at the base



Lateral Force vs. Lateral Displacement

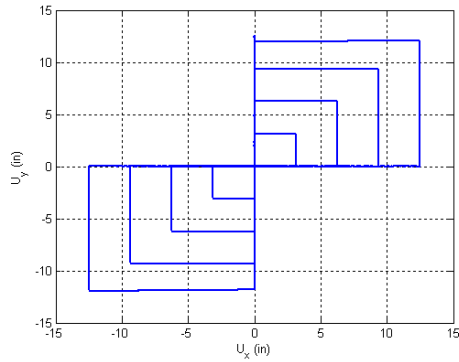
Base Moment vs. Top Displacement



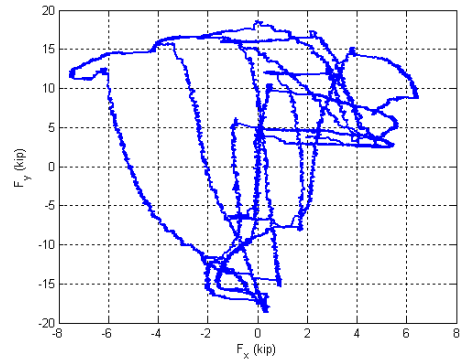
Base Moment vs. Top Rotation

Base Moment vs. Base Curvature

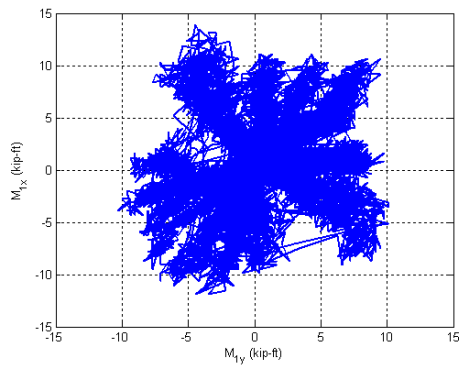
Figure B.88. Experimental results from LC2b in the specimen 12Rw-26-5



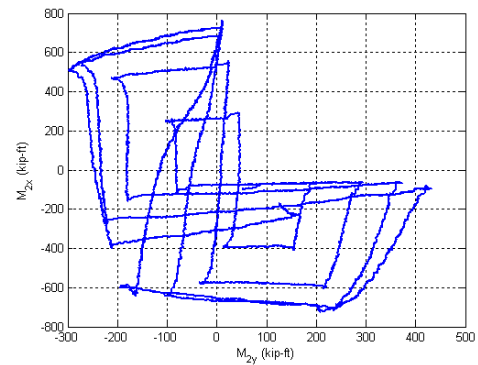
Y Displacement vs. X Displacement



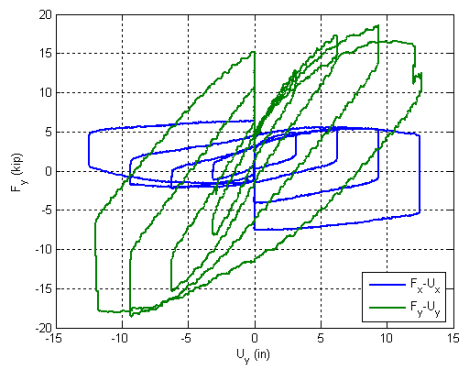
Y Force vs. X Force



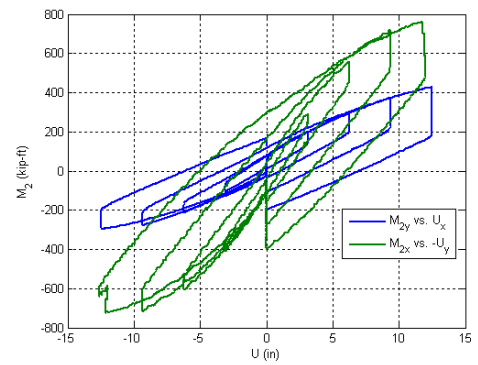
X Moment vs. Y Moment at the top



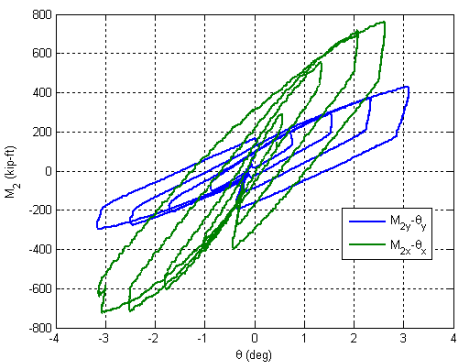
X Moment vs. Y Moment at the base



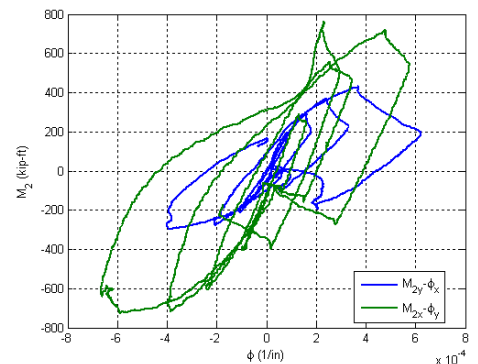
Lateral Force vs. Lateral Displacement



Base Moment vs. Top Displacement

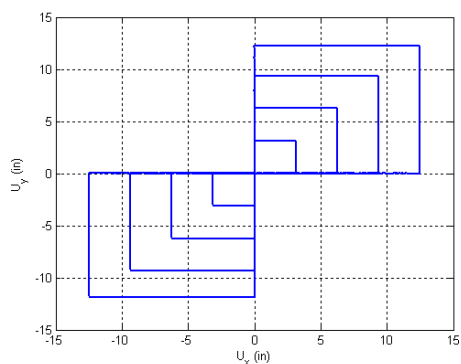


Base Moment vs. Top Rotation

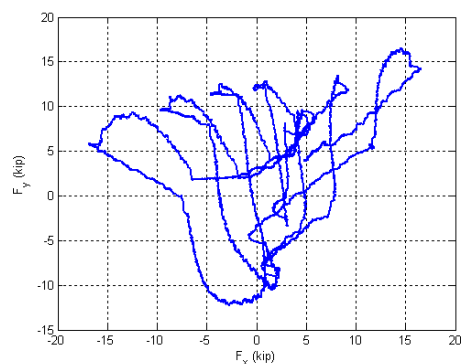


Base Moment vs. Base Curvature

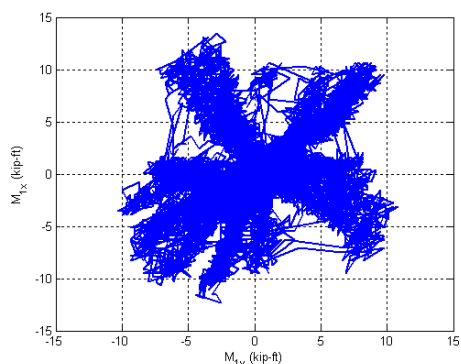
Figure B.89. Experimental results from LC3a in the specimen 12Rw-26-5



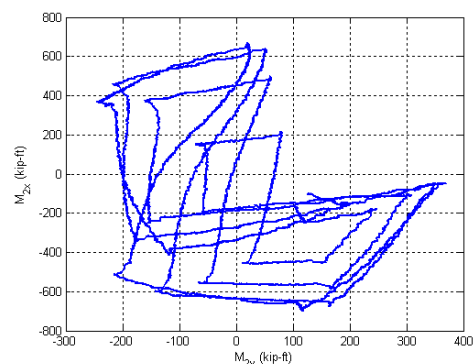
Y Displacement vs. X Displacement



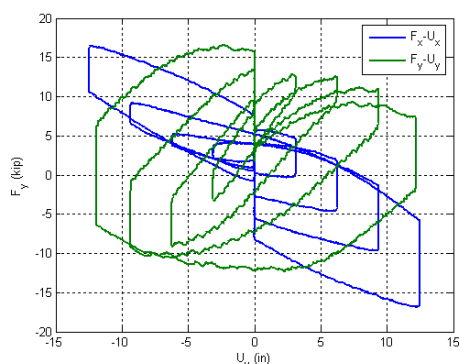
Y Force vs. X Force



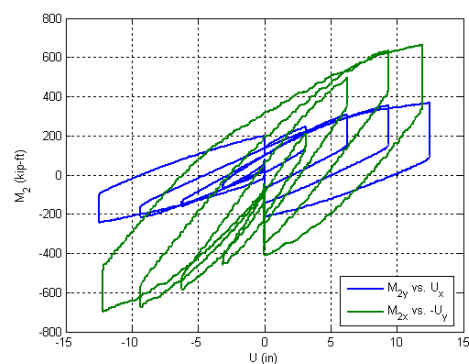
X Moment vs. Y Moment at the top



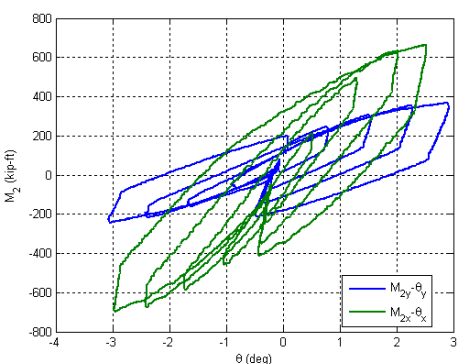
X Moment vs. Y Moment at the base



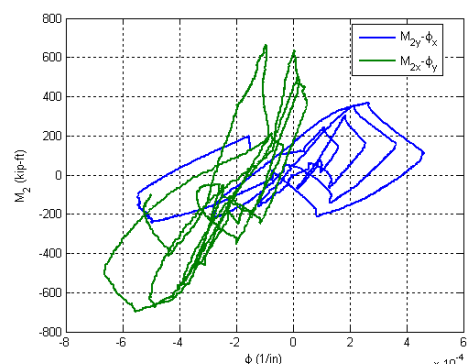
Lateral Force vs. Lateral Displacement



Base Moment vs. Top Displacement

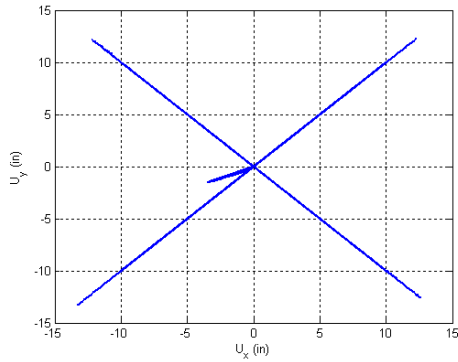


Base Moment vs. Top Rotation

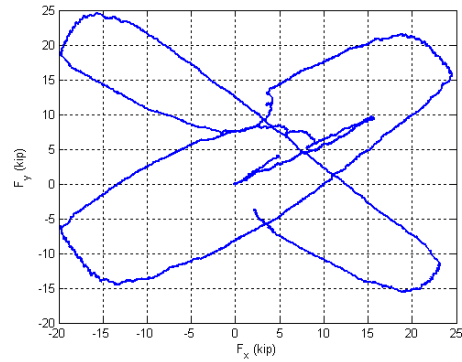


Base Moment vs. Base Curvature

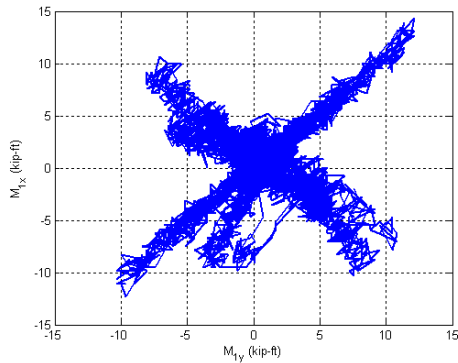
Figure B.90. Experimental results from LC3b in the specimen 12Rw-26-5



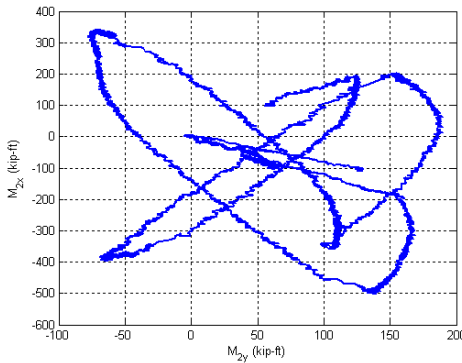
Y Displacement vs. X Displacement



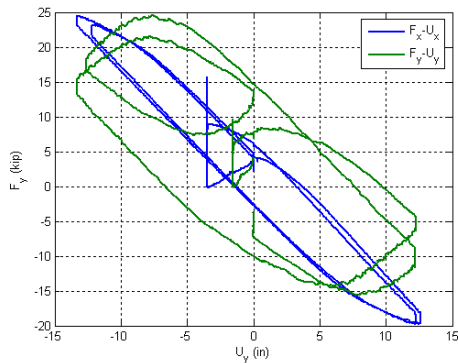
Y Force vs. X Force



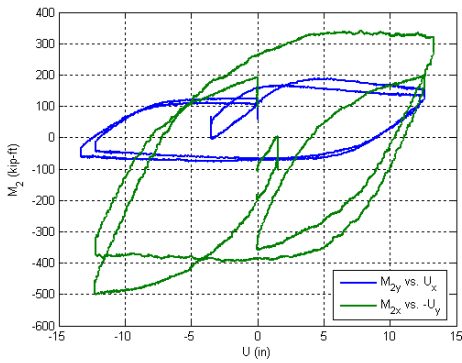
X Moment vs. Y Moment at the top



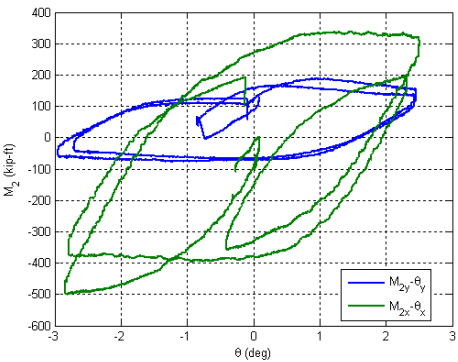
X Moment vs. Y Moment at the base



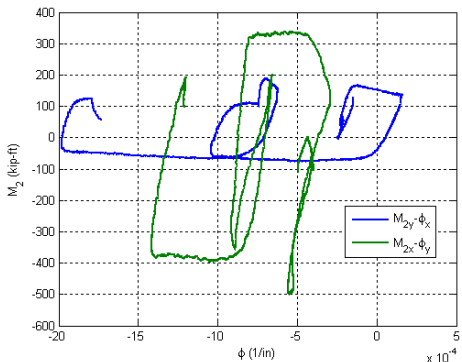
Lateral Force vs. Lateral Displacement



Base Moment vs. Top Displacement



Base Moment vs. Top Rotation



Base Moment vs. Base Curvature

Figure B.91. Experimental results from LC4 in the specimen 12Rw-26-5

B.13. Specimen 13Rs-26-5

Description:

- Specimen number: 13
- Composite Cross-section: CCFT
- Steel cross-section: HSS20x12x0.25
- Design concrete strength: 5 ksi
- Design specimen length: 26 ft
- Pouring date: 03/27/2009
- Testing date: 06/11/2009

Parameters:

- Specimen length: 26' 1 3/4"
- Initial out-of-plumbness: $U_{xo} = 0.68'' / U_{yo} = 0.00''$
- Steel yielding stress: $F_y = 55.5$ ksi
- Steel ultimate stress: $F_u = 73.2$ ksi
- Concrete strength at the 28th day: $f_c' = 7.3$ ksi
- Concrete strength at the testing day: $f_c = 8.3$ ksi
- Concrete Young's modulus: $E_c = 5000$ ksi
- Concrete tensile strength: $f_t = 0.6$ ksi

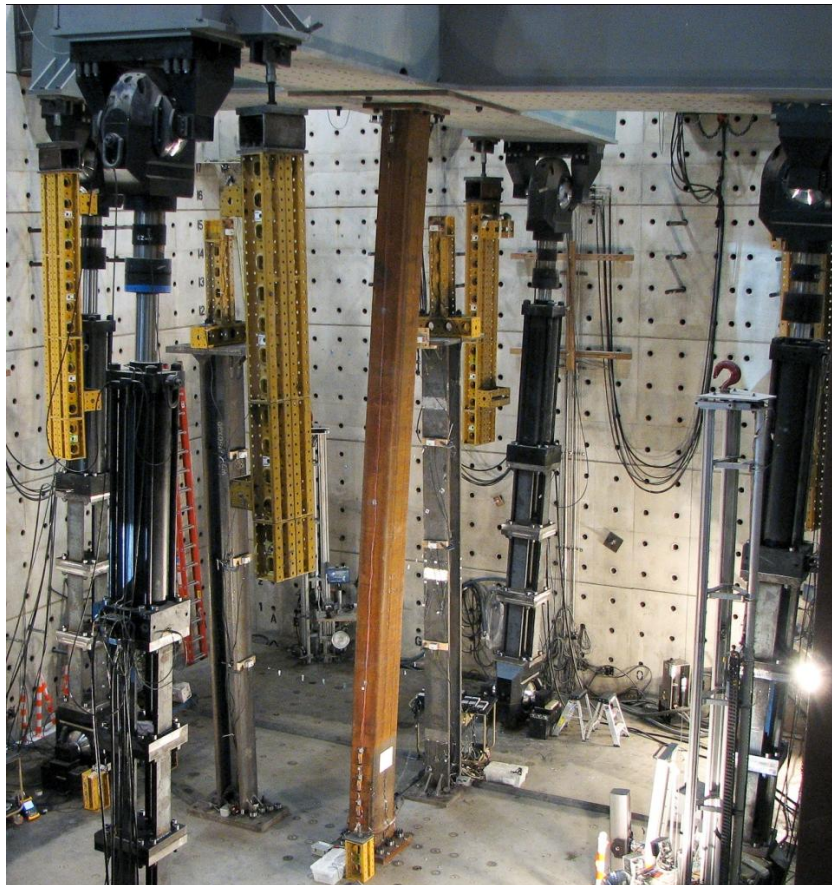


Figure B.92. Specimen 13Rs-26-5

Table B.13. Load protocol summary for the specimen 13Rs-26-5

LC1 - Incremental compression loading in two cycles until the maximum load is reached. The top is forced to be free at X ($K_x=2$) and fixed at Y ($K_y=0.5$).

Step	DOF						Stop Criterion
	X	Y	Z	RX	RY	RZ	
1	$F_x = 0$	$U_y = 0$	$U_z \downarrow$	$R_x = 0$	$M_y = 0$	$R_z = 0$	max P
2	$F_x = 0$	$U_y = 0$	$U_z \uparrow$	$R_x = 0$	$M_y = 0$	$R_z = 0$	P = 0
3	$F_x = 0$	$U_y = 0$	$U_z \downarrow$	$R_x = 0$	$M_y = 0$	$R_z = 0$	max P
4	$F_x = 0$	$U_y = 0$	$U_z \uparrow$	$R_x = 0$	$M_y = 0$	$R_z = 0$	P = 0

LC2a - Cyclic uniaxial lateral displacements with constant compression force ($-F_z = P = 400$ kips). The top was forced to have zero moments in Y and fixed rotation in X.

Step	DOF						Stop Criterion
	X	Y	Z	RX	RY	RZ	
1	$U_x \uparrow$	$U_y = 0$	P = 400k	$R_x = 0$	$M_y = 0$	$R_z = 0$	+1% drift
2	$U_x \downarrow$	$U_y = 0$	P = 400k	$R_x = 0$	$M_y = 0$	$R_z = 0$	-1% drift
3	$U_x \uparrow$	$U_y = 0$	P = 400k	$R_x = 0$	$M_y = 0$	$R_z = 0$	+2% drift
4	$U_x \downarrow$	$U_y = 0$	P = 400k	$R_x = 0$	$M_y = 0$	$R_z = 0$	-2% drift
5	$U_x \uparrow$	$U_y = 0$	P = 400k	$R_x = 0$	$M_y = 0$	$R_z = 0$	+3% drift
6	$U_x \downarrow$	$U_y = 0$	P = 400k	$R_x = 0$	$M_y = 0$	$R_z = 0$	-3% drift
7	$U_x \uparrow$	$U_y = 0$	P = 400k	$R_x = 0$	$M_y = 0$	$R_z = 0$	+4% drift
8	$U_x \downarrow$	$U_y = 0$	P = 400k	$R_x = 0$	$M_y = 0$	$R_z = 0$	-4% drift
9	$U_x \uparrow$	$U_y = 0$	P = 400k	$R_x = 0$	$M_y = 0$	$R_z = 0$	+5% drift
10	$U_x \downarrow$	$U_y = 0$	P = 400k	$R_x = 0$	$M_y = 0$	$R_z = 0$	-5% drift
11	$U_x \downarrow$	$U_y = 0$	P = 400k	$R_x = 0$	$M_y = 0$	$R_z = 0$	$U_z = 0$

LC2b - Cyclic uniaxial lateral displacements with constant compression force ($-F_z = P = 600$ kips). The top was forced to have zero moments in Y and fixed rotation in X.

Step	DOF						Stop Criterion
	X	Y	Z	RX	RY	RZ	
1	$U_x \uparrow$	$U_y = 0$	P = 600k	$R_x = 0$	$M_y = 0$	$R_z = 0$	+1% drift
2	$U_x \downarrow$	$U_y = 0$	P = 600k	$R_x = 0$	$M_y = 0$	$R_z = 0$	-1% drift
3	$U_x \uparrow$	$U_y = 0$	P = 600k	$R_x = 0$	$M_y = 0$	$R_z = 0$	+2% drift
4	$U_x \downarrow$	$U_y = 0$	P = 600k	$R_x = 0$	$M_y = 0$	$R_z = 0$	-2% drift
5	$U_x \uparrow$	$U_y = 0$	P = 600k	$R_x = 0$	$M_y = 0$	$R_z = 0$	+3% drift
6	$U_x \downarrow$	$U_y = 0$	P = 600k	$R_x = 0$	$M_y = 0$	$R_z = 0$	-3% drift
7	$U_x \uparrow$	$U_y = 0$	P = 600k	$R_x = 0$	$M_y = 0$	$R_z = 0$	+4% drift
8	$U_x \downarrow$	$U_y = 0$	P = 600k	$R_x = 0$	$M_y = 0$	$R_z = 0$	-4% drift
11	$U_x \downarrow$	$U_y = 0$	P = 600k	$R_x = 0$	$M_y = 0$	$R_z = 0$	$U_z = 0$

LC3a - Cyclic biaxial lateral displacements (8 shape) with constant compression force ($-F_z = P = 300$ kips). The top was forced to have zero moments.

Step	DOF						Stop Criterion
	X	Y	Z	RX	RY	RZ	
1	$U_x \uparrow$	$U_y \uparrow$	$P = 300k$	$M_x = 0$	$M_y = 0$	$R_z = 0$	+/-1% drift
2	$U_x \downarrow$	$U_y \downarrow$	$P = 300k$	$M_x = 0$	$M_y = 0$	$R_z = 0$	+/-2% drift
3	$U_x \uparrow$	$U_y \uparrow$	$P = 300k$	$M_x = 0$	$M_y = 0$	$R_z = 0$	+/-3% drift
4	$U_x \downarrow$	$U_y \downarrow$	$P = 300k$	$M_x = 0$	$M_y = 0$	$R_z = 0$	+/-4% drift

LC3b - Cyclic biaxial lateral displacements (8 shape) with constant compression force ($-F_z = P = 500$ kips). The top was forced to have zero moments.

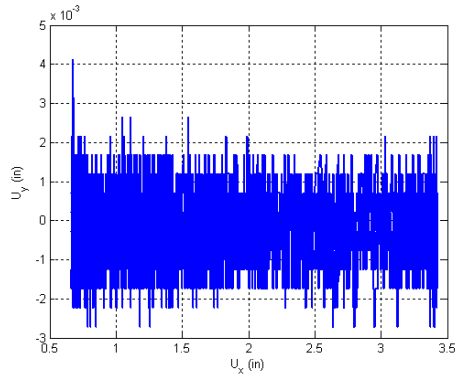
Step	DOF						Stop Criterion
	X	Y	Z	RX	RY	RZ	
1	$U_x \uparrow$	$U_y \uparrow$	$P = 500k$	$M_x = 0$	$M_y = 0$	$R_z = 0$	+/-1% drift
2	$U_x \downarrow$	$U_y \downarrow$	$P = 500k$	$M_x = 0$	$M_y = 0$	$R_z = 0$	+/-2% drift
3	$U_x \uparrow$	$U_y \uparrow$	$P = 500k$	$M_x = 0$	$M_y = 0$	$R_z = 0$	+/-3% drift
4	$U_x \downarrow$	$U_y \downarrow$	$P = 500k$	$M_x = 0$	$M_y = 0$	$R_z = 0$	+/-4% drift

LC4a - Incremental compression loading until the maximum load is reached. The top is forced to be free at X ($K_x=2$) and fixed at Y ($K_y=0.5$)..

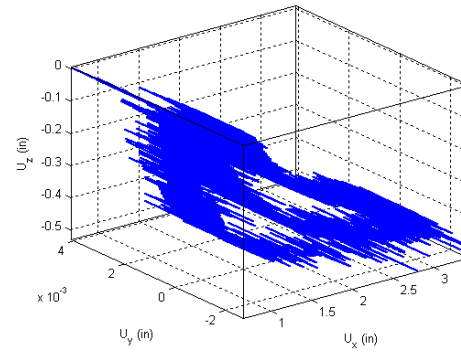
Step	DOF						Stop Criterion
	X	Y	Z	RX	RY	RZ	
1	$F_x \rightarrow 0$	$F_y \rightarrow 0$	$F_z \rightarrow 0$	$M_x = 0$	$M_y = 0$	$R_z = 0$	$F_x=F_y=0$
2	$F_x = 0$	$U_y = 0$	$U_z \downarrow$	$R_x = 0$	$M_y = 0$	$R_z = 0$	$P = P_{max}$

LC4b - Cyclic uniaxial lateral displacements (4 corners) with constant compression force ($-F_z = P = 600$ kips). The top is forced to be free at all the time.

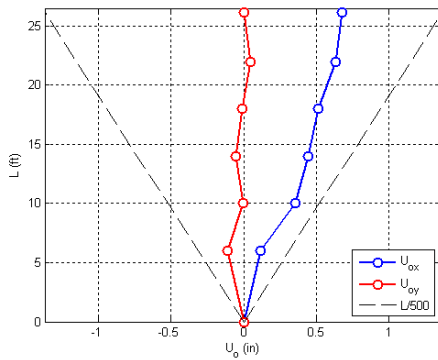
Step	DOF						Stop Criterion
	X	Y	Z	RX	RY	RZ	
1	$U_x \uparrow$	$U_y \uparrow$	$P = 600k$	$M_x = 0$	$M_y = 0$	$R_z = 0$	max stroke
2	$U_x \downarrow$	$U_y \downarrow$	$P = 600k$	$M_x = 0$	$M_y = 0$	$R_z = 0$	max stroke
3	$U_x \rightarrow 0$	$U_y \rightarrow 0$	$P = 600k$	$M_x = 0$	$M_y = 0$	$R_z = 0$	$U_x=U_y=0$



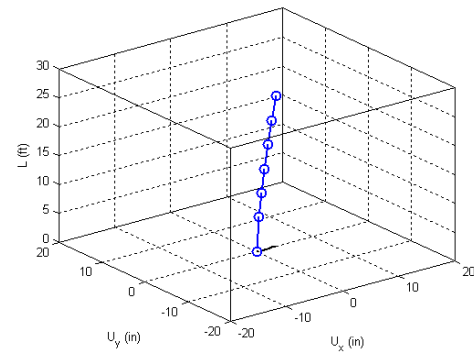
Y displacement vs. X displacement



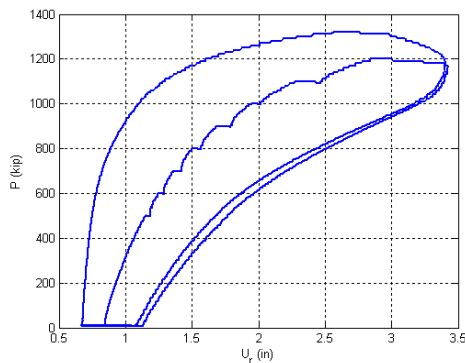
Z displacement vs. X and Y displacement



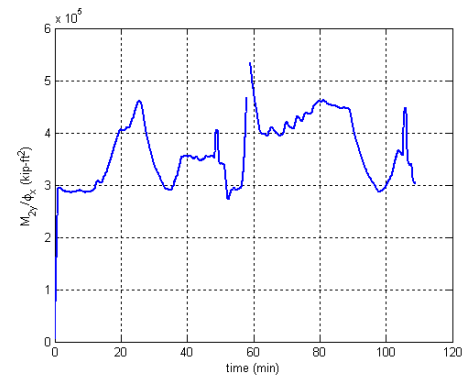
Initial deflected shape



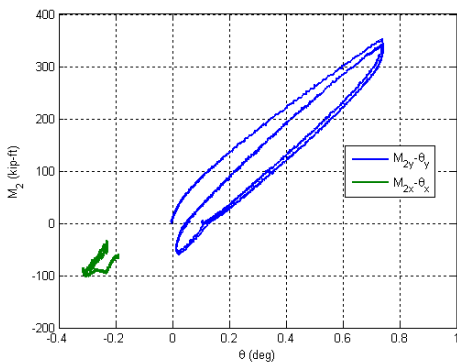
Maximum lateral displacement



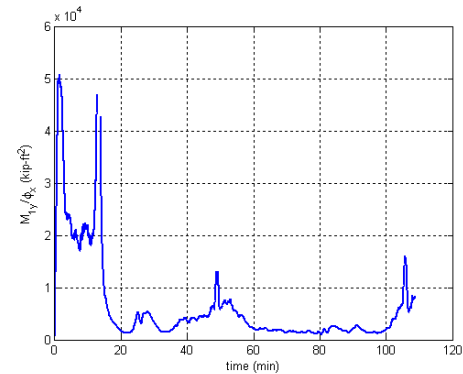
Axial force vs. lateral displacement



Axial force vs. base moments

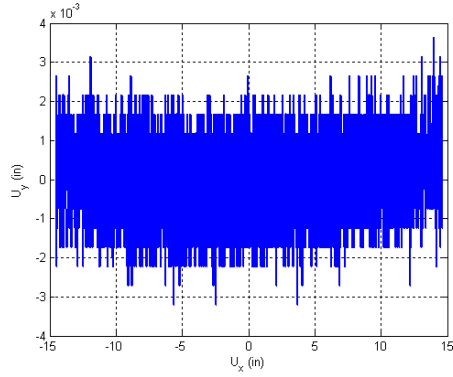


Base moment vs. base curvature

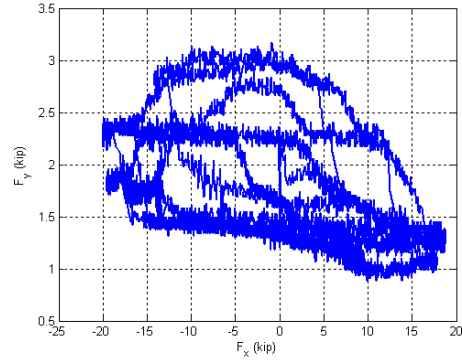


Base moment vs. top rotation

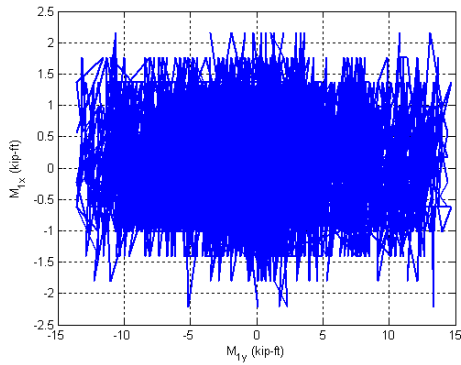
Figure B.93. Experimental results from LC1 in the specimen 13Rs-26-5



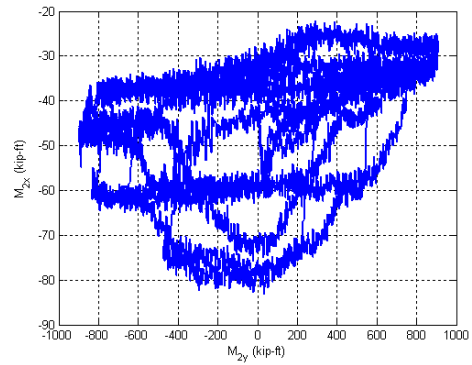
Y Displacement vs. X Displacement



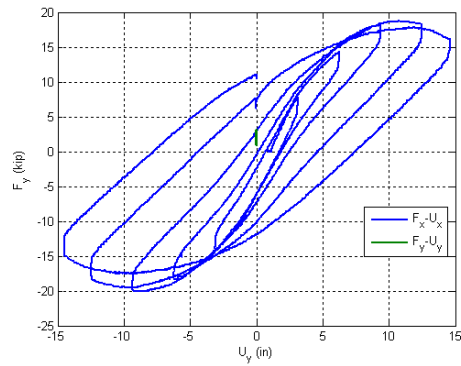
Y Force vs. X Force



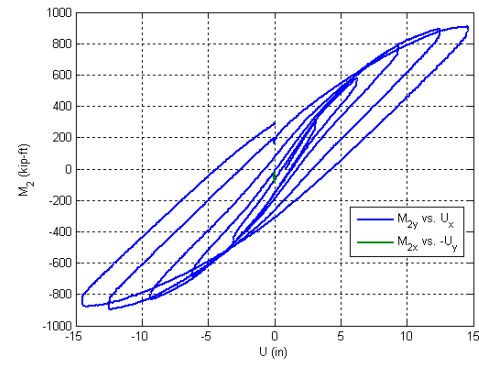
X Moment vs. Y Moment at the top



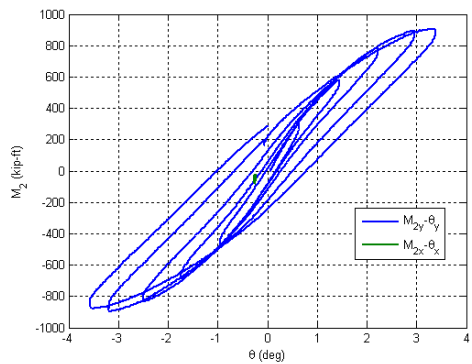
X Moment vs. Y Moment at the base



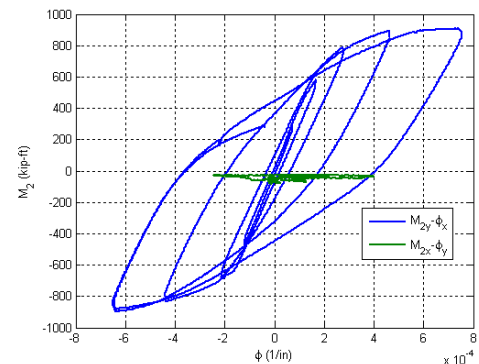
Lateral Force vs. Lateral Displacement



Base Moment vs. Top Displacement

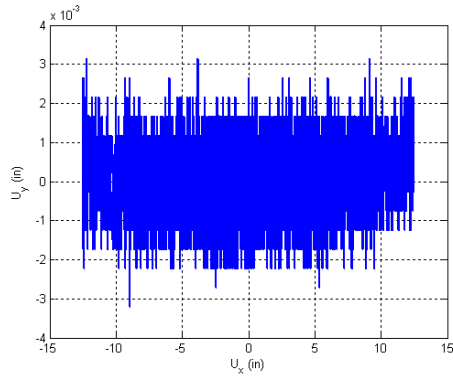


Base Moment vs. Top Rotation

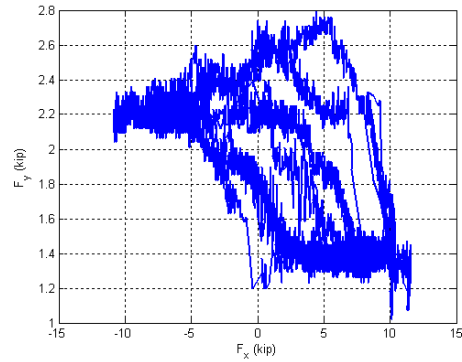


Base Moment vs. Base Curvature

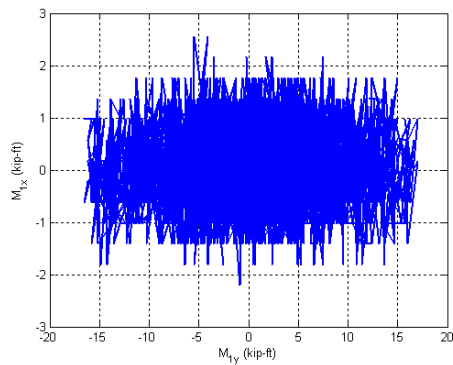
Figure B.94. Experimental results from LC2a in the specimen 13Rs-26-5



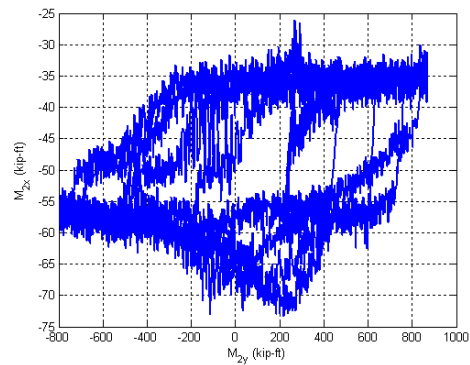
Y Displacement vs. X Displacement



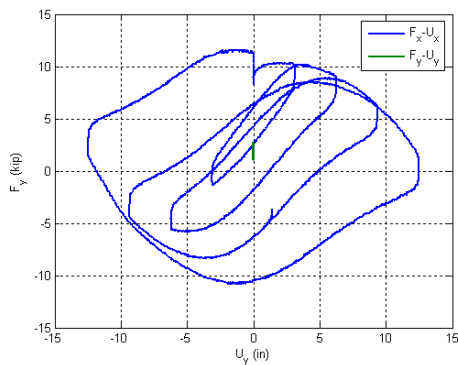
Y Force vs. X Force



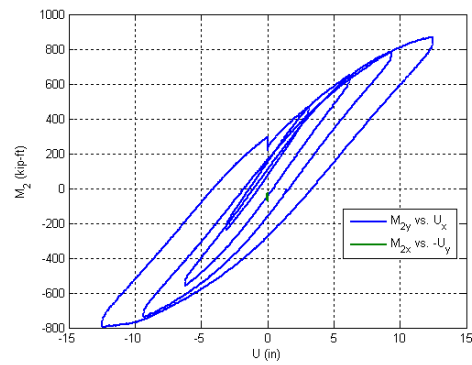
X Moment vs. Y Moment at the top



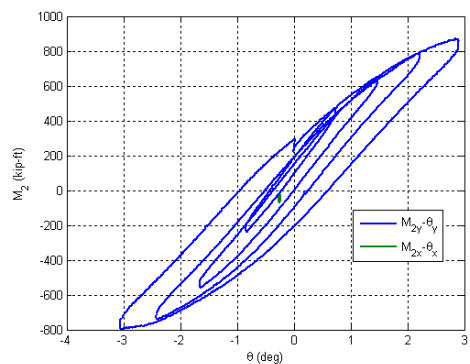
X Moment vs. Y Moment at the base



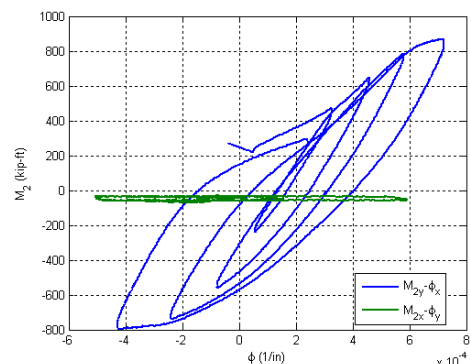
Lateral Force vs. Lateral Displacement



Base Moment vs. Top Displacement

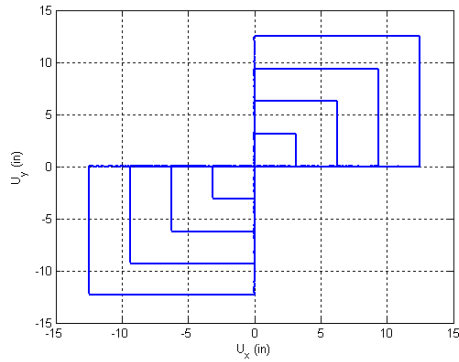


Base Moment vs. Top Rotation

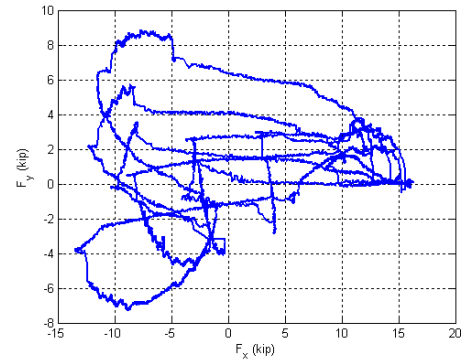


Base Moment vs. Base Curvature

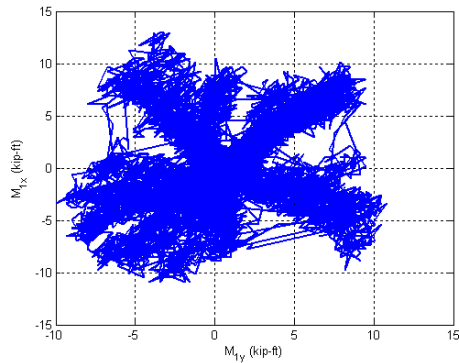
Figure B.95. Experimental results from LC2b in the specimen 13Rs-26-5



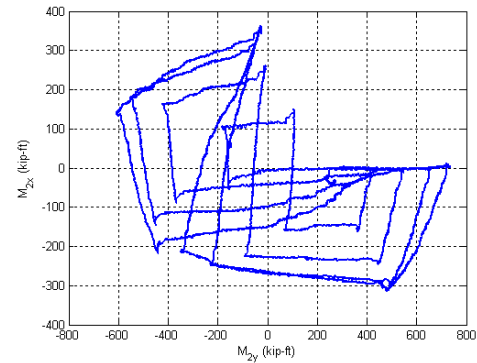
Y Displacement vs. X Displacement



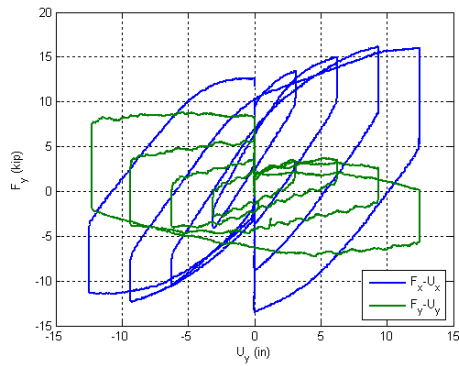
Y Force vs. X Force



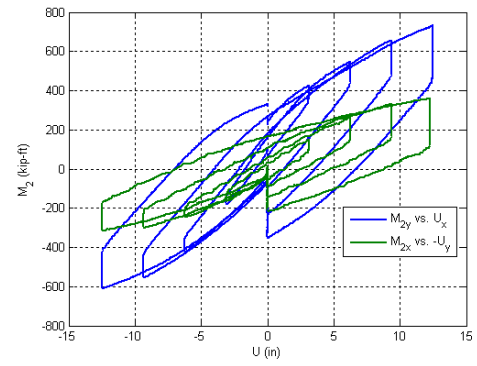
X Moment vs. Y Moment at the top



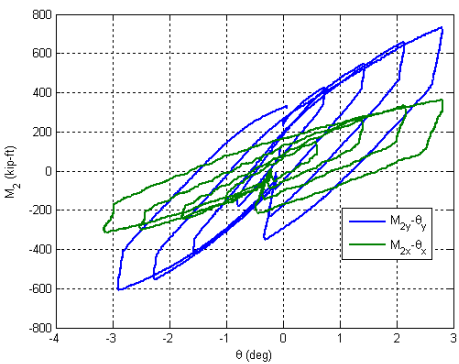
X Moment vs. Y Moment at the base



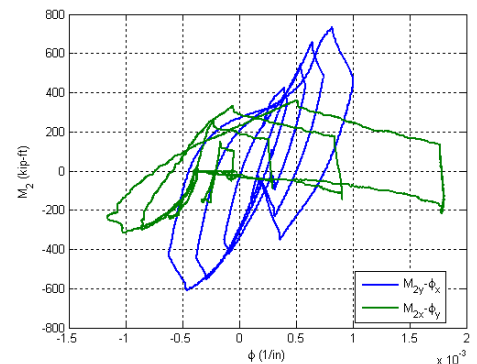
Lateral Force vs. Lateral Displacement



Base Moment vs. Top Displacement

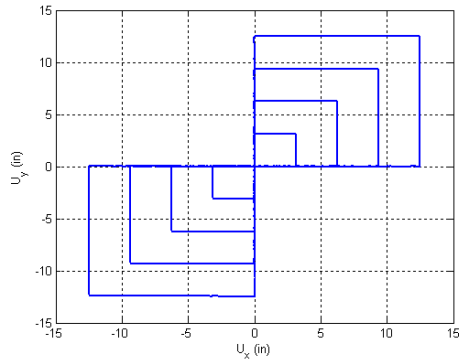


Base Moment vs. Top Rotation

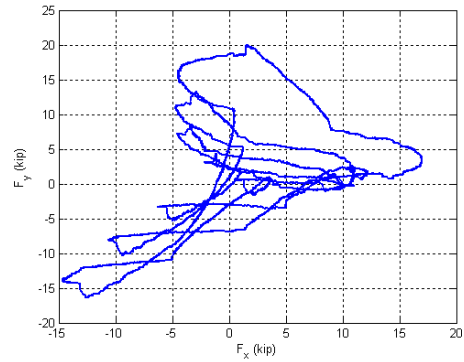


Base Moment vs. Base Curvature

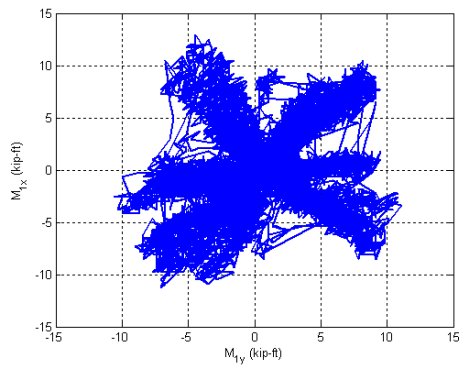
Figure B.96. Experimental results from LC3a in the specimen 13Rs-26-5



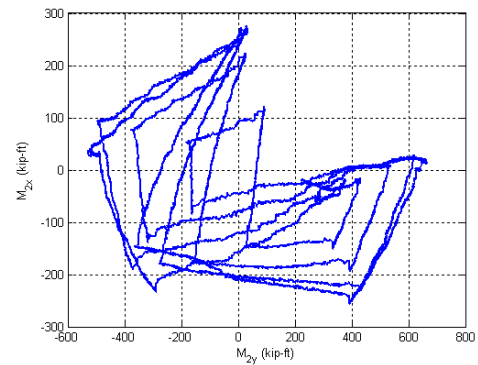
Y Displacement vs. X Displacement



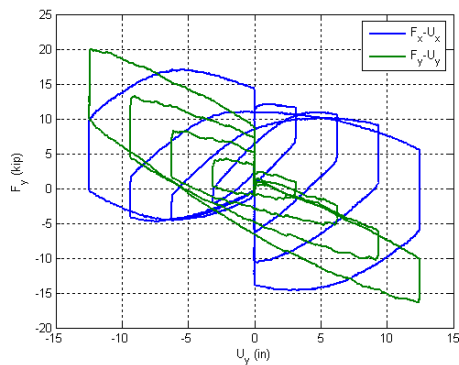
Y Force vs. X Force



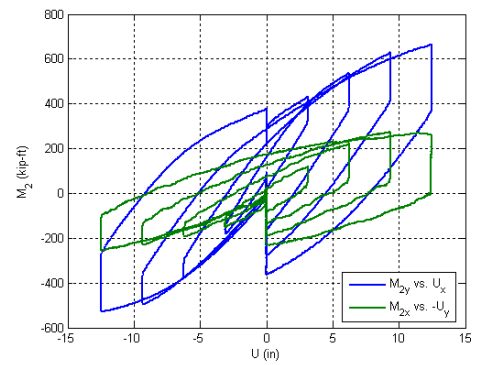
X Moment vs. Y Moment at the top



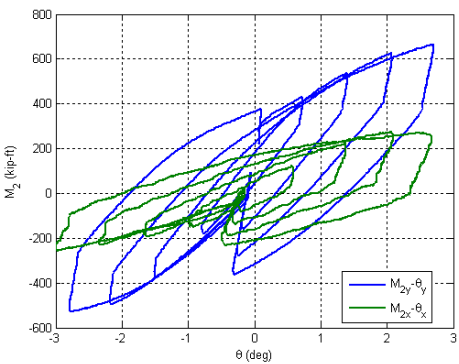
X Moment vs. Y Moment at the base



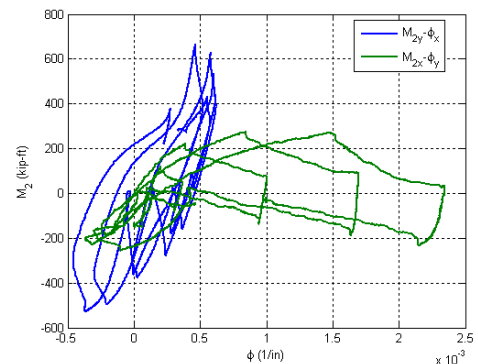
Lateral Force vs. Lateral Displacement



Base Moment vs. Top Displacement

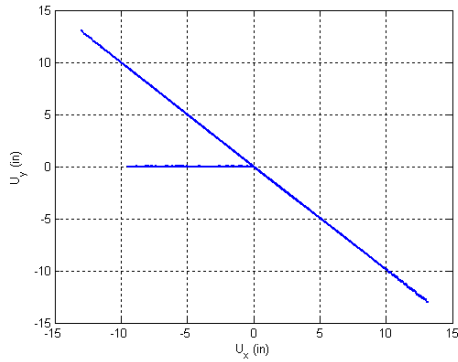


Base Moment vs. Top Rotation

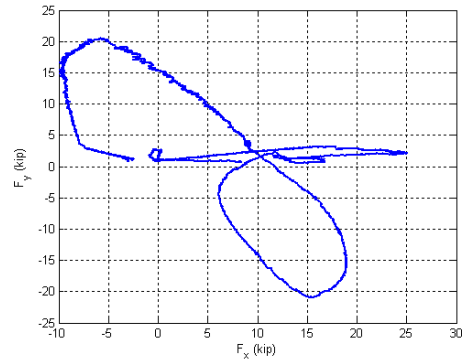


Base Moment vs. Base Curvature

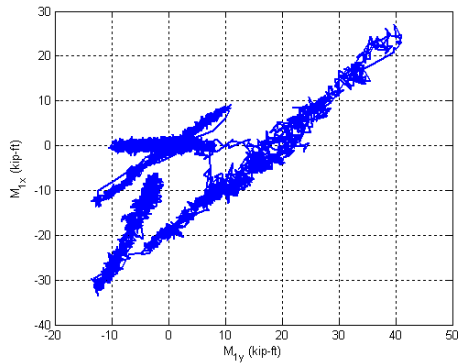
Figure B.97. Experimental results from LC3b in the specimen 13Rs-26-5



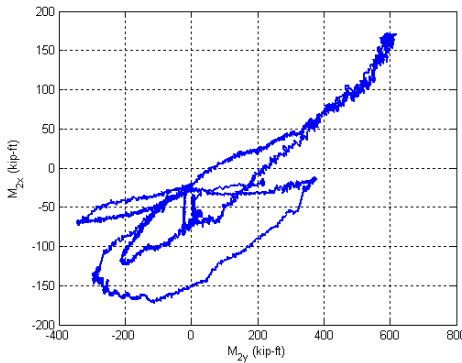
Y Displacement vs. X Displacement



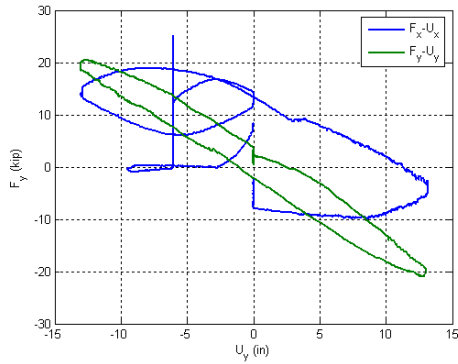
Y Force vs. X Force



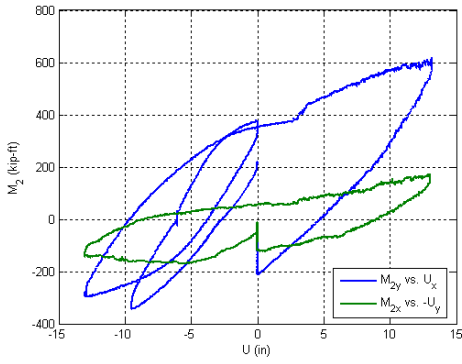
X Moment vs. Y Moment at the top



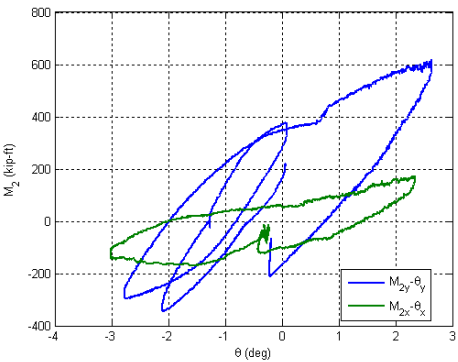
X Moment vs. Y Moment at the base



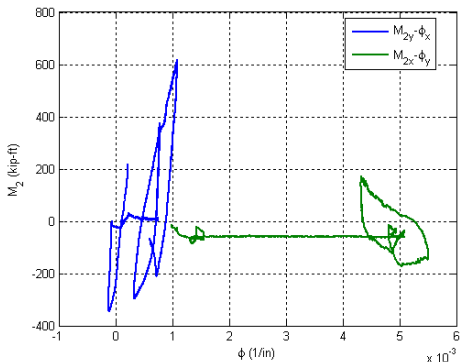
Lateral Force vs. Lateral Displacement



Base Moment vs. Top Displacement



Base Moment vs. Top Rotation



Base Moment vs. Base Curvature

Figure B.98. Experimental results from LC4 in the specimen 13Rs-26-5

B.14. Specimen 14C12-26-12

Description:

- Specimen number: 14
- Composite Cross-section: CCFT
- Steel cross-section: HSS12.75x0.25
- Design concrete strength: 12 ksi
- Design specimen length: 26 ft
- Pouring date: 03/27/2009
- Testing date: 06/16/2009

Parameters:

- Specimen length: 26' 1 1/2"
- Initial out-of-plumbness: $U_{xo} = 0.12'' / U_{yo} = -0.66''$
- Steel yielding stress: $F_y = 55.5$ ksi
- Steel ultimate stress: $F_u = 66.8$ ksi
- Concrete strength at the 28th day: $f_c' = 11.5$ ksi
- Concrete strength at the testing day: $f_c = 11.6$ ksi
- Concrete Young's modulus: $E_c = 5800$ ksi
- Concrete tensile strength: $f_t = 0.76$ ksi

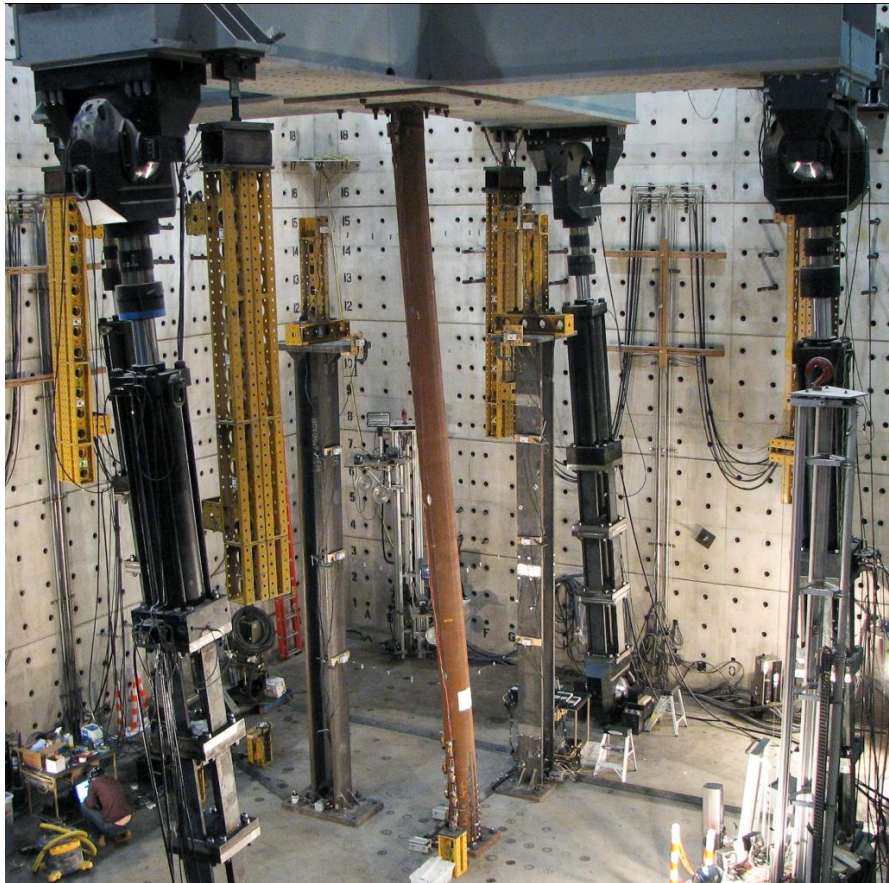


Figure B.99. Specimen 14C12-26-12

Table B.14. Load protocol summary for the specimen 14C12-26-12

LC1 - Incremental compression loading in two cycles until the maximum load is reached. The top is forced to be free at all the time.

Step	DOF						Stop Criterion
	X	Y	Z	RX	RY	RZ	
1	$F_x = 0$	$F_y = 0$	$U_z \downarrow$	$M_x = 0$	$M_y = 0$	$R_z = 0$	$P = 150k$
2	$F_x = 0$	$F_y = 0$	$U_z \uparrow$	$M_x = 0$	$M_y = 0$	$R_z = 0$	$P = 0$
3	$F_x = 0$	$F_y = 0$	$U_z \downarrow$	$M_x = 0$	$M_y = 0$	$R_z = 0$	max P
4	$F_x = 0$	$F_y = 0$	$U_z \uparrow$	$M_x = 0$	$M_y = 0$	$R_z = 0$	$P = 0$

LC2a - Cyclic uniaxial lateral displacements with constant compression force ($-F_z = P = 100$ kips). The top was forced to have zero moments.

Step	DOF						Stop Criterion
	X	Y	Z	RX	RY	RZ	
1	$U_x \uparrow$	$U_y \downarrow$	$P = 100k$	$M_x = 0$	$M_y = 0$	$R_z = 0$	+2% drift
2	$U_x \downarrow$	$U_y \uparrow$	$P = 100k$	$M_x = 0$	$M_y = 0$	$R_z = 0$	-2% drift
3	$U_x \uparrow$	$U_y \downarrow$	$P = 100k$	$M_x = 0$	$M_y = 0$	$R_z = 0$	+4% drift
4	$U_x \downarrow$	$U_y \uparrow$	$P = 100k$	$M_x = 0$	$M_y = 0$	$R_z = 0$	-4% drift
5	$U_x \uparrow$	$U_y \downarrow$	$P = 100k$	$M_x = 0$	$M_y = 0$	$R_z = 0$	+stroke
6	$U_x \downarrow$	$U_y \uparrow$	$P = 100k$	$M_x = 0$	$M_y = 0$	$R_z = 0$	-stroke
7	$U_x \downarrow$	$U_y \uparrow$	$P = 100k$	$M_x = 0$	$M_y = 0$	$R_z = 0$	$U_z = 0$

LC2b - Cyclic uniaxial lateral displacements with constant compression force ($-F_z = P = 200$ kips). The top was forced to have zero moments.

Step	DOF						Stop Criterion
	X	Y	Z	RX	RY	RZ	
1	$U_x \uparrow$	$U_y \downarrow$	$P = 200k$	$M_x = 0$	$M_y = 0$	$R_z = 0$	+2% drift
2	$U_x \downarrow$	$U_y \uparrow$	$P = 200k$	$M_x = 0$	$M_y = 0$	$R_z = 0$	-2% drift
3	$U_x \uparrow$	$U_y \downarrow$	$P = 200k$	$M_x = 0$	$M_y = 0$	$R_z = 0$	+4% drift
4	$U_x \downarrow$	$U_y \uparrow$	$P = 200k$	$M_x = 0$	$M_y = 0$	$R_z = 0$	-4% drift
5	$U_x \downarrow$	$U_y \uparrow$	$P = 200k$	$M_x = 0$	$M_y = 0$	$R_z = 0$	$U_z = 0$

LC3a - Cyclic biaxial lateral displacements (8 shape) with constant compression force ($-F_z = P = 150$ kips). The top was forced to have zero moments.

Step	DOF						Stop Criterion
	X	Y	Z	RX	RY	RZ	
1	$U_x \uparrow$	$U_y \uparrow$	$P = 150k$	$M_x = 0$	$M_y = 0$	$R_z = 0$	+/-1% drift
2	$U_x \uparrow$	$U_y \downarrow$	$P = 150k$	$M_x = 0$	$M_y = 0$	$R_z = 0$	+/-2% drift
3	$U_x \downarrow$	$U_y \downarrow$	$P = 150k$	$M_x = 0$	$M_y = 0$	$R_z = 0$	+/-3% drift
4	$U_x \downarrow$	$U_y \uparrow$	$P = 150k$	$M_x = 0$	$M_y = 0$	$R_z = 0$	+/-4% drift

LC1' - Incremental compression loading in two cycles until the maximum load is reached. The top is forced to have free displacement and fixed rotation at all the time.

Step	DOF						Stop Criterion
	X	Y	Z	RX	RY	RZ	
1	$F_x = 0$	$F_y = 0$	$U_z \downarrow$	$R_x = 0$	$R_y = 0$	$R_z = 0$	max P
2	$F_x = 0$	$F_y = 0$	$U_z \uparrow$	$R_x = 0$	$R_y = 0$	$R_z = 0$	P = 0

LC2a' - Cyclic uniaxial lateral displacements with constant compression force ($-F_z = P = 300$ kips). The top was forced to have fixed rotations.

Step	DOF						Stop Criterion
	X	Y	Z	RX	RY	RZ	
1	$U_x \uparrow$	$U_y \downarrow$	P = 300k	$R_x = 0$	$R_y = 0$	$R_z = 0$	+2% drift
2	$U_x \downarrow$	$U_y \uparrow$	P = 300k	$R_x = 0$	$R_y = 0$	$R_z = 0$	-2% drift
3	$U_x \uparrow$	$U_y \downarrow$	P = 300k	$R_x = 0$	$R_y = 0$	$R_z = 0$	+4% drift
4	$U_x \downarrow$	$U_y \uparrow$	P = 300k	$R_x = 0$	$R_y = 0$	$R_z = 0$	-4% drift
5	$U_x \uparrow$	$U_y \downarrow$	P = 300k	$R_x = 0$	$R_y = 0$	$R_z = 0$	+stroke
6	$U_x \downarrow$	$U_y \uparrow$	P = 300k	$R_x = 0$	$R_y = 0$	$R_z = 0$	-stroke
7	$U_x \downarrow$	$U_y \uparrow$	P = 300k	$R_x = 0$	$R_y = 0$	$R_z = 0$	$U_z = 0$

LC3a' - Cyclic biaxial lateral displacements (8 shape) with constant compression force ($-F_z = P = 450$ kips). The top was forced to have fixed rotations.

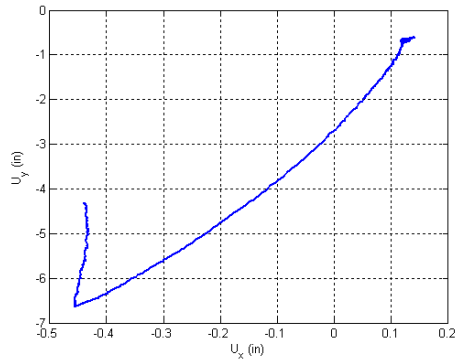
Step	DOF						Stop Criterion
	X	Y	Z	RX	RY	RZ	
1	$U_x \uparrow$	$U_y \uparrow$	P = 450k	$R_x = 0$	$R_y = 0$	$R_z = 0$	+/-1% drift
2	$U_x \downarrow$	$U_y \downarrow$	P = 450k	$R_x = 0$	$R_y = 0$	$R_z = 0$	+/-2% drift
3	$U_x \downarrow$	$U_y \uparrow$	P = 450k	$R_x = 0$	$R_y = 0$	$R_z = 0$	+/-3% drift
4	$U_x \uparrow$	$U_y \downarrow$	P = 450k	$R_x = 0$	$R_y = 0$	$R_z = 0$	+/-4% drift

LC4a - Incremental compression loading until the maximum load is reached. The top is forced to have free displacement and fixed rotation at all the time.

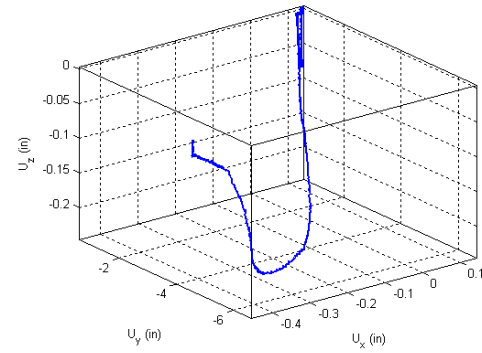
Step	DOF						Stop Criterion
	X	Y	Z	RX	RY	RZ	
1	$F_x = 0$	$F_y = 0$	$U_z \downarrow$	$R_x = 0$	$R_y = 0$	$R_z = 0$	max P
2	$F_x = 0$	$F_y = 0$	$U_z \uparrow$	$R_x = 0$	$R_y = 0$	$R_z = 0$	P = 300k

LC4b - Cyclic uniaxial lateral displacements (4 corners) with constant compression force ($-F_z = P = 300$ kips). The top is forced to have fixed rotations.

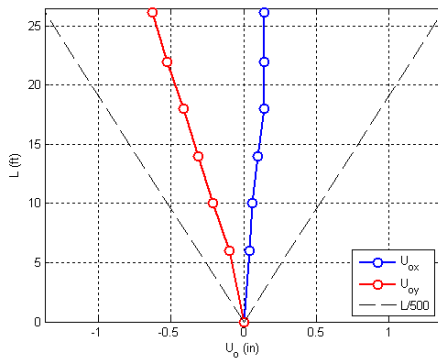
Step	DOF						Stop Criterion
	X	Y	Z	RX	RY	RZ	
1	$U_x \uparrow$	$U_y \uparrow$	P = 300k	$R_x = 0$	$R_y = 0$	$R_z = 0$	max stroke
2	$U_x \downarrow$	$U_y \downarrow$	P = 300k	$R_x = 0$	$R_y = 0$	$R_z = 0$	max stroke
3	$U_x \rightarrow 0$	$U_y \rightarrow 0$	P = 300k	$R_x = 0$	$R_y = 0$	$R_z = 0$	$U_x = U_y = 0$
4	$U_x \uparrow$	$U_y \downarrow$	P = 300k	$R_x = 0$	$R_y = 0$	$R_z = 0$	max stroke
5	$U_x \downarrow$	$U_y \uparrow$	P = 300k	$R_x = 0$	$R_y = 0$	$R_z = 0$	max stroke
6	$U_x \rightarrow 0$	$U_y \rightarrow 0$	P = 300k	$R_x = 0$	$R_y = 0$	$R_z = 0$	$U_x = U_y = 0$



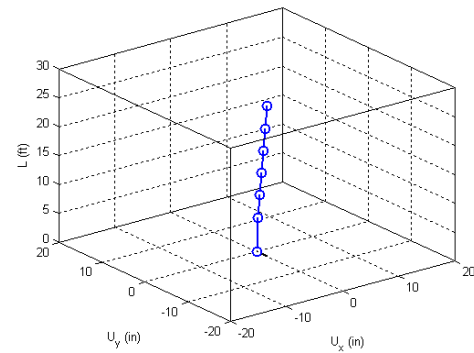
Y displacement vs. X displacement



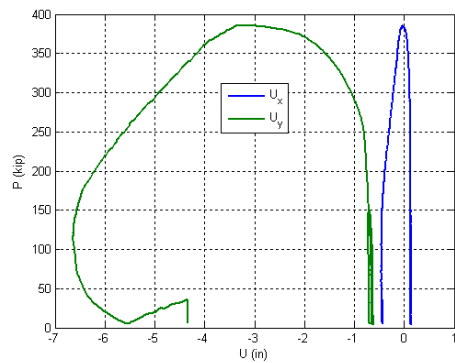
Z displacement vs. X and Y displacement



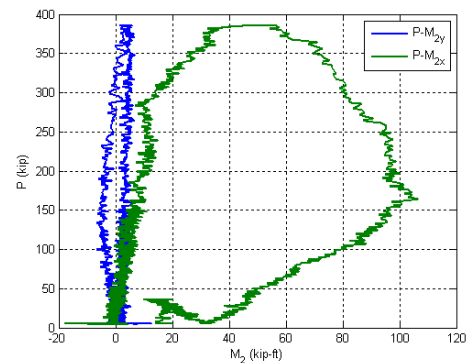
Initial deflected shape



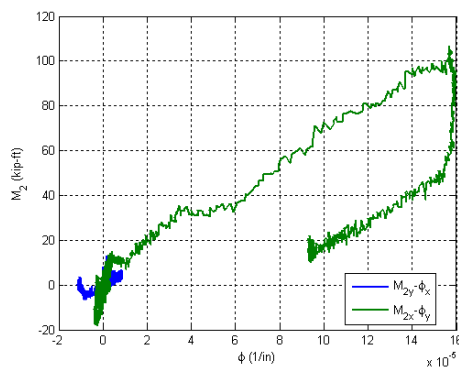
Maximum lateral displacement



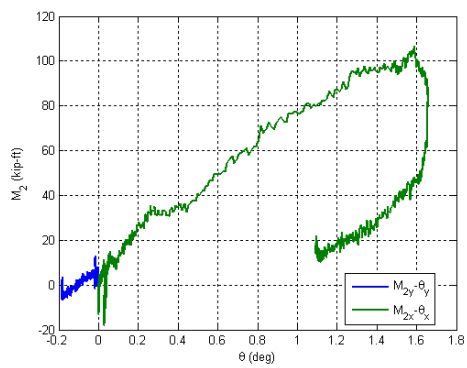
Axial force vs. lateral displacement



Axial force vs. base moments

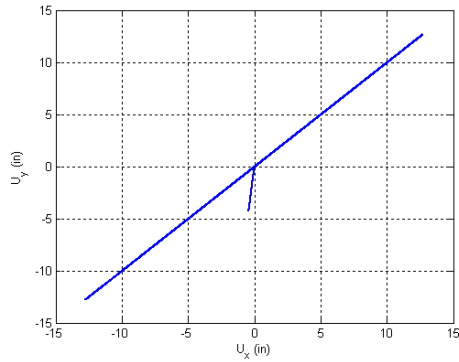


Base moment vs. base curvature

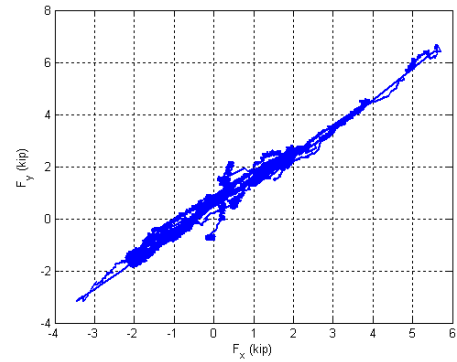


Base moment vs. top rotation

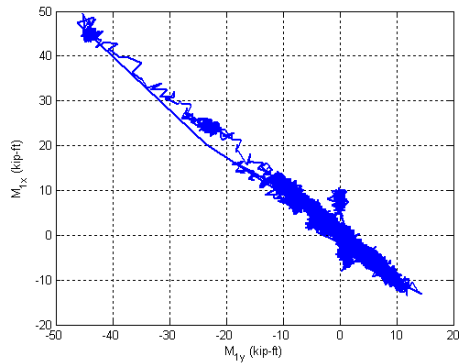
Figure B.100. Experimental results from LC1 in the specimen 14C12-26-12



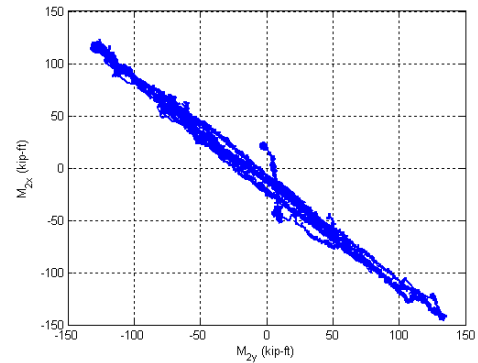
Y Displacement vs. X Displacement



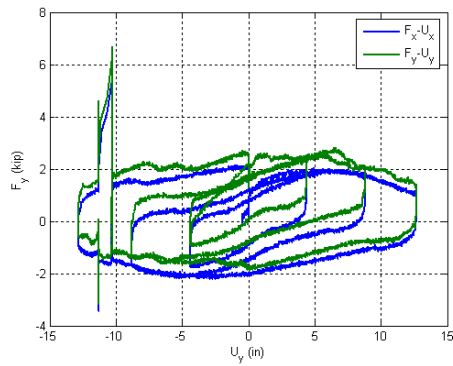
Y Force vs. X Force



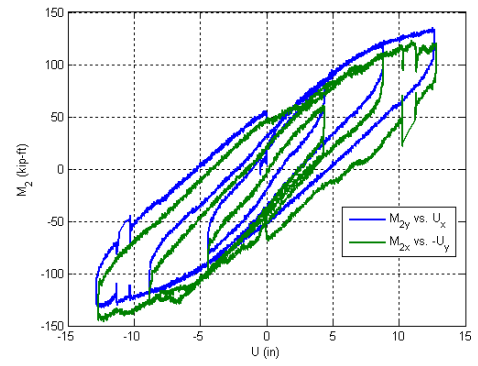
X Moment vs. Y Moment at the top



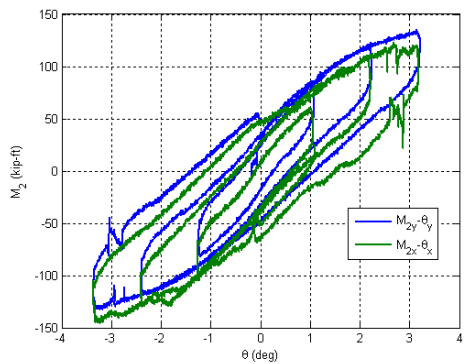
X Moment vs. Y Moment at the base



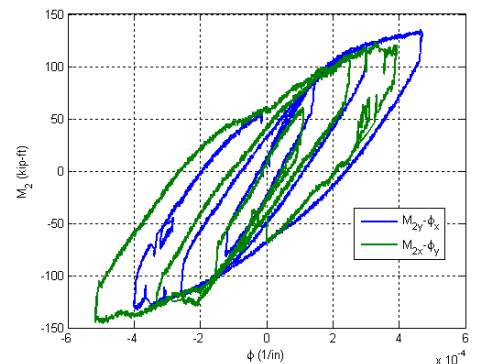
Lateral Force vs. Lateral Displacement



Base Moment vs. Top Displacement

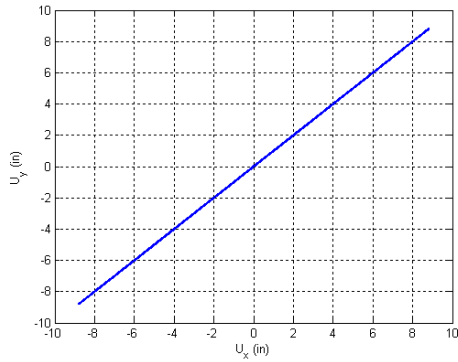


Base Moment vs. Top Rotation

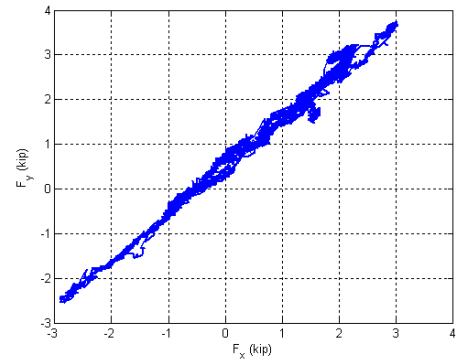


Base Moment vs. Base Curvature

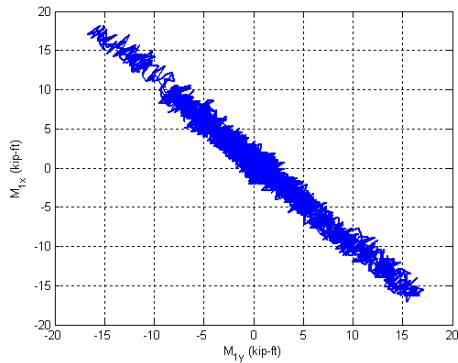
Figure B.101. Experimental results from LC2a in the specimen 14C12-26-12



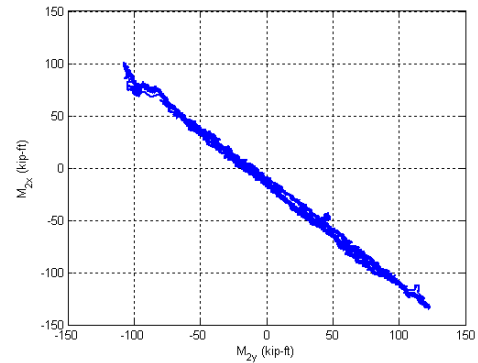
Y Displacement vs. X Displacement



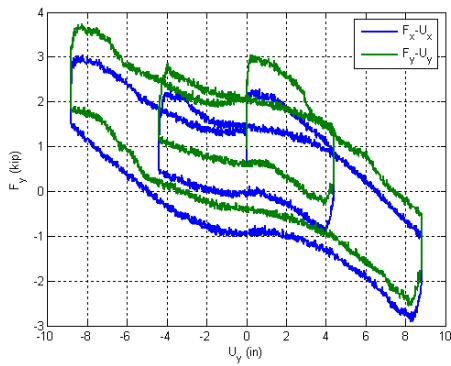
Y Force vs. X Force



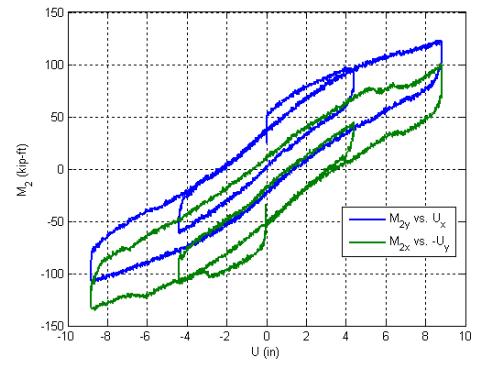
X Moment vs. Y Moment at the top



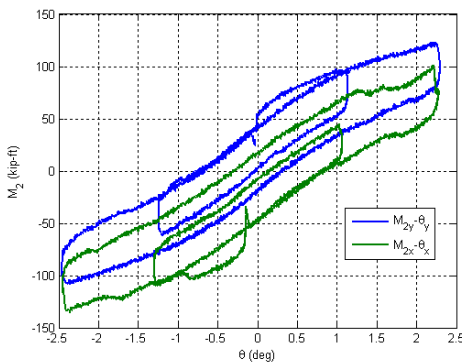
X Moment vs. Y Moment at the base



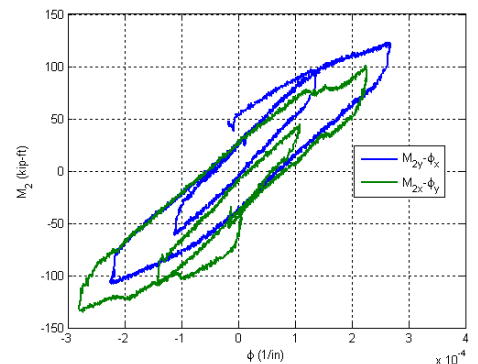
Lateral Force vs. Lateral Displacement



Base Moment vs. Top Displacement

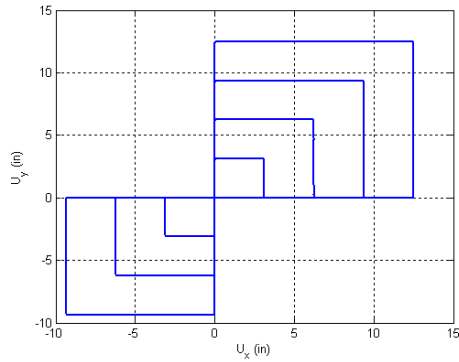


Base Moment vs. Top Rotation

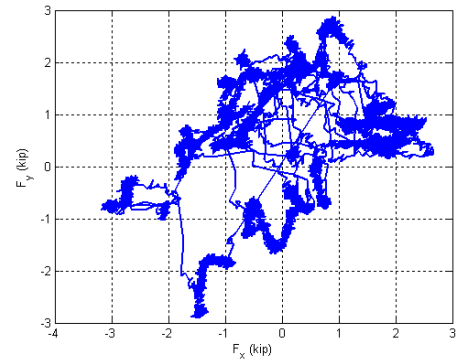


Base Moment vs. Base Curvature

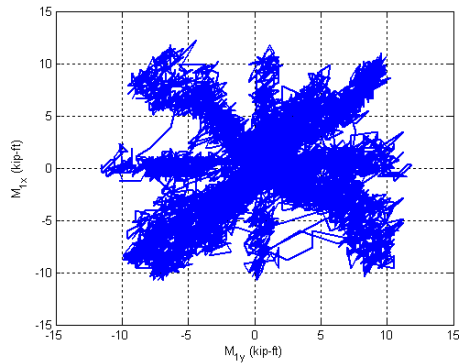
Figure B.102. Experimental results from LC2b in the specimen 14C12-26-12



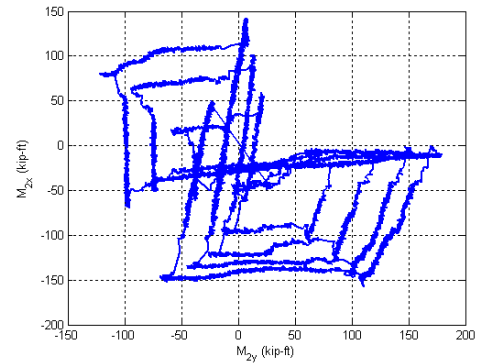
Y Displacement vs. X Displacement



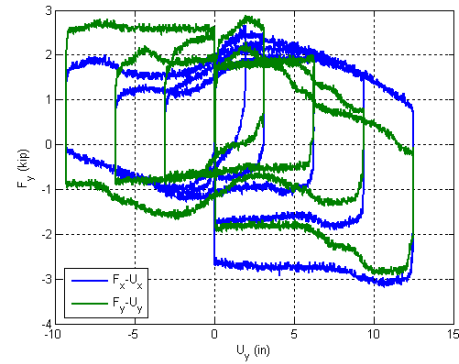
Y Force vs. X Force



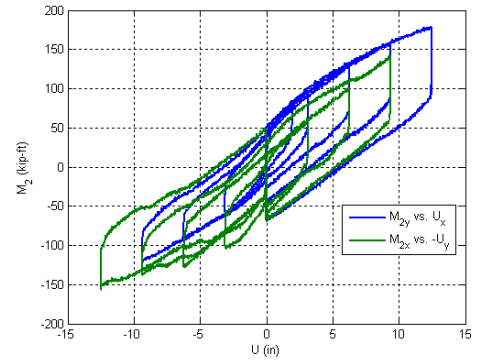
X Moment vs. Y Moment at the top



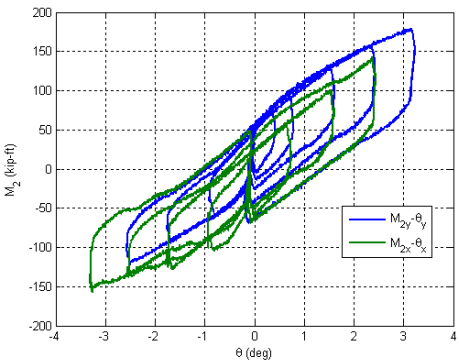
X Moment vs. Y Moment at the base



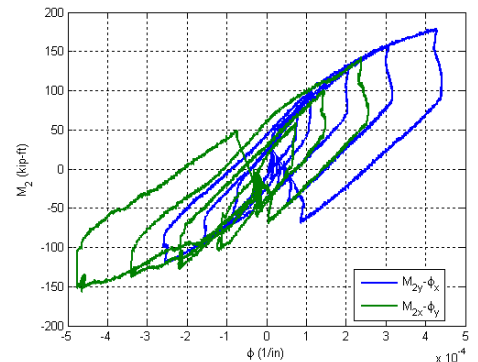
Lateral Force vs. Lateral Displacement



Base Moment vs. Top Displacement

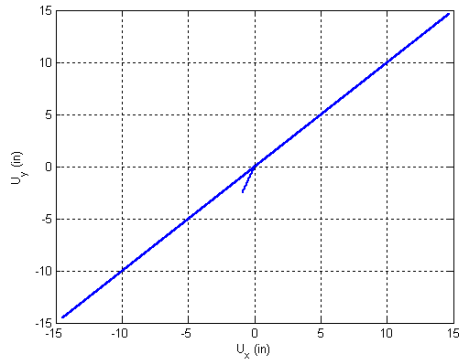


Base Moment vs. Top Rotation

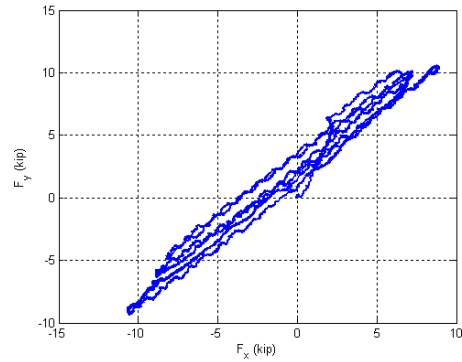


Base Moment vs. Base Curvature

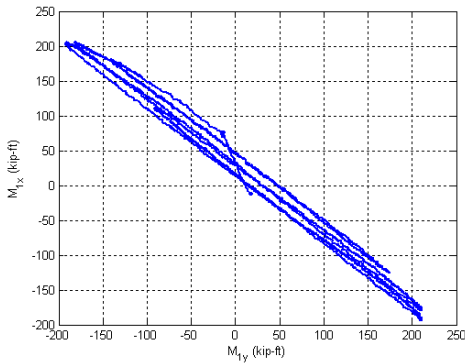
Figure B.103. Experimental results from LC3a in the specimen 14C12-26-12



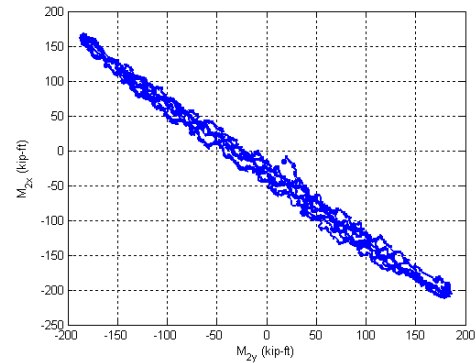
Y Displacement vs. X Displacement



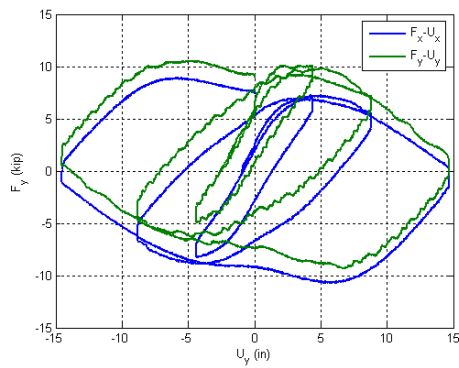
Y Force vs. X Force



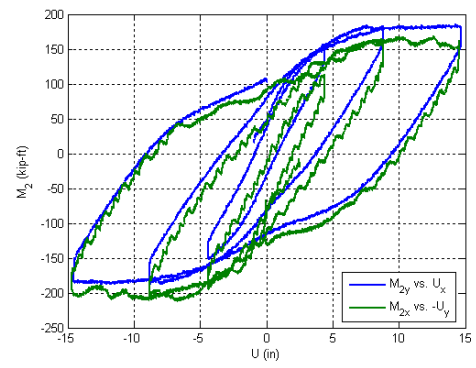
X Moment vs. Y Moment at the top



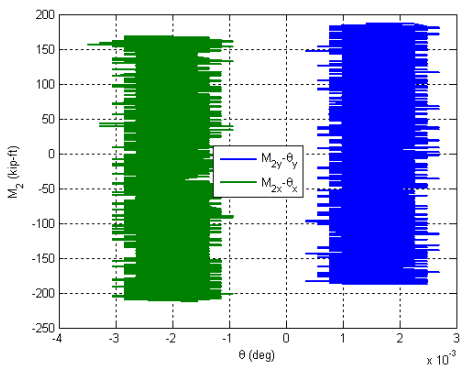
X Moment vs. Y Moment at the base



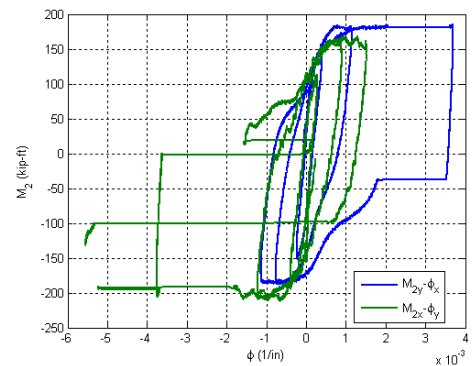
Lateral Force vs. Lateral Displacement



Base Moment vs. Top Displacement

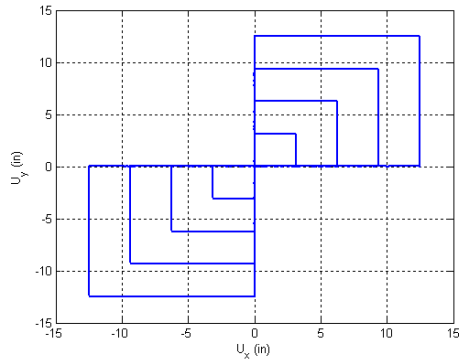


Base Moment vs. Top Rotation

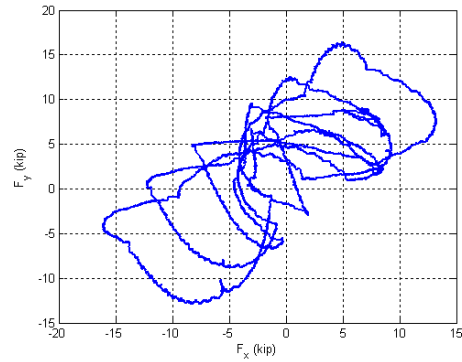


Base Moment vs. Base Curvature

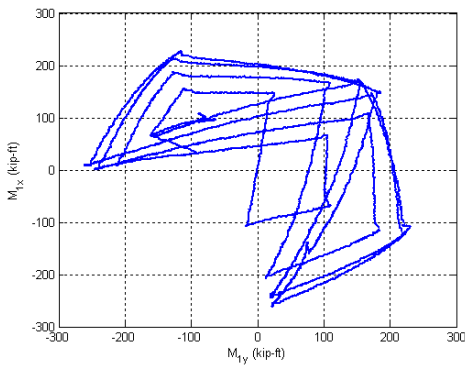
Figure B.104. Experimental results from LC2a' in the specimen 14C12-26-12



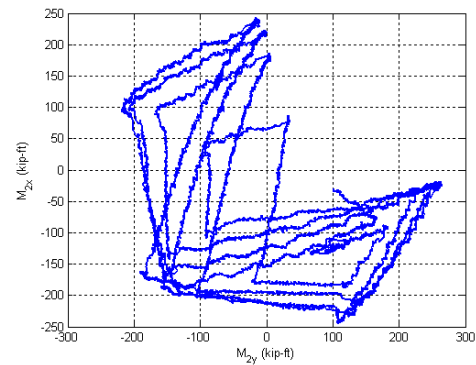
Y Displacement vs. X Displacement



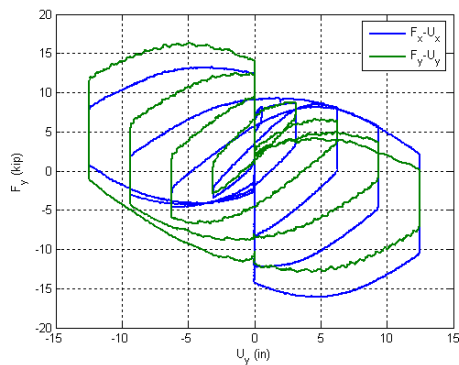
Y Force vs. X Force



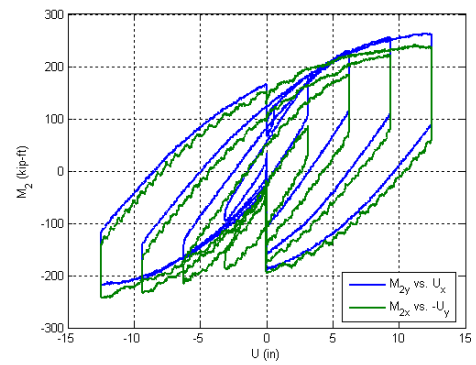
X Moment vs. Y Moment at the top



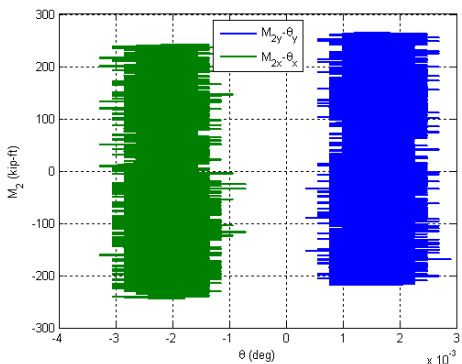
X Moment vs. Y Moment at the base



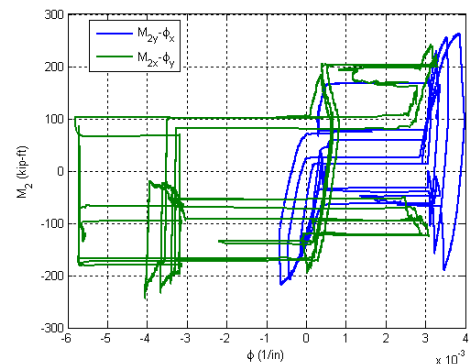
Lateral Force vs. Lateral Displacement



Base Moment vs. Top Displacement

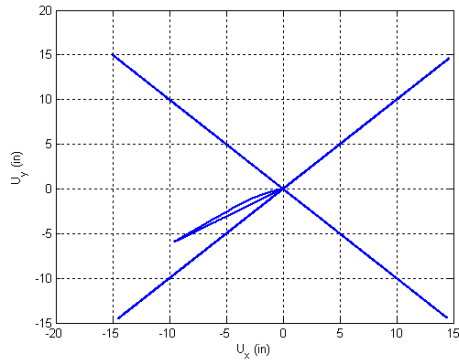


Base Moment vs. Top Rotation

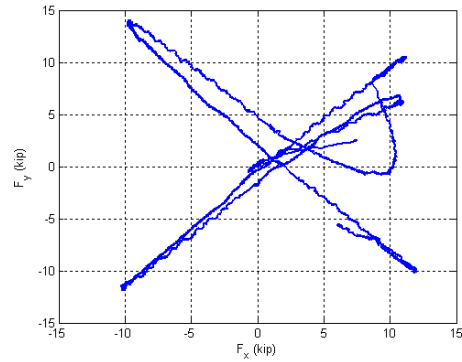


Base Moment vs. Base Curvature

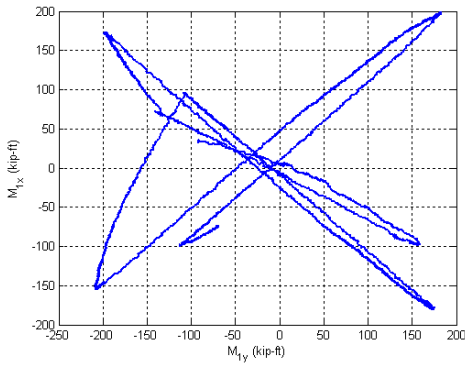
Figure B.105. Experimental results from LC3a' in the specimen 14C12-26-12



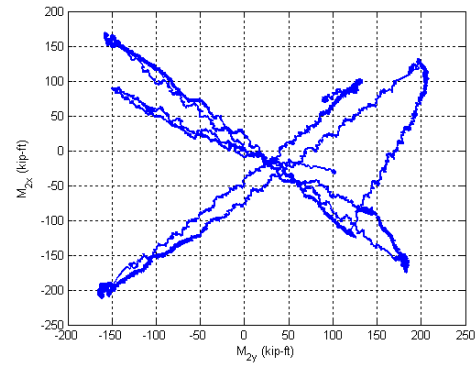
Y Displacement vs. X Displacement



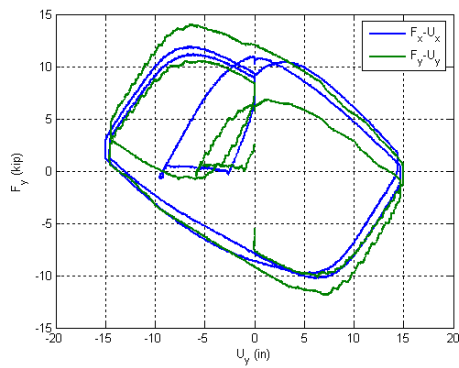
Y Force vs. X Force



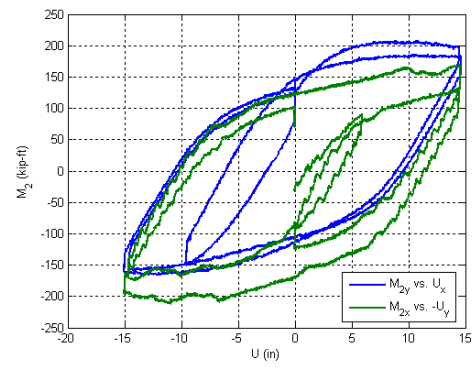
X Moment vs. Y Moment at the top



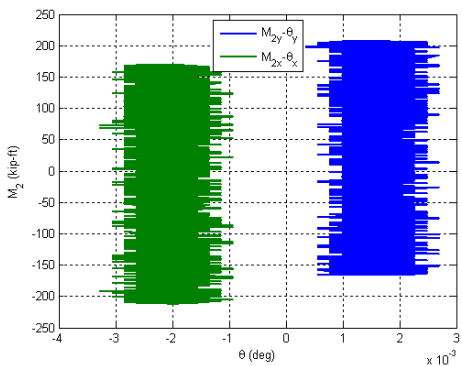
X Moment vs. Y Moment at the base



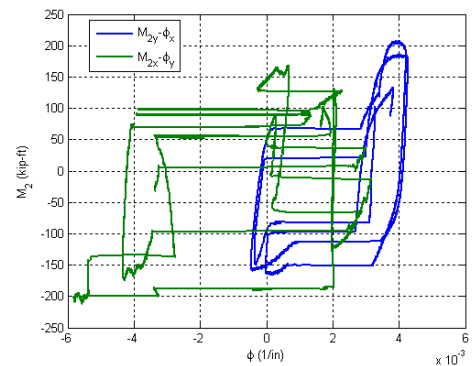
Lateral Force vs. Lateral Displacement



Base Moment vs. Top Displacement



Base Moment vs. Top Rotation



Base Moment vs. Base Curvature

Figure B.106. Experimental results from LC4 in the specimen 14C12-26-12

B.15. Specimen 15C20-26-12

Description:

- Specimen number: 15
- Composite Cross-section: CCFT
- Steel cross-section: HSS20x0.25
- Design concrete strength: 12 ksi
- Design specimen length: 26 ft
- Pouring date: 03/27/2009
- Testing date: 06/29/2009

Parameters:

- Specimen length: 26' 2"
- Initial out-of-plumbness: $U_{xo} = 0.24'' / U_{yo} = 1.62''$
- Steel yielding stress: $F_y = 42.5$ ksi
- Steel ultimate stress: $F_u = 65.8$ ksi
- Concrete strength at the 28th day: $f_c' = 11.5$ ksi
- Concrete strength at the testing day: $f_c = 11.6$ ksi
- Concrete Young's modulus: $E_c = 5800$ ksi
- Concrete tensile strength: $f_t = 0.76$ ksi

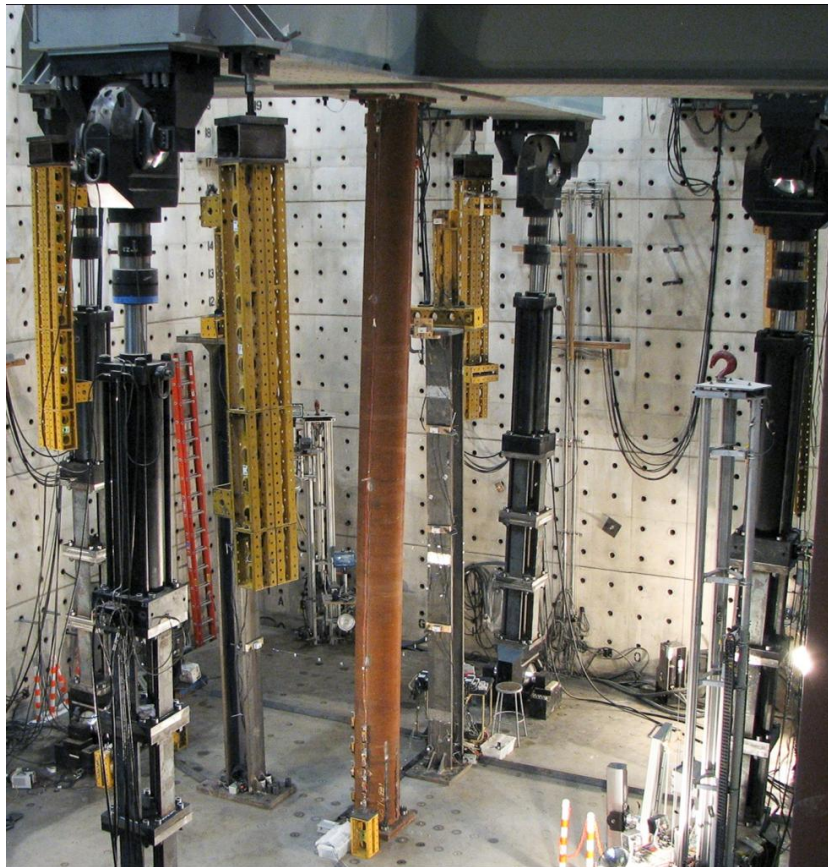


Figure B.107. Specimen 15C20-26-12

Table B.15. Load protocol summary for the specimen 15C20-26-12

LC1 - Incremental compression loading in two cycles until the maximum load is reached. The top is forced to be free at all the time.

Step	DOF						Stop Criterion
	X	Y	Z	RX	RY	RZ	
1	$F_x = 0$	$F_y = 0$	$U_z \downarrow$	$M_x = 0$	$M_y = 0$	$R_z = 0$	max P
2	$F_x = 0$	$F_y = 0$	$U_z \uparrow$	$M_x = 0$	$M_y = 0$	$R_z = 0$	P = 0
3	$F_x = 0$	$F_y = 0$	$U_z \downarrow$	$M_x = 0$	$M_y = 0$	$R_z = 0$	max P
4	$F_x = 0$	$F_y = 0$	$U_z \uparrow$	$M_x = 0$	$M_y = 0$	$R_z = 0$	P = 0

LC2a - Cyclic uniaxial lateral displacements with constant compression force ($-F_z = P = 400$ kips). The top was forced to have zero moments.

Step	DOF						Stop Criterion
	X	Y	Z	RX	RY	RZ	
1	$U_x \uparrow$	$U_y \downarrow$	P = 400k	$M_x = 0$	$M_y = 0$	$R_z = 0$	+/-1% drift
2	$U_x \downarrow$	$U_y \uparrow$	P = 400k	$M_x = 0$	$M_y = 0$	$R_z = 0$	+/-2% drift
3	$U_x \uparrow$	$U_y \downarrow$	P = 400k	$M_x = 0$	$M_y = 0$	$R_z = 0$	+/-3% drift
4	$U_x \downarrow$	$U_y \uparrow$	P = 400k	$M_x = 0$	$M_y = 0$	$R_z = 0$	+/-4% drift
5	$U_x \uparrow$	$U_y \downarrow$	P = 400k	$M_x = 0$	$M_y = 0$	$R_z = 0$	+/-5% drift
6	$U_x \downarrow$	$U_y \uparrow$	P = 400k	$M_x = 0$	$M_y = 0$	$R_z = 0$	+/-6% drift
7	$U_x \downarrow$	$U_y \uparrow$	P = 400k	$M_x = 0$	$M_y = 0$	$R_z = 0$	$U_z = 0$

LC2b - Cyclic uniaxial lateral displacements with constant compression force ($-F_z = P = 800$ kips). The top was forced to have zero moments.

Step	DOF						Stop Criterion
	X	Y	Z	RX	RY	RZ	
1	$U_x \uparrow$	$U_y \downarrow$	P = 800k	$M_x = 0$	$M_y = 0$	$R_z = 0$	+/-1% drift
2	$U_x \downarrow$	$U_y \uparrow$	P = 800k	$M_x = 0$	$M_y = 0$	$R_z = 0$	+/-2% drift
3	$U_x \uparrow$	$U_y \downarrow$	P = 800k	$M_x = 0$	$M_y = 0$	$R_z = 0$	+/-3% drift
4	$U_x \downarrow$	$U_y \uparrow$	P = 800k	$M_x = 0$	$M_y = 0$	$R_z = 0$	+/-4% drift
5	$U_x \downarrow$	$U_y \uparrow$	P = 800k	$M_x = 0$	$M_y = 0$	$R_z = 0$	$U_z = 0$

LC3a - Cyclic biaxial lateral displacements (8 shape) with constant compression force ($-F_z = P = 200$ kips). The top was forced to have zero moments.

Step	DOF						Stop Criterion
	X	Y	Z	RX	RY	RZ	
1	$U_x \uparrow$	$U_y \uparrow$	P = 200k	$M_x = 0$	$M_y = 0$	$R_z = 0$	+/-1% drift
2	$U_x \uparrow$	$U_y \uparrow$	P = 200k	$M_x = 0$	$M_y = 0$	$R_z = 0$	+/-2% drift
3	$U_x \uparrow$	$U_y \uparrow$	P = 200k	$M_x = 0$	$M_y = 0$	$R_z = 0$	+/-3% drift
4	$U_x \uparrow$	$U_y \uparrow$	P = 200k	$M_x = 0$	$M_y = 0$	$R_z = 0$	+/-4% drift

LC3b - Cyclic biaxial lateral displacements (8 shape) with constant compression force ($-F_z = P = 600$ kips). The top was forced to have fixed rotations.

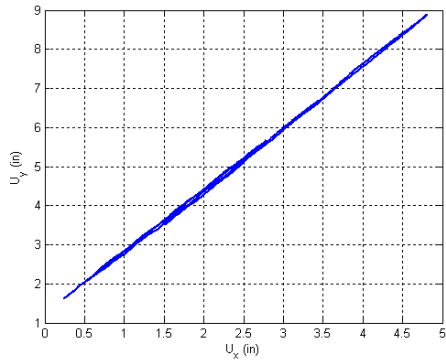
Step	DOF						Stop Criterion
	X	Y	Z	RX	RY	RZ	
1	$U_x \uparrow$	$U_y \uparrow$	$P = 600k$	$R_x = 0$	$R_y = 0$	$R_z = 0$	+/-1% drift
2	$U_x \downarrow$	$U_y \downarrow$	$P = 600k$	$R_x = 0$	$R_y = 0$	$R_z = 0$	+/-2% drift
3	$U_x \uparrow$	$U_y \uparrow$	$P = 600k$	$R_x = 0$	$R_y = 0$	$R_z = 0$	+/-3% drift
4	$U_x \downarrow$	$U_y \downarrow$	$P = 600k$	$R_x = 0$	$R_y = 0$	$R_z = 0$	+/-4% drift

LC4a - Incremental compression loading until the maximum load is reached. The top is forced to be free at all the time.

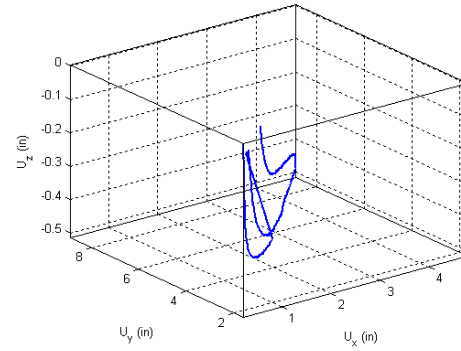
Step	DOF						Stop Criterion
	X	Y	Z	RX	RY	RZ	
1	$F_x = 0$	$F_y = 0$	$U_z \downarrow$	$R_x = 0$	$R_y = 0$	$R_z = 0$	max P
2	$F_x = 0$	$F_y = 0$	$U_z \uparrow$	$R_x = 0$	$R_y = 0$	$R_z = 0$	$P = 500k$

LC4b - Cyclic uniaxial lateral displacements (4 corners) with constant compression force ($-F_z = P = 300$ kips). The top is forced to be free at all the time.

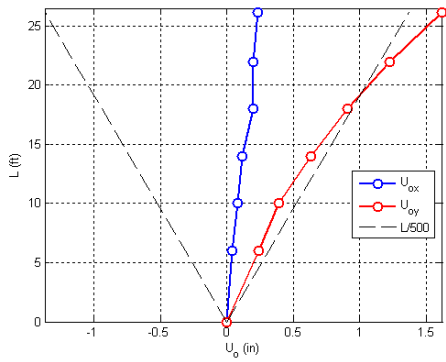
Step	DOF						Stop Criterion
	X	Y	Z	RX	RY	RZ	
1	$U_x \uparrow$	$U_y \uparrow$	$P = 500k$	$R_x = 0$	$R_y = 0$	$R_z = 0$	max stroke
2	$U_x \downarrow$	$U_y \downarrow$	$P = 500k$	$R_x = 0$	$R_y = 0$	$R_z = 0$	max stroke
3	$U_x \rightarrow 0$	$U_y \rightarrow 0$	$P = 500k$	$R_x = 0$	$R_y = 0$	$R_z = 0$	$U_x=U_y=0$
4	$U_x \uparrow$	$U_y \downarrow$	$P = 500k$	$R_x = 0$	$R_y = 0$	$R_z = 0$	max stroke
5	$U_x \downarrow$	$U_y \uparrow$	$P = 500k$	$R_x = 0$	$R_y = 0$	$R_z = 0$	max stroke
6	$U_x \rightarrow 0$	$U_y \rightarrow 0$	$P = 500k$	$R_x = 0$	$R_y = 0$	$R_z = 0$	$U_x=U_y=0$



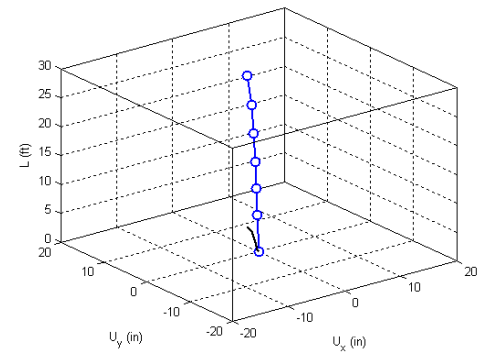
Y displacement vs. X displacement



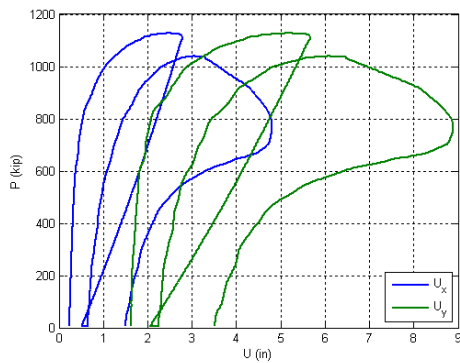
Z displacement vs. X and Y displacement



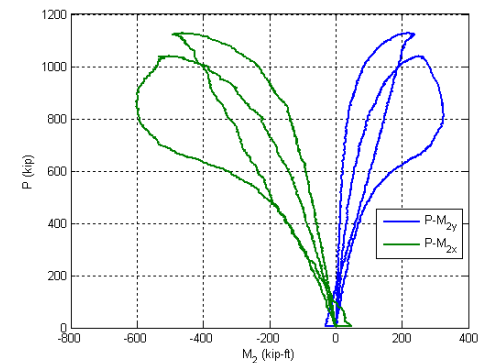
Initial deflected shape



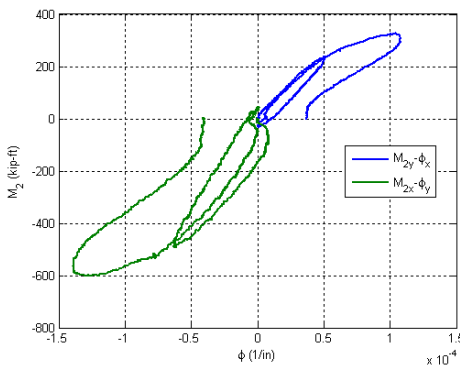
Maximum lateral displacement



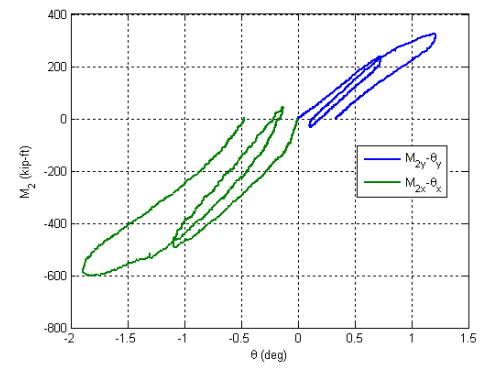
Axial force vs. lateral displacement



Axial force vs. base moments

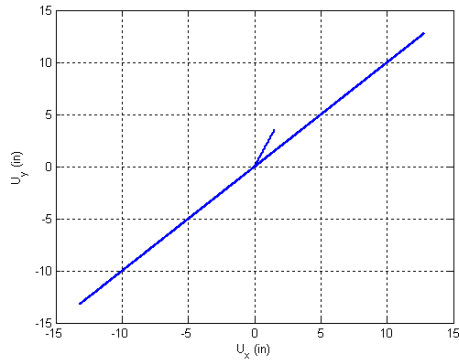


Base moment vs. base curvature

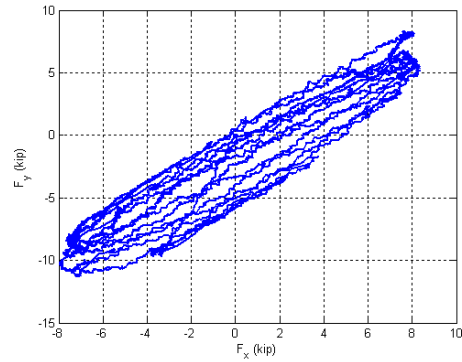


Base moment vs. top rotation

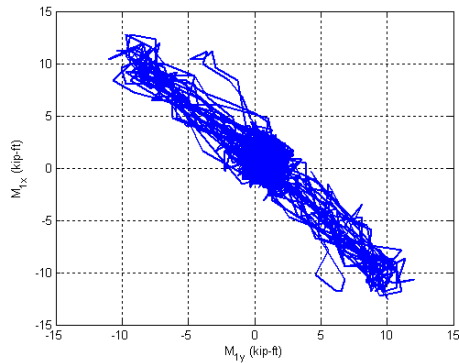
Figure B.108. Experimental results from LC1 in the specimen 15C20-26-12



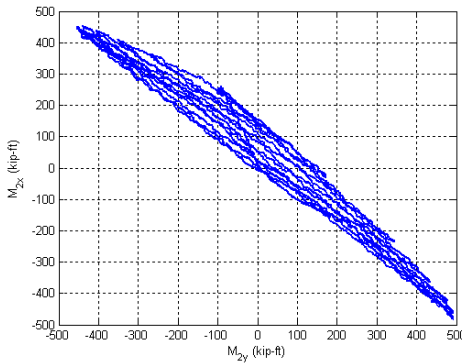
Y Displacement vs. X Displacement



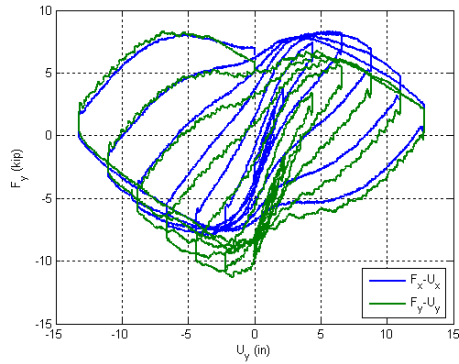
Y Force vs. X Force



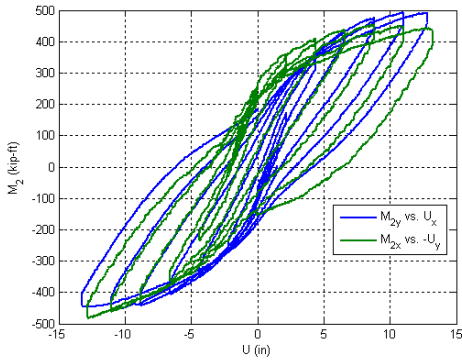
X Moment vs. Y Moment at the top



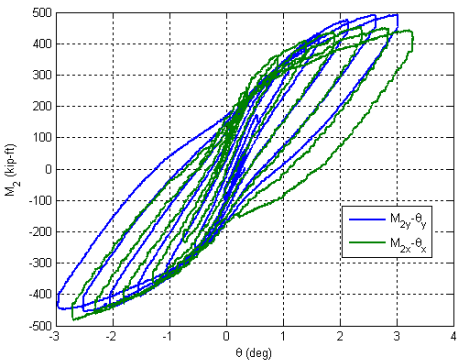
X Moment vs. Y Moment at the base



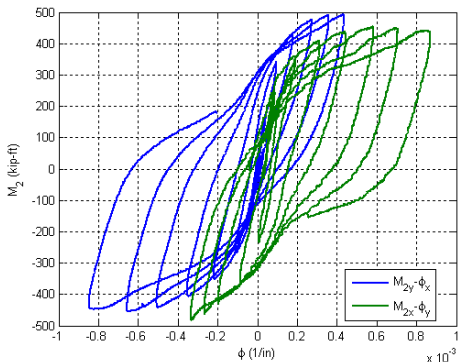
Lateral Force vs. Lateral Displacement



Base Moment vs. Top Displacement

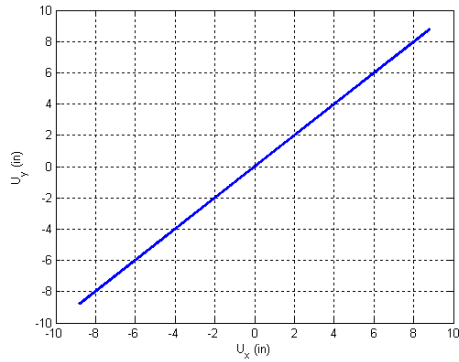


Base Moment vs. Top Rotation

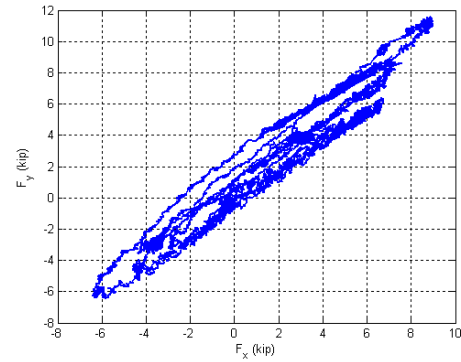


Base Moment vs. Base Curvature

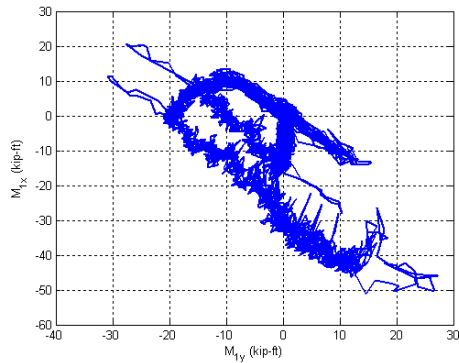
Figure B.109. Experimental results from LC2a in the specimen 15C20-26-12



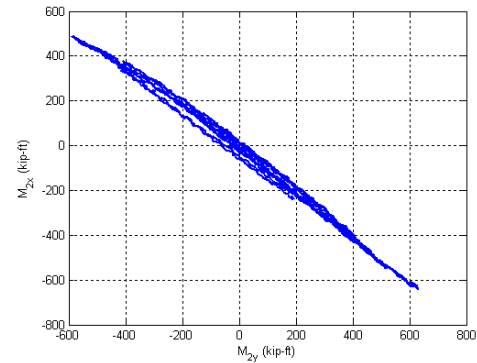
Y Displacement vs. X Displacement



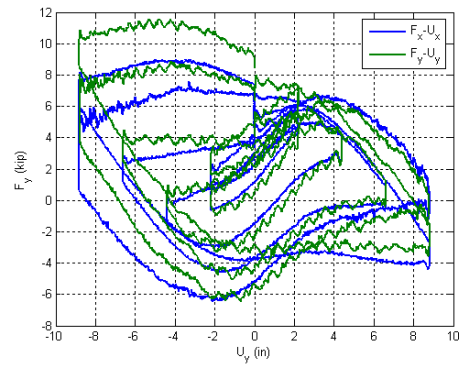
Y Force vs. X Force



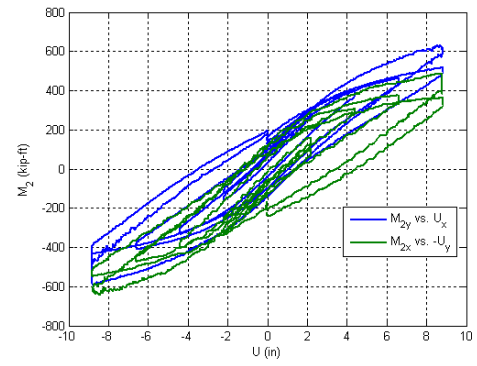
X Moment vs. Y Moment at the top



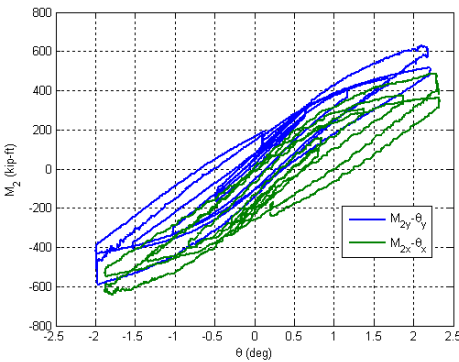
X Moment vs. Y Moment at the base



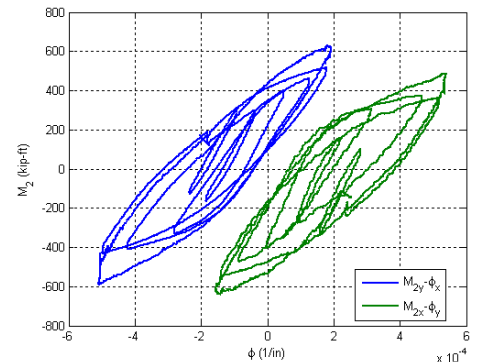
Lateral Force vs. Lateral Displacement



Base Moment vs. Top Displacement

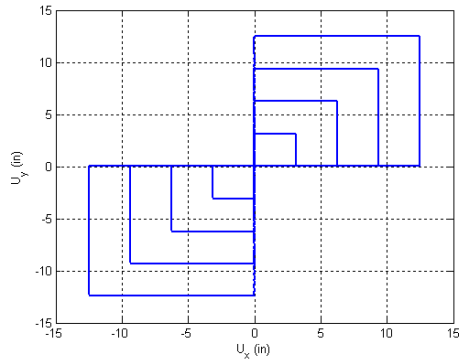


Base Moment vs. Top Rotation

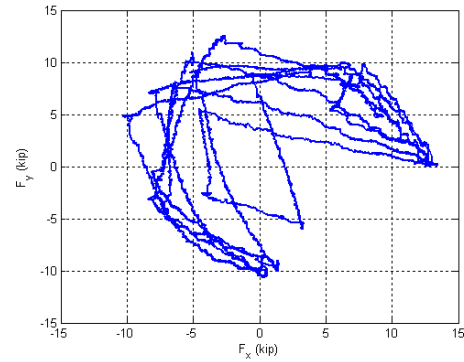


Base Moment vs. Base Curvature

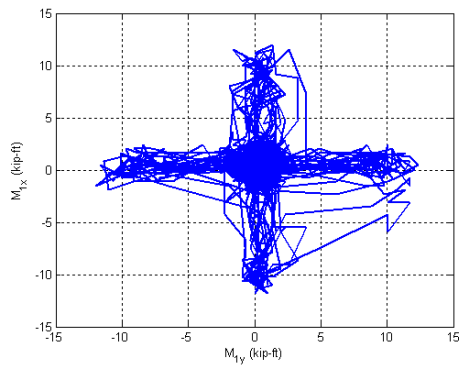
Figure B.110. Experimental results from LC2b in the specimen 15C20-26-12



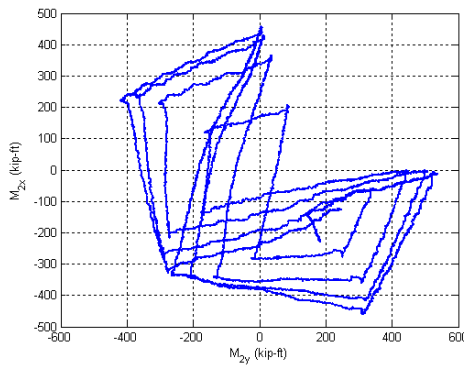
Y Displacement vs. X Displacement



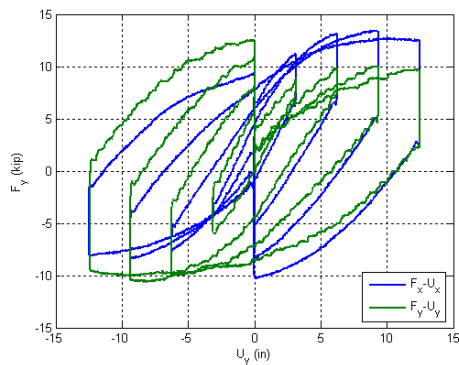
Y Force vs. X Force



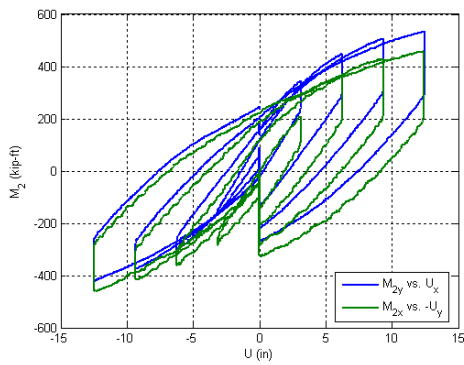
X Moment vs. Y Moment at the top



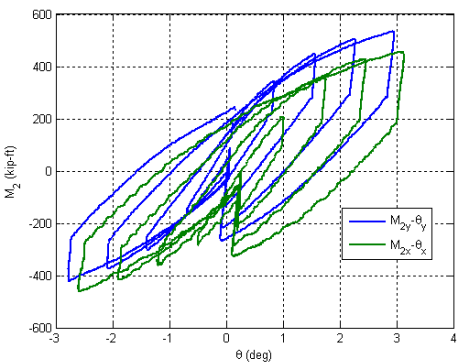
X Moment vs. Y Moment at the base



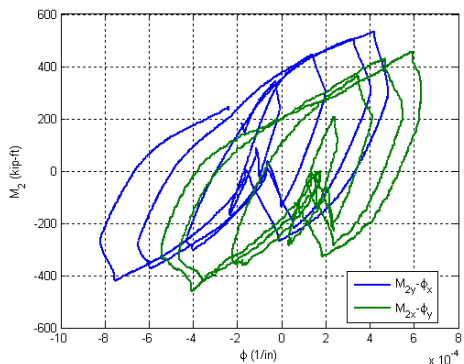
Lateral Force vs. Lateral Displacement



Base Moment vs. Top Displacement

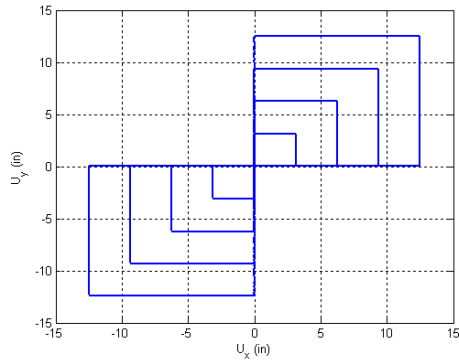


Base Moment vs. Top Rotation

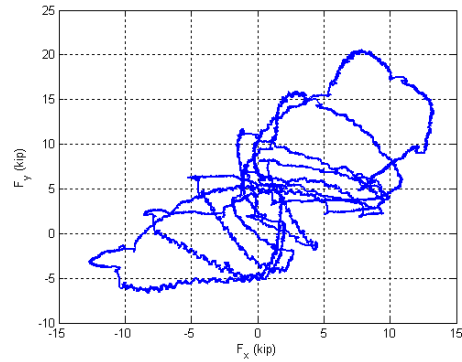


Base Moment vs. Base Curvature

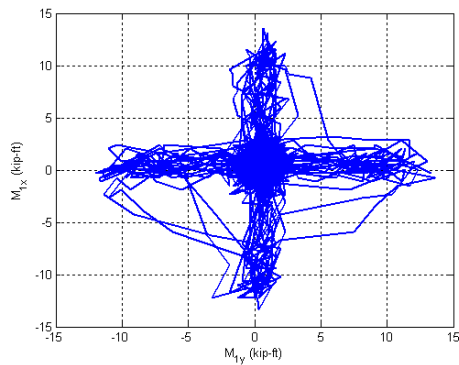
Figure B.111. Experimental results from LC3a in the specimen 15C20-26-12



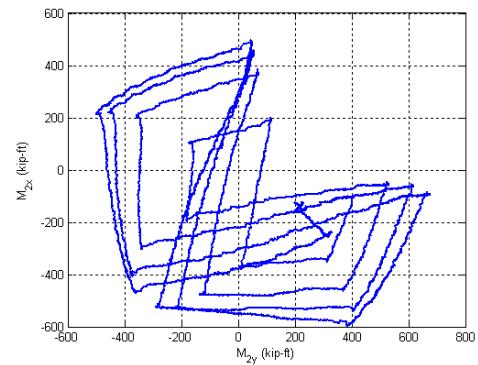
Y Displacement vs. X Displacement



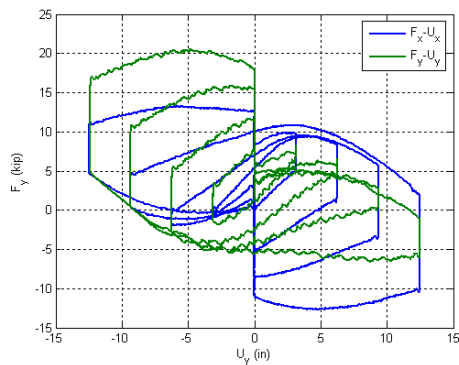
Y Force vs. X Force



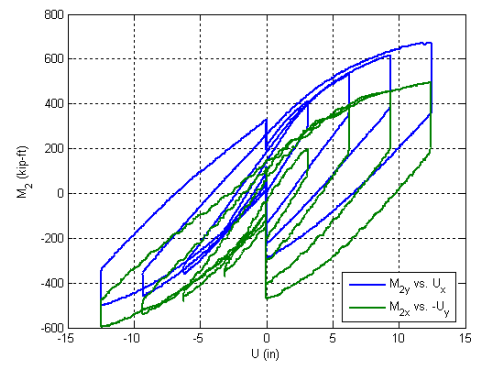
X Moment vs. Y Moment at the top



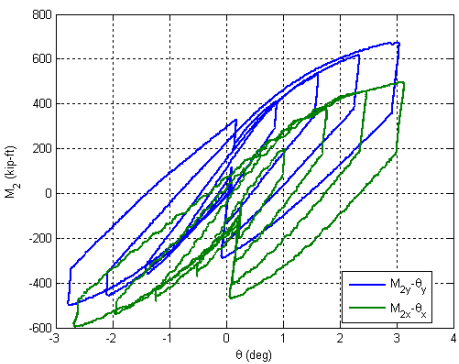
X Moment vs. Y Moment at the base



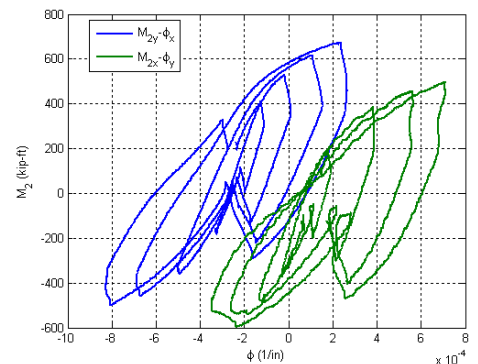
Lateral Force vs. Lateral Displacement



Base Moment vs. Top Displacement

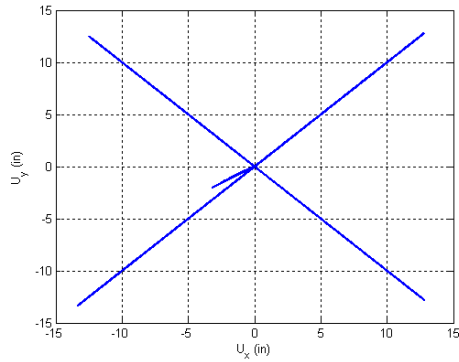


Base Moment vs. Top Rotation

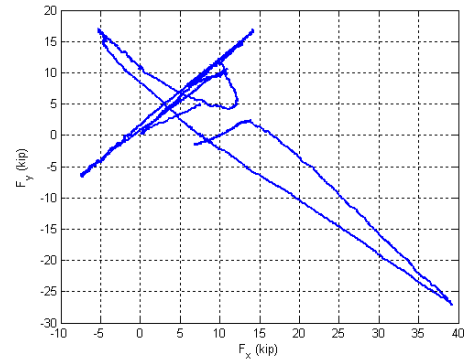


Base Moment vs. Base Curvature

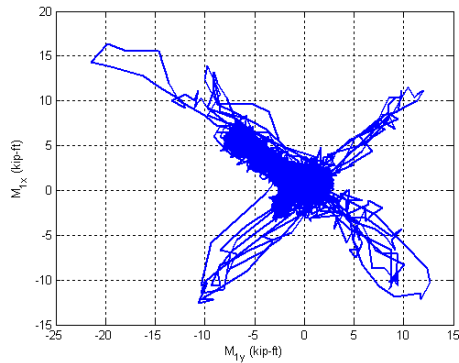
Figure B.112. Experimental results from LC3b in the specimen 15C20-26-12



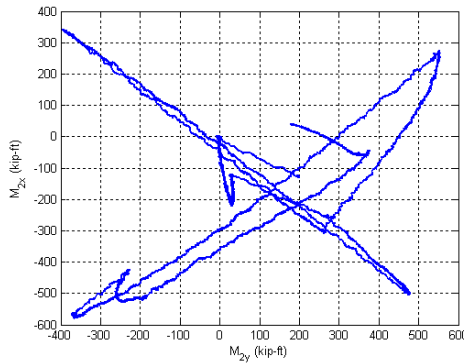
Y Displacement vs. X Displacement



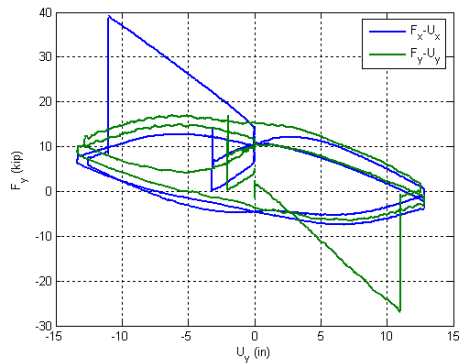
Y Force vs. X Force



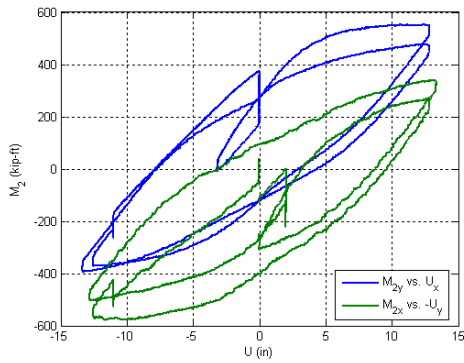
X Moment vs. Y Moment at the top



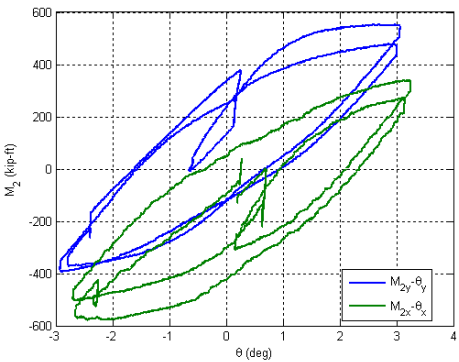
X Moment vs. Y Moment at the base



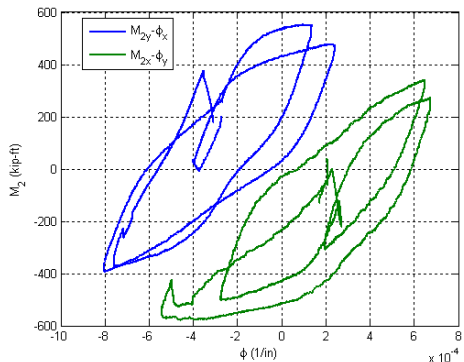
Lateral Force vs. Lateral Displacement



Base Moment vs. Top Displacement



Base Moment vs. Top Rotation



Base Moment vs. Base Curvature

Figure B.113. Experimental results from LC4 in the specimen 15C20-26-12

B.16. Specimen 16Rw-26-12

Description:

- Specimen number: 16
- Composite Cross-section: RCFT
- Steel cross-section: HSS20x12x0.25
- Design concrete strength: 12 ksi
- Design specimen length: 26 ft
- Pouring date: 03/27/2009
- Testing date: 07/07/2009

Parameters:

- Specimen length: 26' 1 1/4"
- Initial out-of-plumbness: $U_{xo} = -0.58'' / U_{yo} = 0.00''$
- Steel yielding stress: $F_y = 55.2$ ksi
- Steel ultimate stress: $F_u = 73.4$ ksi
- Concrete strength at the 28th day: $f_c' = 11.5$ ksi
- Concrete strength at the testing day: $f_c = 11.7$ ksi
- Concrete Young's modulus: $E_c = 5800$ ksi
- Concrete tensile strength: $f_t = 0.76$ ksi

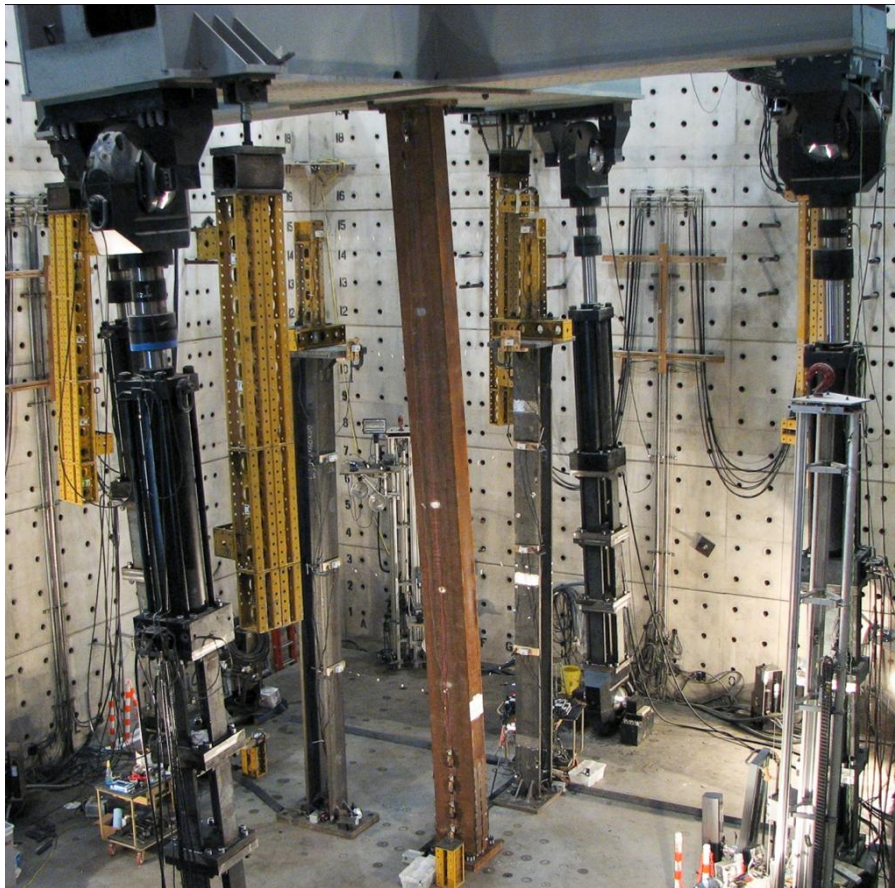


Figure B.114. Specimen 16Rw-26-12

Table B.16. Load protocol summary for the specimen 16Rw-26-12

LC1 - Incremental compression loading in three cycles until the maximum load is reached. The top is forced to be free at X ($K_x=2$) and fixed at Y ($K_y=0.5$).

Step	DOF						Stop Criterion
	X	Y	Z	RX	RY	RZ	
1	$F_x = 0$	$U_y = 0$	$U_z \downarrow$	$R_x = 0$	$M_y = 0$	$R_z = 0$	max P
2	$F_x = 0$	$U_y = 0$	$U_z \uparrow$	$R_x = 0$	$M_y = 0$	$R_z = 0$	P = 0
3	$F_x = 0$	$U_y = 0$	$U_z \downarrow$	$R_x = 0$	$M_y = 0$	$R_z = 0$	max P
4	$F_x = 0$	$U_y = 0$	$U_z \uparrow$	$R_x = 0$	$M_y = 0$	$R_z = 0$	P = 0
5	$F_x = 0$	$U_y = 0$	$U_z \downarrow$	$R_x = 0$	$M_y = 0$	$R_z = 0$	max P
6	$F_x = 0$	$U_y = 0$	$U_z \uparrow$	$R_x = 0$	$M_y = 0$	$R_z = 0$	P = 0

LC2a - Cyclic uniaxial lateral displacements with constant compression force ($-F_z = P = 200$ kips). The top was forced to have zero moments in Y and fixed rotation in X.

Step	DOF						Stop Criterion
	X	Y	Z	RX	RY	RZ	
1	$U_x \uparrow$	$U_y = 0$	P = 200k	$R_x = 0$	$M_y = 0$	$R_z = 0$	+1% drift
2	$U_x \downarrow$	$U_y = 0$	P = 200k	$R_x = 0$	$M_y = 0$	$R_z = 0$	-1% drift
3	$U_x \uparrow$	$U_y = 0$	P = 200k	$R_x = 0$	$M_y = 0$	$R_z = 0$	+2% drift
4	$U_x \downarrow$	$U_y = 0$	P = 200k	$R_x = 0$	$M_y = 0$	$R_z = 0$	-2% drift
5	$U_x \uparrow$	$U_y = 0$	P = 200k	$R_x = 0$	$M_y = 0$	$R_z = 0$	+3% drift
6	$U_x \downarrow$	$U_y = 0$	P = 200k	$R_x = 0$	$M_y = 0$	$R_z = 0$	-3% drift
7	$U_x \uparrow$	$U_y = 0$	P = 200k	$R_x = 0$	$M_y = 0$	$R_z = 0$	+4% drift
8	$U_x \downarrow$	$U_y = 0$	P = 200k	$R_x = 0$	$M_y = 0$	$R_z = 0$	-4% drift
9	$U_x \uparrow$	$U_y = 0$	P = 200k	$R_x = 0$	$M_y = 0$	$R_z = 0$	+5% drift
10	$U_x \downarrow$	$U_y = 0$	P = 200k	$R_x = 0$	$M_y = 0$	$R_z = 0$	-5% drift
11	$U_x \downarrow$	$U_y = 0$	P = 200k	$R_x = 0$	$M_y = 0$	$R_z = 0$	$U_z = 0$

LC2b - Cyclic uniaxial lateral displacements with constant compression force ($-F_z = P = 400$ kips). The top was forced to have zero moments in Y and fixed rotation in X.

Step	DOF						Stop Criterion
	X	Y	Z	RX	RY	RZ	
1	$U_x \uparrow$	$U_y = 0$	P = 400k	$R_x = 0$	$M_y = 0$	$R_z = 0$	+1% drift
2	$U_x \downarrow$	$U_y = 0$	P = 400k	$R_x = 0$	$M_y = 0$	$R_z = 0$	-1% drift
3	$U_x \uparrow$	$U_y = 0$	P = 400k	$R_x = 0$	$M_y = 0$	$R_z = 0$	+2% drift
4	$U_x \downarrow$	$U_y = 0$	P = 400k	$R_x = 0$	$M_y = 0$	$R_z = 0$	-2% drift
5	$U_x \uparrow$	$U_y = 0$	P = 400k	$R_x = 0$	$M_y = 0$	$R_z = 0$	+3% drift
6	$U_x \downarrow$	$U_y = 0$	P = 400k	$R_x = 0$	$M_y = 0$	$R_z = 0$	-3% drift
7	$U_x \uparrow$	$U_y = 0$	P = 400k	$R_x = 0$	$M_y = 0$	$R_z = 0$	+4% drift
8	$U_x \downarrow$	$U_y = 0$	P = 400k	$R_x = 0$	$M_y = 0$	$R_z = 0$	-4% drift
9	$U_x \uparrow$	$U_y = 0$	P = 400k	$R_x = 0$	$M_y = 0$	$R_z = 0$	+5% drift
10	$U_x \downarrow$	$U_y = 0$	P = 400k	$R_x = 0$	$M_y = 0$	$R_z = 0$	-5% drift
11	$U_x \downarrow$	$U_y = 0$	P = 400k	$R_x = 0$	$M_y = 0$	$R_z = 0$	$U_z = 0$

LC3a - Cyclic biaxial lateral displacements (8 shape) with constant compression force ($-F_z = P = 300$ kips). The top was forced to have zero moments.

Step	DOF						Stop Criterion
	X	Y	Z	RX	RY	RZ	
1	$U_x \uparrow$	$U_y \uparrow$	$P = 300k$	$M_x = 0$	$M_y = 0$	$R_z = 0$	+/-1% drift
2	$U_x \downarrow$	$U_y \downarrow$	$P = 300k$	$M_x = 0$	$M_y = 0$	$R_z = 0$	+/-2% drift
3	$U_x \uparrow$	$U_y \uparrow$	$P = 300k$	$M_x = 0$	$M_y = 0$	$R_z = 0$	+/-3% drift
4	$U_x \downarrow$	$U_y \downarrow$	$P = 300k$	$M_x = 0$	$M_y = 0$	$R_z = 0$	+/-4% drift

LC3b - Cyclic biaxial lateral displacements (8 shape) with constant compression force ($-F_z = P = 500$ kips). The top was forced to have zero moments.

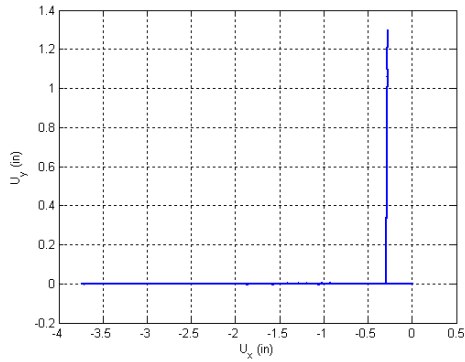
Step	DOF						Stop Criterion
	X	Y	Z	RX	RY	RZ	
1	$U_x \uparrow$	$U_y \uparrow$	$P = 500k$	$M_x = 0$	$M_y = 0$	$R_z = 0$	+/-1% drift
2	$U_x \downarrow$	$U_y \downarrow$	$P = 500k$	$M_x = 0$	$M_y = 0$	$R_z = 0$	+/-2% drift
3	$U_x \uparrow$	$U_y \uparrow$	$P = 500k$	$M_x = 0$	$M_y = 0$	$R_z = 0$	+/-3% drift
4	$U_x \downarrow$	$U_y \downarrow$	$P = 500k$	$M_x = 0$	$M_y = 0$	$R_z = 0$	+/-4% drift

LC4a - Incremental compression loading until the maximum load is reached. The top is driven with different BCs for both X and Y.

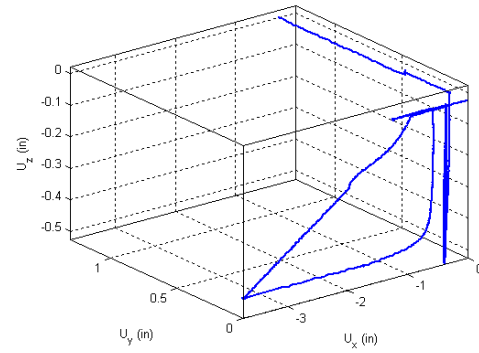
Step	DOF						Stop Criterion
	X	Y	Z	RX	RY	RZ	
1	$F_x \rightarrow 0$	$F_y \rightarrow 0$	$F_z \rightarrow 0$	$M_x = 0$	$M_y = 0$	$R_z = 0$	$F_x=F_y=0$
2	var	var	$U_z \downarrow$	var	var	$R_z = 0$	$P = P_{max}$

LC4b - Cyclic uniaxial lateral displacements (4 corners) with constant compression force ($-F_z = P = 600$ kips). The top is forced to be free at all the time.

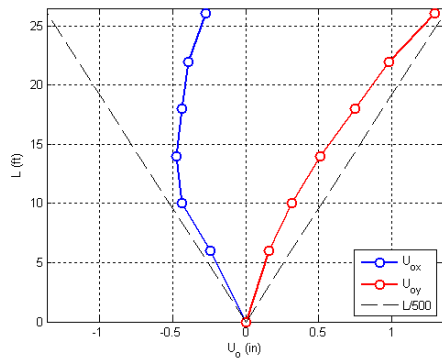
Step	DOF						Stop Criterion
	X	Y	Z	RX	RY	RZ	
1	$U_x \uparrow$	$U_y \uparrow$	$P = 600k$	$M_x = 0$	$M_y = 0$	$R_z = 0$	max stroke
2	$U_x \downarrow$	$U_y \downarrow$	$P = 600k$	$M_x = 0$	$M_y = 0$	$R_z = 0$	max stroke
3	$U_x \rightarrow 0$	$U_y \rightarrow 0$	$P = 600k$	$M_x = 0$	$M_y = 0$	$R_z = 0$	$U_x=U_y=0$
4	$U_x \uparrow$	$U_y \downarrow$	$P = 600k$	$M_x = 0$	$M_y = 0$	$R_z = 0$	max stroke
5	$U_x \downarrow$	$U_y \uparrow$	$P = 600k$	$M_x = 0$	$M_y = 0$	$R_z = 0$	max stroke
6	$U_x \rightarrow 0$	$U_y \rightarrow 0$	$P = 600k$	$M_x = 0$	$M_y = 0$	$R_z = 0$	$U_x=U_y=0$



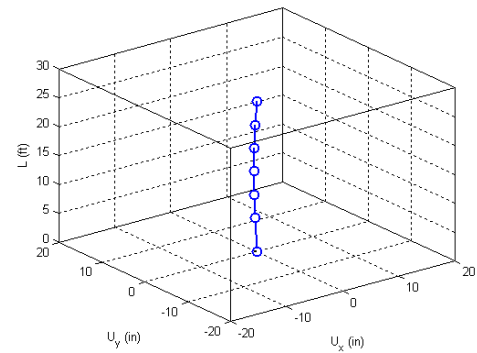
Y displacement vs. X displacement



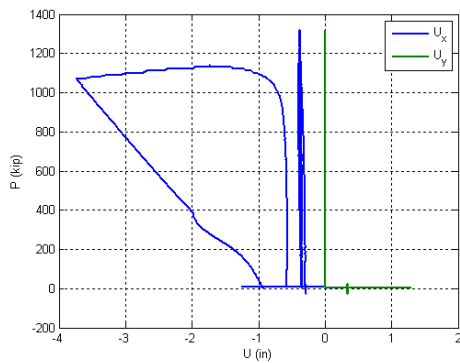
Z displacement vs. X and Y displacement



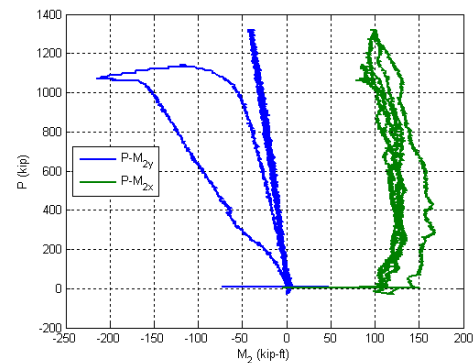
Initial deflected shape



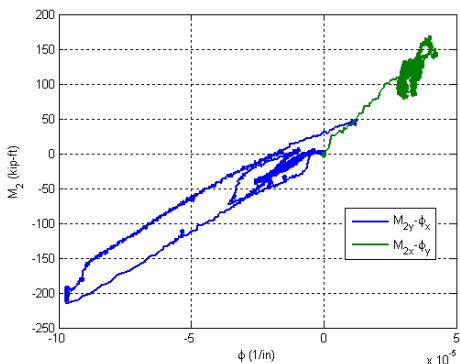
Maximum lateral displacement



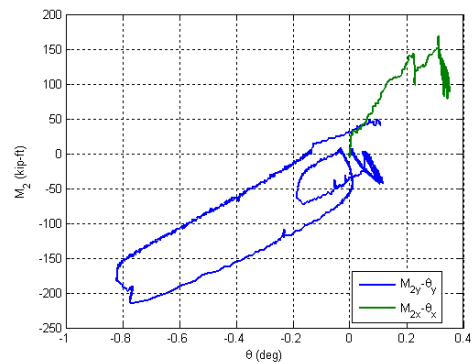
Axial force vs. lateral displacement



Axial force vs. base moments

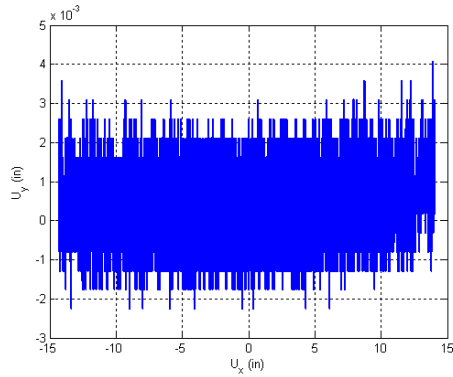


Base moment vs. base curvature

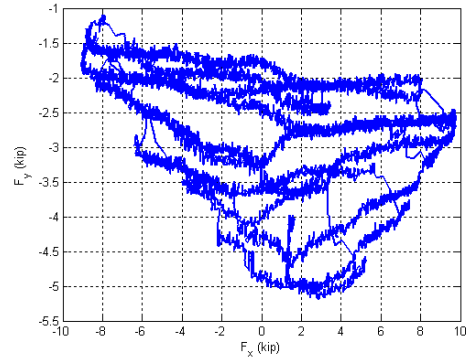


Base moment vs. top rotation

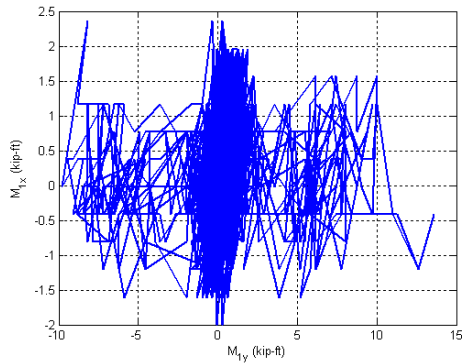
Figure B.115. Experimental results from LC1 in the specimen 16Rw-26-12



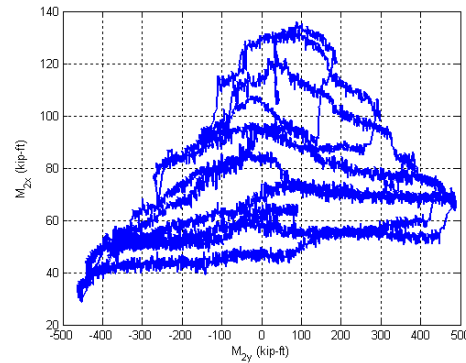
Y Displacement vs. X Displacement



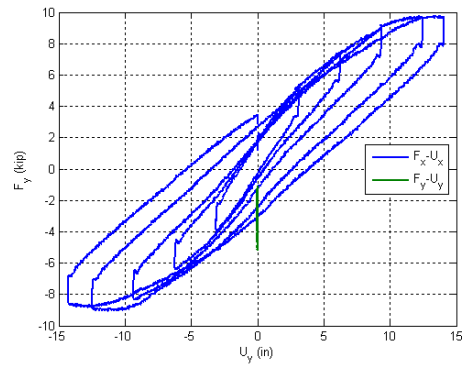
Y Force vs. X Force



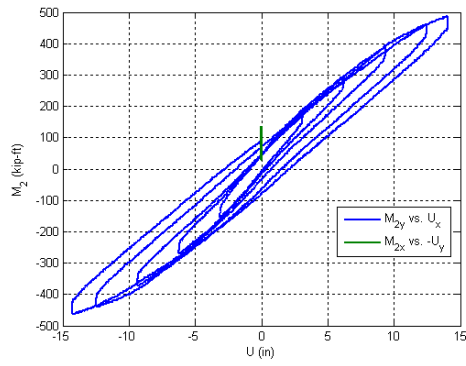
X Moment vs. Y Moment at the top



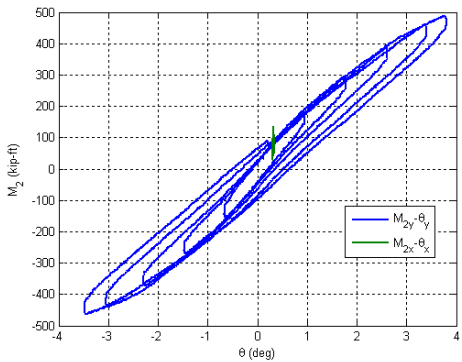
X Moment vs. Y Moment at the base



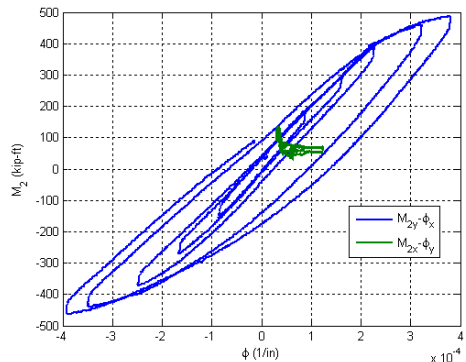
Lateral Force vs. Lateral Displacement



Base Moment vs. Top Displacement

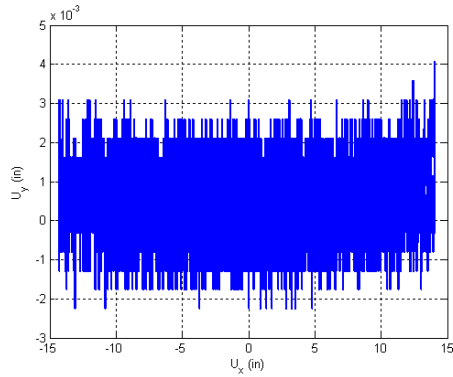


Base Moment vs. Top Rotation

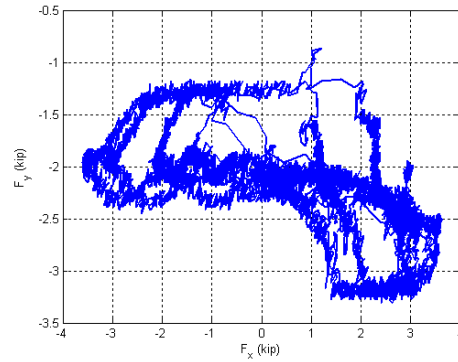


Base Moment vs. Base Curvature

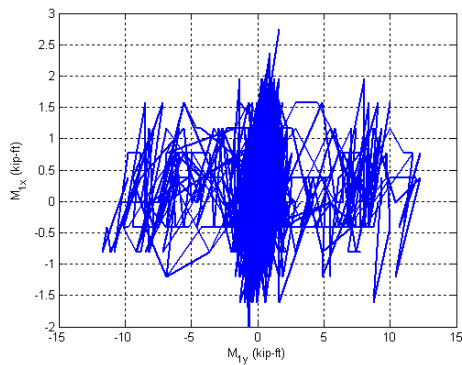
Figure B.116. Experimental results from LC2a in the specimen 16Rw-26-12



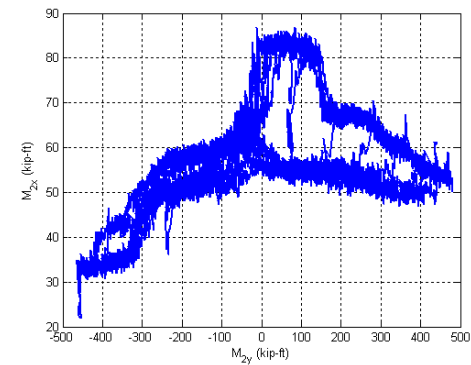
Y Displacement vs. X Displacement



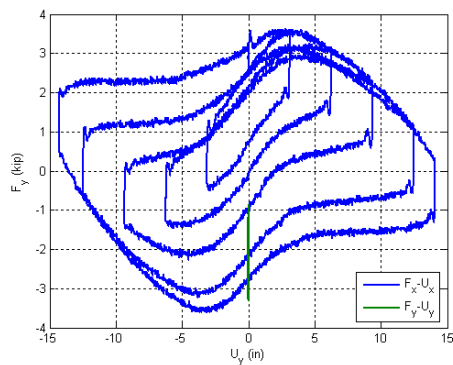
Y Force vs. X Force



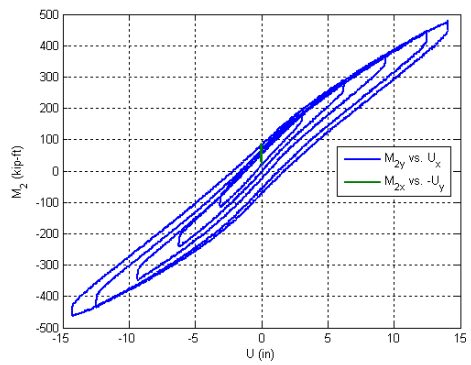
X Moment vs. Y Moment at the top



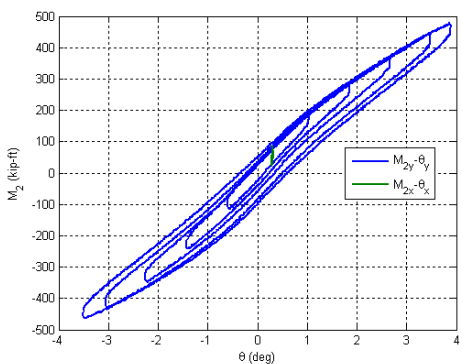
X Moment vs. Y Moment at the base



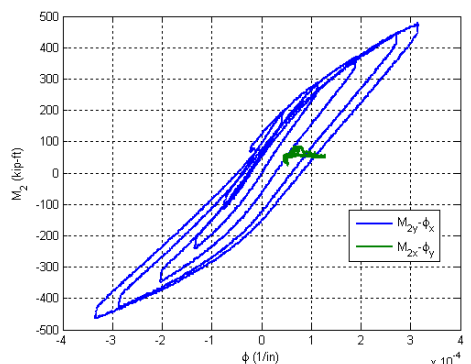
Lateral Force vs. Lateral Displacement



Base Moment vs. Top Displacement

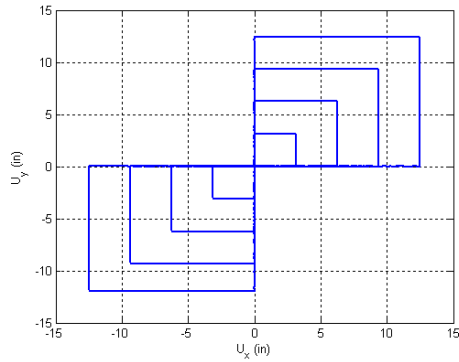


Base Moment vs. Top Rotation

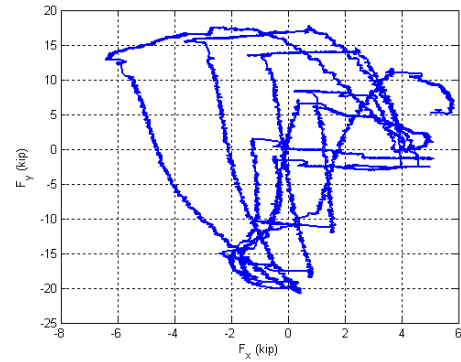


Base Moment vs. Base Curvature

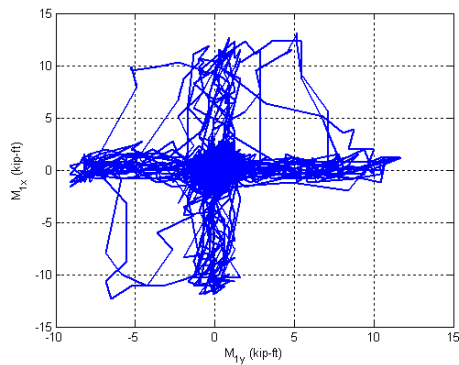
Figure B.117. Experimental results from LC2b in the specimen 16Rw-26-12



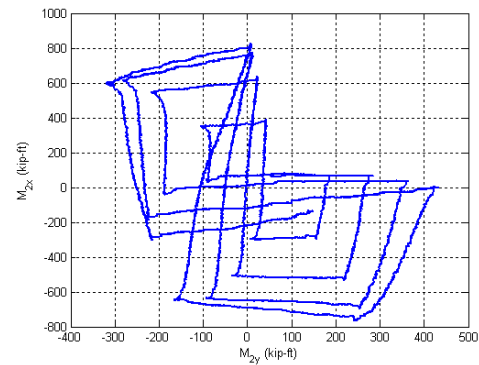
Y Displacement vs. X Displacement



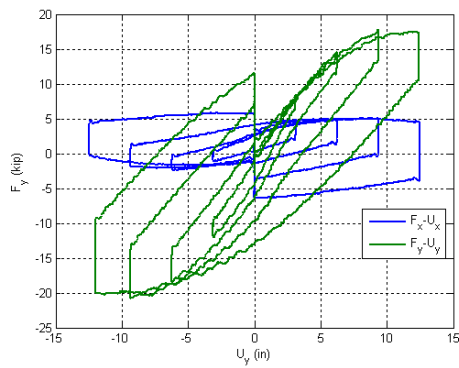
Y Force vs. X Force



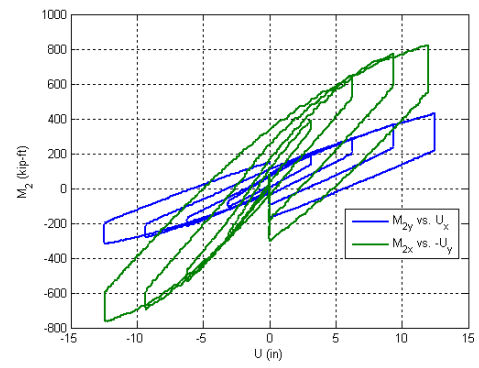
X Moment vs. Y Moment at the top



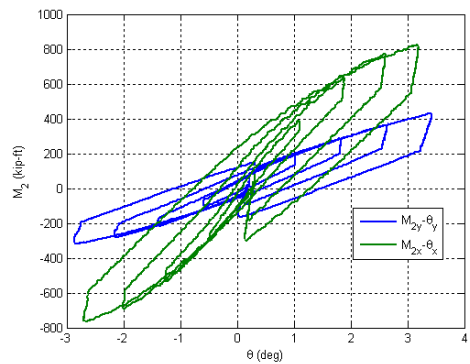
X Moment vs. Y Moment at the base



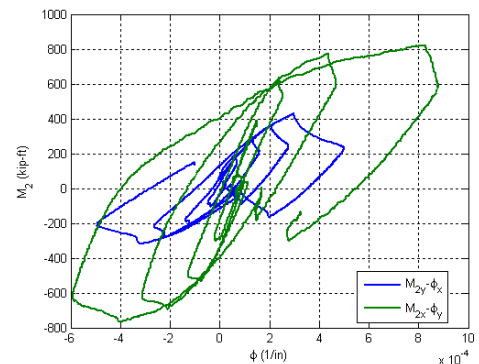
Lateral Force vs. Lateral Displacement



Base Moment vs. Top Displacement

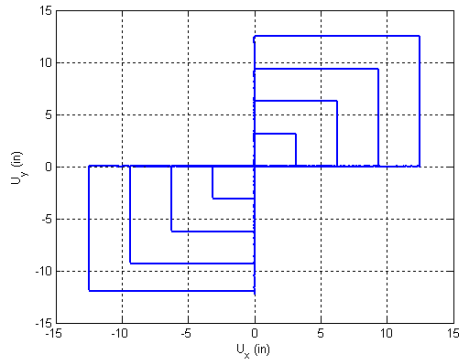


Base Moment vs. Top Rotation

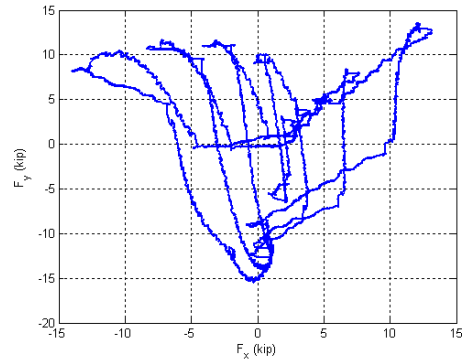


Base Moment vs. Base Curvature

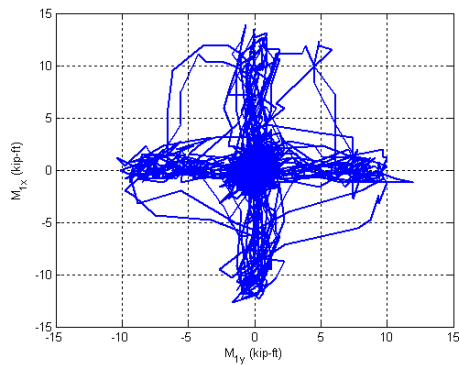
Figure B.118. Experimental results from LC3a in the specimen 16Rw-26-12



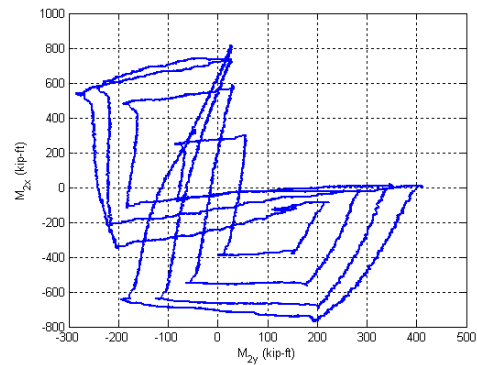
Y Displacement vs. X Displacement



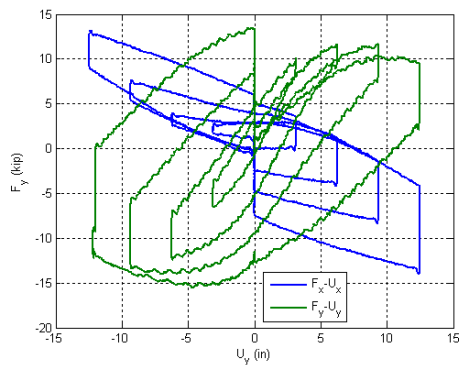
Y Force vs. X Force



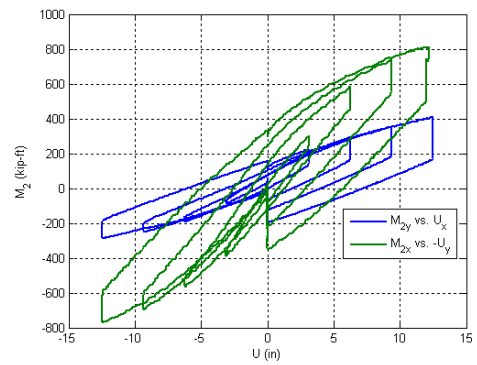
X Moment vs. Y Moment at the top



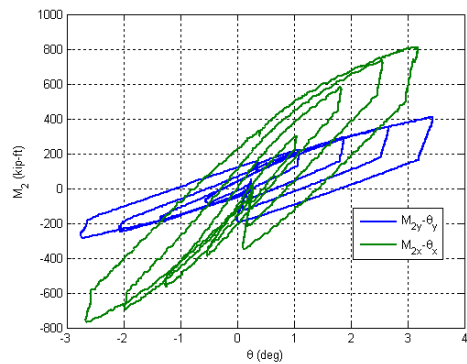
X Moment vs. Y Moment at the base



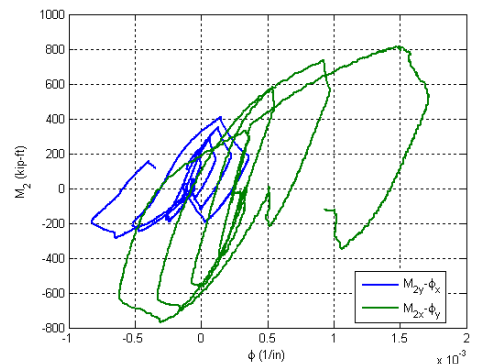
Lateral Force vs. Lateral Displacement



Base Moment vs. Top Displacement

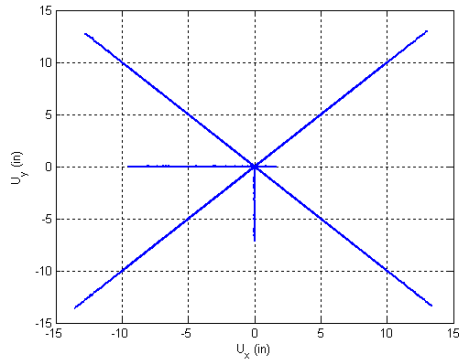


Base Moment vs. Top Rotation

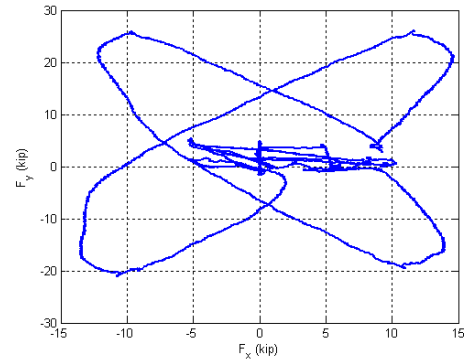


Base Moment vs. Base Curvature

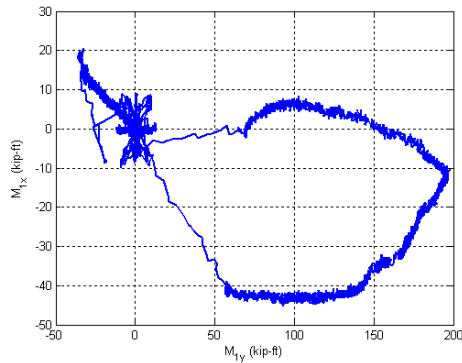
Figure B.119. Experimental results from LC3b in the specimen 16Rw-26-12



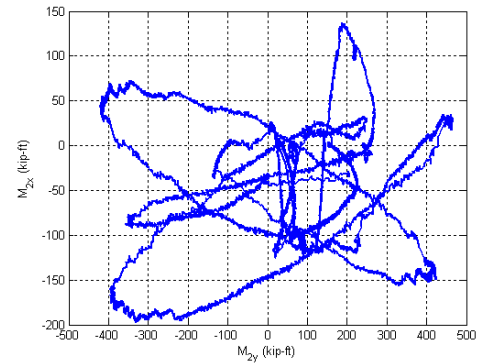
Y Displacement vs. X Displacement



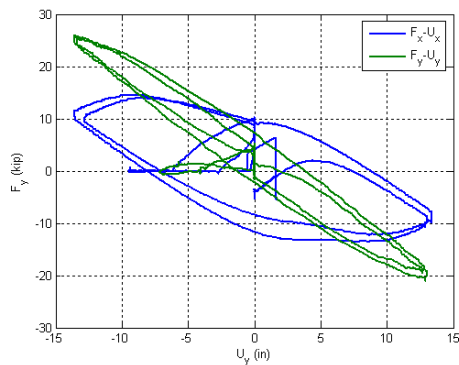
Y Force vs. X Force



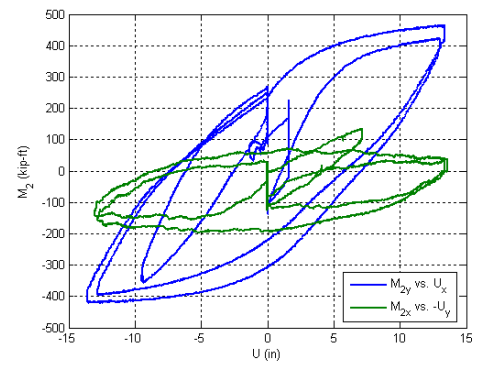
X Moment vs. Y Moment at the top



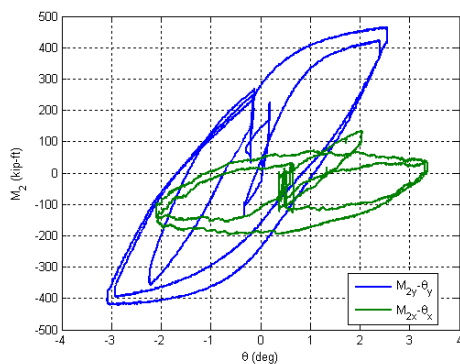
X Moment vs. Y Moment at the base



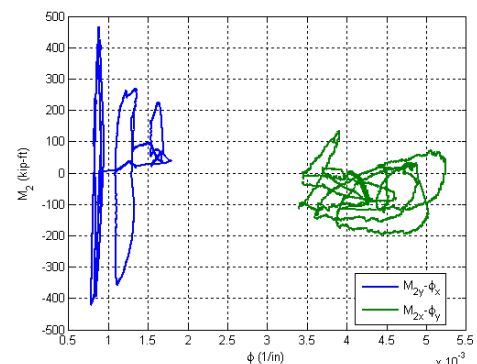
Lateral Force vs. Lateral Displacement



Base Moment vs. Top Displacement



Base Moment vs. Top Rotation



Base Moment vs. Base Curvature

Figure B.120. Experimental results from LC4 in the specimen 16Rw-26-12

B.17. Specimen 17Rs-26-12

Description:

- Specimen number: 17
- Composite Cross-section: RCFT
- Steel cross-section: HSS20x12x0.25
- Design concrete strength: 12 ksi
- Design specimen length: 26 ft
- Pouring date: 03/27/2009
- Testing date: 07/16/2009

Parameters:

- Specimen length: 26' 1 1/2"
- Initial out-of-plumbness: $U_{xo} = 1.64'' / U_{yo} = 2.22''$
- Steel yielding stress: $F_y = 55.1$ ksi
- Steel ultimate stress: $F_u = 71.9$ ksi
- Concrete strength at the 28th day: $f_c' = 11.5$ ksi
- Concrete strength at the testing day: $f_c = 11.7$ ksi
- Concrete Young's modulus: $E_c = 5800$ ksi
- Concrete tensile strength: $f_t = 0.76$ ksi

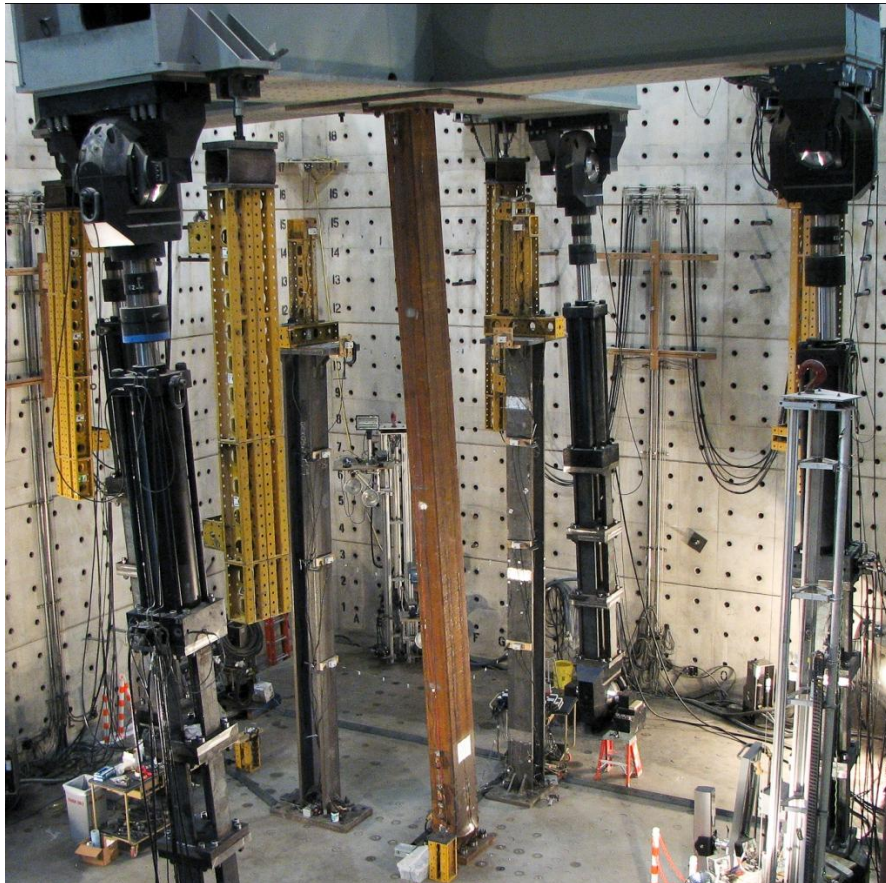


Figure B.121. Specimen 17Rs-26-12

Table B.17. Load protocol summary for the specimen 17Rs-26-12

LC1 - Incremental compression loading in three cycles until the maximum load is reached. The top is forced to be free at X ($K_x=2$) and fixed at Y ($K_y=0.5$).

Step	DOF						Stop Criterion
	X	Y	Z	RX	RY	RZ	
1	$F_x = 0$	$U_y = 0$	$U_z \downarrow$	$R_x = 0$	$M_y = 0$	$R_z = 0$	max P
2	$F_x = 0$	$U_y = 0$	$U_z \uparrow$	$R_x = 0$	$M_y = 0$	$R_z = 0$	P = 0
3	$F_x = 0$	$U_y = 0$	$U_z \downarrow$	$R_x = 0$	$M_y = 0$	$R_z = 0$	max P
4	$F_x = 0$	$U_y = 0$	$U_z \uparrow$	$R_x = 0$	$M_y = 0$	$R_z = 0$	P = 0

LC2a - Cyclic uniaxial lateral displacements with constant compression force ($-F_z = P = 400$ kips). The top was forced to have zero moments in Y and fixed rotation in X.

Step	DOF						Stop Criterion
	X	Y	Z	RX	RY	RZ	
1	$U_x \uparrow$	$U_y = 0$	P = 400k	$R_x = 0$	$M_y = 0$	$R_z = 0$	+1% drift
2	$U_x \downarrow$	$U_y = 0$	P = 400k	$R_x = 0$	$M_y = 0$	$R_z = 0$	-1% drift
3	$U_x \uparrow$	$U_y = 0$	P = 400k	$R_x = 0$	$M_y = 0$	$R_z = 0$	+2% drift
4	$U_x \downarrow$	$U_y = 0$	P = 400k	$R_x = 0$	$M_y = 0$	$R_z = 0$	-2% drift
5	$U_x \uparrow$	$U_y = 0$	P = 400k	$R_x = 0$	$M_y = 0$	$R_z = 0$	+3% drift
6	$U_x \downarrow$	$U_y = 0$	P = 400k	$R_x = 0$	$M_y = 0$	$R_z = 0$	-3% drift
7	$U_x \uparrow$	$U_y = 0$	P = 400k	$R_x = 0$	$M_y = 0$	$R_z = 0$	+4% drift
8	$U_x \downarrow$	$U_y = 0$	P = 400k	$R_x = 0$	$M_y = 0$	$R_z = 0$	-4% drift
9	$U_x \uparrow$	$U_y = 0$	P = 400k	$R_x = 0$	$M_y = 0$	$R_z = 0$	+5% drift
10	$U_x \downarrow$	$U_y = 0$	P = 400k	$R_x = 0$	$M_y = 0$	$R_z = 0$	-5% drift
11	$U_x \downarrow$	$U_y = 0$	P = 400k	$R_x = 0$	$M_y = 0$	$R_z = 0$	$U_z = 0$

LC2b - Cyclic uniaxial lateral displacements with constant compression force ($-F_z = P = 800$ kips). The top was forced to have zero moments in Y and fixed rotation in X.

Step	DOF						Stop Criterion
	X	Y	Z	RX	RY	RZ	
1	$U_x \uparrow$	$U_y = 0$	P = 800k	$R_x = 0$	$M_y = 0$	$R_z = 0$	+1% drift
2	$U_x \downarrow$	$U_y = 0$	P = 800k	$R_x = 0$	$M_y = 0$	$R_z = 0$	-1% drift
3	$U_x \uparrow$	$U_y = 0$	P = 800k	$R_x = 0$	$M_y = 0$	$R_z = 0$	+2% drift
4	$U_x \downarrow$	$U_y = 0$	P = 800k	$R_x = 0$	$M_y = 0$	$R_z = 0$	-2% drift
5	$U_x \uparrow$	$U_y = 0$	P = 800k	$R_x = 0$	$M_y = 0$	$R_z = 0$	+3% drift
6	$U_x \downarrow$	$U_y = 0$	P = 800k	$R_x = 0$	$M_y = 0$	$R_z = 0$	-3% drift
7	$U_x \uparrow$	$U_y = 0$	P = 800k	$R_x = 0$	$M_y = 0$	$R_z = 0$	+4% drift
8	$U_x \downarrow$	$U_y = 0$	P = 800k	$R_x = 0$	$M_y = 0$	$R_z = 0$	-4% drift
9	$U_x \uparrow$	$U_y = 0$	P = 800k	$R_x = 0$	$M_y = 0$	$R_z = 0$	+5% drift
10	$U_x \downarrow$	$U_y = 0$	P = 800k	$R_x = 0$	$M_y = 0$	$R_z = 0$	-5% drift
11	$U_x \downarrow$	$U_y = 0$	P = 800k	$R_x = 0$	$M_y = 0$	$R_z = 0$	$U_z = 0$

LC3a - Cyclic biaxial lateral displacements (8 shape) with constant compression force ($-F_z = P = 200$ kips). The top was forced to have zero moments.

Step	DOF						Stop Criterion
	X	Y	Z	RX	RY	RZ	
1	$U_x \uparrow$	$U_y \uparrow$	$P = 200k$	$M_x = 0$	$M_y = 0$	$R_z = 0$	+/-1% drift
2	$U_x \downarrow$	$U_y \downarrow$	$P = 200k$	$M_x = 0$	$M_y = 0$	$R_z = 0$	+/-2% drift
3	$U_x \uparrow$	$U_y \uparrow$	$P = 200k$	$M_x = 0$	$M_y = 0$	$R_z = 0$	+/-3% drift
4	$U_x \downarrow$	$U_y \downarrow$	$P = 200k$	$M_x = 0$	$M_y = 0$	$R_z = 0$	+/-4% drift

LC3b - Cyclic biaxial lateral displacements (8 shape) with constant compression force ($-F_z = P = 600$ kips). The top was forced to have zero moments.

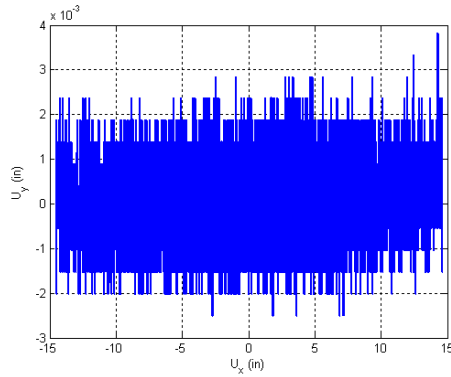
Step	DOF						Stop Criterion
	X	Y	Z	RX	RY	RZ	
1	$U_x \downarrow$	$U_y \downarrow$	$P = 600k$	$M_x = 0$	$M_y = 0$	$R_z = 0$	+/-1% drift
2	$U_x \uparrow$	$U_y \uparrow$	$P = 600k$	$M_x = 0$	$M_y = 0$	$R_z = 0$	+/-2% drift
3	$U_x \downarrow$	$U_y \downarrow$	$P = 600k$	$M_x = 0$	$M_y = 0$	$R_z = 0$	+/-3% drift
4	$U_x \uparrow$	$U_y \uparrow$	$P = 600k$	$M_x = 0$	$M_y = 0$	$R_z = 0$	+/-4% drift

LC4a - Incremental compression loading until the maximum load is reached. The top is driven with different BCs for both X and Y.

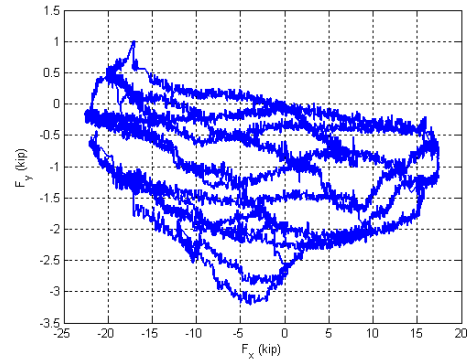
Step	DOF						Stop Criterion
	X	Y	Z	RX	RY	RZ	
1	$F_x \rightarrow 0$	$F_y \rightarrow 0$	$F_z \rightarrow 0$	$M_x = 0$	$M_y = 0$	$R_z = 0$	$F_x=F_y=0$
2	var	var	$U_z \downarrow$	var	var	$R_z = 0$	$P = P_{max}$

LC4b - Cyclic uniaxial lateral displacements (4 corners) with constant compression force ($-F_z = P = 600$ kips). The top is forced to be free at all the time.

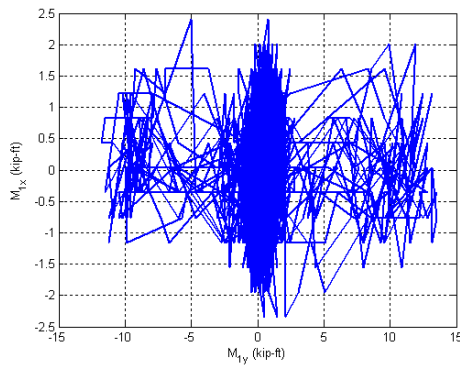
Step	DOF						Stop Criterion
	X	Y	Z	RX	RY	RZ	
1	$U_x \uparrow$	$U_y \uparrow$	$P = 600k$	$M_x = 0$	$M_y = 0$	$R_z = 0$	max stroke
2	$U_x \downarrow$	$U_y \downarrow$	$P = 600k$	$M_x = 0$	$M_y = 0$	$R_z = 0$	max stroke
3	$U_x \rightarrow 0$	$U_y \rightarrow 0$	$P = 600k$	$M_x = 0$	$M_y = 0$	$R_z = 0$	$U_x=U_y=0$
4	$U_x \uparrow$	$U_y \downarrow$	$P = 600k$	$M_x = 0$	$M_y = 0$	$R_z = 0$	max stroke
5	$U_x \downarrow$	$U_y \uparrow$	$P = 600k$	$M_x = 0$	$M_y = 0$	$R_z = 0$	max stroke
6	$U_x \rightarrow 0$	$U_y \rightarrow 0$	$P = 600k$	$M_x = 0$	$M_y = 0$	$R_z = 0$	$U_x=U_y=0$



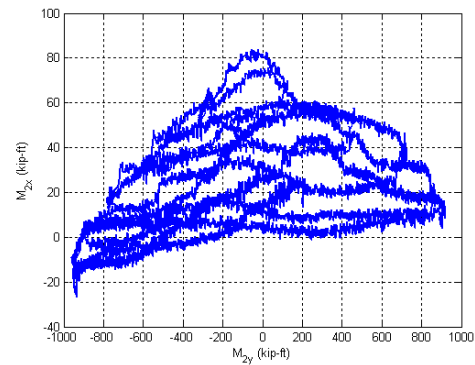
Y Displacement vs. X Displacement



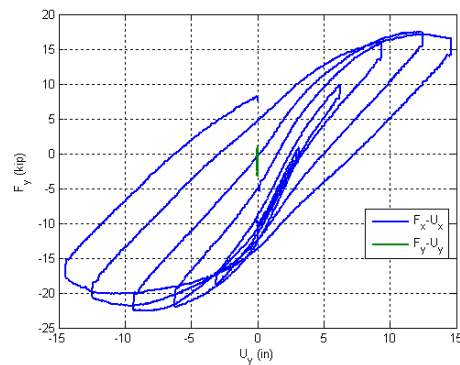
Y Force vs. X Force



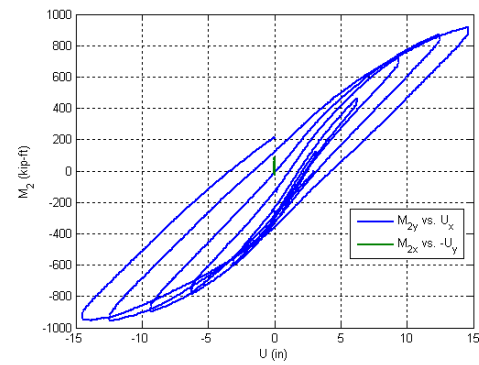
X Moment vs. Y Moment at the top



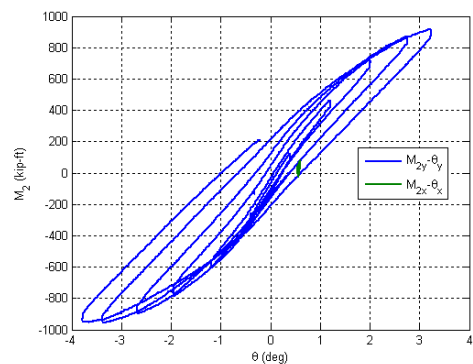
X Moment vs. Y Moment at the base



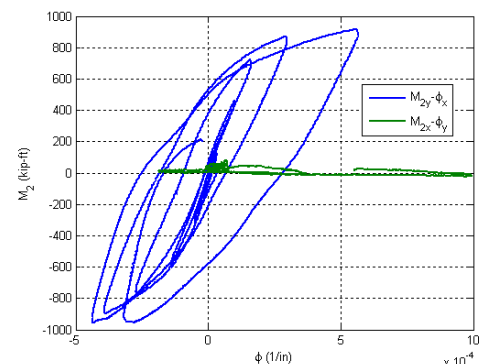
Lateral Force vs. Lateral Displacement



Base Moment vs. Top Displacement

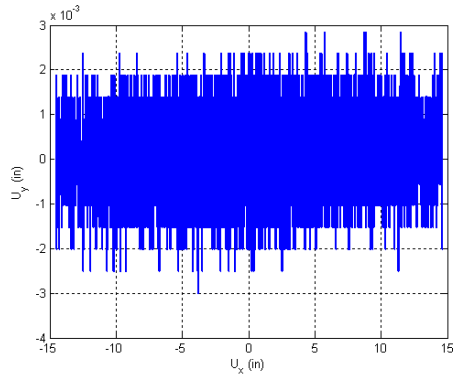


Base Moment vs. Top Rotation

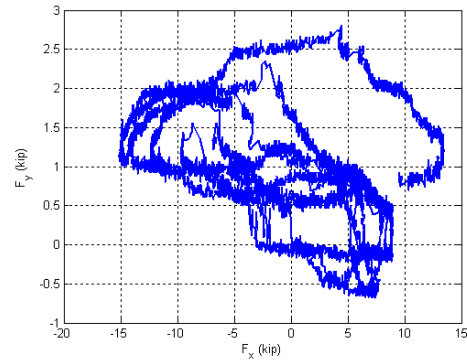


Base Moment vs. Base Curvature

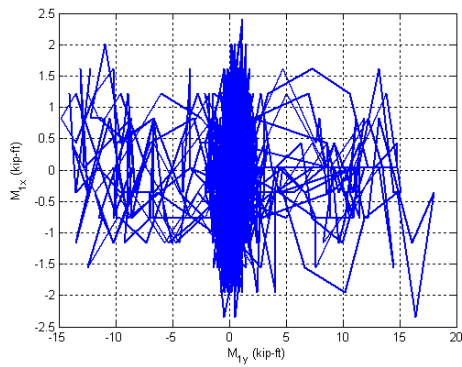
Figure B.122. Experimental results from LC2a in the specimen 17Rs-26-12



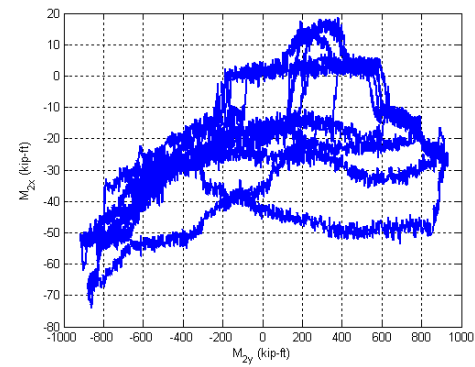
Y Displacement vs. X Displacement



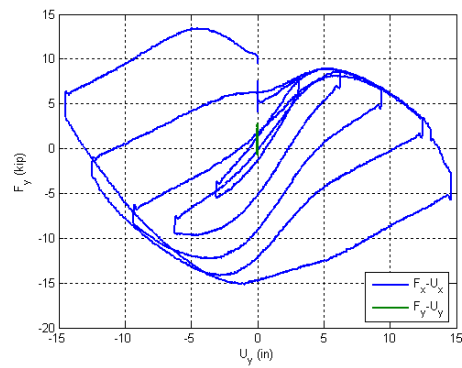
Y Force vs. X Force



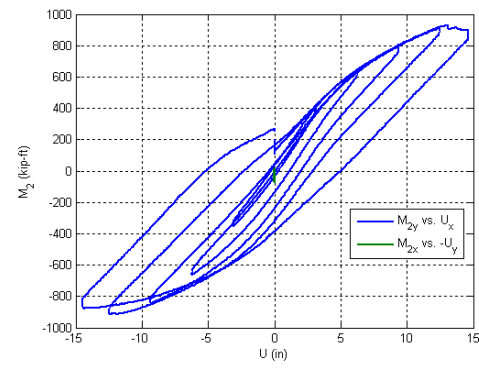
X Moment vs. Y Moment at the top



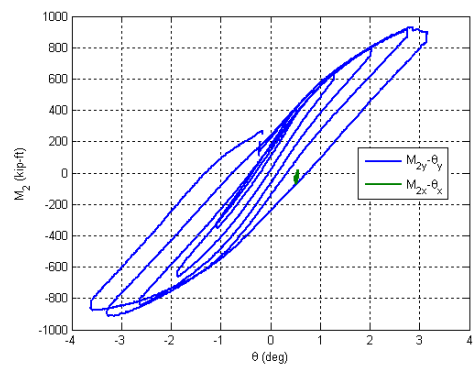
X Moment vs. Y Moment at the base



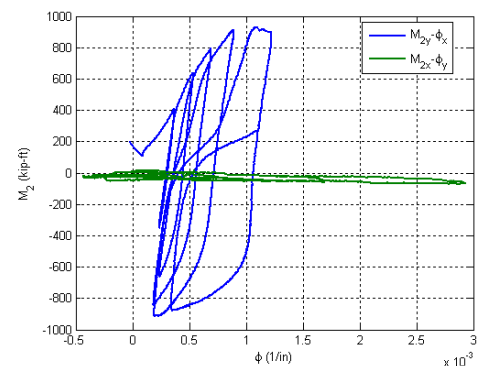
Lateral Force vs. Lateral Displacement



Base Moment vs. Top Displacement

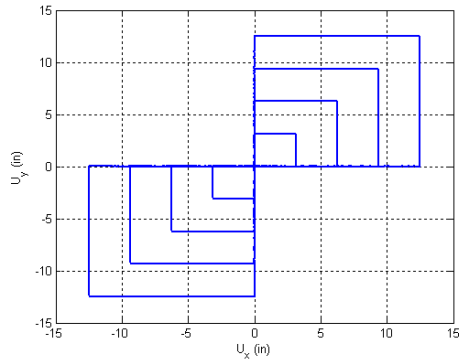


Base Moment vs. Top Rotation

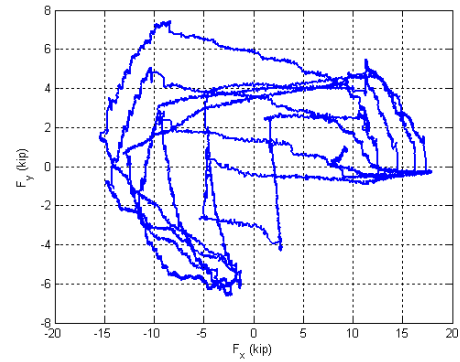


Base Moment vs. Base Curvature

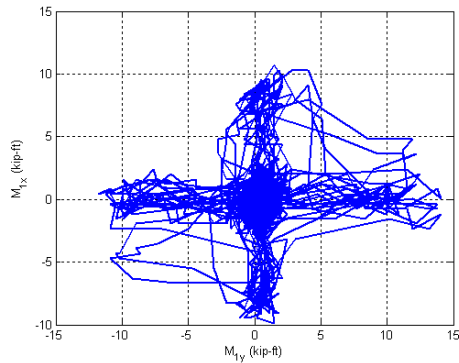
Figure B.123. Experimental results from LC2b in the specimen 17Rs-26-12



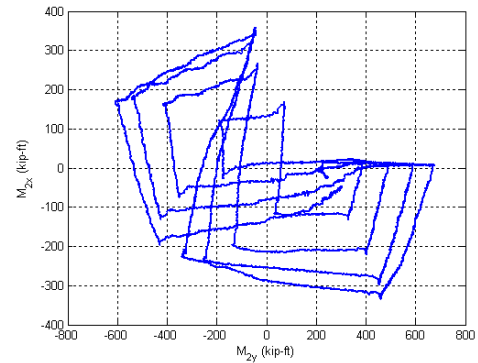
Y Displacement vs. X Displacement



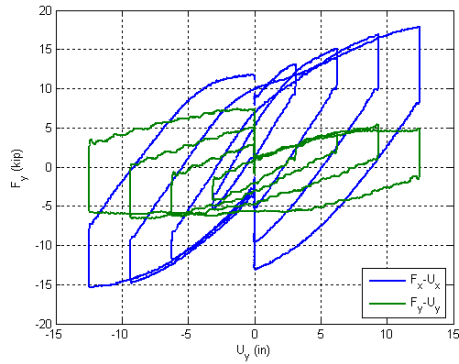
Y Force vs. X Force



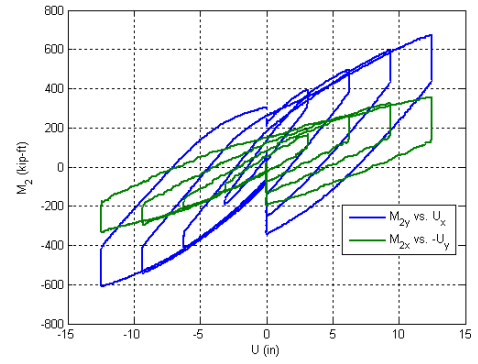
X Moment vs. Y Moment at the top



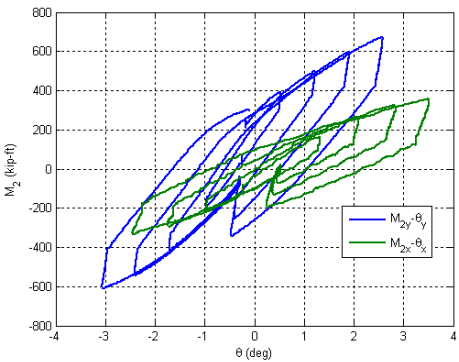
X Moment vs. Y Moment at the base



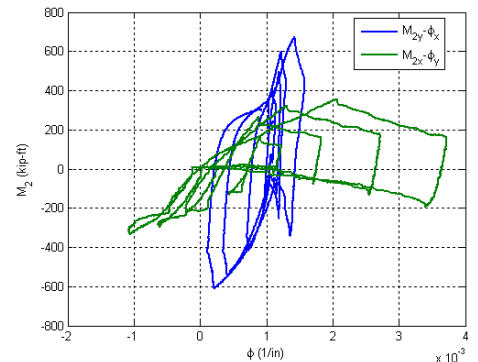
Lateral Force vs. Lateral Displacement



Base Moment vs. Top Displacement

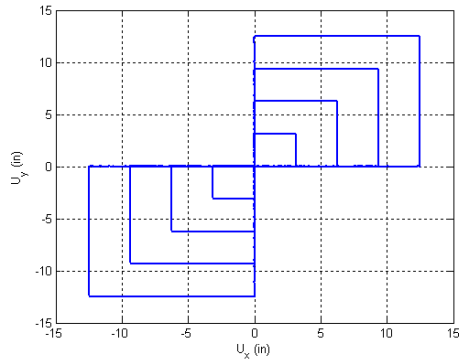


Base Moment vs. Top Rotation

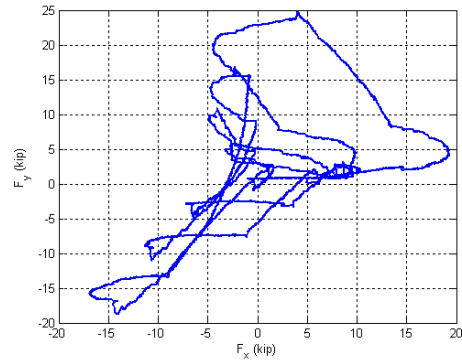


Base Moment vs. Base Curvature

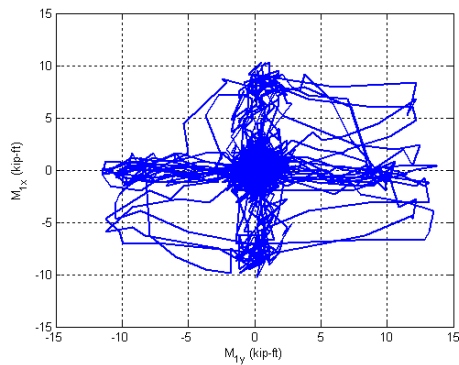
Figure B.124. Experimental results from LC3a in the specimen 17Rs-26-12



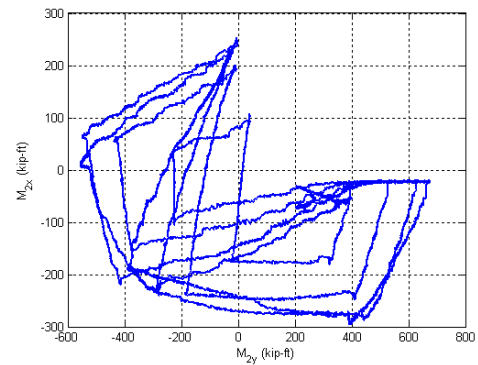
Y Displacement vs. X Displacement



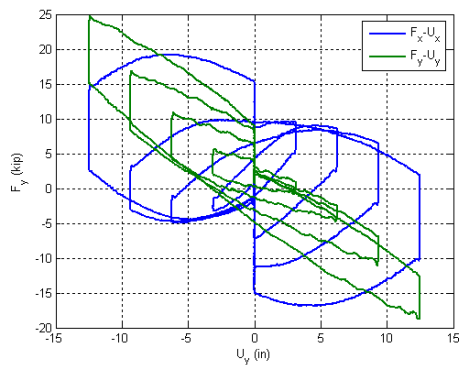
Y Force vs. X Force



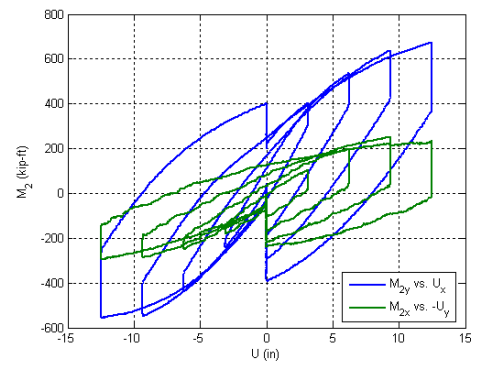
X Moment vs. Y Moment at the top



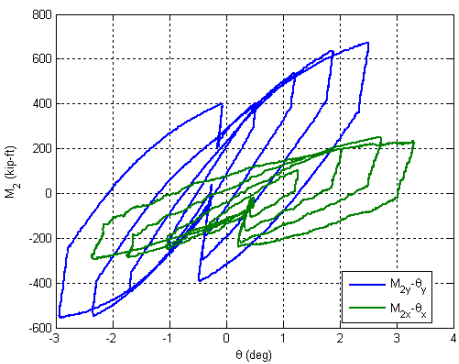
X Moment vs. Y Moment at the base



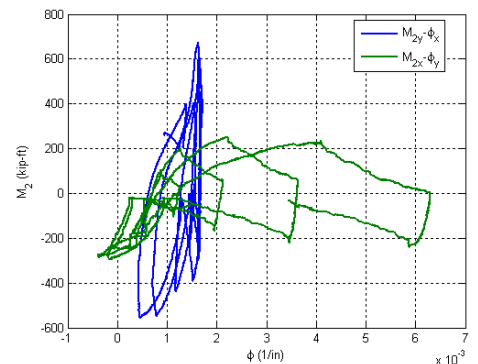
Lateral Force vs. Lateral Displacement



Base Moment vs. Top Displacement

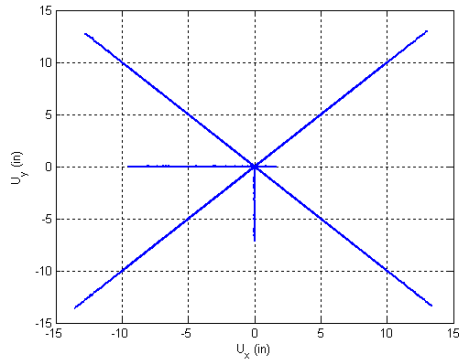


Base Moment vs. Top Rotation

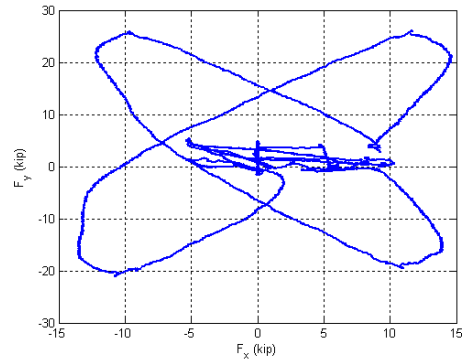


Base Moment vs. Base Curvature

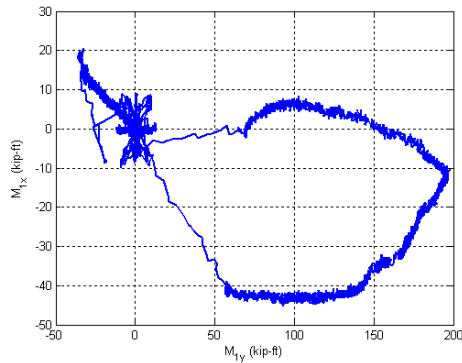
Figure B.125. Experimental results from LC3b in the specimen 17Rs-26-12



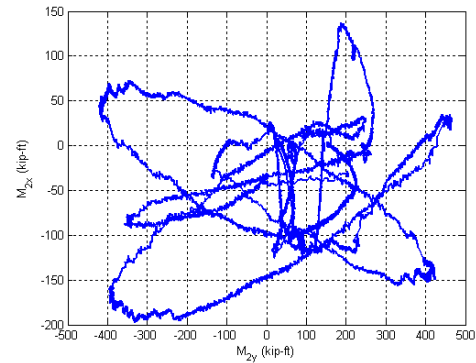
Y Displacement vs. X Displacement



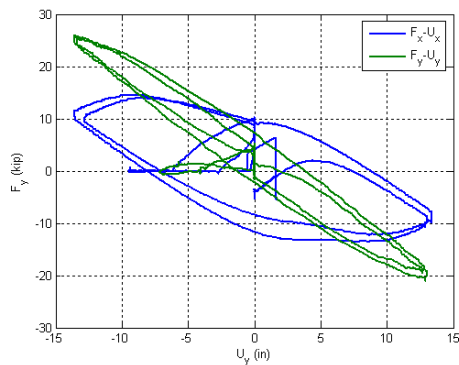
Y Force vs. X Force



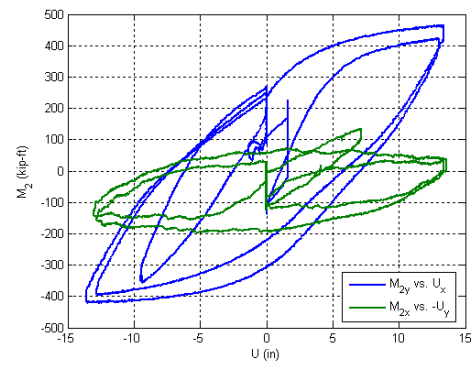
X Moment vs. Y Moment at the top



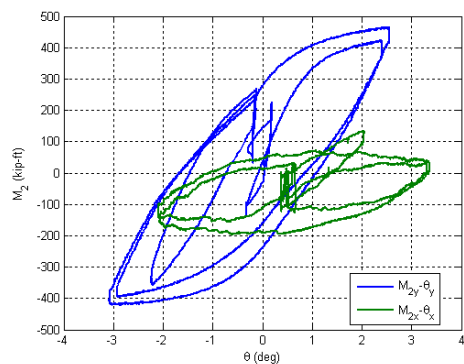
X Moment vs. Y Moment at the base



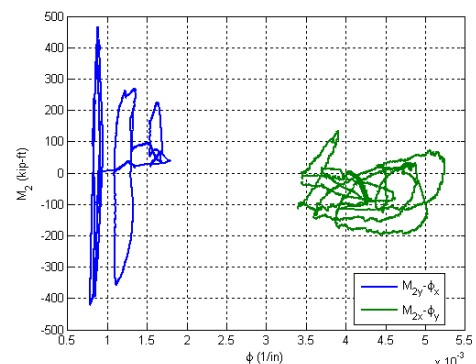
Lateral Force vs. Lateral Displacement



Base Moment vs. Top Displacement



Base Moment vs. Top Rotation



Base Moment vs. Base Curvature

Figure B.126. Experimental results from LC4 in the specimen 17Rs-26-12

B.18. Specimen 18C5-26-12

Description:

- Specimen number: 18
- Composite Cross-section: CCFT
- Steel cross-section: HSS5.563x0.123
- Design concrete strength: 12 ksi
- Design specimen length: 26 ft
- Pouring date: 03/27/2009
- Testing date: 07/29/2009

Parameters:

- Specimen length: 26' 5/8"
- Initial out-of-straightness: $U_{xo} = -0.50'' / U_{yo} = 0.36''$
- Steel yielding stress: $F_y = 55.6$ ksi
- Steel ultimate stress: $F_u = 70.7$ ksi
- Concrete strength at the 28th day: $f_c' = 11.5$ ksi
- Concrete strength at the testing day: $f_c = 11.7$ ksi
- Concrete Young's modulus: $E_c = 5800$ ksi
- Concrete tensile strength: $f_t = 0.76$ ksi

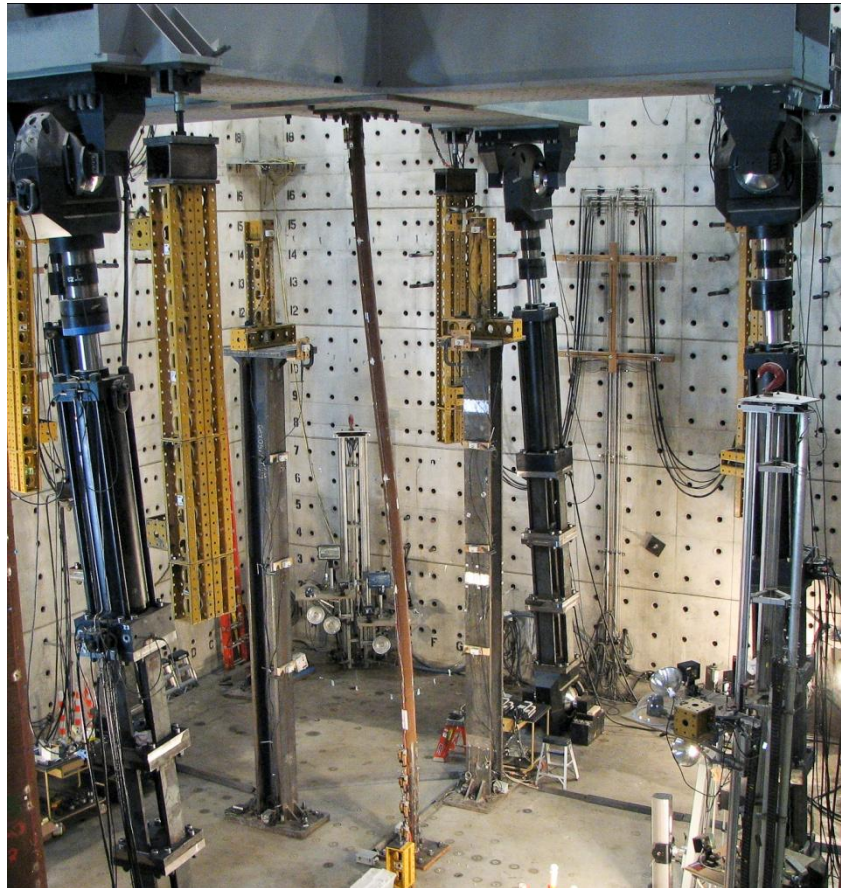


Figure B.127. Specimen 18C5-26-12

Table B.18. Load protocol summary for the specimen 17Rs-26-12

LC1 - Incremental compression loading in three cycles until the maximum load is reached. The top is forced as (1) free translation-fixed rotation ($K=1$), and (2) double fixed ($K=0.5$).

Step	DOF						Stop Criterion
	X	Y	Z	RX	RY	RZ	
1a	$F_x = 0$	$F_y = 0$	$U_z \downarrow$	$R_x = 0$	$R_y = 0$	$R_z = 0$	max P
1b	$F_x = 0$	$F_y = 0$	$U_z \uparrow$	$R_x = 0$	$R_y = 0$	$R_z = 0$	P = 0
2a	$U_x = 0$	$U_y = 0$	$U_z \downarrow$	$R_x = 0$	$R_y = 0$	$R_z = 0$	max P
2b	$U_x = 0$	$U_y = 0$	$U_z \uparrow$	$R_x = 0$	$R_y = 0$	$R_z = 0$	P = 0

LC2a - Cyclic uniaxial lateral displacements with constant compression force ($-F_z = P = 15$ kips). The top was forced to have fixed rotations.

Step	DOF						Stop Criterion
	X	Y	Z	RX	RY	RZ	
1	$U_x \uparrow$	$U_y \uparrow$	P = 15k	$R_x = 0$	$R_y = 0$	$R_z = 0$	+/-1% drift
2	$U_x \downarrow$	$U_y \downarrow$	P = 15k	$R_x = 0$	$R_y = 0$	$R_z = 0$	+/-2% drift
3	$U_x \uparrow$	$U_y \uparrow$	P = 15k	$R_x = 0$	$R_y = 0$	$R_z = 0$	+/-3% drift
4	$U_x \downarrow$	$U_y \downarrow$	P = 15k	$R_x = 0$	$R_y = 0$	$R_z = 0$	+/-4% drift
5	$U_x \uparrow$	$U_y \uparrow$	P = 15k	$R_x = 0$	$R_y = 0$	$R_z = 0$	+/-5% drift
6	$U_x \downarrow$	$U_y \downarrow$	P = 15k	$R_x = 0$	$R_y = 0$	$R_z = 0$	+/-6% drift
7	$U_x \uparrow$	$U_y \uparrow$	P = 15k	$R_x = 0$	$R_y = 0$	$R_z = 0$	+/-7% drift
8	$U_x \downarrow$	$U_y \downarrow$	P = 15k	$R_x = 0$	$R_y = 0$	$R_z = 0$	$U_z = 0$

LC2b - Cyclic uniaxial lateral displacements with constant compression force ($-F_z = P = 25$ kips). The top was forced to have fixed rotations.

Step	DOF						Stop Criterion
	X	Y	Z	RX	RY	RZ	
1	$U_x \uparrow$	$U_y \uparrow$	P = 25k	$R_x = 0$	$R_y = 0$	$R_z = 0$	+/-1% drift
2	$U_x \downarrow$	$U_y \downarrow$	P = 25k	$R_x = 0$	$R_y = 0$	$R_z = 0$	+/-2% drift
3	$U_x \uparrow$	$U_y \uparrow$	P = 25k	$R_x = 0$	$R_y = 0$	$R_z = 0$	+/-3% drift
4	$U_x \downarrow$	$U_y \downarrow$	P = 25k	$R_x = 0$	$R_y = 0$	$R_z = 0$	+/-4% drift
5	$U_x \uparrow$	$U_y \uparrow$	P = 25k	$R_x = 0$	$R_y = 0$	$R_z = 0$	+/-5% drift
6	$U_x \downarrow$	$U_y \downarrow$	P = 25k	$R_x = 0$	$R_y = 0$	$R_z = 0$	+/-6% drift
7	$U_x \downarrow$	$U_y \downarrow$	P = 25k	$R_x = 0$	$R_y = 0$	$R_z = 0$	$U_z = 0$

LC3a - Cyclic biaxial lateral displacements (8 shape) with constant compression force ($-F_z = P = 20$ kips). The top was forced to have fixed rotations.

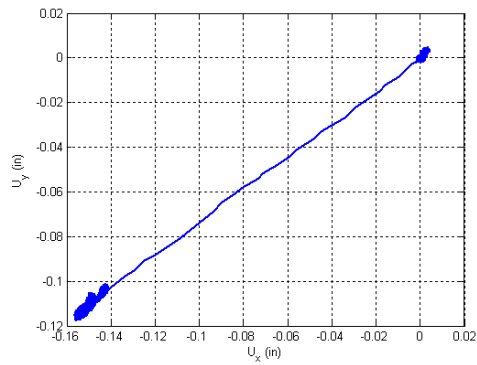
Step	DOF						Stop Criterion
	X	Y	Z	RX	RY	RZ	
1	$U_x \uparrow$	$U_y \uparrow$	P = 20k	$R_x = 0$	$R_y = 0$	$R_z = 0$	+/-1% drift
2	$U_x \downarrow$	$U_y \downarrow$	P = 20k	$R_x = 0$	$R_y = 0$	$R_z = 0$	+/-2% drift
3	$U_x \uparrow$	$U_y \uparrow$	P = 20k	$R_x = 0$	$R_y = 0$	$R_z = 0$	+/-3% drift
4	$U_x \downarrow$	$U_y \downarrow$	P = 20k	$R_x = 0$	$R_y = 0$	$R_z = 0$	+/-4% drift

LC4a - Incremental compression loading until the maximum load is reached. The top is driven with different BCs for both X and Y.

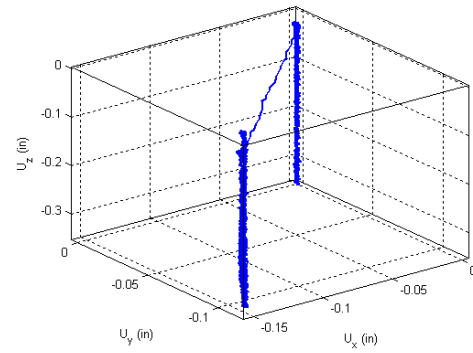
Step	DOF						Stop Criterion
	X	Y	Z	RX	RY	RZ	
1	$F_x \rightarrow 0$	$F_y \rightarrow 0$	$F_z \rightarrow 0$	$M_x = 0$	$M_y = 0$	$R_z = 0$	$F_x=F_y=0$
2	var	var	$U_z \downarrow$	var	var	$R_z = 0$	$P = P_{\max}$

LC4b - Cyclic uniaxial lateral displacements (4 corners) with constant compression force ($-F_z = P = 40$ kips). The top was forced to have fixed rotations.

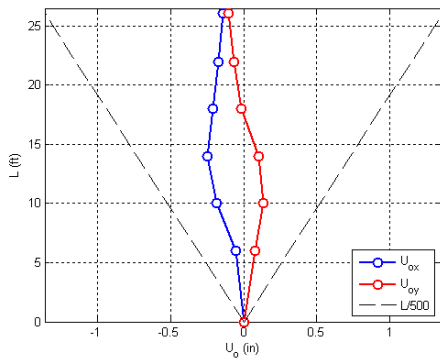
Step	DOF						Stop Criterion
	X	Y	Z	RX	RY	RZ	
1	$U_x \uparrow$	$U_y \uparrow$	$P = 40k$	$R_x = 0$	$R_y = 0$	$R_z = 0$	max stroke
2	$U_x \downarrow$	$U_y \downarrow$	$P = 40k$	$R_x = 0$	$R_y = 0$	$R_z = 0$	max stroke
3	$U_x \rightarrow 0$	$U_y \rightarrow 0$	$P = 40k$	$R_x = 0$	$R_y = 0$	$R_z = 0$	$U_x=U_y=0$
4	$U_x \uparrow$	$U_y \downarrow$	$P = 40k$	$R_x = 0$	$R_y = 0$	$R_z = 0$	max stroke
5	$U_x \downarrow$	$U_y \uparrow$	$P = 40k$	$R_x = 0$	$R_y = 0$	$R_z = 0$	max stroke
6	$U_x \rightarrow 0$	$U_y \rightarrow 0$	$P = 40k$	$R_x = 0$	$R_y = 0$	$R_z = 0$	$U_x=U_y=0$



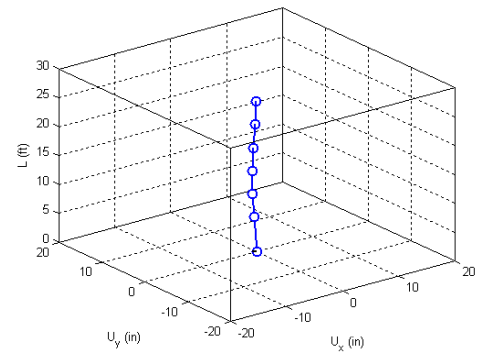
Y displacement vs. X displacement



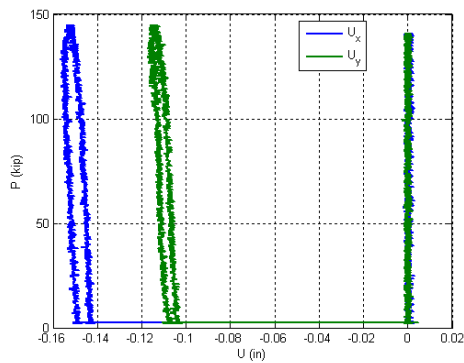
Z displacement vs. X and Y displacement



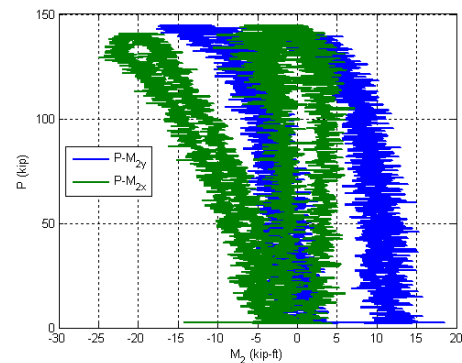
Initial deflected shape



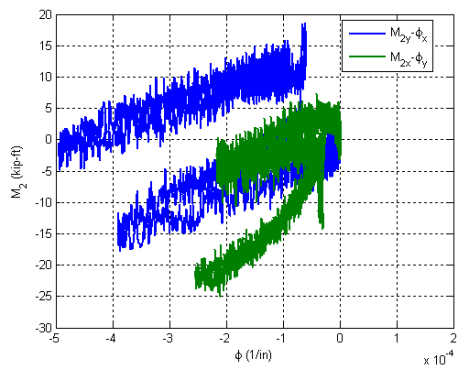
Maximum lateral displacement



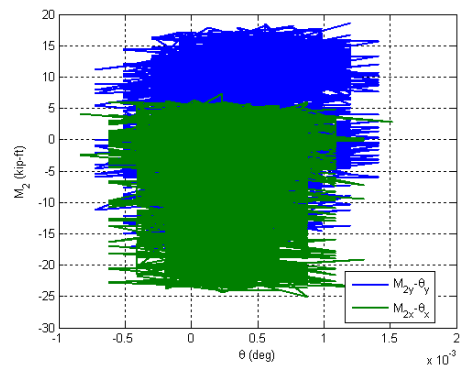
Axial force vs. lateral displacement



Axial force vs. base moments

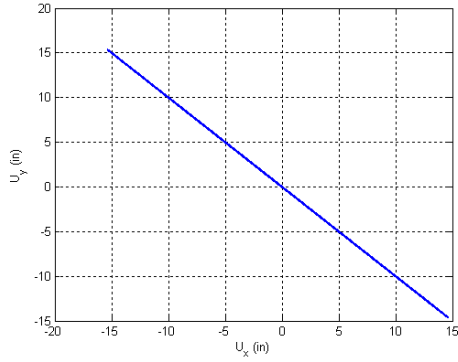


Base moment vs. base curvature

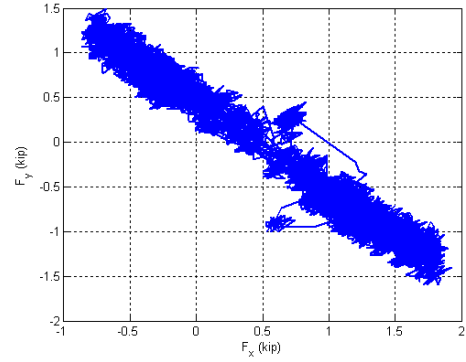


Base moment vs. top rotation

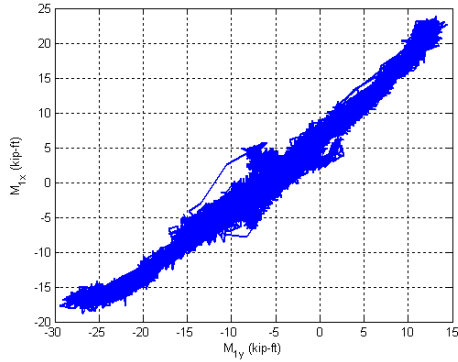
Figure B.128. Experimental results from LC1 in the specimen 18C5-26-12



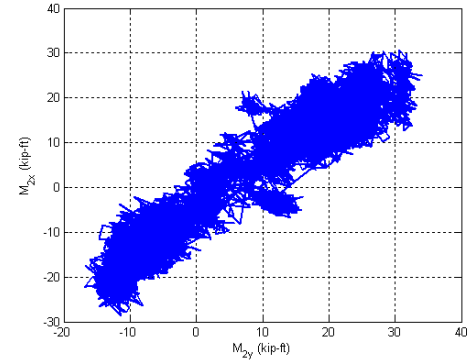
Y Displacement vs. X Displacement



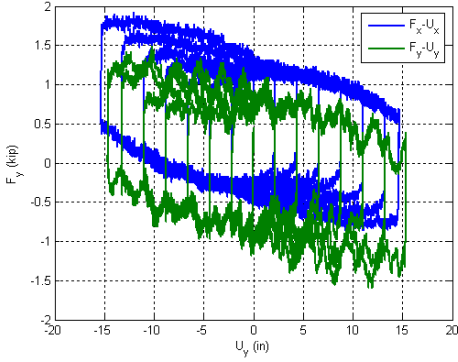
Y Force vs. X Force



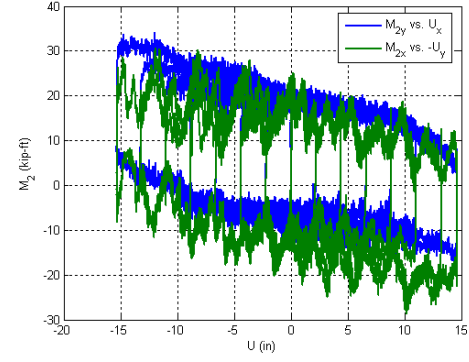
X Moment vs. Y Moment at the top



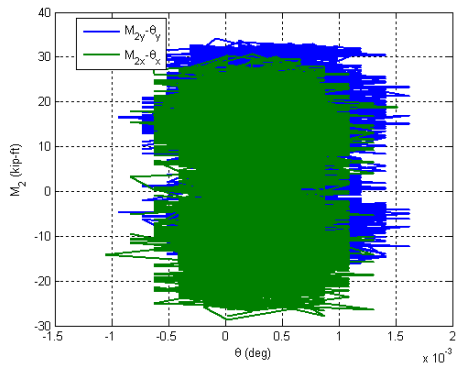
X Moment vs. Y Moment at the base



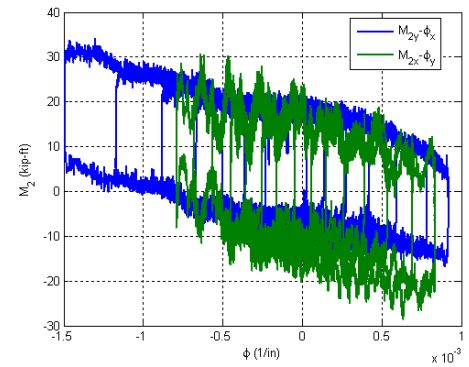
Lateral Force vs. Lateral Displacement



Base Moment vs. Top Displacement

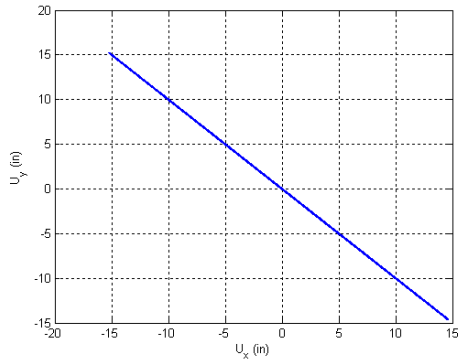


Base Moment vs. Top Rotation

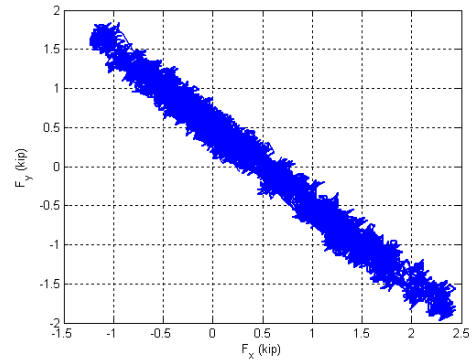


Base Moment vs. Base Curvature

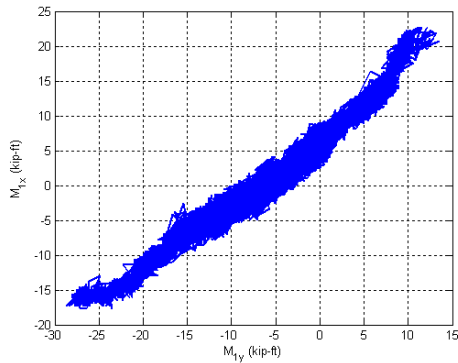
Figure B.129. Experimental results from LC2a in the specimen 18C5-26-12



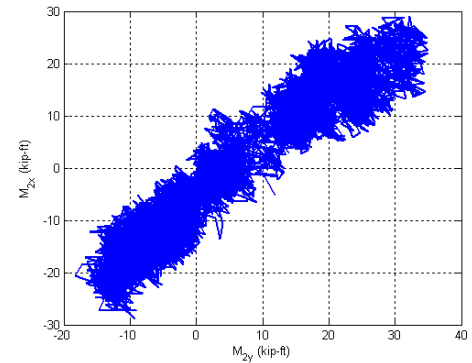
Y Displacement vs. X Displacement



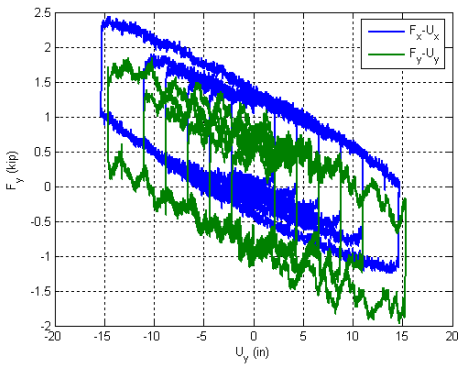
Y Force vs. X Force



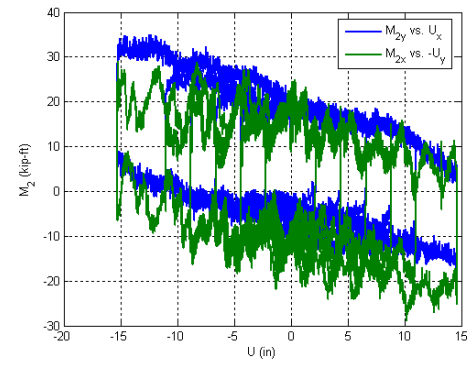
X Moment vs. Y Moment at the top



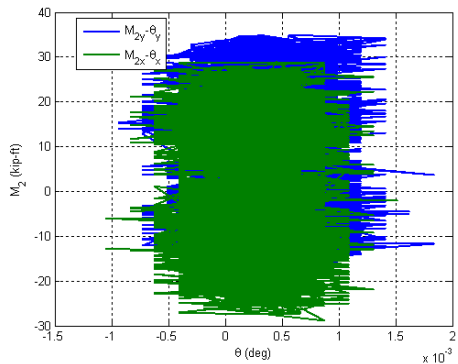
X Moment vs. Y Moment at the base



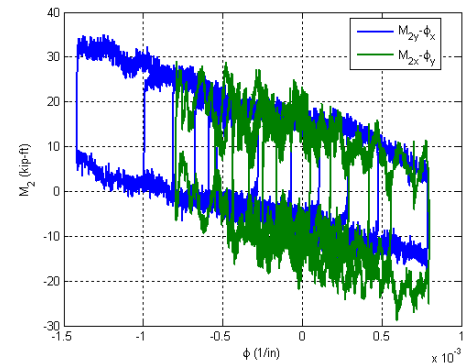
Lateral Force vs. Lateral Displacement



Base Moment vs. Top Displacement

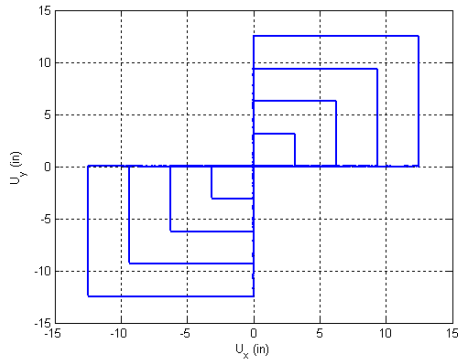


Base Moment vs. Top Rotation

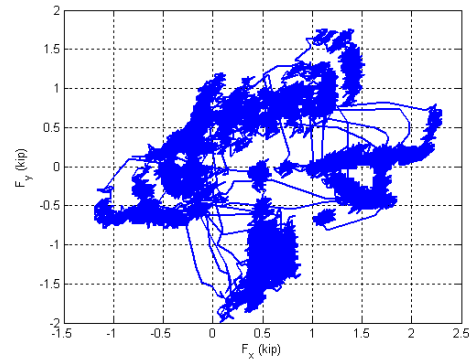


Base Moment vs. Base Curvature

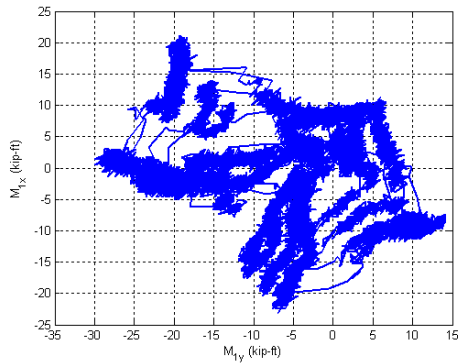
Figure B.130. Experimental results from LC2b in the specimen 18C5-26-12



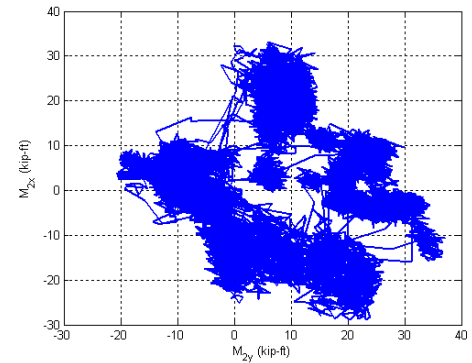
Y Displacement vs. X Displacement



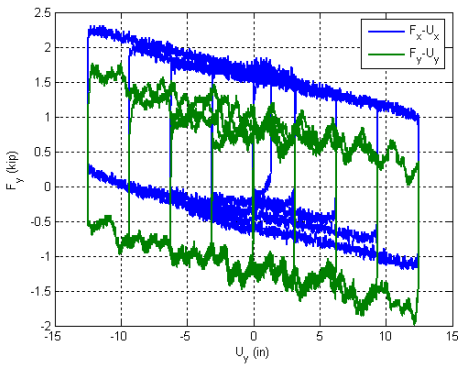
Y Force vs. X Force



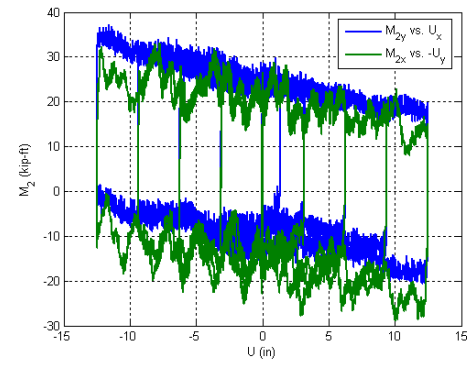
X Moment vs. Y Moment at the top



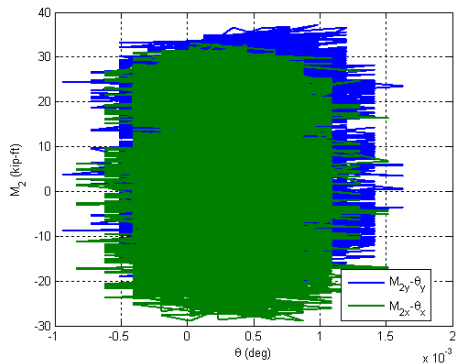
X Moment vs. Y Moment at the base



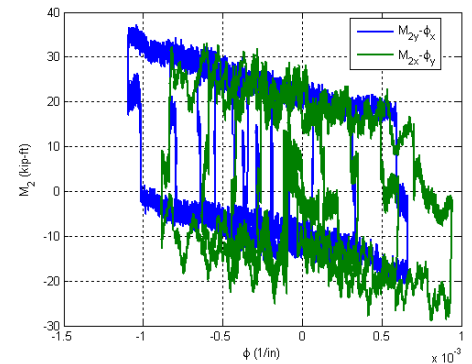
Lateral Force vs. Lateral Displacement



Base Moment vs. Top Displacement

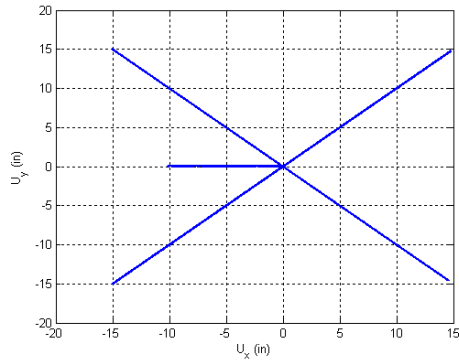


Base Moment vs. Top Rotation

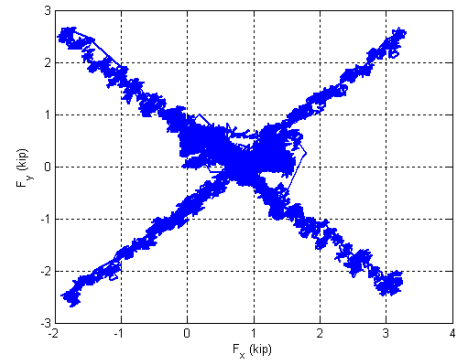


Base Moment vs. Base Curvature

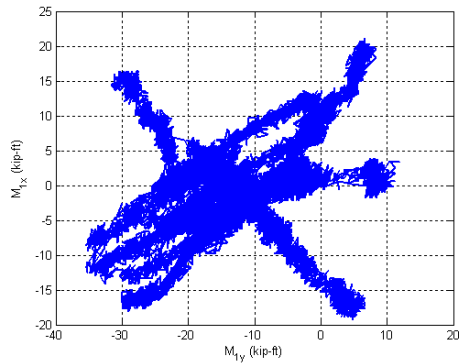
Figure B.131. Experimental results from LC3 in the specimen 18C5-26-12



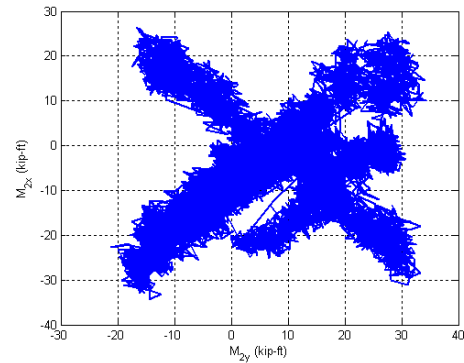
Y Displacement vs. X Displacement



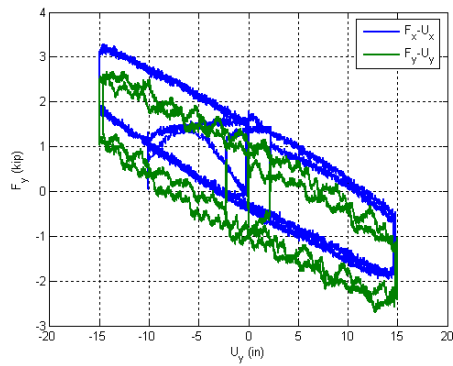
Y Force vs. X Force



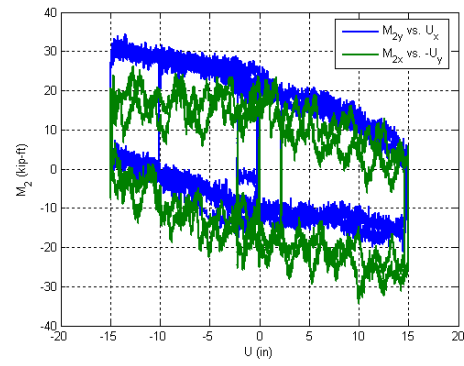
X Moment vs. Y Moment at the top



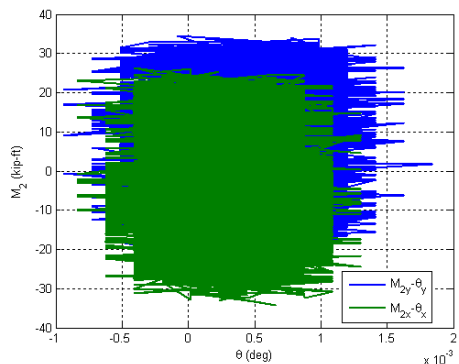
X Moment vs. Y Moment at the base



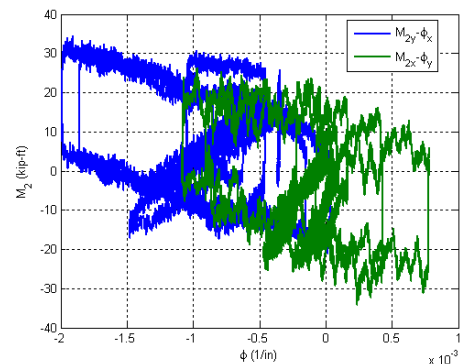
Lateral Force vs. Lateral Displacement



Base Moment vs. Top Displacement



Base Moment vs. Top Rotation



Base Moment vs. Base Curvature

Figure B.132. Experimental results from LC4 in the specimen 18C5-26-12

REFERENCES

- ABAQUS. (2010). *ABAQUS FEA*. SIMULIA. ABAQUS Inc.
- ACI-117. (2006). "Standard Specifications for Tolerances for Concrete Construction and Materials." American Concrete Institute.
- ACI-318. (2008). *Building Code Requirements for Structural Concrete and Commentary*.
- Aho, M. (1997). "A database for encased and concrete-filled columns." Georgia Institute of Technology, School of Civil and Environmental Engineering.
- AIJ. (2001). *Standard for Structural Calculation of Steel Reinforced Concrete Structures*. Architectural Institute of Japan (AIJ).
- AISC. (2005a). *Specifications for structural steel buildings. ANSI/AISC 360-05*. American Institute of Steel Construction.
- AISC. (2005b). *Seismic Provisions for structural steel buildings. ANSI/AISC 341-05*. American Institute of Steel Construction.
- AISC. (2005c). *Commentary on the specifications for structural steel buildings*. American Institute of Steel Construction.
- AISC. (2005d). *Code of Standard Practice for Steel Buildings and Bridges (AISC 303-05)*. ; American Institute of Steel Construction.
- AISC. (2010a). *Specifications for structural steel buildings. ANSI/AISC 360-10*. American Institute of Steel Construction.
- AISC. (2010b). *Seismic Provisions for structural steel buildings. ANSI/AISC 341-10*. American Institute of Steel Construction.
- ASCE. (1997). *Effective Length and Notional Load Approaches for Assessing Frame Stability: Implications for American Steel Design*. (R. Q. Bridge, M. J. Clarke, R. T. Leon, E. M. Lui, T. M. Sheikh, D. W. White, and J. F. Hajjar, eds.), American Society of Civil Engineers. Institute Structural Engineering.
- ASTM. (2009). "Standard Specification for General Requirements for Rolled Structural Steel Bars, Plates, Shapes, and Sheet Piling."
- Aval, S. B. B., Saadeghvaziri, M. A., and Golafshani, A. A. (2002). "Comprehensive Composite Inelastic Fiber Element for Cyclic Analysis of Concrete-Filled Steel Tube Columns." *Journal of Engineering Mechanics*, 128(4), 428-437.
- Beck, J., and Kiyomiya, O. (2003). "Fundamental Pure Torsional Properties of Concrete Filled Circular Steel Tubes." *Proceedings of JSCE (Japan Society of Civil Engineers)*, 739(739), 285-296.
- Bergmann, R., Matsui, C., Meinsma, C., and Dutta, D. (1995). *Design guide for concrete filled hollow section columns under static and seismic loading*. CIDECT, Construction with hollow steel sections. Verlag TÜV Rheinland.
- Bjorhovde, R. (1972). "Deterministic and probabilistic approaches to the strength of steel columns." *Ph. D. Dissertation, Department of Civil Engineering, Lehigh University, Bethlehem, Pennsylvania, USA*.

- Bradford, M. A., Loh, H. Y., and Uy, B. (2002). "Slenderness limits for filled circular steel tubes." *Journal of Constructional Steel Research*, 58(2), 243-252.
- Budynas, R. G. (1999). *Advanced strength and applied stress analysis*. McGraw-Hill.
- Cai, S. H., and Gu, W. L. (1985). "Behavior and ultimate strength of long concrete-filled steel tubular columns." *Journal of Building Structures*, 6, 32-40.
- Chang, G. A., and Mander, J. B. (1994). *Seismic Energy Based Fatigue Damage Analysis of Bridge Columns: Part I - Evaluation of Seismic Capacity*. National Center for Earthquake Engineering Research, State University of New York at Buffalo, Department of Civil Engineering.
- Chen, W. K., and Lui, E. M. (1987). *Structural Stability: Theory and Implementation*. Prentice Hall.
- Davids, A., and Merriel, A. (2004). "Latitude Reaches Skyward in Steel." *Steel Australia*, 17(1).
- Denavit, M. D. (2010). "Characterization of behavior of composite members and frames and applications for design." University of Illinois at Urbana-Champaign, Urbana-Champaign, IL, USA.
- Denavit, M. D., and Hajjar, J. F. (2010). *Nonlinear Seismic Analysis of CCFT Members and Frames*. Department of Civil and Environmental Engineering University of Illinois at Urbana-Champaign, Urbana-Champaign, IL, USA.
- Denavit, M. D., Hajjar, J. F., Perea, T., and Leon, R. T. (2010). "Cyclic evolution of damage and beam-column interaction strength of concrete-filled steel tube beam-columns." *9th US National and 10th Canadian Conference on Earthquake Engineering*, Toronto, Canada.
- Elremaily, A., and Azizinamini, A. (2002). "Behavior and strength of circular concrete-filled tube columns." *Journal of Constructional Steel Research*, 58(12), 1567-1591.
- Eurocode 4. (2004). "Eurocode 4: Design of composite steel and concrete structures - Part 1-1: General rules and rules for buildings."
- French, C. W., Schultz, A. E., Hajjar, J. F., Shield, C. K., Ernie, D. W., Dexter, R. J., Du, D. H. C., Olson, S. A., Daugherty, D. J., and Wan, C. P. (2004). "Multi-Axial Subassemblage Testing (MAST) System: Description And Capabilities." *Proceedings of the 13th World Conference on Earthquake Engineering*, Vancouver, B.C., Canada.
- Fukumoto, Y., Nethercot, D. A., and Galambos, T. V. (1983). "Experimental data for the buckling of steel structures - NDSS." *Proceedings of the 3rd International Colloquium on Stability of Metal Structures*, Toronto, Canada., 609-630.
- Furlong, R. W. (1967). "Strength of Steel-Encased Concrete Beam Columns." *Journal of Structural Division, ASCE*, 93(ST5), 113-124.
- Goode, C. D. (2007). *ASCCS Database of Concrete-Filled Steel Tube Columns*. ASCCS.
- Goode, C. D., and Lam, D. (2008). "Experimental data analysis of concrete-filled steel columns." *Composite Construction VI*.

- Gourley, B. C., and Hajjar, J. F. (1993). *A Synopsis of Studies of the Monotonic and Cyclic Behavior of Concrete-Filled Steel Tube Members, Connections, and Frames*. Department of Civil and Environmental Engineering, Institute of Technology, University of Minnesota., Minneapolis, MN.
- Gourley, B. C., Tort, C. T., Denavit, M. D., Schiller, P. H., and Hajjar, J. F. (2008). *A Synopsis of Studies of the Monotonic and Cyclic Behavior of Concrete-Filled Steel Tube Members, Connections, and Frames*. Department of Civil and Environmental Engineering, University of Illinois at Urbana-Champaign, Urbana, Illinois.
- Hajjar, J. F. (2000). "Concrete-filled steel tube columns under earthquake loads." *Progress in Structural Engineering and Materials*, 2(1), 72–81.
- Hajjar, J. F., French, C. W., Schultz, A. E., Shield, C. K., Ernie, D. W., Dexter, R. J., Du, D. H., and Bergson, P. M. (2002). "A system for multi-axial subassembly testing (MAST): initial developments." *Proceedings of the American Society of Civil Engineers Structures Congress, Denver, Colorado, April 4–6, 2002*, 313–314.
- Hajjar, J. F., Schiller, P. H., and Molodan, A. (1998). "A distributed plasticity model for concrete-filled steel tube beam-columns with interlayer slip." *Engineering Structures*, 20(8), 663–676.
- Han, L. H., Yao, G. H., and Tao, Z. (2007a). "Performance of concrete-filled thin-walled steel tubes under pure torsion." *Thin-Walled Structures*, 45(1), 24–36.
- Han, L. H., Yao, G. H., and Tao, Z. (2007b). "Behaviors of concrete-filled steel tubular members subjected to combined loading." *Thin-Walled Structures*, 45(6), 600–619.
- Hatzigeorgiou, G. D. (2008). "Numerical model for the behavior and capacity of circular CFT columns, Part I: Theory." *Engineering Structures*, 30(6), 1573–1578.
- Horton, W. H., Cundari, F. L., and Johnson, R. W. (1971). *Applicability of the Southwell Plot to the Interpretation of Test Data Obtained from Stability Studies of Elastic Column and Plate Structures*.
- Izzuddin, B. A., Karayannis, C. G., and Elnashai, A. S. (1994). "Advanced Nonlinear Formulation for Reinforced-Concrete Beam-Columns." *Journal of Structural Engineering-Asce*, 120(10), 2913–2934.
- Janss, J. (1974). *Charges Ultimes des Profils Creux Remplis de Beton Charges Axialement*. Centre de Recherches Scientifiques et Techniques de L'industrie des Fabrications Metalliques (CRIF), Brussels.
- Kawaguchi, J., Morino, S., Shirai, J., and Tatsuta, E. (1998). "Database and structural characteristics of CFT beam-columns." *Proceedings of the Fifth Pacific Structural Steel Conference*, Seoul, Korea.
- Kent, D. C., and Park, R. (1971). "Flexural members with confined concrete." *Journal of the Structural Division*, 97(7), 1969–1990.
- Kim, D. K. (2005). "A Database For Composite Columns." Georgia Institute of Technology.

- Kitada, T., and Nakai, H. (1991). "Experimental Study on Ultimate Strength of Concrete Filled Square Steel Short Members Subjected to Compression or Torsion." *Proceedings of Third International Conference on Steel-Concrete Composite Structures, Fukuoka, Japan*.
- Knowles, R. B., and Park, R. (1970). "Axial Load Design for Concrete Filled Steel Tubes." *Journal of the Structural Division, ASCE*, 96(ST10), 2125-2153.
- Lee, G., Xu, J. S., Gong, A., and Zhang, K. C. (1991). "Experimental studies on concrete filled steel tubular short columns under compression and torsion." *Proceedings of the third international conference on steel-concrete composite structures*, Association for International Cooperation and Research in Steel-Concrete Composite Structures, Fukuoka, Japan, 143-148.
- Leon, R. T., Aho, M. F., and Kim, D. K. (2005). *A database for encased and concrete-filled columns*. Georgia Institute of Technology, Atlanta, Georgia.
- Leon, R. T., and Hajjar, J. F. (2008). "Limit state response of composite columns and beam-columns part II: Application of design provisions for the 2005 AISC specification." *Engineering Journal*, 45(1), 21 - 46.
- Leon, R. T., Kim, D. K., and Hajjar, J. F. (2007). "Limit state response of composite columns and beam-columns part 1: Formulation of design provisions for the 2005 AISC specification." *Engineering Journal*, 44(4), 341 - 358.
- Liew, J. Y. R., and Chen, H. (2004). "Explosion and fire analysis of steel frames using fiber element approach." *Journal of Structural Engineering-Asce*, 130(7), 991-1000.
- Lin, C. Y. (1988). "Axial Capacity of Concrete Infilled Cold-Formed Steel Columns." St. Louis, Missouri, U.S.A., 443-457.
- Luksha, L. K., and Nesterovich, A. P. (1991). "Strength testing of large-diameter concrete filled steel tubular members." *Proceedings 3rd ASCCS International Conference on Composite Construction*, Fukuoka, Japan, 67-70.
- Lundberg, J. E., and Galambos, T. V. (1996). "Load and resistance factor design of composite columns." *Structural Safety*, 18(2-3), 169-177.
- Mander, J. B., Priestley, M. J. N., and Park, R. (1988). "Theoretical Stress-Strain Model for Confined Concrete." *Journal of Structural Engineering*, 114(8), 1804-1826.
- Martinez-Romero, E. (2003). "Tres casos de edificios de acero en construccion compuesta."
- Mizuno, E., Shen, C., Tanaka, Y., and Usami, T. (1992). "A Uniaxial Stress-Strain Model for Structural Steels under Cyclic Loading." Y. Fukumoto and G. C. Lee, eds., CRC Press, Boca Raton, Florida.
- Nakahara, H., Sakino, K., and Inai, E. (1998). "Analytical model for compressive behavior of concrete filled square steel tubular columns." *Transactions of the Japan Concrete Institute*, 20, 171-178.
- Nakahara, H., and Sakino, K. (2000). "Flexural Behavior of Concrete Filled Square Steel Tubular Beam-Columns." Auckland, New Zeland.

- Nishiyama, I., Morino, S., Sakino, K., Nakahara, H., Fujimoto, T., Mukai, A., Inai, E., Kai, M., Tokinoya, H., Fukumoto, T., Mori, K., Yoshioka, K., Mori, O., Yonezawa, K., Uchikoshi, M., and Hayashi, Y. (2002). *Summary of research on concrete-filled structural tube column system carried out under the US-Japan cooperative research program on composite and hybrid structures*. BRI Research, Building Research Institute, Japan.
- Nukala, P. K. V. V., and White, D. W. (2004). "A mixed finite element for three-dimensional nonlinear analysis of steel frames." *Computer Methods in Applied Mechanics and Engineering*, 193(23-26), 2507-2545.
- OpenSees. (2010). *Open system for earthquake engineering simulation*. Pacific Earthquake Engineering Research Center. University of California, Berkeley, CA, USA.
- O'Shea, M. D., and Bridge, R. (1997). *Tests on Circular Thin-Walled Steel Tubes Filled with Very High Strength Concrete*. The University of Sydney.
- Park, R., and Paulay, T. (1975). *Reinforced concrete structures*. Wiley-Interscience.
- Paulay, T., and Priestley, M. J. (1992). *Seismic design of reinforced concrete and masonry buildings*. John Wiley & Sons New York, NY.
- Popovics, S. (1973). "A numerical approach to the complete stress-strain curve of concrete." *Cement and Concrete Research*, 3(5), 583-599.
- Richart, F. E. (1928). "Tests of the effect of brackets in reinforced concrete rigid frames." *Bureau of Standards Journal of Research*, 1(1), 189-253.
- Roik, K., and Bergmann, R. (1989). *Report on Eurocode 4, Clause 4.8 and 4.9. Composite Columns Harmonization of European Construction Codes*. Minister für Raumordnung, Bauwesen und Städtebau der Bundesrepublik Deutschland, Bochum, Germany.
- Roik, K., and Bergmann, R. (1992). "Composite columns." *Constructional steel design*, Elsevier Sc. Publ., New York, 443-470.
- Sakino, K., Nakahara, H., Morino, S., and Nishiyama, I. (2004). "Behavior of Centrally Loaded Concrete-Filled Steel-Tube Short Columns." *Journal of Structural Engineering*, 130(2), 180-188.
- Sakino, K., and Sun, Y. (1994). "Stress-strain curve of concrete confined by rectangular hoop." *Structural and Construction Engineering, AIJ*, (461), 95-104.
- Shakir-Khalil, H., and Al-Rawdan, A. (1996). "Experimental behaviour and numerical modelling of concrete-filled rectangular hollow section tubular columns." *Composite Construction in Steel and Concrete III*, 222-235.
- Shanmugam, N. E., and Lakshmi, B. (2001). "State of the art report on steel-concrete composite columns." *Journal of Constructional Steel Research*, 57(10), 1041-1080.
- Shen, C., Mamaghani, I. H. P., Mizuno, E., and Usami, T. (1995). "Cyclic Behavior of Structural Steels. II: Theory." *Journal of Engineering Mechanics*, 121(11), 1165-1172.
- Spacone, E., and Filippou, F. (1995). "A fiber beam element for nonlinear dynamic analysis of reinforced concrete structures." *10th Conference on Engineering Mechanics*, University of Colorado at Boulder, Colorado, USA., 818-821.

- SSRC. (1998). *Guide to Stability Design Criteria for Metal Structures, 5th Edition*. (T. V. Galambos, ed.), Wiley.
- SSRC. (2010). *Guide to Stability Design Criteria for Metal Structures*. (R. D. Ziemian, ed.), Wiley.
- SSRC Task Group 20. (1979). "A specification for the design of steel-concrete composite columns." *Engineering Journal, AISC*, 16(4), 101-115.
- Sulyok, M., and Galambos, T. V. (1995). "Reliability of composite columns and beam-columns in EC4." *Proc. Int. Coll. on Stability of Steel Structures*, Budapest, Hungary., 11257-11265.
- Susantha, K. A. S., Ge, H., and Usami, T. (2001). "Uniaxial stress-strain relationship of concrete confined by various shaped steel tubes." *Engineering Structures*, 23(10), 1331-1347.
- Taucer, F., Spacone, E., and Filippou, F. C. (1991). *A fiber beam-column element for seismic response analysis of reinforced concrete structures*. Earthquake Engineering Research Center., Berkeley, CA., 138.
- Timoshenko, S. (1930). *Strength of materials*. Van Nostrand, New York,
- Timoshenko, S. (1961). *Theory of elastic stability*. McGraw-Hill, New York,
- Timoshenko, S., and Gere, J. M. (1972). *Mechanics of materials*. Van Nostrand Reinhold Co., New York,
- Tomii, M., and Sakino, K. (1979a). "Experimental Studies on the Ultimate Moment of Concrete Filled Square Steel Tubular Beam-Columns." *Transactions of the Architectural Institute of Japan*, 275, 55-63.
- Tomii, M., and Sakino, K. (1979b). *Elastoplastic behavior of concrete filled square steel tubular beam-columns*. Architectural Institute of Japan.
- Tort, C., and Hajjar, J. (2007). *Reliability-based performance-based design of rectangular concrete-filled steel tube (RCFT) members and frames*. University of Minnesota., Minneapolis, MN.
- Uy, B., and Bradford, M. A. (1996). "Elastic local buckling of steel plates in composite steel-concrete members." *Engineering Structures*, 18(3), 193-200.
- Uy, B., and Das, S. (1997). "Wet Concrete Loading of Thin-walled Steel Box Columns During the Construction of a Tall Building." *Journal of Constructional Steel Research*, 42(2), 95-119.
- Uy, B., and Das, S. (1999). "Bracing of thin walled steel box columns during pumping of wet concrete in tall buildings." *Thin-Walled Structures*, 33(2), 127-154.
- Varma, A. H. (2000). "Seismic Behavior, Analysis, And Design of High Strength Square Concrete Filled Steel Tube (CFT) Columns." Lehigh University.
- Viest, I. M., Colaco, J. P., Furlong, R. W., Griffs, L. G., Leon, R. T., and Wyllie, L. A. (1997). *Composite Construction Design for Buildings*. McGraw-Hill.
- White, D. W. (1986). *Material and geometric nonlinear analysis of local planar behavior in steel frames using interactive computer graphics*. Cornell University.

- White, D. W., and Hajjar, J. F. (1997). "Buckling Models and Stability Design of Steel Frames: a Unified Approach." *Journal of Constructional Steel Research*, 42(3), 171-207.
- Xu, J. S., Zhou, J., and Lee, G. (1991). "Experimental studies on concrete filled steel tubular medium and long columns under compression and torsion." *Proceedings of the third international conference on steel-concrete composite structures (I)*. Fukuoka, Japan: ASCCS, Association for International Cooperation and Research in Steel-Concrete Composite Structures, Fukuoka, Japan, 159–164.
- Young, W., and Budynas, R. (2001). *Roark's Formulas for Stress and Strain*. McGraw-Hill Professional.

VITA

Tiziano Perea

Tiziano Perea was born on January 10, 1973 in Tulancingo, Hidalgo, Mexico. He earned a Bachelor of Science degree in Civil Engineering from the Universidad Popular Autónoma del Estado de Puebla (UPAEP) in 1996, and a Master of Engineering degree from the Universidad Nacional Autónoma de México (UNAM) in 1999. He worked as structural engineer from 1996 to 1997, and as an Assistant Professor at the Universidad Autónoma Metropolitana (UAM) in Mexico City from 2000 to 2005. Afterward, he continued his graduate studies at the Georgia Institute of Technology, where he earned a Master of Science degree in Civil Engineering in 2007, and then pursuing a Doctor of Philosophy degree in Civil Engineering with a minor in Mechanics under the supervision of Prof. Roberto T. Leon. Mr. Perea will return to the Universidad Autónoma Metropolitana (UAM) in Mexico City as an Associate Professor in 2011.